SET 2015 NOTTINGHAM

14ᵗʰ International Conference on Sustainable Energy Technologies

25ᵗʰ to 27ᵗʰ August 2015, Nottingham, UK

SUSTAINABLE ENERGY FOR A RESILIENT FUTURE

CONFERENCE PROCEEDINGS
VOLUME I

The University of Nottingham

UNITED KINGDOM · CHINA · MALAYSIA

W SSET
World Society of
Sustainable Energy Technologies

Proceedings of the
14th International Conference on
Sustainable Energy Technologies – SET 2015
25th to 27th August 2015, Nottingham UK

Sustainable Energy for a Resilient Future

Volume I

Edited by

Lucelia Rodrigues

SET 2015 Co-Chair and Chair of the Scientific Committee
Architecture, Energy & Environment Research Group
Department of Architecture and Built Environment
Faculty of Engineering, University of Nottingham

Supported by the Conference Organising Committee:

Chair: Professor Saffa Riffat
Co-chair: Professor Mark Gillott
Event Manager: Zeny Amante-Roberts
Administrative Manager: Claire Hardwidge
Proceedings Support: Phil Roberts
Marketing: Guillermo Guzman
Webmaster: Johnny Mistry

Reference to a conference paper:

To cite a paper published in these conference proceedings, please substitute the highlighted sections of the reference below with the details of the article you are referring to:

Author(s) Surname, Author(s) Initial(s), 2016. 'Title of paper'. In: Rodrigues, L. ed., Sustainable Energy for a Resilient Future: Proceedings of the 14th International Conference on Sustainable Energy Technologies, 25-27 August 2015, Nottingham, UK. University of Nottingham: Architecture, Energy & Environment Research Group. Volume X, pp XX-XX. Available from: eprints.nottingham.ac.uk [Last access date].

Version: 07.07.2016

FORWARD

Dear Reader,

I am delighted to present to you the 14th International Conference on Sustainable Energy Technologies SET 2015 conference proceedings volume I.

We are all aware of the impact of climate change on our environment and the importance of sustainable energy technologies to reduce energy consumption. The SET conferences are multi–disciplinary, peer-reviewed international events on sustainable energy sources and technologies that provide a forum for the exchange of latest technical information, the dissemination of the high-quality research results, the presentation of the new developments in the area, and the debate and shaping of future directions and priorities for sustainable development and energy security.

The SET conferences have been running for the past 14 years. Previous conferences were held in Portugal (Porto 2002), China (Chongqing, 2003), United Kingdom (Nottingham, 2004), China (Jinan, 2005), Italy (Vicenza, 2006), Chile (Santiago, 2007), South Korea (Seoul, 2008), Germany (Aachen, 2009), China (Shanghai, 2010), Turkey (Istanbul, 2011), Canada (Vancouver, 2012) and, China (Hong Kong, 2013) and Switzerland (Geneva, 2014).

We have had a very successful SET conference at Nottingham in 2015 organized by the University of Nottingham, United Kingdom, and the World Society of Sustainable Energy technologies (WSSET). The SET 2015 conference covered a wide range of topics on sustainable technologies including energy, buildings, transport and industry. Lectures were given by eminent keynote speakers and technical sessions focused on important research topics related to sustainable technologies and eco-buildings.

Over 300 delegates from 42 countries attended the event. The SET 2015 conference received over 500 abstracts and 214 papers have been published in the conference proceedings.The proceedings have therefore been divided into three volumes; I introduce here Volume I which is a collection of excellent works on energy technologies and renewable energy.I hope you enjoy as much as I did the breadth of work you will find in this book.

On behalf of the Organizing Committee, I would like thank the conference co-chairpersons Professor Mark Gillott and Dr Lucelia Rodrigues for their dedicated work to organize the conference and also our sponsors including Solar Ready Ltd, Vale Windows Company Ltd, Ecosmart Solution, PCM Products Ltd and Oxford press. I would also like to thank the Advisory Committee, the Scientific Committee and all staff and students who gave their time and energy to make this a very successful event.

Professor Saffa Riffat
Chair in Sustainable Energy Technologies
President of the World Society of Sustainable Energy Technologies
SET 2015 Chairman

CONFERENCE PROCEEDINGS STRUCTURE

Volume I

Energy Technologies & Renewables

Keynote Speaker Professor Chi-Hwa Wang: "Challenges on the Co-gasification of Woody Biomass and Solid Waste: A Singapore Story on Waste Minimization and Energy"

Session 1: Biofuels & Biomass

Session 5: Building Energy Systems

Session 9: Low-carbon/ Low-energy Technologies

Session 13: Biomass Systems

Session 16: Solar Energy

Session 17: Biomass & Biofuels

Session 20: Solar Energy

Session 21: Solar Energy

Session 22: Solar Energy

Session 25: Building Energy Technologies

Session 26: Solar Energy

Session 29: Low-carbon/ Low-energy Technologies

Session 32: Heat Pumps

Session 33: Low-carbon/ Low-energy Technologies

Session 36: Low-carbon/ Low-energy Technologies

Poster Session A

Poster Session B

Poster Session C

Poster Session E

Volume II

Energy Storage & Conversion

Keynote Speaker Professor Tianshou Zhao: "Innovating Energy Storage Technologies for a Sustainable Energy Future"
Session 2: Heating and Cooling Systems
Session 6: Heating and Cooling Systems
Session 10: Ventilation and Air Conditioning
Session 14: Smart and Responsive Buildings
Session 18: Phase Change Materials
Session 23: Smart and Responsive Buildings
Session 30: Heating and Cooling System
Session 34: Carbon Sequestration
Poster Session A
Poster Session C
Poster Session D

Policies & Management

Keynote Speaker Chris Twinn: "The goalposts are changing – are we ready for the new direction?"
Session 4: Environmental Issues and the Public
Session 8: Energy and Environment Security
Session 12: Energy and Environment Policies
Poster Session A
Poster Session D

Volume III

Sustainable Cities & Environment

Keynote Speaker Professor Matheos Santamouris: "Urban Warming: Evidence, Impacts and Mitigation"
Keynote Speaker Professor Edward NG : "Sustainable Living in Compact Urban and Built Environment in the Tropics"
Session 3: Sustainable and Resilient Cities
Session 7: Energy Demand and Use Optimization
Session 11: Energy Efficiency in Buildings
Session 15: Green and Sustainable Buildings
Session 19: Green Buildings and Materials
Session 24: Energy Efficiency in Buildings
Session 27: Energy Efficiency in Buildings
Session 28: Energy Efficiency in Buildings
Session 31: Energy Efficiency in Buildings
Session 35: Energy Efficiency in Buildings
Poster Session A
Poster Session D
Poster Session E

CONTENTS

ENERGY TECHNOLOGIES & RENEWABLES

Keynote Speaker Professor Chi-Hwa Wang: "Challenges on the Co-gasification of Woody Biomass and Solid Waste: A Singapore Story on Waste Minimization and Energy"

Dr Chi-Hwa Wang is currently a Professor of Chemical and Biomolecular Engineering at the National University of Singapore (NUS). He is also the Assistant Dean for Research at the Faculty of Engineering, NUS (2006-2008), and (ii) Faculty Fellow, Singapore-MIT Alliance (2001-2006).

He received his B.S. degree (Chemical Engineering) from the National Taiwan University, M.S. degree (Biomedical Engineering) from Johns Hopkins University, M.A. and PhD degrees (both in Chemical Engineering) from Princeton University, respectively. He was holding several visiting appointments throughout different stages of his career: National Taiwan University (1999-2000, 2002, Visiting Assistant Professor), Kyoto University (2003, JSPS Visiting Fellow), Cambridge University (2004, Sabbatical Academic Visitor), Massachusetts Institute of Technology (2004, Visiting Associate Professor). He is the recipient of the following teaching awards and recognitions: Princeton University [Hoechst Celanese Excellence in Teaching Award (1993, 1994), E-Council Excellence in Teaching Award (1995)], National University of Singapore [Teaching Honours List Award (1997 & 1998), Teaching Commendation List (2006, 2007, 2008, 2009)].

His current research interests include transport & reaction in particulate systems and drug delivery systems. He was an Executive Editor for Advanced Powder Technology (Elsevier, 2009-2012). He is on the editorial boards of Journal of Controlled Release (2009 - present), Powder Technology (2008- present), and Advanced Powder Technology (2009 - present). He is active in the organizing committees of international conferences on the subject areas of chemical engineering and particle technology. To name a few examples in year 2012: 14th Asia Pacific Confederation of Chemical Engineering Congress (Chair, Scientific and Technical Committee, 5th Asia Particle Technology Symposium (Conference Chair). He is currently an Executive Editor for Chemical Engineering Science (Elsevier, 2013 - present).

Dr Chi-Hwa Wang's recent research program aims at developing expertise in the interface of "particle technology", "drug delivery systems" and "coal and biomass gasification". His cumulative research publications include 160 international refereed journal papers on the subjects of chemical engineering fundamentals and powder technology (with more than 3507 citations, h-index = 34) and 175 conference papers. The focus of his recent research development is on the subject of clean coal and biomass co-gasification technology, particularly in the application targeting at solving problems on energy and environmental sustainability and waste-to-energy technology.

SESSION 1: BIOFUELS & BIOMASS

335: Technological and commercial maturity of aviation biofuels

REBECCA MAWHOOD[1], EVANGELOS GAZIS[1*], RAPHAEL SLADE[1]

[1] *Imperial Centre for Energy Policy and Technology, Imperial College London*
* Correspondence: e.gazis@imperial.ac.uk

Airline operations generated 705 Mt of CO_2 in 2013, representing around 2% of global anthropogenic CO_2 emissions [1]. 99% of airline emissions are caused by the combustion of kerosene [2,3]. Aviation biofuels (biojet) have the potential to provide a near-term solution to the twin challenges of decarbonisation and security of fuel supply. However, production costs of biomass-derived kerosene are considerably higher than the selling price of petroleum-derived kerosene due to the relative immaturity of conversion technologies, small number of producers and competition with other biofuel markets.

This paper reviews the commercial and technological maturity of various technologies for converting biomass to synthetic jet fuel and evaluates them according to their Fuel Readiness Level (FRL). This work is part of the EIT Climate KIC project 'Fuel Supply Chain Development and Flight Operations' (RENJET) which aims to accelerate the development of renewable jet fuel, simultaneously increasing availability and stimulating demand

Keywords: biofuels, biojet, aviation

1. INTRODUCTION AND AIM

Airline operations generated 705 Mt of CO_2 in 2013, representing around 2% of global anthropogenic CO2 emissions [1]. 99% of airline emissions are caused by the combustion of kerosene [2,3]. Aviation biofuels (biojet) have the potential to provide a near-term solution to the twin challenges of decarbonisation and security of fuel supply. However, production costs of biomass-derived kerosene are considerably higher than the selling price of petroleum-derived kerosene due to the relative immaturity of conversion technologies, small number of producers and competition with other biofuel markets.

This paper reviews the commercial and technological maturity of various technologies for converting biomass to synthetic jet fuel and evaluates them according to their Fuel Readiness Level (FRL). This work is part of the EIT Climate KIC project 'Fuel Supply Chain Development and Flight Operations' (RENJET) which aims to accelerate the development of renewable jet fuel, simultaneously increasing availability and stimulating demand.

2. METHODOLOGY

This work draws on an extensive literature review and uses the Commercial Aviation Alternative Fuels Initiative's Fuel Readiness Level scale [4] to evaluate seven conversion pathways.

Published, peer-reviewed studies and grey literature were reviewed through a `rapid evidence assessment' to identify potential conversion pathways that would be relevant to the study. Six of the conversion pathways were identified by this screening activity: biomass to liquids (BTL) (Fischer-Tropsch process), hydrotreated depolymerised cellulosic jet (HDCJ), alcohol to jet (ATJ), fermentation to jet (FTJ), aqueous phase reforming (APR) and lignin to jet (LTJ). The most technologically advanced pathway – hydroprocessed esters and fatty acids (HEFA) – was excluded because since it is considered economically unattractive for deployment at scale. However, it remained in the analysis as a reference technology.

The pathways were characterised according to their technological and commercial maturity, progress towards international certification, compatibility with existing infrastructure, economic viability and the opportunity costs of producing biojet.

3. FINDINGS

Biojet production pathways vary considerably in terms of their technological and commercial maturity, with the most highly developed being in the very early stages of commercialisation. The breadth and depth of available data is considerably greater for pathways which are at the higher end of the FRL scale and/or which are being pursued by multiple developers.

BTL is the most advanced of the pathways reviewed (FRL 7-8). Several fuel developers are involved with this pathway and BTL jet fuel is certified for use by the ASTM. The first commercial-scale plant is expected to become operational by 2015, with other similar projects due for completion around 2020. The findings regarding other technologies are summarised in Fig. 1.

Overall, biojet currently presents a risky investment proposition. Whilst some pilot and/or demonstration projects may be financed 'on balance sheet', investment in large-scale facilities is likely to be limited by the cost of and access to finance. Policy support will be necessary to promote deployment at scale in the short-to-medium term, to enable the realisation of potential cost reductions.
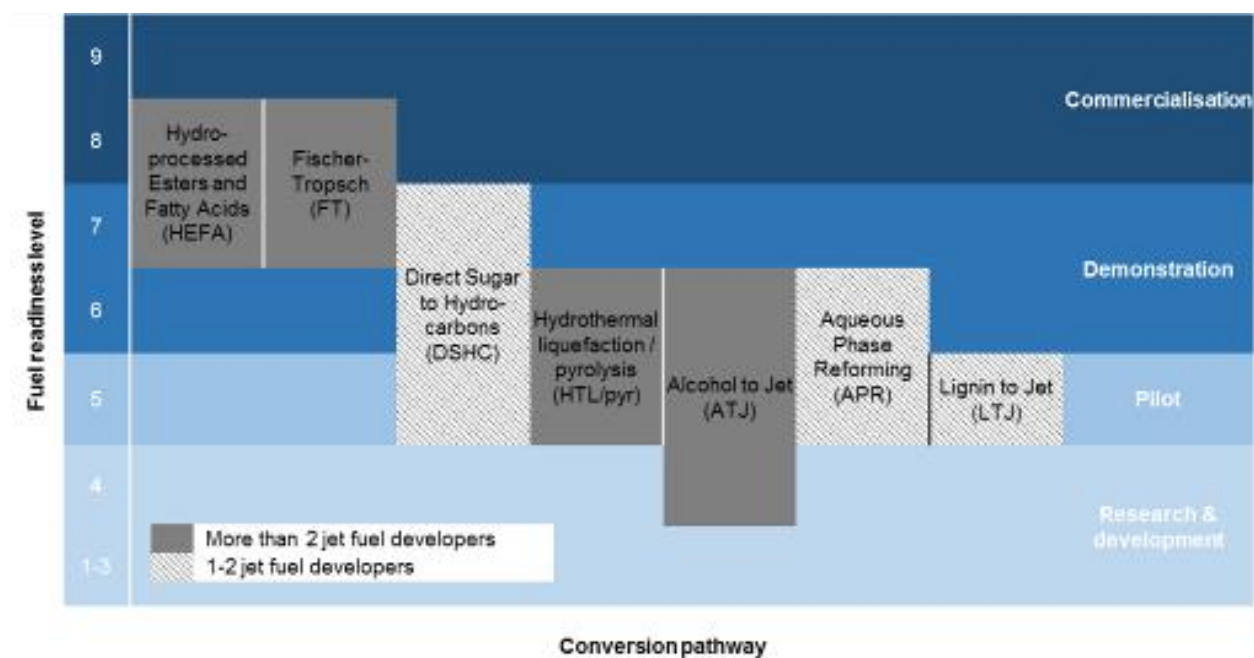
Figure 1 Current Fuel Readiness Levels of biojet conversion technologies.

4. REFERENCES

[1] Air Transport Action Group (ATAG). Aviation: Benefits Beyond Borders. Geneva, Switzerland. 2014

[2] Commercial Aviation Alternative Fuels Initiative (CAAFI). Path to Alternative Jet Fuel Readiness. 2013

[3] FAAIJ, A. & van Dijk, M.. White Paper on Sustainable Jet Fuel. SkyNRG. 2012

[4] CAAFI. Fuel Readiness Level. Available: http://www.caafi.org/information/pdf/FRL_CAAFI_Jan_2010_V16.pdf [Accessed April 2014].

430: Production and testing of biodiesel methyl ester fuels from Nigerian tropical seed oil feedstocks

GILLIAN OGBENE IGBUM[1] ANDREW C. ELOKA-EBOKA[2], SAMUEL JACOB. ALIYU [3]

[1] *Department of Chemistry, Benue State University, Makurdi, Nigeria.*
[2] *Discipline of Mechanical Engineering, University of KwaZulu-Natal, Howard College, Durban, South Africa.*
[3] *Department of Mechanical Engineering, Landmark University, Omu Aran, Nigeria.*
ogbenebenny@yahoo.com, fatherfounder@yahoo.com, sjaliyu@gmail.com

The urgent need for alternative energy, climate change mitigation and environmental protection in the world today cannot be over-emphasized. Researchers are at top gear in search of non-edible energy crops. The huge environmental benefits of renewable energy notwithstanding, new discoveries in this area arise every day. The potentials of selected tropical seed-oils for biodiesel production and utilization as fuels were therefore explored and subsequently produced. The seed-oils studied include: Sand box tree, fluted pumpkin seed and wild melon seeds. Oils of these seeds were extracted, optimized, synthesized and characterized as biodiesel fuels by transesterification process using different alcohol/oil ratios of (4:1 and 6:1) and catalysts types (NaOH and KOH) at optimization temperatures of 38oC and 55oC and reaction time of 5 mins and 30 mins respectively. Optimized biodiesel produced were investigated for their chemo-physical properties in conformity with ASTM standards of biodiesel. Results showed that sandbox tree seeds, wild melon seeds and pumpkin seeds have high percentage oil content (69.32%; 70.24% and 46.88%) respectively. They also hold great potentials as feedstock for biodiesel production. The chemo-physical properties and their biodiesel fuels and blends with automotive gas oil (AGO) fell within specification. Pumpkin seed oil however showed highest average percentage optimized yield of biodiesel (97%) in (1 wt of oil), NaOH catalyst, and alcohol to oil ratio of 6:1 at a reaction temperature of 55oC. Under the giving conditions, biodiesel fuels and blends were successfully produced from the selected feedstock with properties very close to those AGO. They can therefore be commercialized for large scale utilization as biodiesel fuels or as blends for the replacement of environmentally unfriendly fossil fuels.

Keywords: production, testing, tropical Nigerian seed oils, biodiesel, feedstocks, methyl ester, renewable energy

1. INTRODUCTION

Vegetables oils and esters are receiving increasing attention as non-toxic, biodegradable and renewable alternative diesel fuels. Limited energy resources and increasingly strict emission regulations have motivated an intense search for alternative transportation fuels over the last three decades. Biodiesel is an oxygenated, sulphur-free, biodegradable, non-toxic and environmentally friendly alternative diesel fuel. Biodiesel is defined as the alkyl monoesters of fatty acids from renewable resources such as vegetable oils, animal fats and waste restaurant greases. One of the alternative characteristics of biodiesel is that its use does not require any significant modifications of the diesel engines, so the engines do not have to be dedicated for biodiesel alone. However, similar to alcohol fuels, biodiesels have lower engine content and different physical properties than diesel fuels [1, 2, 3]

Biodiesel refers to a diesel-equivalent, processed fuel derived from biological sources. Though derived from biological sources, it's a processed fuel that can be readily used in diesel-engine vehicles, which distinguishes biodiesel from the Straight Vegetable Oils (SVO) or Waste Vegetable Oils (WVO) used as fuels in some modified diesel vehicles [4]. The problem associated with the use of heat vegetable oils are injector fouling; ring sticking and varnish build up on the high viscosity of vegetable oils and to the reactivity of the polyunsaturated fatty acids components of the triglycerides. Researchers have shown that viscosity as a major constraint and other attendant problems can be overcome by different reactions to form alkyl esters (biodiesel). Most of the biodiesel produced today is by transesterification, because the process does not require exotic materials of construction, there is direct conversion to methyl esters with no intermediate steps under a low temperature and pressure environment and a high percentage (98%) of the input is converted to the final product with minimal side reaction time [5]. The production of biodiesel yields 3.24 times more energy than required to produce, which is better than the 1.24 to 1 ratio of ethanol. In order for biodiesel to replace petroleum-based diesel, it must be produced in sufficient quantities.

This may not be a problem as many companies have invested significantly for the construction of production plants for biodiesel in the world. The current capacity for producing biodiesel is estimated to around sixty and eighty million gallons per year, however, this can be quickly increased as needed [6]. Nigeria's contribution to biodiesel production has just begun with researches towards its eventual kick off. At present, the emphasis is on biofuel/bioethanol production with the federal government's establishment of its plants and ethanol crop plantation across the country. In fact, within the last few years, Nigerian's government has seen the need to de-emphasis the total dependence on petroleum based fuels. Recent informed survey has indicated that at the present rate of energy consumption, since the fossil oil is the major source of energy, there is continued decline in the quantity of crude petroleum which serves as the main source for diesel oil production. Moreover, the rate of replacement is not commensurate to the rate of consumption. For instance, at the end of 1986, there was sufficient oil remaining to last 34 years, natural gas for some 58 years, and coal, 219 years in Nigeria [7].

Long before these resources are finally exhausted, oil in particular will become scarce and heading for extinction and of course more expensive. Here in our country Nigeria, bulk and sustainable production of biodiesel is yet to be explored to greater extents. With the turn of events in Nigeria where our refineries are almost down and we have been heavily dependent on importation of fuel, the development of this promising biofuel sector to improve the economic fundamentals for biodiesel production is imperative. Biodiesel can meet growing energy demands in a sustainable manner, since it can be produced in large quantities, it is environmentally friendly and the cost of production can be encouraged by promoting the agricultural sector. This sector can also provide job opportunities and reduce our dependence on foreign oil and improve our domestic economy.

The ability to achieve higher yields and higher oil contents is crucial to the success of any sustainable biodiesel industry. The objectives of this study was to extract oil from some Nigerian tropical seed oils (sandbox sees oil, fluted pumpkin seed and wild melon seeds); produce and characterize biodiesel fuels from them; and then evaluate their properties with ASTM standards of biodiesel. This research will enhance alternative sourcing of fuel which is sustainable, renewable, and environmentally friendly. Motivation for the study is the fact that biodiesel is an ecologically friendly fuel, it can be produced from renewable materials; the cost of production can be viewed from an angle where it is possible to produce biodiesel in domestic homes since the feedstocks are readily available. Therefore people leaving in areas outside townships can produce and access biodiesel at any point in time with proper awareness and empowerment. Considering that the manufacturing processes are quite straight Biodiesel decomposes biologically with no harm to soil or ground water and hence can minimize issues of spillage with the following benefits:

- Contains no carcinogenic polyaromatic components.
- Reduces soot emission up to 50%.
- Contains only a minute amount of sulphur (0.001%).
- It is very safe to handle and store (flash point above 150%).
- Reduces air pollution and related public health risks.
- Properties of diesel fuel can be measured by ASTM standards. These procedures can be carried out using various forward and can be produced even in smaller batch quantities is an advantage.

1.1. Cost of Biodiesel Production (Efficiency and Economic Argument)

Biodiesel cost two to three times as much to make as it costs to produce fossil diesel. This is the reason why the British Government has agreed to reduce the fuel duty rate, so that the use of an environmentally friendly fuel may be promoted. The environmental benefits of biodiesel should not be confused with claims made for versions of fossil fuels such as green diesel or city diesel! All fossil fuels including Compressed Natural Gas (CPG) liberate vast amounts of carbon dioxide, which is now universally acknowledged as contributing to global climate change. The carbon has been stored for many millions of years – hence the expression "fossil fuels".

The plants from which bio fuels are made extract carbon dioxide from the atmosphere sequestrate a considerable proportion of it in plant roots left in the soil and then liberate the rest when the fuel is used, no additional carbon dioxide is produced, as a useful by – product, oxygen is produce by the plants from which biodiesel are made, which is a bit of luck for us. Biodiesel is made from plants which grow again on the same plot of land, year after year. The fuel is therefore sustainable.

The cost of biodiesel varies. If vegetable oil and the production chemicals (alcohol and catalyst) are readily available then biodiesel can cost as little as 50cents per gallon to produce. For this reason, biodiesel is available for approximately one dollar more than petroleum diesel. As the demand for biodiesel increases so will production capacity. This will bring the price down. One must be cautious when comparing the cost of alternative fuels with any petroleum fuels, which includes not only our payment upon filling up, but also our taxes for subsidizing the industry and the detriment of our health, environment and international relations.

Using biodiesel decreases our dependence on foreign oil and improves our domestic economy. For those in developing nations, biodiesel may offer independence from expensive oil markets and empowerment to meet their energy needs from a locally and renewable sources. This is especially true for isolated communities where in many cases two gallons of diesel are burnt just to transport one gallon of diesel and the price of diesel can be over seven dollars a dollar. For instance, from cultivation of palm trees, not as a monoculture but ecologically diverse, with many different forest products, with the oil, one can produce biodiesel and edible oils, as well as lubricants, soaps and other products. With the leftover biomass, one can generate electricity, steam and ethanol. And in future, develop hydrogen gas from the electrolysis of water molecules.

There is potential for every poor agricultural region to augment the value of their agricultural products and reduce their dependence on other sources of fuel. Micro-credit can be used to start the biodiesel process with very minimal cost and commonly available materials most agricultural region could reduce the parity of their agricultural product or even increase the value of that product. [8]. Global biodiesel production reached 3.8 million tons in 2005. Approximately 85% of biodiesel production came from the European Union. In 2007, in the United States, average retail (at the pump prices, including federal and state taxes of B2/B5) was lower than petroleum diesel by about 12 cents and B20 blends were the same as petro-diesel. However, as part of a dramatic shift in diesel pricing over the last year, by July 2009, the US DOE was reporting average cost of B12 15 cents per gallon higher than petroleum diesel ($2.69/gal Vs $2.54/gal). B99 and B100 generally cost more than petro-diesel except where local governments provide subsidy [9].

1.2. Review of Selected Feedstocks for biodiesel production

Fluted Pumpkin: (*Telfairia occidentalis)* is a tropical vine grown in West Africa as a leaf vegetable and for its edible seeds. Common names for the plant include fluted gourd, fluted pumpkin. The leaves used as

vegetable are common in every household in Nigeria. The fruit of the plant which contains the oil seed is a large pod; reaching 13 kg has not been explored for edibility.

Fig. 1: Fluted pumpkin seed pods and vegetables

The chemical composition and functional properties of the fluted pumpkin (*Telfairia occidentalis*) seeds and fatty acid composition of its oils have been evaluated. Results of proximate analysis showed moderate percentage of crude protein (17.50±0.12%), carbohydrate (17.96±0.35%), ash (5.67±0.10%) and high percentage crude fat (42.17±0.27%) but low moisture content (6.67±0.01%). Mineral composition revealed that the seed flour contains mostly potassium (1824mg/100g wet sample) followed by magnesium (535mg/100g wet sample) and sodium (280mg/100g wet sample). The physiochemical analysis of the oil revealed an acid value of 3.56±0.45, saponification value of 188.24±2.12, iodine of 78.26±1.24, free fatty acid 4.5±0.15 and refractive index of 1.471. Five fatty acids were detected in the oil. The unsaturated fatty acids were composed mainly of oleic (61.83%) and linoleic (16.44%) while the unsaturated fatty acids mainly of palmitic acid (21.20%). It can be considered as a good protein ingredient as it was found to have a low gelation capacity of 14% (wlv), foaming capacity 12.8±1.10%, water and oil absorption capacities of 90.2±0.2% and 183.4±2.5% respectively. The seed proteins have minimum solubility at pH 5.0 [10]. The study did not investigate the oils suitability for biodiesel use or for other industrial application. The lipids content of the seeds were found to be 13.15% and an iodine value of 115.60 indicating a semi drying oil consisting predominantly polyunsaturated fatty acids mainly oleic and linoleic fatty acids. These classes of oils whose iodine value is between 100-150 possess the property of absorbing oxygen on exposure to the atmosphere; though not sufficiently to qualify them as drying oils. They become thicken and remain sticky but do not form a hard dry film. The results indicate that the oil contained higher proportions of low molecular weight fatty acids. Acid values indicate that the oils could be stored for a long time without deterioration. The free fatty acid value was 1.74% implying non rancid oil, the peroxide values obtained was 2.26 and the specific gravity and refractive index (25^oC) was 0.92 and 1.46 respectively [11]. The advantageous effect of the pumpkin seed oil has been proved on prostate hypertrophy, inflammations and treatment of arteriosclerosis [12].

Sandbox tree *(Hura crepitans)* also known as Possumwood and Jabillo, is an evergreen tree of the spurge family (*Euphorbiaceae*), native to tropical regions of North and South America in Amazon Rainforest. It is recognized by the many dark, pointed spines and smooth brown bark. These spines have caused it to be called Monkey no-climb. The fruit is a large capsule with explosive dehiscence. When ripe, pods catapult the seeds as far as 100 meters (300 ft). It has also been known as the Dynamite tree, so named for the explosive sound of the ripe fruit as it splits into segments. This tree prefers wet soil, and partial shade or partial sun to full sun. It is often cultivated for shade. Fishermen have been said to use the milky, caustic sap from this tree to poison fish. The Caribs made arrow poison from its sap. The wood is used for furniture under the name "hura". Before more modern forms of pens were invented, the trees' unripe seed pods were sawed in half to make decorative pen sandboxes (also called pounce pots), hence the name 'sandbox tree' [13]. The berries look-alike structure is actually their male flowers that have no petals. Male flowers grow on long spikes; female flowers are solitary. When ripe, pods catapult the seeds as far as 100 meters and are considered an invasive species in some country as their seeds can germinate and grow in deep shade, allowing the plant to invade undisturbed forest. These seeds are emetic and when green, very purgative. Oils extracted from the derived seeds are also as a purgative. It's pale, yellow or brown soft wood is used for furniture under the name Hura. In summary, the sandbox tree often can be found in nearly pure stand on most loam soil in the flat coasted region. The leaves are used against eczema. In Africa, it's invasive in Tanzania was reported [14].

Figure 2: Dry and pulverised seeds of Sandbox tree plant

Wild melon *(Cucumeropsis manni)* is specie of melon native to tropical Africa west of the Rift valley area, where it is grown for food and as a source of oil. The heart-shape or roughly palmate leaves are up to 12cm long and 14 wide. It bears small yellow male and female flowers with petals under a centimetre in length. The fruit is egg-shape or an elongated ovate shape up to about 19cm long and 8 wide and cream in colour with green streaks. The fruits and white seed are edible. The plant is grown more often for the seed oil than for the fruit [15].

Figure 3: dehusked seeds of Wild Melon

2. MATERIALS AND METHODS

2.1. Sample Collection and Preparation

The seeds were collected from different growing regions of Nigeria, prepared, dehusked and dried. They were thereafter pulverized and ready for oil extraction using the soxhlet apparatus. Soxhlet extraction method was used for the extraction in these cases; this is carried out on a comparative scale using organic solvent petroleum ether and hexane. Soxhlet extractor uses a refluxing or siphoning action to leach out oil from ground seeds. It is a continuous counter current process with the raw materials flowing in one direction against the solvent. Petroleum ether (60-80°C) and hexane (60-80°C) were used to extract oils from the three oil seed samples using bulk soxhlet extractor, 4 litres by volume. Laboratory Rotary evaporator was employed to concentrate the oil and to recover the solvent for re use. Soaking method was equally used for the extraction; petroleum ether was poured into closed containers containing powdered seeds and allowed to stand for about two days. The oil-solvent product was evaporated to yield oil.

Figure 4: seed oils of Fluted Pumpkin (TVO), Wild melon (CVO) and Sandbox tree seeds (HVO)

2.2. Physiochemical properties of seed oils

Both preliminary and actual experimental determinations of varying chemo-physical analysis were conducted for all seed oil samples using ASTM methods. Parametric analysis include: determination of kinematic viscosity (ASTM D445); the test method specifies a procedure for the determination of the kinematic viscosity, v, of liquid petroleum products, both transparent and opaque, by measuring the time for a volume of liquid to flow under gravity through a calibrated glass capillary viscometer. Determination of free fatty acid profile of the neat vegetable oils and the methyl esters obtained using GC spectrometer was carried out on a Shimadzu GC-17A chromatograph equipped with a FID detector equipped with a mass spectrometer detector Shimadzu GC-MS-QP 5050 using an identical column. One µm of each diluted sample with analytical grade dichloromethane was injected. [28; 134; 135]; determination of moisture content/volatile matter (ASTM 4377 method); determination of density/specific gravity (ASTM D4052/ISO-AOAC methods); determination of acid value and fatty acid value (FA); determination of saponification value

[138]: Saponification value is the number of milligrammes of KOH required to neutralize the fatty acids resulting from the complete hydrolysis of 1g of the sample, because it is a measure of both free and combined acids, it is usually large compared to the acid values of most edible oils; determination of peroxide value/stability (AOCS–AOAC method): Peroxide value studies the stability of vegetable oils, monitors the development of rancidity through the evaluation of the quantity of peroxide generated in the product. It is the measure of its content of oxygen which is a very important indicator for biodiesel's combustion in the engine. Fresh oils usually have peroxide values below 10m Eq/kg; and the determination of Iodine value which measures the degree of unsaturation in vegetable oils.

2.3. Preparation of Biodiesel (Methyl Esters)

For biodiesel production, a batch 100ml of each oil sample was measured, and poured into a large beaker. The oil was pre-treated by heating to a temperature of 110°C using Bunsen burner to remove the remains of solvent or moisture content in it and the temperature was monitored using a thermometer until it drops to the required temperature. The heated oil was then poured into a reactor, with the reactor still switched off, the prepared methoxide from the pet bottle was emptied into the oil in the reactor and the reactor switched on, the mixture was reacted for the required time of mixing and was switched off and allowed to stop rotating. The mixture was immediately transferred to a one litre pet bottle and closed tightly .The pet bottle occasionally opened to allow some air into the pet bottle in order to avoid contraction due to cooling of the oil. The mixture allowed to settle for 24hours after which a dark colour glycerine by-product was observed separated from the pale liquid above which is the biodiesel at the top layer. It should be noted that the biodiesel varies somewhat in colour according to the oil used and so does the bye-product layer at the bottom [16].

Figure 5: Glycerine obtained when NaOH and KOH were each used as catalysts

2.4. Biodiesel Washing

The biodiesel was turned into a separatory funnel and covered by a lid and equal amount of tap water added. The funnel swirled severally, after which it was allowed to settle for some few minutes and the water drained off from the bottom by opening the tape. This procedure was repeated twice using two different separatory funnel i.e. in each washing, a separatory funnel is used until washing was affected. After washing, the biodiesel was heated to 1100C and allowed to cool. The essence of the heating was to dry the oil [16].

2.5. Determination of the Effect of Catalyst Type on the Yields, Viscosity and Specific Gravity of the Methyl Esters

Base catalysts (NaOH and KOH) were used. Catalysed processes dominate current commercial production. These reactions are relatively fast but are sensitive to water content and free fatty acids. Typical base concentrations are 0.3 to 1.5% based on the weight of oil. When sodium methoxide is used, the concentration can be 0.5% or less. Most researchers use NaOH as the catalyst. There are some operations that use KOH, in spite of the higher cost, because the potassium can be precipitated as K_3PO_4, fertilizer, when the products are neutralized using phosphoric acid. This can make meeting water effluent standards a bit more difficult because of limits on phosphate emissions. The effects of the use of these catalysts were determined at different ratios and proportions

2.6. Preparation of Methoxide

To prepare methoxide, 1g of KOH or NaOH was measured into a handy-sized light plastic bag using the scale (weighing balance) and 20ml of methanol was also measured using a graduated measuring cylinder and this was turned into a pet bottle. The KOH or NaOH from the plastic bag was mixed with the methanol and the container closed tightly, the container was swirled several times until all the lye is

completely dissolved [16]. This solution was directly used in the transesterification process of biodiesel production.

2.7. Other ASTM Quality Evaluations [17]

Determination of the kinematic viscosity; density/specific gravity; determination of flash point; determination of pour point (ASTM D97 method); determination of cloud point; ASTM D 2709 standard test method for water and sediment in middle distillate fuels by centrifuge (biodiesel limit – 0.05 volume %); determination of carbon residue (ASTM D189 method); and free glycerine and total glycerine. For biodiesel, gas chromatography (GC) forms the basics of the standard ASTM D6584, which is the prescribed method for measuring free and total glycerol. It determines the amount of glycerol (in derivatized form), mono- and diacylglycerol (both also in derivatized form), triacylglycerols, and methyl esters in a biodiesel sample. The derivatised glycerol is the first material to elute, followed sequentially by the methyl esters and the derivatized monoacylglycerols, diacylglycerols and triacylglycerols. The sample is usually dissolved in an organic solvent because a sample needs to be derivatized in order to obtain a useful gas chromatogram. Glycerol and the mono- and diacylglycerols contain free hydroxyl groups causing this material not to perform well in GC. Derivatization (in the case of biodiesel with a silylating agent) improves their performance considerably.

Derivatization can provide better resolution between compounds with similar properties. After injection into the gas chromatograph, the sample is separated on a column. A column is a long, thin path (capillary) tube that contains a material with which the sample components interact more or less strongly depending on their structure (polarity) while it is heated. Usually, the solvent used and, if applicable, residual derivatizing agent used for preparing the sample are the first materials to elute (come out) from the GC and was registered by means of a detector. The identity of the structure was established using a spectroscopic method of detection in combination with a chromatographic method to yield more detailed information and in this case however, GC-MS, the combination of gas chromatography with mass spectroscopy [18]. The sample was analysed by gas chromatography, after silylating with N-methyl-N-trimethylsilyltrifluoracetamide (MSTFA). Calibration was achieved by the use of two internal standards and four reference materials. Mono-, di-, and triglycerides were determined by comparing to monoolein, diolein, and triolein standards respectively. Average conversion factors are applied to the mono-, di-, and triglycerides to calculate the bonded glycerin content of the sample.

2.8. Preparation of Methoxide

Some crude vegetable oils contain phospholipids that need to be removed in a degumming process. Phospholipids can produce lecithin, a commercial emulsifier [19]. Hydration method was used in this process. Because of the hydrophilicity of phospholipids, hot water (80°C) was added into the oil at a ratio of 3% of the total weight of the oil with stirring for 30minutes. The phospholipids solubility is therefore significantly reduced and so separated from the oil by natural sedimentation within 24 hours. The hydration method features a simple process, easy operation, and high yield refining, but non-hydratable phospholipids cannot be removed by this method.

3. RESULTS

Table 1: Physiochemical properties of Fluted pumpkin, Sandbox and Wild melon seed oils

Samples	Fluted Pumpkin (TVO)	Sandbox(HVO)	Wild Melon (CVO)
Moisture Content (%)	0.60	0.40	0.64
Specific gravity	0.92	0.92	0.92
Iodine Value (Wij's)	118.02	127.53	113.68
Free Fatty Acid Value (mg/KOH)	1.87	2.38	2.73
Acid Value (mg/KOH)	3.76	4.76	5.43
Peroxide Value (mg/kg)	13.20	15.00	8.62
Viscosity (mm^2/s)	11.22	6.44	9.32
Percentage Yield (%)	46.88	69.32	70.24
Saponification Value (mg/KOH))	188.24	193.20	203.39

Table 2: Free fatty acid composition of Neat Vegetable oils

Fatty Acid	Carbon atoms	HVO	CVO	TVO	Units
Stearic	$C_{18:0}$	0.03	-	2.17	%
Myristic	$C_{14:0}$	4.33	4.33	5.22	%
Palmitic	$C_{16:0}$	18.66	22.19	22.93	%
Linolenic	$C_{18:3}$	9.24	9.11	21.08	%
Linoleic	$C_{18:2}$	18.13	20.53	20.24	%
Oleic	$C_{18:1}$	6.14	11.35	7.29	%
ΣSFA		23.02	26.72	30.32	%
ΣUFA		33.51	40.99	48.61	%
U/S		1.46	1.53	1.60	%
L/L		0.51	0.44	1.04	%

Table 3: Free Fatty Acid Methyl Ester (FAME) composition of Biodiesel

Fatty Acid	Carbon atoms	HVO-ME	CVO-ME	TVO-ME	Units
Methyl Stearate	$C_{18:0}$	0.97	2.17	3.08	%
Methyl Myristate	$C_{14:0}$	6.28	5.97	6.19	%
Methyl Palmitate	$C_{16:0}$	31.28	27.51	29.36	%
Methyl Linolenate	$C_{18:3}$	26.55	8.33	26.17	%
Methyl Linoleate	$C_{18:2}$	25.28	18.06	24.37	%
Methyl Oleate	$C_{18:1}$	8.17	20.69	9.17	%
ΣSFA		38.53	35.65	38.63	%
ΣUFA		60.00	47.08	59.71	%
U/S		1.56	1.32	1.55	%
L/L		1.05	0.46	1.07	%

Table 4: Oxidative stability => Degree of unsaturation of the neat vegetable oils

Oil	DU
HVO	60.88
CVO	90.60
TVO	89.93

$DU = C_{n:1(Wt\%)} + 2C_{n:2,3(Wt\%)}$

Table 5: Long Chain Saturated Factor (LCSF) and Cold Filter Plugging Point (CFPP)

Oil	LCSF (^oC)	CFPP (^oC)
HVO	1.881	-10.567
CVO	3.173	-9.503
TVO	3.378	-5.864

LCSF (^oC) = (0.1 x $C_{16:0}$ + 0.5 x $C_{18:0}$ + 1 x $C_{20:0}$) + 1.5 x ($C_{22:0}$ + 2 x $C_{24:0}$)

CFPP (^oC) = 3.1417 x LCSF – 16.477

Table 6: The heat of combustion (KJ/kg) and the absolute viscosity (Inη)

Oil	H (KJ/kg)	Inη
HVO	39539.54	96.01
CVO	39197.15	94.76
TVO	39759.41	93.96
CSVO	39964.85	91.99

Where

IV = Iodine value;

SV= Saponification value

Heat of Combustion = 47,465 – [4.187(IV) + 38.31(SV)] KJ/kg

Viscosity $\text{In}\eta$ = -4.7965 + 2525.92962(1/T) + 1.6144 [$(SV)^2/T^2$] – 101.06 x $10^{-7}(IV)^2$

Table 7: Heating values of the neat vegetable oils and their methyl esters

S/No.		HHV (Btu/lb)	LHV (Btu/lb)
1	TVO	16914	15674
2	TVO-ME	17020	16159
3	HVO	17384	16813
4	HVO-ME	17995	16918
7	CVO	17834	16508
8	CVO-ME	17913	16717

HHV= higher heating value; LHV= lower heating value; Btu/lb = British thermal unit per pound

4. DISCUSSION

4.1. Preparation of Methoxide

Analysis of the chemo-physical properties of the seed oils is shown in Table 1 and Fig. 6. The iodine value of CVO, TVO, HVO, was 113.68, 118.02 and 127.53 respectively as shown. The results indicate that all the oils are semi-drying constituting predominantly polyunsaturated fatty acids mainly oleic, linoleic and linolenic fatty acids. This class of oils whose iodine value is between 100 – 150 poses the property of absorbing oxygen on exposure to the atmosphere; though do not do so sufficiently to qualify them as drying oils. They become vicsous and remain sticky but do not form a hard-dry film [20, 21]. The saponification values of CVO, TVO and HVO was found to be 203.39, 188.24 and 193.20 respectively. ANOVA analysis shows significant difference ($P < 0.05$) in the chemo-physical properties including saponification value. Saponification value indicates the average molecular weight of oil. A high saponification value implies greater proportion of fatty acid of low molecular weight. The results indicate that all the oils contained higher proportions of low molecular weight of fatty acids. The values compared favourably with the saponification values of palm oil (196 - 205), olive oil (185 - 196), soya bean oil (193) and linseed oil (193 - 195) [22].

CVO, TVO and HVO acid values were found to be 5.43, 3.76 and 4.76 (mg/kg) respectively. There was significant difference ($P < 0.05$) in the acid content. Acid value of oil measures the extent to which the glycerides had been decomposed by lipase action. The decomposition is usually accelerated by heat and light. The acids that are usually formed include free fatty acids, acid phosphates and amino acids. Free fatty acids are formed at a faster rate than the other types of acids [23]. The low acid values also indicate that the oil could be stored for a long time without deterioration. The free fatty acid values for CVO, TVO and HVO were found to be 2.73, 1.87 and 2.38 respectively. A significant difference was obtained in free fatty acid content (See Fig. 1). The values obtained were below 3.0% FFA content recommended for biodiesel feedstock and 5.0% FFA for non-rancid oils [24]. This implies that the oil samples studied are not rancid and are good feedstocks for biodiesel production. The peroxide values of CVO, TVO and HVO were found to be 8.62, 13.20 and 15.00 respectively. There was significant difference ($P < 0.05$) in the peroxide values of the oils. The peroxide value is the measure of oxidative stability of oil. High peroxide values are associated with rates of oxidation across the double bonds in unsaturated fatty acids in the presence of enzyme or certain chemical compounds. Variation of peroxide value could be due to the number of unsaturated fatty acid content, since rate of auto-oxidation of fats and oils increase with increasing level of un-saturation. The low peroxide values of the oils indicate that they are less liable to oxidative rancidity at room temperature [20, 21]. The specific gravity of the oils (CVO, TVO and HVO) was found to be 0.92, 0.92 and 0.92 respectively. There was no significant difference at $P < 0.05$ in this property of the oils. The values for density for these oils were 1.46, 1.47, 1.47 and 1.46 respectively. The viscosity of CVO, TVO and HVO was found to be 9.32, 11.22 and 6.44(mm^2/s). There was significant difference at $P < 0.05$. This viscosity indicates that all the oils were free flowing. The moisture content (%) was found to be 0.64 (CVO), TVO and HVO was 0.60 and 0.40 respectively. Moisture content for biodiesel production should be as low as <0.5%. For these oils, the oils were usually heated to remove any moisture present before use for preparation of biodiesel.
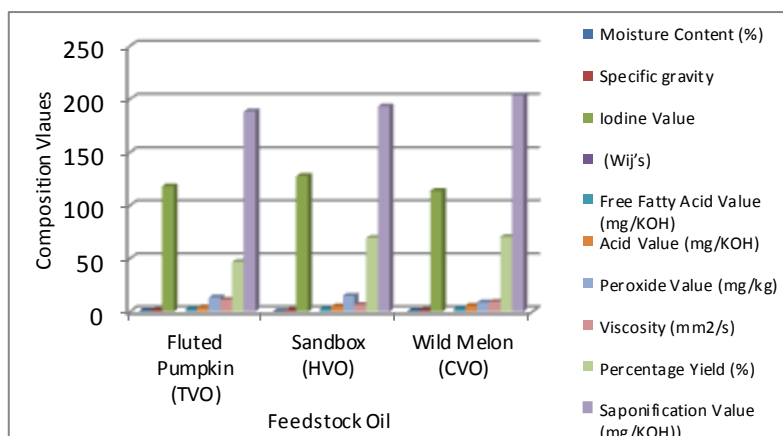
Fig. 6: Chemo-physical properties of the seed oils studied

4.2. Free Fatty Acid Profile

Compared to diesel fuel, biodiesel is chemically simple since it contains only six to seven fatty acid esters. However, different esters vary in terms of important fuel properties such as total and free glycerine, cetane number, viscosity, cloud point, pour point, density and degree of unsaturation. This is as a result of the presence of impurities. It is also affected by the choice of feedstock [25]. For diesel engine, the best alternative fuel like biodiesel, the most critical fuel quality parameter is the total glycerine content. Higher cetane number is desirable whereas high viscosity and higher cloud point and pour point are undesirable [160]. Biodiesel as a whole has potential to contain glycerol in the form of free glycerine, mono -, di- and tri-glycerides [26]. Free and bonded glycerine content reflects the quality of biodiesel [27]. A high content of free glycerine may cause problem during storage or in the fuel system due to separation of the glycerine. High total glycerine content can lead to injection fouling and may also contribute to the formation of deposits in injection nozzles, pistons and valves [27, 28]. High concentrations of mono- or di-glycerides in biodiesel not only affect the fuel quality but also indicate incomplete reaction during production [28]. Total glycerine includes the sum of free glycerine and mono-, di- and triglyceride in % mass- 0.020 maximum for free glycerine and 0.240 maximum for total glycerine in % mass [28]. Free glycerine can cause fuel separation and materials compatibility problems. Glycerides have much higher boiling point than biodiesel and conventional diesel fuel and can lead to engine deposits and durability problem [30]. In this work, three tropical Nigerian feedstocks were analysed for their fatty acid composition. Figure 7 and 8 show the acids compositions of the neat oil with palmitic acids and polyunsaturated acids dominating in the all feedstocks.

All the oil contains mostly linolenic, linoleic and palmitic acids. These properties are same as those of cottonseed oil composed primarily of unsaturated linolenic and the saturated palmitic which gave 98.6% optimum yield of methyl ester [31]. TVO (Fluted pumpkin) has been planted in several tropical regions. The seed contains about 46.88% oil. Different types of vegetable oils have different types of fatty acids. Of importance are the combustion and flow properties of biodiesel fuel which are determined primarily by FFA content of the vegetable oil. The oil fraction of TVO consists of both saturated (22.93% palmitic acid, 2.17% stearic and 5.22% myristic acid) and unsaturated fatty acids (21.08% linolenic acid and 20.24% linoleic acid and 7.29% oleic acid). Statistically, significant difference at ($p<0.05$) was observed in fatty acid compositions of these oils as shown in Figure 7 and 8.

Biodiesel obtained from Fluted pumpkin (TVO-ME) shows conversion from oil to about 98.34% of the methyl ester, with unsaturated acid to 59.71% (methyl linolenate 26.17%, methyl linoleate 24.37% and methyl oleate, 9.17%) and the saturated fats 30.63% (methyl palmitate, 29.36%, methyl stearate, 3.08% and methyl myristate, 6.19%). Comparing the composition of TVO-ME to TVO, statistical analysis shows significant difference ($p<0.05$) as shown. HVO (Hura crepitans) is native to a number of countries including Australia, Nigeria. Sandbox tree can grow in tropical (region). It is a tree of 90 – 130 feet height (25m), with spread branches. It is a fast growing tree with the potential for high oil seed production. It's non-edible oil. These properties support the suitability of this plant for large scale vegetable oil production required by a suitable biodiesel industry.

Seed of Hura crepitans yields 69.32% oil by weight. The fatty acid composition of Hura crepitans was reported. Statistical analysis showed significant difference in the fatty acid composition. The predominant fatty acid is palmitic acid and linoleic fatty acids with18.66% and 18.13%respectively. The total unsaturated

acid is 33.51% (comprising of 9.24% linolenic acid, 18.13%, linolenic acid and 6.14%, oleic acid). The total methyl ester conversion is about 98.53%, 60.00% of this conversion was from the unsaturated fatty acid (methyl linolenate, 26.55%; methyl linoleate, 25.28% and methyl oleate, 6.17%), while the 38.53%, from the saturated fatty acid as shownn. The results showed no significant difference ($p=0.05$) to the composition of HVO.
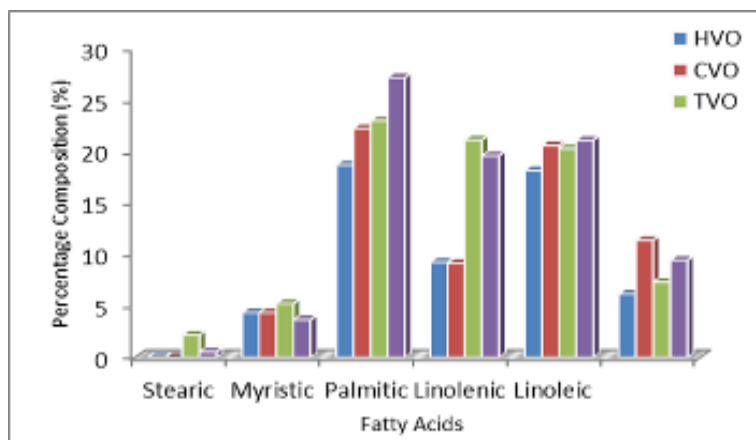
Fig. 7: Fatty acids composition of the seed oils of study
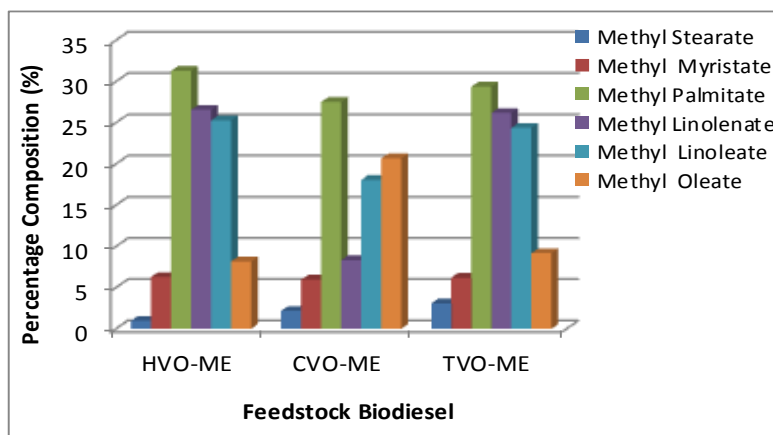
Fig. 8: Fatty acids composition of produced biodiesel (FAME)

CVO – The fatty acid composition of Wild melon (*Cucumeropsis manii*) oil and biodiesel is reported in Table 2 and 3 and Figure 7 and 8. A total of 69.68% were identified in Cucumeropsis manii. It comprises of 26.72% saturated fatty acids and 40.99% unsaturated fatty acids. The maximum composition is palmitic acid which is 22.19%, and traces of myristic acid (4.33%), linoleic acid (20.53%), linolenic acid (9.11%) and oleic acid (11.35%) were found. Statistical analysis shows significant difference ($p<0.05$). The moderate unsaturated fatty acids are considered optimum to turn a fuel at which polymerization during combustion would be substantially less than what would occur with highly polyunsaturated fatty acid derived fuel. CVO-ME gave 82.73% conversion into methyl esters as depicted in Table 3 with the unsaturated fatty acid having a conversion of 47.08% and saturated fatty acid comprising of 35.65%, which showed no significant difference ($p>0.05$) to fatty acid composition of CVO, the vegetable oil investigated for their suitability as biodiesel resources are those which occur abundantly in the specific region. While the suitability of any material as fuel, including biodiesel, can be influenced by contaminants arising from product or other sources, the nature of the fuel components ultimately determines the fuel properties included as specification in standards can be traced to the structure of the fatty esters comprising biodiesel. Since the transesterification reaction of oil or fats leads to a biodiesel fuel corresponding in its fatty acid profiles with that of the parent oil or fats, biodiesel is a mixture of fatty esters with each ester component contributing to the properties of the fuel [30]. Analytical indices related to vegetable oils can be distinguished as structure or quality indices. Structure indices are iodine value; a measure of total unsaturation of an oil, saponification value; an indicator of average molecular weight and hydroxyl value, which is applicable to fatty compounds (or their mixtures) containing hydroxyl groups, such as castor and lesquerell oils.

Quality indices are the free fatty acids, peroxide, anisidine, phosphorus and other similar values. Generally, quality indices relate to the quality of vegetable oil obtained after processing and possible further derivatization as well as after extended storage and/or the presence of naturally occurring non-fatty materials. Quality indices were formerly termed processing – related parameters but the term quality indices appears to be more general. In some cases, oils are subjected to reactions, and the nature of the resultant products requires the inclusion of additional quality indices. For instance, in the case of methyl ester production from vegetable oils for biodiesel use, the additional quality indices would include free and total glycerol content (free glycerol arising from the clearage of fatty acid chain, total glycerol including glycerol bound in the form of mono- and di-glyceride) [32].

The properties of biodiesel that are determined by the structure of component fatty esters include ignition quality (cetane number CN), heat of combustion (gross calorific value H), oxidation stability, viscosity, cold flow [33].
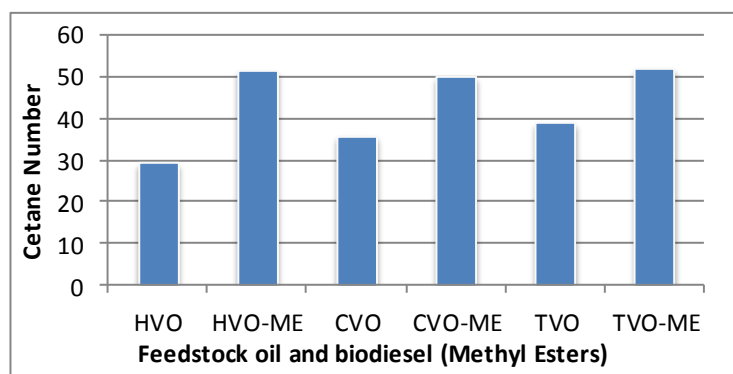
Figure 9: Biodiesel quality (Cetane Number) of biodiesel feedstocks

It is well known that the cetane number of biodiesel depends on the feedstock used for it production. The longer the fatty acid carbon chains and the more saturated the molecules the higher the cetane number [34, 35]. Ramos et al. [32] reported a linear relationship between the degree of unsaturation, and cetane number of biodiesel. The higher the degree of unsaturation,, the lower the cetane number. It was noted that diesel engine vary widely in their cetane requirements, the lower the engine speed, the lower the cetane number (as low as 20) of the fuel it can use [36]. Figure 9 shows the values of CN of FAME under study [49 < CN < 65] fell within range acceptable in the broad range of diesel engines with TVO-ME and HVO-ME having a cetane number of 51.5 and 51.1 respectively. CVO-ME has cetane numbers of 49.6 and. Cetane numbers for neat oils were also obtained using the cetane number for individual pure fatty acids and the corresponding fatty acids compositions in Tables 2 and 3. Figure 9 shows the profile of cetane number of neat oils and their corresponding FAME which were greatly enhanced in the FAME. Cetane number is one of the prime indicators of the quality of diesel fuel. It relates to the ignition delay time of a fuel upon injection into the combustion chamber. The shorter the ignition delay time, the higher the cetane number and vice versa [37]. Research has revealed that there is a correlation between high cetane number and low NOx emission. The cetane number of biodiesel is generally higher than conventional diesel. The effect of blending biodiesel on cetane number is almost linear for mixtures of esters with biodiesel fuel or diesel fuel [159] .Research has also shown that the values of cetane number from different feedstock vary widely with soya-beans oil derived biodiesel. The value ranges from 48 to as high as 67 with the ASTM D613 standard specification requirement of 47 minimum [38]. These empirical data suggest that the mixture of the locally available vegetable oils may be processed safely to methyl ester that would meet the requirement for use in diesel engines.

5. CONCLUSION

Biodiesel production is worthy of continued study and optimization of production procedures because of its environmentally beneficial attributes and its renewable nature. A reduced cost option is to produce biodiesel from non-edible oils. Another option for cost reduction is to reduce the cost of processing through optimizing the process variables that affect the yield and purity of biodiesel. Feedstocks comprising three edible/non-edible oils of Nigerian tropical origin (Sandbox tree, Fluted pumpkin and wild melon seeds) were studied for production of biodiesel (methyl esters) because of their availability in abundance in the locality of study. Base catalysis was used for the transesterification reaction with methanol at two different oil/alcohol molar ratios (4:1 and 6:1). Two catalyst type; KOH and NaOH were also used and two reaction times (5min and

30 mins) and at two reaction temperatures (38° and 55^oC). The catalyst concentration was kept constant. These process variables were used to achieve biodiesel with optimum yields, viscosity, and specific gravities. Neat oils were extracted from these feedstocks and pre-treatment by degumming was achieved to remove phospholipids. Physiochemical properties of the oils were obtained which shows that all the oils were suitable feedstock for biodiesel production. Free fatty Acid composition of the oil shows that all the oils contains mainly saturated and polyunsaturated fatty acids which compared favourably with common feedstocks like cottonseeds oil composed primarily of unsaturated linolenic and the saturated palmitic acids which gave 98.6% optimum yield. The fatty acid composition obtained were used to determine fuel properties like ignition quality (cetane number), heat of combustion (gross calorific value H), oxidative stability, viscosity and cold flow properties. The results shows all the vegetable oils under study are suitable for biodiesel on the basis of these fuel properties.

6. REFERENCES

[1]   TAT, M.E. and Van Gerpen, J.H. (1999). The kinematic viscosity of biodiesel and its blends with diesel fuel. Journal of America oil Chemists Society, vol. 76 (12): 1511-1513.

[2]   TAT, M.E. and Van Gerpen, J.H. (2009). The specific gravity of biodiesel and its blends with diesel fuel. *Journal of America Oil Chemist Society*, vol. 77 (2): 115-119.

[3]   TAT, M.E. Van Gerpen, J.H, Soylu S. Canakci, M., Monyem, A. and Wormley S. (2006). The speed of sound and isentropic bulk modulus of biodiesel at 21oC from atmospheric pressure to 35MPa. *Journal of America Oil Chemists Society*, vol. 77 (3): 285-289.

[4]   Biodiesel, Wikipedia, the free encyclopaedia, August 2006. Pp.1. Retrieved from "http://en.wikipedia.org/wiki/biodiesel"

[5]   BÜNGER, J., Krahl, J., Baum, K., Schröder, O., Müller, M., Westphal, G., Ruhnau, P., Schulz, T. G., Hallier, E. and Baum, K. (2002). Cytotoxic and mutagenic effects, particle size and concentration analysis of diesel engine emissions using biodiesel and petro-diesel as fuels. Archives of Toxicology vol. 74 (8): 490 - 498.

[6]   YAP, A. and Quinn, N. (Ed.) (2004). Biodiesel- Fuel for the future. Environmental Technology. pp 2, 3, 8.

[7]   AJIWE, V.I.E, Ajibola, V.O, and Martins, C.M.O.A. (2002). Pentadethamacrophylla (oil bean) oil, its methyl-ester and ester-diesel blends. Alternative source of diesel. African Journal of Science, vol 3(2): 587-600.

[8]   Fueling for the Future (Cu Biodiesel 2004) University of Colorado. http://www.biofuels.fsnet.co.uk Pp 1-23.

[9]   Biodiesel (2010). The free encyclopedia–Wikipedia. Pp 1-18. Retrieved from "http://en.wikipedia.org/wiki/biodiesel.

[10]   AKINTOYO, E.T (1997). Chemical composition and physiochemical properties of fluted pumpkin (Telfairia occidentalis seed and seed oil. Rivista Italian Delle Sostanze Grasse, vol. 74(1): 13-15.

[11]   ANHWANGE, B.A., Ikyenge B.A., Nyiatagher D.T., Ageh J.T. (2010). Chemical analysis of Citrullus lanatus, Cucumeropsis   manii, and Telfairia occidentalis. Journal of Applied Science Research, vol. 6(3): 265-268.

[12]   JEFFREY, C. (1990). Systematic of the Cucurbitaceous: an overview, in: Bates D.M., Robinson R.W., and Jeffrey C. (Ed). Biology and utilization of the cucurbitaceous. Cornel Univ. Press, Ithaca, New York Pg. 3 -28.

[13]   MATAMOLA, M. (2009). Trees with many names- hura crepitians, stubborn limpet, lively Tuas Shore, Sandballs party. Manta's Experience. (Online pictures).

[14]   BURKIL, H.M. [1994]. Useful plants of West Tropical Africa, Vol.2, families E.I., Royal Botanical Garde, Kew.

[15]   OBUTE, G.C., Ndukwu, B.C., and Chukwu, O.F. (2007). Targeted mutagenesis in Vignaungui Culata (L), Walp and Cucumeropsis Manii   (Naud) in Niger. African Journal of Biotechnology, vol. 6 (21): 2467-2472.

[16]   KEITH, A. (2010). Make your own biodiesel http://journeytoforever.org/   P1-30.

[17]   ASTM (American Society) for Testing Materials (2003). ASTM Standards Methods, ASTM pub; Philadelphia.

[18]   VAN GERPEN J.H, Shanks B., Pruszko R., Clements D. and Knothe G. (2002- 2004). Biodiesel Production Technology. National Renewable Energy Laboratory (NREL/SR-510-36244). Pp. 1-105

[19]   VAN GERPEN, J.H., Dvorak, B. (2002). The effect of phosphorus level on the total glycerol and reaction yield of biodiesel bioenergy, in the 10thBiennial Bioenergy Conference, Boise.

[20]   ODOEMELAM, S.A. (2005): Proximate composition and selected physiochemical properties of the seeds of African oil bean (Pentacle thramarcrophlla). Pakistan Journal of Nutrition, vol. 4 (6): 382-383.

[21]   ANYASOR, G.N., Ogunwenmo K.O., Oyelana O.A., Ajayi D. and Dangana, J. (2009). Chemical analyses of groundnut (Arachis hypogaea) oil, Pakistan Journal of Nutrition, vol. 8 (3): 269-272.

[22]   FOLKAID, G. and Sutherland, J. (1994). Moringa oleifera – a multi-purpose tree. Footsteps, No. 20. Pp.109-111. In: Intermediate Technology Publication.

[23]   BANMER, M. (1996). Food-producing tree and shrubs of West Africa. Serie-Etudes-et-Recherches (Senegal) No.168-170, 252-260.

[24].   SAVAGE, G.P., McNeil, D.L. and Dutta, P.C. (1997). Lipid composition and oxidation stability in New Zealand. Journal of American Oil Chemist's   Society, vol. 74: 755-9.

[25]   CHANDRA, B. (2004). The critical review of biodiesel as a transportation fuel in Canada. Principle of GCSI-Global change strategies international incorporation, Canada.

[26]   RUPPET, G. and Hall, E. (2004). Standard testing method for determination of free and total glycerine in B100 biodiesel methyl esters by GC by ASTM D6584. ASTM International. West Conshohocken PA.

[27]   FAUSTO, M., Cavagnino, D., Cadoppi, A. (2007). Determination of free and total glycerine in pure biodiesel (B100) by GC in compliance with   EN14105, LC/GC Europe. Dec. 2:24.

[28]   ASTM D6584 – 10. (2010). Standard test methods for determination of   total,mono-,di-and   triglycerides. http://www.astm.org/standards/D6584.html.

[29]   MCCORMIOK, T.L., Alleman, R. M. and Moens. L. (2005). Survey of the quality and stability of biodiesel and biodiesel blends in the United States in 2004, NREL Technical Report.

[30]   GEORGIOS, K., Georgios, A. and Stamos, S. (2011). Tetramethylguanidine as an efficient catalyst for transesterification of waste frying oils. *Applied Energy*, vol.88: 3645-3650.

[31]   OKOEGWALE, E.E., Ogie O. and Idialu J.E (2009) Comparative tracheary elements characteristics of Canarium schweinfurthii Engl. and Dacroydes edulis (G. Don) H.J. Lam growing in derived savanna and rainforest regions of Edo State, Nigeria. Nature and Science, 7(6): 1-10

[32]   RAMOS, M.J., Fernandes, C.M., Casas, A., Rodrigues, L. and Perez, A. (2009). Influence of fatty acid and composition of raw materials on biodiesel properties. *Bioresource Technol.*, vol.100: 261-268.

[33]   REFAAT, A.A. (2009) A review correlation between the chemical structure of biodiesel and its physical properties*. Int. J. Environ.Sci.Tech.* 6 (4): 677-694.

[34]   BAJPAI, D. and Tyagi, U.K. (2006) Biodiesel, source, Production, composition, properties and its benefit. J. Oleo Sci., vol. 55: 487-502.

[35]   VAN GERPEN, J.H. (2005). Biodiesel processing and production. *Fuel processing technology,* vol.86: 1097-1107.

[36]   OKIEMEN, F.E. and Omosigho, H.N. (2008). On the fuel properties of methyl esters of palm kernel oil. Niger, J. Appl. Sci., vol.26: 90-94.

[37]   CHANDRA, B. (2004). The critical review of biodiesel as a transportation fuel in Canada. Principle of GCSI-Global change strategies international incorporation, Canada.

[38]   OMOSIGHO, H.N. and Okieimen, F.E. (2009). Studies on the fuel properties of vegetable oils. *Niger, J. Appl. Sc.*, vol.27: 9-14.

31: Novel two-stage high-solid anaerobic digestion of food waste and grass

WANGLIANGA LI[1], LOH KAI CHEE[2], TONG YEN WAH[*, 1, 2],
PENGHUI GAO[1], ZHANG JINXINA[1], LIM JUN WEI[1]

1 NUS Environment Research Institute, National University of Singapore, 5A Engineering Drive 1, Singapore 117411, Singapore
2 Department of Chemical and Biomolecular Engineering, National University of Singapore, 4 Engineering Drive 4, Singapore 117585, Singapore
Corresponding author at: NUS Environment Research Institute, National University of Singapore, 5A Engineering Drive 1, Singapore 117411, Singapore. Tel.: +65 6516 8467; fax: +65 6779 1936. E-mail address: chetyw @nus.edu.sg (Y.W. Tong).

A high-solid two-stage process was proposed to increase biogas yield, to improve the efficiency and to stabilize the digestion process of horticultural waste (HW) and food waste (FW). In this two-stage process, high-solid codigestion of FW and chicken manure (CM) was carried out in the first stage and then, transferred and codigested with grass in the second stage. When volatile solid (VS) ratio of FW, CM and grass was 4:5:5, after 70 days, the cumulative methane yield was about 203 mL/g VS. The optimized operation parameter for the two-stage is VS ratio of FW/CM/grass as 4:5:5, duration of first stage as 3 days. Compared with the codigestion of FW, CM and grass, the biogas yield of the two-stage process increased by 28% and the duration of digestion was 52 days, 18 days shorter. Under the optimal condition, the VS removal exceeded 55%. The composition analysis revealed that cellulose and hemicellulose contributed to the production of biogas.

Keywords: Food waste; Yard waste; High-solid; Digestion; Bioga

1. INTRODUCTION

Horticultural waste (HW), food waste (FW) and animal manure take up most of organic fractions of MSW, which are appropriate to be disposed with AD because of high organic content and moisture content. However, high-solid anaerobic digestion of HW is limited by low hydrolysis rates, low digestion efficiency, and inhibition of volatile fatty acids (VFAs), because its AD process is very easy to become acidified due to the accumulation of long chain fatty acids (LCFAs) and VFAs. Although FW is a promising organic substrate for AD due to its high potential for methane production, high organic matter content results in the failure of the single-phase AD because of the rapid production of large amounts of VFA at the initial stage. Digestate recycling can improve biogas yield and realize full utilization of organic waste, which can be realized in two-stage process.

The two-stage system has advantages over one-stage process since it can enrich different bacteria in each digester and increase the digestion stability. Therefore, compared with one-stage AD, the two-stage AD has better performance in acid production and methane yield and has a higher removal of suspended solids (SS) and chemical oxygen demand (COD) (ZHANG B., 2014;ZUO Z., 2014;YABU H., 2011.) Even though two-stage AD has been studied for many years, the two-stage process in solid state has never been reported. The new technology allows high organic loading rate and treatment capacity, meantime its biogas is a highly convenient bioenergy. After the solid-state AD, the solid residue can be disposed via further treated via thermal conversion if the residue has suitable heating value. The volume of waste is in fact greatly reduced and the solid residue of AD has low contents of organic matters and moisture after producing biogas and removing leachate via solid-state AD.

This study aims to develop a novel two-stage high-solid digestion process to dispose solid waste of FW, grass and CM economically and technically. The effect of different alkalis on the performance of the two-stage dry digestion was further studied by detecting the biogas yield and the variations in COD, ammonia nitrogen concentration and total solids (TS) of the substrate.

2. EXPERIMENT AND METHODS

2.1. High-solid codigestion of grass and chicken manure

Biogas and methane production of the cosubstrate with the mixture of grass, CM and FW was evaluated using batch experiment in 250 mL flask. The C/N ratio of grass/chicken manure was about 21.70. The flasks were sealed using rubber stoppers, and incubated at 35 ±1°C for up to 40 days. Biogas production was collected with Tedlar bags.

2.2. Two-stage bioreactors Configuration

Fig.1 Scheme of the semi-continuous two-stage system with recirculation.

The scheme of the two-stage digestion system was presented in Fig.1. Codigestion of FW and CM was carried out in first-stage digester. Then, the digestate was transferred to second-stage with a pump and mixed with grass. If necessary, the effluent produced in second-stage digester was recirculated back to the

first-stage digester. In order to separate particulate matter from the effluent, the outlet of the second-stage digester was equipped with a sedimentation tank consisting of a filter, to separate and settle the large particles before pumping the liquid to the first-stage digester.

3. RESULTS AND DISCUSSION

3.1. Substrates characterization

Table 1 Physical properties of grass, FW and CM

Feed	Grass	CM	FW
C, %	41.08	28.16	50.48
N, %	1.02	3.48	2.84
C/N ratio	40.27	8.09	17.77
S, %	<0.50	1.09	<0.50
Total solid,%	89.58	72.26	29.32
Volatile solid ,%	77.61	38.38	26.03
Composition analysis			
Neutral detergent soluble, %	16.68	73.00	79.18
Cellulose, %	42.49	15.30	10.03
Hemicelluloses, %	27.14	4.07	2.33
Lignin, %	12.67	6.03	8.48
Ash, %	0.67	1.62	0.00

In this study, grass, FW and CM were used as the substrates. Physical properties of the substrates were measured in terms of TS, VS, elemental analysis and composition analysis, as shown in Table 1. For the three substrates, the organic fraction contributed to the major part of the biomass, representing a TS content of 89.86%, 72.26% and 29.32% in grass, CM and FW, respectively. VS of them are 77.61%, 38.38% and 26.03%, respectively. Based on elemental analysis, the C/N ratio of grass, CM and FW is 40.27, 8.09 and 17.77, respectively. The C/N ratios of all the different samples were not in the range of 20–30 which was proposed to be most suitable for optimum operation of the AD. While, from the composition analysis, we can see that the content of NDS, cellulose, hemicellulose, lignin and ash content of grass was 16.68%, 42.49%, 27.14%, 12.67% and 0.67%. While, for CM and FW, the content of NDS fraction was more than 70%. The contents of lignin and hemicellulose of them were only about 10%.

3.2. High-solid codigestion of FW, grass and CM

The VS ratio of grass, FW and CM is 4:4:5. Fig.2 showed the cumulative biogas yield, cumulative methane yield and methane concentration of codigestion. It can be seen that biogas was produced on the 1st day, then, no biogas produced until the 9th day. From the 9th day, biogas was produced until the 75th day. The cumulative biogas yield of cosubstrate was about 322 mL/g VS and the cumulative methane yield was about 203 mL/g VS. The pH value decreased from 7.03 to 5.49 in 5 days of digestion, which can inhibit the digestion process significantly. Then the pH value increased slowly since the 15th day. The possible reason is that the hydrolysis of FW is much faster than the digestion of CM. After the 15th day, ammonia was produced from the digestion of CM which has buffer effects and can increase the pH value. Thus, the pH value was in the range of 7.06 to 8.09 after the 25th day.

Fig.2 Cumulative biogas yield, methane yield and methane concentration of codigestion

3.3. HRT of first-stage on digestion performance

The effects of HRT of first-stage on total biogas yield of two-stage process were studied with TS 20%, VS ratio of FW: CM: grass as 4:5:5. The first-stage duration was chosen as 1 day, 2 days, 3 days, 4 days and 15 days. With the same total organic wastes, the FW/grass ratio on cumulative biogas yield and cumulative methane yield and HRT was tested. When the digestate of FW/CM was transferred on the 1st day, 2nd day, 4th day, 5th day and 7th day, the pH value of FW/CM digestion system was 6.50, 6.96, 6.96, 6.87 and 6.78. It can be concluded that the pH value decreased little after 7 days of codigestion. Codigestion with CM can make the digestion process more stable. Fig.5 showed the total biogas yield with different first-stage HRT. Fig.3 showed the total methane yield with different first-stage HRT. When first-stage HRT was 3 days, the biogas yield and methane yield were highest.

Fig. 3 HRT of first-stage on cumulative methane yield

4. CONCLUSIONS

When FW was used as sole substrate, fast hydrolysis led to the sharp decrease of pH value to below 4.0 and thus, led to the failure of digestion within 3 days. The highest biogas yield and methane yield were obtained with the FW/grass ratio (VS ratio) 1:2.

The hydrolytic retention time (HRT) 1 day, 2 day, 3 day, 4 day and 7 day of first stage on digestion performance was also studied. The optimal HRT of the first stage is 3 day.

Biogas yield can be increased through two-stage process than codigestion.

Under the optimal condition, the volatile solid (VS) removal efficiencies exceeded 55%.

5. ACKNOWLEDGEMENTS

6. REFERENCES

ZHANG B., HE P. He, 2014. Performance assessment of two-stage anaerobic digestion of kitchen wastes. Environ Technol, 35(10),1277–1285.

YABU H., Sakai C., Fujiwara T., et al. 2011.Thermophilic two-stage dry anaerobic digestion of model garbage with ammonia stripping. J Biosci Bioeng, 111 (3), 312–319.

ZUO Z., Wu S., Zhang W., Dong R., 2014. Performance of two-stage vegetable waste anaerobic digestion depending on varying recirculation rates. Bioresour Technol. 162, 266–272.

SESSION 5: BUILDING ENERGY SYSTEMS

82: Thermodynamic optimization for central heating system by using industrial waste heat through absorption heat transformer

YIN ZHANG, FEI XIONG, WENXING SHI, YINPING ZHANG[*], XIN WANG

Department of Building Science, Tsinghua University, Beijing, China
* Corresponding author: zhangyp@tsinghua.edu.cn

Urban heating energy consumption in northern China accounts for 40% of total building energy consumption. Meanwhile there are large quantities of low grade waste heat discharged into the environment during industrial processes in northern China. Utilizing these industrial waste heat for central heating in winter is of great importance in energy saving and has raised more concerns during recent years. However, in traditional systems, the low grade waste heat is often used to produce relatively low temperature supply water through heat exchangers, often leading to large mass flow rate in the primary network, which results in huge pump energy consumption after long distance delivery, since the heating users are often far away from the industrial heat sources. To break through such application bottleneck, the key is to increase the temperature difference between the supply and the return water, and decreasing the mass flow rate in the primary network. In this paper, based on the concept of heat adaptor, two kinds of heat adaptors, absorption heat transformer and absorption heat pump, are used at heat source and substations respectively to take place of heat exchangers in central heating system, to decrease the mass flow rate in the primary network. Aiming to minimize the pump energy consumption, the thermodynamic model of the new system is built and the optimal supply and return water temperatures can be obtained through extreme principle. The illustrative example indicates that the optimal supply water temperature in primary network is much higher than the waste heat temperature when the absorption heat transformer is utilized. The results also show that the delivery pump energy consumption can be decreased by almost 96% for the ideal heat adaptor system after optimization, compared to absorption heat exchange system. The theoretically ideal system deduced out in this paper is significant for guiding the optimization design of practical central heating systems using industrial waste heat.

Keywords: Waste heat, Heat engine, Heat pump, Absorption cycle, Extremum principle

1. INTRODUCTION

Urban heating energy consumption in northern China accounts for 40% of total building energy consumption and the percentage keeps increasing during recent years (Tsinghua University Building Efficiency Research Center, 2014: Page 42). Meanwhile there are large quantities of low grade waste heat discharged into the environment during industrial processes in northern China (Fang, 2013: Page 236). Utilizing these industrial waste heat for central heating in winter is of great importance in energy saving and has raised more concerns during recent years (Heitner, 1982: Page 8 and Anish, 2009: Page 412). However, in traditional central heating systems using industrial waste, the low grade waste heat is often used to produce relatively low temperature supply water through heat exchangers at the heat source (Zhu, 2013: Page 56). Moreover, the return water temperature in the primary network is relatively high (>60℃), due to the temperature limitation of heat exchangers at the substations (Jia, 2001: Page 4258 and Li, 2011: 4572). So the relatively low temperature difference between supply and return water leads to large mass flow rate in the primary network, which results in huge pump energy consumption after long distance delivery, since the heating users are often far away from the industrial heat sources.

To solve these problems, Fu et al (2010: Page 78) proposed the absorption heat exchanger and applied the new system to take the place of heat exchangers in central heating system in Northern China, in order to increase the supply and return water temperature difference in the primary network (Li, 2011: Page 4574). Zhang et al (2014: Page 275) put forward a new concept of heat adaptor and found that the thermal performance can be greatly improved after bringing in heat-work conversion devices on the basis of heat exchanger. Nevertheless, existing researches consider the central heating system as closed systems, regardless of the environmental influence, so they failed to obtain the theoretical optimal system form.

In this paper, by resorting to the concept of heat adaptor, two new heat adaptor systems are built for the heat source and the substations respectively. And the best system form is deduced out after thermodynamic optimization through extremum principle. The preliminary results indicate that when the return water temperature in the primary network equals the ambient temperature, the heating capacity reaches the maximal value. It also shows that the optimal supply water temperature is much higher than the waste heat source temperature after utilizing absorption heat transformer. Thus the delivery pump energy consumption in the primary network can be decreased dramatically. This work is of great significance in design and evaluation of practical central heating systems.

2. THERMODYNAMIC MODEL OF NEW SYSTEM BASED ON HEAT ADAPTOR

2.1. Traditional System

Figure 1 shows the traditional central heating system using industrial waste heat. In the traditional systems, heat exchangers are widely used at both heat source and substations. However, the supply and return water temperature difference in the primary heat network ($T_{pri,s}$-$T_{pri,r}$) is restricted by the heat exchangers, in terms of that the supply water temperature can't be higher than the heat source temperature ($T_{pri,s}<T_{source}$) and the return water temperature can't be lower than the water temperature in the secondary network ($T_{pri,r}>T_{sec,s}$) (Li, 2011: Page 4572). As a result, the mass flow rate in the primary network (m_{pri}) is relatively high, increasing the circulation pump energy consumption.
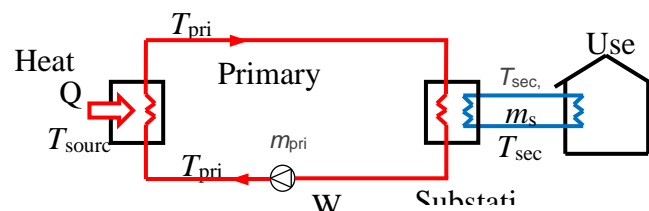
Figure 2: Schematic diagram of traditional central heating system based on heat exchangers

2.2. New System Based on Heat Adaptor

Some researchers focus on addressing the problem to save the delivery energy consumption. It is found that the key solution is to increase the supply water temperature and reduce the return water temperature in the primary network (Fu, 2010: Page 77). Nevertheless, existing researches failed to obtain the theoretical optimal system. Based on the concept of heat adaptor (Zhang, 2014: Page 275 and Zhang,

2015: Page 2), two new thermodynamic systems are established for the heat source and substations respectively, in order to find the best system form (Figure 2).
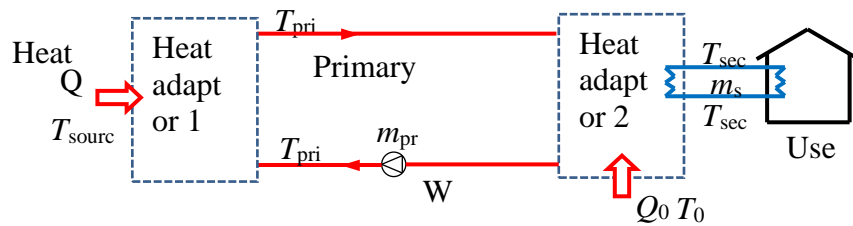
Figure 2: Schematic diagram of new central heating system based on heat adaptor

Figure 2 shows that heat adaptor 1 utilizes the heat source from industrial waste to heat the water from $T_{pri,r}$ to $T_{pri,s}$. The function of heat adaptor 2 is to make full use of the heat carried by the primary network to produce required hot water in the secondary network. The main objective is to increase the temperature difference in the primary network ($T_{pri,s}-T_{pri,r}$) to decrease the mass flow rate (m_{pri}) and save water pump energy. Based on the concept of heat adaptor, heat-work conversion devices (heat engine and heat pump) are introduced and the new system is shown in Figure 3.
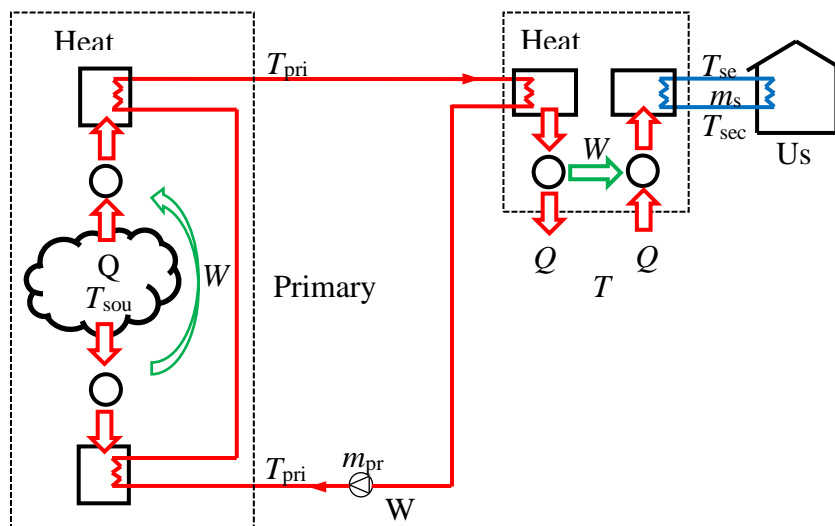
Figure 3: New thermodynamic model by using heat engine and heat pump

For heat adaptor 1, heat engine works under temperature difference between heat source and return water in the primary network to generate some power. Then the heat pump can be driven by the generated power to heat the supply water, by using the waste heat source again. Thus in theory, the supply water temperature can be higher than the waste heat source temperature itself, due to the function of the heat pump. For heat adaptor 2, except for considering making full use of the heat carried in the primary network, it is hoped that some free energy can be obtained from the environment after introducing the heat pump (Zhang, 2015: Page 2).

2.3. Optimization Model

In engineering field, the energy amount and temperature of industrial waste heat source (Q, T_{source}), coupled with the ambient temperature (T_0), are often known. In addition, the supply and return water temperature ($T_{sec,s}$, $T_{sec,r}$) and mass flow rate (m_{sec}) in the secondary network are determined by users. The undetermined parameters are temperatures and mass flow rate in the primary network ($T_{pri,s}$, $T_{pri,r}$, m_{pri}). And the main purpose is to find the optimal supply and return water temperatures to save the circulation pump energy consumption. According to the inverse-problem-based variation method (Zhang, 2015: Page 6), the optimization model is established as follows.

Known: $T_{sec,s}$, $T_{sec,r}$, T_0, T_{source}, Q, m_{sec};

Unknown: $T_{pri,s}$, $T_{pri,r}$;

Objective: minimize $m_{pri} = f(T_{pri,s}, T_{pri,r})$;

Constraint conditions:

Equation 1: Energy conservation.

$$Q = m_{pri}c_p(T_{pri,s} - T_{pri,r}) = m_{sec}c_p(T_{sec,s} - T_{sec,r}) + (Q_{01} - Q_{02})$$

Equation 2: Entropy increase for heat adaptor 1.

$$\Delta S_1 = m_{pri}c_p \ln\frac{T_{pri,s}}{T_{pri,r}} - \frac{Q}{T_{source}} \geq 0$$

Equation 3: Entropy increase for heat adaptor 2.

$$\Delta S_2 = m_{pri}c_p \ln\frac{T_{pri,r}}{T_{pri,s}} + m_{sec}c_p \ln\frac{T_{sec,s}}{T_{sec,r}} + \frac{Q_{01} - Q_{02}}{T_0} \geq 0$$

Where:

- Q_{01}/ Q_{02} = heat released to/obtained from the environment for heat adaptor 2 (kW)
- m_{pri}/ m_{sec}= mass flow rate in the primary/secondary network (kg/s)
- $T_{pri,s}$/$T_{pri,r}$ = supply/return water temperature in the primary network (K)
- $T_{sec,s}$/$T_{sec,r}$ = supply/return water temperature in the secondary network (K)
- T_0 = ambient temperature (K)
- c_p= specific heat capacity of water (4.19 kJ/kg K)

To obtain the theoretical optimal system, it is assumed that both heat engine and heat pump are ideal devices, so that there is no irreversible loss for both processes (ΔS_1=0, ΔS_2=0). In such situation, it can be obtained that

Equation 4: Expression of mass flow rate ratio.

$$\frac{m_{pri}}{m_{sec}} = \frac{T_{sec,s} - T_{sec,r} - T_0 \ln\dfrac{T_{sec,s}}{\bullet T_{sec,r}}}{T_{pri,s} - T_{pri,r} + T_0 \ln\dfrac{T_{pri,r}}{T_{pri,s}}}$$

When $T_{pri,r}$=T_0, it is found that

Equation 5: Necessary and sufficient conditions.

$$\begin{cases} \dfrac{\partial(m_{pri}/m_{sec})}{\partial T_{pri,r}} = 0 \\ \dfrac{\partial^2(m_{pri}/m_{sec})}{\partial T_{pri,r}^2} > 0 \end{cases}$$

Equation 5 means when $T_{pri,r}$=T_0, m_{pri} reaches the minimum value, when m_{sec} is given (Zhang, 2015: Page 2). Then $T_{pri,s}$ and m_{pri} can be expressed by

Equation 6: The optimal supply water temperature.

$$T_{pri,s} = \exp\left(\frac{Q}{m_{pri}c_pT_{source}}\right)T_0$$

Equation 7: The optimal mass flow rate.

$$m_{pri} = \frac{T_{sec,s} - T_{sec,r} - T_0 \ln\dfrac{T_{sec,s}}{\bullet T_{sec,r}}}{T_{pri,s} - T_0 + T_0 \ln\dfrac{T_0}{T_{pri,s}}} m_{sec}$$

According to the established model, in practical engineering field, the optimal supply and return water temperatures as well as the mass flow rate in the primary network can be obtained. Then based on the hydraulic model, the circulation pump energy consumption in the primary network can be expressed by

Equation 8: The pump energy consumption.

$$W = \lambda \frac{L}{d} \frac{v^2}{2} m_{pri} = \lambda \frac{L}{d} \frac{m_{pri}}{2} \left(\frac{\frac{m_{pri}}{\rho}}{\frac{1}{4}\pi d^2} \right)^2 = \frac{8\lambda L}{\pi^2 \rho^2 d^5} m^3 = S m_{pri}^{\ 3}$$

Where:

- S = hydraulic resistance coefficient (W s^3/m^3)
- λ= frictional resistant coefficient
- L = length of the primary network pipe (m)
- d = diameter of the primary network pipe (m)
- ρ = water density (1000 kg/m3)
- v = flow velocity (m/s)

The following section makes comparative analysis on the pump energy consumption between traditional and new systems.

3. ILLUSTRATIVE EXAMPLES AND APPLICATION

3.1. Heat-exchanger-based System

As mentioned in the introduction, the heating users are often far away from the industrial heat sources. So the industrial waste heat is usually utilized to produce hot water through heat exchanger near the heat source. Then after long distance delivery in the primary heat network, the carried heat is transferred to the water in secondary network through heat exchangers at substations (Figure1). It is assumed that the industrial waste heat amount is 100 MW, with temperature of 363 K. The parameters in the secondary network are determined by users (e.g., $T_{sec,s}$=333 K, $T_{sec,r}$=318 K). For the network hydraulic parameters, suppose that λ=0.025, L=100 km, d=400 mm, ρ=1000 kg/m^3, c_p=4.19 kJ/kg K.

For traditional heat-exchanger-based systems, the supply and return water temperatures in the primary network are determined by the heat source and the parameters in the secondary network respectively. In the ideal situation that the two heat exchangers in Figure 1 are of infinite heat exchange area, there is $T_{pri,s}$=T_{source}=363 K, $T_{pri,r}$=$T_{sec,s}$=333K. Then according to Equations 1 and 8, it can be calculated out that m_{pri}=796 kg/s, W=99863 kW. Hence it is crystal clear that the delivery energy consumption almost equals the delivered energy itself for traditional heat-exchanger-based system.

3.2. Absorption-heat-exchanger-based System

To reduce the mass flow rate in the primary network and save pump energy consumption, Fu et al. (2010: Page 78) combined the absorption heat pump and heat exchanger together, and proposed the concept of absorption heat exchanger. Figure 4 gives the specific process of absorption heat exchanger.
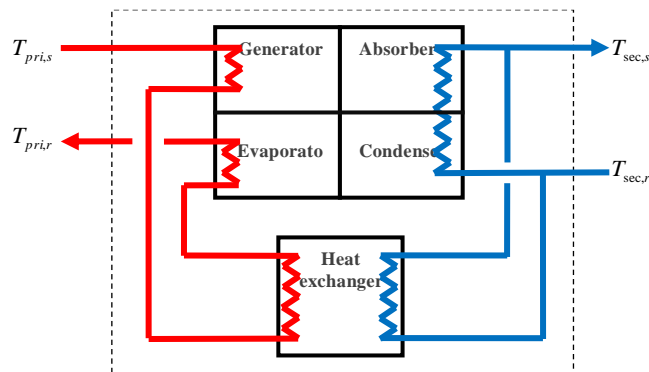
Figure 4: Schematic diagram of absorption heat exchanger (Fu, 2010)

Absorption heat exchangers have been applied to central heating systems to take the place of traditional heat exchangers at substations. The demonstration project in northern China shows that the return water temperature in the primary network ($T_{pri,r}$) can be decreased dramatically to 298 K (Fu, 2010: Page 80). In

45

that situation, for the aforementioned calculation conditions ($T_{pri,s}$=363 K, Q=100 MW), it can be obtained that m_{pri}=341 kg/s, W=7851 kW. Thus the pump energy consumption can be reduced by almost 92%, compared to traditional heat-exchanger-based system.

3.3. Heat-adaptor-based System

As shown in Figure 3, heat engine and heat pump are all ideal devices, so that there is no irreversible loss during these two processes (ΔS_1=0, ΔS_2=0 in Equations 2 and 3). For heat adaptor 2 at the substation, the heat engine works between the primary network supply water temperature and the ambient temperature and the heat pump obtains free energy from the environment, in order to decrease the return water temperature in the primary network. The calculation results of heat adaptor 2 are shown in Figure 5.

It is clear that the mass flow rate (m_{pri}) in the primary network decreases first and increases after the minimum with increasing return temperature ($T_{pri,r}$). When $T_{pri,r}$=T_0, m_{pri} reaches the minimal value. The reason is that with the decreasing T_{pri}, the average temperature of heat source decreases, lowering the COP of the heat engine. On the other hand, the available heat energy in the primary network ($T_{pri,s}$-$T_{pri,r}$) increases with lower $T_{pri,r}$. So there exists the best value for $T_{pri,r}$, to minimize the mass flow rate (m_{pri}). However, heat adaptor 1 near the heat source is a closed system, to increase the supply water temperature. When the optimal $T_{pri,r}$ is obtained by heat adaptor 2, the corresponding $T_{pri,s}$ can be derived from Equation 6. Supposing that the ambient temperature (T_0) is 273 K, for the same conditions ($T_{pri,s}$=363 K, Q=100 MW), it can be obtained that $T_{pri,r}$= T_0=273 K, $T_{pri,s}$= 471 K. Then the mass flow rate, coupled with the pump energy consumption can be calculated out that m_{pri}=121 kg/s, W=351 kW. Thus the pump energy consumption can be reduced by almost 96%, compared to absorption-heat-exchanger-based system.

(a)

(b)
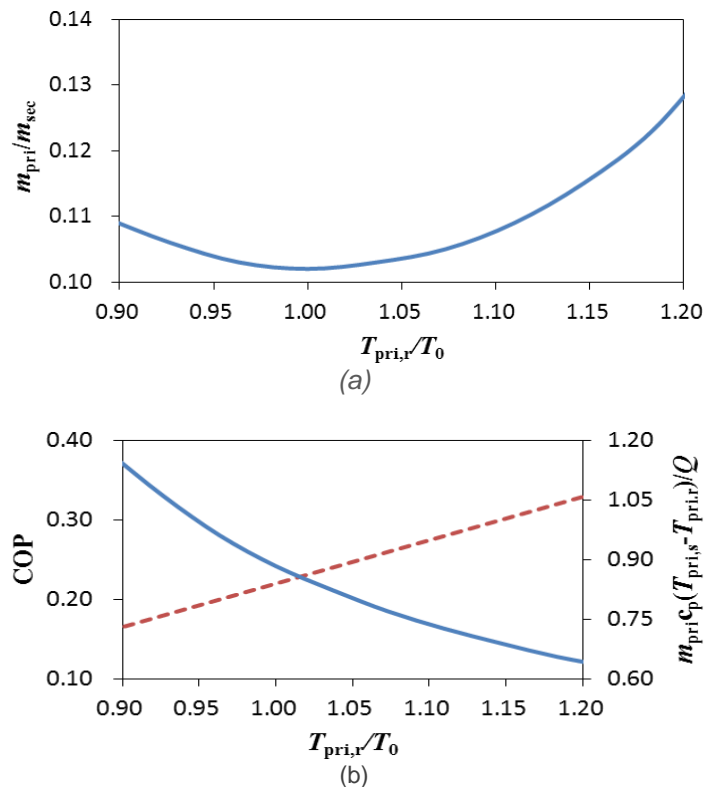
Figure 5: System performance with changing return water temperature: (a) mass flow rate ratio; (b) heating power and COP

3.4. Application

In the aforementioned heat-adaptor-based system, both the heat engine and the heat pump are ideal devices. For heat adaptor 2, it is an open system where heat-work conversion happens between the working fluids and the environment. As Figure 6 shows, the Organic Rankine Cycle (ORC) heat engine, combined with the air-source heat pump, can fulfil the requirement in heat adaptor 2.
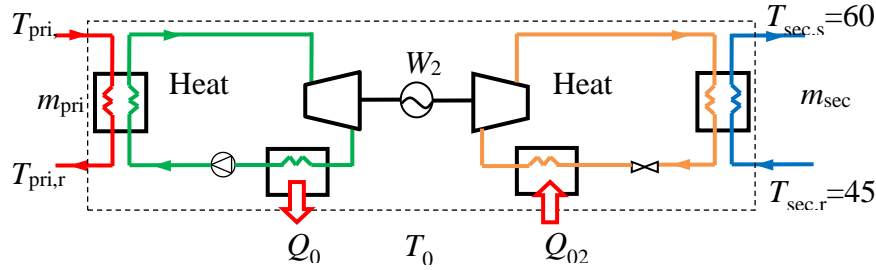
Figure 6: Heat engine and heat pump in heat adaptor 2

However, some other devices are needed in practical engineering field, since there is no ideal heat-work conversion equipment. From the thermodynamic perspective, an absorption heat pump can be regarded as a heat engine combined with a heat pump (Zhang, 2014: Page 276). Hence the heat adaptor 2 can be substituted by the absorption heat pump. Whereas the traditional absorption heat pump cannot be utilized in heat adaptor 1, even though it is also viewed as heat pump and heat engine.

For heat adaptor 1, the industrial waste heat is used as the heat source not only for the heat engine but also for the heat pump. Moreover, the output temperature ($T_{pri,s}$) is higher than the input one (T_{source}), which means that the absorption temperature should be higher than the generation temperature for the absorption cycle, so that absorption heat pump cannot meet such demand. Absorption heat transformer is another form of absorption cycle and used to upgrade the low-grade waste heat (Ma, 2003: Page 798). The main function of absorption heat transformer is to increase the temperature, when the heat source temperature is not high enough to drive the traditional absorption heat pump. Therefore, according to the schematic diagram in Figure 3, the specific process is established in Figure 7 for heat adaptor 1, based on the absorption heat transformer.
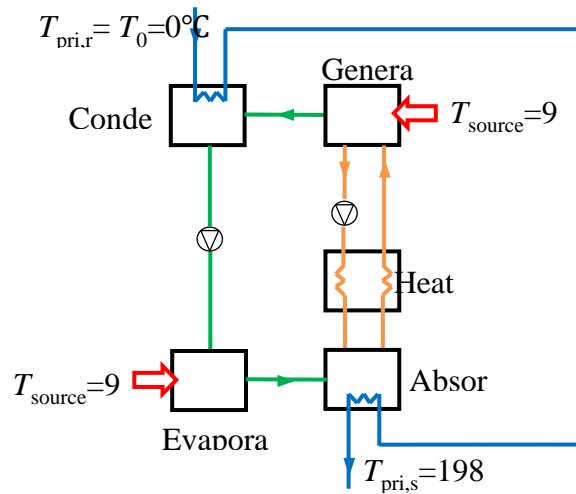
Figure 7: Absorption heat transformer in heat adaptor 2

In Figure 7, the industrial waste heat (T_{source}=363 K) input into both generator and evaporator to drive the absorption cycle. The main difference between absorption heat transformer and absorption heat pump centers on that the refrigerant pump takes the place of throttle valve and the solution pump is set in reverse direction, because the temperature and pressure in absorber and evaporator is higher than that in generator and condenser. Furthermore, the return water in the primary network is heated in series by the condenser and the absorber, since the condensing heat is often taken away by other natural cold sources for most absorption heat transformer. Thus in ideal situation that the irreversible loss is neglected, the water temperature can be increased from 273 K to 471 K, which is much higher than the heat source itself.

4. CONCLUSIONS

In this paper, based the concept of heat adaptor, two different kinds of heat adaptors, absorption heat transformer and absorption heat pump, are used at heat source and substations respectively to take place of heat exchangers in central heating system utilizing the industrial waste heat. Aiming to decrease the mass flow rate in the primary network and save the pump energy consumption, the thermodynamic model

of the heat-adaptor-based system is built and the optimal supply and return water temperatures can be obtained through extreme principle. The illustrative example indicates that the optimal return water temperature just equals the ambient one and the optimal supply water temperature in the primary network is much higher than the waste heat source temperature. The results also show that the delivery pump energy consumption can be decreased by almost 96% for the ideal heat-adaptor-based system when the absorption heat transformer is used, compared to absorption heat exchange system. Although the conclusion may be quite different for non-ideal devices in real applications (e.g., the efficiency of practical Organic Rankine Cycle is much lower than the ideal one), the theoretically ideal system deduced out here is somehow significant for guiding the optimization design of practical central heating systems using industrial waste heat. To emphasize, aimed at maximizing/minimizing objective parameter, the extremum-based optimization method used here should be also applicable if the practical conditions are used. How to apply the new approach to optimize a practical system with non-ideal devices should be an interesting and important topic for future research.

5. ACKNOWLEDGEMENT

6. REFERENCES

ANISH P, Austine A, Paulien H, 2009. Recycling industrial waste heat for sustainable district heating -- a multi-actor perspective. *International Journal of Environmental Technology and Management*, 10(3/4): 412-426.

FANG H, Xia JJ, Zhu K, et al, 2013. Industrial waste heat utilization for low temperature district heating. *Energy Policy*, 62: 236-246.

FU L, Li Y, 2010. A district heating system based on absorption heat exchange with CHP systems. *Frontiers of Energy and Power Engineering in China*, 4(1): 77-83. (In Chinese)

HEITNER KL, Brooks PP, 1982. Industrial-waste heat for district heating. *Energy Engineering*, 79(6): 7-17.

JIA L, Peng XF, Yan Y, et al, 2001. Effects of water vapor condensation on the convection heat transfer of wet flue gas in a vertical tube. *International Journal of Heat and Mass Transfer*, 21 (44): 4257 – 4265.

LI Y, Fu L, Zhang SG, et al, 2011. A new type of district heating system based on distributed absorption heat pumps. *Energy*, 36: 4570-4576.

MA XH, Chen JB, Li SP, et al, 2003. Application of absorption heat transformer to recover waste heat from a synthetic rubber plant. *Applied Thermal Engineering*, 23: 797–806.

Tsinghua University Building Efficiency Research Center, 2014. 2014 Annual Report on China Building Energy Efficiency. Beijing: China Building Industry Press. (In Chinese)

ZHELEV TK, Semkov KA, 2004. Cleaner flue gas and energy recovery through pinch analysis. *Journal of Cleaner Production*, 12 (2): 165 - 170.

ZHANG Y, Shi WX, Zhang YP, 2014. From heat exchanger to heat adaptor: concept, analysis and application. *Applied Energy*, 115: 272-279.

ZHANG Y, Shi WX, Zhang YP, et al, 2015. Application of heat adaptor: thermodynamic optimization for central heating system through extremum principle. The 7th International Conference on Applied Energy, Abu Dhabi.

ZHANG YP, Zhang Y, Shi WX, et al, 2015. A new approach, based on the inverse problem and variation method for solving building energy and environment problems: preliminary study and illustrative examples. *Building and Environment*, in press.

ZHU K, Xia JJ, Jiang Y, 2013. Optimization for industrial waste heat extraction process for central heating system. *HV&AC*, 43(10): 56-60. (in Chinese)

339: Heating and ventilation flow pulsation for energy saving and indoor air quality

M. EMBAYE[1], R. K. AL - DADAH[2], S. MAHMOUD[3]

1 School of Mechanical Engineering,
University Of Birmingham,mxe964@bham.ac.uk
2 School of Mechanical Engineering,
University Of Birmingham, R.K.AL-DADAH@bham.ac.uk
3 School of Mechanical Engineering
University Of Birmingham S.M.MAHMOUD@bham.ac.uk

Heating and ventilation of buildings is the second largest energy consumption after transportation and significantly contribute to the CO_2 emission. The current heating and ventilation systems operate at constant flow strategy with On/Off control which leads to higher energy consumption. Therefore there is a need for alternative ways of operating the heating and ventilation systems so that energy can be saved without compromising the occupant's wellbeing including indoor CO_2 and humidity levels. Flow pulsation has been applied for various applications to enhance heat transfer for heating and cooling appliances. This work mathematically investigates the effect of radiator hot water and inlet air ventilation pulsation for a living room in a 4 bedroom house with 5 occupants to improve the energy consumption and indoor air quality (IAQ) using demand based embedded control system in MatLab/Simulink software. The developed model is targeting to control the indoor air quality and thermal indoor comfort of occupants, including temperature of 20± 2 (OC), CO_2 level of 1000 ± 100 (PPM) and relative humidity of 50± 10 (%). Flow pulsation for both heating and ventilation was applied at flow frequency of 0.016 (Hz) with the amplitudes of the water and air flow pulsation vary depending on heated space environment. Results showed that pulsating the flow of hot water through the panel radiators of the central heating system can achieve an average of 20(%) energy saving compared to the constant flow currently use. Also, using pulsating air flow to the heated space (for ventilation purpose) can achieve energy saving of 34.5% in the fan power consumption of the ventilation system by keeping the level indoor CO_2 concentration and relative humidity at an acceptable level. The significant saving achieved by flow pulsation indicates the potential of using this approach to reduce energy consumption and improve the indoor air quality.

Keywords: Heating and ventilation, flow pulsation, indoor thermal comfort and indoor air quality

1. INTRODUCTION

Energy consumption in buildings in Europe accounts for 40% of primary energy use and 50% of the extracted natural resources according to Energy Performance Buildings Directive 2010/31/EU. This requires efficiency improvements to be implemented in all the new buildings in order to achieve the target of nearly zero energy buildings after 2020. From the 40% energy share for buildings; 60% of the energy demand is used for heating and ventilation system, this can reach 80% if the hot water is added (Mandley et al., 2015, p851). Finding alternative operating condition for the heating and ventilation system that improve the efficiency of the HVAC appliance without compromising occupant's thermal comfort and indoor quality will contribute to the reduction of energy consumption in buildings (Luisa et.al., 2014, p.68). The indoor environmental comfort can be classified into 4 main categories; indoor air quality; thermal comfort, acoustic comfort and visual comfort as shown in figure 1.
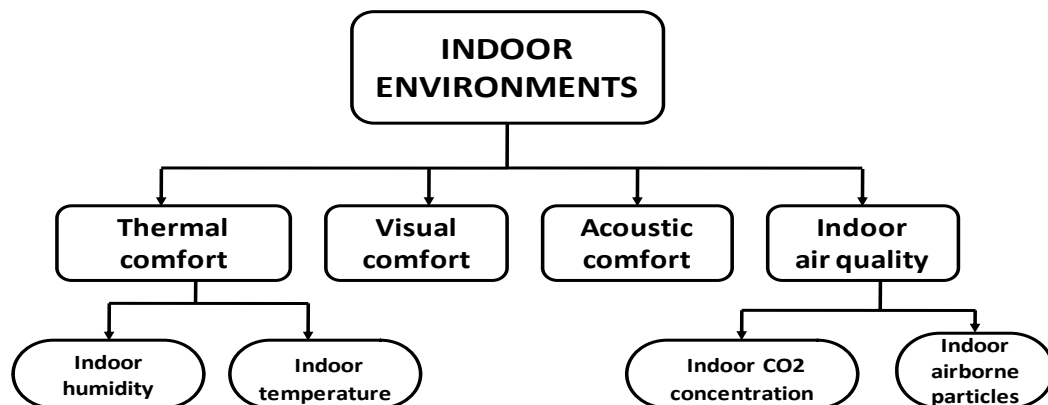
Figure 1: description of the indoor environments

There are various heat transfer enhancement methods including; rough surfaces; nanofluids; fluid slipping enhancers, surface coating, fin attachments, mechanical mixing device, vibration, magnetic fields and flow pulsation (Beck et al., 2004, p.1291; Ploskic et al., 2011, p.176). Flow pulsation is an effective method of heat transfer enhancement applied for various industrial applications including heat exchangers, pulse combustors, electronic cooling devices, cooling system of nuclear reactors. Up to 60% heat transfer enhancement was achieved by applying pulsed flow for different applications (Li et al., 2013; Hamida et al., 2002; p.1767; Jafari et al., 2013, p146).

Investigating the indoor environmental condition of occupants' satisfaction is the most common practice for the thermal indoor comfort and the indoor air qualities perceptions. According to ISO7730, 2005 indoor thermal comfort is defined as state of mind in terms of satisfaction with thermal environment which depends on the individual psychology and physiologies; it can be also defined as the interaction of the air ventilation supply and the heating source of the space to be heated. Indoor air quality is the overall results of the interaction between building volume (envelope) incoming outdoor air; air ventilation system, indoor occupants and contaminant sources (Zhu et al., 2007, p.1711; Sarbu et al., 2013 p.410. (Anna et al., 2014, p.319) investigated experimentally and numerically the effect of CO_2 sensor position used to control the room ventilation system and concluded that positioning the CO_2 sensor at the centre of the room gives accurate measurement of concentration regardless of the room height. The heating ventilation and air conditioning (HVAC) system is designed for extreme condition capacities of the space to be heated or cooled. The load of the buildings envelope scenario keeps changing throughout the day which depends on the occupants, ambient temperature, solar load, lighting and equipment loads. For the case of heating and ventilation appliance the design capacity is always larger than the operating condition of the actual load demand of the heated space. Therefore the deviation from the design leads to imbalance of the occupants comfort and high energy consumption of the buildings if the system is running without appropriate control system (Beghi et al., 2014, p.773). 50% of energy consumption can be saved if the ventilation system of the room is controlled using carbon dioxide (CO_2) concentration response (Warren and Harper, 1991, p.87). Demand based Controlled Ventilation (DCV) was developed to control the level of indoor CO2 concentration and reduce energy consummation. According to the result of the study carried out based on the ASHRAE Standards 62.1 2010 for building about 23% of energy can be saved using the DCV control strategy compared to the traditional control system (Nassif. 2012, p.72). (West et al., 2014, p.271; Liao et al., 2004, p.1013) developed a model predictive control (MPC) system to optimize the thermal comfort, indoor air quality (IAQ) including CO2 and energy consumption of the heating and ventilation system and concluded that about 19% to 32% energy reduction can be achieved.

This work will invigilate the performance of heating and ventilation system at different flow strategies (constant and pulsed flow cases) in terms of energy consumption using embedded control simulation in Matlab/Simulink. The work includes; indoor CO_2 concentration response control, indoor Humidity, and complete central heating system (boiler, panel radiator and room) model. The proposed work aims to save energy by changing the constant flow strategy to pulsed flow for both ventilation and heating systems.

2. MATHEMATICAL MODELLING OF HEATING AND VENTILATION

Figure 2 shows a typical central heating system consisting of heat source (boiler), flow distribution components (circulation pump, valves, and pipes), heat emitter (panel radiator), heated or conditioned space (room). Heat sources other than the radiator are; solar heat gain and internal gain (light, occupants and computers). The main heat losses from the proposed room are; heat loss by ventilation, heat loss through the window, and heat loss through building structure. Each of the components are modelled mathematically as individual and then compiled to represent an integrated central heating system. All the indoor conditions including temperature, humidity level, and CO2 concentration are calculated dynamically using the mass and energy balance equations.
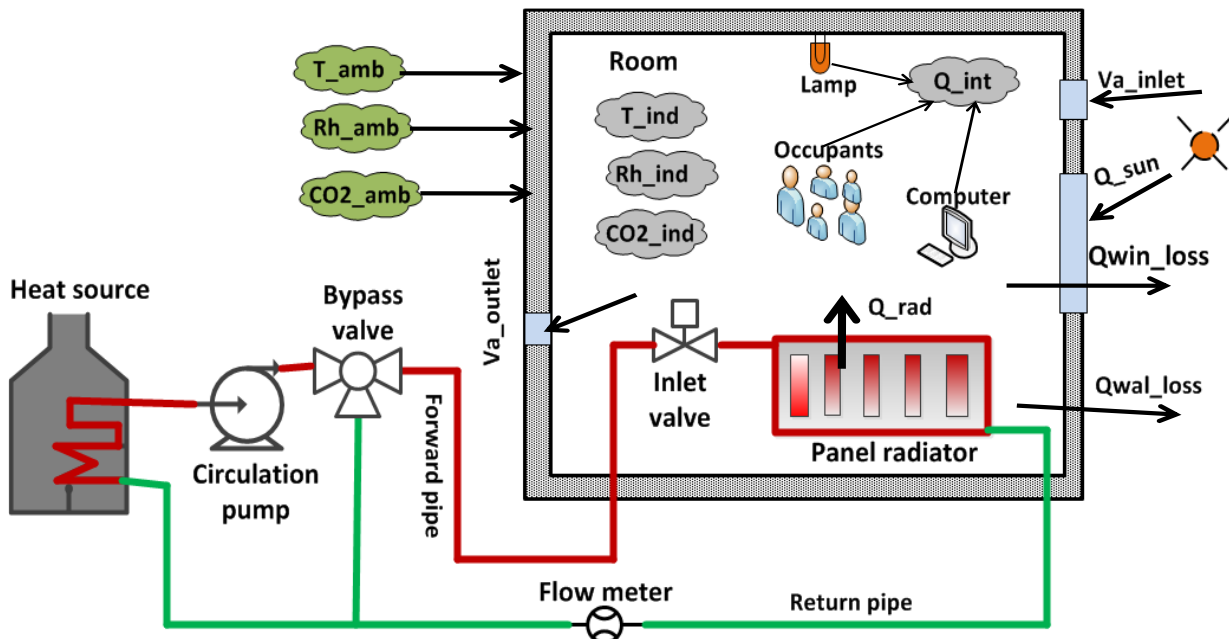
Figure 2: schematic description of the central heating system for proposed work

2.1 Indoor temperature model

The indoor comfort temperature can be calculated dynamically using energy balance equations by integrating the boiler (heat source), radiator (heat emitter), room envelope (heat gains and loss), and ventilation system (heat loss).

The boiler heat balance is expressed using equation 1 to 3 based on the 90% efficiency from the manufacturer for Combi-boiler with stainless steel heat exchangers, (Georgina, 2009; White, 2010, p.22)

$$\dot{Q}_b = \dot{m}.C_p.(T_{out} - T_{in}) \tag{1}$$

$$(MCp)_{hex} + (MCp)_w \cdot \frac{d}{dt}\left(\frac{T_{in} + T_{out}}{2}\right) = \eta * Q_b - \dot{m}.C_p.(T_{out} - T_{in}) \tag{2}$$

$$T_{out} = 2\int\left(\frac{\eta .Q_b}{(MCp)_{hex} + (MC_p)_W} - \frac{\dot{m}.C_p}{(MCp)_{hex} + (MC_p)_W}(T_{out} - T_{in})\right)dt \tag{3}$$

Where: $\dot{Q}$, η, M, T, C_p, $\dot{m}$, t, b, hex, out, in, w, are heat output rate (W); efficiency (%) mass (kg) Temperature (°C), specific heat capacity respectively, mass flow rate (kg/s), time (s), boiler, heat exchanger, outlet, inlet, and water respectively. T

The heat balance of the heat emitter (hydronic panel radiator) is expressed using equations 4 to 7.

$$\dot{Q}_s = \dot{m}_w . C_w . \left(T_{rad,in} - T_{rad,out} \right) \qquad (4)$$

$$\dot{Q}_{rad} = U_{rad} A_{rad} (LMTD) \qquad (5)$$

Where :

$$\frac{1}{U_{rad}} = \frac{1}{h_{rad,in}} + \frac{L_{rad}}{k_{rad}} + \frac{1}{h_{rad,out}}$$

$$LMTD = \frac{T_{rad,\,in} - T_{rad,\,out}}{\ln\left(\dfrac{T_{rad,\,in} - T_{ind}}{T_{rad,\,out} - T_{ind}} \right)}$$

$$\left(C_{p,rad} M_{rad} + C_{p,w} M_w \right) \frac{d}{dt} \left(\frac{T_{rad,\,out} + T_{rad,\,in}}{2} \right) = C_{p,w} \dot{m}_w (T_{rad,\,in} - T_{rad,\,out}) - U_{rad} A_{rad}(LMTD) \qquad (6)$$

$$T_{rad,out} = 2 \int \left(\frac{C_{p,w} m_w}{C_{p,rad} M_{rad} + C_{p,w} M_w}(T_{in,rad} - T_{rad,out}) - \frac{h_{rad} A_{rad}}{C_{p,rad} M_{rad} + C_{p,w} M_w}(LMTD) \right) dt$$

(7)

Where: A, $\dot{Q}$, k, L, LMTD, M, h, U, T, C_p, $\dot{m}$, t, s, rad out, in, ind and w area (m²) heat rate (W) thermal conductivity (W/m.K), thickness (m), log mean temperature difference in (°C), mass (kg), local heat transfer coefficient (W/m².K), over all heat transfer (W/m².K), temperature (°C), specific heat capacity (J/kg.K), mass (kg/s), time (s), supply, radiator, outlet, inlet, indoor and water respectively.

The heat loss through the room envelope, heat loss and heat gain through the window, internal heat gain, and heat loss due to ventilation (sensible and latent heat loss) are mathematically calculated using equations 8 to 14.

$$\dot{Q}_{wi} = A_{wi} U_{wi}(T_{so} - T_{ind}) + I.SHGC.A_{wi} \qquad (8)$$

Where :

$$T_{so} = T_{amb} + \frac{\alpha.I}{h_{amb}}$$

$$\dot{Q}_{env} = (UA)_{wall}(T_{ind} - T_{amb}) + (UA)_{roof}(T_{ind} - T_{amb}) + (UA)_{floor}(T_{ind} - T_{soil}) \qquad (9)$$

Where :

$$U = \frac{1}{R_{tot}} \quad and \quad R_{tot} = \frac{1}{h_{ind}} + \sum_0^j \frac{L_j}{k_j} + \frac{1}{h_{amb}}$$

$$\dot{Q}_{s,vent} = \rho_a . \dot{V}_a . C_{p,a}.(T_{ind} - T_{amb}) \qquad (10)$$

$$\dot{Q}_{l,vent} = \rho_a . h_{fg} . \dot{V}.(\omega_{in} - \omega_{amb}) \qquad (11)$$

Where :

$$\dot{V} = \frac{ACH.V_{rm}}{3600}$$

$$\dot{Q}_{int} = People + computer + electrical\ light \qquad (12)$$

$$V_{rm} . \rho_a C_{p,a} d \frac{Trm}{dt} = \dot{Q}_{rad} + \dot{Q}_{gain} - \dot{Q}_{l.vent} - \dot{Q}_{s.vent} - \dot{Q}_{env} - \dot{Q}_{win} \qquad (13)$$

$$T_{rm} = \int \frac{1}{V_{rm} . \rho_a C_{p,a}} (\dot{Q}_{rad} + \dot{Q}_{gain} - \dot{Q}_{s.vent} - \dot{Q}_{l.vent} - \dot{Q}_{env} - \dot{Q}_{wi}) dt \qquad (14)$$

Where: $\dot{Q}_{env}$, $\dot{Q}_{wi}$, A, U, T_{so}, T_{ind}, T_{amb}, I, SC, α, h_{amb}, h_{ind}, k_j, L_j, R_{tot}, ω_{in}, ω_{amb}, h_{fg}, $\dot{V}$, $\dot{Q}_{s,vent}$, $\dot{Q}_{l,vent}$, $\dot{Q}_{int}$, Vrm, $\dot{V}$, ρ, Cp, a and ACH, are heat loss by room envelope (W), heat of window (W), surface area (m²),

over all heat transfer coefficient (W/m^2·K), solar temperature (^{o}C), indoor temperature (^{o}C), outdoor temperature (^{o}C), solar heat flux (W/m^2), solar heat gain coefficient (0.87), absorbance of surface or solar radiation (-), outdoor heat transfer coefficient (W/m^2·K), indoor heat transfer coefficient (W/m^2·K), thermal conductivities of jth wall (W/m.K), thickness of jth wall (m), total thermal resistance (K.m^2/W), indoor specific humidity (kg/kg), outdoor specific humidity (kg/kg), heat vaporization of water (kJ/kg), sensible heat ventilation and latent heat of ventilation (W), internal gain (W), volume of room (m^3), volume flow rate (m^3/s), density (kg/m^3), specific heat capacity (kJ/kg), air and air change (1/hr) respectively .

2.2 Indoor humidity level model

According ASHRAE 55-1992 relative humidity (RH) is defined as the presence of water vapour in air that can cause discomfort for the indoor occupants (Rodrigues and Gomes, 2014, p.53). To avoid the discomfort due to indoor humidity; it is recommended that humidification processes is required in order to keep indoor air relative humidity at the range of 25%- 60%. Humidity can be defined as specific humidity, absolute humidity and relative humidity and it is represented mathematically using mass balance equations 15- 20.

$$P_{s,amb} = \frac{e^{\left(77.345 +0.0057T_{amb} - \frac{7235}{T_{amb}}\right)}}{T_{amb}^{8.2}} \quad (15)$$

$$\omega_{amb} = \frac{0.622.Rh_{amb}.P_{s,amb}}{P_{atm}-(Rh_{amb}.P_{s,amb})} \quad (17)$$

$$P_{s,ind} = \frac{e^{\left(77.345 +0.0057T_{ind} - \frac{7235}{T_{ind}}\right)}}{T_{ind}^{8.2}} \quad (16)$$

$$Rh_{ind} = \frac{\omega_{ind}.P_{atm}}{P_{s,ind} - (\omega_{ind} + 0.622)} \quad (18)$$

$$\rho V_{rm} \frac{d\omega_{ind}}{dt} = (M_{fresh})(\omega_{amb} - \omega_{ind}) + M_{pp} + M_{add/rev} \quad (19)$$

$$\omega_{ind} = \int \frac{(\dot{m}_{fresh})(\omega_{amb} - \omega_{ind}) + M_{pp} + M_{add/rev}}{\rho_a V_{rm}} \quad (20)$$

Where: Rh, ω , $\dot{m}$, $P_{s,ind}$, V_{rm}, $P_{s,amb}$, M_{pp}, $M_{add/rev}$,T and P_{atm} are; relative humidity (%), specific humidity (kg/kg), mass flow rate of air (kg/s), indoor saturation pressure (Pa), volume of the room (m^3), saturation pressure of the ambient air (Pa), moisture generation rate from occupants (kg/s), moisture generated by conditioning added or removed (kg/s), temperature (^{o}C), and atmospheric pressure (Pa) respectively.

2.3 Concentration of CO2

Indoor CO_2 concentration is an indicator of the indoor air quality which is recommended to be 1800kg/m^3 (1000ppm) and also the CO_2 concentration difference of the indoor air and outdoor air should be about 700PPM with outdoor ranges from 350 to 400 PPM (White, 2010, p.22). ASHARAE also predicted higher ventilation than the recommended flow rate; if the indoor heat gain is not compensated by air cooling supply. The metabolic rate (Met) of occupants which depends human activities vary form 0.005l/s (1 Met) to 0.01l/s (2Met) (Sougan and Damiano, 2004, p.47). Indoor CO_2 concentration can be modelled using mass balance expressed in equation 21 and 22.

$$V_{rm} \frac{dC_{ind}}{dt} = G + \dot{V}C_{out} - \dot{V}C_{ind} \quad (21)$$

$$C_{ind} = \int \left(\frac{G + \dot{V}C_{out} - \dot{V}C_{ind}}{V_{rm}}\right) dt \quad (22)$$

Where: C_{ind}, C_{out}, G, and $\dot{V}$ are indoor CO_2 concentration (PPM), outdoor CO_2 concentration (PPM), human CO_2 generation rate (PPM).

3. MATLAB/SIMULINK MODELLING

In this work a living room(salon) with 5 people inside was considered with dimensions of 4m width, 5m length, 2.7m high and 2*1.5m^2 of window. A typical UK winter average ambient temperature, relative humidity, and CO_2 was applied at 5°C, 80% and 400PPM respectively. ASHRAE 62-1999 recommended an acceptable ventilation flow rate of 7.5 l/s per person and 0.6l/m^2 of floor area in the occupied zone. The recommended ventilation flow rate is able to dilute the CO2 generated by respiration of the occupants and remove air born contaminates as well as supply adequate oxygen to the occupants of the room. The model was a typical central heating system using radiator as heat emitter and controlled fan ventilation fresh air system. The work present was aimed to investigate the indoor thermal comfort condition and indoor air quality (IAQ) including humidity, temperature and CO_2 concentration. The room was modelled base on inlet mass flow rate for the radiator hot water, fan ventilation fresh air at constant flow strategy and pulsed flow strategy. Thus results are investigated the indoor comfort level and the energy saving due to the pulsed flow compared to the constant flow cases. Table 1 and Figure 3 represent the thermal properties of the materials for the proposed room and the inlet mass flow profiles respectively. The hot water supply to the radiator was applied at 0.024 (kg/s) for constant flow case. And average flow rate of 0.0192(kg/s) at flow amplitudes of 0.0384 (kg/s), and frequency 0.016 (Hz) was applied for the radiator pulsed flow case. The fresh air supply to the ventilations fan was applied at 10 (l/s) per person for constant flow case. And average flow rate of 6.6 (l/s) per person at flow amplitudes of 13.2 (l/s) and flow frequency of 0.016 (Hz) was applied for the ventilation at pulsed flow case.

Table 1 the thermal properties of buildings materials and hydronic panel radiator heater used for this work

Components	Materials	K [W/m.K]	c [J/kg.K]	U [W/m^2.K]	ρ[kg/m^3]	UA [W/K]
Internal wall	Plasterboard	0.16	840	0.35	950	13.23
External wall	Brick	0.77	800	0.86	1700	9.3
Window	Glass	0.96	750	3.1	2400	9
Floor	Screed	0.41	840	0.35	1200	7
Ceiling	Wood wool	0.10	1000	0.3	500	6
Radiator	Steel (AISI 316)	205	900	8.5	2700	18.7
Room envelope	Air	0.025	1005	-	1.2	-
Door	wood	0.14	1200	-	650	-
working fluid	Water	-	4180	-	1000	-

(a)   (b)
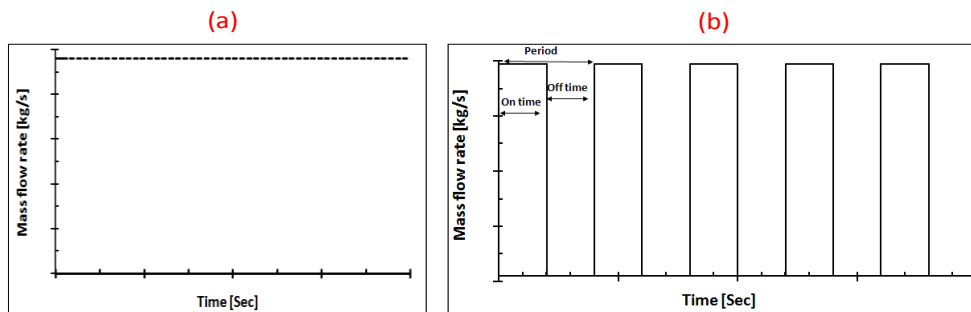
Figure 3 (a) the constant inlet mass flow profiles and (b) pulsed flow inlet mass flow rate profile of the proposed work for the heating and ventilation appliances

Figure 4 shows the complete integrated model developed in Simulink embedded user defined function. The developed model include room model, boiler model, radiator model and the PID control system to manipulate the indoor temperature, humidity and CO_2 level at constant and pulsed flow cases.
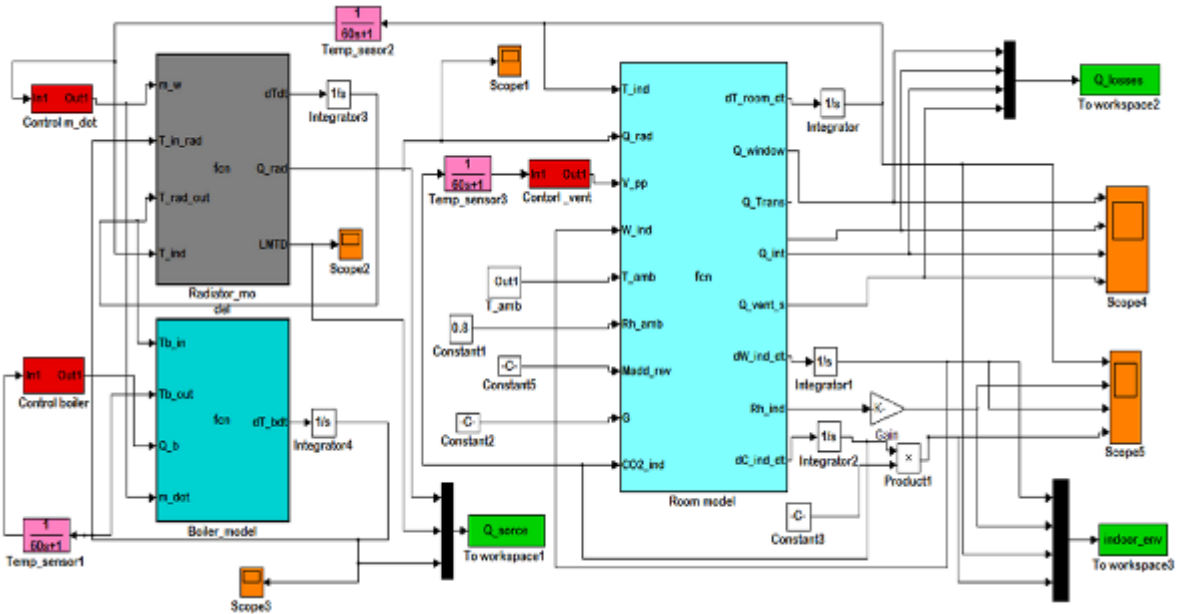
Figure 4 the MatLab/Simulink model of the proposed room for the constant and pulse flow cases

4. SIMULINK RESULTS OF ROOM MODEL AT CONSTANT AND PULSED FLOW CASES

Results are analysed based on the indoor thermal comfort (temperature and humidity), indoor air qualities (CO_2 concentration) and the associated energy saving due to flow pulsation compared to the constant flow. Energy saving was analysed based on the ratio of heat output rate for heating and ventilation to the inlet average mass flow rate supply of hot water and fresh air (rate of specific heat output). Figure 5 shows the boiler outlet temperature (inlet to the radiator) and the log mean temperature difference (LMTD) of the radiator for both pulsed and constant flow cases. As shown in figure 5a 75 (^{o}C) of average boiler outlet temperature is achieved and also in figure 5b the LMTD of the radiator is 50 (^{o}C) is achieved, results are complied with the criteria of BS EN 442 radiator standards.
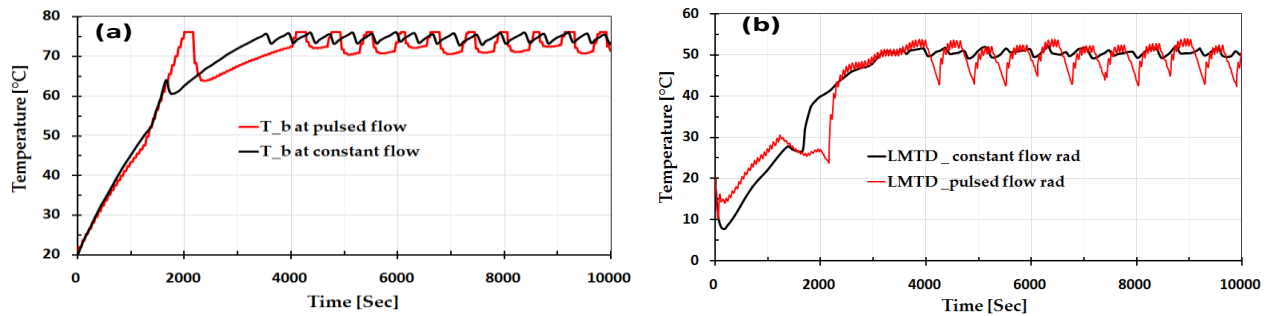
Figure 5 (a) Boiler outlet temperature and (b) LMTD of the panel radiator for both constant and pulsed flow cases

Figure 6 shows the heat output of the radiator at constant and pulsed flow cases and the specific heat output of the corresponding values. As shown in figure 6(b) the specific heat output of the radiator at pulsed flow is higher compared to the constant flow trend. The higher the specific heat output; the lower the hot water mass supplied to the radiator and then results lower energy consumption for the heating system. This clearly highlights the potential of flow pulsation to enhance the panel radiator of heating system.
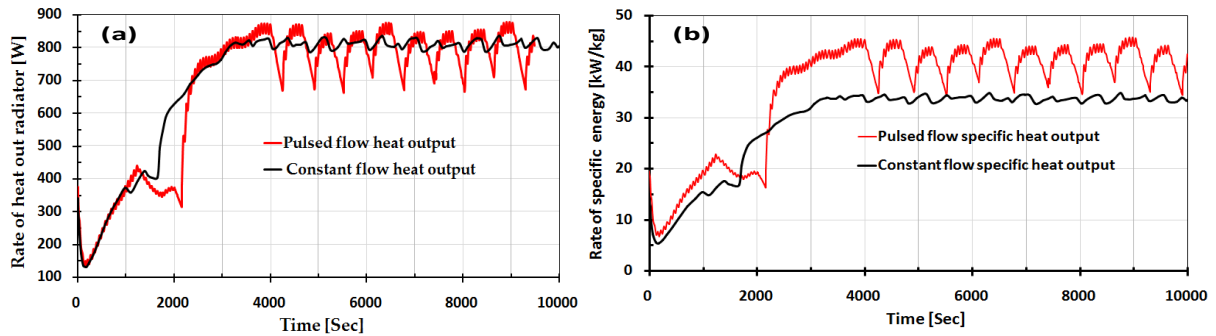
Figure 6 (a) rate of heat output of the radiator (b) specific heat output ofradiator

Figure 7 shows the internal heat gain form computer, human being, electrical equipment, and also the heat loss due to the building structure and heat loss through the window glazing. The internal gained was assumed as a constant supply of heat to room according ASHRAE; a seated person can release about 100W and sensible heat to the room and also the electrical equipment contribute about 200W overall total energy of 700W of heat was gained internally. The heat loss through the window and building structure depends on the outdoor temperature.
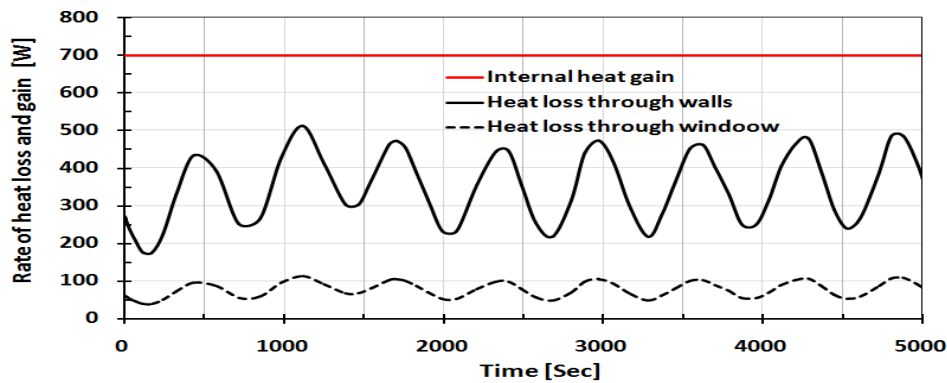
Figure 7 the internal heat gain, heat loss due to building structure and heat loss through windows

Figure 8 shows the heat loss due to ventilation for both constant flow and pulsed flow cases. The energy consumption for ventilation of space depends on the mass flow rate of fresh air to the fan and hence higher is the specific heat of the ventilation (energy density), the lower is the mass flow rate of fresh air that leads to lower energy loss by ventilation. The specific heat of the ventilation trends shown in figure 8b clearly highlights the potential of applying flow pulsation in saving energy for ventilation compared to the constant flow cases.
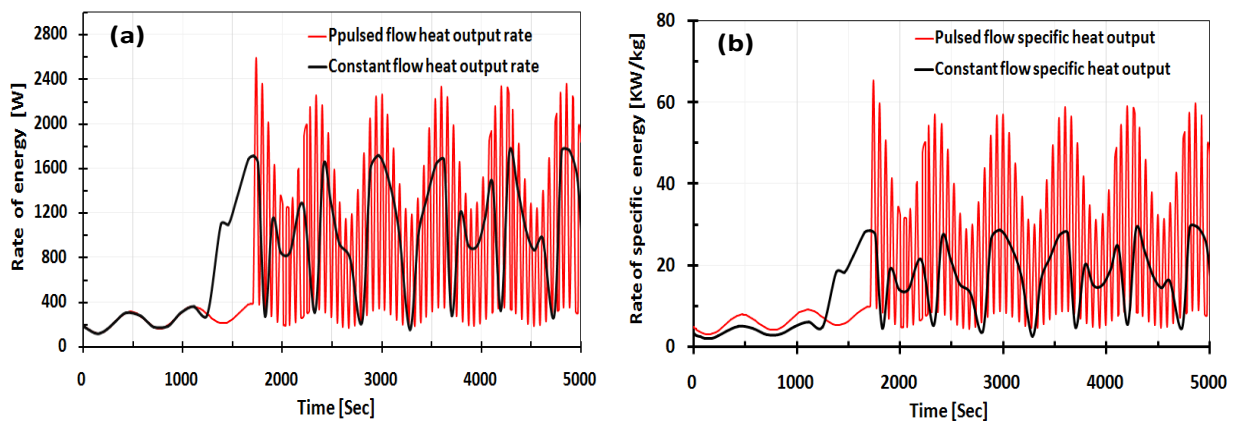
Figure 8 (a) ventilation rate of energy output and (b) ventilation specific energy rate

Figure 9 shows the indoor environment of the proposed room including the temperature profile, relative humidity and CO2 concentration. Saving energy in building must not compromise the occupants comfort at any time and hence in this model the comfort level of indoor environment was carefully analysed and the proposed pulsed flow strategy is targeted the energy consumption reduction without compromising the occupants wellbeing.   Based on that all results are fulfilled the indoor comfort standard of ISO 7730-2005, ASHRAE 55-1992, and ASHRAE 62-1999 which are adapted by the international community of building service. According the results gained from the Simulink model for this work the indoor temperature achieved at 20±1.5 in (ºC), indoor relative humidity of 50 +5 in (%) and the indoor CO_2 concentration of 1000±50 in (PPM).
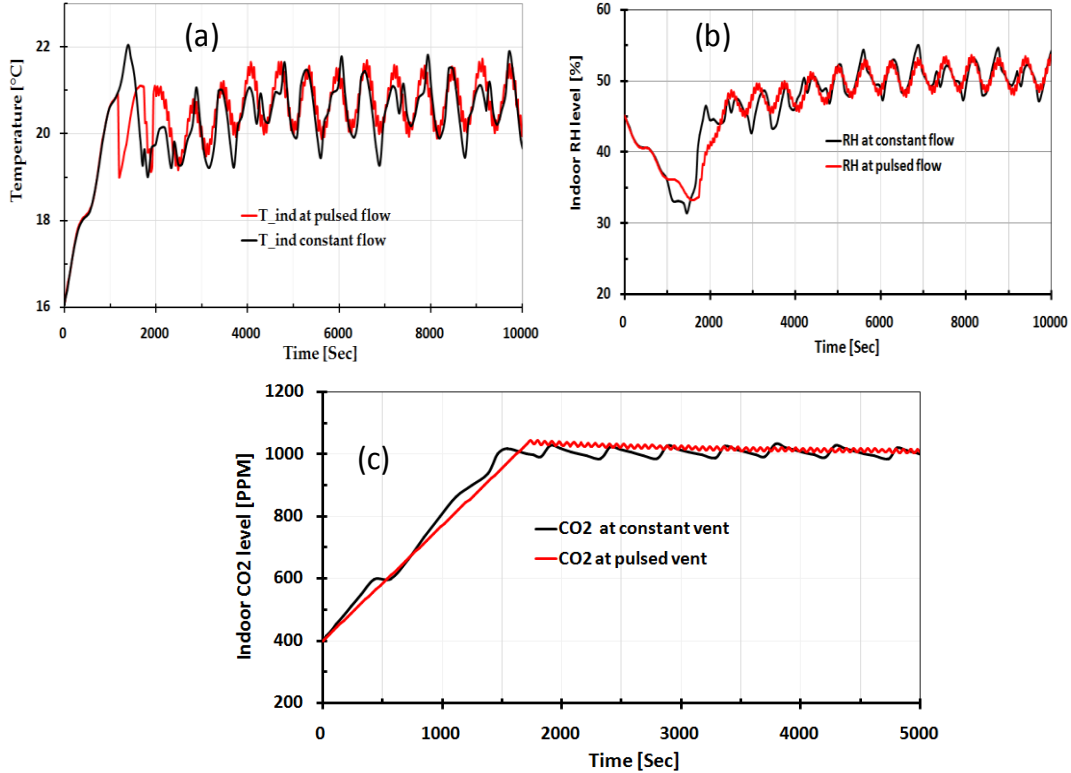
Figure 9 (a) indoor temperature, (b) indoor humidity and (c) indoor CO2 concentration

In figure 10 the energy saving or reduction of energy consumption was shown based on the energy density (specific heat energy) produced by the heating radiator and ventilation fan. The driving force for energy consumption in heating and ventilation system is the mass flow rate and hence the energy saved in percentage due to the applied pulsed flow case compared to the constant flow case is calculated using equation 23.

$$ES = (\frac{\dot{m}_{CF} - \dot{m}_{PF}}{\dot{m}_{CF}}) \times 100 \qquad (23)$$

Where: $\dot{m}_{CF}$ the mass flow rate of air and hot water (kg/s) at constant flow cases, $\dot{m}_{PF}$ mass flow rate air and hot water at pulsed flow cases (kg/s) and ES (%) is the energy saving. According the obtained results about 20% of energy can be saved for the heating radiator and 34.5 % for the ventilation fan by applying the pulsed flow case without affecting the occupants comfort zone. The presented work results clearly highlight the potential of using flow pulsation to enhance the specific heat output of the heating and ventilation systems and hence saving significant amount of energy in the building service industries.
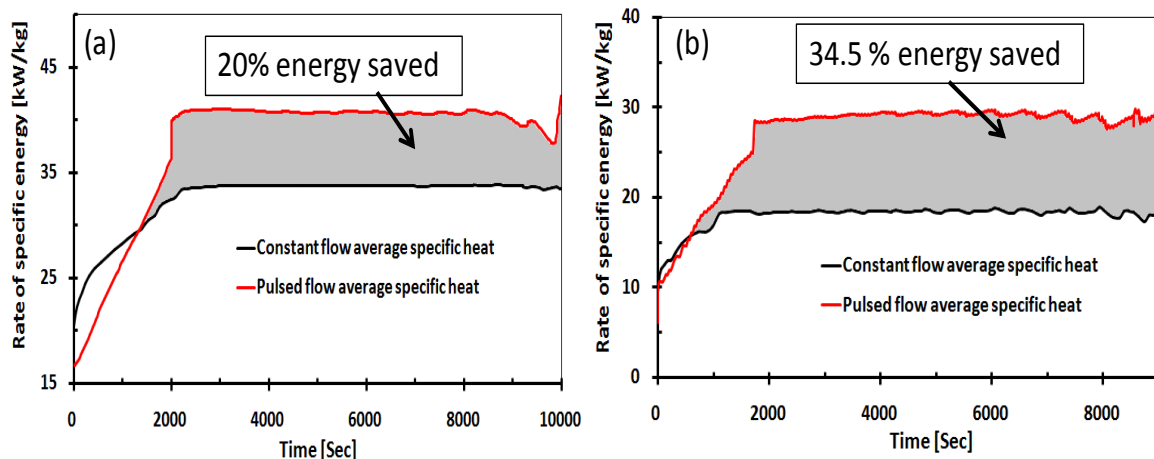
Figure 10 the saved energy due pulsed flow compared to the constant flow case (a) saved for heating and (b) saved energy for ventilations

5. CONCLUSION

This work mathematically investigates the effect of flow pulsation for radiator hot water and fan inlet air ventilation applied for a living room of 4 bedroom house with 5 occupants on energy consumption. A demand based embedded control system was developed using MatLab/Simulink software to assess the indoor thermal comfort and indoor air quality (IAQ). The developed model aimed to control the indoor air quality and thermal indoor comfort of occupants, including temperature of 20± 2 (^{O}C), CO_2 level of 1000 ± 100 (PPM) and relative humidity of 50± 10 (%) [3]. Flow pulsation for both heating and ventilation was applied at flow frequency of 0.016 (Hz) with the amplitudes of the water and air flow pulsation vary depending on heated space environment.

Results showed that using flow pulsation in hydronic panel radiators based central heating system can achieve an average of 20 (%) energy saving compared to the constant flow currently use. Also, using pulsating air flow to the heated space (for ventilation purpose) controlled on the basis of indoor CO_2 concentration achieved energy saving of 34.5% from the fan power consumption. The demand based proposed control system on the basis of indoor CO_2 concentration is able to keep indoor air qualities (CO_2) and indoor relative humidity at an acceptable level of 1000±50 PPM and 50±5 % respectively. The significant saving achieved by flow pulsation indicates the potential of using this approach to reduce energy consumption and improve the indoor air quality for buildings.

6. REFERENCES

ANNA B., Zbigniew P., Zbigniew B. (2014) Experimentally validated CFD analysis on sampling region determination of average indoor carbon dioxide concentration in occupied space. Building and Environment, 72, pp. 319-331.

BECK S.M.B., Grinsted S.C., Blakey S.G. and Worden K. (2004) Novel design for panel radiators. Journal of applied Thermal Energy, 24, pp. 1291–1300.

BEGHI A., Cecchinato L., Rampazza M. and Simmini F. (2014) Energy efficiency control of HVAC systems with ice cold thermal energy storage. Journal of process control, 24, pp.773-781.

GEORGINA O. (2009), In-situ monitoring of efficiencies of condensing boilers and use of secondary heating, Department of Energy and Climate Change. Available from https://www.gov.uk/government [accessed 20/04/2015]

HAMIDA H.N., Sabry M.N., Abdel-Rahim A. and Mansour H. (2002) Theoretical analysis of heat transfer   in laminar pulsating flow. International Journal of heat and mass transfer, 45, pp.1767-1780.

JAFARI M., Farhad M., Sedighi K. (2013) Pulsating flow effects on convection heat transfer in corrugated channel. Heat and Mass transfer, 45, pp.146-154.

LI G., Zheng Y., Hu G. and Zhang Z. (2013) Experimental investigation on heat transfer enhancement   from an inclined heated cylinder with constant heat input power in infrasonic pulsating flows. ETF.

LIAO Z. and Dexter A.L. (2004) A simplified physical model for estimating the average air temperature in   multi-zone heating systems. Building and Environment, 39, pp. 1013 – 1022.

LUISA P.D., Daniela R., Paolo S. C. and Manuel G. S. (2014) Assessment of indoor air quality and   thermal comfort in Portuguese secondary class rooms: Methodology and results. Building and environment, 81, pp.69-80.

MANDLEY S., Harmsen, R. and Worrell E. (2015) Identifying the potential for resources and embodied energy savings within the buildings sector. Energy and Buildings, 86, pp 841–851.

NASSIF N. (2012) A robust CO2 based demand controlled ventilation control strategy for multi-zone HVAC systems. Energy and Buildings, 45, pp. 72-81.

OLAYIWOLA B. and Walzel P. (2008) Cross-flow transport and heat transfer enhancement in laminar pulsed flow. Chemical Engineering and Processing, 47, 929-937.

PLOSKIC, A. and Holmberg S.(2011) Low temperature baseboard heaters with integrated air supply analytical and numerical investigations. Energy and Environment 46, pp. 176-186.

RODRIGUES A.N. and Gomes M. G. (2014) Natural ventilation of room with atmospheric-vent water heater in both on-and off-states. Energy and Buildings, 74, pp. 53-60.

SARBU I. and Sebarchievici C. (2013) Aspect of indoor environmental qualities assessment in buildings. Energy and Buildings, 60, pp.410-419.

SOUGAN D.S. and Damiano L. (2004) CO2-based demand control ventilation (DCV). ASHRAE Journal, pp. 47-53.

WARREN B. F. and Harper N. C. (1991) Demand controlled ventilation by room C02 concentration: a comparison of simulated energy savings in an auditorium space. Energy and Buildings, 17, pp. 87-96.

WEST S.R., Ward J.K. and J. Wall. (2014) Trial results from model predictive control system and optimization system for commercial building HVAC. Building and Energy, 72, pp. 271-279.

WHITE. A. S. (2010) Simulation of Domestic Boiler Control. International journal of simulation system science and technology, 11, pp. 22-32.

ZHU C., Li N., Re D. and Guan J. (2007) Uncertainty in indoor air quality and grey system method. Building and environment, 42, pp. 1711-1717.

23: Experimental investigation of CO2 gas cooler/condenser in a refrigeration system

KONSTANTINOS M. TSAMOS[1], YUNTING [1], IDEWA SANTOSA[1], SAVVAS TASSOU[1]

[1] *RCUK National Centre for Sustainable Energy Use in Food Chains, Brunel University, Kingston Lane, Uxbridge, UB8 3PH, UK, Konstantinos.Tsamos@brunel.ac.uk*

Natural refrigerants including CO2 have been recognized as the most promising working fluids and have been widely applied in refrigeration systems over the last decade. Owing to its attractive thermo-physical properties and negligible environmental impact, the CO2 refrigerant can be used as a replacement for convectional HFC working fluids. Normally, CO2 refrigeration systems can be classified into three different groups as indirect, cascade and all CO2 transcritical booster structures. The CO2 booster system has some advantageous over the others in terms of functions and sizes etc. However, the performance of such system still requires further investigation and improvement.

This study focused on the experimental investigation into the performance comparison of two CO2 finned-tube gas coolers/condensers with different design structures and their effects on the overall performance of a CO2 booster refrigeration system. The integrated CO2 booster refrigeration system consisted of two variable speed semi-hermetic compressors, a gas cooler/condenser, a liquid receiver, electrically operated expansion valves, a medium temperature display refrigeration cabinet and an additional water/glycol load. The refrigeration system and especially the CO2 gas cooler/condenser had been comprehensively instrumented to enable detailed monitoring of the system and the heat exchanger at different operating states. Results for the system performance were obtained and analysed for different CO2 gas coolers/condensers. The results include the effect of heat exchanger designs and fan operations on the system performance. In addition, the controls of supercritical and subcritical pressures and cooling capacity are described.

Keywords: heat exchanger, CO2 booster refrigeration system, COP, optimal designs, control strategies

1. INTRODUCTION

Refrigeration technology is an essential utility used in the food retail sector to ensure proper merchandising and safety of the food products by enabling the long-term storage for frozen foods and short-term storage for chilled foods. Two temperature levels are required in the food retail sector for frozen and chilled products -18°C to -35°C for frozen and -1°C to 7°C for chilled. Due to the huge amount of the refrigerant fluids used to cover the needs of food storage, the vapour compression refrigeration systems are responsible for greenhouse gas emissions (GHG) to the environment. The GHG emissions from refrigeration systems can be split into two main categories: direct and indirect emissions. The direct emissions are created by leakage of refrigerant with high global warming potentials (GWP) such as fluorocarbons including the HFC's. On the other hand, the indirect emissions produced from the energy required to operate the refrigeration systems (Tassou, 2011). Therefore, reducing both direct and indirect emissions is become an important objective for the researchers and public companies around the world. Potential actions to reduce the indirect emissions are reported including the new guidance for buying new refrigeration equipment with low cost indirect emissions, more sophisticated performance information for new large systems and preparation of guidance on indirect emissions reduction opportunities for existing systems (DEFRA-SKM Enviros, 2011). The actions can be taken to reduce the direct emissions divided into two sections for existing and new system installations. The suggested actions for the existing systems include the regularly maintenance of the equipment used. For the new installation system the use of more environmental friendly refrigerants such as CO_2 is recommended (DEFRA-SKM Enviros, 2011). CO2 is an ozone friendly substance with zero Ozone Depletion Potential (ODP), negligible direct Global Warming Potential (GWP<1), non-toxic and non-flammable. Along with the excellent environmental characteristics, the CO2 has favourable thermo-physical properties in terms of higher density, specific heat, volumetric cooling capacity, latent heat and thermal conductivity. The use of CO2 as a refrigerant create a great opportunities to eliminate entirely the direct GHG emissions to the atmosphere and diminish potentially the indirect effects by optimising the system designs and operations. The CO2 has 28 times higher density than the ammonia and 7 times higher than R-134a at the same temperature. The high gas density of CO2 enables a greater cooling capacity to be achieved comparing with other refrigerants for the same volume flow. This allows the use of smaller suction pipes and smaller compressor size. The use of smaller compressor decrease indirect emissions of the system (Pearson, 2014).

In the application of CO_2 as a refrigerant to food retail refrigeration systems, a number of different design approaches can be adopted that fall into three major categories: indirect/secondary, subcritical cascade systems and all-CO2 system. For an indirect system, the CO2 is commonly used as a two-phase secondary coolant while a HFC refrigerant such as R404A is conventionally charged in the primary side. The performance characteristics of the R404A indirect system using CO2 as a secondary refrigerant has been analysed experimentally and the optimum design parameters for this particular system was discuss (Yoon, 2014). In a cascade layout, the system constitutes of two single stage sub-systems, integrated by a cascade heat exchanger. The CO2 is applied in the low cascade side while a working fluid such as R404A, NH3 or hydrocarbon is operated in the high cascade side. The performance of subcritical cascade systems in supermarket applications has been reported by a number of investigators (Hinde, 2009). The performance of an ammonia/CO2 cascade refrigeration system for a supermarket application has been theoretically and experimentally investigated. The authors have reported that the cascade arrangement could provide better COP compared to a conventional R-404A system (Sawalha, 2006). All-CO2 system, the CO2 refrigerant is the only working fluid employed without need of a second refrigerant on the high pressure side. The main advantages of the CO2 booster system over other ones include the simpler design requirements, less installation cost and less environmental impacts from the refrigerant leakage comparing with cascade systems use a HFC's as a secondary fluid. However, the CO2 as a working fluid has a quite low critical temperature of 31.1°C and very high critical pressure of 73.8 bar. Consequently, the CO2 operates in relatively high pressure comparing with other refrigerants. In case the ambient temperature is higher than the critical temperature, the CO2 is not condensate in the high pressure-side of the system. The high pressure-side in the system can thus act as either a condenser or gas cooler depending on the ambient conditions. This necessitates high pressures which can lead to high power consumption. Therefore, the pressure of the gas cooler becomes very important operating parameters which need to be controlled in order to obtain best performance of the system. To understand the performance of a CO2 air cooled gas cooler, a series of tests were conducted at different operating conditions using a purposely designed test facility (Hwang, 2005). The effects of air and refrigerant side flow parameters on the heat exchanger heat transfer and hydraulic behaviours were examined. In addition, the temperature profiles along the heat exchanger circuit pipes were measured. Apart from the overall performance investigations of the CO2 gas coolers, the in-tube cooling processes of CO2 supercritical flow were extensively tested and correlated, which is helpful to understand the CO2 heat transfer and hydraulic behaviours in the heat exchangers

(Srinivas, 2002; Yoon, 2003). The CO2 finned-tube gas cooler/condenser performances have been investigated extensively. Experimental and theoretical methods used to investigate the effect of their integration with associated systems are still rather limited (Chang, 2007). To some extent, this could lead to inaccurate design and mismatching of the heat exchanger size and control when applied to a real system.

In this experimental research, two different sizes and designs of CO2 finned-tube gas cooler/condensers are purposely selected in order to be integrated with the existed CO2 booster system with specially designed measurement facilities. Extensive measurements based on different air volume flow rates have been carried out and some meaningful effects on the system performance have been obtained from the analysis of the test data. These data include heat exchanger designs, air flow rates, supercritical and subcritical pressure controls and cooling capacity controls.

2. TEST FACILITY

The tested gas cooler/condenser and integrated CO2 booster system shown in Fig. 1. CO2 booster system consists of the gas cooler/condenser which located at the top of the refrigeration plant; inside the plant room an ICMT motorized valve and ICM by-pass valve, a liquid receiver, a CO2 accumulator and two semi-hermetic compressors have been installed. A medium temperature (MT) direct expansion (DX) open vertical multi-deck refrigerated display was used for the investigations and the tests were carried out at controlled conditions in an environmental chamber. An additional CO2/Brine load has been installed at the top of the plant room in order to balance the capacity of the compressor.
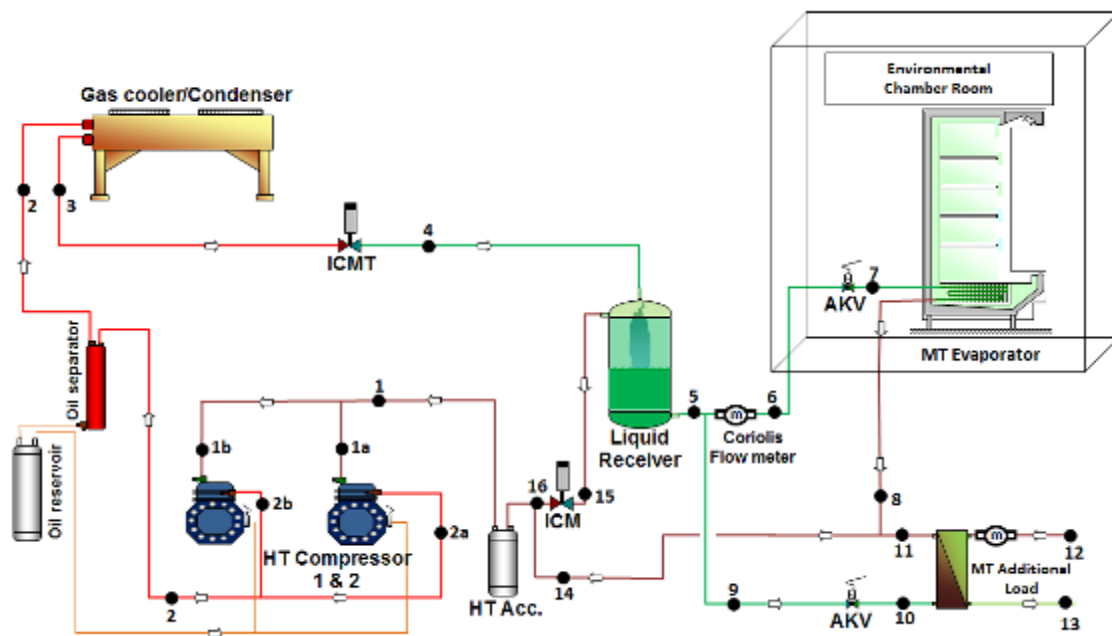
Figure 3 - CO2 Booster system test rig

The system is divided into three pressure sections, high, intermedium and medium; where the high pressure section begins at the outlet of the compressor and continues through the gas cooler/condenser and inlet line of ICMT motorized valve. Intermediate pressure section exists at the outlet of the ICMT valve and through the receiver where the flow is divided into gas and liquid. The gas phase returns back to the compressor suction line through the by-pass ICM valve. The liquid flows to the expansion valve where the medium pressure level begins. The liquid is expanded prior to MT display cabinet. The gas outlet from the MT flows back and mixing with the gas by-pass from the receiver before enter to compressor suction line and complete the circuit. The test facility is equipped with Danfoss controls and was comprehensively instrumented with pressure transducers, thermocouples and coriolis refrigerant flow meter to enable the detailed experimental investigation of the system and individual component under different operating conditions. Fig. 2 shows the relative installation position of the main components in the system.

The thermodynamic analysis and control optimisation of a similar CO2 booster system have been explained in more details by the authors (Ge, 2009; Ge, 2011). The overall system performance has been investigated experimentally at different operating conditions and controls when two different sized and designed gas

coolers/condensers are installed separately. A purposely test rig has been built in order to examine extensively the performance of CO_2 gas cooler/condenser with different structure designs. This purposely test rig allows to investigate the system under various operating conditions without affect from the ambient temperature.
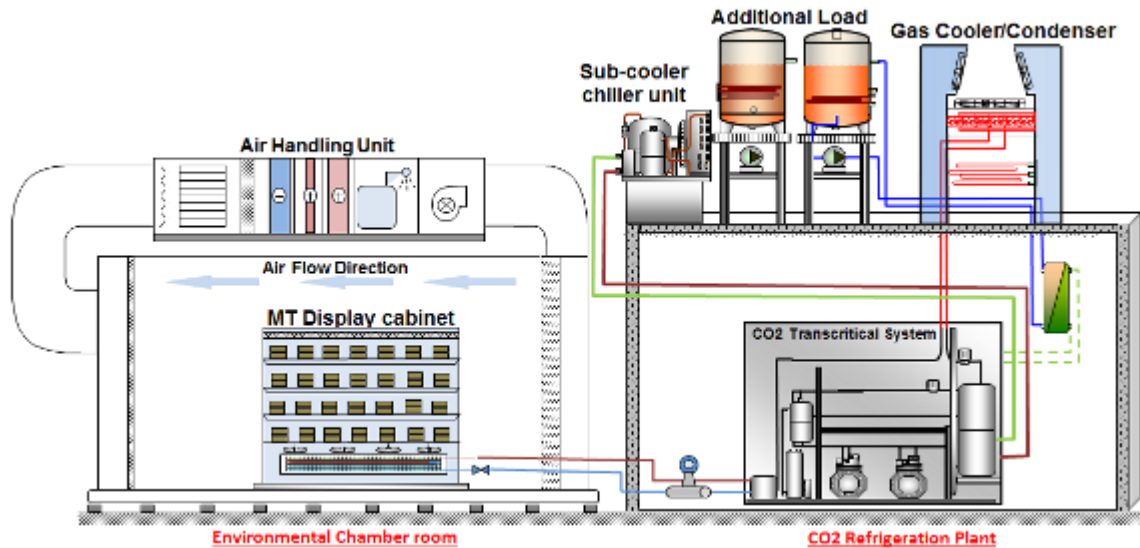
Figure 4 - Simplified diagram of the main component installation
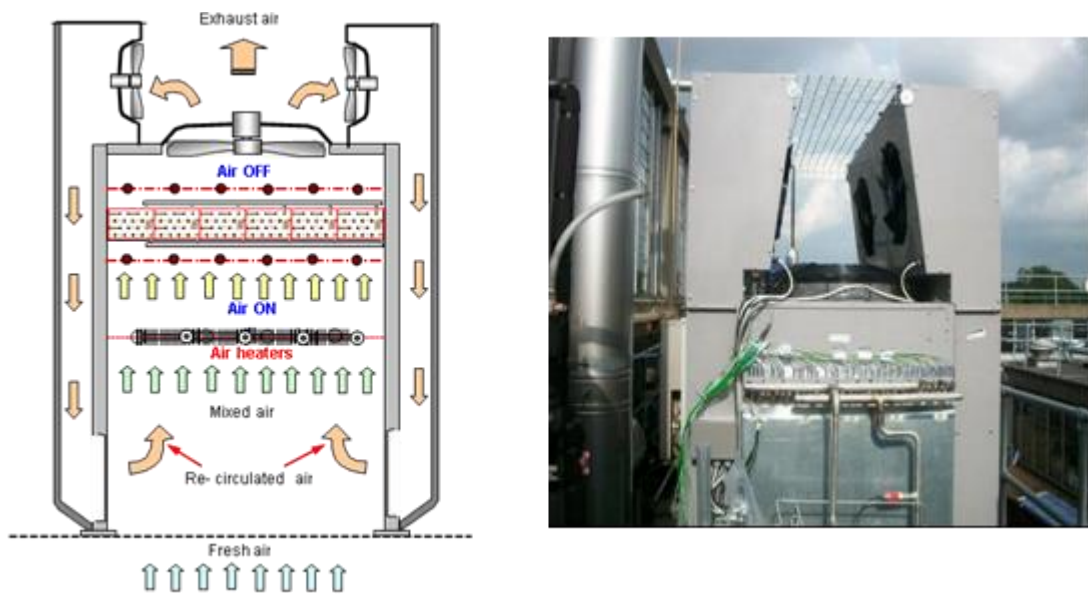
Figure 5 – Gas cooler/condenser test unit

This purposely gas cooler/condenser test unit shown in Fig. 3. The CO_2 heat exchanger is suspended tightly between two upright metal frames. Two propeller air fans are installed above the heat exchanger and controlled by variable speed control to maintain the requirement fixed air flow passing through. There are a number of smaller air fans installed oppositely along the direction of the pipe length, which will be switched on if the air inlet temperature is required to be higher than the ambient. The hot exhaust air from the coil will flow back through the return air tunnels then return air grills and mix with lower temperature ambient air flow. In the case the mixed air flow temperature is still lower than the required set point, an electric air heater which is installed at the air inlet section just below the heat exchanger will be controlled on to maintain the air inlet Remperature at the designed temperature. With the variable controlled main air fans, recirculate air fans and air inlet heaters the gas cooler air on parameters, temperature and flow rate, can be well controlled to specified values.

The test rig has been instrumented   comprehensively to detailed measurement data and overall performance description of the heat exchanger itself and its integrated CO_2 refrigeration system. The instrumentation devices used on the test unit are temperature and pressure measurements, air flow velocity and air pressure drop sensors. T-type thermocouples measure the air-inlet and air-outlet temperatures in 24 points respectively. For the refrigerant side, two pressure transducers are installed inside inlet and outlet headers of the heat exchanger to measure overall and heat exchanger refrigerant side pressure drops. A large amount of T-type thermocouples are attached and proper insulated on all the pipe bends along the pipes of one circuit to obtain the refrigerant temperature variation from the inlet to outlet. The refrigerant mass flow rate passing through the gas cooler/condenser it is calculated as the proportional of the heat balance air and refrigerant sides.

3. EXPERIMENTAL PROCEDURE

Fig. 4 shows the two different CO2 gas coolers/condensers which have been purposely designed and manufactured with different pipe arrangements and circuit numbers in order to experimentally examine the effects on the overall system. The coil number 1 is a three rows coil with four pipe circuits and total pipe number of 96. The overall dimension is 1.6m×0.066m×0.82m (L×D×H). Correspondingly, the coil number 2 has two rows and two circuits. The total number of pipe is 64 and overall dimensions 1.6m×0.044m×0.82m (L×D×H). Both coils use a copper pipe with 8mm outer diameter, aluminium fins with 0.16mm thickness and fin density of 453fins/meter. These two heat exchangers were installed in the CO2 system separately and tested at the same operating stages including intermedium and medium temperatures and pressures and air flow parameters. The tests conditions including air flow temperatures were varied from 19°C to 36°C and flow rates were modulated from 2000l/s to 2800 l/s through fan speed controls. Therefore, both heat exchangers operated at both subcritical and transcritical modes. In order to investigate the transient performance, the system was monitored from start up to the point it achieved steady state conditions. Investigations on steady state performance were carried out after the test plant reached the specified steady state conditions. Measured performance parameters from the instrumentation devices such as temperature, pressure and flow rate were logged by data logging every 20 seconds.
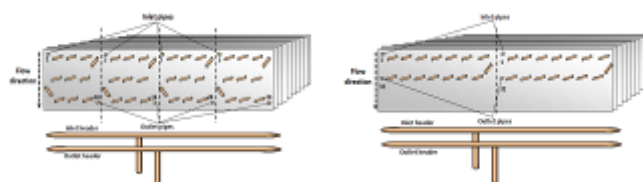
Figure 6 – CO$_2$ heat exchangers

To ensure the precise measurement, all measurement devices were calibrated carefully and the measurement uncertainty values are ±0.5°C, ±5%, ±0.3% and ±0.035% for temperature sensors, air velocity meter, pressure transmitters and refrigerant mass flow rate respectively. Table 1 illustrate the different operating conditions for the experimental investigations of both heat exchangers.

Table 1 - Experimental test conditions

Operating Mode	Coil Type	Air Temp. inlet °C	Main Fan Speed %	Air Volume l/s (x 1000)	Refrigerant Temp. inlet °C	Refrigerant pressure inlet bar
Condenser	3 Rows	19 - 27	50 – 60 - 70	20-24-28	69 - 85	60 - 73
Condenser	2 Rows	19 - 27	50 – 60 - 70	20-24-28	69 - 85	60 - 73
Gas Cooler	3 Rows	28 - 34	50 – 60 - 70	20-24-28	86 - 115	75 - 90
Gas Cooler	2 Rows	28 - 34	50 – 60 - 70	20-24-28	86 - 115	75 - 90

4. THERMODYNAMIC ANALYSIS OF THE SYSTEM

Energy and mass balance equations applied for individual components of the CO_2 system. The refrigeration capacity of the evaporator of the MT display cabinet was calculated using the enthalpy difference across the coil and the mass flow rate of the refrigerant. The enthalpy of the refrigerant liquid entering the evaporator and the refrigerant vapour leaving the evaporator were determined from the measurements of temperature and pressure of the refrigerant inlet of the expansion valve and outlet of the evaporator coil

respectively. The thermo-physical properties of the CO2 used for first law of thermodynamic analysis in this paper were calculated by using Engineering Equation Solver (EES ®, 2015).

Equation 1: Mass and Energy balance of the MT evaporator. (Numbers refer to Fig. 1.)

$$\dot{m}_7 = \dot{m}_8 = \dot{m}_{MT}$$

$$\dot{Q}_{MT} = \dot{m}_{MT} \, (\Delta h)_{ref} = \dot{m}_{MT,air} \, c_p \, (\Delta T)_{air}$$

Where:

- $\dot{m}$ = refrigerant mass flow rate (kg/s)
- Q = refrigeration capacity (kW)
- c_p = Specific heat capacity (kJ/kg K)
- Δh = enthalpy difference (kJ/kg)
- ΔT = temperature difference (K)

The additional refrigeration capacity load was calculated from the energy balance between brine and refrigerant side assuming adiabatic heat transfer. The brine mixture properties were determined by using the equations form M. Conde Engineering (2011).

Equation 2: Mass and Energy balance of the Additional Load evaporator. (Numbers refer to Fig. 1.)

$$\dot{m}_{12} = \dot{m}_{13} = \dot{m}_{AL,brine}$$
$$\dot{m}_{10} = \dot{m}_{11} = \dot{m}_{AL,ref}$$
$$\dot{Q}_{AL} = \dot{m}_{11} \, (\Delta h)_{ref} = \dot{m}_{12} \, c_p \, (\Delta T)_{brine}$$

Where:

- $\dot{m}$ = mass flow rate (kg/s)
- Q = refrigeration capacity (kW)
- c_p = Specific heat capacity (kJ/kg K)
- Δh = enthalpy difference (kJ/kg)
- ΔT = temperature difference (K)

The total refrigerant mass flow rate passing through the heat exchanger is calculated by the energy balance of air and refrigerant sides and is assumed to be the same passing through the compressor, ICMT motorized valve and at the inlet of the receiver where the mass flow is divided into gas and liquid form.

Equation 3: Calculation of the refrigerant mass flow rate.

$$\dot{m}_{ref} \, (\Delta h)_{ref} = \dot{m}_{air} \, c_{p,air} \, (\Delta T)_{air}$$

In order to calculate the compressor power consumption, a mathematical model based on the manufacture data (GEA BOCK Compressors, 2009) has been created. The model is divided into subcritical and transcritical operations. However, the former is a function of condensing and evaporating temperatures while the later one is dependent on the compressor suction and discharge pressures. The coefficients from these equations are correlated and listed in Table 2.

Equation 4: Compressor power consumption – Subcritical operation

$$W_{com,sub} = c_1 T_{ev}^2 + c_2 T_{ev} + c_3 T_{cd}^2 + c_4 T_{cd} + c_5 T_{ev} T_{cd} + c_6$$

Equation 5: Compressor power consumption – Transcritical operation

$$W_{com,trans} = c_1 P_{suc}^2 + c_2 P_{suc} + c_3 P_{dis}^2 + c_4 P_{dis} + c_5 P_{suc} P_{dis} + c_6$$

Where:

- - T_{ev} = evaporating temperature (K)
- - T_{cd} = condensation temperature (K)
- - P_{suc} = Suction pressure (Bar),
- - P_{dis} = Discharge pressure (Bar)

It is noted that the manufacture data of compressor power consumption was measured at constant superheat 10 K at compressor inlet. If the actual suction superheat is different from 10 K, the following correlation factor c$_{suc}$ is applied:

Equation 6: Correction factor
$$csuc = \frac{v_{exp}}{v_{10K}}$$

Where:

- - v_{exp} = experimental specific volume at compressor inlet (m^3/kg)
- - v_{10K} = specific volume at 10K superheat (m^3/kg).

Table 2 - Correlated coefficients for the mathematical model

	c1	c2	c3	c4	c5	c6
Subcritical	-1.61804	303.794	-0.23315	-299.358	1.955376	-5696.67
	c1	c2	c3	c4	c5	c6
Transcritical	-1.79591	40.16467	-0.12544	21.38474	1.473649	2520.822

5. TEST RESULTS & DISCUSSION

The COP of the CO_2 refrigeration system is defined as Eq. 7. The refrigeration capacity of the MT cabinet and the additional load can be determined using the thermodynamic relationships from Eq. 1 and 2. The work done by the CO_2 compressor can be calculated by Eq. 4 and 5 for subcritical and transcritical respectively. The power consumption of the extraction fans was determined by recording the power by using a power quality analyser.

Equation 7: System COP
$$COP = \frac{Q_{AL} + Q_{MT}}{W_{com} + W_{fan}}$$

Where:

- - $\dot{Q}_{AL}$ = cooling capacity of additional load (kW)
- - $\dot{Q}_{MT}$ = cooling capacity of refrigeration cabinet (kW)
- - W_{com} = compressor power consumption (kW)
- - W_{fan} = extraction fans power consumption (kW)

Fig. 5 (a) shows the extraction fan power consumption with respect of different air volumetric flow rates. Apparently, the fan power consumption increases with higher air volumetric flow rate and the increase rate is much higher for a higher air flow rate, which effect on the final COP calculation of the system. The influence of the air volume flow rate on the air side pressure drop for both heat exchangers is illustrated in Fig. 5 (b). From the graph, it is seen that the air side pressure drop increases with higher air flow rate and more pressure drop in the 3-row coil due to the higher row number. On the other hand, the higher air flow rate will enhance the air side heat transfer and subsequently improve the system performance.
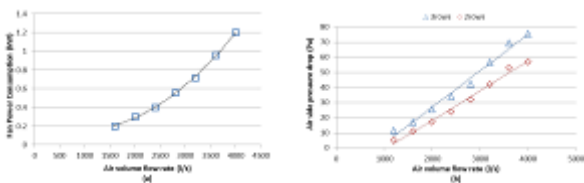
Figure 7 – (a) Fan power consumption for different air volume flow rates

(b) Air side pressure drop with air volume flow rates
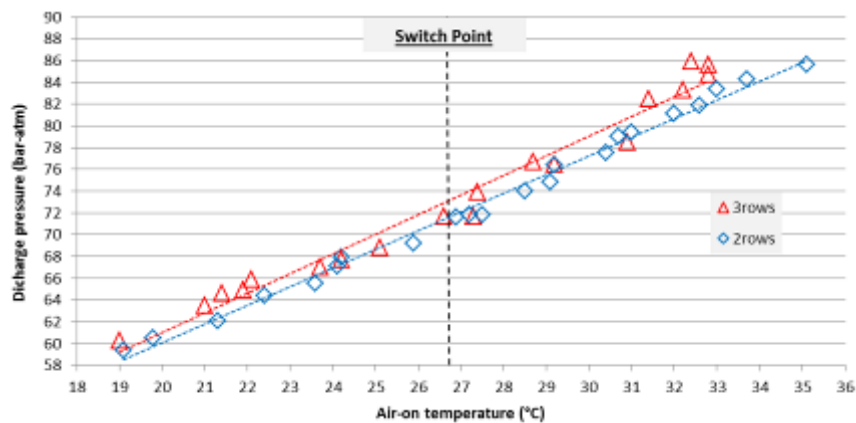
Figure 8 - Relationship between air-inlet temperature and heat exchanger discharge pressure

The intermediate pressure is effect on the cooling COP of the system. The intermediate pressure is controlled by the ICMT valve and ICM by-pass valve; by adjusting both we can control the liquid level inside the receiver. With lower intermediate pressure the refrigerant quality will diminish at the inlet of the receiver and the enthalpy values will be lower at the inlet of MT evaporator (Ge, 2011). In such circumstances, the COP of the system will be increased. Therefore, during the experimental tests the intermediate pressure controlled to be between 30 to 31 bar, slightly higher than the MT evaporating pressure. Moving to the higher pressure side of the system is easily to define that is an optimal high side refrigerant pressure for each ambient temperature in which the COP reaches the maximum values. The optimum high side pressure is operate in irrespective from the intermediate pressure side and is only proportional of the air-inlet temperature and coil structural design. Fig. 6 illustrates the relationship of heat exchanger discharge pressure and air-on temperature at three different fan speeds of 50%, 60% and 70% of the total corresponding to 2000l/s, 2400l/s and 2800 l/s respectively.

It is clear from the linear relationship that there is no any effect from the fan speed on the discharge pressure of the system. In transcritical mode the control strategies involve a PID controller which record the air-on temperature on the gas cooler/condenser and tries to maintain the optimal pressure in the gas cooler. On the other hand, the temperature difference (ΔT) subcooling controls can be used for the subcritical operation. The refrigerant temperature outlet of the condenser used to regulate subcooling degree based on the reference pressure. The condensing temperature of the system varies between 20°C to 28.4°C which is lower than the critical point of the CO_2 refrigerant. The variation of the system cooling capacity and compressor power consumption with respect of varies air-inlet temperatures is shows in Fig. 7(a). The graph illustrates the results for 70% extraction fan speed at 2800l/s. Similar trends can be obtained for 50% and 60% fan speeds. The cooling capacity for the 3-row gas cooler/condenser is higher while the compressor power consumptions are nearly the same for both coils. The higher cooling capacity is the proportional of the bigger refrigerant pressure drop across the coil for the 3-rows coil. This will lead to a higher COP for the system with the 3-row CO_2 coil and different fan speeds, as shown in Fig. 8. M, the COP for both circumstances decreases with higher air-on temperature. The higher COP was found on the 60% main fan speed, corresponding to 2400 l/s of air passing through the coil, and is a proportional to the lower power consumption of the fan when compared with 70% of fixed fan speed.
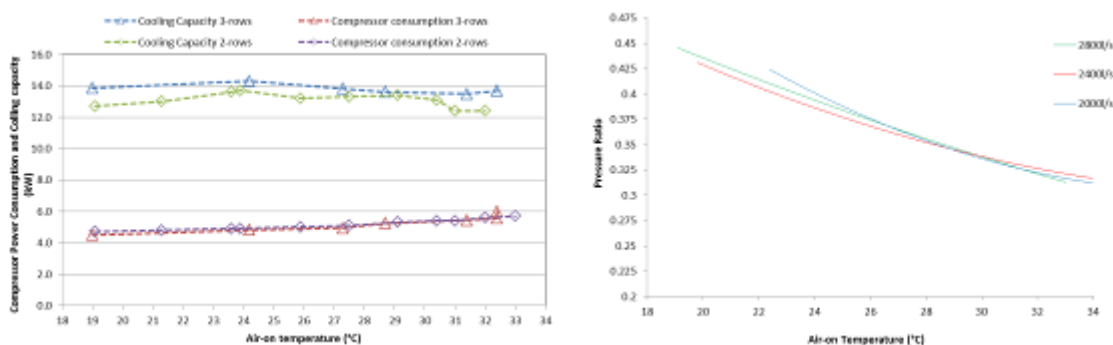
Figure 7 – (a) Effect of air-inlet temperature in compressor power consumption & system cooling capacity

(b) Compressor pressure ratio in different air-inlet temperatures

The system control strategies for this experimental investigation involve a compressor variable speed control system. Fig. 7 (b) shows the pressure ratio with respect of air-inlet temperature for three different air extraction fan speeds. The graphs show that the air fan speed is not effect to the compressor power consumption. On the other hand the power consumption of the compressor it is dependent on the air-inlet condition. As the air-inlet temperature increased the system trying to decrease the pressure ratio and maintain the isentropic efficiency of the compressor in order to keep the power consumption in lower levels.

Test results based on a fixed air extraction fan speed, constant subcooling at 2K for subcritical cycles and constant approach temperature in a transcritical mode. The refrigerant mass flow rate is fairly constant and changed only when the system move from subcritical to supercritical operation and the evaporating temperature was - 8°C (± 1°C).
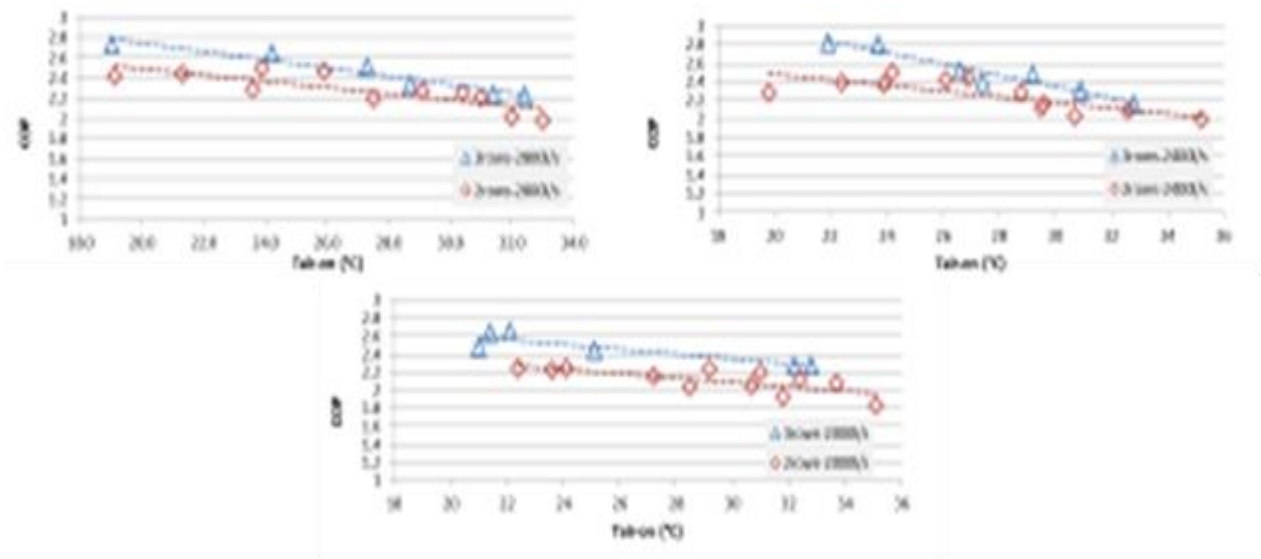
Figure 9 - Variation COP with air-inlet temperature

Take in account the uncertainty of the experimental measured variables which include air mass flow rate and air temperature, refrigerant temperatures, refrigerant pressures, refrigerant mass flowrate and assuming that the individual measurements are uncorrelated and random, the uncertainty in the calculation of COP was determined, using the Engineering Equation Solver (EES) software, to be between ± 5.52% and ± 6.1% for both 3-row and 2-row heat exchanger respectively. The display cabinet evaporator cooling capacity uncertainty calculation was found to be ± 0.77% and the additional load cooling capacity uncertainty calculation is relatively high because the calculation involved the brine side of the system and it's found to be ± 11.22%.

6. CONCLUSION

The CO_2 booster refrigeration system has been demonstrated as a promising solution for use in supermarket applications. This experimental investigation focuses on the effect of different designs of CO2 gas coolers/condensers on the overall performance of a CO2 booster refrigeration system. To achieve this target, two different heat exchangers were designed, manufactured and used in the booster refrigeration system. A number of experiments were carried out with different operating conditions and control strategies of the system. The experimental results show that the system COP and cooling capacity have been improved with the larger CO_2 heat exchanger. On the other hand, the air flow rate and air-side pressure drop have also been investigated. Finally, to achieve the maximum COP of the system a compromise balance has to be considered in the coil design.

7. REFERENCES

CHANG YS, Kim MS., 2007, Modelling and performance simulation of a gas cooler for CO2 heat pump system. HVAC&R Research; 13: 445-456.

DEFRA - Sinclair Knight Merz, 2011, Examination of the Global Warming Potential of Refrigeration in the Food Chain, Evidence review findings, Department for Environment Food and Rural Affairs

EES, 2015. Engineering Equation Solver, version 9.810, www.fChart.com

GE Y.T., Tassou S.A., 2009, Control optimisation of CO2 cycles for medium temperature retail food refrigeration systems, International Journal of Refrigeration 32, 1376-1388

GE Y.T., Tassou S.A., 2011, Thermodynamic analysis of transcritical CO2 booster refrigeration systems in supermarket, Energy Conversion and Management 52, 1868-1875

GEA BOCK Compressors, Product information (12 pages), Available from: http://www.bock.de/en/home.html, (accessed 03/04/2014) - Online published on: 09/06/2009

HINDE, D., Shitong Zha, S., Lan, L., 2009. Carbon dioxide in North American supermarkets. ASHRAE Journal 51, 18-26.

HWANG Y., Jin DDH., Radermacher R., Hutchins JW. 2005, Performance measurement of CO2 heat exchangers, ASHRAE Transactions; 306–316.

M. Conde Engineering, 2011. Thermo-physical properties of brines, Zurich, Switzerland, 9 pgs.

PEARSON A.B., 2014, CO2 as a refrigerant, International Institute of Refrigeration, ISBN: 978-2-36215-006-7

SAWALHA, S., Soleimani, K.A., Rogstam, J., 2006. Experimental and theoretical evaluation of NH3/CO2 cascade system for supermarket refrigeration in laboratory environment. Proc. 7th IIR Gustav Lorentzen Conference on Natural Working Fluids, Trondheim, Norway.

SRINIVAS SP., Groll EA., Ramadhyani S. New correlation to predict the heat transfer coefficient during in-tube cooling of turbulent supercritical CO2. International Journal of Refrigeration 2002; 25 : 887–895.

TASSOU, S.A., Ge, Y., Hadawey, A., Marriott, D., 2011. Energy consumption and conservation in food retailing. Appl. Therm. Eng. 31, 147-156.

YOON J.I., Kwang H.C., Chang H.S., Wen B.Y., Soo J.H., Min J.J., 2014, Performance Characteristics of the R404A Indirect Refrigeration System Using CO2 as a Secondary Refrigerant. International Journal of Engineering Sciences & Research Technology, 459 - 473

YOON SH., Kim JH., Hwang YW., Kim MS., Min K., Kim Y., 2003, Heat transfer and pressure drop characteristics during the in-tube cooling process of carbon dioxide in the supercritical region. International Journal of Refrigeration; 26:857–864.

462: Energy efficiency improvements in paper mills by combined heat and power systems

IMRAN SHABBIR[1], MOJTABA MIRZEIAN[1]

1 University of the west of Scotland, PA1 2BE, Paisley, UK, Imran.shabbir@uws.ac.uk

Cogeneration proved itself as one of the promising energy efficient technique to produce electricity and useful thermal energy from a single fuel source. Detailed study of thermoeconomics parameter relevant for the feasibility study of employing biomass fuel for cogeneration is presented in this study. Three different plant configurations are presented and assessed to improve the energy efficiency of a paper mill. The mill employs biomass, namely rice husk as its energy source which not only enhances the scope and economic feasibility of cogeneration but also has particularly importance from sustainable energy balance and environmental point of view. The options studied are gas turbine, steam turbine and combined cycle and are evaluated on the basis of Simple payback period, Annualised Life Cycle Cost (ALCC) and energy utilisation factor. The result shows that mill have a strong potential of cogeneration and the combined cycle based cogeneration is concluded as a best option as it have least payback period and the least ALCC. It is found that the proposed combined cycle cogeneration in existing set up in mill can provide huge financial savings with payback period of 2.6 yrs.

Paper mill, Gas turbine, Industrial cogeneration, Thermoeconomics, Annulaised Life Cycle Cost analysis

1. INTRODUCTION

Increasing energy prices and strict controls on CO_2 emissions develops an immense pressure to improve energy efficiency in process industries. The cogeneration concepts often called as combined heat and power plant (CHP) refers to the simultaneous production of two useful forms of energies i.e. mechanical or electric and thermal energy from a single fuel source i.e. oil, natural gas, coal or biomass. The basic difference between the CHP and conventional power plant is the utilisation of rejected heat to fulfil the thermal need of the site. The efficiency of converting the fuels available energy into electrical power in conventional power plant is about 30% and rest of fuel energy is lost as waste heat (unless it captures). On top of this further energy losses occur in the transmission and distribution of this electric power to the individual consumer. The overall conversion efficiency of fuel into useful energy in CHP systems can be up to 80%. This not only results in savings of fossils fuels and reduces the emission of greenhouse gases but also reduce the burden on utility network and eliminate the transmission and distribution losses. CHP systems come in wide range of technical characters and also can be designed for site specific needs. The main difference between the CHP systems is the type of prime mover it use i.e. gas turbine, steam turbine, reciprocating engine, fuel cells etc.

CHP feasibility studies for chemical process industries have been reported by many researchers over the years. Mollersten et al. (2003) investigated the potential of CO_2 reduction through energy measures in Swedish pulp and paper industry by employing cogeneration. Velez et al. (2012) presents an overview of the technical and economic aspects, as well as the market evolution of the organic rankine cycle for the conversion of low-grade heat for power generation. The result shows that this technology could facilitate an electricity supply to unconnected areas, the self-production of energy, or even to increase the energy efficiency in the industrial sector respecting the environment. A comparative life cycle assessment is done by Kimming et al. (2011) to supply the power and heat to rural village from biomass produced on farm land in small-scale combined heat and power plant. The result shows that this option would considerably reduce greenhouse gas emissions compared to the scenario based on fossil fuel and have an advantage of utilising a by-product and thus not occupying extra land. Arrieta et al. (2007) performed case study on cogeneration potential in the Columbian palm oil industry. The result of this study shows that in all the analysed cases, the biomass available in the plants not only guarantees the power demands of the process, but also generates surplus electricity. A comparative analysis of different software i.e. Ready Reckoner, EnergyPro, and CHP Sizer used in feasibilities of CHP was done by Hinojosa et al. (2007). The study concluded that software packages are a good start, but they tend to be either overly simple or extremely complicated, and sometimes not very flexible. However, building custom-built generic models that include different technologies, unit sizes, control modes, market restrictions and benefits can be a complex but will be more transparent to the user. Same approach has been used in this study to develop custom-built model for CHP configurations for a paper mill. Different authorities have published guidelines on CHP for improving the energy efficiency i.e. European Commission (1999), Irish CHP Association, The Carbon Trust (2010) & U.S. Environmental Protection Agency (2014). A few of the many other works include, study on cogeneration in a sugar factory has been done by Raghu Ram and Banerjee (2003), preliminary economics of black liquor gasifier/gas turbine cogeneration at pulp and paper mills by Larson et al. (2000) and black liquor gasification integrated in pulp and paper mills by Naqvi et al. (2010). Importance of thermoeconomics analysis have been highlighted by Mazur (2007) and considered CHP as a useful tool for analysing the production process in terms of economic profitability and thermodynamic efficiency with respect to energy resource consumption.

The literature review reveals the fact that a lot of researchers have focused on process industries including paper mills which is an excellent site for CHP. As far as the authors are aware, there are more than 20 registered paper mills in Pakistan and the implementation of cogeneration has not been reported so far. Against this background, the specific objectives of the present work are to analyse the different possible options for cogeneration in a paper mill to highlight the energetic and economic saving potentials.

2. METHODOLOGY

Detailed study on thermoeconomics parameter relevant for the feasibility study of three potential options of employing biomass fuel for cogeneration is presented in this study. In steam turbine cogeneration, superheated steam generated at high pressure is expanded in a back-pressure steam turbine. The expanded steam is then supplied to meet the demand for process heat. The electricity generated in this case is only sufficient to meet part of the total requirement as prime motive is to fulfil the heat demand of mill. The deficit of electricity is bought from the utilities. In gas turbine cogeneration, fuel is burned in combustion chamber of gas turbine to generate electricity and exhaust gases of turbine are utilised for

steam generation in the heat recovery steam generator with the aid of supplementary firing for process heat requirements. This cogeneration option produces sufficient electricity to meet internal demands and excess electricity can sell to utilities. In combined cycle, both gas and steam turbine are employed in one system to gain more benefits out of the system. Fuel is burned in combustion chamber of gas turbine to make electricity first and gas turbine exhaust is utilised in the HRSG for superheated steam generation with the aid of supplementary firing. This superheated steam is then expanded in the steam turbine to make electricity and exhaust of steam turbine is used for process heat requirement. Figure 1, 2 & 3 shows the schematic diagram of the proposed back-pressure steam turbine, gas turbine and combined cycle cogeneration configurations.

For optimisation of energy system in each CHP configurations, suitable operating parameters are first selected to establish the operating conditions (pressure, temperature and mass flow rate of stream entering and leaving each unit and total electric load). The cost of producing process steam and electricity in each CHP configuration is based on "theory of exergetic cost" developed by Lozano and Valero, (1993). This theory present the algebraic cost-balance equations derived from conventional economic analysis and auxiliary cost equations for each subcomponent of CHP system.

2.1. Energetic model of CHP configurations

This section present the proposed models and assumptions used to develop the energy balance in each CHP configuration. The assumption made was as follows: ideal gas principles are applied to air and combustion gases, system operates in steady state, complete combustion reactions, all components were considered adiabatic and all the CHP configuration are aimed to produce fixed rate of steam (8.63 kg/s,10 bars and 180Cᵒ). Figure 1, 2 & 3
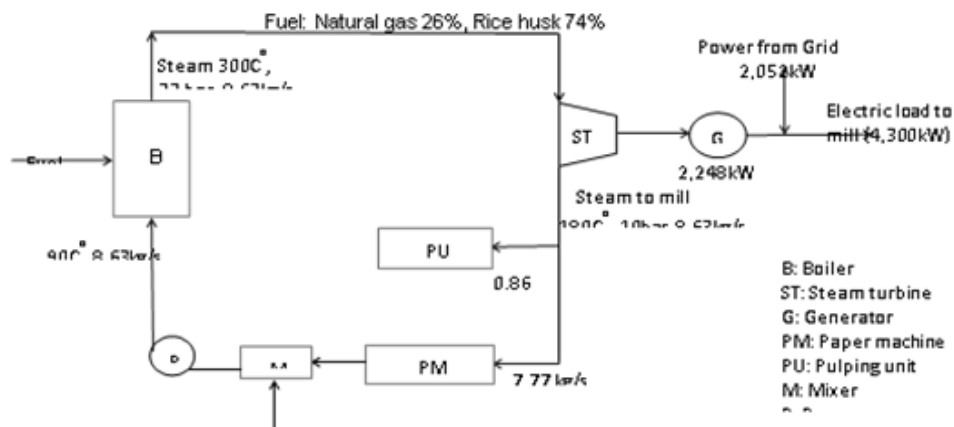
Figure 1: Schematic diagram of the proposed steam turbine cogeneration system
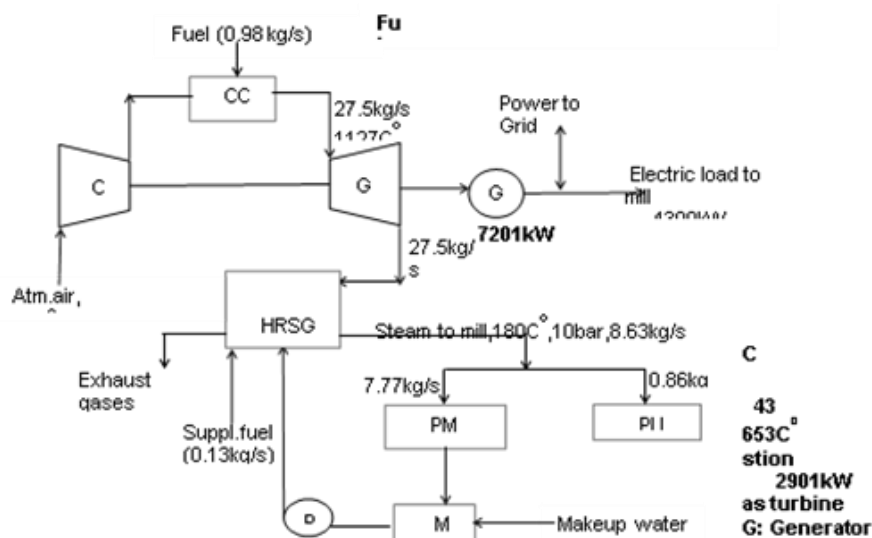
Figure 2: Schematic diagram of the proposed gas turbine cogeneration system
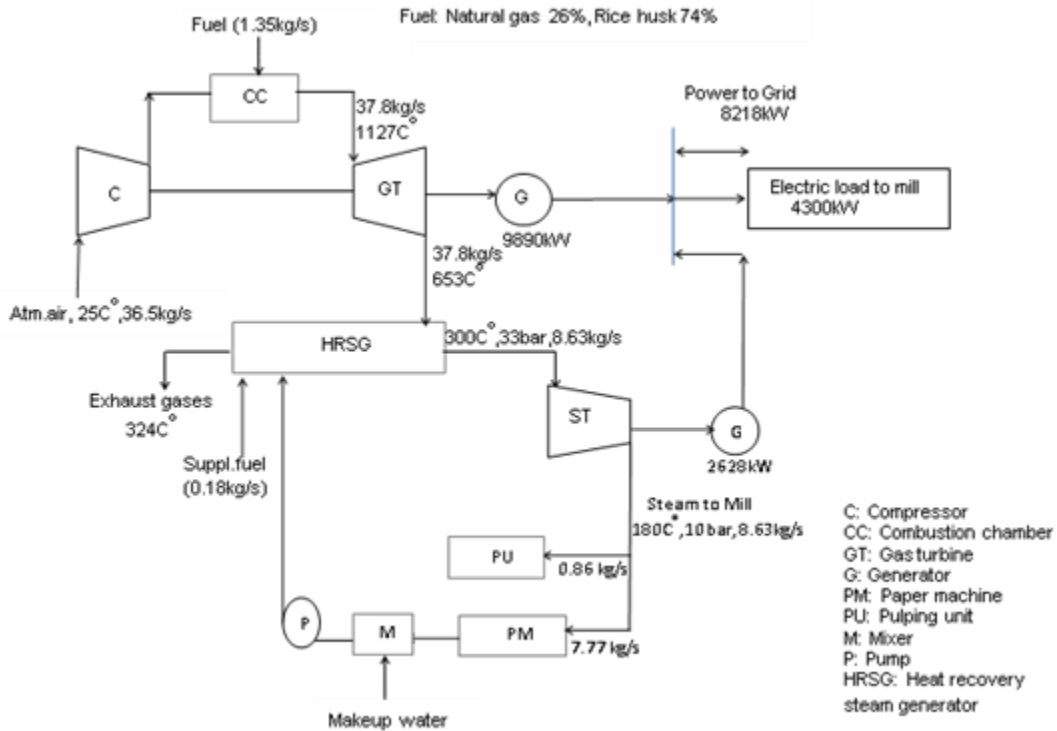
Figure 3: Schematic diagram of the proposed combined cycle cogeneration system

Table 3: Summary of main assumptions made for CHP configurations

Parameter	Value	Parameter	Value
Boiler efficiency	80%	Turbine efficiency	85%
Electric generator efficiency	97%	Compressor efficiency	82%
Specific heat of combustion gas (kJ/kg k)	1.148 (constant)	Combustion chamber efficiency	98%
LHV of fuel (kJ/kg)	28,516	Ambient temperature	288K
Useful life of cogeneration system	30 years	Discount rate of cogeneration system	30%
Maintenance factor (% of total equipment cost)	15%	Price of rice husk ($/kg)	0.08
Price of electricity ($/kWh)	0.225	Price of natural gas ($/kg)	0.279
Selling price of electricity($/kWh)	0.075	Avoided cost of electricity purchase ($/kWh)	0.058

2.2. Economic model of CHP configuration

Profitable deployment of CHP solutions is strongly dependent upon the presence of simultaneous demand of the relevant energy vectors in an extensive time span over the year (Chicco, 2009). Typically, guidelines for industries adopting cogeneration have annual operating hours above 4,500 (Irish CHP Association, U.S. Environmental Protection Agency, 2014). The estimated hours of operation for this analysis is based on current practice in the paper mill, where mill stops its operation twice for fortnights for schedule maintenance and one month complete closure for filling the raw material storage silos. This result in 7,320 estimated hours of operation. In this methodology, the optimisation analysis to evaluate the economics of different cogeneration options is based on Annualized Life Cycle Cost Analysis (ALCC) and Simple Payback Analysis (SPB). All values of cost is in US dollar.

Simple Payback Analysis

Simple payback analysis is the simplest and most commonly used key factor to calculate the time required to recover the capital cost based on annual savings from installation of the project (Meckler & Hyman, 2010). The simple payback period of employing CHP in this case study can be calculated by the following formula:

Equation 1: Simple payback period

$$S_{P.B} = \frac{T_c}{FS_{CHP}}$$

Where:

- $S_{P.B}$ is the simple payback period
- T_C is the total engineering, construction and procurement cost
- FS_{CHP} is the financial Savings from CHP by selling the surplus electricity to the grid

T_c is calculated by following expression,

Equation 2: Total investment cost

$$T_c = I_c + C_O$$

Where:

- I_c is the investment cost of equipment
- C_O is the annual operating cost

However, it is not the most suitable criteria for a long term investment as it does not account for time value of money, escalation etc. (Meckler & Hyman, 2010, Hinojosa et al., 2007). Hence the final optimisation analysis of the chosen CHP system configuration in this study is based on Annualized Life Cycle Cost Analysis (ALCC).

Annualized Life Cycle Cost Analysis

ALCC analysis are used to find the total cost of production throughout its life cycle, which included research and development, construction, operation and maintenance, and disposal (Kawauchi & Rausand, 1999). Mujeebu, M., et al. (2009), developed a simple model for quantifying the annualised life cycle costs of cogeneration as follows:

Equation 3: Total investment cost

$$ALCC = (I_c \times R) + C_o - (FS_{CHP} + C_{pp})$$

Where:

- R is the capital recovery factor
- C_{pp} is the avoided cost of power purchase

Accurate and verified investment cost (I_c) of equipment can only be obtained from vendors of specific models; however a comprehensive way to present the variation of cost with important thermodynamic parameters is in the form of mathematical function as shown in equations (4-11). These equations have been widely used for the calculation of investment costs in different industries (Frangopoulos & Spakovsky, 1993, Lazzaretto & Macor, 1995, Robert F. Boehm, 1987, Valero et al., 1994 and Lian et al., 2010). The cost of installation, electrical equipment, control system, piping and local assembly have also taken into account by the coefficients used in the following equations where I_{BL}, I_P, I_{AC}, I_{GEN}, I_{GT}, I_{ST}, I_{CC}, are the investment costs for boiler, pump, air compressor, electric generator, gas turbine, steam turbine and combustion chamber respectively.

Equation 4: Investment cost of boiler

$$I_{BL} = 740(h_s)^{0.8} \exp\left(\frac{P-2}{14.29}\right) \exp\left(\frac{T-350}{446}\right)$$

Where:

- I_{BL} = Investment cost of boiler
- h_s = Rate of energy generated by boiler

- P = Outlet pressure of boiler
- T = Outlet temperature of boiler

Equation 5: Investment cost of pump
$$I_P = 3540(W_P)^{0.71}$$

Where:

- I_P = Investment cost of pump
- W_P = Work done by the pump

Equation 6: Investment cost of air compressor
$$I_{AC} = \left(\frac{75m_{air}}{0.9 - \eta_{AC}}\right)\left(\frac{P_2}{P_1}\right)\ln\left(\frac{P_2}{P_1}\right)$$

Where:

- m_{air} = mass flow rate of air
- P_1 & P_2 = Compressor inlet and outlet pressure
- η_{AC} = Efficiency of compressor

Equation 7: Investment cost of electric generator
$$I_{GEN} = 60(E_P)^{0.95}$$

Where:

- I_{GEN} = Investment cost of electric generator
- E_P = Power produced by gas & steam turbine

Equation 8: Investment cost of gas turbine
$$I_{GT} = \left(\frac{1536m_G}{0.92 - \eta_{GT}}\right)\ln\left(\frac{P_3}{P_4}\right)\left(1 + \exp(0.036T_3 - 54.4)\right)$$

Where:

- m_G = mass flow rate of gas
- P_3 & P_4 = Gas turbine inlet and outlet pressures
- η_{GT} = Efficiency of gas turbine

Equation 9: Investment cost of steam turbine
$$I_{ST} = 6000(E_P)^{0.7}$$

Where:

- I_{ST} = Investment cost of steam turbine
- E_P = Electric energy produced by steam turbine

Equation 10: Investment cost of combustion chamber
$$I_{CC} = \left(\frac{48.64m_{air}}{0.995 - \dfrac{P_3}{P_2}}\right)\left(1 + \exp(0.018T_3 - 26.4)\right)$$

Where:

- I_{CC} = Investment cost of combustion chamber
- P_2 & P_3 = Inlet and outlet pressure of combustion chamber

Equation 11:
Investment cost of
HRSG

$$I_{HRSG} = \left(\left(\frac{Q_{economizer}}{LMTD_{economiser}} \right)^{0.8} + \left(\frac{Q_{evaporator}}{LMTD_{evaporator}} \right)^{0.8} \right) + 11820F_S + 658F_G^{1.2}$$

Where:

- $Q_{economizer}$, $Q_{evaporator}$ = Heat input into economiser and evaporator
- $LMTD_{economiser}$, $LMTD_{evaporator}$ = Log mean temperature difference of economiser and evaporator

The capital recovery factor R for cogeneration is defined by following formula as formulated by (Beihong & Weiding, 2006):

Equation 12: Capital recovery factor

$$R = \frac{i(1+i)^n}{(1+i)^n - 1}$$

Where:

- i = Interest rate
- n = Useful life of the equipment in years

Where i is the interest rate and n is the useful life of the equipment in years. It is assumed that the values of i and n would be same for gas turbine, steam turbine and reciprocating engine. The CHP plant configuration with the minimum ALCC is selected as the optimal solution from an economic point of view.

3. CASE STUDY

The present method will be applied in three possible cogeneration systems on "Khan Board and paper mill" which is one of the leading paper mill located in Lahore, Pakistan. The demand of this plant is 4,300 kW of electricity and saturated steam of 10 bars with flow rate of 8.63kg/s. Annual average electrical and thermal load requirements of mill are plotted to analyse the scale of energy demand as shown in Figure 4. In the present situation, two boilers operate at a time out of six installed boilers which consumes natural gas and rice husk and electricity is bought from grid.
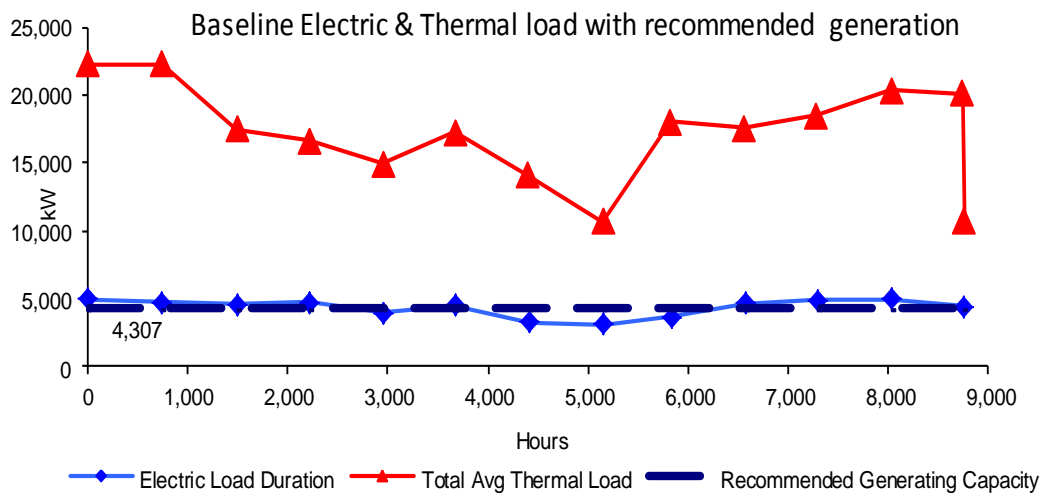
Figure 4: Annual Electric and thermal demand of a mill

Table 4: Investment cost of equipment

Parameter	Cost (US dollar)	Parameter	Cost (US dollar)
IBL	2.19 x 106	IGEN,ST	91,697
IP	34,579	IGT	1.28 x 106
IAC	914,032	IST	1.33 x 106
IGEN,GT	277,144	ICC	47,904
IHRSG	413,545		

4. RESULTS AND DISCUSSIONS

The energy balance of three different CHP options analysed are show in Table 3. Steam requirement is kept constant in all the options. The annual fuel consumption, electricity generation and its export to grid and avoided electricity of all cogeneration options are summarised in Table 4. Results of cost analysis of cogeneration options can be seen in Table 7.

Table 5: Energy balance abstract of studied cogeneration systems

Parameters	Units	Gas turbine	Steam turbine	Combined cycle
Fuel consumption	tonnes / hr	4.01	3.55	5.51
Energy input	MW	31.82	28.13	43.70
Heat requirement (steam)	Kg / s	8.63	8.63	8.63
Electricity production	MW	7.20	2.25	12.52
Process heat recovery	MW	8.77	17.70	7.81
Electrical efficiency	%	22.63	7.99	28.65
Energy utilisation factor		0.50	0.71	0.47

Table 6: Annual fuel consumption and electrical energy data

Parameters	Units	Gas turbine	Steam turbine	Combined cycle
Fuel consumption	tonnes	29,356	25,952	40,318
Electricity production	MWh	52,715	16,455	91,644
Electricity transferred to grid	MWh	21,188	0	60,117
Electricity bought from grid	MWh	0	15,072	0
Avoided electricity purchases	MWh	31,527	16,455	31,527

The annual operating cost of cogeneration consists of fuel, labor, and maintenance cost. Where labor cost is calculated by assuming an automated gas turbine plant of 8 MW, with three shifts per day, which will require 6 operators / shift; thus 18 full time operators (Deshpande et al., 2010; Kalowekamo & Baker, 2009). Assuming 8 hour/shift, 306 days/year and a wage rate of $1.42/h, then the direct labor cost is estimated at 18 people * 8 h/day * 306 days/year * $1.42/h = $62,570/year. Same expression is applied to with assuming 8 operators required for steam turbine and 12 operators for combined cycle labor cost. Several authors (Silveira & Tuna, 2003, C. A. Frangopoulos, 1987 & Lazzaretto & Macor, 1995) have estimated the maintenance cost of natural-gas fired cogeneration plant to be about 6% of the total equipment cost. However, as combustion of biomass fuels produces higher rate of ash fouling and slagging, thus boiler tubes and grates have to be cleaned more often which increase the maintenance cost. Therefore a value of 15% of the total equipment cost is selected for the maintenance cost in this study.

Table 7: Summary of annual operating costs (millions USD) of studied cogeneration options

Description	Gas turbine	Steam turbine	Combined cycle
Fuel cost	3.87	3.42	5.32
Electricity cost	0.00	3.73	0.00
Labor cost	0.062	0.083	0.125
Maintenance cost	0.43	0.54	0.81
Annual operating cost (Co)	4.36	7.77	6.25

It is concluded that the ALCC of combined cycle cogeneration system is least and most economical viable option for paper mill as shown in Table 6. However, as it can be seen from the results in Table 3 that energy utilisation factor is best in steam turbine, though this option does not produce enough electricity even for mill own use. Hence, it's a compromise between energy efficiency and cost between steam turbine and combined cycle. Furthermore, when comparing with the existing facility, the proposed combined cycle cogeneration will save the electricity purchase cost of millions (1.85 USD) besides providing the revenue worth millions (4.52 USD) per year through power export.

Table 8: Comparison of SPB and ALCC of studied cogeneration options

Description Cost (millions US $)	Gas turbine	Steam turbine	Combined cycle
Equipment investment cost	2.93	3.65	5.40
Annual operating cost	4.36	7.77	6.25
Avoided cost of power purchase	1.85	0.96	1.85
Total cost	7.29	11.42	11.65
Financial saving from CHP	1.59	0	4.52
Simple pay back	4.58	0	2.58
ALCC	1.80	7.91	1.5

5. CONCLUSION

Thermoeconomic viability of cogeneration system for a typical paper mill is analysed with different options by employing biomass as its main energy source. It is found that the mill has a good potential for combined cycle cogeneration and is viable in both technical and economic perspectives. The proposed scheme can provide attractive saving in annual operating cost with a simple payback period of 2.6 years. The installation of the cogeneration unit at this industrial plant is thus justified, even without any government incentive policy, provided that the paper mill is eager to avoid the possible risks of power outages. However, government incentives for gas and electricity rates could enhance the economic performance of the cogeneration unit even further. Though cogeneration is not a new idea, unfortunately industries in Pakistan are still either unaware of its benefits or reluctant to take a risk to implement this technique. There is a need of industry and engineering institute partnerships to untapped the benefits of cogeneration practically.

6. REFERENCES

Arrieta, F., Teixeira, F. N., Yáñez, E., Lora, E., & Castillo, E. (2007). Cogeneration potential in the Columbian palm oil industry: Three case studies. Biomass and Bioenergy, 31(7), 503-511.

Beihong, Z., & Weiding, L. (2006). An optimal sizing method for cogeneration plants. Energy and Buildings, 38(3), 189-195.

European Commission, (1999). Training guide on Combined Heat and Power Systems. from http://www.cres.gr/kape/education/3.CHP_en_small.pdf

Deshpande, A., Anitescu, G., Rice, P., & Tavlarides, L. (2010). Supercritical biodiesel production and power cogeneration: technical and economic feasibilities. Bioresource technology, 101(6), 1834-1843.

Frangopoulos, C., & von Spakovsky, M. (1993). A Global Environomic Approach for Energy Systems Analysis and Optimization (Part I).

Frangopoulos, C. A. (1987). Thermo-economic functional analysis and optimization. Energy, 12(7), 563-571.

Hinojosa, L., Day, A., Maidment, G., Dunham, C., & Kirk, P. (2007). A comparison of combined heat and power feasibility models. Applied Thermal Engineering, 27(13), 2166-2172.

Irish CHP Association. A Guide to Combined Heat and Power in Ireland.   Retrieved 06 June, 2015, from http://www.seai.ie/Publications/Renewables_Publications_/CHP/Guide_to_CHP_in_Ire_low_.pdf

Kalowekamo, J., & Baker, E. (2009). Estimating the manufacturing cost of purely organic solar cells. Solar Energy, 83(8), 1224-1231.

Kavvadias, K., Tosios, A., & Maroulis, Z. (2010). Design of a combined heating, cooling and power system: Sizing, operation strategy selection and parametric analysis. Energy Conversion and Management, 51(4), 833-845.

Kawauchi, Y., & Rausand, M. (1999). Life Cycle Cost (LCC) analysis in oil and chemical process industries. Toyo Engineering Corp, Chiba.

Kimming, M., Sundberg, C., Nordberg, Å., Baky, A., Bernesson, S., Norén, O., & Hansson, P.-A. (2011). Biomass from agriculture in small-scale combined heat and power plants–a comparative life cycle assessment. Biomass and Bioenergy, 35(4), 1572-1581.

Larson, E. D., Consonni, S., & Kreutz, T. G. (2000). Preliminary economics of black liquor gasifier/gas turbine cogeneration at pulp and paper mills. Journal of Engineering for Gas Turbines and Power, 122(2), 255-261.

Lazzaretto, A., & Macor, A. (1995). Direct calculation of average and marginal costs from the productive structure of an energy system. Journal of energy resources technology, 117(3), 171-178.

Lian, Z., Chua, K., & Chou, S. (2010). A thermoeconomic analysis of biomass energy for trigeneration. Applied Energy, 87(1), 84-95.

Mazur, V. (2007). Fuzzy thermoeconomic optimization of energy-transforming systems. Applied Energy, 84(7), 749-762.

Meckler, M., & Hyman, L. B. (2010). Sustainable on-site CHP systems.

Mollersten, K., Yan, J., & Westermark, M. (2003). Potential and cost-effectiveness of CO_2 reductions through energy measures in Swedish pulp and paper mills. Energy, 28(7), 691-710.

Mujeebu, M., Jayaraj, S., Ashok, S., Abdullah, M., & Khalil, M. (2009). Feasibility study of cogeneration in a plywood industry with power export to grid. Applied Energy, 86(5), 657-662.

Naqvi, M., Yan, J., & Dahlquist, E. (2010). Black liquor gasification integrated in pulp and paper mills: A critical review. Bioresource technology, 101(21), 8001-8015.

Raghu Ram, J., & Banerjee, R. (2003). Energy and cogeneration targeting for a sugar factory. Applied Thermal Engineering, 23(12), 1567-1575.

Robert F. Boehm. (1987). Design Analysis of Thermal Systems. New York: Wiley & Sons.

Silveira, J., & Tuna, C. (2003). Thermoeconomic analysis method for optimization of combined heat and power systems. Part I. Progress in energy and Combustion Science, 29(6), 479-485.

Soares, J., Szklo, A., & Tolmasquim, M. (2001). Incentive policies for natural gas-fired cogeneration in Brazil's industrial sector—case studies: chemical plant and pulp mill. Energy Policy, 29(3), 205-215.

The Carbon Trust. (2010). Introducing combined heat and power. Retrieved 24 May, 2015, from http://www.carbontrust.com/media/19529/ctv044_introducing_combined_heat_and_power.pdf

U.S. Environmental Protection Agency, (2014). Catalog of CHP Technologies. from http://www.epa.gov/chp/technologies.html

Valero, A., Lozano, M. A., Serra, L., Tsatsaronis, G., Pisa, J., Frangopoulos, C., & Von Spakovsky, M. (1994). CGAM problem: definition and conventional solution. Energy(19), 279-286.

Vélez, F., Segovia, J. J., Martín, M. C., Antolín, G., Chejne, F., & Quijano, A. (2012). A technical, economical and market review of organic Rankine cycles for the conversion of low-grade heat for power generation. Renewable and Sustainable Energy Reviews, 16(6), 4175-4189.

SESSION 9: LOW-CARBON/ LOW-ENERGY TECHNOLOGIES

203: Engine performance and emission characterization of modelled biodiesel fuels from hybridised moringa oleifera and jatropha curcas seed oils

Andrew C. eloka-eboka[1], Freddie L. inambao [2]

[1,2] *Green Energy Solutions Research Group, Discipline of Mechanical Engineering, University of KwaZulu-Natal, Howard College, Durban 4041, South Africa,*
[1] *fatherfounder@yahoo.com,* [2] *eloka-ebokaa@ukzn.ac.za*

Biodiesel fuels are one of the easiest alternative fuels to be utilized in compression ignition engines. They are renewable, environmentally friendly and produce less gaseous and exhaust emissions. A variety of biodiesel feedstocks have been experimented with using different engine types and for various performance evaluations. In this study, overall engine performance tests and gaseous/emission characterizations were conducted in a four stroke versatile internal combustion engine (TD 300) over a wide range of throttle from the feedstocks of Moringa and Jatropha biodiesel and their resultant biodiesel hybrids. The hybrid compositions were J50M50, J40M10, J30M20, J20M30, and J10M40 from crude oil samples (in situ) and: BM50J50, BM40J10, BM30J20, BM20J30 and BM10J40 from produced biodiesel (ex situ). The biodiesel hybrids were produced by transesterification at specific optimization protocols and subjected to a novel approach in biodiesel development and hybridization using in situ and ex situ processes as reported in our earlier studies (Eloka-Eboka and Inambao [16]). The single stock biodiesel of Moringa and Jatropha and their hybrids performed favourably in comparison to AGO following ASTM standardized procedures. The torque, air consumption, ambient air temperature and pressure, specific fuel consumption, brake thermal and mechanical efficiency, brake power, engine noise, exhaust temperature and smoke opacity were determined. Also, gaseous emission was conducted using an online sampler which was subjected to a GC-MS spectrophotometer interacting with a flame induced detector (FID) for all comparisons. Results show greater improvement in performance from the hybrids and Moringa biodiesel with close similarity to AGO. The emissions were however insignificant to the immediate environment as against those of AGO. Biodiesel development continues to be currently researched until the much needed breakthrough is achieved globally.

Keywords: Engine, performance, emission, characterization, biodiesel, Moringa, Jatropha, seed oil, hybrids, hybridization, in situ, ex situ

1. INTRODUCTION

The civilization of any country has come to be reckoned on the basis of the number of automotive vehicles being used by the populace of the country. The tremendous rate at which population explosion is taking place imposes expansion of cities to larger areas and the common person is forced to travel long distances even for his/her routine work [1-3]. This in turn is causing an increase in vehicular population at an alarming rate thereby creating huge pressures for different governments in raising substantive foreign exchange for the import of crude petroleum products to meet the fuel requirements of automobiles and engines. The large amount of pollutants from the exhausts of engine applications running on fossil fuels have drastically increased in proportion to the number of vehicles on roads [4]. In view of the need and heavy demand for diesel fuel involved in transport in the domestic, industrial and agricultural sector and also the fast depletion of unevenly distributed fossil fuels, the search for alternate fuels has become pertinent apart from effective fuel utilization which has been the concern of the engine designers and manufacturers, developers, users and researchers involved in fuel, renewable and alternate fuel research and combustion [5-7].

When Rudolf Diesel [8] first invented the diesel engine, about a century ago, he demonstrated the principle by employing peanut oil and hinted that vegetable oil would be the future fuel in diesel engines. However, the higher viscosity and chemical composition of unprocessed oils and fats have been shown to cause problems in a number of areas: (i) piston ring sticking; (ii) injector and combustion chamber deposits; (iii) fuel system deposits: (iv) reduced power; (v) reduced fuel economy and (vi) increased exhaust emissions. The above mentioned problems can be solved once vegetable oils are converted chemically into biodiesel [6, 7]. Biodiesels derived from vegetable oils present a very promising alternative to diesel fuel since biodiesels have numerous advantages compared to fossil fuels as they are renewable, biodegradable, provide energy security and foreign exchange savings besides addressing environmental concerns and socio-economic issues [9-14]. These biodiesels have lower viscosity, density, molecular weight and ratio of carbon to hydrogen. Experiments were conducted [5-9] with conventional engine fuelled with biodiesel and it was reported that performance was comparable with conventional engines [10, 11, 13]. The drawbacks associated with biodiesel for use as fuels in compression ignition engines call for improvement in biodiesel production and processes [14, 15].

Biodiesel as mono-alkyl ester made from natural and renewable vegetable oil and animal fats based feedstock can be improved upon by chemical processes such as hybridization [16, 17]. Biodiesel is an environmentally friendly alternative diesel fuel consisting of the alkyl esters of fatty acids which are expected to play a significant role in reducing overall CO_2 emissions which will in turn clean and sustain the environment [14, 15]. Biodiesel is produced commercially by a chemical reaction, transesterification, which lowers the viscosity of the vegetable oils, breaks the poly-unsaturated nature of the bonds and improves its performance, combustion and atomization in the combustion chambers. Since biodiesel is an oxygenated, sulphur-free fuel, it typically reduces engine and gaseous emissions except for the oxides of nitrogen (NOX) which are slightly higher than fossil diesel [14, 15]. The chemical and physical properties of the fatty acids, as well as the effect of molecular structure determine the overall properties of biodiesel fuel. Investigations into the impact of FAME properties on diesel engines are highly topical, as hybrids of different feedstocks and higher blends with automotive gas oil (fossil diesel) of biodiesel are introduced [12, 18].

1.1. Emission Effects

Global warming is considered to be one of the greatest environmental threats facing our modernized and technological world. Climate change has mainly been caused by the increase in atmospheric greenhouse gases due to human activities since the start of the industrial era which includes burning fuel to run engines [18]. When fuels are burnt, the exhaust products contain gaseous, solid, and liquid emissions. For internal combustion (IC) engines, there are just a few basic types of emissions to consider: Carbon (IV) oxide, oxides of Nitrogen (NOx), oxides of Sulphur (SOx), Carbon (II) oxide (CO), hydrocarbons (HC), and particulate matter (PM). In addition to these primary pollutants, reactions in the atmosphere generate secondary pollutants, namely acid rain, photochemical smog and tropospheric ozone [18]. Many of these pollutants have serious implications on human health, safety and the environment. Consequently, many countries have established strict environmental regulations that must be met by all automobile manufacturers and fuel developers.

1.2. Status and legislation of biodiesel use in South Africa

Legislation has driven research to satisfy increasingly stringent emission requirements such as improving the combustion process and utilizing advanced after-treatment systems. Another approach has been to develop and popularize electrically powered vehicles and hybrids, and the use of alternative fuels. Of most recent and still at developmental stage is the process of hybridization of different feedstocks of biodiesel to improve general biodiesel fuel properties which this paper is related to. Studies are at top gear at the Biofuel Research Laboratories of the Green Energy Solutions Research group at the University of KwaZulu-Natal, Howard College, Durban, South Africa to make the required breakthrough. Different feedstocks are being experimented with to ascertain fuel properties and performance characterization [16]. Biofuels are expected to play a significant role in reducing overall CO_2 emissions [4]. Also, the possibility of substituting cleaner burning alternative fuels for gasoline and diesel has drawn increasing attention over the past decade [16]. Biofuels produced from sugar cane, corn or other vegetable oils are attracting interest as renewable energy sources that do not increase CO_2 levels [17]. That is why the South African government granted a reduction of 30% fuel tax for biodiesel thus encouraging its utilization in the country [19]. In terms of legislation, the South African Bureau of Standards (SABS) drafted a provisional biodiesel standard (SANS 1935:2011) [20] edition 2 as comparable to the ASTM D6751:2 which was based on European standards with some modification in parameters like the iodine value, and allowing the use of other esters as well [19]. Feedstocks of specific interests include soya oil, corn and physics nuts (Jatropha). Some studies were conducted with the objective of determining the influence of biodiesel development and application on the South Africa's economy without interfering with food production. The outcome was positive with the assessment that biodiesel especially from non-edible sources could replace 20% of imported diesel in the country [19].

1.3. Engine performance

Cetane Index (CN) is one of the main indicators of the ignition quality and combustion miscibility in diesel engines. It is a dimensionless descriptor for the ignition delay time of a fuel upon injection into the combustion chamber. The higher the cetane number, the shorter the ignition delay time and vice versa. It is an acceptable fact that the CN of biodiesel is generally higher than fossil diesel fuel due to the absence of aromatic compounds and unburnt hydrocarbons [20] and better amongst biodiesel hybrids [16,17]. The European standard for biodiesel (EN 14214:2003) specifies the minimum requirements for CN to be 51, since too low cetane number might cause very rapid and incomplete combustion. Like other properties, Cetane number/index number is affected by the molecular structure of the source material FA [21-23]. The CN of biodiesel depends on the distribution of fatty acids in the original oil or fat from which it was produced. The longer the straight chain FA and the more saturated the molecules in the fuel, the higher the CN [7, 10, 20].

Higher Cetane numbers of the fuel was also correlated with reduced NO exhaust emissions for conventional diesel fuel as stated by Knothe and Steidley [22], however this is not always true for all types of engine technologies, as modern engines that are equipped with more sophisticated injection systems that control the rate of injection are less sensitive to CN variations [20, 22-23]. In addition, several other properties of biodiesel are important for determining its suitability as an alternative to petroleum diesel fuel. It is generally known that biodiesel fuels have lower heat release values than petroleum diesel. Fuel density and number of double bonds also have an effect on the fuel's calorific value but not significantly. Hybridization alters this structural sequence to suit desired fuel needs. A review conducted by some biodiesel researchers concluded that the FAMEs have slightly higher combustion efficiency than baseline diesel fuel due to the structural oxygen content of the biodiesel which improves the combustion process, as also and similar observations reported by Lapuerta et al. [24-26].

Lubricity properties of fuel are very critical for reducing friction wear in engine components which are normally lubricated by the fuel rather than crankcase oil. Mechanical wear and fuel leaks can cause many problems in the engine fuelling system, as fuel pumps and injectors depend on the fuel for lubrication of moving parts. It has been known that biodiesel improves the lubricity of diesel fuel, and it is a common practice among most of the diesel fuel producers to add 1-5% of biodiesel in the ultralow Sulfur diesel (ULSD) fuel to improve its lubrication quality [19, 22]. Particulate Matter (solids or liquids) emissions have been of considerable concern with the manufacturers of diesel engines, as it is very visible and often contains some carcinogenic aromatic hydrocarbons such as benzene. According to an EPA technical report issued in 2002 [12, 14], the particulate matter emissions of B100 and B20 are less than petroleum diesel by 47%, and 12% respectively. Lapuerta et al. [24] reported that particulate matter emissions were investigated by a few authors and their results did not show any significant correlation either with the chain length or with the unsaturation level. But Monyem and Van Gerpen et al. [27, 28] reported an increase in particulate matter with increasing number of double bonds in the fatty acid and no significant impact of FA

chain length was observed. NOx formation is influenced by the oxygen concentration in the fuel, combustion duration, and mixture richness in the combustion chamber [2]. The formation of NOx emissions is also effected by fuel properties, such as cetane number, aromatics content and iodine number. Lapuerta et al. [24] reported that the use of biodiesel fuels leads to a slight increase in NOx emissions, especially in the case of highly un-saturated biodiesel fuels.

1.4. Improvement consideration in biodiesel feedstock

When considering the total amount of greenhouse gas emissions it is therefore important to consider the whole production process and what indirect effects such production might cause. The effect on carbon dioxide emissions is highly dependent on production methods and the type of feedstock used. Calculating the carbon intensity of biofuels is a complex and inexact process, and is highly dependent on the assumptions made in the calculation. A calculation usually includes:

1. Emissions from growing the feedstock (e.g. petrochemicals used in fertilizers);

2. Emissions from transporting the feedstock to the factory;

3. Emissions from processing the feedstock into biodiesel.

Based on these, production methodology of biodiesel as a whole is as important as quality of the biodiesel. In cases where there is incomplete transesterification process, the end product(s) may be undesirable for utilization in the engines which may also affect the environment

1.5. Specific study objectives

Engine testing facilities are commonly used in engine development and catalyst performance research laboratories to achieve further emission reductions. A variety of biodiesel feedstocks have been experimented with using different engine types and for various performance evaluations but the aim of this study is overall engine performance tests and gaseous/emission characterizations on a four stroke versatile internal combustion engine (TD 300) over a wide range of throttle from the feedstocks of Moringa and Jatropha biodiesel and their resultant biodiesel hybrids produced by transesterification, at specific optimization protocols and subjected to a novel approach in biodiesel development, viz. a viz hybridization using *in situ* and *ex situ* processes as reported in our earlier studies [16].

In this study, the single stock biodiesel of Moringa and Jatropha and their hybrids were subjected to standardized procedures and compared with AGO. The torque, air fuel ratio, ambient air temperature and pressure, specific fuel consumption, brake thermal and mechanical efficiency, brake power, exhaust temperature and smoke opacity and their individual effects were determined with significant differences; gaseous emissions were also measured to ascertain the level of improvement in performance.

2. MATERIALS AND METHODS

2.1. Development and application of biodiesel production model

The biodiesel production model that was adopted in this study was derived from the production protocol of CSIR-CSMCRI, Bhavnagar [30] for Jatropha biodiesel production patented in the US which was re-evaluated and modified to suit variable feedstocks in this study. The working principle was the free fatty acid neutralization through base wash. The processes involved are a form of oil pre-treatment which conditioned the crude oil for transesterification. The free fatty acid composition of any crude vegetable oil and its neutralization is the main thrust of reaction. Oil with lower free fatty acids requires less treatment procedures and less materials of reaction. The modified model is preceded by several stoichiometric calculations which are then applied in the experimental reactions. The model encompasses a dual way process consisting of two main reactions: base wash/neutralization reaction using strong base, in this case, aqueous solutions of sodium hydroxide (NaOH) was used for base-wash in the first phase while methyl-esterification reaction was performed in the second phase using methanol in the presence of potassium hydroxide (KOH) as catalyst. NaOH interacts better in aqueous medium hence the choice in the base wash while the solubility of KOH in organic solvent makes it the choice in esterification. The effervescence reaction with NaOH in water enhances the dissolution and therefore proper pre-treatment of the crude vegetable oil. The calculations were adopted in excel spreadsheets and values imputed to give required

compositions for the reaction simply by changing the quantity of oil to be transesterified (in kg) and the fatty acid composition. The model generated the required NaOH and water for dissolution and also the required KOH needed to convert the neutralized oil to biodiesel. Expounding on this model is well beyond the scope of this present study.

Before adopting the model, four important experimental and numerical determinations were required:

Determination of the average molecular weight of fatty acids usually adopted for any member of the carboxylic acid family; determination of the weight of the crude oil to be transesterified (in kg): determination of the free fatty acid composition of the crude oil using any method; and determination of the total free fatty acids.

From the experimental and numerical calculations of this model, the following will be determined: The amount of sodium hydroxide (NaOH) required for neutralization/ base wash for any quantity and type of crude vegetable oil; the amount of water (H_2O) needed to dissolve the required sodium hydroxide; the amount of potassium hydroxide required as catalyst for transesterification and the amount of methanol (alcohol) required for the total transesterification of vegetable into biodiesel (methyl esters).

The engine test performance and emission analysis test which followed the model experimentation was conducted at the Biofuels laboratory of the Petroleum Processing Engineering Technology of Petroleum Training Institute, Effurun, Nigeria. A TD 300, a versatile engine test bed with instrumentation for comprehensive investigations into the features and operating characteristics of internal combustion engines was used for the study. It enables a wide range of investigations into the characteristics of four-stroke single-cylinder petrol and diesel engines. For use with engines up to 10 kW: four-stroke diesel and four-stroke petrol engines ideal for group demonstrations and student projects; Includes comprehensive control console and instrumentation; Optional ancillaries available to extend the range of study even further; Quick, convenient and accurate engine mounting and changeover; Test bed includes anti-vibration mounts; Uses four-quadrant drive to start and load the engine, giving excellent stability; Self-sealing couplings enable quick and efficient connection and disconnection of fuel lines with minimum loss or spillage of fuel; Works with TecQuipment's Versatile Data Acquisition System (VDAS®).

The main components of the system are: a heavy fabricated floor-mounting bed; an instrument console with instrument frame; a fuel tank support frame that supports the fuel tank and optional fuel gauge. The bed is held on anti-vibration mounts. It includes a robust trunnion-mounted d.c. machine. An electronic load cell connected to the machine measures the driving torque of the test engine. The engines are supplied pre-mounted on a sturdy precision base plate. When the engine is initially mounted onto the test bed or exchanged with an alternative engine, dowels and slots locate the engine quickly, accurately and reliably. Each engine includes a colour-coded fuel tank with self-sealing couplings. The couplings ensure the engines can be connected and disconnected quickly and efficiently with minimum loss or spillage of fuel. For convenience and safety, the fuel tank can be removed for filling or for storage in a fuel locker when not in use. Removing the fuel tank also prevents unauthorized use of the equipment.

The control has an electrical cabinet which houses a four-quadrant drive to start and load the engine. The motor can also be used to drive the engine while the fuel and ignition are off, so students can establish frictional losses. The control includes an air-box and orifice plate to enable students to measure air flow. The instrumentation and display units are mounted on a sturdy frame, which is part of the control. The control also includes a convenient work top for use as a writing desk, or for positioning other equipment such as a computer. The control and test bed are separate in order to avoid vibration being transmitted from the engine to the measuring devices. In addition, it allows the instrumentation to be thermally and acoustically screened from the test bed, using suitable shielding or a wall. The engines (available separately) include an exhaust thermocouple, dynamometer coupling, colour-coded fuel tank, hoses and fittings. They have modified cylinder heads and cranks for connection to TecQuipment's Engine Cycle Analyzer (ECA100 available separately). An Exhaust Gas Calorimeter (TD300a) is also available to enable students to measure energy lost through exhaust gases and to determine the energy balance of the engine.

2.2. Power, torque and rotational speed relationship employed

The relationship of power, torque and rotational speed according to Serway and Jewett [29] and general engine technology is crucial to engine performance. Mathematically for rotation about a fixed axis or point, the expression is given by:

$$W = \int_{\theta 1}^{\theta 2} \tau \, d\theta \qquad\qquad (5.1)$$

Where W = work, τ = torque, θ_1 and θ_2 are initial and final angular positions.

From the theory of work-energy and power, W is equal to change in rotational kinetic energy, ΔE which is given by;

$$\Delta E = \frac{1}{2} I \, \omega^2 \qquad\qquad (5.2)$$

Where I is the moment of inertia and ω is the angular speed (rpm).

$$P = \tau . \omega \qquad\qquad (5.3)$$

P = power, т = torque and ω = angular velocity.

The power injected by the torque depends on instantaneous angular speed and the power output [29] is determined by the torque applied to the engine generator as schematically presented in Figure 5.1.

$$P = \tau \times \pi \times \omega \qquad\qquad (5.4)$$

2.3. Emissions Determination

The temperature attained at different time and speeds were recorded using the thermocouple and the digital meter. The fuel consumption per sample for the period of the tests (40 minutes) was also recorded. This was accomplished by taking the difference of the volume of the initial fuel used for each run and the final volume after runs for 40 minutes. The amount of flue gas emitted (O2, CO, NO2 and VOCs) at each interval of time, temperature and speed for each sample was recorded in parts per million (ppm) and compared. All the data collected were analyzed, compared and graphs plotted. Inference statistics were used for this analysis and applied for the purpose of this study. The experimental setup used in the present work is shown in Figure alongside portable diesel smoke meter (opacimeter). The engine was loaded with an eddy current dynamometer. The mass flow rate of intake air was measured with an orifice meter connected to a manometer. A surge tank was used to damp out the pulsations produced by the engine, for ensuring a steady flow of air through the intake manifold. The fuel consumption rate was determined using the glass burette and stop watch. The engine speed was measured using a digital tachometer. An AVL 444 Di gas analyzer was used for measuring the exhaust gas components such as CO, HC, and NOx. The smoke density was measured using an AVL 413 smoke meter. The exhaust gas temperature was measured with a k-type thermocouple.

Figure 1: Experimental setup (TD 300/302) Engine test set up and portable diesel smoke meter

Before starting the measurements, some important points were considered in order to get meaningful data from the experiments. The engine was warmed up prior to data acquisition. The lubricating oil temperature was monitored to confirm that the engine was in a sufficiently warmed-up situation. Ambient conditions

should be maintained for different engine runs because the ambient pressure and temperature have an effect on intake air drawn into the engine cylinder, thereby changing the fuel-air mixing as well as combustion process. All the engine test runs were carried out in fair constant ambient conditions. During the tests with hybrids biodiesel, the engine was started with AGO until it warmed up. Then fuel was switched to biodiesel and hybrids. After finishing the tests with biodiesel B100 the fuel was always switched back to diesel and the engine was run until the hybrids biodiesel had been purged from the fuel line, injection pump, and injector in order to prevent starting difficulties at later time.

At the start of each test the test engine was operated with base fuel-diesel for about 30 minutes to attain a normal working temperature condition after that base line data were generated and the corresponding results were obtained. The engine was then operated with hybrids of biodiesel in situ (J50M50, J40M10, J30M20, J20M30, and J10M40) and ex situ (BM50J50, BM40J10, BM30J20, BM20J30 and BM10J40). At every operation the engine speed was checked and maintained constant. All the measurements were repeated thrice, and the arithmetic mean of these three readings was employed for calculation and analysis. The different performance and emission parameters analyzed in the present investigation were brake thermal efficiency (BTE), brake-specific fuel consumption (BSFC), exhaust gas temperature (EGT), carbon monoxide (CO), unburned hydro-carbons (HC), nitrogen oxide (NO), and smoke. Smoke opacity was measured using portable diesel smoke meter (Figure 5.4) according to SAE J1667 standards as adopted by South African National Standards [20].

3. RESULTS AND DISCUSSION

The results show that crude Moringa oil properties which include some chemo-physical properties which are determinants in its characteristics as a feedstock for biodiesel. The chemo-physical and thermal properties have been presented in our previous paper. As this study is primarily concerned with the engine performance and emission characteristics, parameters such as brake specific fuel consumptions (BSFC) on engine loads, brake specific thermal efficiencies (BSTE) on engine loads, exhaust gas temperatures on engine loads, smoke opacity on engine loads were evaluated. Also expressed are the comparisons of thermal and mechanical efficiencies, composition of gaseous emissions and the effects of engine loads on them. These are presented in Table 1, Figures 2 to 8. As can be seen in Table 1, the average biodiesel (B100 and the acceptable biodiesel bend, B20) was compared with conventional AGO for regulated and non-regulated emissions. The emissions of CO, PM and NOx were significantly reduced in biodiesel compared to AGO and B20 (80% of AGO). Sulphates, PAHs and nPAH which were non-regulated also followed the same trend of non-pollution in biodiesel. This was as established by the National Biodiesel Board of the US and was employed as the benchmark (standard/control) for comparison of the hybrids performance of this study. The effects of engine loads on thermal efficiency in Figures 2 and 3 when AGO and biodiesel hybrids were used to power the engine exhibited close comparison with the AGO. The efficiencies increased as the engine load was increased for all the hybrids utilized.

Table 1: Average biodiesel (B100 and B20) emissions compared to conventional diesel. Source: National Biodiesel Board, Biodiesel Fact Sheets, Emissions

Emission Type	B100	B20
	Emissions in relation to conventional diesel	
Regulated		
Total Unburned Hydrocarbons	-67%	-20%
Carbon Monoxide	-48%	-12%
Particulate Matter	-47%	-12%
NOx	+10%	+2% to -2%
Non-Regulated		
Sulfates	-100%	-20%a
PAH (Polycyclic Aromatic Hydrocarbons)b	-80%	-13%
nPAH (nitrated PAH's)b	-90%	-50%c
Ozone potential of speciated HC	-50%	-10%

Figure 2: Effects of engine loads on brake thermal efficiencies of biodiesel and hybrids

Figure 3: Effects of engine loads on brake specific fuel consumption of biodiesel and hybrids

The difference in the response of AGO and biodiesels was quite insignificant even though AGO performed better. At full load, AGO produced 40% thermal efficiency while the hybrid biodiesel fuels produced between 35% and 40%. BM50J50 and BM40J10 were as high as 38%. The presence of oleic acid and the higher oxidative stability of Moringa as a hybridization agent may be responsible for this improved performance. This was due to the higher percentage in brake power as loads are applied. The high presence of dissolved oxygen and complete combustion of the biodiesel hybrids were also responsible which enabled proper atomization of the fuel molecules. Fuel consumption (Figure 3) is also related to the thermal efficiencies which decreased as the loads increased. Biodiesel and hybrids combusted more than AGO so had a lesser consumption rate with superior heating/calorific value, lesser specific gravity and lower mass flow injected into the engine [19]. Viscosity as a property also played a significant role in the atomization of fuel in the combustion chambers. At full load, the specific fuel consumption of AGO was as low as 0.28 kg/kWh while the hybrid biodiesel recorded between 0.30 kg/kWh to 0.42 kg/kWh.

This is quite an improvement from non-hybridized conventional biodiesel fuels as recorded by other researchers. The mono-unsaturated oleic acid which is very prominent in the Moringa hybridizing agent with fatty acid profile of 74.0% as indicated in our earlier studies [16, 17] also made a significant contribution. Oils with high oleic acid content are desirable and give biodiesel fuels a reasonable balance or compromise of fuel properties. Considering that the other saturated fatty acid methyl esters (C20:0 and C22:0) in Moringa biodiesel as well as C22:1 likely have high cetane numbers, a high cetane number of Moringa biodiesel is anticipated [16, 17]. Figures 4 and 5 show the trend of events of the exhaust gas temperature and smoke opacity with increased engine loads. There was a general increase in smoke opacity and exhaust temperature as the engine loads increased. But in comparison to AGO, the biodiesel and the hybrids performed better. At peak load, AGO recorded 380 HSU while the hybrids fell between 290 and 320 HSU; what this means is that AGO produced more smoke than the biodiesel and hybrids. Density/opacity of smoke is used to measure the efficiency of combustion of fuel in the engine. The lower

the better and higher is the environmental protection it offers. The exhaust gas temperature is also closely linked with the former. Fossil AGO recorded higher temperatures than the biodiesel hybrids. At peak load, it was 395°C while the hybrids were between 320°C to 375°C. Biodiesel and hybrids with lesser emissions and lower exhaust gas temperatures are not prone to tail pipe and exhaust corrosion compared to AGO. It must be noted that the quantity of fuel injected into the engine increases with engine load to maintain the power output and therefore the heat released rises proportional to the exhaust gas temperature as the load increases which is also indicative of combustion quality in the chamber.

Figure 4: Effects of engine loads on smoke opacity of biodiesel and hybrids

Figure 5: Effects of engine loads on exhaust gas temperature of biodiesel and hybrids

For all the emissions, CO, CO_2, NOx, VOCs as evaluated in Figures 6, 7 and 8 with AGO, there was a general trend with respect to engine loads. At constant load, there was slight variation with respect to hybrids which was very wide compared to AGO (0.035 and 0.018 %) vol composition of CO_2 at 100 and 50% load respectively while the hybrids fell between 0.02 to 0.017 and 0.008 to 0.02% vol at 100 and 50% respectively. Figures 6 shows that AGO produced a wider variation in composition of CO than biodiesel and hybrids while Figure 7 compared mechanical and thermal efficiencies. The same trend is also observable in Tables 2 with respect to torque, temperature and rotational speed, v in rpm. Between the speed of 1000 rpm to 200 rpm, the torque, and temperature with increase in time from 5 minutes to 40 minutes, the emissions of CO, NOx, CO, VOCs and O_2 increased for AGO and for the hybrids at 50 and 100% load respectively.

Figure 6: Effect of CO emission composition of the hybrids at different loads

Figure 7: Effect of NOx emission composition on the hybrids at different loads

Figure 8: Effect of VOCs emission composition on biodiesel and hybrids at different loads

4. CONCLUSION

The aim of this investigation was to evaluate engine performance and usability of Moringa and Jatropha hybridized biodiesel fuels produced by the model of improved method and by hybridization as a new approach in biodiesel improvement and to characterize the emission from compression ignition engines in accordance to ASTM standards and to compare with AGO (Control). Moringa biodiesel appears to be a biodiesel fuel with one of the highest cetane numbers ever reported as biodiesel fuel. There is no doubt that Moringa is a potentially valuable oil seed crop and that its oil appears to be a viable and promising feedstock for biodiesel production and as a hybridization agent. The performance of the hybrids of Jatropha and Moringa seed oil in the CI engine was very close to the performance of the petroleum diesel (AGO). Therefore, they can be used in CI engines for any diesel engine application without modification both in

rural areas and for meeting the energy requirement in various agricultural operations such as irrigation, threshing, grinding and general farm operations. The CI engine ran successfully during the tests conducted. The hybrids characterized for their improved chemo-physical and stable thermal properties performed favourably compared with conventional diesel (AGO). The specific fuel consumption, thermal and mechanical efficiencies, exhaust gas emission were close to the value obtained from AGO. The overall smoke density produced during combustion were less than those produced by AGO while also all the emissions produced were better and more environmentally friendly, achieving higher energy efficiencies from hybridisation of biodiesel feedstock. All the hybrids showed improved properties compared to the non-hybridised or single stock biodiesel. Recommendation is that other feedstocks should be experimented with hybridisation either *in situ* or *ex situ*. This study has also pointed a direction to researchers to look at other forms of hybridisation of feedstocks such as hybridising not just two feedstock oils (bi-hybridisation) but also poly-hybridisation.

5. ACKNOWLEDGEMENT

6. REFERENCES

[1] KOFFMAN, D., Weiner, R., Pfeiffer, A. and Chapman, S. (2010). Funding the public transportation needs of an aging population: TCRP Project J-11, Task 8, Transit Cooperative Research Program, Nelson\Nygaard Consulting Associates, San Francisco, California.

[2] RAJA, S.A., Robinson, D.S. and Lindon, C.R.L. (2011). Biodiesel production from Jatropha oil and its characterization. Research Journal of Chemical Sciences, 1(1); 81-87.

[3] RAHMAN, K.M., Mashud, M., Roknuzzaman, M.D. and Asadullah, Al G. (2010). Biodiesel from Jatropha oil as an alternative fuel to diesel engine, IJMME-IJENS, 10(3): 1-6.

[4] IBRAHIM, J.S. and Eloka-Eboka, A.C. (2012). Evaluation of levels of automobile exhaust gas pollution in selected cities of Benue State. Advances in Science and Technology, 8(1): 14-18.

[5] AGARWAL, A.K. (1999). Performance evaluation and tribological studies on a biodiesel fuelled compression ignition engine. Ph.D. Thesis, Indian Institute of Technology, Delhi, India.

[6] AJIWE, V.I.E., Ajibola, V.O. and Martins, C.M.O.A. (2001). Vegetable diesel fuels from Castor oil, its methyl-ester and ester-diesel blends. Journal of Applied Sciences, 3(4): 1471-1487.

[7] AJIWE V.I.E., Ajibola, V.O. and Martins, C.M.O.A. (2002). Pentadetha macrophylla (oil bean) oil, its methyl-ester and ester-diesel blends. Alternative source of diesel. Nnamdi-Azikiwe University, Awka. African Journal of Science, 3(2): 587-600.

[8] REDDY, V.S., Ranjan, K.R., Sharma, V.K. and Tyagi, S.K. (2011). Experimental investigation of a diesel engine fuelled with Jatropha curcas L. seed oil, International Journal of Sustainable Energy, 30: sup1, S4-S10.

[9] VAN GERPEN, J.H., Peterson, C.L. and Goering, C.L. (2007). Biodiesel: an alternative fuel for compression ignition engines. Presentation at the 2007 Agricultural Equipment Technology Conference Louisville, Kentucky, USA 11-14 February.

[10] ASTM. (2002). D 6751 Standard specification for biodiesel fuel (B100) blendstock for distillate fuels. West Conshohocken, Penn.: ASTM International.

[11] ASTM. (2006). Standard Specification for Diesel Fuel Oils. West Conshohocken, Penn.: ASTM International.

[12] VAN GERPEN, J.H. 2005. Biodiesel processing and production. Fuel Processing Technology 86: 1097-1107.

[13] MIRUNALINI, T., Anand, R. and Mahalakshmi, N.V. (2006). Jatropha oil as a renewable fuel in a diesel engine. Proceedings of the 3rd BSME-ASME International Conference on Thermal Engineering, 20-22 December, 2006, Dhaka, Bangladesh.

[14] KNOTHE, G. Gerpen, J.H. and Jurgen, K. (2005). The biodiesel handbook. Champaign, Ill: AOCS Press.

[15] IGBUM, O.G., Eloka-Eboka, A.C., Ubwa, S.T. and Inambao, F.L. (2014). Evaluation of environmental impact and gaseous emissions of biodiesel fuels and blends of selected feed-stocks. International Journal of Global Warming, Inderscience Publication Series, Volume 6 No 1: 99-112.

[16] ELOKA-EBOKA, A.C. and Inambao, F.L. (2014a). Hybridisation of feedstocks – a new approach in biodiesel development: A case of Moringa and Jatropha seed oils. Energy Sources Part A (Taylor and Francis) (Accepted and in Press).

[17] ELOKA-EBOKA, A.C. and Inambao, F.L. (2014b). Blending of feedstocks – a new approach in biodiesel development: A case of Moringa and Jatropha seed oils. Proceeding of 22nd Domestic Use of Energy Conference, Cape Peninsula University of Technology, Cape Town, 31st March - 2nd April, 2013: 189-196. (Published in IEEE Explore).

[18] KRISHNA, M.V.S., Chowdary, R.P., Kishen, T., Reddy, K and Murthy, P.V.K. (2013). Performance, emissions and combustion characteristics of waste fried vegetable oil in based biodiesel in high grade low heat rejection diesel engine. British Journal of Applied Science & Technology, 3(4): 1345-1367.

[19] KORBITZ, W. (2005). Status of biodiesel in Asia, the Americas, Australia and South Africa. In: Knothe, G. (Ed.). The Biodiesel Handbook. National Centre for Agricultural Utilization Research, Agric Research Service, USDA, Illinois, USA.

[20] South Africa National Standard (SANS 1935:2011) (2011). Automotive biodiesel – fatty acid methyl esters (FAME) for diesel engines – requirements and test methods. Pretoria: SABS Standards Division.

[21] VAN GERPEN, J.H., Peterson, C.L., Goering, C.E. (2007). Biodiesel: an alternative fuel for compression ignition engines. Presentation at the 2007 Agricultural Equipment Technology Conference Louisville, Kentucky, USA 11-14 February 2007.

[22] KNOTHE, G. and Steidley, K.R. (2005). Lubricity of components of biodiesel and petrodiesel: the origin of biodiesel lubricity. Energy and Fuels, 19: 1192-1200.

[23] AGARWAL, A.K. (2007). Biofuels (alcohols and biodiesel) applications as fuels for internal combustion engines. Progress in Energy and Combustion Science, 33: 233-271.

[24] LAPUERTA, M., Armas, O. and Rodríguez-Fernández, J. (2008). Effect of biodiesel fuels on diesel engine emissions. Progress in Energy Combustion Science, 34: 198-223.

[25] LAPUERTA, M., Armas, O., Ballesteros, R. and Fernández, J. (2005). Diesel emissions from biofuels derived from Spanish potential vegetable oils. Fuel, 84: 773-780.

[26] LAPUERTA, M., Rodriguez-Fernandez, J. and Agudelo, R. (2008). Diesel particulate emissions from used cooking oil. Biodiesel. Bioresour. Technol. 99: 731-740.

[27] MONYEM, A.; Gerpen, J.V. (2001). The effect of biodiesel oxidation on engine performance and emissions. Biomass Bioenergy, 20, 317-325.

[28] MONYEM, A., van Gerpen, J.H. and Canakci, M. (2001) The effect of timing and oxidation on emissions from biodiesel-fueled engines. Transactions of the ASAE, 44: 35-42.

[29] SERWAY, R.A. and Jewett, Jr, J.W. (2003). Physics for scientists and engineers. 6th ed. Pacific Grove, CA: Brooks Cole.

[30] SRINIVASAN, K., Sankaranarayanan, S. and Antonyraj, C.A. (2012). Improved process for the preparation of fatty acid alkyl esters (biodiesel) from triglyceride oils using eco-friendly solid base catalysts. Goggle patents.

113: Performance and emissions prediction of natural gas engine using two-zone combustion model

Yu Ding, La Xiang, Jialin Cui, Kui Wang

College of Power and Energy Engineering, Harbin Engineering University, Harbin, China,
dingyu@hrbeu.edu.cn

Natural gas (NG) is considered as one of the cleanest fuels to replace the conventional fuels such as diesel, petrol because of its rather lower emissions, which has been proven by engine tests at labratories and manufactories in the world. Generally the NG engines share the similar structure profile with diesel or petrol engines, but the combustion characteristics and pollutant emissions are different due to its gaseous properties and higher hydrogen-carbon ratio.

In this paper a two-zone simulation model is built to characterize the thermodynamic state of the burnt zone and unburnt zone separately. Each of them is consisted of properties library, mass balance and composition, gas pressure, heat loss and pollutant formation sub-models, etc. The Vibe function, which is based on the first principle of chain reactions, is used to calculate the heat release rate of NG. In order to obtain the gas properties, the in-cylinder gas is considered as a mixture of three well defined basic mixtures - NG, air and stoichiometric gas, whose properties are the functions of temperature. The purpose of mass balance and composition model is to acquire the mass of each zone and proportions of the three basic mixtures. In the gas pressure model, 'First Law of Thermodynamics' is used to calculate the in-cylinder pressure. The heat transfer coefficient can be estimated using the Woschni formula while the temperatures of the cylinder wall, cylinder cover, piston crown are assumed to be constant. In pollutant formation model, the 'Zeldovich Mechanism' are applied to calculate the NO and concentration in the cylinder.

The simulation model is implemented in MATLAB/SIMULINK environment and provides the prediction of engine performance and pollutant emissions. Furthermore, a comparison is carried out between the two-zone model and a single-zone model, in which the power output and NO concentration are chosen as criterions. It is shown in the results that the two-zone model performs better in the prediction of NO emission with a slight difference in power output.

Keywords: natural gas engine, two-zone, simulation, performance, emissions

1. INTRODUCTION

With the increasing concern on the pollutant emission and energy shortage, it is becomes an inevitable trend to find new alternative fuels in place of diesel and petrol more than ever. Natural Gas (NG) is considered as an appropriate alternative for internal combustion engines because of its cleaner combustion and lower cost (Bhandari et al., 2005, Tilagone et al., 2006). Engines fuelled with NG emit less carbon-monoxide and hydrocarbons compared to gasoline engines, but the NOx emission may not be low enough to meet the increasingly more stringent emission regulations as shown in Figure 10(Ma et al., 2007, Herdzik, 2011).
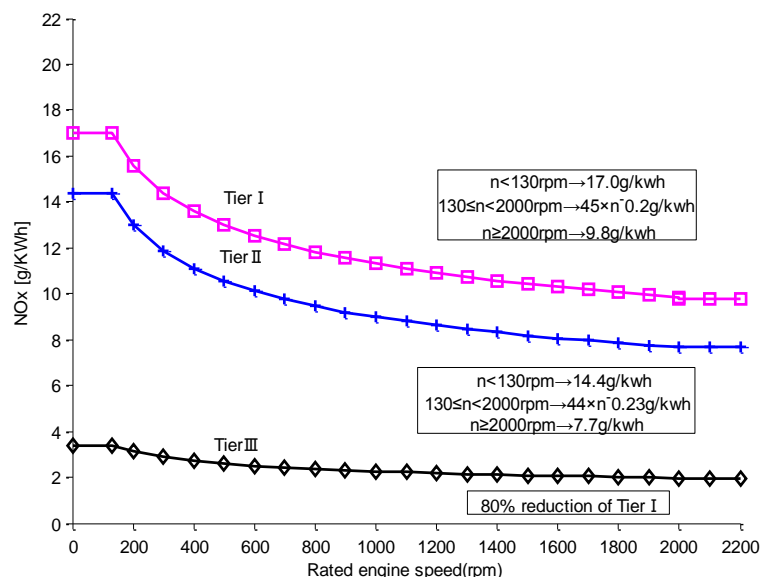
Figure 10: NOx emissions according to MARPOL Annex VI requirements

Simulation models of engine processes are valuable tools to predict engine performance and pollutant emission. Compared to zero-dimensional and multi-dimensional models, the quasi-dimensional models are able to calculate emission levels with a degree of accuracy but without a high computational cost (Verhelst and Sheppard, 2009). For common used quasi-dimensional models of spark ignition engines, the volume ratio of different zones is often determined by applying a flame propagation sub-model, which depends on accurate evaluation of the mean turbulence intensity and laminar flame speed(Metghalchi and Keck, 1982, Gülder, 1991). When the engine in-cylinder process is assumed to be single zone, the simulation procedure is simple to predict the engine performance, but the in-cylinder temperature mixed with the burnt and unburnt zones is relative lower, which results in NO calculation is far from the actual value.

In this paper, a two-zone model is built in the MATLAB/SIMULINK environment to simulate the in-cylinder process of a premixed NG engine, and the two-zone model is compared with a single-zone model to investigate the engine performance and NO emission.

2. MODEL DESCRIPTION

In order to predict the performance and emission of natural gas engine, a two-zone model is built, in which considers the chamber as two parts separated by the flame front. The two-zone thermodynamic model is built on certain assumptions, as outlined as follows:

a) The space inside the cylinder is discretized in two cylindrical zones – burnt zone and unburnt zone, as depicted in Figure 11;
b) The pressure at any time is uniform throughout the cylinder;
c) The in-cylinder temperature is divided as burnt temperature and unburnt temperature, which is uniform in their own zone. There is no heat transfer between the two zones;
d) The unburnt zone is composed of natural gas, air and stoichiometric gas, while the burnt zone is entirely composed of stoichiometric gas. Combustion occurs in the flame front which is negligible in volume;
e) Charge in each zone is assumed to be homogenous and the basic species are considered as ideal but non-perfect gases.
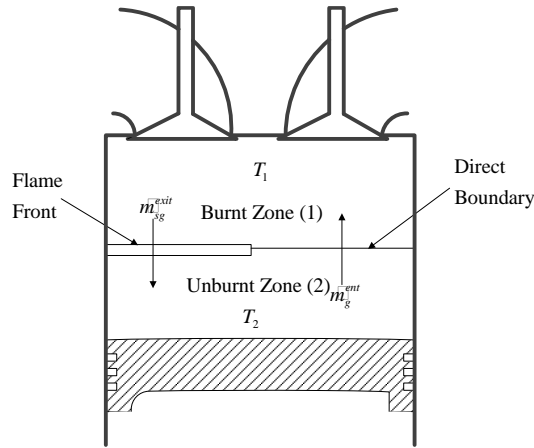
Figure 11: Two-zone model for natural gas engine

2.1. Sub-models for Each Zone

According to the assumptions, sub-models for each zone are zero-dimensional. The subscript 1 and 2 will be respectively used to describe parameters related to burnt zone and unburnt zone. Equation 1 is the core equation of the simulation model for burnt zone, which is derived from the First Law of Thermodynamics by separating temperature terms. The left hand side of Equation 1 is the internal energy variation caused by temperature change. On the right hand side, the five terms orderly represent entering enthalpy flow, exiting enthalpy flow, combustion heat flow, heat loss to the cylinder wall and volumetric work. Since NG shows a main characteristic of premixed combustion, a single Vibe function is applied to simulate the combustion reaction rate (ξ) (Ghojel, 2010). Gas properties parameters (e.g. specific heat, internal energy, gas constant, et) can be obtained by mass fraction (x) and temperature (T). In addition, the Woschni formula is employed to evaluate the heat transfer coefficient (Stapersma, 2008).

Equation 1: Energy conservation in burnt zone

$$m_1 \cdot c_{v,1} \cdot \frac{dT_1}{dt} = \dot{m}_g^{ent} \cdot \left(h_g^{ent} - u_{g,1} \right) - \dot{m}_{sg}^{exit} \left(h_{sg}^{exit} - u_{sg,1} \right) + u_{comb} \cdot \xi - \dot{Q}_{1 \rightarrow wall} - p \frac{dV_1}{dt}$$

Where:

- $\dot{m}_g^{ent}$, $\dot{m}_{sg}^{exit}$ = mass flow entering and exiting the burnt zone (kg/s)
- u_{comb} = specific heat of combustion (J/kg)
- ξ = combustion rate of natural gas (kg/s)

Energy conservation in unburnt zone is presented as Equation 2, in which the terms are similar to Equation 1 except the combustion heat flow.

Equation 2: Energy conservation in unburnt zone

$$m_2 \cdot c_{v,2} \cdot \frac{dT_2}{dt} = -\dot{m}_g^{ent} \cdot \left(h_g^{ent} - u_{g,2} \right) + \dot{m}_{sg}^{exit} \left(h_{sg}^{exit} - u_{sg,2} \right) - \dot{Q}_{2 \rightarrow wall} - p \frac{dV_2}{dt}$$

2.2. Volume Balance between Two Zones

During the in-cylinder process, the volume ratio of burnt zone and unburnt zone changes once combustion begins. So the volume balance is an important element to consider in order to compute the in-cylinder pressure and the volume of the two zones. Figure 12 presents the calculation flow of volume balance, in which the Ideal Gas Law and geometry of the engine are used. To solve this balance, three new parameters are introduced to determine the initial conditions and mass flow of the two zones.

The mass factor S_{mass} is defined as the ratio between initial mass of burnt zone and the whole cylinder. Then the initial mass of burnt zone and unburnt zone can be calculated by Equation 3 and Equation 4.

Equation 3: Initial mass of burnt zone

$$m_{1,0} = S_{mass} \cdot m_0$$

Equation 4: Initial mass of unburnt zone $\qquad m_{2,0} = \left(1 - S_{mass}\right) \cdot m_0$

Where:

- m_0= mass of the whole cylinder at inlet valve close moment (kg)
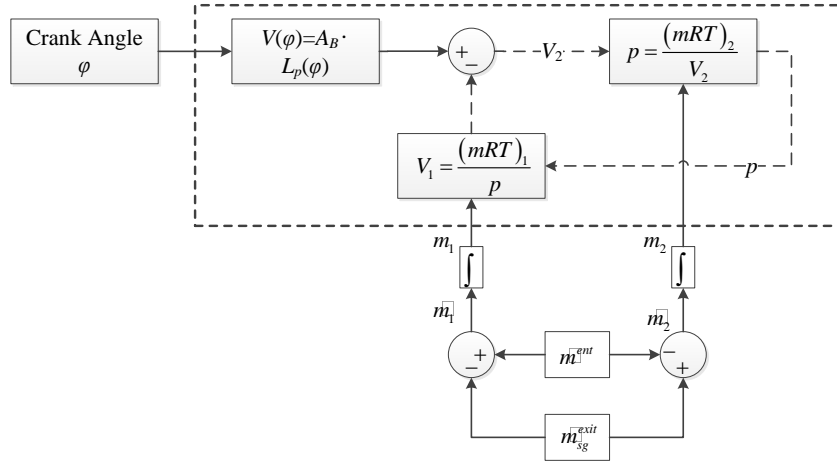
Figure 12: Volume balance

The entrained rate $\overset{\text{ent}}{m_g}$ is fixed by the stoichiometry of fuel σ and the combustion rate ξ on assumption that the unburnt zone is composed of natural gas and air. But in fact it is inevitable for the stoichiometric gas to enter the unburnt zone during the mass exchange process between the two zones. The entrainment factor λ_{ent} is introduced to account for the existence of stoichiometric gas in unburnt zone and the possibility that entrained air could be more than or less than the stoichiometric amount. Then the entrained rate can be computed by Equation 5.

Equation 5: Entrained rate $\qquad \overset{\text{ent}}{m_g} = \xi \cdot \left(1 + \sigma \cdot \lambda_{ent}\right)$

Referring to the literature, on the one hand in the work of Holhbaum (Merker et al., 1993) all the produced gas leaves the burnt zone, and on the other hand in the Heider (Heider, 1995) model the produced stoichiometric gas stays in the burnt zone. Therefore, the Heider-Holhbaum factor S_{HH} is defined as the quotient between the stoichiometric gas flow leaving the burnt zone and the stoichiometric gas production rate. Then the mass flow of stoichiometric gas leaving the burnt zone can be worked out according to Equation 6.

Equation 6: Exiting gas flow $\qquad \overset{\text{exit}}{m_{sg}} = S_{HH} \cdot \xi \cdot \left(1 + \sigma\right)$

2.3. Gas Properties Calculation

In order to obtain the gas properties, the in-cylinder gas is modelled as a mixture of three well defined basic mixtures –air, natural gas and stoichiometric gas. Since the concentrations of N, O and NO are smaller than that of other combustion intermediate products by several orders of magnitude, they are not taken into account when calculating the gas properties. Then the constituents of the three basic mixtures are assumed as follow:

a)   Air: Fixed-fraction dry air (N_2, O_2, Ar, CO_2) and water vapor (H_2O);
b)   Natural gas: CH_4, C_2H_6, C_3H_8, n-C_4H_{10}, i-C_4H_{10}, C_5H_{12}, N_2;
c)   Stoichiometric gas: N_2, O_2, Ar, CO_2, H_2O.

The 'specific heat of combustion' can be calculated by the internal energy of fuel, air and stoichiometric gas in Equation 7.

Equation 7: Specific heat of combustion $u_{comb} = u_f + \sigma \cdot u_a - (1+\sigma) \cdot u_{sg}$

Where:

- σ = ratio of air and fuel
- u_f, u_a, u_{sg} = specific internal energy of natural gas, air and stoichiometric gas (J/kg)

Gas properties of the basic mixtures are functions of in-cylinder temperature and the mixture fraction since each species are considered as ideal but non-prefect gases in the model. Therefore the specific heat of in-cylinder gas can be calculated according to Equation 8. Specific internal energy, specific enthalpy and gas constant can be worked out in the same way.

Equation 8: Specific heat in constant volume $c_v = x_a \cdot c_{v,a} + x_f \cdot c_{v,f} + x_{sg} \cdot c_{v,sg}$

Where:

- x_a, x_f, x_{sg} = mass fraction of air, natural gas and stoichiometric gas in each zone
- $c_{v,a}$, $c_{v,f}$, $c_{v,sg}$ = specific heat in constant volume of air, natural gas and stoichiometric gas (J/kg/K)

2.4. NO Concentration Calculation

While nitric oxide (NO) and nitrogen dioxide (NO_2) are usually grouped together as NO_x emissions, NO is the predominant oxide of nitrogen produced inside the engine cylinder. In this paper the formation of NO from nitrogen and oxygen is described by the well-known Zeldovich mechanism. The integrated mechanism contains three equilibrium reactions presented as Equation 9.

Equation 9: The extended Zeldovich mechanism

$$O + N_2 \underset{k_{b1}}{\overset{k_{f1}}{\rightleftarrows}} NO + N$$
$$N + O_2 \underset{k_{b2}}{\overset{k_{f2}}{\rightleftarrows}} NO + O$$
$$N + OH \underset{k_{b3}}{\overset{k_{f3}}{\rightleftarrows}} NO + H$$
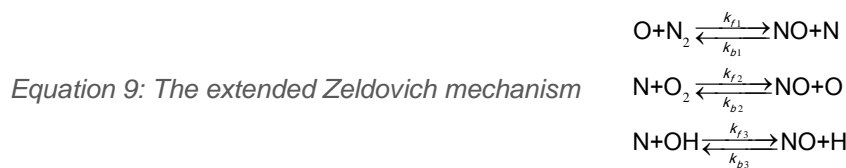
Since the third equilibrium reaction in Equation 9 contributes little to NO formation (Heywood, 1988) and slows down the calculation speed of the simulation model, the author uses the first two reactions to calculate NO concentration, i.e. the basic Zeldovich mechanism. The NO concentration can be computed with temperature according to Equation 10 on assumption that the main species are in equilibrium.

Equation 10: NO concentration $\dfrac{d(NO)}{dt} = k_{f1}(O)(N_2) - k_{b1}(NO)(N) + k_{f2}(N)(O_2) - k_{b2}(NO)(O)$

Where:

- ( ) = concentrations of different species (mol/cm^3)
- k_{f1}, k_{b1}, k_{f2}, k_{b2} = temperature related reaction rate coefficients (cm^3/mol/s)

3. RESULT AND ANALYSIS

A SI natural gas engine test bed is used in this paper to verify the simulation model. The general data of the engine is in Table 1.

Table 9: The dimensions of engine using in the model

Parameter	
Bore [mm]	135
Stroke [mm]	140
Nominal Engine Speed [rpm]	1500

Nominal power per cylinder [kW]	23.8
Compression Ratio	11:1
IC [CA,ABDC]	48
EO [CA,BBDC]	48

3.1. Analysis of the Defined Parameters

After the model is implemented in MATLAB/SIMULINK environment, the simulation results indicate that the three parameters S_{mass}, λ_{ent} and S_{HH} show significant influence on the thermal state in burnt zone. In order to establish the range of validity for the three parameters, the simulation must achieve the same indicated mean effective pressure (imep) as 5.95bar measured from the test bed. The max temperature T_1^{max} in burnt zone is chosen as a second restriction since the thermal NOx formation occurs in the regions with gas temperature well above 2000K(Stiesch, 2003). Table 10 shows the constraint range of the three parameters with the result that imep changes from 3 to 7 bar and T_1^{max} rests in 1500~3500K.

Table 10: Parameter range in two-zone model

Parameter	
S_{mass}	0.03 – 0.45
λ_{ent}	0.6 – 1.5
S_{HH}	0.1 – 0.6

3.2. Simulation results of the two-zone model

The three defined parameters in two-zone model are selected as $S_{mass} = 0.045$, $\lambda_{ent} = 1.4$, $S_{HH} = 0.2$ to ensure that the indicated mean effective pressure equals 5.95bar. Figure 13 shows the normalized reaction co-ordinate – also referred as fuel burnt percentage – which is computed by the single Vibe function. The Vibe parameters are acquired by a heat-release calculation from the measured pressure in the SI natural gas engine. Since NG shows a main characteristic of premixed combustion, the heat combustion flow centralizes in the prior period of the combustion as presented in Figure 14.
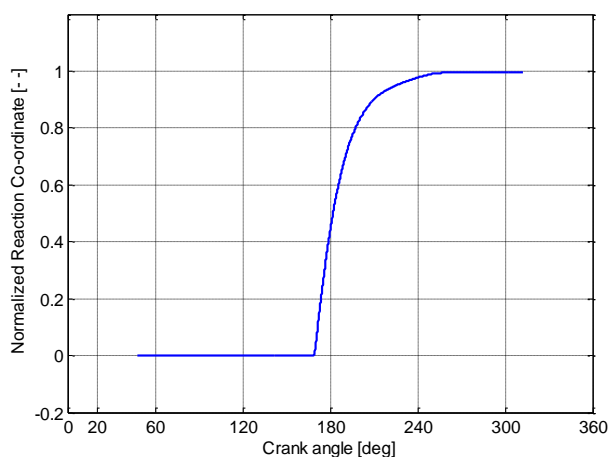
Figure 13: Normalized Reaction Co-ordinate
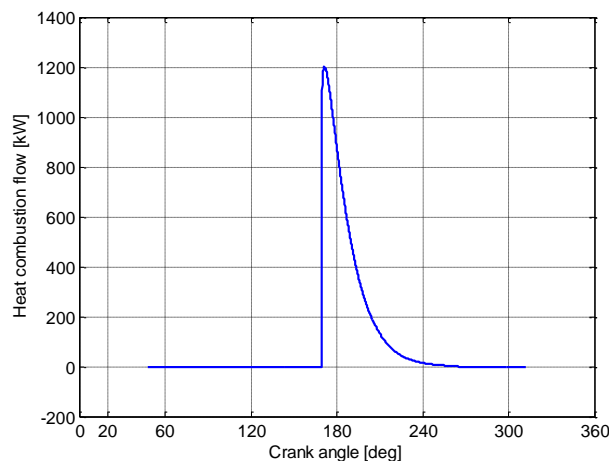
Figure 14: Heat combustion flow

Figure 15 illustrates the specific heat of combustion which has a straightforward impact on heat combustion flow in the model. The simulation result fluctuates around NG LHV (4.885×10^4 kJ/kg, at p=0.1 Mpa, T=25 °C) and the relative error is smaller than 0.82%. The heat of combustion calculated in the model depends on temperature, not kept constant, which makes the in-cylinder process closed to the reality. In Figure 16, the specific heat at constant volume of burnt zone and unburnt zone do not coincide with each other during the compression period mainly because the compositions in these two zone are ausumed differently. Later in the cumbustion and expansion period, higher temperature in burnt zone results in larger value for the specific heat at constant volume.

Due to the temperature difference between the two zones, the heat loss from in-cylinder gas to cylinder wall is also divided into two parts as shown in **Error! Reference source not found.**. There is some heat input (negative heat loss flow) at the beginning of compression because the temperature of inlet fresh charge is lower than that of the cylinder wall. After combustion begins, heat loss in burnt zone is much larger than that in unburnt zone since the temperature is much higher in burnt zone. **Error! Reference source not found.** shows the in-cylinder mass of different zones. The gas mass in burnt zone increases rapidly with the combustion process while mass in unburnt zone decreases correspondingly. However, the total mass in whole cylinder keeps constant because all the fuel has entered the cylinder before the inlet valve closes.
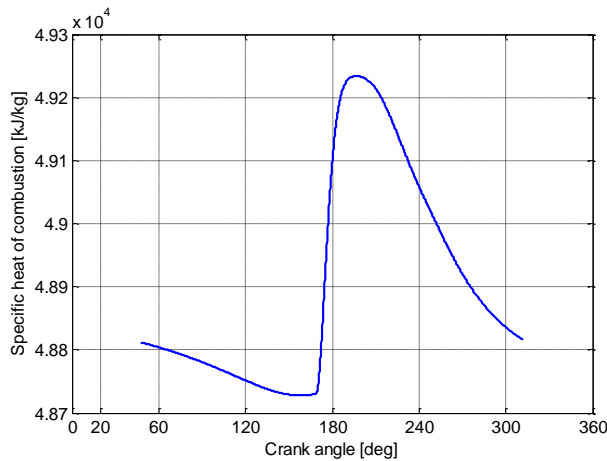
Figure 15: Specific heat of combustion
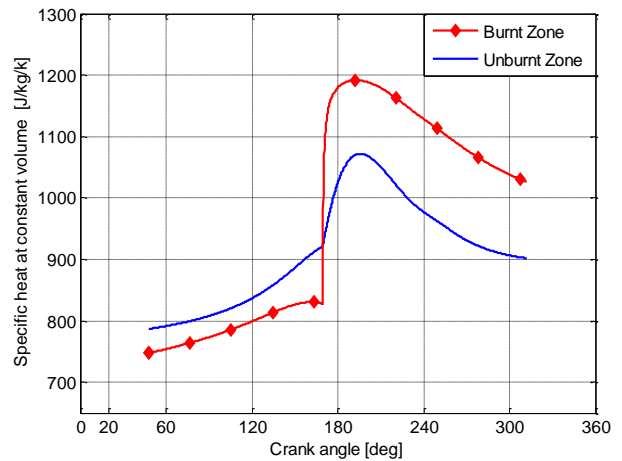
Figure 16: Specific heat at constant volume
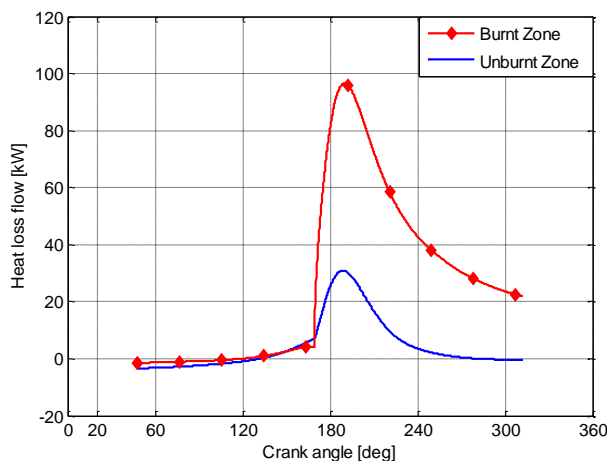
Figure 17: Heat loss
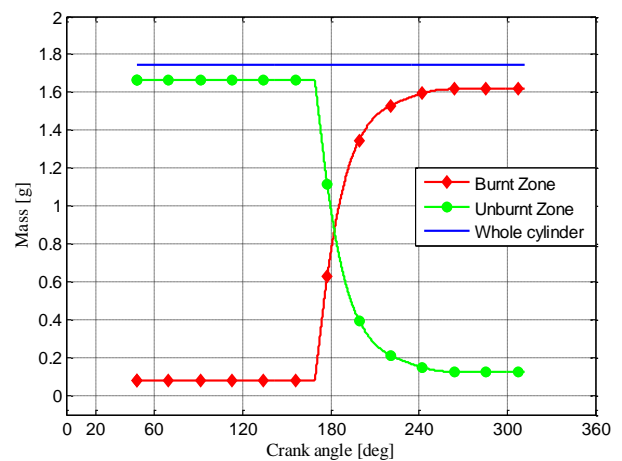
Figure 18: In-cylinder mass

3.3. Comparison with Single-zone Model

The main difference between quasi-dimensional and zero-dimensional models relies in the extension of the basic mass and energy balances with some simplified description of three dimensional phenomena occurring within the cylinder. A comparison between the two-zone model and a single-zone model is carried out to investigate their capacities to predict the engine performance and NO emission. The single-zone model is built on the similar basic of flame zone but without mass and energy exchange.
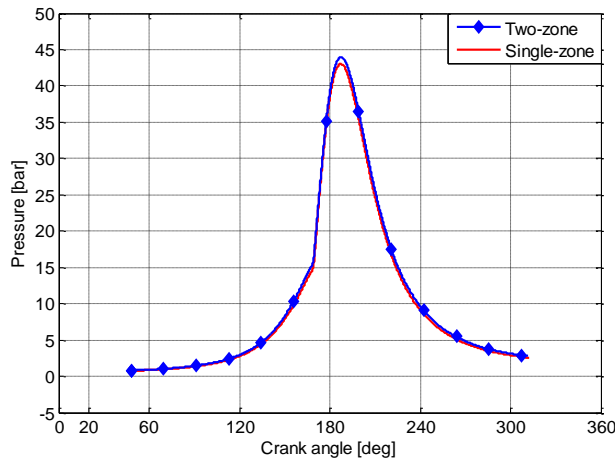
Figure 19: In-cylinder pressure
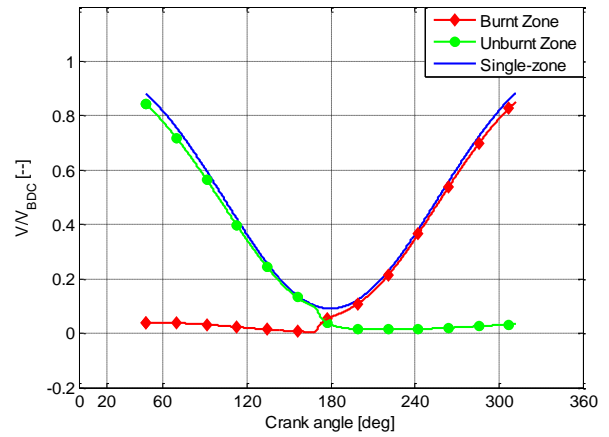
Figure 20: Volume ratio

Figure 19 shows the profile of in-cylinder pressure obtained by the two-zone model and the single-zone model. It is shown in the figures that the curves coincide with each other enough while the peak value of two-zone model is somewhat higher than that of single-zone model. The volume varies of different zones are presented in Figure 20 with the form of ratio to the cylinder volume at the bottom dead centre. Once combustion begins the volume of burnt zone increases fast and nearly occupies the whole cylinder at the end of combustion. However, the unburnt zone still exists at the end of combustion accounting for incomplete combustion in two-zone model.

In Figure 21 the temperature of burnt zone and unburnt zone in two-zone model are compared, as well as the temperature in single-zone model. The peak temperature in burnt zone and unburnt zone respectively reach 2300K and 1050K while that in single-zone model rises to 1950K. Figure 22 shows the NO concentration in different models calculated by the basic Zeldovich mechanism. From the figure we can see that the NO concentration predicted by single-zone model can be neglected compared to the two-zone model. This is mainly because the peak temperature of single-zone model is less than 2000K, above which degree the thermal NO formation begins at large scale. Combining with the engine speed and output power, the final NO emission can be computed to be 7.78g/kW/h, which meets the requirement of Tier Ⅱ but not the Tier Ⅲ.
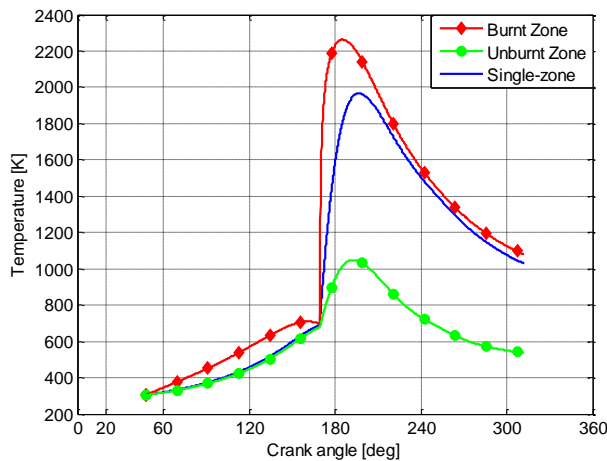
Figure 21: In-cylinder temperature
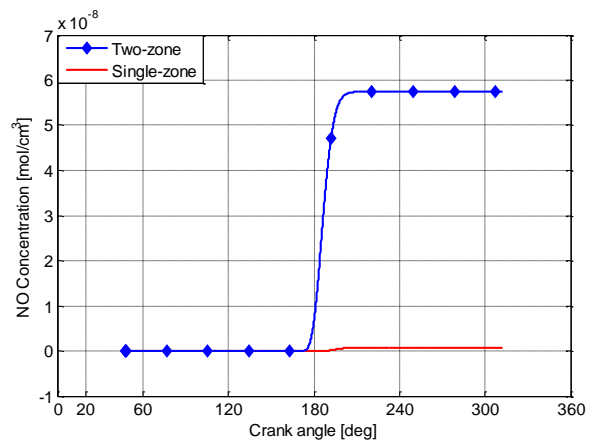
Figure 22: NO concentration

4. CONCLUSION

In this paper a two-zone model of natural gas engine is built on a cylindrical volume assumption for each zone, as well as three new parameters which are defined to descript the mass exchange between the two zones. Then the simulations are carried out to establish the valid range for the three parameters and compare the built two-zone model to a single-zone model. It concludes that the two-zone model shows better accuracy in predicting the NO emission and obtains more engine performance details than single zone model. Nevertheless the three defined parameters (S_{mass}, λ_{ent} and S_{HH}), which determine the two zone

boundary, increase the simulation model uncertainty. The further research will be focused on the parameters definition and application.

5. ACKNOWLEDGEMENT

6. REFERENCES

BHANDARI, K., Bansal, A., Shukla, A. & Khare, M. 2005. Performance and emissions of natural gas fueled internal combustion engine: A review. Journal of Scientific & Industrial Research, 64, 333-338.

G LDER, M. L. 1991. Turbulent premixed flame propagation models for different combustion regimes. Symposium (International) on Combustion, 23, 743–750.

GHOJEL, J. I. 2010. Review of the development and applications of the Wiebe function: a tribute to the contribution of Ivan Wiebe to engine research. International Journal of Engine Research, 11, 297-312.

HEIDER, G. 1995. Two-zone calculation model for the prediction of NO emissions from Diesel engines, 21st CIMAC Cong. Interlaken, Switzerland, D52.

HERDZIK, J. 2011. Emissions from marine engines versus IMO certification and requirements of tier 3.

HEYWOOD, J. B. 1988. Internal Combustion Engine Fundamentals, New York, McGraw-hill.

MA, F., Wang, Y., Liu, H., Li, Y., Wang, J. & Zhao, S. 2007. Experimental study on thermal efficiency and emission characteristics of a lean burn hydrogen enriched natural gas engine. International Journal of Hydrogen Energy, 32, 5067-5075 %@ 0360-3199.

MERKER, G. P., Hohlbaum, B. & Rauscher, M. 1993. Two-zone model for calculation of nitrogen-oxide formation in direct-injection diesel engines. SAE Technical Paper.

METGHALCHI, M. & Keck, J. C. 1982. Burning velocities of mixtures of air with methanol, isooctane, and indolene at high pressure and temperature. Combustion & Flame, 48, 191–210.

STAPERSMA, D. 2008. Emissions and Heat transfer, Royal Netherlands Naval College.

STIESCH, D. I. G. 2003. Modeling Engine Spray and Combustion Processes. Heat & Mass Transfer, 59.

TILAGONE, R., Venturi, S. & Monnier, G. 2006. Natural gas - an environmentally friendly fuel for urban vehicles: the smart demonstrator approach. Oil & Gas Science and Technology-Revue D Ifp Energies Nouvelles, 61, 155-164.

VERHELST, S. & Sheppard, C. G. W. 2009. Multi-zone thermodynamic modelling of spark-ignition engine combustion – An overview. Energy Conversion & Management, 50, 1326–1335.

34: Exergy analysis on the steam gasification of various biomass at the dual fluidized bed gasifier

XIAOMING LI[1], PENG LI[1], JIN BAI[2], JUNXI JIA[1]

[1] College of Power and Energy Engineering, Harbin Engineering University ,NO.145 ,Nantong street,Nangang District, Heilongjiang Province, China, lxmlily2014@126.com.
[1]College of Power and Energy Engineering, Harbin Engineering University, NO.145 ,Nantong treet,Nangang District, Heilongjiang Province, China,lipenglipeng@hrbeu.edu.cn
[2]Institute of Coal Chemistry, Chinese Academy of Sciences.NO.27,Taoyuan South Road. Yingze District, Shanxi Province.stone@sxicc.ac.cn
[1]College of Power and Energy Engineering, Harbin Engineering University,NO.145 ,Nantong Street,Nangang District, Heilongjiang Province, China,jiajunxi99@sohu.com.cn

Gasification of biomass is an attractive technology for combined heat with power production as well as for synthesis processes such as production of liquid and gaseous biofuels. Dual fluidized bed (DFB) technology offers the advantage of a nearly nitrogen-free product gas mainly consisting of H2, CO, CO2 and CH4.

Based on experimental data from literature, exergy analyses was performed for the DFB steam gasification process in this paper. The influence of operating parameters such as steam-to-fuel ratio, gasification temperature, catalyst on the exergy efficiency has been investigated .The results show that the higher gasification temperature results in significantly higher heat value of product gas. In addition, the exergy efficiencies are observed to be higher when steam-to-fuel ratio is lower.With the increase of the bed material content in the catalysts, the exergy efficiency value will also become higher. And different kinds of catalysts always have different exergy ficiency values. The silica sand is suitable bed material for DFB gasifier

Keywords: DFB biomass gasifier, exergy efficiency, catalyst, steam-to-fuel ratio, gasification temperature

1. INTRODUCTION

Under the burden of fossil fuel crisis and expanding energy need, biomass utilization is a useful supplementary way. A promising way to use biomass for production of heat, electricity and other biofuels is through biomass gasification. It is a thermo-chemical process of gaseous fuel production by partial oxidation of a solid fuel. In this process, the chemical energy of the solid fuel is converted into the chemical and thermal energy of the product gas.

Steam gasification leads to a nitrogen-free product gas with a low tar content and a high hydrogen content. Fluidised bed technology is well known for high fuel flexibility and can therefore be applied for various kinds of biogenous feedstock. However, steam gasification is an endothermic reaction and agent requires heat input. One way to provide the required heat is to use a combustion reactor in which the solid char produced from the gasification is combusted and the bed material is heated at the same time. The heated bed material is then circulated to the gasification reactor for heat supply. This dual fluidised bed gasification technology has been successfully demonstrated.

Exergy analysis is quantified in terms of thermodynamic second law and irreversibility, Hence, estimation of exergy of a renewable energy resource is essential to estimate its useful energy availability and for comparing with similar energy resources. Many exergy studies have been conducted on biofuel gasification. Kalinci et al. investigated the exergy efficiencies of an integrated gasifier–boiler power system for hydrogen production via air gasification of six different biomass fuels. Zhang et al. detailed the exergy values and efficiencies of product gas from biomass gasification with air in autothermal gasifiers. Based on chemical equilibrium models, Karamarkovic and Karamarkovic focused on air gasification of biomass with different moisture at different gasification temperatures, Pellegrini and de Oliveira performed an exergy analysis of irreversibilities associated to the process. Jarungthammachote and Dutta used Gibbs energy minimization approach to determine H2 production from biomass steam gasification, exergy efficiency of the process was also evaluated. Based on simulation, Abuadala and Dincer evaluated exergy efficiency of biomass steam gasification. Prins et al. studied the overall exergy efficiencies of converting biomass into gaseous components and char by varying amounts of air and/or steam.

From what has been discussed above ,There are very little analysis about the DFB steam gasification process, which can result in a nitrogen-free product gas with a low tar content and a high hydrogen content and is suitable for different types of biogenous feedstocks. The aim of this paper is to study the influence of operation parameter and biofuel type on the DFB gasification process.

2. EXERGY ANALYSIS

2.1. Exergy Balance

The exergy balance model for the DFB steam gasification is described in this section. The modelling framework is based on the following assumptions:(a) No heat leakage takes place from the gasifier to the environment satisfying the adiabatic condition.(b) At the product side, gases are CO, CO2, H2,CH4, H2O(g), neglecting higher order hydrocarbons.(c) No tar and char are formed.(d) Product gas leaves the reactor at the temperature of the gasifier.The corresponding exergy balance in this gasifier can be written in flow rate form as:

Equation 2: Exergy Balance of DFB gasification $$E_{x.bio} + E_{x.steam} = E_{x.pro} + E_{x.loss}$$

Where:

- $E_{x.bio}$= exergy rate of biofuel,(kW)
- $E_{x.steam}$=exergy rate of gasification agent steam,(kW)
- $E_{x.pro}$= exergy rate of product gas,(kW)
- $E_{x.loss}$= lost exergy rate from DFB gasifier,(kW)

2.2. Total exergy of biofuel and steam

The exergy of biomfuel may be written by a correlation (Szargut, Morris, and Steward 1988) :

Equation 2: exergy of biomass
$$E_{x.bio} = m_{fuel.dry.in} \beta \, LHV_{bio}$$

Where:

- LHVbio= lower heating value of biofuel(kJ/kg).
- $m_{fuel.dry.in}$= mass flow rates of dry component(kg/s).

where the coefficient β in terms of atomic ratios is given by

Equation 3 : Coefficient β
$$\beta = 1.0064 + 0.1519 \frac{w(H)}{w(C)} + 0.0616 \frac{w(O)}{w(C)} + 0.0428 \frac{w(N)}{w(C)}$$

Where:

- w(C),w(H),w(O),w(N)= mass fraction of carbon、hydrogen、oxygen and nitrogen of biofuel,respectively.

The enthalpy exergy of steam as gasification agent is calculated with the equation as followed:

Equation 4 : enthalpy exergy of steam
$$e_{x,steam} = h - h_0 - T_0(s - s_0)$$

Where:

- h= specific enthalpy at the specified state characterized by pressure P and temperature T（kJ/kg）..
- s= specific entropy at the specified state characterized by pressure P and temperature T（kJ/kg.K）
- h_0= specific enthalpy at at the environmental condition with pressure p_0(= 1 atm) and temperature T_0 (= 298 K)（kJ/kg）.
- s_0= specific entropy at the environmental condition with pressure p_0(= 1 atm) and temperature T_0 (= 298 K)（J/kg.K）.

The exergy of steam :

Equation 5: exergy of steam
$$E_{x,steam} = m_{x,steam} \times e_{x,steam}$$

2.3. Total exergy of product gas

Total exergy of the product gas mixture is the sum of its physical and chemical parts and is given by

Equation 6 : Total exergy of product gas
$$E_{x,pro} = E_{x,ph,pro} + E_{x,ch,pro}$$

Where:

- $E_{x.ph,pro}$= physical exergy rate of the product gas mixture ,(kW)
- $E_{x.ch,pro}$=chemical exergy rate of the product gas mixture,(kW)

To simplify the process of calculation, the mixture of product gas is seen as ideal gas.

Equation 7 : enthalpy exergy of product gas
$$e_{x,ph,pro} = h - h_0 - T_0(s - s_0)$$

Equation 8 : (h-h0) of ideal gas
$$h - h_0 = \int_{T_0}^{T} C_{pm,i} dT$$

Equation 9: (s-s0)of ideal gas
$$s - s_0 = \int_{T_0}^{T} \frac{C_{pm,i} dT}{T} - R \ln \frac{p}{p_0}$$

The physical exergy of product gas can be calculated as followed：

Equation10 : physical exergy of product gas
$$E_{x,ph,pro} = n \times e_{x,ph,pro}$$

Where:

- $C_{pm,i}$= molar heat capacity of component i . (kJ /(kmol K)).
- n= mole of product gas.(kmol).
- R=universal gas constant, 8.314J/mol.K.

Equation11 : molecular heat capacity of component i
$$C_{pm,i} = a_0 + a_1 T + a_2 T^2 + a_3 T^3$$

Where the values of a_0, a_1, a_2, a_3 can be found in Table1.

Table 11: the values of a0, a1, a2, a3

Gas	a0	a1×102	a2×105	a3×109
H2	29.11	-0.1916	0.4003	-0.8704
CO	28.16	0.1675	0.5372	-2.222
CO2	22.26	5.981	-3.501	7.469
CH4	19.89	5.024	1.269	-11.01
H2O(g)	32.24	0.1923	1.055	-3.595

The chemical exergy of product gas can be calculated as followed:

Equation12 : molar chemical exergy of product gas $e_{x,ch,pro} = \sum x_i e_{x,ch,i} + RT_0 \sum x_i \ln x_i$

Equation13 : chemical exergy of product gas $E_{x,ch,pro} = n \times e_{x,ch,pro}$

Where:

- x_i= volume fractionof component i.
- $e_{x,ch,i}$= standard chemical exergy of component i (kJ/mol), which can be found in Table 2.

Table 2: the values of standard chemical exergy of various gas components

	H_2	CO	CO_2	CH_4	$H_2O(g)$
$e_{x,ch,i}$ (kJ/kmol)	235.381	275.533	20.138	830.7	8.619

2.4. Evaluation index

The performance of the DFB steam gasification process can be evaluated though three values including exergy efficiency, exergy losses which are defined as followed.

Equation14 :exergy efficiency
$$\eta_x = \frac{E_{x,pro}}{E_{x,bio} + E_{x,steam}}$$

Equation15 : exergy losses
$$E_{x,loss} = E_{x,bio} + E_{x,steam} - E_{x,pro}$$

3. EXPERIMENTAL DATA

The experimental data, which have been reported in previous literatures, include detailed information about product gas at the different operation conditions, thereby being selected for analysis. Biomass used in experiment is Wood pellets, and its high heating value (HHV) is 18.62 MJ kg −1 and low heating value (LHV) 17.12 MJ kg −1 on dry basis. The elemental content (on dry ash free basis) of C, H, O, N and S are 49.20%, 6.49%, 44.20%, 0.10% and 0.01%,respectively. The catalyst employed in experiment is a Ni/olivine catalyst.The yield and composition of product gas at different gasification temperatures and different sfr are given in Table3 and Table4 respectively.The experimental data of catalyst comprising 0, 5, 10, 20, and 43 wt % of the bed material is shown in Table5.The wood/coal mixture(50/50energy%) is chosen to compare with wood pellets. The gas composition of wood pellets and wood/coal mixture is given in the table 6.

Table 3: Product gas composition for the experiments with Wood pellets at different gasification temperatures (sfr=0.8)

temperature	770	800	830	850
CO(% v/v, dry,N_2 free)	30.9	31.8	29.4	27.4
H_2(% v/v, dry,N_2 free)	36.9	38.8	41.9	43.0
CO_2(% v/v, dry,N_2 free)	19.7	19.0	18.6	19.6
CH_4(% v/v, dry,N_2 free)	12.5	10.4	10.1	10.0
Yield(NM^3/h,dry)	22.4939	23.2123	23.8380	24.2343

Table 4: Product gas composition for the experiments with Wood pellets at different sfr

sfr	0.3	0.4	0.5	0.6
CO(% v/v, dry,N_2 free)	28	27.8	27.6	27.2
H_2(% v/v, dry,N_2 free)	41.5	42.3	42.9	43.7
CO_2(% v/v, dry,N_2 free)	19.5	19.7	19.9	20.1
CH_4(% v/v, dry,N_2 free)	8.9	8.7	8.3	8.1
Yield(NM^3/h,dry)	22.248	22.48	22.94	23.175

Table 5: Product gas composition for the experiments with Wood pellets at different wt% of bed material

wt % of the bed material	0	5	10	20
CO(% v/v, dry,N_2 free)	20.2	20.1	19.9	19.8
H_2(% v/v, dry,N_2 free)	37.9	41.7	43.1	44.4
CO_2(% v/v, dry,N_2 free)	25.1	24.8	24.6	24.4
CH_4(% v/v, dry,N_2 free)	10.1	8.52	8.52	7.84
Yield(NM^3/h,dry)	23.1	22.9	23.0	22.8

Table 6: Product gas composition for the experiments with Wood pellets and coal/wood mixture

biomass	Wood pellets	coal/wood mixture
CO(% v/v, dry,N_2 free)	26	23.5
H_2(% v/v, dry,N_2 free)	40.3	45.8
CO_2(% v/v, dry,N_2 free)	21.1	17.5
CH_4(% v/v, dry,N_2 free)	10.1	7.64
Yield(NM^3/h,dry)	24.2	26.1

4. RESULTS AND DISCUSSION

The exergy values of biofuel and steam in different conditions are calculated from Eqs. (2)-(5). The physical exergy of product gas with various temperatures can be calculated from Eqs.(7)-(13), while the standard chemical exergy of component i is shown in Table2. At last exergy efficiency and exergy losses are calculated from Eqs. (14)-(15).

4.1. Variation of the steam-to-fuel ratio

In this work, the different values of the steam-to-fuel ratio (0.3, 0.4, 0.5, 0.6) are taken into account in order to study the influence of sfr on the exergy efficiency in the DFB steam gasification process when the gasification temperature is 1123.15K. It is can be seen from the Figture 1 that the exergy efficiency is decreasing from 69.5% to 68.1%while sfr is changing from 0.3 to 0.6.The decrease in exergy efficiency resulted from the increase in total steam exergy and total exergy of product gas.The total exergy of product gas is mainly determined by the chemical exergy when gaisification temperature is constant. The chemical exergy of product gas decreases with increasing of sfr, because volume concentration of CH4.
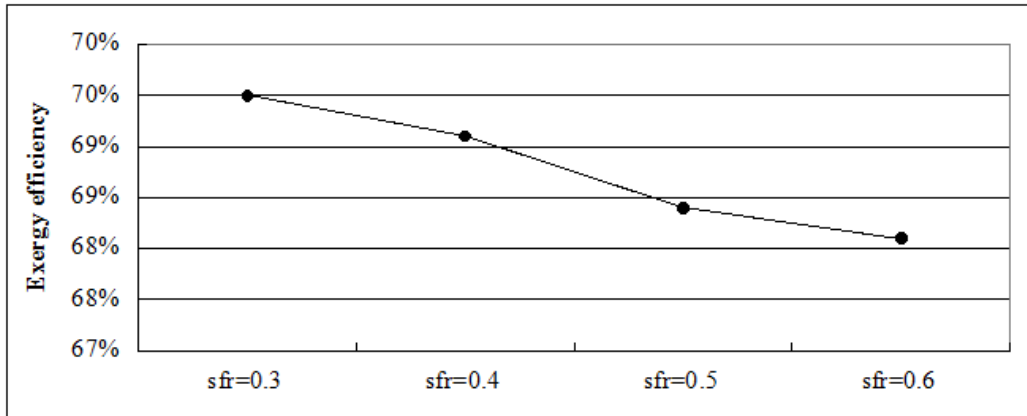
Figure.1 exergy efficiency vs. steam-to-fuel ratio. gasification temperature: 1123.15K.

4.2. Variation of gasification temperature

The influence of different gasification temperatures on the exergy efficiency in the DFB steam gasification process is investigated when other variations (sfr=0.8, catalyst wt-20%) are stable. From Figture 2, the exergy efficiency slightly increases at the beginning while significantly drops with the increasing of the gasification temperature. The increase in exergy efficiency resulted from the increase in the total physical exergy of product gas while temperature increased from 800℃to 830℃.The decrease in exergy efficiency was determined mainly by the decreasing of the chemical exergy of product gas while temperature increased from 700℃to 800℃.
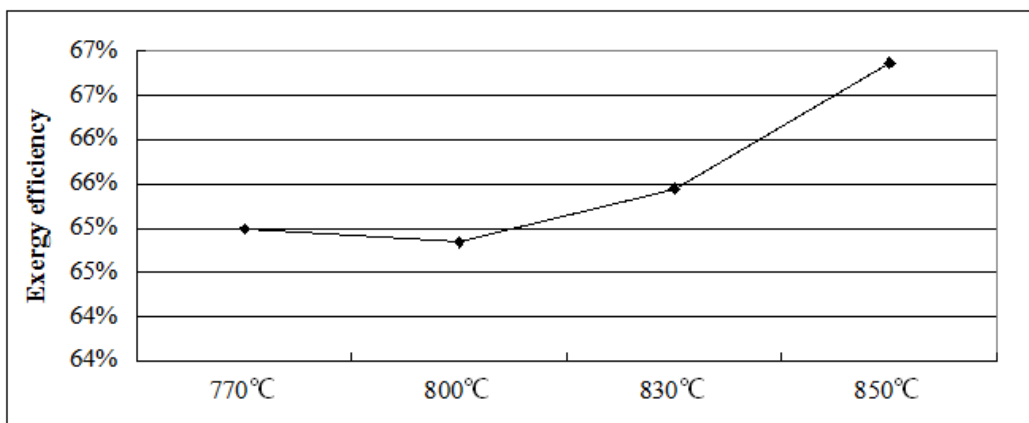
Figure.2 exergy efficiency vs. gasification temperature,sfr=0.8

4.3. Variation of the catalyst and bed material

For bed material, we have studied different content and different kinds of catalysts that have influence on exergy efficiency of the DFB steam gasification process when the gasification temperature is 1123.15K. Firstly, the different content of Ni Olivine has been investigated in our work, including 0%, 5%, 10%, 20%. From Figture.3, the exergy efficiency experiences a upward trend with the increase of content of Ni Olivine. Different kinds of catalysts are also studied in order to find their different influence, including Silica sand, Limestone, Olivine, Fe olivine, Ni olivine. From Table 7, the exergy efficiency values of all the catalysts

mentioned are between 0.59 and 0.70, although Silica sand has the maximum value, 0.670 and Ni olivine has the minimum value, 0.599.

4.4. Variation of the fuel

It is clear (Table 6) that different kinds of fuels have different values of gas composition, which will lead to the different exergy efficiency values of the DFB steam gasification process. So it is also necessary to study the influence of different kinds of fuels. In our work, two different kinds of fuels has been investigated including wood pellets and wood/coal mixture 50:50energy%, when the gasification temperature is 1123.15K and sfr is 0.6. From the table, the values of exergy efficiency of wood pellets and wood/coal mixture 50:50energy% are 66.24% and 77.05, respectively. The mixture of wood and coal can produce higher value than pure wood pellets.
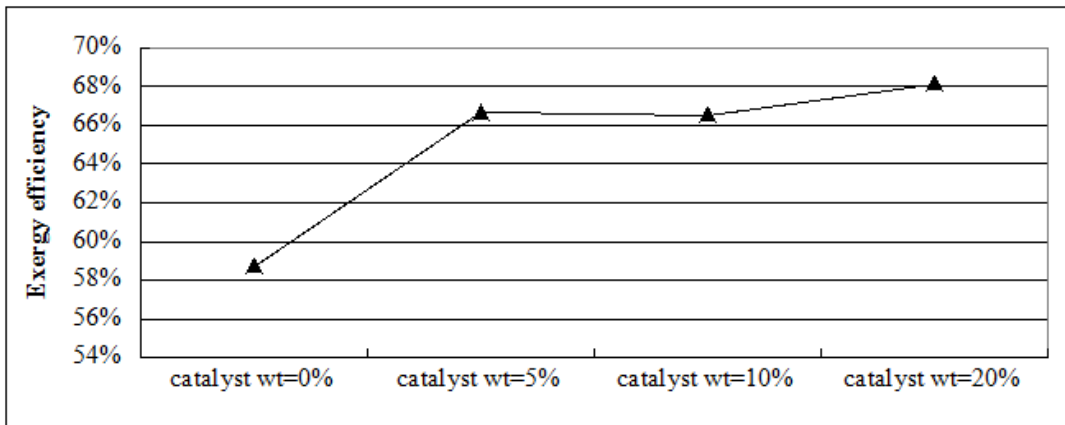
Figure.3 exergy efficiency vs. Catalyst wt . gasification temperature:1123.15K

Table 7: Corresponding values about Variation of the catalyst

Catalyst	Ex,in(kw)	Ex,pro(kw)	Exergy efficiency
Silica sand	439883.8	294868.7	67.0%
Limestone	439883.8	274871.5	62.5%
Olivine	439883.8	285811.2	64.9%
Fe olivine	439883.8	269836.3	61.3%
Ni olivine	439883.8	263871.5	59.9%

Table 8: Corresponding values about variation of the fuel

Fuel	$E_{xm,in}$ (kJ/h)	$E_{xm,p}$ (kJ/h)	$\eta_{ex,p}$
wood pellets	439883. 9	291369.0	66.24
wood/coal mixture 50:50energy%	392285.6	294425.7	75.05

5. CONCLUSION

The influence of various parameters including steam-to-fuel ratio, gasification temperature, fuel and catalyst on the energy and exergy efficiency of the DFB steam gasification process has been investigated. And we can come to the conclusions: (1) the exergy efficiency is rising with the increase of sfr. (2) there is a maximum value of gasification temperature between 1060K and 1080K that can produce the maximum exergy efficiency value. (3)with the increase of the bed material content in the catalysts, the exergy efficiency value will also become higher. And different kinds of catalysts always have different exergy ficiency values. The silica sand is suitable bed material for DFB gasifier according exergy efficiency.

6. ACKNOWLEDGMENT

7. REFERENCES

HOFBAUER, H., Rauch, R., Loeffler, G., Kaiser, S., Fercher, E., Tremmel, H.,2002. Six years experience with the FICFB-gasification process. In:SET 2002-12th European Biomass Conference. ETA, Florence, 982–985.

KALINCI, Y. Hepbasli, A. Dincer, I., 2010. Efficiency assessment of an integrated gasifier/boiler system for hydrogen production with different biomass types. *Hydrogen Energy,* 35, 4991–5000.

ZHANG, Y. , Li, B., Li, H.,2011. Thermodynamic evaluation of biomass gasification with air in autothermal gasifiers, *Thermochim. Acta* 519 ,65–71.

KARAMARKOVIC, R. Karamarkovic, V.,2010.Energy and exergy analysis of biomass gasification at different temperatures, *Energy.* 35.537–549.

PELLEGRINI, L.F. 2007. Exergy analysis of sugarcane bagasse gasification, *Energy* 32 . 314–327.

JARUNGTHAMMACHOTE,S. Dutta, A.,2007, Thermodynamic equilibrium model and second law analysis of a downdraft waste gasifier, *Energy,* 32, 1660–1669.

ABUADALA, A., Dincer, I., 2010, Efficiency evaluation of dry hydrogen production from biomass gasification, *Thermochim. Acta,* 507–508, 127–134.

PRINS, M.J., Ptasinski, K.J.,2003, Thermodynamics of gas–char reactions:first and second law analysis, *Chem. Eng. Sci,*58 ,1003–1011.

PFEIFER, C., Rauch, R.,Hofbauer, H.,2004.In-Bed Catalytic Tar Reduction in a Dual Fluidized Bed Biomass Steam Gasifier. *Ind. Eng. Chem. Res.,* 43(7), 1634-1640.

PFEIFER, C.,Koppatz, S.,Hofbauer, H.,2011,Steam gasification of various feedstocks at a dual fluidised bed gasifier: Impacts of operation conditions and bed materials.*Biomass Conv. Bioref.*1,39-53.

494: Thermodynamic efficiency of IGCC plant with overheated cycle air and two-stage gasification

DENIS SVISHCHEV[1], ALEXANDRE KEIKO[2], IGOR DONSKOY[3],
ALEXANDER KOZLOV[4], VITALY SHAMANSKY[5], ALEXANDER RYZHKOV[6]

[1] *Melentiev Energy Systems Institute (ESI) SB RAS Lermontov Street 130, Irkutsk 664033, Russian Federation, denis.svishchev@gmail.com*
[2] *Melentiev Energy Systems Institute (ESI) SB RAS Lermontov Street 130, Irkutsk 664033, Russian Federation paragraph1@yandex.ru*
[3] *Melentiev Energy Systems Institute (ESI) SB RAS Lermontov Street 130, Irkutsk 664033, Russian Federation donskoy.chem@mail.ru*
[4] *Melentiev Energy Systems Institute (ESI) SB RAS Lermontov Street 130, Irkutsk 664033, Russian Federation kozlov@isem.sei.irk.ru*
[5] *Melentiev Energy Systems Institute (ESI) SB RAS Lermontov Street 130, Irkutsk 664033, Russian Federation vita@isem.sei.irk.ru*
[6] *Ural Federal University (UrFU), 19 Mir Street, Yekaterinburg 620002, Russian Federation af.ryzhkov@mail.ru*

The goals to enhance the efficiency and environmental friendliness of power plants burning fossil coal explain the interests in the technologies of gasification in the combined cycle (IGCC). The research is dedicated to a promising IGCC process flow diagram which suggests an intermediate overheating of the cycle air coming to the combustion chamber of the combined cycle plant. After air processor the air goes to the boiler where it is heated to the temperature of $1000°\,C$. Compared to the classical IGCC plants, the air overheating makes it possible to reduce the capacity of gasifier and gas cleaning system. The plant flow diagram also includes a two-stage MHI gasifier. The gasifier is fed by overheated cycle air, steam and oxygen from the air separation unit. In the research the operating conditions of gasifier and the whole plant are studied. The efficiency of electricity generation without considering auxiliaries reaches 53-54.4%. The hot gas cleaning and oxygen steam gasification is optimal.

Keywords: IGCC, staged gasifier, cycle air heating, oxygen-rich air, equilibrium modeling

1. INTRODUCTION

Nowadays coal energy technologies are developing in the following areas: 1) transition of steam power cycle to the ultra-supercritical parameters; 2) creation and development of solid-fuel combined cycle plants; 3) carbon capture and storage; and 4) production of secondary fuels from coal. The first two areas are competing. Ultra supercritical pulverized coal combustion technology is a little bit more beneficial as compared to internal gasification combined cycle (IGCC), if the carbon capture and storage are not considered (Pettinau, 2013). However, the development of IGCC technologies is important in the long run. This is associated with the inevitable deterioration in the quality of solid fuel and constraints on the carbon dioxide emissions to be imposed in the future.

Most of the operating solid-fuel IGCC plants run on low-ash coal and use steam-oxygen gasification (Sahraei, 2014). This gasification technology is characterized by high fuel conversion. However, the need to apply air separators increases the price of a unit installed capacity. On the contrary, the use of non-enriched air and steam-air mixture causes a decrease in the temperature and rate of the thermochemical process and a considerable increase in the amount of unburned carbon. Unconverted carbon residue can be disposed of in the steam boiler furnace; however, such a solution reduces the combined-cycle output and efficiency of the whole plant.

The working medium of the combined-cycle plant is the products of producer gas combustion in the air forced into the combustion chamber by an air compressor. When compressed, the air is heated from the environment temperature up to 450°C. The technology of the working medium preparation can be improved if the cycle air is heated up to around 1000°C. The air can be additionally heated at the air heater section built into the boiler furnace burning either the carbon residue from the gasification stage or the extra coal. Such an improvement will enhance the efficiency of the plant with air and air-steam gasification, reduce the output of producer gas and consequently the dimensions of the gasifier and gas treatment system.

In order to estimate the technical efficiency of oxygen enrichment and blast overheating, in this research we conducted thermodynamic studies of corresponding process diagram including both the stage of air enrichment and its additional heating (Fig.1). The object of the studies is the IGCC process flow diagram, the subject is the physicochemical processes of the conversion of matter and energy of solid fuel. The objectives of the research are the development of a mathematical model of gasifier and IGCC process flow diagram as well as optimization of their operating parameters.
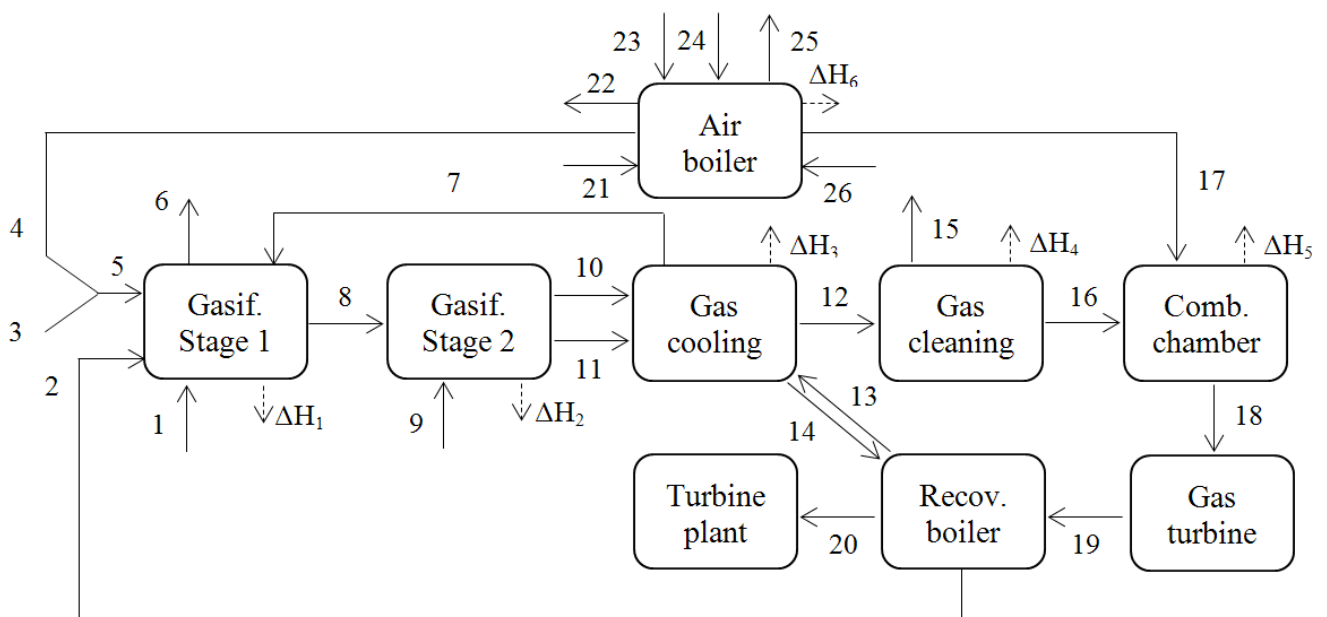
Fig.1. An IGCC process flow diagram

2. METHODS AND APPROACHES

Blocks «Gasification stage 1» and «Gasification stage 2» reflect individual zones of staged gasifier fed by steam of the waste heat recovery boiler and overheated oxygen-enriched (5) cycle air (4). An assumption was made that only gaseous products (8) are transferred from stage 1 to stage 2, and mineral part in the form of melted ash (6) is removed only from stage 1. One of the boiler sections is part of gas cooling stage which provides recovery of sensible heat from the producer gas and solid particles in the steam cycle of the plant. The solid particles are returned to stage 1 of the gasifier. To exclude condensation of water steam, elevated temperature of gas cooling gases is maintained. Further gas cooling and water steam condensation occur at the stage of gas cleaning. Combustion chamber is fed by heated cycle air (17) whose excess is used to maintain the specified combustion temperature. Energy part of the IGCC process flow diagram is represented by gas turbine, waste heat recovery boiler and a steam turbine plant.

The IGCC process flow diagram is characterized by the parameters presented in Table 1. Eight of them are varied and determine various operating conditions of the plant. The total number of calculated conditions makes up z^8, where z – the number of values taken by each parameter. If to take the value z equal to 4, the number of potential operating conditions will exceed 65 thousands which will make their analysis laborious and unrealizable.

Table 1: Initial parameters for the calculation of operating conditions of gasifier and IGCC process flow diagram

No	Parameter	No flow (Fig. 1)	Value
	Constant parameters		
	Gasification stages		
1	Pressure in the gasifier, MPa	-	3
2	Temperature of the first stage, °C	-	1700
3	Initial temperature of the coal, °C	1,9	10
4	Steam temperature, °C	2	320
5	Content of O_2 in the oxygen, %	3	95
6	Oxygen temperature, °C	3	107
7	Total coke residue formation,%	6	2
8	Temperature of cooling gas and coke, °C	7	350
9	Heat losses (stages 1 and 2), %	$\Delta H_1, \Delta H_2$	2
	Stages of gas cooling and cleaning		
10	Temperature of the cooling stage feed water, °C	13	317
11	Steam temperature from cooling stage, °C	14	320
12	Gas cooling heat loss,%	ΔH_3	0,5
13	Pressure of the gas after gas cleaning, MPa.	16	2,959
	Gas combustion chamber		
14	Temperature in chamber, °C	-	1399
15	Pressure in chamber, MPa	-	1,82
16	Heat loss, %	ΔH_5	2
	Air boiler		
17	Blast air temperature before the boiler, °C	21	600
18	Cycle air temperature before the, °C	26	550
19	Coal temperature	23	10
20	Combustion air temperature, °C	24	10
21	Air excess in boiler furnace, -	24	1,2
22	Exhaust gas and ash temperature, °C.	22,25	125

23	Coke residue output, %	25	2
24	Boiler heat loss, %	ΔH_6	5
	Power island		
25	Efficiency of gas turbine,%	-	40,6
26	Efficiency of recovery boiler, %	-	85
27	Steam turbine efficiency, %	-	40,3
28	The plant capacity, MW(elec.)	-	500

Variable parameters

	Gasification stages		
29	Air overheat temperature, °C	4	600-1000
30	The content of O_2 in enriched air, % vol.	5	21-95
31	Steam flow, mole/mole (fuel daf)	2	0-0,6
32	Equivalence ratio, -	-	0,2-0,6
33	The share of coal supplied to the first step, %	1	20-80
34	Coal conversion degree, second stage, %	11	70-100
	Other stages		
35	Cycle air overheating temperature, °C	17	550-1000
36	Gas cooling temperature, cooling stage, °C	16	30-330

In order to reduce the amount of calculated conditions, for some of them we took only the extreme values from the variation range. The share of coal coming to the first stage of gasifier, and oxygen excess were optimized directly in the calculation. Table 2 presents the assumed values of the parameters.

Table 2: Calculated variants of the process flow diagram operation

Air temperature, °C	Coal conversion degree (stage 2), %	O2 content, %	Steam flow, mole/mole (fuel daf)	Cycle air overheating temperature, °C	Gas cooling temperature, °C
600	70				
600	100	21, 25, 43, 95	0, 0.2, 0.4, 0.6	550, 1000	30, 330
1000	70				
1000	100				

2.1. Thermodynamic Model

The mass and energy flows leaving or entering the reactors, and the efficiency indices of individual stages and the whole unit were estimated for all calculated operating conditions. Staged gasification process was calculated using the thermodynamic model of extreme intermediate states with macrokinetic constraints on the coal conversion degree [Gorban, 2006]. In terms of mathematical programming the model has the form:

find

$$\max S(x,T) \qquad (1)$$

subject to

$$Ax = b, \qquad (2)$$

$$x_j \geq 0, \forall j = \overline{1,n} \qquad (3)$$

$$S(x,T) = \sum_j S_j(x,T)x_j \qquad (4)$$

$$H_{hr} = \sum_j H_j(T^{in})x_j^{in} - H \qquad (5)$$

$$x_k \geq \varphi(x, y), \qquad 6)$$

Equations 2 and 3 determine the mass balance. Expression 4 establishes a relationship between entropy and composition vector. Equation 5 sets the constancy of the system enthalpy. H_{hr} is the value of heat exchange between the system and the environment. Expression 6 is a macrokinetic constraint causing the formation of a coke residue. This thermodynamic model allows calculating the composition of the products. To this end it is necessary to set some values: initial composition of a reaction system and its heat exchange with the environment, as well as the composition and quantity of the coke residue. Model (1)-(5) was used to describe the process of producer gas combustion in the combustion chamber and solid fuel combustion in the boiler furnace.

3. THERMODYNAMIC ANALYSIS AND OPTIMIZATION OF THE IGCC SCHEME

In order to reduce the number of analyzed cases the conditions with the coal conversion degree equal to 70% were chosen as a base case. The summarized data on the IGCC plant efficiency are presented in Table 3. Comparison of the conditions makes it possible to draw the following conclusions:

In all the conditions an increase in the oxygen content in the blast leads to an increase in the cold gas efficiency. The efficiency of air conditions of gasification appears to be lower than oxygen conditions by 0.9-3.5% abs, other things equal.

Air heating does not lead to a considerable increase in the plant efficiency and in some cases decreases it. For example in the case of no steam in the gasifying agent, the efficiency drops in all conditions by 02.-1.1% abs.

Presence of steam in the gasifying agent positively affects the efficiency of the plant. The greatest efficiency is achieved when steam consumption reaches 0.4-0.6 mole/mole (daf) for the enriched air, and 0.2 mole/mole (daf) - for bulk oxygen.

Hot gas cleaning enhances the IGCC efficiency by 0.9-3.8% abs, with respect to the cold gas cleaning.

Heating of cycle air is only efficient in the case of cold gas cleaning and gasification with the air containing 21-43% of oxygen. The efficiency of these conditions increases by 1.7% abs. With oxygen as a gasification agent and cold gas cleaning, the efficiency increases or decreases insignificantly. Heating of cycle air in the case of hot gas cleaning reduces the efficiency of all conditions by 0.1% -1% abs, except for the cases of "dry" gasification with air that contains 21-43% of oxygen.

Table 3: IGCC efficiency for a base case

Cycle air and gas temperature		550, 30		550, 330		1000, 30		1000, 330	
Air temperature		600	1000	600	1000	600	1000	600	1000
O_2	Steam								
21	0	49.3	48.5	52.8	51.8	50.7	50.2	53.0	52.3
21	0.2	50.1	50.3	53.7	53.5	51.3	51.4	53.5	53.4
21	0.4	50.2	50.5	53.9	53.9	51.3	51.6	53.6	53.6
21	0.6	50.3	50.6	54.1	54.1	51.4	51.6	53.7	53.7
25	0	50.1	49.4	53.2	52.3	51.3	50.8	53.2	52.7
25	0.2	50.8	50.9	54.0	53.9	51.7	51.8	53.7	53.6
25	0.4	50.9	51.1	54.3	54.2	51.8	51.9	53.8	53.8
25	0.6	50.8	51.0	54.4	54.3	51.8	51.9	53.9	53.8
43	0	51.8	51.4	54.0	53.6	52.3	52.1	53.7	53.4

43	0.2	52.4	52.4	54.8	54.7	52.7	52.7	54.1	54.1
43	0.4	52.3	52.3	54.9	54.9	52.6	52.7	54.2	54.1
43	0.6	52.1	52.1	54.9	54.9	52.5	52.6	54.2	54.1
95	0	53.0	53.0	54.6	54.6	53.1	53.1	54.0	54.0
95	0.2	53.6	53.6	55.4	55.4	53.4	53.4	54.4	54.4
95	0.4	53.3	53.3	55.4	55.4	53.2	53.2	54.4	54.4
95	0.6	53.0	53.0	55.4	55.4	53.1	53.1	54.4	54.4

Notes: O_2 – oxygen content in the enriched air, %; Steam – steam consumption, mole/mole (daf); flow temperatures are presented in °C.

4. CONCLUSION

Further development of the project can follow the path of the analysis of optimum thermodynamic conditions of the gasifier and IGCC scheme by kinetic modeling. Such a study will reveal macrokinetic constraints on thermochemical processes to achieve equilibrium, and take them into account in the thermodynamic models in the future. Refined thus thermodynamic models can be the basis of calculation methods of engineering processes, including solid fuel thermochemical conversion.

Model IGCC must be supplemented by the characteristics of the energy and the compressor equipment, as well as an air separation unit and allows the calculation of net efficiency of the plant.

5. ACKNOWLEDGMENT

6. REFERENCES

Gorban, A., 2006. Thermodynamic Equilibria and Extrema: Analysis of Attainability Regions and Partial Equilibrium. NY: Springer.

Sahraei, H., 2014. A survey on current advanced IGCC power plant technologies, sensors and control systems. Fuel, 137, 245–59.

Pettinau, A., 2013. Combustion vs. gasification for a demonstration CCS (carbon capture and storage) project in Italy: A techno-economic analysis. Energy, 50, 160–9.

SESSION 13: BIOMASS SYSTEMS

9: Effect of different seeding sludge on the energy recovery potential of food waste during anaerobic digestion

JUN WEI LIM[1], JASON TAN[2], KAI CHEE LOH[3], YANJUN DAI[4], YEN WAH TONG[5]

[1] *NUS Environmental Research Institute, National University of Singapore, 5A Engineering Drive 1, Singapore 117411, eriljw@nus.edu.sg*
[2] *Department of Chemical and Biomolecular Engineering, National University of Singapore, 4 Engineering Drive 4, Singapore 117585, a0094613@u.nus.edu*
[3] *Department of Chemical and Biomolecular Engineering, National University of Singapore, 4 Engineering Drive 4, Singapore 117585, chelohkc@nus.edu.sg*
[4] *Institute of Refrigeration and Cryogenics, Shanghai Jiao Tong University, Shanghai, China, yjdai@sjtu.edu.cn*
[5] *NUS Environmental Research Institute, National University of Singapore, 5A Engineering Drive 1, Singapore 117411, chetyw@nus.edu.sg*

Increasing food waste (FW) generation has been a growing environmental challenge for many countries. In Singapore, 796,000 tonnes of FW was generated in 2013, with only 13 per cent of the FW recycled. The recycling rate could be increased by adopting anaerobic digestion (AD), which is a biological process that efficiently converts organic matter into biogas. Due to the high degree of waste stabilisation and controlled methane generation, AD is regarded as a more sustainable treatment method for FW. Seeding sludge contains a consortia of microbes that are responsible for the conversion of organic matter to methane. A suitable seeding sludge can shorten start-up time and enhance biogas production. Therefore, the source of seeding sludge plays a crucial role in the fate of the AD process. The objective of this study was to compare the performance of two different seeding sludge for the AD of FW: (1) anaerobic sludge from water reclamation plants (WRP) in Singapore; and (2) anaerobic sludge from palm oil mill effluent (POME) digesters in Johor, Malaysia. This was achieved by comparing the evolution of bacterial and archaeal communities in anaerobic digesters inoculated with WRP sludge (R1) and POME sludge (R2) over 30 days. Biomass from R1 and R2 were sampled for terminal restriction fragment length polymorphism to detect the shift of microbes throughout the study. This study showed that WRP sludge (R1) took a shorter start-up time as compared to POME sludge (R2). The overall performance of R1 was also superior to that of R2. Information from both reactor performance and microbial community analysis suggested how the differences in the initial microbial consortia of WRP sludge and POME sludge affected the start-up and behaviour of FW anaerobic digesters. Knowledge gained from this study could aid future works in optimising the AD of FW through bioaugmentation.

Keywords: Microbial community profiling, Anaerobic digestion, Seeding sludge

1. INTRODUCTION

Increasing food waste (FW) generation has been a growing environmental challenge for many countries. In Singapore, 796,000 tonnes of FW was generated in 2013, with only 13 per cent of the FW recycled. The recycling rate could be increased by adopting anaerobic digestion (AD), which is a biological process that efficiently converts organic matter into biogas. Due to the high degree of waste stabilisation and controlled methane generation, AD is regarded as a more sustainable treatment method for FW. The AD process converts organic matter into biogas (methane and carbon dioxide) through hydrolysis, acidogenesis, acetogenesis and methanogenesis. These metabolic processes are carried out by a consortia of microbes that are crucial to the efficiency of AD processes. Therefore, the objective of this study was to compare the impact of two different seeding sludge for the AD of FW: (1) anaerobic sludge from water reclamation plants (WRP) in Singapore; and (2) anaerobic sludge from palm oil mill effluent (POME) digesters in Johor, Malaysia. This study monitored the bacterial community structure and dynamics from two laboratory-scale reactors based on their terminal restriction fragment length polymorphism (T-RFLP) profiles. The relationship between microbial community structure and reactor performance was also examined to evaluate the impact of seeding sludge on the start-up and behaviour of FW anaerobic digesters.

2. MATERIAL AND METHODS

2.1. Feedstock and reactor operation

FW was collected from the National University of Singapore (NUS) canteen at the beginning of each month. A representative fraction of the FW collected was blended into puree form and packed into small portions of 30 grams each before being stored in a -20°C freezer. A pack of FW was thawed prior to use and had average pH level of 5.38 ± 0.73, C/N ratio of 19.59 ± 4.20, total solids (TS) of 31.89 ± 1.59% and volatile solids (VS) of 30.83 ± 1.40%. The feedstock for this study consisted of blended FW mixed with 133 ml of deionised water to achieve organic loading rate (OLR) of 1.0 g-VS/L/2d. AD of food waste was performed in laboratory scale (2 L working volume) single-stage reactors. R1 and R2 were initially inoculated with anaerobic sludge collected from water reclamation plant (WRP) in Singapore; and palm oil mill effluent (POME) digesters in Johor, Malaysia, respectively. R1 and R2 were operated in parallel for 30 days at 35°C with hydraulic retention time (HRT) of 30 days.

2.2. Chemical analysis

pH value and biogas production as well as composition were measured once every two days, while TS and VS were measured once weekly according to the Standard Methods [1]. pH value was measured using a portable ExStik PH100 pH meter (EXTECH Instruments), biogas production measured using a 0.5 L jumbo syringe (SGE Analytical Science, Australia) and biogas composition was analysed by gas chromatograph (PerkinElmer, USA) equipped with a thermal conductivity detector (TCD).

2.3. DNA extraction and terminal restriction fragment length polymorphism (T-RFLP)

Sludge samples were collected on days 0 and 22 and genomic DNA was extracted from sludge using soil DNA isolation kit (Norgen Biotek Corporation, Canada) as recommended by the manufacturer. Extracted DNA was used in the subsequent PCR amplification with a domain Bacteria-specific reverse primer 927r (5'-HEX-ACCGCTTGTGCGGGCCC-3') and domain Archaea-specific reverse primer 1100r (5'-VIC-TGGGTCTCGCTCGTTG-3'). Analysis of Bacterial 16S rRNA gene-based terminal-RFLP (T-RFLP) was performed according to a protocol described previously [2]. The amplified PCR products were purified with GeneJET PCR purification kit (Thermo Scientific, United States), and digested with tetrameric restriction nuclease *Msp*I. The digested products were detected by fragment analysis using the Beckman CEQ 8000 system (AIT Biotech, Singapore). The peak area of each operational taxonomic units (OTUs) was divided by the total peak area of all OTUs in each sample and then multiplied by 100 to calculate the relative abundance of each OTU.

3. RESULTS AND DISCUSSION

3.1. Reactor performance

Figure 1 shows the pH levels, biogas production and methane production yields for both R1 and R2 throughout the 30d study. Both R1 and R2 had short start-up times where methane production started to occur after 2 to 4 days. Average biogas productions for R1 and R2 for the study were 619 ± 129 and 299 ± 117 mL/g-VS/2d, respectively. The average methane production for R1 was 317 ± 86 while that for R2 was 97 ± 48 mL/g-VS/2d. As shown in Figure 1, the performances of both R1 and R2 started to decline towards the end of the study (after 20d). This was observed together with a drop in pH levels for both reactors due to a build-up of AD intermediates: mainly propionic acid and butyric acid (data not shown). Propionic acid degrading organisms are known to be the most sensitive acetogenic organisms present in most anaerobic digester ecosystems [3] and the accumulation of propionic acid in reactors often leads to inhibition and reduced biodegradation of biomass. In this study, biogas and methane production was notably higher in the reactor inoculated with WRP sludge (R1) as compared with the reactor inoculated with POME sludge (R2).

3.2. Effect of different seeding sludge on microbial population dynamics as revealed by T-RFLP

Bacterial and archaeal community structures of seeding sludge (0d) and reactor sludge (22d) were monitored for both R1 and R2. The T-RFLP fingerprints of bacterial 16S rRNA gene fragments revealed a total of 9 and 11 bacterial terminal restriction fragments (T-RFs) and a total of 4 and 2 archaeal T-RFs for R1-0d and R1-22d, respectively. On the other hand for R2-0d and R2-22d, there were a total of 11 and 12 bacterial T-RFs and a total of 4 and 4 archaeal T-RFs, respectively. As shown in Figure 2 the bacterial population compositions of R1 and R2 seeding sludge were significantly different. Other than a slightly less diverse bacterial community for R1 seeding sludge, the dominant species for both R1-0d and R2-0d were also different. *Deltaproteobacteria* (T-RF 220 bp and 259 bp), *Bacteroidetes* (T-RF 101 bp, 192 bp, 381 bp and 382 bp) and *Firmicutes* (T-RF 80 bp, 136 bp and 138 bp) represented the dominant bacterial groups for both R1 and R2. As shown in Figures 2a and b, the abundance of *Deltaproteobacteria* decreased from 41% to 18% for R1-0d and R1-22d, respectively. This trend was also observed for R2 as *Deltaproteobacteria* decreased from 25% to 8% for 0d and 22d, respectively (Figures 2c and d). The abundance of *Bacteroidetes* was similar for both 0d and 22d in R1 (maintained at 37% to 39%) while that of R2 decreased from 34% to 14%. The dominant T-RFs present in R1-0d: 101, 192, 197, 220, 259 and 381 bp accounted for more than 90% of total abundance for R1 seeding sludge. Though present in lower abundance, most of these T-RFs were still detected in R1-22d. This indicated that these *Deltaproteobacteria*, *Bacteroidetes* and *Firmicutes* represented the dominant groups that were responsible for the biodegradation of FW into biogas. As shown in Figure 2d, abundance of *Deltaproteobacteria* (T-RFs 220 bp and 259 bp) decreased while that of *Betaproteobacteria* (T-RF 216 bp) increased at the end of the study as compared to the microbial community of the starting seeding sludge. The abundance of *Bacteroidetes* (T-RF 380 bp, 381 bp and 382 bp) also decreased from 31% to 14%.

As shown in Figure 3, the T-RFLP profiles of archaeal populations for R1 and R2 seeding sludge were similar and primarily displayed difference in abundances. The abundance of *Methanosarcinales* (T-RF 76 bp) for R1 was observed to be at 79-81% and that of *Methanomicrobiales* (T-RFs 93 bp, 118 bp and 131 bp) at 19-21% throughout the study. For R2, the abundance of *Methanosarcinales* remained at 71-72% and that of *Methanomicrobiales* at 28-29% throughout the study. In comparison, the bacterial community structures of WRP and POME seeding sludge were significantly different and evolved differently while that of archaeal remained relatively similar for both seeding sludge and during the study period. Since the performance of R1 was superior to that of R2, the microbial consortia present in R1 seeding sludge likely contained the bacterial species important for the conversion of FW into biogas. On the other hand, a significant shift in the T-RFLP profiles was observed for R2. Though the methane production efficiency of R2 was much lower than that of R1, R2 still managed to achieve an average biogas yield of 307mL/g-VS for the first 18d of the study. Therefore it was highly likely that the microbial consortia capable of converting organic matter to biogas was initially present in the POME seeding sludge but they were either out-competed by other microorganisms or washed out during the feeding/discharge process.
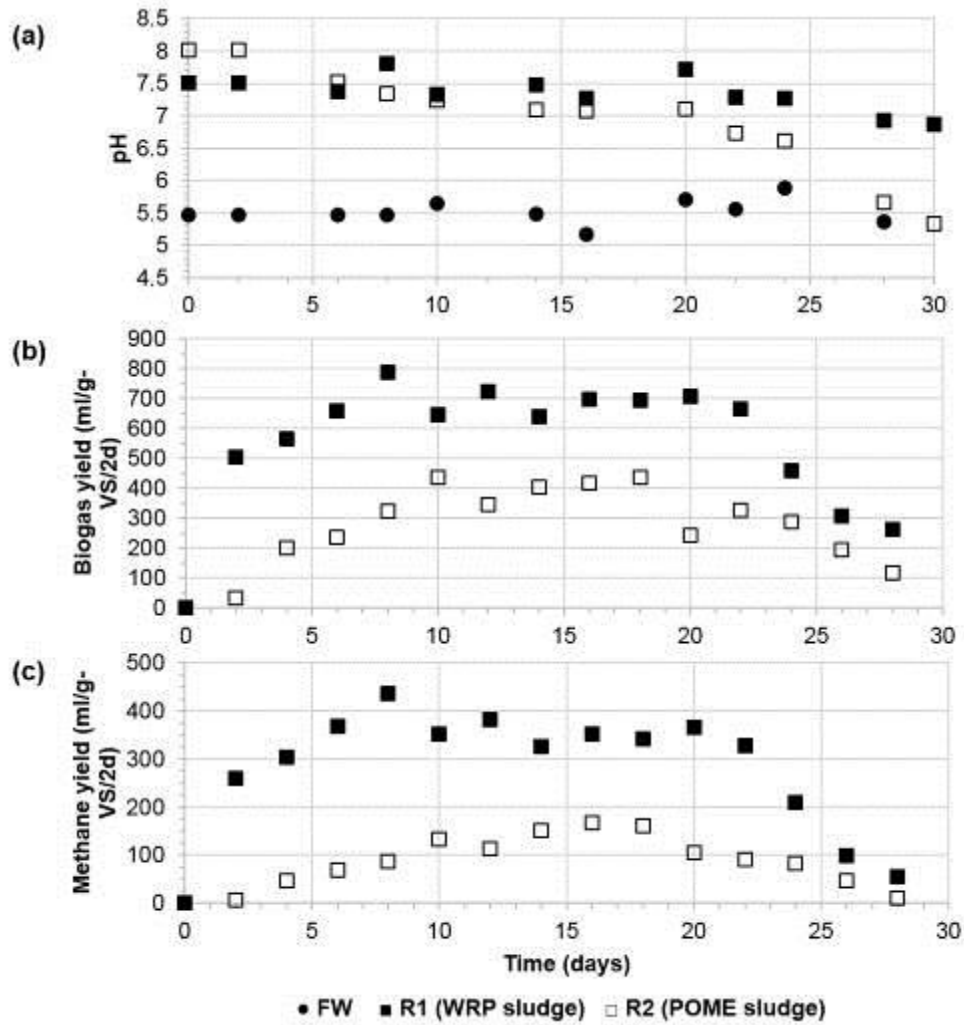
Figure 23: pH and biogas yield for: -●- Food waste, -□- R1 (PUB), and -■- R2 (POME)
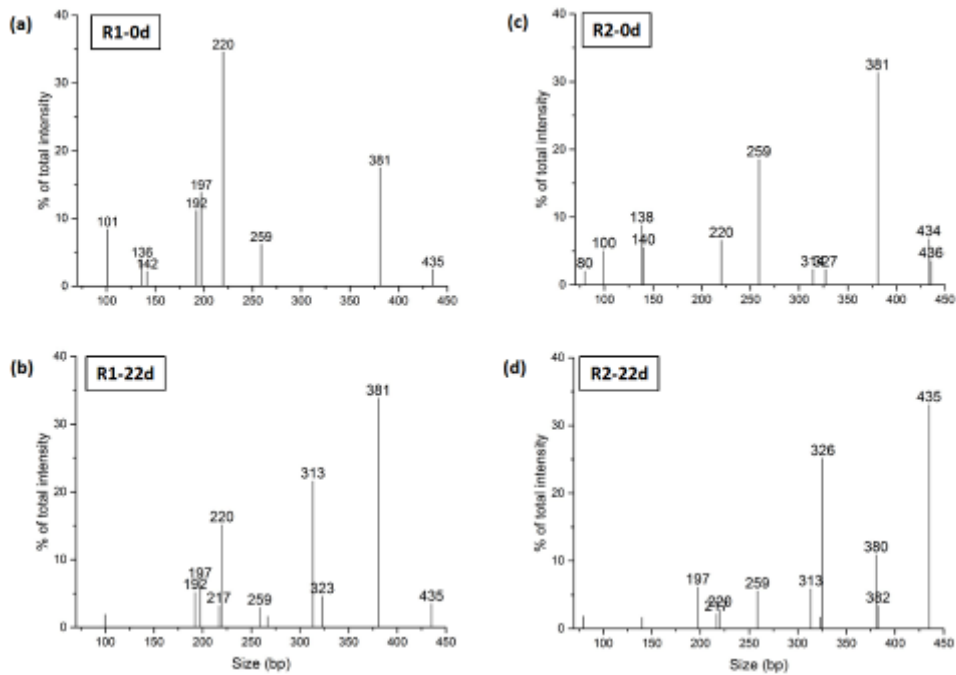
Figure 24: Electropherograms of MspI-digested T-RFLP fingerprints obtained for bacterial populations from (a) R1-0d, (b) R1-22d, (c) R2-0d, (d) R2-22d. The length of T-RFs in base pairs (bp) was indicated.
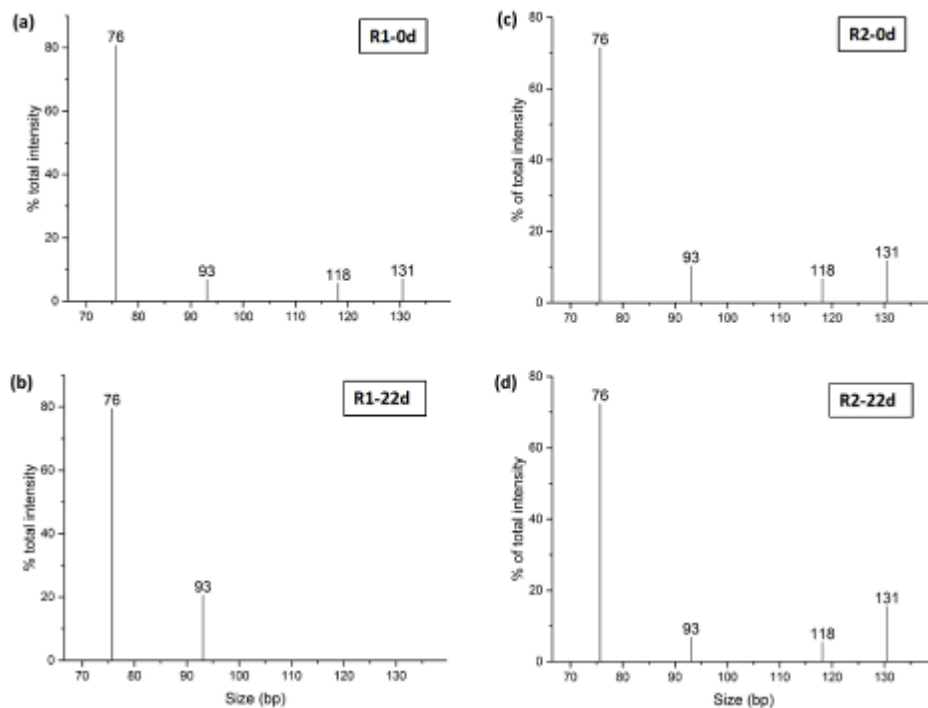
Figure 25: Electropherograms of MspI-digested T-RFLP fingerprints obtained for archaeal populations from (a) R1-0d, (b) R1-22d, (c) R2-0d, (d) R2-22d. The length of T-RFs in base pairs (bp) was indicated.

4. CONCLUSIONS

The performance of FW AD was investigated using a single-stage bioreactor, and the microbial communities were monitored during the anaerobic digestion process. This study showed that the differences in microbial populations present in the inoculum source played an important role in the performance of FW reactors. Anaerobic sludge from WRP in this study was shown to be a more suitable seeding sludge which promoted reactor stability and enhanced biogas production. The methane yield of FW reactors inoculated with WRP sludge was on average 2-3 times higher than that inoculated with POME sludge. T-RFLP analysis showed that the predominant T-RFs that were important for the bioconversion of FW into biogas were present in the WRP seeding sludge and remained as dominant groups until the end of the study.

5. ACKNOWLEDGEMENT

6. REFERENCES

[1] APHA. (1998). Standard methods for the examination of water and wastewater. Washington DC, USA:American Public Health Association.

[2] CHEN, C.-L., Macarie, H., Ramirez, I., Olmos, A., Ong, S.L., Monroy, O., Liu, W.-T. (2004). Microbial community structure in a thermophilic anaerobic hybrid reactor degrading terephthalate. Microbiology, 150 (10), 3429-40.

[3] GUJER, W., Henze, M., Mino, T., Matsuo, T., Wentzel, M., Marais, G. (1995). The activated sludge model No.2: biological phosphorus removal. Water Science and Technology, 31 (2), 1-11.

27: Exergy analyses of an integrated solid oxide fuel cell and biomass gasification system

JUNXI JIA[1], BAOZHI SUN[1]

1College of Power and Energy Engineering, Harbin Engineering University, *jiajunxi99@sohu.com*
1College of Power and Energy Engineering, Harbin Engineering University, *baozhisun@hrbeu.edu.cn*

An integrated process of biomass gasification and solid oxide fuel cells (SOFC) is investigated using energy and exergy analyses. A performance comparison of power systems for different gasification agents is given by thermodynamic analyses. Exergy analysis is applied to investigate exergy destruction in components in the power systems. When using air or oxygen-enriched air as gasification agents, the gasifier reactor causes the greatest exergy destruction.

For the case in which oxygen-enriched air as gasification agent, about 29% of the chemical energy of the biomass is converted into net electric power, while about 17% of it is used to for producing hot water for district heating purposes. The total exergy efficiency of combined heat and power is 29%.For the case in which steam as gasification agent, the highest exergy destruction lies in the air preheater due to the great temperature difference between the hot and cold side. The net electrical efficiency is about 40%. The energy combined heat and power efficiency is almost 36%, which is higher than that when air or oxygen-enriched air as gasification agent.

Keywords: biomass gasification; solid oxide fuel cell; exergy analysis;

1   INTRODUCTION

Biomass is supposed to be one of promising renewable source of energy, which has the advantage of being renewable and available locally (Jefferson, 2006, pp.571-582.). Biomass gasification (BG) technology has been used to produce syngas and electricity, from laboratory scale test to some demonstration scale plants over the years. Although low energy density and seasonal availability of biomass lead to both the high transport cost and high capital cost of biomass plants, it has the greatest potential for being commercialized to produce hydrogen in the future (Abuadala and Dincer, 2012, pp. 415–455).

Biomass can be gasified using steam or air as gasification agent. Air gasification is an exothermic process, which is autothermal (Prokash, 2009, p.833; Thanapa, 2012, p525.). On the other hand steam gasification is an endothermic process, which is allothermal, an external source supplies the necessary heat from the depleted fuel (Umeki, 2010, pp.791-798; Gröbl, 2012, pp.451-461).By supplying steam as the gasification agent, high H_2 yields can be got, however steam gasification consumes lot of energy and the system efficiency may decrease (Masishi and Goswami, 2007, pp. 3831-3840.).

Solid oxide fuel cell (SOFC) is considered one of the most important energy technologies for its high efficiency and low environmental impact. SOFC is fuel flexible and ideal for syngas conversation due to its high operation temperature (Jia, 2013, pp.1821).

Integration of biomass gasification with SOFC has received more attention as a potential substitute for fossil fuels in electric power production. Athanasiou et al. (Athanasiou, 2007, pp. 337-342) investigated the integrated process of biomass gasification and a solid oxide fuel cell .According to some assumptions, the energy balance revealed that the process can be auto-thermal. Furthermore, and due to the utilization of the hydrogen content of steam utilized in the reforming stage, the overall efficiencies to electrical power could reach very high levels. A energy generation system has been analysed by Cordiner et al. (Cordiner, 2007, pp.738-747) where a SOFC is supplied by a biomass gasifier.From a global point of view, the system presents good performance and the electrical efficiency was found to be 43.3%.Karellas et al. (Karellas, 2008, pp.284-291) investigated the performance of a power system which Coupling of the biomass heatpipe reformer with a SOFC for combined heat and power (CHP) production. The results of the simulations verified that high-efficient systems are available, especially when the gasification of biomass takes place in high temperature and low excess steam ratio. The gasification product can be further used in microturbine and SOFC systems.Fryda et al. (Fryda, 2008, pp.281-290) assessed the combination of biomass air gasification with a SOFC and micro gas turbine (MGT) and comparatively investigates three small scale CHP configurations. The results show that the biomass gasification system at elevated pressures with SOFC-MGT proved more efficiency and reached an electrical efficiency of 40.6%.

Gasification agent strongly influences the product gas composition and the performance of the BG-SOFC system. Therefore, the selection of a suitable BG-SOFC system requires a careful evaluation of gasification agent and options for system integration.

As few of references mentioned above compared the effects of gasification agents on the overall performance of power systems. In this paper, a performance comparison of BG-SOFC system for different gasification agents, i.e. air, enriched oxygen and steam is given by thermodynamic analyses. Firstly, a gasifier model is developed to analyze the syngas composition and the adiabatic reaction temperature. Then a system level SOFC model is developed for the purpose of this study, which includes an electrochemical model and takes into account the operating parameters, e.g. temperature, pressure, gas composition and fuel utilization. Energy and exergy analyses are applied to assess the performance of the BG-SOFC systems for autothermal and allothermal gasification. Electrical efficiency, combined heat and power efficiency, exergy destructions and exergy efficiency are calculated to evaluate the performance of the two power systems.

2. SYSTEM DESCRIPTION

A schematic of the integrated biomass gasification and SOFC system is shown in Figure 1 and Figure 2. Biomass enters the dryer and its moisture content is reduced to a level acceptable by the gasifier. Different gasification agents, e.g. air (Fig.1), enriched oxygen (Fig.1, Air separation unit is only valid for this case) and steam (Fig.2) enters the gasifier. The syngas produced by gasification is cleaned up after entering a hot gas cleaning unit according to the tolerance limits of the SOFC. Then, the cleaned syngas enters the SOFC, where electricity is produced. The depleted fuel and air enter the combustor to burn. The burned

gas is used to increase the temperature of air supplied by the blower to the SOFC temperature level. The stream of burned gas supplies heat to the steam generator and then enters to the gasifier in the case of steam gasification. Finally, the stream gives heat to the dryer and goes into the atmosphere.
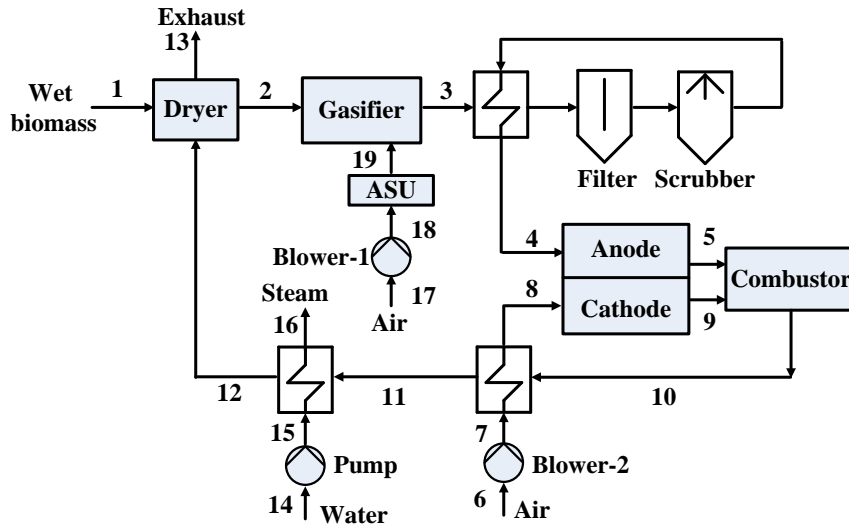
Figure.1 Flow sheet diagram of an integrated biomass air or enriched oxygen gasification and SOFC system (case 1 and 2)
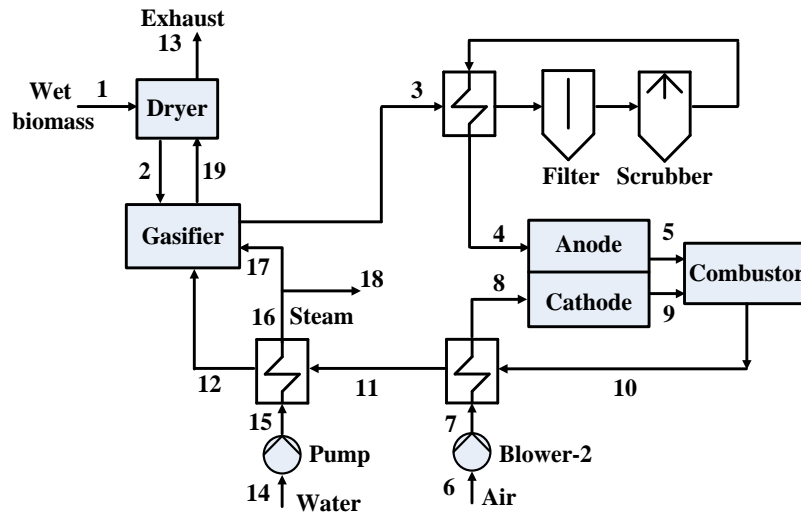
Figure.2 Flow sheet diagram of an integrated biomass steam gasification and SOFC system (case 3-5)

3. MODEL DESCRIPTION

38.10.   3.1 Gasifier model

The global reaction in the gasifier can be written as,

$$CH_a O_b + w H_2 O + m(O_2 + 3.76 N_2) = x_1 H_2 + x_2 CO + x_3 CO_2 + x_4 H_2 O + x_5 CH_4 + 3.76 m N_2 \qquad (1)$$
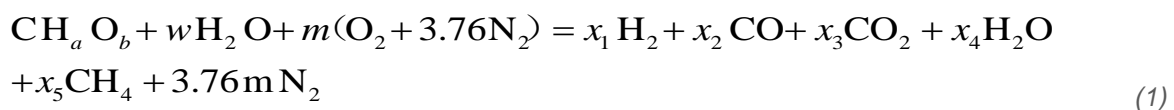
The mass balances for C, H and O are, respectively

$$x_2 + x_3 + x_5 = 1 \qquad (2)$$

$$a + 2w = 2x_1 + 2x_4 + 4x_5 \qquad (3)$$

$$b + w + 2m = x_2 + 2x_3 + x_4 \quad \text{(4)}$$

In order to analyze the effects of the air supply and moisture content of the biomass on the process of gasification, the moisture content (MC) of biomass and equivalence ratio(ER) is defined as follows:

$$MC = \frac{Mass_{water}}{Mass_{water+biomass}} = \frac{18w}{(12 + a + 16b) + 18w} \quad \text{(5)}$$

$$ER = \frac{Air_{actural}}{Air_{stoichiometric}} = \frac{m}{1 + 0.25a - 0.5b} \quad \text{(6)}$$

The two equilibrium reactions in the gasification are

$$C + 2H_2 \leftrightarrow CH_4 \quad \text{(7)}$$

$$CO + H_2O \leftrightarrow H_2 + CO_2 \quad \text{(8)}$$
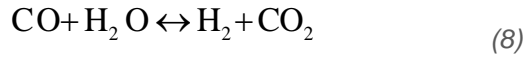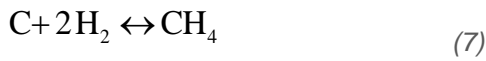
The equilibrium constants for them are

$$K_1 = \frac{P_{CH_4}/P_0}{(P_{H_2}/P_0)^2} = \frac{x_5 n_T}{x_1^2 P_0} \quad \text{(9)}$$

$$K_2 = \frac{P_{CO_2}P_{H_2}}{P_{H_2O}P_{CO}} = \frac{x_1 x_3}{x_2 x_4} \quad \text{(10)}$$

where n_t is the total mole of the syngas, P_0 is total pressure (atm).

At the same time, the equilibrium constant is a function of temperature, written as

$$K_p = \exp(-\frac{\Delta G_T^0}{R_m T}) \quad \text{(11)}$$

Where

$$\Delta G_T^0 = \Delta H_T^0 - T \Delta S_T^0 \quad \text{(12)}$$

Substitution of Eq. (13) and (14) into Eq. (11) and (12) respectively gives:

$$K_1 = \frac{x_5 n_T}{x_1^2 P_0} = \exp[-(G_{T,CH_4}^0 - 2G_{T,H_2}^0)/(R_m T)] \quad \text{(13)}$$

$$K_2 = \frac{x_1 x_3}{x_2 x_4} = \exp[-(G_{T,H_2}^0 + G_{T,CO_2}^0 - G_{T,CO}^0 - G_{T,H_2O}^0)/(R_m T)] \quad \text{(14)}$$

The energy balance equation can be written as (assuming no heat loss and work=0)

$$H_{biomass} + wH_{H_2O} + mH_{O_2} + 3.76mH_{N_2} =$$
$$x_1 H_{H_2} + x_2 H_{CO} + x_3 H_{CO_2} + x_4 H_{H_2O} + x_5 H_{CH_4} + 3.76mH_{N_2} \quad (15)$$

with

$$H(T) = \Delta H_f^0 + \Delta H = \Delta H_f^0 + \int_{298}^{T} C_p dt \quad (16)$$

The six variables x_1, x_2, x_3, x_4, x_5 and T are determined by six equations (2), (3), (4), (13), (14) and (15).The values of the thermodynamic properties are adopted from Perry and Green. (Perry and Green, 1997).

Once the equilibrium constants are calculated by Eq. (15) and (16) at a tentative temperature, the x_1, x_2, x_3, x_4, x_5 is determined by solving the equations using Newton-Raphson method. Then, the gasification temperature is obtained by Eq. (15) using bisection method. This temperature is taken as the initial temperature for the next iteration until the convergence is obtained.

The present model has been validated against the experimental results of Jayah et al. (Jayah, 2003,pp. 459-469) shown in the Table 1.This work did not take into account the thermal loss in the gasifier,the value of methane is slightly inferior to that of experiment. At the same time, the hydrogen content is slightly higher than the real value. However, the good agreement between the model prediction and the experiment shows the present model is reliable.

Table 1. Comparison between model results and experimental results of Jayah et al. (MC=0.185, ER=0.40)

Gas composition (%)	CO	H_2	CO_2	CH_4	N_2
Experimental	19.6	17.2	9.9	1.4	51.9
This work	21.83	20.30	8.26	1.0	48.61

3.2 Solid oxide fuel cell model.

In general, the ideal reversible potential of H_2-O_2 SOFC can be calculated by the Nernst equation:

$$E_0 = \frac{-\Delta G_0}{2F} + \frac{RT}{2F} \ln \frac{p_{H_2} \cdot (p_{O_2})^{1/2}}{p_{H_2O}} \quad (17)$$

Nernst potential is reduced to the terminal voltage by the sum of the local voltage polarizations. The three polarizations are ohmic, activation and concentration polarization. Therefore the cell terminal voltage is given:

$$V = E_0 - \eta_{act,\ a} - \eta_{act,c} - \eta_{ohm} - \eta_{con} \quad (18)$$

Where V is the cell potential. The detailed description of the electrical simulation of SOFC can be found in (Paola,1998,pp. 3995-4007;Norman,1995,pp. 3792-3800;Jia,2007,pp. 696-705;Jia,2008,pp. 554-564;Jia,2011,pp. 1068-1075).

3.3 Energy and exergy efficiency

The performance of biomass gasification and SOFC power system can be evaluated by energy and exergy efficiency. Energy efficiency is defined as the ratio of useful energy products to total energy inputs. At the

same time, exergy efficiency is given as the ratio of useful exergy products to total exergy inputs, and then the inefficiencies due to irreversibilities can be found in (Dincer, 2012).

Net electrical power output of the system is defined as:

$$W_{net} = W_{SOFC} - W_{blower} - W_{pump} \qquad (19)$$

The heating production for user in Fig.1 is shown as:

$$Q = \dot{n}_{14} \cdot (\bar{h}_{16} - \bar{h}_{14}) \qquad (20)$$

The heating production for user in Fig.2 is shown as:

$$Q = (\dot{n}_{16} - SB \cdot \dot{n}_{CH_{1.44}O_{0.66}})(\bar{h}_{18} - \bar{h}_{14}) \qquad (21)$$

SB is molar ratio of steam entering the gasifier to drybiomas,in this study , which is choose as 0.05,0,1 and 0.15,respectively, in case 3,case 4 and case 5.

Both physical and chemical exergy at inlet and outlet are calculated for gasification, electrochemical reaction and combustion. The specific flow exergy is expressed by the sum of specific physical and chemical exergy.

$$ex = ex^{ph} + ex^{ch} \qquad (22)$$

The physical exergy can be defined as

$$ex^{ph} = h - h_0 - T_0(s - s_0) \qquad (23)$$

The chemical exergy for an ideal gas mixture can be written as

$$ex^{ch} = \sum_i x_i (ex_i^{ch} + RT_0 \ln x_i) \qquad (24)$$

where x_i is the molar fraction, ex_i^{ch} the standard chemical exergy of species i which can be taken from Szargut and Morris (Szargut and Morris, 1988).

For a general process, an overall exergy balance can be written as:

$$(\sum Ex_i)_{in} = (\sum Ex_j)_{out} + \sum Ex_{dest} \qquad (25)$$

where
$$(\sum Ex_i)_{in} = Ex_{air} + Ex_{drybio} + Ex_{biomoist} + Ex_{water} \qquad (26)$$
$$(\sum Ex_j)_{out} = Ex_{product\ gas} + Ex_{exhaust} + W_{net} + Ex_{steam} \qquad (27)$$

The exergy destruction ratio of component is defined as the ratio of exergy destruction to total exergy input. It can be written as

$$\eta_{dest,gasifier} = \frac{(Ex_{dest})_i}{(\sum Ex_i)_{in}} \qquad (28)$$

The overall system performance is investigated by electrical efficiency, combined heat and power efficiency and exergy efficiency, which can be expressed as,

$$\eta_{el} = \frac{W_{net}}{n_{biomass} \cdot LHV_{biomass}} \qquad (29)$$

$$\eta_{CHP} = \frac{W_{net} + Q}{n_{biomass} \cdot LHV_{biomass}} \qquad (30)$$

$$\eta_{ex} = \frac{W_{net} + Ex_{steam}}{(\sum Ex_i)_{in}} \qquad (31)$$

4. RESULTS AND DISCUSSION

The input data used in this study is shown in Table.2

The compositions of syngas leaving the gasifier are shown in Table 3. It can be seen that when enriched oxygen is used as gasification agents instead of air, molar fraction of all species except N_2 increases since less N_2 enters the gasifier. When using steam as gasification agent, molar fraction of H_2, CO and CH_4 is higher than those cases when using air or enriched oxygen.

Exergy destruction ratios in different components are shown in Fig.3. Exergy efficiencies of components are shown in Table 4. It clearly shows that the largest exergy destruction lies in the gasifier in case 1 and 2, whereas the destruction in heater is the highest due to the great temperature difference between the hot and cold side of the heater when steam as the gasification agent. It should be noted that the exergy destruction ratio for air preheater is 22%, which is the largest one among all the components in case 3.The exergy destruction in SOFC is moderate compared to other components. The exergy destruction in steam generator decreases from case1 to case 3, since most of steam is sent to the gasifier to product hydrogen and less steam is sent for producing heat. The exergy destruction in the combustor results from mixing loss and irreversible combustion process.

Table 2 Input data

Environmental	
Ambient temperature	25℃
Ambient pressure	1.013bar
Biomass data	
Type of biomass	wood
Ultimate analysis /wt% (dry)	50% C, 6% H, 44% O
Moisture content in biomass	40%
Gasifier	
Gasifier operating temperature	800℃
Gasifier operating pressure	1.013bar
Moisture content of biomass entering gasifier	10%
Molar fraction of air(case 1)	21%O_2,79%N_2
Molar fraction of enriched oxygen(case 2)	35%O_2,65%N_2
Molar ratio of steam entering gasifier to dry biomass	0.05(case3),0.1(case4)0.15(case5)
SOFC	
SOFC operating temperature	800℃
Anode inlet temperature	750℃
Fuel utilization	0.85
Air utilization	0.12
DC/AC inverter efficiency	95%
Peripheral equipment	
Isentropic efficiency of blower	0.53
Pressure ratio of blowers	1.2
Isentropic efficiency of water pump	0.85
Pressure ratio of water pump	1.2
Exhaust temperature (No.13)	130℃

Table 3. Compositions of syngas for different gasification agents. (800℃)

	H_2	CO	CH_4	CO_2	H_2O	N_2
Case 1 : Air	20.37	23.08	0.19	8.69	7.00	40.67
Case 2:Enriched O_2	27.83	31.22	0.34	9.79	7.84	23.42
Case 3: Steam (SB=0.05)	45.31	50.05	0.78	2.11	1.74	0
Case 4: Steam(SB=0.1)	45.43	47.42	0.78	3.40	2.97	0
Case 5: Steam(SB=0.15)	45.47	44.99	0.79	4.55	4.2	0
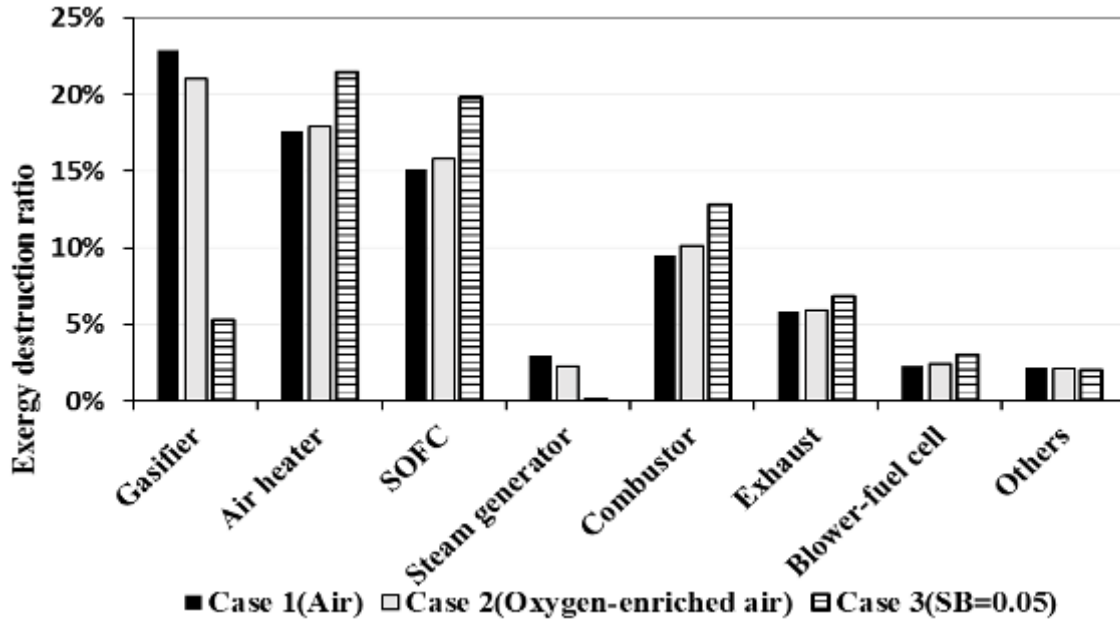
Figure.3 Exergy destruction ratios for different components in case 1-3.

The power input, output for components, net power and heat output is shown in Table 4 .It can been seen that the net power output for steam gasification (case3-5) is higher, however the heat for user in these systems is lower than case1-2 because more energy is spent in the gasification process (case3-5), thus less energy is left for producing steam. In the case of steam gasification(case3-5),the heat increasing ,whereas the net power output hardly change as SB increasing, since we assume the fuel utilization of SOFC as constant in the modeling, hence more steam remains for producing heat for user. The power to heat ratio are 93, 7.9 and 4.1 for case3-5, respectively.

Table 4 Power input, output for components, net power and heat output (W)

	Wblower,biomass	Wblower,SOFC	WSOFC	Wnet	Heat
Case 1 : Air	482	10672	57390	46236	34534
Case 2:Enriched O2	414	10832	57739	46492	27614
Case 3: Steam (SB=0.05)	0	10625	59475	48850	522
Case 4: Steam(SB=0.1)	0	10625	59200	48575	6146
Case 5: Steam(SB=0.15)	0	10625	58953	48328	11964

The total performance of five power systems is compared by the calculation of the electrical efficiencies, combined heat and power efficiencies and exergy efficiencies for case1-5 as shown in Fig.4.It is evident that the electrical efficiencies are between 28% and 29% for case1 and case 2, and they increase to 40% for case3-5.The combined heat and power efficiency varies from 40% to 50%.The exgergy efficiencies for case 1 and 2 are 28% and 29%,and they increases slightly from 35% to 37% for case 3-5.
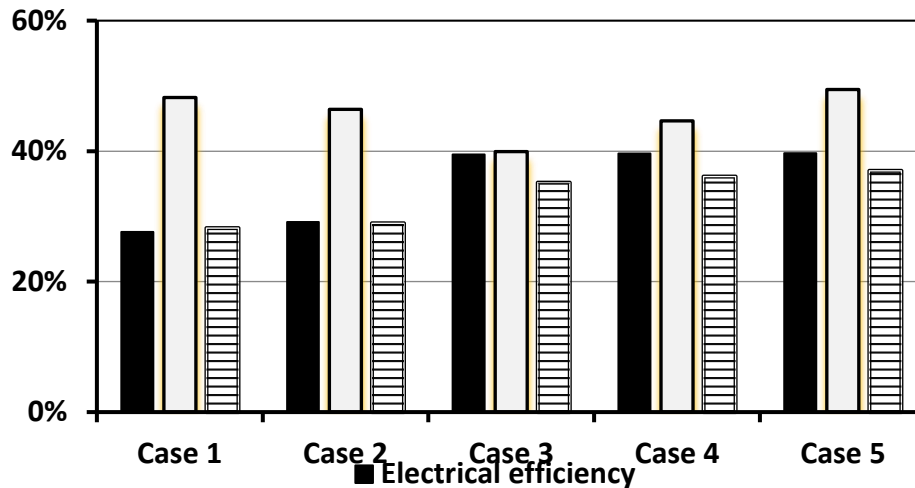
Figure.4 Electrical efficiencies, combined heat and power efficiencies and exergy efficiencies for five cases

5. CONCLUSIONS

An integrated SOFC and biomass gasification system using air, enriched air, and steam as gasification agent is investigated by thermodynamic model. Energy and exergy analyses are carried out to access the performance of five cases.

It is found that the adiabatic gasification temperature increases with higher air supply and lower moisture content of the biomass. When using steam as gasification agent, molar fraction of H_2, CO and CH_4 in syngas is higher than those cases when using air or enriched oxygen.

When using enriched oxygen as gasification agent, the gasifier reactor caused the greatest exergy destruction giving rise to a loss corresponding to 21% of the system exergy input. However, for steam gasification power systems(case 3-5), the magnitude of exergy destruction for gasifier is much lower than that for case1 and 2.The largest exergy destruction lies in heat exchanger, which is approximately 22% of the system exergy input.

The net electrical efficiencies of the power systems for air and enriched oxygen gasification are 27% and 29%.For the power systems of steam gasification, the net electrical efficiencies reaches 40%. The exergy efficiencies of the power system(case 3-5) of steam gasification is about 36% which is 8% higher than those of case1 and 2.It can be concluded that steam should be selected as a gasification agent in term of a better overall thermodynamics performance of the BG-SOFC system.

The future work about this study will include a more comprehensive multi-dimensional gasifier model and optimization study of the power system configuration with micro gas turbine.

6. ACKNOWLEDGMENT

7. REFERENCES

[1] ABUADALA, A. and Dincer, I. (2012).A review on biomass-based hydrogen production and potential applications.International Journal of Energy Research, 36, 415–455.

[2] ATHANASIOU, C., et al. (2007).From biomass to electricity through integrated gasification/SOFC system-optimization and energy balance.International Journal of Hydrogen Energy, 32, 337-342.

[3] CORDINER, S., et al (2007).Analysis of a SOFC energy generation system fuelled with biomass reformate. Applied Thermal Engineering, 27, 738-747.

[4] DINCER, I. et al. (2012).Exergy: Energy, Environment and Sustainable Development.2nd ed. London: Elsevier.

[5] FRYDA, L., et al. (2008).Integrated CHP with autothermal biomass gasification and SOFC-MGT, Energy C onversion and Management, 49,281-290.

[6] GRÖBL, T., et al (2012).Biomass steam gasification for production of SNG – Process design and sensitivity analysis. Applied Energy , 97, 451-461.

[7] JAYAH, T., et al. (2003). Computer simulation of a downdraft wood gasifier for tea drying. Biomass and Bioenergy, 25,459-469.

[8]JEFFERSON, M. (2006). Sustainable energy development: performance and prospects. Renewable Energy, 31,571-582.

[9] JIA, J., et al. (2007).A mathematical model of a tubular solid oxide fuel cell with specified combustion zone. Journal of Power Sources, 171,696-705.

[10] JIA, J., et al. (2008). Effect of operation parameters on performance of tubular solid oxide fuel cell. AIChE Journal, 54,554-564.

[11] JIA, J., et al. (2011).Effects of gas recycle on performance of solid oxide fuel cell power systems, Energy, 36, 1068-1075.

[12]JIA J, et al. (2013). Performance comparison of three solid oxide fuel cell power systems, International Journal of Energy Research, 37, 1821-1830.

[1]KARELLAS, S., et al. (2008). An innovative biomass gasification process and its coupling with microturbine and fuel cell systems. Energy, 33,284-291.

[14]MASISHI, R., and Goswami, Y. (2007).Thermodynamic optimization of biomass gasifier for hydrogen pro duction. International Journal of Hydrogen Energy, 32, 3831-3840.

[15] NORMAN, F., et al. (1995).A mathematical model of a solid oxide fuel cell. Journal of the Electrochemical Society, 42, 3792-3800.

[16] PAOLA, C., et al. (1998) Modelling of solid oxide heat exchanger integrated stacks and simulation at high fuel utilization. Journal of the Electrochemical Society, 145, 3995-4007.

[17] PERRY, R., and Green, D. (1997).Perry's Chemical Engineers' Handbook, 7th edn, New York: McGraw Hill. [4] Thanapa, S, et al (2012).Fixed bed gasification of dairy biomass with enriched air mixture. Applied Energy, 97, 525-531.

[18] PROKASH, C.et al. (2009).Modelling of a downdraft biomass gasifier with finite rate kinetics in the reduction zone. International Journal of Energy Research, 33, 833–851.

[19] SZARGUT, J. and Morris D. (1988) Exergy analysis of thermal, chemical and metallurgical processes. New York: Hemisphere.

[20] THANAPA, S, et al (2012).Fixed bed gasification of dairy biomass with enriched air mixture. Applied Energy, 97, 525-531.

[21] UMEKI, K., et al. (2010). High temperature steam-only gasification of woody biomass. Applied Energy, 87, 791-798.

30: Three-stage anaerobic co-digestion of high-solids food waste and horse manure

JINGXIN ZHANG[1], KAI CHEE LOH[2], YEN WAH TONG [1,2]*, WANGLIANG LI[1], JUN WEI LIM[1]

1NUS Environmental Research Institute, National University of Singapore, Singapore
2Department of Chemical & Biomolecular Engineering, NUS, Singapore
* Corresponding author. Tel: +65 65168467, Fax: +65 67791936, E-mail: chetyw @nus.edu.sg

The hydrolysis and acidogenesis were the rate-controlling steps in the overall anaerobic digestion (AD) process. Considering the optimum conditions for different AD stage were diverse, the development of multi-stage AD system was likely to enhance each stage of AD through optimizing control respectively. This study developed a highly integrate three-stage anaerobic digester (HM3) to bond the advantages of dry AD and wet AD for anaerobic co-digestion of food waste and horse manure. The digester design was mainly comprised of three chambers i.e. high-solids hydrolysis stage, high-solids acidogenesis stage and wet methanogensis stage. Through comparing the treatment performance with other two control digesters, HM3 presented 11.2 ~22.7% higher methane yield. The improved methane yield was mainly attributed to the functionalized partitioning in this integrated digester, which significantly accelerated the solubilization of solid organic matters and the formation of organic acids as well as ammonia in the high-solids hydrolytic and acidogenic stage respectively. Additionally, HM3 also showed the highest volatile solids reduction rate among the three digesters. Real-time PCR and pyrosequencing analysis indicated that the abundance and biodiversity of microorganisms including bacteria and archaea in HM3 was much higher than that in the control reactors. Moreover, different dominant bacterial communities with various functions were enriched in the high-solids hydrolytic stage e.g. Lactobacillaceae and Pseudomonadaceae, acidogenetic stage e.g. Porphyromonadaceae and Enterobacteriaceae and wet methanogenic stage e.g. Aminobacterium, Clostridium and Proteiniphilum. The bioaugmentation and functional partition in this three-stage anaerobic digester enhanced the transformation from particulate organic matter to soluble substrate and methanogenesis, which is meaningful for its application in practice.

Keywords: Anaerobic; Three-stage anaerobic digestion; High-solids anaerobic digestion; Wet anaerobic digestion; Microbial community.

1. INTRODUCTION

Anaerobic digestion (AD) is a commonly used and cost-effective technology for solid organic waste and high-strength wastewater treatment, simultaneously with the recovery of bioenergy recovery e.g. CH4. According to the difference of total solids (TS) in the AD system, AD was categorized into wet AD system (TS < 15%) and high-solids AD system (15%<TS<40%). The widely application of AD is mainly attributed to its low capital and operating cost, high potential of methane production and extensive feedstock e.g. food waste, animal manure and waste activated sludge. However, AD of single substrates such as food waste usually presents some drawbacks e.g. imbalance of C/N ratio, lack of nutrients and low buffering ability (Mata-Alvarez et al., 2014). To overcome this issue, anaerobic co-digestion (AcoD), the simultaneous AD of two or more substrates, is developed as a cost-effective alternative to improve methane yields and economic viability of AD plants (Banks et al., 2011; Fang et al., 2011).

At present, most of the developed anaerobic digesters in practice belong to single-stage and wet anaerobic systems (total solids < 15%) (Nagao et al., 2012), due to its high treatment capacity and methane yields. However, wet AD usually need high water consumption, digester volume and expensive post-treatment cost (Kothari et al., 2014). In view of this, high-solids AD (total solids >15%) attracts much more attention recently because of its reduced cost and digester volume, as well as potential by-products (Li et al., 2011). Usually, AD undergoes the three stages: hydrolysis, acidogenesis and acetogenesis/methanogenesis (Martin et al., 2003), in which the hydrolysis is commonly considered as the rate-limiting step during the whole anaerobic process especially for the AD of high molecular compound and granular substrates. Comparing to wet AD, high-solids AD is more susceptible to the rate of hydrolysis due to high-solids feedstock and less mass transfer rate, especially for AD of agriculture-based waste such as farm waste and animal manures. To accelerate the hydrolysis step, several pretreatment approaches were applied such as microwave, ultrasound, thermal and chemical. The purpose of these methods is to improve the solubilization and biodegradability of solid organic waste that will be utilized by methanogens in the final methanogenesis stage for methane production. However, these pretreatment methods are inevitable to cause high expense, energy waste and introduce some unwanted chemicals. It is reported that biological solubilization process was an effective method for the pretreatment of organic waste, during which organic particles were microbiologically solubilized and the size of waste particle was also reduced prior to AD (Gonzales et al., 2005). Obviously, biological pretreatment process help to enhance the hydrolysis rate at a lower cost as compared with other physical or chemical pretreatment methods. It was assumed that biological hydrolysis process possibly accelerated the solubilization process of high-solids organic wastes to improve the mass transfer rate and further enhance the subsequent acidogenesis and methanogenesis.

In this study, a highly integrated three-stage anaerobic digester (TSAD) was developed for AcoD of high-solids food waste (FW) and horse manure (HM), which separated the entire anaerobic process into three stages i.e. high-solids hydrolysis stage, acidification stage and wet methane-producing stage. This TSAD reactor could be considered as a coupling of high-solids biological hydrolysis, acidogenesis and wet methanogenesis. The functional partitioning in this high-solids combined wet TSAD system is expected to enhance hydrolysis and acidogenesis of FW and HM and further improve the whole treatment performance through applying optimal conditions in each stage of them such as optimum pH control. It is reported that the optimum pH for hydrolysis and acidogenesis were 5.5 and 6.5 respectively (Kim et al., 2003), and the suitable range of pH for methanogenesis was 6.5-8.2 (Lee et al., 2009). However, most of studies are focus on the wet AD or high-solids AD while few researches have been reported on the development of an integrated anaerobic digester containing high-solids AD stage and wet AD stage. Moreover, the type of feedstock will significantly affect the community structure of functional microorganisms and reactor performance. However, the commonly used animal manures in AcoD are pig manure and cow manure while less attention has been paid to other livestock e.g. horse manure (Mata-Alvarez et al., 2014). In light of this, this study will first seek to develop a method and apparatus for three-stage anaerobic digestion. The possibility and potential of this TSAD system for AcoD of FW and HM were evaluated. The synergistic effect and interaction between bacterial and archaeal communities in this TSAD system were also investigated in-depth.

2. METHODOLOGY

2.10. Experimental set-up and reactor specification

A three-stage anaerobic digester (TSAD) was developed, which separated the entire anaerobic process into three stages i.e. high-solids hydrolysis stage, acidification stage and wet methane-producing stage. The simulated schematic diagram of this TSAD system. Chamber level 1, level 2 and level 3 correspond to high-solids hydrolysis stage, acidification stage and wet methane-producing stage respectively. To simply the experimental design and comparison among traditional one-stage AD, two-stage AD and TSAD, three continuous stirred-bank reactors (CSTR) were operated in parallel for anaerobic co-digestion of FW and HM methane production, with HM1, HM2, HM3 representing the one-stage AD, two-stage AD and TSAD respectively. The feeds for each AD were separately prepared according to the following procedures: (1) Fresh FW and HM (mass ratio 1:1) from the freezer was used as the feed of one-stage AD (HM1). (2) Fresh FW and HM (mass ratio 1:1) was placed in a 2 L hydrolysis glass reactor (Regard it as chamber level 1) and TS adjusted to 20% with the addition of seeding sludge. During this hydrolysis stage, the reactor was operated at 35 oC with a stirrer speed of 150 rpm and optimum pH was maintained at 5.5 ± 0.2 via the addition of sodium bicarbonate (Kim et al., 2003). After 2 days operation, the hydrolyzed FW and HM was stored in the freezer at -20 oC as the feed of two-stage AD (HM2). (3) The hydrolyzed FW and HM from step (2) was added with the seeding sludge to reduce the inhibition of VFAs and hydrolysis products and enhance acidification process. The pH was controlled at 6.5 ± 0.2, to provide the optimal conditions for acidogenesis (Kim et al., 2003). After 2 days' operation, the acidized FW was stored in the freezer at -20 oC as the feed of TSAD (HM3). Table. S1 summarizes the type of feed for each AD.

The CSTRs (HM1, HM2 and HM3) are made of 1 L glass reactor with an effective volume of 0.8 L. A magnetic stirrer revolving at a speed of 800 rpm was used to ensure even mixing. The three CSTRs were operated at 35 oC in parallel. These three AD were operated in a semi-continuous mode (feeding every two or three days) with gradual increase in OLR from 2.51, 3.76, 6.27, 8.15 and 12.54 g VS/L. This experiment conduct two parallels at the same experimental conditions. The data collected from the liquid samples and gas samples were the mean value of these two parallels.

Inoculums and substrates

The seed sludge was collected from a large-scale anaerobic digester at Ulu Pandan Water Reclamation Plant of Singapore. The ratio of volatile suspended sludge (VS) to total suspended sludge (TS) was 0.75 with initial TS of 13.2 g/L.

FW and HM were obtained from a restaurant of National University of Singapore and Singapore turf club respectively. After removing any bones and non-biodegradable waste like plastic bag, FW was smashed by a FW disposer and then stored with HM at -20 oC freezer to prevent biological decomposition. The detailed characteristics of FW and HM are listed in Table. S2.

Analysis

COD and ammonia were determined using HACH color meter (DR900, America) according to the manufacturer's instructions. The pH was recorded using a pH analyzer (Agilent 3200M, America). TS and VS were determined based on the weighing method after being dried at 103-105 oC and burnt to ash at 550oC. The CH_4 production was determined using a gas chromatograph (Clarus 580 Arnel, PerkinElmer, America) equipped with a thermal conductivity detector. Volatile fatty acids such as acetic acid, propionic acid and butyric acid were determined by a gas chromatograph (Clarus 580GC, PerkinElmer, America) equipped with a flame ionization detector. C and N element contents in FW were determined using an elementar (vario MICRO cube, HANAU, Germany). The genomic DNA of the sample was extracted using an extraction kit (MO BIO Laboratories, Inc. Carlsbad, USA) according to the manufacturer's instructions.The diversity of microbial communities was deeply investigated by IIlumina Hiseq 2000 pyrosequencing technology. A set of bacterial primers 341F (5' – CCTACGGGNGGCWGCAG- 3') and 805R (5' - GACTACHVGGGTATCTAATCC - 3') was used to amplify the hypervariable V3 – V4 region of bacterial 16S rRNA gene.

3. RESULTS AND DISCUSSION

3.1 High-solids hydrolytic and acidogenic stage

The hydrolytic and acidogenic efficiency in the first and second stage of the developed three-stage anaerobic digester were shown in Table. 1. After hydrolysis stage, the degree of solubilization of FW and HM increased from 19.1 in the initial to 33.6%. The hydrolysis yield was lower than those obtained by Bouallagui et al. (2004) (46~53%) for hydrolysis of fruit and vegetable wastes operating at an HRT of 3 days. The low hydrolysis rate might be attributed to the bio-refractory organics containing in HM such as undigested grass that contained high content of cellulose and hemicellulose (Brown and Li, 2013) and its relatively short retention time of 2 days. However, the hydrolysis rate was in agreement with the results obtained by De La Rubia etal. (2009) (hydrolysis rate: 20.5~30.1%) for hydrolysis of sunflower oil cake. After the acidogenic stage, the hydrolysis yield of FW and HM further increased to 45%. As compared with high-solids hydrolytic stage, acidogenic stage also contributed to the increased degree of solubilization in some content.

During hydrolytic and acidogenic stage, the pH tended to decrease accompanied with VFA generation such as acetic acid, propionic acid and butyric acid etc. The VFAs except acetic acid will be further utilized by acetogenic bacteria to produce acetic acid and hydrogen. Finally, acetic acid and hydrogen are used for methane production. Hence, VFA accumulation during hydrolytic and acidogenic stage are very important. As shown in Table. 1, the degree of acidification raised slightly from 44 to 50% after high-solids hydrolysis stage. After acidogenic stage, the degree of acidification increased sharply to 62.8%, indicating that soluble COD was mainly consist of VFA that was in agreement with the results of De La Rubia et al. (2009). These results indicated that acidogenic stage contributed to the most of the increased acidification yield as compared with the high-solids hydrolytic stage. As the end-product of AD of N-rich organic feedstock, ammonia concentration also increased from 0.58 ± 0.04 to 1.31 ± 0.06 mg/g VS after high-solids hydrolytic stage. During the following acidogenic stage, ammonia concentration further raised to 9.93 ± 0.1 mg/g VS. The amount of ammonia releasing in the acidognic stage showed 11.8 times higher than that in high-solids hydrolytic stage. The relatively low degree of acidogenetion and ammonia in hydrolysis stage may not be limited by the hydrolysis, but the hydrolyzed products generated from complex organic compounds could be inhibitors (Chen et al., 2008). As the dispensable nutrient for the growth of microorganisms and buffering agent ($CxHyCOOH + NH_3 \times H_2O \rightarrow CxHyCOO^- + NH_4^+ + H_2O$), ammonia plays an very important role in the performance and stability of AD. Therefore, the increased ammonia content was likely to enhance the performance of the following methanogenesis.

Table 1

Characteristics of food waste and horse manure

Parameter	pH control	SCOD (g COD/g VS)	TCOD (g COD/g VS)	TVFA (g COD/ g VS)	Ammonia (mg/ g VS)	[1]Degree of solubilisation (%)	[2]Degree of acidification (%)
Fresh mixture of FW and HM	6.0 ± 0.1	0.25 ± 0.04	1.31 ± 0.07	0.11 ± 0.01	0.58 ± 0.04	19.1%	44%
FW and HM after hydrolysis	5.5 ± 0.3	0.44 ± 0.03	1.31 ± 0.07	0.22 ± 0.03	1.31 ± 0.06	33.6%	50%
FW and HM after hydrolysis and acidogenesis	6.5 ± 0.3	0.59 ± 0.05	1.31 ± 0.07	0.37 ± 0.02	9.93 ± 0.1	45%	62.8%

1. The degree of solubilization can be expressed as the quotient between soluble COD and total COD (TCOD) of solid sample (Demirel and Yenigun, 2004).
2. The degree of acidification was defined as the ratio of COD-equivalent TVFA to the soluble COD (De La Rubia *et al.*, 2009).

3.2 Methanogenic performance comparison among one-stage AD, two-stage AD and Three-stage AD

HM1, HM2 and HM3 were fed using the fresh FW and HM, hydrolyzed FW and HM and acidified FW and HM respectively. As shown in Fig. 1A, the accumulated methane yield increased gradually with the increasing of OLR from 2.5 to 12.5 g VS/L. After 60 days' operation, the accumulated methane yield of HM3 raised to 55.7 L at a OLR of 12.5 g VS/L, which was 22.7% times higher than that of 45.4 L in HM1. It is assumed that high-solid hydrolysis and acidogenesis stage helped to enhance the solubilisation of FW and HM and VFA formation that might further accelerate the process of VFA consumption by ethanogens and methane production in HM3. This assumption was confirmed by the results of VFA concentration in these three digesters. From Fig. 1C, VFA concentration in these three digesters increased with the increase of OLR. However, the VFA content in HM3 was still lower than that of HM1 and HM2, indicating that the VFA consumption rate in HM3 was faster. As compared with HM3, the accumulated methane yield of HM2 showed 10.9% lower value. The improved methane yield might be attributed to the positive effect of acidogenic stage which significantly accelerated the VFA accumulation and further enhance the

solubilization of FW and HM (Table. 1). From Fig. 1B, the pH value among HM1, HM2 and HM3 were maintained between 7.09 and 8.05 during the whole experimental operation. With the increase of OLR, HM2 and HM3 presented a slightly higher pH value as compared with HM1. Anyway, the pH value in these three reactors was kept in the proper range for methanogenesis even exposed to high OLR (Lee et al., 2009). This result was in agreement with the reports of Zhang et al. (2013) who found that AD system stability was improved using co-substrate of FW and cattle manure because of high buffering ability via adding cattle manure while mono-AD system only fed with FW failed and soured. Similar to other manure such as cattle or chicken manure, the addition of horse manure can also enhance buffering ability of AD system. However, the improved performance of HM3 might not be due to the high buffering ability but the enhanced hydrolysis and acidogenesis efficiency of FW and HM.
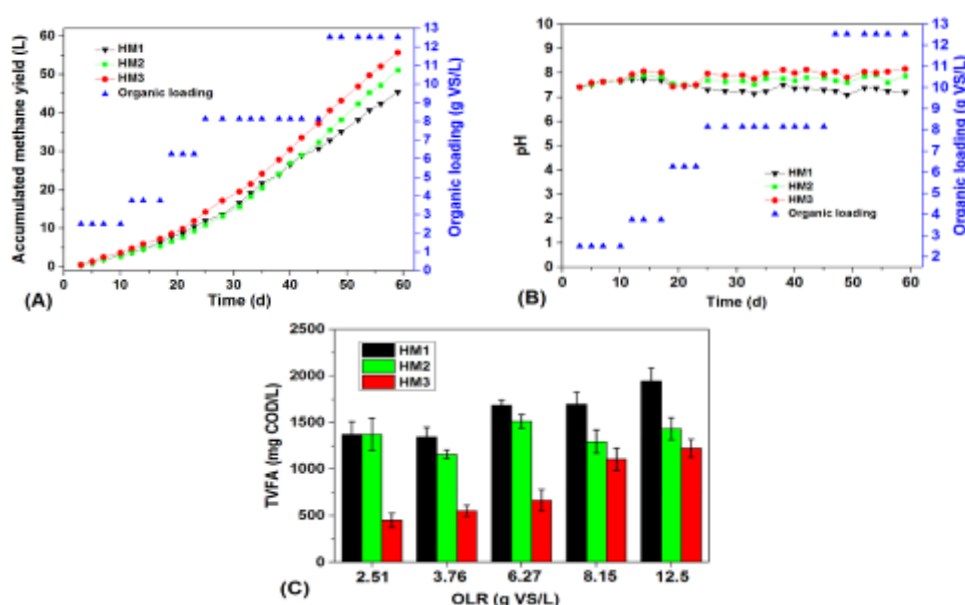
Fig. 1 – Comparison of (A) accumulated methane yield, (B) pH and TVFA concentration among the three ADs (HM1, HM2 and HM3). HM1: one-stage AD; HM2: two-stage AD; HM3: three-stage AD

3.3 Analysis of the bacterial community

After high-through put pyrosequencing, a total of 21524 (HM1), 24306 (HM2), 20013 (HM3) and 38768 (seed sludge) effective reads were obtained from the sludge samples. Sequence similarity is set 0.97 and operational taxonomic units (OTUs) is considered to be close to genus probably. At a 0.3 distance, the observed OTUs were 1217 (HM1), 1279 (HM2), 1520 (HM3) and 7054 (seed sludge) respectively, suggesting that the species in HM3 was more richness as compared with HM1 and HM2. To study the bacterial communities in-depth among these three digesters, the sequence taxonomic classification was conducted. The relative abundances of species were identified at the genus level. There were more than 31 different dominant species in there three digesters except unclassified. Thereinto, nine dominant species i.e. Aminobacterium (10.1%), Clostridium (8.3%), Proteiniphilum (8.4%), Saccharofermentans (6.7%), Eubacterium (5%), Syntrophomonas (4.3%), Petrimonas (3.3%), Thermoflavimicrobium (2.9%) and Flavonifractor (1.4%) in HM3 were mainly contributed to the different bacterial community structure among the three digesters, and the abundance of these nine species in HM3 was higher than that in HM1 and HM2.

4 CONCLUSIONS

A novel method and apparatus for three-stage anaerobic digestion was put forward in this study with the aim to improve treatment performance of high-solids organic waste and biochemical methane potential. Functional partitioning in this highly integrated digester enhanced the hydrolysis of solid organic matter and acidogenesis efficiency, which further accelerated the methanogenesis by improving the availability of soluble organic acids and nutrients for methanogens. The results showed that three-stage anaerobic digester had 11.2 ~ 22.7% more methane yield as compared with the control digesters. Different microbial communities were enriched and distributed in the three stages of one digester, suggesting that the bioaugmentation in each stage of AD helped to improving the hydrolysis, acidogenesis and overall

performance. This integrated digester can be considered as the coupling of high-solids AD and wet AD, which is meaningful for improving OLR, methane yield and reducing digester volume.

5   ACKNOWLEDGMENTS

6   REFERENCES

ALKAYA, E., Demirer, G.N., 2011. Anaerobic acidification of sugar-beet processing wastes: Effect of operational parameters. Biomass and Bioenergy 35, 32-39.

BANKS, C.J., Salter, A.M., Heaven, S., Riley, K., 2011. Energetic and environmental benefits of co-digestion of food waste and cattle slurry: A preliminary assessment. Resources, Conservation and Recycling 56, 71-79.

BOUALLAGUI, H., Torrijos, M., Godon, J.J., Moletta, R., Ben Cheikh, R., Touhami, Y., Delgenes, J.P., Hamdi, M., 2004. Two-phases anaerobic digestion of fruit and vegetable wastes: bioreactors performance. Biochemical Engineering Journal 21, 193-197.

BROWN, D., Li, Y., 2013. Solid state anaerobic co-digestion of yard waste and food waste for biogas production. Bioresource Technology 127, 275-280.

CHEN, Y., Cheng, J.J., Creamer, K.S., 2008. Inhibition of anaerobic digestion process: A review. Bioresource Technology 99, 4044-4064.

DE LA RUBIA, M.A., Raposo, F., Rincón, B., Borja, R., 2009. Evaluation of the hydrolytic–acidogenic step of a two-stage mesophilic anaerobic digestion process of sunflower oil cake. Bioresource Technology 100, 4133-4138.

DEMIREL, B., Yenigun, O., 2004. Anaerobic acidogenesis of dairy wastewater: the effects of variations in hydraulic retention time with no pH control. Journal of Chemical Technology and Biotechnology 79, 755-760.

FANG, C., Boe, K., Angelidaki, I., 2011. Anaerobic co-digestion of by-products from sugar production with cow manure. Water Research 45, 3473-3480.

GONZALES, H.B., Takyu, K., Sakashita, H., Nakano, Y., Nishijima, W., Okada, M., 2005. Biological solubilization and mineralization as novel approach for the pretreatment of food waste. Chemosphere 58, 57-63.

KIM, J., Park, C., Kim, T.-H., Lee, M., Kim, S., Kim, S.-W., Lee, J., 2003. Effects of various pretreatments for enhanced anaerobic digestion with waste activated sludge. Journal of Bioscience and Bioengineering 95, 271-275.

KOTHARI, R., Pandey, A.K., Kumar, S., Tyagi, V.V., Tyagi, S.K., 2014. Different aspects of dry anaerobic digestion for bio-energy: An overview. Renewable and Sustainable Energy Reviews 39, 174-195.

LEE, D.H., Behera, S.K., Kim, J.W., Park, H.-S., 2009. Methane production potential of leachate generated from Korean food waste recycling facilities: A lab-scale study. Waste Management 29, 876-882.

LI, Y., Park, S.Y., Zhu, J., 2011. Solid-state anaerobic digestion for methane production from organic waste. Renewable and Sustainable Energy Reviews 15, 821-826.

MARTIN, D.J., Potts, L.G.A., Heslop, V.A., 2003. Reaction mechanisms in solid-state anaerobic digestion - I. The reaction front hypothesis. Process Safety and Environmental Protection 81, 171-179.

MATA-ALVAREZ, J., Dosta, J., Romero-Güiza, M.S., Fonoll, X., Peces, M., Astals, S., 2014. A critical review on anaerobic co-digestion achievements between 2010 and 2013. Renewable and Sustainable Energy Reviews 36, 412-427.

MIRON, Y., Zeeman, G., Van Lier, J.B., Lettinga, G., 2000. The role of sludge retention time in the hydrolysis and acidification of lipids, carbohydrates and proteins during digestion of primary sludge in CSTR systems. Water Research 34, 1705-1713.

NAGAO, N., Tajima, N., Kawai, M., Niwa, C., Kurosawa, N., Matsuyama, T., Yusoff, F.M., Toda, T., 2012. Maximum organic loading rate for the single-stage wet anaerobic digestion of food waste. Bioresource Technology 118, 210-218.

SHAH, F.A., Mahmood, Q., Rashid, N., Pervez, A., Raja, I.A., Shah, M.M., 2015. Co-digestion, pretreatment and digester design for enhanced methanogenesis. Renewable and Sustainable Energy Reviews 42, 627-642.

WRIGHTON, K.C., Agbo, P., Warnecke, F., Weber, K.A., Brodie, E.L., DeSantis, T.Z., Hugenholtz, P., Andersen, G.L., Coates, J.D., 2008. A novel ecological role of the Firmicutes identified in thermophilic microbial fuel cells. Isme Journal 2, 1146-1156.

ZHANG, C., Xiao, G., Peng, L., Su, H., Tan, T., 2013. The anaerobic co-digestion of food waste and cattle manure. Bioresource Technology 129, 170-176.

SESSION 16: SOLAR ENERGY

49: Performance test of a solar concentrating system with cylindrical fresnel lens

HONGFEI ZHENG, XINGLONG MA

School of Mechanical Engineering, Beijing Institute of Technology, Beijing 100081, China,
hongfeizh@bit.edu.cn

An experiment was carried out on a solar concentrating system with cylindrical Fresnel lens which was produced industrially. Each concentrator is consist of four cylindrical Fresnel lens, a secondary reflector and a vacuum-tube receiver, and the aperture area is 2.5m2. The vacuum-tube receiver is placed at the focus of the concentrator, and the secondary reflector is used for concentrating the deflected rays caused of incidence error. This solar concentrating system has the advantages of low cost, less weight, compact volume and modularization. The Fresnel lens is fabricated by injection moulding and the material is PC. Compared with the trough type solar concentrator, its advantages also include with better anti-wind, snow and dusty performance. Besides, the driving torque is small. The optical simulation about the system is completed before experiment to obtain the optical efficiency of the concentrator for different incidence angles and therefore determine the allowable tracking error. It has been found that about 90% of the incident lights can still be gathered by absorber when the error of tracking is 1.5 degrees. Optical efficiency measurements have been carried out and the system is driven to real-time tracking. Some experimental results have been introduced including the collecting heat efficiency with the solar radiation. The experimental data generally agrees with the simulation result. In addition, the losses of system also analysed. As the results, this system can be considered to be an effective structure as a medium temperature solar collector.

Key words: Solar concentrator, Fresnel lens, Compound cylindrical concentrator, High temperature collection

1. INTRODUCTION

In 1920s, Augustin-Jean Fresnel invented a "whirling lens" which was consisted of several circular lenses in order to fabricate a lens with larger aperture, and which is called Fresnel lens. Compare to conventional lenses, Fresnel lens has prominent advantages such as small volume, light-weight, mass production with low cost as well as effectively increase the energy density [1]. However, limited by material technology, lenses were made of quartz glass generally so that it was very difficult to take shape. Until 1951, Millar OE [2] designed and fabricated the world's first plastic Fresnel lens by injection moulding. Millar OE discovered that the superficial quality and concentrating precision of plastic Fresnel lens are very close to vitreous lens. Boettner EA et al. [3] described the design and construction of Fresnel-type optics particularly suitable for used with area-type photoelectric receivers which was a point-focus system. The lens was flat plate structure and manufactured by lathe. In 1970s, the study on Fresnel lens was mainly focused on its performance. Nelson DT et al. [4] designed a line-focus Fresnel lens used for heating water. The result showed the temperature of the focus was 143℃, but the average optical efficiency was only 50%. Krichman et al. [5] prompted a new kind of line-focus convex-shaped Fresnel lens. He had proved that the geometrical concentration ratio of it was very close to the theoretical value, which provided a new idea of shaped-Fresnel lens' studying. Nakata. Y et al. [6] designed an imaging point-focus spherical Fresnel lens. The lens has well concentration homogeneity. The transmittance is reaching to 83%. It was traced by polar axis and applied for low power photovoltaic power generation. Khalile. J et al. [7] designed a flat plate line-focus Fresnel lens. The experimental result illustrates that the middle part of the lens has high optical efficiency, but optical efficiency dropped rapidly when closing to the edge. The average optical efficiency was barely 58%. In 21st century, the studies were particularly emphasized on application of Fresnel lens. Adeff et al. [8] built a thermoacoustically driven thermoacoustic refrigerator power by solar thermal energy. A 0.457m diameter Fresnel lens focused sunlight onto the hot end of a 0.0254m diameter reticulated vitreous carbon prime mover stack, heating it to 475℃, thereby eliminating the need for the most troublesome component in a heat driven prime mover, the heat exchanger. The high intensity sound waves produced by the prime mover could drive the refrigerator to produce 2.5W of cooling power at a cold temperature of 5℃ and a temperature span of 18℃. Tsangrassoulis A et al. [9] combined Fresnel lens with core liquid fibre to realize the solar daylighting. The development of a method to control the light output from a prototype hybrid lighting system which transported daylight from a heliostat with a concentrating Fresnel lens to a luminaire in a windowless room, via a large core liquid fiber optic. The main artificial lighting system was located outside of the building. Yabe T et al. [10] employed 1.3m^2 area size Fresnel lens to achieve the solar-energy-pumped laser. All the elements were fixed in one unit and moves together. Once alignments of the laser cavity were fixed, realignment would not be necessary even if all the system moved following the sun. The energy conversion efficiency was 11%-14%. Thorsten Hornung et al. [11] set up a systems with Fresnel lens concentrator and solar cells to estimate the influence of temperature of Fresnel lens on energy generation. One Fresnel lens was kept at a constant temperature and another with a realistic temperature. Compared to the simulation, poly Fresnel lenses and SOG Fresnel lenses show comparable energy harvesting efficiency and are closing to market locations. Pei-Wen Li et al. [12] developed a fundamental modeling for the optical features and control algorithm for a solar stove heat collection system which uses a giant Fresnel lens. The results of the analysis have been incorporated into the control algorithm which has been implemented in the control system of a prototype solar stove which successfully demonstrated the predicted efficient solar tracking. M. Hasan Nia et al. [13] designed an electricity and preheated water cogeneration system by Fresnel lens and thermoelectric module. The experimental result revealed that matched load output power is 1.08W with 51.33% efficiency under radiation intensity of 705.9W/m^2. With respect to the performance of Fresnel lens, Naichia Yeh et al. [14] develops a formulation that helps to quantify the linear lens' transmittance loss and prism-tip scattering loss, which briefly examines the Fresnel lens development since 1970s and investigates the losses inherent in the linear Fresnel lenses. Chung-Feng Jeffrey Kuo et al. [15] analysed and evaluated important parameters in fabrication of Fresnel lens solar collector (melt temperature, mould temperature, packing pressure, and injection speed) based on its two qualities (ratio of power efficiency and percentage error of groove filling ratio). Taguchi method was applied in the experiment and the optimal combination of parameters was found. The concept and designing method of cylindrical compound Fresnel solar concentrator can be found in reference [16]. In this work, the performance of the compound cylindrical solar concentrator was mainly investigated.

2. PERFORMANCE OF CYLINDRICAL FRESNEL LENS

The structure of the Fresnel lenses was shown in figure1, which size is 0.64m×1.0m. The outer diameter of the cylindrical Fresnel lens is 1.0m. The cylindrical Fresnel lens is made of PC material (The relative index of refraction is 1.6) and the focal length is 0.95m. It has been found in reference [16] that the focus turns shorter when the incident light deviates from the normal incidence. Figure 2 shows the shape of focus

of normal incidence. The focus of the cylindrical Fresnel lens is consist of two parts, the high-bright area in center and the coma areas distribute in two sides. When incident lights deviate from the normal incidence, the change focus was shown in figure 3. It can be inferred that: (1) the gradient of focal length turns faster when the tilt angle become larger. When the tilt angle reaches to 45°, the focal length approaches to the half of the original. (2) The focal area is consisted of two parts, the high-bright area in center and the coma area. The width of high-bright area changes lightly, even in 45°, the width is still less than 60mm. While the total width is changing severely especially when the tilt angle larger than 20°due to the coma area.
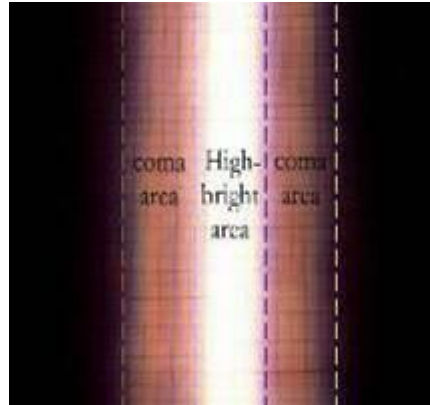
Figure 1: The photo of cylindrical Fresnel lens   Figure 2: The focus of cylindrical Fresnel

Because of the focal length will turn shorter when the incident light deviates from the normal incidence, the focal area will turn wider in the original focus place. Considering the width of receiver is always wider than the focus, it can adjust the position of receiver to adapt the tilt incidence. In this way, the width of focal area in different positions which are shorter than the original focal position change with different tilt incidence were shown in figure 4. It can be found that the light areas turn thinner first, then increase fast. As to the evacuated-tube receiver (with 80mm width), it can be chosen to set in the 850mm position where the incident light can be received totally when tilt angle is in ±29°.
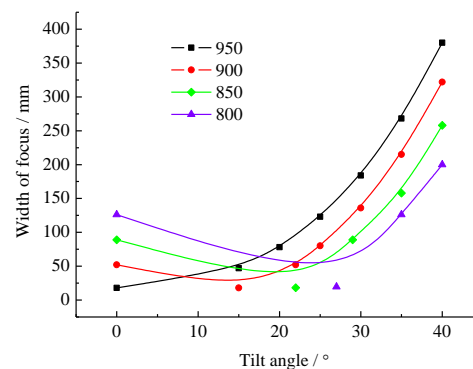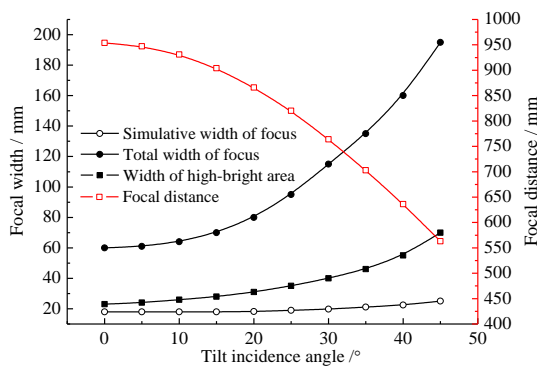
Figure 3: The change of focus with tilt incidence   Figure 4: The width of focal areas in different positions

3. SET-UP OF EXPERIMENTAL SYSTEM

The schematic diagram of the solar concentrating system is shown in figure 5. The main optical elements of the concentrator include cylindrical Fresnel lensed and secondary reflectors.
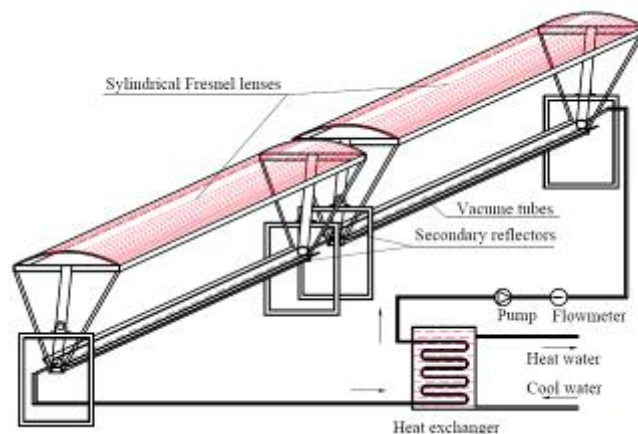
Figure 5: The schematic diagram of concentrating system

The incident solar beam will be converged by cylindrical Fresnel lenses and secondary reflectors. The converged lights reach to the evacuated-tube receiver where the radiant energy is collected. However, some of the concentrated rays would not reach to the vacuum-tube receiver due to the errors of fabrication and trace. In this case, the secondary reflector reflects the runaway rays to the evacuated-tube receiver again. Ultimately, the collected heat will be taken away by the circular work fluid. Figure 6 is the photo of experimental test system.

Figure 6: The photo of testing system

The vacuum-tube receiver is an evacuated glass tube with two plate heat transfer fins inside. The glass tube is 4.0m length and Φ102mm diameter. The size of plate heat transfer fin is 0.08m×1.9m. A coating is spread on the surfaces of the fins to increase the adsorptivity and decrease the emittance simultaneously, and the adsorptivity is 0.93. Two copper pipes with diameter of Φ12mm are connected to the fins in their symmetric lines respectively to conduct heat. A spring tube is welded between two copper pipes to avoid the stress of thermal expansion. Two vacuum-tube receiver were used.

The vacuum-tube receiver is set in the vicinity of the focus of concentrators where 0.4m apart from the rotating center of the concentrator. According to the above introduction, the focus is 0.45m apart from the rotating center so there was a distance of 0.05m between the focus and vacuum-tube receiver. The heat transfer working fluid is conductive oil and the volume is 15L, which is equivalent to 12.5kg in normal condition. The conductive oil is pumped by a thermostable oil pump, of which the rated flow is 25L/min. The specific heat capacity of conductive oil is changing with temperature, but it is not serious. It can be managed as follow: during the lower temperature (≤100℃), the average specific heat capacity is 2.55 kJ/(kg•℃) and in the higher temperature (100~300℃),the average specific heat capacity is 2.75 kJ/(kg•℃). The heat lord is water, with volume 200L .Three temperature measuring points were distributed in the oil tank and the inlet and the outlet of the vacuum-tube receiver respectively. One flow rate meter and one irradiance sensor were used, so that the parameters can be recorded completely.

4. MATHEMATICAL MODEL OF ENERGY CONSERVATION

4.1. Mathematical model

In this experiment, the conductive oil in oil tank and oil pipes is constant. The temperature of the oil will rise up persistently with continuously heat. Meanwhile, the temperature difference between oil and surroundings will increase, which would lead to the increase of heat dissipation. Finally, when the heat dissipation is equal to the radiant energy that the concentrator collected, oil temperature will reaches to the peak. The system will approaches to the thermal equilibrium state. Heat dissipation will appears in everywhere from vacuum-tube receiver to oil tank. The total heat-dissipation area and the heat resistances are not easy to figure out because of the structures of vacuum-tube receiver, oil pipes and oil tank are so complex that the shapes of thermal insulation materials is uneasy to define. Thus, several assumptions are given as follow: (1) considering the heat dissipation of vacuum-tube receiver, oil pipes and oil tank as an equivalent parameter, which can be defined as equivalent coefficient of heat transfer. (2) The working environment is in a constant state. The temperature of surroundings, wind speed, solar irradiance etc. are constant. (3) The physical properties of the equipment and heat isolation materials are not changing with temperature. In this case, an analysis in accordance with the law of conservation of energy is given as follow.

(1) Time from t_1 to t_2, the received radiant energy of solar concentrator is:

$$\Delta Q_{rad} = 0.93 I_{ave} A \eta_o (t_2 - t_1) \qquad (1)$$

Where 0.93 is the absorptivity of the receiver, ΔQ_{rad} is the received radiant energy, A is the light receiving area of concentrator, which includes two parts, one part is A_1, the receiving area of cylindrical Fresnel lenses, and another part is A_2, the receiving area of parabolic reflectors. η_o is the optical efficiency, and I_{ave}

is the average solar irradiance, which could be calculated as:
$$I_{ave} = \frac{1}{t_2 - t_1} \int_{t_1}^{t_2} I \, dt \qquad .$$

(2) Time from t_1 to t_2, the energy obtained by conductive oil is:

$$\Delta Q_{rec} = \bar{c}_p m [T(t_2) - T(t_1)] \qquad (2)$$

Where ΔQ_{rec} is the increment of intrinsic energy of conductive oil. $\bar{c}_p$ is the average specific heat capacity. m is the mass of conductive oil and $T(t)$ is the real time temperature of conductive oil.

(3) Time from t_1 to t_2, the heat dissipation is:

$$\Delta Q_{dis} = \int_{t_1}^{t_2} U A_{eq} [T(t) - T_{sur}] dt \qquad (3)$$

Where ΔQ_{dis} is heat dissipation. UA_{eq} is the equivalent coefficient of heat transfer.

According to the conservation of energy:

$$\Delta Q_{rec} + \Delta Q_{dis} = \Delta Q_{rad} \qquad (4)$$

Then an equation will be obtained combining to formulas (1, 2 and 3):

$$\int_{t_1}^{t_2} U A_{eq} [T(t) - T_{sur}] dt + \bar{c}_p m [T(t_2) - T(t_1)] = 0.93 I_{ave} A \eta_o (t_2 - t_1) \qquad (5)$$

When t_2 approaching to t_1 illimitably, we can sign $dt = t_2 - t_1$. Both sides of equation (5) divide dt and utilize mean value theorem, an differential equation will be derived as (6):

$$UA_{eq}T(t) + \bar{c}_p m \frac{dT(t)}{dt} = 0.93 I_{ave} A\eta_o + UA_{eq}T_{sur} \qquad (6)$$

Then solve the differential equation:

$$T(t) = \frac{\beta}{\alpha} + \left(T_{sur} - \frac{\beta}{\alpha} \right) e^{-\alpha t} \qquad (7)$$

Where $\quad \alpha = \dfrac{UA_{eq}}{\bar{c}_p m}, \quad \beta = \dfrac{0.93 I_{ave} A\eta_o + UA_{eq}T_{sur}}{\bar{c}_p m}$

The function (7) illustrates that the temperature curve of heat load is conformed to exponential function and it would be approaching to the maximum value β/α ultimately, where is the thermal equilibrium state. The growth rate of temperature curve and the maximum temperature are determined by heat capacity of heat load $c_p m$, the equivalent coefficient of heat transfer UA_{eq}, temperature of surroundings T_{sur} and the received solar energy $I_{ave}A\eta_o$. Then analyze performance parameters of solar concentrating system.

4.2 Optical efficiency of concentrator ηo

Optical efficiency of concentrator η_o is defined as a ratio between the radiant energy that pass through the concentrator and the original radiant energy reaches to the concentrator, which reflects the "energy transmitting efficiency" of a concentrator. There are several energy losses including diffuse reflection, light-blocking and adsorption of materials. Particularly, the reflective loss would occur directly on the surfaces of transmission-type concentrators. In order to guarantee the measuring result of η_o to be more precise, it must avoid the energy loss of the heat system as far as possible. Thus, the experimental data at the beginning of test should be used for calculating the optical efficiency for the temperature difference between system and surroundings is very tiny at this time and the heat dissipation can be ignored. The data in the first minute during the test is extracted out to calculate the optical efficiency. The formula of is η_o:

$$\eta_o = \frac{c_{p0} \rho v_L (T_o - T_i)}{60 I_{ave} A} \qquad (8)$$

Where c_{p0} is the specific heat capacity of conductive oil in normal temperature and ρ is the intensity. v_L is the volume flow (L/min) of oil pump. T_i, T_o are the temperature of inlet and outlet of the vacuum-tube receiver respectively.

4.3 Collection efficiency η_c

The collection efficiency η_c is a matric that indicates the percentage of final heat we could use to the total radiant energy reaching to the concentrator. The average collection efficiency from t_1 to t_2 can be calculated as formula (19):

$$\eta_{cave} = \frac{\bar{c}_p m [T(t_2) - T(t_1)]}{I_{ave} A (t_2 - t_1)} \qquad (9)$$

When time interval shorten infinitely, the average irradiance would approach to the instantaneous irradiance, that is $\quad \eta_c = \lim_{t_2 \to t_1} \eta_{cave}$. So the collection efficiency can be calculated as (10):

$$\eta_c = \frac{\overline{c}_p m}{I_{ave} A} \cdot \frac{dT(t)}{dt}$$

(10)

When $t_1=0$ and $t_2=60s$, it could be derived that $\eta_c=\eta_o$. It indicates that the collection efficiency is equal to optical efficiency at the beginning of the experiment.

4.4 Receiving efficiency of concentrator ηrec

The receiving efficiency of concentrator is defined as a ratio between the energy that received by the vacuum-tube receiver and the radiant energy collected by Fresnel lenses and reflectors, which illustrates the collection ability of a concentrator when incident rays are deviated from normal incidence. During time t_1 to t_2, the average receiving efficiency can be calculated by (11):

$$\overline{\eta}_{rec} = \frac{\overline{c}_p m[T(t_2) - T(t_1)] + UA_{eq}[\frac{T(t_2)+T(t_1)}{2} - T_{sur}]}{0.93 I_{ave} A \eta_o}$$

(11)

5 RESULT DISCUSSION

5.1 Optical efficiency

Optical efficiency of concentrator is defined as a ratio between the radiant energy that pass through the concentrator and the original radiant energy reaches to the concentrator, which reflects the "energy transmitting efficiency" of a concentrator. In this experiment, the solar concentrator was set at east-west direction. The real-time tracing was adopted in tracing the elevating angle of the sun, so the solar concentrator is horizontal. The experimental data in one minute at the beginning of test is given in table 1. At this time, the working fluid is not passing through the water tank. The measuring value of volume flow of oil pump was 2.76 L/min. It could be calculated from table 1 that the optical efficiency of the solar concentrator is 83.1%.

Table 1: The temperature difference of inlet and outlet of the receiving tube in one minute at the beginning of testing

Local time / hh:mm:ss	11:30:00	11:30:20	11:30:40	11:31:00
T_i /°C	33.1	35.9	37.1	38.5
T_o /°C	59	61.1	62.1	63.2
$(T_o$-$T_i)$ /°C	25.9	25.2	25	25.3

(T_I——Temperature of inlet, T_o——Temperature of outlet)

5.2 Characteristic of collection performance

The performance of temperature of the concentration system is shown in figure 7. It can be perceived that the effective working time is about 6 hours a day, which is from 9:00 AM to 3:00 PM. When time between 10:00 AM and 2:00 PM, the temperature of the water is rising linearly that means the collection ability of the concentrator is stable during this time. The highest temperature of 200L water is approaching to 75°C after one day heating with average solar irradiance 875W/m^2.
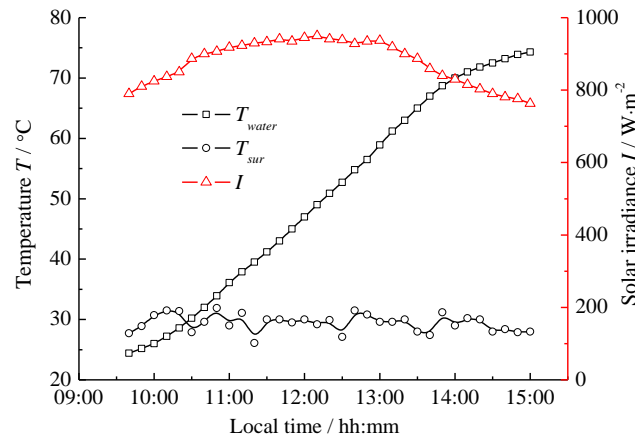
Figure 7: Temperature performance

The collection efficiency of the concentrating system was figured out and shown in figure 8. Corresponding to the temperature performance, the collection efficiency keeps higher than 35% during 10:00 AM to 14:00 PM. However, it is lower before 10:00 AM and after 14:00 PM due to the tilt incidence. Because of the solar concentrator was set as east-west direction, the tilt incidence angle was very large in the early morning and late afternoon. For example, the tilt incidence angle was larger than 30 º before 10:00 AM and after 14:00 PM, which would decrease the receiving efficiency that will be analysed later. Thus, the concentrating system has 4 hours working time with higher efficiency and the most effective tilt incidence angle is within ±30º.
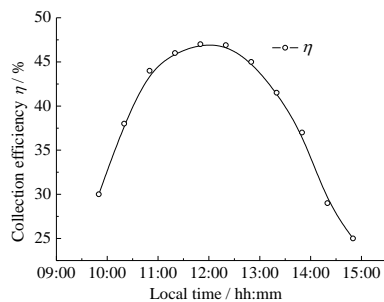
Figure 8: Collection efficiency
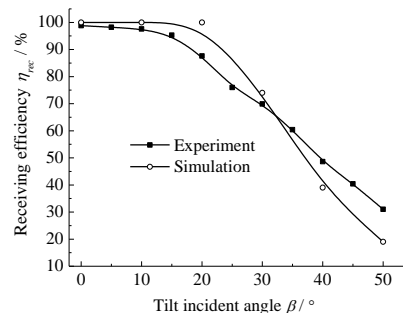
Figure 9: Variation of the receiving efficiency with tilt angle.

5.3 The receiving efficiency ηrec

The receiving efficiency is mainly influenced by the tilt incidence. As a matter of fact, what tilt angle primarily influences on is the focus of Fresnel lenses. If the focus changed, the receiving efficiency would change with it because of the receiving area of the vacuum-tube is constant. The change of the focus would make some lights escape from the receiving area. The receiving efficiency was tested in different tilt angles in this experimental. Thinking over all the heat loss throughout the concentration, η_{rec} was calculated and figure out in figure 9. Make a comparison to the simulative result in reference [16], it can be conclude that the receiving efficiency is very close to the simulative result when the incident light approaching to the normal incidence. When tilt angle is not lower than 15°, the receiving efficiency is still higher than 90%. While the tilt angle increases continuously, the receiving efficiency is declining sharply. There appears an intersectional point when tilt angle nearly equals to 30° and the receiving efficiency is still higher than 70%, approximately, which demonstrates that when set the concentrator in E-W direction, it can work 4 hours with receiving efficiency is above 70%. That means, even though the concentrator is stationary, it can still utilize the most intense solar irradiance of a day efficiently from AM 10:00 to PM2:00. When tilt angle is larger than 30°, the receiving efficiency of experiment is larger than simulative result on the contrary. Two reasons can explain this conclusion. First, according to the simulative result, the focal distance would become shorter when the incident light deviates from normal incidence. Thus, the vacuum-tube receiver is set in a place where higher the focus 50mm to make up for the tilt incidence. Second, diffuse reflection and

end effect of solar concentrator were not thought about in simulation. Actually, if the incident lights shoot into the solar concentrator in a large tilt angle, the effect of diffuse lights from surroundings will become more obvious. In other words, during the large tilt angle conditions, the received lights in actual weather are more than the theoretical. Therefore, the receiving efficiency of experiment is becoming larger than simulative result when tilt angle exceeds 30°.

6   CONCLUSION

In this study, a compound cylindrical solar concentrating system has been set up and investigated in actual weather condition. According to the experimental results, we can draw conclusions as follow:

(1) The optical efficiency of the cylindrical Fresnel lens is 83.1%.

(2) The experimental results show that the collection efficiency of the concentrator is above 45% during midday. And the most effective working incidence angle of the cylindrical Fresnel lens is within ±30º.

(3) The receiving efficiency could be improved effectively by adjusting the position of receiver.

7   ACKNOWLEDGEMENT

8   REFERENCES

[1] W.T. XIE, Y.J. Dai, R.Z. Wan, K. Sumathy. Concentrated solar energy applications using Fresnel lenses: A review. Renewable and Sustainable Energy Reviews. 2011, 15(2011): 2588–2606.

[2] MILLER OE, Mcleod JH, Sherwood WT. Thin sheet plastic Fresnel lenses of high aperture. Journal of the Optical Society of America. 1951;41(11):807–15.

[3] BOETTNER EA, Barnett NE. Design and construction of Fresnel optics for photoelectric receivers. Journal of the Optical Society of America. 1951;41(11):849–57.

[4] NELSON DT, Evans DL, Bansal RK. Linear Fresnel lens concentrators. Solar Energy 1975;17(5):285–9.

[5] KRICHMAN EM, Friesem AA, Yekutieli G. Highly concentrating Fresnel lens. Applied Optics. 1979, 18(15): 2688-2695.

[6] NAKATA Y, Shibuya N, Kobe T, Okamoto K, Suzuki A, Tsuji T. Performance of circular Fresnel lens photovoltaic concentrator. Japanese Journal of Applied Physics. 1980; 19(2):75–80.

[7] KHALIL E.J.AL-JUMAILY, MUNADHILA.K.A.AL-KAYSI. The study of the performance and efficiency of flat linear Fresnel lens collector with sun tracking system in Iraq. Renewable Energy. 1998, 14(1-4): 41-48.

[8] ADEFF JA, Hofler TJ. Design and construction of a solar-powered, thermoacoustically driven, thermoacoustic refrigerator. Journal of Acoustical Society of America. 2000; 107(6): 37-42.

[9] TSANGRASSOULIS A, Doulos L, Santamouris M, Fontoynont M, Maamari F, Wilson M, et al. On the energy efficiency of a prototype hybrid daylighting system. Solar Energy. 2005; 79(1): 56–64.

[10] YABE T, Ohkubo T, Uchida S, Yoshida K, Nakatsuka M, Funatsu T, et al. High efficiency and economical solar-energy-pumped laser with Fresnel lens and chromium codoped laser medium. Applied Physics Letters. 2007; 90(26): 1–3, 261120.

[11] Thorsten HORNUNG, Marc Steiner, Peter Nitz. Estimation of the influence of Fresnel lens temperature on energy generation of a concentrator photovoltaic system. Solar Energy Materials & Solar Cells. 2012; 99(2012): 333-338.

[12] Pei-Wen LI, Peter Kane, Matthew Mokler. Modeling of solar tracking for giant Fresnel lens solar stoves. Solar Energy. 2013, 96(2013): 263–273

[13] M. Hasan NIA, A. Abbas Nejad, A. M. Goudarzi, M. Valizadeh, P. Samadian. Cogeneration solar system using thermoelectric module and Fresnel lens. Energy Conversion and Management. 2014; 84(2014): 305-310.

[14] Naichia YEH. Analysis of spectrum distribution and optical losses under Fresnel lenses. Renewable and Sustainable Energy Reviews. 2010; 14 (2010): 2926–2935.

[15] CHUNG-FENG, Jeffrey Kuo, Feriyonika, Chung-Ching Huang, Yong-Lin Kuo. Analysis of processing parameters in fabrication of Fresnel lens solar collector. Energy Conversion and Management. 2012; 57 (2012): 33–41.

[16] Hongfei ZHENG, Chaoqing Feng, Yuehong Su, Jing Dai, Xinglong Ma. Design and experimental analysis of a cylindrical compound Fresnel solar concentrator. Solar Energy. 2014; 107 (2014): 26–37.

54: An experimental study on the thermal performance of multi-surface compound trough solar air concentrators with dual collector tubes

HAOSHU LING[1], CHAO CHEN[1], HONG QIN[2], NA LI[1],
MINGXING ZHANG[1], HONGFEI ZHENG[3], SHEN WEI[4]

*1 Beijing University of Technology, Beijing, PR China. Email: linghaoshu@163.com,
chenchao@bjut.edu.cn*
2 Guangzhou Vocational College of Science and Technology, Guangzhou, PR China
3 School of Mechanical and Vehicular Engineering, Beijing Institute of Technology, Beijing, PR China
4 School of Civil and Building Engineering, Loughborough University, LE11 3TU, UK

A multi-surface compound trough solar air concentrator (MCTSAC) with dual collector tubes (DCTs) was developed and introduced in the paper, in order to improve the thermal performance and the air flow rate of MCTSACs with a single collector tube (SCT). In the study, the thermal performance of MCTSACs with DCTs and those with a SCT was compared using real measured data. Additionally, the influence of factors, i.e. air velocity inside the collector tube, solar radiation, inclination angle and length of the MCTSAC, on the thermal performance of MCTSACs has been evaluated. Experimental results have reflected that comparing to MCTSACs with a SCT, MCTSACs with DCTs perform significantly better in both thermal performance and air flow rate, with an increase of 18% for both mean heat collection and mean thermal efficiency. Furthermore, solar radiation has shown a positive impact on the thermal performance, whilst inlet temperature performed a negative impact. When the air velocity inside the collector tube was around 1.8m/s with the inclination angle set as 23°, the MCTSACs with DCTs performed the best.

Keywords: multiple clamber trough solar air concentrator, dual collector tubes, thermal performance, influential factor, comparative experiment

1. INTRODUCTION

Due to the limitation in the specific heat and the density of air, the thermal efficiency of solar air collectors is generally low. To solve this problem, many studies have been carried out, mainly focusing on compound parabolic concentrators (CPCs), whose thermal efficiency can reach 75%, larger than that of either flat solar air collectors or vacuum tube solar air collectors.

In order to collect up-to-date information on the thermal performance of CPC solar collectors, Singh and Eames (2011) have reviewed factors that influence the natural convective heat transfer correlations in cavities. From the review, they suggested that enclosure shape, geometry, orientation and thermal boundary conditions at cavity surfaces are influential. Similarly, Tchinda (2008) developed a mathematical model that can be used to calculate the thermal performance of an air heater with a truncated CPC, based on which the effect of air mass flow rate, wind speed and collector length on the thermal performance of CPC solar collectors have been identified. Kim and Seo (2008) carried out both experimental and numerical studies in order to evaluate the thermal performance of CPC solar collectors, and they suggested that the thermal efficiency of tracking CPC solar collectors can be up to 59.56%. Zhao et al. (2006) proposed a mathematical model of CPC heat pipe evacuated tubular solar collectors. Using this model, they pointed out that solar radiation had a positive effect on the collectors' thermal efficiency. Sun et al. (2009) also performed a numerical study exploring how to improve the thermal efficiency of CPCs. In the study, they found that the optimum truncation was from 0.5 to 0.8. Xue et al. (2011) developed a new type of multi-surface compound solar trough concentrators, which increases the performance of solar heat receivers and expands its usable situations.

The research group authoring this paper (Chen et al. 2014) has also developed a specific type of the multi-surface compound trough solar air concentrator (MCTSAs) with a single collector tube (SCT), its maximum daily cumulative heat collection rate can be 6.2 MJ/(m^{2}d). However, the MCTSAC with SCT has a major disadvantage in the small air flow rate. In order to solve this problem, a MCTSAC with dual collector tubes (DCTs) has been developed by the research group. This paper expresses results of a comparative study on the thermal performance of the two types of MCTSACs (i.e. that with DCTs and that with a SCT), and influence from air velocity inside the collector tube, solar radiation, inclination angle and length of the MCTSAC, on the collectors' thermal performance have also been suitably evaluated and discussed.

2. MATERIALS AND METHODS

2.1. MCTSACs

Figure 1 presents the design of two types of MCTSACs, one with a SCT and another with DCTs. They are composed of six components: 1) multiple curved reflector surfaces; 2) an insulation layer; 3) an outer protective layer; 4）one or two collector tubes; 5) a heat collecting screen inside the collector tube and 6) a glass cover.

a) With a SCT   b) With DCTs

Figure 26: MCTSAC design

During the daytime, some solar radiation irradiates directly on the heat collecting screen inside the collector tube of MCTSACs, and some others irradiates on the multiple curved reflector surfaces and then this part of radiation will be reflected to the heat collecting screen. The solar radiation absorbed by the heat collecting screen will increase the surface temperature of the screen. When air is sent to the collector tube and go

through the heat collecting screen, the large temperature difference between the air and the heat collecting screen causes strong convective heat transfer, so the air can be heated.

2.2. Experimental Setup

The experimental setup, as shown in Figure 2, consists of 1) two sets of MCTSACs either both with a SCT or both with DCTs; 2) a fan; 3) an anemometer and 4) a temperature measurement device. Main structural parameters of MCTSACs used in this study are list in Table 1.
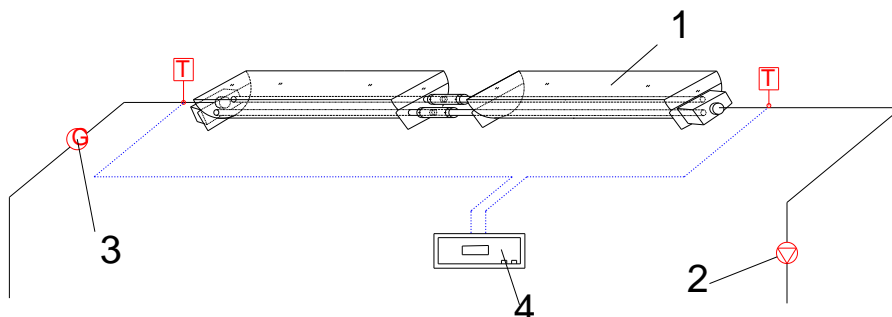

Figure 2: The system diagram of experimental setup

Table 12: Main structural parameters of the MCTSACs

Length (m)	Width of glass cover (m)	Diameter of collector tube (m)	Diameter of heat collecting screen (m)
4	0.55	0.11	0.075

During the experiment, the following parameters have been monitored: inlet and outlet air temperatures, air temperature inside the collector tube, air velocity, solar radiation, ambient temperature and inclination angle. In order to accurately measure the inlet and outlet air temperature, three T-type thermocouples with an accuracy of ±0.5°C have been located at both inlet and outlet, and the average value of them was used in the later analysis. Inside the collector tube, twelve T-type thermocouples were used to monitor the air temperature distribution along the length direction. Air velocity was measured and recorded by a Testo 435 hot-wired anemometer, with a measurement error lower than 0.01m/s. A PC-3 portable weather station was used to collect and record ambient temperature and solar radiation. It has an accuracy of ±0.4°C for temperature measurement and ±10W/m^2 for solar radiation measurement. The inclination angle of MCTSACs was measured by a protractor, which has an accuracy of ±0.5°. All measurement was based on an interval of one minute.

Table 2 presents the experimental definitions of this study. In the experiment, when evaluating the influence of a specific parameter on the performance of solar collectors, its value is changed gradually while keeping other factors constant. Case 1 is designed to evaluate the influence from the air velocity inside the collector tube, and other cases are defined for solar radiation (Case 2), inlet air temperature (Case 3) and inclination angle (Case 4). Case 5 focused on the influence from the length of MCTSACs. However, as this parameter is not changeable in the study, the later analysis was based on measurement at different points along the length direction of the tube, at various solar radiation conditions.

Table 2: Experimental definitions of the study

	Air velocity inside collector tube m/s	Solar radiation W/m^2	Inlet air temperature °C	Inclination angle °
Case 1	1.4, 1.6, 1.8, 2.0, 2.2	900	10	23
Case 2	1.8	500, 600, 700, 800, 900, 1000	10	23
Case 3	1.8	900	5, 10, 15, 20, 25	23
Case 4	1.8	900	10	18, 20, 22,23,24, 26,28
Case 5	1.8	300, 500, 700, 900	10	23

2.3. Performance indicators

In the study, indicators, namely outlet temperature, heat collection rate and thermal efficiency, have been adopted for evaluating the performance of MCTSACs with either a SCT or DCTs, based on Equations 1-3.

Equation 3: Outlet temperature

$$T_0 = \frac{1}{3} \sum_{i=1}^{3} T_{o,i}$$

Equation 2: Heat collection rate

$$Q = \frac{\pi}{4} d^2 v \rho Cp (T_0 - T_i)$$

Equation 3: Thermal efficiency

$$\eta = \frac{Q}{BLI}$$

Where:

- T_o= mean outlet air temperature (°C)
- $T_{o,i}$= air temperature of NO.i T-type thermocouple at outlet (°C)
- Q= heat collection rate (W)
- d= diameter of the collector tube (m)
- ρ= density of air (kg/m^3)
- v= air velocity inside the collector tube (m/s)
- Cp= specific heat of air (J/(kg °C))
- T_i= average inlet air temperature (°C)
- η= thermal efficiency (%)
- B= width of the glass cover (m)
- L= length (m)
- I= solar radiation (W/m^2)

3. RESULTS AND DISCUSSIONS

3.1. Influence from Air Velocity Inside the Collector Tube (Case 1)

The influence of air velocity inside the collector tube on the thermal performance is demonstrated in Figure 3, based on the experimental conditions defined in Case 1 (Table 2). With the increase of air velocity, the outlet temperature of MCTSACs decreases linearly, for both the one with a SCT and the one with DCTs. Additionally, both heat collection rate and thermal efficiency are generally proportional to the air velocity. However, when air velocity is bigger than 1.8m/s, the increase of both heat collection rate and thermal efficiency seems to be weaker. Therefore, an optimal air velocity value should be around 1.8m/s and this range needs to be determined in the future study with more experimental conditions.

When provided with air with the same velocity in the collector tube, the total air flow rate of MCTSACs with DCTs was two times as much as that of MCTSACs with a SCT. Although the outlet temperature of MCTSACs with DCTs was 13.4°C lower than that of MCTSACs with a SCT, both heat collection rate and thermal efficiency of the MCTSAC with DCTs were better than that of the MCTSAC with a SCT. The average heat collection rate of MCTSACs with DCTs at various air velocity conditions was 826W, 1.18 times bigger than that of MCTSACs with a SCT. The average thermal efficiency of the MCTSAC with DCTs was 42%, 6% increase than the MCTSAC with a SCT. Therefore, comparing to MCTSACs with a SCT, those with DCTs have improvement in both air flow rate and thermal performance.

Outlet temperature and heat collection rate | (b) Thermal efficiency
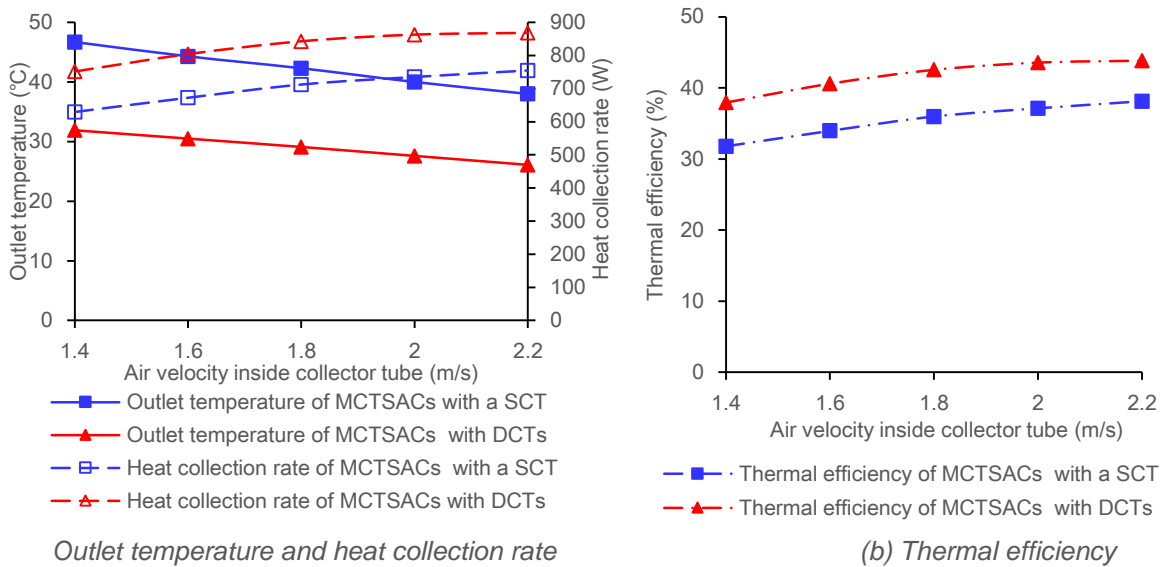
Figure 3: Influence from of air velocity inside the collector tube

3.2. Influence from Solar Radiation (Case 2)

The evaluation of influence of solar radiation on the thermal performance of solar collectors was carried out under the experimental conditions defined in Case 2 (Table 2). The comparison of all indicators is presented in Figure 4. With the increase of solar radiation, both outlet temperature and heat collection rate for both types of MCTSACs perform an increase trend. The outlet temperature of MCTSACs with DCTs is 10.4°C lower than that of MCTSACs with a SCT. However, the heat collection rate of MCTSACs with DCTs shows an opposite trend, as the heat collection rate of MCTSACs with DCTs is 1.2 times bigger than that of MCTSACs with a SCT. Furthermore, the results also show that solar radiation can also influence the thermal efficiency, and the thermal efficiency of MCTSACs with DCTs is always better than that of MCTSACs with a SCT. The average difference between them at various solar radiation conditions is 7%.

Outlet temperature and heat collection rate | (b) Thermal efficiency
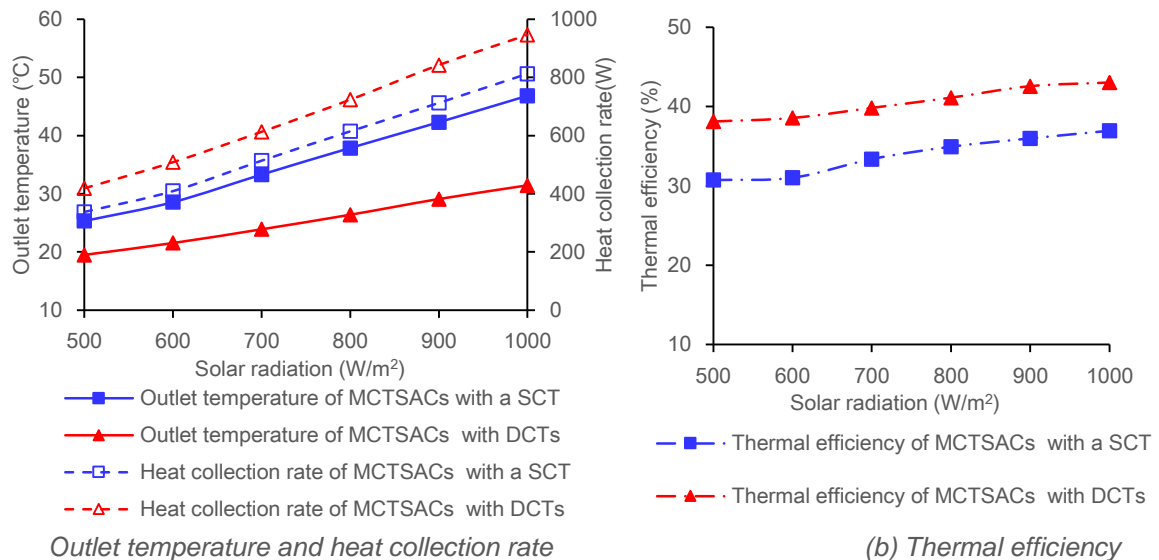
Figure 4: Influence from solar radiation

3.3. Influence from Inlet Temperature (Case 3)

Outlet temperature and heat collection rate   *(b) Thermal efficiency*
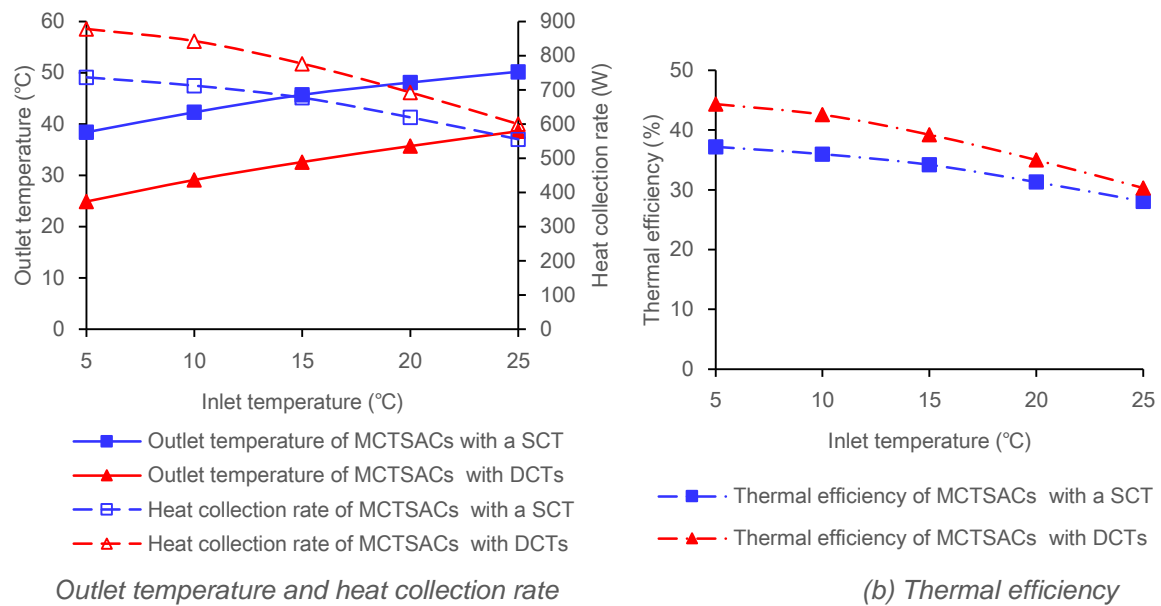
Figure 5: Influence from inlet temperature

Figure 5 shows the influence of inlet temperature on the thermal performance of solar collectors, using the experimental conditions defined in Case 3 (Table 2). With the increase of inlet temperature, the outlet temperature of MCTSACs with both a SCT and DCTs shows an increase trend. However both heat collection and thermal efficiency go down. The reason is that with the increase of inlet temperature, the temperature difference between the air and the heat collecting screen decreases, hence the convection heat transfer reduces.

Similar to the previous results, the outlet temperature of MCTSACs with DCTs is less than that of MCTSACs with a SCT, but both the heat collection rate and the thermal efficiency of MCTSACs with DCTs are better than that of MCTSACs with a SCT. The average outlet temperature of MCTSACs with DCTs is 32.2 °C, but that of MCTSACs with a SCT is 44.9 °C. Additionally, the average heat collection rate of MCTSACs with DCTs is 758W, which is 1.15 times bigger than that of MCTSACs with a SCT. The average thermal efficiency of MCTSACs with DCTs is 38.3%, also 1.15 times bigger than that of MCTSACs with a SCT. However, with the increase of inlet temperature, the difference between MCTSACs with DCTs and that with a SCT decreases, for both of heat collection rate and thermal efficiency.

3.4. Influence from the Inclination Angle (Case 4)

The influence of the inclination angle on the thermal performance of MCTSACs with DCTs is reflected in Figure 6, whose experimental conditions are based on the definitions in Case 4 (Table 2). It can be observed that the thermal performance of MCTSACs with DCTs reach the pick when the inclination angle is 23°, with an outlet temperature of 29.1 °C, a heat collection rate of 842.7 W, and a thermal efficiency of 42.6%. Based on these results, it is suggested that the inclination angle should be chosen as 23°.

Figure 7 depicts the temperature distribution of air along the length direction, based on the experiment conditions defined in Case 5 (Table 2). Apparently, with the increase of the length, the air temperature increases as well, for all solar radiation conditions. When the length is bigger than 2m, the increasing rate seems to be lowered. As shown in the previous results, the outlet temperature of MCTSACs with DCTs is less than that of MCTSACs with a SCT. Therefore, we can increase the length of MCTSACs with DCTs to increase its outlet temperature, hence improve the heat collection rate.

Outlet temperature and heat collection rate

(b) Thermal efficiency
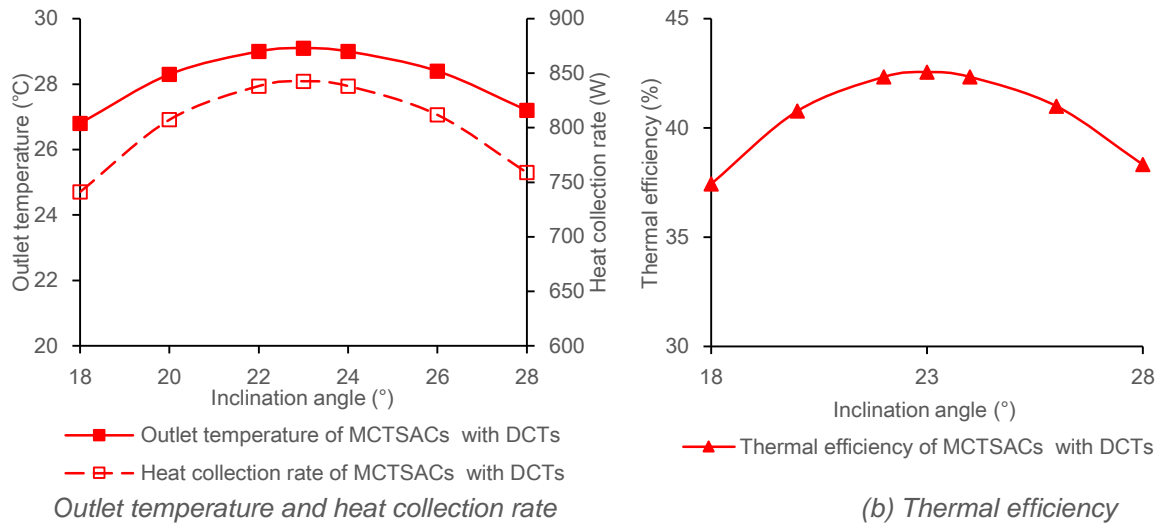
Figure 6: Influence from the inclination angle

3.5. Influence from the Length of the Tube (Case 5)
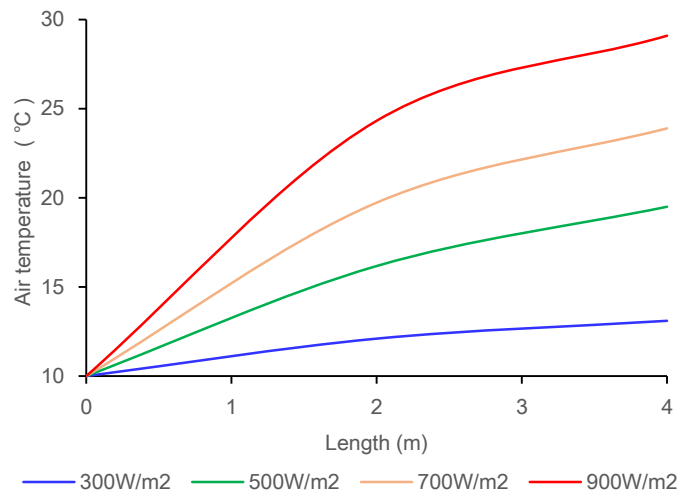
Figure 7: Influence from the length of the tube

4. CONCLUSION

In order to improve the thermal performance and air flow rate of MCTSACs with a SCT, a MCTSAC with DCTs is developed and expressed in the paper. The thermal performance of MCTSACs with DCTs and that of MCTSACs with a SCT was compared using results from a real experiment, and conclusions are as follows:

1. Comparing to MCTSACs with a SCT, MCTSACs with DCTs can significantly improve both air flow rate and thermal performance of the solar collector. The total air flow rate of MCTSACs with DCTs is two times as much as that of MCTSACs with a SCT, and the average heat collection rate and the average thermal efficiency of MCTSACs with DCTs grow by 17.8%.

2. For MCTSACs with DCTs, an optimal air velocity inside the collector tube should be around 1.8m/s, and an optimal inclination angle is considered to be 23°.

3. The outlet temperature of MCTSACs with DCTs is less than that of MCTSACs with a SCT. To compensate this disadvantage, we can increase the length of MCTSACs with DCTs to improve its outlet temperature and heat collection rate.

5. ACKNOWLEDGEMENT

6. REFERENCES

CHEN Z., Chen C., Ling H., Zheng H., Guan Y., 2014. Experimental study on thermal performance for the specialized multiple curved surfaces trough solar air collector dedicated to solar greenhouse. Building Science, 30, 58-63.

KIM Y., Seo T., 2008. An evaluation on thermal performance of CPC solar collector. International Communications in Heat and Mass Transfer, 35, 446-457.

SINGH H., Eames P., 2011. A review of natural convective heat transfer correlations in rectangular cross-section cavities and their potential applications to compound parabolic concentrating solar collector cavities. Applied Thermal Engineering, 3, 2186-2196.

SUN C., Xia X. Tan X., 2009. Concentrating characteristic and improved scheme analysis for space solar collector. Acta Energiae Solaris Sinica, 30, 895-899.

TCHINDA R., 2008. Thermal behaviour of solar air heater with compound parabolic concentrator. Energy Conversion and Management, 49, 529-540.

XUE X., Zheng H., Tao T., Xie G., He K., 2011. Theoretical analysis of a novel multi-surface compound solar trough concentrator. Acta Energiae Solaris Sinica, 32, 843-848.

ZHAO Y., Zhang H., Zhan D., Zhuang J., 2006. Design and heat transfer analysis of CPC heat pipe evacuated tubular collectors. Petro-Chemical Equipment, 35, 28-31.

100: Heat transfer analysis of ferrofluids based solar parabolic trough collectors

MUSTAFA, ALSAADY, YUYING, YAN, RABAH, BOUKHANOUF

HVACR & Heat Transfer Group, Faculty of Engineering, University of Nottingham, University Park, Nottingham NG7 2RD, UK

The paper is concerned the use of ferrofluids in solar parabolic trough collectors enhances thermal efficiency of solar collectors. Ferromagnetic nanoparticles dispersed in common heat transfer fluids (ferrofluids) exhibit better thermos-physical properties compared to the base fluids. By applying the right magnetic intensity and magnetic field direction, the thermal conductivity of the fluid enhanced more than conventional nanofluids. Therefore, ferrofluids based concentrating solar collector design is slightly different from conventional solar collectors. External magnetic source is installed to alter the thermos-physical properties of the fluid. In this paper, a heat transfer model based on energy balance of the solar collector is presented. The balance includes the direct thermal solar irradiation on the collector, optical losses, thermal losses, and heat gain of solar absorber. Various nanoparticle concentrations (<0.05 %) at the operational temperatures between 300 K and 500 K were used in the current study. The model was compared to experimental data that used conventional heat transfer fluid. The results of the model were in a good agreement with the experimental data. Using ferrofluids as a heat transfer fluid increases the efficiency of solar collectors. Increasing the concentration of particles increase the efficiency of the collector. In the presence of external magnetic field, the solar collector efficiency increase to the maximum. At higher temperatures, the ferrofluids shows much better efficiency than convectional heat transfer fluid. The ferrofluids shows better heat transfer coefficient and decrease the surface temperature of the absorber. Ferromagnetic particles build a chain like structure in the presence of external magnetic field allowing faster heat transfer throw conduction.

Keywords: Solar Energy, Nanofluids, Ferrofluids, Parabolic Trough Collector, Thermal Efficiency

1. INTRODUCTION

The world recognizes the environmental issue, the shortage, and the rising price of fossil fuel. Eventually, this will constrain the use of fossil fuels in the future. Therefore, the use of renewable energy has had increased curiously. Solar energy is sufficient, clean renewable source, and it is available in both direct and indirect forms (Thirugnanasambandam et al., 2010). However, the levelized costs of solar energy ($194/MWh) are still much higher than conventional energy ($43/MWh) despite continues decline of solar energy costs (Timilsina et al., 2012). The cost of solar collectors is one of the main factors hindering their implementation. Researchers, attempt to improve the solar collector efficiency to ease this problem (Al-Shamani et al., 2014b).

Heat transfer can be enhanced by increasing the thermal conductivity of the heat transfer fluid (HTF). Suspending nano sized metal particles in common fluids (nanofluids) can significantly increase the thermal conductivity (Alsaady et al., 2014).   In recent years, many researchers have investigated the effects of nanofluids on the enhancement if heat transfer in thermal engineering devices, both theoretically and experimentally.   Researches have applied variety of preparation methods, characteristics and different models for the calculation of Thermo-physical properties of nanofluids (i.e. thermal conductivity, viscosity, density, specific capacity) (Ettefaghi et al., 2013, Fakoor Pakdaman et al., 2012, Fan and Wang, 2011, Ghadimi et al., 2011, Han, 2008, Ramesh and Prabhu, 2011, Saidur et al., 2011). Heat transfer can be enhanced by increasing the thermal properties of heat transfer fluid (nanofluids). In theory, nanofluids illustrating extraordinary thermo-physical properties are appropriate to increase the efficiency of any thermal management systems by selecting base fluids with applicable nanoparticle materials, dispersion agents, nanoparticle sizes, and concentrations (Wu and Zhao, 2013). A Special branch of nanofluids is Ferrofluid. Ferrofluids also known as magnetic nanofluids (MNF) are stable liquid dispersions of colloidal magnetic nanoparticles. Their magnetic and thermo-physical properties differentiate them than other nanofluids (Cowley and Rosensweig, 1967) Due to the intrinsic magnetic property of solute particle, the thermo-physical characteristics of ferrofluids properties such as thermal conductivity and viscosity can be effectively controlled by external magnetic field (Odenbach, 2002).

Using nanofluids in solar thermal energy harvesting have several advantages. First, very small quantity of nanoparticles are needed to make an efficient absorber (<1% by volume) (Taylor et al., 2011). Also, the extremely small size of the particles allows them to pass through conventional pumps and plumbing (Wang and Mujumdar, 2007). Another reason is the significant enhancement in wide range of thermal, optical, and catalytic properties over bulk properties. Recent studies, showed improvement in the efficiency of solar collector by using nanofluids with different solar collector design (Al-Shamani et al., 2014a).

In this paper, a novel design of solar parabolic trough collector is numerically investigated. The solar collector is a concentrated solar collector. A one-dimension model is used to calculate the solar collector efficiency. The Thermo-physical properties were calculated and determined from experimental data. The result of the model is illustrated and discussed.

2. THERMO-PHYSICAL PROPERTIES OF FERROFLUIDS

The thermo-physical properties of the base fluids (synthetic oil) and the nanoparticles (Fe_3O_4) including density, viscosity, thermal conductivity and specific heat are strongly dependent on the operational temperature. Using the correlation of thermos-physical properties of ferrofluids and base fluid were determined from (Chandrasekar et al., 2009, Snow, 2010, Sokhansefat et al., 2014, Syam Sundar et al., 2013).

The change of ferrofluids thermo-physical properties in the presence of external magnetic field was investigated by many researchers (Alsaady et al., 2014). The mechanisms proposed to explain the change in the thermos-physical properties is the formation of chain like magnetite particles in the ferrofluids induced by an external magnetic field. The thermal conductivity increases with increasing volume fraction and magnetic intensity (Nkurikiyimfura et al., 2013). When the magnetic field increases, the chain length increase, creating more bridge of thermal energy conduction along magnetic field direction. As the magnetic field intensity increases, the interaction among particles increases, leading to increase in the viscosity also called the magnetoviscous effect (Shima and Philip, 2011).The heat capacity is assumed to be the same in the presence of magnetic field. Many researchers consider the change of ferrofluids heat capacity in the presence of magnetic field to be slight and it is not taken into account in the model. Table 1 summarises the properties used in the model.

Table 1 Ferrofluids properties in the absence and the presence of external magnetic field with volume concentration of 0.05%.

T(°C)	B= 0 Gauss				B= 25 Gauss				B= 50 Gauss			
	$\square\square$	$\square\square\square$	225	325	$\square\square$	$\square\square\square$	225	325	$\square\square$	$\square\square\square$	225	325
$\square$ (kg/m3)	1197	1145	1040	935	1197	1145	1040	935	1197	1145	1040	935
$\square$ (mPa s)	2.86	1.75	0.69	0.34	2.93	1.79	0.71	0.34	3.35	2.05	0.81	0.39
$\square$ (W/(m K)	0.125	0.116	0.096	0.076	0.228	0.210	0.174	0.139	0.390	0.359	0.298	0.237
Cp (J/kg K)	1832	1922	2101	2281	1832	1922	2056	2281	1832	1922	2056	2281

3. FERROFLUIDS PARABOLIC TROUGH COLLECTOR (FPTC)

The ferrofluid based solar parabolic trough collector (FBTC) is a solar collector that uses ferrofluids (magnetic nanofluids) as a heat transfer medium. The main difference between the conventional solar parabolic trough collector and FPTC is the magnet or electromagnet found in FPTC design as shown in figure 1. Ferrofluids and nanofluids have the advantage of having higher thermal conductivity then conventional heat transfer medium. Moreover, the external magnet creates a magnetic field that increases the thermal conductivity of ferrofluids.
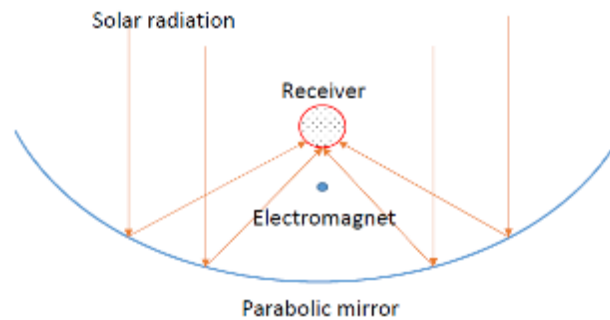

Figure 1: The basic design of ferrofluids based concentrating solar collector.

3.1 FPTC Model

The thermal analysis model determines the performance of a parabolic trough solar collector's linear receiver, also called solar absorber, using nanofluids as heat transfer fluid (HTF). Thermodynamics equations, heat transfer, and all parameters used in the model are discussed. Parameters include solar absorber geometries, nanofluids thermal and optical properties, flow rate, wind speed, ambient temperature, inlet and outlet temperatures of nanofluids, heat gain, heat losses, and optical losses. Modelling assumptions are also discussed.

The solar absorber performance model is based on an energy balance between the solar collector and the atmosphere. The energy balance includes the direct thermal solar irradiation on the collector, optical losses, thermal losses, and heat gain of solar absorber. For solar absorber shorter than 100 m a one dimensional energy balance gives acceptable results. For longer receivers a two dimensional energy balance becomes necessary. All equations and correlations necessary to predict there terms in the energy balance are depending on the collector type, solar collector condition, optical properties, HTF, and ambient conditions.

Figure 2 shows the one-dimensional steady-state energy balance for a cross section of an solar absorber, with and without the glass envelope intact, and Figure 2 b shows the thermal resistance model and subscript definitions. For clarity, the incoming solar energy and optical loses have been omitted from the resistance model. The optical losses are due to imperfections in the collector mirrors, tracking errors, shading, and mirror and solar absorber cleanliness. The effective incoming solar energy is absorbed by the glass envelope ($\dot{q}'_{5,SolAbs}$) and absorber selective coating ($\dot{q}'_{3,SolAbs}$). Some energy is absorbed into the selective coating is conducted through the absorber ($\dot{q}'_{23,Cond}$) and transferred to the HTF by convection ($\dot{q}'_{12,Conv}$): remaining energy is transmitted back to the glass envelope by convection ($\dot{q}'_{34,Conv}$) and radiation ($\dot{q}'_{34,rad}$). The energy from radiation and convection then passes through the glass envelope by conduction ($\dot{q}'_{45,Cond}$)

and radiation ($\dot{q}'_{12,Conv}$) and along with energy absorbed by the glass envelope ($\dot{q}'_{5,SolAbs}$) is lost to the environment by convection ($\dot{q}'_{56,Conv}$) and radiation ($\dot{q}'_{57,rad}$).

The flux directions are shown in Figure 2. Therefore, the energy balance equations are determined by conserving energy at each surface of the solar absorber cross-section.

$$\dot{q}'_{12,Conv} = \dot{q}'_{23,Cond} \qquad (1)$$
$$\dot{q}'_{3,SolAbs} = \dot{q}'_{34,Conv} + \dot{q}'_{34,rad} + \dot{q}'_{23,Cond} \qquad (2)$$
$$\dot{q}'_{34,Conv} + \dot{q}'_{34,rad} = \dot{q}'_{45,Cond} \qquad (3)$$
$$\dot{q}'_{45,Cond} + \dot{q}'_{5,SolAbs} = \dot{q}'_{56,Conv} + \dot{q}'_{57,rad} \qquad (4)$$
$$\dot{q}'_{HeatLoss} = \dot{q}'_{56,Conv} + \dot{q}'_{57,rad} \qquad (5)$$

The model assumes all temperatures, heat fluxes, and thermodynamics properties are uniform around the circumference of the solar absorber. Temperatures and properties are independent of angular and longitudinal solar absorber directions.
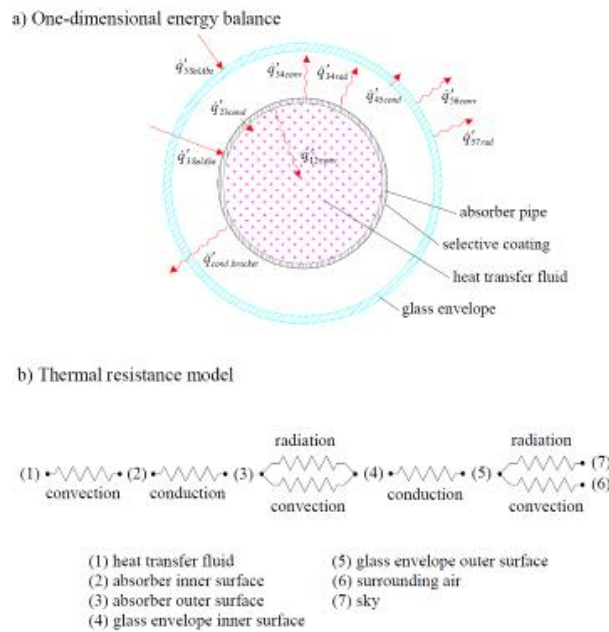
Figure 2: a) one dimensional steady state energy balance and b) thermal resistance model for a cross section of a solar absorber.

From Newton's law of cooling, the convection heat transfer from the inner surface of the absorber tube to the HTF is

$$\dot{q}'_{12,Conv} = h_1 D_2 \pi (T_2 - T_1) \qquad (6)$$
$$\text{With } h_1 = Nu_{D2} \frac{k_1}{D_2} \qquad (7)$$

Where h_1 HTF convection heat transfer coefficient at T_1, D_2 inner diameter of the absorber tube, T_2 mean (bulk) temperature of the HTF, T_2 inner surface temperature of absorber tube, Nu_{D2} Nusselt number based on D_2, and k_1 thermal conductivity of the HTF at T_1. The Nusselt number depends on the type of flow through solar absorber. At typical operating conditions, the flow in a solar absorber is well within the turbulent flow region. However, during off solar hours or when less energy output is required, the flow in the solar absorber may become transitional or laminar because the viscosities of HTF at lower temperatures. In this model, we study the solar absorber performance only under the turbulent flow.

For the convective heat from the absorber to the HTF, The Nusselt number correlation for turbulent and transitional cases (Reynolds number > 2300) is used. Furthermore, a correction factor is added to improve the accuracy of Nusselt number.

$$Nu_{D2} = \left(1 - 0.14\left(\frac{D_3}{D_2}\right)^{0.6}\right)\frac{f_2/8(Re_{D2}-1000)Pr_1}{1+12.7\sqrt{f_2/8}\left(Pr_1^{2/3}-1\right)}\left(\frac{Pr_1}{Pr_2}\right)^{0.11} \qquad (8)$$

With $f_2 = (1.82\, log_{10}(Re_{D2}) - 1.64)^{-2}$ *(9)*

$Pr = \frac{C_p\mu}{k}$ *(10)*

Where f_2 is the friction factor for the inner surface of the absorber tube, Pr_1 is Prandtl number evaluated at the HTF temperature T_1, Pr_2 is Prandtl number at the absorber inner surface temperature T_2, and D_2 is the absorber inner diameter, and D_3 is the absorber outer diameter. The correlation is valid for $0.5 < Pr_1 < 2000$ and $2300 < Re_{D2} < 5e6$. Except for Pr_2, all fluid properties are evaluated are the mean HTF temperature, T_1.

Fourier's law of conduction through a hollow cylinder describes the conduction heat transfer through absorber wall.

$$\dot{q}'_{23,Cond} = 2\pi k_{23}(T_2 - T_3)/ln(D_3/D_2) \qquad (11)$$

Where k_{23} is the absorber thermal conductivity at the average temperature $(T_2 + T_3)/2$, T_2 is the absorber inner surface temperature, T_3 is the absorber outer surface temperature. The conduction coefficient depends on the absorber material type. In this model a stainless steels, H321H is chosen. Conductive resistance through the selective coating has been neglected.

Convection and radiation heat transfer occur between the absorber and the glass envelope. The heat transfer mechanism depends on the annulus pressure. The solar absorber annulus is under vacuum (pressure <1). Therefore, the heats transfer between the absorber and glass envelope occurs by free-molecular convection.

$$\dot{q}'_{34,Conv} = \pi D_3 h_{34}(T_3 - T_4) \qquad (12)$$

With

$h_{34} = \frac{k_{std}}{(D_2/2 \ln(D_4/D_3) + b\lambda(D_3/D_4 + 1))}$ *(13)*

$b = \frac{(2-a)(9\gamma-5)}{2a(\gamma+1)}$ *(14)*

$\lambda = \frac{2.331E(-20)(T_{34}+273.15)}{(p_a\delta^2)}$ *(15)*

Where h_{34} is the convection heat transfer coefficient for the air in annulus at temperature T_{34}, T_4 is the inner glass envelope surface temperature, D_4 is the inner glass envelope surface diameter, k_{std} is the thermal conductance of the air at standard temperature and pressure (0.02551 W/m-K), b is the interact coefficient of air (1.571), λ is the mean free path between collisions of molecule, a is the accommodation coefficient, γ is the ration of specific heats for air (1.39), T_{34} is the average temperature $(T_3 + T_4)/2$, p_a is the air pressure, and δ is the molecular diameter of air (3.53e-8 cm).

The radiation heat transfer between the absorber and glass envelope $\dot{q}'_{34,rad}$ is estimated with the following equation

$$\dot{q}'_{34,rad} = \frac{\sigma\pi D_3\left(T_3^4-T_4^4\right)}{(1/\varepsilon_3+(1-\varepsilon_4)D_3/(\varepsilon_4 D_4))} \qquad (16)$$

Where σ is the Stefan-Boltzmann is constant, ε_3 is the absorber selective coating emissivity, and ε_4 is the glass envelope emissivity. Several assumptions were made in deriving this equation: non-participating gas in the annulus, grey surface, diffuse reflections and irradiation, and long concentric isothermal cylinders. In addition, the glass envelope is assumed to be opaque to infrared radiation. Some of these assumptions are not accurate. However, the errors associated with those assumptions should be relatively small.

The heat will transfer from the glass envelope to the atmosphere by convection and radiation. The convection will be either forced or natural, depending on whether there is wind. Radiation heat loss occurs due to the temperature difference between the glass envelope and sky. The convection heat transfer from the glass to envelope to the atmosphere $\dot{q}'_{56,Conv}$ is the largest source of heat loss, especially if there is a wind. From Newton's law of cooling

$$\dot{q}'_{56,Conv} = h_{56}\pi D_5 (T_5 - T_6) \qquad (17)$$

$$h_{56} = \frac{k_{56}}{D_5} Nu_{D5} \quad (18)$$

Where h_{56} is the glass envelope outer surface temperature, T_5 glass envelope outer surface temperature, T_6 is the ambient temperature, k_{56} is the thermal conductivity of air at $T_{56} = (T_5 + T_6)/2$, D_5 is the glass envelope outer diameter, Nu_{D5} average Nusselt number based on the glass envelope outer diameter.

The Nusselt number depends on whether the convection heat transfer is natural (no wind) or forced (with wind).

If there is no wind, the convection heat transfer from glass envelope to the environment will be by natural convection. For this case, the correlation developed by Churchill and Chu will be used to estimate Nusselt number

$$Nu_{D5} = \left[0.6 + 0387 \left\{ \frac{Ra_{56}}{\left[1+(0.559/Pr_{56})^{\frac{9}{16}} \right]^{\frac{16}{9}}} \right\} \right]^2 \qquad (19)$$

$$Ra_{56} = \frac{g\beta(T_5 - T_6)}{(\alpha_{56}v_{56})} \ (20)$$

$$\beta = \frac{1}{T_{56}} \ (21)$$

$$Pr_{56} = \frac{\alpha_{56}}{v_{56}} \qquad (22)$$

Where Ra_{56} is the Rayleigh number of air based on the glass envelope outer diameter D_5, g is the gravitational constant, α_{56} is the thermal diffusivity, β is the volumetric thermal expansion coefficient, Pr_{56} is the Prandtl number for air at T_{56}, and v_{56} is the kinematic viscosity for air at T_{56}. The correlation is valid for $105 < Ra_{56} < 1012$, and assumes a long isothermal horizontal cylinder.

If there is wind, the convection heat transfer from the glass envelope to the environment will be forced convection. The Nusselt number in the in this case is estimated with Zhukauskus correlation for external forced convection flow normal to an isothermal cylinder.

$$Nu_{D5} = CRe_{D5}^m Pr_6^n \left(\frac{Pr_6}{Pr_5} \right)^{1/4} \qquad (23)$$

This correlation is valid for $0.7 < Pr_6 < 500$, and $1 < Re < 106$. All fluid properties are evaluated at the atmospheric temperature, T_6, except Pr_5, which is evaluated at the glass envelope outer surface.

The radiation transfer between the glass envelope and sky is caused by the temperature difference between the glass envelope and sky. To approximate this, the envelope is assumed to be small convex grey object in a large blackbody cavity (sky). The net radiation transfer between the glass envelope and sky becomes

$$\dot{q}'_{57,rad} = \sigma D_5 \pi \varepsilon_5 (T_5^4 - T_7^4) \qquad (24)$$

Where ε_5 is the emissivity of the glass envelope outer surface, and T_7 is the effective sky temperature. The sky, espically during less than conditions, does not act like a blackbody; however, it is common practice to model it as such and to use an effective compensate for the difference. To simplify the model, the effective sky temperature is approximated as being below 8C below the ambient temperature. The glass envelope absorptance and emissivity are constants (independent of temperature) (a=0.002, e=0.86).

The optical losses and solar absorption – given the direct normal irradiation, solar angle, and optical properties of the trough mirrors and absorber components – is very difficult to model accurately. Because of this, optical efficiency terms are estimated and combined to form effective optical efficiency. The optical efficiency is estimated to calculate the solar absorption. The equation for the solar absorption n the glass envelope becomes

$$\dot{q}'_{5,SolAbs} = \dot{q}'_{si}\eta_{env}\alpha_{env} \qquad (25)$$
$$\text{With } \eta_{env} = \sum \varepsilon'_i K \qquad (26)$$

Where $\dot{q}'_{si}$ is the solar irradiation per receiver length, η_{env} is the effective optical efficiency at glass envelope, α_{env} is the absorptance of the glass envelope, ε'_i is the optical efficiency terms, and K is the incident angel modifier. The optical effective includes the absorber shadowing, tracking error, geometry error, clean mirror reflectance, dirt on mirrors, and dirt on absorber. The incident angle modifier is added to account for incident angle loses. The effective optical efficiency is estimated from the data published in a report by NREL [Price et al. 2002]. The solar irradiation $\dot{q}'_{si}$ in equation 24 is determined by multiplying the direct solar irradiation by the projected normal reflective surface area of the collector (aperture area) and dividing by the receiver length.

The solar energy absorbed by the absorber occurs very close to the surface; therefore, it is treated as a heat flux. The equation for the solar absorption in the absorber becomes

$$\dot{q}'_{3,SolAbs} = \dot{q}'_{si}\eta_{abs}\alpha_{abs} \qquad (27)$$
$$\text{With } \eta_{abs} = \eta_{env}\tau_{env} \qquad (28)$$

Where η_{abs} is the effective optical efficiency at absorber, α_{abs} is the abosrptance of absorber, τ_{env} is the transmittance of the glass envelope. The solar collector efficiency is calculated as follow:

$$\eta_{Colector} = \frac{\dot{q}'_{12,Conv}}{\dot{q}'_{si}} \qquad (29)$$

3.2 Model Validation

In order to validate the heat transfer model, it was compared with experimental data obtained from Sandia National Laboratory (SNL) (Dudley et al., 1994). The numerical model was also compared with other numerical model (Forristall, 2003). The experimental results were fir a solar collector assembly (LS-2) module placed at the AZTRAK rotating platform at SNL, Due to limitations in the experimental set up, a 5 cm flow restriction device (solid plug) was cantered in the inside diameter of the absorber tube. Two different selective coating were used in the test: black chrome and cermet. Cermet has better radiative properties (low emissivity) at high temperatures than black chrome, and does not oxidize if the vacuum is lost (Dudley et al., 1994). The test was performed in various conditions. All the conditions and specifications used in the experimental test are summarized in table 2. A silicone heat transfer fluid (Syltherm 800) was used in the experimental set up.

The ferrofluids uses Syltherm 800 as based fluid and Fe_3O_4 nanoparticles. Three different volume fractions are considered 0.01%, 0.03%, and 0.05%.In the presence of magnetic field; it is assumed that the enhancement in the properties is independent of temperature, and no effect on heat capacity.

The input data for the model include the direct normal insolation, wind speed, ambient temperature, inlet bulk temperature of HTF, outlet bulk temperature of HTF, HTF volume flow rate. The output data include the difference between the average HTF and the ambient temperature, solar absorber heat loss per collector area, HTF heat gain, and collector efficiency.

Table2: Specifications for AZTRAK test data, (Dudley et al., 1994)

Module size	7.8 x 5 m	Condition of receiver annulus	Vacuum intact
Rim angle Reflectors	70°	Atmospheric air pressure	0.83 atm
	12 thermally sagged panels	Heat transfer fluid	Syltherm 800
	Second surface silvered	Average Solar irradiance	1000 W/m^2
	Low iron glass	Average wind speed	2.5 m/s
Aperture Area	39 m^2	Average atmospheric temperature	25 °C
Focal Length	1.84 m		
Concentration ratio	71		
Receiver	Evacuated tube design		

Absorber diameter 70 mm	
Length:4m Pyrex glass envelope 115 mm diameter	
Selective coating: cermet	

4   RESULTS AND DISCUSSION

The results obtained for the collector efficiency and thermal losses are shown in Figs 3-5. For the collector efficiency figure 3, the model for Syltherm follows the trends of the experimental values and all the results are inside the experimental error bars. Higher efficiencies are obtained using ferrofluids even with low volume concentration 0.01%. At higher temperatures, the collector efficiency drops gradually. At low average temperature, the difference between the efficiency of solar collector is small around 2.5%. At high average temperature, the difference increase to reach 7% at average temperature of 325°C. This is due to the enhancement in the convection heat transfer of ferrofluid compared to the base fluid. The improved thermal conductivity of ferrofluids is the most important factor for improving the heat transfer in parabolic trough collectors. Ferrofluids reduces the thermal resistance at interfaces and minimizes the temperature difference between the absorber surface and the heat transfer fluid. Figure 4 illustrate the convective heat transfer coefficient of ferrofluids at different volume concentration. The ferrofluids at high average temperature are more efficient compared to base fluid. At 325°C the heat transfer coefficient of ferrofluids with 0.05% volume fraction is 796 W/m^{2}K, where at the same temperature the base fluid heat transfer coefficient is only 394 W/m^{2}K. The heat transfer coefficient curve has a peak, where the heat transfer coefficient decrease with increasing temperature. This is because a vapour film, which acts as an insulation due to the low thermal conductivity of the vapour, covers a large fraction of the absorber surface. Figure 5 shows the efficiency of FPTC with 0.05% volume fraction ferrofluids in the presence of external magnetic field. The efficiency increase with increasing the magnetic field intensity. The ferromagnetic particles creates a chain-like structure in the presence of external magnetic field, which improve the heat transfer performance. Even though the magnetization of ferromagnetic particles decreases with increasing temperature, it was neglected in this study. Decreasing the magnetization will make the chain particles shorter and will affect the thermos-physical properties of ferrofluids.
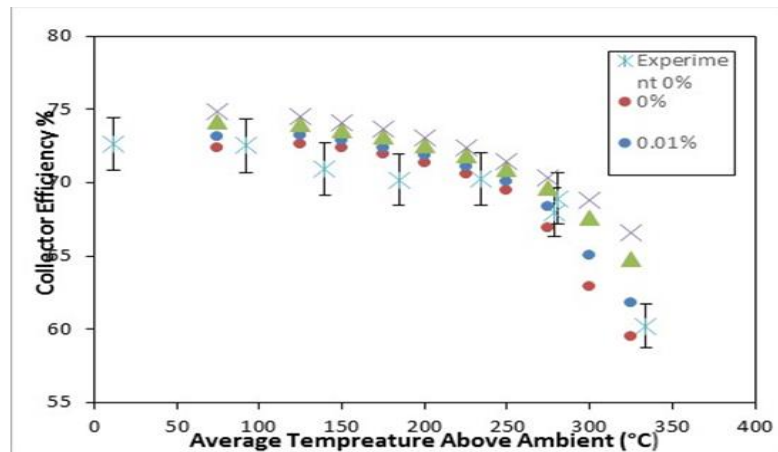

Figure 3: comparison of calculated ferrofluid collector efficiency with different volume fraction and experiment data.
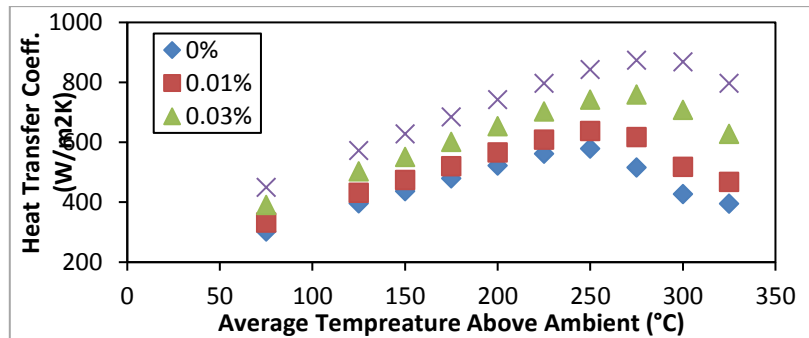
Figure 4: Convective heat transfer coefficient of different volume fraction vs average temperature of ferrofluids above ambient.
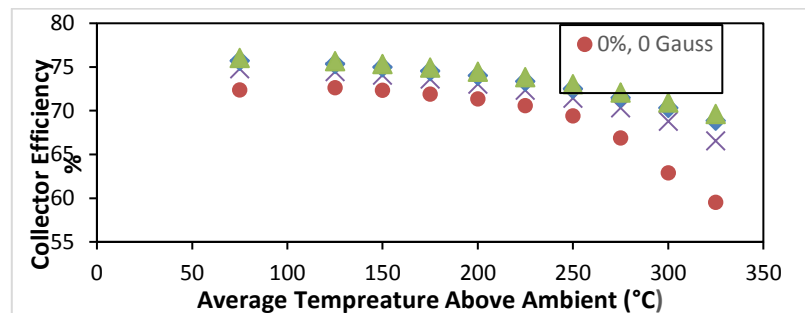

Figure 5: Ferrofluids solar collector efficiency in the presence of external magnetic.

5 CONCLUSION

The thermal behaviour of ferrofluids consisting of synthetic oil and Fe_3O_4 throughout a solar parapolic trough collector tube (L=7.8, and D=0.07 m) has been investigated. The heat transfer model showed a good agreement with experimental data. The results illustrate that the thermal efficiency of the solar collector enhanced when nanoparticles are added to the base fluid. Moreover, in the presence of external magnetic field the thermal efficiency increased further. At higher temperature, ferrofluids showed much better results, around 10% higher than conventional heat transfer fluids. The heat transfer coefficient is increased as the concentration of the nanoparticles in the base fluid is increased. Utilizing ferrofluids in concentrating solar collectors has environmental benefits and causes improving heat transfer, consequently reducing the needed heat transfer area of collectors. These advantages could be achieved with little change on the system.

4. REFERENCES

AL-SHAMANI, A. N., Yazdi, M. H., Alghoul, M., Abed, A. M., Ruslan, M., Mat, S. & Sopian, K. 2014a. Nanofluids for improved efficiency in cooling solar collectors–A review. Renewable and Sustainable Energy Reviews, 38, 348-367.

AL-SHAMANI, A. N., Yazdi, M. H., Alghoul, M. A., Abed, A. M., Ruslan, M. H., Mat, S. & Sopian, K. 2014b. Nanofluids for improved efficiency in cooling solar collectors – A review. Renewable and Sustainable Energy Reviews, 38, 348-367.

ALSAADY, M., Fu, R., Li, B., Boukhanouf, R. & Yan, Y. 2014. Thermo-physical properties and thermo-magnetic convection of ferrofluid. Applied Thermal Engineering.

CHANDRASEKAR, M., Suresh, S., Srinivasan, R. & Bose, A. C. 2009. New analytical models to investigate thermal conductivity of nanofluids. Journal of Nanoscience and Nanotechnology, 9, 533-538.

COWLEY, M. & Rosensweig, R. E. 1967. The interfacial stability of a ferromagnetic fluid. J. Fluid Mech, 30, 671-688.

DUDLEY, V., Kolb, G., Sloan, M. & Kearney, D. 1994. SEGS LS2 solar collector—test results. Report of Sandia National Laboratories, Report No. SANDIA94-1884.

ETTEFAGHI, E.-O.-L., Ahmadi, H., Rashidi, A., Nouralishahi, A. & Mohtasebi, S. S. 2013. Preparation and thermal properties of oil-based nanofluid from multi-walled carbon nanotubes and engine oil as nano-lubricant. International Communications in Heat and Mass Transfer, 46, 142-147.

FAKOOR PAKDAMAN, M., Akhavan-Behabadi, M. A. & Razi, P. 2012. An experimental investigation on thermo-physical properties and overall performance of MWCNT/heat transfer oil nanofluid flow inside vertical helically coiled tubes. Experimental Thermal and Fluid Science, 40, 103-111.

FAN, J. & Wang, L. 2011. Review of heat conduction in nanofluids. Journal of heat transfer, 133, 040801.

FORRISTALL, R. E. 2003. Heat transfer analysis and modeling of a parabolic trough solar receiver implemented in engineering equation solver, National Renewable Energy Laboratory.

GHADIMI, A., Saidur, R. & Metselaar, H. 2011. A review of nanofluid stability properties and characterization in stationary conditions. International Journal of Heat and Mass Transfer, 54, 4051-4068.

HAN, Z. 2008. Nanofluids with enhanced thermal transport properties.

NKURIKIYIMFURA, I., Wang, Y. & Pan, Z. 2013. Effect of chain-like magnetite nanoparticle aggregates on thermal conductivity of magnetic nanofluid in magnetic field. Experimental Thermal and Fluid Science, 44, 607-612.

ODENBACH, S. 2002. Magnetoviscous Effects in Ferrofluids, Springer.

RAMESH, G. & prabhu, N. K. 2011. Review of thermo-physical properties, wetting and heat transfer characteristics of nanofluids and their applicability in industrial quench heat treatment. Nanoscale research letters, 6, 1-15.

SAIDUR, R., Leong, K. Y. & Mohammad, H. A. 2011. A review on applications and challenges of nanofluids. Renewable and Sustainable Energy Reviews, 15, 1646-1668.

SHIMA, P. D. & Philip, J. 2011. Tuning of Thermal Conductivity and Rheology of Nanofluids Using an External Stimulus. The Journal of Physical Chemistry C, 115, 20097-20104.

SNOW, C. L. M. 2010. The Heat Capacity and Thermodynamic Properties of the Iron Oxides and Their Relation to the Mineral Core of the Iron Storage Protein Ferritin.

SOKHANSEFAT, T., Kasaeian, A. B. & Kowsary, F. 2014. Heat transfer enhancement in parabolic trough collector tube using Al2O3/synthetic oil nanofluid. Renewable and Sustainable Energy Reviews, 33, 636-644.

SYAM SUNDAR, L., Singh, M. K. & Sousa, A. C. M. 2013. Investigation of thermal conductivity and viscosity of Fe3O4 nanofluid for heat transfer applications. International Communications in Heat and Mass Transfer, 44, 7-14.

TAYLOR, R. A., Phelan, P. E., Otanicar, T. P., Adrian, R. & Prasher, R. 2011. Nanofluid optical property characterization: towards efficient direct absorption solar collectors. Nanoscale research letters, 6, 1-11.

THIRUGNANASAMBANDAM, M., Iniyan, S. & Goic, R. 2010. A review of solar thermal technologies. Renewable and sustainable energy reviews, 14, 312-322.

TIMILSINA, G. R., Kurdgelashvili, L. & Narbel, P. A. 2012. Solar energy: Markets, economics and policies. Renewable and Sustainable Energy Reviews, 16, 449-465.

WANG, X.-Q. & Mujumdar, A. S. 2007. Heat transfer characteristics of nanofluids: a review. International journal of thermal sciences, 46, 1-19.

WU, J. M. & Zhao, J. 2013. A review of nanofluid heat transfer and critical heat flux enhancement—Research gap to engineering application. Progress in Nuclear Energy, 66, 13-24.

255: Experimental study of a new space heating system combining Chinese Kang and solar energy

HAOFANG ZHENG*[1], JIE JI*[2], CHAO GOU3, WEI WEI[4]

1,2,3,4 Department of Thermal Science and Energy Engineering,
University of Science and Technology of China
#96 Jinzhai Road, Hefei City, Anhui Province, People's Republic of China
1 zhavefun@mail.ustc.edu.cn
2 2jijie@ustc.edu.cn

In the present work, a new space heating system has been designed and experiments have been conducted on its performance .The new system consists of a solar Kang system and solar air heaters for room heating. Kang is a kind of heatable brick bed. The solar Kang is heated by circulating hot water which is provided by solar collector. The experiments are conducted in a family house in Qinghai province in the north-west of China. Three different working modes have been tested. 1, Solar Kang working alone. 2, Solar air heaters. 3, Solar Kang and Solar air heaters combined. Kang is heated by circulating hot water from 21:30 to 9:00. The air vents of solar air heaters are open from 9:30 to 16:50 in the afternoon. Results show that the surface of the Kang can maintain a temperature range from 27℃ to 38℃ during its working hours. The solar Kang can perfectly meet the demand of thermal comfort in the sleeping hours. The performance of air heaters is less ideal. The average air temperature in the room is 8.7℃ during the day, 4℃ higher than the reference room, 4℃ higher than environment temperature.

1. INTRODUCTION

Energy consumed in buildings accounts for approximately one third of the whole energy consumption, and about 40% of them are consumed in lighting, ventilating, space heating or cooling, and water heating. Therefore, how to reduce energy consumption of space heating, cooling and hot water and how to transform energy supply methods are of great significance for reducing the energy consumption.

In the past decades, solar thermal application has drawn increasing attention and very successfully developed. In 1990s, Yakubu et al. presented an user-experience survey about living in passive solar homes (Li, G., et al., 2014); Zhai et al. analysed two kinds of roof solar collectors and found that the heat collecting efficiency was higher for the double pass than that of the single pass design (Zhai, 2005) . The design of polymer flat plate solar collectors was optimized by Do Ango et al. (Do Ango, 2013). Summers et al. designed and optimized a solar air collector with integrated phase change material storage (Summers, 2012). Tromb wall also showed great potential in energy saving in buildings. (Sun, 2007) As a common point, solar air collectors that serve as passive heating equipment may become inefficient or even infeasible under poor weather condition if thermal storage is not available. So, to economically storage and efficiently use solar energy is as important as collecting the energy. (Tian, 2013)

Winter is very cold in the north of China. Thus space heating during winter is in great demand. In the rural areas of northern China, Chinese Kangs are widely used in nearly 85% of rural homes for space heating. In recent years, Chinese Kang has arouse much research interest. Zhuang et al. (zhuang, 2009) gave a thorough review of the traditional grounded Kang and elevated Kang, including their thermal performance. Ren et al. put forward an up-to-date Kang design (Ren, 2013), with details about the proposed structure, material, construction, performance as well as energy-saving potential. Several scholars developed numerical models for Kang. For example, a thermal and airflow model for elevated Kang was developed by Zhuang et al. (Zhuang, 2009) ; Cao et al. established a set of models to simulate the energy performance of a Kang heating system in Chinese detached house, and accomplished this with experimental field study (Cao, 2009). Traditional fire Kang is composed of a stove, a Kang body and a chimney though the Kang body. The Kang body serve as bed as well as bench. Traditional fire Kang uses biomass fuel as its energy source. By burning wood and straw in the stove, Kang is heated by hot fume which went through the flue in the Kang. The heated Kang body will release heat into the room as well as providing a comfortable sleeping environment. As a method to improve domestic thermal environment, traditional fire Kang is effective and economical, but it also has certain defects. Firstly, there is always serious air pollution during heating season caused by the burning of fuel. And it also presents a safety risk if the ventilation is not ideal. Secondly, fire Kang has low energy efficiency. Thirdly, fire Kang requires a lot of human labour to keep it functioning and the temperature of the Kang body is hard to control.

Solar energy, due to its advantages of renewable and environmentally friendly, is an important alternative to fossil fuels. To improve existing Kang system, a new space heating system combing Kang and solar energy has been designed. The system consists of a solar Kang subsystem and solar air heater subsystem. Solar Kang uses solar energy in place of biomass fuel. By introducing solar energy into the application of Kang, the system is able to meet the demand of indoor thermal comfort with less air pollution, less energy consumption and more convenience for the users.

2. SYSTEM DESCRIPTION AND EXPERIMENTAL SETUPS

2.1 System description

The new system consists of a solar Kang subsystem and a solar air heater subsystem.

The solar Kang system consists of a Kang body, solar collectors, a circulation pump and interconnecting pipework. Solar energy is collected by solar collectors and stored in thermal insulated water tank in form of sensible heat. When Kang needs heating, hot water will be pumped into the water pipe circuit buried in the body of Kang.

The solar air heater subsystem consists of air heaters and air vents. The air vents are built though the south wall to connect the air duct in the solar heaters with indoor space. The air heaters are mounted upon the south wall of the room. The air vents are open during day so the air in the duct of the solar air heaters is heated and brought into the room by natural convection.

2.2 Experimental setups

Experiments on the system are conducted in Guide (101.47 ºE, 36.02 ºN), Qinghai province in the north west of China. Components of the system are manufactured and installed in a family house's bedroom. The room has an area of 20 square meters, including a small kitchen. The outer walls (the south, north and east walls) of the room have extra insulation layers.

The solar collectors are installed on the roof of the house. The collectors used in the experiment are all glass evacuated tube collectors. The collectors have a total area of 4.94 m^2. The volume of the water tanks is 330 L. The Kang body is built in the room 0.6 meters away from the south wall. Kang body is of dimensions 2m by 1.8m by 0.45 m(height), with the following five layers from top to bottom: cement layer (30 mm), sand layer (30 mm), thermal insulation layer (20 mm), and concrete layer(100 mm),as displayed in Fig. 1. a. The vertical surfaces of the Kang body are covered with thermal insulation material. Conductive water pipe is buried in the Kang as shown in Fig. 2. The water pipe in the Kang was arranged in the shape showed in Fig. 1. B. in order to obtain a uniform distribution of temperature for the Kang surface. The pipework connecting the Kang and the water tank is wrapped by insulation material to reduce heat loss.

The solar air heaters are installed on the south wall of the room, as shown in Fig. 2. The two solar heaters have a total area of 4m^2.
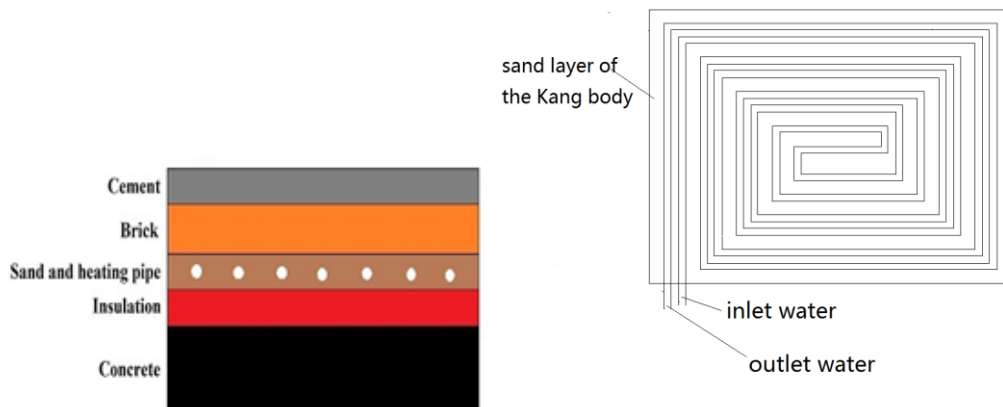
Fig. 1.a: Structure of the Kang body   Fig. 1.b: Layout of the water pipe in the Kang

In the experiments, Copper-constantan thermocouples were used to measure the thermal progresses of the space heating system and the room. Nine thermocouples were placed uniformly on the surface of the Kang body, and the temperature of inlet/outlet hot water was measured by two thermocouples attached to the water pipe, as shown in Fig. 3. The temperature in the water tank is measured by a thermocouple placed in the middle of the water tank. Four thermocouples were placed at opening of the air vents of the solar air heaters. 6 thermocouples were placed on the four walls, the roof and the floor. Thermocouples were also used to measure the ambient temperature and the temperature of the reference room.

The flow rate of the hot water which goes through the Kang body was measured and recorded by flowmeter.

Two pyranometers were used to measure the solar radiation quantity received by the solar collectors and solar air heaters. One pyranometer was hanged upon the south wall besides the solar air heaters. The other was placed on the roof of the room beside the solar collector as the same setting angle as the solar collectors.

Fig. 2: Solar air heaters on the south wall

Fig. 3: Thermocouples placed on the surface of Kang body

3   RESULTS AND DISCUSSION

To assess and compare the performance of the two subsystems, three different working modes were tested in the experiments:

1, the solar Kang subsystem and solar air heater subsystem working together.

2, the solar Kang subsystem working alone.

3, the solar air heaters working alone.

Mode 1: The solar Kang subsystem and solar air heater subsystem working together.

During the tests of this mode, the air vents of the solar heaters are open from 9:45 to 16:45. The circulation pump of the solar Kang was on form 21:00 to 9:30. The data used here is from experiments carried out in 29th, December, 2014.

Fig. 4 shows the weather condition and solar radiation of the day. Fig. 5 and Fig. 6 show the working performance of the Kang system and solar air heaters respectively.
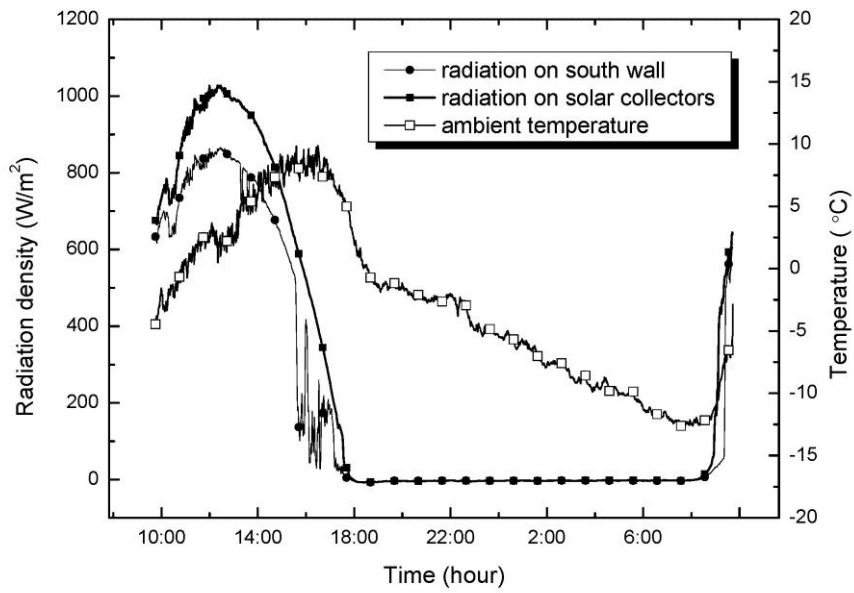
Fig.4: Radiation and ambient temperature in 29th, December, 2014.

In Fig.4 the weather condition and solar radiation of the day is showed. The ambient temperature fluctuates from   -12.4℃ to 9.8℃. The average ambient temperature is -2.88℃.

The performance of the solar Kang subsystem
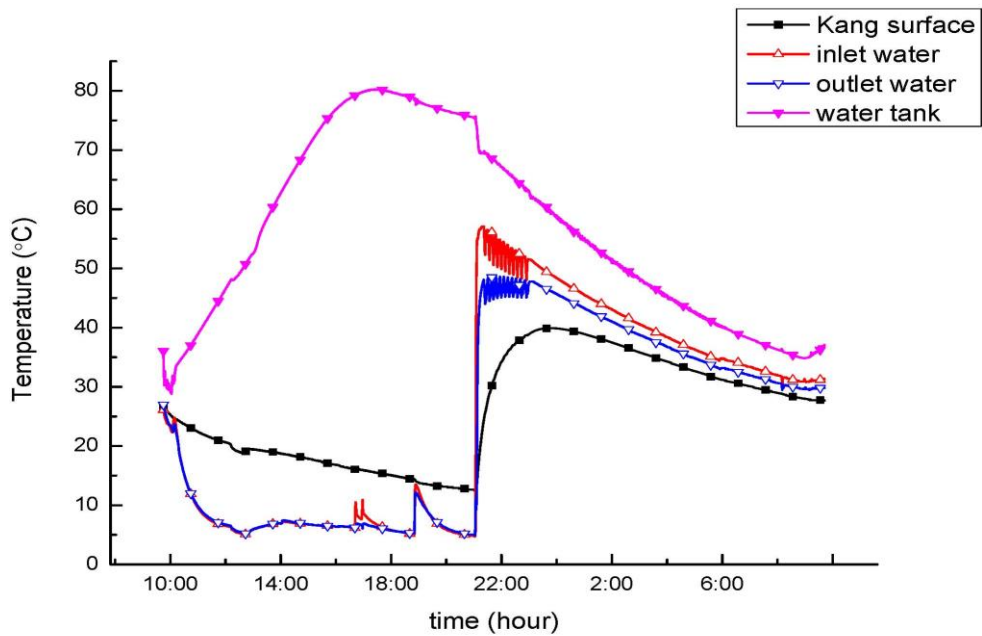
Fig.5 Work condition of the Kang in 29th, December, 2014.

The vibration of the inlet/outlet water temperature showed in Fig.3 is caused by the high temperature protection system, which turns off the circulation pump when the temperature in the water pipe gets too

high. At the beginning, the temperature in the water tank is too high, thus the circulation pump worked intermittently. When the pump is on, the flow rate though the Kang was steadily 0.033kg/s.

The temperature of the Kang surface was obtained by averaging the readings of the 9 thermocouples placed on the surface of the Kang. The graph shows that the temperature of the Kang surface varies from 34.2 ℃ to 27.9℃ from 22:00 to 9:00. The temperature reaches 40℃ as its climax at 24:00. The average temperature of the Kang during the sleeping hours is 34.56℃.

The temperature reached 40℃ around 24:00, which is too high for thermal comfort. This problem can be solved by modifying the controlling system of the Kang. To avoid overheating of the Kang, a temperature probe should be placed on the surface of the Kang body, when the temperature on the Kang surface gets too high, the circulation pump should be turned off temporarily.

The solar Kang system provided a heated bed with an average temperature of 34.56℃.The result shows that the solar energy collected by the solar collectors is sufficient to provide a comfortable thermal environment throughout the night. And by heating the Kang body throughout the night, the solar Kang system provided a thermal sleeping environment steadier than traditional Kang.

The performance of the solar air heater subsystem
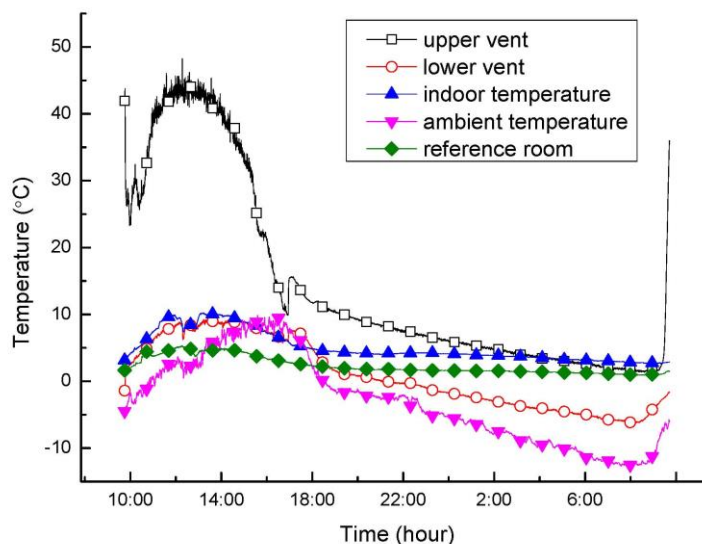
Fig.6: The performance of the solar air heaters in 29th, December, 2014

The indoor air temperature was obtained by averaging the readings of the three thermocouples placed in the middle of the room. The air vents of the solar air heaters were open from 9:45 to 16:45. During these hours, the average indoor air temperature was 8.1℃, while the average ambient temperature was 4℃, and the average temperature in the reference room was also 4℃. The solar air heaters increased the indoor approximately by 4℃.

The performance of the solar air heaters were influenced by the thermal condition of the room. The room is the test is larger than usual bedrooms, and it also has a large window space. The performance of the solar air heaters could be improved by improving the heat insulation of the room.

The result of the experiments shows that the solar air heaters are insufficient to provide a satisfactory indoor thermal environment, but it can still be a prominent auxiliary method for indoor space heating.

Mode 2: The solar Kang subsystem working alone

During the tests of mode 2, the air vents of the solar heaters are closed. The circulation pump of the solar Kang is on from 22:00 to 9:30.The data used here is from experiments carried out in 19th, January, 2015.

Fig.7 shows the weather condition and solar radiation of the day. The ambient temperature fluctuated from -10.7℃ to 9.1℃. The average ambient temperature is -2.9℃.

Fig. 7: Radiation and ambient temperature in 19th, January, 2015.

Comparison of Mode 1 and Mode 2
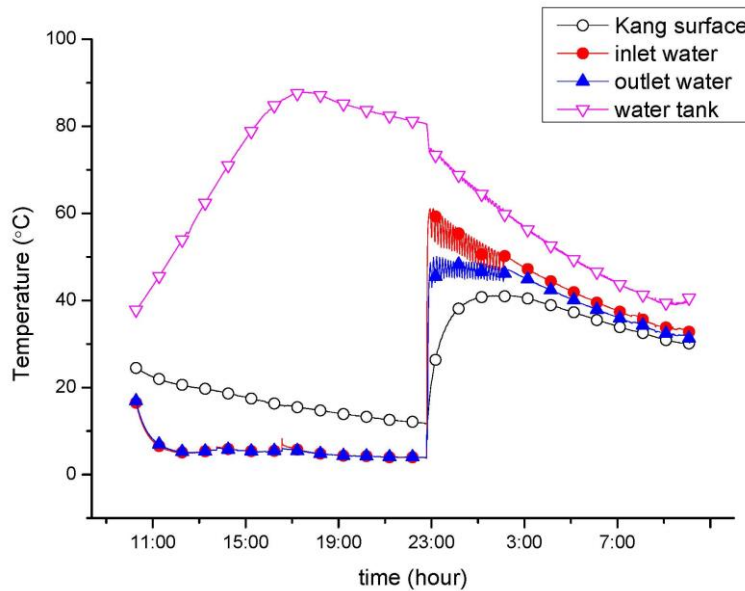
Fig. 8: Working condition of the Kang in 19th, January, 2015.

From Fig.8 it can be seen that the performance of solar Kang subsystem in mode 2 was similar with it in mode 1. The shutdown of solar air heater subsystem does not affect the working of the solar Kang

subsystem. During the sleeping hours, the temperature of the surface of the Kang varies from the average temperature of the Kang surface is 35℃.
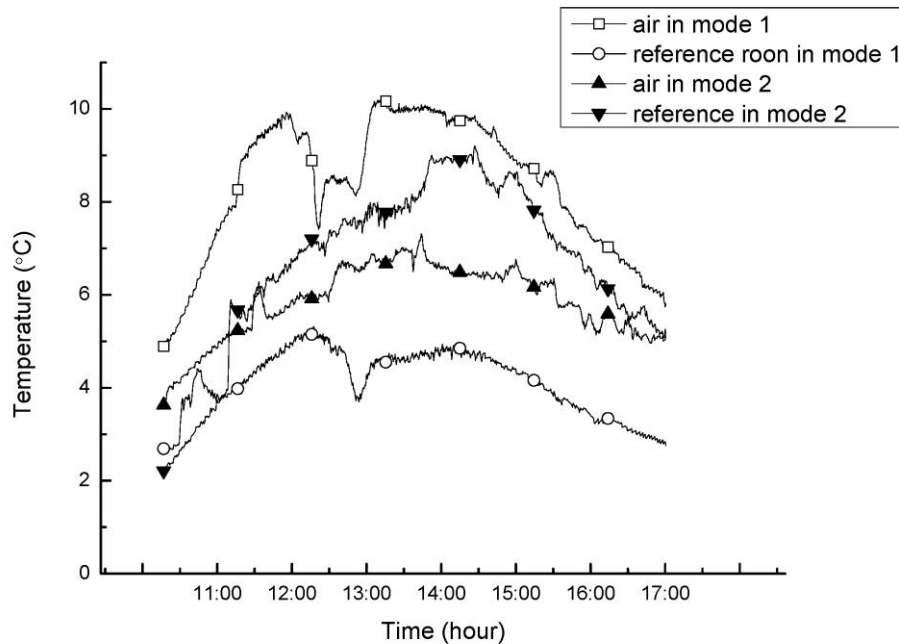
Fig. 9: The indoor air temperature in mode 1 and mode 2 during day

In Fig.9 air temperature in the test room and reference room under mode 1 and mode 2 was compared. In mode 2, the indoor air temperature is lower than the air temperature in the reference room. During the day, from 10:00 to 17:00, the average indoor air temperature of the test room in mode two is 4.5℃， while the average air temperature in the reference room is 6.7 ℃. The average air temperature in the test room in mode 2 is 2.2℃ lower than the reference room. In mode one, the average air temperature in the test room is 4℃ higher than that in the reference room.

The comparison of air temperature in mode 1 and mode 2 shows that the solar air heaters have distinct effect over indoor temperature during the day.

Mode 3： The solar air heaters working alone.

The data is from experiments carried out in 10th, January, 2015.

During the tests of mode 3 the circulation pump of the solar Kang is turn off. The air vents of the solar air heaters are open from 9:50 to 16:50.

In Fig. 10 the weather condition and solar radiation of the day is shown. The ambient temperature fluctuates from 13.4℃ to 10.0℃. The average ambient temperature is -3.6℃.
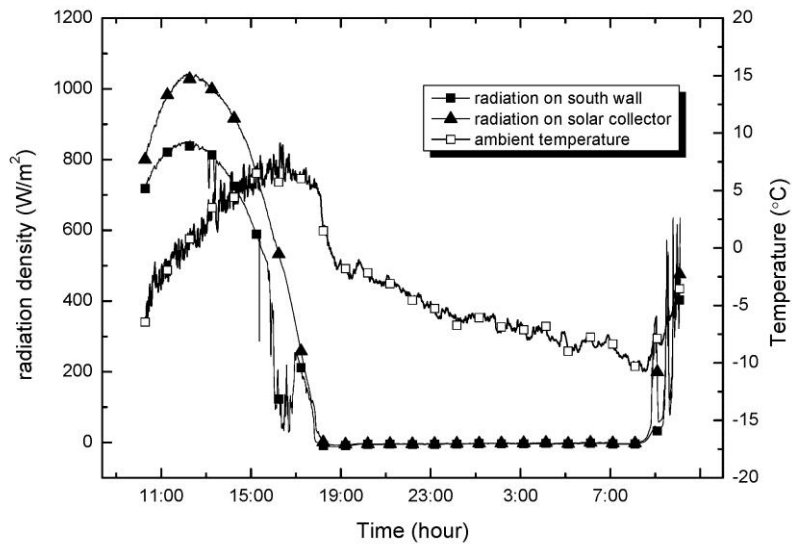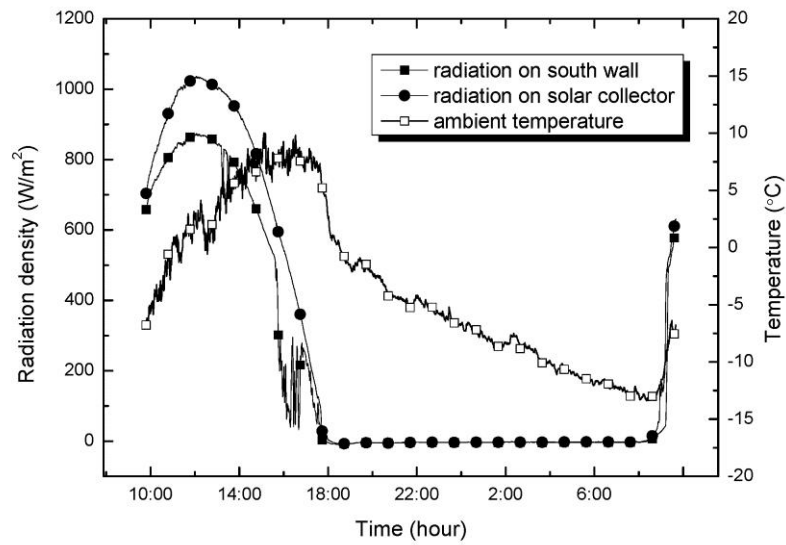
Fig.10: Radiation and ambient temperature in 10th, January, 2015.
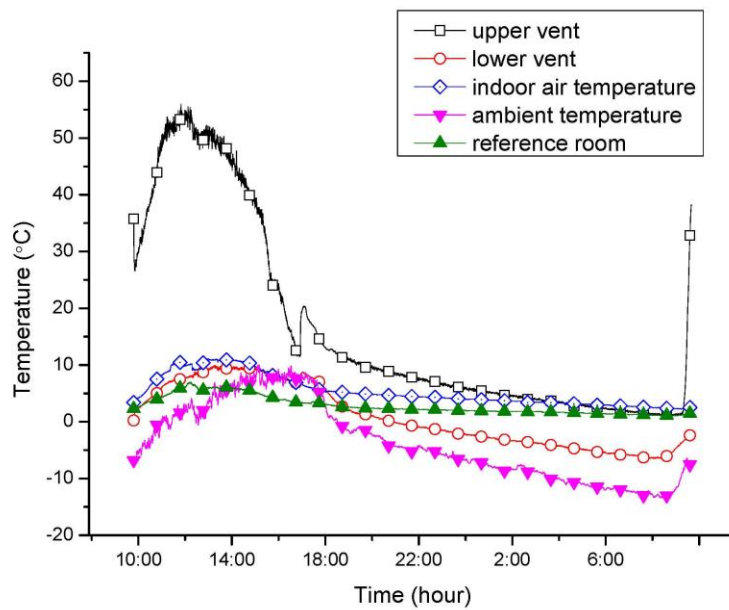
Fig.11: The performance of the solar air heaters in 10th, January, 2015.

During the day, the average indoor air temperature is 8.9℃, while the average ambient temperature is 3.6 ℃, and the average temperature in the reference room is also 4.9℃. The solar air heaters increased the indoor approximately by 4℃.

The air temperature in the test room reached 11℃ as maximum temperature. In The experiments in 10th, January, 2015, the test room maintained an air temperature above 10℃ from 11:30 to 15:00.

The result is consistent with the result of experiments of mode 1.

4   CONCLUSION

A new system combining the solar air heaters with the solar Kang has been successfully developed. Experiments were conducted on the performance of the system. Three different operating modes was tested. Highly encouraging results were obtained.

During the night, the solar Kang can maintain a temperature above 30℃. As a method of providing a comfortable thermal environment for sleeping, the solar Kang is a perfect substitute for traditional fire Kang. Considering solar Kang's advantage in reducing energy consumption and air pollution, it is a distinct improvement to replace traditional space heating Kang system with solar Kang.

While the effect of the solar air heater system is less ideal, it can still be improved in many aspects. In a smaller and better insulated room, the indoor air temperature would be maintained at a higher level.

The thermal environment provided by the system is comfortable and stable. Comparing to traditional fire Kang, this new system is more economical and environment friendly, and the new system can also bring the users a lot convenience for it can work automatically. As a whole, the new system is a very competent and beneficial substitute for the traditional fire Kang system.

5   ACKNOWLEDGED

6   REFERENCES

Cao, G.Y., et al.,2011, Simulation of the heating performance of the Kang system in one Chinese detached house using biomass. Energy and Buildings. **43**(1): p. 189-199.

Do Ango, A.C.M., M. Medale, and C. Abid, 2013, Optimization of the design of a polymer flat plate solar collector. Solar Energy. **87**: p. 64-75.

Li, G., et al., 2014, Experimental investigation of energy and exergy performance of short term adsorption heat storage for residential application. Energy. **65**: p. 675-691.

Ren, H.G. and G.W. Li, 2013, Structure Updates Chinese Kang Technical Countermeasures. Architecture, Building Materials and Engineering Management, Pts 1-4. **357-360**: p. 2308-2311.

Summers, E.K., M.A. Antar, and J.H. Lienhard, 2012, Design and optimization of an air heating solar collector with integrated phase change material energy storage for use in humidification-dehumidification desalination. Solar Energy. **86**(11): p. 3417-3429.

Sun, W., et al., 2007, Numerical study of performance of Trombe wall with PV cells. Proceedings of Ises Solar World Congress 2007: Solar Energy and Human Settlement, Vols I-V: p. 397-400.

Tian, Y. and C.Y. Zhao, 2013, A review of solar collectors and thermal energy storage in solar thermal applications. Applied Energy. **104**: p. 538-553.

Zhuang, Z., et al., 2009, Chinese kang as a domestic heating system in rural northern China-A review. Energy and Buildings. **41**(1): p. 111-119.

Zhuang, Z., Y.G. Li, and B. Chen, 2009, Thermal storage performance analysis on Chinese kangs. Energy and Buildings. **41**(4): p. 452-459.

SESSION 17: BIOMASS & BIOFUELS

46: Energy valuation of the abattoir waste by co-digestion process: biogas production

MAAMAR FEDAILAINE[1,2], KARIMA MOUSSI[1], SABAH ABADA[1], MERYEM SABER[1]

[1] *Centre de Développement des Energies Renouvelables, CDER, B.P. 62, Route de l'Observatoire, Bouzaréah, Algiers, Algeria, m.fedailaine@cder.dz, k.moussi@cder.dz, s.ababa@cder.dz, m.saber@cder.dz.*
2 Laboratoire de stockage et valorisation des énergies renouvelables, LSVER. Faculté de chimie, USTHB, BP 32 El Alia, Bab Ezzouar, Algiers, Algeria.

Anaerobic digestion is a natural process of organic substrates degradation using bacteria to produce biogas as renewable energy. Further to this clean energy, this process contributes to ensure a sustainable waste treatment process to protect the environment.

The aim of the present work is to study at laboratory scale, the biogas production from co- digestion of fatty acids of slaughterhouse waste and digested sludge from wastewater treatment plant. During this experience, we followed the parameters that influence directly the anaerobic digestion, namely the evolution of pH and the optical density. In addition, a kinetic production of biogas was daily measured. These tests were successful in obtaining the combustible biogas with a high rate of methane

Keywords: *Biomethanisation, anaerobic co-digestion, slaughterhouse waste.*

1. INTRODUCTION

Anaerobic digestion is a natural process of fermentable organic substrates degradation using anaerobic bacteria that produce biogas, which is a mixture of methane and other gas such as (CO_2, H_2, H_2S, NH_3, etc ...).

Organic substrates include a wide variety of wastes derived from human activities (sludge, agricultural and municipal wastes), food transformations (milk, meat,…), etc.

The produced biogas is usually converted to a valuable energy, such as heat and electricity, or purified to reach biomethane (Pöschl et al., 2010) , (Holm-Nielsen et al., 2009) and (Roque et al., 1981).

Slaughterhouse and meat transformation wastes present very interesting substrates regarding their high rate of fatty compounds characterized by a high methane potential. They are usually codigested with other substrates in order to improve biogas production (Holm-Nielsen et al., 2009) and (Roque et al., 1981).

Sheep fats was chosen as a principal substrate to study the methanisation process under specific operating conditions. To simulate a basic biogas installation with a low degree of technology, a non-homogeneous mixing with a temperature gradient were considered at laboratory scale.

Inoculum added to this reactor was a digested sludge taken from an industrial digester for urban sludge treatment. PH, redox potential, optical density, and gas production were estimated during the entire process.

2. MATERIALS AND METHODS

Continuous fermentation process in a 10 L digester with a working volume of 8 L was considered to investigate biogas production under the set operating conditions. Feeding was ensured by introducing the substrate at several time periods.

To increase contact area between the substrate and the liquid, a mechanical mixing with continuous heating of sheep fat and water were considered to initiate previous substrate hydrolysis.

Figure 1: Anaerobic Digester.

Table 1: Principal characteristics of organic load.

Digester	Fats	Digested sludge	Mixture
Quantity introduced in the reactor	250 (g)	167.5 (g)	10 (L)
pH	-	7	7.0
Potential red mix / Ox (m eV)	-	-	-7.2

2.1 Physico-chemical analysis

They focused mainly on pH, red-ox potential which are daily monitored and optical density analyzed at different periods.

It should be noted that the pH is related to hydrogen ions and together with redox potential allow predicting the reactivity of the chemical species.

2.2 Optical density

The optical density is generally correlated with the chemical oxygen demand COD. The absorbance of the various samples with a scanning from 200 to 800 nm have been measured to select the appropriate Wavelength.

Sample are analyzed after filtration, centrifugation (3500 rmp for 5 min) and dilutions (100 µl of the sample in 1900 µl of distilled water). The UV-Visible spectrophotometer used for our analysis is PerkinElmer's LAMBDA 25.

2.3 Biogas production

Quantitative monitoring of the produced biogas is an important step for the optimal use of the co-digestion (digested sludge and fats). Graduated bags with a maximum amount of 2000 ml are used for biogas measurement and storage (Figure 1).

3 RESULTS AND DISCUSSION

3.1 Operating pH
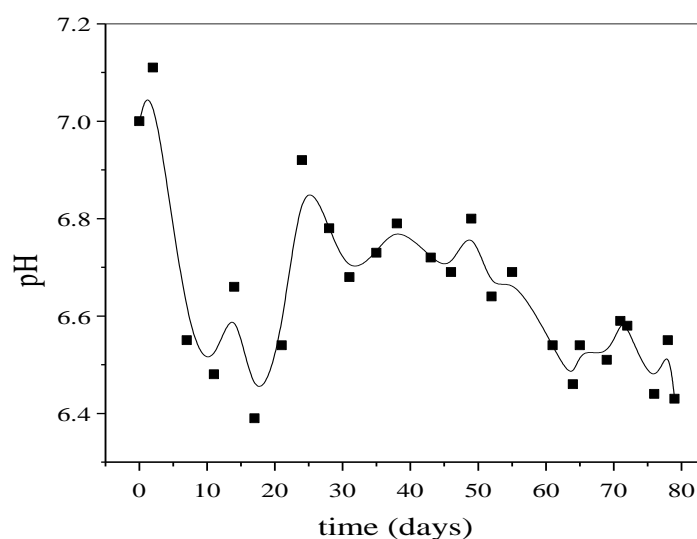
Figure 2: Monitoring pH during the biogas production.

The pH represents a very important indication of a correct global behavior of the digester. If the pH is above 8.5, biogas will be rich in H_2S (Graieb et al., 1988). However, when it is relatively acid, the bacteria will be inhibited (Roque et al., 1981). In our case the pH did not exceed 7.2 (Figure 3), but it has reached a minimum value of 6.39, which illustrates the step of acidogenesis. In this case, the digester does not require any pH adjusting.

Furthermore, the substrate is continuously added to the reactor to ensure bacteria nutrition and at the same time neutralizing the reaction medium.

Figure 3 exhibits a general pH behavior for anaerobic digestion phenomena. The process starts with a decrease in pH values (from 7.1 to 6.39) for the first sixteen days (hydrolysis and acidogenes steps). From the 17 [th] day, it starts to increase to a maximum value of 6.9 until 24 days (acetogenesis and methanogenic). After 24 days, the pH remains between 6.8 and 6.5.

3.2 Oxydo-reduction potential:

Microbial processes were often accompanied by redox reactions, the microorganisms develop chemical energy that they need for their maintenance and growth. In pure culture, methanogens requires low red-ox potential below -300 meV, which indicates the anaerobic fermentation condition (Glauser et al., 1993),(De La Farge et al., 1995) . In a digester in full swing as our case (Figure 3), the potential varies between -50 to 0 meV as indicated by Glauser (Glauser et al., 1983).
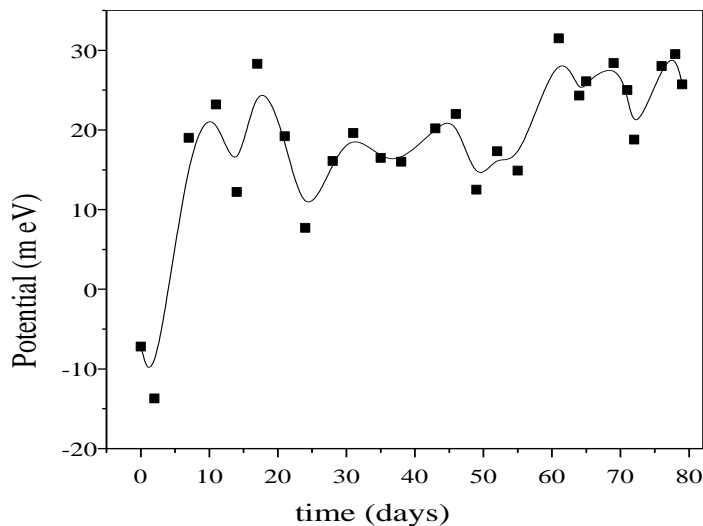
Figure 3: Monitoring of potential in biogas production.

3.3 Measuring the optical density

Figure 4 show the evolution of absorption spectra as a function of time of the anaerobic digestion.
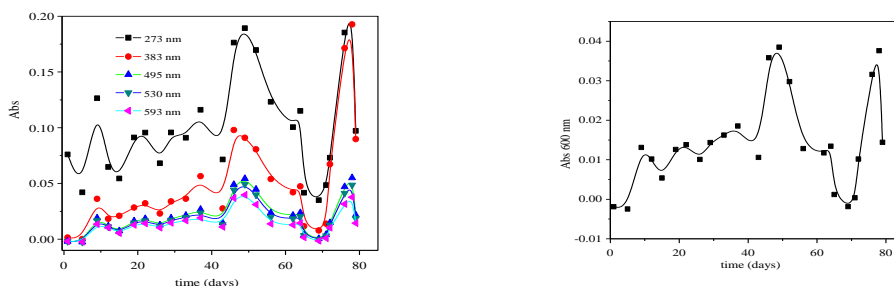
Figure 4: a) optical Plots of OD versus time and at different wavelengths b) Absorbance at 600 nm.

Changes in the optical density at different wavelengths showa low degradation of organic matter that can be due to different parameter as the non regular mixing , temperature and solubility of the grease that are non uniform in the reactor, etc. This may be due also to the continuous feeding of the substrate (each 3 or 4 days).

3.4 Kinetic of gas production
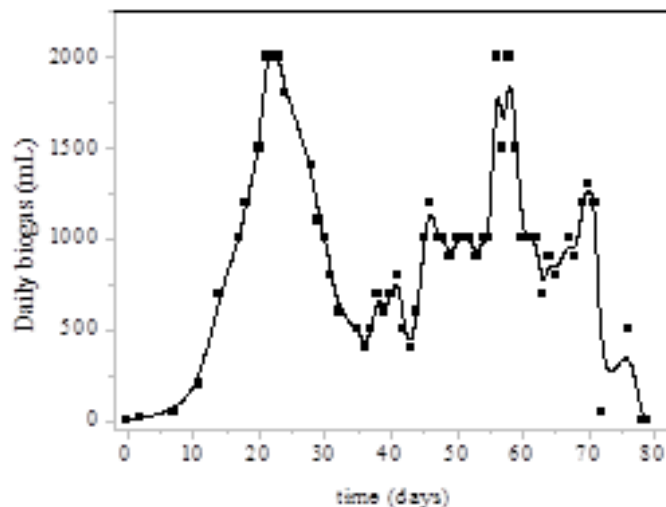
Figure 5: Kinetics of daily gas productivity.

The gas production in the experimental digester increases continuously after 7 days (which corresponds to the latency or hydrolysis step)to reach a stable level of production (2000 ml). This possibly corresponds to the multiplication of bacteria populations and substrate feeding,

3.5 Quantitative gas production
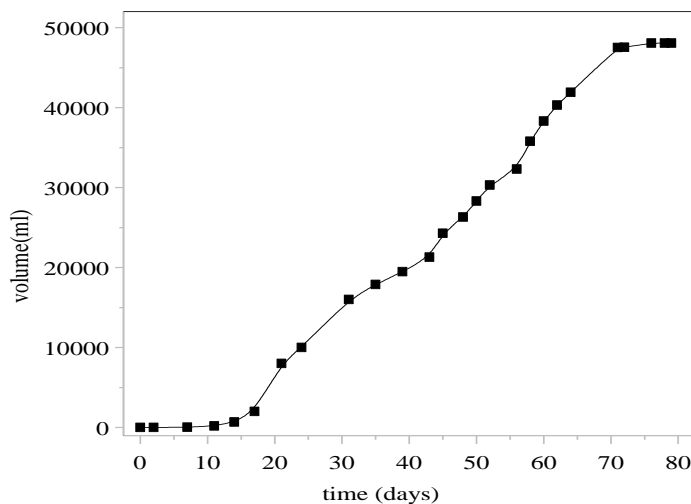
Figure 6: Cumulative quantity produced biogas.

Figure 6 show the evolution of cumulative gas production. For an operating time less than 80 days, the amount of biogas produced is about 49 L.

3.6 The calorific value of biogas

Figure 7: methane flame that confirms the biogas enrichment.

The calorific value of biogas depends on its composition and specifically its methane content (which varies from 50% to 80% for a correct anaerobic digestion). The biogas flammability test illustrated in Figure 7 gives an idea about the energy efficiency of the produced biogas.

4   CONCLUSIONS

In this study biomethanation of fat and digested sludge as inoculum source is investigated under critical operating conditions. It is shown that it is possible to produce about 49 L of biogas during an operating time less than 80 days.

The quantitative gas production is recorded daily and a volume of 2000 ml can be reached after three consecutive days in the optimal production step (between 20 and 25 days).

The biogas flammability test, gave us an idea about the efficiency of the sample used and the methane as major component. A more detailed analysis is however, necessary to quantify the biogas composition and the impact of such as operating conditions.

5   REFERENCES:

PÖSCHL. M., Ward, S., Owende, P., 2010. Evaluation of energy efficiency of various biogas production and utilization pathways. Applied Energy, (87), 3305-3321.

HOLM-NIELSEN. J. B., Al Seadi. T., Oleskowicz-Popiel. P., 2009. The future of anaerobic digestion and biogas utilization. Bioresource Technology, (100), 5478-5484.

ROQUE. H., 1981. Fondements théoriques du traitement biologique des eaux: Traitement anaérobie, Chap. 3-6, 1476-1532.

DE LA FARGE. B.,1995. Le Biogaz procédés de fermentation méthanique. Masson, paris, ISBN : 2-225-84257-4, ISSN : 1248-4806.

GRAIEB. M., 1988. Étude et réalisation d'une installation de méthanisation avec chauffage. Mémoire de Spécialisation, Institut National Agronomique de Tunis, Tunisie.

GLAUSER, M., Membrez, Y.,1993. Association romande pour la protection des eaux et de l'air (ARPEA), Digestion des déchets et effluents industriels et ménagers, office fédéral des questions conjoncturelles, Énergies renouvelable (3003),724.231.

315: Performance and emission profile of micro-algal biodiesel in compression ignition engine

ANDREW C. ELOKA-EBOKA[1], BABATUNDE F. BAKARE [2], CHIEMELA . ONUNKA [3]

[1,] 2 *Faculty of Engineering, Centre for Renewable Energy Research and Waste Management Research Niche Areas, Mangosuthu University of Technology, Umlazi, Durban, South Africa,*
fatherfounder@yahoo.com
3 *Department of Mechanical Engineering, Mangosuthu University of Technology, Umlazi, Durban, South Africa*

Micro-algae are a large and diverse group of simple typically autotrophic organisms which have the potential to produce greater amounts of non-polar lipids and biomass than most terrestrial biodiesel feedstocks. Having emerged as one of the most promising sources for biodiesel production. They are gaining research interests in the current energy scenario due to their phenomenal growth potential (< 21 days log phase) in addition to relatively high lipids production which are also excellent source of biodiesel. In this study, engine performance and emission profile was performed using biodiesel fuels and blends from micro-algal technology in a compression ignition engine. The technology of micro-algae involved open pond cultivation and the use of photo-bioreactor model BF-115 Bioflo/celli Gen made in the US of 14 litre capacity (200 Lux light intensity) and flowrate of 2.5L/min. The micro-algal species used were Chlorella vulgaris and Scenedesmus spp. The biodiesel produced were blended with conventional diesel (AGO) at different proportions. The performance parameters evaluated include: engine power, torque, brake specific fuel consumption (BSFC), smoke opacity, thermal gravimetry, thermal efficiency, exhaust gas temperatures and lubricity while the varying effects of emission pollutants during combustion were also studied. Results showed that viscosity, density and lubricity have significant effects on engine output power and torque than when throttled with AGO which was used as control. Combustion efficiency and emission profile were better than the AGO due to the oxygenated nature of the micro-algal biodiesel which brought about complete combustion. A striking deduction arrived is that oxygen content of the algal biodiesel had direct influence on smoke opacity and emissions in the engine and also thermo-gravimetrically stable for other thermal applications. The engine tests (BSFC, BTE, ThE, MechE, EGT) and overall emissions (CO_2, CO, VOCs, HC, SOx, NOx) were within acceptable limits and comparable with AGO. The implication of the study is that Micro-algal technology is feasible and can revolutionise development in biodiesel industry

. Keywords: emission profile, microalgal technology, biodiesel, compression ignition engine, open pond cultivation, photobioreactor, performance. hybridization, in situ, ex situ

1. INTRODUCTION

There is constant rising worldwide demand for motor and power generation fuels together with environmental concerns in terms of greenhouse gases, climate change mitigation, economic growth and stability and the ongoing depletion of oil reserves. These are all major factors for the development of economically, rational, renewable energy technology platforms [1,2]. Engineers and scientists are therefore motivated to think about various alternative sources of improved energy. The importance of developing CO_2 neutral fuel sources has been highlighted by the detailed modeling of climate change effects, its global and national economic impacts and the increasing competition for fossil fuel reserves [3,4]. Of these, climate change appears to be the most time-constrained driver of renewable energy technology development. This is because a reduction in CO_2 emissions of 25 – 40% by 2020 and 80 – 90% by 2050 is predicted to be required to limit global temperature increases to less than the $2^{o}C$ limit agreed at the 2009 Copenhagen Climate Change Summit [3].

In recent years, a lot of thrusts have been put on the search for the potential biomass feedstock from different sources, which can be converted to liquid as well as gas fuels for energy generation. Various feedstocks have been identified as alternative sources of energy fuels. They range from various kinds of bio-wastes, energy crops (edible and non-edible oil seeds); and recently various aquatic plants identified as bio-oil sources. As a result, interests have been arisen on the possibilities of using algae as a source of bio-oil and bio-gas for energy applications [5].

Algae are basically a large and diverse group of simple, typically autotrophic organisms, ranging from unicellular to multi-cellular forms. These have the potential to produce considerably greater amounts of biomass and lipids per hectare than any kind of terrestrial biomass [5]. As these can be cultivated on marginal lands, therefore do not compete with food or other crops. Algae can be cultivated photo-synthetically using sunlight for energy and CO_2 as a carbon source. They may be grown in shallow lagoons or raceway ponds on marginal lands or closed ponds. Plastic tubes in ponds offer up to seven times the productivity of open ponds. A number of closed photo-bio-reactors have been investigated for cost effective production of the algae [5]. The commercial viability of algae-based biofuels production shall eventually depend on economics of the technology. Regardless of whatsoever advances might come in terms of technological and biological innovations, the hard fact remains that the commercial marketplace shall have an enthusiasm for funding capital intensive energy projects, by ensuring the risk-return ratio to the acceptable stratum for debt and equity financiers.

Microalgae feedstocks are gaining interest in the present day energy scenario due to their fast growth potential coupled with relatively high lipid, carbohydrate and nutrient contents. All of these properties render them an excellent source of biofuels such as biodiesel, bioethanol, and bio-methane; as well as other products. A critical evaluation of available information suggests that the economic viability of the production process in terms of minimizing the operational and maintenance cost along with maximization of oil-rich microalgae production is the key factor, for successful commercialization of algae-based fuels. The engine performance test of produced biodiesel from species of microalgae was conducted in this study. In evaluating the performance of the produced biodiesel in an internal combustion engine, certain chemo-physical properties were evaluated. But it is beyond the scope of this present study.

1.1 Biodiesel as a Diesel Engine Fuel

Diesel engines produce mechanical power from conversion of the chemical energy contained in the fuel. Energy is released by the combustion and oxidisation of the fuel inside the engine. The fuel-air mixture prior to combustion and the products from combustion are the working fluids. The boundary work which provides the desired power output occurs directly between these working fluids and the mechanical components of the engine [6]. Since the advent of the diesel-powered engine, compression ignition engine technology has been under continuous development. However, the basic components of the engine (Figure 1) have been unchanged, with the main difference between a modern day engine and its predecessor being its combustion performance [7].

Biodiesel can be used in modern diesel engines in its pure form (B100), or blended with petroleum diesel in any ratio [8]. There is an increasing body of literature reporting on research into diesel engine performance and engine emissions when fuelled with biodiesel. The schematic in Figure 1 describes the combustion, exhaust and fuel feed/injection systems of the diesel engine. The diesel (compression-ignition) engine is an internal combustion engine in which ignition of the fuel that has been injected into the

combustion chamber is initiated by the high temperature which the diesel achieves when greatly compressed. This is called adiabatic compression. It has the highest efficiency of any standard combustion engine because of very high compression ratio achievable and also inherent lean burn that allows for heat dissipation by excess air which is very much available in biodiesel than conventional AGO due to high oxygenated nature which allows for complete combustion with lower exhaust elimination [9]. The fuel injection system contains feed pumps and filters, fuels tanks to account for low pressure and temperature maintenance at levels below flash points of the fuel. Biodiesels generally possess high flash points as one of its advantages.
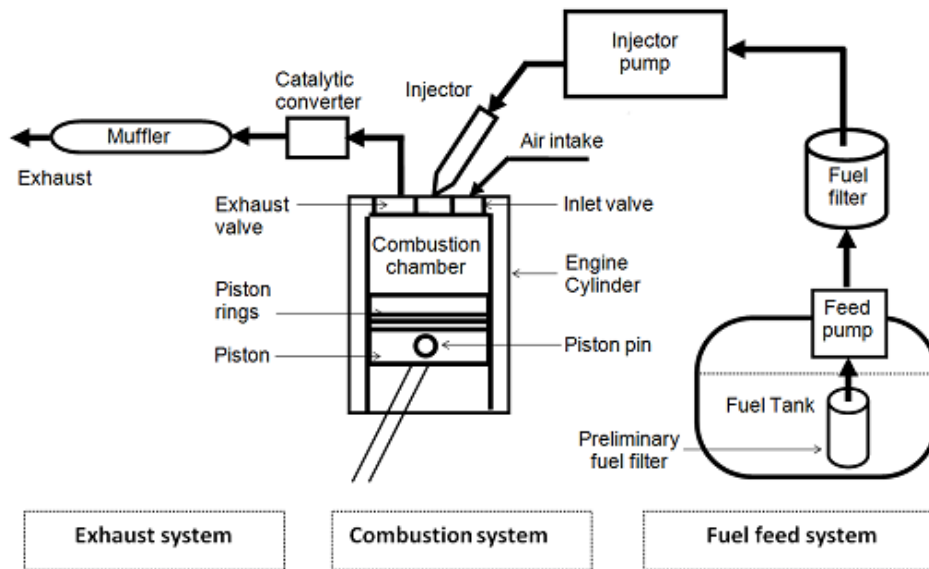
Figure 1: Schematic diagram of a typical diesel engine fuel system

1.2 Engine performance

Diesel engine performance parameters evaluated with biodiesel fuels in literature typically includes engine power, torque, brake specific fuel consumption (BSFC), thermal efficiency, and exhaust gas temperature (Table 1). While illustrating the effect of biodiesel on engine power and/or torque, it is commonly argued that biodiesel drops engine power and torque. This is mainly due to the lower heating value of biodiesel compared with petroleum diesel. [10] ran a four-cylinder diesel engine with waste frying oil methyl ester (WFOME), varying the engine speed from 1750 to 4400 rpm. They found on average a 4.5% and 4.3% reduction in power and torque respectively. Similar results have been reported in many other studies, with some fluctuations in the reduction percentage. Some of these studies are summarized in Table 1.

Studies found that the loss of power was 7.14% for biodiesel when compared to diesel on a three-cylinder, naturally aspirated (NA) submarine diesel engine at full load, yet the loss of heating value of biodiesel was about 13.5% when compared to diesel [11-13]. Hansen et al. [12] observed that the brake torque loss was 9.1% in biodiesel at 1900 rpm as the results of variation in heating value (13.3%), density and viscosity. Findings from these studies confirm that the lower heating value of biodiesel is not the only factor which influences engine power and torque. Other biodiesel fuel properties including viscosity, density and lubricity have significant effects on engine output power and torque. For instance, higher viscosity of biodiesel improves air-fuel mixing by enhancing spray penetration, and thus recovery in power and torque when compared to diesel [14,15]. Higher viscosity can also reduce engine power by decreasing combustion efficiency due to poor fuel injection atomisation [16]. On the other hand; the higher density of biodiesel improves engine power and torque. Moreover the high lubricity in biodiesel may result in reduced friction power loss, and this will subsequently recover engine output power and torque [17]. Therefore, it is not surprising that some studies have reported increased power and torque from engines when running on biodiesel; power and torque increased with an increase in biodiesel percentage in blends while running an engine. Usta [18] also found similar results when using tobacco seed oil in a four-cylinder turbo-charged diesel engine.

Furthermore, negligible variation in engine power and torque between biodiesel and petroleum diesel has also been found [19]. More interesting results have been reported by Haşimoğin et al. [20] while using

waste cooking oil biodiesel in a four-cylinder turbo-charged diesel engine operating between 1100 and 2800 rpm. This study found lower engine torque and power at lower engine speeds (1100 to 1600 rpm) while power and torque increased at medium and high engine speeds. However, Carraretto et al. [21] has overcome the power loss of biodiesel engine by optimising biodiesel combustion through reducing the injection advance. It is therefore evident that power and torque developed in biodiesel engines is not only dependent on feedstock and fuel properties, but also on the engine type and operating conditions, such as engine speed, load, injection timing and injection pressure. Similar correlations have been found in the literature for other performance parameters such as brake specific fuel consumption, thermal efficiency, exhaust gas temperature and combustion characteristics [13, 16, 22].

1.3 Exhaust Emissions

Combustion chemistry in internal combustion engines (ICE) is very complex and depends on fuel types and operating conditions. In the combustion chamber, hydrocarbon reactions are generally grouped into three distinct steps.

Table 1: Performance and emission of diesel engines with biodiesel

Fuel Type	Engine	Test condition	Increase/Decrease Vs AGO (diesel) (↓↑)									
			Power	Torque	BSFC	BTE	EGT	CO	CO_2	NOx	PM	HC
Soybean	IC	1400-2000rpm	↓	↓	↑			↓		↓		↓
Cottonseed	IC	850rpm			↑	↓		↓		↑	↓	
Sunflower	IC	1000-3000rpm	↓	↓	↑	↓	↓	↓		↓		
Waste Cooking	4C	1750-4400rpm	↓	↓	↑			↓	↓	↓		
Cottonseed	4C	1500rpm	↓	↓	↑	↓		↓	↓	↑	↓	
Sunflower	4C	1100-2800rpm	↓	↓	↑	↓	↑				↓	
Soybean	4C	1400rpm	↓	↓	↑	↓	↓	↓		↑	↓	↓
Waste cooking	4C	800-1400rpm	↓	↓	↑	↑	↓		↓	↑		
Waste cooking	IC	1400-200rpm	↓	↓	↑	↓	↓		↓	↑		
Mahua	4C	1600rpm			↑	↓	↑		↓	↑		
Tobacco	4C	1500-300rpm	↑	↑		↑	↓	↓		↑		
Rapeseed	4C	1200-2400rpm	↑	↑				↓		↑		
Cotton seed	IC	1200-2500rpm	↑	↑		↑	↓	↓		↑		

Source: Jahirul *et al.* (2013).

The first step is the breakdown of hydrocarbons; the second step is the oxidation of hydrocarbons and hydrogen; the third step is the oxidation of combustion reaction products. The exhaust gas from diesel engines contains many components including carbon dioxide (CO_2), carbon monoxide (CO), hydrogen (H_2), oxygen (O_2), sulphur oxides (SOx), unburned hydrocarbons (HC), particulate matter (PM), and nitrogen oxides (NOx). These pollutants have various potential adverse health and environmental effects. Numerous studies have been conducted to investigate the effect of biodiesel on exhaust emissions in diesel engine applications. The emission parameters investigated include carbon dioxide (CO_2), carbon monoxide (CO), hydrocarbon (HC), nitrogen oxides (NOx), sulphur oxides (SOx) smoke, particulate matter (PM). Most of the studies found a sharp reduction in all exhaust emissions when biodiesel was used was compared with petroleum diesel fuel (except NOx). However, a reduction in NOx in biodiesel use has also been reported in some other literature. In general, biodiesel contains about 10% oxygen by mass, while diesel has little to no oxygen. Biodiesel fuels result in more complete combustion and thereby reduces exhaust emission, and various researchers have postulated reasons for this outcome. The percentage change in emissions varies amongst these studies. The variety of results reported can be attributed to variations in the fuel properties and chemical structure of the biodiesels used, varying feedstocks and due to the variety of engines used in tests. For example, Lin et al. [24] conducted an experiment with biodiesel from eight different feedstocks and found a significant reduction in PM emissions (50 – 73%). While conducting experiments with coconut, jatropha and rapeseed oil biodiesel, Lance et al. [25] showed that rapeseed oil biodiesel tended to give amongst the highest NOx emissions. Similarly, variations in emissions from biodiesels using different feedstocks have been reported in many other recent studies [26-28]. Monyem and Gerpen [15] found that oxidized biodiesel can significantly reduce emissions while investigating the effect of biodiesel oxidation on

diesel engine emissions. This study found that oxidized biodiesel resulted in approximately 15% less CO emissions and 21% less HC emission when compared with un-oxidized biodiesel.

1.4 Interest in Microalgae

The interest has always been to utilize eukaryotic algae for the renewable production of several bio-energy carriers, including starches for alcohols, lipids for diesel fuel surrogates, and H_2 for fuel cells. Relative to terrestrial biofuel feedstock, algae can convert solar energy into fuels (chemical energy) at higher photosynthetic efficiencies, and can thrive in salt water systems [5]. Photosynthesis is the fundamental driving force that supports all biofuel synthetic processes, converting solar energy into biomass, carbon storage products (such as carbohydrates and lipids which is the building block of fats and oil) and/or hydrogen [29].

There are already major problems of air pollution resulting from CO_2 evolution and future crisis of energy due to shortage of energy sources in the world. Greenhouse gas emissions and fossil fuels combustion are calamities that have bedevilled our environments. Energy requirements are increasing continuously, because of increases in industrialization and population. The basic sources of this energy are petroleum, natural gas, coal, hydro and nuclear. The major disadvantage of using petroleum based fuels is atmospheric pollution created by the use of petroleum diesel. Petroleum diesel combustion is a major source of greenhouse gas (GHG). Apart from these emissions, petroleum diesel is also major source of other air contaminants including NOx, SOx, CO, particulate matter and volatile organic compounds (VOCs). Biomass is one of the better sources of energy. The burning of enormous amount of fossil fuel has increased the CO_2 level in the atmosphere, causing global warming. The use of microalgae as a source of biofuel production has gained enormous research interests. Microalgae are able to photosynthetically convert carbon dioxide into potential biofuel feedstocks, as well as food, feeds, and high value bio-actives [30]. Micro algal crops, unlike other oil crops, are able to grow extremely fast and can double their biomass within a period of 24 h [30, 31]. Algalogy and similar studies are presently dominating studies biodiesel at the moment.

2. METHODOLOGY

2.1 Biodiesel production from Microalgae

Samples of *Chlorella vulgaris*, *Scenedesmus obliquus*, *Senechococus spp* and *Duneliella spp.* that have been prepared and stored as innocula in the laboratory controlled conditions were cultivated in an open pond of plastic tank, 850L capacity and in a photobioreactor of 14L. In the both methods, nutrient (broth agar) were inoculated and allowed to grow for 21 days. The accumulated biomasses on harvest were subjected to solvent extraction of its lipids. The extracted oils were converted to algal biodiesel by transesterification process. Simple transesterification approach adopted was: settling up for solvent recovery after oil extraction: saponification reagent (SR) (methanol: H_2O at the ratio of 1:1, methylation reagent (MR) (3.25 of 6 M HCl: 2.75 methanol) and extractive reagent (ER) (Hexane: diethyl ether at the ratio of 1:1 were deployed. The biodiesel was used to power a four stroke diesel engine TD 300.

2.2 Engine Performance Test/Analysis

The engine test performance and emission analysis test was conducted at the Biofuels laboratory of the Petroleum Processing Engineering Technology of Petroleum Training Institute, Effurun, Nigeria. TD 300, a versatile engine test bed with instrumentation for comprehensive investigations into the features and operating characteristics of internal combustion engines was used for the study at the petroleum Training Institute. It enables a wide range of investigations into the characteristics of four-stroke single-cylinder petrol and diesel engines. It is for use with engines up to 10 kW: four-stroke diesel and four-stroke petrol engines (available separately). It is a versatile regenerative engine test set with comprehensive controls and instrumentation. The equipment is fully compatible with TecQuipment's Versatile Data Acquisition System (VDAS, available separately). Using VDAS enables accurate real-time data capture, monitoring and display, calculation and charting of all relevant parameters on a computer (PC available separately) making tests quick and reliable. The main components of the system are: a heavy fabricated floor-mounting bed, an instrument console with instrument frame, a fuel tank support frame that supports the fuel tank and optional fuel gauge. The bed is held on anti-vibration mounts. It includes a robust trunnion-mounted DC machine. An electronic load cell connected to the machine measures the driving torque of the test engine. Each engine includes a colour-coded fuel tank with self-sealing couplings. The couplings ensure the

engines can be connected and disconnected quickly and efficiently with minimum loss or spillage of fuel. For convenience and safety, the fuel tank can be removed for filling or for storage. The control console has an electrical cabinet which houses a four-quadrant drive to start and load the engine. The motor can also be used to drive the engine while the fuel and ignition are off, so that frictional losses can be established. The control console includes an air-box and orifice plate to measure air flow. The instrumentation and display units are mounted on a sturdy frame, which is part of the control console. The control console also includes a convenient work top for use as a writing desk, or for positioning other equipment such as a computer (computer not included). The control console and test bed are separate in order to avoid vibration being transmitted from the engine to the measuring devices. In addition, it allows the instrumentation to be thermally and acoustically screened from the test bed, using suitable shielding or a wall. The engines (available separately) include an exhaust thermocouple, dynamometer coupling, colour-coded fuel tank, hoses and fittings. They also have modified cylinder heads and cranks for connection to TecQuipment's Engine Cycle Analyser (ECA100 available separately). An Exhaust Gas Calorimeter (TD300a) is also available to enable students to measure energy lost through exhaust gases and to determine the energy balance of the engine.

In the performance experiment, the following were tested, analyzed and recorded: torque, exhaust temperature, low and high speeds, specific fuel consumption, engine flue gas emissions, O_2, CO_2, VOCs and NOx; smoke opacity using smoke meter and vibration. Having powered the diesel engine for 30 minutes of continuous run using the AGO (conventional diesel) to stabilize it, the engine was put to a hold, drained off of the AGO and ready for testing. Samples of biodiesel and blends, experimental AGO were measured out using measuring cylinder. 1000mls of each sample were poured into sample bottles. They were intermittently poured into the storage tank of the diesel engine which was modified to suit the purpose of the test. A standard 1000ml container was constructed for use as fuel tank and was directly connected to the injector combustion chamber so that precise data will be collected without difficulty and ran for 40 minutes for each sample. A total of 15 samples and AGO were ran and tested for the parameters already established. All the biodiesel and samples were able to power the engine creditably well without any aorta of difficulty. The speeds (rpm) were measured for each sample at different temperatures and time; using the rated power of the engine and the power-torque-speed relationship, the torque at different speeds were determined.

The relationship is given as P = 2πrpm (1)
Where, P = rated power; π = 3.142; rpm = number of revolutions in rpm; T = torque.

At the start of each test the test engine was operated with base fuel-diesel for about 30 minutes to attain a normal working temperature condition after that base line data were generated and the corresponding results were obtained. At every operation the engine speed was checked and maintained constant. All the measurements were repeated thrice, and the arithmetic mean of these three readings was employed for calculation and analysis. The different performance and emission parameters analyzed in the present investigation were brake thermal efficiency (BTE), brake-specific fuel consumption (BSFC), exhaust gas temperature (EGT), carbon monoxide (CO), carbon dioxide, unburned hydro-carbons (HC), nitrogen oxide (NO), and smoke.

3. RESULTS

Table 2: Physico-chemical Properties of Biodiesel of produced microalgal oil

Microalgal biodiesel	EC (wt %)	CN	SV (MgKOH)	IV (gl$_2$ 100g^{-1})	DU (wt %)	LCSF (wt %)	CFPP (ºC)
Chlorella vulgaris (BA1)	99.8	56.7	225.1	65.4	74.1	6.7	4.4
Scenedesmus (BA2)	99.8	56.1	217.5	65.0	67.8	11.9	20.4
Dunelliela (BA3)	99.8	52.2	220.8	83.6	98.0	2.6	-8.5
Synechoccocus (BA)	99.8	54.6	217.9	68.2	52.7	6.6	4.3

EC: ester content; CN: cetane number; SV: saponification value; DU: degree of unsaturation; LCSF: CFPP: Cold filters clogging point.

Table 3: Gaseous emission characteristics of biodiesel

Algae Biodiesel	CO_2 ($\mu g/m^3$)	NOx (ppm)	CO (ppm)	SOx (ppm)	SPM ($\mu g/m^3$)	HC (%)	VOC (%)	Toluene (ppm)	Benzene (ppm)	Ethyl Benzene (ppm)	Xylene (ppm)
AGO	22.6	178	35.8	200	224	171	114	11.14	30.96	30.84	5.79
BA1	19.87	137	10.22	163	131	93	138	6.21	10.13	13.84	15.77
BA2	19.88	136	10.14	159	128	91	133	7.84	10.26	15.09	15.77
BA3	19.87	133	10.12	156	128	86	121	7.93	10.29	15.62	15.80
BA4	20.03	121	9.65	153	128	79	110	7.94	11.12	20.16	15.83
B20	20.14	105	8.74	128	103	53	64	20.13	33.68	39.36	21.31

Table 4: Engine exhaust emissions of algal biodiesel and AGO

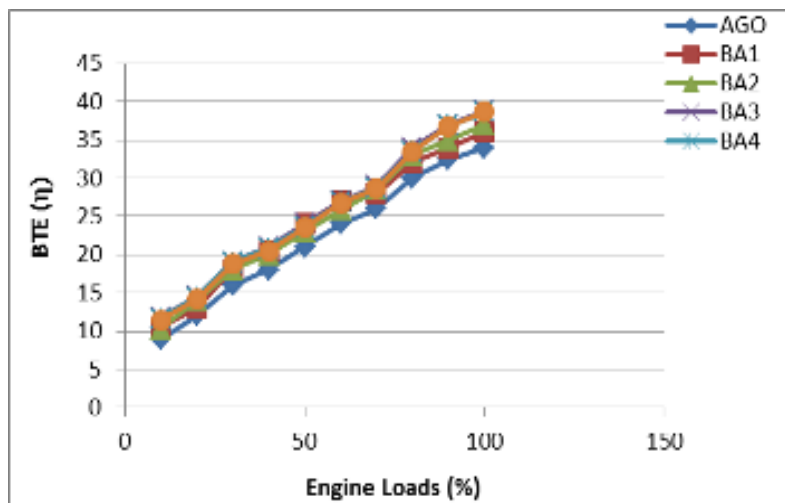| Algae Biodiesel	CO (ppm)		SOx (ppm)		HC (ppm)		NOx (ppm)		VOCs (ppm)	
Engine Load	50 (%)	100(%)	50(%)	100(%)	50(%)	100(%)	50(%)	100(%)	50(%)	100(%)
AGO	0.035	0.018	150	200	171	220	420	660	1.85	3.4
BA1	0.018	0.009	110	140	80	84	435	678	0.50	0.85
BA2	0.020	0.012	115	146	78	85	438	682	0.50	0.88
BA3	0.0209	0.0119	116	148	76	87	436	680	0.51	0.89
BA4	0.0208	0.0118	117	150	75	88	436	681	0.51	0.89

Figure 2: Effects of engine loads on the brake thermal efficiency
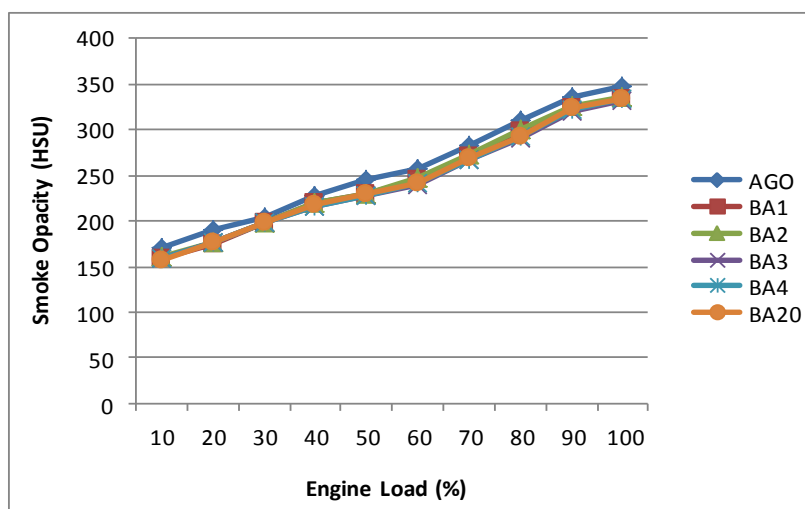
Figure 3: Effects of engine Loads on smoke density
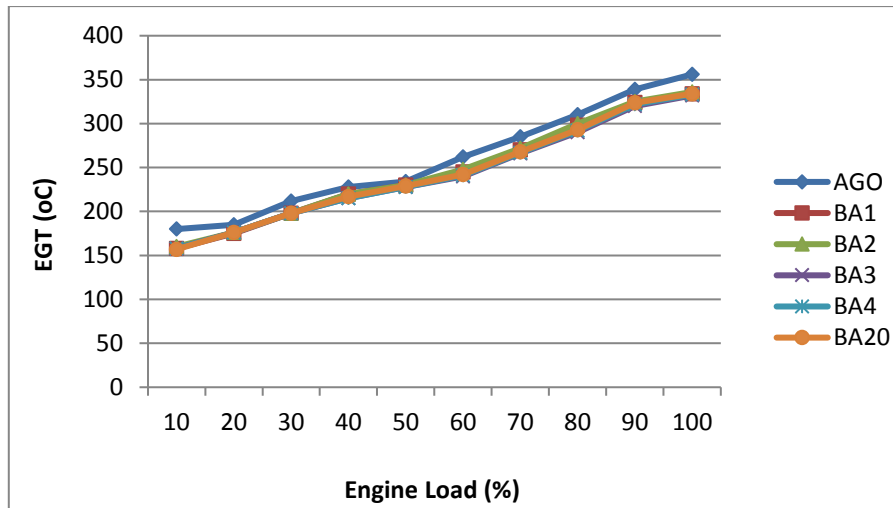
Figure 4: Effects of engine loads on exhaust gas temperature
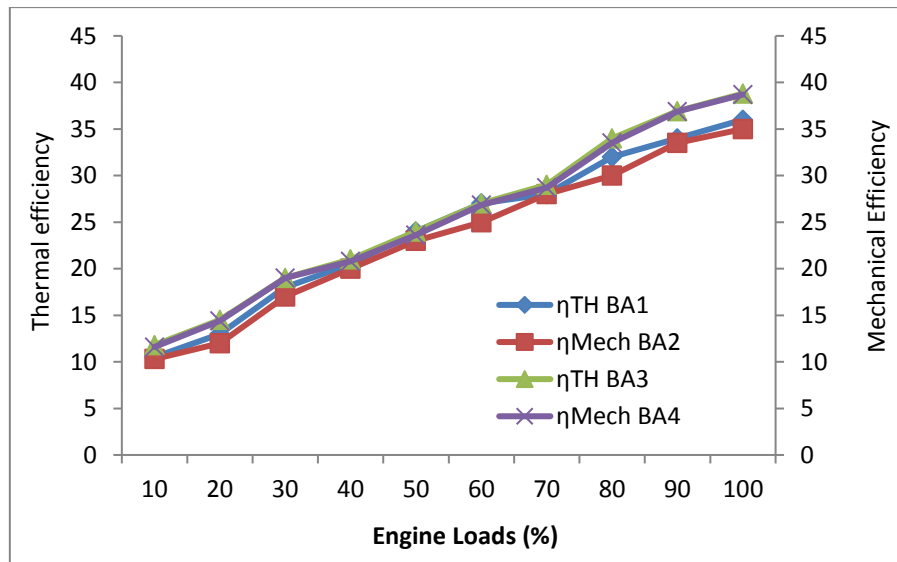
Figure 5: Effects of engine loads on thermal and mechanical efficiencies

Table 5: Engine emission and performance of AGO for comparison

Speed (rpm)	Torque (Nm)	Temperature (° C)	Time (mins)	CO (ppm)	NO_2 (ppm)	VOCs (ppm)	O_2 (ppm)
1000	6.9	73	5	36	7.8	0.9	19.2
1200	5.8	74	10	40	9.0	1.1	19.4
1400	4.9	92	25	47	13.7	1.6	19.6
1600	4.3	101	20	47	15.7	2.0	19.8
1800	3.8	105	30	53	16.5	2.2	19.9
2000	3.4	107	40	58	18.2	2.4	20

4. DISCUSSION

4.1 Engine Performance Test and Emissions

This section discusses general information on the engine performance tests and gaseous emission (from gas emission analyser) experimented in the compression ignition engine and some chemo-physical properties as presented in Tables 2, 3, 4, 5 and Figures 3 to 5. Biodiesel usually contains higher CO_2 emission than AGO and it is observable in in this study. Of particular interest is NOx which is expected to be higher in the algal biodiesel than AGO, but incidentally was not very high in the case of this study. Generally, the fatty acid composition of biodiesel which contains both (saturated and polyunsaturated fatty acids) is the main index that determines its interaction/behaviour in the engine. Also the ester content (EC),

Cetane number index (CN), saponification value (SV), iodine value (IV), degree of unsaturation (DU) and cold filter clogging points as indicated in Table 2. Even though polyunsaturated fatty acids produce more NOx than saturated fatty acids, but in this case a balance in composition was observed between saturation and poly-unsaturation which may be responsible for the low NOx levels. PM, HC and CO emission is independent of the feedstock of the biodiesel. Aromatic pollutants in biodiesel generally have lower emission compared to AGO, although emissions of benzene and several other VOCs sometimes increase as have been reported. The specific fuel consumption (SFC), specific fuel consumption rate (SFCR), brake thermal efficiency (BTE) are quite lower in AGO than in the algal biodiesel and blends by about 5% - 31% as the speed increases. At elevated temperatures, the performance of the engine improves with relatively better burning of fuel resulting in decreased CO in all the biodiesel even though similar characteristics was not noticed in AGO performance. Oxygen content in biodiesel had direct influence on smoke opacity. The smoke density was noticed to be reduced as the temperature increases in all the fuels samples (biodiesel, hybrids and AGO) but with higher densities in AGO. This and other trends are mainly due to the presence of internal availability of oxygen in the biodiesel and neat burning of fuel at elevated temperatures. Chemo-physical properties are indispensable indicators for the performance of biodiesel and once they fell within the ASTM limit will have significant performance and less emission which are biodegradable, non-toxic and environmentally friendly. Individual emissions and engine performance results are discussed subsequently.

4.2 Carbon (II) oxides (CO) and carbon (IV) oxides

Table 4 presents the emissions of carbon monoxide and carbon (IV) oxide pollutants from algal biodiesel and blends and AGO from the CI engine during performance testing at constant maximum speed of 2000rpm and at 100% load; Table 49 brings out the emissions of carbon (II) oxides across different speeds (1000, 1200, 1400, 1600, 1800 rpms) and engine torques (range of 3.4 to 6.9 Nm) at different exhaust temperatures using AGO as control while Table 50 displays the emission at 50% and 100% loads for all the biodiesel fuels, blends and hybrids. Figure 45 is the effects of engine speeds on the emissions of CO. AGO recorded the highest CO and CO2 emission all through the performance tests (22.6ppm) and (35.8µg/m3) measured separately at different units respectively. All the biodiesel were quite lower than the AGO. This can be accounted for by the usual complete combustion of highly oxygenated biodiesel during combustion than the AGO (Monyem and Van Gerpen, 2001; Monyem et al 2001; Agarwal, 1999). It is the major advantage of using biodiesel as fuels. Lower gaseous emission, environmental friendliness and biodegradability are all important characteristics. Biodiesel generally atomises during combustion due to the presence of methyl chain of the alcohol used during transesterification and so produces lesser CO_2 and CO (Agarwal, 1999). The effects of these emissions on engine and vice versa further explains this with a sharp disparity between emissions from biodiesel and AGO. Biodiesel fuels are also carbon neutral fuels and so its contribution to carbon emission is quite minimal.

4.3 Nitrogen Compounds (NOx)

Tables 2 and 3 present the emissions of nitrogenous compounds (NOx) pollutants from studied biodiesel, blends and hybrids and AGO from the CI engine during performance testing at constant maximum speed of 2000rpm and at 100% load; Table 49 brings out the emissions of carbon (II) oxides across different speeds (1000, 1200, 1400, 1600, 1800 rpms) and engine torques (range of 3.4 to 6.9 Nm) at different exhaust temperatures using AGO as control while Table 50 displays the emission at 50% and 100% loads for all the biodiesel fuels, blends and hybrids. AGO recorded the highest NOx emission all through the performance tests (22.6ppm) and (18.8µg/m3) respectively. All the biodiesel samples were quite higher than the AGO. The reason for high NOx formation at the exhaust of biodiesel than AGO is NOx formation from atmospheric nitrogen is highly dependent on the temperature, which is due to high activation energy needed for the reactions involved, and these reactions are determined by the equivalence ration, oxygen concentration and combustion temperature as well. The extra oxygen available in biodiesel causes increase in local temperature in the combustion chamber together with higher viscosity, density and bulk modulus, higher cetane index. These also affect the injection and combustion behaviour of the fuel. Most researchers have also reported increments in NOx from biodiesel (Monyem and Van Gerpen, 2001; Monyem et al 2001; Agarwal, 1999). From the present study and other studies, the NOx is the single most critical increasing emission exhibited by biodiesel due the established reason and implication so far adduced. Table 3 presents the emissions of SOx pollutants from studied biodiesel, blends and hybrids in comparson with AGO from the CI engine during performance testing at constant maximum speed of 2000rpm and at 100% load, AGO recorded the highest sulphur oxides emission all through the performance tests (200ppm) against the emissions of the biodiesel (<< 180ppm) respectively. These are contained in the exhaust diesel system and can cause adverse health effect (Igbum et al. 2014). Sulphur compounds are acidic and can cause corrosion of tail pipes. Biodiesel however is preferable in this case because, the emissions are quite

minimal. Not much could be discussed about the emissions of sulphur compounds as they are not very common or critical pollutant. Most literatures have rarely addressed its contribution as an exhaust gas emission.

4.4 Hydrocarbons (HC, VOCs, PAHs)

Table 2, 3 and 4 presents the emissions of hydrocarbons (HC) pollutants from algal biodiesel and blends with AGO from the CI engine during performance testing. Hydrocarbon (HC) emissions may include VOCs, PAHs and others (toluene, benzene, methyl benzene, xylene at trace levels). Diesel particulates can be characterized in terms of specific metals, elemental carbon, and organic compounds. However, it is not practically possible to speciate all organic hydrocarbons, which may number in thousands. The main source of HCs in engines is due to the incomplete combustion caused as a result of bulk quenching of flames in a fraction of the engine cycles where combustion is especially slower (Agarwal, 1999; Ramadhas et al. 2005). AGO therefore recorded the highest HC emission (very high) of HCs all through the performance tests (171ppm at 50% load and 220ppm at 100% load) and (18.8µg/m3) respectively while biodiesel samples were between 70 and 86ppms at 50% and 100% loads. Engine loads did not have any significant effects on the HC emission from biodiesel unlike those from the AGO. The VOCs from AGO which are very toxic are quite significant (1.83ppm at 50 % load and 3.4ppm at 100% load). Biodiesel and hybrids produced insignificant VOCs which are quite below toxicity levels. Soot formation is also linked to the formation of VOCs because the emission mechanism for synthesized organic compounds links to the mechanism of soot formation which is also by the presence of NOx.

4.5 Effect of Loads on Engine Power, Torque and Efficiencies

The effects of engine loads on brake thermal efficiencies of the algal biodiesel and AGO were evaluated in this study (Figures 2, 3, 4 and 5). Brake thermal efficiency is the ratio of brake power output to power input. It increased as the percentage of engine loads increased in all the samples (algal biodiesel with AGO) but the level of increase is lowest in AGO. Brake thermal efficiencies rise from lower to higher load level. It is because of higher power output or work done at high load level which makes for higher brake thermal efficiency. Efficiencies of 100% Algal biodiesel were approximately higher than in AGO with (η = 9 at 10% load which later peaked to 35 maximum at 100% load); BA1 and BA2 performed at efficiency of 12 at 10% load and also peaked to η = 40). Other algal biodiesel efficiencies were between η = 10 to 12 at 10% loads up to 35 at 100% load. The reason is that algal biodiesel has higher efficiency of combustion ll. Biodiesel from algae, therefore, may account for better combustion and therefore they have better energy conversion rate compared to diesel fuel. Variations in heating values, density and viscosity clearly influence engine torque and power. Biodiesel with lower heating values, densities and higher lubricity has significant effects on engine power and torque. Although, biodiesel has slightly higher density than petroleum diesel, it contains slightly less energy on a volumetric basis. This has been shown to result in a slight loss of engine power. Higher viscosity in biodiesel improves air-fuel mixing by enhancing spray penetration and homogenization in the combustion chamber and therefore greater recovery in power and torque when generally compared to fossil diesel (AGO). Oner and Altun, 2009 observed same in their study of biodiesel and blends in four stroke engine. In the case of this study, the response was closely comparable to AGO meaning that algal biodiesel has better biodiesel performance than other first and second generation feedstocks. It is therefore evident that power and torque generated in biodiesel engines is dependent on feedstock and fuel properties. Higher viscosity can also reduce engine power by decreasing combustion efficiency due to poor fuel injection atomisation (Aydin and Bayindir, 2010). On the other hand, the higher density of biodiesel improves engine power and torque. Moreover the high lubricity in biodiesel may result in reduced friction power loss, and this will subsequently recover engine output power and torque (Ramadhas *et al.* 2005). Therefore, it is not surprising that some studies have reported increased power and torque from engines when running on biodiesel.

4.6 Effects of Engine Loads on Smoke Density

Biodiesel from algae being highly oxygenated contains higher concentrations of oxygen which will allow faster and more complete combustion compared to fossil diesel fuel and this no doubt influences the amount or density of exhaust smoke to be released to the environment from the compression ignition engine. This is the trend observed in this study. In Figure 3, fossil diesel (AGO) produced higher smoke density (between 148 to 385 HSU (Hattridge Smoke Unit)) than all the algal biodiesel as the engine loads increased from 10 to 100%. All algal biodiesel samples produced very close density of smoke amongst themselves (between 120 to 350 HSU) lesser than AGO. The reason for this result is that in the diesel combustion process, some of fuel droplets may never vaporize, and thus, never burn. But the fuel does not

remain unchanged; the high temperatures in the combustion chamber cause it to decompose. Later, these droplets may be partly or completely burned in the turbulent flame. If they are not completely burned, they will be emitted as droplets of heavy liquid or carbon particles (Agarwal, 1999). The conversion of fuel to particulate matter is most likely to occur when the last bit of fuel is injected in a cycle, or when the engine is being operated at high speed and high load. At higher speeds and loads, the total amount of fuel injected increases and the time available for combustion decreases resulting in higher smoke emission. Also, fuel rich region or no enough oxygen and mistimed fuel injection can substantially increase PM or smoke emission. These limitations are more obtainable in AGO than algal biodiesel because of its lean oxygen availability. The smoke emission in biodiesel fuels varies with the oxygen content of the fuel and the more oxygen content in the fuel, the less the smoke emission. In the case of algal biodiesel, they are nontoxic and biodegradable; over 90% of it will degrade within 28 days in soil or water (Chuk, 2007), and this biodegradability of biodiesel in natural environment makes it an attractive fuel.

4.7 Effects of Engine Load on Exhaust Gas Temperature

The ignition delay is a symbol of ignition ability of a fuel. The shorter ignition delay means the better ignition ability. From the experimental results, the ignition delays of methyl ester (algal biodiesel) fuels are shorter than that of the diesel fuel at every load levels in Figure 4 which clearly brought about the increase in the temperature of the exhaust gas. From this result, it can be said that the ignition abilities of biodiesel fuels are better than that of the diesel fuel. Comparing the ignition ability of biodiesel fuels and AGO, this inference is matching with the cetane number index which presented higher cetane index for all biodiesel samples thereby conferring on them higher degree of ignition quality. CN is one of the main indicators of the ignition quality and combustion smoothness in diesel engines. It is a dimensionless descriptor for the ignition delay time of a fuel upon injection into the combustion chamber. The higher the CN, the shorter the ignition delay time and vice versa. It is an acceptable fact that the CN of biodiesel is generally higher than fossil diesel fuel due to the absence of aromatic compounds (Van Gerpen, 2005).

4.8 Comparison of Thermal and Mechanical Efficiencies

After looking at the brake thermal efficiencies of the algal biodiesel samples and blends together with AGO and observing the effects of engine loads on them from 10 to 100%, BA1 to BA4 (100% algal biodiesel) were isolated in order to compare the effects of engine loads on thermal and mechanical efficiencies in Figure 5 since biodiesel fuels reflected higher brake thermal efficiencies than the AGO as discussed in the previous subsection. The effect was that as the engine load increased, both thermal and mechanical efficiencies increased as well almost linearly and parallel to each other. Both efficiencies are influenced by the increased combustion rate and increased heat produced together with increased torque, speed and overall power.

5. CONCLUSION

Oxygen content in the algal biodiesel had direct influence on smoke opacity and gaseous emissions in CI engines. The smoke density reduces as temperature increases in all the fuels samples (algal biodiesel and AGO) but with higher densities in AGO. This trend is mainly due to the presence of internal availability of oxygen in the biodiesel and neat burning of fuel at elevated temperatures. Chemo-physical properties of biodiesel are the most important and indispensable factors to be considered in the production of biodiesel. Once they meet the ASTM standards, the fuels are unarguably acceptable for application in the CI engines.

Variations in heating values, density and viscosity clearly influence engine torque and power. Biodiesel with lower heating values, densities and higher lubricity has significant effects on engine power and torque. Although, biodiesel has slightly higher density than petroleum diesel, it contains slightly less energy on volumetric basis. Higher viscosity in biodiesel improves air-fuel mixing by enhancing spray penetration and homogenization in the combustion chamber and therefore greater recovery in power and torque when generally compared to fossil diesel (AGO). Higher brake specific fuel consumption of the biodiesel is due to lower net calorific value of fuels.

Algal biodiesel being highly oxygenated contains higher concentrations of oxygen which allows faster and more complete combustion compared to fossil diesel fuel and this no doubt influences the amount or density of exhaust smoke to be released to the environment from the compression ignition engine.

Algal oil is thermo-gravimetrically very stable for any thermal application. There is therefore no hindrance to conversion to biodiesel via any known process.

6. REFERENCES

SINGH, S.P. and Singh, D. (2010). Biodiesel production through the use of different sources and characterization of oils and their esters as the substitute of diesel: a review. Renew Sust Energy Rev; 14:200–16.

STEPHENS, E., Ross, I.L., Mussgnug, J.H., Wagner, L.D., Borowitzka, M.A., Posten, C., Kruse, O. and Hankamer, B. (2010). Future prospects of microalgal biofuels production systems: Trends in Plant Science Vol. 15 No. 10. 554 – 564. Elsevier Ltd.

IPCC (2009). Intergovernmental Panel on climate change: Fourth Assessment report, Trends in Plant System.

STERN, N. (2006). The economics of climate change, HM Treasury. www.biofuelstp.eu/algae.html Algal biofuels - Algae for production of biofuels: assessed on 8/3/11.

BEER, L.L., Boyd, E.S., Peters, J.W. and Posewitz, M.C. (2009). Engineering algae for bio-hydrogen and biofuels production: Current Option in Biotechnology, 20: 264 – 271.

HEYWOOD, J.B. (1998). Internal Combustion Engines Fundamentals; McGrawHill: New York, NY, USA.

FERGUSON, C.R.; Kirkpatrick, A.T. (2001) Internal Combustion Engine, 2nd ed.; John Wiley Sons: New York, NY, USA.

LEBEDEVAS, S.; Vaicekauskas, A. (2006) Research into the application of biodiesel in the transport sector of Lithuania transport. Transport, 21, 80–87.

JAASLELAINEN, H. and Khar, M.K. (2013). Fuel Injection system components. DieseNet Technology Guide, EcoPoint Inc. Revision 2013.06

UTLU, Z.; Koçak, M.S. (2008). The effect of biodiesel fuel obtained from waste frying oil on direct injection diesel engine performance and exhaust emissions. Renew. Energy, 33, 1936 –1941.

KARABEKTAS, M. (2009). The effects of turbocharger on the performance and exhaust emissions of a diesel engine fuelled with biodiesel. Renew. Energy, 34, 989–993.

HANSEN, A.C.; Gratton, M.R.; Yuan, W. (2006). Diesel engine performance and NOx emissions from oxygenated biofuels and blends with diesel fuel. Trans. Am. Soc. Agric. Biol. Eng., 49, 589–595.

MURILLO, S.; Miguez, J.L.; Porteiro, J.; Granada, E.; Moran, J.C. (2007). Performance and exhaust emissions in the use of biodiesel in outboard diesel engines. Fuel, 86, 1765–1771.

ONER, C. and Altun, S. (2009). Biodiesel production from inedible animal tallow and an experimental investigation of its use as alternative fuel in a direct injection diesel engine. Appl. Energy, 86, 2114–2120.

MONYEM, A.; Gerpen, J.V. (2001). The effect of biodiesel oxidation on engine performance and emissions. Biomass Bioenergy, 20, 317–325.

AYDIN, H. and Bayindir, H. (2010). Performance and emission analysis of cottonseed oil methyl ester in a diesel engine. Renew. Energy, 35, 588–592.

RAMADHAS, A.S., Muraleedharan, C.; Jayaraj, S. (2005). Performance and emission evaluation of diesel engine fueled with methyl esters of rubber seed oil. Renew. Energy, 30, 1789–1800.

USTA, N. (2005). An experimental study on performance and exhaust emissions of a diesel engine fuelled with tobacco seed oil methyl ester. Energy Convers. Manag., 4615, 2373–2386.

PAL, A.; Verma, A.; Kachhwaha, S.S.; Maji, S. (2010). Biodiesel production through hydrodynamic cavitations and performance testing. Renew. Energy, 35, 619–624.

HAŞIMOĞLU, C.; Ciniviz, M.; Özsert, İ.; İçingür, Y.; Parlak, A.; Sahir Salman, M. (2008). Performance characteristics of a low heat rejection diesel engine operating with biodiesel. Renew. Energy, 337, 1709–1715.

CARRARETTO, C.; Macor, A.; Mirandola, A.; Stoppato, A.; Tonon, S. (2004). Biodiesel as alternative fuel: Experimental analysis and energetic evaluations. Energy, 29, 2195–2211.

RAHEMAN, H.; Ghadge, S.V. (2007). Performance of compression ignition engine with mahua Madhuca indica biodiesel. Fuel, 8616, 2568–2573.

JAHIRUL, M.I., R. J. Brown, W. Senadeera, I. M. O'Hara, and Z.D. Ristovski (2013). The Use of Artificial Neural Networks for Identifying Sustainable Biodiesel Feedstocks. Energies 2013, 6, 3764-3806.

LIN, C.Y.; Lin, H.A.; Hung, L.B. (2006) Fuel structure and properties of biodiesel produced by the peroxidation process. Fuel, 85, 1743–1749.

LANCE, D.L.; Goodfellow, C.L.; Williams, J.; Bunting, W.; Sakata, I.; Yoshida, K.; Taniguchi, S., Kitano, K. (2009). The Impact of Diesel and Biodiesel Fuel Composition on a Euro V HSDI Engine with Advanced DPNR Emissions Control; SAE Technical Paper No. 2009-01-190; SAE International: Washington, DC, USA.

SAHOO, P.K.; Das, L.M.; Babu, M.K.G.; Arora, P.; Singh, V.P.; Kumar, N.R. (2009) Comparative evaluation of performance and emission characteristics of Jatropha, Karanja and Polanga based biodiesel as fuel in a tractor engine. Fuel, 889, 1698–1707.

OZSEZEN, A.N.; Canakci, M.; Turkcan, A.; Sayin, C. (2009) Performance and combustion characteristics of a DI diesel engine fueled with waste palm oil and canola oil methyl esters. Fuel, 884,629–636.

BANAPURMATH, N.R.; Tewari, P.G.; Hosmath, R.S. (2008). Performance and emission characteristics of a DI compression ignition engine operated on Honge, Jatropha and sesame oil methyl esters. Renew. Energy, 339, 1982–1988.

SKJANES, K., Knutsen, G. kallqvist, T. and Lindblad, P. (2008). H2 production from marine and freshwater species of green algae during sulfur deprivation and considerations for bioreactor design. International Journal of Hybrid Energy (33): 511 – 521.

CHRISTI, Y. (2007). Biodiesel from microalgae. Biotechnology Advances: 25 (3): 294 – 306.

CHISTI, Y. (2008). Biodiesel from microalgae beats bioethanol. Trends Biotechnol. 26, 126–131.

153: Esterification of oleic acid with methanol by a sulfonated carbon-based solid acid microspheres (SCMs)

HONGLEI ZHANG[1, 2], ZHENG MA[1], CHUANGSHENG JIANG[1],
JIARUI GAO[1], GEORGE Z. CHEN[2, 3, 4], TAO WU [1*], FENG HE [5*]

[1] Faculty of Science and Engineering, The University of Nottingham Ningbo China, Ningbo, 315100, P.R. China
2 Department of Chemical and Environmental Engineering, Energy and Sustainability Research Division, The University of Nottingham, Nottingham, NG7 2RD, UK
3 International Academy of Marine Economy and Technology, The University of Nottingham Ningbo China, Ningbo, 315100, P.R. China
4 Center for Sustainable Energy Technology, The University of Nottingham Ningbo China, Ningbo, 315100, P.R. China
5 College of Biological and Environmental Engineering, Zhejiang University of Technology, Hangzhou, Zhejiang 310032, China.

A carbon-based solid acid microspheres rich of sulfonated groups (-SO3H) was prepared by simple hydrothermal and sulfonation method using cheap glucose as raw material. The green, non-corrosive, renewable and environmental friendly carbon material was used as heterogeneous catalysts for the esterification of oleic acid with methanol for biodiesel production. The structure and properties of the carbon microsphere were characterized by using Field-Emission Scanning Electron Microscope (FESEM), Transmission Electron Microscope (TEM), Fourier Transform Infrared Spectroscopy (FTIR), Thermo Gravimetric Analysis (TGA) and Differential Scanning Calorimeter (DSC), elemental analysis, N2 adsorption–desorption test and acid-base titration. It is found that the carbon microspheres prepared under the optimal reaction conditions showed smooth surfaces, uniform particle sizes and good dispersion. The sulfonated carbon-based solid acid microspheres showed high acidity and comparable activities to sulfuric acid for the esterification reaction of oleic acid with methanol. Reaction parameters including methanol/oleic acid mass ratio and catalyst usage amount were studied to get optimal esterification reaction conditions. The catalysts showed high reusability although there is some loss in acidity due to the leaching of active sites, the sulfonated groups.

Keywords: Biodiesel production, Carbohydrates, Esterification, Hydrothermal method, Solid acid catalyst

1. INTRODUCTION

Biodiesel is a non-petroleum-based fuel consists of alkyl esters derived from renewable lipid feedstock such as vegetable oil or animal fat (1). Compared with regular diesel, biodiesel is more biodegradable, has lower CO_2 and sulfur emissions and almost none particulate pollutants (2).However, biodiesel is not competitive with fossil fuels due to higher cost of raw material and production (3). One way to reduce the cost is to select cheaper oil feed like waste cooking oils (WCO) (4). But the WCO pretreatment is still a problem due to its high free fatty acids (FFAs) content that produces soap during base transesterification (4). Therefore, the esterification of FFAs in WCO was often firstly carried out using homogeneous strong acid-catalysts, such as sulphuric and hydrochloric acid (5). However, the use of H_2SO_4 causes many problems, such as difficulty of separation from reaction medium, formation of large amount of wastewater and significant corrosion of equipment (6). Consequently, it is desirable to develop a highly active, inexpensive, green and reusable heterogeneous acid catalyst (7).

Many solid acid catalysts have been proposed to replace liquid acids because they are non-corrosive and easy to be separated from reaction mixture. Typically, solid acids include ion-exchange resin (4, 8), zeolites (2, 9), mesoporous materials (3, 10-12) and SO_3H-functionalized carbon microspheres (13-18). Among them, SO_3H-functionalized carbon microspheres with regular spherical shapes and controllable sizes, which are attractive metal-free, stable and recyclable catalysts to achieve sustainable reactions, have emerged as stable and highly active acid catalysts for various acid-catalyzed reactions like esterification, hydrolysis and dehydration. Some methods have been developed for the synthesis of carbon microspheres. The hydrothermal method is unique because of its simple operational and mild reaction condition requirements (19, 20).

In this work, a sulfonated carbon-based solid acid microsphere was prepared by using glucose as raw material. The carbon microspheres were used as catalyst in esterification of oleic acid with methanol for biodiesel production. The structure and properties of the carbon material were investigated by SEM, TEM, FTIR, TGA-DSC, elemental analysis and N_2 adsorption–desorption test. The catalytic properties (catalytic activity and reusability) were also investigated.

2. EXPERIMENTAL

2.1 Preparation of sulfonated carbon-based solid acid microspheres (SCMs)

The overall preparation procedure of the sulfonated carbon-based solid acid microspheres is listed in Figure 1. The hydrothermal carbonization of glucose was carried out according to the following procedure: 9 g of glucose was dissolved in water (50 mL) and mixed into a homogeneous aqueous glucose solution and then transferred to a stainless steel autoclave with a 80 mL capacity, where it was heated up to 200 °C and maintained at this temperature for 4 h. Then, the solution was cooled to room temperature naturally. The black precipitate was collected by filtration, sequentially washed with boiling water, pure ethanol, and acetone to get carbon-based microspheres (CMs). The obtained sample was then dried in a vacuum at 60 °C for 24 h. 1 g of the solid product was then treated with 200 mL concentrated sulfuric acid (98 %) at 150 °C under nitrogen atmosphere for 15 h. The sulfonated sample was collected by filtration, washed in succession with boiling water for 5-10 times, and then refluxed with toluene to remove the un-bonded polycyclic aromatic compounds. The solid obtained on the filter was vacuum-dried overnight at 60 °C to get sulfonated carbon-based solid acid microspheres.
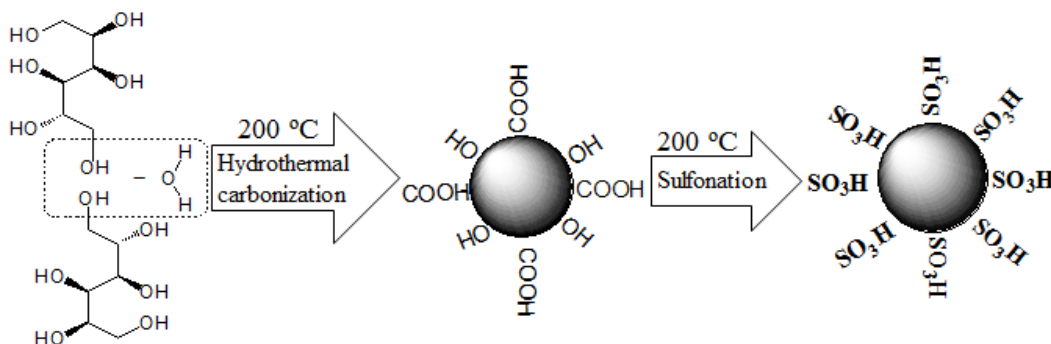

Figure 1 The illustration of the preparation method of SCMs

2.2 Characterization

The morphology of the samples prepared was inspected under a Zeiss Ultra plus Field-Emission Scanning Electron Microscope (FESEM) (Zeiss Co.) equipped with an energy dispersive X-ray (EDX) detector operating at an accelerating voltage of 10 kV. A TEM measurement was carried out on a JEOL JEM 2100 UHR transmission electron microscope operated at 200 kV. The IR spectra of the samples were characterized by Fourier Transform Infrared Spectroscopy (FTIR) TENSOR-37 (Bruker Co.) operated by Attenuated Total Reflectance (ATR) in the wave number range of 4000-500 cm^{-1}. The elemental composition (C, H, O, N and S) of the samples was studied with a Perkin-Elmer 2400 Series II CHNS/O analyzer (PerkinElmer Co.). The textural properties of calcined samples were measured based on N$_2$ adsorption–desorption isotherms using a Micromeritics ASAP 2020M apparatus. The specific surface area (S$_{BET}$) was calculated using the Brunauer–Emmett–Teller (BET) method. The thermal stability of the membranes was investigated using a STA449 F3 Jupiter Thermo Gravimetry (Netzsch Co.). Thermo Gravimetric Analysis (TGA) was carried out under an air atmosphere at a heating rate of 10 °C min^{-1} from 50 to 900°C. Differential Scanning Calorimeter (DSC) measurements were carried out concurrently in the range of 50 to 900 °C. Total acidity indicates the number of milli-equivalents of ions (H$^+$) in dry catalyst of unit quality (8) Total acidity of the catalysts was obtained using the acid-base titration method. The reported values were the mean of at least five measurements and the average experimental error was ±5 %.

2.3 Catalytic activity test

Esterification reactions of oleic acid with methanol (Scheme 1) were performed in a three-necked batch reactor (250 mL) equipped with a reflux condenser and a mechanical stirrer at atmospheric pressure. The oleic acid was first introduced into the reactor and heated to the desired temperature. Then the desired amount of the methanol and the catalyst were added into the reactor and the reaction began at pre-determined conditions. The primary reaction conditions were as following: oleic acid, 10 g; methanol, 20 g; catalyst loading 0.2 g; mechanical stirring, rate 360 rpm; reaction temperature, 65 °C; and reaction time, 8 h, except otherwise mentioned. The samples were taken out from the reactor every hour and the composition were tested on a Gas chromatography (GC7890B, Agilent Technologies) with a flame ionization detector equipped using a HP-5 column to get esterification yield. After completion, the reaction mixture was poured into a separating funnel and allowed to settle for 1 h to separate the excess methanol and the biodiesel. The biodiesel was further purified by decompression distillation to remove excess methanol and other impurities. After each run, the catalysts were filtrated from the reaction solution and dispersed in deionized water. Then the samples were first washed with ethyl ether twice to remove the adsorbed organic components and then washed with ethanol, boiling DI water twice, respectively. Afterward, the sample dispersed in deionized water was sonicated for another 30 min. The recovered catalysts were then dried in a vacuum oven at 50 °C for 24 h to remove residual water completely before reuse.

$$R_1\text{-COOH} \; + \; \text{HO-R} \; \underset{}{\overset{\text{Catalyst}}{\rightleftharpoons}} \; R_1\text{-COOR} \; + \; H_2O$$

Scheme 1 The esterification of free fatty acid to free acid methyl ester (biodiesel)

3. RESULTS AND DISCUSSION

3.1 Catalyst Characterization

The surface morphology of the CMs and SCMs prepared were investigated by using SEM and the results are listed in Figure 2. The carbon-based solid acid microspheres showed spherical structure with uniform size (about 1.2 µm) and smooth surfaces. It is noted that the sulfonated carbon-based solid acid microspheres show similar spherical structure with the raw carbon microspheres, suggesting that the sulfonation process did not change the morphology or the particle size of the carbon microspheres. The BET surface area of the two samples calculated nitrogen gas absorption method were 1.9 and 2.2 m^2 g^{-1}, respectively, suggesting both the two samples have no porosity and the carboxyl, hydroxyl and sulfonated groups were at the external surface of the microspheres (as shown in Figure 1). This character will be beneficial for reactants to flow smoothly onto the catalytic active sites and promote the esterification reaction.
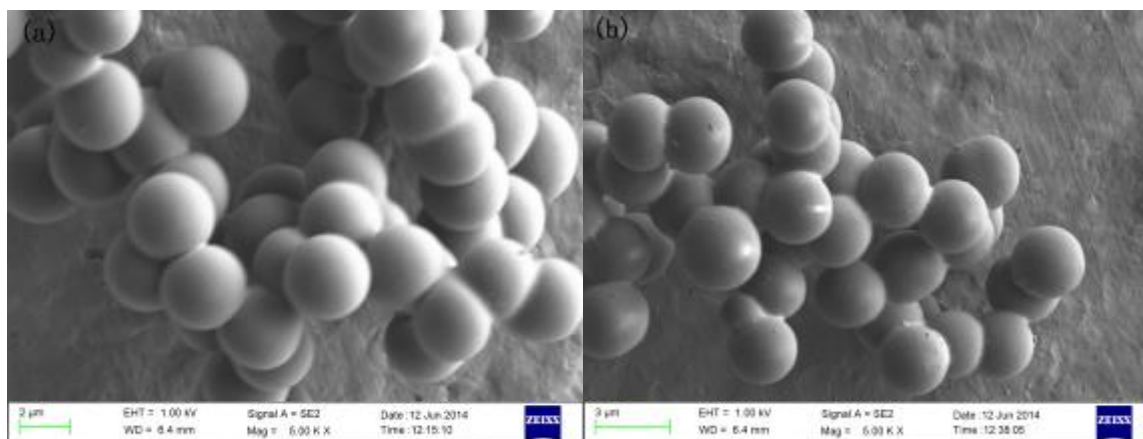
Figure 2 SEM of CMs (a) and SCMs (b).

The FTIR spectra of CMs and SCMs are shown in Fig. 3. Both the two samples show the same peaks associated with –OH vibration at 1260 cm^{-1},[21] C=C stretching vibration at 1630 cm^{-1},[22] C=O stretching vibration of the –COOH groups at 1730 cm^{-1},[23] the stretching vibration of O–H at 3430 cm^{-1} [24]. These peaks suggest that there are –OH, -COOH groups on both CMs and SCMs, which is in good accordance with the preparation method illustrated in Figure 1. However, a sharp peak appeared for the SCMs at 1040 cm^{-1},[20] which is due to symmetric O=S=O stretching vibrations of –SO$_3$H groups, suggesting the presence of sulfonated groups in SCMs [19]. Both the two curves can be used to confirm the present of oxygen-containing groups during carbonization and Sulfonation process.
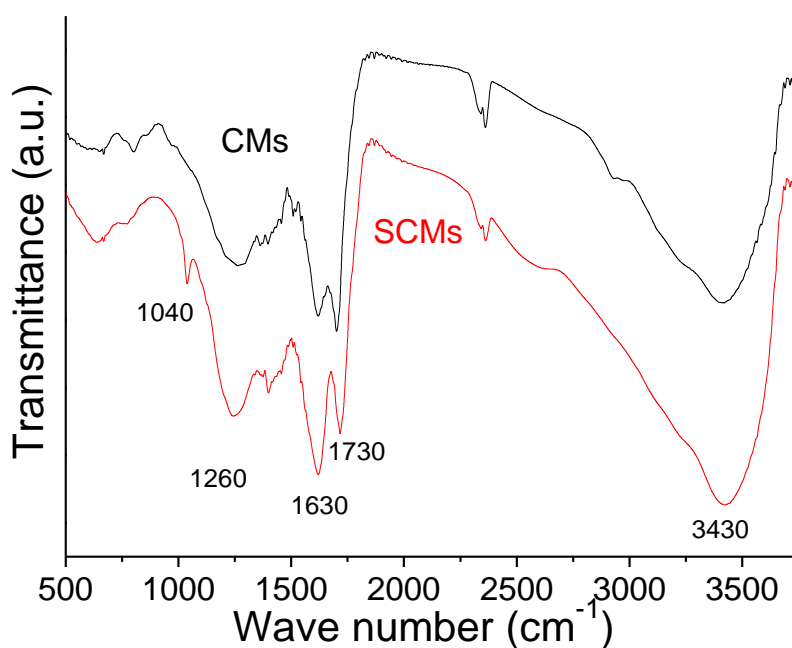
1.

Figure 3 FTIR spectra of CMs and SCMs

Thermo Gravimetric Analysis (TGA) and Differential Scanning Calorimeter (DSC) of CMs and SCMs were carried out under air atmosphere and the results are illustrated in Figure 4 (a, and b). CMs shows excellent thermal stability, and the weight loss is only observed at over 500 °C, which is assigned to the decomposition of graphene framework, suggesting that there are almost no functional groups in the raw CMs. However, there are mainly two weight loss peaks for SCMs from the TGA curve of SCMs. The first weight loss below 450 °C (centering at 350 °C as shown in Figure 4 (b)) is aroused is a result of the decomposition of –SO$_3$H and –COOH groups. The weight loss in the first stage is about 40 wt. %, which is in good agreement with the elemental analysis results (see Table 1). The second peak over 500 °C is assigned to the decomposition of carbon framework. The DSC curves of all the samples matching their TGA curves well.
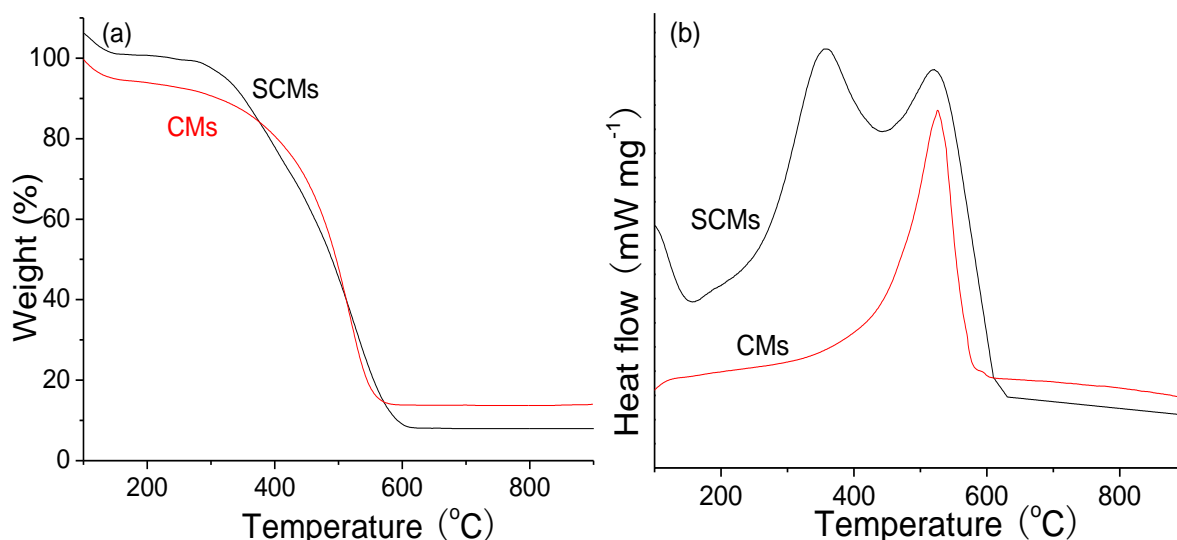
Figure 4 TGA (a) and DSC (b) curves of the CMs and SCMs

As shown in Table 1, the data originated from elemental analysis show that both the two samples contain abundant hydrogen and oxygen content from incompletely carbonization. However, the sulfur content in CMs is only 0.24 % but 1.73 % for SCMs, suggesting the sulfur content associated to the –SO$_3$H groups were fixed in the sulfonated carbon-based acid microspheres.

Table 1 Elemental analysis and BET surface area results of CMs and SCMs

Samples	Carbon	Hydrogen	Nitrogen	Sulfur	Oxygen	S$_{BET}$ (m^2 g^{-1})
CMs	63.06	4.35	0.31	0.24	32.04	1.9
SCMs	58.82	3.32	0.33	1.73	35.8	2.2

3.2 Catalytic performance of SCMs

Then, SCMs was used in esterification of oleic acid with methanol to evaluate their catalytic activity and the results are shown in Figure 5 and Table 2. The results of esterification catalyzed by CMs, Amberlyst-15, H$_2$SO$_4$ and that without catalyst are also compared. The yield was approximately 4.2 % when no catalyst was used and oleic acid itself acts as a weak acid catalyst. The CMs could only slightly promote esterification to the yield of 27 % as it does not contain any catalytic active sites. SCMs exhibits a higher catalytic activity than Amberlyst-15, a widely used commercial cation exchange resin, although it has a higher –SO$_3$H density as shown in Table 2. This is mainly due to the fact that sulfonated microspheres contains abundant –COOH groups, which can promote the esterification by adsorbing the water produced. The excellent catalytic performance is also associated with its smaller particle size and uniform particle size.
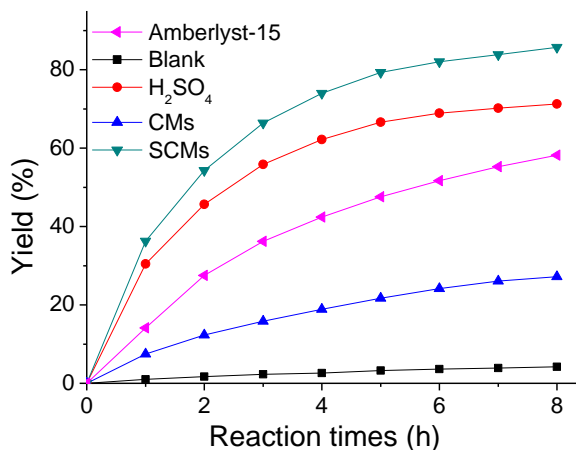

Figure 5 Esterification reaction catalyzed by different catalysts

Table 2 Catalytic activities on the esterification reaction by various catalysts (reaction conditions: oleic acid, 10 g; methanol, 20 g; catalyst loading 0.2 g; mechanical stirring, rate 360 rpm; reaction temperature, 65 ºC; and reaction time, 8 h)

Catalysts	-SO$_3$H Density (mmol g^{-1})	Total acidity (mmol g^{-1})	S$_{BET}$ (m^2 g^{-1})	yield (%)
Blank	—	—	—	4.2
H$_2$SO$_4$	—	20.40	—	71.3
CMs	0.07	0.21	1.9	27.2
SCMs	0.54	2.16	2.2	85.7
Amberlyst-15	4.9	4.7	30	58.2

3.3 Effect of methanol/oleic acid mass ratios on the esterification

To study the effect of methanol/oleic acid mass ratios on the esterification reaction, different experiments were carried out with the methanol/oleic acid mass ratios of 1.5:1 to 4.0:1. The results are shown in Table 3. It can be seen that yield increased from 66.7 % to 86.2 % with the increase of the methanol/oleic acid mass ratio from 1.5:1 to 2.5:1, equivalent to the increase of reactant concentration. However, the yield decreased from 86.2 % to 74.3 % when the mass ratio increased from 2.5:1 to 4:1. This is mainly because excess methanol would adsorb on the catalyst surface and thus inhibits the increment of yield or even deactivates the catalyst. Thus the optimized methanol/oleic acid mass ratio was 2.5:1 in the reaction system.

Table 3 Effect of methanol/oleic acid mass ratio (Reaction conditions: oleic acid, 10 g; catalyst loading 0.2 g; mechanical stirring, rate 360 rpm; reaction temperature, 65 ºC; and reaction time, 8 h)

Methanol /oleic acid mass ratio	1.5	2	2.5	3	3.5	4
Yield (%)	66. 7	75.3	86.2	81.3	78.4	74.3

3.4 Effect of catalyst amount

Different experiments were carried out with different loading amounts of SCMs and the results were shown in Table 4.The reaction could not precede efficiently with a small amount of catalyst as there were not enough catalytic active sites. The yield increased with the increment of catalyst loading within 0.25 g. When the catalytic membrane loading exceeded 0.25 g, the yield didn't increase with the amount of catalyst. The optimized loading amount was 0.25 g.

Table 4 Effect of catalyst amount (Reaction conditions: oleic acid, 10 g; methanol, 25 g; mechanical stirring, rate 360 rpm; reaction temperature, 65 ºC; and reaction time, 8 h)

Catalyst amount (g)	0.1	0.15	0.2	0.25	0.3
Yield (%)	77.2	86.46	90.28	94.04	94.31

3.5 Effect of reaction temperatures

Effect of reaction temperature on esterification is shown in Figure 6. It is found that yield increased greatly with the increase of reaction temperature from 40 to 65 °C and the yield of 60 °C is almost the same with that of 65 °C. This is mainly because increasing temperature can result in promotion of the molecule motion and mass transfer rate. However, the yield decreases from 87 % to 72 % when the temperature further increases to 70 °C, which is because when the reaction temperature exceeds the boiling point of methanol, it will vaporize and form a large number of bubbles and thus inhibit the reaction. The optimal reaction temperature is 65 °C.
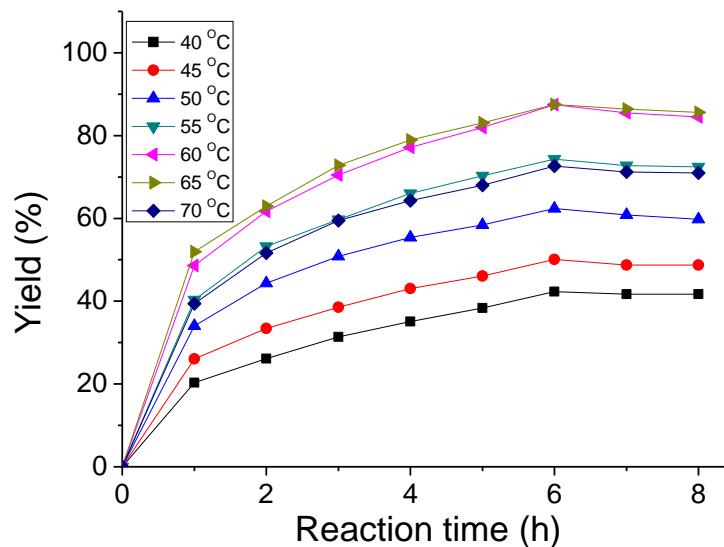
Figure 6 Effect of reaction temperatures

3.6 Effect of stirring rate

As methanol are not totally miscible with oleic acid, it is believed that esterification reaction is a relatively slow process since esterification can only occur in the interfacial regions. So vigorous stirring is required to increase the contact area between the two immiscible reactants. To investigate the effect of mechanical stirring rate on the reaction, esterification was conducted with different stirring rates of 120, 240, 360 and 480 revolutions per minute (rpm), respectively and the results are shown in Figure 7. It is observed that the yieldsare very lowe when the rates are 120, and 240 rpm and the yields are only 74 %, and 81 %, respectively after 8 h. However, the yield at 360 and 480 rpm are almost the same (over 90 %). Considering the productiong cost, the optimal stirring rate is 360 rpm.
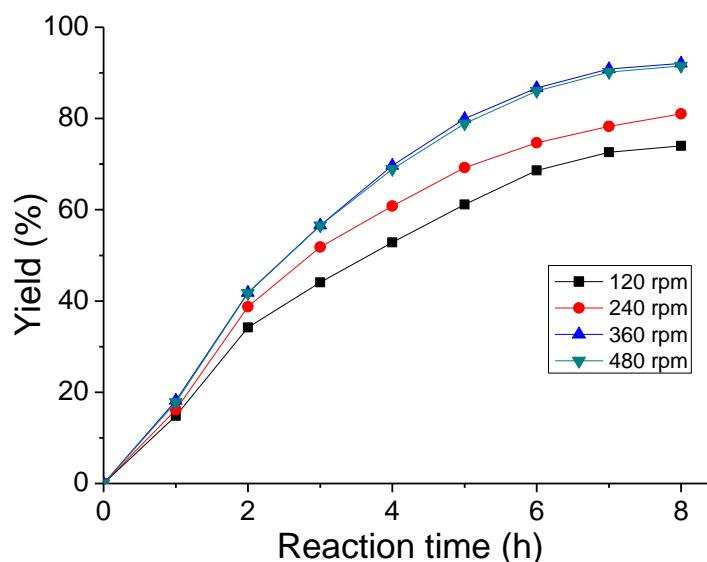

Figure 7 Effect of stirring rate on esterification

3.7 Reusability of the SCMs

In order to investigate the reusability of the sulfonated carbon-based solid acid microspheres, the used catalyst was collected, washed with water and employed in the esterification for six runs under the optimal

reaction conditions and the results were shown in Figure 8. It can be seen that SCMs showed good catalytic activity at the first run, with the yield of 92 %. A slight deactivation occurred after the first run. And the yield kept approximate 84 % after five runs, indicating the high catalytic performance and stability for producing biodiesel.
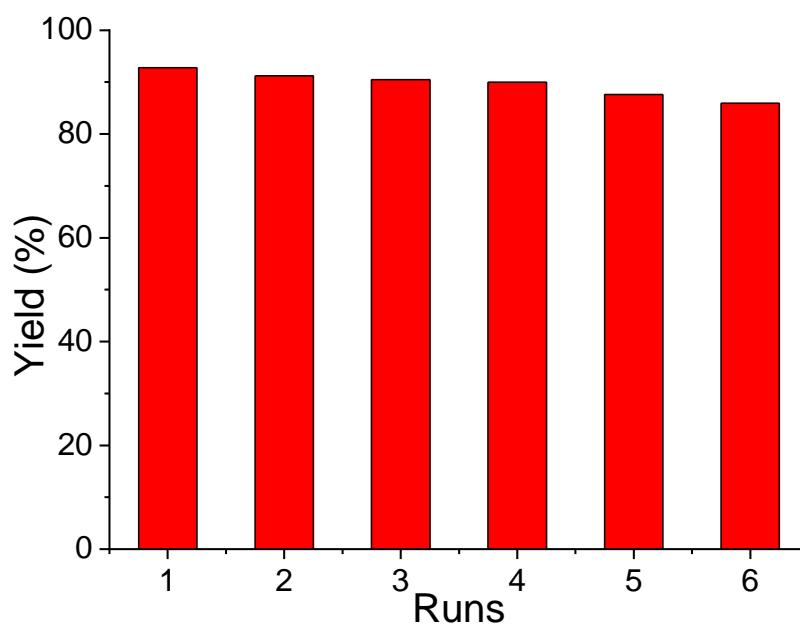

Figure 8 The catalytic performance of the membrane versus recycling times

4. CONCLUSION

In conclusion, a sustainable route for the synthesis of sulfonated carbon-based solid acid microspheres for biodiesel production by using glucose as raw materials. The catalyst showed higher catalytic performance compared with sulfuric acid and Amberlyst-15 in esterification of oleic acid with methanol. This is mainly due to the fact that sulfonated microspheres have uniform particle size and better affinity with reactants. The catalyst is green, non-corrosive, renewable and environmental friendly, may have great potential in industrial production of biodiesel.

5. REFERENCES

(1). MA, F. and Hanna, M. A., Bioresour. Technol., 1999, 70, 1-15.

(2). NARKHEDE, N. and Pate,l A., Ind. Eng. Chem. Res., 2013, 52, 13637-13644.

(3). DHAINAU,t J., Dacquin, J.P., Lee, A. F. and Wilson, K., Green Chem., 2010, 12, 296-303.

(4). ZHANG, H., Ding, J. and Zhao, Z., Bioresour. Technol., 2012, 123, 72-77.

(5). DESIMONE, J. M., Science 2002, 292, 799-803

(6). JI, J., Zhang, G., Chen, H., Wang, S., Zhang, G., Zhang F. and Fan, X., Chem. Sci., 2011, 2, 484-487.

(7). HARA M., Yoshida, T., Takagaki, A., Takata, T., Kondo, J. N., Hayashi, S. and Domen, K., Angew. Chem. Int. Ed. , 2004, 43, 2955-2958.

(8). ZHANG, H., Ding, J., Qiu, Y. and Zhao, Z., Bioresour. Technol., 2012, 112, 28-33.

(9). ŽILKOVÁ, N., Bejblová, M., Gil, B., Zones, S. I., Burton, A. W., Chen, C. Y., Musilová-Pavlačková, Z., Košová, G. and Čejka, J., J. Catal., 2009, 266, 79-91.

(10). PESARESI, L., Brown, D. R., Lee, A. F., Montero, J. M., Williams, H. and Wilson, K., Appl. Catal., A 2009, 360, 50-58.

(11) C. PIREZ, J.-M. Caderon, J.-P. Dacquin, A. F. Lee and K. Wilson, ACS Catal., 2012, 2, 1607-1614.

(12). PIREZ, C., Lee, A. F., Manayil, J. C., Parlett, C. M. A. and Wilson, K., Green Chem., 2014, 16, 4506-4509.

(13) OKAMURA, M., Takagak, A., Toda, M., Kondo, J. N., Domen, K., Tatsumi, T., Hara, M. and Hayashi, S., Chem. Mater., 2006, 18, 3039-3045.

(14). KITANO, M., Arai, K., Kodama, A., Kousaka, T., Nakajima, K., Hayashi, S. and Hara, M., Catal. Lett., 2009, 131, 242-249.

(15). HARA, M., Energy Environ. Sci., 2010, 3, 601-607.

(16). HARA, M., Top. Catal., 2010, 53, 805-810.

(17). FUKUHARA, K., Nakajima, K., Kitano, M., Kato, H., Hayashi, S. and Hara, M., ChemSusChem 2011, 4, 778-784.

(18). SUGANUMA, S., Nakajima, K., Kitano, M., Hayashi, S. and Hara, M., ChemSusChem, 2012, 5, 1841-1846.

(19). MACIA-AGULL, J. A., Sevilla, M., Diez, M A. and Fuertes, A. B., ChemSusChem, 2010, 3, 1352-1354.

(20). LIANG, X., Zeng, M. and Qi, C., Carbon, 2010, 48, 1844-1848.

(21). MARCANO, D C., Kosynkin, D V., Berlin, J M., Sinitskii, A, Sun, Z, Slesarev, A, Alemany, L B., Lu, W and Tour, J. M., ACSnano, 2010, 4, 4806-4814.

(22). MAZZOTTA, M. G., Gupta, D., Saha, B., Patra, A. K., Bhaumik, A. and Abu-Omar, M. M., ChemSusChem, 2014, 7, 2342-2350.

(23). ZHU, M., He, B., Shi, W., Feng, Y., Ding, J., Li, Zeng, J. and F., Fuel, 2010, 89, 2299-2304.

(24). LIU, X. Y., Huang, M., Ma, H. L., Zhang, Z. Q., Gao, J. M., Zhu, Y. L., Han, X. J. and Guo, X. Y., Molecules, 2010, 15, 7188-7196.

222: Design and testing of a bubbling fluidized bed reactor for biomass oxy-fuel combustion

Farooq SHER[1], Hao LIU[2], Chenggong SUN[3], Colin SNAPE[4]

[1] Faculty of Engineering, University of Nottingham, University Park, Nottingham NG7 2RD, UK. Farooq.Sher @nottingham.ac.uk
[2] Faculty of Engineering, University of Nottingham, University Park, Nottingham NG7 2RD, UK. Liu.Hao @nottingham.ac.uk
[3] Faculty of Engineering, University of Nottingham, University Park, Nottingham NG7 2RD, UK. Chenggong.Sun @nottingham.ac.uk
[4] Faculty of Engineering, University of Nottingham, University Park, Nottingham NG7 2RD, UK. Colin.Snape @nottingham.ac.uk

The continual use of fossil fuels results in an increase in CO_2 concentration in the atmosphere which leads to global climate change. The huge energy demand of our society is causing fossil fuel resources to diminish rapidly. Therefore, it is critical to search for alternative renewable energy resources to protect the environment and to meet the future energy demands. Biomass is abundant, inexpensive and has the potential to replace fossil fuels. Oxy-fuel combustion is one of three main CO_2 capture technologies that can be applied to commercial power plants. The combustion of biomass in an oxy-fuel power plant could yield a significant, additional CO_2 reduction, or even lead to negative CO_2 emissions. However, biomass oxy-fuel combustion technology is still in the developing phase and further research is still required in order to fully clarify the consequences of its implementation in power plants. In the present study a bubbling fluidized bed reactor (BFBR) with a capacity of 20 kW is designed, manufactured and successfully tested for biomass combustion. A sintered plate was used as the distribution plate and Garside 14/25 sand with a sauter mean diameter (d_{32}) of 0.78 mm was used as the bed material. The minimum fluidization velocity (U_{mf}) of 0.51 m/s was experimentally determined with air at ambient temperature. The biomass screw feeder was tested with three different types of biomass feedstocks: wood pellets (WP), miscanthus pellets (MP) and straw pellets (SP). The feeder was found to be able to provide continuous and smooth feeding without any blockage for all three types of biomass pellets. The temperature profiles in the BFBR during combustion were found to be smoothly distributed along the reactor throughout the operation. With the help of a water-cooling heat extraction probe, the average temperatures within the main combustion zones were successfully controlled to be in the range of 750–850 oC. The concentrations of the main components in the flue gas have shown the expected dependencies on the stoichiometric ratio (SR). The average values of the flue gas components CO_2, CO, O_2 and NOx were found to be in the range of 14.85–18.64%, 0.29–0.70%, 1.67–5.94% and 40.08–63.30 ppm respectively with a different SR ratio from 1.10 to 1.45. The average temperatures distribution throughout the reactor were in the range of 655–850 oC.

Keywords: Bubbling fluidized bed reactor (BFBR), Minimum fluidization velocity, Biomass and Combustion.

1. INTRODUCTION

It has been accepted worldwide that the global warming is by far the greatest threat and challenge to human being. The current warming trend is of particular significance because most of it is very likely human-induced and proceeding at a rate that is unprecedented in the past 1,300 years (Shuit, Tan et al. 2009). Ever since the Industrial revolution began about 150 years ago, man-made activities have added significant quantities of greenhouse gases (GHGs) to the atmosphere. An increase in the levels of GHGs could lead to greater warming, which, in turn, could have an impact on the world's climate, leading to the phenomenon known as climate change. Strategies and technologies for reducing greenhouse gases such as CO_2, CH_4, SO_X and NO_X have been studied in much detail. However, carbon dioxide (CO_2) is the largest contributor among well-mixed long-lived heat-trapping greenhouse gases, accounting for more than 63% of the total that contributes to global warming (Vijaya Venkata Raman, Iniyan et al. 2012), which is released through human activities such as burning fossil fuels, transportation, building heating and cooling. Moreover, power plants are major source for the CO_2 emissions causing about 41% of the total emissions. Capturing CO_2 at large point sources, where it is quite concentrated, makes sense as the power plants and the industry emits 41% and 17% of the CO_2 respectively. (Kiesgen De Richter, Ming et al. 2013).

A variety of technologies for capturing CO_2 from a mixture of gases are commercially available and widely used today. The choice of technology is dependent on the requirements for product purity and on the conditions of the gas stream being treated (such as its temperature, pressure, CO_2 concentration, the type and level of trace species or impurities). CO_2 capture technologies are usually classified into three categories post-combustion, pre-combustion and oxy-fuel combustion. Either pre-combustion or post-combustion systems, depending on whether carbon in the form of CO_2 is removed before or after a fuel is burned. A third approach, called oxy-fuel or oxy-combustion, does not require a CO_2 capture device. In oxy-fuel pure oxygen rather than air is used for combustion. This eliminates the large amount of nitrogen in the flue gas stream. After the particulate matter (fly ash) is removed, the flue gas only consists of water vapour and CO_2 plus smaller amounts of pollutants such as sulphur oxides (SO_x) and nitrogen oxides (NOx) (Wall 2007). However, oxy-fuel combustion process is still in the developing phase and much research is still required in order to fully clarify the consequences of its implementation in power plants.

The reality is that the world today relies on fossil fuels for over 85% of its energy use. Biomass is a carbon neutral resource in its life cycle. It is the fourth largest source of energy in the world after coal, petroleum and natural gas, providing about 14% of the world's primary energy consumption. Therefore, biomass is being considered as an important energy resource all over the world. Biomass is used to meet a variety of energy needs, including generating electricity, fuelling vehicles and providing process heat for industries. Among all the renewable sources of energy, biomass is unique as it effectively stores solar energy. It is the only renewable source of carbon that can be converted into convenient solid, liquid and gaseous fuels through different conversion processes (Saxena, Adhikari et al. 2009). The fluidized beds appear to be the most efficient and suitable for converting biomass (agricultural and wood residues etc.) into energy among the proven combustion technologies. The inherent advantages of fluidized beds, like high efficiency even with low grade fuels, compact combustion chamber with high heat and mass transfer rates, relatively low combustion temperatures and subsequently low emissions of NOx, fuel flexibility and easy temperature control; make fluidized beds an attractive option for the utilization of biomass (Natarajan, Nordin et al. 1998). In recent years, fluidized bed combustion has received wide attention given its potential as an economic and environmentally acceptable technology for burning low-grade coals, biomass and organic wastes, and mixtures of these fuels (Gungor 2013). Biomass fluidized bed combustion requires the most attention in order to gain a deeper understanding of the combustion behaviour under oxy-fuel conditions.

The aim of the present study was to design, manufacture, commission and testing of bubbling fluidized bed reactor (BFBR) for biomass combustion in air and oxy-fuel environment. Understanding the combustion rates of biomass is an important step towards the proper designing of biomass fluidized bed reactor on a large scale.The experimental work reported here is divided into two sections: analytical analysis and preliminary testing of newly commissioned BFBR. The characterization of biomass was carried out using thermo-gravimetric analysis technique. The second section investigates the hydrodynamic behaviour of a cold BFBR proposed for the continuous combustion of biomass. The sintered distribution plate was used for fluidization study as well as for the minimum fluidization velocity (U_{mf}) calculations. Newly designed biomass screw feeder was calibrated and tested using three types of biomass feedstocks; wood pellets (WP), miscanthus pellets (MP) and straw pellets (SP), all of these feedstocks were produced within the UK. Combustion experiments were conducted at temperatures up to 850 °C to investigate the combustion parameters of selected biomass under different operating conditions like air flow rate, level of excess air, temperature and feed rate.

2. EXPERIMENTAL DESIGN

The design of a fluidized bed reactor involves a careful evaluation of fuel characteristics followed by the selection of operating parameters: temperature, pressure, gas velocity, gas and solids residence time. The current design of the fluidized bed is the key to successful and efficient operation of a reactor. The schematic diagram of the bubbling fluidized bed reactor (BFBR) system is illustrated in Figure 1. This consists of the main reactor, water-cooling heat extraction probe, single screw feeding unit, cyclone and data acquisition devices. The specifications of reactor are; plenum (diameter 101.6 mm, height 300 mm); bed region (diameter 101.6 mm, height 800 mm); free-board region (diameter 152.4 mm, height 1.05 m).

The main bed region of the reactor was constructed of high grade 312 stainless steel. The freeboard region of the reactor was constructed of 316 stainless steel. The total height of the reactor is approximately 2.2 m. High grade stainless steel flanges were used while connecting bed region section with free board region and plenum. The distribution plate was flanged between plenum and bed region section of the reactor.

Two semi cylindrical ceramic fibre heaters (model: VS106J18T-B001R) 2100 watt, 600 mm long, 165 mm internal diameter manufactured by Watlow US were installed in series across the main body of the bed region. These heaters have a heating capacity up to 1000 °C. Another samox heavy insulated heating tape (model: STH052-120) 940 watt, 12.7 mm wide, 305 mm long, heating capacity up to 750 °C manufactured by Omega UK was installed on the flexible steel hose (diameter 50.8 mm) to preheat the air before entering into the reactor. The maximum working temperature of this stainless steel hose is 650 °C. The installed heaters were only used to get the required temperatures for combustion inside the reactor; once combustion started the heaters were switched off. A series of thermocouples (T), air staging points (S) and pressure sensors (P) were

Figure 27: Schematic diagram of bubbling fluidized bed

also installed in the reactor to monitor the fluidization and combustion process. P1, P2 and P6 were the positions of pressure sensors used to measure pressure drop across the distribution plate.
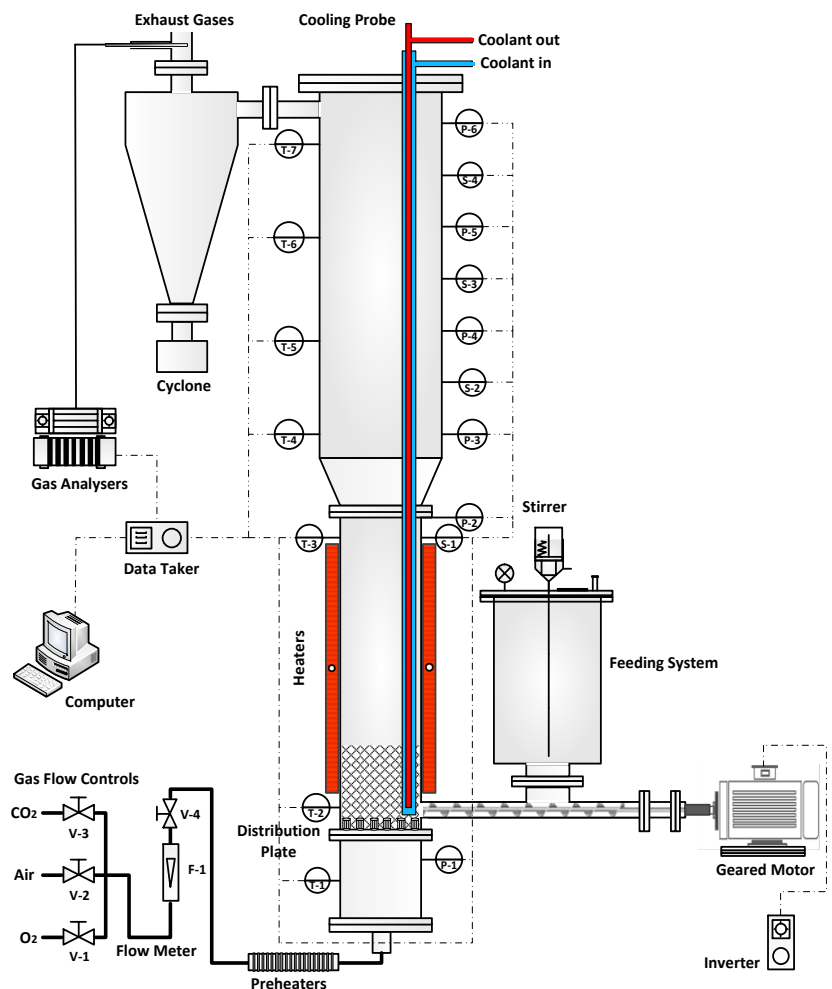
For biomass combustion it is crucial to control temperatures inside the reactor for that water-cooling heat extractions probe (length 2 m, outer pipe 12 mm and inner pipe 6 mm diameter) was installed from the top of the reactor all way down to the sand bed. A screw feeder has been designed, it is very important to ensure that the biomass particles completely fall away or swept away in order to prevent blockage, which can lead to serious physical deformation. The feeding unit consists of a cylinder shaped hopper (600 mm height and 280 mm diameter), a screw (35 mm diameter) with 38 mm pitch flight, which was connected with a geared motor made by SEW Eurodrive which was controlled by a power flex inverter made by Allen Bradley. An overhead stirrer was also installed for breaking bridging in the hopper. All parts were carefully adjusted to ensure continuous and reliable feeding during combustion. The gases from the fluidized bed reactor usually need to be cleaned of entrained particles, the cyclone separators are typically used for such applications. A reverse flow cyclone separator (1.08 m height, 280 mm top and 76 mm bottom diameters)

was installed at the exit of the reactor. Momentum pushes the incoming particles toward the wall where centrifugal forces cause gas-solid separation. A gas cooling probe was used for flue gas to cool it down before entering into the analyzers. To find out the most favorable fluidization conditions, a sintered plate was used as distribution plate. For continuous air supply through a flexible stainless steel hose (diameter 50.8 mm); a blower fan (model 34-2 QZ, speed 290 RPM) manufactured by Fans and blower Ltd UK was installed.

3. MATERIALS AND METHODS

3.1 Distributor type

A sintered distribution plate was used for fluidization and minimum fluidization velocity (U_{mf}) calculations, its specifications are given in Table.1. Air at ambient temperature and pressure was used for the fluidization in the BFBR.

Table 13: Specifications of distributor.

Distributor Type	Material	Thickness mm	Diameter mm	Pore size mm
Sintered plate	Stainless steel frits	12	115	0.002

Garside 14/25 sand with a sauter mean diameter (d_{32}) of 0.78 mm was used as the bed material. Cold rig experiments were conducted with and without sand for comparison of pressure drop across the distributor.

3.2 Materials characterization

Three biomass feedstocks; wood pellets (WP), miscanthus pellets (MP) and straw pellets (SP) were selected for the experiments. Proximate and ultimate analysis were conducted using a thermo-gravimetric analyzers TGA-Q500 and CE Instruments Flash EA 1112 series, respectively; results are reported in Table 2. The proximate TG method involves heating the sample under N_2 at a rate of 10 °C/min to 110 °C then holding for 10 min to obtain the weight loss associated with moisture. The temperature was then ramped from 110 °C at a rate of 20 °C/min to 950 °C and held for 10 min to obtain the weight loss associated with volatiles release. The air was then introduced into the furnace chamber and hold up for 30 min to fully oxidize the carbon in the char and the weight loss associated with this was the fixed carbon. The remaining material after combustion was the ash.

Table 2: Ultimate and proximate analysis of biomass fuels.

Biomass Fuels	Ultimate analysis[a]					Proximate analysis[c]				HHV[e] (MJ/kg)
	C (%)	H (%)	N (%)	O[b] (%)	S (%)	M (%)	VM (%)	FC (%)	Ash (%)	
Wood pellet (WP)	47.02	6.17	0.07	46.75	0.00	6.34	84.94	14.28	0.79	18.83
Miscanthus pellets (MP)	42.67	5.86	0.44	51.04	0.00	6.91	78.29	16.33	5.38	16.40
Straw pellets (SP)	41.32	5.69	1.18	51.81	0.00	6.41	72.28	18.22	9.50	15.56

M: moisture, VM: volatile matter, FC: fixed carbon, LHV: lower heating value, HHV: higher heating value.

[a] On dry basis except as denoted in the table.

[b] Calculated by difference.

[c] On dry basis except moisture which is as received basis.

[d] As received basis.

[e] Calculated based on (Channiwala and Parikh 2002).

3.3 Operating conditions

All the devices, including pressure transducer, flow meters and gas analyzers were calibrated before starting the experiments. The reactor was topped up with 3.2 kg of sand up to a height of 250 mm in a stationary state from distributor for all the experiments. Before each experiment the hopper was filled with the selected type and amount of biomass. The reactor was heated up using main and preheater to the desired temperature for combustion (i.e. +515 °C), once the temperature has reached to the set point, the biomass from the hopper was fed gradually into the reactor using screw feeder. The water-cooling heat extraction probe was introduced into the reactor to control excessive temperatures during combustion, the required water flow rate was adjusted using rota meter. Stoichiometric ratio (SR) for the combustion was varied from a range of 1.0 to 4.5 to investigate the effect of SR on the flue gas composition, temperatures and heating values. The flow rate of the air supplied for combustor was kept constant, but biomass feed rate was varied according to SR to ensure the total amount of air supplied into the whole system remain constant. Some air was also flushed through the sealed feeder hopper to prevent backfire as well as to stop hot gases and sand coming into the feeding pipe. Experiments were conducted using 10%, 15%, 30% and 45% excess air levels. The average temperature above the distributor was used as bed temperature. The successful measurements recorded, when the temperatures reached the steady state. The operated parameters are listed in Table 3.

Table 3: BFBR operating conditions for wood pellet combustion.

Parameters	Values
Stoichiometric Ratio (SR)	1.0 – 4.5
Primary air flow rate (L/min)	300
Secondary (feeder) air flow rate (L/min)	50
Excess air (%)	10 – 45
Main heaters temperature setup (^{o}C)	850
Preheater temperature setup (^{o}C)	450
Cooling water flow rate (L/min)	1.2
Biomass feed rate (kg/h)	3 – 4

The flue gas after the cyclone was passed through a water cooling probe, which was finally sent to the online gas analyzers for analysis after removing particles and moisture. Temperatures were measured inside the reactor at different heights through the installed thermocouples. All variables in the rig temperatures, pressures and gas composition were measured and data was stored each 10 s by the data taker system through software. At the end of the experiment, rig was cool down to room temperature before it shut down.

4. RESULTS AND DISCUSSION

4.1 Minimum fluidization and physical properties

Fluidization occurs when solid particles are suspended in an upward flowing stream of fluid. The solid particles swirl around the bed rapidly, creating excellent mixing among them. The material fluidized is almost a solid and the fluidizing medium is either a liquid or gas, in the present case is gas (air). The characteristics and behaviour of a fluidized bed are strongly dependent on both the solid and gas properties. The minimum fluidization velocity (U_{mf}) is the point of transition between a fixed bed regime and a bubbling regime in a fluidized bed. Minimum fluidization velocity is one of the most important normalized parameters when characterizing the hydrodynamics in a fluidized bed reactor (Caicedo, Ruiz et al. 2002).

Usually, the minimum fluidization velocity is obtained experimentally, and there are several techniques reported in the literature to find out the minimum fluidization velocity in a multiphase flow system (Gupta and Sathiyamoorthy 2010). The most common method measures the pressure drop across the bed as a function of the superficial gas velocity. The point of transition between a fixed bed regime and a bubbling regime is denoted by a constant pressure line in a plot of pressure verses superficial gas velocity; this point marked the minimum fluidization velocity. Several equations have been reported in the literature for determining the minimum fluidization velocities of single component particles as well as for binary mixtures of the same material with different particle sizes. In the present work minimum fluidization velocity was determined from the abscissa of the point from which the pressure drop remained constant. The following equation, widely used in the literature (Wen and Yu 1966, Kunii and Levenspiel 1991) to calculate minimum fluidization velocity, was employed:

$$Re_{p,mf} = \sqrt{33.7^2 + 0.0408\,Ar} - 33.7 \tag{1}$$

Where *Re* and *Ar* represents Reynolds and Archimedes numbers respectively, defined as:

$$Re_{p,mf} = \frac{\rho_g\,U_{mf}\,d_p}{\mu_g} \tag{2}$$

$$Ar = \frac{\rho_g\,(\rho_p - \rho_g)\,g d_p^3}{\mu_g^2} \tag{3}$$

According to (Wen and Yu 1966, Grace 1986) Equation 1 can be further simplified into the form of Equation 4.

$$U_{mf} = 0.202 \sqrt{\frac{d_p(\rho_d - \rho_g)\,g}{\mu_g}} \tag{4}$$

Where ρ_s and ρ_g are densities of sand particles and gas respectively, d_p is the particle diameter, μ_g is the gas viscosity and *g* is the acceleration due to gravity. The theoretical value of minimum fluidization velocity was calculated using equations 1-4.

Initially two types of fluidization experiments with and without sand were performed to determine minimum fluidization velocity. The air flow rate was gradually increased and at each increment the pressure drop (ΔP) was recorded using a pressure transducer. The linear fit correlation from the experiments without sand is shown in Figure 2(a). Similarly, the results from the experiments with sand are presented in Figure 2(b). There is a drag exerted on the sand particles by the flowing gas, at low air flow rates the pressure drop resulting from this drag was small. At the air flow rate of 100 L/min, the pressure drop of 17.8 mbar was recorded. It is evident from Figure 2(b), when the air flow is increased to a certain level about 250 L/min with a pressure drop of 27 mbar, the total drag on the sand particles become equal the weight of the bed, and the particles begin to lift at this stage bed just become fluidized.

The highest value of pressure drop recorded was 36 mbar at an air flow rate of 800 L/min. Whereas, at the same air flow rate the pressure drop due to only sand particles was 30 mbar. It is also evident from Figure 2(b) that the entire pressure drop is not due to the weight of sand but also due to the pore resistance of the distributor. At higher air flow rates, the bed pressure drop also shows a slight decrease, which could be attributed to the frictional forces on the walls of the reactor (Hilal, Ghannam et al. 2001). From visual observations at air flow rates above the point of minimum fluidization >250 L/min, fluidized bed appears much like a vigorously boiling liquid; bubbles of gas rise rapidly and burst on the surface, and the emulsion phase is thoroughly agitated. The bubbles form near the bottom of the bed, close to the distributor plate. From the experimental data the value of minimum fluidization velocity was found to be 0.51 m/s, whereas the theoretical calculated value was 0.40 m/s. This difference between theoretical and experimental values could be attributed with different diameters of the sand particles.

Biomass fuels usually pose difficulties in handling and feeding due to their poor flow characteristics. Screw feeders are most popular volumetric feeding devices which are able to deliver bulk solids over a wide range of feed rates. The advantages of using screw feeder for biomass are low cost, flexibility of use, functional reliability, easy to install and less environmental pollution risks. The feeder for the present study was designed to
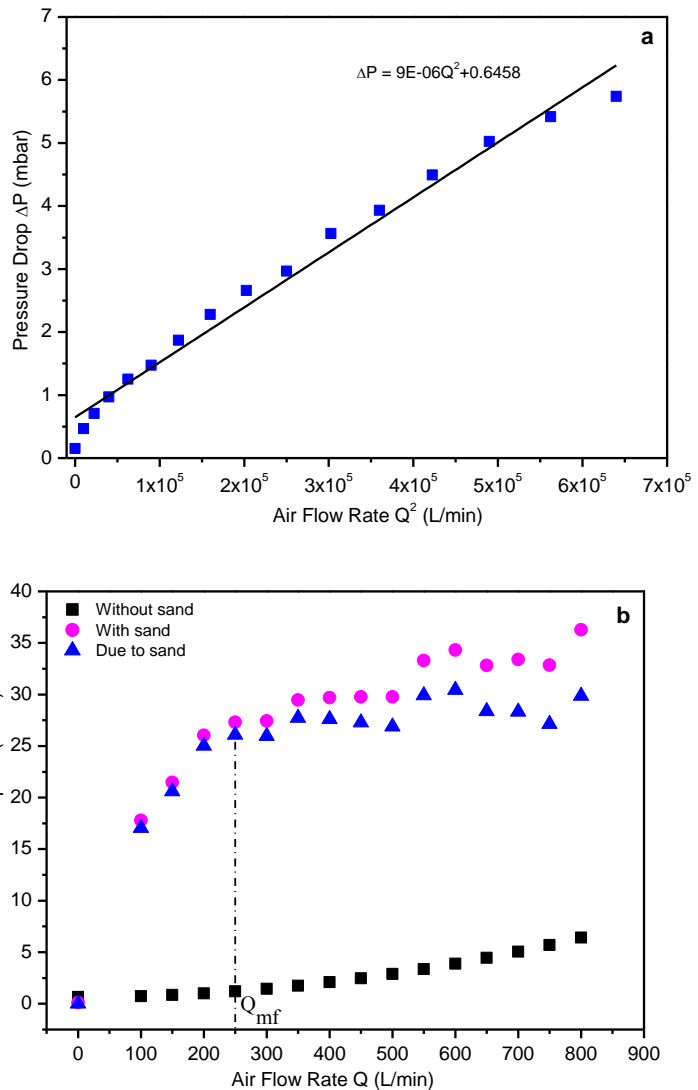

Figure 2: Pressure drop measurements with sintered distribution plate; a) without sand, b) with sand.
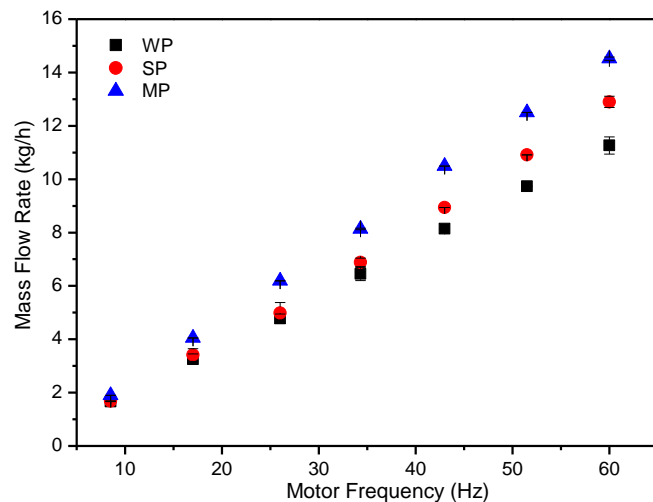

Figure 3: Biomass feeding rate at different frequencies.

deliver 3–5 kg/h of biomass on a continuous, steady state and accurate basis. Three types of biomass feedstocks; wood pellets (WP), miscanthus pellets (MP) and straw pellets (SP) size range from 10–20 mm were tested in the newly designed feeding system. It is clear from Figure 3 that MP feed rate was the highest, followed by SP and WP at the end. The flow rate of a screw feeder depends on a number of factors like geometry of the screw, rotational speed, inclination, geometry of the feed hopper and flow ability of the material (Yu and Arnold 1995). If the biomass entering the screw is compressible, the mass delivered per unit time varies. As the screw rotates, particles move in a helical path of the opposite hand to that of the screw. The feed rates for the present study were found to be very smooth at low rpm but a little variation in the feed rates were observed at higher rpm. It is also clear from the results that the volumetric capacity is linearly proportional to the motor frequency.

4.2 Temperature profiles

The combustion experiments in the present study were performed using wood pellet (WP) as a fuel. The feed rates were varied according to different excess air levels. Table 3 states the operating conditions and other variables for these combustion experiments. The effect of these variables on temperature profiles, combustion efficiency and flue gas composition was studied.

The whole combustion process is divided into three stages; achievement of bed temperatures, steady-state combustion and final measurements. After achieving bed ignition temperature about 515 °C, the biomass was fed into the reactor. The temperatures in the bed region during combustion were maintained in the range of 750–850 °C. Overall, temperatures in the reactor were controlled by the water-cooling heat extraction probe, which was inserted from the top of the reactor. The temperatures of the cooling water in and out were monitored throughout the experiments to get the exact amount of heat released from the system. A window of 45 min during combustion of the biomass was studied only when the system had reached a steady state. One way of ensuring that steady state had been attained was by monitoring the flue gas composition and temperature profiles as a function of time. When the composition of the gaseous species did not vary, it was assumed that the system had reached a steady state, then readings were recorded for that specific case. Figure 4 illustrates that the BFBR running very smooth even after 4 h, since the time elapsed after feeding. Windows a, b, c and d correspond to stoichiometric ratios (SR) 1.45, 1.30, 1.15 and 1.10 respectively at steady state conditions. It is also evident from Figure 4 that the combustion process is stable throughout the experiment.
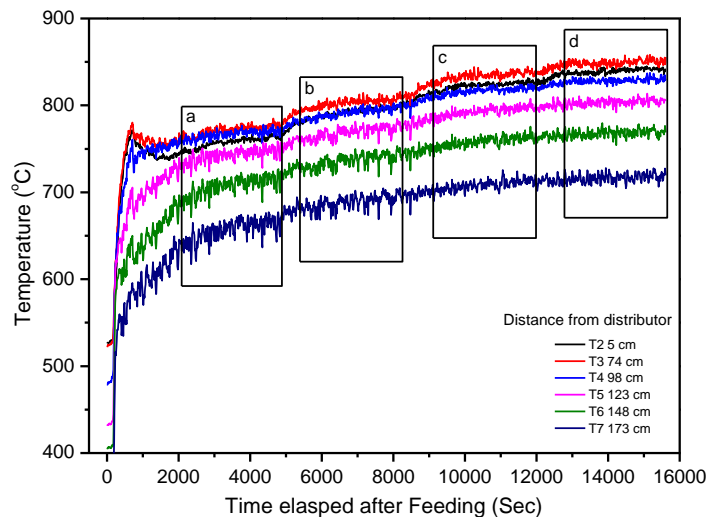

Figure 4: Steady state temperature profiles against time; a) SR 1.45, b) SR 1.30, c) SR 1.15 and d) SR 1.10.
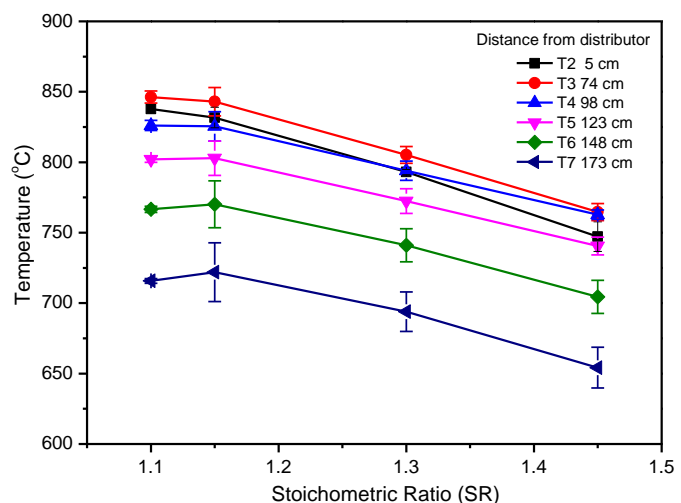

Figure 5: Temperature profiles at different locations against various SR.

The temperature gradient inside the fluidized bed is another important characteristic. Figure 5, represents the temperature profiles along the height of the reactor at different SR. The results are presented that SR influence the temperatures inside the reactor, which is more significant in the bed region T2–T3. With an overall observations temperatures increase with the decreasing SR but after a certain value of SR 1.15, temperatures show decreasing trend in the freeboard region. This could be attributed to some incomplete combustion due to less availability of excess air, which is also proved by a higher CO concentration shown in Figure 6. This low air flow rate promotes a poor mixing of the bed. If the air flow rate grows further, the strong combustion zone will move to the top of the freeboard region (Armesto, Bahillo et al. 2002). On the other hand the temperatures in the bed region show increasing trend even after SR 1.15. It is also evident from the Figure 5 that the main combustion process is happening mainly between T2 and T4 zones. The highest average peak temperature of 847 °C corresponding to the zone T3 at SR 1.15 was recorded. Above this zone the temperatures decrease slowly until the end of the expanded bed. Further up the temperature T7 decreases strongly with a lowest measurement of 650 °C near the exit of the BFBR. All the temperature profiles except T2 in the main bed region, have achieved stable and homogeneous distributions throughout the combustion process. This unusual variation in the T2 inside the bed region could be associated with complex bed hydrodynamics of BFBR. The differences in the profiles are also a consequence of the strong influence of the operating conditions (Permchart and Kouprianov 2004).

4.3 Flue gas composition

The components of the flue gas were mainly carbon dioxide (CO_2), carbon monoxide (CO), unreacted oxygen (O_2) and nitrogen oxides (NOx). The variations in the composition of these species are shown in Figure 6 and 7. The stoichiometric ratio (SR) plays an important role in the emission characteristics during combustion. At lower SR 1.10 the composition of CO_2, CO, O_2 and NOx was found to be 18.64%, 0.71%, 1.67% and 40.08 ppm respectively. It is evident from Figure 6 that by increasing SR the concentration of O_2 and NOx increases, whereas CO_2 and CO decreases. At highest value of SR 1.45 the composition of CO_2, CO, O_2 and NOx was recorded as 14.85%, 0.29%, 5.94% and 68.30 ppm respectively. At lower SR the temperature of a burning particle may be lower than the high one, which may result as extended values of CO and CO_2 (Lin, Dam-Johansen et al. 2003). The CO concentration also shows a strong dependency on SR. The CO concentration changed between 0.2% to almost 0.7%. Highest value of 0.7% for CO at SR 1.10 was observed, when the bed average temperature T2 was 837 °C (highest). The emissions of CO are a complex function of many factors like low combustion temperatures, low quality of the mixture between the air and the biomass and low residence time of the combustible gases in the combustion zone (Alonso, Diego et al. 2014).

Flue gas concentration, combustion temperature and excess air ratio can be taken as the important parameters that represent the combustion conditions. Since, excess air ratio was nearly kept constant during all the experiments; hence O_2 is
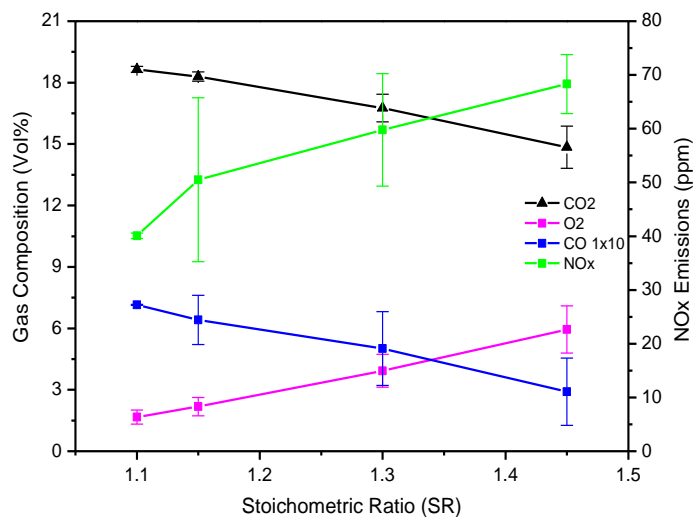

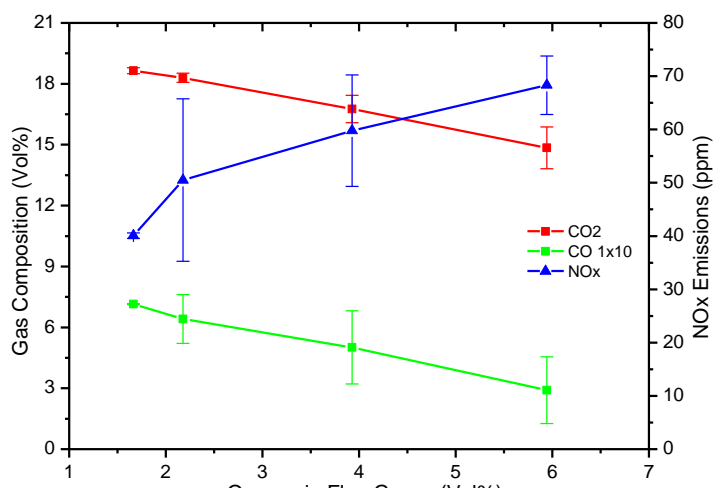**Figure 6:** Flue gas compositions against different SR.

Figure 7: Flue gases composition against oxygen in flue gas.

adopted as a representation parameter over the other components in the flue gas. Figure 7 represents the average gas composition against O_2 in flue gas during combustion. The average NOx concentration increases, whereas CO and CO_2 concentrations decrease with an increase in O_2 level in the flue gas. The CO emissions are high at low SR ratios means with less O_2 in flue gas, which was also observed at the beginning of an experiment, especially, when the temperature of freeboard is lower than at the moment of the experiment reaches the steady-state conditions (Johansson, Tullin et al. 2003). The maximum CO emission obtained during the combustion at SR 1.10 was recorded as 0.7%. The plots of CO_2 and O_2 show a symmetrical relationship with averaged values of around 17% and 4% respectively at SR equal to 1.30. Figure 7 also represents low NOx with maximum value 68.30 ppm at SR 1.45, the main reason for this is because the wood pellets (WP) contains the lowest N contents among the other studied fuels, which is also listed in Table 2.

5. CONCLUSIONS

A pilot scale bubbling fluidized bed reactor (BFBR), capacity 20 kW was designed, set up and successfully tested. The effect of distributor, i.e., sintered plate on the flow behaviour of the bed has been studied. Garside 14/25 sand with a stationary height of 250 mm was used as bed material; the bed height and weight were kept constant throughout all the experiments. In order to fluidize the bad material, a specific gas velocity is required to overcome the distributor resistance and solids bed weight. The value of minimum fluidization velocity (U_{mf}) was found to be velocity of 0.51 m/s. The biomass volume delivered by feeder in a given time depends on the screw flight diameter, shaft diameter, pitch and the fullness of the screw. A continuous, smooth and reliable biomass feeding of wood pellets in the range of 3–4 kg/h was successfully achieved during combustion. The influence of the stoichiometric ratio (SR) on temperatures and flue gas composition was also studied during combustion experiments. The temperatures in the bed were evenly distributed; the average temperatures in the main reaction zone were in the range of 750–850 ^{o}C. The composition of the flue gas heavily dependent on SR. The average concentrations of the four main components of the flue gas CO_2, CO, O_2 and NOx were in the range of 14.85–18.64%, 0.29–0.70%, 1.67–5.94% and 40.08–63.30 ppm respectively with SR from 1.10 to 1.45. In future other biomass feedstock will be tested using same reaction conditions under the air, then under oxy-fuel environment.

7. REFERENCES

Alonso, M., M. Diego, C. Pérez, J. Chamberlain and J. Abanades (2014). "Biomass combustion with in situ CO 2 capture by CaO in a 300kW th circulating fluidized bed facility." International Journal of Greenhouse Gas Control **29**: 142-152.

Armesto, L., A. Bahillo, K. Veijonen, A. Cabanillas and J. Otero (2002). "Combustion behaviour of rice husk in a bubbling fluidised bed." Biomass and Bioenergy **23**(3): 171-179.

Caicedo, G. R., M. G. Ruiz, J. J. P. Marqués and J. G. Soler (2002). "Minimum fluidization velocities for gas–solid 2D beds." Chemical Engineering and Processing: Process Intensification **41**(9): 761-764.

Channiwala, S. and P. Parikh (2002). "A unified correlation for estimating HHV of solid, liquid and gaseous fuels." Fuel **81**(8): 1051-1063.

Grace, J. R. (1986). "Contacting modes and behaviour classification of gas-solid and other two-phase suspensions." The Canadian Journal of Chemical Engineering **64**(3): 353-363.

Gungor, A. (2013). "Simulation of co-firing coal and biomass in circulating fluidized beds." Energy Conversion and Management **65**: 574-579.

Gupta, C. K. and D. Sathiyamoorthy (2010). Fluid bed technology in materials processing, CRC Press.

Hilal, N., M. Ghannam and M. Anabtawi (2001). "Effect of bed diameter, distributor and inserts on minimum fluidization velocity." Chemical Engineering and Technology **24**(2): 161-166.

Johansson, L., C. Tullin, B. Leckner and P. Sjövall (2003). "Particle emissions from biomass combustion in small combustors." Biomass and bioenergy **25**(4): 435-446.

Kiesgen De Richter, R., T. Ming and S. Caillol (2013). "Fighting global warming by photocatalytic reduction of CO2 using giant photocatalytic reactors." Renewable and Sustainable Energy Reviews **19**: 82-106.

Kunii, D. and O. Levenspiel (1991). Fluidization engineering, Butterworth-Heinemann Boston.

Lin, W., K. Dam-Johansen and F. Frandsen (2003). "Agglomeration in bio-fuel fired fluidized bed combustors." Chemical Engineering Journal **96**(1): 171-185.

Natarajan, E., A. Nordin and A. Rao (1998). "Overview of combustion and gasification of rice husk in fluidized bed reactors." Biomass and Bioenergy **14**(5-6): 533-546.

Saxena, R., D. Adhikari and H. Goyal (2009). "Biomass-based energy fuel through biochemical routes: a review." Renewable and Sustainable Energy Reviews **13**(1): 167-178.

Shuit, S. H., K. T. Tan, K. T. Lee and A. H. Kamaruddin (2009). "Oil palm biomass as a sustainable energy source: A Malaysian case study." Energy **34**(9): 1225-1235.

Vijaya Venkata Raman, S., S. Iniyan and R. Goic (2012). "A review of climate change, mitigation and adaptation." Renewable and Sustainable Energy Reviews **16**(1): 878-897.

Wall, T. F. (2007). "Combustion processes for carbon capture." Proceedings of the Combustion Institute **31**(1): 31-47.

Wen, C. and Y. Yu (1966). "A generalized method for predicting the minimum fluidization velocity." AIChE Journal **12**(3): 610-612.

Yu, Y. and P. Arnold (1995). Estimate of the volumetric efficiency of a screw feeder. 5th International Conference on Bulk Materials Storage, Handling and Transportation: Proceedings, Institution of Engineers, Australia.

SESSION 20: SOLAR ENERGY

64: Performance investigation on vertical diffusion multi-effect solar still with parallel feed

H Sharon[1], K S Reddy[2]

[1,2]Department of Mechanical Engineering, Heat Transfer and Thermal Power Laboratory, Indian Institute of Technology Madras, email id: [2]ksreddy@iitm.ac.in
Tel.:+91 44 22574702; fax: +91 44 22574652

Solar thermal distillation of saline water is an effective way to meet the clean water demands of remote and rural population. Multi-effect solar stills have been widely acknowledged for their high distillate productivity. Most of the multi-effect solar stills studied are of horizontal type which has reduced distillate yield compared to vertical multi-effect diffusion solar stills. In this work, a new configuration of vertical diffusion multi-effect solar still has been proposed and it has been optimized using transient mathematical modelling. The feed water separately heated in solar collector is distributed equally in all effects such that glass reflectors, heat pipes which were used for heating the first effect of previous configurations have been avoided which increases the safety and handling flexibility of the present unit. The optimum number of effects and diffusion gap was found to be 5 and 10 mm, respectively. The distillate yield from the unit was highly dependent on the diffusion gap, mass flow rate of feed water circulated through the solar collector and feed water salinity. Distillate yield was found to decrease with the increase in salinity of feed water and maximum distillate yield was recorded as 8.25 kg/m^2-d and 6.07 kg/m^2-d during summer for feed water with 0 and 10 wt% salinity, respectively. The yield from the unit supplied with hot feed water from evacuated heat pipe solar collector is higher than the yield from the unit supplied with hot feed water from solar flat plate collector.

Keywords: solar thermal; solar distillation; vertical still; water; multi-effect;

1. INTRODUCTION

Scarcity of clean drinking water is a major problem in different parts of the globe. Desalination of saline water is an effective solution to tackle this problem (Ranjan et al., 2013; Pillai et al., 2013). Hence, development of suitable desalination technologies has been a wide area of interest for most of the researchers. Conventional large scale desalination units consume large amount of non-renewable energy and cause degradation to environment (Kalogirou, 2005). For remote and rural areas, desalination units powered by renewable energy are found to be cheap because of the elimination of large pipelines from decentralised fossil fuel powered desalination units (Jijakli et al., 2012). Solar energy is a widely accepted alternative to conventional energy sources and is available almost in all parts of the globe (Bozkurt et al., 2012). Basin type solar stills developed initially, has been tested for its capability to meet the fresh water demands of remote population and different techniques has also been adopted to enhance the yield of these stills (Muftah et al., 2014). Multiple effect solar stills are found to be more attractive because of their high yield (Zurigat et al., 2004; Nishikawa et al., 1998). Multiple effect solar stills that were widely studied are mainly of horizontal type. The yield of these units can be enhanced further by reducing the gap between the evaporating and condensing surface but this causes contamination of the distillate by saline feed water (Tanaka et al., 2000a). The above mentioned problem has been effectively eliminated by vertical multiple effect diffusion stills which are more compact, portable and high productive (Elsayed et al., 1984; Tanaka et al., 2000b)

Vertical multiple effect diffusion still coupled with basin type still was capable to produce 15.4 kg/m^2-d of distillate which is 40% higher than the yield from conventional multiple effect stills (Tanaka et al., 2000a; Tanaka et al., 2000b). In order to reduce the bulkiness of the previous system, vertical multiple effect diffusion still was coupled with heat pipe solar collector and was capable of producing 21.8 kg/m^2-d of distillate during sunny days (Tanaka et al., 2004a). The productivity of the unit was found to increase with the increase in number of effects, feed water inlet temperature, reduction in diffusion gap and by choosing proper tilt angle for heat pipe solar collector (Tanaka et al., 2004b). Vertical multiple effect diffusion solar still with a diffusion gap of 5 mm coupled with flat plate reflector was capable of producing nearly 13.3 kg/m^2-d of distillate (Tanaka, 2009). Vertical multiple effect diffusion still integrated with portable electric generator was found to generate distillate at a faster rate by effectively utilizing the waste exhaust heat (Tanaka and Park, 2010). From, the mentioned literatures it could be inferred that vertical multiple effect diffusion stills are high productive, compact and found to be suitable for rural and remote locations.

Generally, in the available vertical multiple effect diffusion still configurations, only the first effect is heated by solar radiation or by heat transfer fluids and the latent heat of condensation is used for preheating the feed saline water in the next effects. In the present investigation, a new type of vertical diffusion still configuration has been proposed in which the feed water is directly heated in solar collector (flat plate collector or evacuated heat pipe collector) and is distributed equally in all effects simultaneously such that heat pipes, flat plate mirrors integrated with the distillation units are avoided which increases the safety and handling flexibility of the distillation unit. The impact of number of effects, diffusion gap, mass flow rate of feed water and salinity of feed water on distillate yield of the proposed unit was simulated using transient mathematical modelling and the results were found to be fruitful.

2. PARALLEL FEED VERTICAL DIFFUSION MULTI-EFFECT SOLAR STILL

The schematic representation of the parallel feed vertical diffusion multi-effect solar still supplied with hot feed water from solar flat plate collector and evacuated heat pipe solar collector along with its necessary energy transport process is shown in Figure 1. and Figure 2., respectively. The vertical diffusion multi-effect still consists of a number of vertical partitions (usually thin metal sheets), feed water distributing unit and condensate collection unit. One surface of the metal sheet partition acts as evaporating surface for the heated feed water while the other surface act as condensing surface for the water vapour evaporated from previous partition. Each such evaporator-condenser unit is called as an effect. The feed water which is directly heated in solar collector is distributed equally to all effects, hence called parallel feed and is allowed to flow as a thin film over the evaporating surfaces. The thin film of heated water gets evaporated in the evaporating surface of the metal partition and the water vapour moves towards the condensing surface due to partial pressure difference. During condensation process, the latent heat of condensation of the water vapour from previous effect is rejected to the next effect there by enhanced evaporation begins in next effect and similar process is repeated in other effects. The condensate is collected using suitable provisions kept below at the condensing surface and the unevaporated brine is rejected from the distillation unit.

3. MATHEMATICAL MODELLING

The following assumptions have been made during modeling of the parallel feed vertical diffusion multi-effect solar still (Tanaka et al., 2000a)

a) The distillation unit is air tight and free from leakage
b) The diffusion gap between the metal partitions is very small such that convection is arrested
c) Heat transfer from the evaporating to condensing surface is by conduction, radiation and evaporation
d) The thickness of the fluid film flowing over the evaporating surface is assumed to be very thin and the brine leaves the distillation unit at the evaporating surface temperature
e) Heat loss through the top and bottom surfaces of the distillation unit is negligible
f) Heat transfer from the last metal partition to the ambient is by convection and radiation
g) Constant water level is maintained in the feed water tank

Figure 28: Schematic representation and energy transport process in parallel feed vertical diffusion multi-effect solar still supplied with hot water from Solar Flat Plate Collector (FPC)

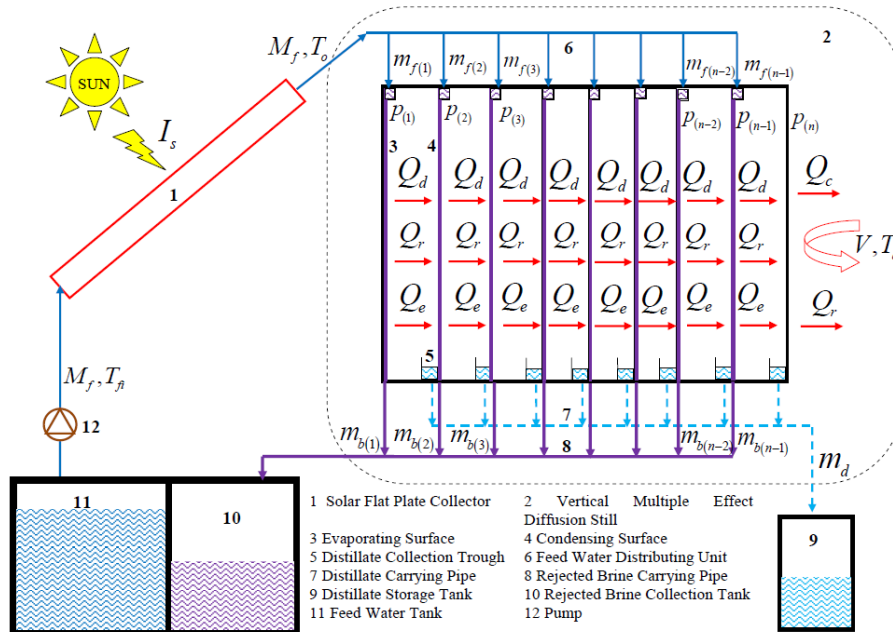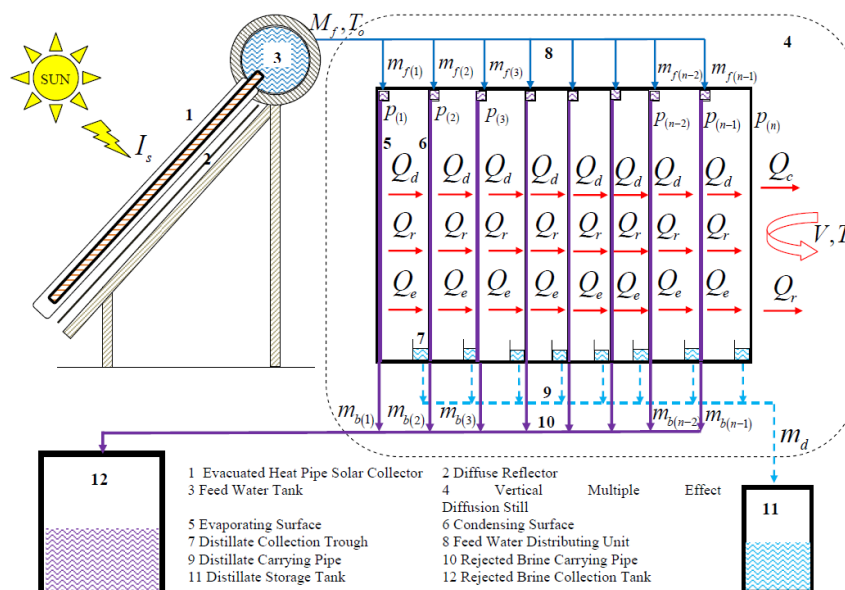*Figure 2: Schematic representation and energy transport process in parallel feed vertical diffusion multi-effect solar still supplied with hot water from Evacuated Heat Pipe (EHP) Solar Collector*

The energy balance for different components of the proposed distillation unit is given below:

Equation 4: Energy balance for the feed water tank integrated with EHP

$$(MC)_w \frac{dT_w}{dt} = Q_u + M_f c_f T_a - M_f c_f T_o - Q_{l(w-a)}$$

Equation 2: Energy balance for the first effect of the distillation unit

$$(MC)_{p(1)} \frac{dT_{p(1)}}{dt} = m_{f(1)} c_f T_o - \left(Q_d + Q_r + Q_e\right)_{(p(1)-p(2))} - m_{b(1)} c_{b(1)} T_{fo(1)}$$

Equation 3: Energy balance between the effects

$$(MC)_{p(i)} \frac{dT_{p(i)}}{dt} = m_{f(i)} c_f T_o + \left(Q_d + Q_r + Q_e\right)_{(p(i-1)-p(i))} - \left(Q_d + Q_r + Q_e\right)_{(p(i)-p(i+1))} - m_{b(i)} c_{b(i)} T_{fo(i)}$$

$$i = 2,3,......,(n-1)$$

Equation 4: Energy balance for the nth condensing surface or metal partition exposed to ambient

$$(MC)_{p(n)} \frac{dT_{p(n)}}{dt} = \left(Q_d + Q_r + Q_e\right)_{(p(n-1)-p(n))} - \left(Q_c + Q_r\right)_{(p(n)-a)}$$

Where:

- c_f = specific heat capacity of feed water (J/kg-K)
- c_b = specific heat capacity of the rejected brine (J/kg-K)
- $(MC)_P$ = heat capacity of metal partition (J/K)
- $(MC)_w$ = heat capacity of water mass in feed water tank of EHP solar collector (J/K)
- m_b = mass flow rate of rejected brine from each effect (kg/s)
- m_f = mass flow rate of heated feed water distributed through each effect (kg/s)
- T_{fo} = temperature of the rejected brine (K)
- T_o = outlet temperature of feed water leaving the solar collector (K)
- T_p = temperature of metal partition (K)

Equation 5: Conductive heat transfer between evaporating and condensing surfaces

$$Q_{d(p(i-1)-p(i))} = \frac{K_h A_p}{W}\left(T_{p(i-1)} - T_{p(i)}\right)$$

Where:

- A_p = area of evaporating/condensing surface (1.0 m^2)
- K_h = thermal conductivity of humid air (W/m-K)
- W = diffusion gap (m)
- $T_{p(i-1)}$ = temperature of the evaporating surface ($^\circ$C)
- $T_{p(i)}$ = temperature of the condensing surface ($^\circ$C)
- $Q_{d(p(i-1)-p(i))}$ = conductive heat transfer between evaporating and condensing surface (W)

Equation 6: Evaporative heat transfer between evaporating and condensing surfaces

$$Q_{e(p(i-1)-p(i))} = \frac{D P_t h_{fg} A_p M_v}{\bar{R} W T_m} \ln\left[\frac{P_t - P_{(T_{p(i)})}}{P_t - P_{(T_{p(i-1)})}}\right]$$

Where:

- D = diffusivity of water vapour in air (m^2/s)
- P_t = total pressure (101325.0 Pa)
- $P_{(T_p(i))}$ = partial pressure of water vapour at the condensing surface (Pa)
- $P_{(T_p(i-1))}$ = partial pressure of water vapour at the evaporating surface (Pa)
- $Q_{e(p(i-1)-p(i))}$ = evaporative heat transfer between evaporating and condensing surface (W)
- h_{fg} = latent heat of vaporization of water (J/kg)
- M_v = molecular weight of water vapour (18.0 kg/kmol)
- $\bar{R}$ = universal gas constant (8314.0 J/kmol-K)
- T_m = mean temperature of evaporating and condensing surface (K)

Equation 7: Mean temperature of evaporating and condensing surface.

$$T_m = \frac{\left(T_{p(i-1)} + 273.0\right) + \left(T_{p(i)} + 273.0\right)}{2.0}$$

Equation 8: Radiative heat transfer between evaporative and condensing surfaces

$$Q_{r(p(i-1)-p(i))} = \frac{\sigma A_p \left(\left(T_{p(i-1)} + 273.0\right)^4 - \left(T_{p(i)} + 273.0\right)^4\right)}{\left(\frac{1}{\varepsilon_p} + \frac{1}{\varepsilon_p} - 1.0\right)}$$

Where:

- σ = Stefan-Boltzmann constant (5.67 x 10^{-8} W/m^2-K^4)
- ε_p = emissivity of metal partition (0.21)
- $Q_{r(p(i-1) - p(i))}$ = radiative heat transfer between evaporative and condensing surface (W)

Equation 9: Convective heat transfer from the last partition to ambient

$$Q_{c(p(n)-a)} = \left(5.7 + 3.8(V)\right) A_p \left(T_{p(n)} - T_a\right)$$

Where:

- V = wind velocity (m/s)
- T_a = ambient temperature ($^\circ$C)
- $Q_{c(p(n) - a)}$ = convective heat transfer from last partition to ambient (W)

Equation 10: Radiative heat transfer from the last partition to ambient

$$Q_{r(p(n)-a)} = \sigma A_p \varepsilon_p \left(\left(T_{p(n)} + 273.0\right)^4 - \left(T_a + 273.0\right)^4\right)$$

Where:

- $Q_{r(p(n) - a)}$ = radiative heat transfer from last partition to ambient (W)

Equation 11: Outlet fluid temperature of solar flat plate collector

$$T_o = \left(\frac{I_s\left(\tau_g \alpha_b\right)}{U_l} + T_a\right)\left[1 - \exp\left(\frac{-A_c U_l F'}{M_f c_f}\right)\right] + T_{fi} \exp\left[\frac{-A_c U_l F'}{M_f c_f}\right]$$

Where:

- I_s = incident solar radiation on the south facing solar collector (W/m^2)
- U_l = overall heat loss coefficient (7.0 W/m^2-K)
- A_c = aperture area of solar flat plate collector
- M_f = mass flow rate of feed water circulated through the solar collector (kg/s)
- F' = collector efficiency factor (0.95)
- T_{fi} = temperature of feed water entering the solar collector (K)

Equation 12: Useful heat energy gained by the EHP solar collector (Xiong et al., 2013)

$$Q_u = A_e \eta_e I_s$$

Where:

- Q_u = useful heat energy gained by the EHP solar collector (W)
- A_e = Solar radiation receiving area of EHP solar collector (m^2)
- η_e = Efficiency of EHP solar collector ($\eta_e = 0.635 - 1.96\left(\frac{T_w - T_a}{I_s}\right)$)

The coupled differential equations used for modeling the parallel feed vertical diffusion multi-effect solar still were first discretized using finite difference technique and were converted to algebraic equations. The obtained algebraic equations were solved by iteration method using the program written in FORTRAN

language. The necessary inputs like solar radiation intensity, wind velocity and ambient temperature for each day has been given as inputs using separate input files. Time step size of 10 s and convergence criteria of 0.001 was used. The temperature of different components of the unit were assumed to be at ambient condition initially and were used to calculate the necessary heat transfer coefficients which were then substituted in their respective equations to obtain the new temperature values. If the difference between the temperature values of new and previous iteration matches the convergence criteria, the new temperature value obtained was used as initial condition for obtaining the temperature at next time step and if the value doesn't match the convergence criteria the new temperature value was used as initial condition for the next iteration for the same time step. Whenever the solution converges, the outputs from the FORTRAN program were saved in an excel file and were further used for plotting and discussion.

4. RESULTS AND DISCUSSION

The simulations were carried out for the month of April (summer) and December (winter) to optimize the number of effects, diffusion gap and mass flow rate of feed for parallel feed vertical diffusion multi-effect solar still. The solar radiation profile and ambient temperature for month of April and December used for simulation is shown in **Figure 3**.
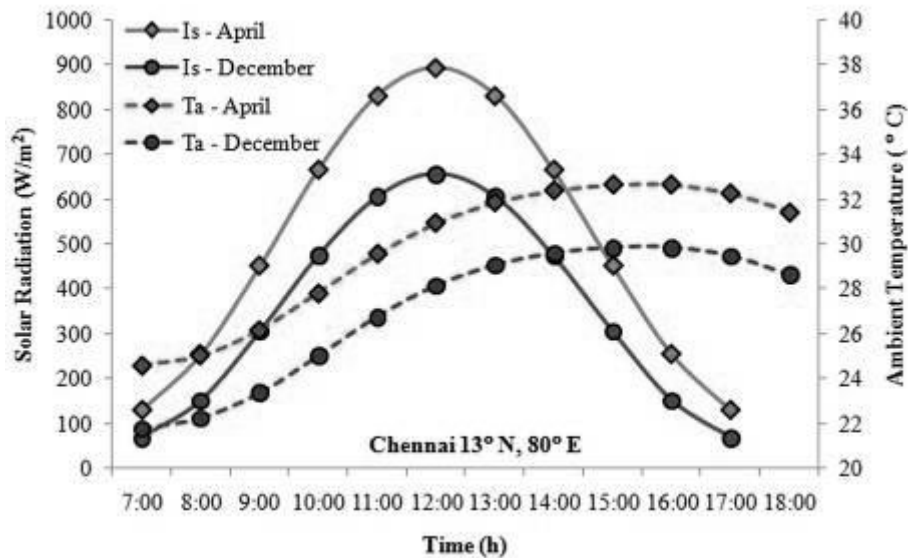

Figure 3: Solar radiation and ambient temperature profile of Chennai

4.1 Impact of Number of Effects on Distillate Yield

The variation of distillate yield with respect to number of effects is graphically depicted in Figure 4. The simulation was carried out by considering a feed water flow rate of 0.005 kg/s and diffusion gap of 10 mm. The distillate yield was found to increase with the increase in number of effects from one to five, but further increase beyond five has shown only negligible enhancement in yield. Nearly, 79.74% and 58.99 % increase in yield was noticed by increasing the effects from one to five for the distillation unit supplied with hot feed water from EHP solar collector during summer and winter, respectively. Incorporation of an additional effect beyond five has shown only 2.87% and 2.61% increase in yield during summer and winter, respectively. Hence, the optimum number of effects can be fixed as five. The marginal increase beyond five effects was mainly due to the reduced temperature difference between the effects which acts as a main driving force for mass transfer (REDDY et al., 2012). The yield from the distillation unit with five effects supplied with hot feed water from solar flat plate collector is nearly 13.66% and 12.60% lower than the unit supplied with hot feed water from EHP solar collector during summer and winter, respectively. The cumulative yield from each effect of vertical diffusion solar still with five effects is shown in Figure 5. The yield was found to be enhanced in the latter effects due to the addition of latent heat of condensation from the former effects which helped the occurrence of enhanced evaporation.
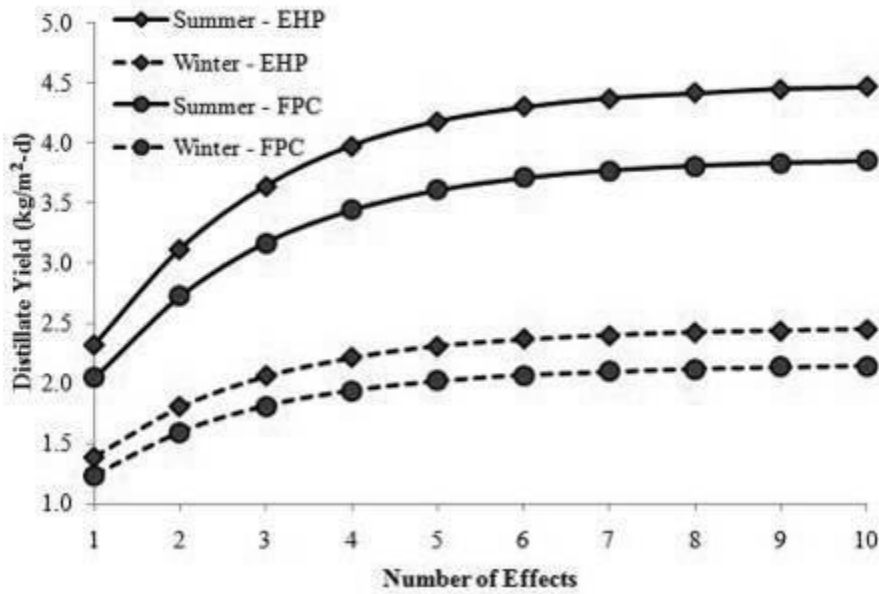
Figure 4: Effect of number of effects on the distillate yield of parallel feed vertical diffusion multi-effect solar still
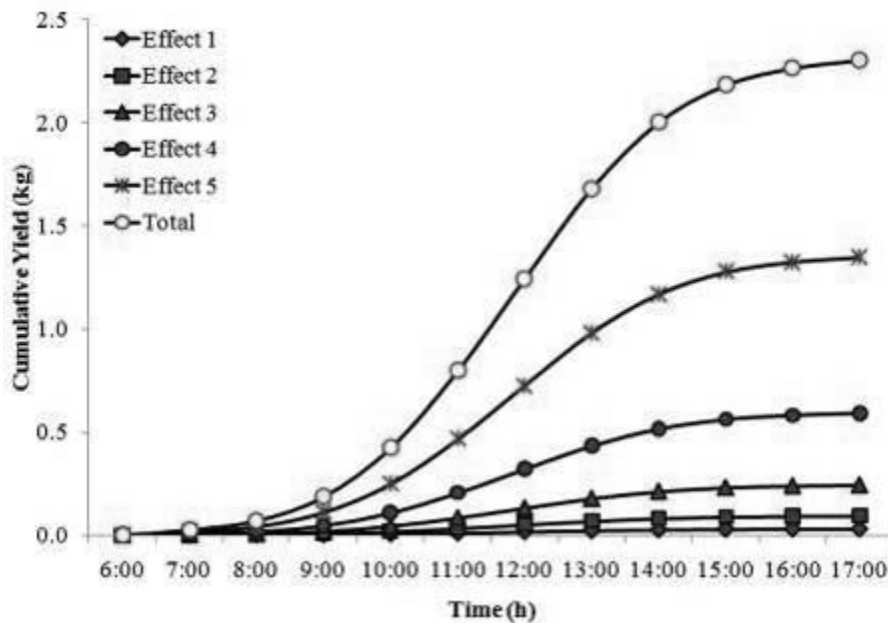

Figure 5: Cumulative yield from parallel feed vertical diffusion multi-effect solar still for the month of December

4.2 Impact of Diffusion Gap on Distillate Yield

The variation of distillate yield with respect to diffusion gap between the effects is shown in Figure 6. The simulation was carried out by considering a feed water flow rate of 0.005 kg/s and by considering five effects. The distillate yield was found to decrease with the increase in diffusion gap between the effects. The decrease was mainly due to the increased thermal resistance offered by the humid air against the diffusion of water molecules towards the condensing surface (TANAKA et al., 2004b). In case of inclined and horizontal stills reduced gap can cause contamination of the distillate with the feed saline water but no contamination has been reported for vertical stills even for a gap of 3 mm (TANAKA et al., 2004b). Therefore, distillate of high quality can be obtained from vertical diffusion type stills. Nearly, 48.20% and 52.17% reduction in yield was noticed by increasing the diffusion gap from 10 mm to 25 mm during summer and winter, respectively for the unit supplied with hot feed water from EHP solar collector. The optimum gap can be fixed as 10 mm based on daily yield and fabrication point of view. For diffusion gap of 10 mm the distillate yield from the unit supplied with hot feed water from EHP collector is nearly 15.83% and 14.42% higher than the unit supplied with hot feed water from FPC.
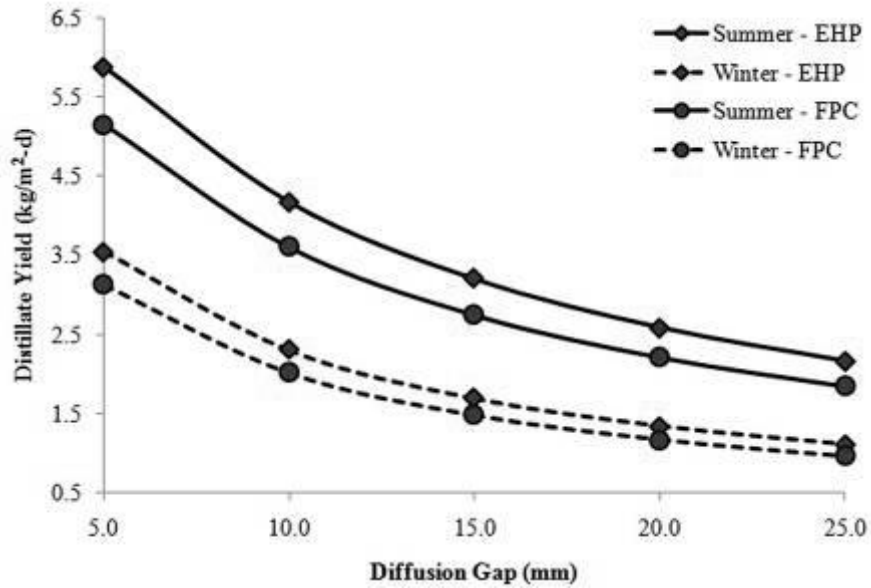
Figure 6: Effect of diffusion gap on distillate yield of parallel feed vertical diffusion multi-effect solar still

4.3 Impact of Feed Water Flow Rate on Distillate Yield

Saline water contains dissolved gases within them which will evolve when heated at or above 100 °C which in turn causes bubble formation along the wick surface and leads to poor evaporation of the heated water resulting in low yield of diffusion still (CHONG et al., 2014). Hence, for proper operation of the unit it is necessary to select proper mass flow rate of the feed water. The variation of distillate yield with respect to mass flow rate of feed water circulated through the solar collector is shown in Figure 7. The simulation was carried out for a five effect distillation unit with a diffusion gap of 10 mm. The yield was found to enhance from 3.26 kg/m^2-d to 8.25 kg/m^2-d and 2.83 kg/m^2-d to 7.01 kg/m^2-d for the unit supplied with heated feed water from EHP and FPC, respectively during summer by reducing the feed water mass flow rate from 0.006 kg/s to 0.003 kg/s.
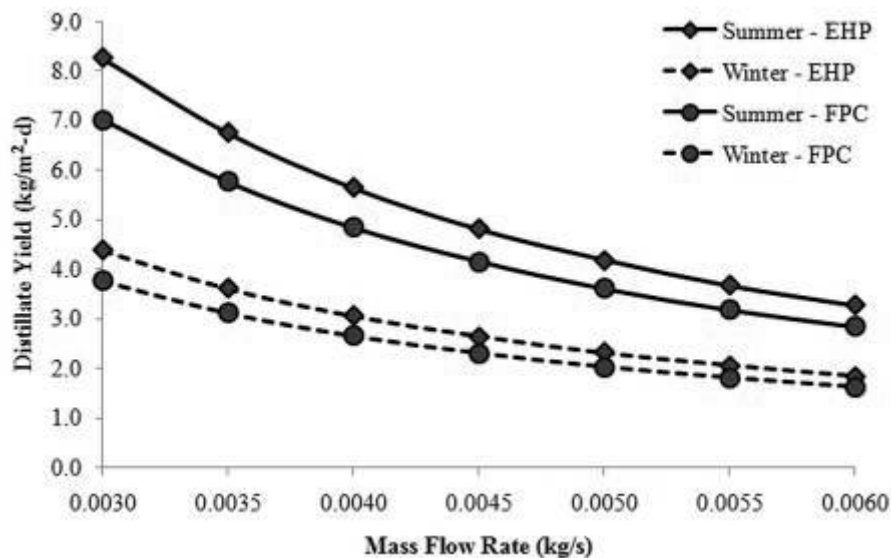
Figure 7: Effect of mass flow rate of feed water on distillate yield of parallel feed vertical diffusion multi-effect solar still

4.4 Impact of Salinity of Feed Water on Distillate Yield

The variation of distillate yield with respect to salinity of feed water is graphically depicted in Figure 8. The salinity of feed water considered in this study ranges between 0 to 10 wt%. The distillate yield was found to decrease with the increase in salinity of the feed water. The distillate yield during summer for the unit supplied with hot feed water from EHP collector is 8.25 kg/m^2-d and 6.07 kg/m^2-d for feed water with salinity

0 wt% and 10 wt%, respectively. As the salinity increases, boiling point elevation increases resulting in reduced vapor temperature which causes reduced partial pressure difference between the evaporating and condensing surface leading to reduced mass transfer (REDDY et al., 2012). During summer, yield from the unit supplied with hot feed water from FPC is around 7.01 kg/m^2-d for feed water with 0 wt% salinity which is higher than the yield from the unit treating feed water with 10 wt% salinity by around 38.81%. Both the units recorded minimum yield during winter due to the availability of low solar radiation.

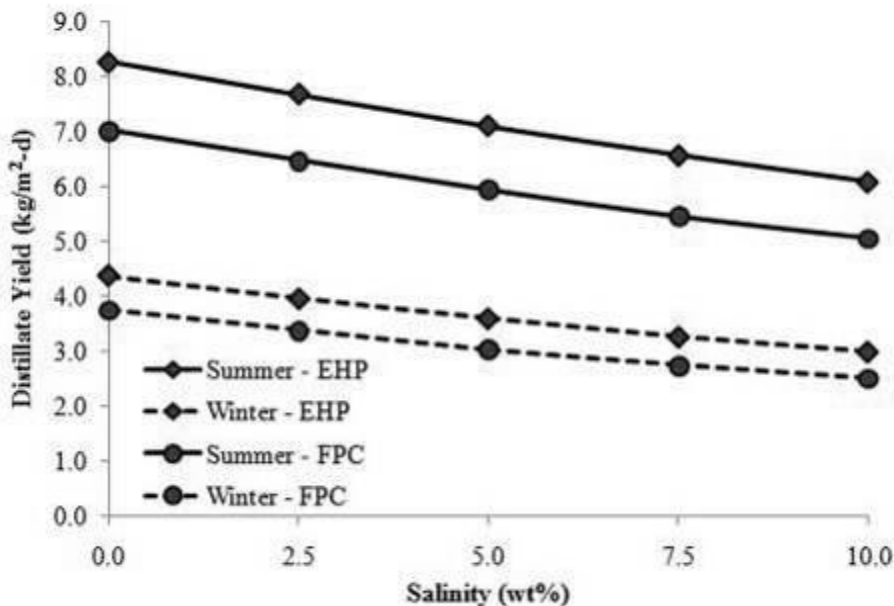*Figure 8: Effect of feed water salinity on distillate yield of parallel feed vertical diffusion multi-effect solar still*

5   CONCLUSION

In this work, parallel feed vertical diffusion multi-effect solar still has been simulated and optimized using transient mathematical modelling. The impact of number of effects, diffusion gap, mass flow rate and salinity of feed water has been discussed briefly. The optimum number of effects, diffusion gap and mass flow rate was found to be 5, 10 mm and 0.003 kg/s, respectively. The distillate yield was affected by salinity of feed water and climatic conditions. The maximum distillate yield of 8.25 kg/m^2-d was recorded for the unit supplied with hot feed water from evacuated heat pipe solar collector during summer for feed water of 0 wt% salinity. Minimum distillate yield of 2.51 kg/m^2-d was recorded for the unit supplied with hot feed water (10 wt% salinity) from flat plate collector. during winter. The unit can be fed with hot feed water from any source which is an added advantage compared to previous configurations. The distillation unit was found to be highly suitable for rural applications because of its compactness, high yield, increased safety and handling flexibility.

6   ACKNOWLEDGEMENT

7   REFERENCES

BOZKURT, I., Karakilcik, M., Dincer, I., 2012. Energy efficiency assessment of integrated and nonintegrated solar ponds. International journal of low-carbon technologies, 0, 1-7.

CHONG, TL., Huang, BJ., Wu, PH., Kao, YC., 2014. Multiple-effect diffusion solar still coupled with a vacuum-tube collector and heat pipe. Desalination, 347, 66-76.

ELSAYED, MM., Fathalah, K., Shams, J., Sabbagh, J., 1984. Performance of multiple effect diffusion stills. Desalination, 51, 183-199.

JIJAKLI, K., Arafat, H., Kennedy, S., Mande, P., Theeyattuparampil, VJ., 2012. How green solar desalination really is? Environmental assessment using life-cycle analysis (LCA) approach. Desalination, 287, 123-131.

KALOGIROU, S., 2005. Seawater desalination using renewable energy sources. Progress in energy and combustion science, 31(3), 242-281.

MUFTAH, AF., Alghoul, MA., Fudholi, A., Abdul-Majeed, MM., Sopian, K., 2014. Factors affecting basin type solar still productivity: A detailed review. Renewable and sustainable energy reviews, 32, 430-447.

NISHIKAWA, H., Tsuchiya, T., Narasaki, Y., Kamiya, I., Sato, H., 1998. Triple effect evacuated solar still system for getting fresh water from seawater. Applied thermal engineering, 18, 1067-1075.

PILLAI, R., Libin, AT., Mani, M., 2013. Study into solar-still performance under sealed and unsealed conditions. International journal of low-carbon technologies, 0, 1-11.

RANJAN, KR., Kaushik, SC., Panwar, NL., 2013. Energy and exergy analysis of passive solar distillation systems. International journal of low-carbon technologies, 0, 1-11.

REDDY, KS., Ravi KUMAR, K., O'donovan, TS., Mallick, TK., 2012. Performance analysis of an evacuated multi-stage water desalination system. Desalination, 288, 80-92.

SINGH, AK., Tiwari, GN., Sharma, PB., Khan, E., 1995. Optimization of orientation for higher yield of solar still for a given location. Energy Conversion and Management, 36(3), 175-187.

TANAKA, H., Nosoko, T., Nagatta, T., 2000. A highly productive basin-type-multiple-effect coupled solar still. Desalination, 130, 279-293.

TANAKA, H., Nosoko, T., Nagatta, T., 2000. Parametric investigation of a basin-type-multiple-effect coupled solar still. Desalination, 130, 295-304.

TANAKA, H., Nakatake, Y., 2004. A vertical multiple-effect diffusion-type solar still coupled with a heat-pipe solar collector. Desalination, 160, 195-205.

TANAKA, H., Nakatake, Y., Watanabe, K., 2004. Parametric study on a vertical multiple-effect diffusion-type solar still coupled with a heat-pipe solar collector. Desalination, 171, 243-255.

TANAKA, H., 2009. Experimental study of vertical multiple-effect diffusion solar still coupled with a flat plate reflector. Desalination, 249, 34-40.

TANAKA, H., Park, CD., 2010. Distillation utilizing waste heat from a portable electric generator. Desalination, 258, 136-142.

XIONG, J., Xie, G., Zheng, H., 2013. Experimental and numerical study on a new multi-effect solar still with enhanced condensation surface. Energy Conservation and Management, 73, 176-185.

ZURIGAT, YH., Abu-Arabi, MK., 2004. Modelling and performance analysis of a regenerative solar desalination unit. Applied thermal engineering, 24, 1061-1072.

78: Thermodynamic analysis of solar hybrid coal-fired power system

HUI HONG[1,*,] SHUO PENG[1,2], WEI HAN[1], HONGGUANG JIN[1]

1 Institute of Engineering Thermophysics, Chinese Academy of Sciences, Beijing 100190, China
2 University of Chinese Academy of Sciences, Beijing 100049, China

Integrating solar energy with fossil fuel is a cost-efficient way to use solar energy to generate electricity in the near and mid-terms. In a solar hybrid coal-fired power system, concentrated solar heat is used to replace the extracted steam from the coal-fired power plant to generate electricity. Previous researches proposed several system configurations where solar heat is used to substitute extracted steam with different temperature and pressure in the coal-fired power system. The contribution of solar heat to the work output for such hybrid power system has been pointed out. However, the inherent reason of solar-to-electricity increased by solar hybridization with fossil fuel has rarely been examined. In this paper, on the basis of the concept of energy level, the correlation of the solar-to-electricity efficiency with the reduced exergy destruction of solar hybridization process is fundamentally derived and their interaction is revealed. In addition, the thermodynamic performance of a typical 330 MW solar hybrid coal-fired power system is evaluated by using the derived equations. The result obtained in this study is expected to provide a basic principle for designing the solar hybrid coal-fired power system.

Keywords: Solar hybrid coal-fired power system; Net solar power output; Exergy destruction; Energy level;

1. INTRODUCTION

Solar energy hybridization with fossil fuel is one proven option to overcome the problems of pollution and increasing fuel prices in the near and mid-terms [1]. For some countries like China, whose primary energy is coal, solar hybrid coal-fired power system is a promising technology. It utilizes concentrated solar heat below 300 °C to substitute the extracted steam in Rankine power cycle to heat the feed water. Through this process, the steam that was to be extracted can efficiently expand in the steam turbine to generate electricity [2].

The first experimental solar hybrid coal-fired power plant was built in Colorado in 2010, which integrated a previously existing 44MW coal-fired power plant and a 4MW CSP installation [3]. In the previous thermodynamic studies, Yang's research group pointed out the thermodynamic advantages with different solar replacements for the extraction steam based on the first law of thermodynamics. The results indicated that the solar-to-electricity efficiency of the solar hybrid coal-fired power plant is higher than that of a solar-only power plant [4-5]. The replacement of higher grade extraction steam can facilitate better thermal performance and efficiency [6]. Peng et al. [7] analyzed the hourly thermodynamic performances of a typical 330 MW coal-fired power plant on typical days under different output work load operation. Besides that, researchers have contributed to the thermodynamic performance analysis based on the second law of thermodynamics. Zhai et al. [8] have studied a 600 MW solar hybrid coal-fired power plant by analyzing the exergy efficiency for different solar irradiation. Hong et al. [9] investigated the exergy destruction of a solar-hybrid coal-fired power plant using the energy-utilization diagram methodology (EUD methodology). Peng et al. [10] analyzed the exergy destruction in key components on off-design conditions, and compared with solar-only thermal power plant. Although previous efforts pointed out the distribution of exergy destruction in each component of solar hybrid coal-fired power system, there are two questions have remained

---

[1] JAMEL, M.S., Rahman, A., Shamsuddin, A.H., 2013. Advances in the integration of solar thermal energy with conventional and non-conventional power plants. Renewable and Sustainable Energy Reviews 20, 71-81.

[2] HU, E., Yang, Y., Nishimura, A., Yilmaz, F., Kouzani, A., 2010. Solar thermal aided power generation. Applied Energy, 87, 2881-2885.

[3] National renewable energy laboratory, 2010, http://www.nrel.gov/csp/news/2010/870.html.

[4] Yan, Q., Yang, Y., Nishimura, A., Kouzani, A., Hu, E., 2010. Multi-point and Multi-level Solar Integration into a Conventional Coal-Fired Power Plant. Energy Fuels, 24 (7), 3733-3738.

[5] YANG, Y., Yan, Q., Zhai, R., et al, 2011. An Efficient Way to Use Medium-or-Low Temperature Solar Heat for Power Generation-Integration into Conventional Power Plant. Applied thermal engineering 31, 157-162.

[6] HOU, H., Mao, J., Yang, Y., Luo, N..2012. Solar-Coal Hybrid Thermal Power Generation- an Efficient Way to Use Solar Energy in China, International Journal of Energy Engineering 2 (4), 137-142.

[7] PENG, S., Hong, H., Wang, Y., Wang, Z., Jin, H., 2014. Off-design Thermodynamic Performances on typical days of a 330 MW Solar-hybrid Coal-fired Power Plant in China. Applied Energy, 130, 500-509.

[8] ZHAI, R., Zhu, Y., Yang, Y., Tan, K., Hu, E., 2013. Exergetic and Parametric Study of a Solar Aided Coal-Fired Power Plant. Entropy 15 (3), 1014-1034.

[9] HONG, H., Zhao, Y., Jin, H., 2011. Proposed Partial Repowering of a Coal-Fired Power Plant Using Low-Grade Solar Thermal Energy. International J. Thermodynamics, 14 (1), 21-28.

[10] Peng, S., Wang, Z., Hong, H., Xu, D., Jin, H., 2014. Exergy Evaluation of a Typical 330 MW Solar Hybrid Coal-fired Power Plant. Energy Conversion and Management, 85, 848-855.

unknown: what is the reason of the reduced exergy destruction of solar hybridization process, and why is the net solar-to-electricity efficiency improved.

Here, the present study is to derive the correlation equation between the net solar power output and the exergy destruction in the solar hybrid coal-fired power system, to reveal the role of the reduced exergy destruction in improving the net solar-to-electricity efficiency, and to evaluate a typical 330 MW solar hybrid coal-fired power system by applying the derived equations.

2. EXPRESSION OF THEORETICAL SOLAR-TO-ELECTRICITY EFFICIENCY

According to the Appendix, the solar power output can be calculated by subtracting equation (A6) from equation (A5)

$$W_{solar} = \Delta E_s + \left(\Delta EXL_{H-fos} - \Delta EXL_{H-hyb} \right) \tag{1}$$

It can be seen that the net solar power output depends on the exergy of solar heat and the reduction of exergy destruction in the feed water heater after hybridization. For a given exergy of solar heat, the increase of the net solar power output can be achieved by reducing the exergy destruction in the feed water heater.

According to Ishida [11], the exergy destruction in the feed water heater is obtained on the basis of the concept of energy level. Thus, ΔEXL_{H-hyb} and ΔEXL_{H-fos} is separately given as

$$\Delta EXL_{H-hyb} = Q_{solar}(A_{abs} - A_{water}) \tag{2}$$
$$\Delta EXL_{H-fos} = Q_{solar}(A_{steam} - A_{water}) \tag{3}$$

where A_{abs} is the energy level of the thermal oil, A_{water} is the energy level of the feed water, and A_{steam} is the energy level of the steam extractions.

Inserting equations (2) and (3) into equation (1) result in

$$W_{solar} = \Delta E_s + Q_{solar}(A_{steam} - A_{abs}) \tag{4}$$

Then, the net solar-to-electricity efficiency of the solar hybrid system can be given as

$$\eta_{hyb} = \frac{W_{solar}}{IS} = \frac{\Delta E_s}{IS} + \frac{Q_{solar}(A_{steam} - A_{abs})}{IS} \tag{5}$$

where I is the direct normal insolation, S is the aperture area of the solar collector.

According to Edward A. Fletcher [12], ΔE_s is expressed as $\Delta E_s = IS \times \eta_{col} \times \eta_{carnot}$. η_{col} is the collector efficiency, η_{carnot} is the carnot efficiency corresponding to the receiver temperature. Since the product of η_{col} and η_{carnot} is the theoretical solar-to-electricity efficiency of the solar-only power system, η_{hyb} can be rewritten as

$$\eta_{hyb} = \eta_{only} + \eta_{col}(A_{steam} - A_{abs}) \tag{6}$$

It can be seen that η_{hyb} is related to two factors. First part is the theoretical solar-to-electricity efficiency of the solar-only power system (η_{only}). Second part is the product of collector efficiency (η_{col}) and the energy level difference ($A_{steam} - A_{abs}$). If $A_{steam} > A_{abs}$, the solar-to-electricity efficiency of the hybrid system will

[11] ISHIDA, M., Kawamura, K., 1982. Energy and exergy analysis of a chemical process system with distributed parameters based on the energy-direction factor diagram. Industrial Engineering and Chemistry Process Design and Development 21, 690–695.

[12] FLETCHER, E.A., Moen, R.L., 1977. Hydrogen- and Oxygen from Water, Science, 4308, 1050-1056.

be higher than that of the solar-only system. On the contrary, if $A_{steam} < A_{abs}$, the solar-to-electricity efficiency of the hybrid system will be lower than that of the solar-only system.

Figure 1 shows the effect of the receiver temperature on the theoretical solar-to-electricity efficiency. For a given receiver temperature, the theoretical solar-to-electricity efficiency of the hybrid system is higher than that of the solar-only system. That is because the available energy of the extracted steam is higher than that of solar heat. On the other hand, the same with the solar-only system, the theoretical solar-to-electricity efficiency of the solar hybrid system rises as the increase of the receiver temperature. When the receiver temperature is 300-400°C, the theoretical solar-to-electricity efficiency reaches to a peak value.

Figure 2 presents the effect of A_{steam} on the theoretical solar-to-electricity efficiency. At a given energy level difference, as A_{steam} increases, η_{hyb} rises at first, and then goes down. When A_{steam} is 0.5~0.6, the theoretical solar-to-electricity efficiency gets a peak value. That is because the available energy of extracted steam rises as A_{steam}. As the further increasing of A_{steam}, the collector efficiency decreases, resulting in the reduction of η_{hyb}. It is also observed that, when Asteam is relatively low, η_{hyb} is almost the same for different energy level difference. The result points out the optimal energy level of the extracted steam substituted by solar energy.
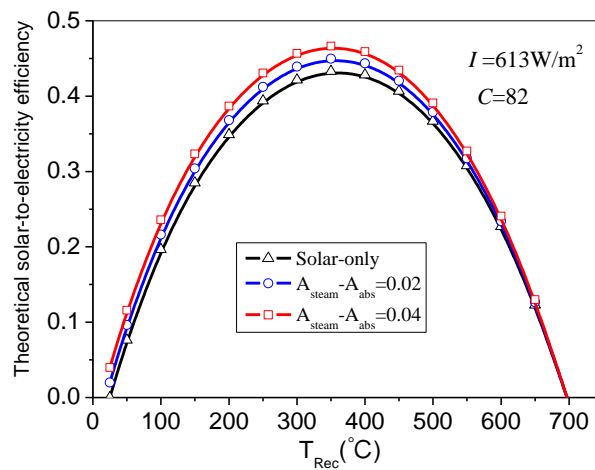

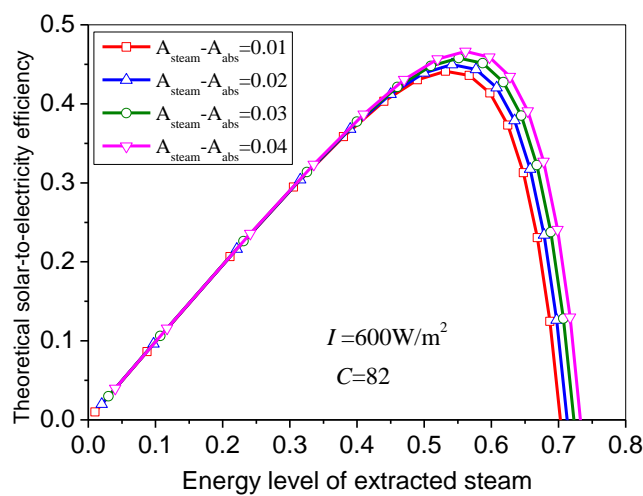Figure 1. Effect of receiver temperature on the theoretical solar-to-electricity efficiency

Figure 2. Effect of Asteam on the theoretical solar-to-electricity efficiency

3. APPLICATION IN A TYPICAL 330 MW SOLAR HYBRID COAL-FIRED POWER SYSTEM

A simplified diagram for a solar aided coal-fired power plant is given in Figure 3 and its state parameters are shown in Table 1. The solar-hybrid coal-fired power plant is located in Changji City, Sinkiang province of China. This plant includes a boiler system with reheating processes; a power system consisting of high, intermediate, and low-pressure turbines; and a feed-water heater system including seven feed water heaters that extracted steam from different stages of the steam turbine. Concentrated solar heat is used to substitute the first grade of extracted steam (SWH in Figure 3). When solar irradiation is insufficient to totally replace the first-stage extracted steam, the total flow of the feed water at the inlet of the first feed water heater is separated into two parts. One part is introduced into the previous H1, whereas the other flows into the solar feed water heaters (SWH). In this way, the feed water can be simultaneously heated by the extracted steam of the turbine and the concentrated solar heat.

According to the local meteorological condition and the actual operational data in 2011 of the 330 MW coal-fired power plant, the annual output work load is about 75%, and the annual average solar irradiation is about 613 W/m^2. The Luz LS-3 collector with N-S axis tracking mode is used. The parabolic trough collector aperture area was assessed to be 70650 m^2. The weather data of Changji City was offered by NREL's standard system advisor model library (SAM).
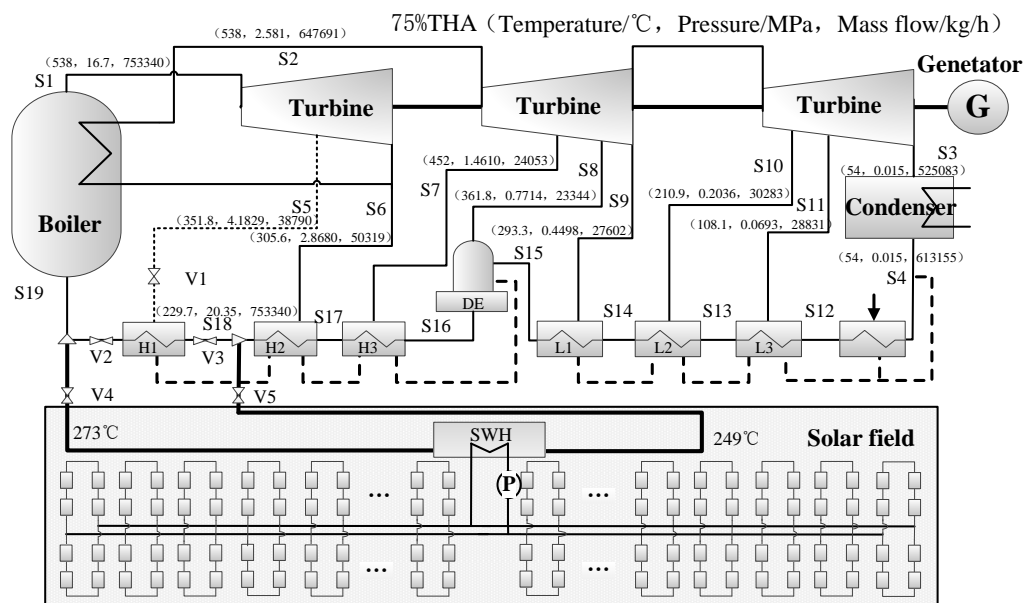

Figure 3. Schematic diagram of the solar hybrid coal-fired power plant

Table 1. State parameters of solar aided coal-fired power plant

Items	Temperature (100%/75%/50% load, °C)	Pressure (100%/75%/50% load, MPa)	Mass flow (100%/75%/50% load, kg/h)
1	538/538/538	16.7/16.7/16.7	1034601/753340/499300
2	538/538/538	3.472/2.581/1.751	875791/647691/435982
3	54/54/54	0.015/0.015/0.015	688877/613155/418291
4	54/54/54	0.015/0.015/0.015	822023/613155/418291
5	380.1/351.8/344	5.7114/4.1829/2.8226	61830/38790/21686
6	329.7/305.6/299.4	3.8574/2.8680/1.9459	75873/50319/28926
7	451/452/453.9	1.9557/1.4610/0.9993	36195/24053/12774
8	359.9/361.8/364.8	1.0278/0.7714/0.5301	33892/23344/14351
9	290.8/293.3/396.9	0.5969/0.4498/0.3104	40170/27602/17012
10	208/211/215	0.2558/0.1934/0.1340	43210/30283/19129
11	106/108/111	0.0873/0.0658/0.0454	48378/28831/13144
12	93.1/85.6/76.2	1.724/1.724/1.724	822023/613155/418291
13	125.4/116.4/105.2	1.724/1.724/1.724	822023/613155/418291

14	153.9/143.2/130.2	1.724/1.724/1.724	822023/613155/418291
15	182.7/170.1/155.8	16.7/16.7/16.7	1034601/753340/499300
16	209.7/195.6/178.5	16.7/16.7/16.7	1034601/753340/499300
17	246.4/229.7/209.4	16.7/16.7/16.7	1034601/753340/499300
18	272.1/252.8/230.4	16.7/16.7/16.7	1034601/753340/499300

For a typical solar hybrid cycle, the turbine efficiency and the exergy destruction in the steam turbine should be considered. A typical 330 MW solar hybrid coal-fired power plant is selected for consideration. Then equation (1) can be rewritten as

$$W_{solar} = \Delta E_s + Q_{solar}(A_{steam} - A_{abs}) + \left(\Delta EXL_{st-fos} - \Delta EXL_{st-hyb} \right) \tag{7}$$

The turbine efficiency is defined as the ratio of the actual enthalpy drop and the ideal enthalpy drop. The actual enthalpy drop is the output work, and the ideal enthalpy drop is the sum of the output work and the exergy destruction. Thus, the exergy destruction of the steam turbine before and after hybridization can be given as

$$\Delta EXL_{st-fos} = \left(\frac{1}{\eta_{tur}} - 1 \right) W_{fos} \tag{8}$$
$$\Delta EXL_{st-hyb} = \left(\frac{1}{\eta_{tur-hyb}} - 1 \right) W_{hyb} \tag{9}$$

η_{tur} and $\eta_{tur-hyb}$ are separately the turbine efficiency before and after hybridization. W_{fos} and W_{hyb} are separately the output work before and after hybridization.

Inserting equations (8) and (9) into equation (7) results in

$$W_{solar} = Q_{solar} A_{steam} \eta_{tur-hyb} + \left(\frac{\eta_{tur-hyb}}{\eta_{tur}} - 1 \right) W_{fos} \tag{10}$$

Then, the net solar-to-electricity efficiency can be expressed as

$$\eta_{hyb-real} = \frac{W_{solar}}{IS} = \eta_{col} A_{steam} \eta_{tur-hyb} + \frac{\left(\frac{\eta_{tur-hyb}}{\eta_{tur}} - 1 \right) W_{fos}}{IS}$$

$$= f\left(\eta_{col}, \ A_{steam}, \ \eta_{tur}/\eta_{tur-hyb}, \ W_{fos} \right) \tag{11}$$

It can be seen from this equation that the solar power output of the solar hybrid coal-fired power system is related to two parts: one part is the power output of the incremental extracted steam. The other part is the variation of the power output caused by the fluctuant of turbine efficiency. Figure 4 presents the comparison of the theoretical and the practical net solar-to-electricity efficiency. It can be seen that $\eta_{hyb-real}$ is about 20% lower than η_{hyb}. The first reason is that the practical net solar-to-electricity efficiency considered the exergy destruction in the steam turbine. The second reason is that the collector efficiency of the theoretical solar-to-electricity efficiency did not consider the optical loss. There are two ways to improve the solar-to-electricity efficiency. The first way is to enhance the turbine efficiency ratio ($\eta_{tur}/\eta_{tur-hyb}$), in order to reduce the impact of the fluctuant of turbine efficiency. The second way is to reduce the cosine loss of the solar collector. If these two factors are handled suitably, the practical net solar-to-electricity efficiency could increase about 10%, as shown the blue line in Figure 4.
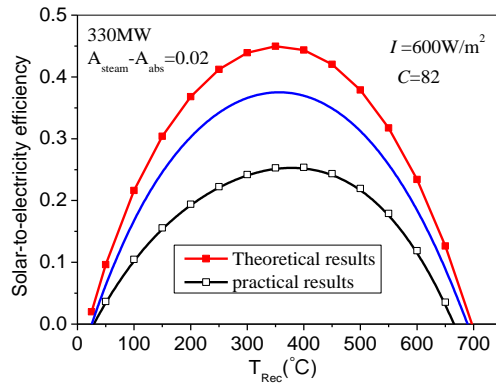
Figure 4. Effect of turbine efficiency on the net solar-to-electricity efficiency

4. FEATURE OF SOLAR THERMAL POWER GENERATION

Equation (11) turns out that the net solar-to-electricity efficiency $\eta_{hyb-real}$ is the function among the collector efficiency (η_{col}), the energy level of extracted steam (A_{steam}), the ratio of turbine efficiency ($\eta_{tur}/\eta_{tur-hyb}$) and the output work before hybridization (W_{fos}). These key parameters also depend on DNI, incident angle and the output work load. Therefore, these three key impact factors are discussed here.

4.1 Exergy Destruction Variance with DNI, Incident Angle and Output Work Load

According to equation (1), the reduction of exergy destruction in the feed water heater is a main factor to influence the power output of the solar hybrid cycle. Therefore, the effect of DNI and incident angle on the reduction of exergy destruction under different output work load is analyzed.

As shown in Figure 5, at a given output work load, the reduction of exergy destruction in the feed water heater rises as DNI increase at first, and then goes down. When DNI is relatively low, the exergy destruction in the solar receiver decreases as DNI increases. Thus, the reduction of exergy destruction in the feed water heater increases. When DNI reaches to the peak value, although the provided solar heat solar energy can be used to entirely replace the extracted steam, the amount of solar heat exceeds in the requirement of the feed-water, causing the more solar energy being abandoned. Correspondingly, the effect of reducing the exergy destruction in the solar-feeding water heat will become worse.
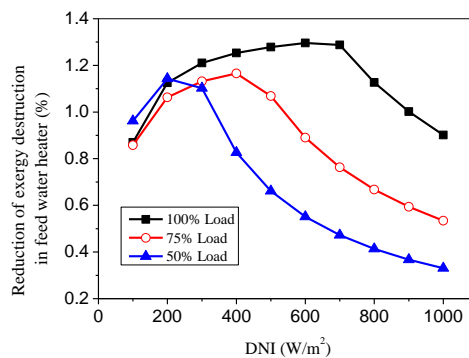

Figure 5. Effect of DNI and incident angle on exergy destruction under different output work load

4.2 Parameters Interaction Between Solar Field and Steam Turbine

The ratio of flow rate (m_{back}/m_{main}) is an important parameter to connect the solar field and the power block. Figure 6 shows the variation of m_{back}/m_{main} with DNI and incident angle. At a given output work load, m_{back}/m_{main} increases and then reaches to a peak value and keeps constant, as DNI rises first. It is due to the fact that the amount of the absorbed solar heat rises with the increase of DNI, meaning more extracted steam flow rate entering into the steam turbine to generate power. It can also be seen that m_{back}/m_{main} under 50% output work load rises more sharply than that under 75% and 100% output work load. The reason is

that the parameter of extracted steam under 50% output work load is lower than the other two output work load. Therefore, the flow rate of the extracted steam drops more sharply as the increase of DNI.

Solar collector efficiency is an important factor to influence the solar-to-electricity efficiency which is influenced by the output work load. Figure 7 illustrates the variation of solar collector efficiency with output work load for different DNI and incident angle. When solar heat input entirely replaces the extracted steam (I=800 W/m², θ= 10° in Figure 7), solar collector efficiency is increased as the output work load increases. That is because the feed water flow rate rises as output work load increases, bringing about the increase of the amount of the absorbed solar heat. For a certain DNI and solar incident angle, the solar collector efficiency simultaneously increases. When solar heat input partly replaces the extracted steam (I=400 W/m² and θ = 40° in Figure 7), the amount of the absorbed solar heat keeps constant for a given DNI and solar incident angle. With the increase of the output work load, the receiver temperature increases, decreasing the solar collector efficiency.
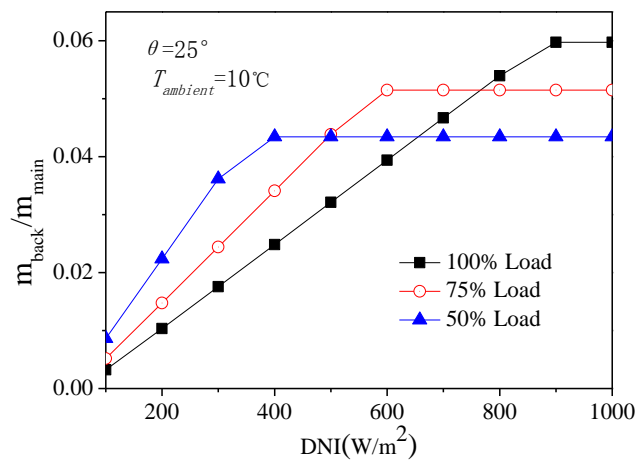
Figure 6.Variation of mback/mmain with DNI and incident angle under different output work load
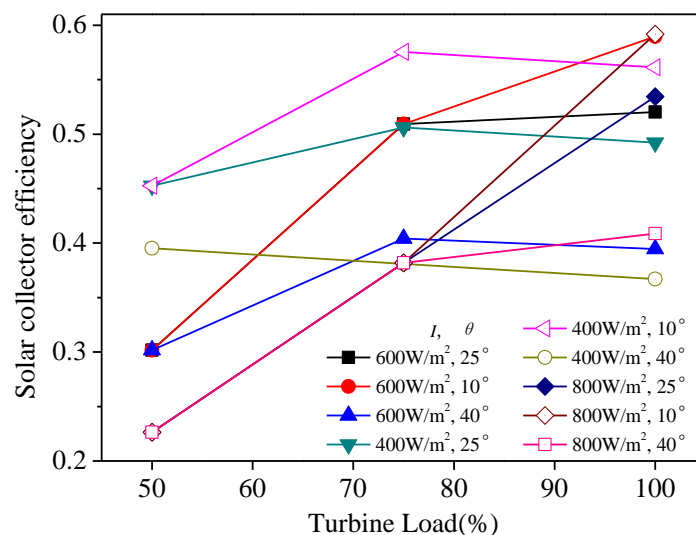
Figure 7.Variation of solar collector efficiency with the output work load

4.3 Behaviour of Net Solar Power Output and Net Solar-to-Electricity Efficiency

Solar share. Here, the contribution of solar output work to the hybrid system is defined as solar share. Figure 8 shows the variation of solar share with the variation of the output work load. When the solar heat input is relatively high (I=800 W/m², θ= 10° in Figure 8), the amount of the absorbed solar heat is determined by the required heat of the feed water heater (H1 in Figure 3). Thus, the exergy destruction in the feed

water heater decreases as output work load increases, as shown in Figure 5. As a result, the net solar power output rises as the output work load increases, increasing solar share. When the solar heat input is relatively low (I=400 W/m^2 and θ = 40° in Figure 8), solar share declines as the increase of the output work load. That is because the amount of the absorbed solar heat is constant for a certain DNI and solar incident angle. Since the total power output rises as the output work load increases, solar share correspondingly declines.
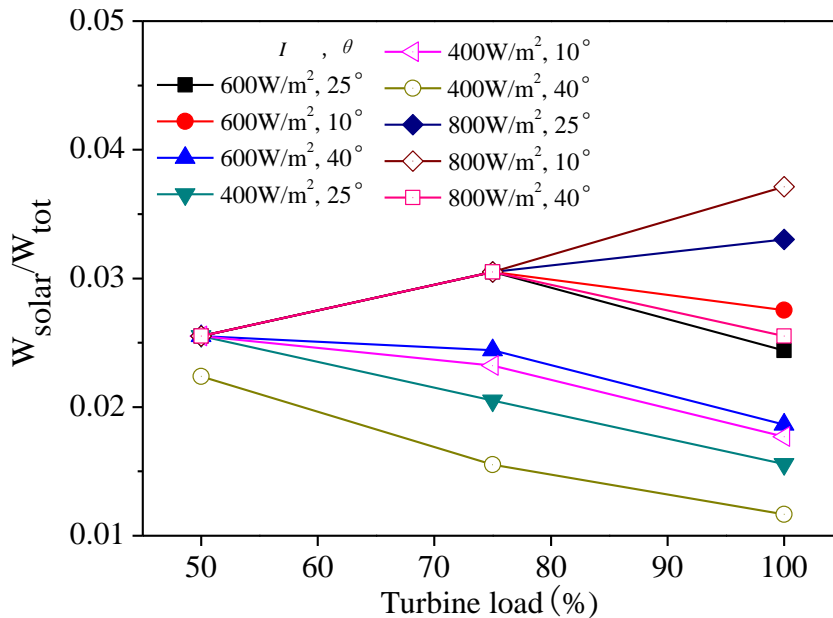

Figure 8.Effect of output work load on power solar share for different DNI and incident angle

Net solar-to-electricity efficiency. Figure 9 shows the variation of the net solar-to-electricity efficiency. At a given output work load, the net solar-to-electricity efficiency rises as the increase of DNI. That is because the reduction of exergy destruction in the feed water heater increases, as shown in Figure 5. As DNI continues to rise, the efficiency improvement is limited by the required heat duty of the feed water heater. It also can be seen that the required DNI for the peak net solar-to-electricity efficiency rises as the increase of the output work load. That is because the heat duty in the feed water heater rises as the output work load increases. Therefore, more solar heat is needed for the peak value, corresponding to higher DNI.

On the other hand, as the increase of incident angle, the net solar-to-electricity efficiency firstly keeps constant, and then decreases. The turning point of these three output work load is respectively 10°, 30°, 50°, when DNI is 600 W/m^2. That is because when the incident angle is relatively small, the reduction of exergy destruction in feed water heater keeps constant. Thus, the net solar power and the net solar-to-electricity efficiency do not vary. With the further increase of incident angle, the reduction of the exergy destruction in the solar feed water heater varies slowly, decreasing the net solar power and the net solar-to-electricity efficiency correspondingly. .
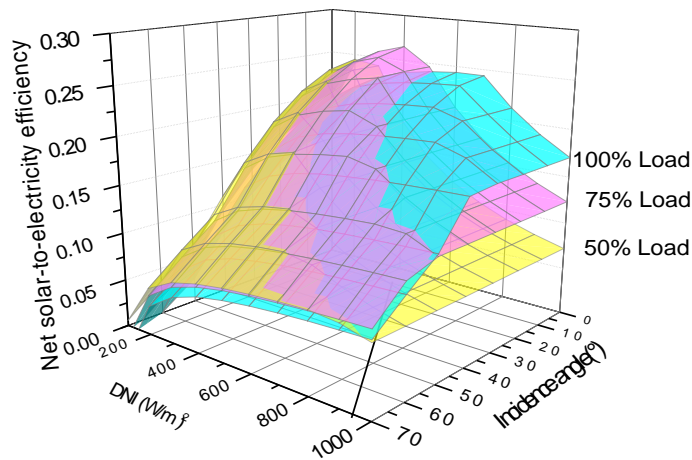
Figure 9. Influences of DNI and θ on net solar-to-electricity efficiency for different output work load

5   CONCLUSION

This paper revealed a mechanism of solar heat hybridization with coal-fired power system. The correlation of the solar–to-electricity efficiency with the reduced exergy destruction of solar hybridization process is fundamentally derived and their interaction is revealed. It is found that the net solar-to-electricity efficiency of hybrid system is higher than the theoretical solar-to-electricity efficiency of solar-only power system. The higher part is the product of collector efficiency and the energy level difference between the extracted steam and the feed water. When the energy lever of extracted steam is 0.5~0.6, the theoretical solar-to-electricity efficiency gets a peak value. Based on the derived equations, a typical 330 MW coal-fired power plant is evaluated. Effects of three key parameters including DNI, incident angle and output work load, on the thermodynamic performances were examined. At a given output work load, as the increase of DNI, the net solar-to-electricity efficiency gets a peak value. As the increase of incident angle, the net solar-to-electricity efficiency firstly keeps constant, and then decreases. This research can provide deeply understanding of improving the solar-to-electricity efficiency of solar hybrid coal-fired power system.

6   ACKNOWLEDGEMENTS

7   APPENDIX

7.1 Energy and Exergy Balance Equations before and after Hybridization

Figure 10 (a) shows the energy conversion process of the feed water heated by solar heat. Figure 10 (b) shows the energy conversion process of the feed water heated by the extracted steam. They both compose three energy transformation processes: the feed water preheating process in the feed water heaters, the steam generation and superheating process in the boiler, and steam expanding process in the turbines. The energy balance equations can be separately expressed as:

$$Q_f + Q_{sol} + \Delta H_w = \Delta H_{st} \tag{A1}$$
$$Q_f + \Delta H_{ex} + \Delta H_w = \Delta H_{st} \tag{A2}$$

where Q_{sol} is the solar heat input, Q_f is the input heat of fuel, ΔH_w is the enthalpy of feed water, ΔH_{ex} is the enthalpy of extracted steam.

For both systems, the exergy balance equations can be separately expressed as:

$$\Delta E_f + \Delta E_s + \Delta E_w = W_{hyb} + \Delta EXL_{hyb} \qquad (A3)$$
$$\Delta E_f + \Delta E_w = W_{fos} + \Delta EXL_{fos} \qquad (A4)$$

where ΔE_s is the exergy of solar heat, ΔE_f is the exergy of fuel, ΔE_w is the exergy input of feed water. W_{ST-hyb} is the total power output of the hybrid system, W_{ST-fos} is the power output of the coal-fired system, ΔEXL_{hyb} is the exergy destruction of the hybrid system, ΔEXL_{fos} is the exergy destruction of the coal-fired system.
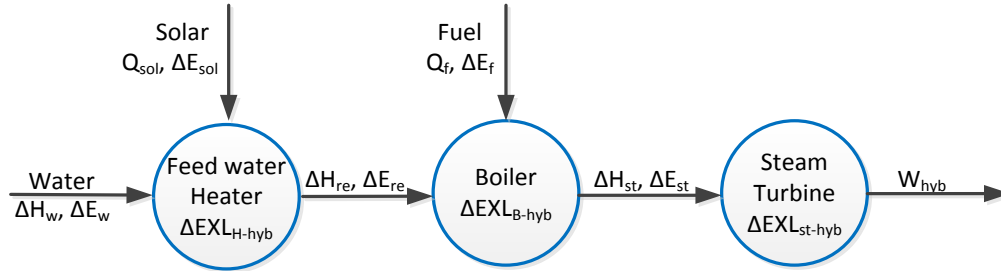

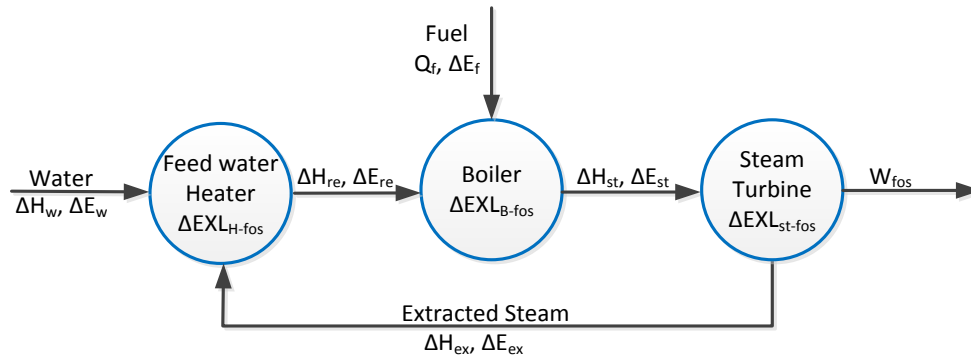Figure 10 (a) Energy and exergy flow of feed water heated by solar heat (After hybridization)

Figure 10 (b) Energy and exergy flow of feed water heated by extracted steam (Before hybridization)

According to Figures 10 (a) and (b), the exergy destruction of both systems involves in three processes: the exergy destruction in the feed water heater, the exergy destruction in the boiler, and the exergy destruction in the steam turbine. For simplification, the boiler is not considered to be refitted. The temperature at the inlet of the boiler and the main steam temperature after the boiler keep the same before and after hybridization. Thus, the exergy destruction occurring in the boiler can be considered as the same before and after hybridization. Furthermore, the variation of the steam flow in the steam turbine is not considered. Then, the change of exergy destruction in the steam turbine is also neglected.

Then equations (3) and (4) can be written as:

$$\Delta E_f + \Delta E_s + \Delta E_w = W_{hyb} + \Delta EXL_{H-hyb} \qquad (A5)$$
$$\Delta E_f + \Delta E_w = W_{fos} + \Delta EXL_{H-fos} \qquad (A6)$$

where ΔEXL_{H-hyb} and ΔEXL_{H-fos} are separately the exergy destruction in the feed water heater after and before hybridization.

8 REFERENCES

[] JAMEL, M.S., Rahman, A., Shamsuddin, A.H., 2013. Advances in the integration of solar thermal energy with conventional and non-conventional power plants. Renewable and Sustainable Energy Reviews 20, 71-81.

[2] HU, E., Yang, Y., Nishimura, A., Yilmaz, F., Kouzani, A., 2010. Solar thermal aided power generation. Applied Energy, 87, 2881-2885.

[3] National renewable energy laboratory, 2010, http://www.nrel.gov/csp/news/2010/870.html.

[4] Yan, Q., Yang, Y., Nishimura, A., Kouzani, A., Hu, E., 2010. Multi-point and Multi-level Solar Integration into a Conventional Coal-Fired Power Plant. Energy Fuels, 24 (7), 3733-3738.

[5] YANG, Y., Yan, Q., Zhai, R., et al, 2011. An Efficient Way to Use Medium-or-Low Temperature Solar Heat for Power Generation-Integration into Conventional Power Plant. Applied thermal engineering 31, 157-162.

[6] HOU, H., Mao, J., Yang, Y., Luo, N..2012. Solar-Coal Hybrid Thermal Power Generation- an Efficient Way to Use Solar Energy in China, International Journal of Energy Engineering 2 (4), 137-142.

[7] PENG, S., Hong, H., Wang, Y., Wang, Z., Jin, H., 2014. Off-design Thermodynamic Performances on typical days of a 330 MW Solar-hybrid Coal-fired Power Plant in China. Applied Energy, 130, 500-509.

[8] ZHAI, R., Zhu, Y., Yang, Y., Tan, K., Hu, E., 2013. Exergetic and Parametric Study of a Solar Aided Coal-Fired Power Plant. Entropy 15 (3), 1014-1034.

[9] HONG, H., Zhao, Y., Jin, H., 2011. Proposed Partial Repowering of a Coal-Fired Power Plant Using Low-Grade Solar Thermal Energy. International J. Thermodynamics, 14 (1), 21-28.

[0] Peng, S., Wang, Z., Hong, H., Xu, D., Jin, H., 2014. Exergy Evaluation of a Typical 330 MW Solar Hybrid Coal-fired Power Plant. Energy Conversion and Management, 85, 848-855.

[1] ISHIDA, M., Kawamura, K., 1982. Energy and exergy analysis of a chemical process system with distributed parameters based on the energy-direction factor diagram. Industrial Engineering and Chemistry Process Design and Development 21, 690–695.

[2] FLETCHER, E.A., Moen, R.L., 1977. Hydrogen- and Oxygen from Water, Science, 4308, 1050-1056.

91: Simulation and experimental research on the solar absorption cooling system driven by linear fresnel reflector solar collectors with thermal storage

L.Y. Zhou [1], Y.J. Dai [2], R.Z. Wang [3]

1 Institute of Refrigeration and Cryogenics, Shanghai Jiao Tong University, Shanghai 200240 PR China, zhoulingyu@sjtu.edu.cn

2 Research Centre of Solar Power and Refrigeration, Shanghai Jiao Tong University, Shanghai 200240 PR China, yjdai@sjtu.edu.cn

3 Research Centre of Solar Power and Refrigeration, Shanghai Jiao Tong University, Shanghai 200240 PR China, rzwang@sjtu.edu.cn

1 Mechanical Engineering Department, VGU, Jaipur, Rajasthan (India)

A novel solar hybrid system, composed of linear Fresnel reflector (LFR) solar collectors, a single/double effect absorption chiller, a thermal storage tank with intermediate-temperature molten salt and assistant components, is investigated both theoretically and experimentally in this paper. Compared with conventional solar cooling system, this system is designed for operating with different modes under various solar irradiances and requirements of load. Under a typical meteorological day in summer condition, theoretical analysis on the performances of solar collectors, absorption chiller and the entire system employing MATLAB software, has been implemented. Meanwhile, an experimental system is built to validate the theoretical model. It is found that the simulation and test results have a good agreement with each other. For the solar collector with rectangle cavity receiver, under the highest temperature of 180oC, the average thermal efficiency of 38% can be obtained. For the absorption chiller, the operating mode automatically changes as the variation of hot water inlet temperature. The COP of the single/double effect can reach up to 0.7 and 1.2 under the single and double effect modes. Thermal storage tank designed for storing and releasing thermal energy can support the absorption chiller operate under the single effect for 2 hours. Besides, the experiment results show that this hybrid system can be available for a whole day in typical summer condition.

Keywords: Solar energy; Linear Fresnel reflector solar collector; Single/double effect absorption chiller; Molten salt energy storage.

1. INTRODUCTION

Linear Fresnel reflector (LFR) solar collector is a kind of concentrate solar collector which is the development and optimization of parabolic trough solar collector. Compared to the parabolic trough solar collector, the predominant merits of LFR solar collector is that it requires minimal manufacturing, operation and maintenance cost [1]. Due to its technical and economic superiority, whereby its simplicity in structural design and low manufacture costs, it is now becoming a potential method to solar power, solar cooling and mid-temperature industrial utilization.

Nowadays lots of concentrate solar collector systems focus on high temperature solar power and pay less attention to mid-temperature solar field, such as solar cooling and industrial heating. Bermejo et al. [2] set up a double effect absorption cooling system which is driven by LFR solar collector. The rated cooling capacity is 180kW, daily average collector efficiency is 35%, the highest collector efficiency is 40%, and daily COP of chiller is 1.1. Chemisana et al.[3, 4] also carried out a solar cooling system driven by linear concentrate Fresnel solar collector which provided energy to a double effect LiBr absorption chiller. The rated COP is 1.35 and operation temperature of chiller is between 150-170°C. This system can operate for about 5hours from 10:00am to 3:00pm in the typical summer condition through simulation. Besides, the distinctive between double effect absorption chiller driven by linear concentrate solar collector and single effect absorption chiller driven by vacuum tube collector was also investigated. Results showed that the LFR solar collector system has its own advantages and disadvantages.

Energy storage is now becoming quite essential in energy systems, especially for low grade thermal energy, such as solar thermal or waste heat. Phase change materials (PCMs) have been widely investigated and applied in heat pumps, solar engineering, and spacecraft thermal control applications[5]. Molten salts working as mature PCM have been used in some solar power plants and industrial applications due to its ideal phase change temperature and latent heat. Anica Trp et al.[6] carried out a numerical method of phase change heat storage based on enthalpy method and investigated the heat transfer process in shell and tube heat exchanger. Also, comparison between the performance of one material and two materials was obtained and some key factors which influents the heat transfer performance were summarized. L. Xia et al.[7] also studied the heat transfer characteristics of PCMs based on effective packed bed model with enthalpy method. Simulation with ANSYS software was utilized to predict the performance and the result was validated by experiment.

Though several solar cooling systems have been investigated and some new materials or methods of thermal storage were also studied, the research and application of single/double effect solar absorption cooling system with thermal storage was limited. In this paper, thermal storage system was added into the cooling system which can switch between single and double effect based on the hot water inlet temperature of chiller to make the system operate stably and flexibly. MATLAB software was utilized to simulate the performance of solar collector, absorption chiller and system operating one day in typical summer condition. Theoretical results were validated with experiment data and results showed that the system can be available for a whole day in typical summer condition.

2. SYSTEM DESCRIPTION

This solar absorption cooling system driven by LFR solar collector with thermal storage was erected and tested at Shanghai (31.25°N and 121.47°E). Four major components consist of this hybrid system: LFR solar collector, Single/double effect absorption chiller, thermal storage tank with intermediate-temperature molten salt and other assistant components including cooling tower, plate heat exchanger, fan coil and other pipelines or valve parts.

2.1 LFR solar collector

LFR solar collector was chosen to be the heat source of this system. The schematic and photograph of LFR solar collector are shown in Figure 1.

There were 24 heat collector units in total, and each of them contained 10 rows of mirrors with mirror elements of dimension$6\text{m} \times 0.38\text{m} \times 2.2\text{mm}$. Mirrors were slight curved with a curvature radius of 5m. To avoid blocking between adjacent mirrors and shading of incident irradiance, the shift between each row was set to 8cm which was calculated based on the research by Mathur et al.[8]. The geometrical shape of cavity receiver was rectangle because of its high optical efficiency (just lower than Arc-shape cavity

receiver[9]) and minimal manufacturing, operation and maintenance costs. It comprised of 3copper pipes (Di=38mm) which was set 4.5m above the mirror field. In order to minimize radiative and convection heat lost, black chromium selective coating was covered on the outer pipes surface. Radiative properties of surface coating were assumed to be constant reflecting the mean absorption and emissivity values. To reduce the convective heat loss, ultra-white glass (2mm in thickness) was covered on the cavity receiver. Besides, sufficient phenolic foam was provided to wrap the back of the copper pipes to reduce the conductive heat loss. The structure and photograph of rectangular cavity receiver are shown in Figure 2 and other main parameters of LFR collector were shown in Table.1.

This system presented was placed in North-South direction and driven by stepper motors in which the position of motors can be controlled and adjusted precisely without feedback mechanism. Stepper motors were controlled by a sun tracking controller based on the ATmega128 MCU (Micro programmed Control Unit) with a real timer chip ensuring a stable and reliable operation with an accuracy of 10s/month. Position of sun based on solar altitude (α_s) and azimuth (γ_s) angle was predicted using solar position algorithm[10] within a variation of 0.0003o. The angle between mirror surface and ground served as the tracking angle β_s[11,12]. In the process of controlling, CPU read real time from the real timer chip and calculated the solar altitude and azimuth angle. These angles were then utilized to predict the tracking angle of the LFR system every 10s. The subdivision number of stepper motors was set to 12,000. That is, stepper motor took 12,000 steps for turning one cycle with a minimum stepping angle of 0.03o. When $\beta(t + \Delta t) - \beta(t) > 0.03$o, the control system sent N pulses and the mirror is rotated by 0.03o$\times N$. The number of pulses was calculated using the following equation:

Equation 5:
$$N = \frac{\beta(t+\Delta t)-\beta(t)}{0.03}$$
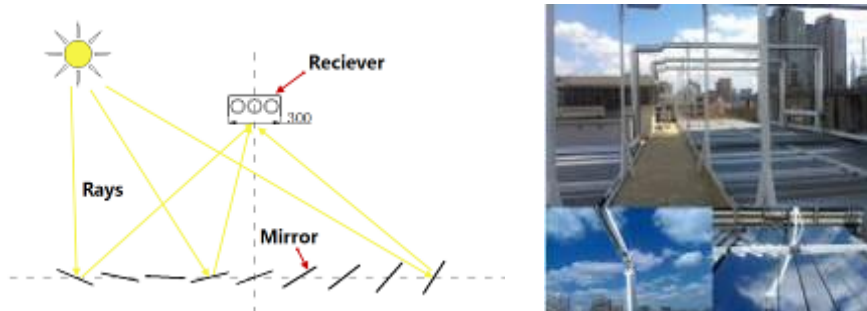
Figure 1 Schematic and photograph of LFR solar collector
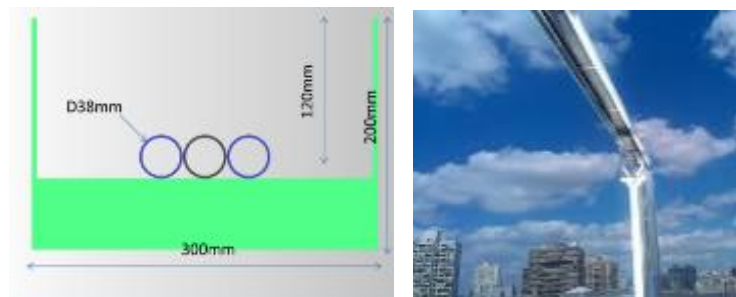
Figure 2 Rectangular cavity receiver

Table.1 The design and operation parameters for the solar collector

Parameters	Values	
	Mirror field 1	Mirror field 2
Number of units	11	13
Collector area	252 m^2	298 m^2
Connection tube length	66 m	78 m
Arch height	2.2mm	
Mirror length	6m	
Cavity receiver height	4.5 m	
Absorber area	1.8m^2/unit	
Working fluid	THERMINOL® 55	
Mass flow	1.34kg s^{-1}	
Mirror chord length	38cm	

2.2 Single /double effect absorption chiller

This LiBr absorption chiller was a new kind of chiller which can change mode from traditional single effect to double effect. Schematic and photograph of it are shown in Figure.3. This chiller is driven by hot water produced by LFR solar collector. When the hot water temperature is low, it's operating under single effect mode. As the hot water temperature rises, it's operating under double effect mode so that improving the efficiency of the solar cooling system. According to the simulation, when hot water temperature is higher than 85oC, it's operating under single effect, its rated cooling capacity is 91kW and COP is about 0.7. As hot water temperature rises higher than 145oC, it's operating under double effect, its rated cooling capacity is 134kW and COP reaches up to 1.2. The operation parameters of absorption chiller are shown in Table.2.

Figure.3 Schematic and photograph of absorption chiller

Table.2 The operation parameters of the absorption chiller
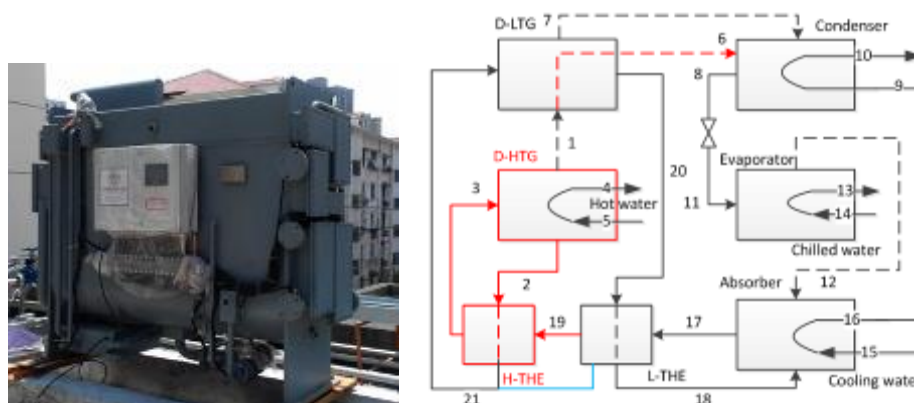
Parameters		Values	
Cooling capacity		134kW	91kW
Hot water	Volume flow	11.0m³/h	11.0 m³/h
	Inlet/outlet temp.	150°C/140°C	105°C/95°C
Cooled water	Volume flow	23.0m³/h	
	Inlet/outlet temp.	12°C/7°C	12°C/8.4°C
Cooling water	Volume flow	44m³/h	
	Inlet/outlet temp.	31°C/36°C	31°C/35.3°C
Capacity adjustment range		20~100%	

2.3 Thermal storage tank with intermediate-temperature molten salt

This thermal storage tank is designed for supporting absorption chiller operate under single effect for 2hours. Considering the stability, storage capacity and cost, materials of thermal storage tank was chosen to be molten salt which is a combination of 7%$NaNO_3$, 53%KNO_3 and 40%$NaNO_2$. The physical parameters were obtained by experiments are shown in Table.3. Through calculation, the thermal storage tank capacity is 1150MJ. Salt mass can be obtained as:

Equation 2:

$$M_{th} = \frac{Q_{th}}{C_{p,th}T_{th} + H}$$

Where:

- T_{th}=temperature difference of sensible heat (°C), in present study it's designed to be 40.
- $C_{p,th}$=specific heat capacity of molten salt (kJ/kg K)
- H= phase change latent heat (kJ/kg)

As salt density is 1978kg/m³, through calculation, the volume of salt is 4.4 m³. Considering 10% margin, 4.84 m³ is the final volume of storage tank. For further considering technology maturity of materials, manufacturing and maintenance costs, mature shell and tube heat exchanger is chosen to be the device.

Molten salt is put into cylindrical shell, and thermal oil flows as working fluid in the tubes inside of shell. Figure.4 shows the Photograph of the thermal storage tank.

Table 3Thermophysical parameters of the molten salt

Molten salt	Phase change temp. ºC	*H* Phase change latent heat kJ/kg	ρ density kg/m^3	C_p Specific heat capacity kJ/(kg K)
HITEC	142	75.3	1978	1.424

Fig.4 Photograph of the thermal storage tank

2.4 System operation modes

Schematic of system operation modes is shown in Figure.5. According to the difference of working fluid and functions, this system can be divided in two parts: heat source thermal oil system and air conditioning water system. Heat source thermal oil system consists of LFR solar collector, thermal storage tank and electric heater. Ari conditioning system consists of absorption chiller, cooling tower and AC terminals. Heat source thermal oil system can operate in six modes under different methods of energy driving and storage. The operating mode switches automatically relying on solenoid valves. Description of different operating modes are shown below in details.
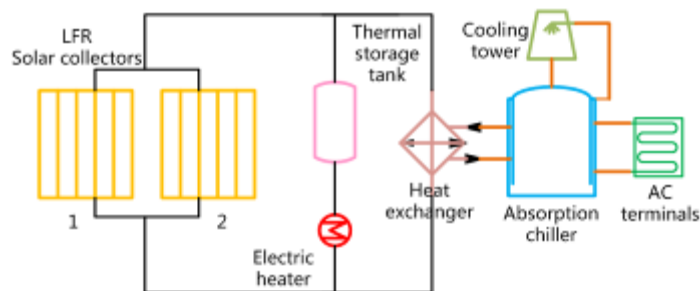

Figure.5 Schematic of the hybrid system

1) Solar direct driving mode. In the daytime LFR solar collector drives absorption chiller directly with present irradiance as it is abundant enough for this system. In this case, thermal storage tank is bypassed. And heat transfers from solar collector to chiller through heat exchanger. Generally this case occurs in typical summer condition.

2) Solar direct driving + excess energy stored mode. This mode is based on previous mode. On the basis of driving absorption chiller, if solar irradiance is far abundant to drive absorption chiller, then excess energy will be stored in thermal storage tank. In this case, energy storage tank is connected. Working fluid, whereby thermal oil flows in two different ways: one is transferring heat from solar collector to absorption chiller through exchanger, the other is for storing energy in thermal storage tank.

3) Thermal storage tank driving mode. Absorption chiller starts working from 8:00 or even earlier in the morning. That means the temperature of hot water which drives absorption chiller has to be high enough. But solar collector can't be driven to that temperature by solar irradiance in the early morning as it is quite low. In this case, thermal storage tank is used to be the heat source which drives absorption chiller.

4) Solar + thermal storage tank driving mode. As solar irradiance decreases from noon to afternoon, the temperature of solar collector also decreases. Meanwhile, the building load still exists. Besides, solar collector will not be available in short term cloudy day. In both cases, thermal storage tank is connected and works as a supplement.

5) Electric storage mode. The price of electricity is lower than daytime from 10:00pm to next morning which known as valley price. Energy storage tank can be heated by electricity in this period.

6) Solar thermal storage mode. For weekends or holidays, air conditioning is not used. In this case, solar irradiance will be transferred into heat then stored in thermal storage tank.

3 THEORETICAL ANALYSIS

In present simulation, a steady-state model was employed to calculate the parameters of system. Here are a few assumptions:

1) LFR solar collector: a) there is no heat loss in connecting tubes, except cavity receiver; b) there is no heat capacity in cavity receiver and tube wall.

2) Absorption chiller: a) outlet solution state of high voltage generator, low voltage generator and absorber is saturation; b) outlet cooled water of condenser and refrigerant steam of evaporator is saturation; c) there are no heat loss in generators and evaporator.

3) All heat loss and pressure drop of working fluid is ignored and measurement errors of temperature and pressure are considered negligible.

3.1 Thermal analysis of LFR solar collector

For LFR solar collector, cavity receiver works for absorbing heat. According to energy balance, the heat absorbed by cavity is equal to the difference of heat reflected to cavity surface by mirrors and heat loss of cavity, which is shown as the following relationship:

Equation 3:

$$Q = mc_p(T_0 - T_i) = A_c I_b \eta_{opt} - Q_{loss}$$

Where:

- Q=useful energy (W)
- Q_{loss}=heat loss (W)
- A_c=total mirror area (m²)
- I_b=solar irradiance (W/m²)
- T_0=outlet temperature (ºC)
- T_i=inlet temperature (ºC)
- m=mass flow (kg/s)

In which Q_{loss} represents the heat loss including conductive, convective and radiative loss respectively. Taking this into account, Eq. (4) is shown as the following equation:

Equation 4:

$$Q = \eta_0 A_c I_b - A_a[\varepsilon_a \sigma(T_s^4 - T_{amb}^4) + h(T_s - T_{amb})] - A_e \frac{\lambda}{L}(T_s - T_{amb})$$

Where:

- T_s=reviever surface temperature (ºC)
- T_{amb}=ambient temperature (ºC)
- h=heat convection coefficient (W/m² K)
- λ= heat conduction coefficient (W/m K)

For concentrating collectors, the heat loss can be thought as a direct ratio with the temperature difference of receiver surface and environment [10]. Hence the heat loss can be expressed as:

Equation 5:

$$Q_{loss} = U_L A_a (T_s - T_{amb})$$

According to Eq. (4) and Eq. (5), the heat loss coefficient is shown as the following equation:

Equation 6:

$$U_L = \frac{A_a[\varepsilon_a \sigma(T_s^4 - T_{amb}^4) + h(T_s - T_{amb})] + A_e \frac{\lambda}{L}(T_s - T_{amb})}{A_a(T_s - T_{amb})}$$

As Eq. (6) shows, the heat loss coefficient is a function related to radiation, convection and conduction. In this equation, several parameters such as heat transfer coefficient h and average surface temperature T_s related to materials properties and air flow condition of cavity surface are quite complex to obtain. Hence it can't be used to predict the thermal performance such as outlet temperature and collector efficiency. For this case, the way of predicting U_L is testing the inlet and outlet temperature T_i, T_o. Then obtaining the heat Q absorbed by receiver and heat loss Q_{loss}. Finally the conclusion is a relationship between heat loss coefficient U_L and inlet temperature T_i which can be utilized to simulate the collector performance.

3.2 Simulation and analysis of absorption chiller

Theoretical analysis and calculation were based on energy balance and mass balance of solution for both single and double effect. For each component, energy and mass balance equations were established. The input parameters were temperature and flow of hot water, and output parameters were cooling capacity, COP and cooled water temperature.

For the transition mode between single and double effect, it is a moving process which based on the change of the way and flow of solution. In this mode, the flow pattern of solution changes from single effect to double effect as the temperature of hot water rises. So it's not accurate to simulate this mode in steady state or quasi steady state condition. For this situation, G.P. Xu and Y.Q. Dai [13,14] did researches about double effect series flow type absorption chiller and double effect Parallel flow type absorption chiller. S.C. Kaushik and Akhilesh Arora [15] studied the energy and exergy of single effect and series flow double effect water–lithium bromide absorption refrigeration systems both theoretically and experimentally. Conclusions showed that the transition mode between single and double effect is not continued. As the single effect mode reaches to rated condition, cooling capacity and COP stop rising. In this situation, excess energy is utilized to preheat and generate HTG. As this process continues to a certain extent, the chiller starts to operate in double effect. Hence in this paper, combined experiment results, the absorption chiller operates under double effect as the hot water inlet temperature reaches higher than 145°C and operates under single effect as the hot water inlet temperature is lower than 145°C.

4   RESULTS AND DISCUSSION

The results are mainly consist of LFR collector, absorption chiller and whole system performance in typical summer condition because of the page limit.

4.1 Performance of LFR solar collector

Figure.6 shows the receiver surface temperature curve of experiment which based on a typical sunny day. The experiment was conducted on June 10th 2014. As recorded, the average solar irradiance is about 680W/m² and ambient temperature is about 26.8°C respectively. The experiment started from 11:00am as LFR collector was exposed to the effective incident ray. It can be seen that the temperature increased sharply at the 60 min of beginning. The receiver reached to quasi steady state within about 80 min and the maximum temperature is 180°C.

Heat loss of LFR collector was obtained by experiments for testing different receiver inlet temperatures within a range of 70°C to 180°C. Experiments were conducted on June 24th 2014. In the process of experiment, the average solar irradiance is about 650W/m² and ambient temperature is about 25.4°C respectively. Eq. (7) was used to evaluate U_L. The mathematical relationship between U_L and T_i is shown as the following equation:

Equation 7:

$$U_L = 5.311e^{0.0117T_i}$$

Thermal efficiency of LFR collector is determined by obtaining instantaneous efficiency values for a combination of incident solar irradiance, ambient temperature and collector temperature. Simulations and Experiments for LFR collector were conducted under various fluid inlet temperatures. Efficiency plots draw against $(T_s - T_{amb})/I_b$ are shown in Figure.7 As shown, when bulk temperature of fluid was 85°C, thermal efficiency was 52%; bulk temperature of fluid was 105°C, thermal efficiency was 45%; bulk temperature of fluid was 150°C, thermal efficiency was 32%. As the ratio $(T_s - T_{amb})/I_b$ increased, the efficiency decreased, which showed that higher collector temperature led to lower efficiency due to the increase of the heat loss. The average deviation between simulation and experiment was about 15%. This deviation may be due to manufacturing imperfections of collector. Furthermore, in simulation it was assumed that cavity receiver was totally insulated, while the fact in experiment it was impossible. Hence the deviation between simulated and experimental results can be considered to be acceptable.
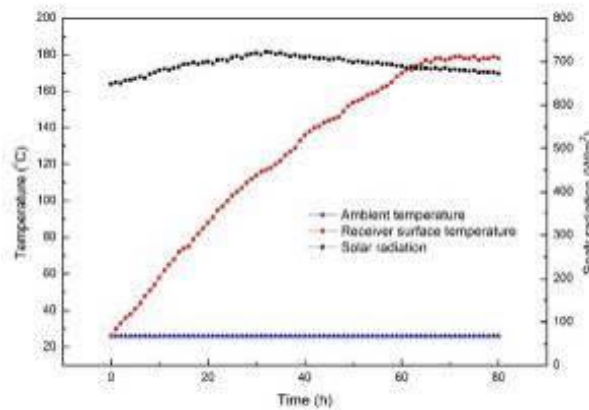

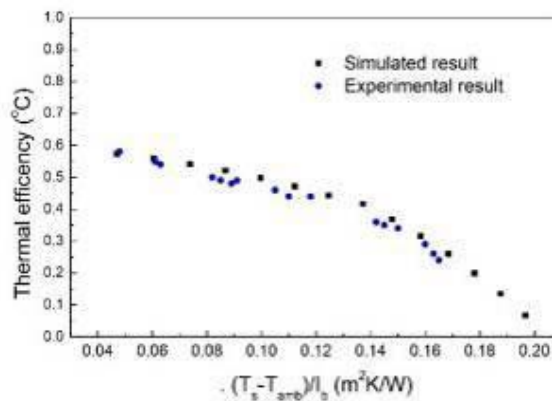*Figure.6 Time-stagnation temperature plot for the LFR system*

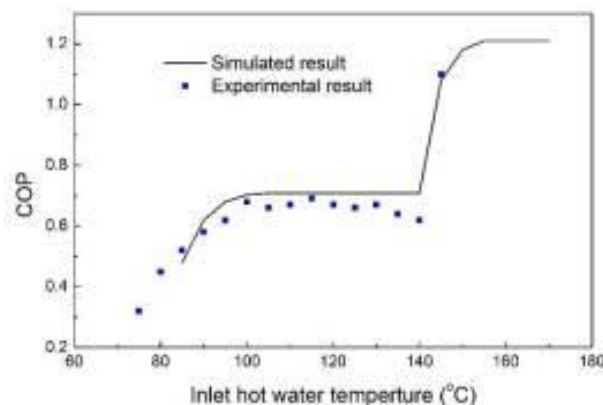*Figure.7 Simulated and experimental thermal efficiency of LFR collector*

Figure.8 COP curve of chiller

4.2 Performance of absorption chiller

Figure.8 shows the COP curve of absorption chiller. It can be found that COP increased as the hot water inlet temperature increased. From experiment, the minimum temperature of driving chiller was about 75°C. As the temperature increased till 105°C, which is the rated temperature of driving chiller for single mode, COP reached to 0.7. After that, both COP and cooling capacity stopped increasing. This was due to the structure and design principle of single/double effect chiller, which is the COP and cooling capacity will not continue to increase as soon as they reach to their rated values. Meanwhile the access energy will be taken into HTG to preheat it as the inlet temperature continues to increase. The chiller started to operate under double effect when HTG was driven by enough energy. For double effect mode, the hot water inlet temperature was 150°C and rated COP was 1.2. Besides, from experimental results it should be noted that the transition mode between single and double effect (135°C-140°C), COP declined to some extends. This was due to operation of HTG and some related pumps when operation mode transited from single to double effect that led to some excess energy costs.

4.3 System performance in typical summer condition

System performances in typical summer condition are shown as below. Figure.9 shows the hot water inlet/outlet temperature curves of the absorption chiller. From the very beginning of morning, solar irradiance, as well as the temperature of working fluid was low, hence the fluid temperature was not high enough to drive the chiller. In this case, the chiller was driven by thermal storage tank and operated in single effect mode for 2hours. Meanwhile, the LFR collector operated and the working fluid was kept being heated in the cavity receiver. After a period, the temperature of working fluid increased and till it was high enough to drive the chiller. This process cost about 2hours from the beginning of operation. Then the chiller was driven by LFR solar collector and continued to operate in single effect mode. As the temperature of working fluid increased, the operation modes of chiller changed from single effect to double effect when the temperature was higher than 145°C. In the noon time, the chiller operated in double effect for 2~3hours. In this period, excess energy would be stored into the storage tank based on the actual situation, whereby the temperature of working fluid was higher than 150°C. According to the test, the average temperature of storage tank raised from 113.6°C to 124.5°C. In the late afternoon, the decrease of solar irradiance led to the decrease of temperature of working fluid. In current experiment, the temperature of working fluid was unable to drive chiller at about 5:00pm, whereby the temperature was lower than 85°C. In this case, thermal storage tank back to operated and provided energy for chiller till the end of that day. Figure.10 shows the COP curve of the absorption chiller. From that it can be seen this system is available for whole day in typical summer condition. The average COP of whole day is 0.88.
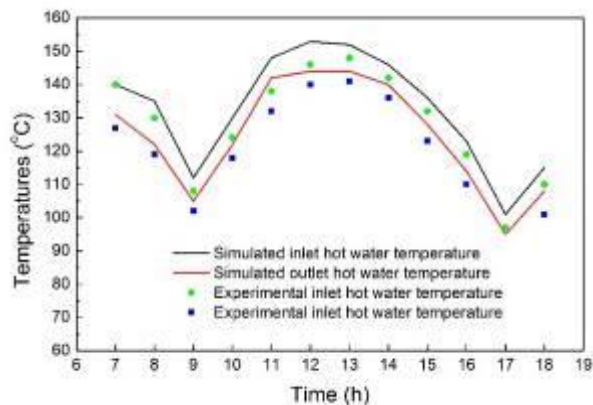
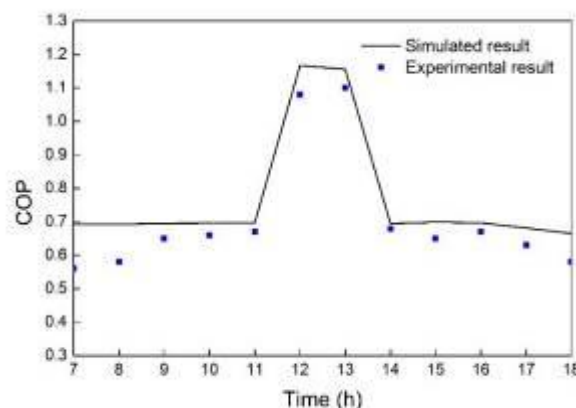*Figure.9 Hot water inlet/outlet temperature curves of the absorption chiller*

Figure.10 COP curve of the absorption chiller

5   CONCLUSION

A novel solar hybrid system, composed of linear Fresnel reflector (LFR) solar collectors, a single/double effect absorption chiller, an intermediate temperature molten salt thermal storage tank and assistant components was investigated both theoretically and experimentally in this paper. Corresponding conclusions are drawn below:

- For LFR solar collectors with rectangle cavity receiver, the value of overall heat loss coefficient varied from 8.5 to 24.2 W/m² K within the tested working fluid inlet temperature range, the highest temperature is 180°C tested in a typical summer day and the thermal efficiency obtained from experimental results is about 38% within a temperature range of 80°C-160°C.
- For the absorption chiller, the operating mode automatically changes as the variation of hot water inlet temperature. The COP of the single/double effect can reach up to 0.7 and 1.2, as well as the temperature of chiller water can reach up to 8.4°C and 7°C under the single and double effect mode.
- The whole day operation of hybrid system was simulated by MATLAB software and validated by experiments in a typical summer day. It showed that this system can be available for whole day combined with thermal storage tank. The chiller can operated under double effect mode for 2~3hours in the noon, which highly improve the energy efficiency of the system.

6   REFERENCES

[1] GHARBI NE, Derbal H, Bouaichaoui S, Said N. A comparative study between parabolic trough collector and linear Fresnel reflector technologies. Energy Procedia 2011;6:565-72.

[2] BERMEJO P, Pino FJ, Rosa F. Solar absorption cooling plant in Seville. Sol Energy 2010;84:1503-12.

[3] CHEMISANA D, Rosell JI. Design and optical performance of nonimaging Fresnel transmissive concentrator for building integration applications [J]. Energy Conversion and Management 2011; 52(10): 3241-3248.

[4] CHEMISANA D, López-Villada J, Coronas A, Rosell JI, Lodi C. Building integration of concentrating systems for solar cooling applications. Applied Thermal Engineering 2013;50:1472-9.

[5] FARID MM, Khudhair AM, Razack SAK, Al-Hallaj S. A review on phase change energy storage: materials and applications. Energy Conversion and Management 2004;45:1597-615.

[6] TRP A, Lenic K, Frankovic B. Analysis of the influence of operating conditions and geometric parameters on heat transfer in water-paraffin shell-and-tube latent thermal energy storage unit. Applied Thermal Engineering 2006;26:1830-9.

[7] XIA L, Zhang P, Wang RZ. Numerical heat transfer analysis of the packed bed latent heat storage system based on an effective packed bed model. Energy 2010;35:2022-32.

[8] S.S. MATHUR, T. Kandpal, B. Negi, Optical design and concentration characteristics of linear Fresnel reflector solar concentrators dII. Mirror elements of equal width, Energy Convers. Manage. 31 (1991) 221 e232.

[9] XIE WT, Dai YJ, Wang RZ. Theoretical and experimental analysis on efficiency factors and heat removal factors of Fresnel lens solar collector using different cavity receivers. Sol Energy 2012;86:2458-71.

[10] J.A. DUFFIE, WA. Beckman. Solar engineering of thermal processes[M]. New York: Wiley Inter science

[11] REDA I, Andreas A. Solar position algorithm for solar radiation applications. Sol Energy 2004;76:577-89.

[12] J.E. BRAUN, J.C. Mitchell, Solar geometry for fixed and tracking surfaces, Sol. Energy 31 (1983) 439 e444.

[13] Q P. XU, Y.Q. Dai, K.W. Tou, et al. Theoretical analysis and optimization of a double-effect series-flow-type absorption chiller. Applied Thermal Engineering, 1996,16(12):975-987.

[14] Q P. XU, Y.Q. Dai. Theoretical analysis and optimization of a double-effect parallel-flow-type absorption chiller. Applied Thermal Engineering, 1997,17(2):157-170.

[15] KAUSHIK SC, Arora A. Energy and exergy analysis of single effect and series flow double effect water–lithium bromide absorption refrigeration systems. International Journal of Refrigeration 2009;32:1247-58.

SESSION 21: SOLAR ENERGY

182: Investigation on the overall energy performance of an a-si based photovoltaic double-skin facade in Hong Kong

Jinqing PENG[1,2], Lin LU[1], Hongxing YANG[1], Aotian SONG[1], Tao MA[1]

[1] *The Hong Kong Polytechnic University, Hong Kong China, bellu@polyu.edu.hk (L. LU)*
[2] *Hunan University, Changsha China, jallenpeng@gmail.com (J. PENG)*

This paper simulates the annual overall energy performance of an amorphous silicon (a-Si) based photovoltaic double-skin facade (PV-DSF) in Hong Kong. Based on EnergyPlus, a numerical simulation model was developed to simulate the thermal, power and daylighting performances of the ventilated PV-DSF simultaneously. The overall energy performance of the optimized PV-DSF was calculated. Per unit area of such PV-DSF was able to generate about 38 kWh electricity yearly in Hong Kong. The studied PV-DSF is also featured with pretty good thermal and daylighting performances. A great amount of solar heat gain was blocked by the PV module, which resulted in a lower solar heat gain coefficient (SHGC) for the PV-DSF. At noon of sunny day, the maximum daylighting illuminance reached 470 lux, which was very close to the design illuminance level. Thus, if combined with a dimmable lighting control system, the semi-transparent PV-DSF could reduce considerable lighting energy use. Moreover, with the efficiency improving of semi-transparent PV modules, the overall energy performance of PV-DSFs would be further improved, and thus it would be more and more promising.

Keywords: building integrated photovoltaic (BIPV), double-skin facade, semi-transparent a-Si, overall energy performance

1.   INTRODUCTION

In 2012, about 68% of the total electricity end-use was consumed by buildings in Hong Kong and this proportion has been increasing over recent years. Among the various types of building energy uses, space air-conditioning has accounted for more than 45% [1]. Windows, as important links between buildings and outdoors, not only allow occupants access to outdoor views but also bring sufficient natural lighting and beautiful building appearance. However, the extensive use of windows also results in negative impact on air-conditioning energy use as their thermal insulation performance are bad, which increase the solar heat gain in summer and heat loss in winter. Thus, it is crucial to develop energy efficient curtain walls/facades which can not only bring sufficient natural lighting but also considerably reduce heat transfer between the outside and the inside of buildings. Semi-transparent thin-film PV (STPV) windows/facades, which refer to use semi-transparent PV modules to replace traditional glass windows/facades, have attracted much attention of researchers in recent years due to their good energy efficient performance levels [2-6]. They can not only generate electricity in situ through photovoltaic effect but also significantly reduce the air-conditioning cooling load by effectively blocking solar heat gain [7-9]. Moreover, it can also make full use of daylighting by adjusting the transmittance of PV modules according to lighting requirements. Through literature review, two severe drawbacks were found for the existing single pane PV windows/facades [10]. Firstly, during BIPV operating, the PV module's temperature is very high due to its high sunlight absorption. The maximum temperature of a semi-transparent a-Si PV module installed on the south-facing facade could reach up to 60 °C. Such high surface temperature would result in serious thermal discomfort in the indoor room if the PV modules are directly used as building facades. Secondly, the heat losses of a single skin STPV window are very serious in winter nights due to its high thermal emissivity and U-value, which severely restrict their applications in cold climate zones. Thus, in order to reduce the thermal discomfort feeling as well as the heat losses, a possible solution is to combine the BIPV facade technology with the double-skin facade (DSF) technology to avoid the overheating and severe heat loss problems. In our previous publication, a novel ventilated photovoltaic double-skin facade (PV-DSF) was developed and its overall energy performance was demonstrated by long-term outdoor test campaign [11-12]. In this study, a comprehensive simulation model based on EnergyPlus was introduced to simulate the thermal, power and daylighting performances of PV-DSF simultaneously, so as to reveal its energy saving potential in Hong Kong.

2. SIMULATION MODEL

As shown in Figure 1, the studied PV-DSF consisted of an outside layer of semi-transparent a-Si PV panels, an inner layer of an openable window as well as an intermediate 400 mm air ventilation cavity. The ventilation design makes cold air enter the airflow cavity through the bottom inlet louvre, then exchange heat with the PV panels as well as the inside windows and finally exhaust a considerable amount of waste heat via the upper outlet louvre. Previous experimental studies demonstrated that such ventilation can not only reduce the cooling load by 15%, but also enhance the PV module's energy output by about 3% [11-12].
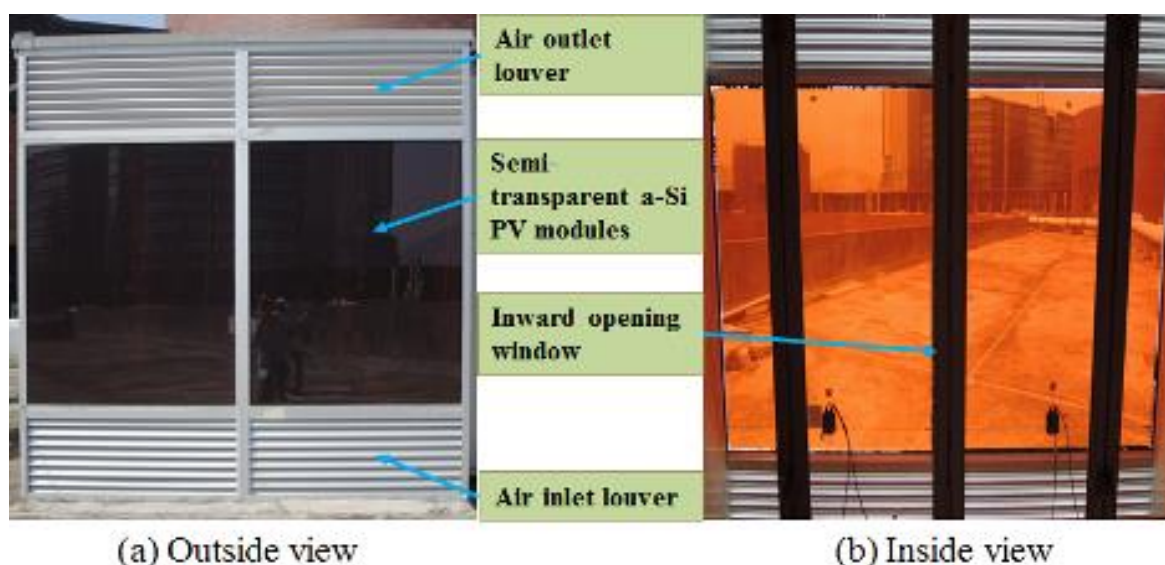

Figure 1: The real picture of the ventilated PV-DSF system

Although massive experimental data was collected during outdoor experiments for the PV-DSF, the experimental scenarios were impossible to cover all the situations and variables. Thus, a numerical simulation model based on EnergyPlus was developed in this study to comprehensively simulate its overall energy performance. The PV power module, airflow network module, daylighting module as well as the Window glass module in EnergyPlus were utilized to simulate the power, thermal and daylighting performances, respectively.

2.10. 2.1 Power output performance

The weather data of typical meteorological year (TMY) in Hong Kong were adopted in this simulation. The annual horizontal global solar radiation is about 1350 kWh/m^2 and the incident solar radiation upon the south-facing vertical facade is about 673 kWh/m^2. Figure 2 presents the monthly incident solar radiation on the south-facing facade in the typical meteorological year. It is obvious that the south-facing facade received more solar radiation in winter season in Hong Kong. This is because that the latitude of Hong Kong is lower than the Tropic of Cancer, thus the PV-DSF installed on the south-facing facade could not receive much solar radiation in summer season. The monthly energy output of the south-facing PV-DSF is shown in Figure 3. It is found that energy output in winter season was much more than that in summer season for the south-facing PV-DSF in Hong Kong. The maximum monthly energy output was about 16.1 kWh, occurring in December. The minimum monthly energy output occurred in June, was only 4.6 kWh. The annual energy generation was about 109 kWh.

The maximum power output of the PV-DSF in each month was also presented in Figure 3. The results showed that the maximum power output, occurring in December, was about 135 W, which was close to the rated power output of the PV-DSF under STC. The maximum power output in June was only 25W because the beam solar radiation was fully obstructed in this month. The annual energy output of per unit area of the PV-DSF was also calculated, it was 38 kWh/m^2. Figure 4 presents the monthly energy output of per unit area of the PV-DSF. The maximum monthly energy output was about 5.6 kWh/m^2. In order to determine which orientation is the best orientation for PV-DSF installation in Hong Kong, the annual energy output of PV-DSFs under different orientations was simulated. As shown in Figure 5, the annual energy output of PV-DSF varied with orientations. In terms of energy performance, the best orientation for PV-DSF installation is 40 degrees south by west, in which the PV-DSF generates the maximum electricity of 39.4 kWh/m^2/yr. In addition, west facade is more suitable than the east facade for PV-DSF installation in terms of energy generation in Hong Kong.
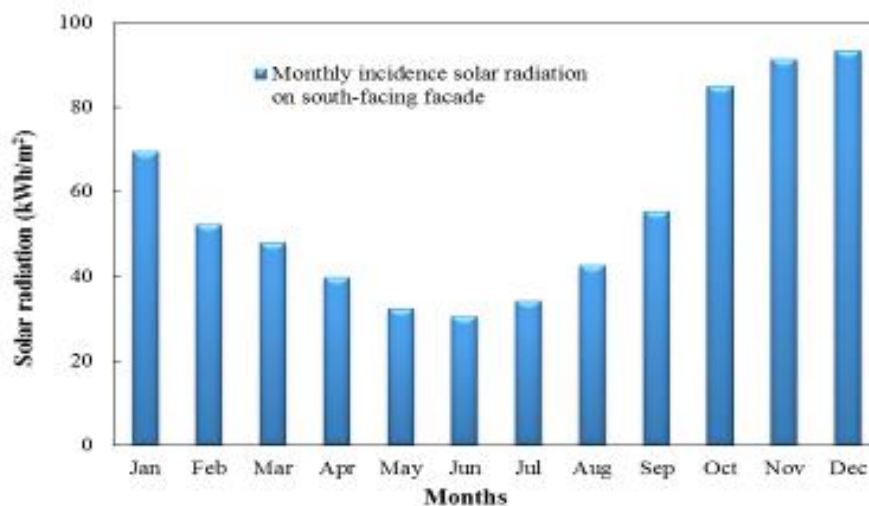
Figure 2: Monthly incident solar radiation on the south-facing facade in TMY in HK
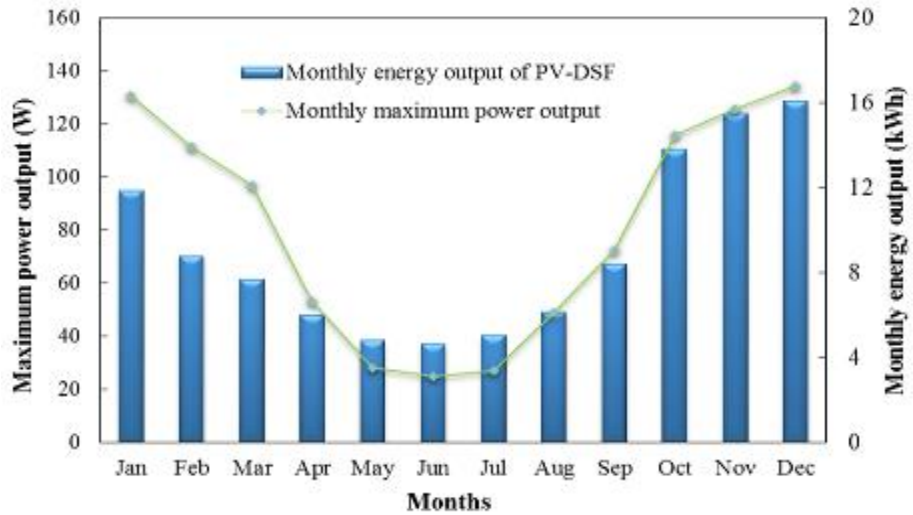
Figure 3: Monthly energy output and the maximum power output of the PV-DSF in Hong Kong
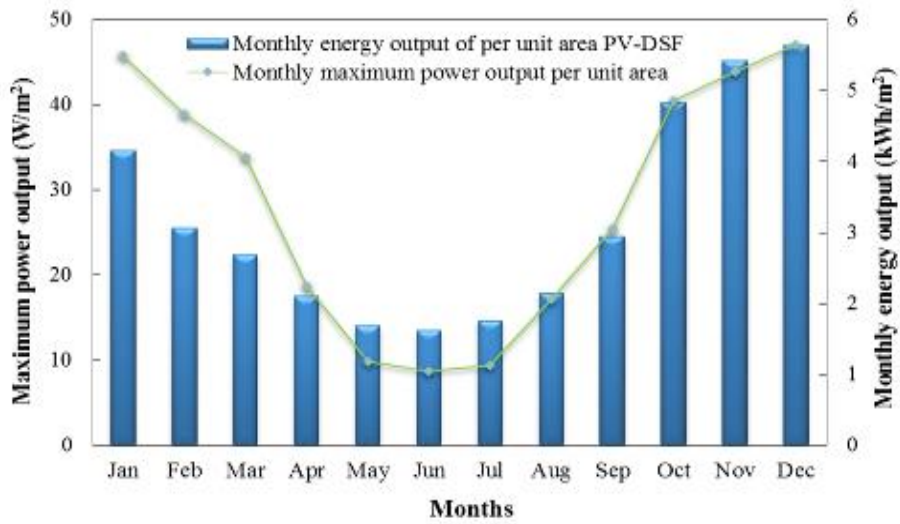
Figure 4: Monthly energy output of per unit area of the PV-DSF in TMY
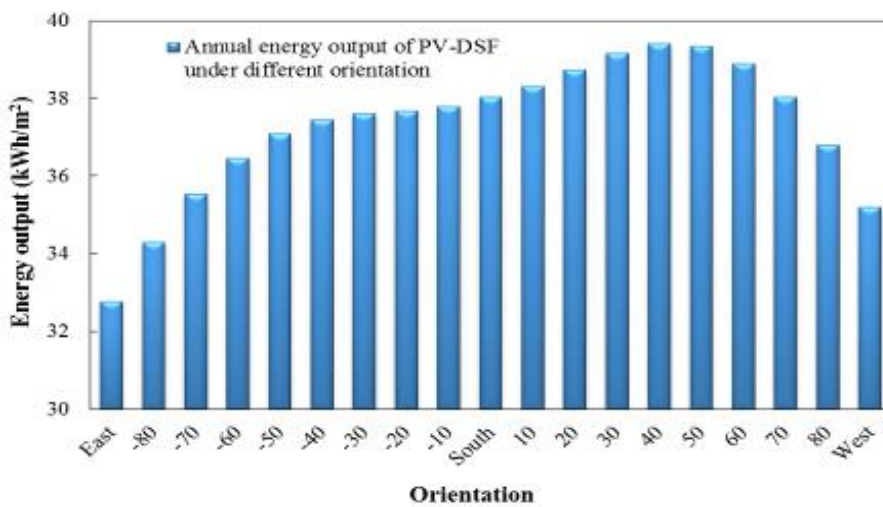
Figure 5: The annual energy outputs of PV-DSFs in different orientations in HK

2.2 Thermal Performance

Except for power generation in situ of buildings, PV-DSF could also significantly reduce the building energy use by bringing down the air-conditioning cooling/heating loads. As the transmittance of the semi-

266

transparent PV module is low, solar radiation would be blocked significantly when transmitting through the PV module. Figure 6 presents a comparison of the monthly solar energy incident upon the PV module and the transmitted one. The external PV module of the PV-DSF reduced the solar radiation energy from 340 MJ/m^2 to 48 MJ/m^2 in December. A great amount of solar heat gain was blocked by the PV module, which resulted in a lower solar heat gain coefficient (SHGC) for the PV-DSF.

The monthly heat gain and heat loss rates of the internal window of the PV-DSF are presented in Figure 7. It is found that the monthly average heat gain rate was low even though in summer season. The main reasons can be explained: 1) a large amount of solar radiation was blocked and absorbed by the external PV modules and, hence, the transmitted solar radiation was reduced dramatically; and 2) the ventilation air flow between the external PV module and the internal window removed a certain amount of waste heat via heat convection. Thus, the final heat gain rate of the PV-DSF was significantly reduced. As shown in Figure 7, another thing worth to note is that the heat loss rate of the internal window was very high. This is because that heat loss transferred from interior to exterior in the form of long-wave thermal radiation, but the PV-DSF can't block the infrared thermal radiation. In other word, even though the PV-DSF can absorb and block a large amount of incident solar radiation, especially the visible light, it can't block the thermal radiation emitting from the indoor room to the sky as its thermal emissivity is high. Thus, for cold climate zones application, the internal window of the PV-DSF should adopt low-e glasses rather than normal clear glasses to reduce heat losses in winter.
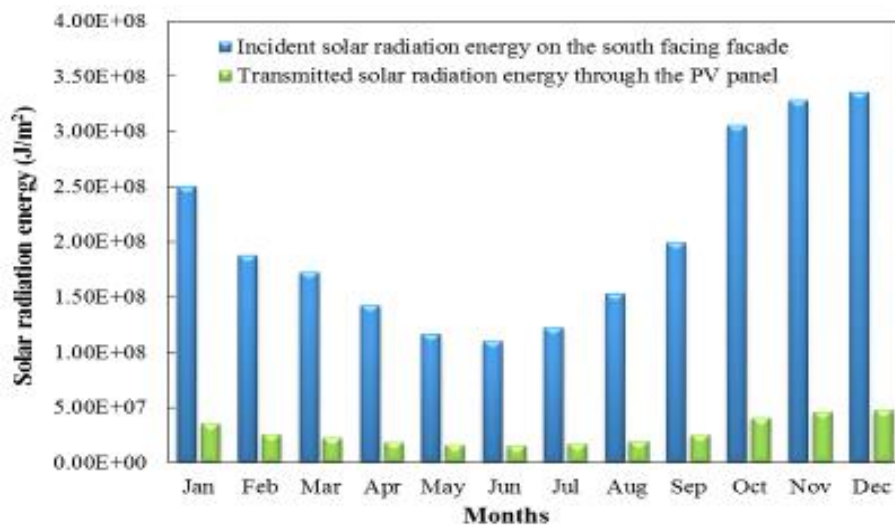

Figure 6: Comparison of the monthly solar energy incident upon and transmitted of the PV module
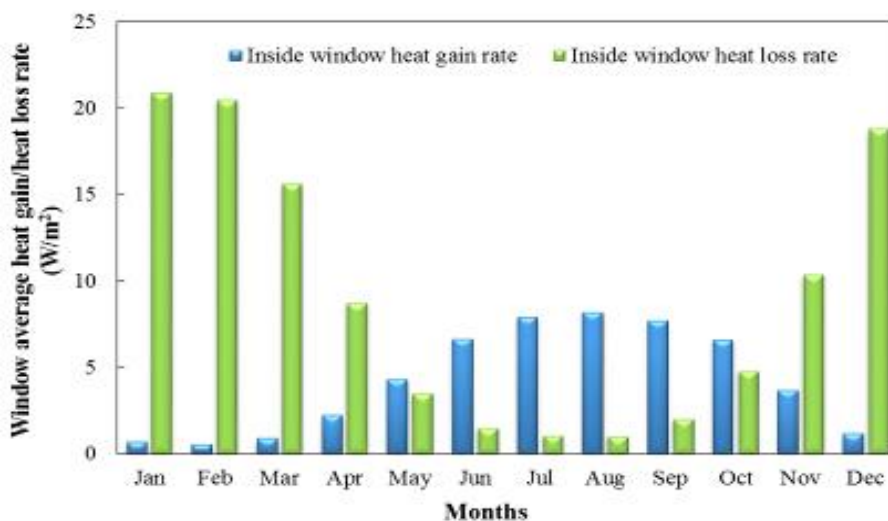

Figure 7: Monthly heat gain and heat loss rates of the internal window of the PV-DSF

2.3 Daylighting Performance

The measured optical data showed that the semi-transparent a-Si PV module had a very high absorptivity in visible light range. The good news of this is that the a-Si PV module could convert a large amount of visible light into electricity and at the same time reduce the solar heat gain significantly. However, the higher the visible light absorptivity of the PV module, the lower the daylighting illuminance in the office room. In order to investigate the impacts of high visible light absorptivity on the daylighting performance of the PV-DSF, the hourly daylighting illuminance was simulated. Figure 8 presents the monthly average daylighting illuminance. Having the similar trends of the monthly energy output, the PV-DSF had better daylighting performance in the winter season because the incident solar radiation was much higher in this season in Hong Kong. In December, the monthly average daylighting illuminance level reached 175 lux, which is about one third of the design lighting illuminance of 500 lux.

For a dimmable lighting control system, the variation of monthly average daylighting illuminance would result in a variation of the monthly lighting electricity use. The energy consumption of artificial lighting can be calculated by multiplying the rated lighting power without daylighting with the real-time daylighting lighting power multiplier [13]. Figure 9 presents the monthly average daylighting lighting power multiplier as well as the minimum power multiplier in each month. The lower the power multiplier, the less the lighting energy use. As shown in Figure 9, the daylighting lighting power multipliers in winter season were obviously lower than those in summer season, which means that less lighting electricity was needed in winter to reach the design illuminance level. In addition, it is found that the minimum hourly daylighting lighting power multipliers on certain days in December and January were only 0.1, which means that during a certain time of these days the daylighting illuminance level was very high and only one tenth of the rated lighting power was needed to reach the design illuminance level.
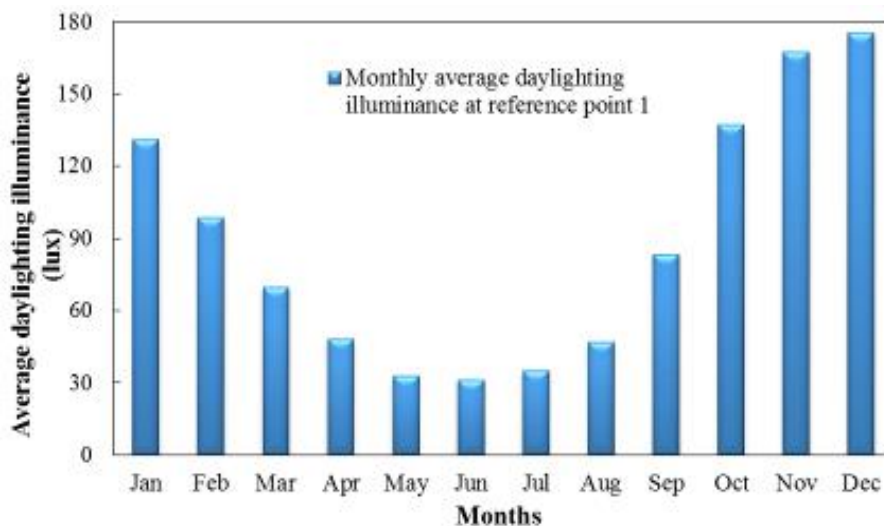
Figure 8: Monthly average daylighting illuminance in Hong Kong

The monthly lighting energy use was calculated by multiplying the rated lighting power with the monthly average daylighting lighting power multiplier and the results are presented in Figure 10. As it was found that the monthly lighting energy use was close to the monthly energy output of PV-DSF, these two parameters were compared in Figure 10. From October to January of next year, the monthly energy output was higher than the lighting energy use because the daylighting lighting power multipliers were low but the energy output of PV-DSF were large in this season. For summer season from February to September, the opposite was true for both the results and the reasons. The annual total energy output of the PV-DSF was about 109 kWh, which was lower than the annual lighting energy use by 45 kWh.

It was further found that the lowest daylighting lighting power multiplier occurred on January 5 and December 9. Figure 11 shows the daylighting illuminance level and the corresponding daylighting lighting power multiplier of these two days. It is found that the maximum daylighting illuminance reached 470 lux at 13:00 PM, which is very close to the design illuminance level. The corresponding daylighting lighting power multiplier was 0.1, which is the minimum lighting power output factor of the dimmable lighting system.
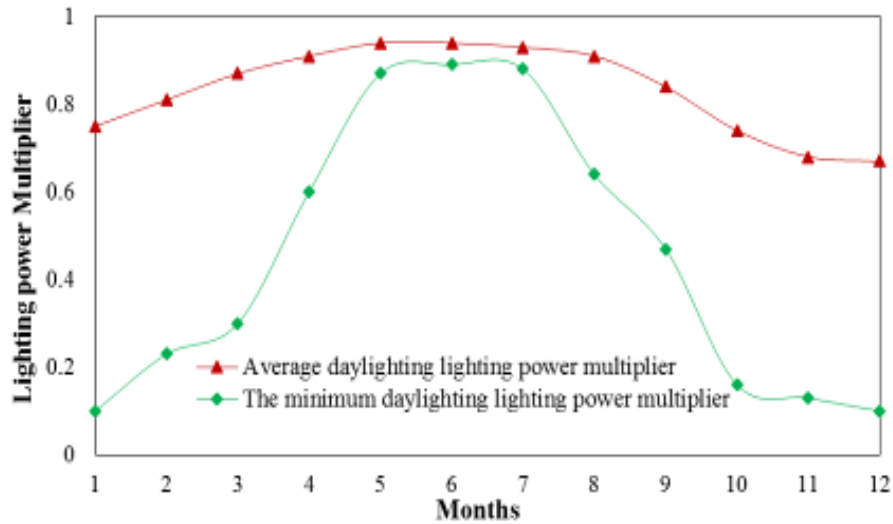
Figure 9: Monthly average daylighting lighting power multiplier and the minimum daylighting lighting power multiplier
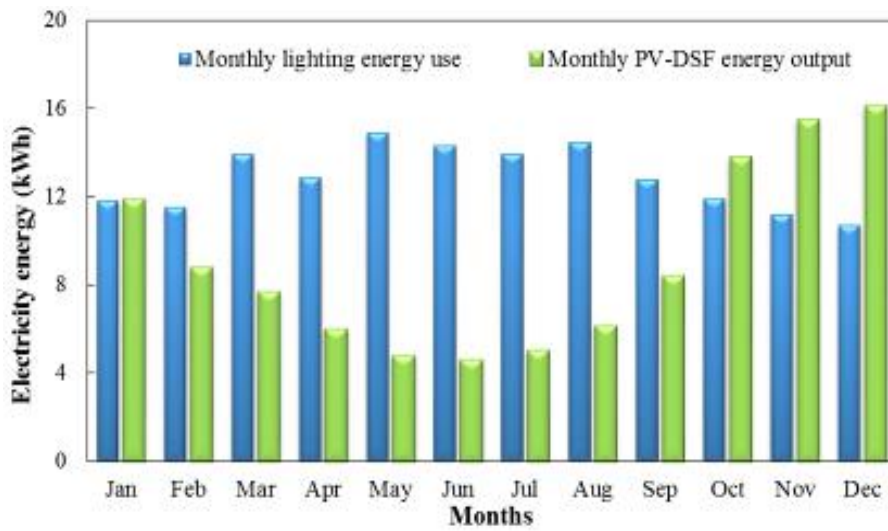
Figure 10: Monthly lighting energy use and energy output of the PV-DSF
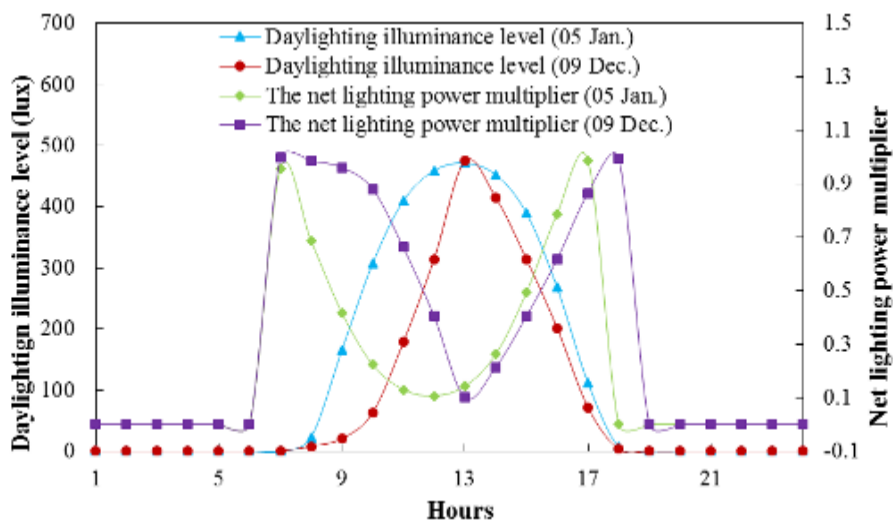
Figure 11: The daylighting illuminance level and the corresponding daylighting lighting power multiplier on December 9 and January 5

3. OVERALL ENERGY PERFORMANCE IN HONG KONG

The annual power, thermal and daylighting performances of the PV-DSF were all simulated in the previous sections. In this section, the overall energy performance of the office room installed with this PV-DSF was analysed.

Figure 12 presents the monthly electricity flows, including the consumed and generated electricity in each month. Most of electricity was consumed by the air-conditioning, especially for air cooling and fan using. The heating electricity use was very small and can be ignored. Counting in the monthly energy output, the monthly net electricity use of the office room was calculated and presented in Figure 12. In winter season, viz. January, February and December, the office room consumed the lowest electricity, about 7.3 kWh/m². In summer season, due to the higher cooling electricity use and the lower energy output of PV-DSF, the net electricity use reached up to 23.2 kWh/m² in August. The annual net electricity use of the office room was 981 kWh and the net electricity use of per unit area was 185 kWh/m²/yr.
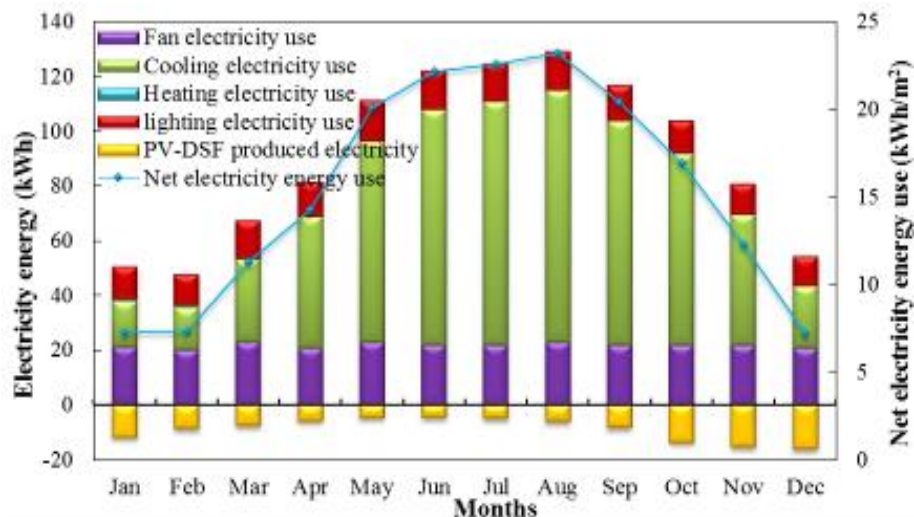
Figure 12: Electricity flows and net electricity use in each month in HK

4. CONCLUSIONS

In this paper, a numerical model was developed based on EnergyPlus to simulate the thermal, power and daylighting performances of a ventilated photovoltaic double-skin facade (PV-DSF). The simulation results showed that per unit area of such PV-DSF was able to generate about 38 kWh of electricity yearly in Hong Kong. It is worth noting that the efficiency of the semi-transparent PV modules used in the PV-DSF was only 6.2%, if high efficiency CdTe PV modules are to be used, the annual power output could be doubled. The PV-DSF studied also possessed good thermal and daylighting performances. As the transmittance of the semi-transparent PV module was low, a great amount of solar heat gain was blocked by PV modules, which resulted in a lower solar heat gain coefficient (SHGC) for the PV-DSF. The maximum monthly average daylighting illuminance level reached 175 lux, which was about one third of the design lighting illuminance. On sunny days, the maximum daylighting illuminance reached 470 lux, which was very close to the design illuminance level. Thus, if combined with a dimmable lighting control system, the energy consumption of artificial lighting can be reduced significantly. Finally, the monthly overall energy performance and net electricity use of the office room equipped with the PV-DSF were calculated. The office room consumed the lowest electricity about 7.3 kWh/m² in the winter season and the largest electricity of 23.2 kWh/m² in August. The annual net electricity use of the office room was 981 kWh and the net electricity use of per unit area was 185 kWh/m²/yr.

5. REFERENCES

[1] Hong Kong energy end-use data 2014. Electrical and Mechanical Services Department, Hong Kong. http://www.emsd.gov.hk/emsd/e_download/pee/HKEEUD2014.pdf

[2] HAN, J., Lu, L., Peng, J.Q., Yang, H.X., 2013. Performance of ventilated double-sided PV façade compared with conventional clear glass façade. Energy and Buildings; 56: 204-209.

[3] CHEN, F.Z., Wittkopf, S.K., Ng, P.K., Du, H., 2012. Solar heat gain coefficient measurement of semi-transparent photovoltaic modules with indoor calorimetric hot box and solar simulator. Energy and Buildings; 53: 74–84.

[4] FUNG, Y.Y., Yang, H.X., 2008. Study on thermal performance of semi-transparent building-integrated photovoltaic glazings. Energy and Buildings; 40: 341-350.

[5] PARK, K.E., Kang, G.H., Kim, H.I., Yu, G.J., Kim, J.T., 2010. Analysis of thermal and electrical performance of semi-transparent photovoltaic (PV) module. Energy; 35: 2681-2687.

[6] YOON, J.H., Song, J.H., Lee, S.J., 2011. Practical application of building integrated photovoltaic (BIPV) system using transparent amorphous silicon thin-film PV module. Solar Energy; 85: 723-733.

[7] MIYAZAKI, T., Akisawa, A., Kashiwagi, T., 2005. Energy savings of office buildings by the use of semi-transparent solar cells for windows. Renewable Energy; 30: 281–304.

[8] CHOW, T.T., Li, C.Y., Lin, Z., 2010. Innovative solar windows for cooling-demand climate. Solar Energy Materials and Solar Cells; 94:212-220.

[9] PENG, J., Lu, L., Yang, H., Han, J., 2013. Investigation on the annual thermal performance of a photovoltaic wall mounted on a multi-layer façade. Applied Energy;112:646-656.

[10] OLIVIERIA, L., Caamano-Martina, E., Olivierib, F., Neila, J., 2014. Integral energy performance characterization of semi-transparent photovoltaic elements for building integration under real operation conditions. Energy and Buildings; 68: 280–291.

[11] PENG, J.Q., Lu, L., Yang, H.X., 2013. An experimental study of the thermal performance of a novel photovoltaic double-skin facade in Hong Kong. Solar Energy; 97: 293-304.

[12] PENG, J.Q., Lu, L., Yang, H.X., Ma, T., 2015. Comparative study of the thermal and power performances of a semi-transparent photovoltaic façade under different ventilation modes. Applied Energy; 138: 572-583.

[13] Input Output Reference-The Encyclopedic Reference to EnergyPlus Input and Output. US Department of Energy.

471: Dust accumulation and PV power output in the tropical environment of Barbados

Darlene A. Field[1], Thomas Rogers[1], Andrea Sealy[2]

[1] *The University of the West Indies, Cave Hill Campus, St. Michael, Barbados*
[2] *Caribbean Institute of Meteorology and Hydrology, Husbands, St. James, Barbados*

Barbados has implemented attractive incentives geared towards increasing its renewable energy capacity to at least 29% of the total energy mix by 2029. Existing incentives include the removal of import duties for renewable energy systems and the introduction of net metering in the form of a renewable energy rider, effectively establishing compensation of up to US$0.16 per kWh for energy supplied to the grid. These changes, in addition to the rapid reduction in price of global solar photovoltaic (PV) modules – from US$4 per Wp in 2009 to under US$1 (Wp) at the end of 2014 – have resulted in a considerable increase in PV installations on the island. Grid-connected solar PV installed capacity has risen from zero in 2009 to over 7MWp by the end of 2014.

As installations continue to increase, there is a need to fully understand the effect of the Caribbean's unique environment on PV performance. Barbados, the easternmost island in the Caribbean, has a strong solar irradiance with 'cooling' winds, and is a good environment for PV utilisation. However, as dust concentrations in the atmosphere vary, so will their accumulation rates onto module surfaces and hence the irradiance received by the cells. Dust accumulation rates are increased by lower tilt angles and increased relative humidity. Rainfall and wind are considered good natural methods for cleaning module surfaces, however they are only effective during intense showers and high winds. In addition, the properties of the dust determine the rate of accumulation based on the ability of dust particles to stick to the module surface.

In this paper, we describe the effect of dust accumulation on four types of PV modules installed at three sites in Barbados – designated as urban, suburban and rural-coastal sites. Crystalline silicon modules were connected separately across resistors and the power output obtained at each site. The power output for April 2015 is described, including a period before and after cleaning.

Keywords: solar PV, module performance, dust accumulation, Caribbean

1. INTRODUCTION

Caribbean territories are considered as small island developing states and all except Trinidad and Tobago are heavily dependent on imported fossil fuels. With electricity tariffs averaging US$0.35 per kWh, policies geared towards increasing renewables in the local energy mix have been drafted and are starting to be implemented (REN21, 2014).

With earlier success in the development of a solar water heating industry (Epp, 2009), Barbados has taken steps toward achieving its target of 29% renewables in the energy mix by 2029 (REN21, 2014, Ministry of Housing, 2004). Attractive incentives promoting RE technologies include the suspension of import and environmental duties for renewable energy systems and the introduction of net metering in the form of a renewable energy rider in 2009, which allows the customer to obtain up to US$0.16 per kWh in compensation for energy supplied to the grid (FTC, 2013). The steep decline in global photovoltaic (PV) module prices, from US$4/Wp in 2009 to US$0.78/Wp as of January 2015 along with the abovementioned incentives has greatly encouraged the local PV market (Solarbuzz, 2015). This is demonstrated by the increased PV capacity from 1.2MWp in 2012 to over 7MWp in January 2015, which is encouraging for a country with a peak demand of 155MW (Shirley and Kammen, 2013).

PV systems are an excellent alternative source of energy compared to that of imported fossil fuels and as such, the effect of the local environment on PV performance needs be fully understood. This includes not only the effect of local weather, but also of non-direct parameters in the form of dust accumulation. In this paper, we look at PV modules installed at three locations, locally defined as urban, suburban and rural-coastal. These locations are classified based on their approximate distance from the major conurbation of Bridgetown, the commercial centre of Barbados. It was expected that there will be higher levels of organic-based dust particles in the urban setting due to an increased human presence and hence activity, especially during the daytime. This also includes exhaust from vehicular traffic. This increased amount of carbon-based dust can affect PV performance due to absorption of irradiance, with less transmission to the solar cells when compared to dust-types (El-Shobokshy and Hussein, 1993). The dust composition in suburban locations is expected to be more vegetation-based as well as soil-based. Rural-coastal regions are expected to have higher concentrations of inorganic-based dust particles due to rocky terrain and proximity to the sea. The rural-coastal installation is located on a cliff overlooking the Atlantic sea and is subject to the sea spray from prevailing trade winds, and hence increased sea salt accumulation.

2. DUST

Dust is defined as small dry solid particles with diameters less than 500µm (Mekhilef et al., 2012, Mani and Pillai, 2010). Dust accumulated on a surface causes a chain reaction of more accumulation, resulting in an exponential decline in irradiance reaching PV cells, ultimately causing a reduction in the output current and hence power (Qasem et al., 2012). The particles of dust are a combination of both naturogenic and anthropogenic activities occurring at or near the location (Al-Ammri et al., 2013). Naturally occurring activities include the migration of dust plumes from North Africa via the Atlantic trade winds, known colloquially as Saharan dust (Prospero, 2011). This approximately week-long journey from Africa brings a mineral based dust consisting of potassium, calcium, iron, phosphorous and other trace minerals (Prospero and Mayol-Bracero, 2013). Human activities producing significant dust in the atmosphere include construction, exhaust from gasoline-based vehicles and the burning of cane fields during the annual dry-period at the end of the sugar-cane season.

Dust in the atmosphere settles onto the surface of PV modules, reducing the irradiance received by the solar cells, thus reducing module power. A further increase in atmospheric dust will therefore increase dust accumulation rates onto module surfaces. Factors affecting dust accumulation rates on a PV module surface include dust properties, PV tilt and orientation, wind velocity, ambient temperature, and humidity (Catelani et al., 2012, Mekhilef et al., 2012, Prospero, 2011). The local environment includes not only weather patterns but also vegetation coverage, the local anthropogenic activities and surface properties (Prospero, 2011, Mani and Pillai, 2010).

2.1 The Barbados Environment and Dust

Barbados, the easternmost island of the Caribbean and located at 13.2°N and 59.6°W, has a hot, humid climate all year round with little variation. A 30-year mean of climatological data gives average temperatures varying from 25.7°C to 27.8°C and rainfall between 41 mm (February) and 185mm

(November) with an average of 12 rainy days per month. Relative humidity values vary from 77% to 83% and average wind speeds of 4.9 m/s (at 10m height) in the direction of ENE to ESE (Barbados Meteorological Services, 2011). Barbados experiences a daily average of eight hours of sunshine producing an insolation of 5.7 kWh/m^2/day year round (Rogers et al., 2012). With such a high solar resource and cooling winds, Barbados is a very good environment for solar PV use.

PV modules are installed at lower tilt angles in Barbados due to the country's latitude as well as for hurricane damage prevention for roof-mounted installations. Hence dust settlement is greater with increased accumulation rates. However higher wind speeds reduce the amount of dust that settles onto a surface and also increases the amount of dust in the atmosphere (especially during dry periods) (Mekhilef et al., 2012). According to Hoffman and Maag (1980), this is based on the properties of dust and relative humidity. Finer dust particles affect PV performance compared with coarser particles as their smaller size increases the chances of uniformly covering a surface. Carbon based particulates from combustion has the greatest negative effect as they more effectively absorb solar radiation which in turn never reaches the modules and leads to elevated module temperatures (El-Shobokshy and Hussein, 1993).

3. METHODOLOGY

Three sites were located along the south of Barbados, and together represent typical urban, suburban and rural-coastal conditions for the island, and indeed the Caribbean. The urban assembly was located at Harrison College in Bridgetown (labelled as 'HC'), the suburban assembly was located The Caribbean Institute for Meteorology and Hydrology (CIMH) in Husbands, St. James, and the rural-coastal assembly was located at Deebles Point (DP) in St. Phillip which are all shown in Figure 29. Figure 30 shows that the assemblies at Harrison College (a) and CIMH in (b) were rooftop installations, while the Deebles Point assembly in (c) was ground-mounted. These installation heights were used to be representative of solar PV systems typically installed in these different terrain types.

Figure 29. Locations of urban (HC), suburban (CIMH) and rural-coastal (DP) sites in Barbados

The modules used in this study are common to those used by local installers of PV systems. Each module was connected separately to a load of equivalent resistance (4.5Ω). Current, voltage and temperature of each module, along with module planar irradiance, were recorded at 5-minute intervals from 5am through to 7pm. Weather data, which included ambient temperature, wind speed, relative humidity and rainfall were collected from weather stations installed at each site. The rated power for each module and temperature coefficients are given in Table 14.

Table 14: Rated power and temperature coefficients of modules used in this study

Label	Technology	Rated power (W)	Temperature coefficient for P_{MAX}(%/°C)
mo-1	monocrystalline	270	0.45
mc-2	Multicrystalline	250	0.44
mc-3	Multicrystalline	255	0.40
mc-4	Multicrystalline	250	0.43

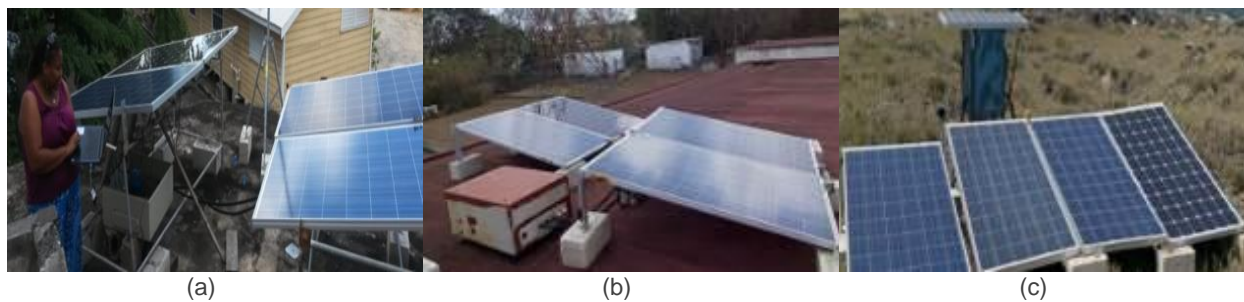(a)   (b)   (c)

Figure 30: The three assemblies at HC (a), CIMH (b) and DP(c).

4. RESULTS AND DISCUSSION

The modules at all sites were cleaned after one-month exposure. The modules from the rural-coastal site (DP) were only exposed for three weeks as data collection begun one week after the other two assemblies were cleaned. The power was computed from the current and voltage values obtained. However, the increased power output would not have been immediately observed from cleaning the module surfaces as there are other parameters affecting performance which obscure the results. The main parameters affecting performance are temperature and irradiance (Field, 2011). It is therefore necessary to exclude their effects and isolate the effect of dust accumulation.

4.1 Excluding the Effect of Temperature

The raw power was corrected by determining the new value had the modules been in operation at 25°C. This temperature-corrected power, P_T, was determined based on the difference in operational temperatures of the modules and adjusted based on the temperature coefficient values given in the manufacturers' specifications. These P_T are now such that the temperature effect is excluded.

Figure 31 shows that the normalised temperature-corrected power (in Watt per peak Watt) generated by each module for the month of April. It is observed that there is a direct and strong relationship with irradiance and the changes in power correspond to the changes in irradiance regardless of cleaning.

Irradiance levels at the rural-coastal location were 28% and 12% higher than urban and suburban locations respectively. One reason could be the reduction in tall structures as one moves out of the urban location. Also tall trees were not located along the cliffs of the coastal location. This increased irradiance was one reason for the increased PV performance in the rural-coastal location. Module performance at the urban site was noticeably lower and this could also be attributed it having the lowest irradiance level of the three sites.

At the same site all modules' performance were within an average of 2.5% of each other except for the urban site where performances varied by as much as 10%. Mc-3 and mc-4 were the top power generators and the output from mo-1 should have been greater based on its higher efficiency and so was considered the worst performing module. This further concludes that monocrystalline does not work best in tropical climes.

As the P_T values are still heavily affected by irradiance and the effect of dust accumulation is still obscured. The effect of irradiance still had to be excluded.

4.2 Excluding the Effect of Irradiance

Figure 31 shows the overwhelming effect on PV power output. To therefore further isolate the effect of cleaning the irradiance effect will now be done by developing a relationship between irradiance and power output. P_T values were plotted against planar irradiance from two days before to two days after cleaning and the relationship was evaluated using the curve-fitting tool in MATLAB. This was determined to be a fifth degree polynomial given by Equation 6 and illustrated by Figure 32 using mc-3 at each of the three sites. Equation 6 was then used to compute the power based on irradiance values and the respective constant coefficients for each module. This would be the power change due to only irradiance, P_H.

Equation 6: Equation representing the relationship between power output and irradiance
$$P_T = aH^5 + bH^4 + cH^3 + dH^2 + eH + f$$

Where:

- P_T = temperature-corrected power output from each module (W)
- H = incident planar irradiance incident on the module surface (W/m^2)
- a, b, c, d, e, f = constant coefficients

4.3 Isolating the Effect of Dust Accumulation

We have now excluded the dependence of PV power output on temperature and irradiance. To further isolate the effect of cleaning, a comparison of the change in power from the day before cleaning (labelled as -1) and the day after cleaning (labelled as +1) was done. The indicators in this comparison were the changes in irradiance corresponding to the change in P_T ($\triangle P_T$) and to the change in P_H (ΔP_H). If the irradiance decreased from day -1 to day +1, then ΔP_T would be less than ΔP_H. If, however ΔP_T is larger than ΔP_H, then there is an increase in power that will be attributed to the cleaning of the modules and which would lessen the decrease in power due to reduced irradiance. These values are shown in Table 15. The negative signs represent a decrease in power (due to reduced irradiance) from day -1 to day +1. The power output the day before cleaning and the day after cleaning was observed.

Table 15: Change in power output for each module from cleaning. Note: The negative signs shows that there was a decrease in power (due to irradiance) from day -1 to day +1.

	Change in power output values computed from the normalised real data, ΔP_T			Change in power output values computed from Equation (1), ΔP_H			$\Delta P_H - \Delta P_T$		
	HC	CIMH	DP	HC	CIMH	DP	HC	CIMH	DP
mo-1	0.053	-1.01	5.38	-0.508	-12.26	19.04	-0.561	-11.25	13.66
mc-2	4.52	-2.55	13.94	-4.0883	-10.70	17.63	-8.61	-8.15	3.69
mc-3	0.0056	-5.20	13.24	-15.47	-17.82	19.42	-15.48	-12.62	6.18
mc-4	2.02	-4.14	12.71	-10.21	-16.99	19.34	12.23	-12.85	6.63

Table 15 showed that the power output was positively affected by the environment of the rural-coastal location (DP). One reason for the increase in power after cleaning was the increased sea salt in the atmosphere coming from the Atlantic Ocean coastline, which was in close proximity to the assembly (20m). The solubility of the salt crystals allow them to use the humid air as a vehicle for transportation. They are therefore more able to cleave to the module surfaces, especially during the dawn when dews evaporate. This adherence reduces the effectiveness of high winds in removing dust from the surfaces.

It should also be noted that the phenomenon of particles adhering to the modules' surfaces, at the urban and suburban locations also occurred. This was due to evaporation of water off the surfaces after rainfall which is mainly due to the low tilts of the modules. This is usually observed at the base of the modules, which results in a degree of shading of the bottom row of cells. The other cells of these modules however would not experience this phenomenon as acutely as the sea salt in the rural-coastal location, and so would be cleaned from higher winds and rainfall. It was expected for the urban environment to be most affected

due to the absorption ability of carbon-based dust. However, due to the components of the dust, the wind was more able to clean the module surfaces than the salt deposits.
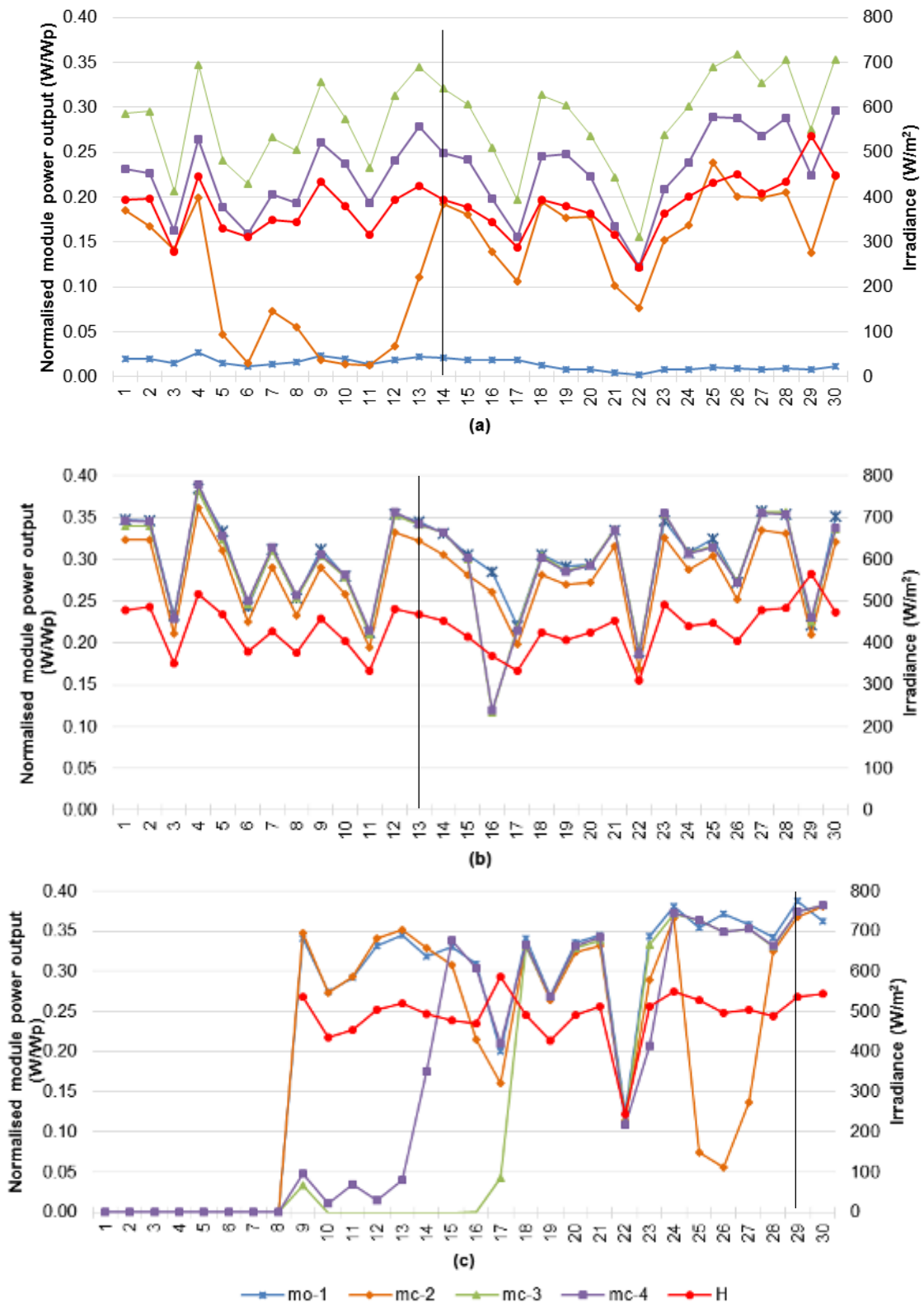
Figure 31: Module power output and irradiance profiles for April 2015 at (a) urban location (HC), (b) suburban location (CIMH) and (c) rural-coastal location (DP). The black lines indicate cleaning days.
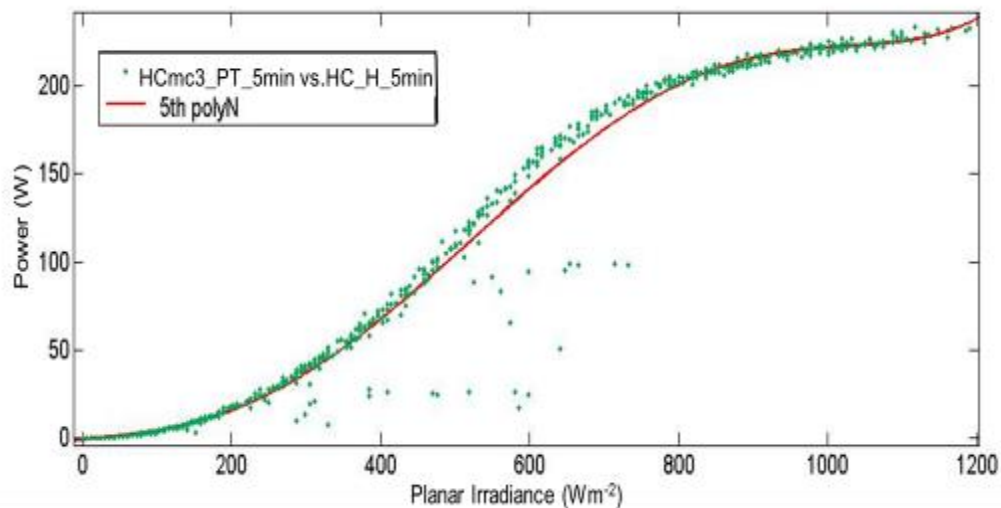
(a)
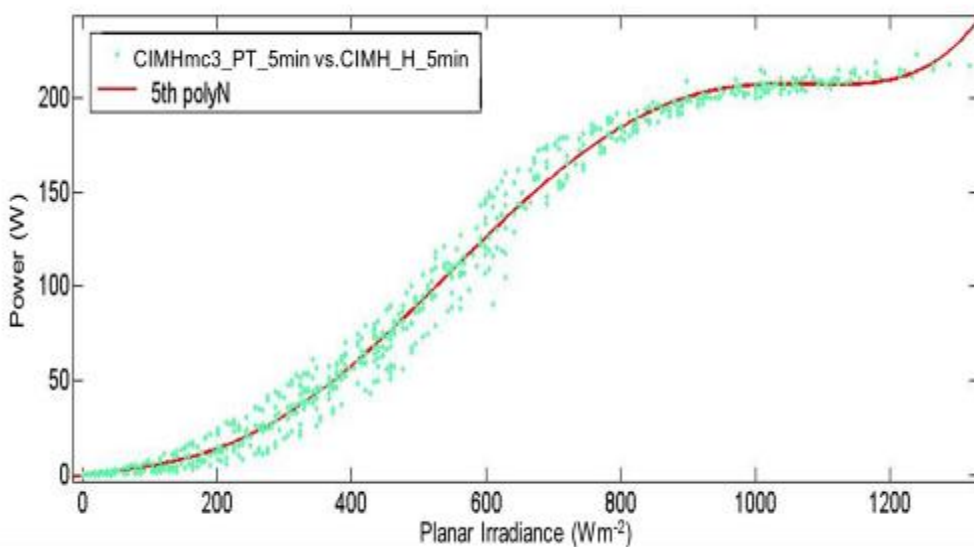
(b)
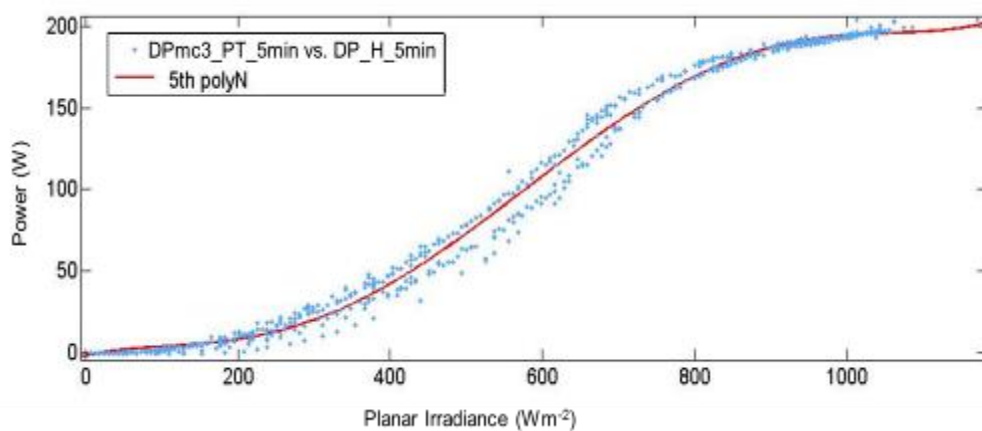
(c)

Figure 32: Polynomial curve fit, one for each site, illustrating the relationship between the temperature-corrected power and planar irradiance for mc-3 at the urban site (a), suburban site (b), and the rural-coastal site (c).

5. CONCLUSION

For the island of Barbados, irradiance levels within three locations differed by as much as 28% and at a given site in the month of April, and normalised module power output were different from each other by as much as 10%. Irradiance had a strong influence on module power output which obscured the effect of other parameters. The relationship between irradiance and power output was therefore determined and characterised as a fifth degree polynomial. This relationship was then used to obtain a power profile of each solar PV module performance at the different locations; thus excluding the effect of irradiance.

After excluding the effects of both irradiance and temperature, it was observed that dust accumulation was strongly affected by terrain and particulate properties. Sea salt in the atmosphere sticks to module surfaces thereby reducing the effectiveness of high wind speeds to remove dust from module surfaces. This occurred especially at daybreak, when dew evaporates from module surfaces increasing the amount of salt particles that accumulate onto them. It was noted that only the modules at the rural-coastal site showed a substantial increase in performance after cleaning.

The main limitation of this experiment was the cleaning of one of the three sites two weeks after the other two. This was due to that site being set up after the others. The differing conditions for those two weeks could have affect the power output and changes that were not included in the study. Another limitation was that rainfall was not tracked with data which would have aided comparative cleaning of the modules at some of the sites. Finally dust accumulation included bird droppings especially at the CIMH site, which may have elevated the decrease in power output due to dust. Future work will focus on collecting data on the same days. The amount of dust collected will be based on the days of no rainfall.

6. ACKNOWLEDGEMENTS

7. REFERENCES

AL-AMMRI, A. S., Ghazi, A. & Mustafa, F. Dust effects on the performance of PV street light in Baghdad city. Renewable and Sustainable Energy Conference (IRSEC), 2013 International, 2013. IEEE, 18-22.

BARBADOS METEOROLOGICAL SERVICES. 2011. *Barbados Weather Climate Data* [Online]. Bridgetown, Barbados: Author. Available: http://www.barbadosweather.org/barbados-weather-climate-data.php [Accessed March 18 2013].

CATELANI, M., Ciani, L., Cristaldi, L., Faifer, M., Lazzaroni, M. & Roussi, M. Characterization of Photovoltaics Panels: the Effect of Dust. Instrumentation and Measurement Technology Conference 2012 Graz, Austria. IEEE, 1-4.

EL-SHOBOKSHY, M. S. & Hussein, F. M. 1993. Effect of dust with different physical properties on the performance of photovoltac cells. *Solar Energy,* 5**,** 505-511.

EPP, B. 2009. The Barbados model: A success story in 3 acts. 2013. Available: http://www.solarthermalworld.org/content/barbados-model-success-story-3-acts [Accessed January 19, 2013].

FIELD, D. 2011. The Performance Characteristics of Commercially Available Photovoltaic Technologies under Jamaica's Climatic Conditions; MPhil Thesis. University of the West Indies Mona Campus.

FTC 2013. Renewable Energy Rider Deciison. Barbados: Fair Trading Commision

MANI, M. & Pillai, R. 2010. Impact of dust on solar photovoltaic (PV) performance: Research status, challenges and recommendations. *Renewable and Sustainable Energy Reviews,* 14**,** 3124-3131.

MEKHILEF, S., Saidur, R. & Kamalisarvestani, M. 2012. Effect of dust, humidity and air velocity on efficiency of photovoltaic cells. *Renewable and Sustainable Energy Reviews,* 16**,** 2920-2925.

MINISTRY OF HOUSING, L. A. T. E., GOVERNMENT OF BARBADOS 2004. The Barbados Sustainable Development Policy. Bridgetown, Barbados: "National Commission on Sustainable Development"

PROSPERO, J. M. 2011. Long term trends in African dust transport to the Caribbean: African sources, changing climate, and future scenarios. *First International Workshop on the Long-Range Transport and Impacts of African Dust on the Americas.* Puerto Rico.

PROSPERO, J. M. & Mayol-Bracero, O. L. 2013. Understanding the Transport and Impact of African Dust on the Caribbean Basin. *Bulletin of the American Meteorological Society,* 94**,** 1329-1337.

QASEM, H., Betts, T. R., Müllejans, H., Albusari, H. & Gottschalg, R. 2012. Dust-induced shading on photovoltaic modules. *Progress in Photovoltaics: Research and Applications*.

REN21 2014. Renewable 2014 Global Status Report. REN21 Secretariat Paris.

ROGERS, T., Chmutina, K. & Moseley, L. L. 2012. The potential of PV installations in SIDS–an example in the island of Barbados. *Management of Environmental Quality: An International Journal,* 23**,** 284-290.

SHIRLEY, R. & Kammen, D. 2013. Renewable energy sector development in the Caribbean: Current trends and lessons from history. *Energy Policy,* 57**,** 244-252.

SOLARBUZZ. 2015. *Module Pricing* [Online]. Available: http://www.solarbuzz.com/facts-and-figures/retail-price-environment/module-prices [Accessed January 20, 2015 2015].

401: A novel multifunctional PV/thermal/daylighting (PV/T/D) panel based on incorporation of miniature prismatic structure and transpired solar collector

Yuehong Su[1]*, Xu Yu[1], Hongfei Zheng[2], Saffa Riffat[1]

[1] 1Institute of Sustainable Energy Technology, Department of Architecture and Built Environment, University of Nottingham, University Park, NG7 2RD, UK, yuehong.su@nottingham.ac.uk
[2] School of Mechanical Engineering, Beijing Institute of Technology, Beijing 100081, China, author email address

This study presents a novel multifunctional PV/Thermal/Daylighting (PV/T/D) roof panel suitable for atrium buildings and large green houses. The panel contains an array of miniature dielectric compound parabolic concentrators (CPCs) to provide concentration of the solar radiation coming from a certain range of sky angles and meanwhile allow the rest of solar radiation to transmit for daylighting. As a result, the panel will also provide a solar shading function and an option to incorporate concentrating PV for PV/Thermal applications. A novel heat recovery design using the concept of transpired solar collection is adopted to remove heat rejection from PV cells and reduce heat gain to the atrium (or green house) space to mitigate the summer overheating problem. Design and fabrication of a small sample panel consisting of an array of miniature CPCs are described. A commercial optical analysis software Photopia is used to predict the transmittance values of the dielectric CPC panel and meanwhile CFD modelling is employed to predict the performance of heat recovery. Some preliminary testing of this panel under real sky conditions is also described. Furthermore, the energy performance of the proposed roof panel is evaluated for an educational building in Nottingham using EnergyPlus simulation.

Keywords: daylighting, shading, PV/thermal, dielectric CPC, multifunctional, panel, Photopia simulation, testing

1. INTRODUCTION

Daylighting is always a favoured feature in architectural design. It is due to not only its potential of reducing electricity consumption by replacing artificial lights, but also its ability of providing visual comfort and necessary view outside for building occupants [1, 2]. Atrium is one of the main applications of daylight in architecture, the aim of atrium design is to provide additional quality of daylighting from the horizontal surface of the building; it is an effective daylighting design especially when the building is close to nearby obstructions [3]. However, penetrating daylight sometimes means penetrating excessive heat into the buildings. Some research indicated that the temperature gap between the lowest and highest points of atrium could be as high as 7°C [4]. In recent years, daylighting technologies like semi-transparent PV, non-removable prismatic panels, glazing with silica aerogel have been put into practice to reject excessive heat gain from the skylight [5-7]. The Compound Parabolic Concentrators (CPC) technology was widely used as non-tracking solar concentrator to improve the efficiency of solar PV cell and solar thermal. According to optical properties of solid dielectric Compound Parabolic Concentrators (CPCs), it might have the potential to be an alternative for roof panel in the atrium or greenhouse buildings. Previous studies on the dielectric solid CPC showed its great potential on the combined application of daylighting control and electricity generation by PV cell [8]. But it was only a preliminary simulation and testing using only a single unit of solid CPC element. Meanwhile, instead of a single CPC element, a panel with an array of miniature solid CPCs is required to act as a roof panel. On the other hand, when the sunlight is concentrated onto the solar cell attached to solid CPC base, the concentrated heat could result in the increase of PV cell surface temperature. And the rejected heat from the cell would also flow into the building to cause overheating if the system is not properly designed. Therefore, employment of PV/Thermal system is necessary to reduce the PV cell surface temperature and reutilisation of excessive heat.

The aim of this paper is to propose an innovative roof panel design which could comprehensively utilise solar energy for daylighting, PV and thermal application (PV/T/D system). First of all, the design principle of the PV/T/D system is introduced. Then the commercial ray-tracing simulation software PHOTOPIA was used to investigate the PV/daylighting performance of the system. The light transmittance and optical efficiency were used to indicate the daylighting and solar concentration performance of CPC panel, respectively. Afterwards, a preliminary investigation on the PV/Thermal performance of the system is taken through a parametric study with the help of CFD modelling. Lastly, the proposed roof panel was used to replace a conventional atrium roof for an education building in Nottingham, and its energy performance was evaluated by building energy simulation software EnergyPlus.

2. PRINCIPLE

According to the optical properties of Compound Parabolic Concentrators (CPCs) and the law of refraction at the air-acrylic interface, a solid CPC, which is made of high transmittance acrylic, should have wider half acceptance angle, i.e. outer half acceptance angle. When the incidence angle is within the outer half acceptance angle, most of the incidence light will be concentrated to the base of CPC, the concentrated light can be absorbed to generate heat and electricity if PV cells are attached on base of CPC. On the other hand, some of the light will be escaped from the side of CPC if the light incidence angle is larger than the outer half acceptance angle. These are mainly diffusion nature light under overcast sky and direct sunlight in winter and in summer morning and afternoon, which can be applied as beneficial daylighting into the building interior. This forms the main theory of combined daylighting and PV application of solid CPC. **Figure 1** shows the light path in the solid CPC [9].

When designing a CPC roof panel consisting of many miniature solid CPC rods, several factors need to be considered such as the thickness of the panel, i.e. height of the solid CPC, which associates with light transmittance; material consumption and weight of roof panel; the conjunction between the miniature CPCs; manufacturing workmanship and so forth. After a parametric study of all the possible influential factors on the optical performance of the roof panel, a 507.2mm*500mm dielectric CPC panel consisting of 28 dielectric CPC rods was designed for the experimental study, see Figure 2. The whole panel is made of clear acrylic. The front aperture width of each truncated dielectric CPC rod is 18mm and the base width is 5mm to give a geometrical concentration ratio of 3.6. The inner half acceptance angle of the full CPC is 14.48°.
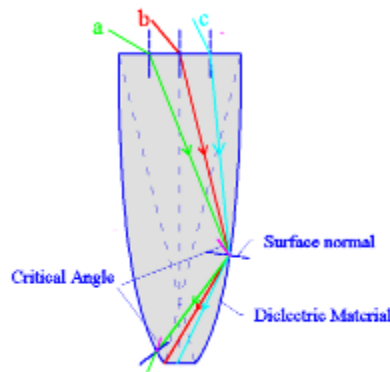
Figure 1: light path in the dielectric solid CPC. (a: beyond half acceptance angle; b: equal to half acceptance angle; c: within half acceptance angle)

(a)   (b)
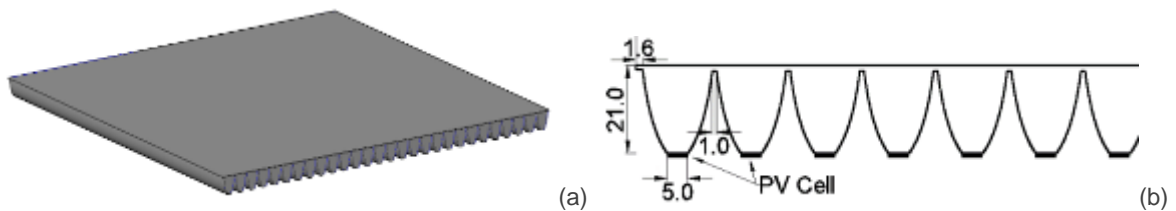
Figure 2: a) 3D model of the dielectric CPC panel; b) cross-section plan of dielectric CPC panel (part)

On the other hand, the concentred heat on the base of dielectric CPC could result in both low electrical efficiency for PV module and transmission of unwanted heat into the atrium during summer, which is the common issue for the transparent façade or skylight buildings and causes overheating and increased cooling load for buildings. As a result, removing of concentrated heat on the solar cell is the main purpose of the dielectric CPC roof panel design. The previous researches on PV/T systems lead the authors to explore the possibility of using the removed heat to heat the air for thermal application, which could form the multifunctional PV/Thermal/Daylighting application of the dielectric CPC panel. The design of the air heater is inspired by the unglazed transpired solar collector (UTC). Three main functions needs to be considered when designing of the ventilation chamber dielectric CPC roof panel, arranged according to the level of priority.

1) Prevent the convection heat loss from roof penal to atrium space so that the indoor thermal comfort could be guaranteed with minimum cooling demand.
2) Reduce the operation temperature of PV module attached on the base of dielectric CPC panel to improve its electrical efficiency.
3) Utilise the removed heat for thermal application such as drying food, air or water preheating.

Figure 3 illustrate the basic design of the PV/T/D system with dielectric CPC panel; a transparent acrylic sheet with many round perforations is attached some distance from the base of dielectric CPC panel to form the plenum for this system. An exhaust fan is installed in the air outlet to provide required suction during operation. The concentrated heat on the PV module at base of dielectric CPC is partially transferred to plenum air and the warmed air could be exhausted and used for thermal application. And at the same time, the temperature of PV module could be reduced to improve its efficiency; and most importantly, the heat flow from the dielectric CPC panel to atrium space could be minimized.

a)   b)
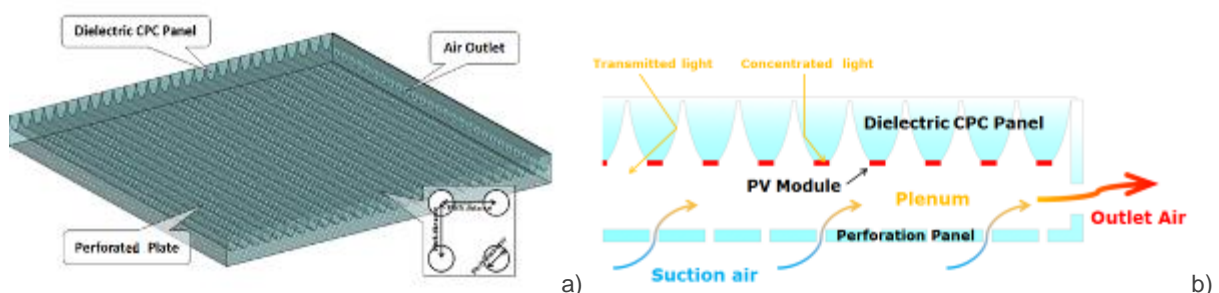
Figure 3: a) PV/T/D system configuration; b) vertical section and schematic diagram of PV/T/D panel.

3. OPTICAL SIMULATION AND TESTING

The daylighting and solar concentration performance were simulated using Photopia. In this case, the daylight model was taken to simulate skylight and changeable sun positions. In the Photopia, the light source can be imported as "Lamp", and the daylight modelling, which consists of sky dome (represents diffused skylight) and sun disk (represents sun) is one of the "Lamps" based on the IESNA RP-21 daylight equation. Moreover, and the sun (solar disk) position and lumen output of both sun and sky can be adjusted to model the sun under various solar altitudes and azimuths. In order to have the knowledge of seasonal variance of its optical performance, the simulation focused on four typical days in the year, which were summer and winter solstices, and two equinoxes. The sky condition of sunny and overcast were also simulated separately. The location of Nottingham, UK was chosen (53°N, 1.2°W). In order to achieve seasonal daylighting control (transmission of daylight in heating season to allow solar heat gain and shading of daylight in cooling season to prevent overheating), the CPC panels were aligned E-W direction and tilted 35 degree to the south. The concept of light transmittance, which stands for the ratio of transmitted light through the panel to incidence light on the panel, was used to represent the daylight illumination ability of CPC panel; while concept of optical efficiency, which has been widely used to represent the solar concentration effects and is defined as the ratio of the received solar radiation on the base of dielectric CPC to the incidence solar radiation on the panel surface. To validate the Photopia simulation results, a simple outdoor testing under real sky condition in Nottingham was also taken. The methods to measure light transmittance and optical efficiency were presented in previous researches [8-9].
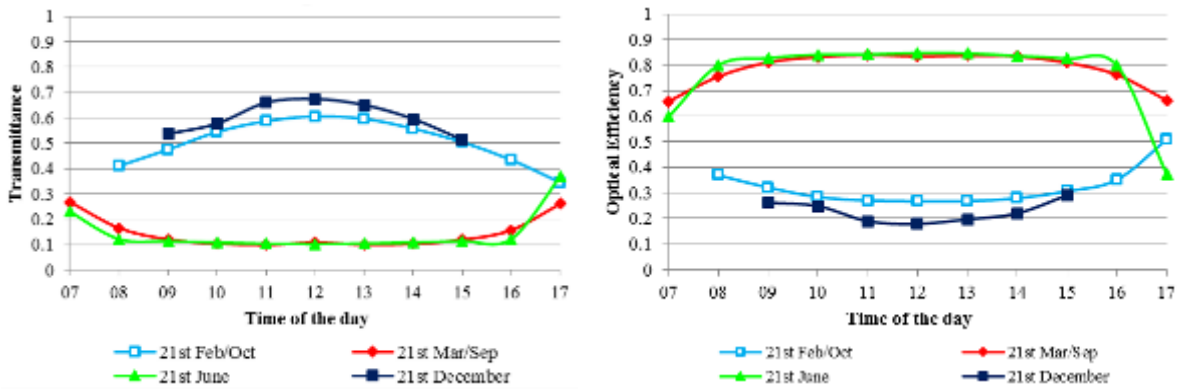
Figure 4: simulated transmittance (left) and optical efficiency (right) of 35° tilted EW-dielectric CPC panel on representative days in Nottingham (sunny sky)
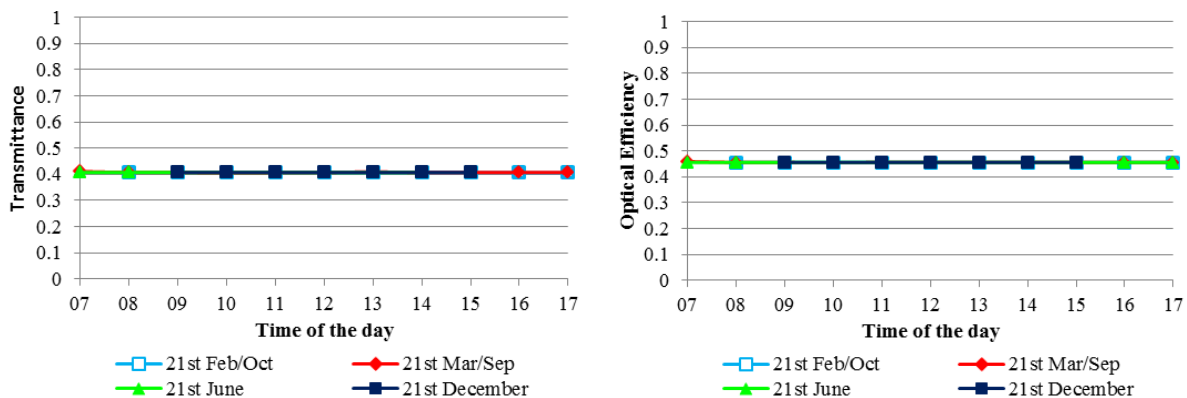
Figure 5: simulated transmittance (left) and optical efficiency (right) of 35° tilted EW-dielectric CPC panel on representative days in Nottingham (overcast sky).

Figure 4-5 indicated the simulated annual variance of light transmittance and optical efficiency in Nottingham for sunny and overcast sky condition. The results shows that under the optimized tilt angle of 35° for Nottingham, the EW-orientated dielectric CPC panel could fulfil the purpose of seasonal daylight control under sunny condition. The light transmittance could be as high as 70% in heating season, and the transmitted sunlight is beneficial to provide extra solar heat gain. On the other hand, the transmittance could reduce to about 10% in cooling season to provide shading to the building, and at the same time, the amount of direct sunlight blocked by the dielectric CPC panel could be concentrated on the PV cell to increase its power output efficiency. Meanwhile, the transmittance and optical efficiency of dielectric CPC panel under simulated overcast sky in Nottingham would keep constant throughout the year, which is 0.4 for light

transmittance and 0.45 for optical efficiency. These values are acceptable for daylight transmission under overcast sky. Similarly, the measured results on one summer and one winter sunny days in Nottingham (Figure 6-7) shows a same trend in the optical properties of dielectric CPC panel despite some differences between the simulated and measured results. The causes for these gaps might be explained by difference between simulated and real weather conditions, the manufacturing precision of dielectric CPC panel and unavoidable measuring errors. Therefore, the above simulation and field measurement results indicated that the EW-orientated dielectric CPC panel is an efficient daylight control device in terms of the multifunction of seasonal daylighting control and solar concentration for enhanced PV output per area.
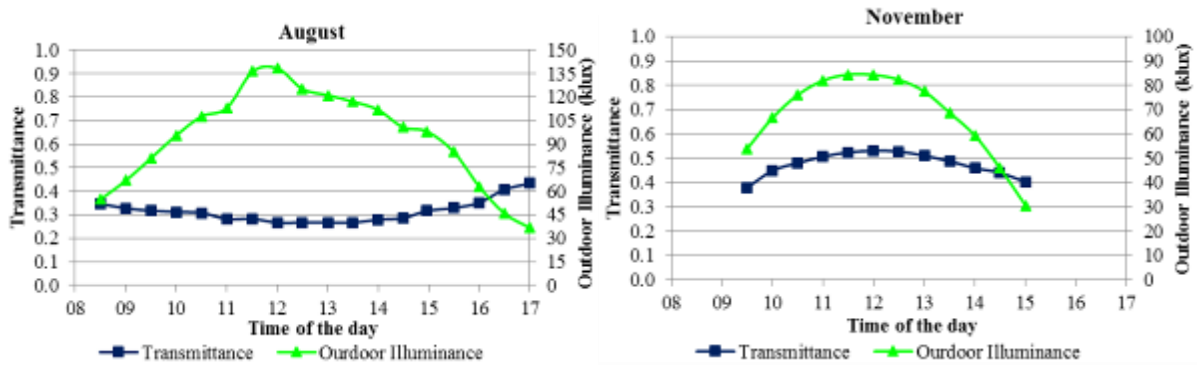
Figure 6: Measured light transmittance of 35° tilted EW-dielectric CPC panel in 8th August and 19th November in Nottingham (sunny)
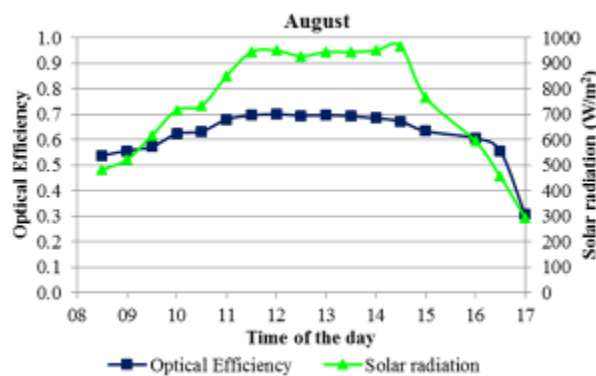
Figure 7: Measured optical efficiency of 35° tilted EW-dielectric CPC panel in August in Nottingham

4. CFD SIMULATION AND PRELIMINARY TESTING OF PV/THERMAL

In this part of the paper, the thermal performance of the designed PV/T/D system is firstly investigated numerically with the aid of computational fluid dynamics (CFD). The heat transfer and air flow through the system are modelled by commercial CFD software (Fluent). A parametric study would be taken to evaluate the influence of suction velocity on the PV/T/D system performance in terms of the design criteria such as approach velocities, plenum height, pitch and perforation dimension, porosity and solar radiation levels. After that, some experimental results would be obtained under the solar simulator and real sky using the experimental chamber to verify the feasibility of the designed PV/T/D system.

4.1 System geometry and simulation settings

The dimension of the whole system is listed in Table 1. The dielectric CPC panel, perforated plate and side walls are all made of acrylic with high light transmittance to guarantee the daylight transmission. Due to the limitation of computer process speed and capability, and ensure the quality of mesh and accuracy of the results, a reduced system domain was sketched with symmetry boundary conditions to reflect the thermal and flow performance of the whole system. The reduced system domain built in Ansys DesignModeler is shown in Figure 8. The domain of numerical simulation has three regions. Region 1 is the solid region for dielectric CPC panel, whose upper surfaces are exposed to the ambient air; Region 2 and 3 are the fluid regions for plenum air and atrium air, respectively, and these two regions are separated by the perforated plate.. The boundary conditions for each domain were set in accordance to previous similar researches [10]. The Meshing component contained in the ANSYS Workbench Package was used to generate mesh. The automatic meshing method (Combines Tetrahedrons & Sweep based on complexity of the geometry)

was applied to split the geometry into several cells. For the sizing control, the function of Curvature and Proximity was used as the geometry contained both curved and narrow surface. It was indicated that a large number of cells are required to be placed within the slots where the temperature and velocity gradients are expected to be significant (Badache et al., 2013). Therefore, the minimum cell size was determined by the perforation diameter in each case. Figure 9 illustrates the example of the mesh for perforation diameter of 3mm. As to the solution methodology, the governing equations were solved numerically by the widely used Fluent software. The convergence criteria were set to be 10^{-5} for the mass and momentum equations and 10^{-6} for the energy equation. The required output could be obtained directly from the results using the Fluent post processing software.

Table 1: Table for the dimension of dielectric CPC air heater

Component of air heater	Dimension
Width and length of air heater	500mm*504mm
Height of air heater	30mm
Num. of dielectric CPCs for panel	28
Dimension of each dielectric CPC	
Front aperture width:	18mm
Base aperture (PV) width:	5mm
Length:	500mm
Pitch dimension of perforation plate	9mm
Perforation Porosity	2%
Thickness of perforation plate and side walls	6mm
Num. of Air outlet	28
Diameter of air outlet	4-5mm
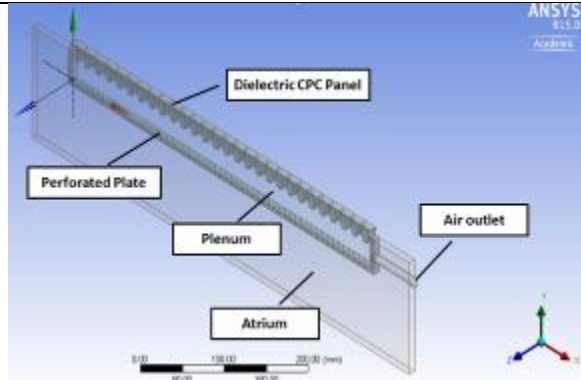
Figure 8: Simplified system domain and three regions in the Ansys DesignModeler

4.2 Parameters input and output for parametric study

Earlier studies on UTC have shown that the key parameters influencing the efficiency of UTC collector is the approach velocity, which normally varies from 0.01-0.05m/s [10]. The output parameters include: a) air temperature rise; b) heat recovery system efficiency; c) PV operation temperature; d) distribution of heat flux. The heat recovery efficiency is used to identify the system thermal performance and defined as the ratio of the useful heat delivered by the heat recovery system to total solar energy input on the base of dielectric CPC (PV cell). Therefore:

$$\eta_{air.heater} = \frac{\dot{m}_{air.out} * c_{p.air} \left(T_{atrium} - T_{out}\right)}{A_{pv}I_{pv}} \qquad (1)$$

4.3 CFD simulation results and discussion

The influence of approach velocity on the thermal collector efficiency (using Equation 1) is numerically represented in Figure 9a, outlet temperature rise and PV operation temperature, respective, under fixed solar radiation, perforation and plenum dimension. The outlet air temperature rise and PV temperature would decrease with rising approach velocities and opposite trend is found for the thermal collector efficiency. Given the solar radiation of 1000W/m², perforation diameter of 1.5mm, pitch distance of 9mm and plenum height of 10mm, the thermal collector efficiency increases rapidly from 0.01m/s to 0.03m/s, and tends to be nearly constant after 0.03m/s. For example, the thermal efficiency increases 22.12% for a change in approach velocity from 0.01 to 0.03m/s while 6.9% in approach velocity from 0.03 to 0.05m/s. The results are generally consistent with earlier study of UTC collector by Kutscher et al [12]. The collector thermal efficiency could be as high as above 80% for the designed PV/T/D system. It seems that higher

approach velocity is preferred for higher thermal efficiency and lower PV operation temperature; however, more power input for suction blower is required to meet the target approach velocity. A comprehensive trade-off for the velocity determination is required.

Meanwhile, in the previous section, it has been discussed that the concentrated heat on the PV module would be transferred to three destinations: ambient air through the upper surface of dielectric CPC panel; plenum air then to air outlet; and atrium air through the perforation plate, respectively. Figure 9b further illustrated the proportion of heat transfer in each destination. It could be found that the heat flux to the plenum air dominate in three heat transfers, especially in high approach velocities and its percentage increases with the rising velocity. As the air flow rate is proportional to the approach velocity, increasing in approach velocity means linear increase in air flow rate in plenum, as a result, the effect of convection heat transfer to the plenum would be enhanced due to the increased air flow rate under the PV module, and consequently the heat flux to the ambient air and atrium air would be reduced with rising approach velocity. However, there seems to be no obvious reduction in heat flux to atrium air with the changing approach velocity. It should be further mentioned that the amount of heat flux to atrium air would be taken back to the plenum by suction air due to the suction effect of the perforation plate. Therefore, the actual heat flux to the atrium should subtract the heat that is taken back to the plenum. According to the previous researches, for perforation plate, if a minimum pressure drop of 25Pa and a minimum approach velocity of 0.02m/s are provided, the convective heat loss could be neglected since the convective boundary layer is continuously sucked off [12]. As a result, almost all the heat flow through the perforation plate could be drawn back to the plenum and the amount of heat flow down to the atrium space could be small and neglected; and this result could fulfil the first design criteria for the PV/T/D system.
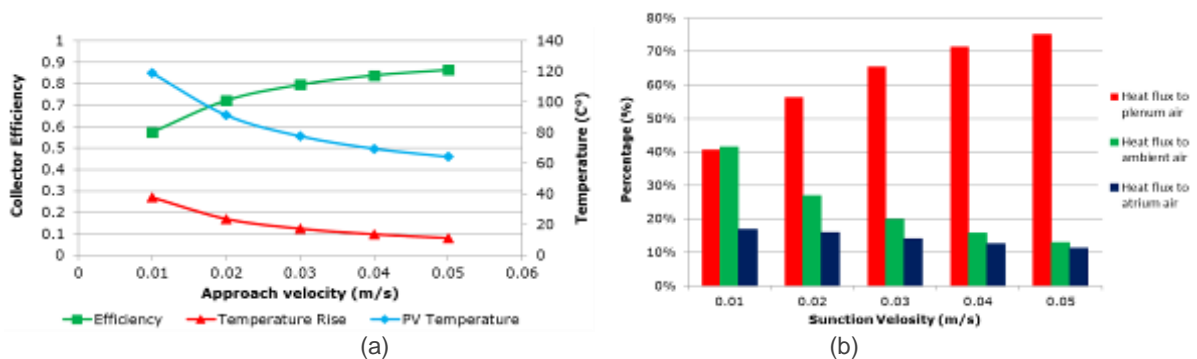
Figure 9: a) : the effects of approach velocity on the temperature of PV cell, outlet temperature rise and thermal efficiency of the system (left), and on the proportion of heat transfer to each destination (right).

4.4 Testing under real sky in Nottingham

The prototypes of PV/T/D system was built in the wooden cubic chamber, which is similar to the one used in the daylight testing. The vertical layout of the system is schematically sketched in Figure 10a. The thermal performance of the PV/T/D system was tested under sunny sky condition in Nottingham. The experimental chamber was tilted in a certain angle such that the dielectric CPC panel could directly face the sunlight (Figure 10b). During the experiment, the air was drawn by from the interior experimental chamber by circular pipe line which is connected to the exhaust fan. The speed of the fan (air flow rate) was controlled by its voltage input.

The outdoor testing and the results were showed in Figure 11, it could be observed that the solar radiation level during testing is about 600-700W/m², which is close to the one provided by solar simulator during indoor testing. The results showed that the PV temperature could only reach about 37°C under steady state, this is due to the low ambient temperature of 8°C and high wind spend of 2m/s on the outdoor testing day. Therefore, the convective heat loss on the dielectric CPC panel surface is much higher than that under the indoor testing condition (15°C and no wind), this could be observed on the difference of CPC surface temperature between indoor and outdoor testing results. However, similar to the indoor testing results, a clear increase in air outlet temperature and decrease in PV surface temperature could also be observed when the air suction fan was turned on.
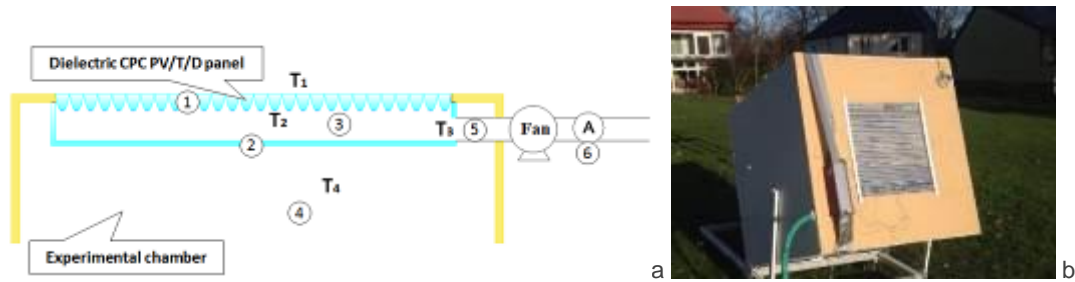
Figure 10：a) vertical layout of the experimental set-up: 1) dielectric CPC panel; 2) perforated plate; 3) plenum; 4) chamber interior; 5) air outlet; 6) anemometer ; b) : the experimental rigs under outdoor testing
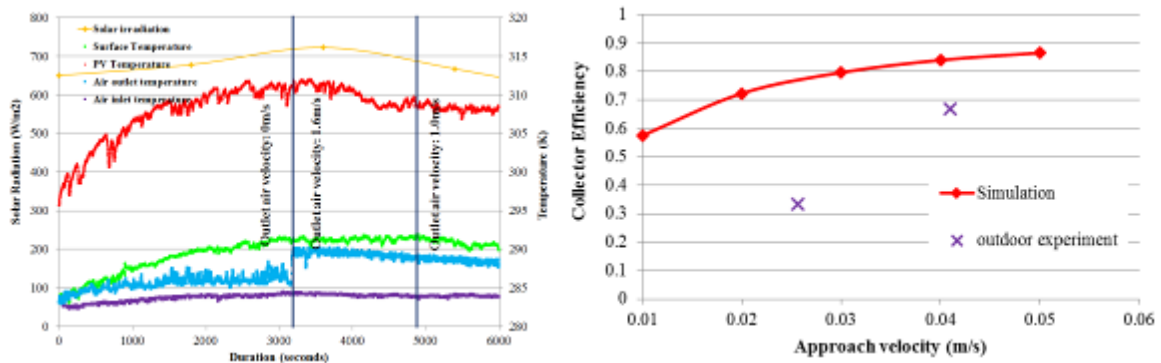
Figure 11: Outdoor testing results on a sunny winter day in Nottingham

5. A CASE STUDY ON APPLICATION OF THE PV/T/D PANEL

The annual energy performance of the dielectric CPC roof panel in terms of lighting and heating/cooling was also evaluated through a case study of an educational atrium building at the University of Nottingham. The original atrium roof which uses conventional double glazing window was replaced by the proposed CPC roof panel, and the lighting and heating/cooling energy consumption using these two types of roof glazing would be compared. The building energy simulation software EnergyPlus was used to assist the evaluation process.

5.1 Methodology

The process of the assessment was as follows:

1) The simplified model of ESLC was built in the SketchUp, and the model was divided into two zones: one zone for central atrium space, and another one for the adjacent rooms. The central atrium zone was the main interest in this part.
2) The model was imported into the EnergyPlus, The weather data of Birmingham was used, as Birmingham is the closest city to Nottingham whose weather data is available in EnergyPlus Weather Data. To simplify the simulation, the default inputs to the EnergyPlus IDF Editor were used, other than the daylighting control strategies and atrium roof glazing setting. For the daylighting control strategy in atrium, the daylighting corresponsive dimming control was applied to achieve the minimum illuminance level of 800lux for atrium space, two illuminance sensors were used and each monitors 50% of the atrium area. The default fraction values were also used for the minimum light output and its corresponding minimum light power input. For the roof glazing setting, the normally used double glazing (3mm clear glazing-13mm gas-3mm clear glazing) with visible light transmittance of 0.806 and solar transmittance of 0.7 was used.
3) The hourly output of the illuminance levels at each monitoring points and the hourly solar heat gain through atrium windows using double glazing were obtained in the EnergyPlus output. These two parameters were the main interests in this part of the study, as the main function of the dielectric CPC roof panel is to selectively control the amount of daylight as well as solar heat penetrating through the transparent roofs.
4) In the last step, the hourly illuminance levels at each monitoring points and the hourly solar heat gain through atrium windows using dielectric CPC roof panel were manually calculated, the changes in these two parameters were proportional to changes in the visual and solar transmittance. The hourly light transmittance for dielectric CPC panel has already been estimated in the previous study. It should be

mentioned that for the solar and visual transmittances for the dielectric CPC panel were assumed to be same.

5.2 Results and discussion

Useful daylight illuminance (UDI)

The useful daylight illuminance is one of the most commonly used dynamic or climate-based daylighting assessment metrics. Generally, 100lux and 2000lux are set to be the lower and upper thresholds, the upper bin ($UDI_{>2000lux}$) presents the times when oversupply of daylight happens, which could lead to visual and thermal discomfort; the lower bin ($UDI_{<100lux}$) presents the time when there is insufficient daylight and the intermediate bin ($UDI_{100-2000lux}$) presents useful daylight. Therefore, the proportion of useful daylight illuminance was the first parameter to assess the daylighting performance of the atrium space using double glazing or dielectric CPC roof. The results were presented in Figure 12, which clearly showed that for double glazing roof, over 75% of the daylit period would exceed the upper threshold of UDI. It means that in most of the time, the benefits of daylighting would be eclipsed by the excessive daylight provision, and effective shading strategies are required to guarantee the indoor visual and thermal comfort, otherwise the increased energy consumption is required. On the other hand, the $UDI_{>2000lux}$ using dielectric CPC would be largely reduced to less than 20%, and about 78% of the daylit period was in the range of useful daylight. As a result, it could be concluded that replacing the double glazing with the dielectric CPC roof panel could increase the visual comfort level in the atrium space.
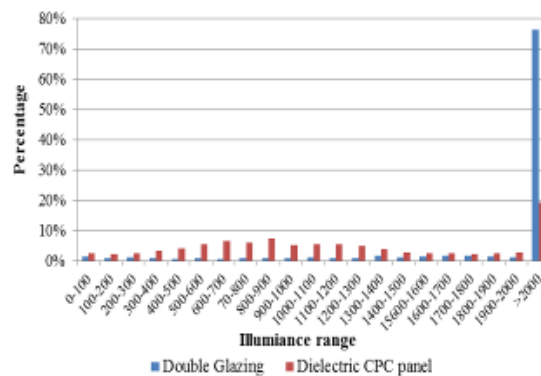
Figure 12: comparison of dieletric CPC panel and double glazing in terms of percentage useful illuminance level.
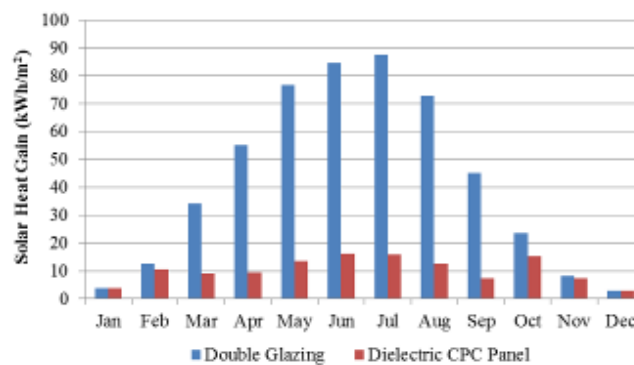
Figure 13: comparison between dielectric CPC panel and double glazing in terms of their direct solar heat gains in Nottingham.

Solar hear gain

Solar heat gain through the window is one of the most important factors influencing the building energy performance. It could contribute to the heating load reduction in winter but increase the cooling load in winter. Effective shading strategies are all focusing on active control of direct solar heat gain through windows. It has been investigated that the dielectric CPC panel has the ability to actively control the light and solar transmittance throughout the year. The results in Figure 13 further confirm this advantage in terms of solar heat gain through the window. It could be recognised that compared to traditional double

glazing, the solar heat gain through dielectric CPC panel could largely be reduced in summer while their differences in winter was quite small. The estimated data showed that there is 81.5% reduction in solar heat gain from March to September while during rest of the year; there is only 10.8% reduction in heat gain, which showed that dielectric CPC panel is an effective shading device in terms of solar heat gain control. The annual reduction in direct solar heat gain could be as high as 75.46% compared to the double glazing atrium windows.

Annual solar energy collection and conservation by PV cell

The calculation of the electricity generation by PV cell is achievable once the optical efficiency of dielectric CPC; local hourly direct normal and horizontal diffuse solar irradiation values and PV efficiency are given. The hourly optical efficiency of dielectric CPC was estimated previously, the hourly solar irradiation values are available in the EnergyPlus weather data, and the PV efficiency is assumed to be 15% in this study. Su et al [13] had presented a method to estimating the solar energy collected by EW orientated trough CPC with certain tilt angle using the EnergyPlus weather data. The component of the direct solar irradiation on the normal plane of a tilted surface I_t is calculated as:

$$I_t = I_n \sin\theta_h \cos\beta + I_n \cos\theta_h \cos\gamma \sin\beta \quad (2)$$

- Where I_n is the direct normal solar radiation (W/m²); θ_h is the solar altitude; β is the tilt angle of surface; γ is solar azimuth angle.
- Then the hourly I_t value multiplies the corresponding optical efficiency to give the collected direct solar radiation. While for the diffused solar radiation, a contant optical efficiency under overcast sky might be used, which is 0.45. It should be mentioned that a correction factor might be employed to consider the effect of tilt angle when the EnergyPlus horizontal diffuse solar irradiation data were used. The correction factor was calculated as $(1-\beta/180)$. As a result, the total energy generated by PV cell could calculated by 15% of sum of collected direct and diffused solar radiation by dielectric CPC panel.

Figure 14 illustrates the monthly power generated by PV cells attached under the dielectric CPC panel based on estimated hourly estimated optical efficiency. It could be observed that more solar energy could be converted during summer period than winter as most of the solar radiation in summer could be concentrated on the PV cells. It was calculated that the annual power generated by PV cells could be 290.65kWh/m² for Nottingham.
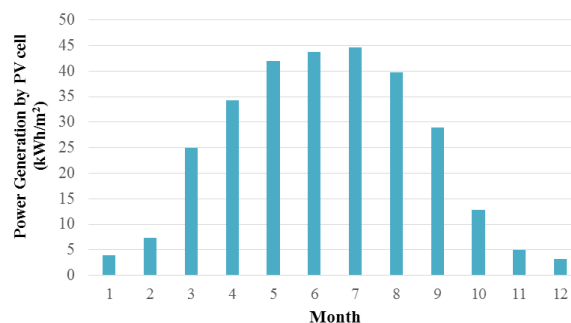
Figure 14: Monthly power generation by PV cell for this case study

6. CONCLUSIONS

Daylight is an energy efficient solution for illumination and visual comfort in buildings. However, successful daylight design requires effective daylight control technology to eliminate the negative impact such as overheating, unbalanced indoor daylight distribution and glare. With this in mind, this paper presents a novel multifunctional roof panel which might be applied in atrium and large green house. The working principle of the panel is based on the non-imaging low-concentration solar collector: dielectric Compound Parabolic Concentrator (CPC). Detailed study on the dielectric CPC has found that there would be some light escaping from side wall of CPC when the incident light is beyond CPC acceptance angle, which could actually be used for indoor daylight provision; while the incident light concentrated on the base of CPC could be used for concentrating PV application. Therefore a dielectric CPC panel which consists of many miniature dielectric CPC rods is designed and manufactured, its function of hybrid PV/Daylight is

investigated through PHOTOPIA simulation and outdoor testing, both simulated and measured results showed that under sunny condition, only 10-15% of light could be transmitted through the panel in cooling season, and the rest of the light is used for concentrating PV application; while light transmittance of about 40-60% is achievable in winter period, when daylight is desired. Additionally, constant light transmittance of about 40% is achievable under overcast sky. The above figures could verify the seasonal daylight control ability of the panel. On the other hand, for the designed panel, the rejected heat on PV could still flow into the building. As a result, a PV/Thermal system is designed using the concept of transpired solar collector to remove the rejected heat on PV cell and reutilize it for thermal application such as drying and hot water. The design parameter of approach velocity is numerically investigated by CFD simulation. The prototype of the system is built and measured under real sky. Both simulated and measurement results showed that the heat recovery efficiency could be 40-80% depending on different approach velocities; and little amount of rejected heat could transfer from the PV cell to the building interior. The hybrid PV/Thermal application seems to be achievable. Lastly, the energy performance for the EW-orientated dielectric CPC panel is investigated by building energy simulation software EnergyPlus and its weather data. An example case on an educational building with a central atrium in Nottingham shows that: compared to the conventional double glazing window, there is 55% increase in useful daylight illuminance (500-2000lux); 81.5% reduction in window solar heat gain in cooling season and only 10.78% reduction in window solar heat gain in heating season; there is also a power generation of 290.65W/m^2 from PV cells. Therefore, the proposed multifunctional roof panel for PV/Thermal/Daylight application could comprehensively utilise the solar energy and provide thermal comfort and visual indoor environment with reduced energy consumption.

7. ACKNOWLEDGMENT

8. REFERENCES

[1] LI DHW, Lam TNT, Wong SL: Lighting and energy performance for an office using high frequency dimming controls. Energy Conversion and Management 2006, 47(9-10):1133-1145.

[2] IHM P, Nemri A, Krarti M: Estimation of lighting energy savings from daylighting. Building and Environment 2009, 44(3):509-514.

[3] RAN Yi LS, Yuehong Su, and Saffa Riffat: Daylighting performance of atriums in subtropical climate. International Journal Low-Carbon Technology 2009, 4(4):230-237.

[4] JONES PJ, Whittle GE: Computational fluid dynamics for building air flow prediction—current status and capabilities. Building and Environment 1992, 27(3):321-338.

[5] JAMES PAB, Jentsch MF, Bahaj AS: Quantifying the added value of BiPV as a shading solution in atria. Solar Energy 2009, 83(2):220-231.

[6] LORENZ W: A glazing unit for solar control, daylighting and energy conservation. Solar Energy 2001, 70(2):109-130.

[7] BURATTI C, Moretti E: Glazing systems with silica aerogel for energy savings in buildings. Applied Energy 2012, 98(0):396-403.

[8] YU, X., Su, Y., Zheng, H. & Riffat, S: 2014. A study on use of miniature dielectric compound parabolic concentrator (dCPC) for daylighting control application. Building and Environment 2014, 74, 75-85.

[9] LI, G., Su, Y., Pei, G., Zhou, H., Yu, X., Ji, J. & Riffat, S: An Outdoor Experiment of a Lens-Walled Compound Parabolic Concentrator Photovoltaic Module on a Sunny Day in Nottingham. Journal of Solar Energy Engineering 2013, 136, 021011-021011.

[10] LEON, M. A. & Kumar, S: Mathematical modeling and thermal performance analysis of unglazed transpired solar collectors. Solar Energy 2007, 81, 62-75.

[11] BADACHE, M., et al., Experimental and numerical simulation of a two-dimensional unglazed transpired solar air collector. Solar Energy, 2013. 93: p. 209-219.

[12] KUTSCHER, C. F. Heat Exchange Effectiveness and Pressure Drop for Air Flow Through Perforated Plates With and Without Crosswind. Journal of Heat Transfer 1994, 116, 391-399.

[13] YUEHONG Su, Saffa B. Riffat, Gang Pei, Comparative study on annual solar energy collection of a novel lens-walled compound parabolic concentrator (lens-walled CPC), Sustainable Cities and Society, Volume 4, October 2012, Pages 35-40.

140: A novel way to calculate the light transmittance loss of glass for photovoltaic (PV) modules according to known accumulated dust density

Yu. JIANG*, Lin. LU

[1] *Renewable Energy Research Group, Department of Building Services Engineering, The Hong Kong Polytechnic University, Kowloon, Hong Kong Special Administrative Region, China, jy293251@sina.com*

Accumulated dust will decrease the light transmittance of glasses for Photovoltaic (PV) modules and thus has a negative effect on the energy conversion efficiency of (PV) modules greatly. However, there has been no model to accurately calculate the change of light transmittance of PV modules based on known accumulated dust density. In this paper, a novel way is built to calculate light transmittance resulting from accumulated dust. This way considers two processes. One is light refraction process and the other is light extinction process. For engineers, if they measure the refraction and extinction parameter of local accumulated dust, the light reduction can be calculated by this model easily. In addition, for Arizona Dust, the refraction parameter is 1.5459 and the extinction parameter is 0.028 based on the experimental results.

Keywords: Accumulated dust, Photovoltaic(PV) modules, Light transmittance, Dust density, Extinction coefficient

1. INTRODUCTION

Solar energy is a major renewable and green energy for human beings. Among the various technologies to use solar energy, photovoltaic technology, can convert solar energy into utilized electricity directly based on the effect of photovoltaic. The most common commercial form of photovoltaic technology, photovoltaic (PV) modules, can be seen everywhere due to the low cost and easy installation.

However, one general phenomenon, accumulated dust, can have a negative effect on the performance of energy output of PV modules. Many researchers have reported this negative in their academic reports. For example, The research on the effect of accumulated dust on PV modules has been undertaken for more than seventy years. Salim et al. were the first group to investigate the impact of accumulated dust on a PV system (Salim et al. 1988). Their results showed that the degradation in performance of tested PV system was 32% in 8 months. In addition, Wakim studied the performance of solar panels in Kuwait and found that the reduction was 17% in 6 days (Wakim, F. 1981) What's more, Said investigated the effect of accumulated dust on a PV panel in a special environment (Said. 1990). His result showed that the efficiency degradation rate was 7% per month. To explain the mechanism of this reduction, Michalsky did the experiment about the impact of dust accumulation with the help of pyranometers and found the reduction in the solar transmittance by 5% over 10 days (Michalsky. 1988). In recent years, the basic results from researchers have not changed, namely, the effect of accumulated dust is not positive for the performance of PV modules. These results are summarized as follows: In Dhahran-KSA, the reduction of PV power output after six months of outdoor exposure is 50% (Adinoyi et al. 2013). In Arar-KSA, the average degradation is 2.78% per day (Ibrahim. 2011). Mohandes et al. reported a 10% reduction after a five-week exposure experiment in UEA (Mohandes et al. 2009). In 2013, Touati et al. found that the reduction was 10% after a 100-day outdoor experiment in Qatar (Touati et al. 2013). In 2006, Elminir et al. reported the maximum reduction so far (Elminir et al. 2006). They pointed out that the reduction in the output of PV modules is nearly 60-70%. Actually, the degradations of PV module performance due to accumulated dust in different areas are various because it is highly dependent on the location and weather conditions.

Even though many researchers have proved the negative influence of accumulated dust on the light transmittance of PV modules, there is no accurate way to calculate the change of light transmittance and the accumulated density. In this paper, the optics mechanism of thin film is used to build a reliable way to calculate the relationship between the light transmittance change and accumulated density. This approach can help us to understand the influence of accumulated dust further and instruct people to estimate the influence of accumulated dust more accurate.

2. THEORETICAL ANALYSIS

In fact, accumulated dust on PV modules can be regarded as a thin film due to two reasons. The first reason is that the height of accumulated is low. Another reason is that the distribution of accumulated particles is uniform, so there is no defect in the accumulated dust area. Then the influence of accumulated dust on the incident light can be divided into two parts. The first part is refraction, which means that the accumulated film can refract the incident solar light. Another phenomenon is that the left energy after refraction of light is absorbed by the accumulated thin film. So this novel method to estimate the influence of accumulated dust on the incident light is calculating this two separated process. The details of computational formula are described below.

2.1 Refraction process by accumulated dust film

Because the first phenomenon of accumulated dust on the incident sunlight is refraction, the refraction can be estimated by Fresnel formula. In addition, to simplify the calculation process, the direction of incident light is perpendicular to the surface, then the equation can be simplified as:

$$Er = E_0 \times \frac{4 \times n1 \times n2}{(n1 + n2)^2}$$

(1)

Where

- E_0 = the energy of incident sunlight
- E_r = the left energy of sunlight after refraction by accumulated dust film
- $n1$ = the refraction index of atmosphere
- $n2$ = the refraction index of accumulated dust

For accumulated dust, the principal component is quartz, so $n2$ equals 1.5459 when wavelength equals to 550nm.

2.2 Absorption process by accumulated dust film

Due to the assumption of the thin film, the change of energy in the accumulated dust film due to the absorption can be calculated by the following equation.

$$E_a = E_r \times \exp(-\frac{2\pi k}{\lambda} \cdot h)$$

(2)

where

- E_a = the left energy after absorption by accumulated dust film
- h = the height of accumulated dust film
- k = the extinction coefficient
- λ = the wavelength of incident light

For this study, the extinction coefficient of utilized dust is unknown, so one approach to verify the thin film assumption is obtaining the extinction coefficient of several samples.

So the light transmittance T can be defined as follows:

$$T = \frac{E_a}{E_0}$$

(3)

2.3 The experimental validation

One indoor deposition experiment was conducted in a chamber. Four glass samples were put on the middle area of the chamber. When all the experimental facilities were well set, aerosol generator was turned on to inject dust into the chamber for about 15 minutes. The aerosol particle would naturally deposit onto the sample glasses placed in the central area of the chamber. This deposition process could last 12 hours or more. After 24 hours, it can be assumed that the particle deposition process is completely finished. The chamber was opened and the deposition was measured by one high-accuracy digital microbalance. What's more, the light transmittance was tested by one light measure meter. The wavelength of this light measure meter is 550nm. The deposition dust is Arizona Dust.

3. RESULTS AND DISCUSSIONS

The results of this study have two parts. The first part is the results of deposition density and light transmittance in the deposition experiment. The second part is the extinction coefficient of Arizona Dust. Figure 33: The format painter tool

3.1 Experimental Results

Table.1 shows the results of deposition density and light transmittance. It can be found that light transmittance of the sample with higher deposition density is lower. The reason is that higher deposition

density reveals higher absorptive length. So the higher accumulated dust film can absorb more energy of incident light. There is no doubt that therefore the light transmittance is lower.

Table 1 Results of deposition experiment

Sample Number	Deposition Density (g/m2)	Light Transmittance
1	0.48	0.8948
2	0.61	0.8800
3	0.63	0.8774
4	0.73	0.8661

3.2 Extinction coefficient of Arizona Dust

From equation 1 to equation 3, the extinction coefficient is calculated and Table 2 demonstrates the calculated results.

Table 2 Extinction coefficient of different samples

Sample Number	Extinction Coefficient
1	0.0283
2	0.0280
3	0.0281
4	0.0281

The extinction coefficient of Arizonna Dust is from 0.0280 to 0.0283. It can be found that the extinction coefficient of different samples are equally in value. So this new way and thin film assumption are verified by this unchanged value.

In addition, if people want to obtain the actual light transmittance of accumulated dust by this computing way in different areas, they need to know the extinction coefficient of local dust. The most simple and accurate way is to use light measure meter to get the actual value according to our experiments. It is significant that the required samples are more than four because the actual extinction coefficient has a narrow range, not a definite number. The average extinction coefficient can be obtained by the average of these tested values.

4. CONCLUSION

In this paper, a novel way to calculate the relationship between dust deposition density and light transmittance after the effect of accumulated dust on PV modules is built based on the thin film theory. In addition, an indoor deposition experiment is conducted and this assumption is validated by deposition experiments. Specifically, the extinction coefficient of Arizona Dust ranges from 0.280 to 0.283. Additionally, the effect of refraction is stable and the absorption influences the light transmittance greatly.

5. REFERENCES

SALIM, A. A., Huraib, F. S., & Eugenio, N. N. (1988). PV power-study of system options and optimization. In EC photovoltaic solar conference. 8 (pp. 688-692).

WAKIM, F. (1981). Introduction of PV power generation to Kuwait. Kuwait Institute for Scientific Researchers, Kuwait City.

SAID, S. A. M. (1990). Effects of dust accumulation on performances of thermal and photovoltaic flat-plate collectors. Applied Energy, 37(1), 73-84.

MICHALSKY, J. J., Perez, R., Stewart, R., LeBaron, B. A., & Harrison, L. (1988). Design and development of a rotating shadowband radiometer solar radiation/daylight network. Solar energy, 41(6), 577-581.

ADINOYI, M. J., & Said, S. A. (2013). Effect of dust accumulation on the power outputs of solar photovoltaic modules. Renewable Energy, 60, 633-636.

IBRAHIM, A. (2011). Effect of shadow and dust on the performance of silicon solar cell. Journal of Basic and applied scientific research, 1(3), 222-230.

MOHANDES, B. M. A., El-Chaar, L., & Lamont, L. A. (2009). Application study of 500 W photovoltaic (PV) system in the UAE. Applied Solar Energy, 45(4), 242-247.

TOUATI, F., Massoud, A., Hamad, J. A., & Saeed, S. A. (2013, March). Effects of environmental and climatic conditions on PV efficiency in Qatar. In International Conference on Renewable Energies and Power Quality (ICREPQ'13) (pp. 20-22).

ELMINIR, H. K., Ghitas, A. E., Hamid, R. H., El-Hussainy, F., Beheary, M. M., & Abdel-Moneim, K. M. (2006). Effect of dust on the transparent cover of solar collectors. Energy Conversion and Management, 47(18), 3192-3203.

SESSION 22: SOLAR ENERGY

249: Investigation on the applicability of screw expander in distributed solar thermal electricity generating systems

Pengcheng Li[1], Jing Li*[2], Gang Pei*[3], Jahan Zeb Alvi[4], Jie Ji[5]

[1,2,3,4,5]*Department of Thermal Science and Energy Engineering, University of Science and Technology of China, Jinzhai Road 96, Hefei City, Anhui Province, People's Republic of China*

1lpc1988@mail.ustc.edu.cn
2lijing83@ustc.edu.cn
3peigang@ustc.edu.cn
4alvi@mail.ustc.edu.cn
5jijie@ustc.edu.cn

Screw expander (SE), with high applicability in power conversion with steam-liquid mixture, would be successfully applied in solar electric generating systems (SEGS). A cascade steam-organic Rankine cycle (SORC) integrated with parabolic trough collectors (PTC) was proposed. The top cycle was SE-based steam Rankine cycle (SRC) and the bottom cycle was organic Rankine cycle (ORC). The SRC condensation heat was used to drive the ORC. By comparison with conventional PTC-SEGS, the proposed system averted superheated steam and was suitable for distributed power generation applications. The actual achieved thermal efficiency was lower than the theoretical value when the influence of operating PR on SE efficiency was considered. Maximum thermal efficiencies of 14.26% and 16.00% could be obtained for SORC system with benzene as bottom fluid at the design hot / cold temperatures of 200/40℃ and 200/10℃. The efficiencies exceeded those of cascade organic Rankine cycle (CORC) system by 4.0% and 1.5% respectively, even if the working fluids in CORC were carefully selected and working conditions were optimized

Keywords: screw expander; thermal efficiency; cascade system; pressure ratio

1. INTRODUCTION

Solar thermal power generation industry was booming rapidly in recent years. Parabolic trough collectors (PTC)-based solar electric generating systems (SEGS) were proven to be the most mature and predominant technology. However, turbines were generally adopted in existing PTC-SEGS, which had some inherent disadvantages.

First, only superheated steam (close to or greater than 400 ℃) was admitted entering into turbine to avoid condensation of vapour during the expansion process. Because if any water droplets were formed, high velocities vapour would impinge on the blades of turbine and erode them and also reduce the expander efficiency. High superheat could only be achieved by PTC with characteristics of high geometric concentrating ratio, high tracking accuracy and strict sealing technology. At the same time, there would be limited space in the selection of heat storage material, good insulation technology was required in heat storage device and serious corrosion problems would be inevitable. In addition, high superheat resulted in low average heat-absorbing temperature and thus reducing the efficiency of Rankine cycle (Pei et al., 2011). Some of the PTC would suffer from low heat-collecting efficiency owing to high average working fluid temperature.

Second, usual scale of PTC-SEGS ranged from a few to tens of megawatts, some even reached two or three hundred megawatts of capacity. Millions of square meter of flat land was necessary, which could only be met in the Gobi desert or sparsely populated areas. The matching turbines required multi-stage expansion or extraction recuperator, which resulted in huge, expensive and complex constructed turbines.

The above problems could be solved by the usage of screw expander (SE).

Screw expanders have been used in geothermal power plants since 1970s (PA, 1976). Many successful projects were available in the fields of steel and flue gas waste heat, industrial radiant heat and geothermal utilization (from website). SE had some outstanding merits as compared with turbine: low demand on the quality of the working fluids (superheated or saturated steam, vapor in two-phase region, hot water and hydrotherm were all admittable); stable efficiency because compressed or expanded vapour or gas had little effect on its mode of operation or efficiency (Smith et al., 2011); much lower rotate speed and hence high ratio reduction gearbox as well as relatively expensive lubrication system were needless (Leibowitz et al., 2006); simpler structure, more convenient to maintain and lower power output for individual devices, which were more suitable for small scale power plants. In China, 10 KW to 1.5 MW screw expanders were available in market.

However, SE-based steam Rankine cycle (SRC) had some inevitable defects as well.

First, the design pressure ratio (PR) of SE was small. According to the existing plants, common design PR of SE was about 2 to 8. The resulting high exhaust temperature and pressure could not make the heat source be fully utilized.

Second, the saturation pressure of water at normal ambient temperature was very low. It was difficult to get an outlet pressure of steam expander lower than 0.05bar in practical operation. This technical limit for maintaining a vacuum in the condenser had been pointed out by previous scholars (Li et al., 2013, FJ et al., 2011). It indicated that lower backpressure and larger enthalpy drop were unavailable for steam expander at condensation temperature lower than 33°C, which limited the power output.

The above two difficulties could be overcome by introducing Organic Rankine cycle (ORC).

ORC displayed a number of advantages over SRC. The characteristic of low boiling points of organic fluids enabled efficient use of low-temperature heat sources; immunity from freezing in cold winter owing to the low freezing points; the absence of droplets during the expansion of dry fluids; higher condensation pressures as compared with steam, thus lower condensation temperatures could be obtained and was particularly suitable for distributed applications, etc. SE-based ORC- SEGS could avert most of the shortcomings mentioned above, but the efficiency of single stage system was low due to small design PR of SE.

A cascade steam-organic Rankine cycle (SORC) system with the top SRC and bottom ORC was a promising scheme. Obviously, SORC offered higher power efficiency compared with sole SRC or ORC system (G et al., 1999, A et al., 2013). Besides, a cascade organic Rankine cycle (CORC) system might also be a comparable idea. The objective of this paper was to show different approaches of SE-based PTC-SEGS and compare thermal efficiencies of CORC and SORC.

2. MATHEMATICAL MODEL

2.1 System description and assumptions

SORC was taken as an example (CORC was similar). The schematic diagram was shown in Fig.1. Cycle Ⅰ was direct steam generation (DSG) structure. Cycle Ⅱ was ORC. T–s diagram of SORC was shown in Fig.2. The feasibility of DSG technology was manifested in the Direct Solar Steam project funded by European Union, which had been operated for more than 6000h (M. et al., 2002). DSG in the absorber tubes was deemed as a promising option to improve the competitiveness of PTC-SEGS. Thermodynamic loss within oil–water/steam heat exchanger was avoided and hence higher steam temperatures and higher steam cycle efficiencies could be attained. Besides, a 26% reduction in the levelized electricity cost seemed to be achievable (Eduardo et al., 2002). The main defect was the more complex transient control and no commercially available storage systems. Since a wide range of fluctuation of pressure and flow rate of the heat source was permitted for SE, the requirements on the tracking accuracy, the property of absorber tubes and the investment in PTC could be reduced.
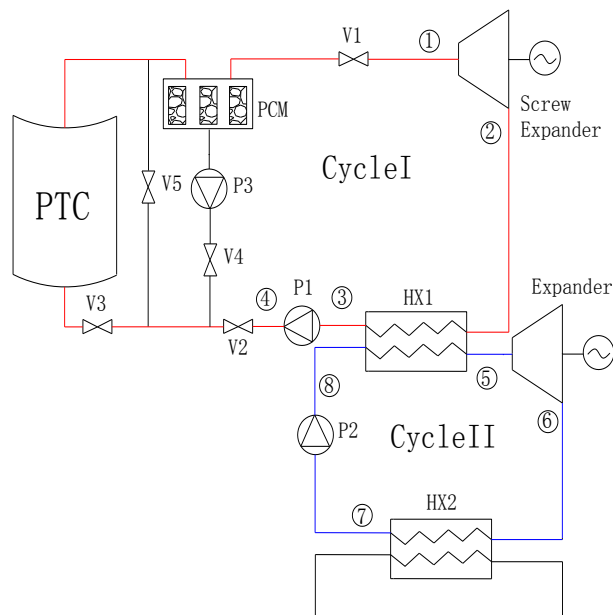
Fig.1.Schematic diagram of SORC system   Fig. 2.T–s diagram with the state points as defined in Fig.1
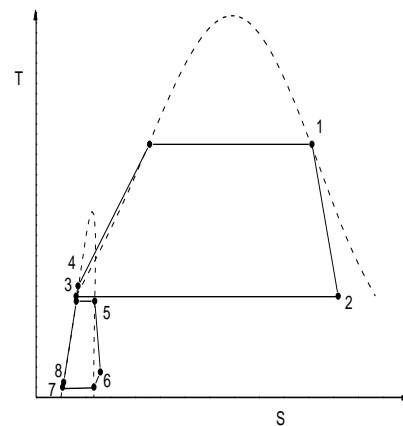
There could be three operating modes for DSG structure.

Ⅰ) The system needed to generate electricity and the solar radiation was abundant. In this mode, valves 1, 2, 3 were open and pump (P) 1 run. Water was heated and vaporized in PTC. The saturated steam flowed into SE, exporting power during the process of enthalpy drop. The outlet vapor was condensed to saturated liquid in heat exchanger (HX) 1, pressurized by P1 and then sent back to PTC. The condensation heat evaporated the organic fluid in Cycle Ⅱ. If the irradiation was too strong, valve (V) 4 would be open and P2 would run to prevent water from being superheated in PTC and part of the solar energy was stored in phase-change material (PCM). It was the simultaneous processes of heat collection and power generation.

Ⅱ) The system did not need to generate electricity but irradiation was well. V3, V4 were open and P2 run. Solar heat was transferred to PCM continuously by water.

Ⅲ) The system needed to generate electricity but irradiation was very weak or unavailable. V1, V2, V5 were open and P1 run. Heat was released by PCM and converted into power by water.

2.2 Calculation models

PTC

The PTC produced by the Industrial Solar Technology Corporation were employed here. The performance formula of single PTC as given by the manufacturer was (Invernizzi et al., 2007):

$$\eta_{PTC}(T) = 0.762 - 0.2125 \times \frac{T - T_a}{G_b} - 0.001672 \times \frac{(T - T_a)^2}{G_b} \qquad (1)$$

where: $\eta_{PTC}(T)$ = heat collecting efficiency of PTC

G_b = beam solar radiation (W/m²)

T = collector inlet temperature (K)

T_a = ambient temperature (K).

Hundreds of collectors were usually required in SEGS, the temperature difference between neighboring collectors was supposed to be small. To calculate the overall collection efficiency, it was reasonable to assume that the average operating temperature of the collectors change continuously from one module to another.

Water in PTC experienced liquid phase and binary phase regions, and finally became saturated gas. Collector efficiency in binary phase region could be calculated with formula (1) as the temperature remained constant. For liquid phase region, in order to reach an outlet temperature T_{out} with an inlet

temperature T_{in} , the required collector area was obtained by
$$A_l = \int_{T_{in}}^{T_{out}} \frac{m_1 \cdot C_p(T)}{\eta \cdot G_b} dT \qquad (2)$$

where m_I = mass flow rate of water in Cycle Ⅰ (kg/s)

C_p = *heat capacity of water. It could be expressed by a first order approximation:* $C_p(T) = C_{p,0} + \alpha(T - T_0)$ *(3)*

where $C_{p,0}$ = heat capacity corresponding to reference temperature T_0 ($kJ/kg \cdot K$)

with $c_1 = 0.2125/G_b$, $c_2 = 0.001672/G_b$, the collector area according to Eqs. (1) - (3) was calculated by

$$A_l = \frac{m_1}{c_2 G_b (\theta_2 - \theta_1)} \left[(C_{p,a} + \alpha\theta_1) \ln \frac{(T_{out} - T_a - \theta_1)}{T_{in} - T_a - \theta_1} + (C_{p,a} + \alpha\theta_2) \ln \frac{\theta_2 - T_{in} + T_a}{\theta_2 - T_{out} + T_a} \right] \qquad (4)$$

where θ_1 and θ_2 = the arithmetical solutions of Eq. (5) ($\theta_1 < 0$, $\theta_2 > 0$) $\quad 0.762 - c_1\theta - c_2\theta^2 = 0 \qquad (5)$

$$C_{p,a} = C_{p,0} + \alpha(T_a - T_0) \qquad (6)$$

Collector efficiency in liquid phase region was calculated by $\eta_l = \dfrac{m_1 \Delta h_l}{G_b A_l} \qquad (7)$

Overall collector efficiency was calculated by $\eta_{PTC} = \dfrac{Q}{G_b(A_l + A_b)} = \dfrac{\Delta h_l + \Delta h_b}{\dfrac{\Delta h_l}{\eta_l} + \dfrac{\Delta h_b}{\eta_b}} \qquad (8)$

where Δh_l and Δh_b = the enthalpy increment of water in liquid and binary phase regions respectively (kJ/kg)

A_l and A_b = the required aperture area in liquid phase and binary phase regions respectively (m^2)

Expanders

The work generated by expanders was defined as $W_{\mathrm{I}} = m_{\mathrm{I}}(h_1 - h_2)\ W_{\mathrm{II}} = m_{\mathrm{II}}(h_5 - h_6)$ (9-10)

The volume ratio (VR) for each expander was defined as: $VR = \dfrac{v_{out}}{v_{in}}$ (11)

where v_{out} and v_{in} = specific volume at outlet and inlet of expander (m^3/kg)

The PR was defined as: $PR = \dfrac{P_{in}}{P_{out}}$ (12)

where P_{out} and P_{in} = pressures at outlet and inlet of expander (MPa).

Heat exchanger

Heat balance in HX1 was given by Eq. (13): $m_{\mathrm{I}}(h_2 - h_3) = m_{\mathrm{II}}(h_5 - h_8)$ 13)

Pumps

The work required by pumps was given by $W_{P1} = m_{\mathrm{I}}(h_4 - h_3)\ W_{P2} = m_{\mathrm{II}}(h_8 - h_7)$ (14-15)

Thermal efficiency (η_T) $\eta_T = \eta_{SORC} \cdot \eta_{PTC} = \dfrac{W_{net}}{G_b \cdot A}$ (16)

where $\eta_{SORC} = \dfrac{W_{net}}{m_{\mathrm{I}}(h_1 - h_4)}$ (17)

$W_{net} = \left(W_{\mathrm{I}} + W_{\mathrm{II}}\right) \cdot \varepsilon_g - \left(W_{P1} + W_{P2}\right)$ (18)

where ε_g = generator efficiency

For CORC, η_{SORC} must be replaced by η_{CORC}, and the other equations remained unchanged.

3. RESULTS AND DISCUSSION

Ten typical organic fluids were selected in Cycle Ⅱ of SORC system. Among them methanol, ammonia and propyne were wet fluids, therefore SE rather than turbine was applicable for wet fluid in Cycle Ⅱ if superheat was not taken into account. Saturation pressures of the fluids at 10℃ were higher than 5kPa. Fixed parameters for calculation were given in Table 1. Fig. 3 shows the variations of η_T of SORC with T_5 when T_H =200℃ and T_L =40℃. T_H was equal to the evaporation temperature in Cycle Ⅰ (T_1). T_L was equal to the condensation temperature in Cycle Ⅱ (T_7). It could be found that methanol showed the highest η_T, followed by benzene. $T_{5,P}$ and $\eta_{T,P}$ at the peak points were (98℃, 14.81%) for methanol and (88℃, 14.61%) for benzene.
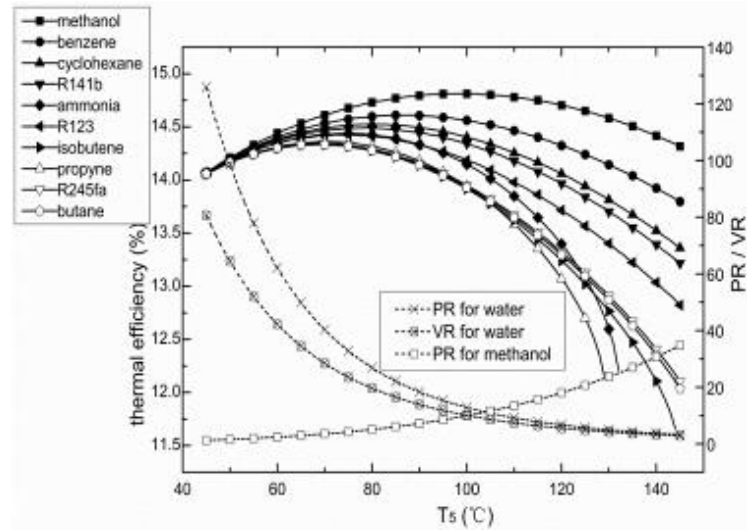
Fig. 3. Variations of η_T of SORC with T_5 when T_H =200℃ and T_L =40℃.

Table 1. Fixed parameters for calculation.

Term	Value
Pinch-point temperature difference	5 K
Pump efficiency, ε_p	0.8
Screw expander efficiency under design condition, ε_{SE}	0.75
Turbine efficiency, ε_{TU}	0.75
Generator efficiency, ε_g	0.95
Beam solar radiation, G_b	800 W/m^2

However, $\eta_{T,p}$ was the theoretic maximum thermal efficiency with the assumption of constant expander efficiency. Given hot /cold side temperatures and working fluid, $T_{5,p}$ might be not the optimum operating T_5 in the cascade system regarding the characteristics of SE. The built-in VR and operating PR were two important parameters for SE. There was a compromise between a lower built-in VR with lower cost and leakage losses, and a higher one with little loss due to under / over-expansion. In practice, a built-in VR from 2 to 5.5 was favorable (V et al. 2014). By comparison with VR, the effect of ill-matching of PR was found to be a more dominant factor on efficiency. It was observed that for a given VR, there was a maximum value of the overall isentropic efficiency and this maximum occured at PR approximately equal to the built-in PR. For a SE with built-in VR of 5, the drop of isentropic efficiency from the maximum was only 10% when the operating PR increased by threefold as the built-in (K. et al. 1990).

The variations of PR and VR for water and PR for methanol were also shown in Fig. 3. The curve of PR for water was above that of VR all along. A built-in VR of 5 corresponded to PR of 5.93 and T_5 =124℃. This was a temperature matching the SE characteristics ($T_{5,ch}$) and enabled a best expansion process. When practical operating T_5 deviated from $T_{5,ch}$, SE would suffer from off-design condition and isentropic efficiency would decrease. It was reasonable to assume an SE efficiency of 0.72, 0.70 and 0.65 when actual PR was around 10, 15 and 21 respectively, according to results by K. et al.

When methanol was taken as bottom fluid in SORC, there were two $T_{5,ch}$ (124 and 84℃) that match built-in PR of 5.93 for top and bottom screw expanders respectively. PR and isentropic efficiency for the other SE and corresponding η_T were listed in the first two lines in Table 2. The third line showed $\eta_{T,P} = 14.04\%$ at $T_{5,P} = 98℃$ when the influence of PR on SE was considered. It was lower than theoretical $\eta_{T,P}$ of 14.81%.

When dry fluids were taken as bottom fluids in SORC, turbine was adopted in Cycle Ⅱ because turbine was able to handle much higher VR compared to volumetric expander. Efficiency over 80% could be achieved for single-stage axial turbine only when the VR was below 50 (Invernizzi et al. 2007). Fortunately, VRs for all the seven dry fluids were below 50 when T_5 ranged from 45 to 145℃, and they were not depicted in Fig. 3. The forth and fifth lines of Table 2 displayed variations of η_T with benzene as the bottom fluid and PR = 5.93 and 15, respectively. Sixth line showed $\eta_{T,P} = 13.42\%$ at $T_{5,P} = 88℃$ when actual PR was

considered. It was also lower than theoretical $\eta_{T,P}$ of 14.61%. Results for the other eight fluids in SORC were similar and the thermal efficiencies were evidently lower than those of with methanol and benzene. It could be seen from Table 2 that highest η_T of SORC was about 14.26% at T$_H$=200℃ and T$_L$=40℃.

Table 2. Comparison results of η_T of SORC and CORC at TH=200℃ and TL=40℃.

Top cycle working fluid	PR(wet fluid)/ VR(dry fluid)	Expander efficiency	Bottom cycle working fluid	T$_5$ (℃)	PR(wet fluid)/ VR(dry fluid)	Expander efficiency	Thermal efficiency(%)
water	5.93	0.75	methanol	124	20.16	0.65	13.58
water	22.73	0.65	methanol	84	5.93	0.75	13.53
water	13.79	0.7	methanol	98	9.35	0.72	14.04
water	5.93	0.75	benzene	124	12.27	0.75	14.26
water	15	0.7	benzene	96	5.98	0.75	14.04
water	19.79	0.65	benzene	88	4.85	0.75	13.42
benzene	11.21	0.75	methanol	85	5.93	0.7	13.71
benzene	5.36	0.75	methanol	118	15	0.7	13.54
benzene	6.14	0.75	benzene	108	8.29	0.75	13.69
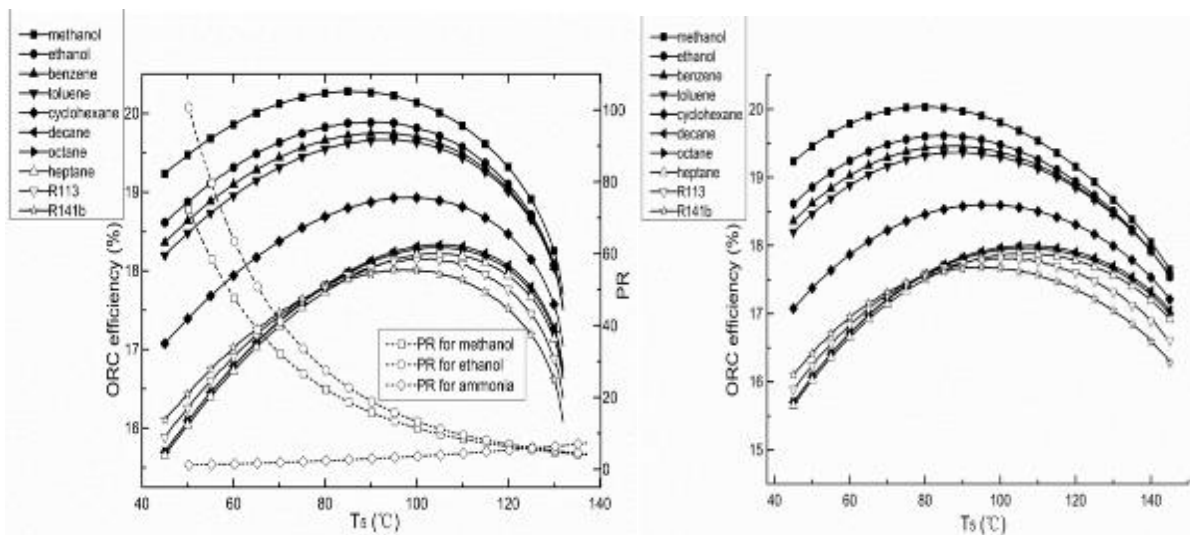
Fig. 4. Variations of η_{CORC} with different top cycle fluids and (a) ammonia; (b) butane as bottom cycle fluid respectively.

For CORC system, different fluids would also result in different heat power conversion efficiencies. The primary step was to screen the most efficient top cycle working fluid. Firstly, ammonia and butane (typical wet and dry fluids) were fixed as bottom cycle working fluids, and the corresponding expanders in bottom cycles were SE and turbine respectively. T$_H$/ T$_L$ was 200/40℃. Ten different fluids with critical temperatures higher than 200℃ were adopted in the top cycle. Fig.4. (a) and (b) show variations of η_{CORC} with T$_5$. Methanol exhibited the highest η_{CORC}, followed by ethanol and benzene in both (a) and (b). Only methanol and ethanol were wet fluids among the ten top fluids. Similar to the situation in Fig.3, off-design conditions for SE were inevitable. Calculation results of η_{CORC} were listed in Table 3. The fifth and last line showed $\eta_{CORC,P}$ for benzene at T$_{5,P}$. The PRs for ammonia in the table were lower than 5.93, therefore efficiency of 0.75 could be achieved by SE with lower built-in PR. Simultaneously, VRs for butane and benzene in the table were much lower than 50, single-stage turbine was sufficient for the power conversion. It could be seen that η_{CORC} with benzene as top cycle fluid was higher than that with methanol and ethanol no matter the bottom fluid was ammonia or butane. Obviously, this superiority was more appreciable when the other seven top cycle fluids were adopted. Therefore, benzene was selected as the most efficient top cycle fluid.

Table 3. Calculation results of η_{CORC} with ammonia and butane as bottom fluids

Top cycle working fluid	PR(wet fluid)/ VR(dry fluid)	Expander efficiency	Bottom cycle working fluid	T_5 (℃)	PR(wet fluid)/ VR(dry fluid)	Expander efficiency	Global ORC efficiency(%)
methanol	5.93	0.75	ammonia	117	5.53	0.75	19.48
methanol	15	0.7	ammonia	92	3.06	0.75	19.42
ethanol	5.93	0.75	ammonia	120	5.89	0.75	19.07
ethanol	15	0.7	ammonia	96	3.39	0.75	19.10
benzene	9.26	0.75	ammonia	92	3.42	0.75	19.75
methanol	5.93	0.75	butane	117	6.49	0.75	19.28
methanol	15	0.7	butane	92	3.21	0.75	19.15
ethanol	5.93	0.75	butane	120	7.10	0.75	18.92
ethanol	15	0.7	butane	97	3.61	0.75	18.80
benzene	12.21	0.75	butane	82	2.89	0.75	19.45

The next step was to screen the most efficient bottom cycle fluid. The ten bottom fluids were the same as in Fig. 3. Variations of η_T of CORC with T5 when T$_H$ =200℃ and T$_L$ =40℃ were shown in Fig.5. Methanol exhibited the highest η_T, followed by benzene. It could be observed by comparison that each curve in Fig. 3 was higher than the corresponding curve in Fig. 5. It indicated η_T of SORC was higher than that of CORC under the assumption of constant expander efficiency. Similar to the above, thermal efficiencies that could be achieved when operating PR was considered were listed in the last three lines in Table 2. It showed maximum η_T of SORC (14.26%) was higher than maximum η_T of CORC (13.71%). The relative increment was about 4%.
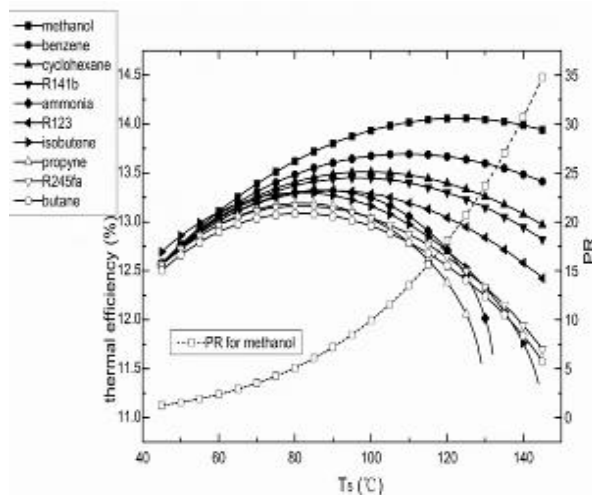
(left) Fig. 5. Variations of η_T of CORC with T5 when TH =200℃ and TL =40℃. (right)

Fig. 6. Variations of η_T of CORC with T5 when TH =200℃ and TL =10℃.

Fig. 7. Variations of η_T of SORC with T_5 when T_H =200℃ and T_L =10℃.

Table 4. Comparison results of η_T of SORC and CORC at $T_H = 200°C$ and $T_L = 10°C$.

Top cycle working fluid	PR(wet fluid)/ VR(dry fluid)	Expander efficiency	Bottom cycle working fluid	T_5 (°C)	PR(wet fluid)/ VR(dry fluid)	Expander efficiency	Thermal efficiency(%)
benzene	39.96	0.75	methanol	45	5.93	0.75	15.53
benzene	19.08	0.75	methanol	67	15	0.7	15.53
benzene	11.54	0.75	benzene	84	15.79	0.75	15.77
water	5.93	0.75	benzene	124	45.16	0.75	15.98
water	15	0.7	benzene	95	21.78	0.75	16.00

Similarly, figures 6 and 7 showed variations of η_T of CORC and SORC with T_5 when $T_H = 200°C$ and $T_L = 10°C$. Each curve in Fig. 7 was higher than the corresponding curve in Fig. 6. Notably, for SORC system, a T_5 that made PRs for both water and methanol below 25 was inexistent. It indicated that no design conditions could make both screw expanders behave well. Methanol was not suitable in this case owing to unacceptably low SE efficiency. Table 4 showed maximum η_T of SORC (16.00%) was higher than maximum η_T of CORC (15.77%). The relative increment was about 1.5%.

In addition, most organic fluids would suffer from thermal instability, flammability or low thermodynamic performance at high temperatures in top cycle. Contrastly, water was of non-fouling, non-corrosiveness, non-toxicity and non-flammability, and had good attainability. Therefore SORC had advantages in security.

4. CONCLUSION

The prominent characteristic in power conversion with steam-liquid mixture made screw expanders suitable for low-medium temperature application. The successful applications of SE in steel waste heat and geothermal power generation would lay solid foundation for its combination with distributed SEGS. The proposed SORC system had advantages over conventional turbine-based PTC-SRC system regarding the lower pressure and temperature in the solar field and better reaction to low ambient temperature. Maximum thermal efficiencies of 14.26% and 16.00% could be achieved with benzene as bottom fluid at T_H / T_L of 200/40 °C and 200/10 °C, respectively.

The CORC system might be a comparable scheme. Benzene was the most efficient top cycle fluid. Calculations showed that maximum thermal efficiencies of SORC exceeded that of CORC by 4.0% at 200/40°C and 1.5% at 200/10°C respectively, even if the working fluids in CORC were carefully selected and working conditions were optimized. SORC had advantages in both thermal efficiency and security.

5. ACKNOWLEDGEMENT

6. REFERENCES

A FAHAD, Al-Sulaiman, 2013. Energy and sizing analyses of parabolic trough solar collector integrated with steam and binary vapor cycles. Energy, 58, 561-570.

D. KRUGER, A. Heller, K. Hennecke, K. Duer, 2000. Parabolic trough collectors for district heating systems at high latitudes—a case study. In: Proceedings of Eurosun '2000 on CD ROM; ISES-Europe.

Eduardo ZARZA, Loreto Valenzuela, Javier Leo ´n, H.-Dieter Weyers, Martin Eickhoff, Markus Eck, Klaus Hennecke, 2002. The DISS Project: Direct Steam Generation in Parabolic Trough Systems. Operation and Maintenance Experience and Update on Project Status. Journal of Solar Energy Engineering, 124, 126-133.

FJ FERNÁNDEZ, MM Prieto, I Suárez, 2011. Thermodynamic analysis of high- temperature regenerative organic Rankine cycles using siloxanes as working fluids. Energy, 36, 5239-5249.

G ANGELINO, C Invernizzi, G Molteni, 1999. The potential role of organic bottoming Rankine cycles in steam power stations. Proceedings of the Institution of Mechanical Engineers, Part A: Journal of Power and Energy, 213, 75.

Invernizzi COSTANTE, Iora Paolo, Silva Paolo, 2007. Bottoming micro-Rankine cycles for micro-gas turbines. Applied Thermal Engineering, 27, 100–110.

K. C. NG, T. Y. Bong and T. B. Lim, 1990. A thermodynamic model for the analysis of screw expander performance. Heat Recovery Systems and CHP, 10, 119–133.

LEIBOWITZ H., Smith I. K., Stosic N., 2006. Cost effective small scale ORC systems for power recovery from low grade heat sources. ASME International Mechanical Engineering Congress and Exposition, 521-527.

Li JING, Pei Gang, Li Yunzhu, Wang Dongyue, Ji Jie, 2013. Examination of the expander leaving loss in variable organic Rankine cycle operation. Energy Conversion and Management, 65, 66-74.

M. ECK, W.-D. Steinmann,2002. Direct Steam Generation in Parabolic Troughs: First Results of the DISS Project. Journal of Solar Energy Engineering, 124, 134–139.

PA House, 1976. Helical-rotor expander applications for geothermal energy conversion. Lawrence Livermore laboratory report UCRL-52043.

Pei GANG, Li Jing, Ji Jie, 2011. Design and analysis of a novel low-temperature solar thermal electric system with two-stage collectors and heat storage units. Renewable Energy, 36, 2324-2333.

SMITH I K, Stosic N, Mujic E, Kovacevic A, 2011. Steam as the working fluid for power recovery from exhaust gases bymeans of screw expanders. Journal of Process Mechanical Engineering, 225, 117-125.

V AVADHANULA, C Lin, 2014. Empirical models for a screw expander based on experimental data from organic Rankine cycle system testing. Journal of Engineering for Gas Turbines and Power, 136, 062601.

http://www.jxhdep.com/en/project.asp

283: Thermal performance of an experimental solar pond provided with heat exchanger in Egypt

Wessam E. Abd Allah1, M.A. Tawfik2, M.K. Abd El-Wahab3

1 University of Zagazig, PO Box 44511, Zagazig City, Egypt. Email: dr.wesam15@yahoo.com
2 University of Zagazig, PO Box 44511, Zagazig City, Egypt. Email: mohamed.ezeldien@yahoo.com
3 University of Zagazig, PO Box 44511, Zagazig City, Egypt. Email: kadryprof@yahoo.com

This work aims to study the availability of absorbing, trapping and exploiting the high radiation- as heat energy- in Egypt. Therefore, a set of practical experiments were conducted to evaluate both the thermal performance of an experimental salinity gradient solar pond (SGSP) and the heat extraction by using an internal heat exchanger (IHE). All experiments were carried out at Faculty of Agriculture, Zagazig University, Egypt (Latitude 30o 35/ N, Longitude 31o 31/ E) during 2013.

The results revealed that, the average temperature stored in the lower convective zone (LCZ) of the pond was about 32.4, 49.3 and 53.2 oC at average penetrated solar radiation flux of 151.8, 239.5 and 298.6 W/m2 for months of January, April and July, respectively .It was found that, about 28.8% of the incident solar radiation on the pond's surface reached the LCZ. Ultimately, the average values of IHE's effectiveness and the thermal efficiency of the pond were 0.505 and 24.5 %, respectively at month of July. Hence, it is clear that, the SGSP has a good thermal performance and suitable for different thermal applications under the Egyptian climate conditions.

Keywords: solar pond, thermal performance, heat extraction, effectiveness, thermal efficiency.

1. INTRODUCTION

Egypt is one of the countries that are located in Sunbelt area of the world and the most suitable for solar energy applications, where it endowed with high solar radiation that ranging between 2000 – 3200 kWh/m²·year from north to south of the country. Thus, it is necessary to devise more economical ways for collecting and storing the solar energy as heat energy in the same medium for a long period of time.

The solar pond is a simple thermal energy storage which works for collecting, trapping and consequently storing the incident solar radiation as a sensible heat at the bottom layer of the pond for long time. The solar pond has three layers namely upper convective zone (UCZ), non-convective zone (NCZ) and lower convective zone (LCZ). The UCZ is made of almost fresh water. The NCZ is made of water with different salinity; at the top of NCZ the salinity of water is similar to that of UCZ water while at the bottom of NCZ the water has salinity close to saturation, while the entire LCZ is made of water with salinity close to saturation. In case of the solar pond, the natural convection is suppressed by the presence of the salinity gradient in the NCZ and hence, the solar energy that is absorbed by the water in the LCZ is trapped and stored (DATE and AKBARZADEH, 2013: page 517).

The advantages of the solar pond are the simplicity of the design, inexpensive construction and easy in maintenance as well as it is considered a potential technique for heat storing, so it can be used as a heat supply with high temperature for short periods in the rural dwellings, settlements in remote regions and the isolated communities. The extracted heat from the pond can be exploited in different thermal applications such as; drying, heating or even desalination.

The incident solar radiation on the surface of pond penetrates across the air-water interface towards the pond's depth to reach the bottom layer causing a continuous increase in temperature at this layer. For efficient operation of a solar pond, the storage temperature should be high to obtain maximum corresponding Carnot efficiency and it's important to maintain this high storage temperature during all seasons by decreasing the amplitudes of the storage temperature variation (AL-JUWAYHEL and EL-REFAEE, 1998: page 1209). The efficiency of a solar pond in collecting energy depends on the stability of the gradient zone and maintaining the state of the salt gradient zone (boundaries, level and salt gradient of the non-convective zone) stable as its initial design is essential to the successful operation of a salinity gradient solar pond (KARIM et al., 2010: page 25).

An experimental and theoretical study of temperature distribution in an insulated solar pond under Jordanian climate conditions was investigated. The maximum temperature of 47 °C was recorded in the LCZ and there is a relationship between the LCZ temperature and the ambient temperature (SAKHRIEH and AL-SALAYMEH 2013: page 728). In solar ponds, temperature difference in the range 40-60 °C is available between the lower convective zone (LCZ) and the upper convective zone (UCZ) (SINGH et al., 2011: page 371). The temperature of the LCZ is observed as maximum as 55.2°C on August, a minimum of 16.9°C on January, and 41.1°C on May (KARAKILCIK et al., 2006: page 732).

The solar pond may serve as an emergency source of energy for a peak load in a short period of time. It may also be used continuously as an energy reserve. The efficiency of the small pond was about 10% in steady state condition (JAEFARZADEH, 2006: page 1864). For any meaningful use of the available heat in the solar pond, it is assumed that, a minimum 20 °C temperature difference must be present between the LCZ temperature and the heat transfer fluid inlet temperature (DATE et al., 2013: page 524). Hence, the current work aims to investigate the thermal performance of an artificially created salinity gradient solar pond and its effect on the potential of heat extraction for the stored heat at LCZ by using an internal heat exchanger (IHE).

2. METHODOLOGY

A theoretical study and practical experiments were carried out to evaluate the thermal performance of an experimental salinity-gradient solar pond (SGSP) and the heat extraction process of the stored heat in the LCZ during months of January, April and July, 2013 at Faculty of Agriculture, Zagazig Univ., Egypt (Latitude 30º 35′ N, Longitude 31º 31′ E).

Regarding the practical experiments, an experimental SGSP - as shown in Figure 1- with area of 150 cm × 150 cm and a depth of 150 cm was constructed from iron-sheets with 0.3 cm in thickness. All the side-walls and bottom of the SGSP were painted from inside and outside with anti-corrosion material then, it painted

with a synthetic black mat paint. The side-walls and the bottom of the SGSP were covered from outside with 15 cm thickness of glass wool as a thermal insulator and it putted on four poles at height of 30 cm above the ground.

The salt solution was prepared by dissolving the salt (NaCl) into the tap water (fresh water) with different concentrations for the different pond's layers. The SGSP was divided into three thicknesses of 15, 60 and 75 cm for the UCZ, NCZ and LCZ, respectively. The UCZ consists entirely of tap water with salt concentration of about 0% and density of 1001 kg/m^3,while the middle layer of NCZ is composed of six adjacent layers with 10cm thickness for each that extended from the adjacent layer to UCZ to the ultimate layer that interfacing the LCZ using salt concentrations of 2, 5, 8, 11, 14 and 17 % .The LCZ represents the heat storage, it had a uniform high salt concentration of 20%.The solar pond's filling process must be started from the bottom layer towards the upper layers, but to avoid the salt diffusion at the adjacent layers of NCZ, the brine has been poured very slowly from the brine's tank using the polystyrene panels. For measuring the density of the different layers of the pond, the samples of the brine were extracted by using hoses that located at height of 7.5, 22.5, 37.5, 52.5, 67.5, 82.5, 97.5, 112.5, 127.5 and 142.5 cm from the pond's surface and measured by an electronic Densimeter.

Regarding the temperature profile of the solar pond, a digital thermometer provided with data logger (monitoring up to 12 sensors) was connected to 12 of thermocouples - Type T- with accuracy of ±0.15 %. These sensors were fixed at height of 5, 10, 15, 30, 45, 60, 75, 90, 105, 120, 135 and 150 cm from the pond's surface to the bottom along the centre of the pond. The values of temperature were recorded every hour from 8:30 am to 15:30 pm. A weather station (WatchDog, model 900 ET) was used to measure the ambient temperature with accuracy of ± 0.7 °C, temperature (-30 -100 °C), solar radiation intensity (1- 1250 W/m^2). Data were recorded each 5 min and averaged for each hour.

The heat extraction was conducted by using an internal heat exchanger (IHE) and an external heat exchanger (EHE).The IHE was fixed on a frame at height of 30 cm from the bottom of solar pond as shown in Figure 2. The IHE was made from copper tubes with an internal diameter of 0.781 cm and external diameter of 0.953 cm. The IHE's tubes were separated by 10 cm distances .Also, the heat extraction system including of an EHE cooled by variable speed fan, flowmeter, controlling valve and pump. The heat removal system based on recirculating tap water with constant flow rate of 0.828 L/min during the thermal loading period that extended from 20th to 27th of July, where, two thermocouples -Type T- were fixed at the inlet and outlet tubes of IHE.
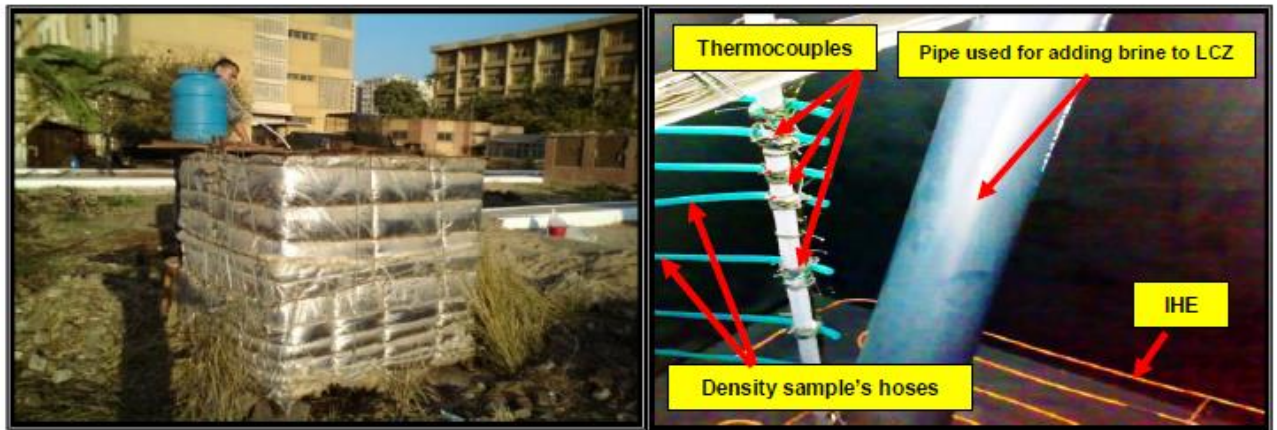
Figure 1: The experimental salinity-gradient solar pond.Figure 2: View from inside the experimental SGSP.

2.1 Thermal Performance of the SGSP

In this work, simple mathematical formulations were used to calculate the net available solar radiation at any depth within pond and thereby the collection efficiency. Moreover, these calculations include the pond's thermal efficiency and IHE's effectiveness during the heat extraction process. To simplify this mathematical method, all the calculations were focused on the direct solar radiation and the heat losses from the side-walls and bottom of the pond were neglected.

The incidence angle of direct solar radiation on the pond's surface is given by (DUFFIE and BECKMAN, 1980: page16):

Equation 7: The incidence angle of solar radiation on pond's surface

$$\theta_i = \cos^{-1}(\cos\phi.\cos\delta.\cos\omega + \sin\phi.\sin\delta)$$

Where:

θ_i= incidence angle of direct solar radiation on the horizontal surface (degrees)

Φ= latitude angle (degrees)

δ= declination angle (degrees)

ω= hour angle (degrees)

For the present work, the angle of latitude (Φ) = 30.58° for Zagazig city, Egypt, while the declination angle can be calculated as:

Equation 2: The angular position of sun at solar noon

$$\delta = 23.45\sin\left(\frac{360(284+n)}{365}\right)$$

Where:

δ= declination angle (degrees)

n= day of the year

The hour angle (ω) was calculated based on the local time as (JAEFERZADEH, 2004: page 284):

Equation 3 : The angular measure of time considered from noon

$$\omega = \frac{2\pi(h-12)}{24}$$

Where:

h= local time (hour)

A portion of the incident solar radiation on the pond's surface will reflect to the air whereas the rest of them will penetrate towards the depth of pond. The penetrated solar radiation (I_o) can be obtained from the incident radiation on the pond's surface (I_h) that measured horizontally by the built-in pyranometer of the weather station as:

Equation 4: Intensity of solar radiation just penetrated the pond's surface

$$I_0 = I_h(1-\rho)$$

 Where:

I_o= solar radiation in water just beneath the pond's surface (W/m²)

I_h= the incident solar radiation flux on the pond's surface (W/m²)

ρ= reflectivity

The reflectivity (ρ) can be estimated as the relation given by (WANG and AKBARZADEH, 1983: page 556)

Equation 5: The reflectivity on the air side

$$\rho = \frac{1}{2}\left(\frac{\sin^2(\theta_i - \theta_r)}{\sin^2(\theta_i + \theta_r)} + \frac{\tan^2(\theta_i - \theta_r)}{\tan^2(\theta_i + \theta_r)} \right)$$

Where:

θ_r = angle of refraction (degrees)

The relationship between the incidence angle (θ_i) and refraction angle (θ_r) is given by Snell's law:

Equation 6: The ratio of refractive index of water to that of air

$$n = \frac{\sin\theta_i}{\sin\theta_r}$$

Where:

n= refractive index (for water=1.33)

The solar radiation (I_o) that penetrated the UCZ surface is decayed gradually with the depth by the effect of the absorption at the different layers of pond. The net radiation stored at depth (x) can be calculated using the mathematical formulations according the model given by (HUSAIN et al., 2004: page 306) as follows:

The formulations started with calculating the available radiation at a depth x (only incident part) using the model given by (BRYANT and COLBECK, 1977: page 321):

Equation 7: The penetrated radiation flux at depth of (x) inside the pond

$$I_x = I_o\left[0.36 - 0.08\ln\left(\frac{x}{\cos\theta_r} \right) \right]$$

Where:

I_X= the penetrated radiation flux at depth x (W/m²)

x= specified depth inside pond (m)

The radiation flux reaching the bottom which can be obtained by substituting (L) in place of (x) in Equation 7 as:

Equation 8: The radiation flux that reached the pond's bottom

$$I_B = I_o\left[0.36 - 0.08\ln\left(\frac{L}{\cos\theta_r} \right) \right]$$

Where:

I_B= radiation flux at the pond's bottom (W/m²)

L= depth of pond (m)

Part of the radiation is absorbed at the bottom and the other is reflected diffusively towards the surface of pond and it equivalent to the beam radiation at 60° for the horizontal receivers (DUFFIE and BECKMAN, 1980: page 226), so the reflected radiation from bottom to depth (x) can be calculated as:

Equation 9: Incoming radiation flux from bottom to surface

$$I_{BR} = I_B . \rho_B \left[0.36 - 0.08 \ln \left(\frac{L - x}{\cos 60°} \right) \right]$$

Where:

I_{BR} = radiation flux reflected from the pond's bottom (W/m²)

ρ_B = pond bottom's reflectivity

The bottom's reflectivity (ρ_B) can be estimated using Equation 5 through replacing the refractive index (n) by ($\frac{1}{n}$) in Equation 6 to find out the relation between incidence angle (θ_i) and refraction angle (θ_r) at the water side as given by (SEZAI and TAŞDEMIROĞLU,1995: page 314).Once the reflected radiation from bottom reach the surface, about 47.7% of these radiation is reflected towards the different depths inside pond (CENGEL and ÖZIŞIK,1984: page 582) and the rest is crossed the pond's surface to air. The surface reflected part from the surface (I_{SR}) to depth (x) is defined as:

Equation 10: The reflected from surface to specified depth

$$I_{SR} = 0.477 I_B . \rho_B \left[0.36 - 0.08 \ln \left(\frac{L + x}{\cos 60°} \right) \right]$$

Where:

I_{SR} = radiation flux reflected back from surface into the body of the pond (W/m²)

The average available of solar radiation flux stored at depth (x) within pond will be:

Equation 11: The net radiation stored at depth (x) $\qquad I_{X_T} = I_B - I_{BR} + I_{SR}$

Where:

- I_{XT}= The net solar radiation flux that stored at depth x (W/m²)

Thus, the collection efficiency of the pond is defined as relation given by (SUBHAKAR and SRINIVASA MURTHY, 1993: page 307):

Equation 12: Collection efficiency $\qquad \eta_c = \dfrac{I_{X_T}}{I_h} \times 100$

Where:

- η_c= the collection efficiency of the pond (%)

2.2 Heat Extraction from the Lower Convective Zone (LCZ)

A portion of the trapped heat at the bottom of the pond is extracted from the LCZ (SUBHAKAR and SRINIVASA MURTHY, 1993: page 307). So, the thermal efficiency represents the heat removal efficiency of the pond that describes the thermal performance of the pond besides the temperature of the LCZ and the collection efficiency. The thermal efficiency can be calculated as the relation given by (LEBLANC et al., 2011: page 3130):

Equation 13: The heat removal efficiency

$$\eta_{th} = \frac{\dot{m}.C_p(T_o - T_i)}{I_h.A_{sp}} \times 100$$

Where:

η_{th}= the thermal efficiency of the solar pond (%)

$\dot{m}$= the average of mass flow rate (kg/s)

C_p= the specific heat of the recirculating fluid (for water= 4184 J/ kg.°C)

T_o= the fluid outlet temperature (°C)

T_i = the fluid inlet temperature (°C)

I_h= the incident solar radiation flux on the pond's surface (W/m^2)

A_{sp}= the surface area of the pond (m^2)

The thermal performance of the internal heat exchanger (IHE) can be described by term of the effectiveness that represents the effectiveness of the heat transfer by the IHE .The IHE's effectiveness can be defined as:

Equation 14: The effectiveness of the IHE

$$\xi = \frac{T_o - T_i}{T_{LCZ} - T_i}$$

Where:

ξ = the effectiveness of the IHE (dimensionless)

T_{LCZ}= the average temperature of the LCZ layer (°C)

3. RESULTS AND DISCUSSION

In this work, the experimental days for each month were selected to be from 15th to 20th for January, 13th to 18th for April and 12th to 17th for July. The variation of the average values of density at the different depths within the solar pond during the five days of each month is depicted in Figure 3. It is obvious that, the density profile of the different inner zones of solar pond before the heat extraction would take the salinity gradient profile shape of the SGSP after the experiment's days of every month. From Figure 3, the average values of density at the UCZ were increased from 1001 kg/m^3 at the beginning of the experiment to reach about 1008, 1016 and 1028 kg/m^3 at January, April and July, respectively, while this value was decreased from 1171 kg/m^3 "'i.e. Initial density" at the LCZ to reach about 1145, 1159 and 1164 kg/m^3 at the mentioned months, respectively. This was attributed to the salt movement from the LCZ to UCZ through the NCZ; either by the evaporation effect at the UCZ during the summer season or by the wind effect in the winter season.Thus, it is necessary to maintain the NCZ layers in stable state and far away from salt diffusion.

Regarding the temperature profile before the heat extraction, the average values of the temperature were increased markedly with pond's depth and would take a shape like the SGSP's temperature profile as seen in Figure 4. It was noticed that, the average temperature of the middle layers in the NCZ were relatively higher than the temperature at the upper interface of this zone for months of January, April and July, whereas the average temperatures at the lower interface of the NCZ were very close to the temperatures of the LCZ .This means that, a portion of the incident solar radiation is absorbed and accumulated as a heat in the NCZ, but this heat may be subjected to lose over the time by conduction to the UCZ through the

upper interface region due to the high difference of temperature. On the other hand, due to the small difference of temperature at the lower interface region of the NCZ, this region and the LCZ would be more stable.
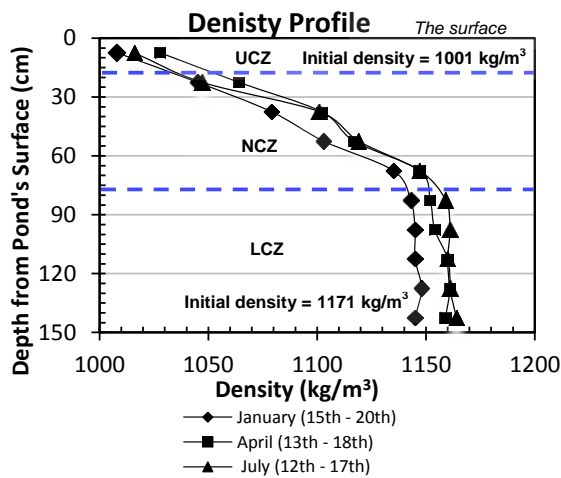

Figure 3: The average values of density at the inner zones of the SGSP for the experiment's months
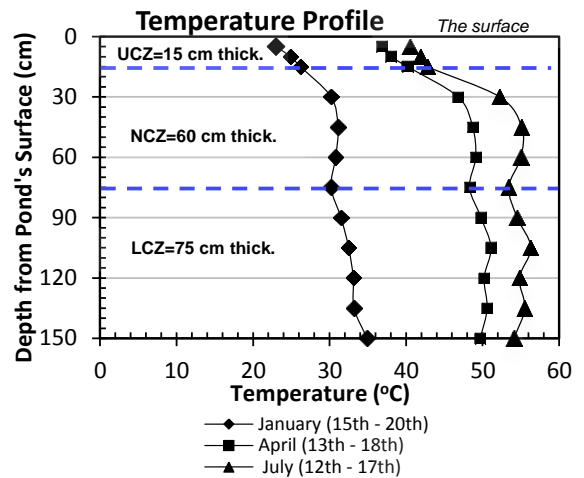

Figure 4: The average values of temperature at the inner zones of the SGSP before heat extraction

Generally, the values of temperature in the pond were varied from month to another depending up on the solar radiation flux (SRF) that measured by the weather station during the experiment's periods, as depicted in Figure 5. As seen in Figure 6, it is clear that the average hourly temperatures for each zone of the pond increased progressively by increasing the SRF as well as the temperatures of both the LCZ and NCZ were very close especially in April and July. It was observed that, the average daily temperature at the LCZ were recorded to be 32.4, 49.3 and 53.2°C at average daily ambient temperature of 16.9, 25.4 and 30.6°C for months of January, April and July, respectively.

Before the heat extraction, the calculations of the reflected, absorbed and stored SRF for the solar pond were obtained from the mathematical formulations that mentioned previously. The calculations indicated that, the maximum average incident SRF on pond's surface at noon were about 540.2, 840.4 and 998.6 W/m2 for January, April and July, respectively as seen in Figure 5.These fluxes were travelled to the LCZ to be 151.8, 239.5 and 298.6 W/m2 "i.e. The average through the thickness of layer" for the same months, respectively with total average of 28.8%, whereas the calculations based on the average daily SRF -as shown in Figure7 - indicated that, the incident SRF on the pond's surface of 330.8, 623.1 and 797.4 W/m2 were travelled downwards to the LCZ to be about 104.2, 183 and 239.2 W/m2 for the same months, respectively with total average of 30.23%. So, there is a small difference between the percentage of the average stored SRF in the LCZ based on the incident SRF at noon and that based on the average daily SRF. According to the calculations based on the average daily of SRF, the average penetrated radiation through the surface of pond (I_o) were about 317.8, 610.3 and 781.3 W/m2 for months of January, April and July respectively, thus about 97.4% of the incident SRF on the pond's surface was penetrated to the pond's depth and about 2.6% was reflected to the surroundings.

From Figure 7, the average absorbed SRF in the UCZ just beneath the surface (IXTS) were about 225.7, 442.1 and 567.7 W/m2 for months of January, April and July, respectively, then these values approached to 156.7, 309.8 and 398.33 W/m2 at the bottom of the UCZ (I_u) and to be 104.2, 183.8 and 239.2 W/m2 at the LCZ "i.e. layer average" for the mentioned months, respectively ,where the values of the stored SRF at the pond's bottom surface were about 96.54, 195.59 and 252.19 W/m2 for the same months, respectively as depicted in Figure 8. This means that about 49.6% of the penetrated SRF (I_o) was absorbed by the UCZ solely for the all mentioned months. Before the heat extraction, the collection efficiency of the pond's layers during the months of experiment is depicted in Figure 9. Because the collection efficiency of the LCZ one of the most important indicator that can describe the thermal performance of the pond. The achievable average collection efficiency at the LCZ was about 29.2, 31.4 and 31.6 % for months of January, April and July, respectively. This means that, the average collection efficiency at the LCZ about 30.7% for all months

of the experiment. Generally, the collection efficiency at the LCZ still low due to the large amount of the SRF that absorbed by the UCZ.

The Average Hourly Solar Radiation Fluxes (SRF) and The Ambient Temperature (TMP)

Average daily SRF = 330.8 W/m²
Average SRF at noon=540.2   W/m²

Average daily SRF = 623.1 W/m²
Average SRF at noon=840.4   W/m²

Average daily SRF = 797.4 W/m²
Average SRF at noon=998.6   W/m²

January   April   July

—— SRF (W/m2)   ----- TMP (oC)
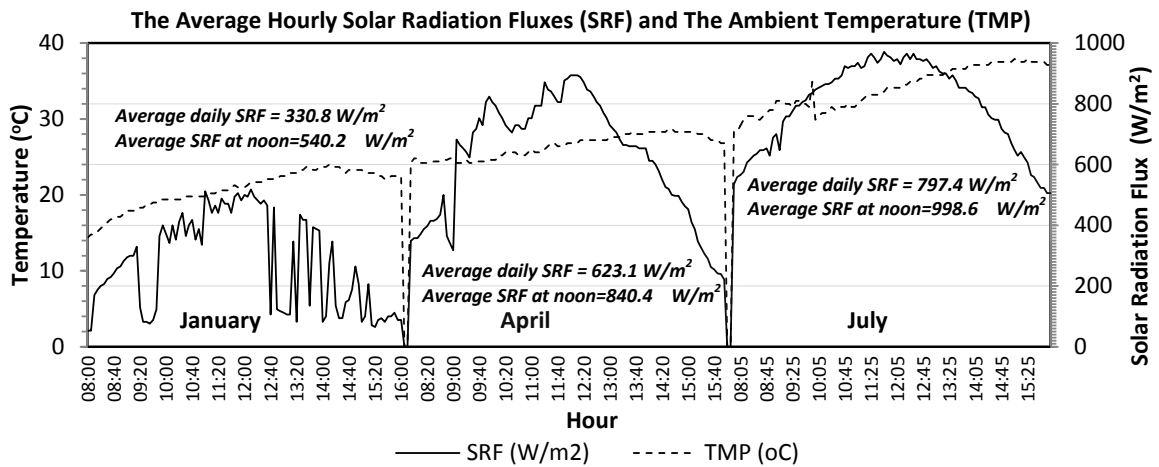
Figure 5: The average daily SRF, average SRF at noon and the TMP for the months of the experiments

Average Hourly Temperatures of The LCZ, NCZ, UCZ and Ambient(TMP) before Heat Extraction

Av. daily LCZ temperature = 32.4 °C
Av. daily Ambient Temperature=16.9 °C

Av. daily LCZ temperature = 49.3°C
Av. daily Ambient Temperature=25.4 °C

Av. daily LCZ temperature = 52.3 °C
Av. daily Ambient Temperature=30.6 °C

January (15ᵗʰ-20ᵗʰ)   *April (13ᵗʰ-18ᵗʰ)*   *July (12ᵗʰ-17ᵗʰ)*

—♦— LCZ   —■— NCZ   —▲— UCZ   —✕— Ambient
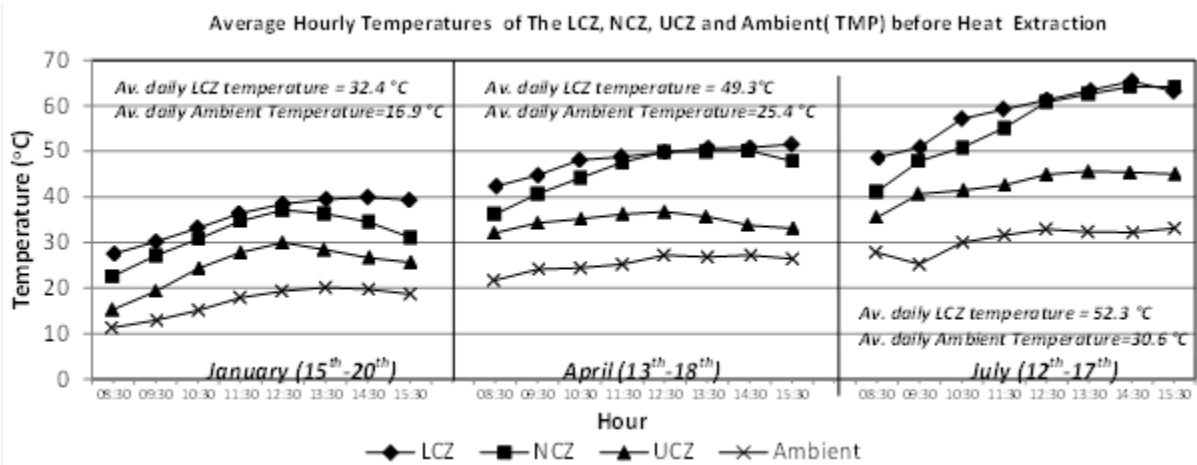
Figure 6: The average hourly temperature of the UCZ,NCZ,LCZ and Ambient for the days of experiment

Average Daily of Solar Radiation Fluxes (SRF)

January   April   July
Months

□ Ih   ■ Io   ▥ IXTS   ▤ Iu   ▦ ILCZ
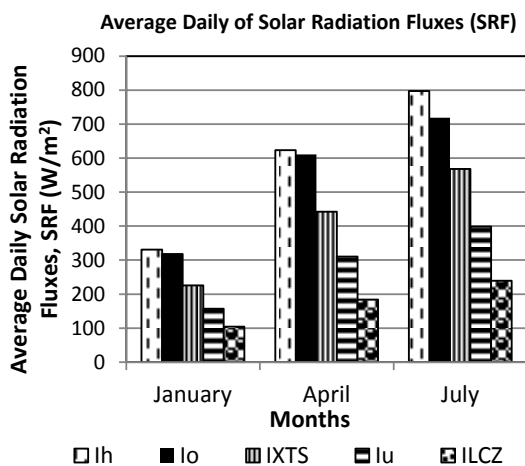
Figure 7: The incident (I_h), penetrated (Io) SRF, the stored radiation beneath surface (I_{XTS}),in UCZ(I_u)and in LCZ (I_{LCZ})

The Stored SRF in The Pond's Zones

The surface
UCZ
NCZ
LCZ

—·— January   ······· April   —— July
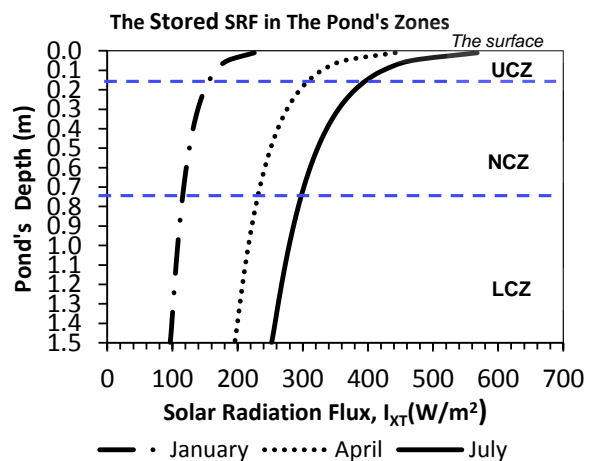
Figure 8: The distribution of the average daily SRF stored in the different depths of the pond

317
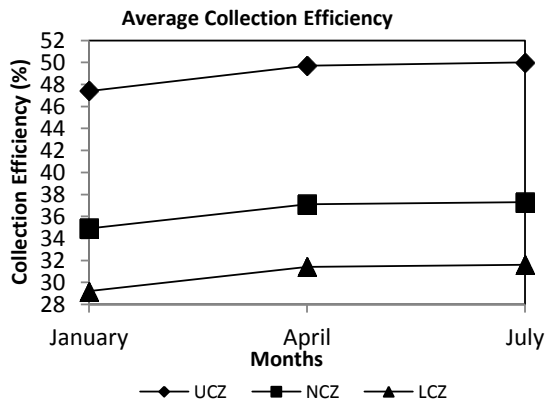
Figure 9: The average collection efficiency of the pond's zones during the experiment's months
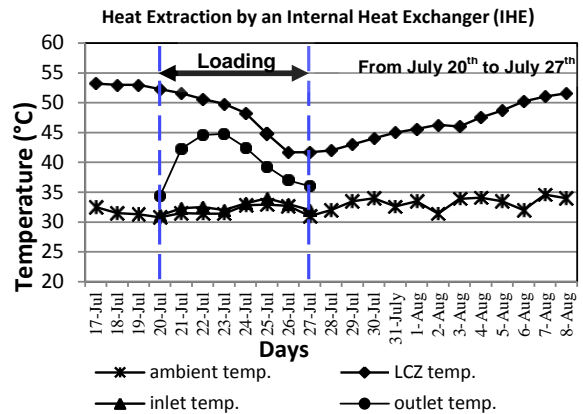
Figure 10: The daily average temperature of the LCZ, ambient ,inlet and outlet of the IHE during the heat extraction
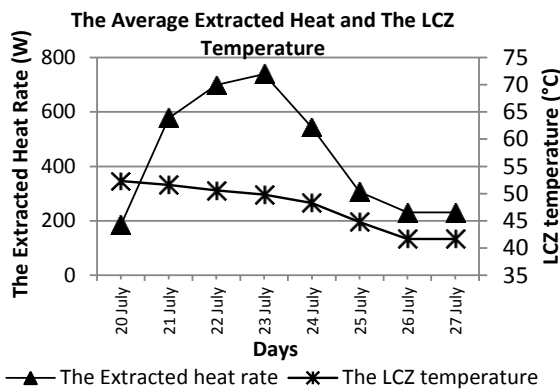
Figure 11: The extracted heat rate and the LCZ temperature during loading period from 20th to 27th of July,2013
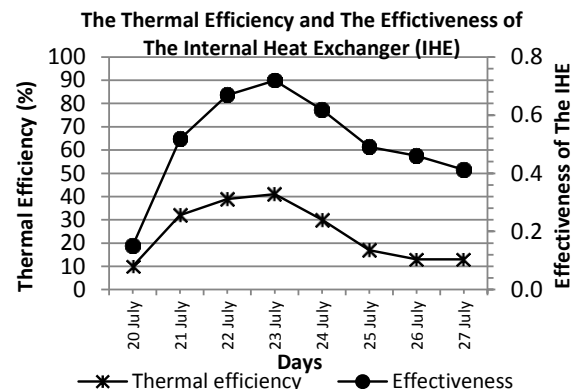
Figure 12: The thermal efficiency of the pond and the IHE effectiveness during loading period

The heat extraction depended upon recirculating the water as heat transfer fluid through a closed loop between the IHE that located at the LCZ and the EHE. The behaviour of the daily average temperatures of LCZ, the fluid's inlet and outlet temperature as well as the ambient are illustrated in Figure 10. It is clear that, the average temperature of the LCZ seems to be constant around 53°C before the heat extraction. In the first four days of the loading period, it was noticed that, the temperature of the LCZ was reduced gradually to be about 48.3° then it dropped to about 41°C in the next two days "i.e. transitional stage" but it tends to be stable at the end of the loading period "i.e. quasi-steady stage" . At the second day after ceasing the loading, the LCZ temperature rose up to 45°C in the next four days then it tends to increase in the next week to be around 52°C. However, the outlet fluid's temperature increased rapidly from about 34.3°C to reach its peak of 44.8°C after the first four days of loading then it decreased till the end of loading.

It was found that, the average inlet fluid's temperatures were - around 33°C- relatively higher than the average ambient temperature which was fluctuated around 31°C during the loading period. Generally, the required minimum difference between the LCZ temperature and inlet fluid's temperature must be about 18 °C to gain a considerable amount of the trapped heat in-pond as well as the fluctuation of the ambient temperature has no clear influence on the LCZ temperature during or after the loading period. From Figure 11, the LCZ temperature decreased steadily during the loading whilst the extracted heat rate increased progressively in the first four days to be about 739 W that corresponding to about 41% and 0.719 for the thermal efficiency and IHE effectiveness, respectively as illustrated in Figure 12. Similarly to trend of LCZ temperature, the extracted heat rate tends to decrease to be about 230.96 W that corresponding to about 13% of thermal efficiency at the seventh day then it would be stable. On the other hand, the IHE effectiveness is reduced to about 0.412 at the end of the loading. Thermally, the solar pond would be exhausted after the seventh day of the heat extraction period and it can be operated with average thermal efficiency of 24.5%, IHE effectiveness of 0.505 and extracted heat rate of 438.3 W.

4. CONCLUSION

The obtained results revealed that, the density of the upper convective zone (UCZ) increased whereas it decreased at the lower convective zone (LCZ) due to the instability of the non-convective zone (NCZ) that caused by the evaporation from UCZ in the summer season and the wind in winter season. The average temperature in the pond was increased with the pond's depth and as the solar radiation flux (SRF) increased. The average daily temperature at the LCZ were about 32.4, 49.3 and 53.2°C at average daily SRF of 330.8, 623.1and 797.4 W/m^2 for months of January, April and July, respectively. The average SRF that stored in the LCZ based on the maximum incident SRF at noon was about 28.8% whilst that based on the average daily SRF was about 30.23% for the mentioned months. About 97.4% of the incident SRF on the pond's surface was penetrated to the pond's depth and about 2.6% was reflected to the surroundings, moreover about 49.6% of the penetrated SRF was absorbed by the UCZ solely. The average collection efficiency at the LCZ was about 30.7% for all months of the experiment. Regarding the summer loading, the minimum temperature difference between the LCZ and inlet fluids must be about 18 °C to gain a considerable amount of the stored heat within the pond. Generally, the solar pond would be exhausted after the seventh day of the heat extraction period and it can be operated with average thermal efficiency of 24.5%, IHE effectiveness of 0.505 and extracted heat rate of 438.3 W.

5. REFERENCES

AL-JUWAYHEL, F., El-Refaee, M.M., 1998.Thermal performance of a combined packed bed-solar pond system-numerical study. *Applied Thermal Engineering*, 18 (12), 1207–1223.

BRYANT, H.C. and Colbeck, I., 1977. A solar pond for London?. *Solar Energy*, 19 (3), 321–322.

CENGEL, Y.A., Özişik, M.N., 1984.Solar radiation absorption in solar ponds. *Solar Energy*, 33 (6), 581–591.

DATE, A., Akbarzadeh, A., 2013.Theoretical study of a new thermodynamic power cycle for thermal water pumping application and its prospects when coupled to a solar pond. *Applied Thermal Engineering*, 58 (1), 511-521.

DATE, A., Yaakob, Y., Date, A., Krishnapillai, S., Akbarzadeh, A., 2013.Heat extraction from Non-Convective and Lower Convective Zones of the solar pond: A transient study. *Solar Energy,* 97 (null issue), 517- 528.

DUFFIE, J.A., Beckman, W.A., 1980.Solar Engineering of Thermal Processes.2nd Edition. New York: John Wiley and Sons, Inc.

HUSAIN, M., Patil, S.R., Samdarshi, S.K., 2004.Simple methods for estimation of radiation flux in solar ponds. *Energy Conversion and Management*, 45 (2), 303–314.

JAEFARZADEH, M.R., 2004.Thermal behavior of a small salinity-gradient solar pond with wall shading effect. Solar Energy, 77 (3), 281–290.

JAEFARZADEH, M.R., 2006.Heat extraction from a salinity-gradient solar pond using in pond heat exchanger. *Applied Thermal Engineering*, 26 (16), 1858–1865.

KARAKILCIK, M., Dincer, I., Rosen, M.A., 2006. Performance investigation of a solar pond. *Applied Thermal Engineering*, 26(7), 727–735.

KARIM, C., Slim, Z., Kais, C., Jomâa, S.M., Akbarzadeh, A., 2010. Experimental study of the salt gradient solar pond stability. *Solar Energy*, 84 (1), 24–31.

LEBLANC, J., Akbarzadeh, A., Andrews, J., Lu, H., Golding, P., 2011.Heat extraction methods from salinity-gradient solar ponds and introduction of a novel system of heat extraction for improved efficiency. *Solar Energy*, 85 (12), 3103–3142.

SAKHRIEH, A., Al-Salaymeh, A., 2013.Experimental and numerical investigations of salt gradient solar pond under Jordanian climate conditions. *Energy Conversion and Management*, 65, 725-728.

SEZAI, I., Taşdemiroğlu, E., 1995.Effect of bottom reflectivity on ground heat losses for solar ponds. *Solar Energy*, 55 (4), 311-319.

SINGH, R., Tundee, S., Akbarzadeh, A., 2011. Electric power generation from solar pond using combined thermosyphon and thermoelectric modules. *Solar Energy*, 85 (2), 371-378.

SUBHAKAR, D., Srinivasa Murthy, S., 1993.Saturated solar ponds: 2. parametric studies. *Solar Energy*, 50 (4), 307-319.

WANG, Y.F., Akbarzadeh, A., 1983.A parametric study on solar ponds. *Solar Energy*, 30 (6), 555-562.

311: Performance evaluation of photovoltaic panel integrated with compound parabolic concentrator (CPC) installed in hot arid area

MOHAMED S. YOUSEF [1], ALI K. ABDELRAHMAN[1], S A. NADA[2] AND S. OOKAWARA[3]

[1] *Energy Resources Engineering Department, Egypt- Japan University of Science and Technology (E-JUST), Alexandria, Egypt, mohamed.mohamed@ejust.edu.eg*
[2] *Department of Mechanical Engineering, Benha Faculty of Engineering, Benha University, Benha, Egypt, samehnadar@yahoo.com*
[3] *Department of Chemical Engineering, Graduate School of Science and Engineering, Tokyo Institute of Technology, Tokyo, Japan, sokawara@chemeng.titech.ac.jp*

Egypt is facing energy crisis despite of the development in every consumption sector. Hence, a search for the efficient utilization of renewable energy, specially the solar energy is a must. The aim of the present work is experimentally and numerically investigating the performance of the photovoltaic (PV) panel integrated with truncated symmetric compound parabolic concentrator (CPC) in hot arid area. For the sake of the experimental work, symmetric CPC with geometrical concentration ratio of (2.4X) has been designed, fabricated and tested. Experiments have been conducted outdoors on the roof top of the Energy Resources Engineering (ERE) building at Egypt-Japan University of Science and Technology (E-JUST) in new Borg El-Arab city, Alexandria, Egypt (Longitude/Latitude: E 029º 42´ / N 30º 55´). A detailed thermal/electrical analytical model was developed and numerically solved using MATLAB software environment to calculate the thermal and electrical performance parameters of the (PV-CPC) system. The Numerical results were in a good agreement with the experimental results. Results showed that PV maximum power was enhanced by 18 % with CPC compared to the non-concentrating one. Although, the results indicate that concentration increases short circuit current (Isc) by 32%, it decreases open circuit voltage (Voc) by 5%. Finally, the proposed (PV-CPC) system yielded promising results in both increasing electrical power production with low cost and provide an advantage for building-integrated PV systems. The study recommends using proper cooling system for further performance enhancement and effective operation of the (PV-CPC).

Keywords: Photovoltaic panel, Compound parabolic concentrator (CPC), Thermal-electrical model, Experimental, Numerical.

1. INTRODUCTION

In Egypt, Solar energy is currently considered the cleanest and the most abundant renewable energy source available to solve the problem of fossil fuel depletion and the dramatically increasing of electrical demand. Therefore, solar energy utilization has become more necessary. Electrical power can be generated from solar energy either by a direct conversion into electrical power by using photovoltaic (PV) technology or by converting it into thermal energy, then to electrical power. The direct conversion of solar radiation into electrical energy through PV technology is still the most suitable and economical way of utilizing solar energy in electric power generation. The widespread of using PV in electric power generation from solar energy is still relatively restricted due to its prohibitively high cost and the needed large areas. Using concentrating photovoltaic technology (CPV) technology has recently appeared to be the best approach to reduce the initial cost of solar PV cells by concentrating solar radiation into a smaller area with less- expensive reflectors. Many researchers have extensively investigated different types of solar concentrators used in CPV technology such as V-trough concentrator and compound parabolic concentrator (CPC). The CPC solar concentrators are considered the most suitable and efficient one for cost saving of electricity production by PV systems. In addition, the CPC concentrators can be utilized indifferent ways such as solar thermal applications, building integrated photovoltaic systems and advantage of the ability to collect solar radiation through large acceptance angle for stationary operation without need for tracking system is encouraging particularly for low concentration systems. Based on these concepts, (Mallick et al. 2004) performed experimental studies on photovoltaic modules equipped with designed an asymmetric compound parabolic photovoltaic concentrator. Although the theoretical geometric concentration ratio of CPC was 2 sun, the maximum output power increased only by 62%. This was attributed to a combination of optical and electrical resistance losses. (Hatwaambo et al. 2008) studied three different low-cost reflector materials, micro reflectors, rolled aluminum foil and anodized aluminum in a low concentrating (PV-CPC) system with a geometrical concentration ratio of 3.6 to concentrate solar radiation across a small module area and reduce the PV module cost. Nevertheless, the results revealed that the short-circuit current increased within a factor of 2.4, the fill factor decreased by 10% under the proposed concentration system due to non-uniform illumination that leads to increase in the resistive losses in the module. They concluded that the rolled aluminum reflector among other's reflector materials had a potential for the use as a PV – CPC reflector for cost reduction. The thermal performance of the evacuated CPC solar collector with a cylindrical receiver has been investigated by (Kim, Han, and Seo 2008) .They numerically presented a comparative study between stationary CPC solar collector and single axis tracking CPC solar collector. Results demonstrated that the thermal efficiency of the tracking CPC solar collector was 14.9% higher than that of the stationary CPC solar collector. (Hedayatizadeh et al. 2013) investigated numerically the thermal and electrical performances of a photovoltaic/thermal water collector integrated with a CPC system with a concentration ratio of 2 sun. They reported that the (PV/T-CPC) integrating system has a considerably positive impact on the thermal and electrical performance of the system. Simulation results were validated with previous experimental data from the literature and a good agreement was achieved. Finally, they presented parametric studies to study the effects of different factors on the thermal and electrical efficiency of the system such as solar radiation, mass flow rate, inlet water temperature and wind speed. (Sellami and Mallick 2013) studied experimentally and numerically the optical efficiency of a PV crossed compound parabolic concentrator (CCPC) system. Results demonstrated that the CCPC system with a concentration ratio of 3.6 provided promising results compared to a 3-D Compound Parabolic Concentrator (CPC) for the use as a static solar concentrator. Numerical results were validated against experimental measurements where a fair agreement was achieved. (Guiqiang et al. 2014) designed and investigated a stationary lens-walled compound parabolic concentrator (CPC) with air gap. They reported that the lens-walled CPC with air gap increases optical efficiency by more than 10% compared with the original lens-walled CPC. Recently, (H. M. Bahaidarah et al. 2014) investigated experimentally and numerically the performance of flat PV string and PV–CPC systems. They presented a comparative study of the two systems with and without cooling. Results revealed that cooling had a significant impact on the output maximum power for the two systems where the maximum power output of the PV–CPC system with cooling was about two times the power of PV module without cooling. Numerical results were compared with experimental data and a good agreement was obtained.

The above literature shows that few studies have investigated the effect of the different operating, design and geometric parameters on the performance of PV panel integrated with CPC collector, however studies for hot arid area are very limited. It is believed that the performance of the PV panel integrated with CPC collector strongly affected by the ambient conditions of the hot arid zones. Therefore, the present study aims to investigate, experimentally and numerically, the performance of the photovoltaic PV panel integrated with truncated symmetric compound parabolic concentrator (CPC) under the conditions of hot arid area. Symmetric CPC with geometrical concentration ratio of (2.4X) has been designed, fabricated and

tested. Moreover, thermal and electrical models are developed using MATLAB software environment to validate the experimental measurements.

2. NUMERICAL MODEL

A schematic diagram and cross- sectional view of the PV-CPC system are shown in Fig. 1. Figure 1 also shows the dimension of the PV panel and the considered elemental length (dx) of the panel for modelling. The geometric and physical specifications of the PV-CPC collector as well as the climatic and operating parameters considered in this study are given in Table 1. The following assumptions have been considered during developing the proposed numerical model (**H. M. Bahaidarah et al. 2014**) : (1) the transmissivity of ethyl vinyl acetate (EVA) is 100%, (2) quasi-steady-state condition is considered for the system, (3) the mean temperature of each layer of PV panel is considered in the analysis, (4) temperatures variation along the thickness and width of the cell layers are negligible, (5) The CPC trough is free from fabrication errors.
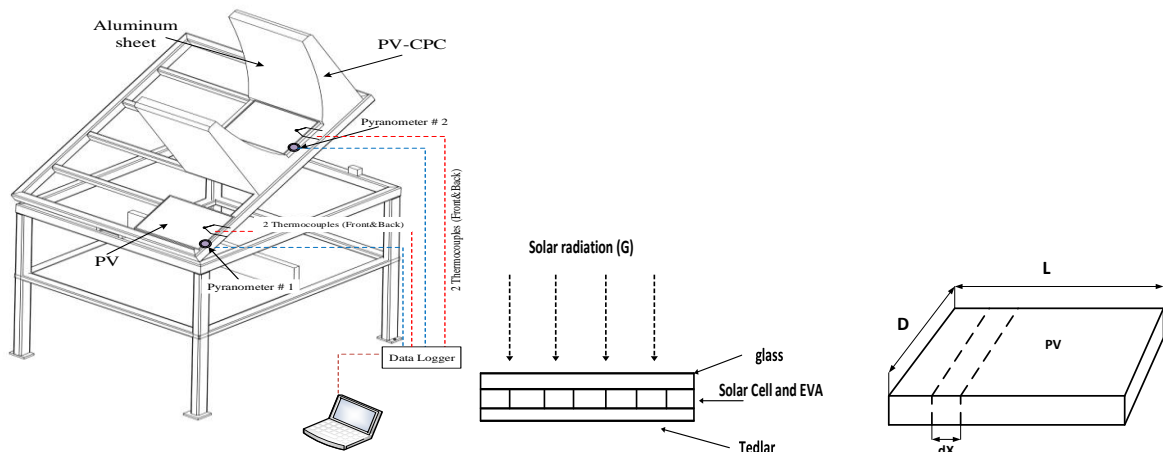
Figure 34: Schematic diagram and cross-sectional view of a (PV-CPC) collector

Table 16: The Values of Climatic, Operating and Design Parameters of the system.

Module type	Polycrystalline (ICO-SPC-10 W)
The length of PV module, L1	0.35 m
The width of PV module, L2	0.245 m
The number of modules in series per string, Nm	1
The number of cells in series in the module, NC	36
The short-circuit current at the reference conditions, $I_{SC,ref}$	o.61 A
The open-circuit voltage at the reference conditions, $V_{OC,ref}$	22.41 V
The maximum power point current at the reference conditions, $I_{mp,ref}$	0.56 A
The maximum power point voltage at the reference conditions, $V_{mp,ref}$	17.9 V
The solar cell temperature at reference conditions, $T_{SC,ref}$	298.15 K
The electrical efficiency at the reference conditions, η_{e1}	12 %
The current temperature coefficient, μ_{Isc}	(.010+/- 0.01) %/ ℃
The voltage temperature coefficient, β	- (0.38 +/-0.01) %/ ℃

2.1 Thermal model

Energy balance principle for the components of a (PV-CPC) collector is applied to calculate the cell and back temperatures. Figure 2 gives the thermal resistant circuit of the different sections of the PV system. The energy balance equations for the overall Glass-Tedlar PV Module reveals that the rate of absorbed

solar energy by solar cell and tedlar equals the sum of overall heat loss from the system. The components of the heat losses are (i) heat loss from the top surface of PV cell to ambient, (ii) heat transfer from PV cell to the back surface of panel, and (iii) the rate of electrical energy produced.
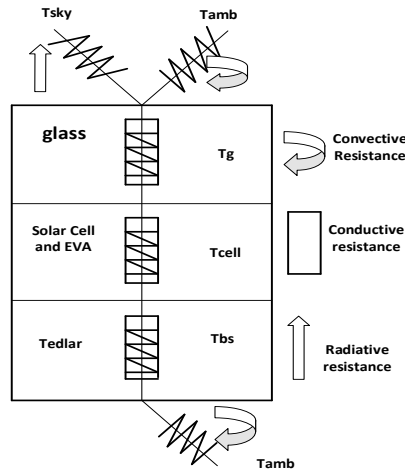
Figure 35: Thermal resistance circuit diagram for a PV-CPC collector

The proof of governing equations on the thermal analysis of PV-CPC collector is not included to have a brief note. More details of the derivation of governing equations are found in (Hedayatizadeh et al. 2013).

The solar cell temperature as a function of back surface temperature of PV panel can be given as:

$$T_{sc} = \frac{(\alpha\tau)_{eff}G + U_t T_{amb} + U_T T_{bs}}{U_T + U_t} \tag{8}$$

The module back surface temperature is given as:

$$T_{bs} = \frac{\left[h_{p1}(\alpha\tau)_{eff}G + U_{tT}T_{amb} + U_b T_{amb}\right]}{U_b + U_{tT}} \tag{9}$$

2.2 Electrical Model

The Five-parameter photovoltaic model by (De Soto, Klein, and Beckman 2006) is utilized in this study for the estimation of the electrical parameters. The solar PV cell is represented by an equivalent electrical circuit which describes the cell as a diode as shown in Fig. 3 and Eq. 3.
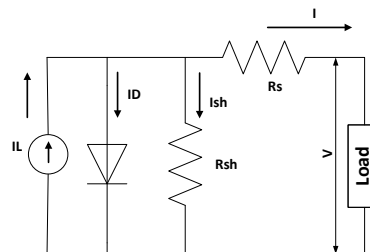
$$I = I_L - I_o\left[\exp\left(\frac{V + I.R_S}{a}\right) - 1\right] - \frac{(V + I.R_S)}{R_{sh}}$$

Equation 10: an equivalent electrical circuit of PV module cell

Figure 36 : Equivalent circuit of a PV

Where:

I, V = Current and voltage at load (A , V)

α = ideality factor

I_L = light current (A)

I_o = diode reverse saturation (A)

R_S = series resistance (ohm)

R_{Sh} = shunt resistance (ohm)

The proof of governing equations on the electrical model of PV-CPC collector is not mentioned to have a brief note. More details of the calculation of five parameters are found in (De Soto, Klein, and Beckman 2006) . The value of five parameters (α_{ref}, $I_{L, ref}$, $I_{o, ref}$, $R_{S, ref}$ and $R_{Sh, ref}$) are obtained by solving five non-linear equations at reference conditions ($G_{, ref}$ =1000 W/m^2, $T_{amb, ref}$ = 25 C°). Next, the five parameters at new climate and operating conditions ($G_{, new}$, $T_{cell, new}$) are calculated (Sobhnamayan et al. 2014).

The maximum power current (I_{mp}) and voltage (V_{mp}) are obtained by simultaneously solving the following equations utilizing the electrical parameters calculated as (H. Bahaidarah et al. 2013):

$$\frac{I_{mp}}{V_{mp}} = \frac{\frac{I_O}{a}\exp\left(\frac{V_{mp}+I_{mp}R_S}{a}\right)}{1+\frac{R_S}{R_{Sh}}+\frac{I_O R_S}{a}\exp\left(\frac{V_{mp}+I_{mp}R_S}{a}\right)} \qquad (11)$$

$$I_{mp} = I_L - I_O\left[\exp\left(\frac{V_{mp}+I_{mp}R_S}{a}\right)-1\right]-\left[\frac{V_{mp}+I_{mp}R_S}{R_{Sh}}\right] \qquad (12)$$

The maximum power (P_{mp}) extracted from the module and maximum power point efficiency (η_{mp}) can be estimated from:

$$P_{mp} = I_{mp}V_{mp} \qquad (13)$$

$$\eta_{mp} = \frac{I_{mp}V_{mp}}{G A_m} \qquad (14)$$

3. EXPERIMENTAL SETUP AND PROCEDURES

An experimental setup has been developed to investigate and evaluate the thermal and electrical performance of PV-CPC system as compared to PV-panel without CPC system. A symmetric 2-dimensional CPC has been designed and fabricated. Mirror aluminum sheets are used as reflecting material for the CPC which has good reflectivity and low cost. A photograph of the experimental setup is shown in Fig. 4 and it consists of the following main components: two identical polycrystalline photovoltaic modules (10W rated power), variable load resistance, CPC concentrator, digital ammeter and weather station. To collect the maximum amount of solar radiation, the tilt angles of the two PV modules and reflectors are selected to be equal the latitude. The PV-CPC trough and PV module were positioned on East-west axis with the aperture tilted 30° from the horizontal toward south. In order to measure the daily global solar radiation incident on the two panels in W/m^2, two pyranometer are used. One for the reference PV panel, and the other for the concentration one. The first one was attached beside the reference module whereas the other pyranometer was attached inside the concentrator beside the concentrated panel. The solar cell front and back temperatures were measured using four standard type K thermocouples attached on the front and at the rear of the panels. Two thermocouples are installed on the front surface of the two modules and the other two are installed on the rear surface of the modules. Wind speed and ambient temperature were measured by Port Log weather station installed beside the proposed system as shown in Fig. 5. Measuring output maximum voltage and current were done manually by utilizing the variation of an Ohmic load. The experimental measurements were recorded every one hour from 08:00 AM to 04:00 PM during a clear day (2nd of March 2015) on the roof top of the Energy Resources Engineering (ERE) department building at Egypt-Japan University of Science and Technology (E-JUST) in new Borg El-Arab city, Alexandria-Egypt.

Figure 37: *a photograph of Experimental setup*

Figure 5: *a photograph of the portable meteorological weather station*

4. RESULTS AND DISCUSSION

4.1 Daily variation of climatic conditions

Climate conditions such as ambient temperature and wind velocity have a great impact on the performance of PV system. The hourly variations of the wind speed and ambient temperature during the test day are shown in Fig 6. Maximum ambient temperature at noon time, daily average temperature and the daily average wind speed were found to be 23℃, 19℃ and 1.4 m/s, respectively.
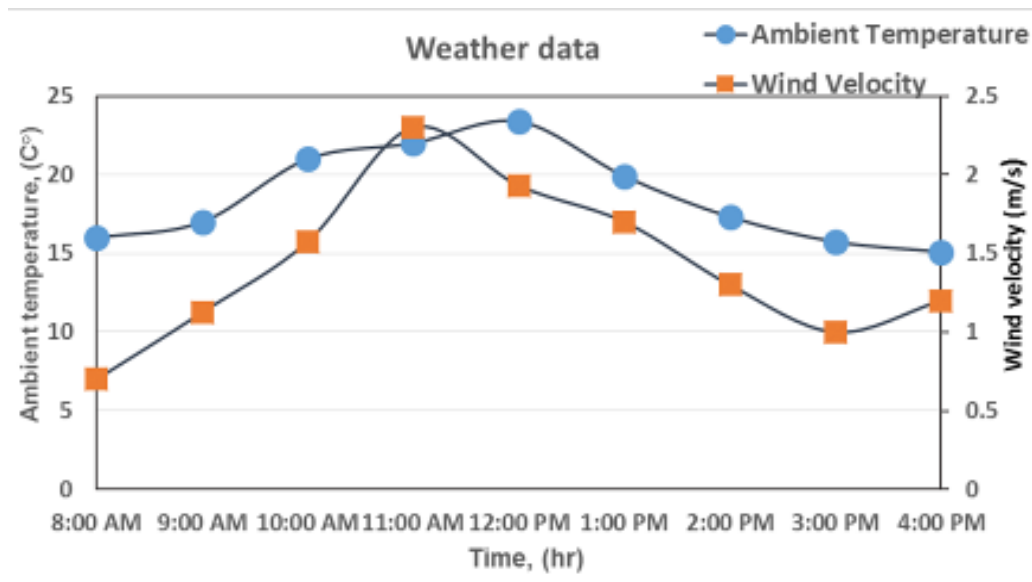
Figure 38: *Variation of ambient temperature and wind velocity during the day*

4.2 Numerical results

The variations of front and back cell temperatures of flat PV module and PV–CPC system are shown in Fig 7. The measured solar radiation for both systems also superimposed on the figure. As expected, the figures indicate that the front cell temperature is always bigger than the back cell temperature and the cell temperatures increase with the increase of solar intensity. The maximum cell temperature occurs at noon (12:00 PM) when the solar intensity is peak. The maximum front and back cell temperatures of PV– CPC system are about 79°C and 69°C, respectively, while those for flat PV module are about 51°C and 45°C, respectively. This indicates that the cell temperature increases as the amount of absorbed radiation increases.
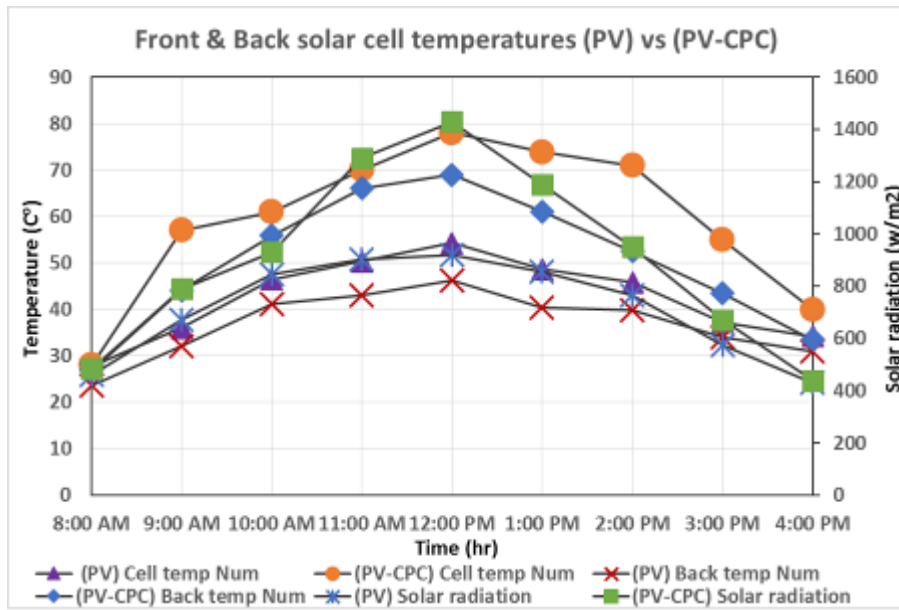
Figure 39: Variations of front and back solar cell temperatures for the two systems

The effect of using CPC concentration system on the short circuit current and open circuit voltage of the PV module are shown in Fig. 8. The figure shows the increase of the short circuit current with increasing the measured solar radiation for both systems. A maximum short circuit current of 0.96 A is obtained with the use of the concentration system at 12:00 PM when the maximum solar intensity was achieved. However, the maximum short circuit current is 0.59 A at the same time for PV without CPC. This reveals that using CPC system increases the short current system by about 70 %. The increase of the short circuit current with using CPC system can be attributed to the increase of the solar radiation received by the PV-CPC system as compared to the flat PV system and to the linearity relation between short circuit current and radiation along the day. In case of open circuit voltage, a minimum open circuit voltage of 18.6 V is obtained with the use of concentration system at noon (12:00 PM) when the maximum solar intensity was achieved. However, the minimum open circuit voltage is 20.1V was achieved at the same time by PV modules without CPC concentration. This reveals that using CPC concentration system reduces the open circuit voltage from PV module by 8%. The decrease of the open circuit voltage by using CPC concentration system can be attributed to the increase in module temperature (see Fig. 7).
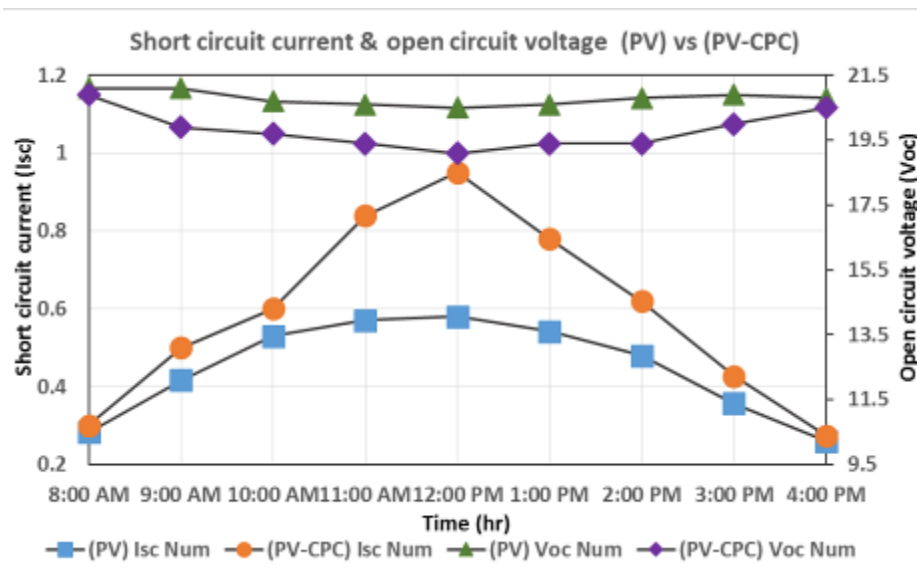
Figure 40: Variations of short circuit current and open circuit voltage for the two systems

Fig. 9 shows the variation of the electrical power and the electrical efficiencies along the day time for both flat PV panel and the PV–CPC system. It is clearly shown from the figure that the power outputs of the PV system and PV-CPC system are peaks at 12:00 PM when the maximum solar intensity was achieved. Also, it can be seen from the figure that at any time the PV–CPC system produces higher power compared to

flat PV panel for the same ambient conditions. The improvement in power produced due to using CPC system increases with increasing the solar intensity. The results reveals that the daily average and maximum power output s of the CPC system obtained at the noon time are higher than those obtained by the flat PV panel by about 18% and 50%, respectively. In case of electrical efficiency. It is clearly shown that the (PV-CPC) system has lower electrical efficiency than the flat PV system. A minimum electrical efficiency of 9.6 % was obtained with the use of the proposed concentration system at noon (12:00 PM) when the solar radiation is maximum. However, the minimum electrical efficiency was 10.7 for PV systems without concentration at the same time. This may be attributed to that the increase of the module losses with the increase of the module temperature which increases with the increase of the absorbed solar radiation. This makes the rate of increase in power of the (PV-CPC) system is lower than the rate of increase in absorbed radiation as the increase in solar radiation is about 30 % due to using concentration system while the increase in the output power was about 18 %. Therefore, it can be concluded that the efficiency of the proposed CPC concentrating system is lower than the flat PV system.

It is should to be noted that the CPC used in this experiment had a theoretical concentration ratio of 2.4, hence, the output maximum power of the (PV-CPC) system was expected to increase by a factor of 2.4. However, the results in fig (9) showed that the output power with using the CPC trough increased by about (18%). This may be attributed to more than one factor. Firstly, the increase in power output due to high concentration is not directly proportional with the solar radiation concentration due to increased ohmic losses in the module. Secondly, high cell temperatures observed by the (PV-CPC) system results in a lower open-circuit voltage as previously mentioned in figure (8). Finally, the observed non-uniform illumination and optical losses which would cause high ohmic losses and produce internal current flow which has negative impact on the panel efficiency.
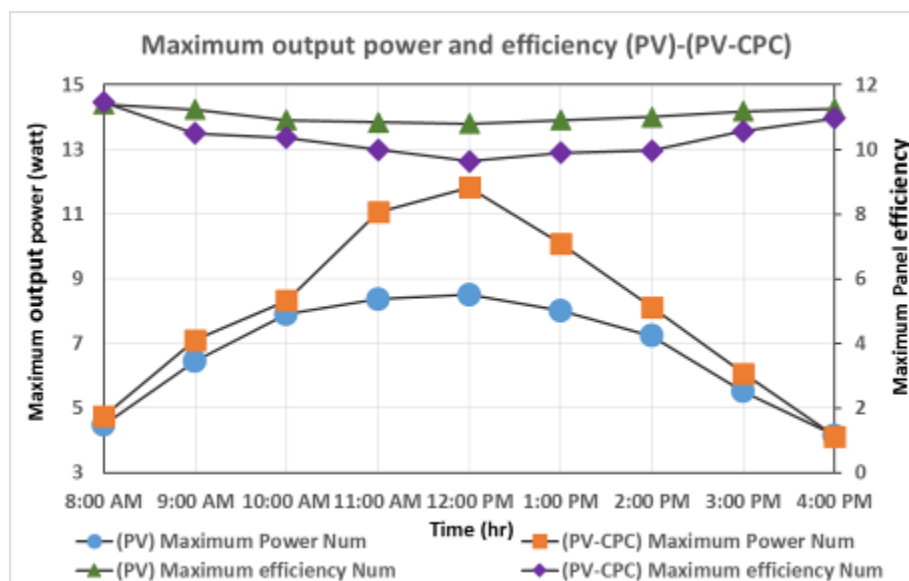
Figure 41: Variations of maximum power point and electrical efficiency for the two systems

4.3 Model validation and comparison between numerical and experimental results

In order to validate the numerical model, the model results are verified with the measured experimental data for both of CPC and flat PV systems. The correlation coefficient (r) and the root mean square percent deviation (e) defined by the following equations are used as measurable of agreements between the numerical and experimental results (H. Bahaidarah et al. 2013) :

$$RMSE(e) = \sqrt{\frac{\sum\left[100 \times \left(X_{\exp,i} - X_{sim,i}\right)/X_{\exp,i}\right]^2}{n}} \qquad (15)$$

$$r = \frac{n\left(\sum X_{\exp} \cdot X_{sim}\right) - \left(\sum X_{\exp}\right) \cdot \left(\sum X_{sim}\right)}{\sqrt{n \cdot \left(X_{\exp}^2\right) - \left(\sum X_{\exp}\right)^2} \sqrt{n \cdot \left(X_{sim}^2\right) - \left(\sum X_{sim}\right)^2}} \qquad (16)$$

Where:

X_{exp} = the values of the experimentally measured parameters

X_{sim} = the values of the numerically estimated parameters

n = the number of the experiments data points.

In order to have a brief note, the comparison of numerical and experimental results for modules temperatures, and modules efficiencies only are shown in figures 10 and 11, however the correlation coefficient (r) and the root mean square percent deviation (e) of these comparison are given in Table 2. Figures [10, 11] and Table 2 show that the numerical results are in a good agreement with the experimental results for all of the parameters.

Table 17: Validation of numerical model

Parameter	PV System		PV-CPC System	
	correlation coefficient (r)	*Root Mean square percent deviation (e)*	*correlation coefficient (r)*	*Root Mean square percent deviation (e)*
Module front temperature	*0.99*	*2.41*	*0.98*	*5.44*
Module back temperature	*0.98*	*4.1*	*0.96*	*5.1*
Maximum Output power	*0.99*	*1.1*	*0.99*	*1.15*
Module efficiency	*0.89*	*1.25*	*0.97*	*1.9*
Short circuit current	*0.99*	*1.1*	*0.99*	*1.15*
Open circuit voltage	*0.92*	*1.25*	*0.97*	*1.9*
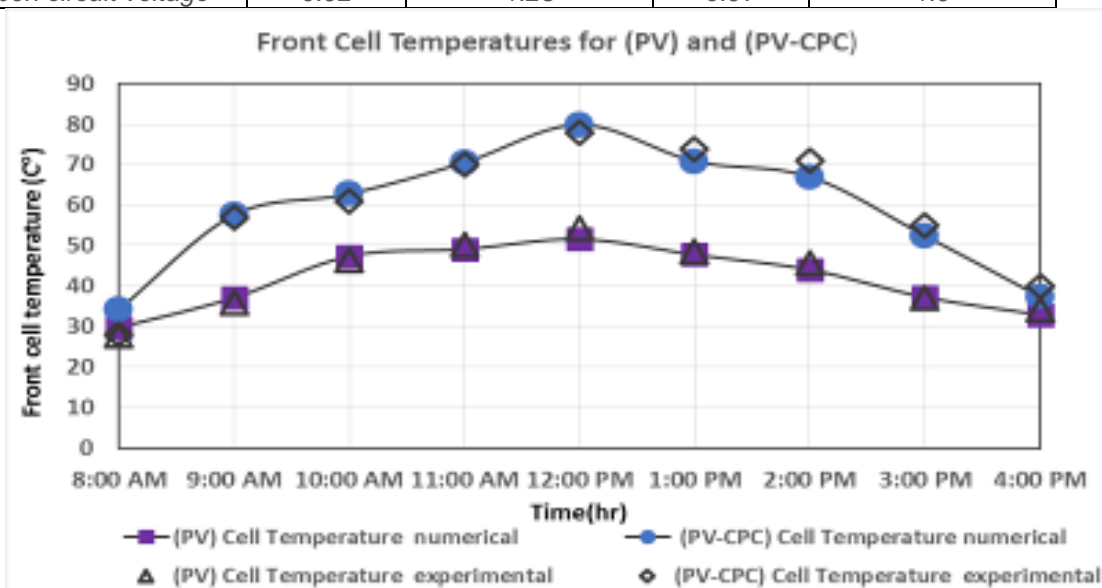
Figure 42: Comparison between numerical and experimental results of Front cell temperatures with and without concentration
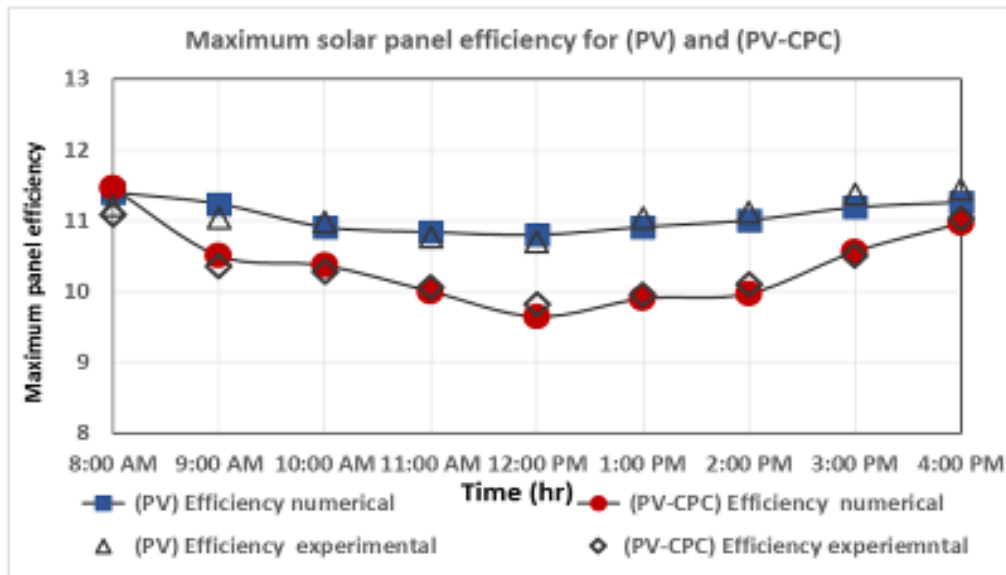
Figure 43: Comparison between numerical and experimental results of maximum output efficiency with and without concentration.

4.4 I-V and P-V curves

Figures 12 shows the average I–V and P-V characteristics values of the two systems obtained from the experimental data. The figure clearly shows that the I–V and P-V curves of the PV-CPC system is higher than that of the PV system without CPC. This reveals that the PV-CPC system provides considerable improvement in the short circuit current and maximum power output with an average increase of 32 % and 18 % respectively. But, it has also a slightly negative impact on the open circuit voltage with an average decrease of 5 %.
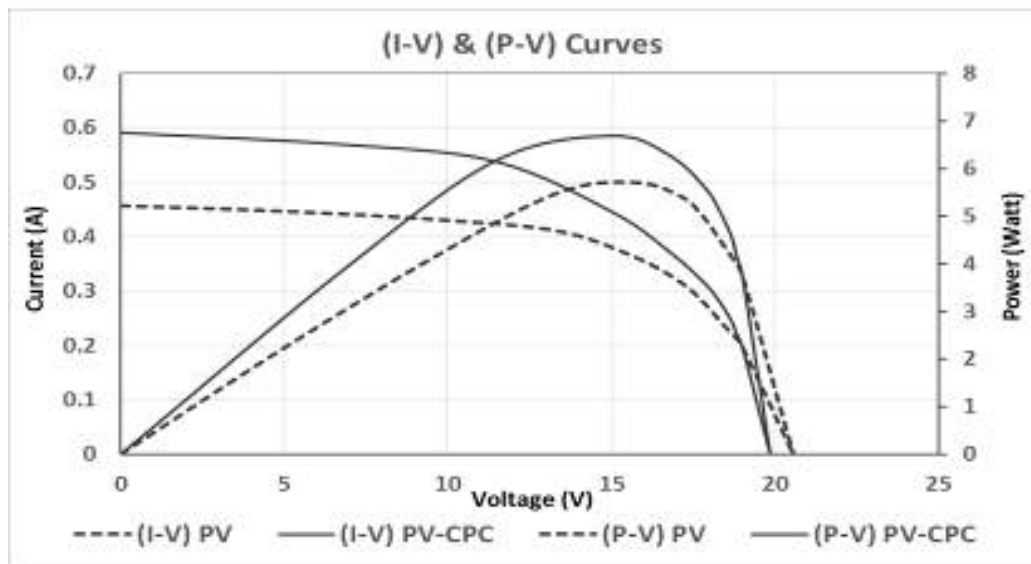
Figure 44: Comparison of (I-V) and (P-V) curves with and without concentration

4. CONCLUSION

Experimental and numerical comparative study has been carried out to study the performance of photovoltaic panel with and without a symmetric compound parabolic concentrator (CPC) in hot arid area. A numerical (thermal and electrical) model has been developed to study different thermal and electrical parameters related to the performance of the proposed system using MATLAB software environment. The results showed that the CPC-PV proposed system is more effective for high levels of solar radiation. In

addition, the system has a considerable positive effect on the maximum output power and the short circuit current with an average increase of 32 % and 18 %, respectively. Conversely, it has a negative impact on open circuit voltage with an average decrease of 5 % due to the higher cell temperature achieved by the system. Numerical results are validated with the experimental results and a good agreement is found. In order to further improve the performance of the (PV-CPC) system, a proper cooling system is recommended. The study reveals that the proposed PV-CPC system can provide a cost effective electrical power generation source integrated with buildings.

5. REFERENCES

BAHAIDARAH, H., Abdul Subhan, P. Gandhidasan, and S. Rehman. 2013. "Performance Evaluation of a PV (photovoltaic) Module by Back Surface Water Cooling for Hot Climatic Conditions." *Energy* 59. Elsevier Ltd: 445–53. doi:10.1016/j.energy.2013.07.050.

BAHAIDARAH, Haitham M., Bilal Tanweer, P. Gandhidasan, Nasiru Ibrahim, and Shafiqur Rehman. 2014. "Experimental and Numerical Study on Non-Concentrating and Symmetric Unglazed Compound Parabolic Photovoltaic Concentration Systems." *Applied Energy* 136. Elsevier Ltd: 527–36. doi:10.1016/j.apenergy.2014.09.060.

DE SOTO, W., S. a. Klein, and W. a. Beckman. 2006. "Improvement and Validation of a Model for Photovoltaic Array Performance." *Solar Energy* 80 (1): 78–88. doi:10.1016/j.solener.2005.06.010.

GUIQIANG, Li, Pei Gang, Su Yuehong, Wang Yunyun, and Ji Jie. 2014. "Design and Investigation of a Novel Lens-Walled Compound Parabolic Concentrator with Air Gap." *Applied Energy* 125. Elsevier Ltd: 21–27. doi:10.1016/j.apenergy.2014.03.042.

HATWAAMBO, Sylvester, Hakan Hakansson, Johan Nilsson, and Bjorn Karlsson. 2008. "Angular Characterization of Low Concentrating PV-CPC Using Low-Cost Reflectors." *Solar Energy Materials and Solar Cells* 92 (11): 1347–51. doi:10.1016/j.solmat.2008.05.008.

HEDAYATIZADEH, M, Y Ajabshirchi, F Sarhaddi, a Safavinejad, S Farahat, and H Chaji. 2013. "Thermal and Electrical Assessment of an Integrated Solar Photovoltaic Thermal (PV/T) Water Collector Equipped with a Compound Parabolic Concentrator (CPC)." *International Journal of Green Energy* 10 (May): 494–522. doi:10.1080/15435075.2012.678524.

KIM, Yong, GuiYoung Han, and Taebeom Seo. 2008. "An Evaluation on Thermal Performance of CPC Solar Collector." *International Communications in Heat and Mass Transfer* 35 (4): 446–57. doi:10.1016/j.icheatmasstransfer.2007.09.007.

MALLICK, T. K., P. C. Eames, T. J. Hyde, and B. Norton. 2004. "The Design and Experimental Characterisation of an Asymmetric Compound Parabolic Photovoltaic Concentrator for Building Fa??ade Integration in the UK." *Solar Energy* 77 (3): 319–27. doi:10.1016/j.solener.2004.05.015.

SELLAMI, Nazmi, and Tapas K. Mallick. 2013. "Optical Efficiency Study of PV Crossed Compound Parabolic Concentrator." *Applied Energy* 102. Elsevier Ltd: 868–76. doi:10.1016/j.apenergy.2012.08.052.

SOBHNAMAYAN, F., F. Sarhaddi, M. a. Alavi, S. Farahat, and J. Yazdanpanahi. 2014. "Optimization of a Solar Photovoltaic Thermal (PV/T) Water Collector Based on Exergy Concept." *Renewable Energy* 68. Elsevier Ltd: 356–65. doi:10.1016/j.renene.2014.01.048.

196: High efficiency absorber with perforated plate for solar air collector

[1]*VINSON ADIDHARMA AUDWINTO, [1]HOY-YEN CHAN,
[2]SINA ENTESHARI, [2]VINESH THIRUCHELVAM

1Solar Energy Research Institute, The National University of Malaysia (UKM),
43600 Bangi, Selangor, MALAYSIA. Email: vinsonaudwinto@gmail.com
2Department of Engineering, Asia Pacific University (APU),
57000 Bukit Jalil, Kuala Lumpur, MALAYSIA

Jet impingement is one of the convective heat transfer methods to transfer heat from a surface to the flowing fluid. This method can be used for many applications as enhancement method to increase the overall performance. The main objective of this research is to study the thermal performance of solar collector under different solar radiation by using jet impingement method.

A solar air collector with jet impingement design was fabricated and tested. A perforated plate of 6mm holes diameter with triangular geometry was designed and installed into the solar air collector. The effect of different irradiance on the rise of temperature was applied to evaluate the thermal performance. The fixed mass flow rate of 0.0076 kg/s was used in the test. It was found that temperature difference between inlet and outlet increases with irradiance. The highest and lowest efficiencies were measured to be 80.40% and 69.60% respectively. From the study, it showed that there are slight increases of thermal efficiency as the solar irradiance increases.

Keywords: Perforated Plate, Jet Impingement, Solar Air Heater, Solar Collector

1. INTRODUCTION

Solar energy is a clean and sustainable energy resource. Due to the increasing cost of fossil fuels and growing distress of global warming, many studies have focused on the applications of solar energy in daily life. The solar air collectors occupy an important place among solar heating systems because of the minimal cost and the direct use of air as the working substance reduces the number of required system components and also can be applied in many applications in space heating and drying agricultural products such as seeds, fruits and vegetables and can also be utilized for heating buildings with auxiliary heaters to save energy in winter-time (Abene et al. 2004; Ammari 2003; Zhao et al. 2011; Sreekumar 2010).

Solar air heater has a simple design and can be fabricated with low cost material. By increasing heat transfer coefficient, it will increase the overall thermal efficiency. Various enhancement methods have been carried out to increase the heat transfer coefficient and also to reduce the heat loss from the absorber. One of them is known as jet impingement solar collector. A simple impinging method was developed in the studied of evaluation of a jet plate solar collector (Choudhury, Garg, and Khas 1991). They found that by using jet impingement method, the performance efficiency of the jet concept air heater is significantly higher than that of the parallel air heater between 10% and 20% depending on the configuration, test condition and flow rate. Therefore, many experimental investigation have been carried out to study the characteristic of the jet impingement including of the effect of jet geometry (Audwinto et al. 2014), jet to jet spacing (Huber & Viskanta 1994), and hole spacing (Belusko et al. 2008).

In the previous investigation, a model of the test rig and perforated plate was developed by Audwinto et.al where the 6mm holes perforated plate was found to achieve the best performance (Audwinto et al. 2014). The present studies, different solar irradiance were applied and their effect on to the test rig was investigated experimentally.

2. MATERIALS AND METHODS

2.1 Experimental Set up

The experiment was carried out indoor by using solar simulator as the light source. It was built with the size of 2mx1m and consists of a total of 35 halogen lamps with individual power of 500 W where voltages controller was used to control the brightness of the solar simulator. As shown in figure 1, perforated plate with size of 99.5cmx68.5cm which have 225 units of holes with the pitch of 40 cm was fabricated.
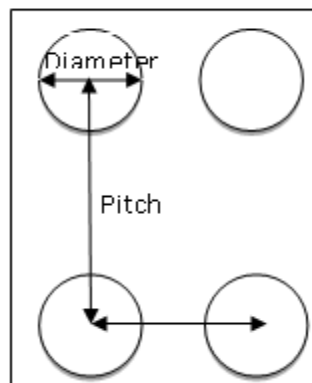
Figure 1: Schematic diagram of perforated plates with square plate design

Absorber plate with the same size as the perforate plate was used in the experiment. A test rig was designed and fabricated as shown in figure 2. It was covered with insulation to prevent heat loss and put on top of the table under the solar simulator where both sides of the test rig were connected to the blower as shown in figure 3.
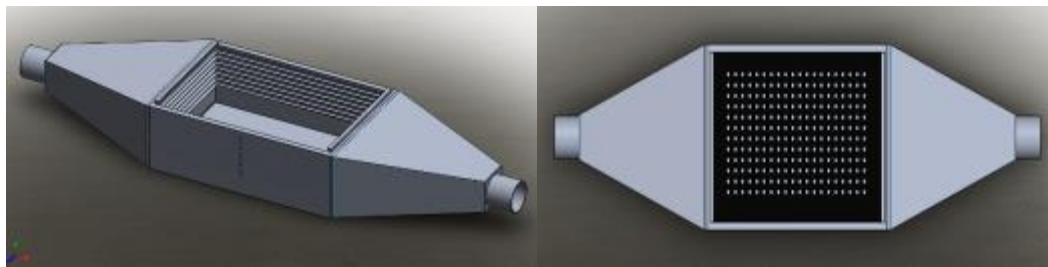
Figure 2: The rig model
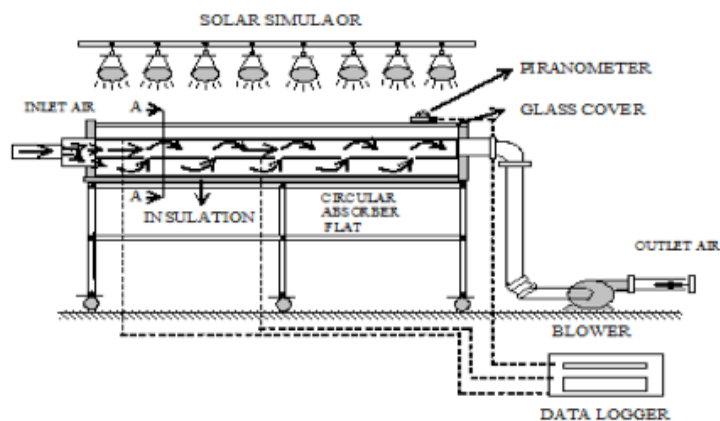
Figure 3: Schematic diagram of a jet impingement solar air collector experimental set up (Audwinto et al. 2014)

2.2 Experimental Procedure

The experiment was conducted under the solar simulator at different irradiance namely; 255, 348, 454, 559, 659, 747, 846, 954 and 1059 W m^{-2}. The flow rate was set to be 0.0076 kg sec^{-1}, the inlet air temperature was maintained at 30 ^{o}C and the jet plate distance was 6 cm. A pyranometer was used to determine the solar irradiance (Wm^{-2}), type-K thermocouple was used to measure the temperature (^{0}C) and Data Taker Series DT80 was used as data acquisition. Lastly the data of the inlet air (T_i), outlet air (T_o), absorber (T_{abs}), upper and lower channel air, jet plate, and glass cover temperatures were collected and analyzed to determine the performance of the solar air collector.

3   DATA ANALYSIS

Jet impingement technology has been an effective method in controlling the fluid flow to increase the convection heat transfer, which directing the air flow go through a nozzle to a target surface as shown in figure 4. This method are widely used in many application such as drying, cooling, and heating (Liu et al. 2014; Amer et al. 2010; Tanda 2011).
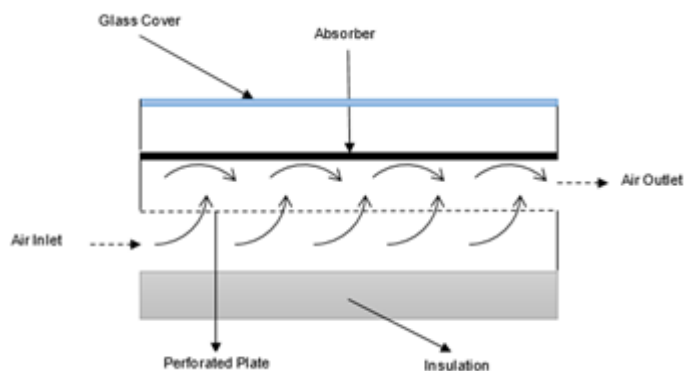
Figure 4: The air flow of the Jet Impingement Solar Air Collector

In this experimental investigation, the thermal performance of the solar air collector was tested indoor under various irradiance. The experimental data were analyzed and shown in the figure 5 and figure 6. From the figure 5 the inlet and outlet temperature difference and the absorber plate temperature increase with irradiance, where the maximum output temperature was found to be 67.9 ^{0}C as shown in figure 6.
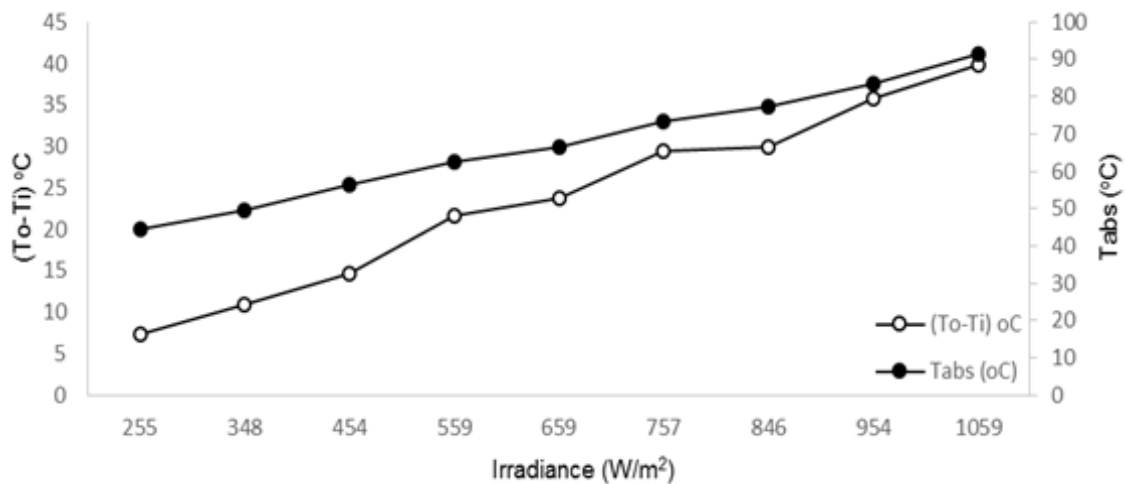
Figure 5: Effect of the irradiance on temperature difference and absorber temperature
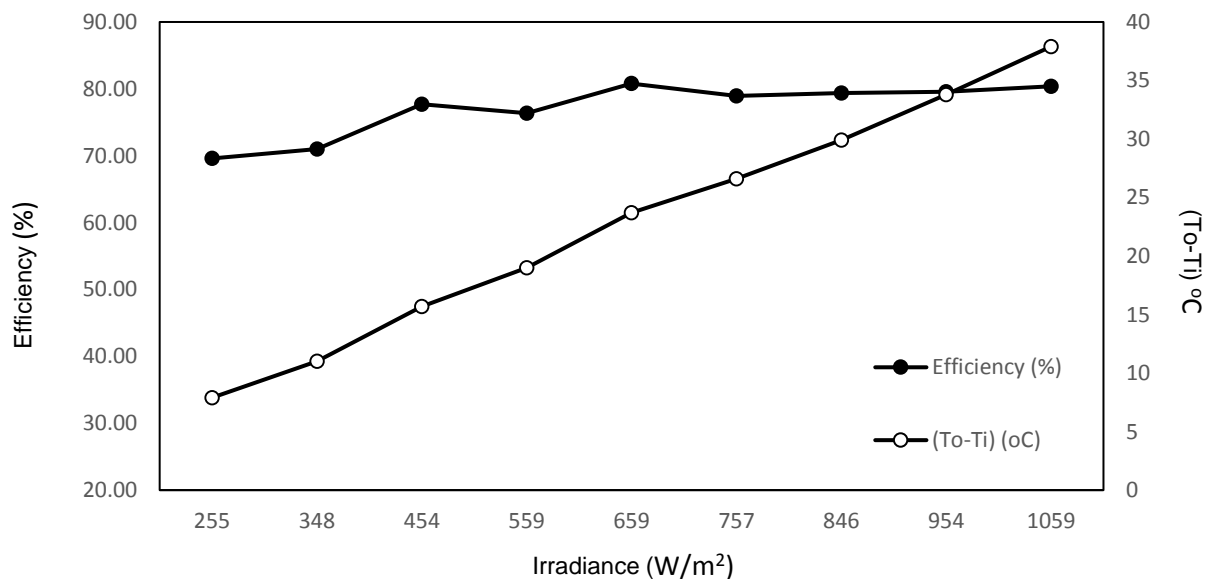
Figure 6: Efficiency and temperature difference against irradiance

The increment of the outlet air temperature is due to the more heat can be extracted from the perforated plate and the absorber plate as the plates temperature increase. Although there is an obvious change in the temperature of solar collector every 100 W/m^2, thermal efficiency is found to be steady ranging from 69.6% to 80.40% as shown in figure 6

4   CONCLUSION

The jet impingement method was studied and analysed in the present investigation showed potential. It is found that the temperature difference increases with the irradiance due to the factor that the air flowing through the impingement extracts the heat from the absorber and the jet plate, where the minimum and maximum of the temperature difference was 7.9 ^{0}C and 37.9 ^{0}C respectively. The highest thermal efficiency achieved by solar air collector is 80.40%. Through this study, it was shown thermal efficiency is not much

affected by the irradiance. Due to this advantage, present design of the solar impingement air collector is suitable for not only the hot climate countries but countries that have low intensity of solar radiation.

5   ACKNOWLEDGEMENT

6   REFERENCES

ABENE, A. et al., 2004. Study of a solar air flat plate collector: use of obstacles and application for the drying of grape. Journal of Food Engineering, 65(1), pp.15–22.

AMER, B.M. a., Hossain, M. a. & Gottschalk, K., 2010. Design and performance evaluation of a new hybrid solar dryer for banana. *Energy Conversion and Management*, 51(4), pp.813–820.

AMMARI, H.D., 2003. A mathematical model of thermal performance of a solar air heater with slats. *Renewable Energy*, 28(10), pp.1597–1615.

AUDWINTO, V.A. et al., 2014. Thermal Analysis of Jet Impingment Solar Air Collector. In *Computer Application in Environmental Sciences and Renewable Energy*. pp. 4–7.

BELUSKO, M., Saman, W. & Bruno, F., 2008. Performance of jet impingement in unglazed air collectors. *Solar Energy*, 82(5), pp.389–398.

CHOUDHURY, C., Garg, H.P. & Khas, H., 1991. Evaluation of Jet Plate Solar Air Heater. , 46(4), pp.199–209.

HUBER, A.M. & Viskanta, R., 1994. Effect of jet-jet spacing on convective heat transfer to confined, impinging arrays of axisymmetric air jets. *International Journal of Heat and Mass Transfer*, 37(18), pp.2859–2869.

LIU, Z. et al., 2014. Numerical simulation on impingement and film composite cooling of blade leading edge model for gas turbine. *Applied Thermal Engineering*, pp.1–12.

SREEKUMAR, a., 2010. Techno-economic analysis of a roof-integrated solar air heating system for drying fruit and vegetables. *Energy Conversion and Management*, 51(11), pp.2230–2238.

TANDA, G., 2011. Performance of solar air heater ducts with different types of ribs on the absorber plate. *Energy*, 36(11), pp.6651–6660.

ZHAO, D.L. et al., 2011. Optimal study of a solar air heating system with pebble bed energy storage. *Energy Conversion and Management*, 52(6), pp.2392–2400.

SESSION 25: BUILDING ENERGY TECHNOLOGIES

11: EcoShopping: energy efficient & cost competitive retrofitting solutions for retail buildings

---

A review of best practice

ANDY LEWRY[1], ED SUTTIE [2]

1 Building Research Establishment (BRE), Watford UK WD25 9XX, LewryA @bre.co.uk
2 Building Research Establishment (BRE), Watford UK WD25 9XX, SuttieE @bre.co.uk

The "EcoShopping" project aims to produce a practical holistic retrofitting solution for commercial buildings, reduce primary energy consumption to less than 80 kWh/(m2.year) and increase the proportion of Renewable Energy Systems (RES) to more than 50% by using state of the art solutions.

The project intends to use and integrate available products and technologies; along with a network to accurately monitor the environmental and occupancy parameters to allow the Building Management System to have better control of the building and fully exploit the thermal mass.

This paper:

– *Introduces the EcoShopping project and the consortium carrying out the work.*

– *Describes the case study building and the initial targets for carbon reduction.*

– *Discusses the results of Work Package 2: which is an assessment of national building codes, Energy Performance Buildings Directive (EPBD) implementation, performance standards and good practice.*

This study identifies that building regulations and their associated codes lay down minimum levels of performance for non-domestic buildings but do not attempt to prompt best practice.

Best practice performance criteria were identified for the majority of technology areas. For such a case study, it is essential that the methodologies are comparable with those already in use and that technologies match or exceed best practice criteria already published. In addition, producing auditable numbers is essential to showing transparency in how the energy savings claimed are justified.

Keywords: ECOSHOPPING: energy efficient, retrofitting, Retail sector, shopping buildings.

1. INTRODUCTION

The "EcoShopping" project (http://ecoshopping-project.eu/) aims to produce a systematic methodology and cost effective solutions for retrofitting commercial buildings. This is to be achieved by improving the insulation and lighting systems; integrating additional RES based HVAC systems; exploiting the building as thermal storage ("mass"); developing an intelligent automation control unit; and improving maintenance and commissioning technologies. The energy efficiency of the commercial building is expected to be enhanced by about 58%.

The "EcoShopping" platform will integrate the existing HVAC systems, such as heating, ventilation, air conditioning, etc.; and interoperate with other ICT- based subsystems (e.g. for security, protection, gas-detection, safety and comfort). The control and management of automation systems will be based on advanced algorithms where the platform will be capable of learning from previous operations and situations. This will be achieved by means of a semi-automatic process of retraining from Internet-based repositories, which allows configuration, personalization and dynamic adaptation to the characteristics of the building and the weather.

The project is budget is 4.10 million €; started in September 2013 with a duration of 4 years, and is co-funded by the European Commission within the 7th Framework Programme. The overall objectives of the project are:

- • To produce a systematic methodology and cost effective retrofitting solutions for commercial buildings by:
  - o Investigating a retrofitting solution with innovative thermal insulation solutions and day-lighting technologies.
  - o Integrating the Intelligent Automation Unit (IAU) concept with a Mobile Robot.
  - o Developing a solution for automatically identifying and predicting failures; and inefficiencies in HVAC system performance.
- • To embody the results in a case study which will:
  - o Demonstrate an RES direct powered DC variable speed heat pump and increase the Building Thermal Mass with a view to reducing the energy consumption.
  - o Target primary energy consumption and reduce to less than 80 kWh/(m^2.year).
  - o Increase the proportion of RES (Renewable Energy Sources) to more than 50%.
- • To carry out a continuous assessment throughout the entire project.

At this point it should be noted that the RES direct powered DC variable speed heat pump is being proposed as a demonstration technology but in itself should perform to the good practice level identified as in work package 2. The phasing of the project is shown in Figure 1 and this paper will introduce the project, the case study and present the results of Work Package 2.
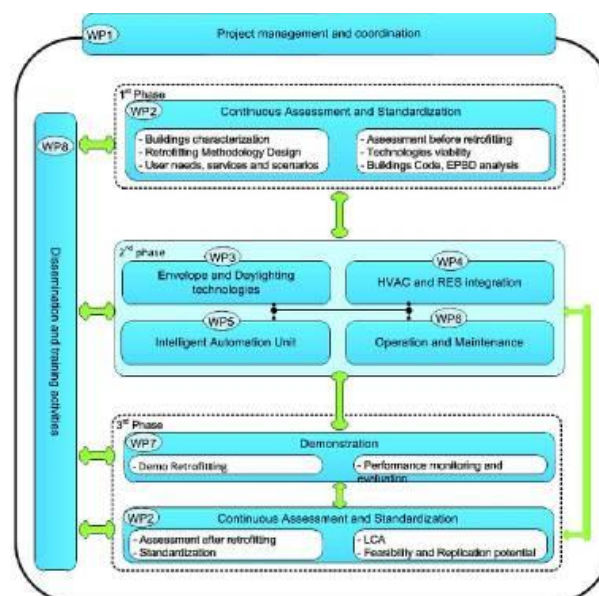
Figure 45: EcoShopping work packages and phasing

2. THE CASE STUDY

The IKVA Shopping Centre is a retail mall in the city of Sopron in Győr-Moson-Sopron County of Hungary. It was built in 1979 and has approximately 3,700 square meters leasable area. The IKVA, due its larger department store size and downtown location, is ideally suited to meet the demands of larger retailers. The retail area mainly consists of large open spaces with only a few pillars, which allows a variety of uses. Operation times of 0800-1900 for 220 working days plus 0800-1300 for 52 days gives a total of 2680 operational hours per annum.

The building has 2 main sections:

- Common area, which consists of 2 storeys with an open parking lot on ground level, and
- Service/office area with 3 storeys and a basement.

Geometry of the building follows functional separation with service and visitor access well separated. The building has a reinforced skeleton structure, 25 cm thick reinforced concrete envelope with a maximum height of 14.90 m; and a flat roof with bituminous waterproofing and polystyrene insulation. There is no insulation on the external walls, which together with the large aluminium frame single-glazed portals in common areas, results in a high overall heat transfer coefficient.

2.1 Pre-retrofit building assessment

The building survey has identified the following systems:

- Heating system: 3 Viessmann Vitodens condensing boilers.
- Cooling system: local split air conditioners.
- DHW: only some local, electrical water heaters.
- Ventilation: 2 AHUs, but these are operated only in summer, 2 hours per day. The heating pipe for heat exchanger of AHU was cut off so the AHU has no heating capability.
- Lighting system: Mainly fluorescent lighting with some tungsten. Many of the fittings are inoperative.
- There is only the basic level of control (on/off for time control plus thermostats) with maintenance staff carrying out this function.

Please note that the Viessmann boilers are relatively new and if replaced this would be on the grounds of demonstrating new or more efficient technologies, not the business case.

2.2 Energy usage and calculations

Natural gas and electricity consumption was collected for the last 3 years:

- Natural gas: ~ 30.000 m^3/annum;
- Electricity: ~124.000 kWh/year.

The first step was to carry out a static energy model calculation in accordance with Hungarian legislation (TNM directive, 2006) which is harmonised with the EPBD (European parliament council on EPBD, 2002). The calculation expresses the primary energy consumption of the heating, domestic hot water, cooling, ventilation and lighting systems. The primary energy factors in Hungary are: e=2.5 for electricity, e=1.0 for natural gas.

Static calculation

Primary energy consumption per systems:

- Heating: 93.71 kWh/(m^2.year);
- Cooling: 11.49 kWh/(m^2.year);
- Lighting: 62.5 kWh/(m^2.year).

The Primary energy consumption was calculated as 167.7 kWh/(m².year) which gave an E rating on the Energy Performance Certification (EPC).

When comparing the actual to modelled consumption the following observations were made:

- Calculated natural gas consumption is 31.400 m³/year; which is close to the real consumption (30.000 m³/year).
- Calculated electricity consumption for lighting and HVAC is 96.000 kWh/year. The real energy consumption much higher (124.000 kWh/year), this was attributed to the additional usage of office equipment, IT technology, etc.

Target value for the IKVA case study is 80 kWh/(m².year); which is just over a 50% reduction in energy usage and would result in an EPC rating of an "A". This is an ambitious target but one that is thought to be achievable.

3. WORK PACKAGE 2: CONTINUOUS ASSESSMENT AND STANDARDISATION

The first deliverable was an assessment of national building codes; EPBD implementation; performance standards and good practice (Lewry, A. J., and Garrido, M. D. C., 2014). This report compares and analyses the national building codes/EBPD implementation and best practices for non-domestic buildings from the European countries (Austria, Croatia, Germany, Hungary, Italy, Poland, Portugal, Spain and the UK) within the project.

3.1 Data collection

The first step was task each of the partners to complete a pro-forma which was designed to capture the following:

- The countries' building energy code and is it mandatory?
- Implementation of the code and mandatory standards.
- Compliance software and targets.
- Requirements in the building code for the building envelope, especially insulation, thermal bridging, pressure testing and overheating.
- Requirements in the building code for the Heating, Ventilation and Air Conditioning (HVAC) systems.
- Requirements in the building code for Domestic Hot Water (DHW).
- Requirements in the building code for the lighting systems.
- Day-lighting requirements of the building code and how is it specified?
- Requirements in the building code for the use of renewables.

Next EPBD implementation was addressed by looking at the following:

- EBPD governance and implementation.
- Are Energy Performance Certificates (EPCs) an operational or asset rating?
- Is the software compatible with that used for building code compliance?
- Are there any other requirements?

Then best practice was examined in each country by asking:

- Is best practice regulated or encouraged through any other means?
- Is the uptake of renewables supported by other government initiatives?

Finally related standards were looked at such as:

- Those that allow electrical connections between renewable energy sources and the electrical grid.
- National regulations related to the procedures of authorization, certification and concession of the transportation and distribution of energy.
- Technical specifications and certification requirements for renewable energy systems.

- Grid obligations of buying the generated renewable energy.
- Mandatory regulation about buying the energy from an existing district heating.
- Any regulation about the thermal reserves in heating/cooling installations.

The data was collected and fully referenced for each of partner countries and captured in the final report as an appendix.

3.2 Analysis and observations

Each of countries building codes, EBPD implementation and good practice were compared. The conclusion was that all the building codes lay down minimum levels of performance for building fabric elements and building services; but not renewables. The codes do not attempt to prompt best practice in any way.

The energy performance of non-domestic buildings as designed is normally calculated holistically by the use of approved software. In the majority of countries the same software is used for both building regulation compliance and the production of EPCs. Because the software is country specific, normally due the local climate and construction data it uses, and therefore it should be the Hungarian software used to assess the design options and overall performance parameters of the building.

Best Practice for Technology areas was identified as lying within either:

- the EU Green Public Procurement (GPP) criteria (EU, 2014), or
- the UK's Enhanced Capital Allowance (ECA) scheme and its Energy Technology List (ETL) (UK DECC (Dept. of Energy and Climate Change), 2014).

Other countries do not seem to be as far advanced down the best practice specification route as the UK; although this may change with the forthcoming implementation of Ecodesign and Eco labelling initiatives. These however are yet to be fully implemented so the best sources of best practice are currently public procurement standards and those in support of government policy vehicles such as tax breaks or feed-in-tariffs.

4. BEST PRACTICE AND STANDARDS TO BE USED ON THE ECOSHOPPING PROJECT

In this section we look at how the best practice specifications and standards identified can be transferred to the EcoShopping project.

4.1 Building fabric

In the context of the project it is proposed that the best fabric u-values identified being used as the backstop (minimum) performance level. Any enhancement of these will be in terms of the cost-effectiveness of the increased thermal performance.

4.2 HVAC services

It is proposed that a renewable powered heat pump is used as are part of the refurbishment to demonstrate this technology. Therefore, the performance should match or exceed those laid down in the criteria of the GPP or ETL to ensure best practice. These criteria lay down best practice performance for Heat pumps, in terms of a Coefficient Of Performance (COP) in Heating mode and an Energy Efficiency Ratio (EER) in Cooling mode for the following technologies:

- Air source: gas engine driven split and multi-split (including variable refrigerant flow);
- Air Source: Packaged Heat Pumps;
- Air Source: Split and Multi-Split (including Variable Refrigerant Flow) Heat Pumps;
- Air Source: Air to Water Heat Pumps;
- Ground Source: Brine to Water Heat Pumps;
- Water Source: Split and Multi-Split (including Variable Refrigerant Flow) Heat Pumps.

The ETL also contains criteria for Heat pump dehumidifiers; Heat pump driven air curtains and CO_2 Heat Pumps for Domestic Hot Water Heating.

As well as Heat pumps and associated technologies the ETL contains best practice criteria for:

- Air to air energy recovery;
- Automatic monitoring and targeting equipment;
- Boilers and boiler equipment;
- Combined heat and power (CHP):
- Compressed air;
- Heat pumps;
- Heating, ventilation and air conditioning (HVAC) equipment;
- Lighting;
- Pipe insulation;
- Motors and drives;
- Solar thermal system
- Refrigeration equipment;
- Uninterruptible power supplies;
- Warm air and radiant heaters.

4.3 Building Controls

The report and the documents it references (Lewry, A. J., 2014) recognise that the control of energy in non-domestic buildings is generally poor, despite the availability of a range of tried and tested systems incorporating both mature and innovative technologies. The installation of HVAC zone controls, optimising controllers (for Wet Heating Systems) and lighting controls is encouraged by the building codes, but their specifications are basic. As controls are one of the most effective solutions in realising energy savings, they should always be part of a refurbishment.

The relatively new European standard EN 15232 on the Energy performance of buildings — Impact of Building Automation, Controls and Building Management (British Standards Institute, 2012), should be used as the methodology for estimating their effect. EN 15232 has a series of classes describing the energy performance – see Figure 2.
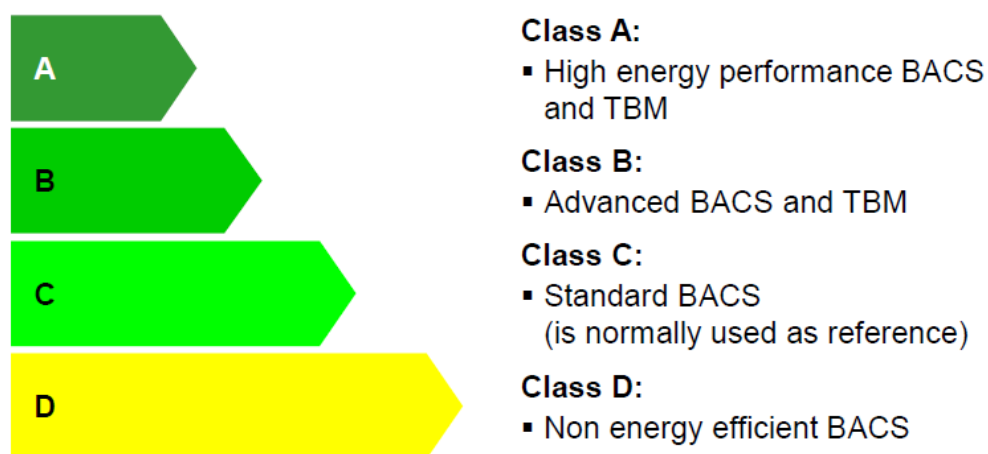
Figure 2: Energy performance classes

Note: Building Automation and Controls Systems (BACS) and Technical Building Management Systems (TBM) in the UK are known as Building Management System (BMS) and Building Energy Management System (BEMS) respectively

To put this into context Class C is what would be required by the current UK building regulations published in November 2013 (UK DCLG (Dept. of Communities and Local Government), 2013). The UK Energy Technology List (ETL) currently has criteria for:

- Heating, Ventilation and Air Conditioning (HVAC) controls (now Building Environment Zone Controls);
- Hot Water Systems Optimising controls (now Heating Management Controllers);
- Lighting controls; and
- Variable Speed Drives (VSDs).

The ETL Building Environment Zone Controls criteria are close to representing good practice when all the criteria are imposed. The criteria above fall slightly short in that summer/winter change over functionality and a requirement for 365 day programming, as defined in BS EN 15500 (British Standards Institute, 2008), have not been included. Joining these together would represent good practice and a specification based on this would probably meet the requirements of Class B of EN 15232, a step up from the building codes but this still falling short of the most efficient operation of a building.

The indicative savings that can be achieved from the implementation of the EN 15232 classes are shown in the table1. This considers Class D of the standard as the baseline; the reason for this is that the majority of buildings will be at this level or below. If we look at the wholesale and trade service buildings line we can see that fitting Class C controls could realise 36% savings, whilst an additional 17% can be achieved through Class B controls. Pre-programmable BEMs would satisfy the Class B criteria but in order to achieve Class A of the standard, programmable BEMs would be required and then the final 9% of energy savings may be realised.

Table 1: Indicatives savings for increasing the class of building controls from Class D of EN 15232

Non-residential building types	% savings from D			
	D	C (Reference)	B	A
	Non energy efficient	Standard	Advanced	High energy performance
Offices	0.00	34	47	54
Wholesale and retail trade service buildings	0.00	36	53	62

This indicates that approximately 62% of savings for a retail building can be achieved by fitting EN 15232 Class A controls (a programmable BEMs) which would achieve the target for the Eco Shopping building without other measures.

Lighting controls are also included within the ETL but are technology specific; the specification covers products that are specifically designed to switch electric lighting on or off, and/or to dim its output. In addition to the functionality covered by the Building Environment Zone Controls described above, lighting controls cover presence detection and daylight detection – with and without dimming. The result is that these could be used as off the shelf specifications for the building control systems.

4.4 Building Controls and zoning

The way a non-domestic building is subdivided into zones will influence the predictions of energy performance and how you set up the control of the building. Therefore, the zoning rules must be applied when assessing a non-domestic building for controls. The end result of the zoning process should be a set of zones where each is distinguished from all others in contact with it by differences in one or more of the following:

- The activity attached to it;
- The HVAC system which serves it;
- The lighting system within it;
- The access to daylight (through windows or roof-lights).

To this end, the suggested zoning process within a given floor plate is as follows:

1. Divide the floor into separate physical areas, bounded by physical boundaries, such as structural walls or other permanent elements.
2. If any part of an area is served by a different HVAC or lighting system, create a separate area bounded by the extent of those services.
3. If any part of an area has a different activity taking place in it, create a separate area for each activity.
4. Divide each resulting area into "zones", each receiving significantly different amounts of daylight, defined by boundaries which are:
    a. At a distance of 6m from an external wall containing at least 20% glazing;
    b. At a distance of 1.5 room heights beyond the edge of an array of roof-lights if the area of the roof-lights is at least 10% of the floor area;
    c. If any resulting zone is less than 3m wide, absorb it within surrounding zones;
    d. If any resulting zones overlap, use your discretion to allocate the overlap to one or more of the zones.

An example of this approach is given in Figure 3. Once the zoning has been carried out consideration can be given to placement of sensors (temperature, occupancy and light levels) with a view to controlling these zones in terms of the services provided.
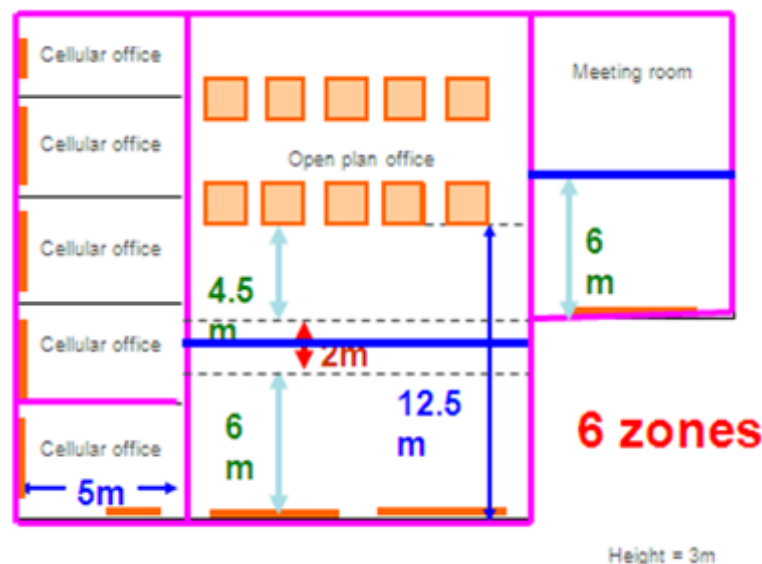
Figure 3: An example of a small office zoned by activity and then daylighting

4.5 Daylighting Standards

The only comprehensive standard found, for non-domestic buildings, was the British Code of Practice for daylighting BS 8206-2 (British Standards Institute, 2008). This standard gives recommendations regarding design for daylight in buildings, which include electric lighting design when used in conjunction with daylight.

BS 8206-2 describes good practice in daylighting design and presents criteria intended to enhance the well-being and satisfaction of people in buildings; these recognise that the aims of good lighting go beyond achieving minimum illumination for task performance.

This revision of BS 8206-2 has been prepared to take account of the publication of two European standards (EN 12464-1 (British Standards Institute, 2011) and EN 15193 (British Standards Institute, 2007)). In particular, some of the manual calculations that appeared in the 1992 edition have been omitted and a new annex on climate-based daylight modelling has been added along with a new clause on daylighting and health

.Simple graphical and numerical methods are given for testing whether the criteria are satisfied, but these are not exclusive and computer methods may be used in practice. Sunlight and skylight data are given.

In addition a new BRE guide (Ticleanu, C., Littlefair, P. and Howlett, G., 2013) provides essential guidance on how to achieve effective and energy-efficient retail lighting and new CIBSE guide 10 provides designers with guidance on lighting for the built environment (CIBSE, 2014).

4.6 Energy auditing and whole building energy savings

There is also a need to carry out an energy audit in order to identify the most appropriate technology areas for any refurbishment.

There is a new European standard for energy auditing (British Standards Institute, 2012) which should be used to identify opportunities for savings and barriers to implementation. Then the data collected can also be used to create meaningful improvement targets through the application of data analysis (Lewry, A. J., 2013).

For a case study such as this it is essential that the methodologies are comparable with those already in use and that technologies match or exceed best practice criteria already published. In addition, producing auditable numbers is essential to showing transparency in how the energy savings claimed are justified. However, refurbishment is not treated consistently and for major works it is suggested the EU GPP criteria of an 20% improvement on the building regulations for new build is aimed for or at least the same performance as the minimum new build criteria, as laid out in the building codes, is reached.

If this is not technically feasible a minimum performance increase, such as achieving a final rating in the top quartile of energy performance should be considered. The top quartile level defined by analysing the database of Energy Performance Certificate (EPC) ratings within the country in which the non-domestic building is situated.

From earlier you can see that this project is far more ambitious and aims for an EPC "A" rating.

4.7 Best practice guidance on the design process

Best practice guidance on low carbon refurbishment of non-domestic buildings has also been identified; this covers both the refurbishment process and the use of renewable technologies (Carbon Trust, 2008). The guidance is structured around a roadmap for the refurbishment process, identifying the key intervention points during the preparation, design, construction and use phases of the project – Figure 4.

4.8 Best practice for renewables

For renewables, the ETL has best practice performance criteria for Heat pumps; Solar Thermal; Combined Heat and Power; Biomass boilers and room-heaters.

The UK Feed-in Tariff (FIT) for generating electricity on-site (UK government, 2014), Renewable Heat Incentive (RHI) (UK government, 2014), and the Microgeneration Certification Scheme ('MCS') (MCS, 2014) contains technology requirements for:

- Solar thermal systems;
- Solar PV systems;
- Small and micro wind turbines;
- Heat pump systems;
- Biomass systems;
- CHP;
- Micro-hydro systems;
- Bespoke Building Integrated Photovoltaic (PV) Products.

These give full product specifications to the current EN and ISO standards and have performance criteria based on these.

For example, MCS includes minimum performance requirements for heat pumps (COPs) and biomass (efficiency) and every MCS installation standard includes a methodology for estimating the annual energy performance of renewable energy systems. In addition, PV has the MCS Guide to the installation of PV

systems which contains a method for estimating the annual electricity generated (AC) in kWh/year of the installed system.

Phase		Low Carbon Refurbishment Process	Page	RIBA Work Stages¹
Prepare	■	Commit to a low carbon refurbishment	7	**Preparation**
	■	Establish a low carbon vision for the refurbishment	7	**A** Appraisal
	■	Develop a low carbon outline brief	7	
	■	Establish the current carbon footprint of the building	8	**B** Design brief
	■	Set carbon targets for the refurbishment	8	
	■	Undertake a pre-refurbishment assessment	9	
	■	Consult stakeholders	10	
	■	Consider a budget for low carbon elements	10	
	■	Appoint a carbon champion	11	
	■	Choose an appropriate design team	11	**Design**
	■	Empower the design team	12	**C** Concept
Design	■	Keep the low carbon theme up front	13	**D** Design development
	■	Develop an integrated low carbon design	13	
	■	Encourage exploration of a wide range of low carbon options	14	
	■	Allow flexibility in design	15	
	■	Use energy modelling data	16	**E** Technical design
	■	Use whole life costing to support low carbon solutions	17	
	■	Manage the budget and scope	17	
	■	Approve the integrated design	18	
	■	Include targets in contracting arrangements	18	**Pre-construction**
Construct	■	Ensure effective project management	19	**F** Production information
				G Tender documentation
	■	Choose an appropriate contractor and subcontractors	19	**H** Tender action
	■	Get buy-in from site workers	19	**Construction**
	■	Monitor site progress against objectives	20	**J** Mobilisation
	■	Ensure high quality commissioning	20	**K** Construction to practical completion
	■	Set up energy monitoring	20	
Use	■	Make sure the occupants understand the building	21	**Post practical completion**
	■	Make sure the building operator understands the building	21	**L** Post practical completion
	■	Conduct a post-occupancy evaluation	22	
	■	Check energy use and comfort conditions and make changes	22	
	■	Make the most of the low carbon building	22	

Figure 4: Good practice roadmap for the Low Carbon refurbishment process

5. CONCLUSION

This study identifies that building regulations and their associated codes lay down minimum levels of performance for non-domestic buildings but do not attempt to prompt best practice. These include minimum performance ("backstop") requirements for building fabric elements and building services; the exception

being true renewables, i.e. solar, hydro and wind based technologies, where there were generally no performance criteria.

This EcoShopping project aims to match the best of these backstop U-values and exceeded them wherever possible. The building codes approach the energy performance of non-domestic building holistically where the overall performance of the building as designed is calculated by the use of approved software. This gives an asset rating which is then deemed as a pass or fail when compared to the performance level required by the individual building code, normally in terms of a target kWh/(m^2.year).

The Primary energy consumption of the case study building was calculated as being 167.7 kWh/(m^2.year); which gave an E rating on the Hungarian Energy Performance Certification (EPC) scale. The target value for the IKVA case study is 80 kWh/(m^2.year); which equates to an approximately 50% reduction in energy usage and would give an EPC rating of an "A". This is an ambitious target but one that is thought to be achievable by the design team.

Best practice performance criteria were identified for the majority of technology areas. The project proposes the use of heat pump technology and the performance of said technology should match or exceed the best practice performance criteria described in the UK's Enhanced Capital Allowance (ECA) scheme and its Energy Technology List (ETL).

The control of energy in non-domestic buildings is generally poor and controls are one of the most effective solutions in realising energy savings. As the level of control specified by building regulations is generally very basic, controls should always be considered as part of a refurbishment and EN 15232 used as the methodology for estimating their effect. EN15232 states indicative savings of 62% may be realised by the installation of an advanced Building Energy Management system (BEMs) in this building type.

For such a case study, it is essential that the methodologies are comparable with those already in use and that technologies match or exceed best practice criteria already published. In addition, producing auditable numbers is essential to showing transparency in how the energy savings claimed are justified.

6. REFERENCES

TNM directive, 2006, Energy Performance of Buildings: 7/2006. (V.24.) customized calculation methods (EPBD) http://net.jogtar.hu/jr/gen/hjegy_doc.cgi?docid=A0600007.TNM

European parliament council on EPBD, 2002, Energy Performance Building Directive (EPBD) implementation and its current recast, Directive 2002/91/ec of the European parliament and of the council of 16 December 2002 on the energy performance of buildings, http://eur-ex.europa.eu/LexUriServ/LexUriServ.do?uri=OJ:L:2003:001:0065:0065:EN:PDF

LEWRY, A. J., and Garrido, M. D. C., 2014, Deliverable D2.1 Assessment of national building codes, EPBD implementation and standards identified, EcoShopping - Energy efficient & Cost competitive retrofitting solutions for Shopping buildings, European Commission within the 7th Framework Programme, V2,.http://ecoshopping-project.eu/document/D2.1%20Assessment%20of%20national%20building%20codes,%20EPBD%20implementation%20and%20standards%20identified_final_14-03-14.pdf

EU, 2014, Green Public Procurement (GPP) criteria, , http://ec.europa.eu/environment/gpp/gpp_criteria_en.htm.

UK DECC (Dept. of Energy and Climate Change), 2014, Enhanced Capital Allowance (ECA) scheme and its Energy Technology List (ETL) - https://etl.decc.gov.uk/etl/site.html.

LEWRY, A. J., 2014, Understanding the choices for building controls, BRE IP 1/14. Bracknell, IHS BRE Press.

British Standards Institute, 2012, BS EN 15232: Energy performance of buildings — Impact of Building Automation, Controls and Building Management.

UK DCLG (Dept. of Communities and Local Government), 2013, Non-Domestic Building Services Compliance Guide (NDBSCG). http://www.planningportal.gov.uk/uploads/br/domestic_building_services_compliance_guide.pdf.

British Standards Institute, 2008, BS EN 15500: Control for heating, ventilating and air-conditioning applications — Electronic individual zone control equipment.

British Standards Institute, 2008, BS 8206-2: Code of Practice for daylighting.

British Standards Institute, 2011, BS EN 12464-1: Light and lighting - Lighting of work places - Indoor work places.

British Standards Institute, 2007, BS EN 15193: Energy performance of buildings, Energy requirements for lighting.

TICLEANU, C., Littlefair, P. and Howlett, G., 2013, The essential guide to retail lighting: Achieving effective and energy-efficient lighting (FB 56), IHS BRE Press.

CIBSE (Chartered Institute of Building Services Engineers), 2014, Lighting Guide 10: Daylighting - A Guide for Designers: Lighting for the Built Environment (SLL LG10),.

British Standards Institute, 2012, BS EN 16247-1 (): Energy audits - Part 1: General requirements.

LEWRY, A. J., 2013, Energy surveys and audits – A guide to best practice. BRE IP 7/13, Bracknell, IHS BRE Press.

Carbon Trust, 2008, CTV 038 Low Carbon Refurbishment of Buildings - A guide to achieving carbon savings from refurbishment of non-domestic buildings, free download from http://www.carbontrust.com.

UK government, 2014, Feed-in Tariff (FIT) for generating your electricity on-site - https://www.gov.uk/feed-in-tariffs.

UK government, 2014, Renewable Heat Incentive (RHI), https://www.gov.uk/government/policies/increasing-the-use-of-low-carbon-technologies/supporting-pages/renewable-heat-incentive-rhi

Microgeneration Certification Scheme ('MCS'), 2012, Guide to the Installation of Photovoltaic Systems, , 10 Fenchurch Street, London EC3M 3BE, 2012, www.microgenerationcertification.org.

138: An innovative external wall insulation system for energy efficient refurbishment of houses

JENNIFER WHITE[1], LUCELIA RODRIGUES[2], MARK GILLOTT[3], RENATA TUBELO[4]

1,2,3,4 Department of Architecture and Built Environment, Faculty of Engineering,
University of Nottingham, Nottingham NG7 2RD, UK
1 j.white@nottingham.ac.uk
2 Lucelia.Rodrigues@nottingham.ac.uk
3 Mark.Gillott@nottingham.ac.uk
4 Renata.Tubelo@nottingham.ac.uk

Energy use from housing contributes in the region of 27% of total UK carbon dioxide and greenhouse gas emissions. Therefore, achieving the national target of an 80% reduction in emissions by 2050 is highly dependent on the reduction of energy consumption in dwellings. Whilst progress is being made towards the improvement of the building fabric of new build dwellings, the existing building stock presents a more complex problem. The UK has over 8.5 million houses that are in excess of 60 years old, which are expected to still be in use for many years and yet need to be made considerably more energy efficient.

There are limited insulation options available to those who occupy solid wall properties, making these particularly difficult to treat. Existing internal and external insulation products tend to be expensive, and installation on site can be time-consuming and weather-dependent. An innovative external insulation system has been developed, which seeks to overcome some of these barriers. The system, which consists of an uPVC shell with an insulating foam core, was designed to fit on most homes, within half the time, in variable weather conditions and using a lower level of installation skills than current systems.

In this study, the authors have analysed the thermal bridging and condensation issues associated with the new product, alongside calculation of a theoretical u-value. Dynamic whole building simulation has been undertaken using a typical Nottingham (UK) property construction, with annual energy demands derived for scenarios both before and after installation of the external insulation system. The results indicate that the innovative external wall insulation panels are able to provide similar levels of improvements in u-values and energy demands/greenhouse gas emissions as compared to more conventional products. It therefore presents a viable alternative to systems that currently exist, thus expanding the number of options available for housing retrofit projects.

Keywords: retrofit, external insulation, social housing, energy efficiency, solid wall properties

1. INTRODUCTION

Whilst much progress is being made towards the improvement of the fabric of new build dwellings in order to enhance thermal performance, the existing building stock presents a more complex problem. The UK has over 8.5 million houses that are in excess of 60 years old (Energy Saving Trust (EST), 2007), resulting in slow progress towards lower domestic carbon emissions through replacement with more efficient properties alone. This poses a dilemma for policy makers, developers and local authorities at the strategic level and home owners at a more localised level – is the best solution to abandon older houses (relocation of occupants and major demolition/rebuild projects) or to refurbish and retro-fit existing properties? (Power, 2008).

Housing demolition rates are relatively low in the UK, and several studies have been undertaken to assess the impact of increased demolition rates within different scenarios to achieve Government energy targets. It has been observed that higher demolition levels may not present a significant contribution in reducing energy demands and carbon emissions, when compared to the impact of wide-scale renovation schemes (Johnston, Lowe, & Bell, 2005; Lowe, 2007; Natarajan & Levermore, 2007).

With this in mind, the role that the improvement of the existing housing stock could have in providing more efficient properties cannot be ignored, although the mechanisms by which this is implemented at Government level could impact upon uptake and effectiveness of improvement measures (Dowson, Poole, Harrison, & Susman, 2012; Killip, 2011). It is largely dependent upon the ability of the wider community to understand the concept of sustainable retro-fit, which may include improvements to the fabric or systems integrated into a dwelling that result in a reduced energy demand, or inclusion of localised power generation from renewable sources (Swan, Ruddock, Smith, & Fitton, 2013).

Research into effective retrofitting practises and new techniques and products is essential in order to inform and aid those undertaking such work at an individual dwelling or whole development scale, and to provide a range of product options to support localised and wide scale refurbishment projects. This study provides a comprehensive theoretical analysis of the potential performance of an innovative external wall insulation product. The system is unique compared to those that are currently available in the marketplace, as it has a competitive cost, a reasonable level of flexibility for its final appearance, and ability to be fitted in all weathers. It also requires a lower level of installation skills than current systems, and may be fitted in most homes with solid walls and other construction types. Therefore, such a product could be beneficial in terms of providing a new and unique system to complement and compete with those already available for mainstream projects, and as an alternative for use in a retrofit context.

2. HOUSING STOCK – THE RETROFIT CHALLENGE

The UK housing stock, being amongst the oldest in the developed world, is also one of the least energy efficient accounting for about 45% of carbon emissions (Stafford, Gorse, & Shao, 2011). Whilst a zero-carbon approach may be suitable for new build dwellings, it should be emphasised that, as demonstrated in Figure 1, only 13% of the English, and total UK, housing stock has been constructed since the introduction of more stringent building regulations implemented in the last two decades. When UK dwellings are considered based on age, type and tenure, Northern Ireland has the newest stock with 61% homes since 1959 and Wales has the oldest housing stock with 61% homes built prior to 1960. However, 84% of all households are located in England and approximately 30% of this housing stock is unlikely to have cavity wall construction and would therefore require either external or internal thermal insulation in order to improve its energy performance (Stafford, Bell, & Gorse, 2012).

Figures 2 and 3 (Department of Energy and Climate Change (DECC), 2013a, 2013b) illustrate that the domestic sector is responsible for a large proportion of both energy consumption and greenhouse gas/carbon emissions within the UK context. With UK Government targets to reduce carbon emission levels to 80% below 1990 levels by 2050 still in place (Department of Energy and Climate Change (DECC), 2008), there is a renewed drive to lower energy use in buildings.
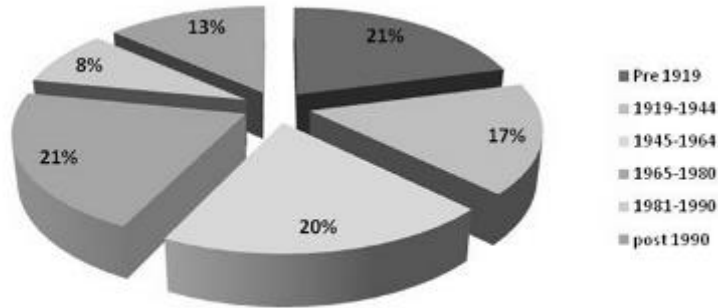
Figure 46: Age Profile of English Housing Stock 2011 (Department for Communities and Local Government (DCLG), 2013)
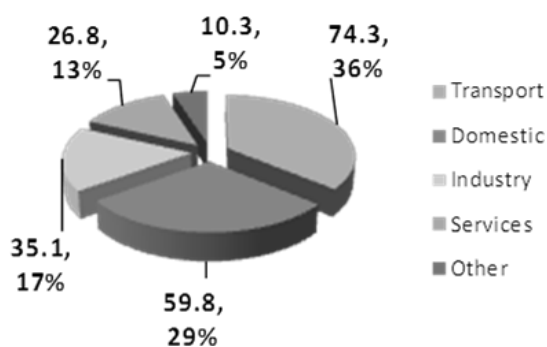
| *Figure 47 - Total UK Energy Consumption by Sector (mtoe, %)* | *Figure 48 - Total UK CO2 Emissions by Sector 2012 (mt, %)* |
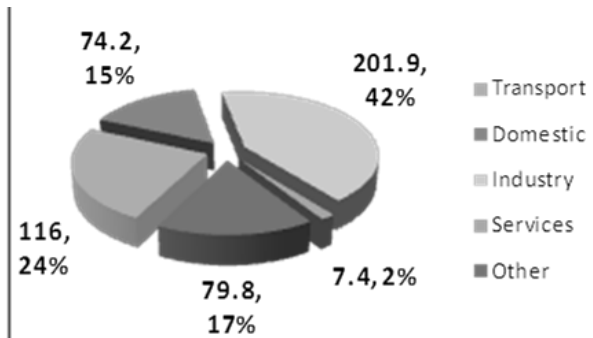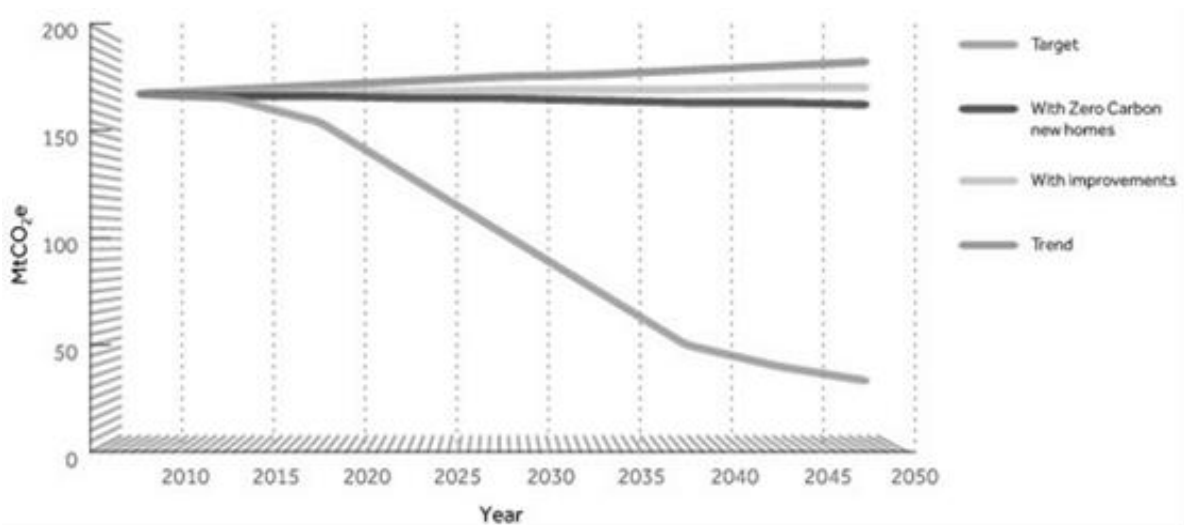
Figure 49: UK Domestic GHG Emissions and Route to 80% Reductions by 2020 (Department of Energy and Climate Change (DECC), 2011)

Demolition rates are currently estimated to be at around 1% of total stock (Kelly, 2010) and current target new-build construction rates are forecast to provide only an additional 9 million homes over the next 15-20 years. It is projected that approximately 75% of the total building stock that will exist in 2050 is already built today (Power, 2010). The emissions level associated with new housing may almost equate to the savings realised by the current rate of improvement of existing buildings. Therefore, whilst zero carbon can be imposed as the standard quality for new build construction, the issue of improving energy efficiency in existing housing is of equal or greater concern and cannot be underestimated in terms of importance (Royal Institute of British Architects (RIBA), 2009).

353

Current improvement programmes may contribute towards a reduction in carbon emissions, as represented by the 'with improvements' line in Figure 4. However, even when taking into consideration the requirement for new dwellings to meet the "zero carbon" standard from 2016, it will be very challenging to meet the 'target' trajectory (Energy Saving Trust (EST), 2010).

The complexity of the problem of retro-fitting energy saving measures in the extensive and diverse aging housing stock is further compounded due to the number of 'hard to treat' properties that exist and comprise over 40% of homes in the UK (Energy Saving Trust (EST), 2008). This includes solid walled, flat roofed, timber framed and high rise buildings, as well as tenements, park homes and those with limited services connections or no loft space (Roaf, Baker, & Peacock, 2008). In such properties, it can be difficult to improve building fabric performance through standard measures such as cavity wall or loft insulation due to the building structure. There is increasing concern that without more pro-active communication, enhanced incentives, and easier to implement solutions, many of the properties in this category will still not be thermally efficient in 2050 (Dowson et al., 2012).

2.1 Potential retrofit solutions: thermal improvements

When considering the energy efficiency of a building, the space heating requirements of a dwelling are dependent upon the balance between whole house heat losses and heat gains (Feist, Pfluger, Kaufmann, Schnieders, & Kah, 2007). In an uninsulated building, up to 35% of total heat losses can occur through the external walls (Woodford, 2014). The choice of materials used to construct the building envelope will therefore have a major impact on thermal performance.

In order to prevent excessive heat loss, a building should be well insulated. This is not problematic in more recent construction types that utilise a cavity wall structure, as using a good quality cavity wall insulation can reduce overall heat losses by up to 60% (Energy Saving Trust (EST), 2010). However, in solid wall structures or those with narrow cavity spaces, such improvements are not possible. External or internal wall insulation may be viable options in these cases.

Internal wall insulation may be cheaper to install than external wall insulation, but it will also reduce the floor area of the rooms in a property as it is installed directly onto the internal surface of the external walls. The work associated with the installation may cause inconvenience to occupants, as it requires the removal of skirting boards and architraves and redecoration will be required following installation (Energy Saving Trust (EST), 2010).

When the external features of a property do not need to be protected and obtaining planning permission is not problematic, external wall insulation may provide a viable alternative. In most cases, it can be applied with minimal disruption, with the added benefit that it will not change the floor area of the property. It may help to increase airtightness and reduce condensation on internal walls (English Heritage, 2014). However, it is generally expensive and can be problematic to install in adverse weather conditions. It may also require extensive enabling works, especially where external walls are not in good condition, and this can increase the cost further.

This study is concerned with an evaluation of the performance of a novel prototype external wall insulation system. Currently, most existing products consist of an insulation panel board fixed onto the external wall and then covered with a wet external render. The new system under consideration is comprised of a prefabricated uPVC panel which is infilled with a rigid polyurethane (PUR) foam. This can be delivered to site as a complete system and can be installed in any weather conditions, as it removes the requirement for a wet render finish to fix and cover the insulation sheets. The aim of this analysis is to investigate the theoretical thermal performance of the prototype product, in order to compare the product to those that are currently available for use in external wall insulation projects.

2.2 Performance analysis

A number of techniques and software programmes were utilised in order to assess the performance of the prototype external insulation system. In order to gain a comprehensive understanding of the properties of the product and the potential for improving energy efficiency of homes, a number of analyses were undertaken. These included:

• Condensation Risk

- • Thermal Bridging
- • Theoretical U-Value
- • Energy Performance using steady state and dynamic building energy models
- • Comparison of prototype product performance with currently available insulation systems

In all cases, a solid brick wall construction was used as a baseline for analysis, with the prototype insulation system included where required. This comprised of a 225mm solid brick envelope, with a 12mm plasterboard internal wall finish. The prototype insulation product was then applied to the wall on top of a breathable membrane and a backing foam of 2mm thickness. A typical semi-detached house design was used, as shown in Figure 5. This represents a very common design of a solid brick wall property in the UK.

Figure 50: Schematic Diagram of the Sample Test Property

2.3 Analysis of Physical Properties

The first stage of the evaluation process involved an initial theoretical performance evaluation of the prototype product. THERM7 software was used to build a model of the panel in order to obtain estimates of the u-value and thermal bridging properties of the system. The isotherms in the insulation panel do not follow a parallel formation, but are wavy due to the different conductivities present in the uPVC and PUR foam fill materials. This causes increased heat flow through the uPVC sections, and also around the fixing elements such as screws and brackets. However, there are no significant heat losses apparent on the internal surface of the wall, and the internal temperature is maintained at approximately 19.2°C. Given that the external and internal temperatures were fixed at 0°C and 20°C respectively within the model, this demonstrates that the panel is providing a good level of insulation and that heat losses from the inside environment are minimal.

Following this work, an assessment of condensation risk within the external insulation panel and at the junction with the external was then undertaken. This work was undertaken using Bentley Hevacomp V8i modelling software. This product utilises the composite/combined method to calculate u-value, in accordance with BS EN ISO 6946. For the condensation analysis, Hevacomp assesses the risk using the principles detailed in BS 5250 and BS EN ISO 13788. This makes the data obtained comparable with the information that is obtained during standard product accreditation tests.

Chartered Institution of Building Engineers (CIBSE) typical annual weather data for the Nottingham area was used within the model to evaluate the product, and the analysis is shown in Figure 51. The wall construction is represented with the internal plasterboard finish shown on the left hand side progressing to the external insulation on the right hand side. It can be seen that the dry bulb temperature within the wall construction is higher than the dew point temperature throughout the structure, meaning that there is minimal risk of condensation forming at any point throughout the external building envelope.
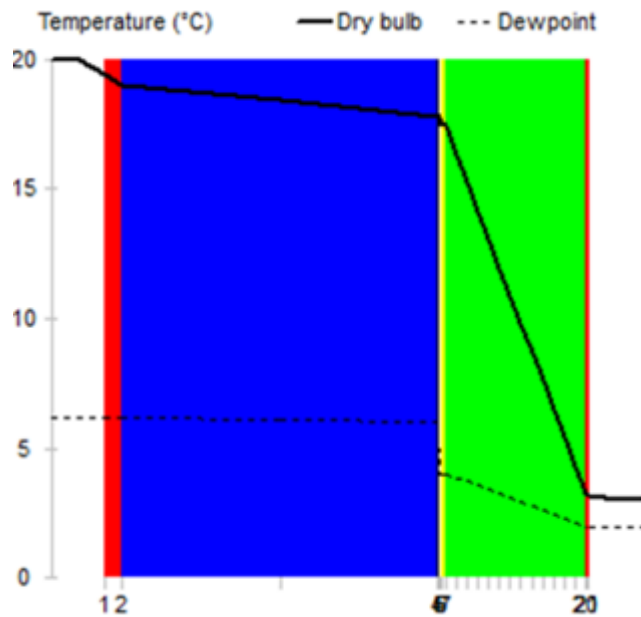
Figure 51: Condensation Risk Analysis

It is interesting to note that when no backing foam material was included in the analysis, the risk of interstitial condensation increased noticeably. This demonstrates the importance of ensuring that there are no air gaps between the external wall and the insulation panel, as this could lead to issues such as mould and degradation of the product.

In terms of theoretical u-value, the Hevacomp V8i software calculated a value of approximately 0.277 W/m^{2}K for this external wall construction, inclusive of the brickwork and the external and prefabricated insulation panel. This did not vary regardless of whether or not the build-up of materials included the backing foam. The u-value derived from Therm 7.2 was slightly different, being 0.239 W/m^{2}K. However, this variance could be due to the simplistic nature of the software assumptions, and the inclusion of moisture in the Hevacomp analysis. However, it is evident that the new insulation panel has the capacity to improve thermal performance of the external wall by a significant amount, as the uninsulated u-values of solid brick construction would be in the region of 2 – 2.1 W/m^{2}K (Baker, 2011; Department of Energy & Climate Change (DECC), 2011).

2.4 Dynamic Building Performance Analysis

EDSL TAS 9.2.1.6 was used in order to assess the potential impact that the prototype external insulation system could have in terms of reducing the space heating energy demands of a standard solid brick semi-detached house with the dimensions detailed in Table 9.

Table 18: Zones and Dimensions of Simulated House

Zone	Area (m^2)	Volume (m^3)
Kitchen/Dining Room	20.10	52.30
Living Room	36.80	36.80
Hallway	6.30	16.60
Landing	5.70	14.60
Bedroom 1	13.70	35.00
Bedroom 2	10.10	25.80
Bedroom 3	6.90	17.60
Bathroom	3.70	9.40

A series of simulations were undertaken, including a solid brick wall with no external insulation, and the same wall construction with the prototype insulation and competing existing products. The following assumptions were included in all of the models:

- CIBSE weather data (TRY) files for the Nottingham are were imported into each model. Such data is considered to be a reliable statistical indicator of the weather patterns of a certain area, as they are based on analysis of trends over a number of years ((CIBSE, 2006);
- Heating and cooling patterns were considered separately within the analysis;
- Space heating was included as a schedule throughout the winter months with a set point internal temperature of 21°C used, and all windows were assumed to be closed;
- Occupancy heat gains were assumed to be 95W per person in bedrooms and 150W per person in living areas;
- Equipment gains were estimated at 1.36 kWh per day and kitchen heat gains calculated to be 4.46 kWh;
- An infiltration rate of 0.5 ACH was applied uniformly throughout the property with windows closed at all times;
- An occupancy schedule was defined and kept consistent for all of the simulations;
- The build-up of all construction elements was kept identical throughout the study, with the exception of the external wall specification as this was altered to reflect application of the different insulation products. The u-values of each component is shown in Table 19.

Table 19: U-Values of Building Elements

Zone	Ground Floor	Roof	Solid Brick Wall	Prototype EWI Applied to Wall
U-Value (W/m²K)	0.50	0.55	2.83	0.25

The energy demand of the property was calculated through the use of the simulation software for both the uninsulated solid brick wall dwelling and for the same construction with the application of the prototype EWI product, as shown in Figure 52. The total heating load for the year is calculated to be 8,824 kWh for the uninsulated property and 4,626 kWh for the same dwelling when the external wall insulation is applied. This equates to a 4,198 kWh (almost 50%) reduction in space heating energy use that can be attributed solely to the installation of the prototype external wall insulation system as all other variables have been kept constant throughout the analysis. The profile of the relative level of reduction remains consistent across each month.

It should be noted that, due to the assumptions made within the model, the space heating requirement may be underestimated during the months of May -September. During these months, the model did not include any space heating usage. The thermal performance of the dwelling may be overestimated, and so it could be that in reality there would be a need for space heating.

The new product was then compared to other more established EWI systems that are currently available in the marketplace. Two wet render systems were included in the external wall construction analysis, one with a 100mm expanded polystyrene (EPS) fill and one with a 100mm polyisocyanurate (PIR) foam fill. This thickness was used in order to compare products on an equal basis in relation to the depth of the insulation and consequent impact on the external wall thickness. This was considered to be important as this characteristic may affect the choice of product used by a builder or property owner/occupier/manager.

Figure 53 includes information relating to the three external wall insulation products that have been used in the analysis. It can be seen that the prototype EWI system performs favourable when compared with more conventional products. The building energy demand associated with the new system is lower than the wet render EPS system but slightly higher than the PIR system. The difference between the three products remains consistent across the monthly profiles.
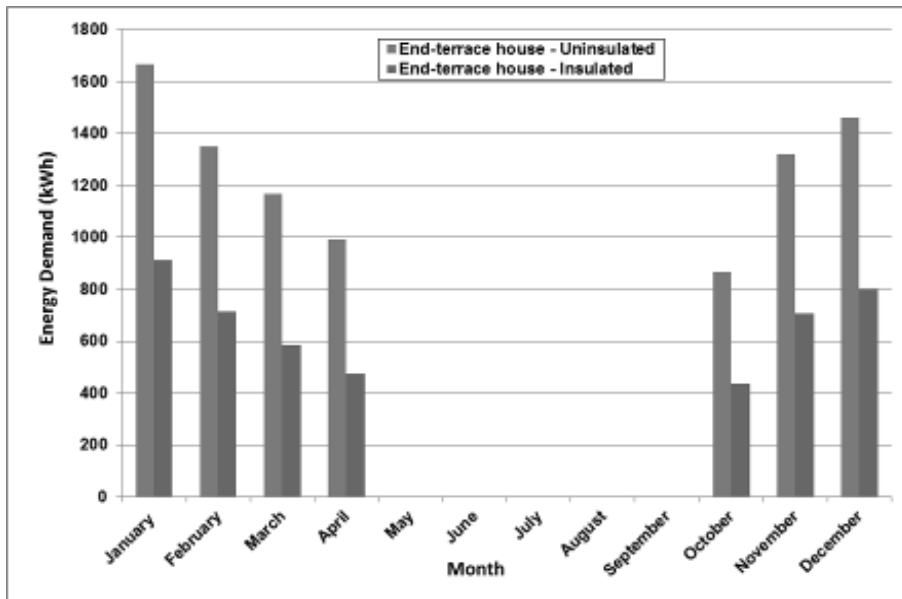
Figure 52: Energy Demand Reduction due to Prototype Insulation System
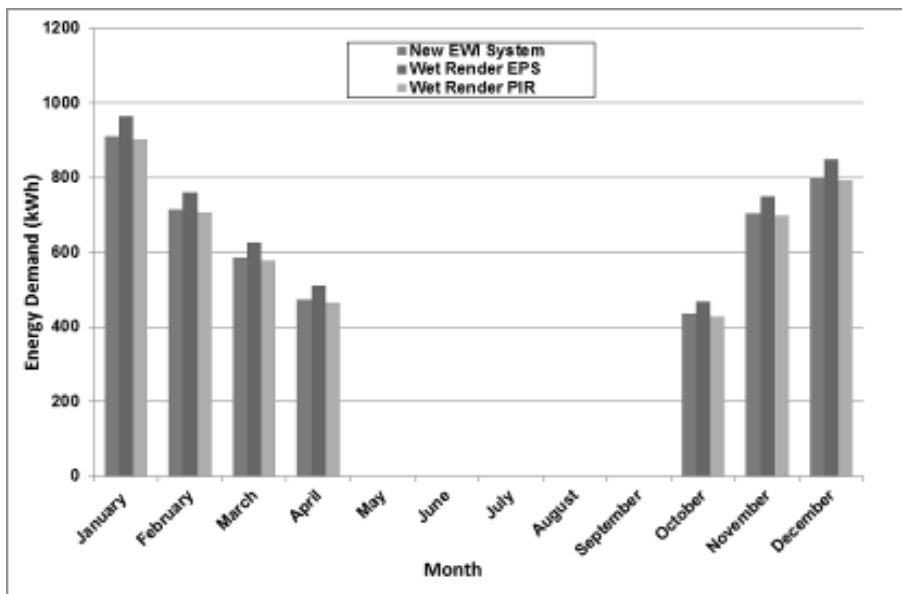
Figure 53: Comparison of Prototype System with other EWI Products

The variance in space heating is relative to the u-value of the various products, as shown in Table 20. The prototype EWI system has a better thermal performance than the Wet Render EPS System, and the Wet Render PIR system has a lower u-value than both of the other products under consideration. A u-value of 0.252 W/m^{2}K was attributed to the prototype system as this is the average value of those calculated using Therm 7.2 and Hevacomp V8i software, being 0.239 W/m^{2}K and 0.277 W/m^{2}K respectively. The solid brick wall u-value is that derived from the TAS 9.2.1.6 software. The variance in performance is reflected in the relative space heating reductions associated with the systems. It can be seen that all of the EWI systems under consideration have a significant effect in reducing the energy load of the uninsulated dwelling.

Table 20: U-Values and Heating Load Summary

	Uninsulated House	Prototype EWI	Wet Render PIR EWI	Wet Render EPS EWI
U-Value (W/m^{2}K)	2.828	0.252	0.229	0.421
Heating Load (kWh)	8824	4626	4537	4928

3. CONCLUSION

The evaluation of the prototype EWI system has demonstrated that the product was able to significantly reduce the energy demand of a solid brick wall dwelling by up to 50%, and achieve levels of thermal performance that are comparable to more established conventional EWI solutions. There are a number of competing products in the marketplace that are currently utilised in both small and large scale installation products. Therefore, the new system would need to offer additional benefits other than simple energy reductions in order to be accepted and used in place of 'known' products.

The main unique selling point of the prototype system is that is does not require a wet render finish. This means that the installation of the product is not weather dependent, which is the case for many conventional systems. It is also prefabricated off-site which simplifies the installation process further and enables it to be completed in less time. These advantages, alongside equivalent thermal performance and potential lower cost, could be sufficient to allow the new system to penetrate the established EWI market.

It should be noted that the performance assessment presented here is based solely in theoretical modelled data. A pilot installation of the prototype product applied to a test dwelling is planned for the near future, in order to gain empirical real-life data relating to the actual impact of the product in terms of reducing energy demands. This will form the basis of a separate publication.

4. ACKNOWLEDGEMENTS

5. REFERENCES

BAKER, P. (2011). U-Values and Traditional Buildings - In Situ Measurements and their Comparison to Calculated Values. Technical Paper 10. Historic Scotland Conservation Group. Edinburgh.

CIBSE. (2006). Environmental Design: Guide A. CIBSE. London.

Department for Communities and Local Government (DCLG). (2013). English Housing Survey Headline Report 2011-2012. DCLG. London.

Department of Energy & Climate Change (DECC). (2011). The Government's Standard Assessment Procedure for Energy Rating of Dwellings 2009 Edition. BRE. Watford.

The Climate Change Act 2008, HMSO, London (2008).

Department of Energy and Climate Change (DECC). (2011). Zero Carbon Non-Domestic Buildings - Phase 3 Final Report. DCLG. London.

Department of Energy and Climate Change (DECC). (2013a). Energy Consumption in the UK. Chapter 1: Overall Energy Consumption in the UK Since 1970. DECC. London.

Department of Energy and Climate Change (DECC). (2013b). Statistical Release - 2012 UK Greenhouse Gas Emissions, Provisional Figures and UK 2011 Greenhouse Gas Emissions, Final Figures by Fuel Type and End-Use. DECC. London.

DOWSON, M., Poole, A., Harrison, D., & Susman, G. (2012). Domestic UK Retrofit Challenge: Barriers, Incentives and Current Performance Leading into the Green Deal. Energy Policy, 50(0), 294-305. doi: http://dx.doi.org/10.1016/j.enpol.2012.07.019

Energy Saving Trust (EST). (2007). Energy-Efficient Refurbishment of Existing Housing (CE83). In EST (Ed.). London.

Energy Saving Trust (EST). (2008). Energy Analysis Focus Report. A Study of Hard to Treat Homes Using the English House Condition Survey - Part 1: Dwelling and Household Characteristics of Hard to Treat Homes. DEFRA. London.

Energy Saving Trust (EST). (2010). Sustainable Refurbishment – Towards an 80% Reduction in CO2 Emissions, Water Efficiency, Waste Reduction, and Climate Change Adaptation, CE309, Energy Saving Trust, London

English Heritage. (2014). External Wall Insulation in Traditional Buildings: Case studies of three large scale projects in the North of England. NDM Heath Ltd. Knaresborough.

FEIST, W., Pfluger, R., Kaufmann, B., Schnieders, J., & Kah, O. (2007). Passive House Planning Package 2007 - Requirements for Quality Approved Passive Houses. The Passivhaus Institut, Darmstadt.

JOHNSTON, D., Lowe, R., & Bell, M. (2005). An Exploration of the Technical Feasibility of Achieving CO2 Emission Reductions in Excess of 60% within the UK Housing Stock by the Year 2050. Energy Policy, 33(13), 1643-1659. doi: http://dx.doi.org/10.1016/j.enpol.2004.02.003

KELLY, M. (2010). Energy Efficiency Resilience to Future Climates and Long-Term Sustainability: The Role of the Built Environment. Philosophical Transactions of the Royal Society. 368, 1083–1089.

Killip, G. (2011). Beyond the Green Deal: Market Transformation for Low-Carbon Housing Refurbishment in the UK. In Proceedings of Retrofit 2012, 24-26 January, Lowry Theatre, Salford Quays, Salford, Manchester, UK: University of Salford. .

Lowe, R. (2007). Technical Options and Strategies for Decarbonising UK Housing. Building Research and Information, 35(4), 412-425.

Natarajan, S., & Levermore, G. (2007). Domestic Futures—Which Way to a Low-Carbon Housing Stock? Energy Policy, 35(11), 5728-5736. doi: http://dx.doi.org/10.1016/j.enpol.2007.05.033

POWER, A. (2008). Does Demolition or Refurbishment of Old And Inefficient Homes Help To Increase Our Environmental, Social and Economic Viability? Energy Policy, 36(12), 4487-4501. doi: http://dx.doi.org/10.1016/j.enpol.2008.09.022

POWER, A. (2010). Housing & Sustainability: Demolition or Refurbishment? Proceedings of the Institution of Civil Engineers – Engineering Sustainability 163(December 2010. DP4), 205-216.

ROAF, S., Baker, K., & Peacock, A. (2008). Evidence on Tackling Hard to Treat Properties. The Scottish Government Housing and Regeneration Department. Edinburgh.

Royal Institute of British Architects (RIBA). (2009). Carbon Literacy Briefing - Executive Summary. RIBA. London.

STAFFORD, A., Bell, M., & Gorse, C. (2012). Building Confidence - A Working Paper. Retrieved 15th September 2013, from http://www.leedsmet.ac.uk/as/cebe/projects/building-confidence.pdf

STAFFORD, A., Gorse, C., & Shao, L. (2011). The Retrofit Challenge: Delivering Low Carbon homes Leeds Sustainability Institute, Leeds Metropolitan University, : Centre for Low Carbon Futures and Energy Saving Trust.

SWAN, W., Ruddock, L., Smith, L., & Fitton, R. (2013). Adoption of Sustainable Retrofit in UK Social Housing. Structural Survey, 31(3), 181-193.

WOODFORD, C. (2014). Heat Insulation. Retrieved 19th May 2014, from http://www.explainthatstuff.com/heatinsulation.html

384: Energy and economic analysis of different solutions for the retrofitting of the heating and cooling plant for a residential care home for elderly people

Marco NORO[1], Giacomo BAGARELLA[2]

[1] Department of Management and Engineering, University of Padua, Stradella S. Nicola, 3, 36100 Vicenza, Italy – marco.noro@unipd.it
[2] Department of Management and Engineering, University of Padua, Stradella S. Nicola, 3, 36100 Vicenza, Italy – bagarella@gmail.com

Since the last decade, European Union policies are oriented to decrease greenhouses emissions and energy dependence. The main incentives are energy saving, renewable energy and cogeneration, as proved by the 2010/31 EU Directive on energy savings in buildings and by the 2012/27/EC Directive on energy efficiency.

At the same time, about 14 % of European population is over 65 years of age, and it is expected that this number will double by 2050. These figures in Italy assume dramatic values, as actually we have 21.4 % of population over 65 (13 million) and we will have 33.6 % (18.7 million) by 2050. Nowadays about 300000 elderly live in just less than 6000 care homes in Italy. These buildings operate 24 hours a day, 365 days a year, with full occupancy. For these reasons reducing energy consumption in residential care homes is important.

This paper focuses on the study of the energy performance of a residential care home for elderly people in Vicenza (North East of Italy). A preliminary energy audit was carried out in order to obtain appropriate information about energy consumption of the building. Moving from the request of the managers responsible for running the care home, a Trnsys simulation model of the building/HVAC plant system was developed with the aim to test different solutions to retrofit the heating/cooling plant.

Some of the best available technologies (photovoltaic, cogeneration, trigeneration, heat pumps) were compared by an energy and economic analysis in order to assess potential energy investment options to make energy efficient informed decisions.

Keywords: energy efficiency; HVAC plant; cogeneration; trigeneration; photovoltaic

1. INTRODUCTION

The goal of the Directive 2012/27/EU on energy efficiency is to achieve the Union's energy efficiency target of 20 % by 2020 compared to 1990 levels and to pave the way for further energy efficiency improvements beyond that date. In Italy, the EU Directive was acknowledged by 102/2014 Decree: among the main issues, the Decree calls on public bodies at all levels to play an 'exemplary role' in energy efficiency, since they have great potential to stimulate market transformation towards more efficient products, buildings and services. Each Member State must therefore ensure that 3 % of the total floor space of heated and/or cooled buildings owned by their central government is renovated each year, taking into account existing obligations in Directive 2010/31/EU.

Among the public (but not only) buildings, residential care homes for elderly people are ones of the most important because of the increasing European population aging. Nowadays about 14 % of European population is over 65 years of age, and it is expected that this number will double by 2050 (Pedro *et al.*, 2011). These figures in Italy assume dramatic values, as actually we have 21.4 % of population over 65 (13 million) and we will have 33.6 % (18.7 million) by 2050 (SCUOLA SUPERIORE DELL'AMMINISTRAZIONE DELL'INTERNO, 2010) (ISTAT, 2006). Nowadays about 1.5 million elderly live in more than 24000 care homes in Europe (300000 elderly live in just less than 6000 in Italy). These buildings operate 24 hours a day, 365 days a year, with full occupancy. For these reasons reducing energy consumption in residential care homes is important.

However, there can be many barriers to the implementation of effective energy saving measures in this sector, in particular lack of financial resources and lack of awareness among the management staff. A recent European research project (Save Age, 2010-2013) firstly recognized energy efficiency importance in residential care homes for elderly people, giving to residential home care managers ideas and suggestions on how to implement energy efficiency strategy and action plan. In this project, both low cost measures, behavioural changes and higher cost measures were promoted (Pedro *et al.*, 2011).

In this context, this paper focuses on the study of the energy performance of a quite new residential care home for elderly people in Vicenza (North East of Italy). A preliminary energy audit was carried out in order to obtain appropriate information about energy consumption of the building. Moving from the request of the managers responsible for running the care home, a Trnsys simulation model of the building and heating/cooling plant system was developed with the aim to test different solutions to retrofit the heating/cooling plant. Some of the best available technologies (photovoltaic, cogeneration, trigeneration, heat pumps) were compared by an energy and economic analysis in order to assess potential investment options to make energy efficient informed decisions. Because of the uncertainty of some variables of the analyses, a sensitivity analysis was further developed in order to make the comparison more consistent.

2. BUILDING DESCRIPTION AND ENERGY LOADS CALCULATION

The considered building is a 29889 m^3 residential care home for elderly people built during the 2002-2004 period and located in Vicenza (North Italy). It is a three floors building (about 2800 m^2 each). The two overground floors host rooms (with bathrooms), halls for meals and recreational activities and some other service rooms (the ground floor hosts also the reception and offices). The underground floor hosts many service and technical rooms (kitchen, storerooms, changing rooms, laundries, surgeries, gym, etc.). In order to estimate (using Trnsys 17) both the annual heating and cooling demands of the building, 3D geometric surface information were firstly required. Hence, a 3D geometric model of the building was developed (Figure 54) using "Trnsys3d for SketchUp".

Figure 54: Photo, 3D model and layout (ground floor) of the considered residential care home.

Once developed the 3D model, geometric information about surfaces were imported in "TRNbuild", where thermophysical properties of both structures and elements were set according to information provided by the studio involved in the building design. The building was divided into 76 thermal zones taking into account own type of use, frequency and occupation time (so scheduling people presence, use of lighting, cooking ovens, refrigeration equipment, personal computers, etc.). Every zone was described by the software in terms of size and orientation of walls, windows, thermal bridges, internal gains, air ventilation and infiltration, internal and inlet air temperature and humidity during heating and cooling seasons. Some information over the year were gathered by interviewing the residential care home staff. Other information were provided by the designer or collected checking the nominal electric consumption of each unit. The main data of the building are reported in Table 21.

Table 21: Main data of the building.

Zone	Vicenza (North Italy)
Heating degree days	2479
Building destination	Residential care home
Internal volume (m3)	29889
Floors	3
External Surface / Heated Volume ratio (m-1)	0.35
Heating period	October 15th – April 15th
Cooling period	April 16h – October 14th
Typical temperature set-point, heating period (°C)	24.0
Typical relative humidity set-point, heating period (%)	-
Typical temperature set-point, cooling period (°C)	26.0
Typical relative humidity set-point, cooling period (%)	50 %
Ventilation flow rate (m3 s-1)	4.09
External walls transmittance (W m-2 K-1)	0.517
Floor transmittance (W m-2 K-1)	0.433
Roof transmittance (W m-2 K-1)	0.287
Windows transmittance (W m-2 K-1)	3.155
Average internal heating gains (W m-2)	4.0
Patients and staff	160

The building model (developed in "TRNbuild") was imported in "Simulation Studio" where it was linked to the models of both heating and cooling systems using "Type 56". An annual simulation of both heating and cooling loads was run with one hour time step: annual heating and cooling energies of the building were estimated to be 622000 kWh and 529000 kWh, with peak loads of 610 kW and 707 kW respectively. Concerning electric loads, there was availability of disaggregated data (on a quarter hourly basis) from local electric distributor for the years 2013 and 2014. Nevertheless, such data was subject to the different environment conditions (e.g. summer 2014 was extremely colder than usual in Italy) and building operating conditions. So, with some approximation based on information found by talks with technical personnel of the home, an hourly electric load profile was built taking into consideration monthly electric consumptions (deduced by electric bills), the actual installed electric power (400 kW) and the real data (Figure 55).
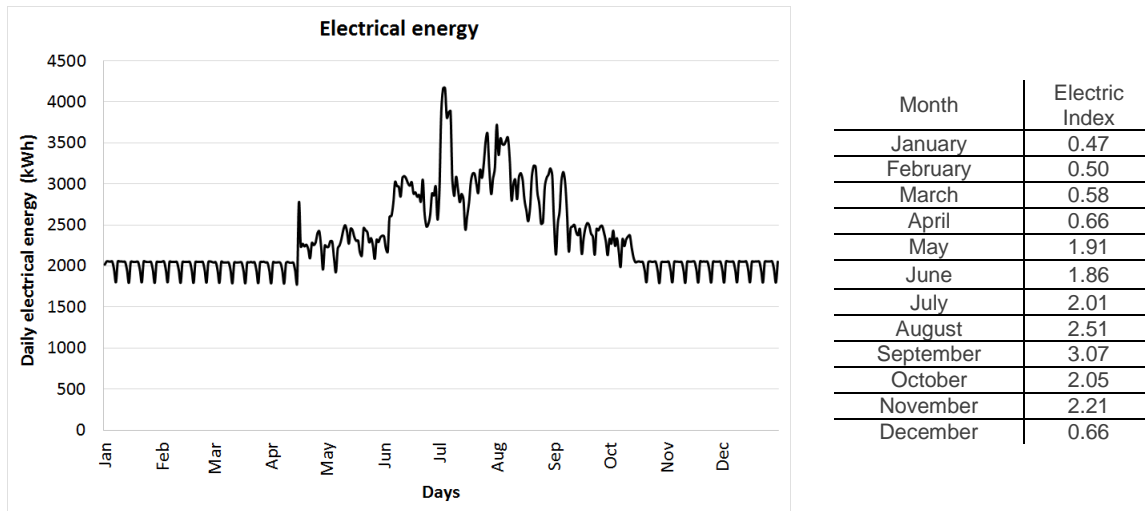
Month	Electric Index
January	0.47
February	0.50
March	0.58
April	0.66
May	1.91
June	1.86
July	2.01
August	2.51
September	3.07
October	2.05
November	2.21
December	0.66

Figure 55: Annual profile of daily electric needs and electric/thermal energy needs ratio (electric index) for the building.

Figure 55 depicts also the "electric index" that is the ratio between electric and thermal (considering domestic hot water) monthly energy needs of the building. Such index is quite variable during the year: in winter thermal needs are almost double the electrical ones, in summer and mid seasons electrical needs are definitely prevailing. Obviously, such variability is even greater in an hourly analysis and makes even more difficult the selection of the appropriate cogenerator (that typically operates at quite constant electric index) as will be described in later section.

3. HEATING/COOLING PLANT DESCRIPTION AND PRIMARY ENERGY CONSUMPTION CALCULATION

The existing heating, ventilation and cooling plant is mixed air/water; it is set up by:

- heating and cooling plant (vapour compression electric chiller and natural gas boilers);
- ventilation and air conditioning plant (many air handling units (AHU) to control relative humidity and for the necessary air changing inside the building; main units are set up by a rotary heat exchanger, pre-heating, cooling and dehumidification and post-heating sections). The common sites of the building (corridors, halls) are served by fan-coils and ventilation air, rooms and bathrooms are served by radiators and ventilation air, service and technical rooms by small AHUs or air heaters;
- air extraction plant (for service rooms).

The object of the work is the energy and economic analysis of the retrofitting of the heating and cooling plant only. The main components are:

- one air/water vapour compression electric chiller (2 circuits - 4 oil free centrifugal compressors per circuit) which provides cold water for fan-coils and cold coils in AHUs. The nominal cooling power is 895 kW, 270 kW is the nominal electric power consumption, EER=3.31. These performances are labelled for summer external air 35 °C and evaporator input/output 12/7 °C;
- two natural gas boilers with two-steps burners (nominal useful power 670 kW, minimum useful power 425 kW each) provide the thermal energy for heating, domestic hot water and post-heating in AHUs during cooling season.

The chiller and the boilers supply three hydraulic circuits. The "hot collector" supplies hot water to the radiators, air heaters, pre and post heating coils in the AHUs. It supplies also the domestic hot water plate heat exchanger that loads a 5000 l tank. The "hot/cold collector" supplies hot (during heating season) or cold (during cooling season) water to the fan-coils. The "cold collector" supplies cold water to the cold coils of the AHUs (obviously during cooling season only). Table 22 reports the temperature set points of the different energy uses. Electric consumptions of pumps and lighting appliances and scheduling of the main equipment (only few equipment/energy uses are different on weekdays with respect to weekends) are not reported for the sake of brevity.

Table 22: Set points and scheduling for the main energy uses and equipment.

Set points
- hot water produced by boilers: 65 to 75 °C (climatic curve in 20/-5 °C external air temperature range)
- hot water supplied to pre and post-heating coils in AHUs: 70 °C
- hot water supplied to radiators: 70 °C (variable by thermostatic valves)
- hot water supplied to fan-coils: 60 °C
- hot water supplied to air heaters: 55 °C
- cold water produced by chiller: 8 °C

Electric uses (other than lighting)
- cold stores, 22 kW, always ON
- ovens, 8 kW, 9.00am-12.00am / 4.00pm-7.00pm
- washing machines, 53.7 kW, 8.00am-9.30am / 10.00am-11.30am
- tumble dryers, 31.1 kW, 9.30am-11.00am / 11.30am-1.00pm
- steam irons, 15 kW, 10.00am-12.00am / 2.00pm-4.00pm

The first step was the simulation by Trnsys model of the just described existing plant ("As Is" solution). The validation of the model was carried out by analysing flow rates and temperatures of the different circuits and by comparing simulated and real energy consumptions of the heating/cooling plant system. Figure 56 reports the annual profiles of monthly electrical energy (EE) and natural gas (NG) consumptions, both simulated and real (referring to 2012, 2103 and 2014 available energy bills). Considering the variability of the environment and building operating conditions, the concordance between simulated and real data is quite good (the slight overestimate of electrical energy consumption during mid seasons is due to the wider cooling period in the simulations with respect to the reality).
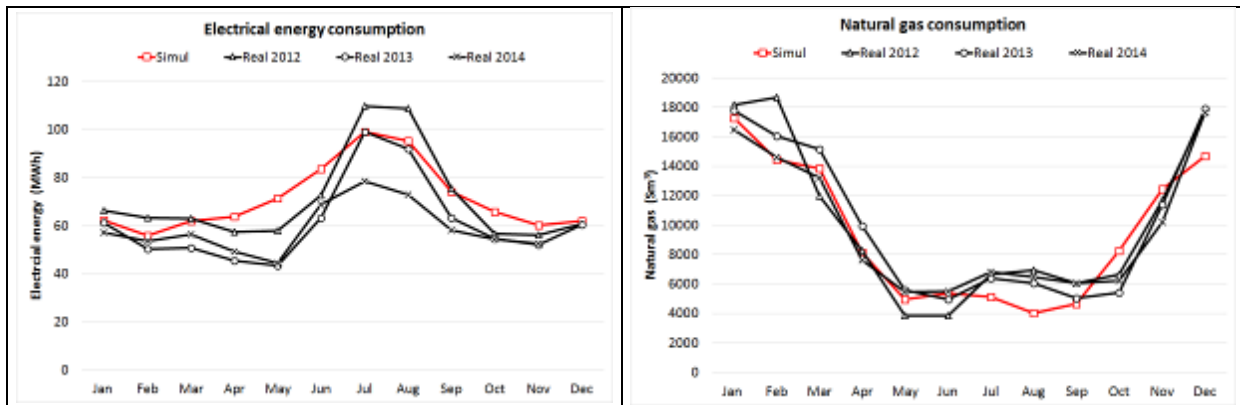
Figure 56: Annual profile of monthly electrical energy and NG consumptions.

4. ALTERNATIVES FOR THE HEATING/COOLING PLANT ENERGY RETROFITTING

Different efficient technologies among the most common known were taken into consideration for the energy improvement of the heating/cooling plant, chosen referring to previous economic estimates in possession of the managers responsible for running the care home. Main technical data of all the equipment considered in the present analysis are reported in Table 23.

For the sake of brevity, extremely concise information are here reported:

- photovoltaics, PV: different kinds of mono and poli-crystalline modules were considered, varying the peak power in the 230-315 W_p range (14-16.9 % nominal efficiency), considering a fixed available area (two terraces of 108 m^2 each on the roof and three parking shelters for 1022 m^2). In one alternative it was supposed to be able to install more PV modules on the roof (available area 350+350 m^2). A penalization factor of -0.60 % per year was considered in order to take into account the annual decrease of useful power. All the other parameters and input in Trnsys model were set in order to suitably simulate the PV plant;
- combined heat and power, CHP (cogeneration): internal combustion engines were considered with two different electrical nominal power (103 and 199 kW) and two different control strategies (electric load following and electric load following but during the 6.00am-9.00pm period only). A smaller size one was further considered (60 kW nominal power, electric - load following);
- combined cooling, heat and power, CCHP (trigeneration): in order to extend the operation hours of the cogeneration plants, three of the previous cases were implemented considering to use the heat

365

produced by the engine also during cooling season by coupling suitable sized lithium bromide-water single effect absorption chiller;

- heat pumps: different sizes of vapour compression air/water heat pumps with both electric (EHP) and natural gas engine (GEHP) were considered. For the characterization of their performances the Authors referred to the UNI/TS 11300-4 and UNI EN 15316-4-2 method (Busato *et al.*, 2012).

Table 23: Main technical data of the equipment considered in the present analysis (V_{oc}=open circuit voltage; I_{sc}=short circuit current; V_{mpp}= voltage at maximum power point; I_{mpp}= current at maximum power point) (*Refer to A7/W45 conditions) (**Electric motor efficiency=0.95 – Internal combustion engine efficiency=0.3 (Busato et al., 2012)).

Alternative	Equipment – Rated data
As Is	-
1,Solon Black 220/16 mono (265 Wp)	Peak power=265 kWp – Rated effic.=16.16 % - Voc=38.1 V – Isc=9.01 A – Vmpp=30.7 V – Impp=8.67 A – Voc (% K-1)=-0.33% - Isc (% K-1)=0.04%
2,Solon Black 220/16 poli (230 Wp)	Peak power=230 kWp – Rated effic.=14.02 % - Voc=36.7 V – Isc=8.24 A – Vmpp=29.6 V – Impp=7.78 A – Voc (% K-1)=-0.32% - Isc (% K-1)=0.05%
3, Abba Solar ASP 60 245-250 poli Plus (250 Wp)	Peak power=250 kWp – Rated effic.=16.16 % - Voc=38.6 V – Isc=8.77 A – Vmpp=30.4 V – Impp=8.24 A – Voc (V K-1)=-0.126 - Isc (A K-1)=0.00563
4, Renesola 156 mono (275 Wp)	Peak power=275 kWp – Rated effic.=16.90 % - Voc=38.3 V – Isc=9.35 A – Vmpp=31 V – Impp=8.87 A – Voc (% K-1)=-0.31% - Isc (% K-1)=0.03%
5, Renesola Virtus II JC315M-24/Abs poli (315 Wp)	Peak power=315 kWp – Rated effic.=16.20 % - Voc=45.1 V – Isc=8.88 A – Vmpp=37.3 V – Impp=8.45 A – Voc (% K-1)=-0.30% - Isc (% K-1)=0.04%
1,Solon Black 220/16 mono (265 Wp)__Plus	Peak power=265 kWp – Rated effic.=16.16 % - Voc=38.1 V – Isc=9.01 A – Vmpp=30.7 V – Impp=8.67 A – Voc (% K-1)=-0.33% - Isc (% K-1)=0.04%
1, 103 kW – el. following	El_pow=103 kWel – Th_pow=170 kWth – El_eff=34.2 % - Tot_eff=90.7 %
2, 199 kW – el. following	El_pow=199 kWel – Th_pow=326 kWth – El_eff=34.7 % - Tot_eff=91.4 %
3, 103 kW – el. following –day time only	As 1, 103 kW – el. following
4, 199 kW - el. following –day time only	As 2, 199 kW – el. following
5, 60 kW - el. following	El_pow=65 kWel – Th_pow=120 kWth – El_eff=30.8 % - Tot_eff=92.5 %
2, 199 kW - el. following - trigeneration	As 2, 199 kW – el. following – Cool_pow=147 kWc – EERabs=0.50
3, 103 kW - el. following – day time only – trigen.	As 3, 103 kW - el. following –day time only - Cool_pow=70 kWc – EERabs=0.50
5, 60 kW - el. following - trigeneration	As 5, 60 kW - el. following - Cool_pow=50 kWc – EERabs=0.48
EHP_99 kWt*	El_pow_compr=29.2 kWel – Th_pow=99.2 kWth – COP=3.1
GEHP_99 kWt* **	NG_consumption=8.6 Sm3 h-1 – Th_pow=99.2 kWth (condenser) + 53.8 kWth (engine heat recovery) – COP=4.0
EHP_209 kWt*	El_pow_compr=57.8 kWel – Th_pow=209 kWth – COP=3.3
GEHP_209 kWt* **	NG_consumption=17.7 Sm3 h-1 – Th_pow=209 kWth (condenser) + 91 kWth (engine heat recovery) – COP=4.1
EHP_311 kWt*	El_pow_compr=86.0 kWel – Th_pow=311 kWth – COP=3.3
GEHP_311 kWt* **	NG_consumption=25.7 Sm3 h-1 – Th_pow=311 kWth (condenser) + 147 kWth (engine heat recovery) – COP=4.2
EHP_424 kWt*	El_pow_compr=116 kWel – Th_pow=424 kWth – COP=3.3
GEHP_424 kWt* **	NG_consumption=35.1 Sm3 h-1 – Th_pow=424 kWth (condenser) + 194 kWth (engine heat recovery) – COP=4.2

It was assumed to maintain the two actually present boilers with the double scope of both thermal integration (e.g. when cogenerator or heat pump cannot satisfy thermal needs) and backup (when cogenerator or heat pump is supposed to be set off because building thermal load is lower than the minimum partial load). Finally, primary energy consumptions were calculated taking into account thermal and electrical nominal efficiencies (on Lower Heating Value) for the cogenerators and nominal performances (COP) for the heat pumps (Table 23), and considering their variations with the partial load (data derived by motors suppliers for the cogenerators – data derived implementing the UNI/TS 11300-4 and UNI EN 15316-4-2 calculation methods for quantifying energy loads and efficiencies of electrical HP-based heating plants).

Investment costs were determined by purchase (1300-1700 € kW$_p^{-1}$ for PV, 1400-2000 € kW$_{el}^{-1}$ for cogeneration, 500-625 € kW$_c^{-1}$ for absorption chillers, 500 € kW$_{el}^{-1}$ and 250 € kW$_{th}^{-1}$ for respectively EHP and GEHP) plus installation, first set up, existing plant adaptation costs (8000-30000 € for the different alternatives). Ordinary maintenance costs were also considered (Bianchi *et al.*, 2009) (Lazzarin and Noro, 2006a) (Lazzarin and Noro, 2006b) (Busato *et al.*, 2012). Table 24 reports on the costs of energy: natural gas and electricity purchased by the local distributors.

Table 24: Costs of the different types of energy sources (*Mean values of 2012, 2013 and 2014 electricity bills, real values were variable month by month) (**0.22 Sm^3 kWh_{el}^{-1} consumed by cogenerators are taxed reduced (and local additional tax is erased) in Italy).

Type of energy source	Cost			Reduced tax**	Tax	Local additional tax**
Natural gas	0.42 €/m3			0.0001348 € Sm-3	0.012498 € Sm-3	0.006249 € Sm-3
Electricity*	Fixed 61 € month-1	Power 2.74 € kW-1 month-1	Energy 0.14 € kWh-1		0.0125 € kWh-1	

Concerning the management of the electricity produced by the cogenerators and photovoltaic plant, there are not economic incentives in Italy for new plants nowadays. For the considered plant size, the only possibility is the so called "ritiro dedicato" (dedicated collection of electrical energy). In this case, electricity produced besides own consumption is sold to the GSE ("Gestore Servizi Energetici", Energy Services Manager) at a constant price (fixed in 5.5 c€ kWh^{-1}), anyhow lower than the saving obtainable with net metering (the saving in purchasing electricity, around 16 c€ kWh^{-1}, Table 24). Nevertheless, net metering option was not considered because of the limited electricity self-production not consumed by the building for the cases here considered.

Finally, the Authors considered the economic gains obtainable by the different co- and tri-generation solutions by means of the White Certificates ("Certificati Bianchi"), an economic incentive credited on the basis of the primary energy savings obtained by the different solutions (the value here considered is 60 € toe^{-1}, 1 White Certificate=1 toe). For the primary energy calculations we considered the conversion factors reported in (AEEG, 2008), i.e. 1 kWh_{pr} kWh_{th}^{-1} and 2.17 kWh_{pr} kWh_{el}^{-1} respectively for natural gas and electricity. For the alternatives here considered, the incomes from the White Certifcates resulted negligible because they did not, or only slightly, satisfy the minimum primary energy saving index provided by the 2004/8/CE European Directive (acknowledged in Italy by the Legislative Decree 8/2/2007, n. 20). This was due to the electric load following operation strategy that implies thermal energy produced by cogenerators to be dissipated when not useful. CCHP alternatives allowed to reduce the heat dissipation. As will be stated in later section, the energy and economic results of cogeneration and trigeneration alternatives that should be operated with a thermal load following strategy would be further improved.

5. RESULTS AND DISCUSSION

The results of the analysis of the different alternatives described in the previous section are reported in terms of energy consumptions and economic viability with respect to the "As Is" solution. Simulations were run with one hour time-step, but annual energy results are here reported for the sake of brevity. To make the conclusions more consistent, a sensitivity analysis was done in order to compensate for the uncertainty of some of the parameters here considered.

5.1 Energy Analysis

Annual balances of the energy vectors used in the building are reported in Figure 57 and Figure 58 respectively for NG and EE. Obviously, installing a PV plant does not affect the NG consumption; the solutions that maximize NG consumptions (even if minimizing the boilers consumption) are the ones with the installation of the 199 kW_{el} nominal power cogenerators, while the solutions minimizing the consumption in absolute terms concern installing the biggest sized electric heat pumps ("EHP_311 kWt" and "EHP_424 kWt"). The balance, in terms of electrical energy, takes into account the "self-produced" and the "sold to grid" electricity: the solutions that minimize the purchase from the grid (by more than 20 times with respect to the "As Is" plant) are the ones that maximize the self-production ("2, 199 kW – el. following" with and without trigeneration). In these cases, a not negligible quote of energy is sold to grid. Anyway, the other CHP and CCHP solutions allow to reduce the electricity from the grid from 2 to 5 times. From this point of view, the most advantageous PV solution is "1, Solon Black 220/16 mono (265 Wp)__Plus", while the mean saving of the other PV alternatives is around 25 %. Obviously, heat pump solutions do not allow electricity saving at all.
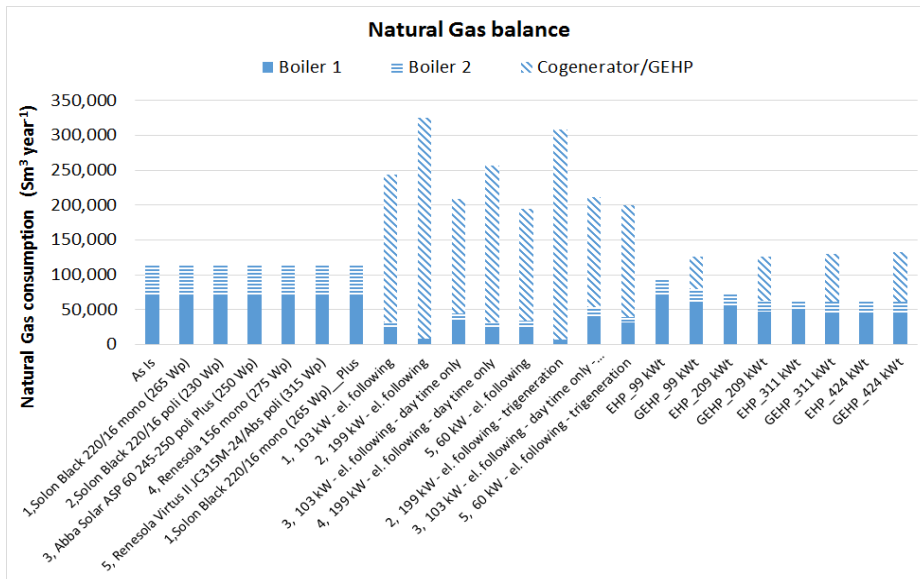
Figure 57: NG annual balance for the different HVAC retrofitting alternatives.
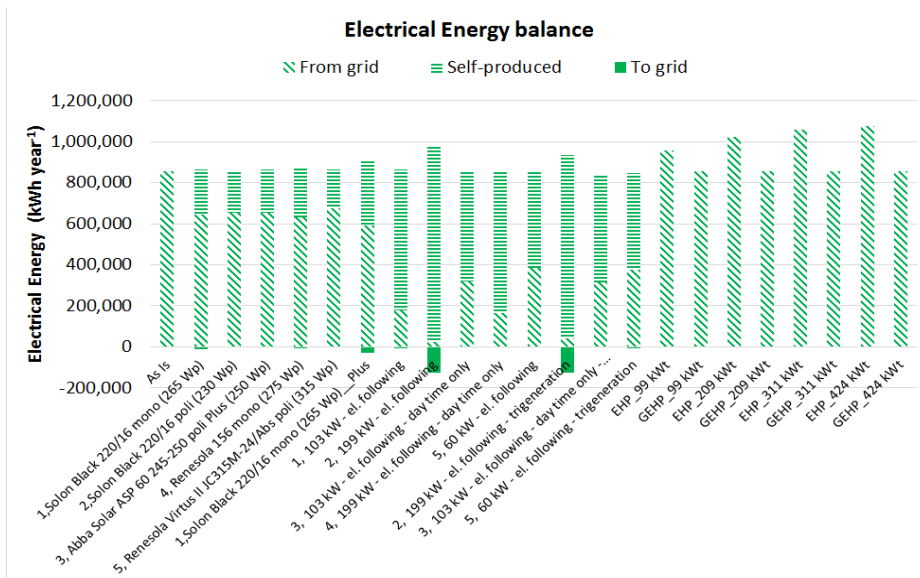

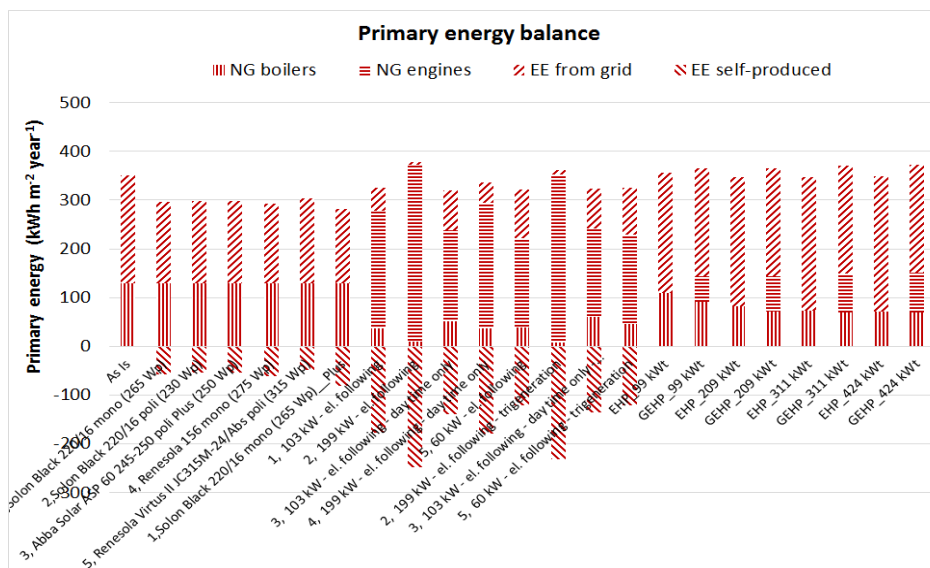Figure 58: EE annual balance for the different HVAC retrofitting alternatives.

Figure 59: Primary energy annual balance (per square meter of building surface) for the different HVAC retrofitting alternatives.

Table 25: Annual Primary Energy consumption of the different solutions, both in absolute (MWh) and specific terms (kWh m⁻²).

Alternative	Total PE		Saving	Alternative	Total PE		Saving
	(MWh)	(kWh m-2)			(MWh)	(kWh m-2)	
As Is	2944	351	-	5, 60 kW - el. following	1689	201	43%
1, Solon Black 220/16 mono (265 Wp)	2015	240	32%	2, 199 kW - el. following - trigeneration	1092	130	63%
2, Solon Black 220/16 poli (230 Wp)	2058	245	30%	3, 103 kW - el. following - day time only - trigeneration	1581	188	46%
3, Abba Solar ASP 60 245-250 poli Plus (250 Wp)	2058	245	30%	5, 60 kW - el. following - trigeneration	1720	205	42%
4, Renesola 156 mono (275 Wp)	1942	231	34%	EHP_99 kWt	2999	357	-2%
5, Renesola Virtus II JC315M-24/Abs poli (315 Wp)	2138	255	27%	GEHP_99 kWt	3067	365	-4%
				EHP_209 kWt	2911	347	1%
1,Solon Black 220/16 mono (265 Wp)__Plus	1694	202	42%	GEHP_209 kWt	3064	365	-4%
1, 103 kW - el. following	1236	147	58%	EHP_311 kWt	2916	347	1%
2, 199 kW - el. following	1101	131	63%	GEHP_311 kWt	3111	370	-6%
3, 103 kW - el. following - day time only	1524	181	48%	EHP_424 kWt	2931	349	0%
4, 199 kW - el. following - day time only	1317	157	55%	GEHP_424 kWt	3135	373	-6%

A more comprehensive comparison, carried out in terms of primary energy (PE), is reported in specific terms (per square meter of building surface) in Figure 59 and in absolute terms as well in Table 25. Self-produced electrical energy accounts for a negative value in terms of consumption, so the best solutions foresee the installation of 199 kW$_{el}$ cogenerator (coupling the absorption chiller allows a very slight improvement). These solutions allow to reduce by 63 % the PE consumption. Anyway, if one looks at the benchmark for Italy suggested by (Pedro *et al.*, 2011) (234 kWh m⁻² year⁻¹), all the CHP and CCHP alternatives and two PV solutions are performant. On the other hand, heat pumps, both electric and natural gas driven, are not advantageous at all and, in some cases, they lead to an increase of the PE consumption. This is due to the penalized operation of air/water heat pumps in the Vicenza winter climate with frequent defrosting necessity (Lazzarin and Noro, 2006a) (Lazzarin and Noro, 2006b) (Busato *et al.*, 2011) and especially due to the high temperature of water at the condenser).

5.2 Economic Analysis

The interest rate, the inflation rate and the period of the economic analysis were fixed in 4 %, 1.8 % and 20 years respectively. From the economic point of view, the comparison between the different alternatives did not consider the investment cost of substituting the existing plant, as it was considered to be a sunk cost. The best solutions (in terms of trade-off between maximum differential - investment alternative versus "As Is" solution - net present worth (NPW) and minimum discounted pay-back period (DPB)) are the CHP/CCHP ones with installed electrical power around or less than 100 kW$_{el}$: NPW is around 630-670 k€ and DPB is between 3 and 4 years (Figure 60); all three are very interesting, also considering that we are talking about the plant of a public building stock (so payback periods can be quite longer than in industry sector). These are also the solutions that allow the minimization of thermal energy dissipation by the cogenerator. From this point of view, it is interesting to observe that a further increase of the economic viability of such alternatives would be obtained by operating the cogenerator with the thermal load following logic. Concerning the "2, 199 kW" solution it is worth to stress that coupling the absorption chiller can improve the economic viability, but even more advantageous is the operation during the day only (respectively NPW increases from 195 to 332 to 423 k€ and DPB decreases from 10.9 to 9.6 to 7.1 years). Photovoltaics is also interesting, even if it allows smaller NPWs (200-300 k€) and longer DPBs (9-11 years). Should be possible to use more surface on the roofs ("1, Solon Black 220/16 mono (265 Wp)__Plus" solution) the economic viability would slightly increase (NPW=440 k€, DPB=8.6 years). It is interesting to observe that heat pump solutions are not advantageous at all as they present a greater than "As Is" solution annual cash flow (Figure 61).
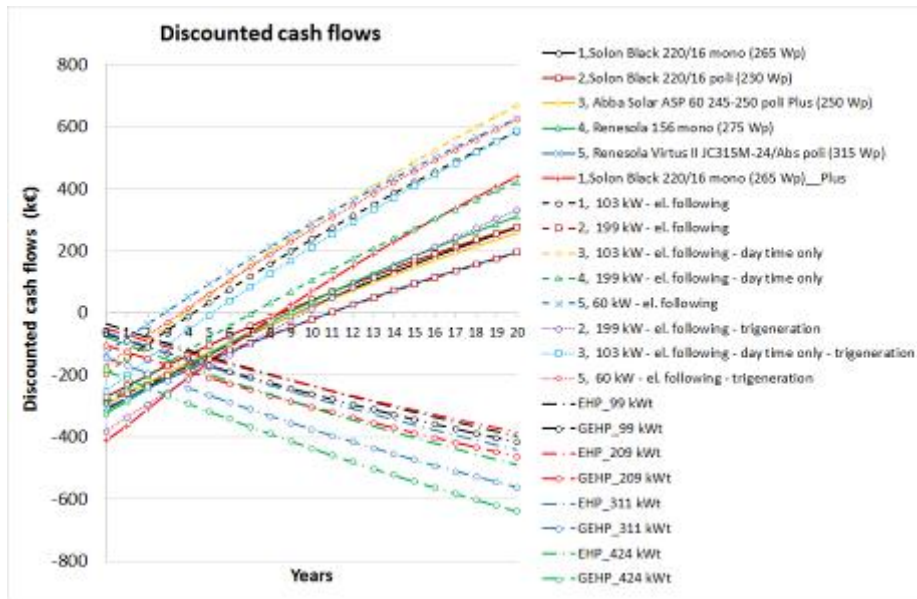
Figure 60: Discounted differential (between the alternatives and the "As Is" solution) cash flows of the different solutions. NPWs can be read at the end of the period of analysis (20 years), DPBs by the interceptions of the curves with the x-axis.
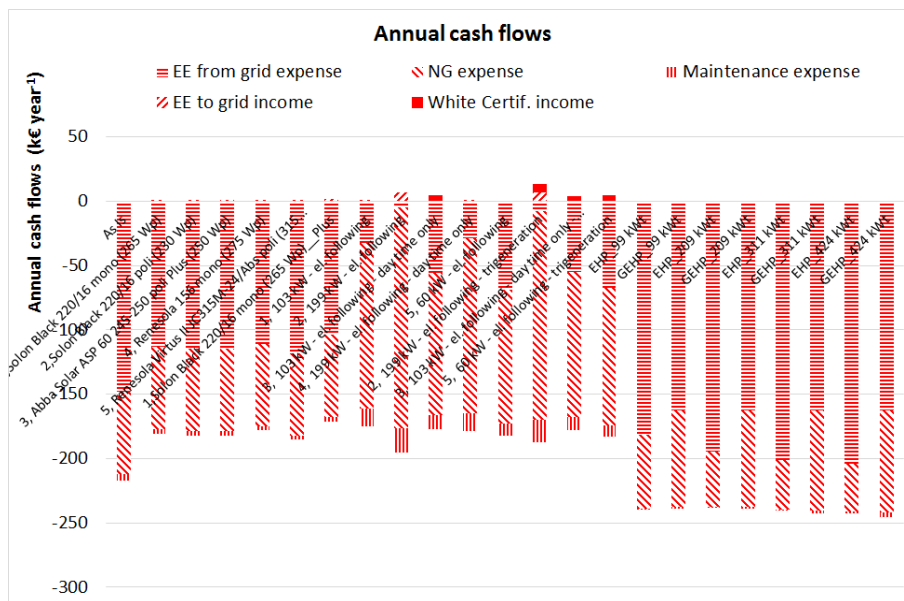
Figure 61: Annual differential (between the alternatives and the "As Is" solution) cash flows of the different solutions spit into the main components (negative values=expenses; positive values=incomes).

5.3 Sensitivity Analysis

These conclusions may be completed by a sensitivity analysis in order to compensate for the uncertainty of some of the parameters here considered, such as natural gas and electrical energy costs. All the cogeneration and trigeneration solutions result to be quite sensitive to the cost of electrical energy purchased from the grid and the cost of natural gas, increasing their economic advantage when increasing the former and decreasing the latter. In particular, the solutions with the largest sized cogenerator (199 kW$_{el}$ rated power) show the faster improvement of the economic viability. It is worth to stress that it is hard to predict which will be the most advantageous solution in the future (i.e. considering an increase of the energy costs) because of the opposing trends of the curves. The air/water HP solutions could become competitive with the CHP/CCHP solutions only in case of a substantial increase in NG cost and above all a decrease of EE cost. From this point of view, a different heat source might be considered (e.g. the ground, as the building is surrounded by a large green surface, or the solar thermal, as there is the possibility to install it). Moreover, a lower condensation temperature (e.g. producing hot water at 45 °C) might be further

considered. Anyway, this one would be only a theoretical option as the substitution of radiators (in both bedrooms and bathrooms) and coils (in the AHUs) would be required. NPWs and DPBs are much less sensitive to the variation of the technology investment cost, set up and adaptation cost and interest rate (results are not reported for the sake of brevity).

6. CONCLUSIONS

Many energy efficiency interventions can be thought to be implemented in residential care homes for elderly people as the greatest part of them are old buildings, i.e. built before regulations on buildings energy performance and economic incentives. In this sense, interventions on the building (e.g. retrofitting of the opaque and transparent surfaces by thermal insulation and windows substituting) are the first ones that should be implemented; installing a solar thermal plant and substituting the old lighting appliances by more efficient ones should be the second ones. In more recent (and so more energy performant) buildings some retrofitting interventions in heating/cooling plant can be analyse. Photovoltaics, cogeneration, trigeneration, electric and gas engine heat pumps were considered in this study and the energy and economic viability were evaluated. Cogeneration with small size engines (with respect to the installed electric power by local distributor) result the most advantageous solutions, whereas coupling a single-effect absorption chiller do not improve the advantage. Photovoltaics as well allow an interesting energy saving with respect to the existing plant, even if with longer payback periods. Air/water heat pumps (the most economic and widespread diffused ones) are not advantageous at all in this case because of the high temperature at condenser and because of the cold and humid winter climate typical of the Po Valley (that implies frequent defrosting of the evaporator coil). The main conclusions of this study will be delivered to the managers responsible for running the residential care home in order to make energy efficient informed decisions.

7. ACKNOWLEDGEMENT

8. REFERENCES

AEEG, 2008. Delibera EEN 3/08, Aggiornamento del fattore di conversione dei kWh in tonnellate equivalenti di petrolio connesso al meccanismo dei titoli di efficienza energetica (*Updating of the kWh/toe conversion factor related to the energy efficiency certificates*, in Italian).

BIANCHI M., Spina P.R., Tomassetti G., Forni D., Ferrero E., 2009. Le tecnologie innovative ed efficienti nei sistemi di generazione in assetto co-trigenerativo e nei sistemi integrati con unità a pompa di calore nelle applicazioni industriali e del terziario (*Innovative and efficient technologies in co-trigeneration plants and in integrated heat pump systems in industrial and commercial applications*, in Italian). Report RSE/2009/18, ENEA.

BUSATO Filippo, Lazzarin Renato, Noro Marco, 2011. Ten years history of a real gas driven heat pump plant: energetic, economic and maintenance issues, *Applied Thermal Engineering*, 31, pp. 1648-1654, doi:10.1016/j.applthermaleng.2011.02.006.

BUSATO Filippo, Lazzarin Renato, Noro Marco, 2012. Energy and economic analysis of different heat pump systems for space heating, *International Journal of Low Carbon Technologies*, 7(2), pp. 104-112, doi:10.1093/ijlct/cts016.

ESTEVES Pedro, Fonseca Paula, Almeida Aníbal, Nunes Urbano, 2011. EU comprehensive document on energy efficiency in Residential Care Homes for the Elderly. SAVE AGE Project. IEE/09/676/SI2.558233.

ISTAT (Italian national statistics institute), 2006. Previsioni demografiche nazionali (*National demographic forecasts*, in Italian).

LAZZARIN Renato, Noro Marco, 2006a. District heating and gas engine heat pump: economic analysis based on a case study, *Applied Thermal Engineering*, 26, pp. 193-199, doi:10.1016/j.applthermaleng.2005.05.013.

LAZZARIN Renato, Noro Marco, 2006b. Local or district heating by natural gas. Which is better from energetic, environmental and economic point of view?, *Applied Thermal Engineering*, 26, pp. 244-250, doi:10.1016/j.applthermaleng.2005.05.007.

SCUOLA SUPERIORE DELL'AMMINISTRAZIONE DELL'INTERNO (SUPERIOR SCHOOL OF ITALIAN MINISTRY OF THE INTERIOR), 2010. Gli anziani in Italia: aspetti demografici e sociali ed interventi pubblici (*Elderly people in Italy: demographic and social aspects and public interventions*, in Italian).

40: Overall energy performance analysis of a living lab building in Denmark

ANA IONESI1,*, MUHYIDDINE JRADI1, CHRISTIAN T. VEJE1

1 Center for Energy Informatics, Campusvej 55, Odense, Denmark
Corresponding Author: ai @mmmi.sdu.dk

Denmark aims to become independent of fossil fuels by 2050 through renewable energy integration as well as improving the efficiency of energy resources utilization. The building sector is one of the major targets where buildings in Denmark contribute to about 40% of the overall Danish energy consumption, mainly for heating, ventilation and lighting. It is estimated that energy savings of 70-75% could be attained in the Danish building sector by 2050 through the implementation of cost effective and energy efficient measures

This paper focuses on evaluating the energy performance under various conditions of a living lab building situated in Vejle, Denmark. An overall energy model for the whole building was developed taking into account the building envelope, construction materials, thermal properties and various building systems and services employed. EnergyPlus was used to model the building and simulate the overall energy performance under Danish regulations and weather conditions. Preliminary validation of the developed model is presented through comparison with real measurements.

Based on the data attained, the energy class in which the building lies will be identified. In addition, an analysis of the main factors that influence the energy performance will be conducted, highlighting the possible areas of improvements in the overall energy performance.

The building management system installed in the building is regularly updated and optimized, and therefore the development of such holistic energy model for the building is crucial to be directly integrated in the overall management strategy to improve the performance of the energy systems and to test different control and optimization strategies.

Keywords: energy efficiency, buildings, simulations, optimization.

1. INTRODUCTION

The Danish energy strategy aims to become independent of fossil fuels by 2050 through renewable energy integration as well as improving the efficiency of energy resources utilization. The buildings sector is one of the major targets where buildings in Denmark contribute to about 40% of the overall Danish energy consumption mainly for heating, ventilation and lighting. It is estimated that energy savings of 70-75% could be attained in the Danish building sector by 2050 through the implementation of cost effective and energy efficient measures (DANISH GOVERNMENT, 2011).

Due to high energy consumption in buildings, the new buildings are expected to meet higher and stricter levels of performance. The tendency is to have sustainable buildings, to use net-zero energy and be grid-friendly, to increase the occupant comfort and reduce the costs (KOLOKOTSA et al., 2011). To attain these goals and decrease the CO_2 footprint of buildings new efficient measures are applied to building envelopes, internal conditions and building services systems (LI et al., 2013). These measures are included in the new standard regulations for buildings.

There are numerous energy performance simulation tools (CRAWLEY et al., 2008) to study energy and thermal comfort in buildings. Most of them consist of a so-called engine, which contains the mathematical and thermodynamic algorithms used to calculate the energy performance. All the simulation results are directly governed by the accuracy of the input data such as: building geometry, internal loads, HVAC systems and components, weather data, operating strategies and schedules, and simulation specific parameters. Due to the fact that the simulations are based on thermodynamic equations, principles and assumptions, the results can be arbitrary incorrect, if some of the assumptions are not satisfied (MAILE et al., 2007).

The monitoring of real energy use in buildings often shows significant differences with respect to predicted energy performance (SCOFIELD, 2013). This discrepancy exists due to numerical errors in simulations as well as experimental errors in the observations. The tool developers have always tried to find a reasonable agreement between these factors in order to achieve a better prediction and more accurate estimates for energy performance. It is important to close this gap in order to generate reliable building energy certificates as well as ensuring a good performance of the building during its operation (DE WILDE, 2014).

In this paper it is described a preliminary energy performance evaluation of the Green Tech House (GTH) as a case study. A building model implemented in EnergyPlus is compared to the predesigned model made to obtain the building certificate. The focus is on the building compliance with the Danish regulations. A pre validation of the developed EnergyPlus model is performed, using real measurements.

2. BUILDING ENERGY SECTOR IN DENMARK

The buildings constructed in Denmark should comply with the Danish Building Regulation 2010 (BR10), which was introduced in January 2011. This standard includes a Class 15 definition for low energy buildings. To have the status of a Class 15 building, it is required that the total demand for energy supply is less than 75% of the permitted limit by the standard for a regular building. Later on, in August 2011, the Class 20 was introduced, defining nearly zero energy buildings. The energy frame of BR10 standards are presented in Table 1.

Table 26: Danish building regulation energy frame

Building type	BR10 Standard	Class 15	Class 20
Residential	52,5 + 1650/A	30 + 1000/A	20
Non-residential	71,3 + 1650/A	41 + 1000/A	25

The values are expressed in KWh/m^2 per year. "A" represents the total ground heated area of the building in m^2.

Around 10% of the new buildings constructed lately in Denmark comply with Class 15. Class 20 it is still voluntary, but it is expected that the municipality will allocate specific areas to comply with this new standard in the near future, as it has been undergone with Class 15 (AGGERHOLM, 2013).

In Denmark all buildings should be certified according to the Energy Performance Certification (EPC) scheme issued by the Danish Energy Authorities (AGGERHOLM et al., 2012). These certificates can be delivered by qualified energy experts using authorized simulation engines (DYRBØL and AGGERHOLM, 2008). Frequently, the predictions of the energy simulations differ from the actual energy consumption of the building.

Be10 is the Danish authorized software to perform the energy rating of buildings. This tool uses a simplified steady state method based on monthly data for climate, heat gains, heat losses and occupancy schedules. Because of its limitation to one zone calculation this tool does not reveal thermal comfort aspects. A comparison between Be10 and a more advanced energy simulation tool (IES-VE) shows that more accurate predictions can be obtained using a full scale dynamic simulation engine (CHRISTENSEN et al., 2013).

3. BUILDING CASE STUDY

In order to carry out a full scale simulation under dynamic conditions, a living lab building situated in Vejle, Denmark, is considered as a case study. The evaluation of the building energy performance is presented in this paper.

3.1 Green Tech House

The considered building, GTH, consists of 3 levels with approximately 3500 m^2 cumulative area having about 60 workplaces per story. The Green Tech House is a commercial Living Lab that has various demonstration spaces equipped with different smart energy solutions. It is designed to accommodate a maximum occupancy capacity of 149 people distributed in classrooms, conferences and seminars spaces for short period rent and permanent offices. The building is connected to a district heating network, and has the possibility of integrating a heat pump, wind turbine and solar panels.

3.2 EnergyPlus Implementation

One of the most used building energy performance simulation tools is EnergyPlus (CRAWLEY et al.,2000). This simulation engine fully integrates the buildings and its HVAC system using the multi zone approach (CRAWLEY et al., 2001). The tool has no graphical interface, allowing third parties developers to add new models providing different interfaces. Based on the available documentation, the GTH is implemented in EnergyPlus. Open studio and SketchUp are used as complementary tools. The geometrical view of the building is shown in Figure 1.

Figure 62: Implementation of GTH in SketchUp.

The overall energy model for the whole building was developed taking into account the building envelope, construction materials, thermal properties and various building systems and services employed. The model is divided into 107 spaces corresponding to specific rooms. All spaces are assigned with a thermal zone. According to the HVAC system specifications, 85 zones are conditioned. The zoning of the building is based on the fact that each room is controlled individually.

4. PRELIMINARY RESULTS

A comparison between the initial design predictions made in Be10 and the results from EnergyPlus is presented to verify the building compliance with the BR10 standards.

4.1 Initial simulation made by designers

In the design phase, the overall energy performance of the building was predicted by the designers using the simplified energy simulation tool developed by the Danish Building Research Institute, Be10. Based on the initial simulations, the overall energy prediction is 40,1 kWh/m^2 per year. According to this, the building is complying with Class 15 standard. As shown in Figure 2, most of the energy is used for heating.
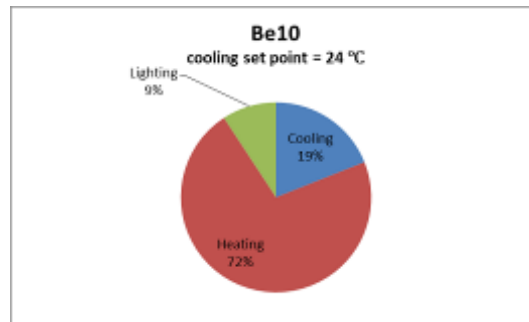
Figure 2: Be10 results (RAMBØL, 2013).

4.2 EnergyPlus simulation

Since at the time when the model was developed, no HVAC system specifications were available for the building, ideal loads simulations are used to get an estimate for the overall energy consumption of the building. This type of simulation assumes that each conditioned thermal zone is equipped with an ideal HVAC system that delivers the required amount of heating / cooling in order to achieve the desired temperatures. The temperature is controlled based on the implemented schedules. All conditioned zones have thermostats. The annual end energy use breakdown results from EnergyPlus for the ideal load simulations are shown in Figure 3.
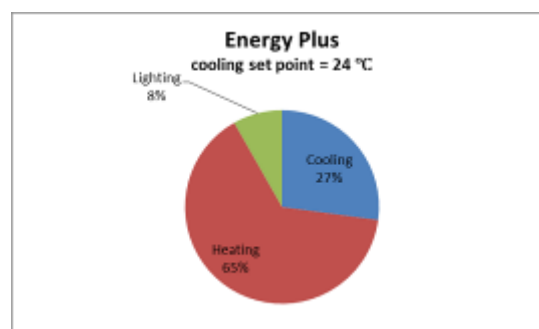
Figure 3: EnergyPlus results

In this case, the building complies with the baseline specification of BR10, but not with the Class 15 as the initial Be10 model suggests. There are major differences between the pre-designed and the as built simulation, especially for cooling demand. The results of the simulations are summarized in Table 2.

Table 2: Energy predictions for GTH building

Simulation Tool	Energy use [kWh/m2 *year]				Compliance
	Heating	Cooling	Lighting	Total	
Be10	28,8	7,6	3,7	40,1	Class 15
EnergyPlus	34,4	14,5	4,4	53,3	BR10

In the Be10 model, the overall heat transfer coefficient for the envelope components are implemented based on the standard requirements, not based on the actual building specifications as in the case of the

EnergyPlus model. Same approach applies for the lighting. Be10 uses a monthly steady state, one zone calculation (CHRISTENSEN et al., 2013), while EnergyPlus uses a multizone dynamic approach.

In Figure 4 and 5 the predictions from EnergyPlus for heating and cooling energy consumption are shown.
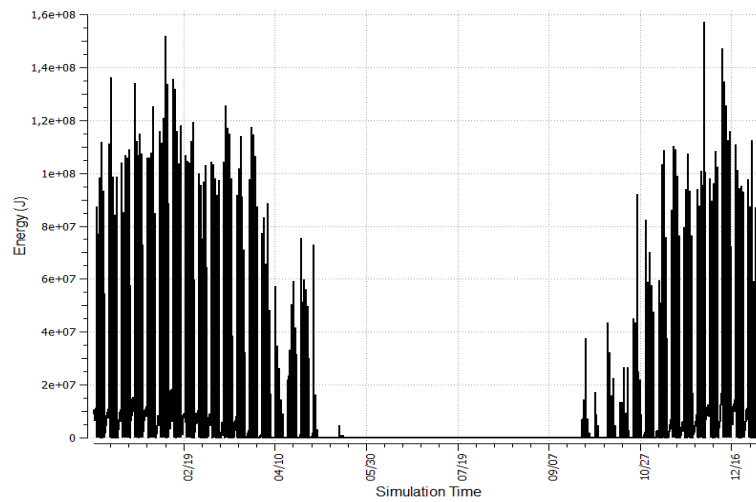
Figure 4: EnergyPlus results – one year predictions for heating demand
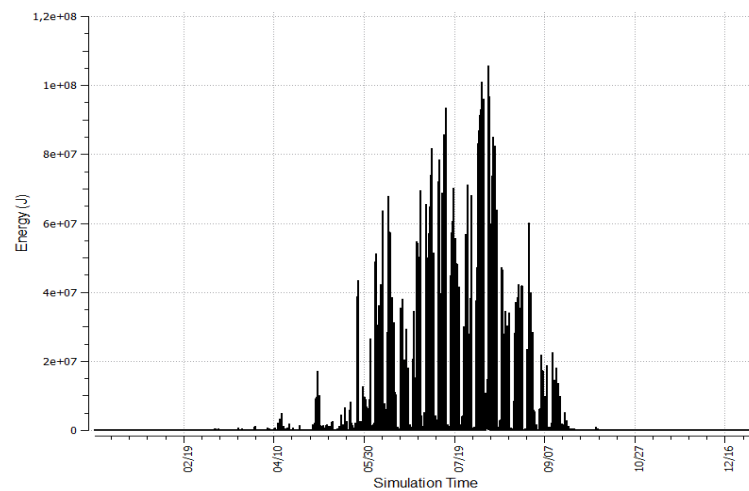
Figure 5: EnergyPlus results – one year predictions for cooling demand
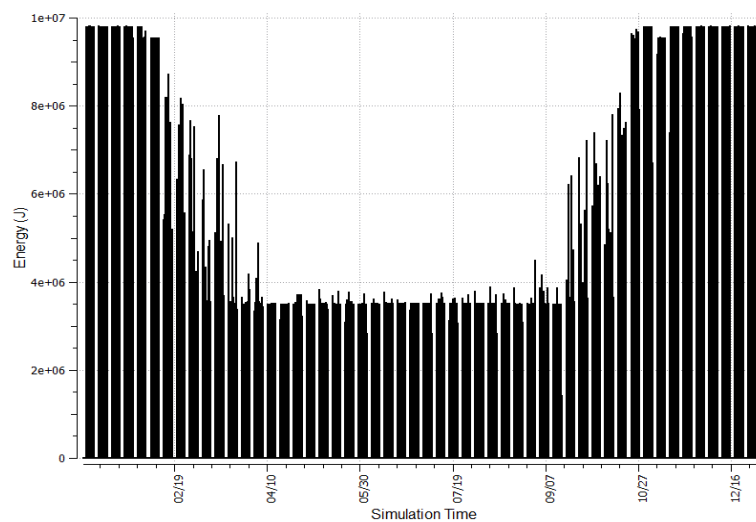
Figure 6: EnergyPlus results – one year predictions for lighting energy consumption

The energy consumption for lighting is shown in Figure 6. There is constant low energy consumption during spring and summer, and an increase in the consumption during the transition between cold and warm season due to daylight variation. The highest energy consumption for lighting is used during winter, approximately double the summer consumption.

5. PRELIMINARY MODEL VALIDATION

A preliminary validation of the developed model is presented, using real measurements from the considered building for the period 01.07.2014 – 01.06.2015. The logged data from the main meters for heating and ventilation are used. Since one month is missing, to perform one year analysis the heating and cooling demand for June is assumed to be the same as in July. The actual energy consumption for lighting could not be recorded as the meters provide only the total power consumption of the building that contains also the electrical energy used by all appliances in the building (computers, kitchen equipment, printing areas and others).

Table 3: Measured data from GTH building

Energy use [kWh/m^2 *year]	Heating	Cooling
	33,95	10,74

The predicted heating demand is very close to the measured heat consumption, with an error of 1,3 %. The major difference between the measured and simulated energy consumption is for the cooling demand. In this case, the predicted value is 35 % higher.

This gap could be due to the following factors:

– the actual occupancy level in the building is lower than what is specified in the implemented schedules,
– the natural ventilation when opening the windows is not taken into account in the simulation model,
– the model does not take into account the energy recovery units for the ventilation system in the building,
– the windows have shading devices that are not modelled in EnergyPlus.
– Based on the measured energy consumption, the building is not complying with Class 15 as predicted by the designers. An overall calibration of the EnergyPlus model needs to be conducted in the next research phases to attain more accurate predictions.

6. SUGGESTIONS FOR IMPROVING ENERGY EFFICIENCY

Using the detailed energy simulation model in EnergyPlus, several scenarios for improving the energy efficiency of the GTH building are presented.

6.1 Lighting Control Based on Occupancy

In the initial model, only daylight factor is taken into account. A new measure was integrated in the EnergyPlus model to simulate the building performance including a lighting control based on vacancy sensors. The results are shown in Figure 6. The baseline model is represented with black and the new model with blue. The yearly energy consumption is 3,7 kWh/m^2 , resulting in a reduction of 0,7 kWh/m^2.

1.1 Model Use in Building Operation

One important factor for closing the gap between predicted and measured energy consumption in buildings is building operation. To ensure a good performance and a reliable control strategy, great interest is directed towards integration of building simulation tools with the BMS (CLARKE et al., 2002). EnergyPlus has a high potential in this area, being already used in a wide range of integration platforms (WETTER, 2011) (PANG, 2011).
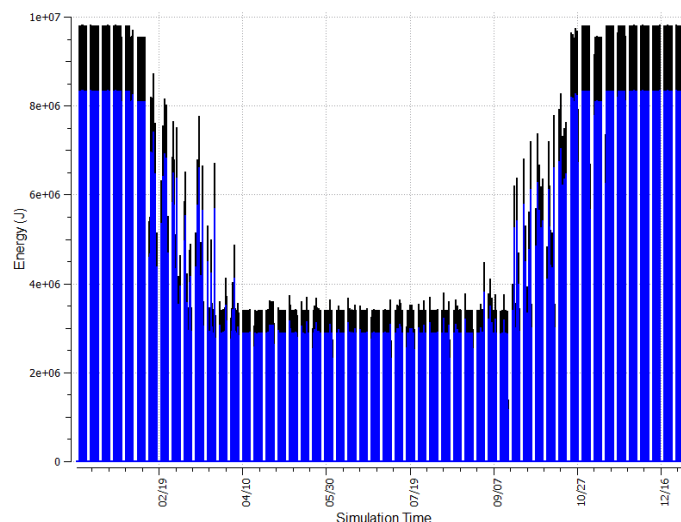
Figure 6: EnergyPlus results – one year predictions for lighting energy consumption using lighting control based on occupancy

2. CONCLUSION

The overall energy performance of the Green Tech House building situated in Denmark was presented in this paper. The building was designed to comply with Class 15 standard. Based on a new implementation in EnergyPlus and the measured heating and cooling energy consumption, the building complies with BR10 standard specification. The major gap between the measurements and predictions is identified in the cooling demand. To close this gap a more detailed full scale validation and a calibration of the model needs to be conducted.

The energy consumption of the building can be reduced with 0,7 kWh/m² by implementing a lighting control based on occupancy. Further work related to renewable energy systems integration and intelligent simulation assisted control will be considered.

The building management system installed in the building is regularly updated and optimized, and therefore the development of such holistic energy model for the building is crucial to be directly integrated in the overall management strategy to improve the overall performance of the energy systems and to test different control and optimization strategies.

3. ACKNOWLEDGEMENT

4. REFERENCES

AGGERHOLM, S, 2013. Cost-Optimal Levels of Minimum Energy Performance Requirements in the Danish Building Regulations; SBi 2013: 25. *SBi: Copenhagen, Denmark*, 42.

AGGERHOLM, S.; Thomsen, K. E.; Wittchen, K. B. , 2012. Implementation of the EPBD in Denmark. Status in November 2010. *Retrieved December*, 2011, 9.

CHRISTENSEN, Jørgen Erik; Schiønning, Peder; Dethlefsen, Espen, 2013. Comparison of simplified and advanced building simulation tool with measured data. In: *13th Conference of International Building Performance Simulation Association*. p. 2356-2363.

CLARKE J. A., et al., 2002. Simulation-assisted control in building energy management systems. *Energy and buildings* 34.9: 933-940.

CRAWLEY, D., et al. , 2001. EnergyPlus: a new-generation building energy simulation program. In: *forum-proceedings-*. American solar energy sock & the American institute of architects. p. 575-580.

CRAWLEY, Drury B. et al., 2008. Contrasting the capabilities of building energy performance simulation programs. *Building and environment* 43: 4, 661-673.

CRAWLEY, Drury B., et al., 2000. Energy plus: energy simulation program. *ASHRAE journal*, 42.4: 49-56.

DANISH GOVERNMENT, 2011. Energy Strategy – from coal, oil and gas to green energy. Ministry of Climate and Energy: The Danish Ministry of Climate and Energy.

DE WILDE, Pieter, 2014. The gap between predicted and measured energy performance of buildings: A framework for investigation. *Automation in Construction*, 41: 40-49.

DYRBØL, Susanne; Aggerholm, Søren, 2008. Implementation of the EPBD in Denmark. Document available at: http://www. epbd-ca. org/Medias/Pdf/2_CO_EPBD_DK. pdf (note EPBD is the Energy Performance of Buildings Directive).

KOLOKOTSA, D., et al. , 2011. A roadmap towards intelligent net zero-and positive-energy buildings. *Solar Energy*, 85.12: 3067-3084.

LI, Danny HW; Yang, Liu; Lam, Joseph C, 2013. Zero energy buildings and sustainable development implications–a review. Energy, 54: 1-10.

MAILE, Tobias; Fischer, Martin; Bazjanac, Vladimir, 2007. Building energy performance simulation tools-a life-cycle and interoperable perspective. *Center for Integrated Facility Engineering (CIFE) Working Paper*, 107: 1-49.

PANG, Xiufeng et al., 2011. Real-time building energy simulation using energyplus and the building controls virtual test bed. 12th Conference of International Building Performance Simulation Association, Sydney.

RAMBOOL, 2013. Green tech house – Energiberegning be10, internal report.

SCOFIELD, John H, 2013. Efficacy of LEED-certification in reducing energy consumption and greenhouse gas emission for large New York City office buildings. *Energy and Buildings*, 67: 517-524.

WETTER, Michael, 2011. Co-simulation of building energy and control systems with the Building Controls Virtual Test Bed. *Journal of Building Performance Simulation*, *4*(3), 185-203.

SESSION 26: SOLAR ENERGY

320: Numerical investigation of thermocline packed bed thermal energy storage system for CSP plants

Ajas Abdulla[1], K. S. Reddy[2]

[1,2] Heat Transfer and Thermal Power Laboratory, Department of Mechanical Engineering, Indian Institute of Technology Madras, Chennai – 600036, INDIA; Email: [2]ksreddy@iitm.ac.in, Tel: +91-44-2257 4702; Fax: +91-44-2257 4652

Thermal energy storage system is becoming indispensable part of any Solar Energy Generation Systems (SEGS) because of its intermittent nature and for enhancing dispatchability of Concentrating Solar Power (CSP) plants. In this study, a two dimensional transient analysis of thermocline sensible heat storage system was carried out numerically to study the discharging characteristics of the packed bed storage system. The governing equation was discretized by finite volume method and coded in MATLAB R2014a. The model takes into account local thermal non-equilibrium between the Heat Transfer Fluid (HTF) and the solid filler bed, thermal diffusion inside HTF, various temperature dependent correlations to obtain the thermo-physical properties for the HTF and considers heat loss through the insulated tank wall henceforth making the model more reliable to design a Thermocline Thermal Energy Storage (TTES) tank. The behaviour of thermocline during discharging and various parameters affecting the performance of the system, namely – tank dimensions, inlet velocity of HTF, storage temperature difference, and cut-off temperature difference criterion were considered. The model was carefully verified based on grid refinement and time step independence studies, and validation of the reference case was done with experimental results in the literature to ascertain the consistency of the proposed model. After validation, all the further analyses were done by taking a modified reference case. It was observed that during discharging, hot region shrinks continuously and the thermocline region is moving upward accompanied by slight expansion and it reached a maximum value of 4.76m inside the tank, almost 1/3rd of the tank height; discharging time increases with height of the tank and decreases with inlet velocity of the HTF; increasing the diameter of tank improves the storage capacity of the system whereas it has no significant influence on the discharging time. It was also obtained that discharging time not only depends on the storage temperature difference, but also with the cut off temperature difference criterion. Discharge time increased from 4.52 hours to 5.32 hours when the cut-off temperature difference was changed from 20 K to 30 K.

Key words: Concentrating solar power, thermocline, packed bed, dispatchability

1. INTRODUCTION

The renewable energy is dramatically gaining its prominence around the globe. The non-polluting, clean and inexhaustible features have made engineers and scientists to do an extensive research on solar energy. CSP have been used for decades to harvest energy from the sun and is used to generate electricity. TES is becoming an indispensible part of any power generating system, especially solar energy systems due to the intermittent and unforeseen weather conditions. TES makes the system more economical by allowing the thermal energy stored in hours of high solar radiation for compensating the intermittency and mismatch between the demand and supply. An affordable energy storage method is thus a crucial element for a successful operation of CSP plants. However, it is also one of the less developed area and only a few CSP plants in the world have tested high temperature TES systems (between 393 K and 873 K) (GIL et al., 2010). TTES system has the potential to reduce the overall cost of the plant since most of the expensive molten salt can be replaced by low cost filler material (GIL et al., 2010). This potential resulted in an increased interest in evaluating such systems through modelling and simulations.

The current study focuses on the thermal performance of a high temperature single-tank sensible thermocline storage tank. Various numerical investigations and comparative analyses were carried out on the thermal and mechanical aspects of high temperature TTES system. The published one and two-dimensional models examined the effect of varying system parameters such as porosity, filler material diameter, tank dimensions etc. on overall performance of the TTES system. The assumption of constant thermo-physical properties, local thermal equilibrium between the HTF and the filler bed or adiabatic conditions of tank wall makes all these models overly simplified. A detailed two-temperature two-dimensional model was presented by (YANG and GARIMELLA, 2010) to study the discharge process of the thermocline system with molten salt and filler material. The same group also conducted a thermo-mechanical analysis of the tank walls to study the thermal ratcheting phenomenon involved with the tank walls (YANG and GARIMELLA, 2010; FLUECKIGER et al., 2011, 2013). (ZANGANEH et al., 2012) came up with a novel tank design to impede thermal ratcheting and experimentally demonstrated a pilot-scale thermal storage unit immersed in the ground to generate thermoclines. (XU et al., 2012) presented a two-dimensional, two-phase model for heat transfer and fluid dynamics within the thermocline storage system. The authors used the model to evaluate different correlations for the interstitial heat transfer coefficient, effective thermal conductivity and the effect of the thermal conductivity of solid fillers. The authors concluded that a uniform cross-sectional temperature can be attained with two insulation layers and that the thermocline region can cover more than 1/3rd of the tank height at its maximum thickness for a tank height of 14 m. (MODI and PE´REZ-SEGARRA, 2014) presented a simplified one-dimensional model to evaluate TTES system performance based on storage temperature difference and the cut-off temperature difference, and their effects on the cycle duration. Authors assumed the effect of thermal conductivity of the filler bed as negligible in their studies. However, it does influence thermal diffusion in the HTF region and the overall performance of the TTES system (FLUECKIGER et al., 2014). The current study attempts to fill these gaps by presenting a two-dimensional, transient, two phase model numerical model for packed-bed TTES system considering local thermal non-equilibrium between the HTF and the filler bed, effect of thermal conductivity of solid filler, various temperature dependent correlations to obtain the thermo-physical properties for the HTF and considers heat loss through the insulated tank wall henceforth making the model more realistic for the evaluation. Various aspects including the behaviour of thermocline inside tank, effect of inlet HTF velocity, storage tank dimension, storage temperature difference and cut-off temperature difference criterion during discharging process will be discussed.

2. MODELLING OF PACKED BED MOLTEN SALT THERMOCLINE STORAGE SYSTEM

The thermocline storage system, as shown in Figure 1, mainly consists of a vertically standing cylindrical tank and the contained storage material, i.e., the molten salt and solid fillers. The tank has inlet/exit ports on the top and bottom for the flow of hot and cold molten salt, respectively. Adjacent to the two exits, distributors are provided to uniformly distribute flow of molten salt through the whole cross section of the packed-bed region. The pack-bed region composes of low cost solid fillers and molten salt takes up the bulk of the tank volume. The tank wall consists of multiple layers (FLUECKIGER et al., 2011); an inner firebrick layer for thermal isolation, a steel shell layer for mechanical support and an outer layer of ceramic fiber for corrosion protection and thermal insulation. During the charging process, the bypassed hot molten salt heated from the solar field enters the storage tank through the port at the top, transfer's heat to the cold solid fillers inside, and leaves the tank through the bottom port with a lower temperature. Thus, energy from the solar field gets stored in the cylindrical tank. During the discharging process, the cold molten salt enters the tank from the bottom port and gets heated by the hot solid fillers in the storage system out of which it emerges as hot molten salt and is sent to the power block for power generation.
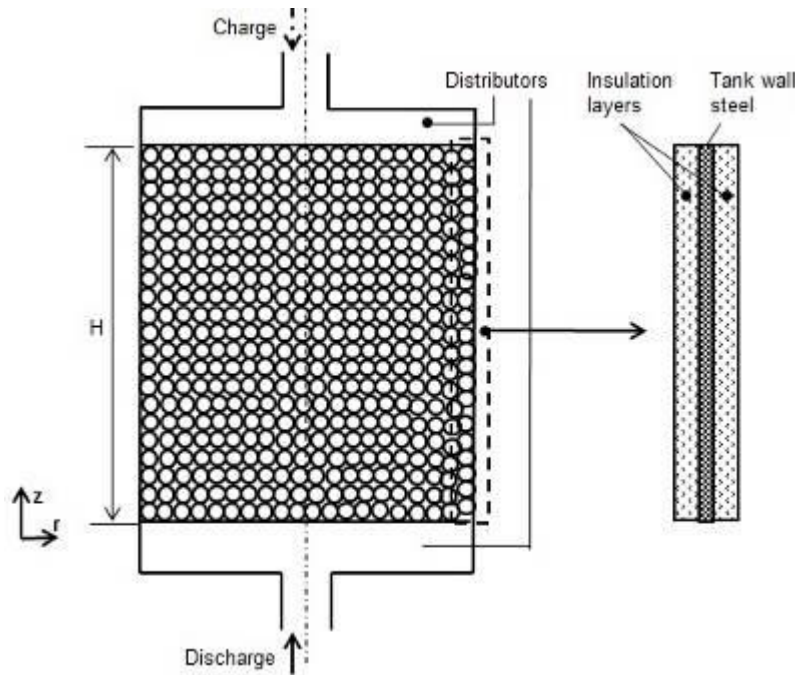
Figure 63: Schematic diagram of the packed bed molten salt thermocline TES and the tank insulation.

In the following, we present a transient, two-dimensional, two phase model to find the characteristics of heat transfer within the packed-bed thermocline storage tank. Since local thermal non-equilibrium exists between the HTF and the filler bed, the energy equations are applied separately to the two phases. The forthcoming assumptions are made to increase the amenability of the governing equations:

- The fluid flow and heat transfer is symmetrical about the axis. Therefore, the governing equations for flow within the storage tank become two-dimensional.
- The filler bed was assumed to be continuous, isotropic and homogeneous.
- The HTF was assumed to have a uniform distribution at the entry to tank.
- Since the filler materials are assumed to be spherical, Conduction in the filler bed was neglected due to inter particle contact resistance.
- The flow of molten salt through the packed-bed region is laminar and incompressible.
- As the temperature profile shows no visible shifts caused by thermal losses in the top and bottom parts of tank, losses from these regions were neglected (MODI et al., 2014).

2.1 Governing Equations

Two-dimensional, two phase model to find the characteristics of heat transfer within the packed-bed thermocline storage tank

Equation 17: Energy balance equation for molten salt.

$$\frac{\partial}{\partial t}\{\in \rho_l \, c_{p_l} \, T_l\} + \frac{\partial}{\partial z}\{\rho_l u \, c_{p_l} \, T_l)\}$$
$$= \frac{\partial}{\partial z}\left(k_{eff} \, \frac{\partial}{\partial z}T_l\right) + \frac{\partial}{\partial r}\left(k_{eff} \, \frac{\partial}{\partial r}T_l\right) + h_i \, (T_s - T_l)$$

Equation 2: Energy balance equation for Filler.

$$\frac{\partial}{\partial t}\left\{(1-\in) \, \rho_s \, c_{p_s} \, T_s\right\} = -h_i \, (T_s - T_l)$$

Where:

- ρ = Density (kg/m³)
- C_p = Specific heat (J/kg-K)
- T = Absolute Temperature (K)
- ϵ = Porosity of the packed bed
- Subscripts *l* and *s* represents molten salt and filler respectively.

2.11. $k_{eff} = k_l \frac{(1+2\beta\emptyset+(2\beta^3-0.1\beta)\emptyset^2+\emptyset^3 0.05e^{4.5\beta})}{(1-\beta\emptyset)}$ The thermal conductivity of rocks in fluid region is represented with an effective thermal conductivity, and is calculated with the Gonzo correlation:

2.12.

2.13. Where: $\qquad \beta = \frac{k_s - k_l}{k_s + 2k_l}$; $-0.499 < \beta < 1$ and $\emptyset = 1-\in$; $0.15 < \emptyset < 0.85$

2.14. $h_i = \frac{(6\,(1-\in)\ k_l\,[2+1.1\,Re_p^{0.6}\,Pr^{1/3}])}{d^2}$ The volumetric heat transfer coefficient hi (W/m³-K) was calculated using the following correlation as mentioned by (XU et al., 2012), where the Re_p is the local Reynolds number based on effective particle diameter, d, and the Prandtl number, Pr, for the HTF.

2.15. $Re_p = \frac{\rho_l du}{\mu}$; $Pr = \frac{\mu\,C_{p_l}}{k_l}$

2.16. $\rho_i c_i \frac{\partial T}{\partial t} = \frac{\partial}{\partial z}\left(k_i \frac{\partial T}{\partial z}\right) + \frac{\partial}{\partial r}\left(k_i \frac{\partial T}{\partial r}\right)$ Where:

Equation 3: Energy balance equation for Insulation material.

Where:

i =   1 - Insulation layer 1; 2 - Steel wall ; 3 - Insulation layer 2

2.2 Computational Domain with Boundary Conditions

Figure 2 shows the Computational domain with boundary conditions applied for the analysis of discharging process. The analysis was axisymmetric since the fluid flow and heat transfer is symmetrical about the axis. In the figure, the temperature and velocity of molten salt are specified at the bottom of tank as the inlet conditions. Adiabatic condition is employed at inlet for the temperature of solid fillers. The top portion represents outlet of the tank, from where the hot molten salt for steam generation is obtained.
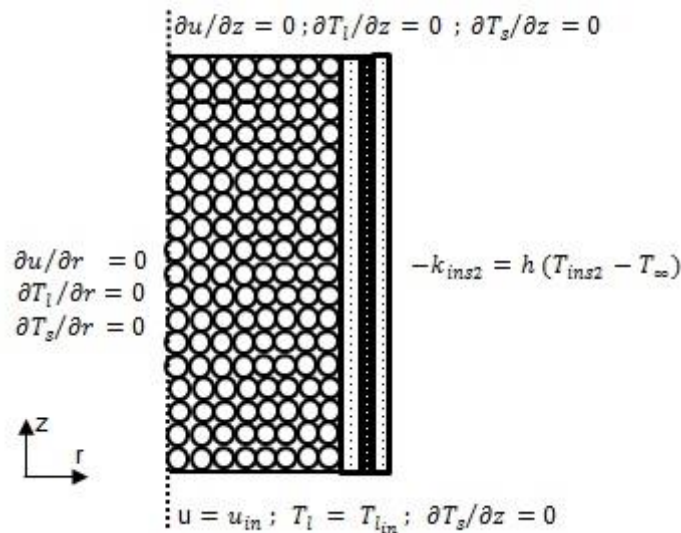
Figure 64: Computational domain with boundary conditions

Left boundary represents the symmetry axis of the cylindrical tank, at which symmetrical boundary conditions are used to the molten salt and solid filler temperatures whereas right end boundary represents the outmost surface (insulation layer 2) of the storage tank open to the ambient air. Heat transport between the surface and ambient air are through forced convection. Heat transfer coefficient, h, in the equation is calculated using Churchill and Bernstein correlation.

From stratification's perspective, the use of Solar Salt gives better performance than the other common HTF's Moreover; Solar Salt provides the highest system storage capacity (MODI et. al, 2014). Hence, Solar Salt was chosen as HTF for the present study. The thermophysical property relations for Solar Salt for a temperature range of 573 K to 873 K are given in Table 1 (ZAVOICO, 2001).

Table 27: Correlations for thermophysical properties of Solar Salt (Zavoico, 2001), T (^{O}C)

Density (kg/m^3)	2090 – 0.636 T
Specific heat capacity (J/kg-K)	1443 + 0.172 T
Absolute Viscosity (kg/m-s)	$2.2714 \times 10^{-4} - 1.20 \times 10^{-4} T + 2.281 \times 10^{-7} T^2 - 1.474 \times 10^{-10} T^3$
Thermal Conductivity (W/m-K)	$0.443 + 1.9 \times 10^{-4} T$

The properties for the solid filler material (quartzite rock and sand mixture) were assumed constant and taken to be: density = 2500 kg/m^3; specific heat capacity = 830 J/kg-K; and thermal conductivity = 5.69 W/m-K. (YANG and GARIMELLA, 2010; XU et al., 2012)

Table 28: The reference case specifications

Parameter	Values
HTF	Solar Salt (60 wt.% NaNO$_3$ + 40 wt.% KNO$_3$)
Filler bed	Quartzite rock and Sand filler
Tank Height , H	6 m
Tank Diameter, D	3 m
Filler bed porosity, ϵ	0.22
Diameter of quartzite rock, d	0.01905 m
HTF inlet flow velocity, u_{in}	4.186×10^{-4} m/s
Hot temperature of the storage system, T_h	673 K
Cold temperature of the storage system, T_c	553 K
Ambient temperature, T_∞	298 K
Wind velocity, v	5 m/s
Cut-off temperature difference at Outlet for Discharge cycle	20

2.17. 2.3 Numerical Model

Solutions to the above energy equations in the porous bed region are obtained via a finite-volume method. The transient term is discretized with a first-order implicit method. Spatial discretization of the convective flux term is accomplished with upwind scheme. The resultant algebraic equations are then solved at each time step with algorithm written in MATLAB 2014a (VERSTEEG and MALALASEKERA, 2007; ANDERSON Jr., 2002). Iterations at each time step proceed until the non-dimensional residual error reduces to less than 10^{-6}. The solution algorithm is described below:

During the discharging process, cold molten salt is pushed to the tank through the bottom port with fixed cold temperature and velocity. At the beginning of the discharging process, the tank is assumed to be filled with molten salt and solid fillers which have the same hot temperature, T_h, and the tank wall is in thermally equilibrium with the interior hot storage material and the outside ambient air. For this, the codes are first run for the tank with an initial uniform hot temperature of T_h and a fixed molten salt velocity (u_{in}) in the storage region. During the running, the molten salt temperature at the inlet port is also fixed as T_c. Finally, a cut-off criterion was set to stop the discharging process as soon as the outlet temperature reached a value 20 K below the storage hot temperature, T_h, (XU et. al, 2012).

3. RESULTS AND DISCUSSIONS

3.1 Model Validation

After grid and time step independence studies, the model was validated against the experimental results obtained by (PACHECO et al., 2002). Figure 3 compares the temperature profiles from his observations (dashed lines) with those obtained from the proposed model (coloured lines) for the reference case. The temperature curve at t = 11:30 from the graph presenting the observations by Pacheco et al. was the initial temperature profiles of the tank for his experiment. Here, the blue coloured line at t = 11:30, somehow close to the observation of Pacheco et al. (dashed blue line), was considered to be the initial condition of the tank for validation. The temperature profiles at the remaining four times (i.e. at t = 12:00, t = 12:30, t = 13:00 and t = 13:30) were obtained by running the code and were used to compare the outputs. It may be observed that the temperature profiles obtained from the current model closely follow the ones from the experimental observations obtained by Pacheco et al. The minor discrepancies can be because the exact experimental

conditions were not available in the literature; hence an approximation based on published data was used as the reference case. Moreover, there may be inherent uncertainties in experimental measurements. Considering all these aspects, results from the proposed model are well matched and assumptions taken for modelling provide a good representation of an operational TTES tank.
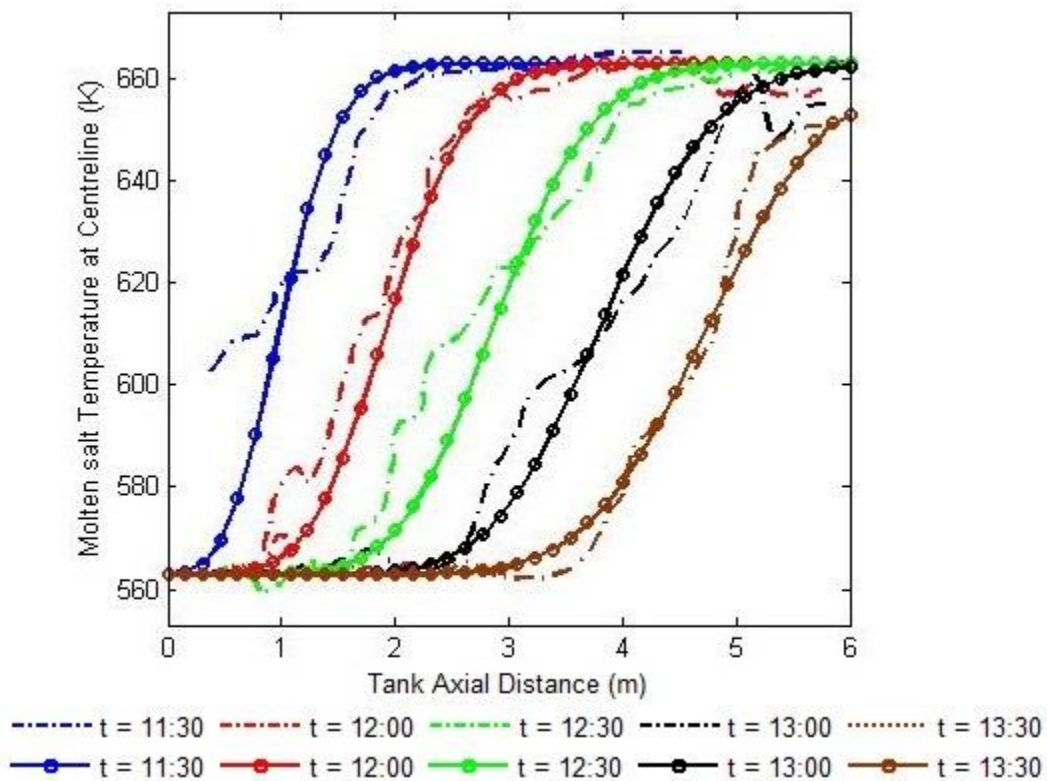
Figure 65: Model Validation against experimental data presented by Pacheco et al. (2002).

The performance of a modified reference case was evaluated by studying the effects of variation in some important system parameters. In the modified reference case, the tank was assumed to have a bed height of 14 m and diameter of 8.6 m. In view of this change, a grid independence test was again performed and a new grid size of 100 x 60 was chosen for the further analysis. These are the only differences from the reference case (Table 2) for the purpose of comparative analysis.

3.2 Thermocline behaviour

The thermocline thickness is an important indicator for the thermal performance of the packed-bed thermocline storage tank. The maintenance of a thin thermocline in the tank is essential to achieve a high discharging efficiency of the storage system. Figure 4 shows the two-dimensional distributions of molten salt temperature for a modified reference case thermocline storage system at different discharging time, i.e., 1 hr, 2 hr, 3 hr and 4 hr. It is clear from figure that the thermocline region is moving upward with the discharging time, accompanied by slight expansion. During discharging, the outlet molten salt temperature remains at the hot temperature of 673 K during the first several hours and starts to decline after about 3.6 hrs since the hot region shrinks continuously with the moving-up of thermocline region. When the thermocline region arrives at the outlet, the hot region disappears and the outlet molten salt temperature starts to decrease. The discharged thermal energy cannot be utilized for useful steam generation when it falls below the threshold value (i.e., 653 K, for cut-off temperature difference of 20 K).
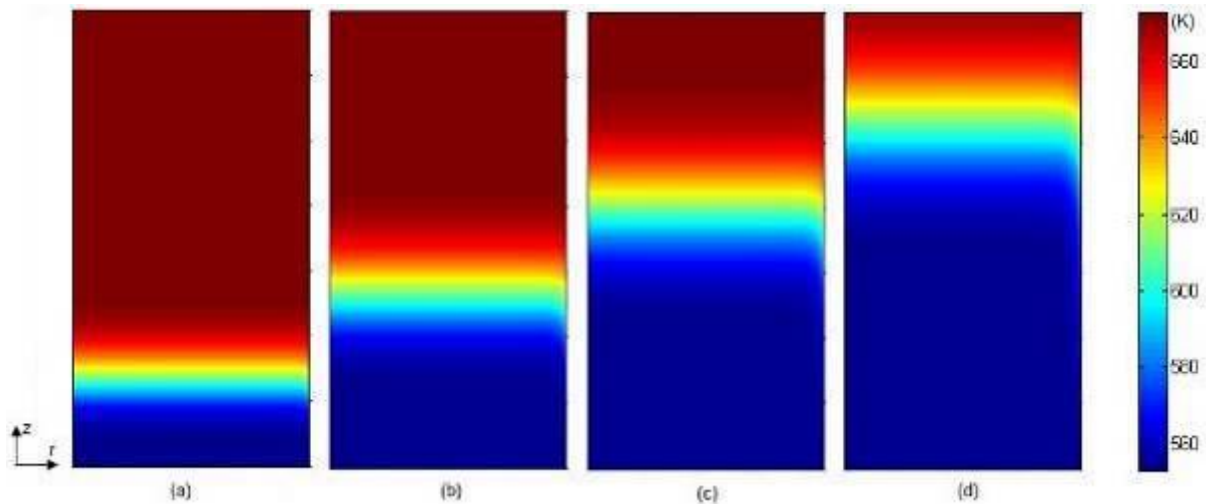
Figure 66: Temperature distribution of Molten salt at different discharging times: a) 1 hr b) 2 hr c) 3 hr and d) 4 hr.

Although the molten salt temperature near the wall can be slightly influenced by the wall temperature, a uniform cross-sectional temperature distribution within the tank was achieved with the help of two insulation layers.
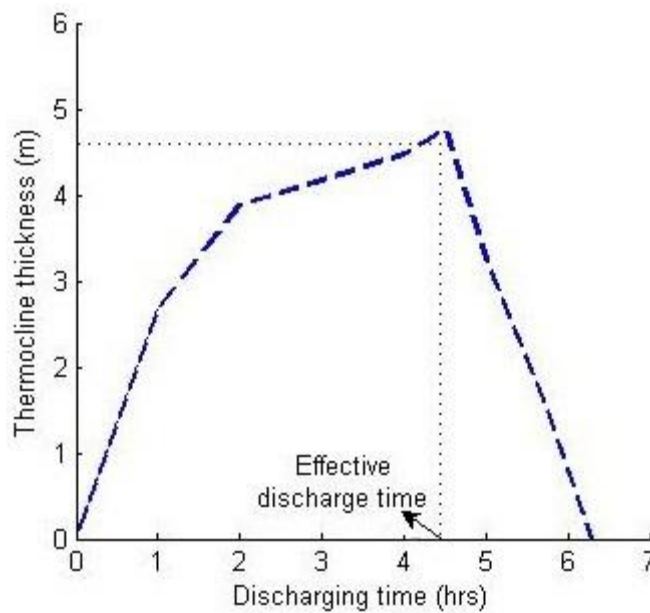
Figure 67: Variation in thermocline thickness with discharge time

Figure 5 shows the variation of thermocline thickness with discharge time. Thermocline thickness increases with time and ascend to a maximum value of 4.76m, almost 1/3rd of the height when it arrives at the outlet. After that, it reduces nearly linearly with fading of the thermocline region.

3.3 Effect of system parameters on performance of TES system

The amount of useful energy that a thermocline system can deliver during a discharge cycle to the total energy initially stored in the thermocline tank is defined as discharge efficiency. Discharge efficiency is higher as the tank discharges more time with other parameters being constant i.e., discharge efficiency is a strong function of the discharging time. Hence, discharging time is taken as the base parameter to analyse various effects of system parameters in this analysis of the modified reference case. The effects of variation in the following system parameters were considered.

Effect of Inlet velocity of HTF:

389

The effect of fluid inlet velocity on the thermal performance is examined in this section by testing different HTF inlet velocities. The inlet HTF temperature, the porosity of the tank and the tank height in this section are 553 K, 0.22, and 14 m. Figure 6 clearly shows that expansion of thermocline is faster as the inlet velocity of molten salt increases which results in reduction in discharging time. Thermocline reaches only half the height of tank with reference velocity whereas it almost reaches the top of the tank with five times increase in the inlet HTF velocity. The molten salt flows faster through the packed-bed with the increase in the inlet HTF velocity, indicating a larger heat discharging rate, and the discharging time decreases significantly.
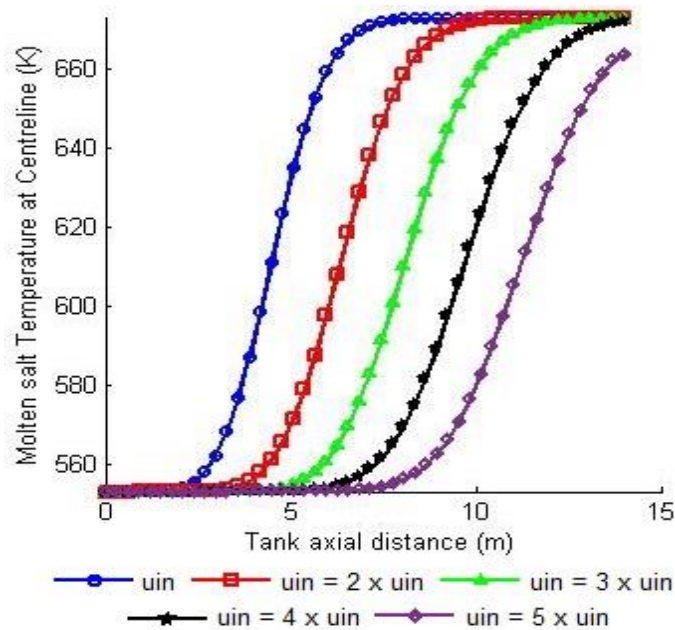
Figure 68: Temperature distribution of Solar salt at various inlet HTF velocities at time = 2 hours.

Effect of Storage tank dimension:

The effect of tank height is shown in Figure 7, in terms of its effect on the temperature history of the molten salt. When the tank height is increased from 6 to 14 m, the discharging time of the system is increased from 1.8 hours to 4.52 hours. Moreover, the capacity of energy storage is proportionally increased by 2.33 times.
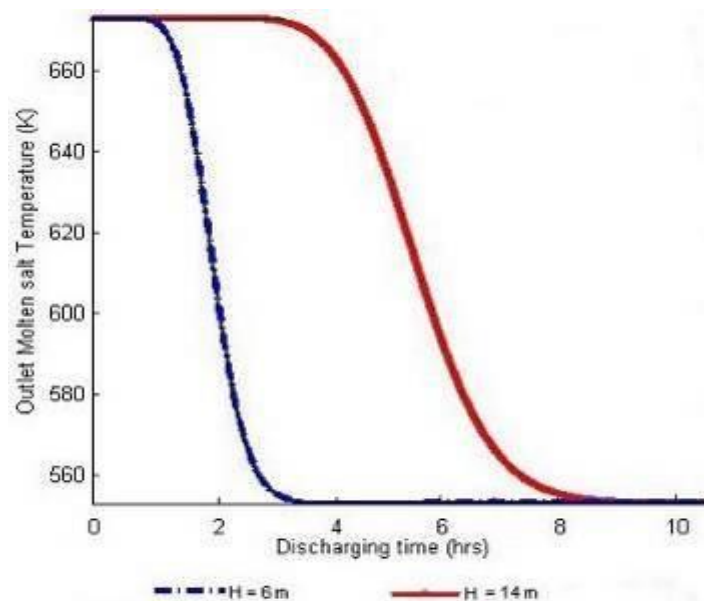
Figure 5: Temperature history of Outlet Molten salt with packed bed height of 6m and 14m.

390

Prior to the thermocline region reaching the tank exit, salt at a constant high-temperature level is available at the outlet. As the thermocline arrives at the exit, the salt temperature begins to drop. Thermocline tanks with a larger height takes more time for the thermocline region to reach the top of tank thereby extend the discharge stage wherein the salt temperature is maintained at a high level. Increasing the diameter of tank doesn't show any noticeable variation. Hence, increasing the tank diameter obviously improves the storage capacity of the tank whereas it has no significant influence on the discharging time.

Effect of Storage Temperature and Cut off temperature difference Criterion:

At higher values of T_h, significantly larger amount of energy was supplied to the storage system. Hence the storage capacity of the tank is larger when operating with a much higher storage hot temperature. From Table 3, it is clear that the discharging time not only depends on the storage temperature difference, but also with the cut off temperature difference.

Table 3: Comparison of discharging time using different values of the cut-off temperature difference

System Parameter	Cut-off Temperature difference (K)	T_h = 673 K	T_h = 838 K
	10	3.24	1.4
Discharging time (hrs)	20	4.52	2.56
	30	5.32	3.84

In this analysis, the cut-off temperature difference was changed to 10 K and 30 K, for two values of the storage hot temperature, such as T_h = 673 K and 838 K (maximum possible achievable temperature in power tower plants with current technology (FLUECKIGER et al., 2014)). The storage cold temperature T_c was kept constant at 553 K for all the above three cases. Discharge time increased from 4.52 hours to 5.32 hours when the cut-off temperature difference was changed from 20 K to 30 K. Increasing cut-off temperature difference allows the tank to operate for a longer duration. However, the increase in cut-off temperature difference is limited by the threshold discharged thermal energy value required for the steam generation.

4. CONCLUSION

Two-dimensional, transient, two phase model for the packed-bed thermocline storage tank for TES system was developed. It was found that thermocline region is moving upward with the discharging time, accompanied by slight expansion and it reached a maximum value of 4.76m, almost 1/3rd of the height, inside the tank. The discharging time decreases with increased inlet velocity of HTF since the expansion of thermocline is faster. Tanks with a larger height take more time for the thermocline region to reach the top of tank thereby extend the discharge stage. When the tank height is increased from 6 to 14 m, the discharging time of the system is increased from 1.8 hours to 4.52 hours. Increasing the diameter of tank obviously improves the storage capacity of the system whereas it has no significant influence on the discharging time. Storage capacity of the tank is larger when operating with a much higher storage hot temperature. But, discharging time not only depends on the storage temperature difference, but also with the cut off temperature difference criterion. Discharge time increased from 4.52 hours to 5.32 hours when the cut-off temperature difference was changed from 20 K to 30 K. The increase in cut-off temperature difference is limited by the threshold discharged thermal energy value required for the steam generation.

5. ACKNOWLEDGEMENTS

6. REFERENCES

ANDERSON Jr. J. D., 2002. Computational Fluid Dynamics-The basics with applications, 1st Edition. New York: McGraw-Hill, Inc.

FLUECKIGER S. M., Yang Z, Garimella S. V., 2011. An integrated thermal and mechanical investigation of molten-salt thermocline energy storage, Applied Energy; 88: 2098–2105.

FLUECKIGER S. M., Yang Z, Garimella S. V., 2013. Review of Molten-Salt Thermocline Tank Modelling for Solar Thermal Energy Storage, Heat Transfer Engineering; 34(10): 787–800.

FLUECKIGER S. M., Iverson B. D., Garimella S. V., Pacheco J. E., 2014. System-level simulation of a solar power tower plant with thermocline thermal energy storage, Applied Energy; 113: 86–96.

GIL A., Medrano M., Martorell I., La´Zaro A., Dolado P., Zalba B., Cabeza L. F., 2010. State of the art on high temperature thermal energy storage for power generation. Part-1 Concepts, materials and modellization, Renewable and Sustainable Energy Reviews; 14: 31–55.

MODI A., Pe´Rez-Segarra C. D., 2014. Thermocline thermal storage systems for concentrated solar power plants: One-dimensional numerical model and comparative analysis, Solar Energy; 100: 84–93.

PACHECO J. E., Showalter S. K., Kolb W. J., 2002. Development of a molten-salt thermocline thermal storage system for parabolic trough plants, Journal of Solar Energy Engineering; 124: 153–9.

VERSTEEG H.K., Malalasekera W., 2007. An introduction to computational fluid dynamics-The finite volume method, 2nd edition. England: Pearson.

XU C., Wang Z., He Y., Li X., and Bai F., 2012. Sensitivity analysis of the Numerical Study on the Thermal Performance of a Packed-Bed Molten Salt Thermocline Thermal Storage System, Applied Energy; 92: 65–75.

YANG Z., Garimella S. V., 2010. Thermal analysis of solar thermal energy storage in a molten-salt thermocline. Solar Energy; 84: 974–85.

ZANGANEH G., Pedretti A., Zavattoni S., Barbato M., Steinfeld A., 2012. Packed-bed thermal storage for concentrated solar power – Pilot-scale demonstration and industrial-scale design, Solar Energy; 86: 3084–3098.

ZAVOICO A. B., 2001. Solar Power Tower: Design Basis Document, California, San Francisco.

278: Nano composite "Vermiculite-CaCl$_2$" matrix for open thermochemical heat storage: Experimental investigation of cyclic behaviour and numerical determination of "operating line"

DEVRIM AYDIN, SEAN CASEY, SAFFA RIFFAT

Faculty of Engineering, University of Nottingham, University Park, Nottingham, NG7 2RD, UK,
ezxda4@nottingham.ac.u

In the last decade, low carbon technologies for reducing the dependency on fossil fuels have been attracting attention. Domestic heating is one of the prior areas needing advanced sustainable technologies to reduce global energy demand. Population growth and the increasing comfort demand in dwellings have caused a sharp rise of fossil fuel consumption in the last 50 years. On the other hand solar energy is counted as one of the promising renewable sources and has a great potential for thermal energy generation. However the mismatch of solar energy availability and building heat loads in winter conditions constitutes a drawback needed to be overcome for increasing solar share in space heating applications. Thermochemical heat storage system is a promising alternative for long term – seasonal storage of solar energy without any heat loss which seems difficult with sensible or latent heat storage systems.

In this study the cyclic behaviour and thermal performance of nano-composite matrix "Vermiculite-CaCl2" is experimentally investigated. A novel open thermochemical reactor consisting of meshed tube diffusers was developed for conducting the experiments. Results showed that "Vermiculite-CaCl2" has a good cyclic behaviour. Additionally it is found that 0, 01 m3 of Vermiculite-CaCl2 can provide an average temperature lifting of air, ΔT~20 °C over 180 minutes corresponding to ~1 kWh heat output. The results suggested a linear correlation between thermal performance and moisture uptake. Concordantly an "operating line" showing the instantaneous ΔT – Δw relation for certain inlet air conditions is numerically generated. Experimental results were used to validate the model and it was found that a numerically achieved operating line is in close approximation with the test results. Determining operating lines will be useful for effective design and control of thermochemical heat storage systems.

Keywords: thermochemical heat storage, Vermiculite, CaCl2, cyclic behaviour, thermal analysis, operating linek

1. INTRODUCTION

Energy technologies and energy management strategies has been gaining attention in the last decade as energy is vital for a safer and sustainable future. Dependency on energy is much higher than in the past due to industrial growth, increasing populations as well as comfort demand. However, recognising that global energy demand is rising but the world can burn only 20% of its established fossil fuel reserves by 2050 if global warming is not to exceed 2 °C represents a major threat to the future of all humans (Berners-Lee and Clark, 2013). The present rate of fossil consumption means that this will be achieved by ~2030.

The domestic sector is counted as the leading energy consumer as more people around the world aspire to comfort living standards which drive the demand for air conditioning and electric power. Urgent solutions are required to increase the share of renewable sources thus reducing the need for fossil fuel driven systems. Within this context, various international agreements such as Kyoto Protocol seek to address this problem (Zhou et al, 2012). In addition EU commission aims to increase the share of renewables to 20% by 2020 in member countries (Böhringer et al., 2009). IEO 2007 report states that buildings are responsible of 40% primary energy consumption, 70% of electricity consumption and 40% of atmospheric emissions in developed countries (Energy Information Administration, 2007, Parameshwaran et al., 2012). Additionally air conditioning (heating, cooling, ventilation) and water heating constitute over half of the energy consumption in buildings (Parameshwaran et al., 2012).

Solar energy is counted as one of the primary renewable energy sources and it has promising potential for thermal applications (space & water heating) in the domestic sector. However the mismatch between solar availability and the building heat load constitutes an obstacle to residential applications usually resulting with a need of auxiliary system/source requirement such as heat pump, electrical resistance or gas heater. Although the combination of multiple systems/sources (Hybrid systems) enables higher utility, at the same time it increases the complexity of the system and also capital and operational costs (Utlu et al., 2014Heat storage systems can considerably improve utility of solar thermal systems as they act as a thermal battery and thermophysically (sensible (SHS) - latent (LHS) heat storage) or thermochemically (thermochemical heat storage (THS)) store energy for later usage. These systems allow short term or long term storage of solar energy. Although SHS and LHS systems are widely researched and they are mature technologies, THS is a relatively new method for storing heat and research on this system is ongoing (Aydin et al., 2015).

Based on previous studies on open THS available in the literature, a novel open THS system using perforated tubes as air/vapour diffusers was developed and the experimental results of the first phase of testing is presented in this paper. Comparative analyses between the results achieved in this testing rig (Gen 3) and a previously developed testing rig (Gen 2) (Casey et al., 2015) was also carried out to demonstrate the achieved improvement. The aim of this paper was to examine a new concept for open THS that can be a model for short/long term heat storage. The authors believe that innovative designs/concepts providing effective heat/mass transfer are vital for achieving commercial level THS systems. Therefore the present study will have a significant influence on further development in this field of research.

2. EXPERIMENTAL SETUP & PROCEDURE

An open thermochemical heat storage system (See: Figure 1) was designed and developed in order to investigate the effectivness of the concept using perforated tubes as air/vapour diffusers. The reactor is rectangular shaped (50mm x 25 mm x 20 mm) and made up of aluminium. Ten perforated tubes with diameter, d = 20mm, made up of 0.55 mm thick perforated aluminium sheet is vertically placed inside the reactor with a horizontal distance of 100 mm between each. The top end of the perforated tubes are sealed in order to achieve sufficient pressure, providing air flow through the holes in the pipe towards the THS material placed in the reactor surrounding the tubes. Humidification of the air is provided using evaporative pads placed inside a rectangular shaped wick chamber. Air flow is parallel to the channels of water holding evaporative pads, enabling humidity enhancement of air before entering the reactor. Xpleair (UK) XID series d = 150 mm, inline duct fan is used for providing air flow and the fan is integrated with the ducting (d = 100 mm) with a 150mm → 100 mm reducer. The whole system is insulated with 25 mm thick glasswool (Izocam, Turkey) including ducting, humidifier and reactor. Temperature and RH were recorded using the EK-H4 Eval Kit for Temperature- Humidity Sensors from Sensiron, AG, Switzerland.

Experimental studies were divided into two phases. The first phase includes a comperative energetic, exergetic and hygrothermal analyses of three selected THS materials' (SIM 3a, SIM 3ad, Zeolite)

performance in the previously developed testing rig (Gen 2) (See: Figure 2) and newly developed one (Gen 3) (See: Figure 1). In the second phase, experimental studies were done in Gen 3, using only SIM 3a, which provided the best performance in first phase. The effect of air flow rate on temperature lifting and moisture uptake is

investigated for optimizing the process performance. Additionally, the cyclic and long term behaviour of SIM 3a is investigated and any correlation between $\Delta w - \Delta T$ is interpreted.
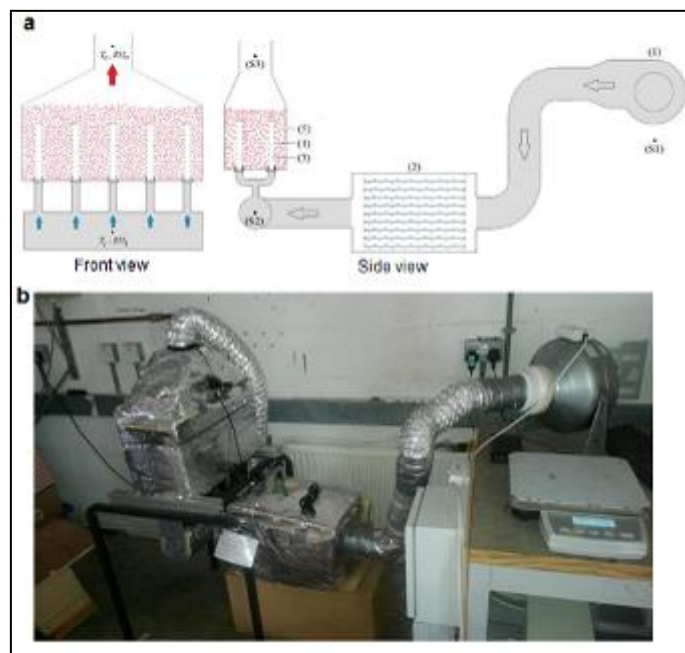
Figure 1: a)Schematic drawing of Gen 3 testing rig, b)View of Gen 3 testing rig
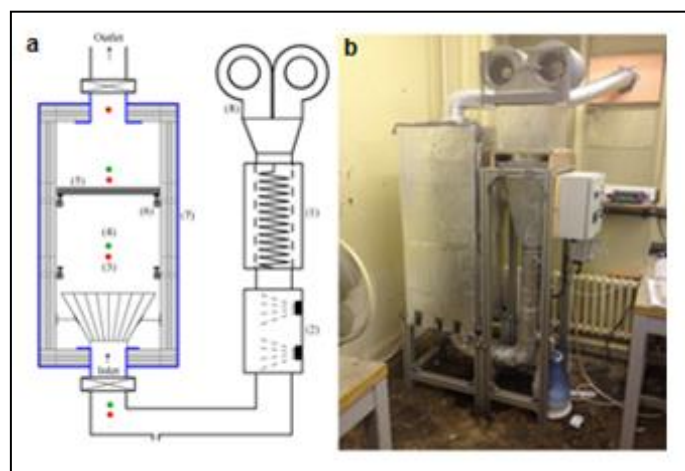
Figure 2: a)Schematic drawing of Gen 2 testing rig, b)View of Gen 2 testing rig

3. THERMAL PERFORMANCE ANALYSIS

In this section energetic and exergetic analysis results based on the experimental data collected during the testing period is presented and discussed. First section of the analysis compares the performances of three different THS materials (Sim 3a, Sim 3ad and Zeolite) in Gen 2 and Gen 3 testing rig. Later, results of the tests with using different mass flow rates, in order to determine best operating conditions of Gen 3 rig is presented. Than four cycle testing results of SIM 3a under determined optimal operating conditions is discussed for investigating cyclic behaviour of this material. Additionally long term performance (20 hours) of the best cycle among the repeated four cycles is illustrated. Formulation used in the analyses is given in Table 1.

Table 1: List of equations used in the analysis (Casey et al, 2015).

Definition	Unit	Equation	Equation No.
Instantaneous heat gain	kW	$\dot{Q}_g = \dot{H}_o - \dot{H}_i$	1a
		$\dot{Q}_g = m_{dr}.c_p.(T_o - T_i)$	1b
Energy density	Wh/g	$E_d = \dfrac{E_{cum,dr}}{\Delta m}$	2
	kWh/m³	$E_{d,dr} = \dfrac{E_{cum,dr}}{V_{ads}}$	3
Mass increase	g	$\Delta m = M_{wv} = M_w - M_d$	4
Mass uptake ratio	---	$f_{dr} = \dfrac{M_{ads,x} - M_{ads,d}}{M_{ads,d}}$	5
Absolute humidity	gr/kg	$w = 216.7.\left[\dfrac{\frac{RH}{100\%}.6.112.exp\left(\frac{17.62.t}{243.12+t}\right)}{273.15+t}\right]$	6
Cumulative thermal energy generation	kWh	$E_{cum} = \dot{m}_{dr}.c_p.\displaystyle\int_0^{t_d}(T_o - T_i)dt$	7
Exergy gain	kW	$\dot{Ex}_g = (\dot{Ex}_o - \dot{Ex}_i)$	8a
		$\dot{Ex}_g = \dot{m}_{dr}.[(h_o - h_i) - T_a.(s_o - s_i)]$	8b
		$\dot{Ex}_g = \dot{m}_{dr}.c_p.[(T_o - T_i) - T_a.ln\left(\frac{T_o}{T_i}\right)]$	8c
COP	---	$COP_{dr} = \dfrac{\dot{Q}_{g,ave}}{\dot{W}_f}$	9

Where:

		Subscripts:	
C_p:	specific heat at constant pressure J/(kgK)	tr:	transferred
E_d:	energy density (kJ/kg)	dr:	discharging
E_{cum}:	cumulative thermal energy (kWh)	a:	air, ambient
η_I:	1st law efficiency (–)	cr:	charging
η_{II}:	2nd law efficiency (–)	ave:	average
Ex:	exergy (kW)	ads:	absorbent
f:	mass uptake ratio	w:	wet
h:	specific enthalpy (kJ/s)	i:	inlet
m:	mass (g, kg)	d:	dry
ma	mass flow rate of air (kg/s)	g:	gain
P:	pressure (Pa)	f:	fan
Q:	energy (kW)	x:	any time during discharging
RH:	relative humidity (%)	rxn:	reaction
S:	entropy (kJ/kg)	cum:	cumulative
t:	time (s, h)	o:	outlet
T:	temperature (∘C, K)	wv:	water vapour
V:	volume (m3)		
w:	absolute humidity (gr/kg)		

3.1 Comparison of Gen 2 and Gen 3 testing rig performances

Inlet- outlet temperatures of SIM 3a, SIM 3ad and Zeolite for two cycles testing in Gen 2 and Gen 3 are presented in Figure 3-5. Additionally, the full data set of test and analysis results are summarized in Table 1. In THS, contrarily to SHS and LHS, effective mass transfer (moisture) is required, which can significantly reduce the performance as the size of the THS increases. Considering that the heat storage capacity of heat storage system is directly proportional to the amount of material used, novel designs providing efficient moisture diffusion are required for efficient sorption process in large size heat storage.

The Gen 2 testing rig has a flatbed sorption unit where the THS material is placed on a perforated tray and air flow is perpendicular to the perforated surface. In this system there was not any additional configuration for improving diffusivity and mass transfer as the primary aim of the testing rig was to test and compare

performance of several SIMs (Salt Impregnated desiccant matrix). Tests conducted in this rig showed that high resistance occurs at the reaction front which both increases the pressure drop and reduces the diffusivity and moisture transfer especially with an increase of the absorption layer. Therefore a new testing rig employing perforated tubes, to prevent the negative effect of the reaction front, demonstrating a concept/design for large scale THS applications was developed (Gen 3).

According to the analysis results, the performance of all three tested materials increased in Gen 3 testing rig. Figure 3 shows the temperature variation of SIM 3ad (Vermiculite-(LiNO$_3$-CaCl$_2$)) over 180 minute testing period both in Gen 2 (Figure 3a) and Gen 3 (Figure 3b). Both the average and peak temperature lifting was higher in Gen 3. Although the temperature lifting of SIM 3ad was poor in Gen 2, it showed a steadier performance over testing in both two cycles. Accordingly the gradients of trend lines after peak points were 0.025 - 0.020 in Gen 2 and 0.065-0.038 in Gen 3 for the first and second cycles respectively. On the other hand energy storage densities (EDS) achieved in Gen 3 is 69.7-90.1 kWh/m3 whereas these values are 83.3-101 kWh/m3 for Gen 2. ΔT_{180}, indicating the temperature lifting at the end of 180 min., is in close approximation with the 1st cycle testing of Sim 3ad in Gen 2 and Gen 3. However in the 2nd cycle of testing, ΔT_{180} is achieved as 16.2 °C for Gen 3 and 13.7 °C in Gen 2. Additionally average temperature lifting over 180 min. was analysed for Gen 2 and Gen 3. It was found that ΔT_{ave} in Gen 2 was 12.4 °C in the 2nd cycle while it was 10.2 °C in the first cycle. For the cycles conducted in Gen 3, ΔT_{ave} was 14.3°C and 18.5°C for 1st and 2nd cycle respectively, indicating an improved, steadier performance.

Two cycles testing results of SIM-3a (Vermiculite-CaCl$_2$) in Gen 2 and Gen 3 testing rigs are presented in Figure 4a and 4b respectively. The results indicate the significant improvement in the Gen 3 rig with average temperature lifting of 23°C and 19.9°C in comparison with 12.8°C and 10.7°C in Gen 2. In both cycles, a sharp drop of outlet temperature is observed in the Gen 2 rig after the peak point following a drop with lower gradient (dT/dt). Therefore ΔT_{180} are 7.8°C and 7.1°C whereas the peak temperature lifting are 24.6°C and 22.6 °C for the 1st and 2nd cycle, indicating a dramatic performance drop during the process. This situation most likely happened as a result of the slower vapour absorption of SIM 3a after the wetting of reaction front. On the other hand peak temperature lifting of SIM 3a over two cycles in Gen 3 rig were 28.6 °C and 25.3 °C while ΔT_{180} were 19.9 °C and 16.5 °C corresponding to a 30% and 34% temperature drop (ΔT_{peak} →ΔT_{180}) in 1st and 2nd respectively. SIM 3a testing in Gen 3 rig demonstrated the most promising results according to all chosen performance criteria such as (energy and exergy output, mass uptake and heat storage density). It should be noted that CaCl$_2$ is highly hygroscopic and this material can absorb moisture until deliquescence occurs. Combination of this remarkable property with the high heat storage density of CaCl$_2$ (45 kJ/mole) makes it a promising candidate for THS applications. Additionally the nano-porous and spongy nature of vermiculite allows high moisture uptake continuously which is the primary factor for high temperature lifting. Therefore CaCl$_2$ as sorption media and vermiculite as the host matrix constitute a spectacular composite absorption material to be used for storing solar energy or waste heat. A direct relation between high mass uptake (0.47 -0.46) and high thermal performance (1123.5 and 971 Wh) of SIM-3a was achieved in the experimental studies. Additionally Sim-3ad showed a similar behaviour with a mass uptake ratio of 0.24 and 0.36 resulting in 697 and 901 Wh thermal energy output supporting the directly proportional relation between mass uptake and thermal performance.

In addition to the SIM 3a and SIM 3ad, Zeolite was also tested. It is widely researched and according to many researchers regarded as the most promising candidate for THS. Although discharging performance of Zeolite seems competitive with Sim 3a, according to testing results, its high regeneration temperature (150-200 °C) is a non-ignorable drawback for usage of this material coupled with solar collectors for regeneration (Casey et al., 2015).

On the other hand, similar to the other tested materials, Zeolites performance is significantly enhanced with the usage of perforated tubes (Gen 3) (see:Figure 5b) in comparison with Gen 2 (see:Figure 5a). A sharp drop is observed between the 2nd cycle of testing of Zeolite in Gen 2 as the ΔT_{180} was 9.5 °C in the 1st cycle whereas it was only 3.6 °C in the following cycle. Conversely steadier performance is achieved in Gen 3 with the ΔT_{180} of 17.7°C and 16.1°C in repeated two cycles respectively. The improved performance in Gen 3 can be explained with a uniform air flow and better diffusivity through the material providing a high absorption rate. This condition is evidenced with the comparison of the ΔRH_{ave} achieved in Gen 2 and Gen 3 and demonstrates three facts;

   i.   Reducing ΔRH_{ave} from 32.5 % (1st cycle) to 24.4 % (2nd cycle) lead to a notable performance drop of Zeolite in Gen 2 testing rig.
   ii.   Steady ΔRH_{ave} 75.3% (1st cycle) → 75.7% (2nd cycle) provided a stable performance of Zeolite without any significant drop in Gen 3 testing rig.

iii.   2.3 (1. cycle) and 3.1 (2nd cycle) times higher ΔRH_{ave} in Gen 3 enabled to achieve 5.2 °C and 9.5 °C higher ΔT_{ave}. *also* 13.8 and 35.2 kWh/m^3 higher E_d than Gen 2 *in 1st and 2nd cycle* respectively
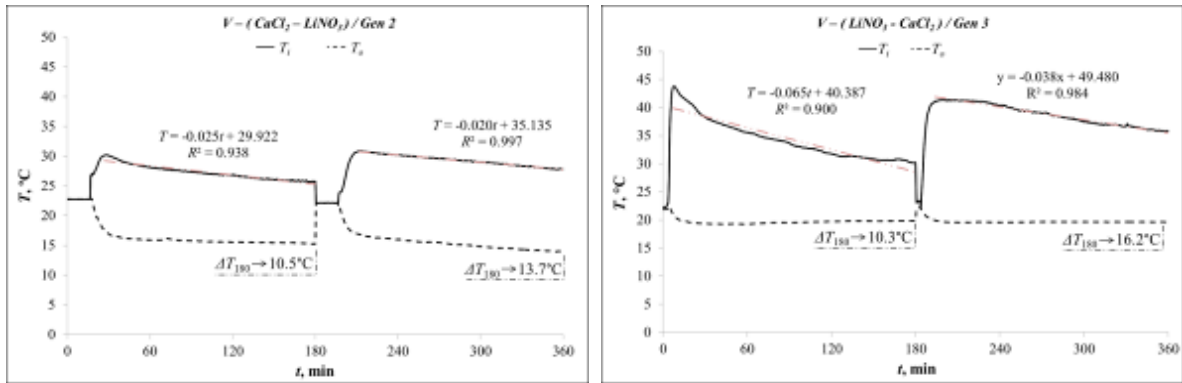
Figure 3: Inlet- outlet air temperature variation over two cycle testing of SIM 3ad in a)Gen 2 (left) and b)Gen 3 (right) testing rig
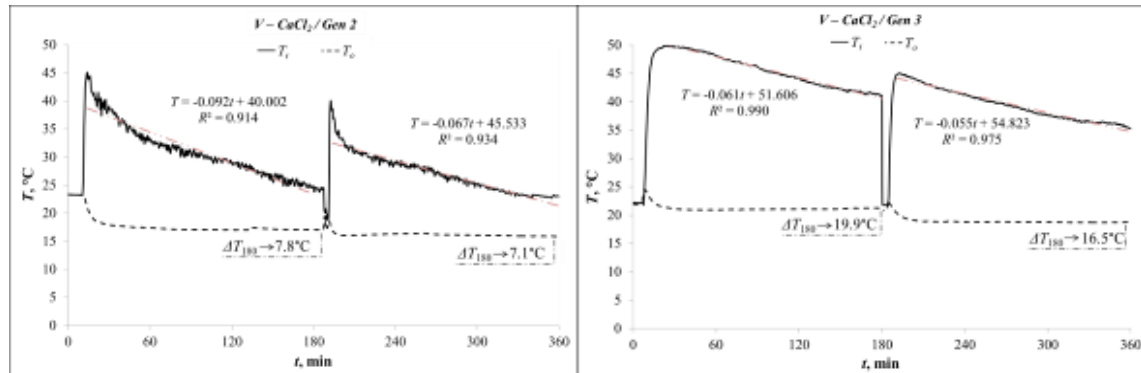
Figure 4: Inlet- outlet air temperature variation over two cycle testing of SIM 3a in a)Gen 2 (left) and b)Gen 3 (right) testing rig
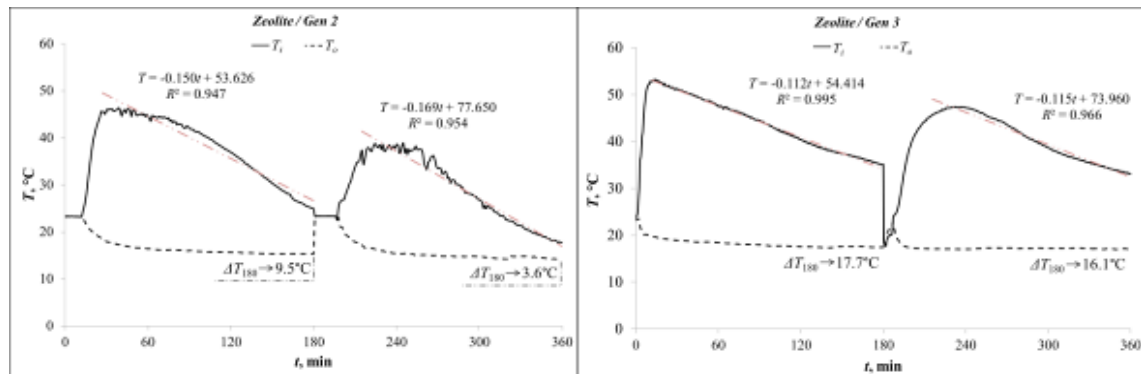
Figure 5: Inlet- outlet air temperature variation over two cycle testing of Zeolite in a)Gen 2 (left) and b)Gen 3 (right) testing rig

Mass flow rate

Although THS is theoretically a simple method for heat storage, it involves a complex process of absorption where mass (moisture transfer from air to the absorbent) and heat (from absorbent to the process air) transfer occur at the same time. Therefore the mass flow rate of inlet air has a significant effect on overall heat storage performance. It includes both the moisture and air that have several influences directly or indirectly related with achievable ΔT. For instance higher mass flow rate of air can provide a higher heat generation as it carries more moisture to the absorbent however this means that a subsequent amount of dry air is needed to heat at the same time. Therefore it can be assumed that increasing humidity has a positive influence on ΔT while increasing the amount of dry air has a negative influence. Although the high humidity drives an increase of heat output, a high rate of moisture absorption also creates a "wetting effect"

on the absorbent which causes sensible cooling of both the absorbent and the process air. Additionally it should be noted that the heat storage capacity of a defined amount of sorption material is limited and a high rate of moisture sorption will lead to a high thermal power release but low process time as the temperature lifting sharply drops in a short period. On the other hand, a low mass flow rate of air may lead to insufficient moisture supply to the absorbent and may not provide enough pressure for uniform air and moisture diffusion through the absorbent. This condition will lead to several undesired consequences such as low temperature lifting, low reaction kinetics, non-uniform moisture sorption and moisture condensation at the reaction front.

Figure 6a and Figure 6b illustrate inlet-outlet air temperature and relative humidity of three different cycles with air flow rates of 0.012 m^3/s, 0.015 m^3/s and 0.02 m^3/s. The results demonstrate a considerably improved performance with 0.015 m^3/s as ΔT_{peak} *and* ΔT_{180} were 28.5 °C and 19.9 °C with this flow rate whereas for air flow rates of 0.02 m^3/s and 0.012 m^3/s $\Delta T_{peak} \rightarrow \Delta T_{180}$ were found as 27.5 °C → 9.7 °C and 24.2 °C → 13.9 °C respectively. In all processes the amount of moisture supplied to the air by the evaporative pads was kept constant. Therefore with the increasing air flow rate, inlet relative humidity showed a decreasing trend. Outlet relative humidity with the highest air flow rate (0.02 m^3/s) was the fastest increasing one among three cycles. It reached to 19% at the end of 180 mins. yielding lower mass uptake ($f = 0.31$) in comparison with 0.012 m^3/s ($f = 0.37$) and 0.015 m^3/s ($f = 0.47$). Obviously mass uptake is crucial for achieving higher performance. Accordingly thermal energy outputs were found as 1.11 kWh, 0.91 kWh and 0.64 kWh for the cycles with air flow rates 0.015 m^3/s, 0.012 m^3/s and 0.02 m^3/s respectively.

THS involves a complex process as discussed in detail here and air flow rate is one of the most important parameters determining its performance. These results demonstrate that there is not any direct relation between the THS performance and air flow rate / humidity and each design may have an unique optimum flow rate which should be carefully analysed (numerically / experimentally) in order to achieve the desired thermal output from the system.
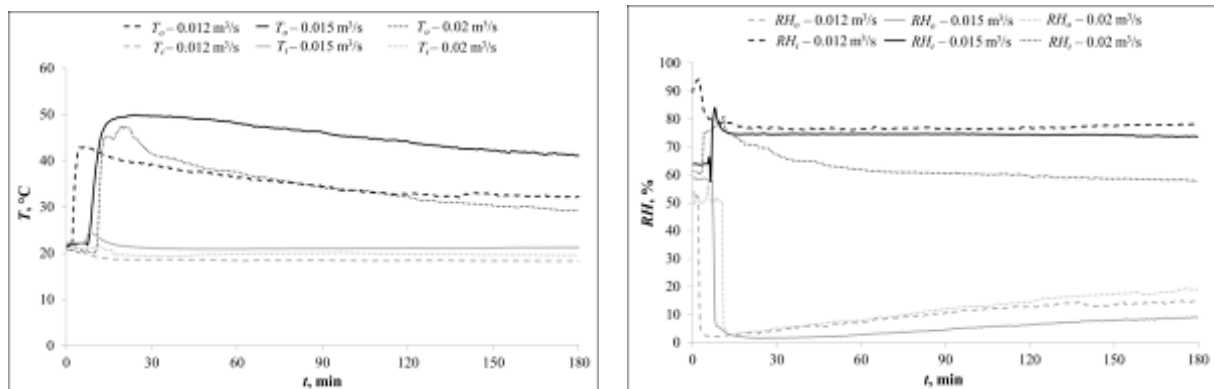
Figure 6: a)Temperature (left) and b)relative humidity (right) variation of Inlet-outlet air for testing SIM 3a in Gen 3 rig with three different air mass flow rat.

3.2 Cyclic Performance of SIM 3a

After selection of the best performing candidate (SIM-3a) and determining the optimum operating conditions of Gen 3 rig, multiple cyclic testing of SIM-3a was performed. The aim was to investigate the cyclic behaviour of this composite absorbent in order to simulate its performance for long term heat storage applications. An air flow rate of 0.015 m^3/s and perforated tubes with hole diameter of $d = 2$mm was used during the tests. Additionally SIM 3a is dried in an electrical oven at $T = 90$ °C for 24 hours following each discharging cycle to simulate the charging cycle7

Figure 7a represents the inlet outlet temperatures and thermal energy output in each cycle whilst Figure 7b illustrates the inlet-outlet *RH* and mass uptake ratio. It is seen from Figure 7a that ΔT_{180} showed a decreasing trend from the 1st cycle to 4th cycle in the order of 19.5 °C → 17.2 °C → 14.8 °C → 13.2 °C as expected. Similarly total energy and exergy outputs were 1.12 kWh → 0.96 kWh → 0.87 kWh → 0.74 kWh and 0.035 kWh → 0.024 kWh → 0.018 kWh → 0.013 kWh in the order of 1st → 4th Cycle respectively. This corresponds to a performance drop of 14% for the 1st→ 2nd cycle, 9% for the 2nd→ 3rd cycle and 14% for the 3rd→ 4th cycle in terms of energy output. One possible reason for the performance drop could be insufficient drying of the material as an electrical oven is used for drying the material. Usage of hot/dry air flow through the material could be more effective as air convection could significantly contribute to moisture

removal from the material. Fully drying the material would enable better cyclic performance of SIM 3a as the material did not show any physical signs of degradation over 4 cycles. The observed performance drop is the result of the reducing trend of mass uptake over the 4 repeated cycles. In Figure 7a and 7b the dashed line represents the thermal energy output and mass uptake respectively. It is clearly seen that the energy output and mass uptake show similar cyclic behaviour indicating a correlation between moisture supplied to the material and temperature lifting.

Figure 8 illustrates the almost linear correlation between instantaneous Δw and achieved ΔT in four repeated cycles. Although there is a slight difference of the line representing each cycle, all of them are in close approximation and therefore can be generalized to simulate THS performance according to the Δw of the process air. For instance ΔT in the range of 20→28.5 °C is achieved for the Δw 9→13 gr/kg in the first cycle. It should be noted that for both the lowest and peak temperature the ratio of $\Delta T / \Delta w = 2.2$ *gr°C/kg (20/9 and 28.5/13)* representing the linear relation between temperature lifting and instantaneous mass uptake of absorbent. A lower performance is achieved in the 2nd cycle due to the ambient conditions and perhaps in sufficient drying of the material. However the similar procedure can be applied to the 2nd cycle as *the ratio of $\Delta T / \Delta w$ for the lowest and peak temperature was found as 2.1 gr°C/kg. The same ratio was also achieved for 3rd and 4th cycle.*

Obviously to get the overall performance of the process and draw a more realistic operating line, it would be necessary to have a considerable amount of repeated cycles (~20 cycles), unique for a certain design-absorbent, indicating the achievable temperature lift for specific amount of Δw. In addition it should be noted that in real winter climate conditions it may not be possible to supply high moisture to the absorbent which could lead to poorer performance. For instance, a $T_a = 10$ °C and $RH_a = 50\%$ corresponds to a $w_a = 3.77$ gr/kg. For these climate conditions, even if the air is saturated to 100% RH, w_a will be limited to 7.5 gr/kg. This value is the maximum that could be supplied to the material and even if all moisture is fully absorbed by the absorbent the achievable ΔT_{peak} is < 20 °C. Therefore in real applications, especially under severe winter conditions pre-heating the air before entering the humidifier by a solar source or recycling a certain amount of the outlet air from the heat storage could significantly improve heat storage performance. Therefore studies on this concept are planned as next step of this research.
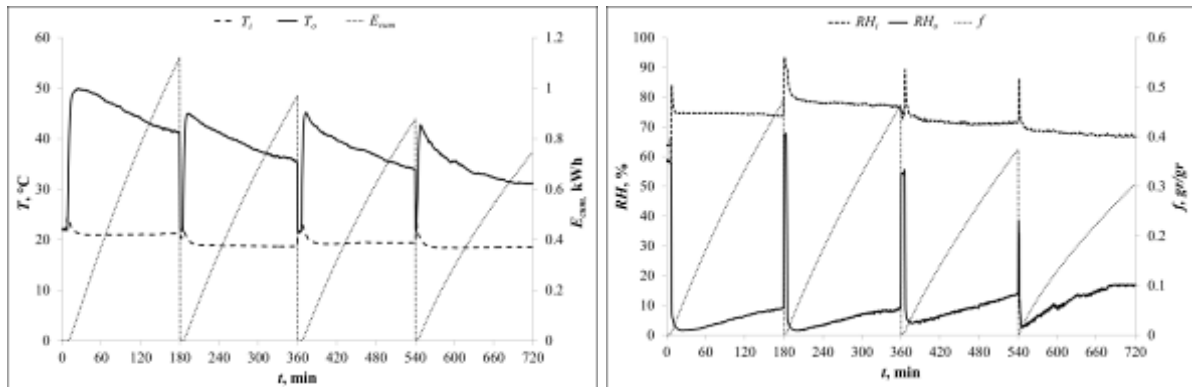
Figure 7: a)Inlet-outlet air temperature variation and cumulative energy generation during four cycle (180 min. each cycle) testing of SIM 3a in Gen 3 rig (left) , b)Inlet-outlet air relative humidity and mass uptake ratio variation four cycle (180 min. each cycle) testing of SIM 3a in Gen 3 rig (right).
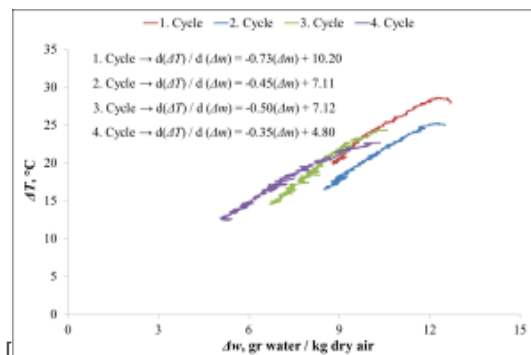
Figure 8: Correlation between instantaneous inlet-outlet absolute humidity difference of air and temperature lifting during four cycle testing of SIM 3a in Gen 3 rig.

3.3 Long cycle performance of SIM-3a

The long term performance of the 1st Cycle of SIM-3a, which provided the most promising results are presented in Figures 9-10. To investigate the maximum thermal energy that can be extracted from SIM-3a in the Gen 3 testing rig, this cycle was allowed to run until $T_o = T_i + 3\ °C$ and this condition was achieved at the end of 20 hours. During that period, total thermal energy output reached 2.93 kWh (see: Figure 9a) in comparison with the 1.12 kWh at the end of first three hours. Similarly mass uptake ratio (f) tripled from the 4th hour (f=0.47) to the 20th hour (f=1.41) (See: Figure 9b). Although thermal energy output considerably increased in 20 hours, conversely thermal power output dropped to 0,03 kW from the peak thermal power output of 0.37 kW. However considering that total energy output of ~3 kWh is achieved only from 0.01 m^3 of storage volume, it can be concluded that THS has a remarkable potential for reducing space requirement for heat storage systems in future low/zero carbon buildings.

Figure 10 illustrates the correlation of $Δw$ and $ΔT$ over 20 hours testing of SIM 3a. Drop of $Δw$ to ~2 gr/kg resulted with ΔT ~ 3 °C at the end of the process. During that period, it had seen that the correlation between $Δw$ and $ΔT$ is almost linear and independent of the time. Recognizing and using this correlation will allow easier and efficient design, control and operating conditions for THS systems.
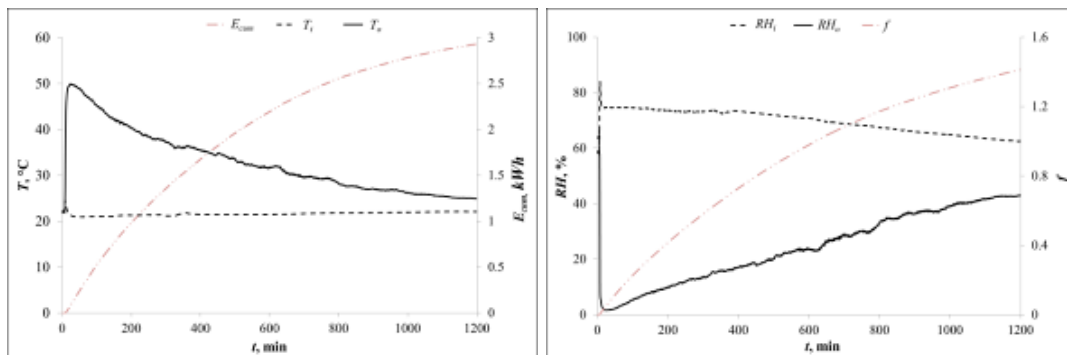

Figure 9:a) Inlet-outlet air temperature variation and cumulative energy generation during 20 hours of testing SIM 3a in Gen 3 rig (left) ,b) Inlet-outlet air relative humidity and mass uptake ratio variation during 20 hours of testing SIM 3a in Gen 3 rig (right).
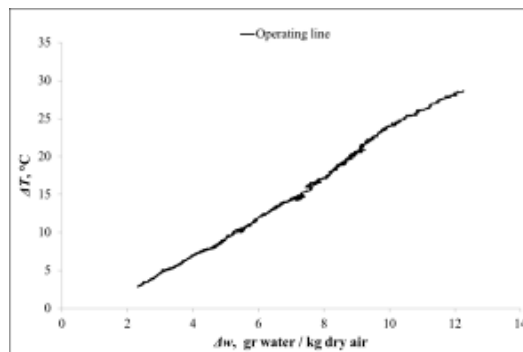
Figure 10: Correlation between instantaneous inlet-outlet absolute humidity difference of air and temperature lifting during 20 hours of testing SIM 3a in Gen 3 rig.

4. CONCLUSION

In this study the thermal performance of three different absorbents was experimentally investigated using two different testing rigs. The aim was to both compare material performance and testing rig performance. The cyclic and long term performance of SIM 3a was also examined experimentally in the Gen 3 rig. Furthermore effect of air mass flow rate on temperature lifting in the discharging process was investigated. The main findings were;

- SIM 3a provided the best performance among the three tested absorbents in terms of thermal performance and multi-cyclic ability. Although Zeolite also presents good thermal properties it fails because of the high regeneration temperature requirement. In addition having a lower cost than Zeolite, SIM 3a has a greater potential for commercial usage. On the other hand, SIM 3ad unexpectedly provided a relatively poor performance against the other tested materials. Although

V-LiNO$_3$ provided a lower temperature lifting in previous testing, its steady performance was the main factor influencing the choice of this material for the present study. The aim was increase performance steadiness of SIM 3a with combining it with LiNO$_3$. However the results showed that SIM 3a has a better performance than SIM 3ad.

- As a result of the tests performed in two different testing rigs, Gen 3 provided an improved performance than Gen 2. Study The results showed that use of perforated tubes enhances moisture and heat transfer. This phenomenon allows for higher and steadier temperature lifting during the discharging process. As the perforated tubes are embedded in the absorbent material they enable air transfer into the absorbent freely, with minimal resistance. Therefore moist air can diffuse through the material uniformly which is one of the challenging issues in thermochemical heat storage systems. However it is concluded that further study on optimizing the size of the perforated tubes and reactor is required to improve system performance.

- The test results showed that among three different air mass flow rates, the middle one (0.015 kg/s) is the optimal one as it provided considerably higher temperature lifting. This result indicates that in thermochemical processes there may not be any direct relation between air mass flow rate and system performance and therefore air mass flow rate should be optimized with numerical or experimental studies in order to achieve the best heat storage performance.

- Cyclic behaviour of the absorbents is one of the key parameters in thermochemical heat storage systems to achieve a steady heat storage performance over repeated cycles. The results showed that SIM-3a has a good cyclic ability as it provided sufficient temperature lifting in all cycles. However further testing will be beneficial for a more realistic judgement. On the other hand, in long cycle testing, SIM 3a provided temperature lifting in the range 30° C → 3° C over 20 hours and an energy storage density of 290 kWh/m^3 which is much higher than conventional sensible (water, soil, concrete) or latent (paraffin) heat storage materials.

- The final output achieved in this study is the evidence that there is a relation between amount of water vapour supplied to the absorbent and the temperature lifting. The importance of this finding is that the low inlet air temperature limits the water vapour that can be added to the air. This phenomenon is highly possible in winter conditions when the heat storage needed to be used. As a result of the low inlet air temperature, low amount of moisture can be added to the absorbent that will possibly result with low temperature lifting. Therefore use of solar energy (if available) or circulating some of the output heat during the discharging process to preheat the incoming air could be alternative solutions to improve heat storage performance.

5. REFERENCES

AYDIN D., Casey S.P., Riffat, S., 2015. The latest advancements on thermochemical heat storage systems. Renewable and Sustainable Energy Reviews. 41, 356–367.

BERNERS-LEE, M. and Clark, M.D., 2013. The Burning Question: We can't burn half the world's oil, coal and gas. So how do we quit? Profile Books LTD, London .

BÖHRINGER, C., Löschel, A., Moslener, U., Rutherford, T.F., 2009. EU climate policy up to 2020: An economic impact assessment. Energy Economics. 31, Supplement 2, 295-305.

BÖHRINGER, C., Rutherford, T.F., TOL, R.S., 2009. The EU 20/20/2020 Targets: An overview of the EMF22 assessment. Energy Economics. 31, 268-273.

CASEY S.P., Aydin, D., Riffat, S., Elvins, J., 2015. Salt impregnated desiccant matrices for 'open' thermochemical energy storage - Hygrothermal cyclic behaviour and energetic analysis by physical experimentation. Energy and Buildings 92, 128–139.

EIA. International energy outlook 2007. Energy Information Administration; 2007

PARAMESHWARAN, R., Kalaiselvam S., Harikrishnan, S., Elayaperumal, A., 2012. Sustainable thermal energy storage technologies for buildings: a review. Renew Sustain Energy Rev.16(5), 2394–433.

UTLU, Z., Aydin, D., Kincay, O., 2014. Comprehensive thermodynamic analysis of a renewable energy sourced hybrid heating system combined with latent heat storage. Energy Conversion and Management. 84, 311–325.

ZHOU, D., Zhao, C.Y., Tian, Y., 2012. Review on thermal energy storage with phase change materials (PCMs) in building applications. Applied Energy. 92, 593-605.

59: Performance analysis of heat pipe-based photovoltaic-thermoelectric generator hybrid system

ADHAM MAKKI[1], SIDDIG OMER[2], SU YUEHONG[3], SAFFA RIFFAT[4]

Institute of Sustainable Energy Technology, Department of Architecture and Built Environment, University of Nottingham, Nottingham, NG7 2RD, UK, 1ezxam1@nottingham.ac.uk , 2siddig.omer@nottingham.ac.uk, 3yuehong.su@nottingham.ac.uk, 4saffa.riffat@nottingham.ac.uk

Photovoltaic (PV) cells can absorb up to 80% of the incident solar radiation of the solar spectrum, however, only certain percentage of the absorbed incident energy is converted into electricity depending on the conversion efficiency of the PV cell technology used, while the remainder energy is dissipated as heat accumulating on the surface of the cells causing elevated temperatures. Temperature rise at the PV cell level is addressed as one of the most critical issues influencing the performance of the cells causing serious degradations and shortens the life-time of the PV cells, hence cooling of the PV module during operation is essential. Hybrid PV designs which are able to simultaneously generate electrical energy and utilize the waste heat have been proven to be the most promising solution. In this study, analytical investigation of a hybrid system comprising of a Heat Pipe-based Photovoltaic-Thermoelectric Generator (HP-PV/TEG) for further enhanced performance is presented. The system presented incorporates a PV panel for direct electricity generation, a heat pipe to absorb excessive heat from the PV cells and assist uniform temperature distribution on the surface of the panel, and a thermoelectric generator (TEG) to perform direct heat-to-electricity conversion. A mathematical model based on the heat transfer process within the system is developed to evaluate the cooling capability and predict the overall thermal and electrical performances of the hybrid system. Results are presented in terms electrical efficiencies of the system. It was observed that the integration of TEG modules with PV cells aid improving the performance of the PV cells through utilizing the waste-heat available, leading to higher output power. The system presented can be applied in regions with hot desert climates where electricity demand is higher than thermal energy.

Keywords: Photovoltaic, Hybrid Photovoltaic System, Heat-Pipe, Thermoelectric Generator

NOMENCLATURE		SUBSCRIPTS	
A	Area [m2]	a	Ambient
C	Specific heat capacity [J/kg K]	b	Base panel
d	Diameter [m]	c	Collector
E	Electrical output [W]	cold	Cold plate of TEG
G	Irradiance [W/m2]	con	Condenser
h	Heat transfer coefficient [W/(m2K)]	eva	Evaporator
I	Electric current [A]	EVA	Ethylene vinyl acetate
k	Thermal conductivity [W/(m. K)]	g	Front glazing
l	length [m]	hot	Hot plate of TEG
R	Thermal resistance [(m2K)/W]	i	inner, differential node "i"
T	Temperature [K]	l	liquid
u	Wind speed [m/s]	n	n-element
V	Voltage [V]	o	Outer
Z	Figure of merit	oc	Open-circuit
p	Heat Pipe, p-element	PV	PV cells
GREEK LETTERS			
$(\tau\alpha)$	Effective transmittance-absorption	r	Reference
α	Absorptivity, Seebeck coefficient [uV/K]	rad	Radiative
β	Temperature Coefficient	s	Thermal insulation
γ	PV cell coverage ratio	sc	Short-circuit
δ	Thickness [m]	Sky	Sky
ε	Emissivity, electrical resistivity [uΩm]	TPT	Tedlar-Polyester-Tellar
η	Efficiency [%]	w	Heat pipe wick
ρ			Density [kg/m3], reflectance
σ			Stefan-Boltzmann constant
τ			Transmittance
μ			Thomson coefficient [uV/K]

1. INTRODUCTION

PV cells absorb up to 80% of the incident solar radiation, however, only a small part of the absorbed incident energy is converted into electricity depending on the conversion efficiency of PV technology used (van Helden et. al, 2004). The remainder energy is dissipated as heat and the PV panel can reach temperature as high as 40°C above ambient temperature. This is due the fact that PV cells converts a certain wavelength of the incoming irradiation that contributes to the direct conversion of light into electricity, while the rest is dissipated as heat (Luque, A, and Steven Hegedus, 2003). The photoelectric conversion efficiency of commercially available single junction solar cells ranges between 6-25% under optimum operating conditions depending on the semiconductor material from which the cell is made (Kurtz S., 2011 and Radziemska, E., 2003). However, PV systems do not operate under standard conditions, thus variation of operating temperature limits the efficiency of a PV system. Such limiting efficiency is associated with the band gap energy of the semiconductor (Luque, A, and Steven Hegedus, 2003, Markvart, T, and K Bogus< 2000). PV cell performance decreases with increasing temperature, fundamentally owing to increased intrinsic carrier concentrations which tend to increase the dark saturation current of the p-n junction (Luque, A, and Steven Hegedus, 2003, and Michael S, 2009). Reduction in band-gap due to high doping also serves to increase the intrinsic carrier concentration (Luque, A, and Steven Hegedus, 2003).The increase in dark saturation current causes the open circuit voltage to decrease linearly which for silicon at 300 K corresponds to about −2.3 mV/°C.

Due to the aforementioned issues of temperature effect on the performance of PV cells, the energy that is not converted into electricity by the PV cells must be extracted to prevent excessive cell heating and deteriorated performance. Therefore, solar cell cooling must be an integral part of PV systems, especially in concentrated PV designs in order to minimize the effect of elevated temperature on the PV module power output. The heat that is a by-product of photovoltaic production of electricity can be utilized in hybrid system designs instead of simply dissipating it to the environment. Hybrid Photovoltaic-Thermal (PVT) systems offer a practical solution to increase the electrical power production from PV panels in addition to the recovery of heat extracted from the panels (Zhang, Xingxing et al., Kern JREC, Zondag HA). Waste heat recovery permits the utilization of waste heat to supply space heating or hot-water heating in a way allowing

improved overall system efficiencies to as high as 70% (Zhang, Xingxing et al., Zondag HA). Several PVT concept designs have been investigated by researchers that utilize different heat extraction mechanisms to achieve optimum cooling of PV cells in addition to permitting efficient waste heat recovery. (Dubey et al., 2009) investigated four different configurations of air-based PVT collectors having air ducts to cool the PV cells. In addition, (Tonui and Tripanagnostopoulos, 2008) investigated the performance of an air-based PVT collector having a thin metal sheet suspended at the middle of the air channel, and finned metal sheet at the back wall of the air duct to improve the temperature regulation of the PV and enhance the thermal efficiency of the hybrid collector. Forced air cooling which is able to provide better heat extraction compared to natural air flow at the expense of parasitic losses was studied by Bambrook and Sproul (2012). Agrawal and Tiwari (2011a) on the other hand presented the concept of series and parallel air flow arrangement of micro-channel solar cell thermal tiles. . Huang et al.(2001) compared the performance of an integrated PVT solar system with conventional solar water heater experimentally. A PVT collector utilising aluminium-alloy flat-box for domestic water heating was also constructed and experimentally investigated in Chow, T. et al. (2006) and He, Wei et al. (2006). Brogren and Karlsson (2002) used active water cooling method to cool a hybrid PV/T system with stationary parabolic reflectors for low concentration ratio. Ji et al. (2009) conducted an investigation on refrigerant-based PVT collectors through a solar-assisted heat pump co-generation system. More recently, Pei et al. (2012) conducted dynamic modelling of a PVT collector utilizing heat pipe for heat extraction for PV modules. Recently, few studies were conducted to investigate the incorporation of PCMs into PV systems to tackle the temperature regulation issues. Incorporation of PCMs in Building Integrated Photovoltaic (BIPV) was discussed in Huang, M.J et al. (2004), Hasan, A. et al. (2010), Ho, C.J. et al. (2013), and Huang, M.J. (2006) while stand-alone PV collectors with PCM thermal storage have also been reported in few literature Maiti, Subarna et al. (2011).

Thermoelectric generators have great potential in waste heat recovery from power plants, automobile vehicles, and solar energy applications where direct heat-to-electricity conversion can occur using a phenomenon called the Seebeck Effect McEnaney, Kenneth et al. (2011), Kraemer, Daniel et al. (2012), El-Genk, Mohamed S (2003), and Harman, T. C. (1958). The utilization of TEG in PV hybrid design permits further electrical conversion and can be adopted in regions where there is higher demand on electricity than heat. In this paper a numerical investigation of a thermoelectric generator, TEG integrated with a PV panel utilizing a heat pipe for heat transport from the PV panel to the TEG is presented.

2. SYSTEM DESCRIPTION AND OPERATION

The proposed system suggests the integration of a PV panel and a TEG with a heat pipe for heat extraction from the PV surface in a hybrid compact design for electricity production, Figure 69. The absorber of the heat pipe-PV/TEG collector consists of an array of solar cells arranged in a linear geometry for electricity production. A heat pipe is chosen to extract excess heat from the solar cells, therefore providing cooling to maintain the solar cells at a lower operating temperature. The extracted heat is transferred via boiling-condensing process to a TEG attached to the condenser section of the heat pipe and waste-heat is recovered via direct conversion of the temperature difference across the plates of the TEG to electrical energy. The layers of the hybrid collector considered in this theoretical investigation are depicted in Figure 69. A layer of PV cells is laminated onto the surface of an aluminium plate base panel. In between the PV layer and the aluminium base panel a layer of black Tedlar-Polyester-Tedlar (TPT) exists in addition to a transparent TPT and Ethylene-Vinyl-Acetate (EVA) layers laid at the top of the PV cells. The TPT layers play role in the electrical insulation of the PV cells in addition to enhancing the absorption of solar radiation Wu, Shuang-Ying et al. (2011). The evaporator section of the heat pipe is attached to the back of the aluminium plate, while the condenser section is attached to a TEG module. On top of the PV cells, a transparent glass cover used to prevent entry of dust particles and rain. Moreover, a thermal insulation layer (Rock Wool) is placed underneath the aluminium plate to minimize thermal losses. All these layers are integrated into one module and are enclosed in a weather tight container. Finally, aluminium heat exchanger housing the condenser section of the heat pipe and attached to the TEG was used to enhance heat transfer from the condenser section to the TEG.
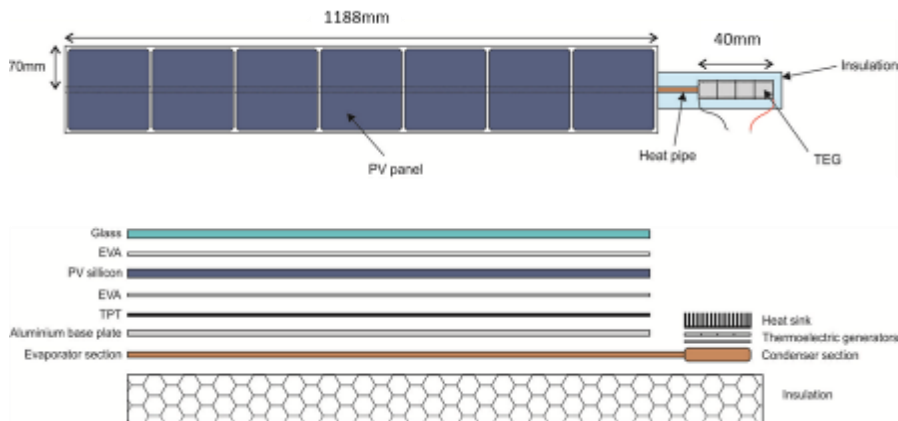
Figure 69 Heat-Pipe based PVT-TEG hybrid collector and its layers

As the solar radiation passes through the transparent glass cover and strikes the PV layer, most of the radiation is absorbed by the PV cells and the black TPT layer. However, part of the absorbed radiation is converted directly into DC electricity according to the Photoelectric effect of silicon PV cells, while the other part is dissipated as thermal energy and is conducted to the aluminium base panel. Therefore, converting the residual radiation transmitted through the PV cells into heat. Heat available at the back surface of the PV layer is conducted along the aluminium plate to the evaporator section of the heat pipe, and to the TEG module via the condenser section of the heat pipe. Such arrangement allows the heat to be conducted to the TEG module through an efficient boiling-condensing process of heat pipe and further electricity generation can be achieved through the *Seebeck* effect. A schematic diagram representing the system operation is shown in Figure 70.
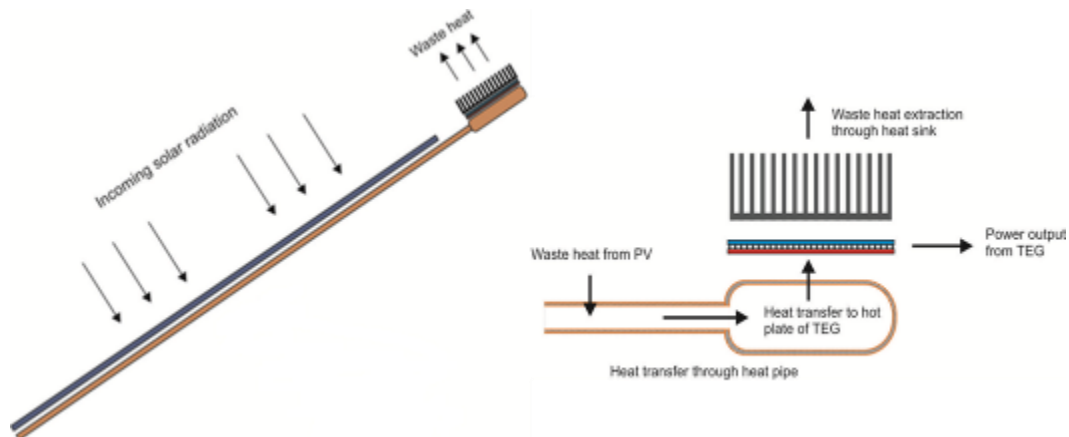
Figure 70 Heat-Pipe based PVT-TEG hybrid collector operation

3. THERMAL MODEL

The mathematical model of the system under investigation was derived based on the energy balance of the design model. The equations consider the three mechanisms of heat transfer, i.e. conduction, convection, and radiation. In this section the derivation of the system performance model is presented. For simplicity the mathematical model is divided into two sections, namely; modelling of the heat pipe-based PVT collector, and modelling of the thermoelectric generator (TEG).

3.1 Heat Pipe-Based Photovoltaic-Thermal (PVT) Collector

The following assumptions were taken into consideration to allow a simplified model of the system:

- The ohm-electrical losses within the PV cells and layer were negligible
- Heat conduction along the length direction of the aluminium base panel was neglected
- Losses at the edge were neglected
- The pressure drop caused by vapour flow along the axial length of the heat pipe was small
- Vapour space of heat pipe operate at constant saturation pressure

- Temperature gradient of the working fluid along the axial length of the heat pipe was neglected

Energy balance of the front glass cover

Referring to Figure 71, the heat flow within a single glazing cover in direct contact with the PV layer can be represented by Equation 18 Chow, T.T. et al. (2007).
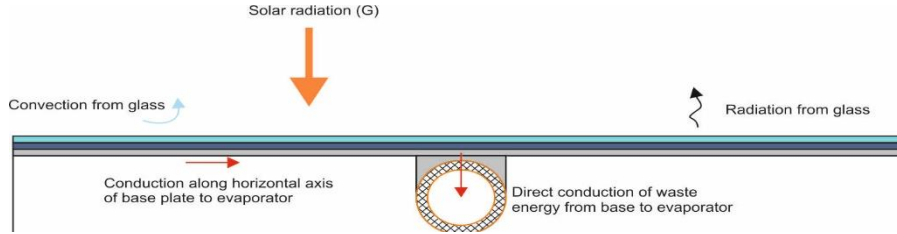
Figure 71 Solar energy conversion and transfer processes

Equation 18:
$$\rho_g \, \delta_g \, C_g \, \frac{\partial T_g}{\partial t} = G \, \alpha_g + h_{wind}(T_a - T_g) + h_{rad(sky-g)}(T_{sky} - T_g) + \frac{(T_{pv} - T_g)}{R_{pv-g}}$$

For a flat plate exposed to the ambient, the convective and radiative heat transfer coefficients are obtained using Equation 19-3 Duffie, John A, and William A Beckman (2006).

Equation 19:
$$h_{wind} = 2.8 + 3u_a$$

Equation 20:
$$h_{rad(sky-g)} = \varepsilon_g \sigma (T_g^2 + T_s^2)(T_g + T_s)$$

The thermal resistance between the front glass and PV layer is given by:

Equation 21:
$$R_{pv-g} = \frac{\delta_{EVA}}{k_{EVA}}$$

Energy balance of PV layer

The time dependent temperature variation for the PV layer is given by the partial differential equation given by:

Equation 22:
$$\gamma \, \rho_{pv} \, \delta_{pv} \, C_{pv} \, \frac{\partial T_{pv}}{\partial t} = G \, (\tau\alpha)_{pv} - \gamma E + \frac{(T_g - T_{pv})}{R_{pv-g}} + \frac{(T_b - T_{pv})}{R_{b-pv}}$$

The electrical power output E is given by Gang, Pei et al. (2012):

Equation 23:
$$E = G(\tau\alpha)_{pv}\tau_{EVA}\eta_r\left[1 - \beta_{pv}(T_{pv} - T_r)\right]$$

The instantaneous PV cell efficiency is calculated based on the panel reference efficiency η_r at reference operating temperature T_r and temperature coefficient β_{pv} using Equation 24.

Equation 24:
$$\eta_{pv} = \eta_r\left[1 - \beta_{pv}(T_{pv} - T_r)\right]$$

The effective transmittance-absorption product of PV layer is calculated according to Equation 25, where α the weighted average of the absorption of PV is cell (α_{pv}) and black TPT (α_{TPT}), $\alpha = \gamma\alpha_{pv} + (1 - \gamma)\alpha_{TPT}$ Duffie, John A, and William A Beckman (2006).

Equation 25:
$$(\tau\alpha)_{pv} = \frac{\tau_g\alpha}{1-(1-\alpha)\rho_g}$$
$$= \frac{\tau_\alpha\tau_\rho\alpha}{1-(1-\alpha)\rho_g}$$

The thermal resistance between the PV layer and base panel (aluminum plate) is given by:

Equation 26:
$$R_{pv-b} = R_{pv} + R_{EVA} + R_{TPT}$$
$$= \frac{\delta_{pv}}{k_{pv}A_{pv}} + \frac{\delta_{EVA}}{k_{EVA}A_{pv}} + \frac{\delta_{TPT}}{k_{TPT}A_{pv}}$$

Energy balance of the aluminum base panel

The time dependent heat conduction along the base panel direction can be considered as one-dimensional transient heat transfer on an infinite flat plate. The base panel is divided into several small segments according to the aluminum sheet width and differential steps used as shown in Figure 72.The temperature distribution across the defined aluminum base panel is assumed to be symmetric relative to the position of the heat pipe evaporator. Hence two energy balance equations are defined here, one associated with the heat pipe node (node=11), and one associated with the surrounding nodes (nodes 1-10 and 12-21).
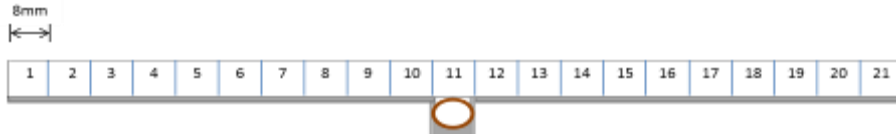
Figure 72 Differential grid diagram of base plate

The energy balance equation of the base panel at the heat pipe node (node=11) is given by Equation 27.

Equation 27:
$$\rho_b C_b = \frac{\partial T_b}{\partial t} = k_b\frac{\partial^2 T}{\partial x^2}$$
$$+ \frac{1}{\delta_b}\left[\frac{T_a - T_b}{R_{b-a}} + \frac{T_{pv} - T_b}{R_{pv-b}}\right.$$
$$\left. + \frac{T_{eva} - T_b}{R_{b-pipe}A_{bi}}\right]$$

The energy balance equation of the differential elements surrounding the heat pipe is given by Equation 28.

Equation 28:
$$\rho_b C_b = \frac{\partial T_b}{\partial t} = k_b\frac{\partial^2 T}{\partial x^2} + \frac{1}{\delta_b}\left[\frac{T_a - T_b}{R_{b-a}} + \frac{T_{pv} - T_b}{R_{pv-b}}\right]$$

The thermal resistance between the base panel and the ambient is obtained through Equation 29.

Equation 29:
$$R_{b-a} = \frac{k_s}{\delta_s} + \frac{1}{h_{wind}}$$

The thermal resistance between the base panel and evaporator section of pipe is given by Equation 30 Lee, H.S. (2010).

Equation 30:
$$R_{b-pipe} = \frac{ln(\frac{d_{o(eva)} + \delta_b}{d_{o(eva)}})}{2\,\pi\,l_{eva}k_b}$$

Energy balance of heat pipe

408

The energy balance of the heat pipe is split into two heat balance equations for both the evaporator and condenser section. The transfer of heat and the associated temperature drops in the heat pipe are represented by thermal resistances given in Equation 31, Lee, H.S. (2010).

Equation 31:
$$R_{eva-con} = R_{p,e} + R_{w,e} + R_{i,e} + R_{w,c} + R_{p-c}$$

Where:

- $R_{p,e}$, Radial conduction resistance across the pipe wall (container wall) at evaporator section
- $R_{w,e}$, Resistance of the liquid-wick combination at the evaporator
- $R_{i,e}$, Thermal resistance occurring at the vapor-liquid interface in the evaporator
- $R_{w,c}$, Resistance of the liquid-wick combination at condenser section
- R_{p-c}, Radial conduction resistance across the pipe wall at condenser section

Equation 32:
$$R_{p,e} = \frac{ln\left(\frac{d_{o,eva}}{d_{i,eva}}\right)}{2\,\pi\,k_p\,l_{eva}}$$

Equation 33:
$$R_{w,e} = \frac{ln\left(\frac{d_{o,wick}}{d_{i,wick}}\right)}{2\,\pi\,l_{eva}\,k_{wick}}$$

Equation 34:
$$R_{i,e} = \frac{2}{h_{eva}\pi\,d_{i,eva}l_{eva}}$$

For a wick lined wall as the case here with the evaporator, the film coefficient h_{eva} is approximately equal to the thermal conductivity of the fluid divided by the wick thickness as Equation 35 Azad, E (2008).

Equation 35:
$$h_{eva} = \frac{k_l}{\delta_{wick}}$$

Equation 36:
$$R_{w,c} = \frac{ln\left(\frac{d_{o,wick}}{d_{i,wick}}\right)}{2\,\pi\,l_{con}\,k_{wick}}$$

Equation 37:
$$R_{p,c} = \frac{ln\left(\frac{d_{o,con}}{d_{i,con}}\right)}{2\,\pi\,k_p\,l_{con}}$$

The thermal resistance associated with the condensing process is given by Equation 38 Gang, Pei et al. (2011).

Equation 38:
$$R_{i,c} = \frac{1}{h_{con}\pi\,d_{i,con}\,l_{con}}$$

Where, h_{con} is the condensing film coefficient, given by Equation 39 Gang, Pei et al. (2011)

Equation 39:
$$h_{con} = 1.13\left[\frac{g\,sin\,\theta\,\rho_l(\rho_l - \rho_v)k_l^3 h_{fg}}{\mu_l \Delta T\,l_{con}}\right]^{\frac{1}{4}}$$

The energy balance equation of the evaporator section is expressed by Equation 40.

Equation 40:
$$M_{eva}C_p\frac{\partial T_{eva}}{\partial t} = \left(\frac{T_{con} - T_{eva}}{R_{eva-con}}\right) + \left(\frac{T_b - T_{eva}}{R_{b-pipe}}\right)$$

The time dependent heat variation within the condenser section of the heat pipe is described by Equation 41.

Equation 41:
$$M_{con}C_p \frac{\partial T_{con}}{\partial t} = \left(\frac{T_{eva} - T_{con}}{R_{eva-con}}\right)$$

3.2 Thermoelectric Generator (TEG)

Modelling of Thermoelectric Generator exposed to transient heat flux can be complicated compared to thermoelectric coolers due to the non-linearity and unknown current in a closed-loop circuit. In thermoelectric generators electric current is generated in a closed-circuit across a load when a temperature gradient is present between the two ends of the device. In this section transient modelling of the thermoelectric generator through the coupling effects governing the conversion which includes, Seebek effect, Peltier effect, Thomson effect, and Joule heating is illustrated. The rational of the transient modelling of the TEG is due to the fact that practical application such as energy harvesting from waste heat sources generally have unsteady heat flux and/or temperature conditions on the hot side of the TEG leading to varying electric currents with time.

To allow simplified model of the TEG the following assumptions are taken into consideration:

- Heat losses due to radiation and convection are neglected
- Flow of heat and current is one-dimensional
- All materials are homogeneous
- The thermal conductivities, electrical resistivity, and specific heat capacities of materials are assumed constant with operating condition ranges

The schematic diagram of the thermoelectric generator shown in Figure 73 consists of two thermoelectric elements, p- and n- elements. To simplify the modelling, the simulation dimension is divided into three frames, namely; (i) Hot plate, (ii) p- and n- elements, and (iii) Cold plate. The power at each junction is induced by the Seebeck and Peltier effects and direction of thermal conduction through the two elements. The direction of current flowing through the load resistor indicates that the device is operating in power generation mode. The governing equations of the p- and n- thermoelectric elements are derived from the energy balance equation of a differential element dx, given by Equation 42: Nguyen et al. (2013).

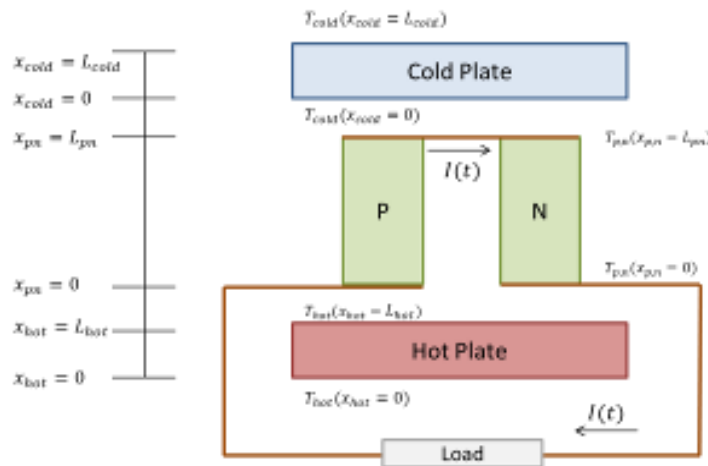*Figure 73 Schematic diagram of Thermoelectric Generator*

Equation 42:
$$A_p C_p \rho_p = k_p A_p \frac{\partial^2 T_p}{\partial x_p^2} + \frac{\varepsilon_p}{A_p} I^2$$
$$- \mu_p I \frac{\partial T_p}{\partial x_p}$$

Equation 43:
$$A_n C_n \rho_n = k_n A_n \frac{\partial^2 T_n}{\partial x_n^2} + \frac{\varepsilon_n}{A_n} I^2$$
$$+ \mu_n I \frac{\partial T_n}{\partial x_n}$$

The thermal energy across the plates is considered a one-dimensional transient heat transfer problem and can be represented by Equation 44-30.

Equation 44:
$$\rho_{hot} C_{hot} \frac{\partial T_{hot}}{\partial t} = k_{hot} \frac{\partial^2 T_{hot}}{\partial x_{hot}^2}$$

Equation 45:
$$\rho_{cold} C_{cold} \frac{\partial T_{cold}}{\partial t} = k_{cold} \frac{\partial^2 T_{cold}}{\partial x_{cold}^2}$$

The initial temperature profiles of the three frames are set to ambient temperature. At boundary $x_{hot} = 0$, the temperature will be conducted from the condenser of the heat pipe through a heat exchanger housing the condenser section. While at the cold side, the boundary at $x_{cold} = L_{cold}$, temperature of 25 °C is assumed. At the interfaces between the hot plate and p- and n-elements the boundary condition is described by Equation 46, while boundary between the p- and n-elements and the cold plate is given by Equation 47.

Equation 46:
$$- A_{hot} k_{hot} \frac{\partial T_{hot}}{\partial x_{hot}} (x_{hot} = L_{hot}) = \alpha_{pn} T_o(t) I(t) - k_p A_p \frac{\partial T_p}{\partial x_p} (x_p = 0) - k_n A_n \frac{\partial T_n}{\partial x_n} (x_n = 0)$$

Equation 47:
$$- A_{cold} k_{cold} \frac{\partial T_{cold}}{\partial x_{cold}} (x_{cold} = 0) = - \alpha_{pn} T_L(t) I(t) + k_p A_p \frac{\partial T_p}{\partial x_p} (x_p = L_p) - k_n A_n \frac{\partial T_n}{\partial x_n} (x_n = L_n)$$

Equation 48:
$$\alpha_{pn} = \alpha_p - \alpha_n$$

In closed-circuit mode, the output voltage generated is essentially the difference between the open-circuit voltage and the voltage drop across the internal resistance and can be computed using Equation 49-35.

Equation 49:
$$V = V_{emf} - IR$$

Equation 50:
$$R = \frac{\varepsilon_p L_p}{A_p} + \frac{\varepsilon_n L_n}{A_n}$$

The open-circuit voltage is calculated using Equation 51.

Equation 51:
$$V_{emf} = T_0 \, \alpha_{pn}(T_o) - T_L \, \alpha_{pn}(T_L)$$

With a load R_L connected to the terminals of the TEG, the electric current can be estimated using Equation 52.

Equation 52:
$$I = \frac{V_{emf}}{R_L + R}$$

The apparent Seebeck coefficient is taken to be related to the Thomson coefficient and can be estimated through the Kelvin relationship given in Equation 53. The Thomson coefficient of both p- and n- elements is assumed independent of temperature.

Equation 53:
$$\alpha_{p,n}(T) = \alpha_{p,n}^{ref} + \mu_{p,n} \, ln\left(\frac{T}{T_{ref}}\right)$$

Substituting Equation 53 into Equation 48 results in the Seebeck coefficient of the device at temperature T, given by Equation 54.

Equation 54:
$$\alpha_{pn}(T) = \left(\alpha_p^{ref} - \alpha_n^{ref}\right) + (\mu_p - \mu_n) \, ln\left(\frac{T}{T_{ref}}\right)$$

411

Several material properties are required to successfully simulate the thermal, electrical and thermos-electrical behaviour of the TEG. Most material properties are obtained from the manufacturers' datasheet, however, some properties as the case for both p- and n- elements are adopted from the literature.

3.3 Photovoltaic-Thermoelectric (PV-TEG) hybrid collector efficiency

The overall energetic (quantity) efficiency is the ratio of generated electricity to incident solar radiation striking on the PV/TEG module surface. It is yielded from the first law of thermodynamics indicating the percentage of the energy converted to electricity from solar radiation. The energetic efficiencies for the PV module and TEG device are given by Equation 55-41 respectively, while the overall efficiency is given by Equation 57.

Equation 55:
$$\eta_{pv} = \frac{E_{pv}}{G.A_{pv}}$$

Equation 56:
$$\eta_{teg} = (1 - \frac{T_{cold}}{T_{hot}})\frac{(1 + Z\bar{T})^{\frac{1}{2}} - 1}{(1 + Z\bar{T})^{\frac{1}{2}} + \frac{T_{cold}}{T_{hot}}}$$

Equation 57:
$$\eta_{pv-teg} = \eta_{pv} + \eta_{teg}$$

4. RESULTS AND DISCUSSION

Results presented in this section take into account the influence of operating conditions on the performance of the hybrid collector under investigations. The results are presented in terms of conversion efficiencies of both PV panel and TEG module as function of irradiance, wind speed, and ambient temperature. To observe the influence of each parameter, simulations were performed by varying one parameters and having the other two at a constant value. As the solar radiation strikes the PV panel and heat is conducted to the TEG through the heat pipe, the temperature at the hot side of the TEG which is available for direct heat-to-electricity conversion and the temperature difference across the TEG plates as a function of irradiance, wind speed, and ambient temperature is shown in Figure 6. It is clear that higher irradiance striking the collector will result in higher temperature difference across the TEG plates. Wind speed affects the natural convection at the surface of the collector, therefore, at low wind speeds, less energy is lost due to natural convection and more heat is available for extraction form the back surface of the PV layer. On the other hand, high ambient temperature also permits higher temperature difference across the TEG plates at the expense of the PV panel performance.

The PV panel and TEG module efficiencies as a function of various operating conditions of irradiance, wind speed, and ambient temperature is shown in Figure 7. Increased irradiance improves the PV panel efficiency as more solar energy is available at the collector per unit area for electricity generation, in addition to increased TEG conversion efficiency as higher radiation permits higher temperature difference across the TEG module plate. However, the PV panel efficiency is enhanced with increased wind speed due to the effect of convection on the surface of the collector, while the TEG module efficiency degrades as less temperature difference is available across the TEG plates for electrical conversion. On the other hand, ambient temperature has an inverse influence on the PV panel efficiency whereas increased operating temperature can lead to efficiency drop to about 7%; however, increased TEG efficiency was observed.

A comparison between the combined efficiency of the collector and the efficiency of a conventional PV panel of the same size as function of operating conditions of irradiance, wind speed, and ambient temperature is shown in Figure 8. It is observed that under all cases the hybrid collector permits further enhanced performance even at high ambient temperature and low wind speeds.CONCLUSIONS

A heat pipe based PV-TEG hybrid collector was investigated to fully harness the energy available from sun. The combined PV-TEG system can be promising in regions where there is high demand on electrical power. A mathematical model based on the heat transfer process within the system was developed to predict the performance enhancement of the hybrid system in terms electrical efficiencies of the system. From the results obtained, the system suggested can be applied in sunny drenched regions with high operating temperature and low wind speeds as in the Middle East and North Africa. Further investigation on the system suggested must be conducted to realize the practicality of the collector. In addition, the assumption

of having constant ambient temperature at the back side of the TEG may not be realized investigation on an arrangement to maintain low temperature at the cold side of the TEG must be considered.
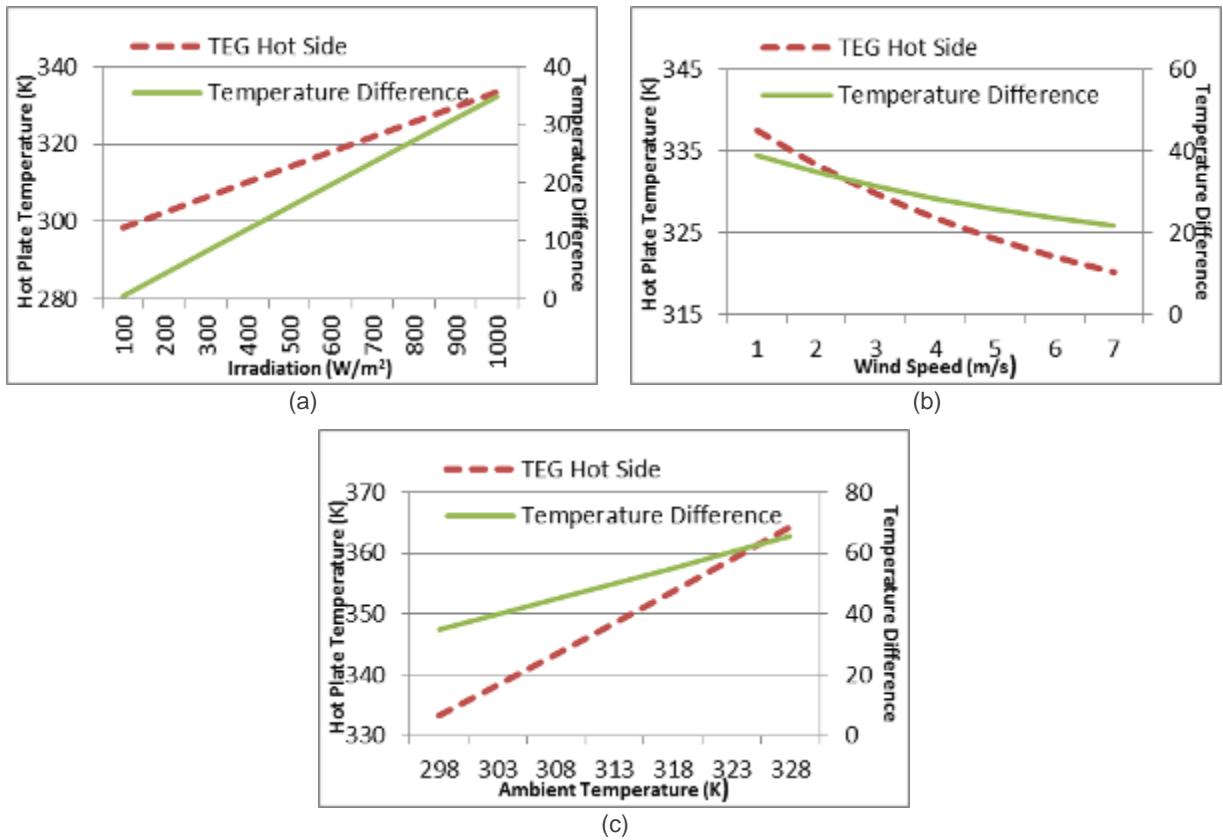

(a)

(b)

(c)

Figure 74

(a)

(b)

(c)

Figure 75

413
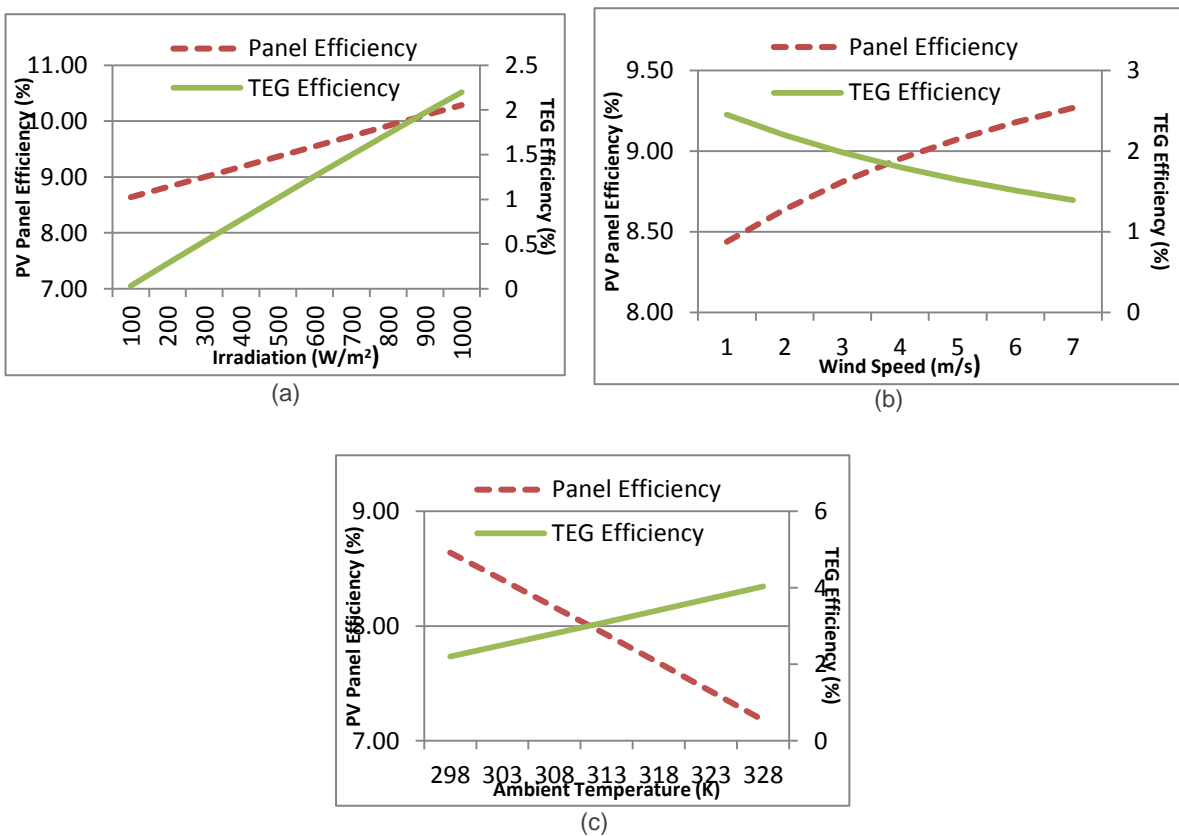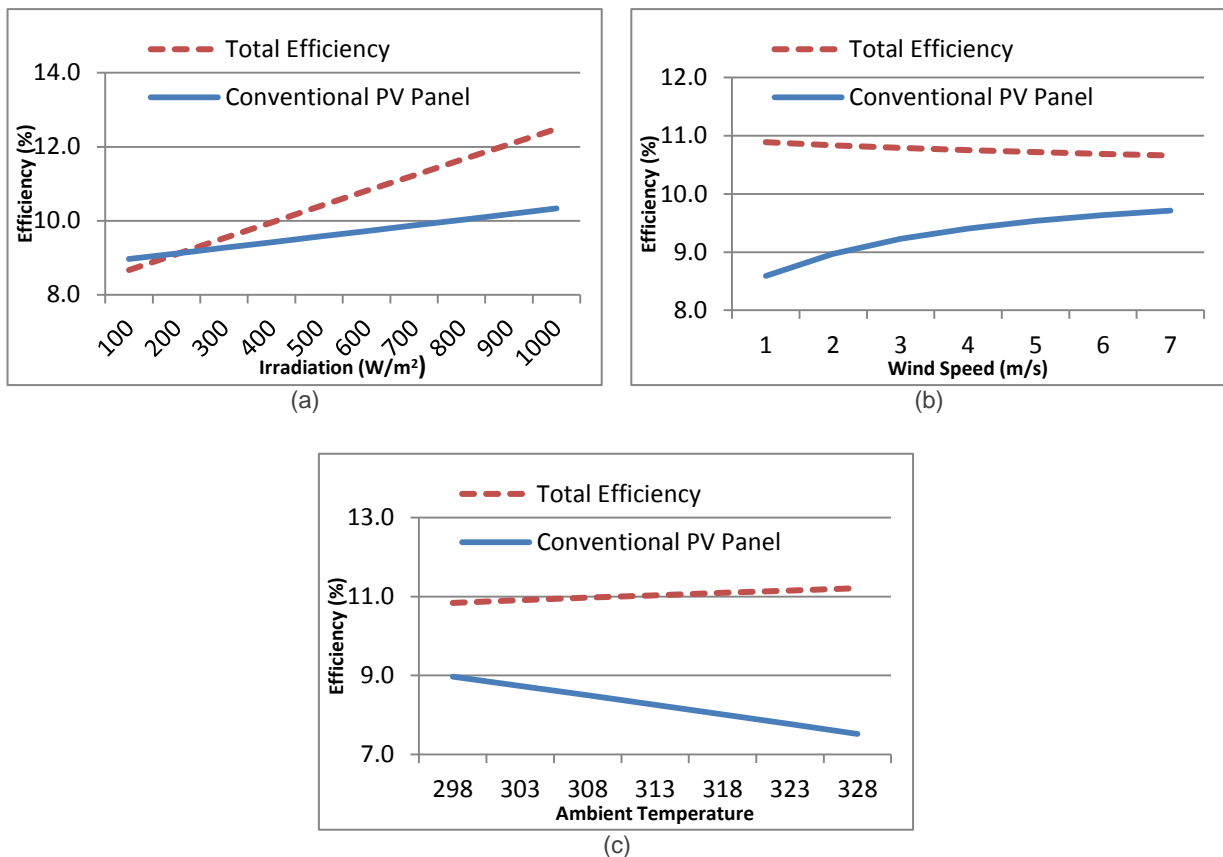
Figure 76

5. REFERENCES

AGRAWAL, Sanjay, and G.N. Tiwari. 'Energy And Exergy Analysis Of Hybrid Micro-Channel Photovoltaic Thermal Module'. *Solar Energy* 85.2 (2011): 356-370. Web.

AZAD, E. 'Theoretical And Experimental Investigation Of Heat Pipe Solar Collector'. *Experimental Thermal and Fluid Science* 32.8 (2008): 1666-1672. Web.

BAMBROOK, S.M., and A.B. Sproul. 'Maximising The Energy Output Of A PVT Air System'. *Solar Energy* 86.6 (2012): 1857-1871. Web.

BROGREN, Maria, Per Nostell, and Björn Karlsson. 'Optical Efficiency Of A PV–Thermal Hybrid CPC Module For High Latitudes'. *Solar Energy* 69 (2001): 173-185. Web.

CHOW, T.T., W. He, and J. Ji. 'Hybrid Photovoltaic-Thermosyphon Water Heating System For Residential Application'. *Solar Energy* 80.3 (2006): 298-306. Web.

CHOW, T.T. et al. 'Performance Evaluation Of Photovoltaic–Thermosyphon System For Subtropical Climate Application'. *Solar Energy* 81.1 (2007): 123-130. Web.

DUBEY, Swapnil, G.S. Sandhu, and G.N. Tiwari. 'Analytical Expression For Electrical Efficiency Of PV/T Hybrid Air Collector'. *Applied Energy* 86.5 (2009): 697-705. Web.

DUFFIE, John A, and William A Beckman. *Solar Engineering Of Thermal Processes*, 4th ed, New York: Wiley, 2006. Print.

EL-GENK, Mohamed S, Hamed H Saber, and Thierry Caillat. 'Efficient Segmented Thermoelectric Unicouples For Space Power Applications'. *Energy Conversion and Management* 44.11 (2003): 1755-1772. Web.

GANG, Pei et al. 'Performance Study And Parametric Analysis Of A Novel Heat Pipe PV/T System'. *Energy* 37.1 (2012): 384-395. Web.

GANG, Pei et al. 'A Numerical And Experimental Study On A Heat Pipe PV/T System'. *Solar Energy* 85.5 (2011): 911-921. Web.

HARMAN, T. C. 'Multiple Stage Thermoelectric Generation Of Power'. *J. Appl. Phys.* 29.10 (1958): 1471. Web.

HASAN, A. et al. 'Evaluation Of Phase Change Materials For Thermal Regulation Enhancement Of Building Integrated Photovoltaics'. *Solar Energy* 84.9 (2010): 1601-1612. Web.

HE, Wei et al. 'Hybrid Photovoltaic And Thermal Solar-Collector Designed For Natural Circulation Of Water'. *Applied Energy* 83.3 (2006): 199-210. Web.

HO, C.J. et al. 'Performance Assessment Of A BIPV Integrated With A Layer Of Water-Saturated MEPCM'. *Energy and Buildings* 67 (2013): 322-333. Web.

HUANG, B.J et al. 'Performance Evaluation Of Solar Photovoltaic/Thermal Systems'. *Solar Energy* 70.5 (2001): 443-448. Web.

HUANG, M.J., P.C. Eames, and B. Norton. 'Thermal Regulation Of Building-Integrated Photovoltaics Using Phase Change Materials'. *International Journal of Heat and Mass Transfer* 47.12-13 (2004): 2715-2733. Web.

HUANG, M.J., P.C. Eames, and B. Norton. 'Phase Change Materials For Limiting Temperature Rise In Building Integrated Photovoltaics'. *Solar Energy* 80.9 (2006): 1121-1130. Web.

HUANG, M.J., P.C. Eames, and B. Norton. 'Thermal Regulation Of Building-Integrated Photovoltaics Using Phase Change Materials'. *International Journal of Heat and Mass Transfer* 47.12-13 (2004): 2715-2733. Web.

JI, Jie et al. 'Distributed Dynamic Modeling And Experimental Study Of PV Evaporator In A PV/T Solar-Assisted Heat Pump'. *International Journal of Heat and Mass Transfer* 52.5-6 (2009): 1365-1373. Web.

KRAEMER, Daniel et al. 'Modeling And Optimization Of Solar Thermoelectric Generators For Terrestrial Applications'. *Solar Energy* 86.5 (2012): 1338-1350. Web.

LUQUE, A, and Steven Hegedus. *Handbook Of Photovoltaic Science And Engineering*. Chichester: Wiley, 2003. Print.

MAITI, Subarna et al. 'Self Regulation Of Photovoltaic Module Temperature In V-Trough Using A Metal–Wax Composite Phase Change Matrix'. *Solar Energy* 85.9 (2011): 1805-1816. Web.

MARKVART, T, and K Bogus. *Solar Electricity*. Chichester: Wiley, 1994. Print.

MCENANEY, Kenneth et al. 'Modeling Of Concentrating Solar Thermoelectric Generators'. *J. Appl. Phys.* 110.7 (2011): 074502. Web.

NGUYEN, Nguyen Q., and Kishore V. Pochiraju. 'Behavior Of Thermoelectric Generators Exposed To Transient Heat Sources'. *Applied Thermal Engineering* 51.1-2 (2013): 1-9. Web.

RADZIEMSKA, E. 'The Effect Of Temperature On The Power Drop In Crystalline Silicon Solar Cells'. *Renewable Energy* 28.1 (2003): 1-12. Web.

TONUI, J.K., and Y. Tripanagnostopoulos. 'Performance Improvement Of PV/T Solar Collectors With Natural Air Flow Operation'. *Solar Energy* 82.1 (2008): 1-12. Web.

VAN HELDEN, Wim G. J., Ronald J. Ch. van Zolingen, and Herbert A. Zondag. 'PV Thermal Systems: PV Panels Supplying Renewable Electricity And Heat'. *Progress in Photovoltaics: Research and Applications* 12.6 (2004): 415-426. Web.

WU, Shuang-Ying et al. 'A Heat Pipe Photovoltaic/Thermal (PV/T) Hybrid System And Its Performance Evaluation'. *Energy and Buildings* 43.12 (2011): 3558-3567. Web.

ZHANG, Xingxing et al. 'Review Of R&D Progress And Practical Application Of The Solar Photovoltaic/Thermal (PV/T) Technologies'. *Renewable and Sustainable Energy Reviews* 16.1 (2012): 599-617. Web.

SESSION 29: LOW-CARBON/ LOW-ENERGY TECHNOLOGIES

166: Numerical simulation of a hybrid concentrated solar power/biomass mini power plant

João Soares[1], Armando Oliveira[1,2]

1 Dept. Mechanical Eng. University of Porto, Rua Dr Roberto Frias 4200-465 Porto-Portugal, joaosoares@fe.up.pt 2 CIENER-INEGI, Rua Dr Roberto Frias 4200-465 Porto-Portugal, acoliv@fe.up.pt

Renewable electricity generation systems are increasingly used as a means of reducing harmful emissions and also reducing operational costs, by comparison with the use of fossil fuels. However, renewable energy sources such as solar energy are characterised by a high degree of intermittence, sometimes unpredictable. This constraint leads to inability to meet the demand of a power system. Hybridisation with more stable renewable sources, such as biomass, represents a resourceful way of meeting energy demands uninterruptedly. Besides stability, hybridisation with biomass allows a fully renewable solution, at the same time promoting security of energy supply.

In this paper, a hybrid renewable electricity generation system is presented and modelled. The system relies on a combination of concentrating solar energy (CSP) and biomass sources to drive an ORC cycle. The solar field is constituted by 12 parabolic trough collectors with a net aperture area of 984 m2. As backup energy, a biogas boiler is used, running on organic food waste. The nominal ORC electrical output is 60 kW. The system was designed and a prototype will be installed in Tunis, in the framework of the REELCOOP project, co-funded by the EU.

A computer model was developed with a combination of EBSILON and EES. EBSILON is used for the solar field (SF) and boiler simulations, and EES for the ORC. Annual simulations were carried out for solar-only and hybrid modes. Distinct operation ranges and boiler sizes were analysed.

The system annual yield is significantly improved with hybridisation, with enhancement of SF and ORC efficiencies. Electrical generation stabilisation was achieved during the whole year with the fulfilment of ORC minimum requirements. On the other hand, hybridisation promoted energy excess mostly in the summer months, demonstrating that hybridisation significantly reduces, but not eradicates, the need of storage.

Keywords: CSP, Biomass, Hybridisation, Generation

1. INTRODUCTION

Renewable electricity generation systems are increasingly used as a means of reducing harmful emissions and also reducing operational costs, by comparison with the use of fossil fuels. However, renewable energy sources such as solar energy are characterised by a high degree of intermittence, sometimes unpredictable. This constraint leads to inability to meet the demand of a power system. Hybridisation with more stable renewable sources, such as biomass, represents a resourceful way of meeting energy demands uninterruptedly. Besides stability, hybridisation with biomass allows a fully renewable solution, at the same time promoting security of energy supply.

Concentrated Solar Power (CSP) plants require abundant solar radiation to be feasible and profitable (Colmenar-Santos et al., 2015), abutting the implementation to remote areas, far-off power consumption centres. Furthermore, the intermittent nature of solar radiation emphasises the generation stability drawback. To overcome such issues, usually CSP plants are designed in the range of 100 MW$_{el}$ (Jin and Hong, 2012), with intensive capital investment and financial risk, taking advantage from economies of scale. One of the main advantages of CSP over other renewable systems is the ability to provide dispatchable power, usually achieved through thermal energy storage (TES). Although energy dispatchability has been widely proven with TES, it is still a costly solution (Coelho et al., 2014).

Facing a huge competition from other non-dispatchable renewable energy technologies (e.g. photovoltaics) (Singh, 2013), hybridisation presents a potential solution for CSP forthcoming. Within the concept of a fully renewable power system, biomass is the ideal contender. The concept of CSP/Biomass hybridisation relies on the ability of both systems to supply thermal energy in order to drive a power generation block.

This synergy's advantages goes further than dispatchability and renewable energy generation: operation stability and flexibility, joint use of power plant equipment (Peterseim et al., 2014) and associated cost reduction, as well as allowing CSP migration from desert areas to load centres(Moreno-Pérez and Castellote-Olmo, 2010). Furthermore, during daylight time, when electricity prices are usually higher, solar radiation is abundant and the system can run with larger solar shares resulting in a reduction of the levelised cost of energy.

In this paper, a simulation model and results for a CSP/Biomass hybrid mini power plant are presented. Annual simulations were carried out for solar-only and hybrid modes. Distinct operation ranges and boiler sizes were analysed. Simulation results are presented, such as: solar field annual generated heat and efficiency, boiler efficiency and biogas consumption, annual generated electrical energy and ORC efficiency, dumped heat, solar and biomass shares, and system global efficiency. Hourly results are presented for standard days, with and without hybridisation, showing the advantages of hybridisation.

The solar field (SF) is constituted by parabolic trough collectors (PTC) with a net aperture area of 984 m^2. As backup energy a biogas boiler is used, running on organic food waste. The nominal Organic Rankine Cycle (ORC) electrical output is 60 kW. The system was designed and a prototype will be installed in Tunis, in the framework of the REELCOOP project, co-funded by the EU (REELCOOP, 2015).

2. THE HYBRID MINI POWER PLANT

The hybrid mini power plant has a nominal electrical output of 60 kW, and relies on a regenerative ORC as generation system, developed by Zuccato Energia. The turbine/generator block was adapted to assure operation at partial load, in order to compensate solar energy fluctuations, with a nominal gross efficiency reaching 13.3%. The ORC will be driven by saturated steam at 170ºC, which allows the power circuit to also operate with available waste heat. Thermal generation will be achieved either from solar energy or biomass, or from the combination of both.

The solar field relies on parabolic trough collector technology, and is constituted by 3 parallel loops of 4 PTM$_x$/hp-36 collectors developed by Soltigua, with a net collecting surface of 984 m^2. Direct Steam Generation (DSG) will be achieved in the solar field, and the recirculation concept was adopted. The solar field will be supplied with subcooled water and partial evaporation will take place in the solar collectors. The water/steam mixture is then separated in a steam drum, and therefore only saturated steam leaves the solar field. The leftover water is then recirculated. Complete evaporation enhances control complexity, implying unnecessary risks over solar collectors' absorbers (Krüger et al., 2014).

Auxiliary energy will be provided by a biogas steam boiler. The biogas will be produced by anaerobic digestion of canteen organic waste remains, showing a potential solution for the problem that waste disposal represents (Oliveira and Coelho, 2013). The system layout allows either hybrid or individual operation with each thermal source (solar-only or biogas-only).

In order to reduce thermal energy waste as well biogas consumption and to compensate short transients from solar power, a storage tank was foreseen in the project. Since the storage tank will be charged with saturated steam from the solar field, an isothermal latent thermal energy storage concept has been adopted. Whilst typical TES systems deal with sensible heat storage by temperature change, the latent heat solution uses Phase Change Materials (PCM).

3. SIMULATION MODEL

The developed simulation model encompasses two stages. First, the solar field, the water/steam cycle and the boiler were analysed using commercial software: EBSILON® Professional. This stage includes the simulation of the thermal generation system, for different operation profiles.

The second stage concerns the power block circuit analysis that was carried out using EES software. The model required that relevant properties of the working fluid (SES36) were introduced, as they were not available either in the EES database or in EBSILON.

EBSILON software was designed for steady state calculations. Yet, the simulations were carried out considering the transient behaviour of the system, on an hour-by-hour basis, using a time-series function.

The simulation layout is presented in Figure 1. The solar field is constituted mainly by one loop of four parabolic trough collectors, the sun, distributing and collecting headers, and the feed and recirculating pumps. The boiler was modelled through a heat injection component, and the regenerative ORC was simulated using EES.
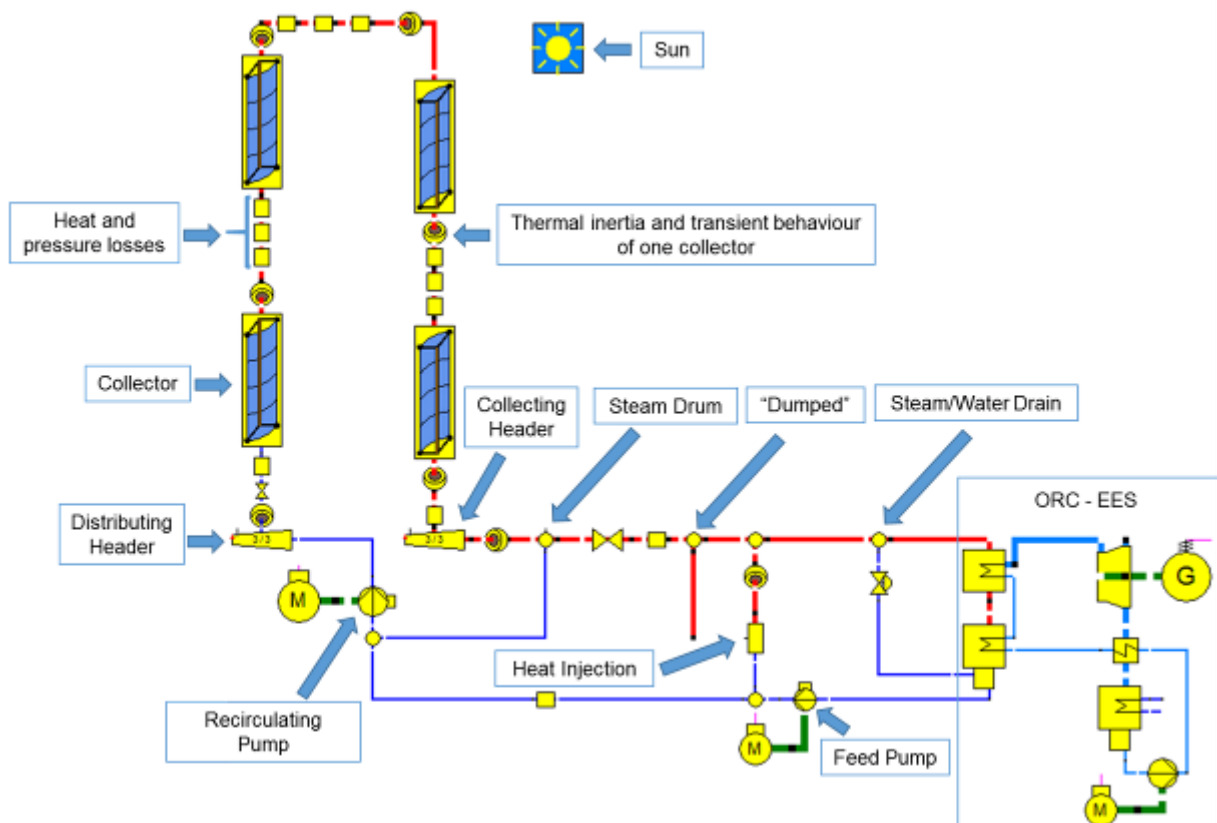

Figure 77: Simulation Layout

The Sun acts as interface between the meteorological data and incident radiation on the collectors, based on DIN 5034 standard. Meteorological data were obtained using Meteonorm software for the prototype site location (Tunis, Tunisia). Heat and pressure losses on the solar field pipes and headers were considered as well. The one-loop simplification was used in order to reduce the computational effort, yet the other two loops were accounted for through the use of the distributing and collecting headers.

The solar collectors were modelled with EBSILON´s line focusing solar collector component and manufacturer´s technical information. The solar field thermal inertia and transient behaviour were modelled through the use of an indirect storage (IS) component and a time-series analysis. The use of an IS block was applied to each solar collector and both headers, where the highest thermal gradients are expected to occur.

The indirect storage component calculates the transient heat exchange between the water/steam and either the collector´s absorber tube or piping. The Fourier heat transfer differential equation is discretised in a two-dimensional domain using a finite volume method, and in time by an iterative Crank-Nicholson method (Pawellek et al., 2012). As inputs, the IS block requires the estimated values for the water and steel mass, as well as the inner heat transfer coefficient at design conditions.

Hybridisation was modelled through a heat injection component, representative of the boiler. This component acts as an ideal heat exchanger, promoting the interface between the boiler output and the mass flow rate of water/steam. In order to control the boiler output, a code was created using EbScript to impose operating limits according to the manufacturer data. The boiler output is controlled by the water/steam mass flow rate, acting as an auxiliary heater of the solar field. For simulation purposes, the Viessmann VITOMAX 200-HS model with economiser was used. Two different boiler sizes were the object of analysis, with nominal heat outputs of 380 kWth (0.5 ton/hr of saturated steam) and 530 kWth (0.7 ton/hr of saturated steam), and both with a minimum thermal output of 100 kWth. The transient behaviour of the boiler was considered using the IS component, taking into account that the boiler takes half an hour from cold start to design conditions.

For estimating biogas consumption, a computer model was created using Ebsilon, consisting in a combustion chamber where the mix of air and biogas is burned, retrieving as output the flue gas. The combustion was modelled considering an excess of oxygen in the flue gas of 3%. The control of biogas and air mass flow rate is achieved considering manufacturer's data regarding efficiencies and flue gas temperatures, either for nominal or part load conditions. The flue gas exchanges heat with a steam evaporator and economiser (see Figure 2).
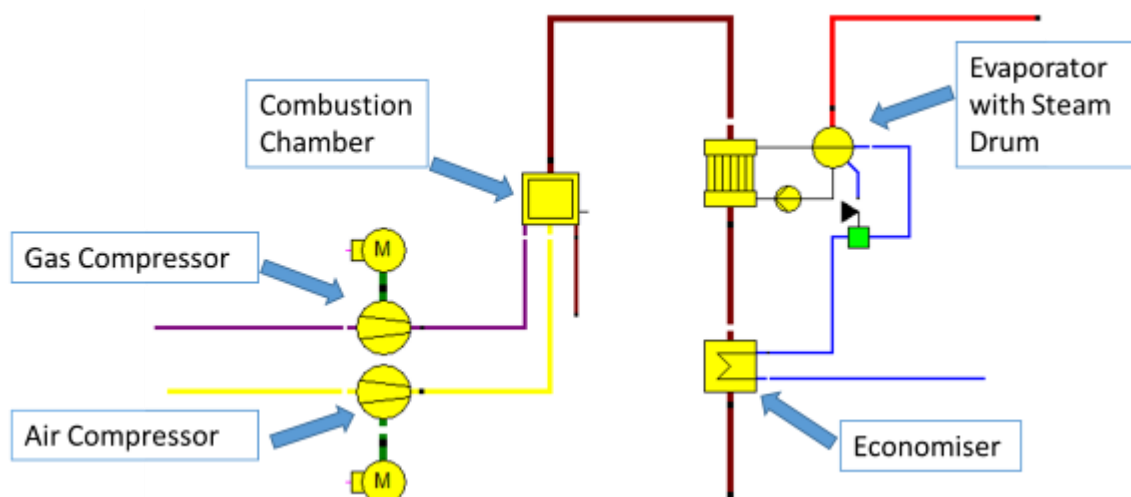
Figure 78: Boiler simulation layout

Biogas consumption was estimated considering a yearly constant low heating value (19.27 MJ/m^3). A study was conducted at ENIT, for estimating biogas production with the local canteen residues. The estimated value is about 60 m^3/day.

The ORC sub-system was simulated using EES, since properties data of the organic fluid (SES36) were not available in the Ebsilon database. It was assumed that the ORC operates at steady-state and thermal

inertia of the power block was neglected. The control was achieved through the organic fluid mass flow rate. Manufacturer´s technical information for the turbine, pump and generator efficiencies were considered. As input the code requires the saturated steam mass flow rate from EBSILON. Neither pressure drops nor efficiencies were considered for the heat exchangers. As main output results the code provides the gross and net electrical power, organic fluid mass flow rate, as well as the parasitic consumption and the condenser thermal requirements.

Solar-only operation mode

The system steam production will be controlled by the mass flow balance at the steam drum. The same concept was used in the simulation model. During system operation the recirculating mass flow rate is kept constant at about 0.5 kg/s. In real conditions the feed water pump will operate when the water level in the steam drum drops below a predefined level. Since the simulations were carried out in an hourly basis, it was assumed that the mass flow rate of the feed water should balance the water removed from the recirculating pump, and so is intrinsically related to the steam quality after the distributing header.

If the saturated steam mass flow rate that leaves the solar field exceeds the maximum requirements of the ORC, it is then separated. In real operation, the solar collectors should change their state to partial defocused in order to control the steam production. In the simulation model, the excess of energy is accounted as dumped, providing an input for a PCM storage tank design. The last separation occurs before the ORC, through a water-steam drainer. This component is mostly used in the warm-up and cool-down profiles, to establish a more realistic thermodynamic balance.

To obtain a more accurate approach in the simulation model, distinct operating profiles were created. A code was developed using EbScript to allow the automatic interchange between the profiles using dynamic variables, e.g. direct normal irradiation, hour of the day.

The solar only operating mode is constituted by four profiles: warm-up, operating, cool-down and stop. At the beginning of the day if DNI exceeds 200 W/m^2 the collectors change their state to focus and the recirculating pump is activated. This represents the warm-up profile. The operation profile starts with solar field steam production, and operates as described before.

At the end of the day, if DNI is less than 200 W/m^2, the collectors change their state to defocus and water circulates until the system cools-down. At night, the system is off, with solar field collectors defocused and the pumps shut-down. Even during the night, the thermal inertia of the system as well as the heat losses to the ambient were considered.

Hybrid operation mode

The analysis was carried out based on the assumption of the system running 12 or 24 hours daily, at ORC minimum and nominal power. Concerning the control, the hybrid mode comprehends four and two operating profiles for the 12 and 24 hours regimes, respectively. The 12-hour operating regime differs from the solar only, on the warm-up and operating profile.

The warm-up begins at 7:00 with the start of the boiler in order to warm-up the ORC and the feed water line of the solar field. If DNI exceeds 200 W/m^2 the recirculating pump is activated and the solar collectors focused. During the operation regime (08:00 to 20:00) the hybrid mode is activated, where the boiler compensates the requirements (nominal or minimum) to drive the ORC turbine. This control is achieved by saturated steam flow rate balance. In preliminary simulation results it was noticed that during summer the system could start earlier (at 7:00), and the 12 hour operation regime acted as constraint to the solar field. To overcome this issue, in the beginning of the day if DNI is above 200 W/m^2 the collectors are focused earlier.

The 24-hour regime just encompasses two operation modes, hybrid and boiler-only. During the daylight period the system operates in hybrid mode, and at night the collectors are defocused and the solar field is cooled down. After that the system relies solely on the boiler.

For both cases the boiler minimum power of 100 kWth was considered, in order to assure electricity generation stability, during the predefined time operating range. Otherwise, the boiler would be submitted

to consecutive startups and shutdowns, and shortages in the electrical generation would be expected, due to solar radiation transients.

4. RESULTS

If the system relies solely on solar energy the annual heat generated is about 663 MWh$_{th}$. Hybridisation improved the solar field output by 3% (Table 1). This outcome is related with the system start-up, since the SF feed water is already warmer, and consequently less solar energy is required to achieve steam generation. Furthermore, this improvement is extended to the solar field annual efficiency.

The second improvement of hybridisation was the extinction of dumping rates associated with scarcity of energy. Almost one quarter of the heat is dumped in the solar-only operation mode, mostly related with energy dearth. The dumping rate results are divided in two items (excess and scarcity), representing the heat dumped due to the excess of energy or due to insufficient energy to drive the ORC turbine, respectively.

The scarcity of energy was surpassed with hybridisation, with the fulfilment of the ORC minimum thermal power requirements. On the other hand, the excess of energy increased. This fact is related with minimum operating conditions of the boiler (100 kW$_{th}$), leading to energy waste predominantly in the summer months, when solar radiation is highly available.

Table 29: Simulation Annual Results

	Solar Only	Hybrid - 24 hours operation			Hybrid - 12 hours operation			
		530 kWth Boiler	380 kWth Boiler	ORC minimum Power	530 kWth Boiler	380 kWth Boiler	ORC minimum Power	
Direct Normal Irradiance - DNI	1799.4	1799.4	1799.4	1799.4	1799.4	1799.4	1799.4	kWh/(m^2.a)
Annual Heat Generated S.F.	663	683	683	683	683	683	683	MWh$_{th}$
Specific Thermal Field Output	674	694	694	694	694	694	694	kWh$_{th}$/m^2
Mean Annual SF Efficiency	37.4%	38.6%	38.6%	38.6%	38.6%	38.6%	38.6%	%
Annual Heat Generated - Boiler	0	3359	2546	1788	1425	1155	865	MWh$_{th}$
Annual Combustion Heat - Boiler	0	3619	2746	1918	1534	1244	928	MWh$_{th}$
Mean Annual Boiler Efficiency	0	92.8%	92.7%	93.2%	92.9%	92.8%	93.2%	%
Annual Biogas Consumption	0	655	497	347	278	225	168	dam^3
Average Biogas Consumption	0	1795	1362	951	761	617	460	m^3/day
Solar Share	100%	17%	21%	28%	32%	37%	44%	%
Dumping Rate - Excess	7.9%	2.5%	3.1%	4.1%	6.5%	7.5%	8.9%	%
Dumping Rate - Scarcity	16.3%	0.0%	0.0%	0.0%	0.5%	0.5%	0.0%	%
Annual Useful Heat - ORC	503	3941	3128	2370	1971	1700	1410	MWh$_{th}$
Annual Power Generated	61	515	380	261	257	213	167	MWh$_{el}$
Mean Annual ORC Efficiency	9.2%	12.7%	11.8%	10.6%	12.2%	11.6%	10.8%	%
ORC - Number of hours running	1420	8760	8760	8760	4380	4380	4380	hr
Annual Dissipated Heat - Condenser	437	3389	2720	2089	1695	1472	1231	MWh$_{th}$
Maximum Heat Dissipated - Condenser	387	387	387	387	387	387	387	kWh$_{th}$
Mean Annual System Efficiency	3.4%	9.6%	8.4%	7.1%	7.8%	7.1%	6.2%	%

The excess of energy can be reduced by implementing a storage tank in the system. The benefits extend beyond the ability to store the excess of solar field thermal energy. If storage capacity can provide more than 30 minutes of thermal energy requirements to drive the ORC turbine, the need of having the boiler in

permanent operation is eliminated. In other words, it can act as system buffer in order to compensate thermal output fluctuations from the solar field and boiler, reducing the amount of wasted biogas.

Despite the discontinuous operation of the boiler, due to the solar irradiance transients, the average biogas boiler efficiency is still high (about 93%) for all cases.

As expected, electric generation significantly increased with hybridisation. If the system depends only on solar energy, electric generation is limited to 1420 hours and 61 MWh$_{el}$, and confined to summer months. In spite of the favourable Tunisian climate, solar radiation monthly values show a noteworthy discrepancy between summer and winter. To enable electrical generation in low radiation months, the solar multiple should be increased leading to costly and oversized systems. On the other hand, even system hybridisation for 12 hours/day at ORC minimum power showed an annual generation of 167 MWh$_{el}$, with a solar share of 44%.

System annual efficiency experienced a huge boost with hybridisation, from 3.5% to almost 10%, due to the high efficiency boiler, along with improved efficiencies of the SF and ORC (Figure 3). In the REELCOOP framework a 10% system efficiency was proposed as target, which is nearly attainable with hybridisation.

One of the main advantages of hybridisation is the stability of the system, in order to promote dispatchability. It can be observed for the 21st of December (Figure 4), where the generator is operating 24 hours at nominal power with the 530 kW$_{th}$ boiler.
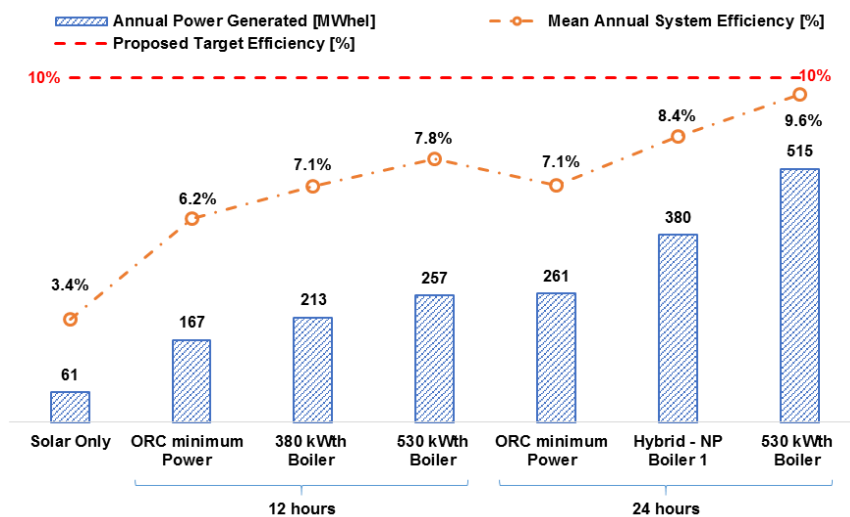

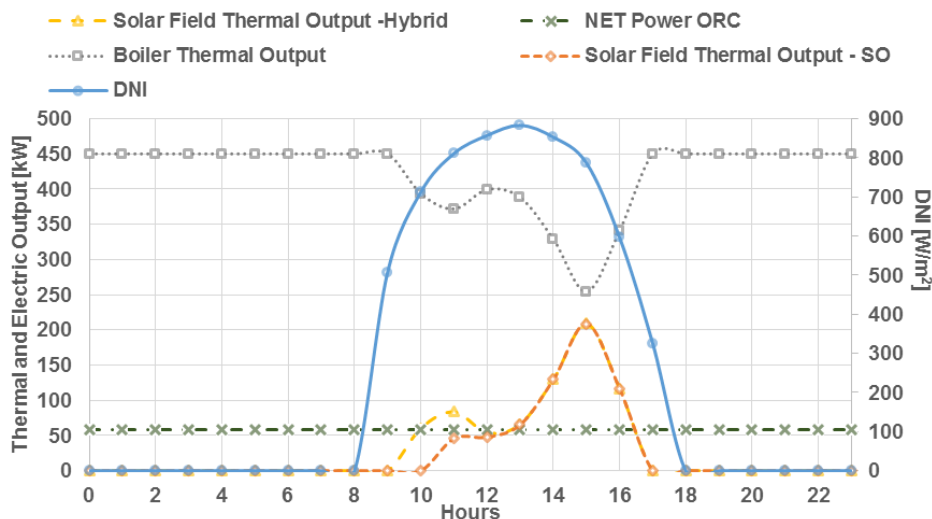Figure 79: Annual power generated and mean annual efficiency

Figure 80: Winter solstice 24-hour hybrid operation with a 530 kWth boiler

On 21st of December, the boiler is supplying 450 kWh$_{th}$ until 9:00am, fulfilling the ORC requirements during night operation. At this time the DNI is above 200 W/m^2, and the collectors change their sate to focus. Steam production from the solar field starts at 10:00 am, with a thermal output of about 50 KW$_{th}$. When compared with solar-only, the steam generation starts one hour later and with half of the hybrid production. During the day the solar field is unable to supply the minimum conditions to drive the ORC turbine. Nevertheless, it contributes to a reduction in the amount of required boiler energy and biogas consumption.

On the Summer solstice (21 June), the generation stability was attained even with the smaller boiler (Figure 5). However, the heat dumped due to excess of energy increased. In such days, the boiler should be used only during start-up and shut-down, reducing the amount of biogas consumption and heat dumped. The boiler starts to operate at 07:00, at minimum power in order to warm-up the SF and ORC. From 8:00 to 20:00 nominal electricity generation is achieved mostly from solar energy.
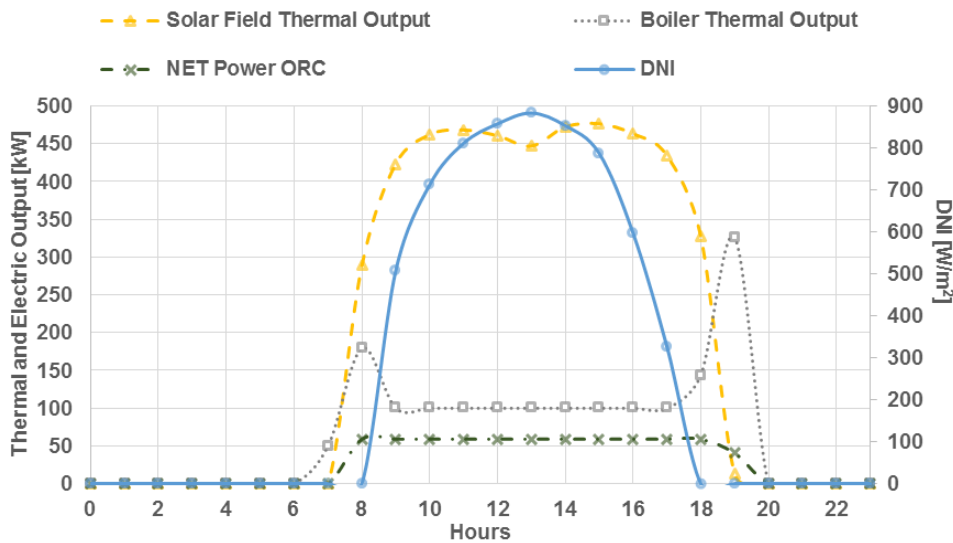

Figure 81: Summer solstice 12-hour hybrid operation with a 380 kWth boiler

Either Summer or Winter solstice results showed that electricity stabilisation can be achieved during the daylight period through hybridisation, moreover with a significant solar share in the summer (75%) and less relevant (13%) in the winter. This synergy is noteworthy, since during the daylight period electricity prices are usually higher, related to peaks in network consumption.

The estimated biogas production of 60 m^3/day is far below the consumption results. On an annual basis the excess of energy related with the boiler minimum operating conditions represents 738 hours of operation and 14 dam^3 annual. If we consider as example the case of 12 hours of operation at minimum power, this represents 9% of the annual biogas consumption and 16% of the running hours. This represents a small contribution to CSP/Biomass hybridisation. Despite hybridisation allowing to relocate a power plant near urban centres where organic wastes are more abundant, the absence of a well-established biomass market represents a drawback to the dissemination of these systems (Colmenar-Santos et al., 2015).

As aforementioned, either solar-only or hybrid operation results showed excess of thermal energy, mostly in the summer months when solar radiation is abundant. The energy waste can be overcome with a storage tank. To define the ideal storage capacity the daily average values of the heat dumped due to energy excess were analysed for the solar-only mode (Figure 6). The analysis was not extended to hybrid mode, since it enhances the heat dumped and consequently the storage capacity. Furthermore, this overestimation can easily be eliminated with a small storage capacity. The maximum value for the average daily dumped heat is 332 kWhth (June) and the minimum is 10 kWhth (December). It is worthy to note that the maximum daily value of the excess heat doesn´t allow to drive the ORC at nominal power for one hour.
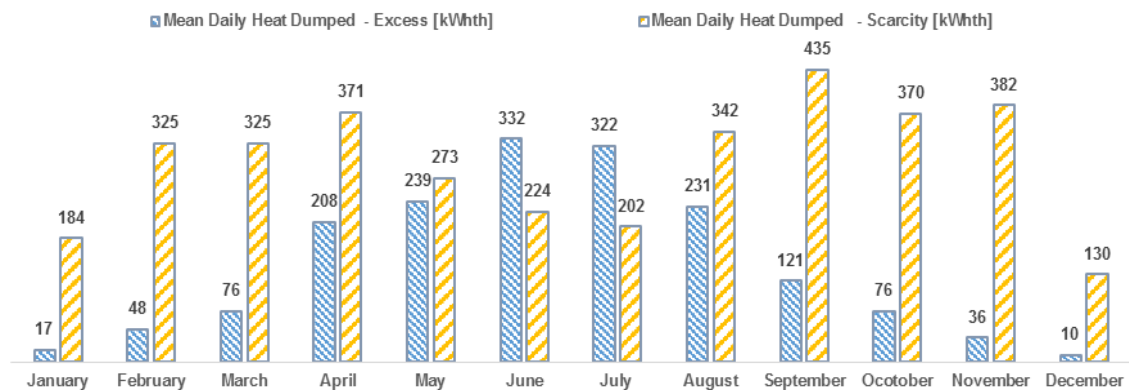
Figure 82: Heat dumped in the solar-only operation mode

5. CONCLUSION

In this paper, a simulation model and results of a hybrid CSP/Biomass Mini Power Plant are presented. The simulations were carried out on an hour-by-hour basis for a typical meteorological year, considering different scenarios regarding operation regimes and boiler sizes.

If power generation is exclusively dependent on the solar field, electrical generation is mostly confined to summer months and negligible in the winter. The annual heat dumping rate ascends to almost one quarter, mostly related with the inability of the solar field to supply the minimum thermal energy to drive the ORC turbine.

System hybridisation proved to stabilise the system regarding electrical power generation during the whole year. Additionally, the downside of the dumped heat, due to scarcity of thermal energy, was surpassed. Hybridisation improvements where extended as well to the SF and ORC efficiencies. The SF efficiency increased 3% since the system is already warmer in the morning, and solar radiation is used exclusively for steam generation. The ORC efficiency increase is in the range of 15% to 38%, and was achieved by a stable operation near turbine design conditions.

On the other hand, there was an increase of the system energy excess due to the downsides of boiler start-up time (about 30 minutes) and minimum operational heat input (100 kW_{th}). The simulated operation profiles were created within the basis of energy dispatchability and demand response ability. Therewith, boiler operation was extended to the system operation range to compensate possible short transient from solar power. This issue can be overcome with the implementation of a storage tank. From simulation results, the maximum average daily dumped heat ascends to 332 kWh_{th}. This value is quite small when compared with the system dimension. For example, it doesn´t allow to run the system for one hour at nominal power. This proves that the solar field design is appropriate and hybridisation significantly reduces (although not totally eliminating) the need of storage.

The improvements in the SF and ORC efficiencies, along with extended operation ranges and a highly efficient boiler, lead to a huge boost on system efficiency, which increases from 3.4% to 9.6%.

As future work, system simulations will include the implementation of a PCM storage tank. More operation strategies, biomass resources, different climatic regions and a cost analysis will be addressed. A prototype of the system is under development, and will be installed in Tunisia during late 2015, for testing during 2016/17, allowing a validation of the simulation results.

6. ACKNOWLEDGMENTS

7. REFERENCES

COELHO, B., Varga, S., Oliveira, A. & Mendes, A. 2014. Optimization of an atmospheric air volumetric central receiver system: Impact of solar multiple, storage capacity and control strategy. Renewable Energy, 63, 392-401.

COLMENAR-SANTOS, A., Bonilla-Gómez, J.-L., Borge-Diez, D. & Castro-Gil, M. 2015. Hybridization of concentrated solar power plants with biogas production systems as an alternative to premiums: The case of Spain. Renewable and Sustainable Energy Reviews, 47, 186-197.

JIN, H. G. & Hong, H. 2012. 12 - Hybridization of concentrating solar power (CSP) with fossil fuel power plants. In: LOVEGROVE, K. & STEIN, W. (eds.) Concentrating Solar Power Technology. Woodhead Publishing.

KRÜGER, D., Kenissi, A., Schenk, H., Bouden, C., Baba, A., Oliveira, A., Soares, J., Bravo, E. R., Cheikh, R. B., Orioli, F., Gasperini, D. & Hennecke, K. 2014. Pre-Design of a Mini CSP plant. International Conference on Concentrating Solar Power and Chemical Energy Systems, SolarPACES 2014. Beijing, China: Elsevier.

MORENO-PÉREZ, Á. & Castellote-Olmo, P. Solar Parabolic Trough - Biomass Hybrid Plants: Features and Drawbacks. International Conference on Concentrating Solar Power and Chemical Energy Systems, SolarPACES 2010, 2010 Perpignan, France.

OLIVEIRA, A. C. & Coelho, B. 2013. REELCOOP project: developing renewable energy technologies for electricity generation. 12th International Conference on Sustainable Energy Technologies (SET2013). Hong Kong.

PAWELLEK, R., Pulyaevrank, S. & Hirsch, T. Transient simulation of a parabolic trough collector in EBSILON. International Conference on Concentrating Solar Power and Chemical Energy Systems, SolarPACES 2012, 2012 Marrakesh, Morocco.

PETERSEIM, J. H., White, S., Tadros, A. & Hellwig, U. 2014. Concentrating solar power hybrid plants – Enabling cost effective synergies. Renewable Energy, 67, 178-185.

REELCOOP. 2015. REELCOOP project [Online]. Available: http://www.reelcoop.com.

SINGH, G. K. 2013. Solar power generation by PV (photovoltaic) technology: A review. Energy, 53, 1-13.

107: Plutonium utilization in HTGR with ThO2 fuel

ABDUL WARIS[1], SYEILENDRA PRAMUDITYA[2],
SIDIK PERMANA[3], ZAKI SU'UD[4]

[1] *Nuclear Physics & Biophysics Research Group, Department of Physics, Faculty of Mathematics and Natural Sciences, Institut Teknologi Bandung, Jl. Ganesa 10 Bandung 40132 INDONESIA, Email: awaris@fi.itb.ac.id*
[2] *Nuclear Physics & Biophysics Research Group, Department of Physics, Faculty of Mathematics and Natural Sciences, Institut Teknologi Bandung, Jl. Ganesa 10 Bandung 40132 INDONESIA, Email: syeilendra@fi.itb.ac.id*
[3] *Nuclear Physics & Biophysics Research Group, Department of Physics, Faculty of Mathematics and Natural Sciences, Institut Teknologi Bandung, Jl. Ganesa 10 Bandung 40132 INDONESIA, Email: psidik@fi.itb.ac.id*
[4] *Nuclear Physics & Biophysics Research Group, Department of Physics, Faculty of Mathematics and Natural Sciences, Institut Teknologi Bandung, Jl. Ganesa 10 Bandung 40132 INDONESIA, Email: szaki@fi.itb.ac.id*

VHTR (very high temperature reactor) is one of Generation IV nuclear reactors. HTGR (high temperature gas cooled reactor) is a VHTR type of reactors with a graphite moderator, helium gas coolant with UO2 fuel and outlet coolant temperature of 900oC or higher than that. In this study, instead of using UO2 fuel, we will evaluate the utilization of PuO2 and ThO2 as a mixed fuel in HTGR. The burnup period is 1100 days, which corresponds to 3 years of fuel cycle length. The reactor 3D calculation was performed by using CITATION-SRAC 2006 code, with the nuclear data library was derived from JENDL3.3. The neutron spectra become harder with the boosting of the plutonium fraction in loaded fuel. Moreover, the neutron spectra at EOC become softer compared to that of BOC. Fascinatingly, U-235 is generated more with the increasing of plutonium fraction.

Keywords: Plutonium, HTGR, ThO2, SRAC, JENDL

1. INTRODUCTION

Spent fuel of pressurized water reactor (PWR) consists of at least 96% of valuable materials (uranium and plutonium isotopes) that can be reused as new fuel (Bernard, 2004). The uncertainty in commercialization of fast breeder reactor (FBR) enforced the nuclear scientists and engineers to find the other way to stabilize the stockpile of plutonium. Reprocessing and recycling of plutonium in the form of mixed oxide (MOX) fuel in PWR is an established industry for several countries, like Japan, UK, and France. Two large-scale fuel fabrication plants, those are MELOX and COGEMA in France have successful operational experiences in fabrication of the later type of fuels. MOX fuel has been utilized in 20 reactors of 900 MWe of PWR type in France since 1987 (Bruna, 2000)

Several studies on the recycling of plutonium together with minor actinides in PWR (Waris, 2001) as well as in boiling water reactors (BWR) (Waris, 2008; Waris, 2012).have been reported. However, these types of reactors are classified as Generation III or III+ reactors. Learning from the Chernobyl, Three Mile Island, and Fukushima Daiichi accidents, since 1990s the studies on the Generation IV reactors have been conducted. The latest reactor types are expected be operated since 2030.

VHTR (very high temperature reactor) is one of Generation IV nuclear reactors. The high temperature gas-cooled reactor (HTGR) is one of VHTR type of reactors which can produce heat with very high temperature heat of more than 950 ^{0}C. As a consequence, HTGR can enrich the nuclear energy utilization to various fields such as for hydrogen production. It also has inherent safety characteristic which can condense safety systems and in due course improve economical advantages over other reactor systems (Shiozawa, 2004).

The research and development activities on high temperature gas-cooled (HTGR) concentrate on HTGR related key technologies and innovation potentials for industrial application in the next decade and to explore new applications like hydrogen production and waste transmutation in the long term. Therefore, in order to establish and upgrade the technological basis for HTGRs and also to use as a tool of basic researches for high temperature and neutron irradiation the Japan Atomic Energy Research Institute (JAERI) has been constructed and operated a 30MW High Temperature engineering Test Reactor (HTTR) (Ogawa, 2004).

HTTR use helium as its coolant and graphite as the moderator with thermal energy of 30 MW. Low enriched UO_2 use for its fuel with prismatic block fuel element type. The block type fuel is adopted in the HTTR, instead of the pebble-bed type fuel (Ogawa, 2004). In this study, the utilization of plutonium in the HTTR core together with thorium oxide (ThO_2) as the loaded fuel has been investigated. At present, the use of thorium become interesting again (IAEA, 2000). However, for employing thorium we need U-233. The use of plutonium can substitute U-233 and may improve the neutronics features of HTTR.

2. METHODOLOGY

The high-temperature engineering test reactor is a block-type HTGR, with 395 ^{0}C and 950 ^{0}C of inlet and outlet gas temperature, respectively. The high outlet gas temperature may enhance the fission product release from fuel since the fuel temperature raises. The HTTR core structure is presented in Figure 1 (Shiozawa, 2004).

The reactor core consists primarily of hexagonal fuel blocks, control rod guide blocks and replaceable reflector blocks. The original HTTR has active core, which is 2.9 m in height and 2.3 m in diameter, consists of 30 fuel columns and 7 control rod guide columns (Fujimoto, 2004). A fuel assembly consists of fuel rods and a hexagonal graphite block. The fuel assembly has three dowels on the top and three mating sockets at the bottom to align the fuel assemblies. TRISO-coated fuel particles with UO_2 kernel, with 600 µm in diameter, are dispersed in the graphite matrix and sintered to form a fuel compact. Fuel compacts are contained in a fuel rod, and then are inserted into vertical holes in the graphite block. The coolant gas flows through gaps between the holes and the rods. General specification of HTTR can be seen in Table 1 (Fujimoto, 2004).
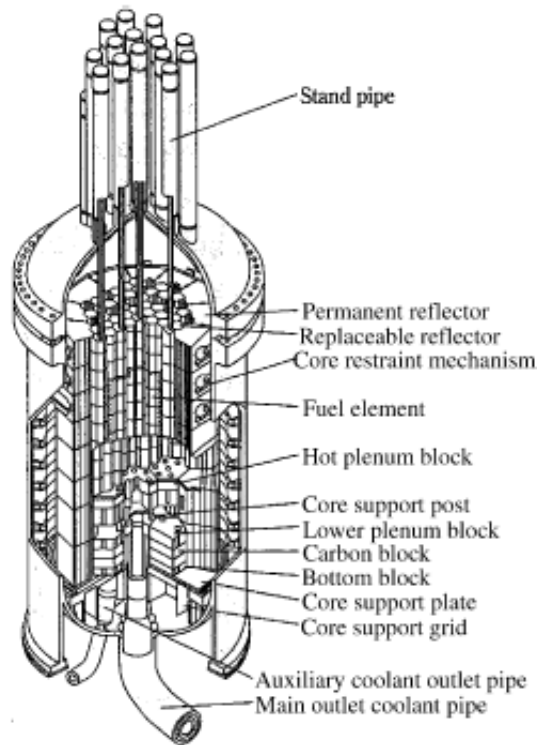
Figure 1 Core structure of HTTR

Table 1 Specifications of HTTR

Parameter	Specification
Thermal power output	30.0 MW
Average power density	2.5 W/cc
Outlet coolant temperature	950 ^{o}C
Inlet coolant temperature	395 ^{o}C
Primary coolant pressure	4 MPa
Material structure	Graphite
Coolant	Helium
Fuel type	$PuO_2 + ThO_2$
Plutonium fraction in fuel	5.0 %, 7.5%, and 10%
Core diameter	230 cm
Core height	290 cm
Burnup period	1100 days

In this study, the plutonium oxide (PuO_2) and thorium oxide (ThO_2) are loaded in the HTTR core as fuel. The isotopic composition of plutonium is given in Table 2. Here we have employed reactor grade plutonium only.

Table 2 Plutonium Composition

Pu	^{238}Pu	^{239}Pu	^{240}Pu	^{241}Pu	^{242}Pu
%	1.81	59.14	22.96	12.13	3.96

In the present paper, the cell burnup calculations have been performed by using and SRAC 2006 code (Okumura, 2006) with nuclear data library is derived from JENDL3.3 (Shibata, 2002)

3. RESULTS AND DISCUSSION

Figure 2 shows the effective multiplication factor (k_{eff}) as a function of operation time. Here the burnup period is 1100 days. As we can see from these figures, the reactor can achieve its criticality condition when the plutonium concentration in the loaded fuel is higher than 7.5%. The effective multiplication factor as a function of burnup is presented in figure 3. The obtained burnup is much smaller than that of the standard HTTR with helium coolant and UO_2 fuel with 6% average enrichment. According to the reference the average burnup of HTTR is 22 GWd/ton and the maximum burnup is 33 GWd/ton (Fujimoto, 2004).

431

Figure 2 Effective multiplication factor vs time

Figure 3 Effective multiplication factor vs burnup

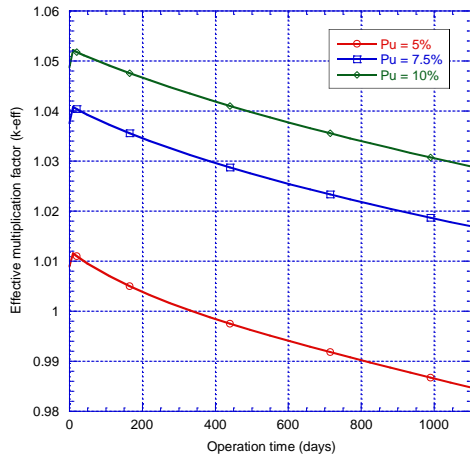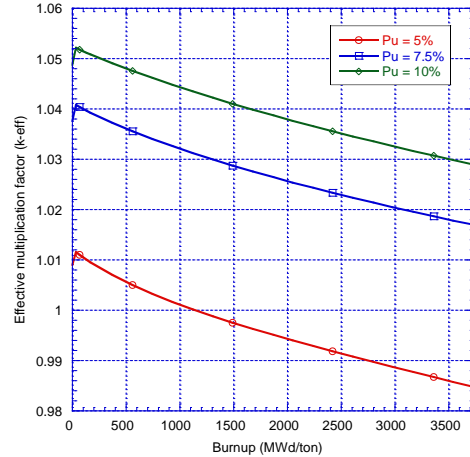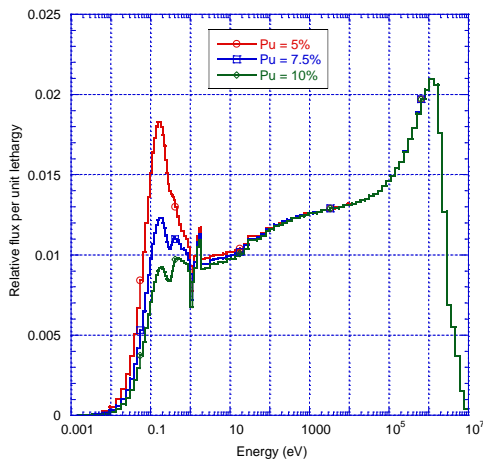Figure 4 Neutron spectra at Beginning of Cycle (BOC)
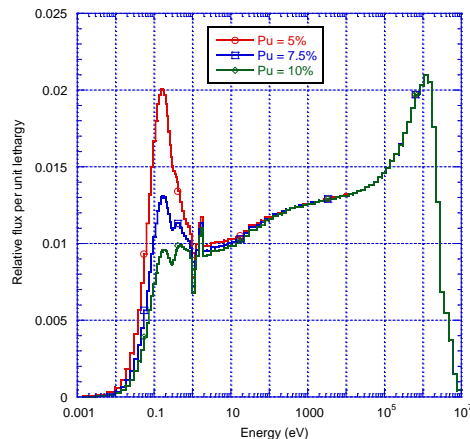
Figure 5 Neutron spectra at End of Cycle (EOC)

The neutron spectra of the helium cooled HTTR with PuO_2 and ThO_2 fuel at the beginning of cycle (BOC) and the end of cycle (EOC) are presented in Figures 4 and 5, respectively. The neutron spectra become harder (shift to higher energy region) with the increasing of the plutonium concentration in loaded fuel. Moreover, the neutron spectra at EOC are softer compared to that of BOC. The standard UO_2 fuelled HTTR with helium coolant has very soft neutron spectra, even much softer compared to the standard pressurized water reactor (PWR) [3]. By employing plutonium in HTTR the neutron spectra become much harder compared to that of the standard UO_2 fuelled HTTR. The later fact also has been observed in PWR (Waris, 2001) and boiling water reactor (BWR) (Waris, 2008). This is due to the presence of fissile plutonium (Pu-239 and Pu-241). In the thermal energy region, the microscopic absorption cross-sections of fissile plutonium are higher than those of U-233 and U-235. As a consequence the flux depression happens and the neutron spectrum becomes harder (Waris, 2001).

Figures 6, 7, and 8 demonstrate the number density of several actinides (thorium, uranium, and plutonium) in the reactor core for 5%, 7.5%, and 10% of loaded plutonium, correspondingly. Logically, the number density of plutonium isotopes increase with the enlarging of plutonium fraction in loaded fuel. On the other hand, the number density of Th-232 decreases with the augmenting of plutonium fraction. Comparison of the number density of U-233 and U-235 in HTTR core for 5%, 7.5%, and 10% of loaded plutonium are shown in Figure 9. Interestingly, the number density of U-235 becomes higher with the raising of plutonium fraction. This means that U-235 may be produced from decay reaction of plutonium isotopes.

432
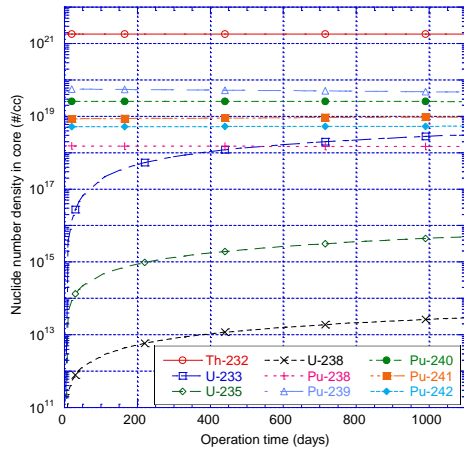
Figure 6 Number density of actinides for 5% Pu
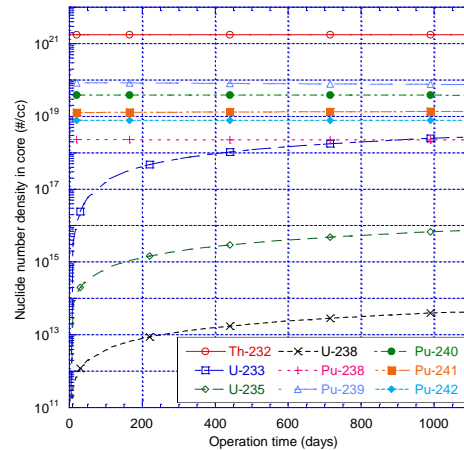
Figure 7 Number density of actinides for 7.5% Pu
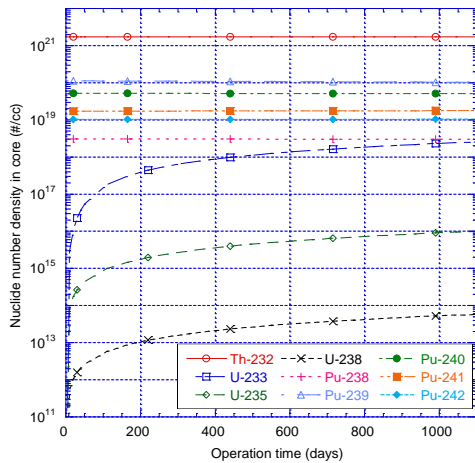
Figure 8 Number density of actinides for 10% Pu
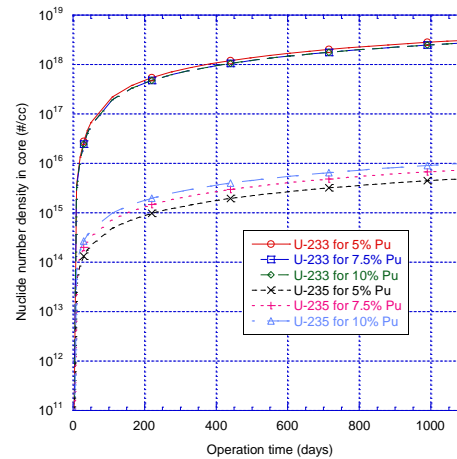
Figure 9 Number density of U-233 and U-235

4. CONCLUSION

Plutonium utilization together with thorium oxide as the loaded fuel in HTTR core has been evaluated. HTTR can obtain its criticality if the plutonium fraction in the loaded fuel is 7.5% or above. The neutron spectra become harder (shift to higher energy region) with the augmenting of the plutonium fraction in loaded fuel. In addition to that, the neutron spectra at BOC become harder compared to that of EOC. Excitingly, U-235 is produced more with the enlarging of plutonium fraction.

5. ACKNOWLEDGMENT

6. REFERENCES

BERNARD, P., 2004, Advances in treatment of wastes from reprocessing of spent fuel, Vienna, Austria, IAEA Scientific Forum

BRUNA, G. B. 2000, Aspects of Physics and Computation of Plutonium Recycling in PWRs: Full MOX Loading and Void Effect, Workshop on Nuclear Data and Nuclear Reactors: Physics, Design and Safety, 13 March – 14 April 2000, Trieste, Italy

WARIS, Abdul, et al., 2001, Characteristics of Several Equilibrium Fuel Cycles of PWR, J. Nucl. Sci. Technol., 38, pp. 517-526

WARIS, Abdul, et al., 2008, Influence of void fraction change on Plutonium and Minor Actinides Recycling in BWR with Equilibrium Burnup, Progress in Nuclear Energy, 50, 2-6, pp.295-298

WARIS, Abdul, et al., 2012, Effect of void-fraction on characteristics of several thorium fuel cycles in BWR, Energy Conversion Management (ECM), 63, pp.11-16

SHIOZAWA, S, et al., 2004, Overview of HTTR design features, Nucl. Eng. Design, 233, pp. 10 -21

OGAWA, M, et al., 2004, Present status of energy in Japan and HTTR project, Nucl. Eng. Design, 233, pp. 5 -10

IAEA, 2000, Thorium based fuel options for the generation of electricity: Developments in the 1990s. Vienna, Austria, IAEA-TECDOC-1155

FUJIMOTO, Nozomu, et al., 2004, Nuclear Design, Nucl. Eng. Design, 233, pp. 23 -26

OKUMURA, K, 2006, SRAC: The Comprehensive Neutronics Calculation Code System, JAERI, Tokai-mura, Japan

SHIBATA, K, et al., 2002, Japanese Evaluated Nuclear Data Library Version 3 Revision-3: JENDL-3.3, JAERI, Tokai-mura, Japan

38: Sustainability aspect of nuclear fuel from loading recycled spent fuel in fast breeder reactor (FBR)

Sidik Permana[1], Abdul Waris[1], Mistutoshi Suzuki[2], Masaki Saito[3]

[1] Bandung Institute of Technology, Jl. Ganesha 10, Bandung Indonesia, psidik@fi.itb.ac.id
2 Japan Atomic Energy Agency, Ibaraki Japan, mitsutoshi.suzuki@jaea.go.jp
3 Tokyo Institute of Technology, Tokyo Japan, msaito@nr.titech.ac.jp

Sustainable energy program including operational energy utilization is one of the key issues for maintaining world energy demand, environmental aspect of energy utilization as well as economical point of view. In case of nuclear energy utilization, maintaining sustainability of nuclear fuel is one of the important issues, especially for the fourth generation of nuclear power plant which can be maintained by utilizing new fresh fuel resources, spent fuel resources as recycled fuel process, and obtaining nuclear fuel breeding resource in the reactors. Utilization of used fuel from recycling resources and fuel breeding resource become the key issue which affects to the reprocessing and refuelling facilities. The study analyses a fast breeder reactor (FBR) type as a reference based and utilizes an established reactor code system of JOINT-FR. Inventory ratio of actinides are evaluated including reactor criticality condition as well as the behaviour of heavy nuclide during reactor operations. Loading MA as trans uranium fuel type in comparing with mixed oxide fuel type gives a significant improvement for plutonium inventory ratio as well as MA inventory ratio. In term of reactor criticality condition, it shows a reduction factor for criticality condition for trans uranium fuel type as MA recycled fuel in comparing with MOX fuel type as a fertile material which absorbs more neutrons which affects to reduction value of criticality and in the same time, conversion process from absorption neutron will produce more fissile materials especially fissile material of plutonium. Recycled material from spent nuclear fuels can be used as new fuel which shows some significant benefits for nuclear fuel sustainability as well as a reduction factor of criticality condition of reactor operation as one of the safety concern in the reactor operation.

Keywords: recycled spent fuel, FBR, plutonium, inventiry ratio, sustainability

1. INTRODUCTION

Spent nuclear fuel (SNF) managements in term of its advantages as an important factor to reduce the environmental impact from nuclear fuel waste, as well as a utilization factor of fuel sustainability for longer fuel utilization and fuel breeding capability in the reactors have been developed. In addition, some important factors are also managed based on SNF from nuclear non-proliferation aspects (Saito, 2002; Meiliza et al, 2008; Permana, 20011a, 2011b, 2009a, 2009b). SNF recycling program can be optimized by adopting reprocessing stage, reused nuclear materials and refabrication processes which can be used as a new fresh fuel and recycling fuel option such as recycling program of uranium and plutonium from SNF of LWR as well as minor actinide (MA). This optimization processes can be conducted in order to reduce the volume of SNF and in the same time its loading process can be used to increase nuclear non-proliferation level of nuclear fuel. Good candidate for recycling program is by adopting fast breeder reactor (FBR) cycle as well as some type of light water reactors (LWR) (Choi and Downar, 1999; Hoffman and Stacey, 2003; Taiwo et al, 2006). FBR has better neutron economy which can be used easier to achieve criticality condition and better transmutation capability because of harder spectrum as well as better nuclear fuel breeding capability. In addition, recycling program of minor actinide (MA) not only will reduce a volume of spent nuclear fuel (SNF), but also will increase the nuclear fuel breeding capability from converted MA into plutonium and in the same time some converted MA to even mass plutonium can be used as control material in term of proliferation resistance aspect especially for plutonium production (Saito, 2002; Meiliza et al, 2008; Permana, 20011a, 2011b, 2009a, 2009b). In the present study, fuel sustainability aspect of nuclear fuel based on recycled spent nuclear fuel in the fast breeder reactor (FBR) has been evaluated for different fuel loading types of mixed oxide (MOX) and uranium-transuranium mixed (UTRU) fuel types. Some inventory ratio analyses based on several important actinides during reactor operation and equilibirum composition have been compared as well as plutonium composition in the core and reactor criticality to evaluate the excess reactivity of the reactor. Loading fuels in the FBR cycle are based on spent nuclear fuel composition of ligh water reactor (LWR).

2. METHOD

Analysis method of this study will focus on the evaluation of FBR performances in term of inventory ratio of nuclear fuel, plutonium isotopes trend composition and criticality condition of the reactor. Methodology analysis will be shown and discussed in this section which will be followed by results and discussion of the results for the next setion and will be resumed in the conclusion. The evaluation is based on fast breeder reactor (FBR) type reactor with some evaluation of fuel composition of ligh water reactor (LWR) spent nuclear fuel which is loaded as loading fuel in the FBR. As mentioned in the previous section, loading fuels which are used in this evaluation based on the reprocessed fuel from LWR which is refabricated as a fresh fuel of mixed oxide fuel (uranium and plutonium, MOX) oxide and it compared with a fuel type of mixed uranium and transuranium (UTRU).

2.1 FBR Design Analysis

FBR analysis is based on the evaluation of reactor condition such as reactor criticality condition and nuclear fuel composition during reacor operation as well as some active core arrangements and fuel cycle schemes. Basic design of FBR evaluation for this analysis is adopting an FBR design of Fast reactor Cycle Technology, FaCT which is used as refference basic design for reactor core evaluation (Ohki et al, 2008). A conventional fuel arrangement of FBR which is used a core-blanket fuel arrangement is adopted. Core fuel region arrangement is dedicated for reactor criticality which is called as driver fuel region of the FBR region and blanket regions arrangement is used for fuel breeding or fuel production purposes to maintain fuel sustainability of the reactor which can be produced during reactor operation as well as some additional fuel production in the core regions. An integrated computational code has been used for evaluating the reactor core behavior as an analysis of space dependence evaluation such as radially and axially fuel arrangement and different fuel types and structure materials as supporting material of FBR design such as fuel cladding material, coolant and others supporting structure of FBR. Time dependence analysis has also been done for the evaluation of reactor condition and fuel behavior during reactor operation or burnup capability of fuel. Those integrated code for the analysis is combined of nuclide data library of FBR based on JENDL data library (Nakagawa and Tsuchihasi, 1984; Fowler et al, 1971; Chiba et al, 2002; Nakagawa et al, 1995). Beside the reactor performances during reactor operation, it can be used also to analyze the fuel inventory at the beginning of operation up to the end of operation as well as the typical composition of fuel in the core and balnket regions. Inventory of actinide can be used to analyze the inventory ratio of several actinide during reactor operation and in the equilibrium condition.

2.2 Loading Fuel of LWR Spent Nuclear Fuel Analysis

As mentioned in the previous section, loading fuel in the FBR is adopted from spent nuclear fuel of LWR. Analysis of fuel behavior of LWR from the fresh nuclear fuel composition up to the end of operation as well as fuel composition after fuels are discharged from the reactor as a cooling time process at certain time of decay process. Fuel behavior analysis of LWR has been done by adopting an ORIGEN code (Ludwig and Croff, 2002). The code is used to optimize the fuel behavior during reactor operation as burnup or irradiation process step and during cooling time process as decay process after fuel discharging process from the reactor. Enrichment of uranium (U-235) and burnup level are used to evaluate the fuel composition as important parameters which is based on 33 up to 60 GWd/t, and 3 % up to 5 % uranium enrichment. In this evaluation a typical fuel composition will be selected to be used for loading fuel in the FBR. Cooling process as decay analysis of fuel composition after discharging process is also evaluated, it used cooling time analysis from 1 year up to 30 years. The composition of LWR SNF will be analysed and focused on actinide composition such as uranium composition, plutonium, minor actinides as well as transuranium fuel compositions. Mixed fuel compsotion from LWR SNF such as mixed uranium and plutonium as MOX fuel or uranium and transuranium mixed fuel as well as uranium and minor actinide (MA) mixed fuel composition will be used and loaded in to the FBR fuel of core regions and blanket regions.

2.3 Plutonium Composition Analysis

Fuel behavior analyses in LWR system as well as FBR system have an important evaluation in term of fuel production which is focused in production rate of fissile material such as fissile uranium as well as fissile plutonium. This fissile production in the reactor can be estimated as fuel breeding or fuel conversion process which is related to the fuel sustainability of the reactor. Nuclear fuel breeding evaluation can be also estimated from the reaction rate ratio of fertile materials to the fissile materials as well as from the mass inventory of fissile production such as production of plutonium. Some main actinides have been adopted such as nuclear fertile materials of U-238 and Pu-240, including Pu-238. In addition, some fissile materials of U-235, Pu-239 and Pu-241 have been used for breeding analysis. Some plutonium isotopes can be produced from some converted U-238 as well as from minor actinide such as production of Pu-238 is estimated from converted minor actinide (MA) which can be used to produce more Pu-239 as fissile material. Another point of view of plutonium isotopes analysis is based on the plutonium proliferation analysis from converted MA into plutonium such as even mass plutonium which is adopted as barrier materil to increase the proliferation resistance aspect based on plutonium production (Saito, 2002; Meiliza et al, 2008; Permana, 20011a, 2011b, 2009a, 2009b).

2.4 Actinide Inventory Ratio

Inventory of actinide as well as other nuclide in the reactor will be analyzed their behavior especially focused on the inventory behavior of actinide. Composition of actinide during reactor operation will be compared with the fresh fuel loading for different fuel loading in the core regions of FBR. At certain irradiation time and in the equilibrum condition, inventory ratio of mass from some actinides are analyzed such as plutonium, MA and transuranium (TRU). Inventory ratio has been analyzed based on the inventory ratio of actinide mass at certain time up to equilibrium discharged fuel to the initial fuel supply. This evaluation has been done to analyze the invetory profile each actinide production during reactor as well as to estimate the inventory balance of nuclear fuel based on input inventory as supply side in comparison with consumption rate and its inventory production. The ratio of inventory is evaluated to estimate the sustainability factor of supply capability for the next step of loading fuel. When the inventory ratio is obtained higher than unity, it can be expected to have more fuel inventory as breeding gain or fuel sustainability capability is achieved.

3. RESULTS AND DISCUSSION

Loading nuclear fuel into the FBR cycle is the main topic to be discussed in this paper which is related to reactor performances and fuel inventory profile as well as some plutonium isotopes behavior during reactor operation. Transuranium fuel which are compared with MOX fuel are used to estimate the different fuel loading for some importance parameters in this evaluation. Reactor operation has a transition behavior for nuclear preactor performance and nuclear fuel behavior as well as the equilibrium condition. The equilibrium fuel condition can be adopted for evaluation because for some estimation target that the reactor has the stable nuclear fuel condition which affect to the reactor core condition such as criticality condition and fuel breeding capability. Inventory of actinide and its ratio which can be used also for estimating a nuclear fuel breeding capability will be shown and discussed based on inventory ratio of element actinide.

Reactor criticality and excess reactivity condition will be shown and evaluated during reactor operation and in equlibrium condition.

3.1 Equlibrium Inventory Ratio

Inventory ratios of produced actinide during reactor operation or cycle operations are obtained and shown in Figures 1 and 2 based on MOX fuel type. Figure 1 shows plutonium inventory ratio of each cyle operation which has its own inventory ratio during cycle operation. Plutonium inventory ratio reaches its ratio from 5-th cycle to 8-th cycle operations. This condition is also obtained by minor actinide (MA) inventory ratio which has an equilibrium ratio from 5th to 8th cycle operation as shown in Figure 2. The trend of both Pu and MA inventory ratios are the same which obtains less ratio at the beginning of cycle than it increases and it reaches an equilibrium condition at the end.

Inventory ratio of Plutonium has relatively higher at the equilibrium cycle in comparing with the ratio at the beginning of cycle (BOC) as shown in Figure 1. In case of inventory ratio of minor actinide (MA), it has relative almost in the same ratio at the equilibrium condition with the BOC as shown in Fig. 2. This fenomena is expected that plutonium production is relatively higher during reactor operation and it increases for longer operation and in the same time, MA inventoris are relatively stable or produce in the same level with the BOC. In transition condition, it can be seen that both plutonium and MA are increasing which shows more actinide productions are obtained and it decreases with operation time and it reaches the equilibrium condition. The existing MA in this evaluation is coming from the fresh fuel of MA which is loaded in the blanket regions. And with increasing operation time or burnup process, MA is also produced during reaction such as in the core region which can contribute to increase the inventory of MA while in the same time some MAs are reducing because of conversion process into another actinide. All reactor operations from the beginning of operation up to the equilibrium of operation or the end of operation shows the inventory ratios of both plutonium and MA are higher than unity. This result shows that actinide production rate in a certain operation periode is higher than the BOC or fresh fuel loading. It can be estimated that plutonium and MA has surplus inventory after reactor operations. In term of sustainability of fuel supply, fuel sustainability can be achieved.

3.2 Actinide Inventory Ratio

Obtained results of some actinides inventory ratios are shown in Figures 3 and 4 based on MOX fuel type for different reactor operation times. Figure 3 shows comparative result of plutonium and MA inventory ratios at BOC and equilibrium condition. It shows plutonium inventory ratio at equilibrium condition is higher than at BOC which means longer operation time produce more inventory of plutonium. In the same time MA inventory ratio at equilibrium condition almost the same with the ratio at BOC. Comparative analysis between inventory ratio of MA and plutonium shows that less inventory ratio is obtained by plutonium at BOC than MA and the opposite trend is shown that inventory ratio of plutonium is obtained higher than MA at equilibrium condition. Figure 4 shows the obtained results for Plutonium and MA plus trasuranium (TRU) composition at the equilibrium condition. Higher TRU inventory mass is obtained in comparison with MA and relatively less ratio than plutonium. This composition can be estimated that by the definition that transuranium or TRU is consist of actinide higher than uranium nuclide and it can be defined as summation of plutonium and MA inventory. This is why the ratio of TRU is in between of ratio of plutonium and MA.
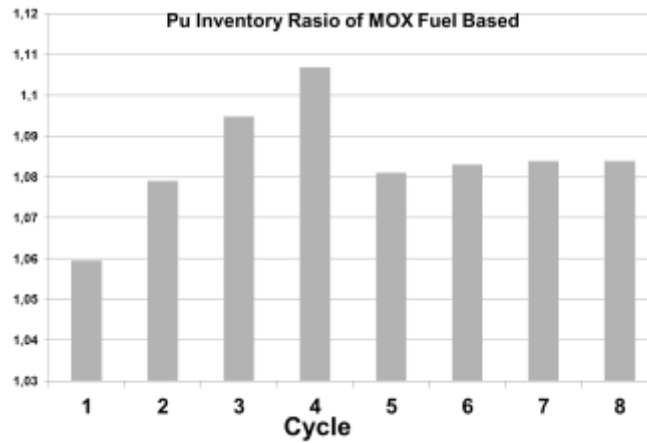
Figure 83: Plutonium Inventory Ratio Based on MOX Fuel of 50 GWd/t SNF LWR
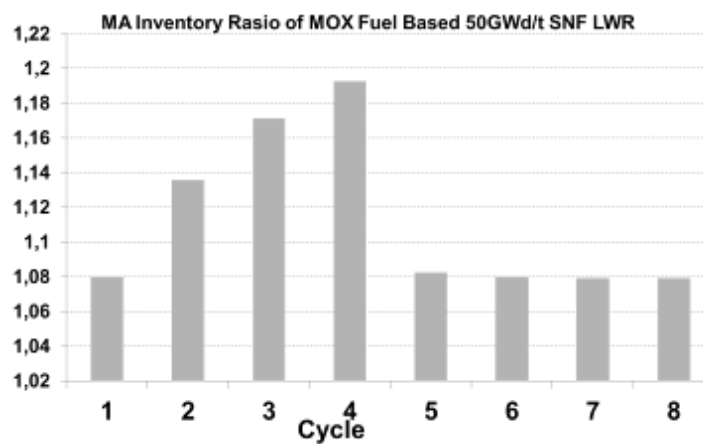

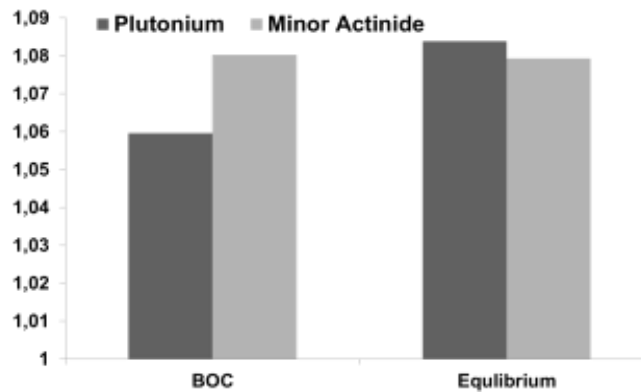Figure 2: Minor Actinide (MA) Inventory Ratio Based on MOX Fuel of 50 GWd/t SNF LWR

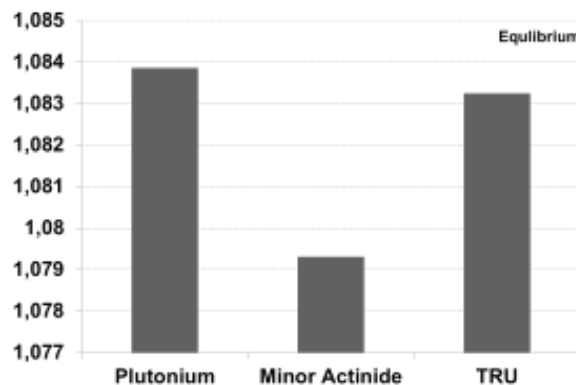Figure 3: Plutonium and Minor Actinide Inventory Ratio at BOC and Equilibrium Cycle

Figure 4: Actinide Inventory Ratio (Pu, MA adn TRU) at Equilibrium Cycle

3.3 Inventory Ratio For Different Fuel Loadings

To evaluate the effect of different fuel loading to the inventory ratio, two different fuel type of MOX and UTRU fuels are compared, and the obtained results are shown in Figure 5 for evaluating plutonium, MA and TRU actinides inventory ratios at equilibrium condition. As mentioned before, inventory ratios of Pu and MA as well as TRU actindes based on MOX fuel composition as fuel loading are obtained higher than unity. However, for UTRU fuel loading type, it shows plutonium and TRU actinide are obtained higher than unity, and inventory ratio of MA is obtained less than unity. Plutonium inventory ratio of UTRU fuel type is achieved higher than MOX fuel loading, however, for MA and TRU inventory ratio of UTRU is less. UTRU fuel type means fuel loading as fresh fuel is consist of uranium and transuranium (TRU) composition which are mixed similar with MOX fuel from uranium and plutonium. TRU composition is based on the composition of plutonium and minor actinide. This UTRU fuel is loaded into the core regions as driver fuel to maintain the reactor in the criticality condition for reactor operation. Some MAs in the core regions are convented into some plutonium isotopes which brings the increase of plutonium inventory. In the same time, more conversion process from MA into plutonium affects to the decresing inventory of minor actinide. This conditin is estimated to produced more plutonium inventory and to reduce the inventory of MA during reactor operation until the equilibrium condition. Less than unity of inventory ratio of MA based on UTRU fuel loading means less actinide production for a certain period of time in comparison with fresh fuel inventory. In case of UTRU fuel loading, fuel sustainability of MA is difficult to be achieved.
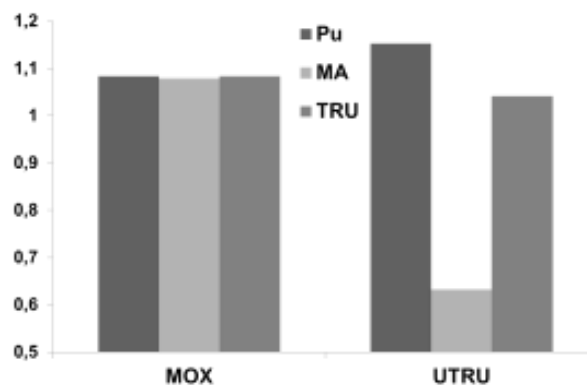
Figure 5: Actinide Inventory Ratio (Pu, MA and TRU) for Different Loaded Fuel Types (MOX and UTRU Fuels)

3.4 Plutonium Production Composition

Plutonium production in the FBR design is interesting to be analyzed not only in term of fuel breeding capability because of more plutonium as good fuel are produce, but also to be considered as control parameter for nuclear non-proliferation aspect based on the material barrier of plutonium. Obtained results of plutonium compositions are shown in Figures 6 and 7 during reactor operation based on MOX fuel loading. Main composition of plutonium isotopes compositions are coming from Pu-239 and Pu-240 as shown in Figure 6 which shows both plutonium isotopes are increasing during reactor operation as well as Pu-241. Pu-238 is slightly deceases and decreasing trend is also obtained by Pu-242. More production of even mass plutonium such as Pu-240 and Pu-238 is effective to increase the proliferation resistance level of plutonium proliferation as well as to reduce the composition of plutonium quality of Pu-239 as good fissile for fuel as well as good candidate for nuclear explosive devices. Comparative composition for all plutonium isotopes also is conducted for fresh fuel condition or BOC (0 day) in comparison with equilibrium condition. Pu-239, Pu-240 and Pu-241 are higher at equilibrium condition than fresh fuel or BOC as shown in Figures 6 and 7, as well as for Pu-238 and Pu-242 are less at equilibrium than BOC. MOX fuel composition is only consist of Pu-238 up to Pu-242 isotopes as plutonium fuel compsotion which is mixed with uranium composition. It requires a conversion process od minor actinide (MA) or other doping material which produces more even mass of plutonium production as a barrier material to reduce odd mass plutonium as plutonium quality of fissile materials (Saito, 2002; Meiliza et al, 2008; Permana, 20011a, 2011b, 2009a, 2009b).
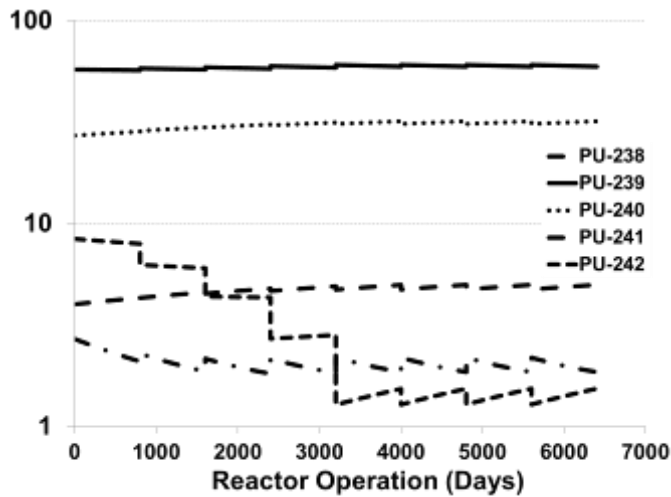
Figure 6: Plutonium Isotopes Compositions Trend During Reactor Operation of MOX Fuel Type
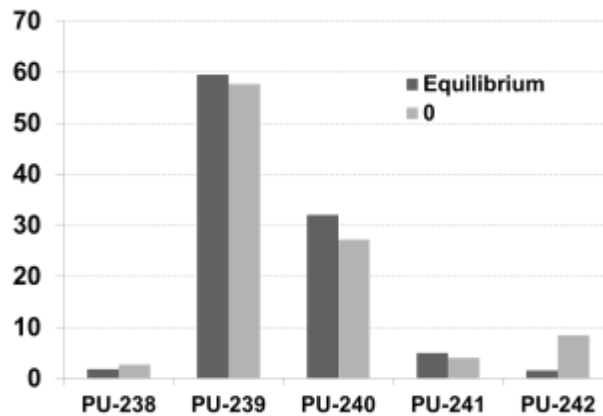
Figure 7: Plutonium Isotopes Compositions at Inner Core at BOC and Equilibrium Cycle of MOX Fuel Type

3.5 Reactor Criticality

In order to evaluate the reactor performance of criticality condition and some effects of different fuel compositios to the reactor critical condition are conducted. Obtained result of criticality condition is shown in Figure 8 and 9 based on different fuel loading and during reactor operation. Figure 8 shows reactor criticality condition during reacor operation from the BOC up to the equilibrium condition. Equilibrium condition for criticality can be achieved from 5-th cycle up to 8-th cycle which can be shown in the figure as a function of reactor operation day which uses 800 days as cycle length. Comparative criticality condition from diffferent fuel loading are obtained in figure 9 at BOC, middle of cycle (MOC) and EOC at equilibrium condition. Both fuel loadings are showing the same trends that longer operation from BOC to MOC up to EOC achieved less critilicaty condition. To achived same reactor condition and smae cycle length, TRU fuel loading is obtained less criticality at BOC and MOC than MOX fuel loading and obtained almost the same criticality condition at equilibrium condition. Less criticality condition for the same cycle operation at the BOC and MOC can be estimated to have less excess reactivity level which means safer in term of criticality condition. UTRU fuel loading which shows less excess reactivity than MOX fuel can be obtained because of some existing minor actinide in UTRU fuel are capturing neutrons to reduce the excess reactivity, however, in the same time they produce more plutonium to compensate the loss of plutonium as fissile material for maintaining reactor criticality. About 8 % excess reactivity from MOX fuel loading can be reduce into 2 % by UTRU fuel loading which means effective to reduce about 6% excess neutron by additional minor actinide in the reactor core. Less excess reactivity is one of the parameters for evaluation of the reactor that shows the sistem is safer for criticality operation, especially for initial stage of operation.
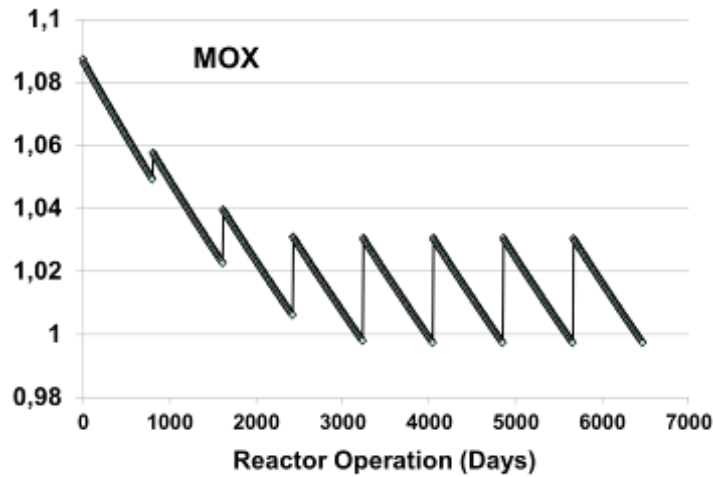
Figure 8 : Criticality Condition of MOX Fuel Type During Reactor Operation
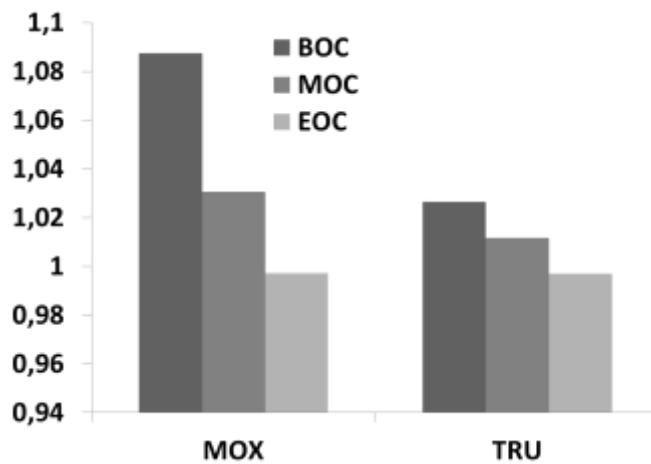
Figure 9 : Criticality Condition of Different Fuel Loading During Reactor Operation

4. CONCLUSION

In the present study, fuel sustainability aspect of nuclear fuel based on recycled spent nuclear fuel in the fast breeder reactor (FBR) has been evaluated for different fuel loading types of mixed oxide (MOX) and uranium-transuranium mixed (UTRU) fuel types. Some inventory ratio analyses based on several important actinides during reactor operation and equilibirum composition have been compared as well as plutonium composition in the core and reactor criticality to evaluate the excess reactivity of the reactor. Loading fuels in the FBR cycle are based on spent nuclear fuel composition of ligh water reactor (LWR). Inventory ratio of Plutonium has a relatively higher at the equilibirum cycle in comparing with the ratio at the beginning of cycle (BOC) and it's ratio of minor actinide (MA), obtains relatively same ratio at the equilibirum condition with the BOC. Inventory ratios of both plutonium and MA in all conditions are higher than unity. In term of sustainability of fuel supply, it can be estimated that plutonium and MA production in the reactor shows its fuel sustainability profile. Plutonium inventory ratio obtains less at BOC than MA, however it becomes higher at equilibirum condition.

Inventory ratios of Pu, MA and TRU actindes for different fuels of MOX fuel and UTRU fuel compositions are obtained higher than unity, however, in case of inventory ratio of MA for UTRU fuel loading is obtained less than unity. Higher inventory ratio of plutonium is achieved higher for UTRU fuel than MOX fuel, however, its less inventory ratio for MA and TRU. In case of UTRU fuel loading, fuel sustainability of MA is difficult to be achieved. Plutonium production in the FBR design is interesting to be analyzed not only in term of fuel breeding capability because of more plutonium as good fuel are produced, but also to be considered as control parameter for nuclear non-proliferation aspect based on the material barrier of plutonium. Main composition of plutonium isotope compositions are coming from Pu-239 and Pu-240 which are increasing during reactor operation as well as Pu-241. Pu-238 is slightly decreasing as well as a decreasing trend is also obtained by Pu-242. More production of even mass plutonium such as Pu-240 and Pu-238 is required from converted minor actinide to increase the proliferation resistance level of plutonium proliferation as well as to reduce

the composition of plutonium quality of fissile materials. UTRU fuel loading obtains less excess reactivity than MOX fuel for about 8 % excess reactivity from MOX fuel loading can be reduce into 2 % by UTRU fuel loading which means less excess reactivity is safer for criticality operation, especially for the initial stage of operation.

5. ACKNOWLEDGMENTS

6. REFERENCES

CHIBA. G et al., 2002, The Revision of Nuclear Constant Set for Fast Reactor JFS-3-J3.2," J. At. Energy Soc. Jpn., 14, 335.

CHOI. H and Downar. T.J., 1999, A Liquid-Metal Reactor for Burning Minor Actinides of Spent Light Water Reactor Fuel—I: Neutronics Design Study , Nucl. Eng. Des., 133, 1–22.

FOWLER. T. B, Vondy. D. R, and Cunningham. G. W, 1971, Nuclear Reactor Core Analysis Code: CITATION, Oak Ridge National Laboratory report, ORNL-TM-2496, Rev2, USA

HOFFMAN. E.A and and Stacey. W. M, 2003, Comparative Fuel Cycle Analysis of Critical and Subcritical Fast Reactor Transmutation Systems", Nucl. Technol., 144, 83.

LUDWIG. S. B. and Croff. A. G, 2002, Origen 2.2 Isotope Generation and Depletion Code Matrix Exponential Method, Oak Ridge National Laboratory.

MEILIZA, Y, Saito, M and Sagara, H, 2008, Protected Plutonium Breeding by Transmutation of Minor Actinides in Fast Breeder Reactor, J. Nucl. Sci. Technol., Vol. 45[3], 230.

NAKAGAWA. M and Tsuchihashi. K, 1984, SLAROM: A Code for Cell Homogenizations Calculation of Fast Reactor, JAERI 1294, Japan Atomic Energy Research Institute.

NAKAGAWA. T. et al., 1995, Japanese Evaluated Nuclear Data Library Version 3 Revision-2: JENDL-3.22, J. Nucl. Sci. Technol., 32, 1259.

OHKI. S, et al., 2008, Design Study of Minor Actinide Bearing Oxide Fuel Core for Homogeneous TRU Recycling Fast Reactor System, The 10th OECD/NEA P&T Meeting, Mito, Japan, October 6-10.

PERMANA, S, Suzuki, M and Saito, M, 2011, Effect of TRU Fuel Loading on Core Performance and Plutonium Production of FBR, Nucl. Eng. Des., 241, 101–117.

PERMANA, S, Suzuki, M and Saito, M, 2001, Basic Analysis on Isotopic Barrier of Material Attractiveness Based on Plutonium Composition of FBR, J. Nucl. Sci. Technol., 48[5], 724-733.

PERMANA. S and Suud. Z, 2009, Core Performance and Plutonium Production of Small Long Life Fast Reactor using Doping Actinides, Proc. of ICAPP, , Tokyo-Japan, May 10-14, 2009.

PERMANA. S, Suud. Z and Suzuki. M, 2009, Trans-uranium doping utilization for increasing protected plutonium proliferation of small long life reactor, Proc. of Global, Paris, France, September 6-11, 2009,.

SAITO, M, 2002, Multi-Component Self-Consistent Nuclear Energy System for Sustainable Growth, Prog. in Nucl. Energy, 40[3-4], 365.

TAIWO. T. A, et al., 2006, Assessment of a Heterogeneous PWR Assembly for Plutonium and Minor Actinide Recycle, Nucl. Technol., 155, 34.

SESSION 32: HEAT PUMPS

143: An irreversibility analysis of the air to air heat pump

SABAN TAMDEMIR[1], ALI KILICARSLAN[2,3]

1 "Ministry of Environment and Urban Planning", Ankara-TURKEY, s-tamdemir@hotmail.com
2 "Hitit University-Department of Mechanical Engineering", 19030 Corum-TURKEY,
alikilicarslan@gmail.com   3Corresponding Author, Telephone: +90(364) 2274533/1236, Fax: +90 (364)
2274535,

Abstract: Second law analysis of thermal systems is very important because it enables us to determine the irreversibilities and entropy generation occurring in the elements of those systems and it also enables us to determine the exergetic efficiencies of the components of thermal systems.

In this experimental study, the air to air heat pump in which R134a is used as refrigerant, that was installed to a room having dimensions of 6000x4000x3800 mm, was tested between the outdoor temperatures of -2.5°C and 4.5°C. The irreversibilities of the compressor, indoor unit, outdoor unit and capillary tube were investigated with respect to the experimental data. Experiments at the same outdoor temperatures were repeated three times under the controlled conditions. Analyses of the results obtained from the experiments were carried out by the computer code that was developed by means of Engineering Equation Solver (EES-V9.723-3D). The irreversibilities of the elements including compressor, indoor and outdoor units and capillary tube increased as the outdoor temperature was increased. The maximum amount of irreversibilities occurred in the compressor while the minimum occurred in the indoor unit.

Keywords: Air to air heat pump; heating; second law; irreversibility; R134

1. INTRODUCTION

The energy applications including heating, refrigerating and air conditioning are the areas in which heat pumps are used. Heat pumps differ from each other in terms of the source that they used (air, water, soil, etc.) and the heat that they conduct (Ceylan, 2010). Air source heat pumps are employed with the applications of different heating systems such as a floor heating system, radiator heating system for homes, etc. and provide an optimum comfort conditions, and the hot water needs are met throughout the year. In addition to the ease of installation, they also don't require a high-cost drilling. They are used in the limited areas because of having a small outdoor unit (Özyİrmidokuz, 2010)**.**

The analysis of heat pump systems in terms of energy is not enough itself. The second law analysis of these systems should also taken into consideration. There are some studies including exergy and irreversibility analyses in the literature.

An experimental air source heat pump study, R410A employed as a refrigerant, was carried out for heating and cooling conditions in North America climatic conditions. It was observed that the second law efficiency is 45 % at an outdoor temperature of -30°C (Bertsch, 2008). Four different types of heat pumps, employing R22 as refrigerant, including air to air, air to water, water to water and water to air were experimentally investigated. Performances, exergy efficiencies and irreversibilities of these heat pumps were compared with each other in terms of heat source temperature and fluid mass flow rate. It was observed that the minimum irreversibilities were obtained by employing "the water to water heat pump" while the maximum ones were obtained with "the air to air heat pump" (Çakır, 2013).

Energetic and exergetic comparison of the ground source heat pump with the air source heat pumps were carried out with resepect to the evaporator and condenser temperatures. It was seen that the ground source heat pump with a condenser temperature of 30 °C is better than air source heat pump (Lohani, 2010). Exergy analysis of multi-purpose heat pump system was carried out. The exergy loss ratios of the components of heat pump including   compressor, condenser, throttling valve and evaporator were determined as a function of water temperatures and compared to that of the conventional air conditioning system (Sun, 2013).

The purpose of this experimental study is to investigate the effect of different outdoor temperatures on the irreversibilities of the components of "the air to air heat pump system" (using R134A as a refrigerant), namely, compressor, indoor unit, outdoor unit and capillary tube.

2. EXPERIMENTAL WORK

Experimental work was carried out at one of the energy labs of Department of Mechanical Engineering of Hitit University, having dimensions of 6000x4000x3800 mm. Air to air heat pump (ASHP) primarily includes the outdoor and indoor units, capillary type capillary tube and reverse valve. The indoor unit includes a forced evaporator which is shown in Figure 1.

Figure 1. Indoor unit of air to air heat pump

Figure 1 also shows that the energy analyzer, electrical control box, data logger and manometers and thermocouples. As it is shown in Figure 2, the outdoor unit consists of a semi hermetic compressor and forced air cooled condenser. Furthermore, Figure 2 depicts the reverse valve, high and low pressure switch, thermocouple and manometer connections. Experiments were performed between the dates of November 2012 and April 2013 at the outdoor temperature ranging from -2.5 °C and 4.5 °C. After the steady-state conditions were reached, three temperature and presssure measurements were obtained for every state points and the average values of these measurements were used in the calculations.

Figure 2. Outdoor unit of air to air heat pump

Air to air heat pump is shown schematically in Figure 3. Refrigerant enters into the compresssor at a low pressure and temperature at state 1 and its pressure and temperature are increased during the compression process at state 2. Inorder to start the heating cycle of the heat pump, the refrigerant is directed to the indooor unit by the reverse valve. At states 3 and 4, refrigerant flows through the indoor unit. During this process, it rejects heat to the room to be heated and then, it flows throughout the capillary tube and its pressure and temperature are reduced to the conditions of the outdoor unit where the refrigerant absorbs heat from the environment. Finally, it comes to the compressor inlet again and the heating cycle is completed.
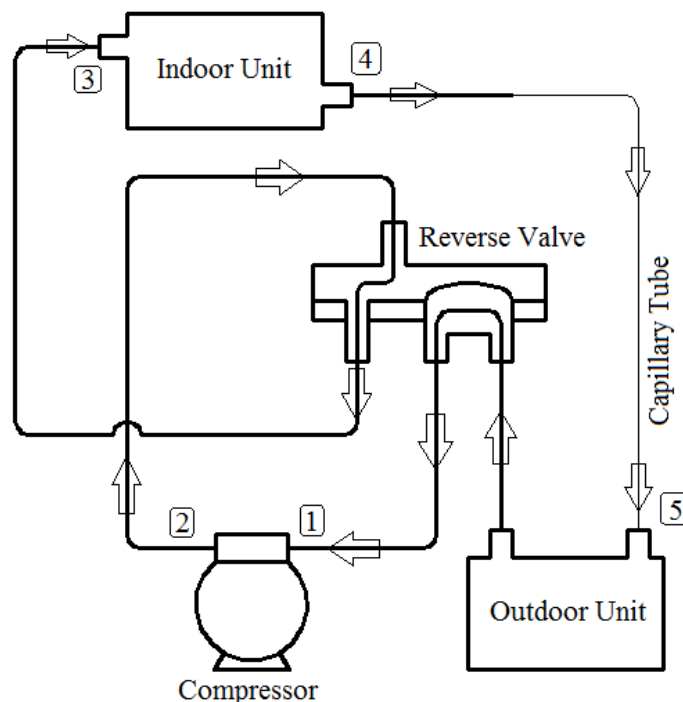
Figure 3. Schematic of air to air heat pump for heating mode

The entropy balance for a control volume can be written as (Borgnakke, 2009),

$$\frac{dS_{cv}}{dt} = \sum \dot{m}_i \, s_i - \sum \dot{m}_i \, s_i + \sum \frac{\dot{Q}_j}{T_j} + \dot{S}_{gen} \qquad (1)$$

where $\dot{S}_{gen}$, $S_{c.v}$, $\dot{Q}_j$ and T_j are the total entropy generated per unit time, the entropy within the boundary of the control volume, the heat transfer rate and absolute temperature at the surrounding boundary, respectively while s is specific entropy of the fluid at the inlet or outlet conditions. According to the Gouy Stodola Theorem, irreversibility rate, $\dot{I}$, can be expresses as (Bejan, 1996)

$$\dot{I} = T_o \, \dot{S}_{gen} \qquad (2)$$

The following assumptions are taken into consideration for the thermodynamic analysis of the air to air heat pump.

- Pressure loss through the elements of the heat pump can be negligible.
- It is presumed that steady-state and uniform flow conditions exist thorough the elements of the heat pump cycle.
- The changes in kinetic and potential energies are negligible.
- The heat loss from the compressor and capillary tube are also negligible.
- The electrical power consumed by the compressor is assumed to be transmitted directly to the refrigerant.

As the above mentioned assumptions are applied to the compressor. The irreversibility rate of the compressor can be expressed as

$$\dot{I}_{comp} = T_0 \, \dot{m}_r \, (s_2 - s_1) \qquad (3)$$

where $\dot{I}_{comp}$ is the irreversibility rate of the compressor, T_0 is the environment temperature, $\dot{m}_r$ is the mass flow rate of refrigerant through the heat pump cycle, s_1 and s_2 are the specific entropies at the compressor inlet and exit, respectively.

In a similar way, if we apply the assumptions to the outdoor unit of the heat pump, one can gets the irreversibility rate for the outdoor unit,

$$\dot{I}_{ou} = T_0 \, \dot{m}_r \left[(s_1 - s_5) - \frac{(h_1 - h_5)}{T_0} \right] \qquad (4)$$

where $\dot{I}_{ou}$ is the irreversibility rate of the outdoor unit, s_5 is the specific entropy at the outdoor unit inlet, h_5 and h_1 are enthalpies at the outdoor unit inlet and outlet, respectively.

The irreversibility rate for the capillary tube can be expressed as

$$\dot{I}_{ct} = T_0 \, \dot{m}_r \, (s_5 - s_4) \qquad (5)$$

where $\dot{I}_{ct}$ is the irreversibility rate for capillary tube. Irreversibility rate of the indoor unit can be written as

$$\dot{I}_{iu} = T_0 \, \dot{m}_r \left[(s_4 - s_3) - \frac{(h_4 - h_3)}{T_{ro}} \right] \qquad (6)$$

where $\dot{I}_{iu}$ is the irreversibility rate of the indoor unit, T_{ro} is the room temperature, s_3 is the specific entropy at the indoor unit inlet, h_3 and h_4 are specific enthalpies at the outdoor unit inlet and outlet, respectively.

3. RESULTS AND DISCUSSION

Experiments with the air to air heat pump are performed between the outdoor temperatures between -2.5 °C and 4.5 °C by using R134a as refrigerant. The experimental results are analyzed by a computer code developed using Engineering Equation Solver (EES-V9.172-3D) (Klein, 2010). Irreversibilities of the indoor and outdoor unit, irreversibility of the compressor, irreversibility of the capillary tube and total irreversibility are determined. The variations of these parameters with respect to the outdoor air temperatures are investigated.
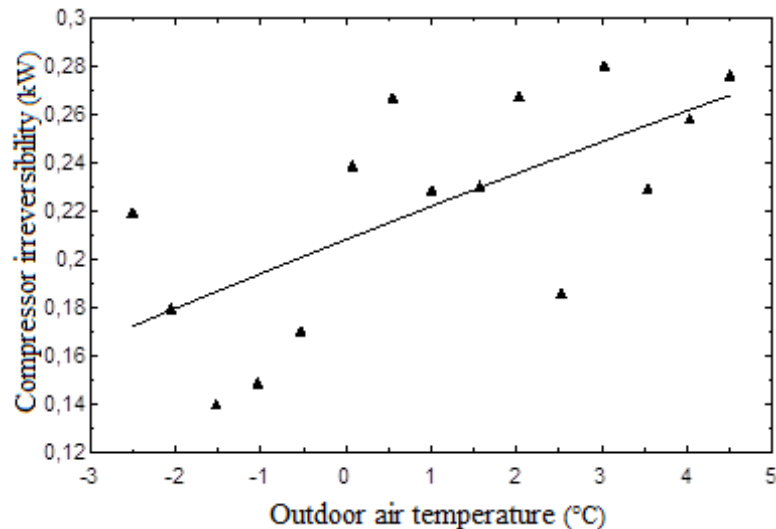
Figure 4. *Compressor irreversibility versus outdoor air temperature*

Figure 4 depicts the irreversibility of the compressor with the outdoor temperature. During the compression process, main sources of irreversibility are fluid friction and nonquasi equilibrium compression. As the outdoor temperature increases, the irreversibility of the compressor increases. At the increasing values of the outdoor air temperatures between -2.5 °C and 4.5 °C, the irreversibility of the compressor changes from 0.17 to 0.27 kW. The percent increase in the irreversibility of the compressor is 58 %. The irreversibility of the compressor increases 0.014 kW per 1 °C temperature difference.
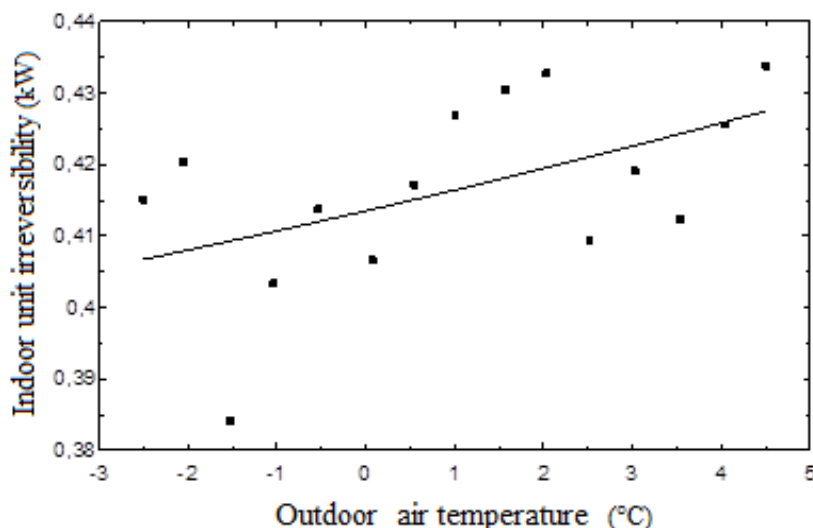
Figure 5. *The irreversibility of the indoor unit versus outdoor air temperature*

Figure 5 depicts the irreversibility of the indoor unit with the outdoor temperature. Irreversibility rate in the indoor unit is mainly caused by the heat transfer between the indoor unit and the room to be heated at a finite temperature difference. As the outdoor air temperature increases, the irreversibility of the indoor unit increases on average. As the outdoor air temperatures ranges from -2.5 °C and 4.5 °C, the irreversibility of the indoor unit varies from 0.405 to 0.430 kW. the irreversibility of the indoor unit has a minimum value of

0.405 kW at the outdoor temperature of -2.5 °C. As it is shown in Figure 5, the irreversibility of the indoor unit of the air to air heat pump approximately increases by 6.17 %.
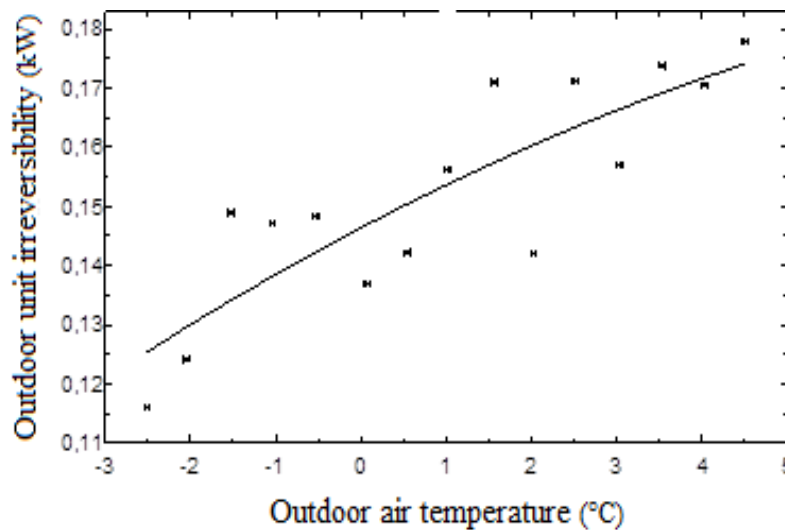
Figure 6. The irreversibility of the outdoor unit versus outdoor air temperature

The irreversibility of the outdoor unit with respect to the outdoor air temperature is shown in Figure 6. The heat transfer at a finite temperature difference between the outdoor unit and environment causes the irreversibility in the outdoor unit. As the outdoor temperature increases, the irreversibility of the outdoor unit increases. As the outdoor air temperatures changes from -2.5 °C and 4.5 °C, the irreversibility of the outdoor unit increases from 0.125 to 0.175 kW. Figure 6 also shows that the increase in the outdoor unit irreversibility is 40 % on average.
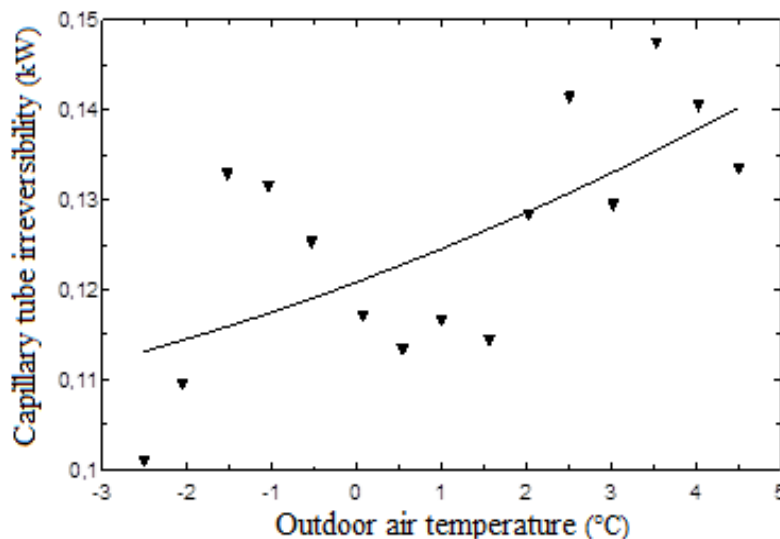
Figure 7. The irreversibility of the capillary tube versus outdoor air temperature

Figure 7 depicts the irreversibility of the capillary tube with respect to the outdoor temperature. Main source of the irreversibility during expansion process is the sudden expansion of refrigerant. The loss in specific refrigeration capacity also increases the irreversibility of the refrigerant in the capillary tube. As the outdoor temperature increases, the irreversibility of capillary tube the increases on average. As the outdoor air temperatures ranges from -2.5 °C and 4.5 °C, the irreversibility of the indoor unit varies from 0.112 to 0.140 kW. As it is compared to the irrreversibilities of the other elements of the air to air heat pump, the second highest irreversibility occur in the capillary tube. The irreversibility of the capillary tube of the air to air heat pump approximately increases by 25 %.
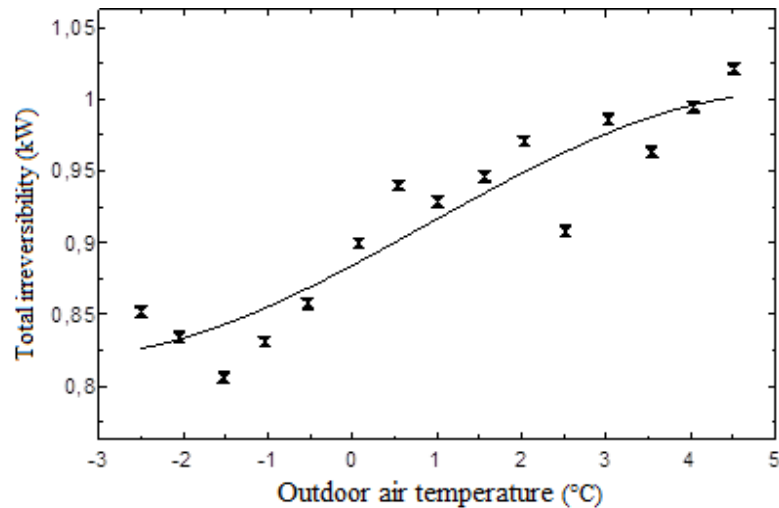
Figure 8. *The total irreversibility of the air to air heat pump versus outdoor air temperature*

The variation of the total irreversibility of the air to air heat pump as a function of outdoor air temperature is depicted in Figure 8. It is clear from the above discussion that the irreversibilities of the elements of the air to air pump increase. As a result of this, the total irreversibility of the air to air heat pump increases as the outdoor air temperature increases. At the increasing values of the outdoor air temperatures between -2.5 °C and 4.5 °C, the the total irreversibility changes from 0.82 to 1 kW. The percent increase in the irreversibility of the compressor is 22 %.

4. CONCLUSIONS

The air to air heat pump in which R134A is used as refrigerant was tested at the outdoor temperatures ranging from -2.5 °C and 5 °C. The main conclusions related to the irreversibilities of the elements of the heat pump are as follows;

- the irreversibilities of the elements including the compressor, indoor unit, outdoor unit and capillary tube increase as the outdoor air temperature increases,
- the minimum irreversibility values occur in the capillary tube while the maximum values occur in the indoor unit,
- the minimum irreversibility increase in the temperature range considered in this study happens in the indoor unit by 6.17 % while the maximum happens in the compressor by 58 %,
- the total irreversibility of the air to air heat pump varies from 0.82 to 1 kW and it increases by 22 % at the outdoor temperatures between -2.5 °C and 5 °C.

5. ACKNOWLEDGMENT

6. REFERENCES

BEJAN A., 1996, Entropy Generation Minimization, CRC Press.

BERTSCH, S.S., Groll, E.A., 2008, Two-stage air-source heat pump for residential heating and cooling applications in northern U.S. climates, International Journal of Refrigeration, (31), 1282 – 1292.

BORGNAKKE C., Sonntag R.E., 2009, Fundamentals of Thermodynamics, seventh ed. Wiley.

CEYLAN, T., 2010, Analysis of heating system of a two floor building with a solar energy assisted air source heat pump and hot water system. M.Sc. Thesis, Gazi University, Graduate School of Natural and Applied Sciences.

ÇAKIR U., Çomaklı K., Çomaklı Ö., Karslı S., 2013, An experimental exergetic comparison of four different heat pump systems working at same conditions: As air to air, air to water, water to water and water to air, Energy, 58, 210-219.

KLEIN, S.A., 2010, Engineering Equation Solver (EES), Professional version V9.723-3D,F-Chart Software.

LOHANI S.P., Schmidt., D, 2010, Comparison of energy and exergy analysis of fossil plant, ground and air source heat pump building heating system, Renewable Energy, 35, 1275–1282.

ÖZYIRMIDOKUZ, M.H., 2010, Exergy Analysis of an Air Source Heat Pump, M.Sc. Thesis, Erciyes University, Graduate School of Natural and Applied Sciences.

SUN X., , J Wu J., Wang R, 2013, Exergy analysis and comparison of multi-functional heat pump and conventional heat pump systems, Energy Conversion and Management, 73, 51-56.

393: Study on performance of multiple air source heat pump system for heating in China

Weili Luo[1,2], Yunkang Sun[1], Yuxiong Xu[1], Ruzhu Wang[1]

[1]*Shanghai Jiao Tong University, Institution of Refrigeraiton and Cryogenics, 800 Dongchuan RD. Minhang District, Shanghai, China, luoweili@sjtu.edu.cn*
[2] *Solar Power and Refrigeration Engineering Research Center, MOE, 800 Dongchuan RD. Minhang District, Shanghai, China*

This paper reports a novel application of an air source heat pump system for cooling, heating and domestic hot water production in Shanghai for a typical apartment. The appliance can supply five functions as space cooling, space cooling plus domestic hot water, space heating, space heating plus domestic hot water, and domestic hot water only. In winter, the system was aim to solve the central heating problem in the area of Yangtze river basin and the operating performance under specified weather conditions. The system was combined with a Low-H2O heat exchanger to decrease the supply water temperature for saving the energy. The heating return water temperature was set at 30oC, 35 oC and 40 oC for heating in winter which lower than the conventional air source heat pump system. When the inlet temperature was set at 30oC, 35oC and 40oC, the power consumption was 27.18kWh, 39.84 kWh, 51.48 kWh, respectively. The power consumption of the system increased 89.2% at the inlet temperature of 40oC and 46.6% at the inlet temperature of 35oC compared with the one at the condition of the inlet temperature of 30oC. When inlet temperature increased from 30oC to 40oC, the COP of the air source heat pump decreased from 3.50 to 2.22 with the percentage of 36.5% at the conditions of the outdoor temperature of 6-7oC. The indoor temperature of the apartment was at the range of 19.4 to 20.9oC with the conditions of the inlet temperature of 30oC and the average temperature 5.1oC.

Keyword: Air source heat pump, energy efficiency, temperature distribution, COP

1. INTRODUCTION

China is a large country with a complex climate. In national standard for China (GB50176-93) (MINISTRY, 1993), it divided into five climate zones as severe cold (SC), cold (C), hot summer and cold winter (HSCW), hot summer and warm winter (HSWW),and temperate (T) zones. For severe cold (SC) and cold (C) zones, they have central heating system. For hot summer and cold winter zones (HSCW), it includes 14 provinces and nearly half of the population of China is living in these places. Furthermore, it didn't have central heating system. It used the individual heating system as air source heat pump air conditioning, floor heating system, electrical heater etc. For an air source heat pump (ASHP) unit, the supplying hot water is about 45oC, so the COP is low as a result of the condensation temperature is very high. And when the surface temperature of the outdoor heat exchanger is lower than both freezing point of water and the air dew point, frost is formed and it badly affects the energy efficiency (Gong, 2013. Ge, 2011. Li, 2012. Liu, 2013. Song, 2015. Vocale, 2014. Wang 2015. Zhu 2015). In the hot summer and cold winter zones (HSCW), an air source heat pump's running time in winter was significantly lower than one in summer because it consumed a lot of electrical energy (Yin, 2013). The machine is at the intermittent operation so it decreased the indoor comfort level. Floor radiant heating system has the advantages of thermal stability, temperature uniformity, no occupied area and big heat capacity, etc. So it was used in South China. But it also has disadvantages. One is that it can supply the heating, but it is not suitable for cooling. Two systems including floor heating and another cooling system are needed for a family. It results in initial cost was big and system was complicated. The other problem was that the system was expensive compared with other heating system such as air source heat pump air conditioning. So a novel air source heat pump cold (hot) water system was conducted in one apartment with 100 m2 residences in Shanghai-a typical city in hot summer and cold winter zones (HSCW). The system can supply heating, cooling as well as domestic hot water in all one. Therefore, we just need one system instead of various equipments for civil family. And as a result of combining of the Low-H2O heat exchangers (Wang, 2014), it can work at the conditions of lower than 0°C with the high efficiency and low electrical consumption because of the supplying hot water temperature is at about 35°C for heating.

2. PROTOTYPE DESCRIPTION

2.1 Low-H2O Heat Exchanger Description

The lowest average outdoor temperature is about 1-2°C for Shanghai. When the outlet hot water temperature is at the range of 45 to 50°C, the air source heat pump maybe can't work properly or run at the condition of a frequent defrosting which will lead to the extremely low efficiency. So it is a good choice to decrease the outlet temperature of the system to solve the running problem or increase the COP of the system. Because of the decreasing outlet temperature, the difference between the hot water and indoor space temperature is also decreased. We named it Low-H_2O heat exchanger that can satisfy the heating capacity with the smaller difference temperature.

2.2 System Description

A prototype was installed in one apartment about 92m^2 in Shanghai Jiao Tong University to study the performance. The room included two bed rooms, one sitting room and a dining room. The schematic of the heat pump system was shown in Figure1. The system can be divided into two parts. The first part for domestic hot water includes four elements: a compressor, a fan-coil heat exchanger, an expansion valve, a double-pipe heat exchanger. A water pump and a water tank are used for circulating domestic hot water in the pipes, as shown in Figure1. The second part consists of a compressor, an outdoor fan-coil heat exchanger with a fan, an indoor plate heat exchanger and expansive valve. The water inlet and outlet temperatures were measured with T-type thermocouples. An ultrasonic flow meter was used to measure the hot water flow rate. A digital power meter was used to measure the overall power consumptions including the compressor, the water pumps and the fans. There are four heat exchangers were placed in bed rooms, sitting room and dining room, respectively. The indoor temperature is controlled by indoor temperature controller and seven temperature and humidity loggers were used to collect the data at the different places of the apartment.
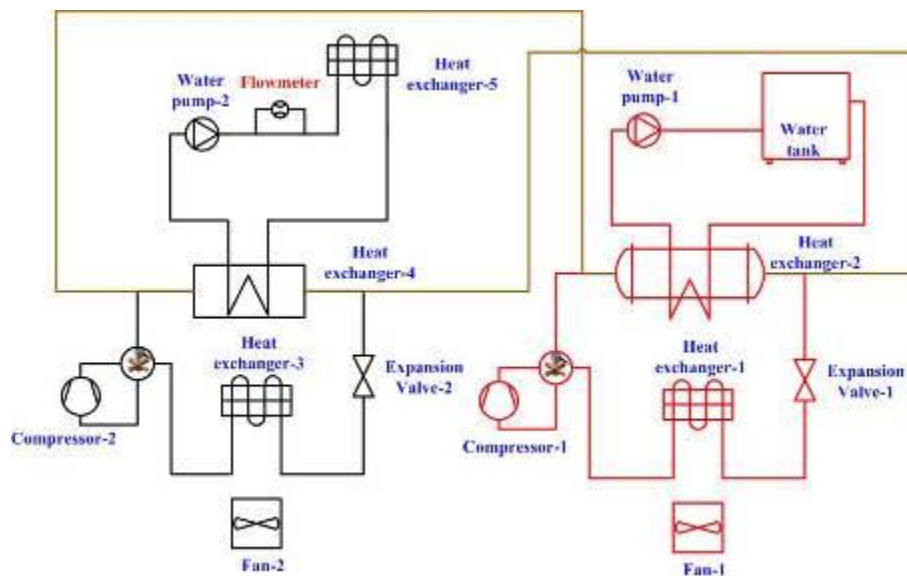
Figure 1: Schematic of the prototype

The appliance can supply five functions as space cooling, space cooling plus domestic hot water, space heating, space heating plus domestic hot water, and domestic hot water only. In our work, the research focused on the performance in heating mode for solving the heating problem in South China.

For domestic hot water only, the water flowed into the double-pipe heat exchanger for heating, and the water tank was used for hot water storage.

For heating mode only, the system was a traditional system except that the terminals were Low-H_2O heat exchanger as shown in the Figure1 as heat exchanger 4.

For heating mode plus domestic hot water, the system included a compressor, an outdoor heat exchanger, an expansion valve, a double-pipe heat exchanger (also called heat exchanger 2 in Figure1) and a plate heat exchanger (named as heat exchanger 4 in Figure1). So, in this mode, three heat exchangers were needed. One was used as an evaporator, and the other two were used as condensers for heating and domestic hot water independently. At some extremely conditions of the heating load was too big to use only one compressor, the other compressor can used for heating space when it didn't working for hot water.

For cooling mode, the system was consisted of a compressor, an outdoor heat exchanger, an expansion valve, a plate heat exchanger.

For cooling mode plus domestic hot water, two compressors were needed. One was used for cooling and another was used for heating the hot water. When the hot water temperature was reached by using this system, just only one compressor was need for cooling. At some extremely conditions of the cooling load was too big to use only one compressor, the other compressor can used for cooling when it didn't working for hot water.

3. EXPERIMENT RESULTS AND DISCUSSION

3.1 Heating capacity

Figure2 showed that the power, heat capacity and power capacity change curves of the novel system with 1hour and 24hours at the different inlet temperature. It was observed the air source heat pump was at the intermittent opening condition when the inlet temperature was at 30°C and 35°C, but it was always running when the inlet temperature was set at 40°C. From the Figure 2(a) and Figure 2(b), it showed that the working time was longer at the inlet temperature of 30°C than one at inlet temperature of 35°C. Accordingly, the stop time was shorter at the inlet temperature of 30°C than one at inlet temperature of 35°C. It illustrated that the heat capacity of the air source heat pump was too big for inlet temperature of 30°C and 35°C and heat capacity was just right for inlet temperature of 40°C. The highest power of the air source heat pump was about 1.8kW, 2.1kW and 2.3kW, respectively. And the highest power of the system was about 2.1kW,

2.4kW and 2.6kW, respectively. It was increased with the inlet temperature. The highest power of the system was 313W which was caused by the water pump. The heating capacity for space heating increased as the hot water temperature increased. It was because when the inlet water temperature was at 30°C, the temperature difference between the indoor temperature and the inlet water temperature was small. When the inlet water temperature water temperature increased to 35°C or 40°C, the temperature difference was become bigger. The heating capacity for space heating increased. The difference between the heating capacities at different inlet temperature was big because of higher indoor temperature and heat losses of the water pipes.

(a)

(b)

(c)

Figure 2: The power, heat capacity and power capacity change curves of the system with 1hour and 24hours (a) 30°C, (b) 35°C, (c) 40°C

3.2 Power Consumption

In this experiment, we studied the influence of the inlet temperature on the indoor temperature and power consumption. We set the inlet temperature at 30°C, 35 °C and 40 °C to calculate the power consumption and collect the indoor temperature change. The experiments lasted at least for 2 days at every inlet temperature. And the data of the system's power consumption which shown in Figure3 was collected from the 00:00 to 23:59 in January from Shanghai. The power consumption was 27.18kWh, 39.84 kWh, 51.48 kWh, respectively. The power consumption of the system increased 89.2% at the inlet temperature of 40°C and 46.6% at the inlet temperature of 35°C compared with the one at the condition of the inlet temperature of 30°C. From the Figure3, it indicated that the power consumption increased a lot when the inlet temperature increased. In addition, according to the policy from the state grid Shanghai municipal electric power company, the electrical prize at the 22:00-06:00 is 0.28RMB/kWh, but the prize is 0.56RMB/kWh at the other time. Table 1 showed the total money per one day for the air conditioning at the different inlet

temperature. So it was feasible to use low-temperature supply water air source heat pump for saving energy and money. When the inlet temperature was 30°C, the night time's temperature was 3.5 °C, and the day time's temperature was 5.9°C. Accordingly, the power consumption was 38% (8h) and 62% (16h) due to the difference temperature of night time and day time.
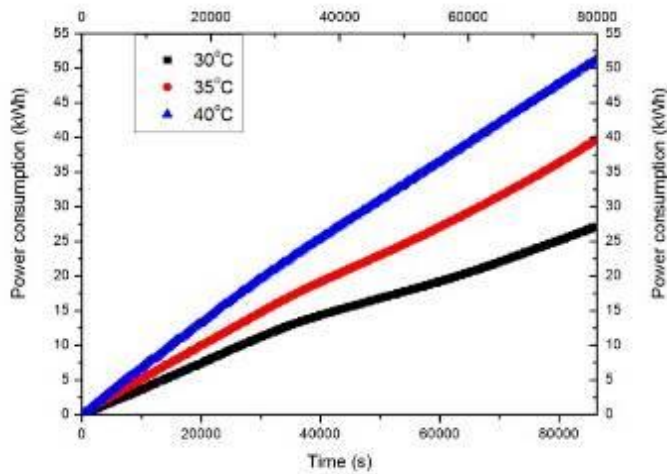
Figure 3: Power consumption of the system for a whole day in January from Shanghai

Table 1: The total money per one day for the air conditioning at the different inlet temperature

Inlet Temperature (°C)	Total Consumption (kWh)	Power Consumption 22:00-06:00 (kWh)	Power Consumption 06:00-22:00(kWh)	Money (RMB/Day)
30	27.18	10.33	16.85	12.3
35	39.84	14.51	25.33	18.2
40	51.48	18.39	33.09	23.7

3.3 Indoor Temperature

In the experiment, we always set the temperature at 20°C using the temperature controller. The accuracy for the temperature controller was 1°C. The sitting room and the bed room south were faced to south and the other rooms were faced north. Table 2 illustrated the indoor temperature of the apartment with the conditions of the inlet temperature of 30°C and the average temperature 5.1 °C. It was observed that the average temperature was at the range of 19.4 to 20.9 °C. The bed room south's temperature was higher than others because of the solar radiation. From the Figure4, it was the typical indoor temperature change of the apartment.

Table 2: The indoor temperature of the apartment at the inlet temperature of 30°C

Location	Average Temperature (oC)	Lowest Temperature (oC)	Highest Temperature (oC)
Sitting Room	19.4	18.1	21.1
Dining Room	19.4	18.4	20.7
Kitchen	19.2	18.5	20.1
Bed Room South	20.9	19.5	22.6
Bed Room North	20	19.2	20.9
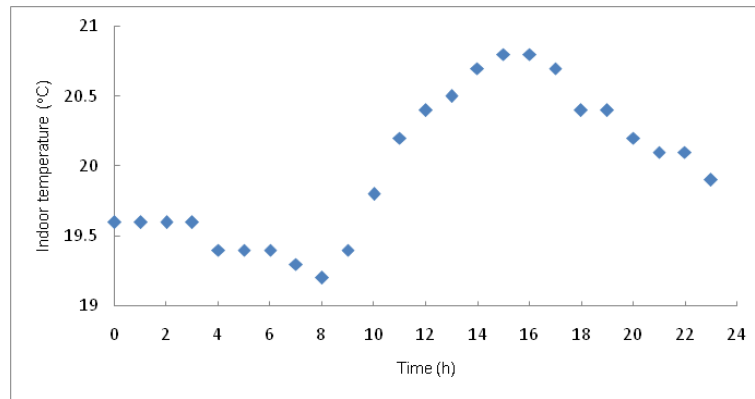
*Figure 4: The indoor temperature of **bed room north for 24h***

3.4 COP Of the Air Source Heat Pump and the System

The system's power consumption included three elements: the air source heat pump, the water pump and the fan in the heat exchanger. When the outdoor temperature decreased, the heat absorbed from outdoor air of air source heat exchanger was declined. In addition, the power of the compressor increased and thus the coefficient of performance (COP) of the system decreased. Table 3 showed that the COPs of the **air source heat pump** and the COPs of the system decreased as the outdoor average temperature decreased. And it also indicated that the COPs decreased as the inlet temperature increased. As a result of the small outdoor temperature at the condition of inlet temperature of 35°C and 40°C, the COPs of the air source heat pump changed a little. The big difference between **the COP of the air source heat pump and the COP of the system was the reason that the consumption of the water pump was big.** As the outdoor temperature dropped to 8.0°C, the **COP of the air source heat pump** was the best when the inlet temperature was 30°C, as shown in Table 3. When the outdoor temperature dropped from 8.0 °C to 6.1 °C, the **COP of the air source heat pump** decreased about 5% and the **COP of the system** decreased 2.3%. That's the reason that the consumption of the air source heat pump decreased with the outdoor average temperature, but the consumption of the water pump almost didn't change with the temperature. When inlet temperature increased from 30°C to 40°C, the COP of the air source heat pump decreased from 3.50 to 2.22 with the percentage of 36.5% at the conditions of the outdoor temperature of 6-7°C. The COP of the system decreased a lot along with the inlet temperature because the condensation temperature increased with the inlet temperature.

Table 3 COP of the air source heat pump and the system at different inlet temperature

Inlet Temperature (oC)	Outdoor Average Temperature (oC)	COP of the Air Source Heat Pump	COP of the System
30	6.1	3.50	2.60
	8.0	3.68	2.66
35	5.0	2.80	2.27
	5.1	2.82	2.29
40	6.6	2.22	1.89
	6.8	2.23	1.92

4. CONCLUSIONS

In this study, the air source heat pump system can supply heating, cooling and domestic hot water in one all. And the air source heat pump system for low-temperature supply water showed superior COP in heating mode at the inlet temperature at 30°C compared with the normal air conditioning with the inlet temperature of 40°C. The performance of a novel heat pump system was investigated in heating mode. The COP of the system is about 3.5 and the COP of the system. The air source heat pump was at the intermittent opening condition when the inlet temperature was at 30°C and 35°C, but it was always running when the inlet temperature was set at 40°C. The heating capacity for space heating increased as the hot water temperature increased. The difference between the heating capacities at different inlet temperature was big because of higher indoor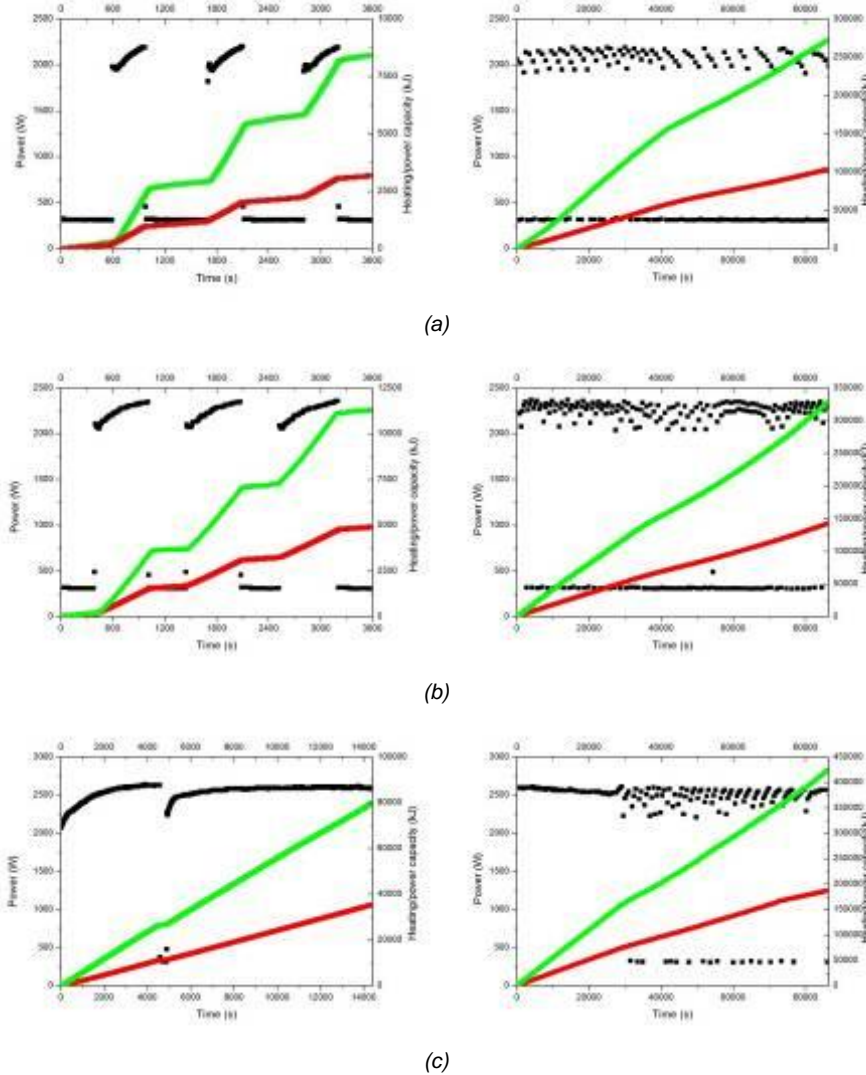 temperature and heat losses of the water pipes. When the inlet temperature was set at 30°C, 35°C and 40°C, the power consumption was 27.18kWh, 39.84 kWh, 51.48 kWh, respectively. The power consumption of the system increased 89.2% at the inlet temperature of 40°C and 46.6% at the inlet temperature of 35°C compared with the one at the condition of the inlet temperature of

30°C. The COPs of the air source heat pump and the COPs of the system decreased as the outdoor average temperature decreased. And the COPs decreased as the inlet temperature increased. When inlet temperature increased from 30°C to 40°C, the COP of the air source heat pump decreased from 3.50 to 2.22 with the percentage of 36.5% at the conditions of the outdoor temperature of 6-7°C. The COP of the system decreased a lot along with the inlet temperature with the condensation temperature increased. The indoor temperature of the apartment was at the range of 19.4 to 20.9°C with the conditions of the inlet temperature of 30°C and the average temperature 5.1°C.

5. REFERENCES

GE Fenghua, Guo Xinglong, Hu Zicheng, Chu Yi, 2011. Energy savings potential of a desiccant assisted hybrid air source heat pump system for residential building in hot summer and cold winter zone in China. *Energy and Buildings*, 42(12), 3521-3527.

GONG Guangcai, Tang Jinchen, LV Dongyan, Wang Hongjin, 2013. Research on frost formation in air source heat pump at cold moist conditions in central south China. *Applied Energy*, 102, 571-581.

LI Xianting, Wu Wei, Zhang Xiaoling, Shi Wenxing, Wang Baolong, 2012. Energy saving potential of low temperature hot water system based on air source absorption heat pump. *Applied Thermal Engineering*, 48, 317-324.

LIU Xiaoyu, Ni Long, Lau Siu-Kit, Li Haorong, 2013. Performance analysis of a multi-functional Heat pump system in heating mode. *Applied Thermal Engineering*, 51(1-2), 698-710.

MINISTRY OF HOUSING AND URBAN RURAL DEVELOPMENT OF THE PEOPLE'S REPUBLIC OF CHINA, 1993. Thermal Design Code for Civil Buildings. 1. Beijing, China Architecture & Building Press, 12-12 (in Chinese).

SONG Mengjie, Pan Dongmei, Li Ning, Deng Shiming, 2015. An experimental study on the negative effects of downwards flow of the melted frost over a multi circuit outdoor coil in an air source heat pump during reverse cycle defrosting. *Applied Energy*, 138, 598-604.

VOCALE Pamela, Morini Gian Luca, Spiga Marco, 2014. Influence of outdoor air conditions on the air source heat pumps Performance. *Energy Procedia*, 45, 653-662.

YIN Ping, 2013. Present situation and proposed approach of heating in Southern China. *Heating Ventilating & Air Conditioning*, 43(6), 50-57. (In Chinese)

WANG Fenghao, Wang Zhihua, Zheng Yuxin, Lin Zhang, Hao Pengfei, HUAN Chao, WANG Tian, 2015. Performance investigation of a novel frost free air source heat pump water heater combined with energy storage and dehumidification. *Applied Energy*, 139, 212-219.

WANG Ruzhu, Zhang Chuan, Chen Jinfeng, Zhai Xiaoqiang, 2014. Heating new mode of high efficiency and comfort for air source heat pump with small temperature difference terminals. *Machinery Industry Standardization & Quality*, 490, 34-38. (In Chinese)

WANG Ruzhu, Zhang Chuan, Zhai Xiaoqiang, 2014. Discussion on the Design Elements of Air Source Heat Pump Air-conditioning, Heating and Hot Water System for Residential Uses. *Chinese Journal of Refrigeration Technology*, 34(1), 32-41. (In Chinese)

ZHU Jiahe, SUN Yuying, WANG Wei, GE Yijing, LI Lintao, C Jingdong, 2015. A novel Temperature Humidity Time defrosting control method based on a frosting map for air source heat pumps. *International Journal of Refrigeration*, 54, 45-54.

388: A comparison study on direct expansion solar assisted heat pump water heater system with different channel pattern roll-bond collectors/evaporators

Yanjun Dai[1], Jinfeng Chen[1], Xiaolin Sun[1], Ruzhu Wang[1]

[1] *Institute of refrigeration and cryogenics, Shanghai Jiao Tong University*

In this paper, three types of roll-bond collectors/evaporators for direct expansion solar assisted heat pump (DX-SAHP) water heater were designed, fabricated and tested. The roll-bond collectors/evaporators were south-faced and wall-mounted for building integration purpose during the experiment. Results show that, under the test conditions, the roll-bond collector/evaporator with honeycomb and rectangle shaped channel pattern shows significant improvement of COP and heating capacity than the conventional channel pattern. Furthermore, compared with the rectangle shaped channel pattern, the honeycomb shaped channel pattern further improved COP by 6.2%. Finally, the DX-SAHP water heater with optimized channel pattern roll-bond collector/evaporator was tested under a series of different weather conditions. With the fixed initial water temperature, the COP of DX-SAHP water heater varied from 1.76 to 5.54 when the operating condition changed. When operating during night, the sky background temperature significantly influenced the COP of the system. Under the same ambient temperature, the results of COP in cloudy and clear night are 2.82 and 1.76 respectively.

Keywords: Solar Heat pump; Collector/evaporator; Channel pattern

1. INTRODUCTION

In a heat pump system, the evaporating temperature has a significant influence on the coefficient of performance (COP). Besides air source, other types of energy such as water and ground source have been used to improve the evaporating temperature. The direct expansion solar assisted heat pump (DX-SAHP) combines solar collector and heat pump together. In this way, solar radiation is used directly as the heat source, which can provide a higher evaporating temperature than other sources [1-5].

The idea of DX-SAHP was first proposed by Sporn and Ambrose in 1955[1], and more studies began since the late 1970s. Performances of various prototypes were tested and analyzed [2-13], and reviews on this topic can also be found [3-5].In a DX-SAHP system, solar collector and evaporator of the heat pump are combined into one single unit. The working fluid evaporates in the collector/evaporator and absorbs heat from solar thermal conversion as well as ambient air. Compared with the conventional solar water heating system with flat plate or evacuated glass tube solar collector, the temperature of working fluid in collector/evaporator of DX-SAHP is much lower, thus it can reach a higher efficiency. While compared with the air source heat pump system, solar radiation can provide a higher evaporating temperature in collector/evaporator of DX-SAHP, resulting in an improved COP.

The most widely used type of collector/evaporator in is bare flat plats made of aluminium or copper in recent researches. Most of those bare plat panels employed simple parallel or S-shaped flow channel patterns. Researchers have made first and second law analysis on the performance of the collector/evaporator and effect of solar radiation, ambient temperature and operating condition et al. has been investigated. While according to the constructal theory analysis of thermodynamics by Bdjan and Lorente [16, 17], geometrical structure (configuration) of the flow channel is also an important factor that affects the thermal performance of the collector/evaporator panel. With channel network optimization, thermal conductive performance of the collector/evaporator can be improved and thus solar energy absorbed by the panel can be transferred to the working fluid more efficiently, resulting in lower average temperature of the panel and higher efficiency of solar utilization.

In this study, the roll-bond panel is used as the collector/evaporator in the DX-SAHP system. The roll-bond panel is one kind of evaporator used a lot in refrigerators and freezers, which is made by welding two aluminium sheets. Compared to the tube and sheet type heat exchanger, it is easy and cheap to manufacture a roll-bond panel with complex flow channel networks. Besides, the roll-bond panel is suitable for the DX-SAHP system for the following advantages: (1) unique design flexibility for the DX-SAHP system; (2) easy to be shaped to fit different applications; (3) easy for design and fabrication; (4) low cost for design and manufacturing; (5) convenient for aluminium recycling.

In this paper, three types of roll-bond collectors/evaporators for direct expansion solar assisted heat pump (DX-SAHP) water heater were designed, fabricated and tested. The thermal performances of the roll-bond collector/evaporators with different types of channel patterns were tested and compared to decide a best flow channel structure.

2. SYSTEM SCHEMATIC AND PROTOTYPE DESIGN

2.1 Schematic of DX-SAHP System

Fig.1 shows the schematic of the DX-SAHP system that consists of a compressor, a hot water tank, a copper coil condenser immersed in the water tank, a thermal expansion valve and a roll-bond solar collector/evaporator. The channel patterns of three roll-bond collectors/evaporators are shown in Fig2. Type I is the traditional S-shaped flow channel, while type II and type III are optimized channel pattern with rectangle and honeycomb shaped channel pattern.
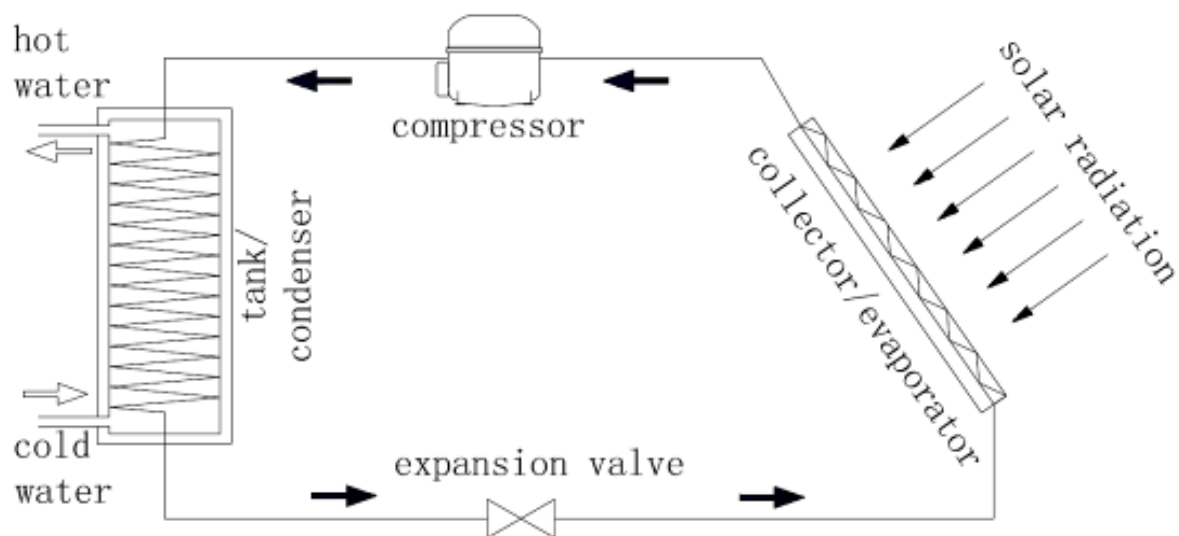
Figure 84: schematic of the DX-SAHP system
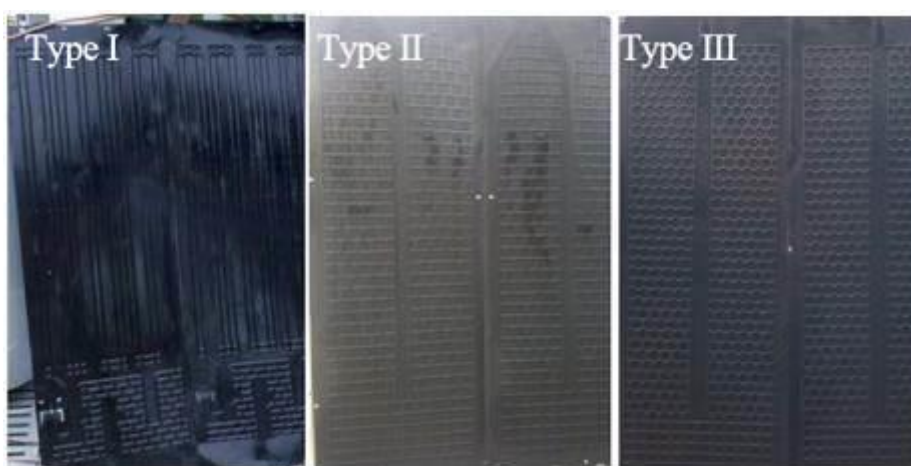
Figure 2: Channel patterns of roll-bond collectors

2.2 Experiment System

As is shown in Fig.3, the collector/evaporator is south-faced vertically because the system is designed to be wall mounted and the main parameters of the system components are listed in Table.1.
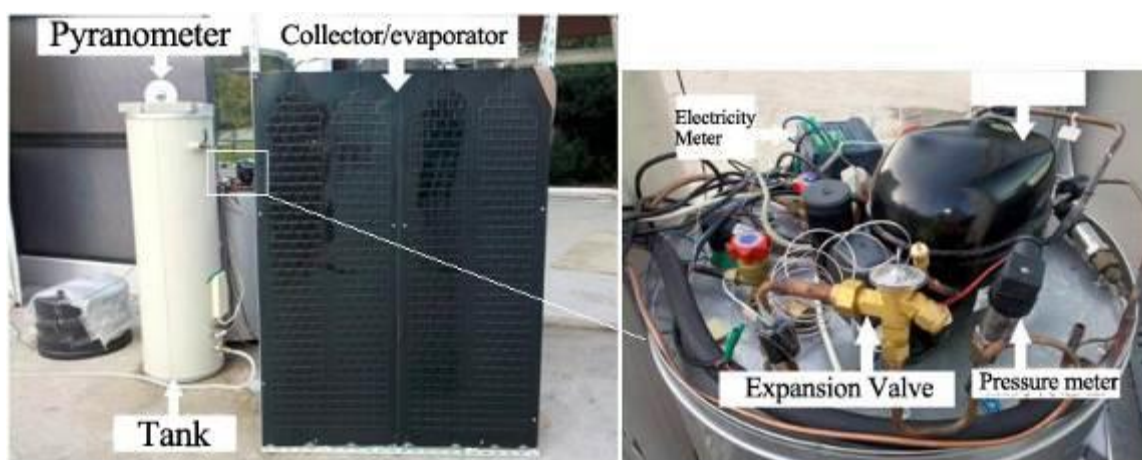
Figure 3: Experiment system of DX-SAHP

Table 30: Main parameters of the experiment system

Component	Parameters
Compressor	Rated power:344W,displacement: 8.77cm3
Collector/evaporator	Area: 1.92 m2, Selective surface: α=0.94, ε=0.2.
Condenser	Length: 30m,Diameter: Φ6.35×0.8mm
Water tank	Volume: 150L
Expansion valve	Thermal expansion valve

As the compressor is the only component that consumes electricity in the system, a single-phase electricity meter was used to measure the power consumption. Platinum resistance thermometers (Pt1000, A class, accuracy ±0.15℃) were used to monitor the temperatures of different components in the system, including water temperature in the tank, suction temperature and exhaust temperature of the compressor and temperature at the outlet of the condenser. Besides, 27 Pt1000 sensors were scattered across the surface of the roll-bond panel to measure surface temperature of the evaporator at different locations as is shown in Fig.4.
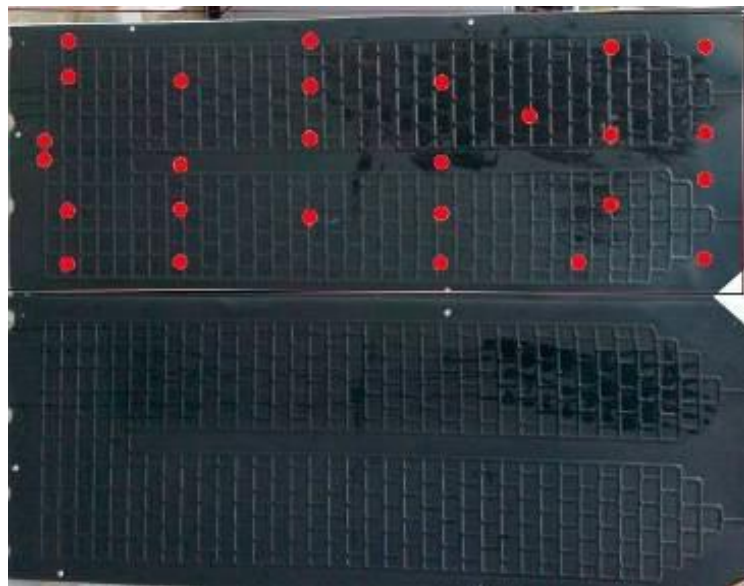
Figure 4: Distribution of measuring points on the surface of the roll-bond panel

During the experiment, the environmental parameters such as solar radiation and dry bulb temperature were also monitored. And the data was collected and handled by a Keithley Model-2700.

2.3 Equations

Equation 58: Quantity of heat energy delivered to water: $Q_c = \rho_w c_w V_w \Delta T_w$
Equation 2: Electricity consumption: $W = \int P_{comp} \, dt$
Equation 3: Coefficient of performance: $COP = \dfrac{Q_c}{W}$
Equation 4: Temperature difference degree: $\Delta T_e = \sum \dfrac{|T_{ei} - T_{em}|}{n}$

Where :

- Q_c= quantity of heat energy delivered to water
- ρ_w= density of water(1kg/L)
- c_w= heat capacity of water(4.2kJ/kg.K)
- V_w= tank volume(150L)
- ΔT_w= water temperature difference of the beginning and the end of the experiment
- P_{comp}= power of compressor
- W= power consumption of compressor

- COP= coefficient of performance of the system
- ΔT_e= temperature difference degree on the collector/evaporator
- T_{ei}= temperature of the ith temperature sensor on the collector/evaporator
- T_{em}= mean surface temperature of the collector/evaporator

3. RESULTS AND DISCUSSIONS

3.1 Performance of the DX-SAHP System

Fig.5 shows COP of the DX-SAHP system using the roll-bond panels with different channel patterns. The weather conditions as well as tap water temperatures are also shown in the figure.
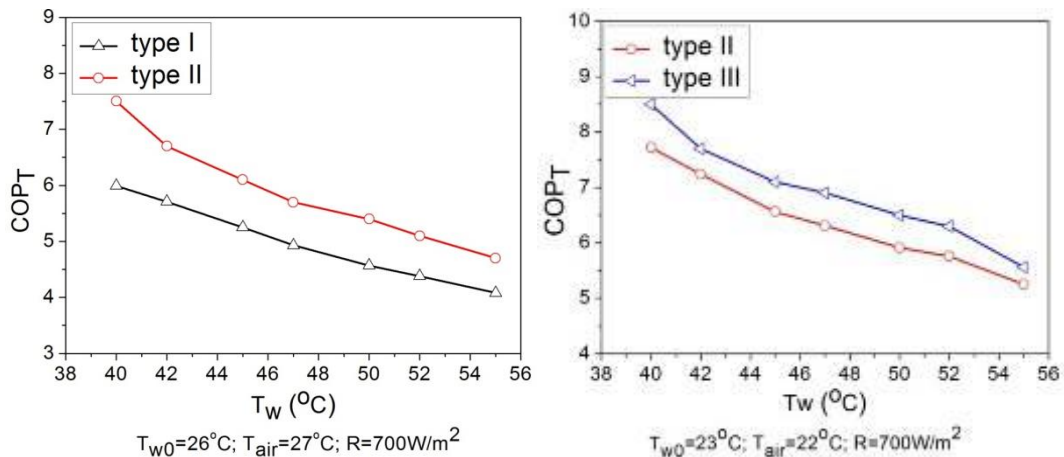
Figure 5: Performances of the DX-SAHP system using roll-bond panels with different types of channel patterns

As shown in Fig.5, T_{w0} is the initial water temperature (tap water temperature). T_w is hot water temperature in the tank. R is the mean value of solar radiation intensity during the operating period. And COP_T is the mean COP value of the DX-SAHP system when water temperature rises from T_{w0} to T_w

Results in Fig.5 show that, compared with the conventional parallel channel pattern(type I), the channel pattern type II enhanced the COP of the DX-SAHP by 17.5%.And compared with the channel pattern type II, the channel pattern type III enhanced the COP by 6.2%.

3.2 Thermal Performances of the Roll-Bond Panels with Different Channel Patterns

In order to further investigate the effect of flow channel pattern on the thermal performance of the roll-bond collector/evaporator, mean surface temperature of the collector/evaporator (Tem) as well as evaporating temperature (T_0) of the DX-SAHP system are compared as shown in Fig.6.
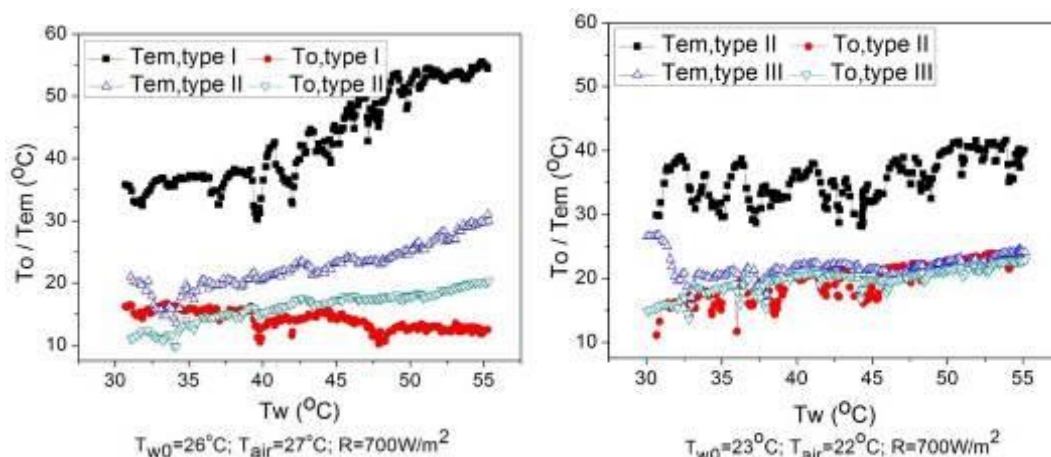
Figure 6: Evaporating temperature and average surface temperature of the roll-bond panel

As shown in Fig.6, T_0 is evaporating temperature of the DX-SAHP system, and T_{em} is the average surface temperature of the roll-bond panel, which is the mean value of the 27 points scattered all over the surface of the panel. Experimental results in the Fig.6 indicate that, compared to roll-bond panel type I, the type II panel shows higher evaporating temperature and lower surface temperature, which will lead to higher COP of the system. In the same way, it could be inferred from Fig.6 that the panel type III performs better than the panel type II. The mean surface temperature of the roll-bond panel type III is very close to the evaporating temperature, indicating good heat conductive properties of the panel.
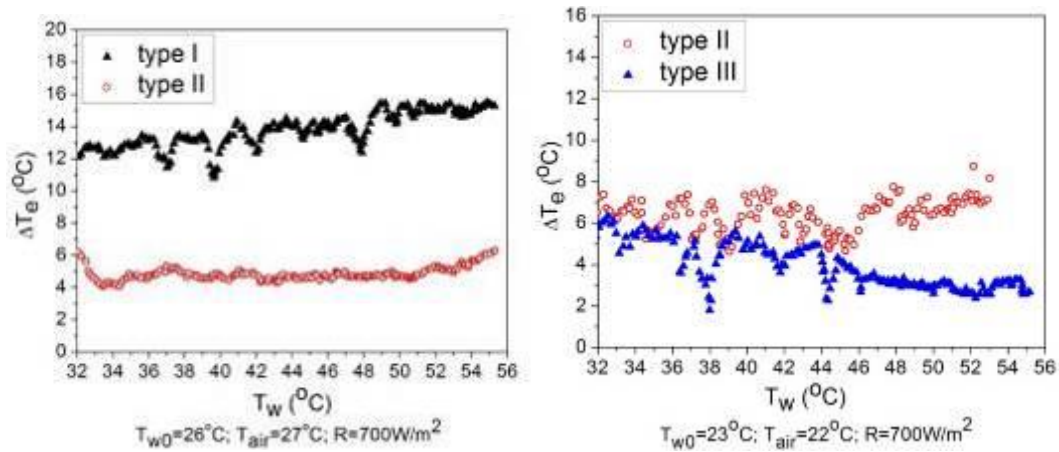
Figure 7: Surface temperature difference of the roll-bond panel

Fig.7 shows the surface temperature differences of different types of roll-bond panels during the water heating process. As shown in Fig.7, the temperature difference degree of the roll-bond panel type I is apparently much higher than that of the roll-bond panel type II. It could be explained that, for the roll-bond panel type I , the thermal conduction performance of the panel is poor, thus local surface temperature of some area is extremely high because the solar radiation received by the panel cannot be absorbed by the working fluid. While at the same time, some other area shows very low temperature because the working fluid cannot get enough heat from the solar radiation and a lower evaporating temperature has to be performed to extract more heat from the ambient air. As for the roll-bond panel type II, the optimized channel pattern improves the heat conduction performance of the roll-bond panel, thus enhances the temperature uniformity as well as solar utilization rate of the panel. And as shown in Fig.7, the roll-bond panel type III shows better temperature uniformity than that of type II, which means, compared to the rectangle channel pattern, the honeycomb shaped channel pattern performs better in improving heat conduction property of the roll-bond panel.

3.3 Test results of Honeycomb Shaped Channel Pattern Under Different Conditions

As is analyzed in section3.1 and 3.2, the honeycomb shaped channel pattern collector/evaporator shows a higher thermal performance than the other two types. Furthermore, a series of experiments under different weather conditions were done to show the feasibility of the DX-SAHP system. The ambient condition and system performance are listed in Table.2.

Table 2: Experiment results of honeycomb shaped channel pattern collector/evaporator under different conditions

	Ambient temperature	Solar radiation	Weather condition	System COP
Case 0	20	700	Sunny day	5.54
Case 1	17	200	Cloudy day	3.57
Case 2	13	0	Cloudy night	2.82
Case 3	13	0	Clear night	1.76
Case 4	17	0	Cloudy night	3.29

As is shown in Table.2, solar radiation intensity has a significant influence on the performance of the DX-SAHP system when comparing case 0 case 1 and case 4. The system COP during night is much lower than it in daytime, because of the lack of solar radiation. The system can only absorb heat in the ambient

air by natural convection when operating without solar radiation, so the evaporating temperature must be much lower than the ambient temperature. Furthermore, low evaporating temperature may lead to frosting problem in Fig.8, which will increase the heat resistance of the collector/evaporator. The difference of system COP between case 2 and case 3 is due to the weather condition. Although the ambient temperature is the same, the sky temperature in cloudy night is higher than it in clear night, thus the heat loss to the sky is lower in case 2. In this way, the evaporating temperature can be higher, which leads to a higher system COP.
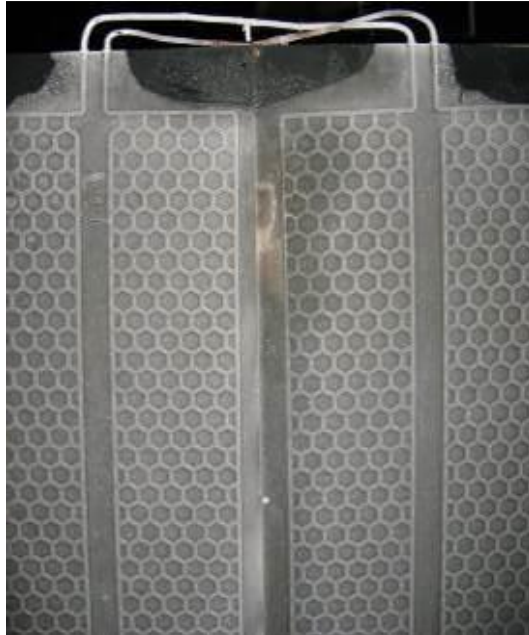
Figure 8: Frosting of collector/evaporator during night condition

4. CONCLUSION

In this investigation, three types of roll-bond collectors/evaporators for direct expansion solar assisted heat pump (DX-SAHP) water heater were designed, fabricated and tested. The roll-bond collectors/evaporators were south-faced and wall-mounted for building integration purpose during the experiment. The experimental results indicate that the roll-bond panels with new types of channel patterns perform better than that with conventional parallel channel pattern, and the following conclusions can be drawn from this study:

(1) The roll-bond panel is suitable to be used as the collector/evaporator of a DX-SAHP system because it provides unique channel network design flexibility, and it is easy and cheap to fabricate.
(2) Performance of the roll-bond collector/evaporator is determined not only by the working conditions and materials, but also by flow channel pattern. The optimized flow channel pattern improves the heat conduction properties of the roll-bond panel, which will lead to a higher evaporating temperature, resulting in better performance of the DX-SAHP system. In the experiment, compared with the panel type I, the panel type II enhanced evaporating temperature by $3℃$. And the panel type III further enhanced evaporating temperature by $1℃$ than type II.
(3) The channel pattern type III (honeycomb shaped) is the best of the three proposed collectors/evaporators. The collector/evaporator with the channel pattern type III shows good temperature uniformity and small difference between the average panel surface temperature and the evaporating temperature. For the panel type III, mean surface temperature difference degree is about $3℃$, and the difference between the average surface temperature and the evaporating temperature is $2℃$. While the corresponding values are $14℃$ and $25℃$ for the panel type I.
(4) With the fixed initial water temperature, the COP of DX-SAHP water heater varied from 1.76 to 5.54 when the operating condition changed. When operating during night, the sky background temperature significantly influenced the COP of the system. Under the same ambient temperature, the results of COP in cloudy and clear night are 2.82 and 1.76 respectively.

5. REFERENCES

[1] P. SPORN, E.R. Ambrose, The heat pump and solar energy, in: Proceedings of the World Symposium on Applied Solar Energy, Phoenix, Ariz, November 1–5, 1955.

[2] W.W.S. CHARTER, L.E. Taylor, Some performance characteristics of a solar boosted heat pump, in: Proceedings of the IIR Conference Towards and Ideal Food Chain, Melbourne, Australia, 1976, pp. 641–648.

[3] O. OZGENER, A. Hepbasli, A review on the energy and exergy analysis of solar assisted heat pump systems, Renewable and Sustainable Energy Reviews 11(2007) 482–496.

[4] A. HEPBASLI, Y. Kalinci, A review of heat pump water heating systems, Renewable and Sustainable Energy Reviews 13 (2009) 1211–1229.

[5] O. KARAA, K. Ulgena, A. Hepbasli, Exergetic assessment of direct-expansion solarassisted heat pump systems: review and modeling, Renewable and Sustainable Energy Reviews 12 (2008) 1383–1401.

[6]SUSHIL K. Chaturvedi, James Y. Shen, Thermal performance of a direct expansion solar-assisted heat pump, Solar Energy, Volume 33, Issue 2, 1984, 155-162.

[7]J. JI, G. Pei, T.T. Chow, K.L. Liu, H.F. He, J.P. Lu, C.W. Han, Experimental study of photovoltaic solar assisted heat pump system, Solar Energy 82 (2008) 43–52.

[8] S.K. CHATURVEDI, M. Abazeri, Transient simulation of a capacitymodulated, direct-expansion, solar-assisted heat pump, Solar Energy 39 (1987) 421–428.

[9] HUANG H, Xinshi G, Yuehong S. Theoretical thermal performance analysis of two solar-assisted heat-pump systems. Int J Energ Res 23(1999) 1–6.

[10] M.N.A. Hawlader, et al,Performance of evaporator-collector and air collector in solar assisted heat pump dryer, Energy Conversion and Management 49(2008) 1612-1619.

[11] S. ITO, N. Miura, K. Wang, Performance of a heat pump using direct expansion solar collectors, Solar Energy 65 (1999) 189–196.

[12] Y.H. KUANG, K. Sumathy, R.Z. Wang. Study on a direct-expansion solar-assisted heat pump water heating system. Int J Energy Res 27(2003) 531–48.

[13] X.Q. KONG, D. Zhang, et al, Thermal performance analysis of a direct-expansion solar-assisted heat pump water heater, Energy 36(12): 6830-6838.

[14] Y. W. LI, R. Z. Wang, J. Y. Wu, Y. X. Xu, Experimental performance analysis and optimization of a direct expansion solar-assisted heat pump water heater, Energy 2007:1361-1374.

[15] Y. W. LI, R. Z. Wang, J. Y. Wu, Y. X. Xu, Experimental performance analysis on a direct expansion solar-assisted heat pump water heater, Applied Thermal Engineering 2007:2858-2868.

[16] A. BEJAN, S. Lorente, Constructal theory of generation of configuration in nature and engineering, Journal of Applied Physics 100(2006): 041301-041327.

[17] A. BEJAN, Constructal-theory network of conducting paths for cooling a heat generating volume, International Journal of Heat and Mass Transfer, 40(1997): 799-816.

SESSION 33: LOW-CARBON/ LOW-ENERGY TECHNOLOGIES

439: Domestic turbine design, simulation and manufacturing for Sub-Saharan Africa energy sustainability

Ebhota WILLIAMS S.[1*] AND Inambao, FREDDIE L.[2]

1, 2Discipline of Mechanical Engineering, Howard College,
University of KwaZulu-Natal, Durban, South Africa
*Correspondence Author: willymoon2001@yahoo.com

The quest for options to the conventional energy sources especially to supply power to remote and rural locations in Sub-Africa has led to several power schemes. The identified options include solar, geothermal, wind and hydro and they belong to renewable energy. However, hydropower has been singled out as the best alternative renewable energy to increase access to power in the region. This study identified inadequate local contents in terms of manufacturing in the small hydropower system technologies in the region as the main hindrance in increasing the rate of power access in Sub-Saharan Africa. The study sees human and manufacturing infrastructure capacities building in small hydropower plant (SHP) technologies as a boost to local production of SHP parts and systems in the region.

For the purposes of design capacity building, a simplified design process was executed for low (3m) and high (60m) heads for Kaplan/Propeller and Pelton pico hydro turbines respectively. The design of a propeller turbine with a river hydrological data of flow rate (Q) 0.2m3/s and head (Hn) 3m using rotational speed (N) of 1500rpm. 6kW turbine power was developed from propeller blade of 0.166m tip diameter (Dt) with specific speed (Ns) of 294. In the case of Pelton turbine, given parameters of flow rate (0.02m3/s), net head (60m) and rotational speed (N) of 1500rpm were used to design a 8.2kW output power Pto of Pelton turbine with specific speed Ns of 26.16. Solidworks modeling and simulation software was used to evaluate the mechanical design of a Pelton bucket. The study concludes that adaptive design and domestic manufacturing are tools for sustainable power development and recommends that a regional joint funding of research on appropriate SHP technologies should be established.

Key words: Power, Design, Turbine, Pelton, Propeller

1. INTRODUCTION

The power situation is Sub-Saharan Africa is in pathetic state despite several remedy interventions. The problems and challenges that trail the power sector in the region seem as fresh as it they were identified in two decades ago and deepened in some areas. Truly, this is heartbroken considering the resources and efforts that have been put to fix it. IRENA (2012) reported that the average rate of electrification in Sub-Saharan Africa is about 35%. It was added that the situation is worse in the rural areas and this was put at below 20%. Further, over 50% of the population in 41 countries in the region has no opportunity to electricity (IRENA, 2012). Some of the factors responsible for this ugly situation are under developed manufacturing infrastructure, over reliance on foreign power technologies, exorbitant cost of power projects and under developed human capacity in power sector.

The search for ways of increasing access to power and alternatives to the conventional energy source (fossil fuel) to supply power to remote and rural areas in the region is massive. This has led to several power schemes. The identified options include solar, geothermal, wind and hydro and they are generally called renewable energies. However, hydropower has been singled out as the best alternative renewable energy with the potential of increasing access to power in the region. This study presents increase in local content in the design and manufacturing of small hydropower system technologies as a potential step to power problems in the region.

2. PRINCIPLE OF OPERATION OF A HYDRO TURBINE

Hydro turbine plants are rotating machines that transform the mechanical energy in flowing water into torque to turn the generator for the purpose of electricity production. Turbine can be categorised into two types, impulse turbines and reaction turbines (Barelli, Liucci, Ottaviano, & Valigi, 2013; Bilal, 2013; Loice & Ignatio, 2013). This classification depends on the water energy transfer method.

For impulse turbines, water is projected from the nozzle as jet and strikes on the buckets that are arranged on the circular edge of the runner. Though, the runner is enclosed in a casing, it is not very important. The buckets are made up double hemispherical cups. The nozzle is the end of penstock while the buckets discharges used water on the tailrace. A schematic diagram of Pelton turbine is shown in Figure 1.

In reaction turbine, the runner or spinning wheel (blade) is completely immersed in the flow and they use water pressure and kinetic energy of the flow. They are appropriate for low to medium head applications. The two main types of reaction turbine are the propeller (with Kaplan variant) and Francis turbines.
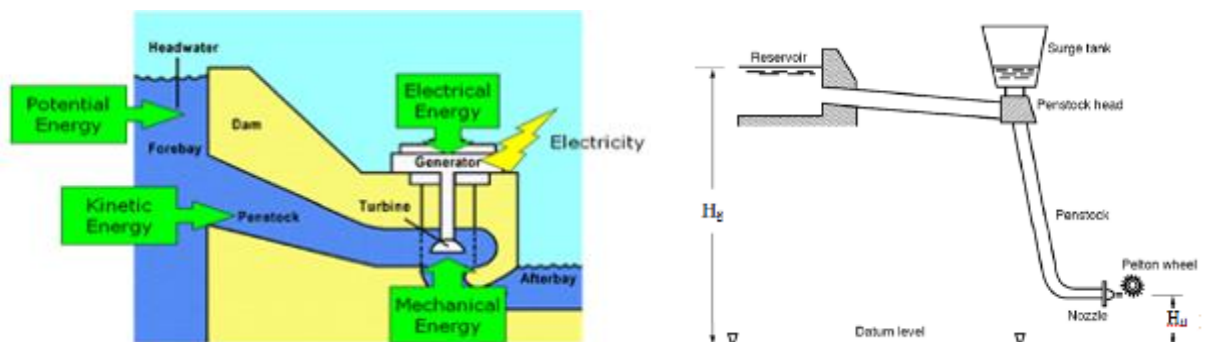
Figure 1: Schematic diagram of a hydro turbine system (Shesha, 2014)

3. HYDRO TURBINE MAIN COMPONENTS

The hydro turbine is composed of the following main components as shown in Figure 1: the ***Dam/Weir –*** is a wall across the river or flow channel to store water. The reservoir created by the dam/weir is termed Headrace; ***the Penstock –*** This is the pipe the connects the headrace to the turbine runner; ***the Runner –*** the part of the layout that converts the energy of the flowing water into torque that drives the generator via shaft is called runner. The runner of a turbine has the wheel and buckets or cups for Pelton turbine; blade and hub for Kaplan, Turgo and Francis turbines. The Shaft – the part that connects the blade and the generator; ***the generator*** – this is the device that receives the mechanical energy through the shaft and

converts this energy into electrical energy. *Tailrace –* the used water flow out of the turbine through a channel called tailrace.

4. HYDRO TURBINE DESIGN AND MANUFACTURING PROCEDURES

There is strong correlation between material selection and manufacturing process. They could be said to be elements of the universal set called *Design Process*. Figure 2 represents the relation that exists between material selection and manufacturing process. For successful product design, the design process should provide an interphase between material selection and manufacturing process. This interphase is subjected to material and manufacturing facility availability. The manufacturing system in Sub Saharan Africa is not as advanced and adequate compared to what is obtainable in Europe and America even in Asia. However, good hydro turbine products can still come out of the region if material and manufacturing inadequacies are factored into the design process early.
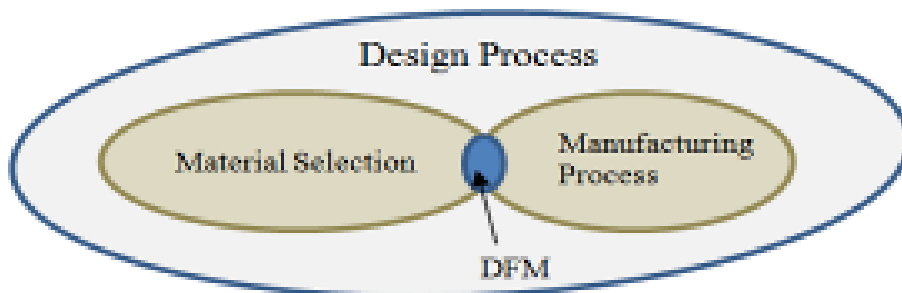
DFM – Design for manufacturing
Figure 2: Correlation between material selection and manufacturing process.

A simplified hydro turbine production procedure can be categorised into twelve sequential steps as shown in Figure 3.
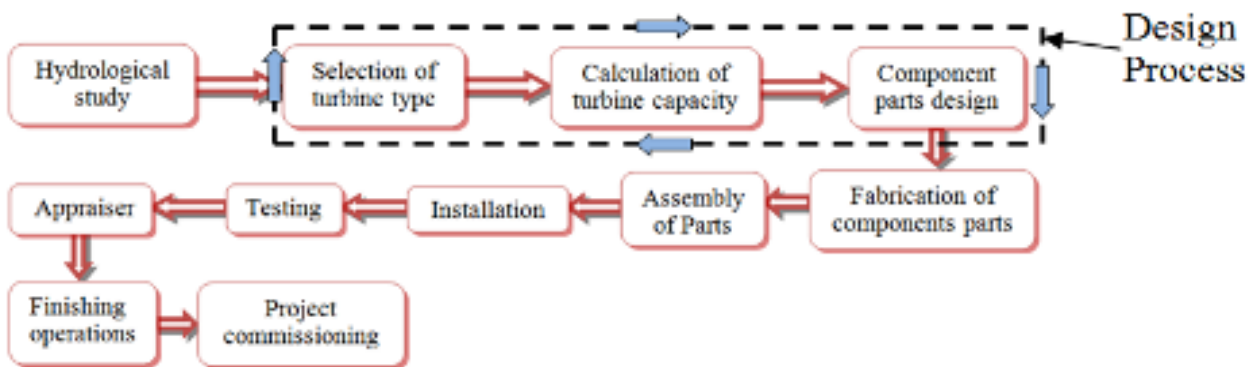
Figure 3: A Production layout Model of a Pico Hydro Turbine System

5. SELECTION OF TURBINE AND DESIGN OF TURBINE

There are two factors that determine the kind of turbine to be used. These factors are products of hydrological study of the hydro potential like river or water falls. The parameters are head (H) and the volumetric discharge (Q) of the river (Figure 4 refers).

The type of turbine to be used according to head classification; the head is classified into low (>10m), medium (10-50m) and high head (above 50m). Table 1 shows type of turbines and the various head domains where they are applied.
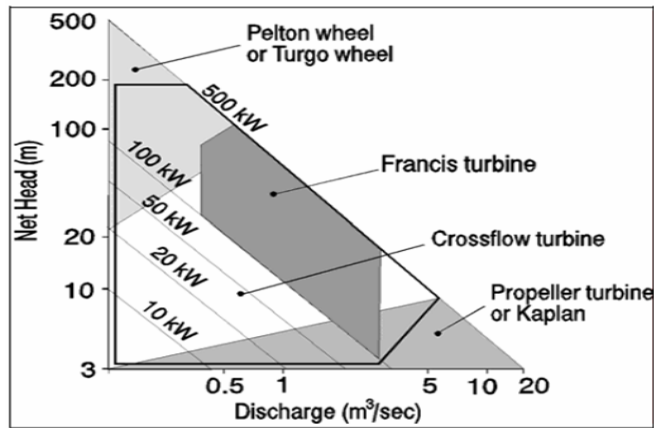
Figure 4: Head-flow Range of Small Hydro Turbines (Paish, 2002)

Table 1: Types of Hydro Turbine and their Applications (John, 2011; Shesha, 2014)

Turbine	Head Classification		
	High (>50m)	Medium (10-50m)	Low (<10m)
Impulse	Pelton, Turgo, Multi-jet Pelton	Crossflow, Pelton, Turgo, Multi-jet Pelton	Crossflow
Reaction		Francis (spiral case)	Francis (open-flume), Propeller, Kaplan, Darius

5.1 The Kaplan/Propeller Turbine

The Kaplan or propeller turbines are very appropriate for low head and large discharge operations. The Kaplan is an adjustable runner blade with high, almost constant efficiency over a wide range of load. The range of Kaplan turbine applications has been greatly improved, which has favoured the improvement of numerous undeveloped hydro sources previously discarded for economic or environmental reasons. The Kaplan Turbine generation efficiency is sometimes over 90% at low heads and high flows (Will, 2010).
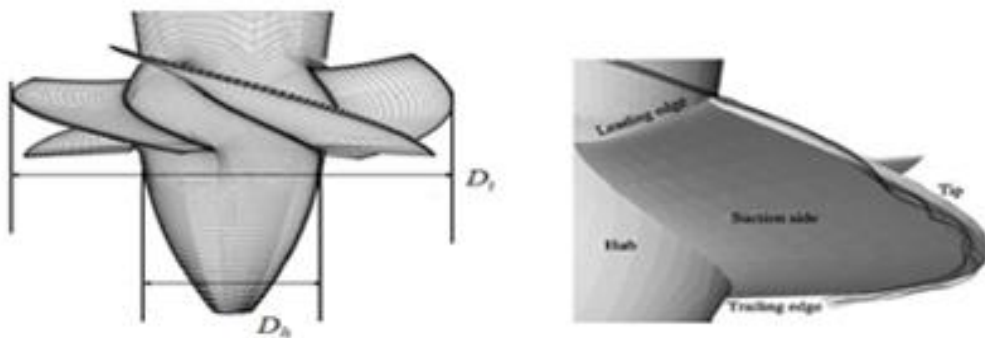
Figure 5: Kaplan/Propeller runner blade parameters and parts

5.2 The Pelton Turbine: Main Elements of a Pelton Turbine System

This turbine is typically used in small-scale micro-hydro systems (with power of up to about 100kW) and a head ranging from 10m to 200m. It consists of a wheel (or runner) with a number of buckets attached around its edge, which are shaped like two cups joined together with a sharp ridge between them as represents by Figure 6. In addition, a notch is cut out of the bucket at the outside end of the ridge. Water is directed to the turbine through a pipe and nozzle to this ridge. Its shape allows for the production of a lot of power from such a small unit and it is easy to manufacture.

As the water strikes at the symmetrical line it then distribute into the two halves of the bucket while some water are reflected back to the nozzle. The angle of jet deflection theoretically for a perfect hemispherical

bucket is 180º. This is not possible to obtain practically rather the angular deflection of 165º is used in practice (Bilal, 2013).

The main parts of Pelton turbine are penstock, spear, nozzle, wheel and buckets, shaft, generator, valves and powerhouse, Figure 7 refers. Water flows from the headrace through the penstock to runner. The penstock has a nozzle at its exit before the runner.

The flow rate of the water jet from the nozzle can be control with the use of spear. This spear helps to adjust the flow rate to balance the change caused by site conditions, see spear in Figure 6.
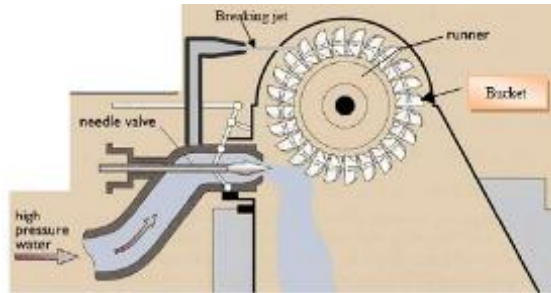
Figure 6: Pelton turbine arrangement
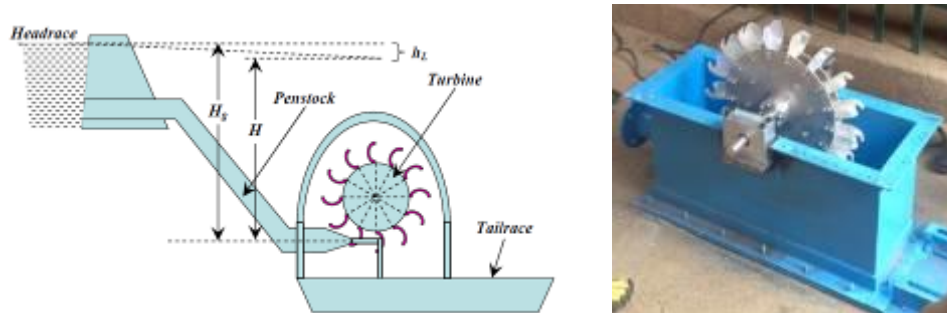
Figure 7: Shows a general layout of a Pelton hydro turbine plant (Shesha, 2014)

5.3 Pelton Design Parameters
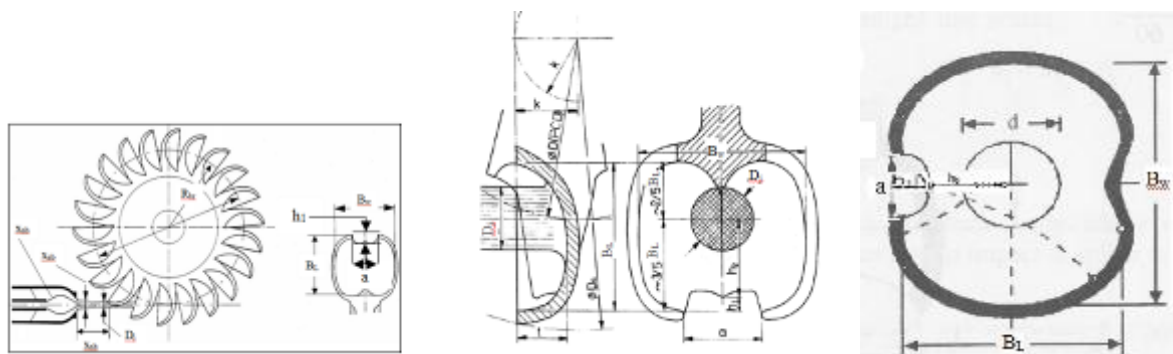
Figure 9: Runner and bucket parameters
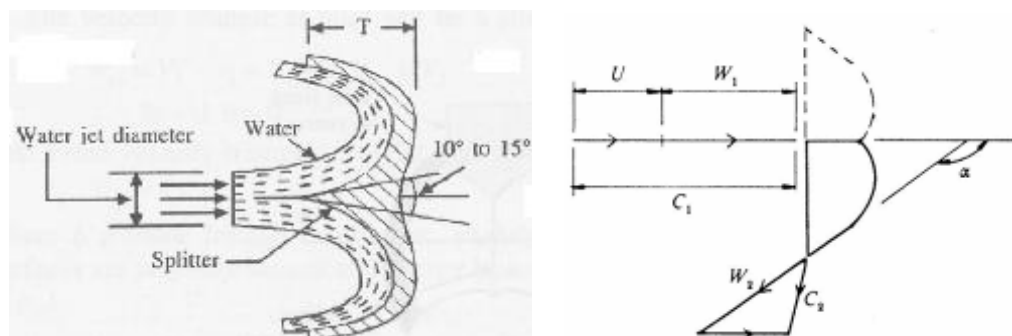
Figure 10: Turbine Velocity diagrams

5.4 Propeller Turbine Design for Low Head

Table 2: Nominal conditions for Kaplan/Propeller turbine design (refer to Figures 5) (Timo, 2007).

Given parameters: $Q = 0.2 m^3/s$; $H_n = 3m$; $\rho = 1000$; $K_u = 1.7$; $N = 400rpm$ and; $\eta = 0.8$				
S/N	Step	Relevant Equations	Input numerical value input	Answer
	Turbine capacity, P.	$P = \rho * g * Q * H_n$	$P = 1000 * 9.81 * 0.2 * 3$	6kW
	Specific speed, N_s	$N_s = \dfrac{N * \sqrt{Q}}{H_n^{0.75}}$	$N_s = \dfrac{1500 * \sqrt{0.2}}{3^{0.75}}$	294
	Velocity, u	$u = K_{ug}\sqrt{2gH_n}$	$u = 1.7 * \sqrt{2 * 9.81 * 3}$	13.04m/s
	The angular velocity of the turbine runner, rad/s	$\omega = \dfrac{2\pi N}{60}$	$\omega = \dfrac{2 * \pi * 1500}{60}$	157rad/s
	The blade tip radius, r_t	$r_t = \dfrac{K_{ug}\sqrt{2gH_n}}{\omega}$	$r_t = \dfrac{1.7 * \sqrt{2 * 9.81 * 3}}{157}$	0.083m
	The blade tip diameter, D_t	$D_t = 2r_t$	$D_t = 2 * 0.083$	0.166m
	The hub diameter, D_h	$\dfrac{D_h}{D_t} = 0.35$	$D_h = 0.35 * 0.166$	0.058m
	Cross sectional area, A	$A = \dfrac{\pi}{4}\left(D_t^2 - D_h^2\right)$	$A = \dfrac{\pi}{4} * \left(0.166^2 - 0.058^2\right)$	0.019m²
	Axial velocity [m/s]	$V_{axial} = \dfrac{4Q}{\pi\left(D_t^2 - D_h^2\right)}$	$V_{axial} = \dfrac{4 * 0.2}{\pi * \left(0.166^2 - 0.058^2\right)}$	10.53m/s
	Flow coefficient, Φ:	$\Phi = \dfrac{Q}{ND_t^3}$	$\Phi = \dfrac{0.2}{1000 * 0.166^3}$	0.044
	Power coefficient, Γ:	$\Gamma = \dfrac{P}{\rho N^3 D_t^5}$	$\Gamma = \dfrac{6}{10^3 * 1500^3 * 0.166^5}$	$1.4 * 10^{-8}$
	Energy coefficient, Ψ:	$\Psi = \dfrac{gH}{N^2 D_t^2}$	$\Psi = \dfrac{9.81 * 3}{1500^2 * 0.166^2}$	$4.7 * 10^{-4}$

Where A - area; Q - flow rate and; r_t - blade radius; r_h - hub radius; D_t - blade diameter and; D_t - hub diameter; K_{ug}, the tip-to-head velocity ratio (D_h/D_t); ρ - density of water (kg/m^3); g - acceleration due to gravity $(9.81m/s^2)$; H_n - net head (m) and; η_{tl} – total efficiency.

5.4 Pelton Design for High Head Design and Simulation of Bucket

Table 3: Nominal Conditions for Pelton Turbine Design (refer to Figure 9 and 10) (Anders & Owen, n.d.; Obretenov, 2006; Shesha, 2014; Will, 2010).

Given quantities: $Q = 0.015 m3/s$; $Hn = 60m$; $Cn = 0.98$; $\rho = 103 Kg/m3$; $x = 0.46$; $nj = 1$; $Lpt = 100m$; $\psi = 0.98$ and; $\theta = 165°$. The generator is rated at 120 watts, and the rotation (N) is 1500 RPM.				
S/N	Parameters	Relevant Equations	Input numerical value input	Answer
	The input power to the turbine, Pti	$P_{ti} = \rho * g * C_n^2 * H_n * Q$	$P_{ti} = 10^3 * 9.81 * 0.98^2 * 60 * 0.015$	8.48kW
	Specific speed (Ns)	$N_s = \dfrac{N * \sqrt{P_{ti}}}{H_n^{\frac{5}{4}}}$	$N_s = \dfrac{1500 * \sqrt{8.48}}{60^{\frac{5}{4}}}$	26.16
	Jet velocity, Vj (m/s)	$V_j = C_n * \sqrt{2 * g * H_n}$	$V_j = 0.98 * \sqrt{2 * 9.81 * 60}$	33.62m/s
	Jet/nozzle diameter, Dj	$D_j = \sqrt{\dfrac{4 * Q}{\pi * n_j * V_j}}$	$D_j = \sqrt{\dfrac{4 * 0.015}{\pi * 1 * 33.62}}$	0.024m

	Tangential velocity of the runner, Vtr	$V_{tr} = x * V_j$	$V_{tr} = 0.46 * 33.62$	15.47m/s
	Runner diameter Dr, (m)	$D_r = \dfrac{60 * V_{tr}}{\pi * N}$	$D_r = \dfrac{60 * 15.47}{\pi * 1500}$	0.20m
	Jet/nozzle cross sectional area, Aj	$A_j = \dfrac{\pi * D_j^{2}}{4}$	$A_j = \dfrac{\pi * 0.024^{2}}{4}$	4.5*10-4
	Nozzle flow rate, Qn (m3/s)	$Q_n = V_j * A_j$	$Q_n = 33.62 * 4.5 * 10^{-4}$	0.015m3/s
	Distance between bucket and nozzle, xnb (m)	$x_{nb} = 0.625 D_r$	$x_{nb} = 0.625 * 0.20$	0.125m
	Radius of bucket center of mass to runner center Rbr(m)	$R_{br} = 0.47 D_r$	$R_{br} = 0.47 * 0.20$	0.094m
	Bucket axial width, B_w (m)	$B_w = 3.4 D_j$	$B_w = 3.4 * 0.024$	0.082m
	Bucket radial length, B_l (m)	$B_l = 3 D_j$	$B_l = 3 * 0.024$	0.072m
	Bucket depth, B_d(m)	$B_d = 1.2 D_j$	$B_d = 1.2 * 0.024$	0.029m
	Cavity Length, h_1 (m)	$h_1 = (0.35) D_j$	$h_1 = (0.35) * 0.024$	0.008m
	Length to Impact Point, h_2 (m)	$h_2 = (1.5) D_j$	$h_2 = (1.5) * 0.024$	0.036m
	Offset of Bucket, k(m)	$k = (0.17) D_j$	$k = (0.17) * 0.024$	0.004m
	Cavity Width, a (m)	$a = (1.2) D_j$	$a = (1.2) * 0.024$	0.029m
	Number of bucket na	$n_b = 15 + \dfrac{D_r}{2 D_j}$	$n_b = 15 + \dfrac{0.20}{2 * 0.024}$	19
	Length of bucket moment arm, L_{ab} (m)	$L_{ab} = 0.195 D_r$	$L_{ab} = 0.195 * 0.20$	0.039m
	Volume of bucket, V_b (m³)	$V_b = 0.0063 * D_r^{3}$	$V_b = 0.0063 * 0.20^{3}$	5.04x10⁻⁵m³
	The output power to the turbine, P_{to} (kW)	$P_{to} = \rho * Q * V_{tr} \left[\dfrac{(V_j - V_{tr}) *}{(1 + \psi * \cos(\phi))} \right]$	$P_{to} = 1000 * 0.015 * 15.47 \left[\dfrac{(33.62 - 15.47) *}{(1 + 0.98 * \cos(15))} \right]$	8.20kW
	Turbine hydraulic efficiency, η_{th}	$\eta_{th} = \dfrac{P_{to}}{P_{ti}} * 100$	$\eta_{th} = \dfrac{8.20}{8.48} * 100$	97%
	Mass of a bucket (Kg)	$M_b = \rho_m * V_b$ ρm =	$M_b = \rho_m * V_b$	
	The torque produced by the turbine, T_t (N-m)	$T_t = \dfrac{P_{to}}{\omega} = Q * D_r * (V_j - V_{tr})$	$T_t = 0.015 * 0.2 * (33.62 - 15.47)$	0.054N-m
	The deflector required force, F_d:	$F_d = \rho * Q * V_j$	$F_d = 1000 * 0.02 * 33.62$	672.4N
	Force acting on the runner	$F_A = 2 * \rho * Q_n * (V_j - V_{tr})$	$F_A = 2 * 1000 * 0.015 * (33.62 - 15.18)$	555.2N

Where C_n – nozzle discharge coefficient (0.98); N – runner speed (rpm); x – ratio of V_{tr} to V_r; Q - flow rate; g - acceleration due to gravity (9.81m/s²); H_n - net head (m); ρ - density of water (kg/m³)

6. MATERIAL SELECTION FOR PELTON BUCKET

Material selection is a very important part of design and manufacturing. One of the variables for design process iteration is material and it influences on manufacturing process. In this study, the selection of material for the bucket was determined by availability, functional requirements, cost and manufacturing facility available. Aluminium alloy (6061-T6) was selected because aluminium is readily available in Sub-Saharan Africa and it can easily be worked upon. Table 4 shows the material properties

Table 4: Material Properties

Model Reference	Volumetric Properties	
	Name: 6061-T6 Aluminum Alloy	Mass: 0.249492 kg
	Model type: Linear Elastic Isotropic	Volume:9.24044e-005 m^3
	Yield strength: 2.75e+008 N/m^2	Density:2700 kg/m^3
	Tensile strength:3.1e+008 N/m^2	Weight: 2.44502 N
	Elastic modulus:6.9e+010 N/m^2	Shear modulus: 2.6e+010 N/m^2
	Poisson's ratio: 0.33	Thermal expansion coefficient: 2.4e-005 /Kelvin

6.1 Evaluation of 6061-T6 Aluminium Alloy: Results of Mechanical Simulation of Pelton Bucket

The necessary design parameters in table 3 were used in the simulation to validate the stress and fatigue of the part (bucket). The results of the simulation are shown is Tables 5 and 6 and diagrams 12 and 13.

Table 5: Mesh Information

	Mesh type	Solid Mesh	Total Nodes	14895
	Mesher Used:	Standard mesh	Total Elements	8568
	Total Nodes	14895	Maximum Aspect Ratio	19.602
	Total Elements	8568	% of elements with Aspect Ratio < 3	97.5
	Jacobian points	4 Points	% of elements with Aspect Ratio > 10	0.0817
	Element Size	4.52077 mm	% of distorted elements (Jacobian)	0
	Tolerance	0.226039 mm	Time to complete mesh(hh;mm;ss):	00:00:07
	Mesh Quality	High		

The static analysis (von Mises) shows that the highest stress (1.95904e+008 N/m^2) as a result of the load is located at node 723 as indicated in Table 6 and Figure 12. This value is less than the material's yield stress of 2.75e+008 N/m^2 as presented in Table 4.

The fatigue distribution along the longitudinal section is shown in Figure 13. The highest fatigue value was recorded at nodal 723 as shown by 13.

The minimum Factor of Safety (FOS) is value at 1.404 and this value was recorded at nodal point 723 as show in Figure 14. However, the FOS is >1. For solidworks software, the FOS benchmark is 1.4. the value of FOS (1.404) recorded from the simulation validates the design good.

Table 6: Study Results for Stress, Displacement and strain

Name	Type	Min	Max
Stress	VON: von Mises stress	1959.97 N/m^2 Node: 812	1.95904e+008 N/m^2 Node: 723
Displacement	URES: Resultant Displacement	0 mm Node: 177	0.209923 mm Node: 435
Strain	ESTRN: Equivalent Strain	5.56279e-008 Element: 3484	0.00172423 Element: 3816

Stress	Displacement	Strain
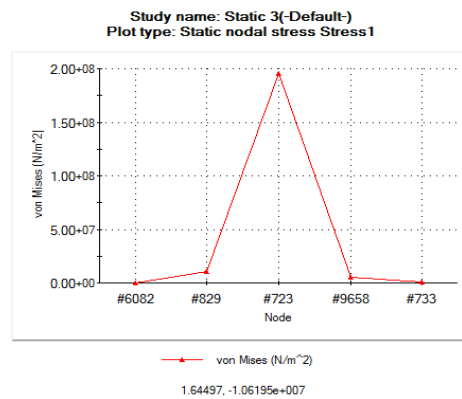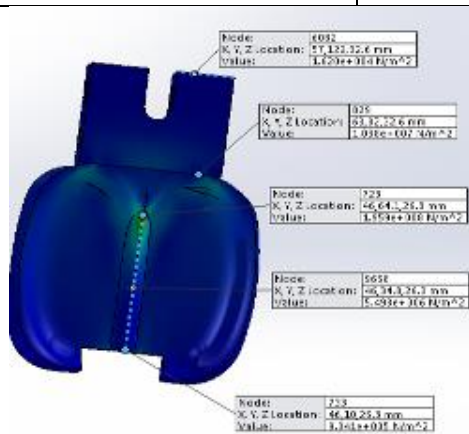
Figure 12: Nodal stress distribution
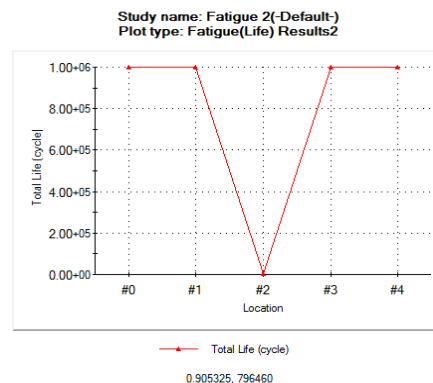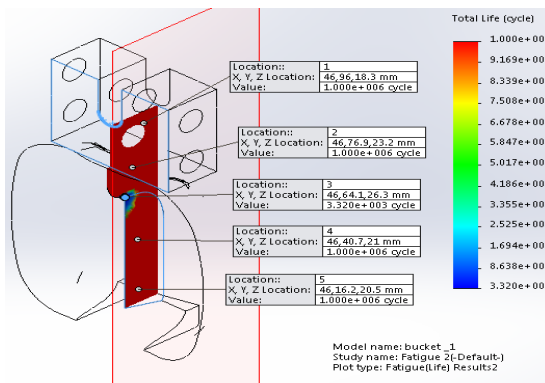
Figure 13: Nodal fatigue distribution
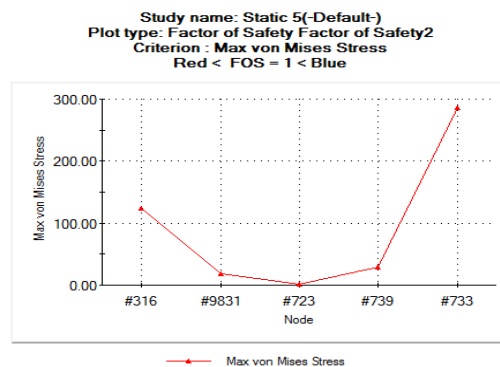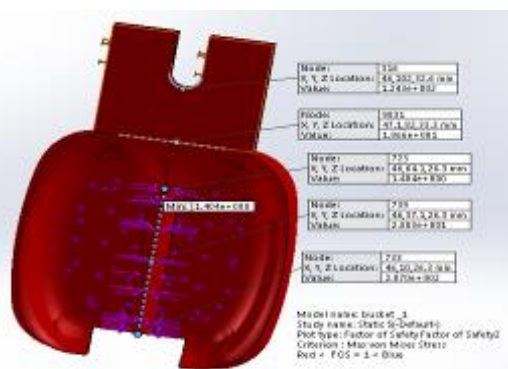
Figure 14: Factor of Safety distribution

7. CONCLUSION

The manufacturing infrastructure in Sub-Saharan Africa is inadequate to support energy sustainability. As a result, the region depends on foreign technology massively and this makes power projects cost very high. This has left the region's socio-economic situation pitiable. In order to increase access to electricity in the region, it is therefore pertinent to building capacity in power technology. The design process should focuses on local contents in terms material selection and manufacturing facility. This study recommends capacity building in small hydropower (SHP) technology, establishment of regional energy research institutions, transformation of research findings into real products, and adopt China's energy development approach of massive use of micro hydro turbines.

8. ACKNOWLEDGEMENT

9. REFERENCES

ANDERS, A., & Owen, S. (n.d.). *Kaplan Turbine From Remote HydroLight* (pp. 49).   Retrieved from www.remotehydrolight.com

BARELLI, L., Liucci, L., Ottaviano, A., & Valigi, D. (2013). Mini-Hydro: A Design Approach in Case of Torrential Rivers. *Energy, 58*, 695-706. doi: http://dx.doi.org/10.1016/j.energy.2013.06.038

BILAL, A. N. (2013). Design of High Efficiency Pelton Turbine for Microhydropower Plant. *International Journal of Electrical Engineering and Technology (IJEET), 4*(1), 171-183.

IRENA. (2012). Prospects for the African Power Sector. United Arab Emirates.

JOHN, F. C. (2011). Turbines.   Retrieved 18/05/2015, 2015, from http://www.jfccivilengineer.com/turbines.htm

LOICE, G., & Ignatio, M. (2013). Efficiencyimprovement of Pelton Wheel and Crossflow Turbines in Micro-Hydro Power Plants: Case Study. *International Journal of Engineering and Computer Science, 2*(2), 416-432.

OBRETENOV, V. S. (2006). Modernization of a Pelton Water Turbine. *Пробл. Машиностроения, 4*, 1-5.

PAISH, O. (2002). Small Hydro Power: Technology and Current Status. Renewable and Sustainable. *Energy Reviews, 6* 537-556.

SHESHA, P. M. N. (2014). Hydraulics and Hydraulic Machines. *VTU Learning*, 1-22. http://elearning.vtu.ac.in/P6/enotes/CV44/Pel_Whe-MNSP.pdf

TIMO, F. (2007). Design of the Runner of a Kaplan Turbine for Small Hydroelectric Power Plants. (Master), Tampere University of Applied Sciences.

WILL, S. (2010). Corazón del Bosque Hydroelectric Scheme: Engineering Design Document. In V. M. 2010 (Ed.), (Vol. 1, pp. 37). Guatemala: Appriopriate Infrastructure Development Group (AIDG).

216: AirAid - an alternative for harnessing wind energy using venturi effect for low-wind regimes

Vishal RAMESH[1], Srinivas MORAPAKALA[2], Nikhil AGARWAL[3]

[1] *Mechanical Engineering Department, BITS-Pilani Hyderabad Campus, Hyderabad, RR District, Telangana State, India, 500078, vishalramesh94@gmail.com*
[2] *Associate Professor, Mechanical Engineering Department, BITS-Pilani Hyderabad Campus, Hyderabad, RR District, Telangana State, India, 500078, morasrini@hyderabad.bits-pilani.ac.in*
[3] *Mechanical Engineering Department, BITS-Pilani Hyderabad Campus, Hyderabad, RR District, Telangana State, India, 500078, agarwal_nikhil@outlook.com*

A new concept in wind energy harnessing is conceived which delivers a significantly higher output and outperforms traditional wind turbines of the same rotor size and design characteristics. The most innovative feature of this concept is that it captures wind at certain speeds but delivers it to the rotor at much higher speeds, increasing the power available at the rotor. Additionally, the requirement of classic, tower mounted turbines is eschewed, mitigating the need for a cumbersome installation of the turbine-generator system at great heights and reducing installation, operation and maintenance costs. Other factors that have undermined the wind industry such as radar impact, aesthetics etc., are addressed. The concept funnels wind through a venturi section that naturally accelerates its flow, increasing a given input velocity of 2 m/s to an average velocity of 10.3 m/s at the rotor, giving a speed ratio of over 5. The CFD analysis is performed on COMSOL using a standard laminar flow model closures with steady flow conditions. The CFD results revealed a non-turbulent velocity distribution near the rotor (no vortex formation), with a minimal variation in the velocity at the rotor's cross section. This shows that because of increased wind velocities, it is possible to have a significant improvement in the power output.

Keywords: Wind energy, wind turbines, ducted turbines, venturi

1. INTRODUCTION

Wind energy has been harnessed for centuries together, with the first windmills being used for purposes like moving boats using sail, cooling houses by circulating the air outside, running machinery in farms and even in production facilities. However, wind power harnessing, today, is far from reaching its full capabilities.

Today, a turbine-generator system mounted at a certain height is the norm. Such systems are well established, particularly in high-wind regimes and manufacturers have improved the energy outputs of such systems, only at the cost of producing ever-larger blades mounted on ever-taller towers. Installed project costs exhibit economies of scale at the lower end of the turbine size range. Based on turbine size – among a sample of projects installed in the United States in 2012 - average installed wind power project costs per kW are seen to rise when moving from projects in the 50-100 MW range to projects of 5 MW or less (Wiser and Bolinger, 2013: page 36). Since 1980, there has been an increasing trend in hub height to meet power demands. Scaling up turbines to lower cost has been effective so far (Philibert and Holttinen, 2013: page 27). This throws in indelible obstacles. A report by NREL cites that 68% of the total land-based project costs is in the turbine itself, of which capital costs amount to 16% and 15% for the tower and rotor, respectively (Tegen, Lantz, Hand et al., 2013: page vii). Such costs may be avoided through the development of ground-based wind turbines. The cost of wind-generated power continues to augment with rising installation, operating and maintenance costs. With tower-mounted turbines, the ease of management, logistics, planning and project site procurement turn into challenges. Moreover, such turbines are a visual distraction and pose a threat to wildlife. They are also subjected to excessive downtime, coupled with being a nuisance aesthetically.

Various concepts, such as Daryoush Allaei's description of a new concept in wind power (Allaei, Andreopoulos, 2014), Grant and Kelly's development of a ducted turbine's model simulation (Grant, Kelly, 2003) et al., have shown substantial progress in harnessing wind energy using ducted turbines. Airborne units have also been developed with turbines at 300-500 m above the ground. A variety of single and multiple array-ducted turbines have also been developed. The single-ducted turbines have been shown to be effective and economical for small wind applications. Attempts have also been made to scale up the single-ducted turbines for utility scale applications. However, due to size and the required speed increase, they have proven to be uneconomical. Even though an array of ducted turbines can generate more electrical energy, they suffer from complexity in actual implementation at utility scale (Allaei, Andreopoulos, 2014: page 337).

Another problem that arises is the issue of wind speeds, which are known to be erratic and directly affect power generation capacity and operating characteristics. In general, a minimum of 2 m/s is required to start rotating the smallest wind turbine. The issue of installing any wind energy system in low-wind regimes has been a pressing one. In this article, the authors offer an emphatic solution to the problem of low-wind regime systems.

2. THE CONCEPT OF AIRAID

While the main intention was to increase the wind velocity from 2 m/s to 10 m/s, it was thought that the use of a venturi action would be appropriate. In other words, if wind is available at 2 m/s and is subjected to venturi action, the wind velocity would increase by a certain fold. This is the very origin of the concept of AirAid. It utilises the use of this venturi action, funnels wind energy to the ground where the rotor is placed, and thus reduces installation, operating and maintenance costs. The plague on fauna is also reduced with absolutely no visible moving parts. Additionally, there's a continuous capture and delivery of wind, reducing the problem of excessive downtime, as wind can be delivered at appropriate cut-in speeds. AirAid features a model whose dimensions are smaller compared to modern wind capturing systems.

2.1 Geometric features of AirAid

The sequence of attainable objectives and associated parts of AirAid are as follows: (1) to capture the incoming wind, (2) to direct the captured wind towards the turbine while increasing its velocity, and (3) to allow the wind to interact with the turbine to generate mechanical work. Figure 1 given below shows the preliminary conceptual model. With regard to capturing the incoming wind, the preliminary model consists of an elbow shaped entry. As the authors have shown in later parts of this article, in order to capture wind from other directions as well, the entry section could be made omnidirectional. The vertical section allows the intake to be placed at a higher elevation so as to minimize wind shear effects. At the same time, the

vertical section was made a converging nozzle so as to enable the venturi action to increase the velocity of flow. A second elbow shaped pipe, at the exit of the vertical nozzle, deflects wind towards the rotor. To further increase the wind speed, a second horizontal nozzle was included before the rotor's hub, thereby allowing the wind turbine to be placed at ground level. The hub houses the blade and the necessary components of the wind energy conversion system. Finally, a diffuser was included to subsequently slow down and expand the wind and enhance its mixing into the surrounding ambient air. In essence, the various parts of AirAid, viz. (1) Intake pipe; (2) Vertical nozzle; (3) Deflecting pipe; (4) Horizontal nozzle; (5) Wind energy conversion system hub; (6) Diffuser; are expected to achieve the above mentioned objectives. After having considered the wind data analysis at the site where the authors were working, available pipes and fittings, available materials etc., the dimensions for various parts were arrived at.
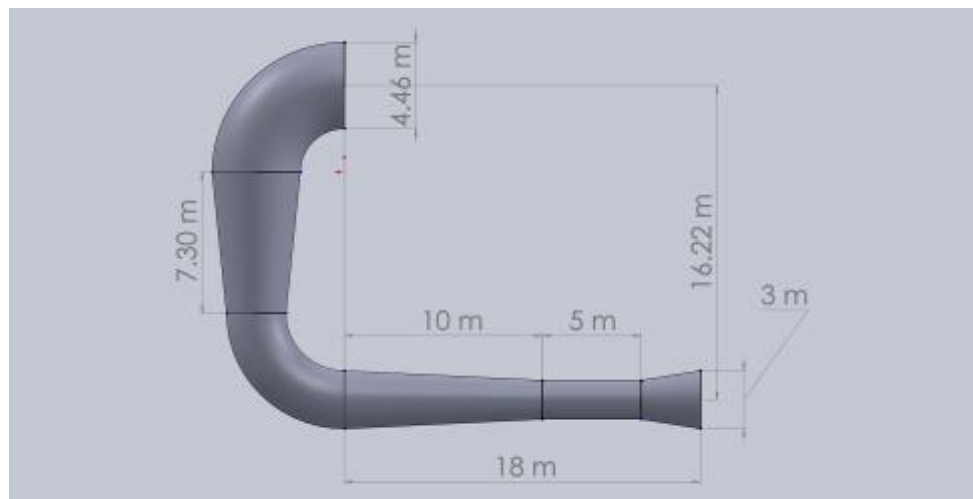
Figure 85: Important dimensions of AirAid: (Anticlockwise from top) Intake pipe, vertical nozzle, deflecting pipe, horizontal nozzle, WECS hub, diffuser

As mentioned above, AirAid consists of two converging nozzles where the effect of venturi action is seen. The entire vertical section is 16.22 m in height from centre-to-centre, which was arrived at by arresting any vertical wind shear effects. In arriving at the diameter of the inlet, the continuity equation for conservation of mass between the inlet and the rotor's section was applied in theory. The input velocity, rotor wind velocity (both related by the speed ratio), and rotor diameter (assumed to be 1 m) were fixed, leading to a diameter of 4.46 m at the inlet. Horizontal wind shear effects were also neglected, making the horizontal distance an insignificant factor in the determination of wind velocity. In the following sections of this article, the authors have presented details about the CFD analysis carried out to study the possibility of having increased velocities with this setup.

3. MODELLING AND ANALYSIS IN COMSOL

A qualitative prediction of any fluid flow is done by incorporating a set of partial differential equations, discretisation and solution techniques, and some software tools. COMSOL, an important multi-physics platform, provides ready-made physics interfaces that may be configured to receive model inputs and used to formulate equations. The CFD module of COMSOL, serving to simulate systems and devices that involve sophisticated fluid flow models, was used as the tool in the analyses of AirAid. Systematically, the methodology used in the CFD module was as follows: after having known the parts and dimensions, a set of underlying equations that govern the physical fluid model were identified, fluid properties and appropriate boundary conditions were defined, mesh elements were selected, and the model was solved numerically using a stationary solver. The authors have described each step of the analysis hereon.

3.1 Governing equations

The continuity equation and the three dimensional Navier-Stokes equation for an incompressible flow with a constant viscosity in rectangular coordinates formed the set of governing equations. Together with the fluid velocity vector, the equations, in their simplified form, are shown below.

Equation 59: Continuity equation for a steady, incompressible flow.

$$\frac{\partial u}{\partial x} + \frac{\partial v}{\partial y} + \frac{\partial w}{\partial z} = \vec{\nabla} \cdot \vec{V} = 0$$

Equation 2: x-component Navier-Stokes equation

$$\rho\left(\frac{\partial u}{\partial t} + u\frac{\partial u}{\partial x} + v\frac{\partial u}{\partial y} + w\frac{\partial u}{\partial z}\right) = \rho g_x - \frac{\partial p}{\partial x} + \mu\left(\frac{\partial^2 u}{\partial x^2} + \frac{\partial^2 u}{\partial y^2} + \frac{\partial^2 u}{\partial z^2}\right)$$

Equation 3: y-component Navier-Stokes equation

$$\rho\left(\frac{\partial v}{\partial t} + u\frac{\partial v}{\partial x} + v\frac{\partial v}{\partial y} + w\frac{\partial v}{\partial z}\right) = \rho g_y - \frac{\partial p}{\partial y} + \mu\left(\frac{\partial^2 v}{\partial x^2} + \frac{\partial^2 v}{\partial y^2} + \frac{\partial^2 v}{\partial z^2}\right)$$

Equation 4: z-component Navier-Stokes equation

$$\rho\left(\frac{\partial w}{\partial t} + u\frac{\partial w}{\partial x} + v\frac{\partial w}{\partial y} + w\frac{\partial w}{\partial z}\right) = \rho g_z - \frac{\partial p}{\partial z} + \mu\left(\frac{\partial^2 w}{\partial x^2} + \frac{\partial^2 w}{\partial y^2} + \frac{\partial^2 w}{\partial z^2}\right)$$

Equation 5: Fluid velocity vector $\overline{V} = u\hat{i} + v\hat{j} + w\hat{k}$

Where:

- ρ = density of air (kg/m^3)
- u, v, w = x, y, z components of fluid velocity vector, respectively
- μ = dynamic viscosity of air (Ns/m^2)
- g = acceleration due to gravity (m/s^2)
- p = local thermodynamic pressure (Pa)

Equation 1 establishes conservation of mass to a differential control volume, Equations 2, 3 and 4 are, essentially, Newton's second law applied to the control volume, and Equation 5 is simply the fluid velocity vector at any point in the flow. The first four equations form a set coupled nonlinear partial differential equations for u, v, w, and p. The equations, being in their differential forms, provide a detailed point-by-point knowledge of the velocity field and pressure at every point in the computational domain. They were solved numerically through the stationary solver in COMSOL, for which a set of boundary conditions were needed.

2.18. 3.2 Characteristics of flow and boundary conditions

Any CFD analysis mandates a set of flow and boundary conditions, after which the model under observation is meshed, the study is carried out and the results are analysed. Some of the important aspects related to characteristics of flow and boundary conditions are as follows:

1. The CFD simulations were based on a steady-state laminar flow of an incompressible Newtonian fluid, air.
2. No rotating turbine was involved in the CFD simulation.
3. No boundary layer elements were used.
4. For boundary conditions,
   a. A uniform input velocity field, representing the free stream wind, was assigned to the entire frontal cross section of the inlet. Its magnitude was set at 2 m/s, as mentioned before.
   b. All the other boundaries were considered slip walls with the exception of the exit cross section in which a pressure-outlet boundary condition was assigned. The assigned pressure was 1 atm.

2.19. 3.3 Meshing

The partial differential equations that govern the fluid flow are usually not amenable to analytical solutions, except in very simple cases. Therefore, flow domains are discretised into smaller subdomains, and the governing equations are then solved inside each of these subdomains. In the present work, the authors have selected three dimensional tetrahedral elements and two dimensional triangular elements as primitives. Tetrahedral elements were selected over hexahedral elements in order to save computational time and effort. Some of the important points with regard to meshing are highlighted.

1. The flow domain was characterized with a mesh of tetrahedral and triangle elements.
2. A 'finer' mesh was used in the study.
3. The total number of elements, with the inclusion of edge and vertex elements, was about 41,000.

4. With 4 variables to each element, the entire flow domain consisted of 164,000 degrees of freedom.

4. RESULTS AND DISCUSSION

The velocity and pressure field, which are properties intrinsic to fluid flow, were calculated numerically through the solver. The velocity distribution was addressed as the critical factor to support the authors' findings.

4.1 Results on Preliminary model

The velocity field plots across two planes of the turbine were observed. Conclusions were drawn through observation of Figures 2 and 3 shown below. Figure 2 shows the distribution at the rotor. It was seen that the velocity at the rotor's section ranges around 10 m/s. The wind speed was increased by a factor of 5, allowing such a turbine to operate at locations whose average wind speeds are 2 m/s. In other words, if a turbine having a cut-in speed of 10 m/s was installed in AirAid, the cut-in speed of the turbine-AirAid system would be 2 m/s. Cut-in speeds are reduced because the system increases wind speeds at the location of the turbine.
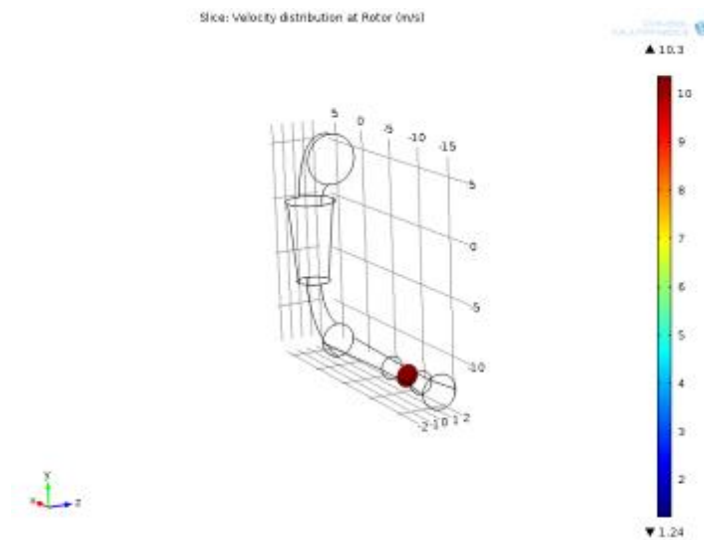
Figure 86: Velocity distribution across the section of the rotor
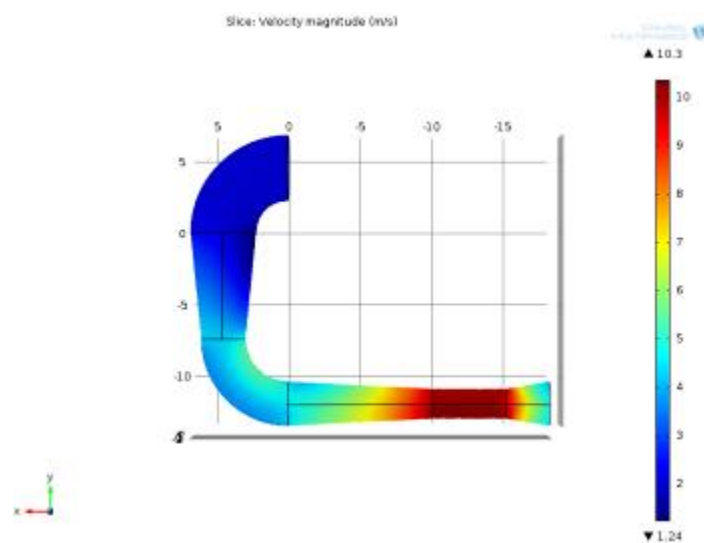
Figure 87: Velocity distribution over the plane of symmetry

Figure 3 presents an observation of the distribution over the plane of symmetry of the entire turbine, essentially displaying the manner in which the wind speed increases. Two important conclusions were made. Firstly, a majority of the speed increase was noticed in the two venturi sections. Secondly, a non-turbulent velocity distribution around the rotor, with no vortex formation, was noticed. Also, the speed ratio of 5 corroborates with the theoretical speed ratio calculated by using the continuity equation between the inlet and the rotor's section.

From the above figures, it was concluded that AirAid presented an emphatic increase in wind velocities at the rotor and can be installed in low-wind regime areas. However, the preliminary model has two major drawbacks: it captures only unidirectional wind and must be yawed to face the incoming wind when necessary. Wind directions are known to be unpredictable and the need to install an active or passive yaw control for any wind turbine is imperative. Hereupon this, transforming AirAid into an omnidirectional wind capturing system through an omnidirectional intake was carried out. AirAid's intake was transformed to have two, four and six inlet sections, all axisymmetric about a vertical axis through the vertical venturi section. The analysis was undertaken separately on each of the three resultant turbines.

4.2 Omnidirectional Intake

For each of the three omnidirectional turbines, the mesh size, wall and outlet boundary conditions were set the same as that of the unidirectional intake. However, in the case of the turbine with two inlets, the input velocity field was assigned as 2 m/s on the left intake and 0.5 m/s on the right intake. This ensures that a substantial portion of wind blows from one particular direction while only a fraction blows from the opposite direction. The presence of a second inlet ensures that even this fraction of wind is captured and concentrated to the rotor. The resultant velocity distribution across the plane of symmetry is shown below in Figure 4.

Figure 4 indicates that the wind velocity around the rotor has increased to about 12 m/s. The second intake effectively captured a portion of wind blowing in the other direction. As the number of inlets was increased to four and six, greater portions of the free stream wind were captured and better speed ratios were obtained, the results of which are shown below in Figure 5 and Figure 6 for four and six inlets, respectively.

Similar to the case of two inlets, the input velocity field for four and six inlets comprised 2 m/s on the leftmost intake and 0.5 m/s on the remaining intakes. Observations of Figures 5 and 6 indicated that the wind velocity at the rotor increased to about 17 m/s and 23 m/s for the four and six inlet turbines, respectively. Although a magnitude of 0.5 m/s on the remaining intakes does not necessarily mimic actual wind conditions, the results indicated that the presence of more inlets did cause increased wind velocities at the rotor. Whatever be the magnitude of wind in other directions, the available energy was captured leading to greater power available at the turbine. Thus, AirAid may also be installed in areas of constantly changing wind direction.

AirAid outperforms traditional wind turbines on several fronts: significantly saving on operation and maintenance costs as all the important rotating parts are housed on ground-level, theoretically improving power coefficient and capacity factor for any installed rotor through enhanced harnessing of the available power in free stream wind, and finally addressing the visual nuisances, aesthetics, and complaints of harm to wildlife. The intake and the turbine-generator system's locations are separate. This allows design engineers to independently size the intake without having to alter the turbine's dimensions, which allows operating at high wind speeds and thus, generating a lot more power with smaller blades while utilising much more efficient generators operating at higher speeds. However, once a turbine is placed in AirAid, it may be so that the increase in resistance will reduce the power available and the output. But mounting a turbine on a tower will also offer resistance to the free stream wind: the case being the same for tower-mounted turbine-generator systems.
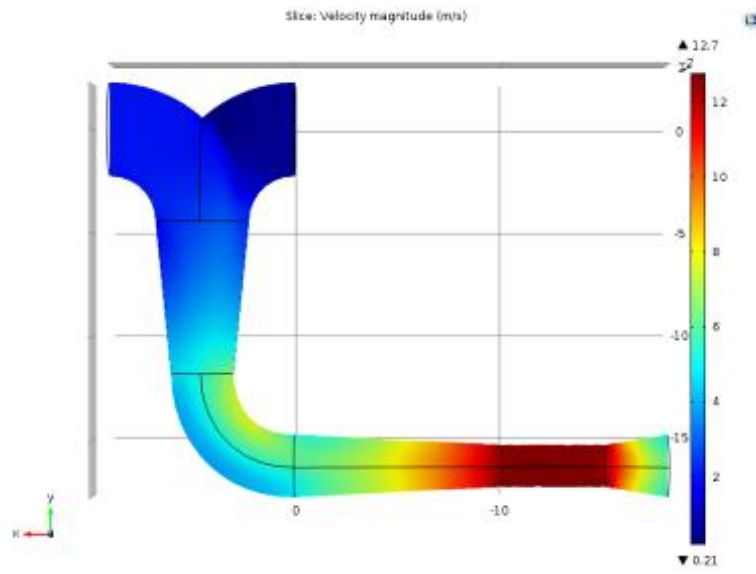
Figure 88: Velocity distribution over the plane of symmetry for two inlets
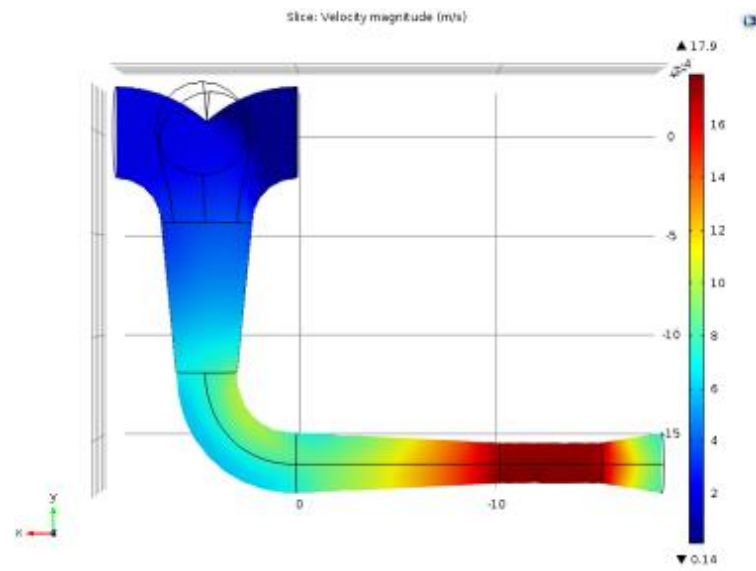
Figure 89: Velocity distribution over the plane of symmetry for four inlets
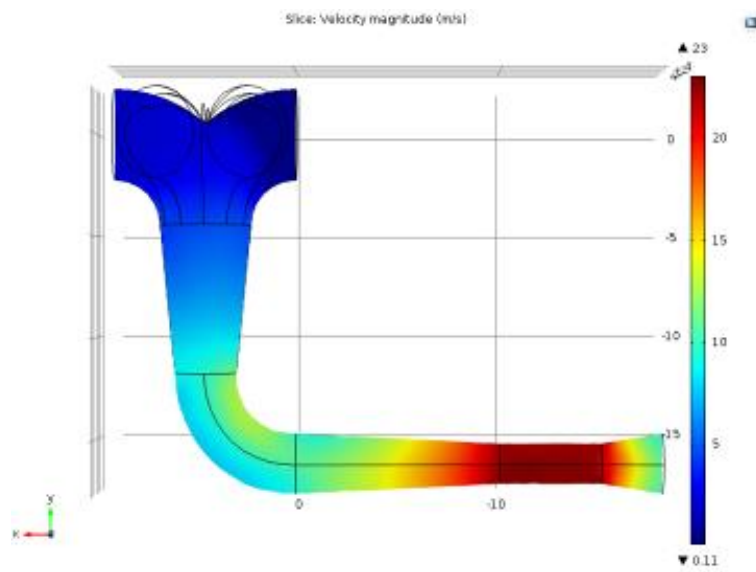
Figure 90: Velocity distribution over the plane of symmetry for six inlets

5. CONCLUSIONS

In this article, the authors have presented an effective alternative to wind energy harnessing and a promising solution to low-wind regime applications. Results indicated an increased wind speed from 2 m/s to 10 m/s for the preliminary unidirectional model, leading to an enhanced available power at the rotor and a speed ratio of 5. The issue of capturing wind from more than one direction was also addressed through the omnidirectional intake. It appeared that omnidirectional capturing led to even higher speeds at the location of the turbine, namely, 12 m/s for two inlets, 17 m/s for four inlets, and 23 m/s for six inlets. The authors' requirements were met by the findings of this article. The key here was to design a system that primarily operates in low-wind areas, but could also be installed in otherwise potential utility-scale wind energy sites. Although substantial progress has been made in ducted turbines designed to work in low-wind regime applications, AirAid works to outperform them by achieving far greater speed ratios. This calls the need for further development of AirAid by modelling it in turbulent conditions and by further scaling and optimizing the model to achieve higher speed ratios for smaller dimensions.

6. REFERENCES

ALLAEI, D., Andreopoulos, Y., 2014. INVELOX: Description of a new concept in wind power and its performance evaluation. Elsevier, energy 69, 336-344.

ALLAEI, D., Andreopoulos,Y., 2013. ASME 2013 7th international conference on energy sustainability & 11th fuel cell science, engineering and technology conference ES-fuel cell. Minneapolis, MN, USA.

GRANT, A., Kelly, Kelly D., 2003. 8th international IBPSA conference. Eindhoven, Netherlands.

PHILIBERT C., Holttinen, H., , 2013. Technology Roadmap Wind energy. 2013 edition. France: IEA publications.

TEGEN, S., Lantz, E., Hand, M., Maples, B., Smith, A., Schwabe, P., 2013. 2011 cost of wind energy review. 2013 edition. USA: National Renewable Energy Laboratory.

WISER, R., Bolinger, M., 2013. 2012 Wind technology market report. 2013 edition. USA: U.S. Department of energy.

257: Renewable energy potential maps for building thermal design in China

Siqiang Lu[1], Kazuo Emura[2], Jun Wang[3], Feng Xiong[4], , Ming Qu[5]

1College of Architecture and Environment, Sichuan University, No. 24, First loop south first section, Chengdu City, Sichuan Province, China, Lusiqiang@scu.edu.cn
2 Graduate School of Human Life Science, Osaka City University, 3-3-138 Sugimoto Sumiyoshi-ku, Osaka-shi, 558-8585,JAPAN, emura@life.osaka-cu.ac.jp
3 College of Architecture and Environment, Sichuan University, No. 24, First loop south first section, Chengdu City, Sichuan Province, China, wangjunhvac@163.com
4College of Architecture and Environment, Sichuan University, No. 24, First loop south first section, Chengdu City, Sichuan Province, China, fxiong@scu.edu.cn
5Sichuan Provincial Architectural Design and Research Institute, No. 688, Tianfu road middle section, Chengdu City, Sichuan Province, China, 306322159@qq.com

Abstract: This paper examines the potential for use of several types of renewable energy through the creation and analysis of maps of potential usage in China. Passive solar potential (PSP) to heat houses, and the nocturnal cold air potential (NCP), the evaporative cooling potential (ECP) and the nocturnal radiative cooling potential (RCP) to cool houses in China are examined. The Standard Year Weather Data for calculating the heat load of buildings is selected to analyzing the regional climate. From it, these potential indictors are evaluated by formulations with showing these attributions. By calculating these indicators at 270 locations throughout China, contour maps are drawn and their indication of potential effect on utilizable renewable energy is analyzed. Through use of these maps, the suitability of these renewable energy technologies in a location can be determined. It is expected that such information on energy conservation can be useful to architects and designers at the first stage of building planning.

Keywords: renewable energy; efficiency; potential map; passive solar; nocturnal cool air; evaporative cooling; nocturnal radiative cooling

1. INTRODUCTION

Methods to make use of renewable energy have been employed since antiquity. Solar energy and wind energy are renewable energy sources, with a small environmental load. The necessity and effectiveness of renewable energy for building plans are quantified as energy sources that can be used according to the seasonal changes in climate. This research is more active than before (Kodama, Y. et al, 1982: page 39;Jiangnan Li, 2009; Ishihara, O. et al,1998: page 15). It is important to China as the economy quickly grows and energy consumption is high and increasing into the future. However, this does not justify the application of any and all renewable energy technology anywhere and everywhere. It is also important to evaluate the effect of using it. Therefore, it is necessary to know the potential for use of renewable energy according to the climate characteristics of the location.

2. WEATHER DATA FOR ANALYSIS

In this paper, the Chinese Standard Weather Data (CSWD) (China Standard Weather Data for Analyzing Building Thermal Conditions, 2005) is used. After comparing the five kinds of Standard Year Weather Data in China and showing the difference between data (Lu, 2009: page 73; Lu 2008: page1), CSWD is adopted for analysis and calculation of the indictors of potential. This data is suitable for the research in that solar radiation data is needed in this study, and the daily solar radiation was measured in many of these stations (270). Figure 1 shows the distribution of these data in China. The number of points located in the west part of China is small. If it is considered that over 94% of the population is concentrated on the eastern part of China, this analysis will be most accurate for the great majority of builders in China, while builders in the west should keep in mind the above facts.
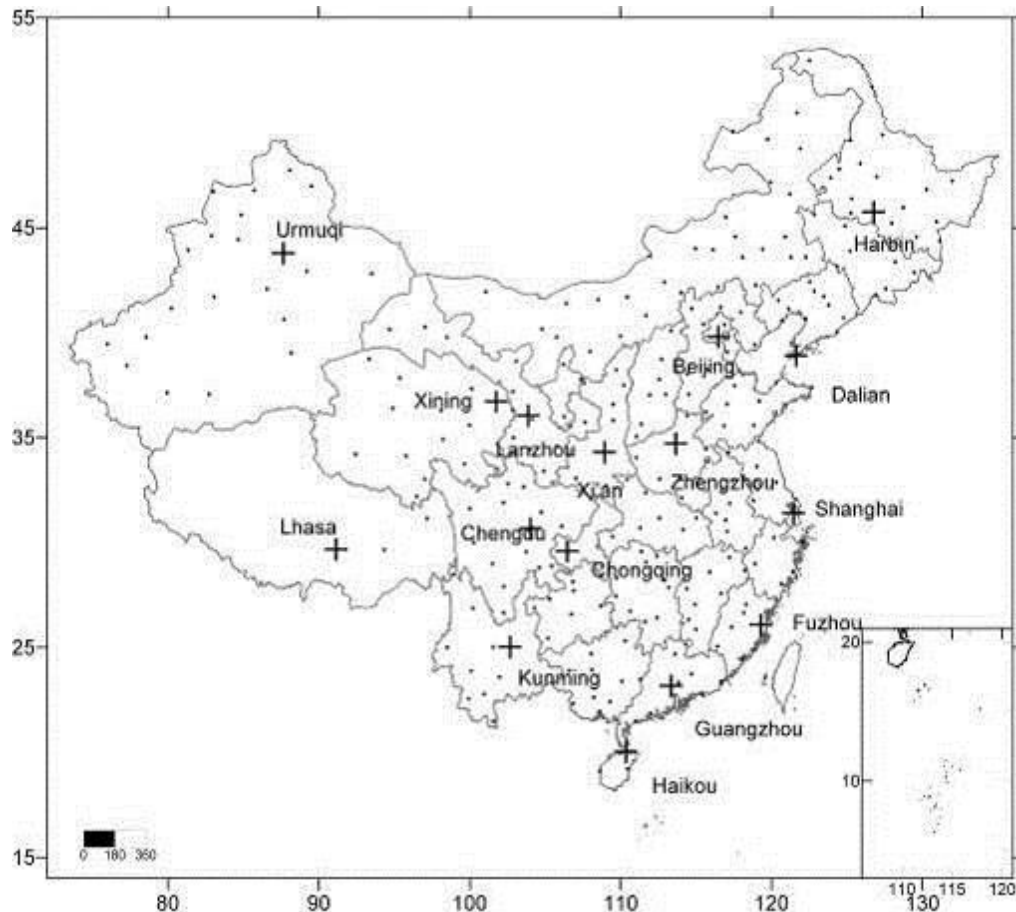
Figure 1: Distribution of all locations

3. RENEWABLE ENERGY POTENCIAL ANALYS

Here, Matusmoto's (2008: page 57) paper is referred to for calculating each indicator on evaluating the potential. Time periods for using renewable energy are divided roughly as "summer" and "winter", though this may differ from an actual situation. The heating season and the cooling season are defined as the days where the daily mean temperature is higher than 22ºC and lower than 18 ºC at each location respectively.

3.1.Passive Solar Potential

Passive construction doesn't rely on the efficient use or generation of power. Instead, the use of renewable energy takes an integral part in devising the plan of construction (Yoshimura, D. and Nishioka, T., 1999: page 477; Osaki, F. and Takahashi, I., 2006: page 585; Qian Wang et al., 2009). The installation of photovoltaic cells and solar water heaters are well-known as examples of solar energy use. The passive solar house uses and/or stores solar energy as heat, and uses the heat to affect the room temperature in the building. This can reduce heating costs and make a comfortable living environment by use of radiant heating. Use of solar energy for heating of buildings is influenced mainly by the south vertical surface. The heating degree day is usually often shown as an indicator of the heating load. The value of cumulative solar radiation on the south vertical surface per heating degree-day is defined as PSP. It is expressed as:

Equation 60: cumulative solar radiation on the south vertical surface per heating degree-day.

$$PSP = \frac{I_s}{HDD_{18-18}}$$

Where

- I_S = the cumulative solar radiation on south vertical surface in the heating season (when average daily air temperature<18 ⁰C)(Wh/m²)
- HDD_{18-18} = heating degree-days when the indoor temperature is set at 18 ⁰C (K·day)

Using the calculated PSP at 270 locations, a contour map is made and shown in Figure 2. For home heating, the PSP value is 150-250Wh/m²·K in most parts of China. It can be seen that the potential use of solar radiation heat is particularly high in the southern seaside region and the southwestern region. As the solar radiation is lower in the Sichuan basin and the value of the heating degree days is large in the north, the PSP potential is small in these two regions.
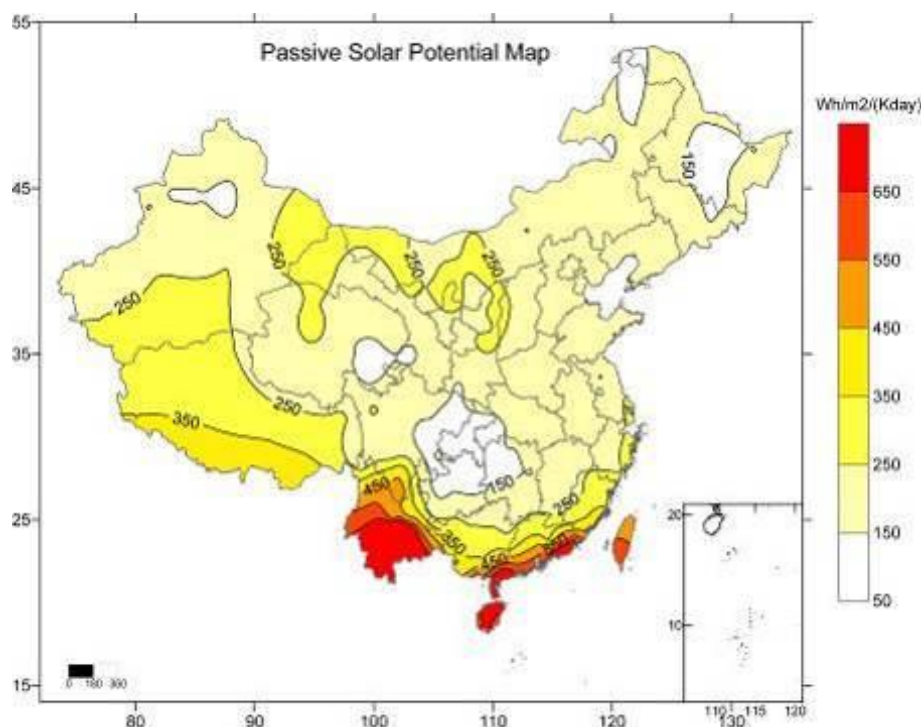
Figure 2: Passive solar potential map in China

3.2 Nocturnal Cold Air Potential

Ventilation cooling is a method of reducing the room cooling load by ventilation and cool storage by cold air at night time (Akabayashi, S. et al., 2003: page 49; Wang, Z. et al., 2006). In a concrete building, as its specific heat capacity is large, it is possible to save the heat in the walls and the floors as a cold source by the air taken in at night time, then those cooled walls and floors can absorb heat from the air and the human body in the room in daytime. As a result, it is possible to reduce the cooling load in daytime. Ventilation cooling is usually used along with nocturnal radiation cooling. The nocturnal cold air potential indicator is

calculated from the difference between the outside average air temperature that is lower than preset temperature (28℃) at night time and 28℃ in the cooling season, and the ECP value at each of the various locations is calculated over the cooling season by:

Equation 2: the value of NCP,

$$NCP = \frac{\sum_{1}^{n_c}(\theta_c - \theta_{night})}{n_c}$$

Where :

- n_c = days of cooling season (-)
- θ_c = the preset temperature of the cooling season (28 ℃ here) (℃)
- θ_{night} = air average temperature during the night period in the cooling season(℃)

The nocturnal cold air potential map is shown in Figure 3. The NCP value of 0-4K is indicated in the eastern region, and there is 6K or more of NCP in the interior area of the northeast and the west. NCP is low and possibly ineffectual in the southeast region. Ventilation cooling can be used as a method of taking the place of the equipment to reduce the cooling load in the region that is not intensely hot in summer. Some effect is expected in central part and west part of China. In contrast, the daily mean temperature is lower than 22℃ even in the cooling season in the Tibetan plateau; the NCP value is 0 because cooling is unnecessary (Lu, Siqiang. et al., 2010)
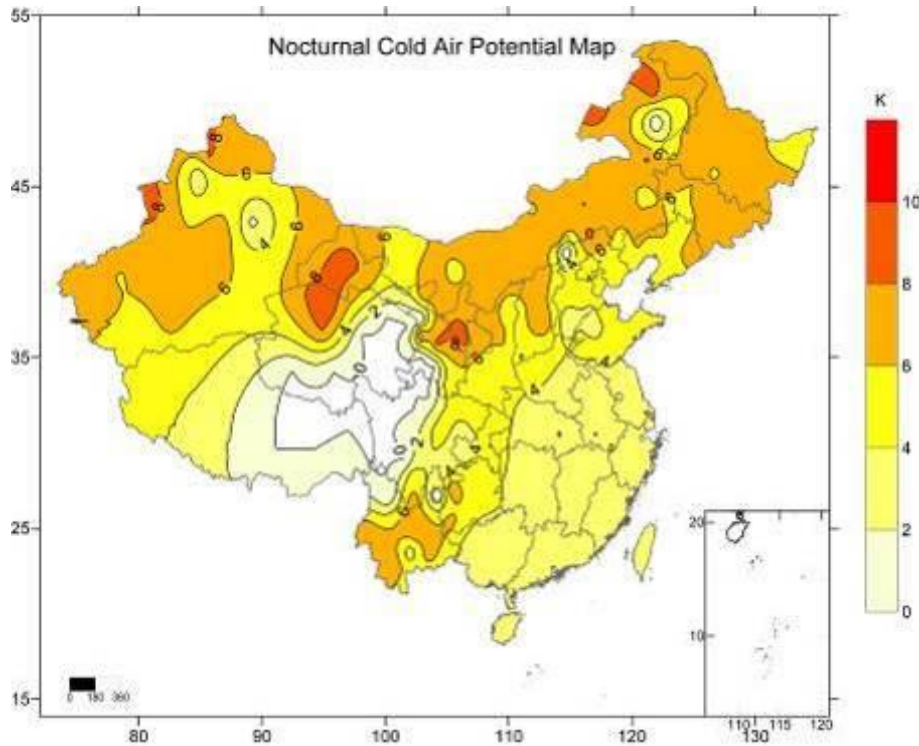
Figure 3: Nocturnal cold air potential map in China

3.3 Evaporative Cooling Potential

Evaporation cooling uses the evaporative latent heat when water evaporates, this can be employed as a method of energy conservation to reduce the cooling load by using the phenomenon at the outer surface of the building to be cooled (Okabe, Y. et al., 2008: page 551;Guo, Xuesen et al., 2009). Roof watering, and improving the air-conditioning efficiency by directing atomized droplets of water onto the outdoor air-conditioning machine, wall cooling with water film are some examples of realizing this effect. Evaporation cooling is strongly influenced by the air temperature, absolute humidity and the wind speed; the ECP value is expressed as:

Equation 3: the value of NCP

$$ECP = \frac{\bar{a} \cdot r}{c}(\bar{x} - \bar{x}_s)$$

Equation 4: the value of convective heat transfer coefficient.

$$\bar{a} = \begin{cases} 4.2 \cdot \bar{\upsilon} + 6.2; & \bar{\upsilon} \leq 5m/s \\ 7.5 \cdot \bar{\upsilon}^{0.78} & ; \ \bar{\upsilon} > 5m/s \end{cases}$$

Where:

- $\bar{a}$ = average convective heat transfer coefficient during the cooling season (W/(m²·K))
- r = he evaporative latent heat of water (2500.8) (J/ (kg·K)
- C= the specific heat of moist air at constant pressure ($c = 1004.6 + 1846 \cdot \bar{x}$) (J/ (kg·K))
- $\bar{x}$ = the average absolute humidity during the cooling season(kg/kg·DA)
- $\bar{x}_s$ = the average absolute saturation humidity during the cooling season(kg/kg·DA)
- $\bar{\upsilon}$ = average wind speed during cooling season (m/s)

If the area where air-conditioning is unnecessary is excluded, the value of ECP is smallest (less than 100W/m²) in south. The ECP value is more than 250W/m² in Xinjiang (western China) and Inner Mongolia (north central China) and 100-200 W/m² in the northeast and northwest of China. When evaporation cooling technology is used, a larger effect is expected.
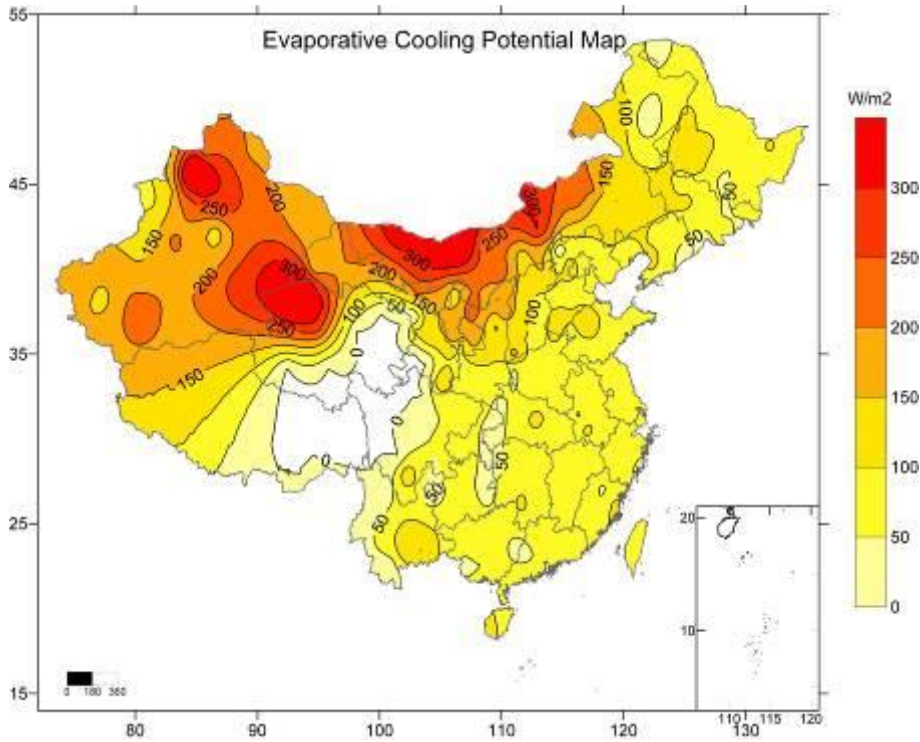
Figure 4: Evaporative cooling potential map in China

2.20. 3.4. Nocturnal Radiative Cooling Potential

The ground surface and air in the vicinity of the ground surface is cooled from the atmosphere by the difference between a downward radiation to ground surface and the radiation of heat to the atmosphere (nocturnal radiation) at night time. This is called nocturnal radiation cooling, and it can be used to reduce the cooling load of the building (Miura, T. et al., 2008: page 559; Peng, 2005)The atmospheric radiation is strongly related to the amount of water vapor in the atmosphere. Nocturnal radiation is stranger from surfaces with a high temperature and when atmospheric radiation is low. The cooling effect can be expected to be higher at night time in areas with dry air and clear sky. In general, the influence of vapor is calculated by using the expression of Brunt based on the outside temperature (Ohashi, K. et al., 1999:page 23). The atmospheric radiation is expressed here by equation 5. The nocturnal radiation cooling potential becomes equation 6 from the thermal radiation of the atmosphere of night time.

Equation 5: the value of the atmospheric radiation.

$$J_A = 109.91 + 4.56\sqrt{e} + 0.25 \cdot \sigma_b \cdot T_{night}^4$$

Equation 6: the value of NCP:

$$RCP = \frac{\sum_{1}^{n_c}(\sigma_b \cdot T_{night}^4 - J_A)}{n_c}$$

Where:

- n_c = days of cooling season (-)
- T_{night}= the average absolute air temperature during the night period (1:00am-sunrise & sunset-24:00pm) in the cooling season (K)
- J_A= the average atmospheric radiation during the night period in the cooling season (W/m^2)
- σ_b= the Stefan-Boltzmann constant ($5.67*10^{-8}$)(W/ (m$^2 \cdot$K^4))
- e= the average vapor pressure during the night period (Pa)

Figure 5 shows the distribution of RCP. The difference between the south and the north is remarkable. It becomes 90W/m^2 or less in most regions in the south. RCP is large in the northern part of Xinjiang, Inner Mongolia and Qinghai.
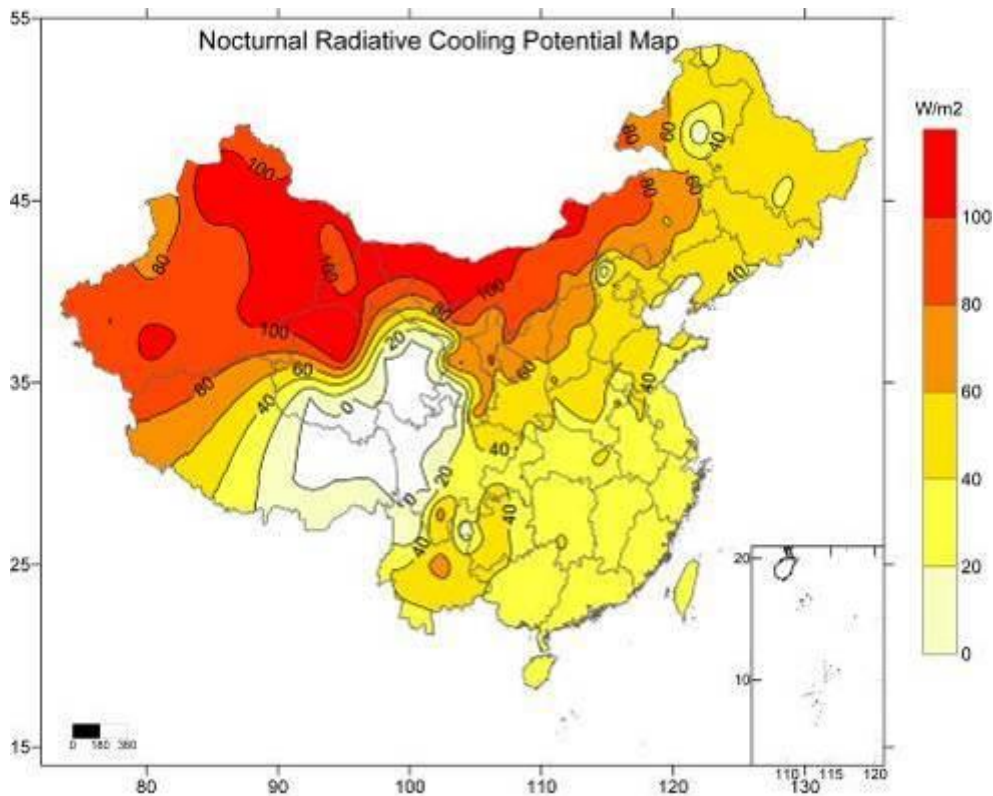
Figure 5: Nocturnal radiative cooling potential map in China

4. CONCLUSIONS

The natural renewable energy potential indictors at 270 points nationwide were calculated by using the Standard Year Weather Data. To apply to all the area of China, a passive solar potential map, a nocturnal cold air potential map, an evaporation cooling potential map and a nocturnal radiative cooling potential map for use in building design were made. The following conclusions can be made:

- Solar radiation heat can be significant for use at the seaside region and the southwest in the heating season.
- Some effect is expected nationwide with nocturnal cold air in summer, excluding the southeast area of China.
- Evaporation cooling is possible to use widely with a value of 50W/m^2 in most areas of China. It may be most advantageous for cooling in Xinjiang and Inner Mongolia.

– The potential of nocturnal radiation cooling is largest Xinjiang, Inner Mongolia and Qinghai. It becomes 40W/m^2 or less in most regions in the southern part of China.

5. ACKNOWLEDGEMENTS

6. REFERENCES

KODAMA, Y. et al. 1982, Regional climate map based on AMeDAS for building design. Summaries of technical papers of Annual Meeting Architectural Institute of Japan, 39-42

LI,Jiangnan. 2009, Design of passive solar building. Solar Energy. No. 10

ISHIHARA, O. et al. 1998, Preparation of meteorological data and climate maps for natural energy utilization. J. Archit. Plann. Environ. Eng., AIJ, No. 509, 15-20

China Meteorological Bureau, Climate Information Center, Climate Data Office and Tsinghua University, Department of Building Science and Technology. 2005, China Standard Weather Data for Analyzing Building Thermal Conditions. China Architecture & Building Press.

LU, Siqiang. et al. 2009, Comparison of standard year weather data of five cities in China. Transactions of the Society of Heating, Air-Conditioning and Sanitary Engineers of Japan, 146, 73-81

LU, Siqiang. et al. 2008, Comparison of standard year data of five cities in China by simulation. Technical Papers of Annual Meeting of IBPSA-Japan, 1-6

MATSUMOTO, S. et al. 2008, Proposal of Natural Energy Utilization Maps for Bioclimatic Environmental Design. Summaries of technical papers of Annual Meeting Architectural Institute of Japan Tohoku Brunch, 57-66

YOSHIMURA, D. and Nishioka, T. (1999) Study on passive solar house in Hokuruku district (No. 2 Comparison of Tokyo and Fukui in heating load saving). Summaries of technical papers of Annual Meeting Architectural Institute of Japan, 477-478

OSAKI, F. and Takahashi, I. 2006, A Trial of supporting residents in lifestyle of passive cooling. Summaries of technical papers of Annual Meeting Architectural Institute of Japan, 585-586

WANG, Qian et al. 2009, Application and development of solar energy heating system. District Heating. No. 1

AKABAYASHI, S. et al. 2003, Study on of the evaluation method of a cross ventilated building performance. J. Environ. Eng., AIJ, No. 568, 49-56

WANG, Z. et al. 2006, Experimental study on night ventilation to improve thermal environment in office rooms. Journal of Harbin institute of technology. Vol. 38(12)

LU, Siqiang. et al. 2010, Distribution characteristics of heat load and correlation with meteorological elements in China. Sichuan Building Science, 36(2)

OKABE, Y. et al. 2008, Study on effectiveness of intermittent evaporation cooling with photocatalyst-coated exterior materials. Summaries of technical papers of Annual Meeting Architectural Institute of Japan, 551-554

GUO, Xuesen et al. 2009, The present condition and prospection of direct evaporative cooling systems. Building Energy & Environment. Vol. 28 (03)

MIURA, T. et al. 2008, Experimental study on evaporation cooling effect by sprayed mist. Summaries of technical papers of Annual Meeting Architectural Institute of Japan, 559-562

PENG, Changhai 2005, Try to discuss the contribution of nocturnal radiation to the thermal surroundings of buildings. Industrial Construction. Vol. 35 (09)

OHASHI, K. et al. 1999, The estimated method and the easy observed method with the atmospheric radiation quantity and nocturnal radiation quantity for the natural energy use. J. Archit. Plann. Environ. Eng., AIJ, No. 522,

SESSION 36: LOW-CARBON/ LOW-ENERGY TECHNOLOGIES

55: Heating and cooling performance of a minitype ground source heat pump system

X.Q. Zhai[1], R.Z. Wang[1]

[1] Shanghai Jiao Tong University, 800 Dongchuan Road, Shanghai, China, xqzhai@sjtu.edu.cn

A minitype GSHP system was designed and installed in the green energy building of Shanghai Jiao tong University for the purpose of satisfying the thermal environment of a meeting room with the covered area of 180 m2. The rated cooling capacity of the heat pump is 22.3 kW with the electricity consumption of 5.3 kW. Correspondingly, the rated heating capacity and electricity consumption in heating mode is 29.5 kW and 6.9 kW, respectively. The ground heat exchanger consists of 9 vertical boreholes. There is a single U-tube with the diameter of 32 mm in each borehole. The whole length of the U-tube is 580 m. The experimental investigation was carried out in both cooling mode and heating mode. After one year, the average temperature of soil was about 18 oC, which is nearly the same as the original soil temperature. The experimental results are instructive to the design and operation of GSHP systems in Shanghai and other cities with similar climatic feature.

Keywords: Ground source heat pump, Heating performance, Cooling performance

1. INTRODUCTION

It was estimated that heating, ventilation and air-conditioning (HVAC) systems accounted for about 65% of the energy consumption in the buildings of China (YANG, 2008). Therefore, it is strongly necessary to reduce the energy consumption in HVAC systems. Recently, both professionals and policymakers have been making great efforts in this aspect (YANG, 2010). It seems that the most effective approach is to improve the utilizations of energy conservation techniques and renewable energy. Ground source heat pump (GSHP) is a highly efficient, renewable energy technology for space heating and cooling. This technology relies on the fact that, at depth, the Earth has a relatively constant temperature, warmer than the air in winter and cooler than the air in summer. A GSHP can transfer heat stored in the Earth into a building during the winter, and transfer heat out of the building during the summer. GSHP technology is receiving increasing interest because of their potential to reduce primary energy consumption and thus reduce emissions of greenhouse gases (MUSTAFA OMER, 2008). It is reported that GSHP technology was well established with over 550,000 units installed worldwide and with more than 66,000 units installed annually. About 80% of the units installed worldwide are domestic (FLORIDES, 2007). GSHP systems have become attractive choices for both residential and commercial buildings because of their higher energy efficiency compared with conventional air-source heat pump (ASHP) systems.

In this paper, a minitype GSHP system was designed and installed in the green energy building of Shanghai Jiao tong University for the purpose of satisfying the thermal environment of a meeting room with the covered area of 180 m². The experimental investigation was carried out in both cooling mode and heating mode.

2. DESIGN OF GROUND SOURCE HEAT PUMP SYSTEM

The ground source heat pump system mainly includes a ground heat exchanger, a minitype ground source heat pump and circulating pumps, as shown in Fig. 1. Table 1 describes the main parameters of the ground source heat pump. The ground heat exchanger (GHE) consists of 9 vertical boreholes, which are divided into 3 groups (GHE I, GHE II and GHE III). There are 3 vertical boreholes with the depth of 80 m in the GHE I. As for GHE II and GHE III, there are also 3 vertical boreholes with the depth of 60 m and 50 m, respectively. Such an arrangement is mainly for the purpose of investigating heat transfer with different depth of the boreholes. Table 2 describes the main parameters of the ground heat exchanger.
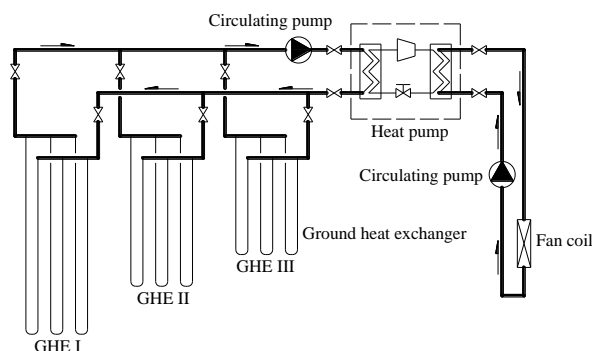
Figure 1: Diagram of ground source heat pump system

Table 1: Parameters of the ground source heat pump

Name	Cooling mode	Heating mode
Rated heat capacity / kW	22.3	29.5
Inlet / outlet temperature / °C	12 / 7	40 / 45
Fluid	Water / R134a	Water / R134a

Table 2: Parameters of the ground heat exchanger

Distance between boreholes / m	5
Depth of boreholes in the GHE I / m	80
Depth of boreholes in the GHE II / m	60
Depth of boreholes in the GHE III / m	50
Diameter of boreholes / mm	160
U-tube material	PE
U-tube type	DN32
U-tube conductivity / W/(m·k)	0.46
Shank spacing between tubes / mm	80
Soil type	sand clay
Soil conductivity / W/(m·k)	1.64

3. PERFORMANCE OF THE GROUND SOURCE HEAT PUMP SYSTEM

The performance of a GSHP system in an archives building has been presented in the research papers of our research group. In this new application case, the experimental results in a typical winter day and a typical summer day were used to show the performance of the GSHP system. The average ambient temperatures in these two days were 2.5 °C and 34.3 °C, respectively.

Fig. 2 (a) shows the variations in inlet and outlet water temperatures of the GHE in typical heating mode. It is observed that the outlet water temperature of the GHE was about 15 °C when the heat pump was turned on at 8:00, then gradually descended, and approached the value of 11.5 °C or so at 10:00. The rate of temperature drop was 1.7 °C/h during this period of time. From then on, the outlet water temperature fell off with the rate of temperature drop of 0.1 °C/h until the heat pump was shut down. It is also deduced that the average outlet water temperatures was 11.3 °C for GHE I, correspondingly, 10.7 °C for GHE II and 10.4 °C for GHE III. The deeper the vertical boreholes, the higher the outlet water temperature of GHE. However, the temperature difference among them was less than 1 °C. As a whole, the average outlet water temperature for the total GHE is 10.8 °C. Besides, the average water temperature of the inlet of the GHE during the operation of the system was concluded to be about 8.2 °C, which was 2.6 °C lower than that of the outlet of the GHE. Taking the total GHE into account, the average heat transfer between ground heat exchanger and soil was 26.5 W/m.

Fig. 2 (b) shows the variations in inlet and outlet water temperatures and heating capacity of the heat pump in typical heating mode. It is observed that both inlet and outlet water temperatures of the heat pump rapidly went up in the first two hours, then gradually rose, and tended to be smooth. The average inlet and outlet water temperatures were concluded to be 36.7 °C and 41.3 °C, respectively. As a result, the system yielded an average heating capacity of 20.9 kW during the all-day operation with an average COP of 3.
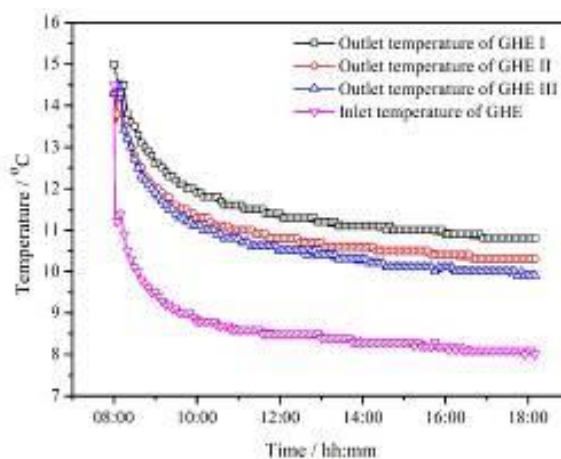
(a) Variations in inlet and outlet water temperatures of GHE
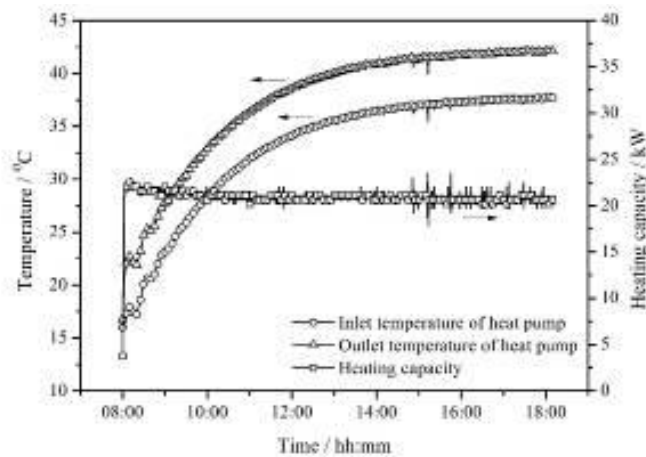
(b) Variations in inlet and outlet water temperatures and heating capacity of the heat pump.

Fig. 2   Operation of the GSHP system in typical heating mode

Fig. 3 (a) shows the variations in inlet and outlet water temperatures of GHE in typical cooling mode. It is observed that the outlet water temperatures of the GHE rapidly increased from 20 ^{o}C to 25 ^{o}C or so in the first hour of operation, then gradually increased with the rate of temperature rise of 0.4 ^{o}C/h. During the operation of the GCHP system, the mean value of outlet water temperature for GHE I was 27.6 ^{o}C, correspondingly, 28.3 ^{o}C for GHE II and 28.9 ^{o}C for GHE III. Therefore, the mean value of outlet water temperature for the total GHE was deduced to be 28.3 ^{o}C. From Fig. 8 (a), it is also obtained that the mean value of inlet water temperature of GHE was 33.6 ^{o}C, which was 5.3 ^{o}C higher than that of outlet water temperature. Thereby, the mean value of heat transfer between ground heat exchanger and soil for the total GHE was deduced to be 48.8 W/m. Besides, it is also noticed that the outlet water temperatures for the three GHEs present a small difference although deeper boreholes are more efficient, which is similar to that in the heating mode. However, the construction cost for deep boreholes is more expensive than that of shallow boreholes. Thus the depth of boreholes for such minitype GCHP systems may be 50-60 m if there is enough space for the installation of ground heat exchangers.

Fig. 3 (b) shows the variations in inlet and outlet water temperatures and cooling capacity of the heat pump in typical cooling mode. It is seen that both the inlet and outlet water temperatures of the heat pump quickly decreased in the first hour of operation, and then varied smoothly. The average inlet and outlet water temperatures of the heat pump were 12 ^{o}C and 7.8 ^{o}C, respectively, with a temperature difference of 4.2 ^{o}C. Accordingly, it was deduced that the average cooling capacity was 17 kW with the COP of 3.2.
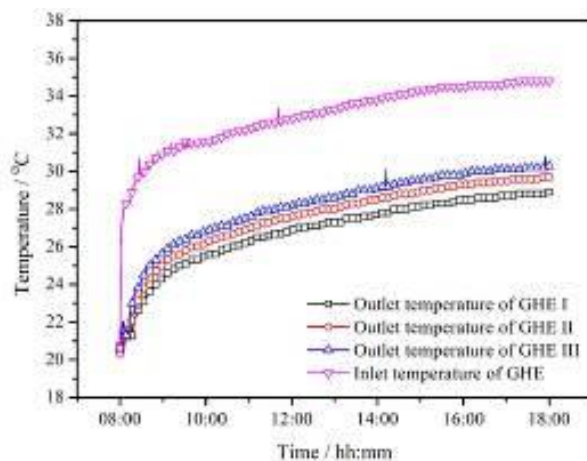
(a) Variations in inlet and outlet water temperatures of GHE
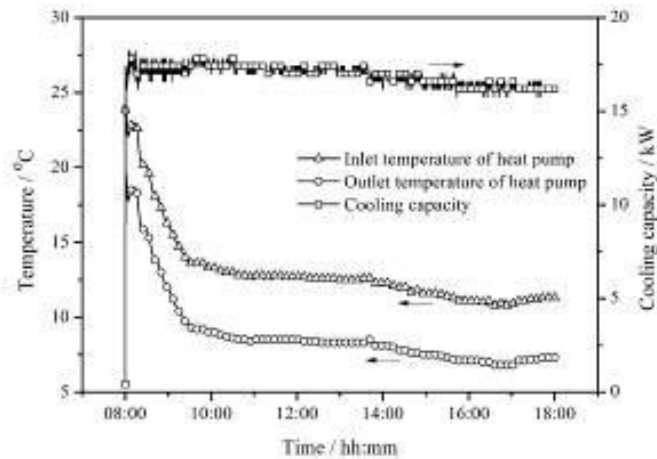
(b) Variations in inlet and outlet water temperatures and cooling capacity of the heat pump

Fig. 3 Operation of the GSHP system in typical cooling mode

The initial temperature of the soil was measured to be 17.8 °C. The variation in temperature of soil after the system had operated for a year is shown in Fig. 4. It showed little variation in the soil temperature even after a year-round operation of the system according to Fig. 4. Consequently, the GCHP system is capable of supplying heating and cooling for the meeting room without affecting the thermal balance in earth energy.

Generally speaking, the air-conditioning systems in Shanghai are air-source heat pumps. The COP of such systems are always lower than 3. Besides, there exists frosting phenomenon for air-source heat pumps in winter because the ambient temperature may be lower than -4 °C, which makes the heating performance worse. The ground temperature is higher than that of the outside air in winter and is lower in summer. A GSHP can be used to extract heat from the relatively warm ground and pump it into the conditioned space. In summer, the process may be reversed and the heat pump may extract heat from the conditioned space and send it out to a ground heat exchanger that warms the relatively cool ground. The experimental results show the applicability of GSHP systems for buildings in Shanghai. Moreover, such minitype GSHP systems can be widely used in dwellings of rural areas in Shanghai, where the space for the installation of ground heat exchangers is usually enough.
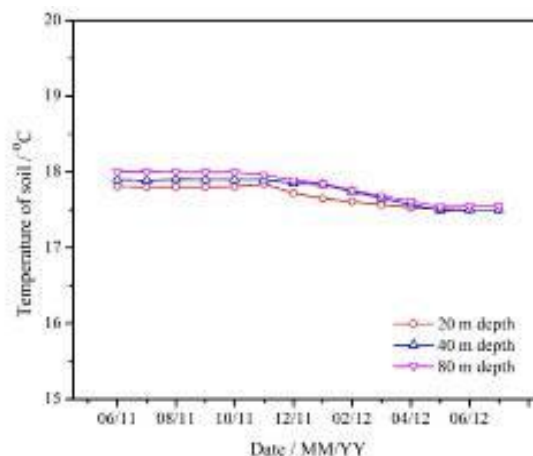
Fig. 4 Variations in temperature of soil.

4.   CONCLUSION

The GSHP system is capable of supplying heating and cooling for the meeting room with the area of 180 m^2 without affecting the thermal balance in earth energy. The average heating capacity was 20.9 kW with the COP of 3 in the typical heating mode. Meanwhile, the average cooling capacity was 17 kW with the COP of 3.2 in the typical cooling mode. The experimental results show the applicability of GSHP systems for buildings in Shanghai. Moreover, such minitype GSHP systems can be widely used in dwellings of rural areas in Shanghai, where the space for the installation of ground heat exchangers is usually enough.

5. REFERENCES

YANG, Liu, 2008. Energy performance of building envelopes in different climate zones in China. Applied Energy, 85, 800-817.

YANG, Wei, 2010. Current status of ground-source heat pumps in China. Energy Policy, 38, 323-332.

MUSTAFA OMER, Abdeen, 2008. Ground-source heat pumps systems and applications. Renewable and Sustainable Energy Reviews, 12, 344-371.

FLORIDES, Georgios, 2007. Ground heat exchangers-A review of systems, models and applications. Renewable Energy, 32, 2461-2478.

244: Experimental study on a direct-expansion solar-assisted heat pump

WENZHU HUANG，JIE JI *， NING XU, FANGLIANG ZHAO, HAOFANG ZHENG

Department of Thermal Science and Energy Engineering, University of Science and Technology of China
#96 Jinzhai Road, Hefei City, Anhui Province, People's Republic of China
Corresponding authors email: jijie@ustc.edu.cn

In this study, a direct expansion solar-assisted heat pump system (DX-SAHP) with bare flat plate collectors is investigated experimentally in the enthalpy difference lab with a solar simulator and tested for space heating under different stable conditions. The influence of solar irradiation and outside temperature on the heating performance of DX-SAHP is analyzed. When outside temperature changes from 5℃ to 15 ℃ with solar irradiation of 300 W/m2， COP increases from 1.83 to 1.99, while the evaporator temperature and the condensing heat exchange rate increases by 8.9℃ and 25%. Moreover, When solar irradiation changes from 100 W/m2 to 300 W/m2 with outside temperature of 15℃， COP of the system increases from 1.85 to 1.99, and the evaporator temperature and the condensing heat exchange rate increases by 2.0℃ and 21.0%, respectively. It is observed that when outside temperature is 7℃, without irradiation, after 30 min the evaporator is seriously frosted and the evaporating temperature is -0.77℃,while under irradiation of 80 W/m2 the evaporator is not frosted and the evaporating temperature and COP is respectively 3.12℃ and 15.5% higher than the former situation.

Keywords: Solar-assisted; Heat pump; COP; Exergy

1. INTRODUCTION

Solar energy has been the subject of many researches, since it is renewable and clean. Heat pump can perform more effectively than common heating system and is widely used. To combine solar energy and heat pump, the concept of direct expansion solar assisted heat pump (DX-SAHP) was first outlined by Sporn and Ambrose[1]. Solar assisted heat pump system is an alternative to use solar energy and improve the conventional heat pump performance. According to the connecting mode of solar collector and evaporator, solar assisted heat pump can be classified as the direct expansion solar assisted heat pump and the indirect expansion solar assisted heat pump.

In a direct expansion solar assisted heat pump, the collector works as the evaporator, where the refrigerant gets evaporated directly. Many experimental and theoretical studies have been reported on DX-SAHP. Krakow and Lin[2] studied the performance of direct expansion solar assisted heat pump systems with unglazed solar collectors and single glazed solar collectors under cold climates. They concluded that the system with glazed solar collectors was preferable to the system with unglazed solar collectors. Huang and Chyng[3] built an integral type solar assisted heat pump water heater with a collector/evaporator and a thermosyphon heat exchanger and studied the performance of the system. The COP of the system was 2.5-3.7 at water temperature between 61 and 25 °C. Kuang and Wang[4] tested a direct expansion solar assisted heat pump system for domestic use. The system can operate under space heating mode, air conditioning mode and water heating mode. The experiments showed that the system obtained COP of 2.6 to 3.3 for space heating and could supply 200 L or 1000 L hot water daily under various weather conditions. However, comprehensive study on DX-SAHP under stable and widely varying conditions is rare.

Parameters that influence the performance of DX-SAHP were studied. Chaturvedi and Abazeri[5] investigated the parameters influencing the performance of a capacity-modulated direct expansion solar assisted heat pump system including the collector area, the compressor speed, the load temperature and refrigerant properties. Chaturvedi et al.[6] developed a variable capacity direct expansion solar assisted heat pump system and modulated the compressor speed to match the heat pumping capacity of the compressor and the evaporative capacity of the collector under different ambient conditions. The influence of the compressor speed on the performance of the system was studied and conclusion was drawn that the compressor speed should be lowered as ambient temperature rises. Ito et al. [7] further studied the influence of the parameters theoretically and experimentally, and optimized the structure parameters of solar collector such as collector area, thickness of the plate and materials of the collector. Hawlader et al.[8] paid attention to the influence of the volume of water tank on the performance of DX-SAHP water heater.

Theoretical investigations of DX-SAHP have been reported: Kong et al.[9] theoretically studied a DX-SAHP water heater and showed that increasing wind speed could increase COP and efficiencies. Moreover, Chow et al. [10]developed a numerical model of DX-SAHP for water heating with an unglazed solar collector. They simulated the performance of the system in a whole year, obtained a year-long average COP of 6.46 in Hong Kong and proved the system promising. Chyng et al.[11] theoretically investigated an integrated solar assisted heat pump water heater with a bare collector and studied its performance in a year. They showed that the daily total COP is around 1.7 to 2.5 year around for the system.

In this paper, a direct expansion solar-assisted heat pump system (DX-SAHP) with bare flat plate collectors is investigated experimentally in the enthalpy difference lab with a solar simulator and tested for space heating under different stable conditions. The influence of solar irradiation and outside temperature on the heating performance of DX-SAHP is analyzed. The frosting performance is also studied under different solar irradiation. The work has good reference value for further experimental and theoretical study of DX-SAHP.

2. EXPERIMENTAL SETUP

2.1 Experimental setup design

The experiments are carried out in an enthalpy difference lab which has two psychometric chambers, named outdoor and indoor chamber, respectively. The outdoor and indoor ambient temperature and humidity can be maintained as constants, by the operating of the indoor and outdoor unit installed in the chambers. An air-enthalpy type calorimeter is located in the indoor chamber, which can measure the heating capacity of the indoor air heat exchanger by the air enthalpy difference method (ASHRAE Standard 116, 1993). Moreover, a solar simulator is configured in the outside chamber to simulate solar irradiation

on the surface of the collectors. As the spectrum distribution satisfies the National Class B level standard, and the heterogeneity and instability of the solar simulator are under 5%, the solar simulator can effectively simulate solar irradiation. In addition, the luminous area is 4 m^2 and the adjustable range of the irradiation is 0 to 1200 W/m^2.

An experimental prototype of DX-SAHP was designed and setup in the enthalpy difference lab, as shown in Fig. 1. The system mainly consists of two collectors, a compressor, an air heat exchanger, and a capillary tube. The two flat plate collectors without back insulation or glazing, called bare collector in this paper, are connected in series. Each of the collectors is made by welding copper coil piping to an aluminum absorber plate with selective absorbing coating on the surface and an aperture area of 2 m^2. As a result, the collector has simple structure and low cost. The collector works as evaporator in the system. An R-22 rotary-type hermetic compressor is used whose rated input power is 750 W. In the experiment, the collector, the compressor and the capillary tube are fixed in the outdoor chamber of the enthalpy difference lab, while the air heat exchanger in the indoor chamber. All components are connected by copper pipe.
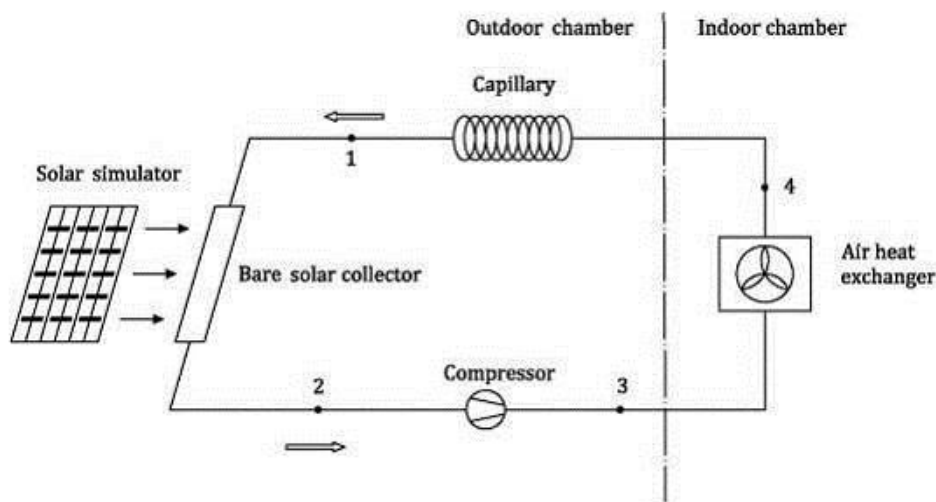
(a)
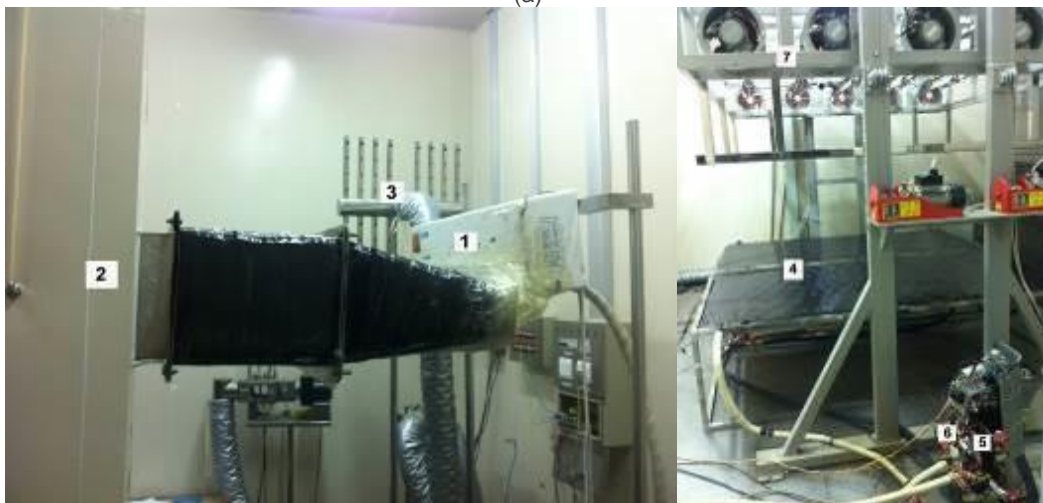
(b)

1. indoor air heat exchanger 2. air-enthalpy type calorimeter 3.indoor sampling device 4. bare flat plate collectors 5. compressor 6.capillary tube

Figure 91: (a) Schematic of the experimental setup of DX-SAHP (b) Photo of the DX-SAHP

2.21. 2.2 Instrumentation

The ambient temperature and humidity is measured by platinum resistance thermometer (with grade A accuracy). The other temperature of the system at various locations is measured by T-type copper-

constantan thermocouples. Except temperature, pressure, irradiation, power consumption and heating capacity are measured and recorded in the experiment. A digital power meter (WT 230) is used to measure the voltage, current and power of the system. The data is recorded automatically every 6 sec interval by a data logger (Angilent 34970A). The detail of the measurement instruments is shown in table 1.

Table 31: Characteristics of sensors and measurement instruments

Parameter	Range	Accuracy	Specification
Temperature/℃	-100-100	±0.2°C	T-type thermocouple
	-200-200	±0.1°C	Pt100 (Grade A accuracy)
Pressure/Mpa	0-2.5	0.3%	Huba pressure sensor
Irradiation/ W·m-2	0~2000	5%	Pyranometer
Power/kW		0.1%	WT230
Heating capacity/kW	0.5~13.5kW	1.2%	Air-enthalpy type calorimeter

3. THERMODYNAMIC ANALYSIS

The mass balance equation can be expressed as

$$\sum \dot{m}_{in} = \sum \dot{m}_{out}$$

Where $\dot{m}_{in}$ is the inlet mass flow rate and $\dot{m}_{out}$ is the outlet mass flow rate.

In this study, the general energy balance can be written as following

$$\dot{Q} + \dot{m}_{in} h_{in} = \dot{W} + \dot{m}_{out} h_{out}$$

Where $\dot{Q}$ is the rate of heat input, $\dot{W}$ is the rate of work output, h_{in} and h_{out} are the enthalpy of inlet and outlet refrigerant.

For the whole system, the energy balance equation is

$$\dot{Q}_{cond} = \dot{W}_{in} + \dot{Q}_{evap}$$

The heat absorbed by the collector is

$$\dot{Q}_{evap} = \dot{m}_r (h_2 - h_1)$$

Where the subscript "1" and "2" stands for the location shown in Fig. 1.

The condensing heat exchange rate can be expressed as follows:

$$\dot{Q}_{cond} = \dot{m}_r (h_3 - h_4)$$

As the condensing heat exchange rate is measured by the air enthalpy difference method, it can also be written as

$$\dot{Q}_{cond} = \dot{m}_a (h_{in} - h_{out}) / [V_n (1 + D_n)]$$

Where $\dot{m}_a$ is the air flow rate, h_{in} and h_{out} are the enthalpy of air entering and leaving the indoor air heat exchanger, V_n and D_n are the specific volume and humidity of air at the nozzle, respectively.

The coefficient of performance of the system is defined as

$$COP = \dot{Q}_{cond} / \dot{W}_{in}$$

4. RESULTS AND DISCUSSIONS

4.1 The influence of ambient temperature on the performance of the system

To investigate the influence of ambient temperature on the thermal performance of the DX-SAHP, experiments are taken under the condition that the solar irradiation is 300W/m² and the temperature of the indoor chamber is 20℃/15℃(DB/WB). The result is shown in Fig.2-5.

As the environment is stable, after nearly 20 min, the system can reach stable operating state. Under the outdoor temperature of 5℃, 10℃ and 15℃, the evaporator temperature is 3.1℃, 7.4℃ and 12.0℃, respectively. As shown in Fig. 2, the evaporator temperature decreases as the ambient temperature decreases. Meanwhile, the evaporator temperature is always lower than the ambient temperature, which leads to heat transfer from the ambient to the collector. It is also observed that the difference between the evaporator temperature and the ambient temperature is 3.0℃, 2.6℃ and 1.9℃ corresponding to the ambient temperature of 15℃, 10℃ and 5℃. Therefore the difference decreases with the decrease of the ambient temperature.
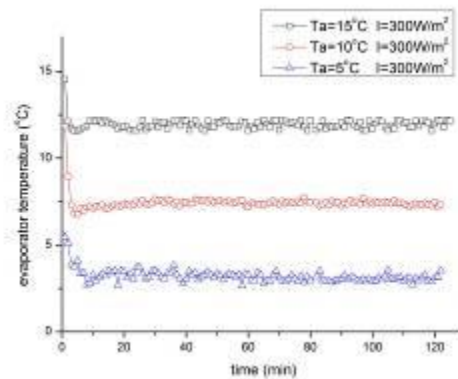
Figure 92: Variation of the evaporator temperature with the ambient temperature of 15, 10, 5℃

The energy consumption of the DX-SAHP increases with the increase of the ambient temperature, as in Fig.3. The specific values of the energy consumption are 0.66 kW, 0.71 kW and 0.78 kW. When the evaporator temperature increases, the evaporating pressure as well as the refrigeration mass flow rate increases, causing the increase of the energy consumption of the compressor.
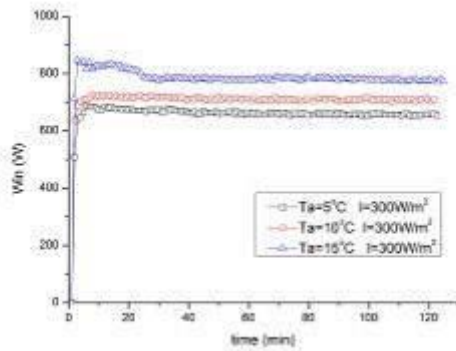
Figure 3: Variation of the energy consumption with the ambient temperature of 15, 10, 5℃

Fig.4 shows the condensing heat exchange rate under the three experiment conditions. The values are 1201 W, 1364 W, 1552 W when the ambient temperature is 5℃, 10℃ and 15℃. Thus, as the ambient temperature increases from 5℃ to 15℃, the system can offer 25% more heat to the indoor chamber.
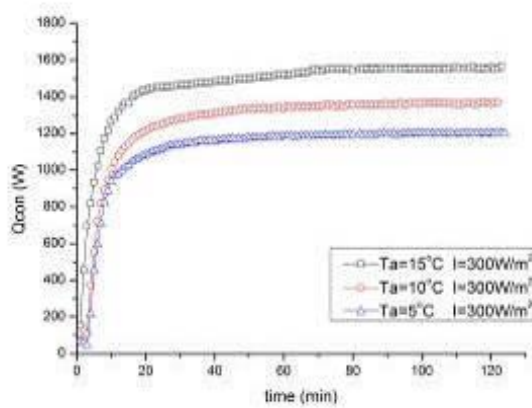
Figure 4: Variation of the condensing heat exchange rate with the ambient temperature of 15, 10, 5℃

In Fig. 5, under the tested conditions, COP is 1.83, 1.91 and 1.99. The increase of COP with the increase of the ambient temperature is not significant, because although the condensing heat exchange rate increases, the energy consumption also increases and to some extent obstacle the increase of COP.
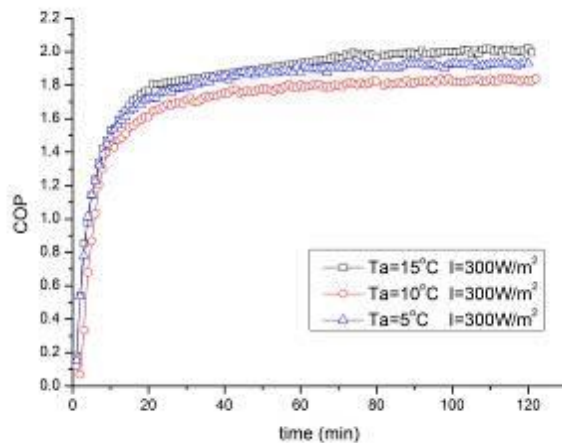
Figure 5: Variation of COP with the ambient temperature of 15, 10, 5℃

4.2 The influence of solar irradiation on the heating performance of the system

To investigate the influence of solar irradiation on the thermal performance of the DX-SAHP, experiments are taken under the condition that the temperature of the indoor chamber is 20℃/15℃(DB/WB) and the solar irradiation is 100 W/m², 200 W/ m², and 300W/ m². The result is shown in Fig.6-9.

Fig. 6 shows that under solar irradiation of 100 W/m², 200 W/ m², and 300W/ m², the evaporator temperature is 10.0℃, 11.0 ℃and 12.0℃, respectively. Therefore, the enhancement of solar irradiation can effectively increase the evaporator temperature. As the evaporator temperature increases, the evaporating pressure and the mass flow rate of refrigerant also increases, which in turn leads to the increase of energy consumption of the system. As shown in Fig. 7, the energy consumption is 707 W, 742 W and 780 W, respectively. Because both the energy consumption and the evaporating heat exchange rate increases, the condensing heat exchange rate increases, as in Fig. 8. The condensing heat exchange rate changes as 1283 W, 1394 W and 1552 W, increased by 21.0%. Fig. 9 depicts that COP of the system also increases with the increase of solar irradiation, with the specific value as 1.85, 1.87 and 1.99.
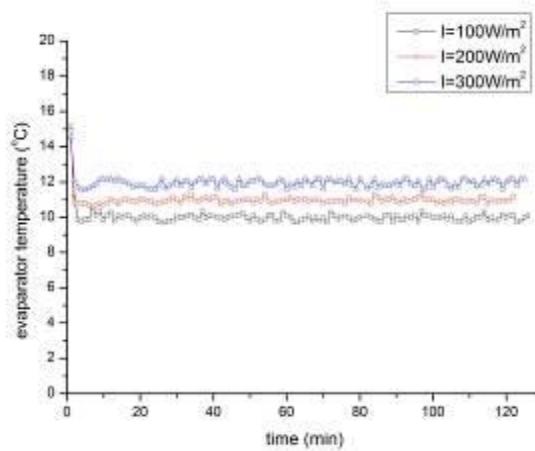
Figure 6: Variation of evaporator temperature with solar irradiation of 100 W/m², 200 W/m², and 300W/ m²
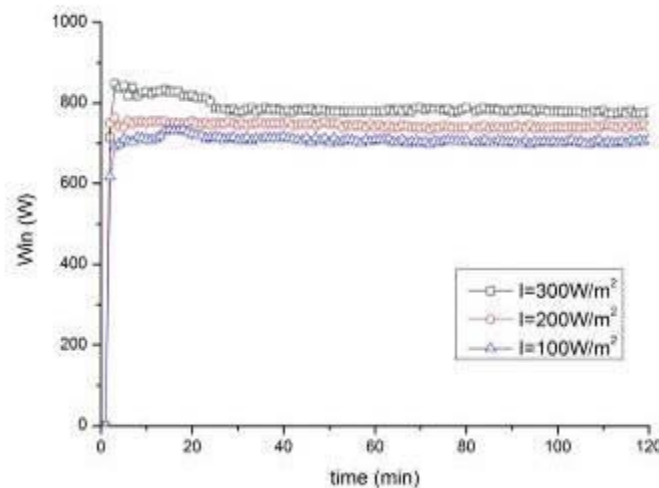
Figure 7: Variation of the energy consumption with solar irradiation of 100 W/ m², 200 W/ m², and 300W/ m²

513
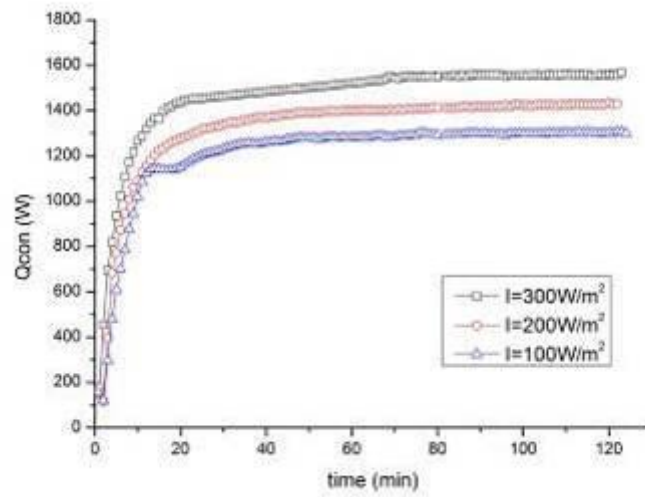
Figure 8: Variation of the condensing heat exchange rate with solar irradiation of 100 W/ m², 200 W/ m², and 300W/ m²
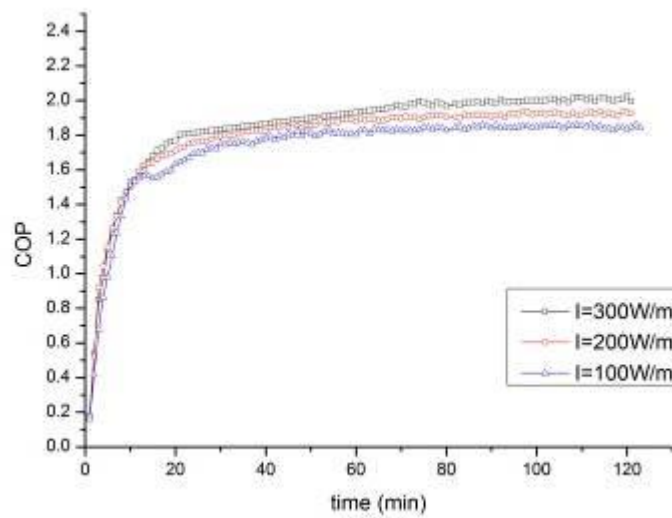
Figure 9: Variation of COP with solar irradiation of 100 W/ m², 200 W/ m², and 300W/ m²
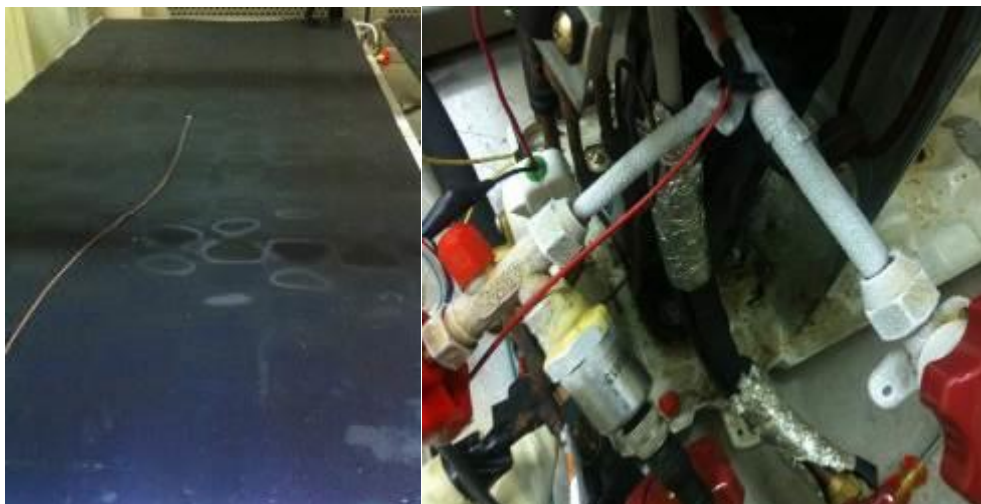
Figure 10: Frost after 30 min with the ambient temperature of 7℃/6℃(DB/WB)
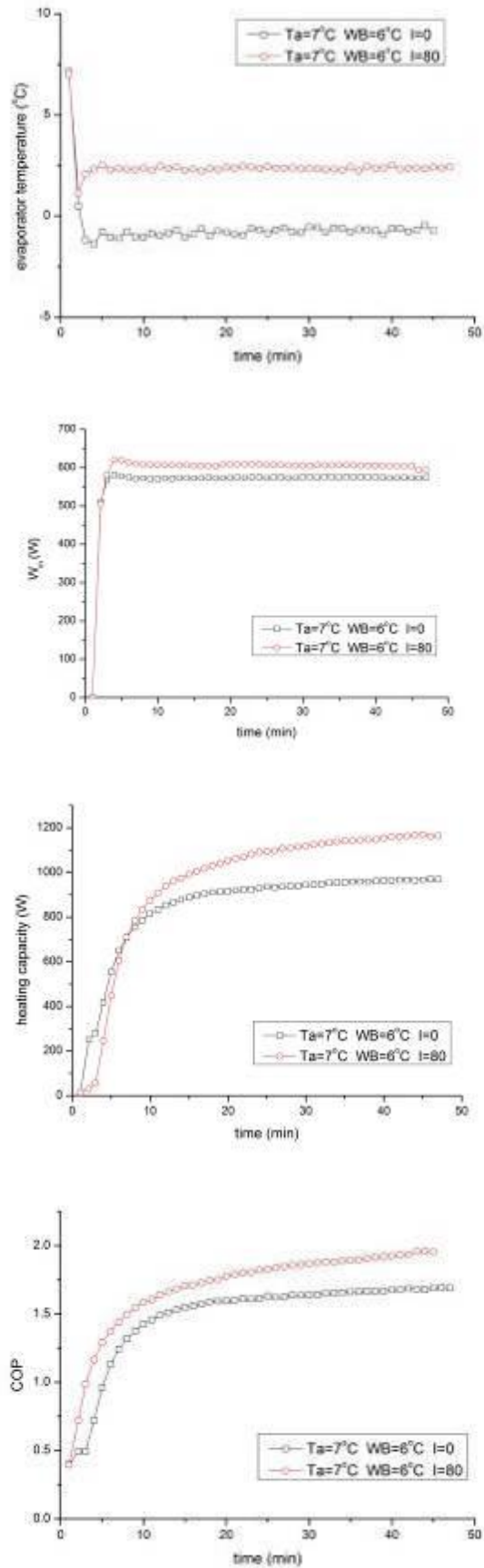
Figure 11: Variation of evaporator temperature, energy consumption, heating capacity and COP with solar irradiation of 0 and 80 W/m²

4.3 The influence of solar irradiation on the frosting performance of the system

To study the influence of solar irradiation on the frosting performance of DX-SAHP, the experiment follows the ANSI-ASHRAE Standard test conditions, which is 20℃/15℃(DB/WB) for the indoor chamber and 7℃/6℃(DB/WB) for the outdoor chamber. Without solar irradiation, after 30 min, the surface of the absorb plate of the evaporator is covered by a layer of frost and the copper pipe of the outlet of the evaporator is frosted, as shown in Fig. 10. As the experiment continues, the frosting will be more serious and decrease the performance of the system. While with solar irradiation of 80 W/m², the evaporator is not frosted during the experiment.

Fig. 11 shows that when the solar irradiation is 0 and 80 W/m², the evaporator temperature is -0.77 ℃ and 2.35 ℃, 3.12℃ higher. The energy consumption is 5.6% higher, the heating capacity increases by 18.1% and COP increased from 1.68 to 1.94 by 15.5%. As the evaporator is not frosted, heat resistance of the evaporator surface is smaller than that of the frosted surface without solar irradiation. At the same time, energy input of the system increases because of solar irradiation, then specific volume of refrigerant decreases and mass flow rate increases, this in turn leads to increase of the energy consumption by 5.6% and increase of the heating capacity of the system by 18.1%. Because the increase of the heating capacity is more significant than that of the energy consumption, COP is improved from 1.68 to 1.94 by 15.5%. The heating performance of the system is enhanced. Therefore, solar irradiation can significantly reduce frosting formation of DX-SAHP and benefit the performance of the system.

5. CONCLUSION

To study the performance of DX-SAHP under different conditions, experiments are carried out in an enthalpy difference lab with a solar simulator. The present study tests the system with the outdoor temperature of 5℃, 7 ℃, 10℃ and 15℃ and solar irradiation is 0, 80 W/m², 100 W/m², 200 W/m² and 300 W/m². The experiment indicates that the increase of ambient temperature and solar irradiation can enhance the heating performance of DX-SAHP. Moreover, solar irradiation can significantly reduce frosting of the system.

(1) When outside temperature changes as 5℃, 10℃ and 15 ℃ with solar irradiation of 300 W/m²，the evaporator temperature of the system is 3.1℃, 7.4℃ and 12.0℃, respectively. the energy consumption are 0.66 kW, 0.71 kW and 0.78 kW, and the condensing heat exchange rate is 1201 W, 1364 W, 1552 W, increases by 25%. COP increases from 1.83 to 1.99. Therefore, the increase of ambient temperature will improve the heating performance of DX-SAHP.

(2) When solar irradiation changes as 100 W/m², 200 W/m² and 300 W/m² with outside temperature of 15 ℃，the evaporator temperature is 10.0℃, 11.0 ℃and 12.0℃

, and the energy consumption is 707 W, 742 W and 780 W, respectively. The condensing heat exchange rate changes as 1283 W, 1364 W and 1394 W, increased by 8.7%. COP of the system increases from 1.85 to 1.99. Conclusion can be drawn that the increase of solar irradiation can enhance the heating performance of DX_SAHP.

(3) It is observed that when outside temperature is 7℃/6℃(DB/WB), without irradiation, after 30 min the evaporator is seriously frosted and the evaporating temperature is -0.77℃,while under irradiation of 80 W/m² the evaporator temperature is 2.35℃, and the evaporator is not frosted. COP increased from 1.68 to 1.94 by 15.5%. Solar irradiation can retard the frost formation of DX-SAHP when the system operates under frosting condition.

6. REFERENCES

1. SPORN P, A.E., The heat pump and solar energy. 1955.

2. K.I Krakow, S.L., A solar source heat pump with refrigerant-cooled solar collectors for cold climates. International Journal of Refrigeration, 1983. 6(1): p. 20-33.

3. HUANG, B.J. and J.P. Chyng, Performance characteristics of integral type solar-assisted heat pump. Solar Energy, 2001. 71(6): p. 403-414.

4. KUANG, Y.H. and R.Z. Wang, Performance of a multi-functional direct-expansion solar assisted heat pump system. Solar Energy, 2006. 80(7): p. 795-803.

5. CHATURVEDI, S.K. and M. Abazeri, TRANSIENT SIMULATION OF A CAPACITY-MODULATED, DIRECT-EXPANSION, SOLAR-ASSISTED HEAT-PUMP. Solar Energy, 1987. 39(5): p. 421-428.

6. CHATURVEDI, S.K., D.T. Chen, and A. Kheireddine, Thermal performance of a variable capacity direct expansion solar-assisted heat pump. Energy Conversion and Management, 1998. 39(3-4): p. 181-191.

7. ITO, S., N. Miura, and K. Wang, Performance of a heat pump using direct expansion solar collectors. Solar Energy, 1999. 65(3): p. 189-196.

8. HAWLADER, M.N.A., S.K. Chou, and M.Z. Ullah, The performance of a solar assisted heat pump water heating system. Applied Thermal Engineering, 2001. 21(10): p. 1049-1065.

9. KONG, X.Q., et al., Thermal performance analysis of a direct-expansion solar-assisted heat pump water heater. Energy, 2011. 36(12): p. 6830-6838.

10. CHOW, T.T., et al., Modeling and application of direct-expansion solar-assisted heat pump for water heating in subtropical Hong Kong. Applied Energy, 2010. 87(2): p. 643-649.

11. CHYNG, J.P., C.P. Lee, and B.J. Huang, Performance analysis of a solar-assisted heat pump water heater. Solar Energy, 2003. 74(1): p. 33-44.

480 : Potential of biogas recovery from landfills for sustainable energy production: a case study from Jordan

HANI ABU QDAIS,

Water and Environmental Engineering, Civil Engineering Department,
Jordan University of Science & Technology, E mail hqdais@just.edu.jo
P.O.Box 3030, Irbid 22110, Jordan

Landfills continue to be part of any municipal solid waste management system. Despite several improvements that took place in landfilling technology, the disposal of solid waste in landfills still imposing adverse environmental impacts. One major impact is the emission of greenhouse gases like methane which has high global worming potential as compared to carbon dioxide.

To minimize the adverse impact of the emitted methane, it is possible to collect the generated methane and utilize it for energy production. This paper is investigating the possibility of collecting the biogas from Al Hosaineyat landfill in northern Jordan for possible energy recovery. Solid waste quantities and composition were evaluated. Daily amount of solid waste disposed at the landfill is about 74 tons with more than 60% of it organic matter.

The amount of methane generated from the landfill was estimated using GASSIM simulation software. It was found that currently (in 2015) the annual methane production is about 2 million M^3/day, while by the peak biogas generation will be one year after the landfill closure (in 2021) and amounting to 2.47 million M^3/day. The annual energetic potential of the landfill was found to be 6.14 GWh and 7.59 GWh in the years 2015 and 2021, respectively.

Keywords: Landfill gas, Energy Recovery, Jordan, Solid Waste, Biogas modelling

1. INTRODUCTION

Despite the efforts that are taking place to reuse and recycle and to divert the solid waste from landfills waste via adopting integrated solid waste management practices, landfills remain and will remain to be one of the most common ways of solid waste disposal (Aljarrah and Abu Qdais, 2006). For example, 55% of the generated solid waste in the United States (USEPA), disposed into landfills, while in Jordan, more than 90% of the solid waste finds its way to the landfills (SWEEPNET,2014).

The landfilling process is usually associated with adverse environmental and health impacts. One of the byproducts of the landfilling process is the landfill gas (Abu Qdais et al 2011), which is mainly composed of methane and carbon dioxide. Since such gases are known as greenhouse gases, they will cause the global warming phenomena when emitted to the atmosphere. Methane gas has a global warming potential 21 times more than the carbon dioxide. In 2011 landfills were the third-largest anthropogenic source of methane emissions in the United States which accounted for 17.5% of the total emissions, (EPA, 2013). In Jordan, about 92% of methane emitted in the country is coming from the disposal of the solid waste in landfills. (SNC, 2009)

Depending on the solid waste composition and age, landfilling process and environmental conditions, the fraction of methane in the biogas stream may range from 50%-60%. Methane is considered as a valuable source that can be utilized to generate energy and at the same time reducing the greenhouse gaseous emissions from the landfills. Using biogas as a fuel source is an environmentally friendly sound option (Zamorano et al 2007).

In Jordan, energy resources have always been scarce. The country has little indigenous energy sources, so almost the 97% of its energy is imported. In 2014, expenditure on energy imports reached approximately 20% of GDP. As a result, Jordan has also set targets regarding its policy for renewable energy resources to be a major contributor in the country's energy mix. The National Energy Strategy 2008-2020 identifies a target of 10% of renewable energy by the year 2020 comprising a ten-fold increase from the share of 1% in 2007. (Jordan Master Energy Strategy, 2007).

The present paper investigates the potential of utilizing the biogas produced from Al Hosaineyat solid waste landfill in Northern Jordan as a source of clean sustainable energy.

1.1 Description of Al Hosaineyat Landfill

Al Hosaineyat Landfill is located in Northern Jordan, east to the main road from Mafraq to Doleil. It is about 21 km south east of Al Mafraq City within the Amman Zarqa water shed. The site has coordinates of 36º20′27.29″ E and 32º15′29.49″N, as shown in Figure 1. The criteria used in the landfill site selection were the low population density and the low land cost. The landfill area is classified as arid region since the average annual rainfall is about 120 mm/year as shown in figure 1.

Solid waste deposition in this landfill was started officially in 1987. The site is currently owned and managed by The Common Services Council (CSC) of Mafraq Governorate which comprises several municipal councils. The estimated remaining useful life of the landfill is about 5 years (up to 2019). However, the CSC is intending to acquire further land to increase the landfill area from 38 hectares to about 50 hectares. This will give more space to dispose more solid waste. The increase in the landfill area will extend the landfill useful life up to the year 2025.
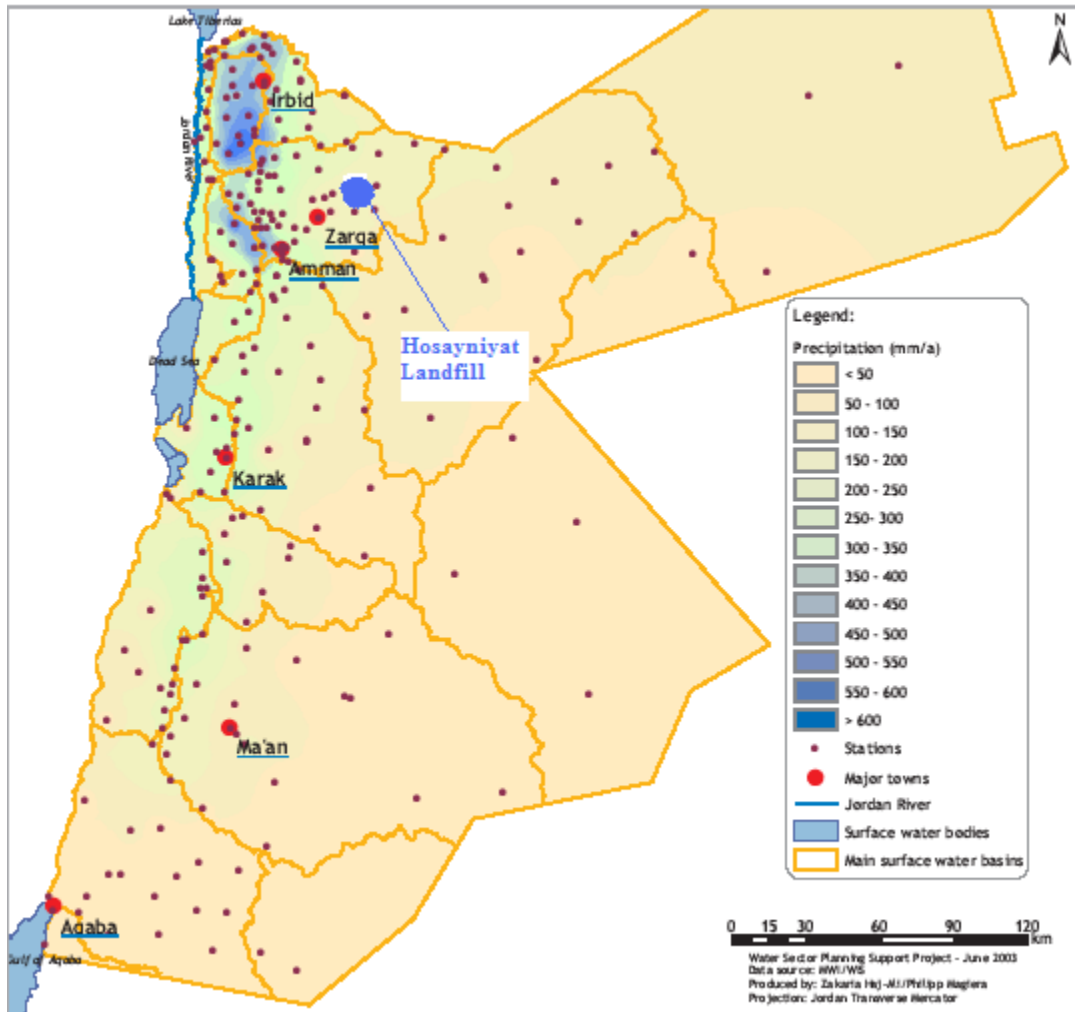
Figure 1. Location of Al Hosayniat landfill in arid region of Northern Jordan

2. SOLID WASTE QUANTITIES AND COMPOSITION

To get information on the quantities of the solid waste being disposed at Al Hosayneyat site, the records of the electronic weighing bridge at the site gate were used. All the collection vehicles that haul the solid waste to the landfill have to go through the weigh bridge where they have been subjected to weighing before and after unloading the solid waste at the landfill

The average daily amount of the municipal solid waste disposed at Al Hosayneyat landfill was found to be 74 tons/day. Figure 2 shows the average daily amounts of municipal solid waste disposed at the site from different municipalities and generators in Al Mafraq Governorate. It can be seen that the bulk amount of solid waste disposed at the site is generated by Al Mafraq Municipality. About 47% (34.63 tons/day) coming from Al Mafraq, while 53% generated by other municipalities and other generators, like Al Al bait University, and military camps.
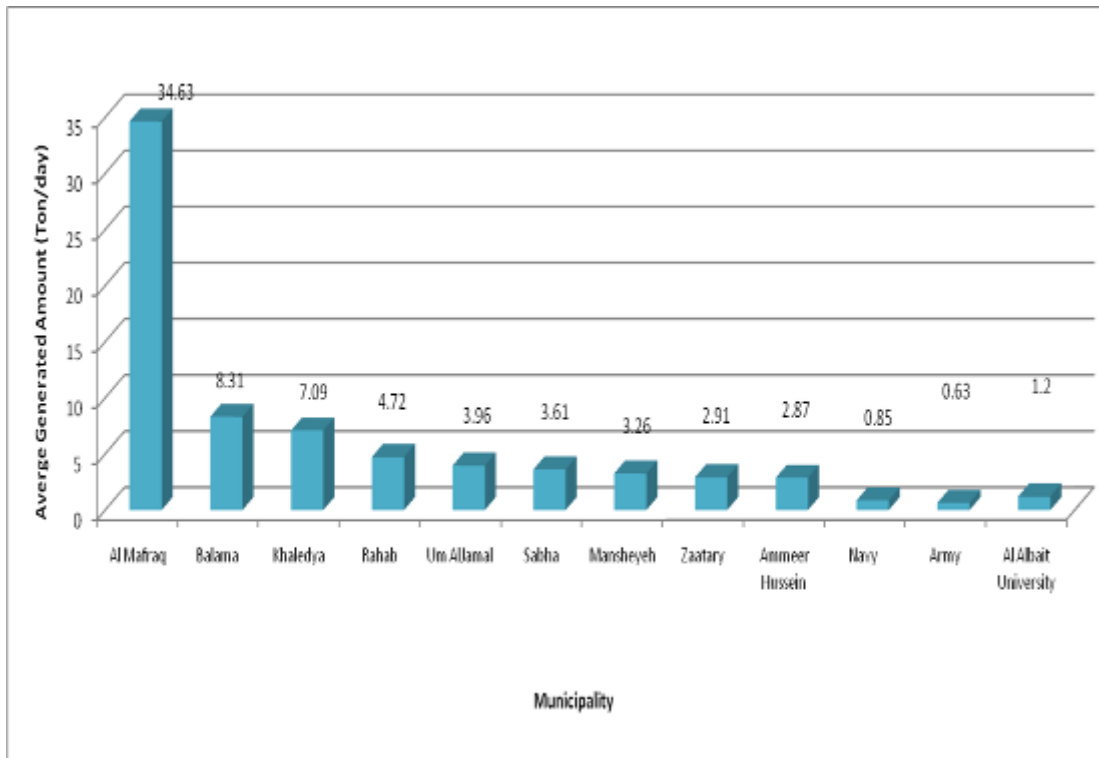
Figure 2. Daily amounts of municipal solid waste disposed at Al Hosaineyat landfill from different Municipalities

The above amounts received by the landfill were measured in 2009, before the influxes of the Syrian refugees. Starting from 2011 as a result of the Syrian refugees influxes the amount of solid waste disposed at the site has been doubled (about 150 tons /day).

The solid waste physical composition was found by sorting method. Randomly selected vehicles were subjected to composition analysis. Vehicle loads were manually sorted into basic components. Each waste component was weighed and recorded as percentage of the total weight. Figure 3 shows average physical composition of the solid waste disposed at Al Husaineyat landfill. It can be noted that the largest fraction of the solid waste is biodegradable organic matter (i.e. food waste and paper) that comprises almost 64% of the total waste disposed at the landfill site, which suggests that that biogas recovery is an option for energy recovery.
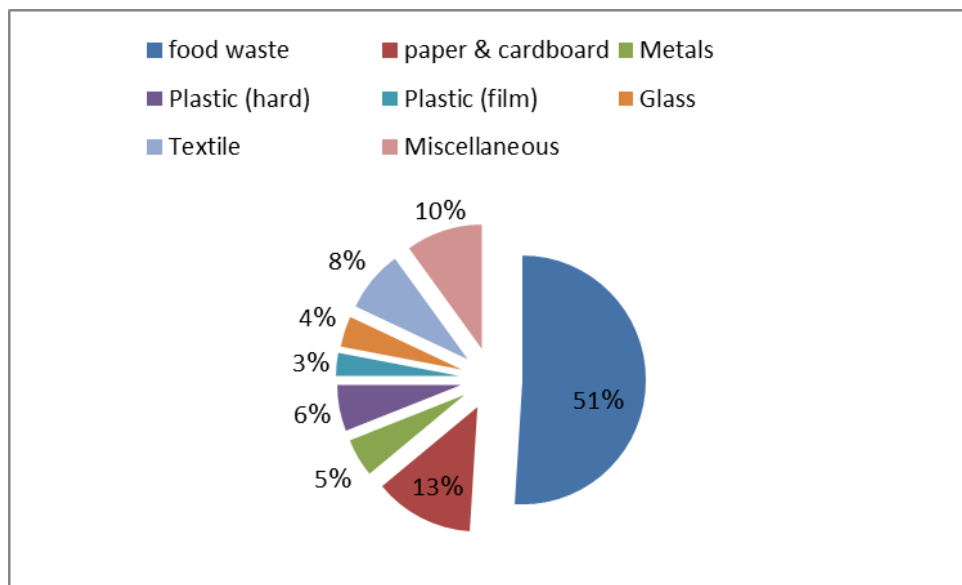
Figure3. Physical composition of the solid waste disposed at Al Hosainiyat landfill

3. MEASUREMENT AND SIMULATION OF METHANE GAS

To measure the concentration of methane in the ambient air at Al Hosaineyat landfill, a gas analyzer was used to measure the concentration of methane, carbon dioxide and sulfur oxide at selected locations. The points of measurement covered the whole area of the landfill including the filling waste of the solid waste and the trenches of animal waste. Figure 4 shows the location of the measurement points at the landfill and the methane concentration at each point. The concentration of methane detected on most of the locations on the site was found to range from 3 to 1750 ppm with an average of 136 ppm.

Landfill gas generation from Al Al Hosaineyat has been simulated from 1986 to 2046 using GASSIM computer software which was developed particularly for simulation of the emissions from landfills. As shown in figure 5, the trend of the simulation follows the triangular shape. In the period from 1986 to 2021; the methane generation increases as well as the waste input quantities. By the year of 2020, the landfill is assumed to be reaching its full capacity and will be closed; hence the methane generation rate will decrease. This can be explained by the fact that the landfill will enter a stage of stabilization where methanogenic bacteria starts to produce less methane amounts due to low moisture content and low fresh biodegradable solid waste.

From Figure 5 it can be noticed that the current annual (year 2015) methane generation from the landfill is about 2 million m^3/year. The maximum methane generation rate is 2.47 million m^3/year. This will be taking place is in the year 2021 (one year after the landfill closure).
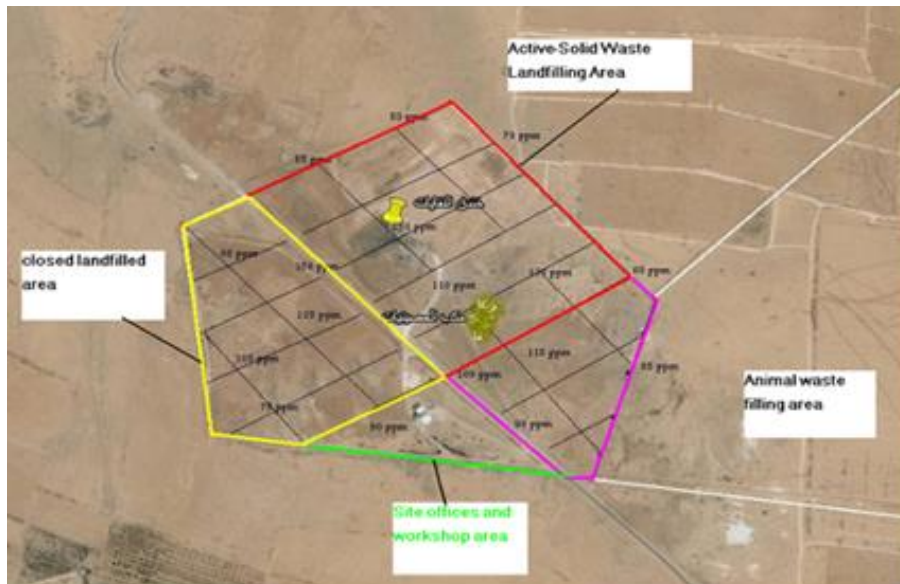
Figure 4. Location of methane measurement points in the landfill
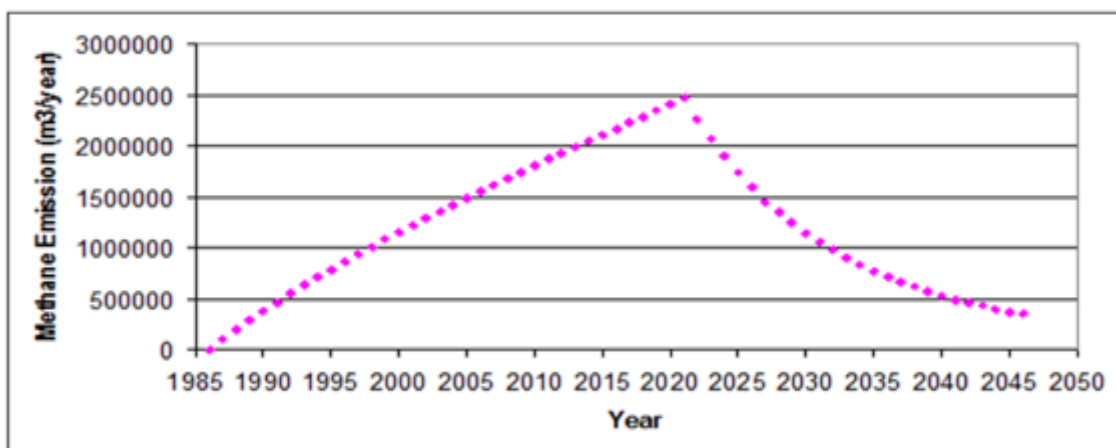
Figure 5. Simulated methane emissions from Al Hosaineyat Landfill

4. LANDFILL ENERGETIC POTENTIAL

Assuming that 70% of the methane produced by the landfill is captured, and the mean lower heating value of methane is 15,800 kJ/Nm^3, the energetic potential of the landfill can be calculated. Table 1 presents the calculated annual energetic potential of the landfill for the period 2015-2021. It can be noted that the maximum energy of 7.59 GWh will be generated in the year 2021. Considering that the average household in Jordan annually consumes 4452 kwh of electricity, the generated energy from landfill methane will be sufficient to supply about 1500 household. As for the global worming potential, capturing such amount of methane, it will avoid releasing of 0.5 million tons of CO_2 equivalent.

Table 1. Estimated Energetic Potential of Al Hosaineyat landfill

Year	Estimated Methane Production M^3/Year	Estimated Methane recaptured (M^3/Year)[*]	Annual Energetic Potential GWh[**]
2015	2,000,000	1,400,000	6.14
2016	2,200,000	1,540,000	6.76
2017	2,250,000	1,575,000	6.92
2018	2,300,000	1,610,000	7.07
2019	2,330,000	1,631,000	7.16
2020	2,400,000	1,680,000	7.37
2021	2,470,000	1,729,000	7.59

[*] methane recaptured is 70% of the estimated methane production

[**] Energetic potential calculated based on mean lower heating value (LHV) of methane 15,800 kJ/Nm^3

5. CONCLUSIONS AND RECOMMENDATIONS

Landfills will remain a part of any integrated solid waste management system. Methane that is emitted from landfill can be utilized for energy recovery. For a country like Jordan, which is lacking indigenous energy sources and fully dependent on imported energy, utilizing renewable energy sources like landfill gas is of great importance. The present study assessed the energy potential of Al Hosaineyat landfill in Northern Jordan. The current annual energy that can be recovered from methane gas that is emitted from the landfill is about 6.14 GWh, while after the landfill closure in the year 2021 the energy potential is about 7.59 GWh. It is recommended to carry out a comprehensive assessment for the Jordanian landfills energetic potential so as to estimate the energy that can be recovered from all landfills in the country.

6. REFERENCES

Abu Qdais H., Maqableh A., Al Nawayseh L, and Al Jammal N. (2011), Energetic and Methane Emission Reduction Potentials from an Unsanitary Landfill, Energy Sources, Part A: Recovery, Utilization, and Environmental Effects, 34:4, pp 360-369

Al- Jarrah O. and Abu Qdais H. (2006) Municipal Solid Waste Landfill Siting Using Intellegent System, Waste Management, 26, pp 299-306

Desideri U., Di Maria F., Leonardi D. and Proietti S. (2003) Sanitary Landfill Energitic Potential Analysis: Areal Case Study, Energy Conversion and Management, 44, pp 1969-1981.

EPA (2013) An Overview of Landfill Gas Energy in the United States U.S. Environmental Protection Agency Landfill Methane Outreach Program (LMOP), july 2013

Master Strategy of Energy Sector in Jordan for the period (2007-2020), Ministry of Energy and National Resources, Amman Jordan, 2007

SNC (2009) Jordan's Second National Communication to the United Nations Framework Convention on Climate Change (UNFCCC), Ministry of Environment Amman, Jordan

SWEEPNET (2014). Country Profile on The Solid Waste Management in Jordan, The Solid Waste Exchange of Information and Expertise in Mashreq and Magreb Countries, Tunis.

Zamorano M., Perez J., Paves I. and Ridao A. (2007) Study of the Energy Potential of Biogas Produced by an Urban Waste Landfill in Southern Spain, Renewable Sustainable Energy Review, 11, pp 909-922

POSTER SESSION A

66: The adaptability of night cooling technology under different climates

Zhongzhe Wu[1] AND Shenyi Wu[1]

1Department of Architecture and Built Environment
University of Nottingham
University Park, Nottingham NG7 2RD, UK

The demanding for cooling in buildings significantly increases worldwide with living standard. In the last few decades, the energy consumption for cooling shared a large part of the total energy consumption in buildings and the trend is still on the rise. The night-time ventilation as a passive cooling method has a potential to reduce the energy consumption for buildings cooling. Employing night cooling ventilation technology can not only save energy, but also improve indoor air quality. However, the effectiveness of the night cooling ventilation is climate dependent. Location has a significant influence on the efficiency of this method. In this study, the adaptability of night ventilation cooling technology under different climate conditions was analysed from a macroscopic view. The analysis was based on the theory of "climate cooling potential" and "climate cooling demand" which is calculated from degree-hours of the difference between the ambient air and inside building temperatures without specifying building parameters.

This study examined the values of the climate cooling potential and the climate cooling demand in 34 cities located in different climate zones. It was found that the potential of night cooling ventilation in the east coast cities of the Pacific and the Atlantic Ocean were always higher than the same latitude cities in west coast.

The study also quantified the effectiveness of night ventilation cooling by simulating a nominal building in different cities with the energy consumption analysis software "design builder". The results showed that among different places, for every 10kh increase of the climate cooling potential, the corresponding indoor temperature could be reduced by approximate 0.12ºC. In the application of the night cooling ventilation combining with air-conditioning system in commercial buildings, the night cooling ventilation showed positive effect when the ratio of local climate cooling potential and demand is larger than 1, i.e., the reduction on HVAC energy consumption for cooling excesses the additional fan power consumed on night cooling.

Keywords: Passive cooling; Night-time ventilation cooling; climate cooling demand; climate cooling potential

Symbols	Definition	Unit
Q_{store}	Heat stored by building thermal mass	(w)
V	Volume of thermal mass	(m^3)
ρ	Density of thermal mass	(kg/m^3)
c_p	Specific heat capacity	($w/kg.^oc$)
T_{max}	The average highest temperature of thermal mass	(^oc)
T_{min}	The average lowest temperature of thermal mass	(^oc)
ΔP_h	Pressure difference	(Pa)
ρ_i	The inside air density respectively	(kg/m^3)
ρ_u	The outside air density respectively	(kg/m^3)
g	Acceleration due to gravity	(m/s^2)
h_o	Vertical distance between the floor plan and the neutral plane	(m)
ΔT	The temperature difference between the internal and external air	(K)
T_i	Inside temperature	(K)
T_u	Outside temperature	(K)
p	The wind pressure	(Pa)
v	Wind speed	(m/s)
ρ_e	The density of external air	(kg/m^3)
g	Acceleration due to gravity	(m/s^2)
T_b	The temperature of building	(^oc)
T_c	The ambient air temperature	(^oc)
$T_{b,h}$	Temperature of building in each hour	(^oc)
h	Hour of the day	$h\epsilon$ [1, 2,..24h]
h_f	The finish hour of the night time ventilation	/
k	The kinetic coefficient of the air	/
h_i	The initial time of night time ventilation	/

1. INTRODUCTION

Natural ventilation is a widely used passive cooling technology for buildings. It is an elementary practice to remove heat from buildings to the ambient air using the ventilation method [1]. Night ventilation is such an example which makes use of the temperature difference between daytime and night for cooling purpose. There are several ways to achieve this. One of these is by introducing the cold outdoor air to cool the building structure. This is normally done during night time when the air temperature is low with the purpose of reducing the indoor temperature for the following day. It is achievable to reduce the peak internal temperature by 2 - 3°C on the following day, if the night cooling strategy is applied in a suitable building design. [2]

Pervious investigations indicated that the climate conditions have a significant effect on the night time ventilation [3] [4], because in order to efficiently cool down the building mass, a sufficiently large temperature difference between the building structure and the ambient air is required. B. Givoni investigated the night-time ventilation in the period of 1990s. [5] He recommended that a suitable region for the application of the night-time ventilation cooling should be with a day time temperature in a range between 30°C and 36°C and the night-time temperature below 20°C. Roaf [6] suggested a criterion for night-time ventilation cooling for buildings that the maximum external air temperature should be less than 31°C, combined with the minimum night time temperature of 20°C. The maximum temperature of the criterion has been taken with the consideration of the climate warming, so he concluded that the reliability of the limiting criterion could be accessed until 2050.

In 2007, N. Artmann evaluated the cooling potential of night-time ventilation for buildings.[11] The concept of climate cooling potential (CCP) was presented in this investigation from analysing the climate data of Europe. The method of degree-hours calculation which is based on a variable building temperature was used and applied to climate data over Europe. This method did not consider any specific parameters but only the climate condition.

Furthermore, the type of night-time ventilation could affect the effectiveness of heat removal directly. According to the statement of J. Pfafferott [8] the night ventilation is based on a free or a hybrid ventilation concept. Natural ventilation in a building is a process of air removing and supplying through an indoor space

without using any mechanical systems.[9] But most of the tall commercial buildings are not suitable for natural ventilation by opening the windows. In this case, hybrid ventilation system should be utilized. In the year 2011, GuoBing Zhou *et al* [10] investigated the performance of a hybrid space-cooling system in a building using SSPCM thermal storage and night ventilation. According to the simulation of the south-facing room model in an office building in Beijing, they indicated that the active system of auxiliary cooling supply is needed to combine with the night ventilation in the hot summer season. This hybrid system could both be used to maintain the maximum indoor temperature of room at daytime and provide enough air change rate during the night time ventilation if SSPCM stores enough cooling energy.

The most of the investigation on the night-time ventilation cooling technology were area specified. There is lack of investigation from the macroscopic view about the suitability of the utilization of night cooling ventilation technology. Moreover, there is lack of a system to quantify the effectiveness of the night cooling ventilation in all over the world.

2. CLIMATE COOLING POTENTIAL AND DEMAND

The "Climate cooling potential" [11], is a summation of products of the air temperature difference between the external and internal and the duration of it. Since the climate cooling potential is not a building–specific parameter, it is convenient to use it for analysing the night cooling potential without considering the building factors. The CCP could be calculated with the following equation:

$$CCP = \frac{1}{N} \sum_{n=1}^{N} \sum_{h=h_i}^{h_f} m(T_b - T_c) \begin{cases} m = 1h & if \ T_b - T_c \ \geq \ \Delta T_{crit} \\ m = 0 & if \ T_b - T_c \ < \ \Delta T_{crit} \end{cases} \qquad (2.1)$$

Where:

- h = hour of the day, hϵ [1, 2,…..24h]
- n = days
- h_i = the initial time of night time ventilation
- h_f = the finish hour of the night time ventilation
- ΔT_{crit} = the threshold value of the temperature difference for the application of time ventilation. The night-time ventilation is only applied when the temperature difference between the building and ambient air is greater than the threshold value ΔT_{crit} = 3K
- T_b = the temperature of building, not a constant value; the subscribes n, h represent day and hour, respectively
- T_c = the ambient air temperature

Similarly, the "climate cooling demand" (CCD) is also a summation of products of the air temperature difference between the external and internal and the duration of it, where T_b is a temperature relates to the thermal comfort range. It can also be calculated as follows:

$$CCD = \frac{1}{N} \sum_{n=1}^{N} \sum_{h=h_i}^{h_f} m(T_c - T_b) \begin{cases} m = 1h & if \ T_c - T_b \ \geq \ \Delta T_{crit} \\ m = 0 & if \ T_c - T_b \ < \ \Delta T_{crit} \end{cases} \quad (2.2)$$

According to N. Artmann, the building temperature was assumed to oscillate harmonically [12][13]. The relationship can be expressed as follows:

$$T_{b,h} = 24.5 + 2.5 \cos\left(2\pi \frac{h - h_i}{24}\right) \qquad (2.3)$$

Where:

$T_{b,h}$ =temperature of building in each hour

h - hour of the day, hϵ [1, 2,…..24h]

h_i = the initial hour of night time ventilation

The first item in the right of Equation 2.3 represents the set thermal comfort temperature. The use of 24.5ºC means that the equation is only suitable for European weather condition. This study was to investigate the different areas of the world, therefore, the thermal comfort temperature was a variable and $T_{b,h}$ should expressed as:

$$T_{b,h} = \alpha + 2.5\cos(2\pi\frac{h-h_i}{24}) \qquad (2.4)$$

Where "α" is a variable determined by the different comfort temperature in different areas of the world. The comfort temperature ranges can be determined by the adaptive model from ASHARE standard 55 shown in Figure 1.
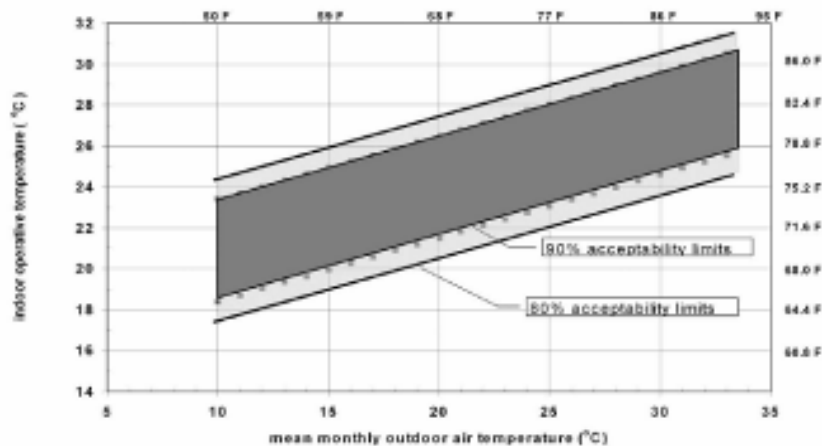
Figure 1: Proposed Adaptive Comfort Standards (ACS)[14]

For example, London's mean temperature in summer is 16.33ºC. Its comfort temperature range could be read from Figure 1 which is 21 - 26ºC, so the value of "a" for London is the average temperature of the comfort range 21 - 26ºC, i.e., 23.5ºC.

3. THE BUILDING MODEL AND LOCATIONS

For the simulation purpose, a nominal building model was set for all climates concerned in this investigation in order to show the effectiveness of the night cooling varying only with the climate. Figure 1 shows the dimension of the nominal building envelope, which was 12m in length, 8m width and 3.5m height. A 30 % of glazing ratio was used on each wall.

The walls of the nominal building were constructed in three layers consisting of 200 mm concrete and 100 mm insulation (polystyrene). The fresh air requirement is set as 10 l/person and the air change rate was 9 ach/h. The mechanical ventilation system was considered to provide the fresh air.2. 4 Locations were selected for the study.

In order to investigate the suitability of night cooling strategy in different areas, 34 cities located in different climate zones of the world were selected. As it shows in the **Error! Reference source not found.** these cities are located in the five different zones of Tropical, Subtropical, Temperate, Mediterranean and mountainous climates.

The weather data were obtained from EnergyPlus weather format which are arranged by world Meteorological Organization region and Country. It included 1042 locations weather in the USA, 71 locations in Canada, and more than 1000 locations in 100 other countries throughout the world. [15]

Table 1 The selected cities in different climate zone

Climate type	Continent	City	Latitude	Longitude	Elevation
Tropical rainy climate	Asia	Singapore	1.22N	103.59E	15
Tropical desert climate	Africa	Cairo	30.08N	31.24E	74
	Asia	Abu Dhabi	24.26N	54.39E	27
Mediterranean climate	Asia	Damascus	33.25N	36.31E	610
	Europe	Sochi	49.27N	39.54E	15
		Rome	41.48N	12.14E	3
		Barcelona	41.17N	2.04E	6
		Athens	37.54N	23.44E	15
	Africa	Casablanca	33.34N	7.04W	61
		Alexandria	31.12N	29.59E	7
	North America	San Francisco	37.46N	122.26W	5
		Los Angeles	34.03N	118.14W	78
	South America	Santiago	33.23S	70.47W	473
Subtropical monsoon climate	Asia	Changsha	28.23N	112.87E	68
		Shanghai	31.13N	121.26E	7
	North America	Atlanta	33.39N	84.26W	307
		Houston	29.48N	95.31W	27
	Oceania	Sydney	33..56S	151.1E	6
Monsoon climate of medium latitudes	Asia	Shenyang	41.77N	123.43E	43
		Seoul	37.34N	126.58E	86
Temperate marine climate	Europe	Oslo	59.54N	10.37E	17
		London	51.09N	0.11W	39
		Paris	48.44N	2.24E	96
	North America	Vancouver	49.18N	123.07W	2
		Seattle	47.44N	122.19W	10
Temperate continental climate	Europe	Helsinki	60.19N	24.58E	56
		Moscow	55.58N	37.25E	189
		Tehran	35.68N	51.35E	1191
	North America	Toronto	43.40N	79.38W	172
		New York	43.14N	75.25W	4
Plateau & mountain climate	Europe	Zurich	47.38N	8.57E	569
	Asia	Lhasa	29.43N	91.02E	3595
	America	Santa Fe de Bogota	4.42N	74.08W	2547
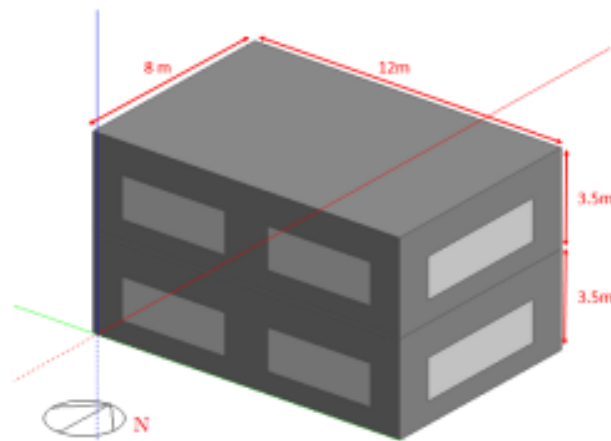
Figure 2 Overview of building model

4. RESULTS AND DISCUSSION

4.1 Geographical climate cooling potential and demand

Since the cities are located at different parts of the world, it is required to define a uniform period of summer time for investigation. For the cities in the Northern Hemisphere, the most of their peak temperature periods are appeared in June, July and August, except the cities in Tropical zone which have almost steady high temperature year around. So, the period of June to August was defined as the summer time for these cities, likewise, for the cities located in the south hemisphere, the period of December to February was defined as the summer time. The night ventilation time in each night was set from 19:00 to 7:00. Table 2 listed the CCP) and CCD values for these cities during the summer time.

In order to further investigate the geographical distribution of climate cooling potential in different locations, cumulative frequency charts were constructed to show the sustained level of the climate cooling potential in summer. This treatment reduced the influence of less frequent but extreme hot or cold days during the whole summer season on the level of the CCP.
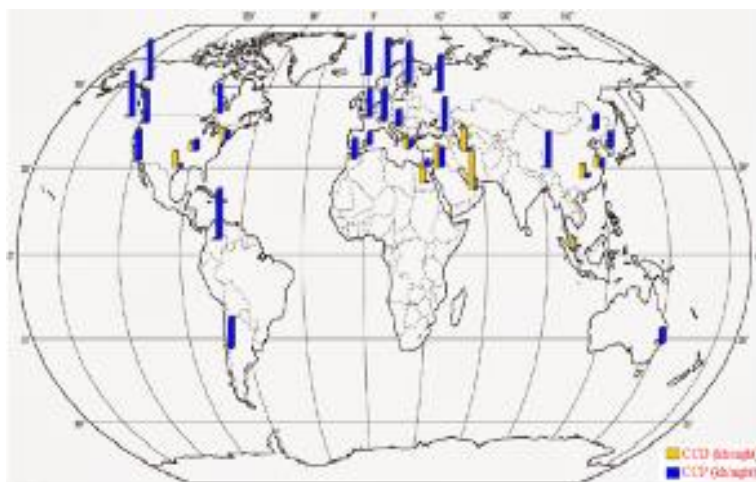
Figure 93 Distribution of climate cooling potential and demand values in chosen cities

Table 32 the values of climate cooling potential and demand in different cities

Climate type	Continent	City	CCP (kh)	CCD (kh)
Tropical rainy	Asia	Singapore	1.635	22.983
Tropical desert	Africa	Cairo	3.830	40.918
	Asia	Abu Dhabi	0.069	100.897
Mediterranean	Asia	Damascus	49.986	58.349
	Europe	Sochi	89.424	9.188
		Rome	46.141	11.532
		Barcelona	29.756	7.303
		Athens	17.900	22.921
	Africa	Casablanca	53.462	12.585
		Alexandria	16.454	7.416
	North America	San Francisco	117.469	1.081
		Los Angeles	77.906	0.000
	South America	Santiago	83.356	10.911
Subtropical monsoon	Asia	Changsha	10.558	34.268
		Shanghai	19.678	28.921
	North America	Atlanta	28.339	22.010
		Houston	7.445	43.018
	Oceania	Sydney	40.161	5.826
Monsoon of medium latitudes	Asia	Shenyang	42.063	9.129
		Seoul	39.062	3.646
Temperate marine	Europe	Oslo	103.872	0.000
		London	109.922	1.001
		Paris	75.242	2.612
	North America	Vancouver	105.256	0.000
		Seattle	84.923	2.024
Temperate continental	Europe	Helsinki	106.199	1.089
		Moscow	94.294	2.707
		Tehran	8.343	61.357
	North America	Toronto	74.869	9.034
		New York	19.031	28.565
Plateau & mountain	Europe	Zurich	83.334	4.286
	Asia	Lhasa	92.399	0.000
	America	Santa Fe de Bogota	129.297	0.000
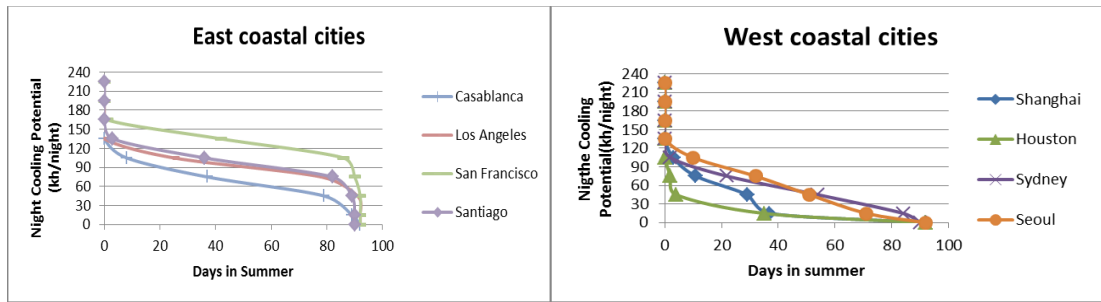
Figure 94: Cumulative frequency distribution of climate cooling potential in summer in west and east coast of ocean

Figure 4 shows the cumulative frequency distribution of CCP for the cities located in west and east coast of the Pacific and Atlantic. With the cold current, the air temperature of the cities at the east coast of these oceans would be lower than that at the other side of the oceans during the summer time. Therefore, there was a big difference in the effectiveness of night cooling ventilation between the east and west coast of the oceans. It can be found that in the range of 30⁰ - 40⁰ northern latitudes, the east coastal cities like Los Angeles and San Francisco always had higher values of CCP than the west coast cities such as Seoul and Shanghai. CCP in Los Angeles and San Francisco could be over 70 kh for more than 80 nights out of 92 summer nights, while this number in Seoul and Shanghai is much lower for about 30 nights. This phenomenon was also found in the south hemisphere. Taking Santiago and Sydney as examples, both cities are located at latitude of 33⁰ S. According to the curve in Figure 4 Santiago had high cooling potential of 75kh in for more than 80 days, however, Sydney in the opposite side of south Pacific to Santiago had only 20 days. Therefore, it can be concluded that the night cooling ventilation strategy in the east coast areas of the Pacific and the Atlantic was more efficient than west coast areas at the same latitude.

4.2 Applicability of night cooling ventilation in different conditions

The effectiveness of night cooling ventilation

The value of climate cooling potential calculated in the previous part shows the potential of it to be used for night cooling in different places; however, it may be convenient to translate it into the effectiveness of night cooling ventilation in terms of the degree of the temperature it can reduce. For this reason, a simulation was carried out to reveal the relationship between them using the software of DesignBuilder – the simulation software based on the calculation platform of energy plus.

According to the previous calculation for different locations, the values of climate cooling potential for these areas vary in the range of 0-120 kh/night. In this study, we divided the range into four levels which were 0 - 30, 30 - 60, 60 - 90, 90 -120. One city was selected for each level as shown in **Error! Reference source not found.**.

Since for the most locations July has the highest average temperature in the whole year, thus, July is chosen as the month for the night cooling effectiveness analysis. By using the nominal building described previously, the hourly average air temperature inside the building for July is calculated.

Table 33: Cooling potential ranges in the typical cities selected in each climate

City	Average Minimum temperature in July (°c)	CCP (kh)/night	CCP Range
Shanghai	25.25	19.67776	0-30
Rome	18.33	46.14149	30-60
Paris	14.60	75.24216	69-90
Helsinki	12.03	106.1993	90-120

Based on simulation results, it can be found that the night cooling ventilation can reduce the average temperature in the day time for the four cities by 3.07°C, 3.50°C, 3.58°C and 4.16°C, respectively.

Figure 95: Average temperature reduction in different cities in July

It is clear that the average temperature reduction during the day time is proportional to the level of climate cooling potential. Shanghai, for example, had average an average of 19kh/night climate cooling potential in summer and the temperature reduction was 3.07°C. Other city like Helsinki, the temperature reduction was 4.16°C for CCP of 106kh/night. This relationship can be expressed in a curve as shown in Figure 96.

Figure 96 Relationship between climate cooling potential and air temperature reduction in building

Night cooling ventilation combined with HVAC

Many tall buildings are not suitable for natural night cooling ventilation by opening windows, particularly for the most of commercial buildings. In this case, the night time cooling ventilation can be achieved from using HVAC system to provide cooling air into building in the night time. For this operation, the energy consumption on circulating cold air should be taken into account. The effect of the night cooling may be measured with a ratio of the extra fan energy consumption to the energy saved in HVAC operation. The extra energy consumption, $P_{fan,night}$, is determined by the operating time of fans to circulate the cold air for night cooling. The operating time of the fan is associated with the night cooling potential, the effectiveness of heat transfer and the amount of cooling to be stored. The larger climate cooling potential and higher effectiveness will lead to a shorter fan operating time while the operating time increases with the amount of cooling to be stored.

In order to investigate the effectiveness of HVAC combining with cooling ventilation, DesignBuilder is used to simulate the night cooling effect on the energy consumption of HVAC system in the building. Since DesignBuilder does not have a special function for nigh cooling simulation, the simulation of the combined HVAC operation was carried out over a period of whole month operation in July. A day's operation was

divided into two sessions with the daytime HVAC operation from 7:00 to 19:00 and the night time ventilation operation from 19:00 to 7:00 next day. The cooling to the building thermal mass in the night time session was fed into the next day operation based on the fact that the building is cooler in the start of HVAC operation. Due to previous night time cooling operation the energy consumption of HVAC operation was somehow reduced depending on the last day's night cooling operation. While the energy consumption for the daytime session is determined from HVAC operation, the energy consumption for the night-time session depended on the length of time the fan operates. With a limited CCP value, the longer running of the ventilation fan did not always deliver more cooling to the building. The duration of fan operation was also restricted in order not to cool the building too cold. Therefore, the duration of the fan operation for night time cooling ventilation had to be considered with the values of CCP.

Table 4 listed the values of seven cities' climate cooling potential, climate cooling demand and their ratio. Singapore has the lowest ratio of 0.071 indicating that the night cooling can only provide 7.1% of cooling demand at the maximum. Helsinki had the highest ratio of 97.56. These cities represented a wide range of variation in the ratio of the climate cooling potential to the climate cooling demand. The fan running time for the night-time cooling ventilation was varied with the ratio according to the available climate cooling potentials to be delivered and the fan's capacity of HVAC.

Table 34 Characteristics of selected cities

City	CCPl(night) (kh)	CCD/(daytime)(kh)	Ratio
Singapore	1.63	22.98	0.071
Shanghai	19.68	28.92	0.68
Atlanta	28.34	22.42	1.29
Alexandria	16.45	7.42	2.22
Toronto	74.87	9.03	8.29
Paris	75.24	2.61	28.81
Helsinki	106.20	1.09	97.56

Table 5 showed the results obtained from the simulations. The figures for HVAC cooling supplied were in kh which was converted from HVAC cooling load.

It should be noted that cooling supplied by HVAC was much greater than the climate cooling demand. The difference represented the cooling load of HVAC required to remove the heat gained directly from radiation to the building while this heat was not considered in calculation of CCD.

Table 35 Fan operation time and night-time cooling delivered

City	Climate potential (kh)	HVAC cooling supplied (kh)	Ratio	Delivered (kh)	t_{op} (h)
Singapore	1.63	425.04	0.071	1.63	1
Shanghai	19.68	487.46	0.68	19.68	2
Atlanta	28.34	303.91	1.29	28.34	4
Alexandria	16.45	295.33	2.22	16.45	3
Toronto	74.87	143.89	8.29	74.87	10
Paris	75.24	91.84	28.81	75.24	2
Helsinki	106.2	47.92	97.56	47.92	1

Table 36 Energy consumption change

Night cooling Cities	Electric Energy for Fan (KWh)			Electric Energy for HVAC (KWh)			$\dfrac{P_{fan,night}}{\Delta P_{HVAC}}$
	No	Yes	Change	No	Yes	Change	
Singapore	87	98.95	11.95	2675.07	2664.42	-10.65	1.122066
Shanghai	92.02	137.33	45.31	3246.37	3207.98	-38.39	1.180255
Atlanta	98.63	124.46	25.83	2110.1	2050.98	-59.12	0.436908
Alexandria	92.47	117.22	24.75	1890.43	1848.83	-41.6	0.594952
Toronto	81.57	131.51	49.94	1128.65	1035.32	-93.33	0.535091
Paris	81.54	85.16	3.62	751.68	745.79	-5.89	0.614601
Helsinki	74.34	76.84	2.5	433.38	429.08	-4.3	0.581395

The column of Delivered (kh) in Table 5 listed delivered the climate cooling potential through night-time ventilation operation. A conversion rate 0.3 was uniformly applied in all cases to reflect the inefficiency of the process to store the cooling in the building. The fan operation time for night time ventilation, t_{op}, was selected with the criterion for maximising the energy saving. The values of t_{op} in the column were obtained from the simulation with the fan running time being rounded to hour. The comparison of the energy consumptions between the operations with and without night-time ventilation cooling was shown in Table 6.

From Table 6, one can find that with the night-time ventilation cooling operation, the fan energy consumption increased while the energy consumption of HVAC in daytime operation decreases. For the cities like Singapore and Shanghai, the energy consumption for the night-time ventilation cooling was greater than the energy saved in daytime operation of HVAC, which results in the ratio of fan power consumption to HVAC saving being greater than 1. All other cities showed energy saving achieved by including night time ventilation cooling.

Figure 7 showed the potential saving can be achieved from night time ventilation against the ratio of CCP to CCD. They can be highlighted as follows:

- For the ratio approximately less than 1, there was no benefit of using night time ventilation. For the city like Singapore, it had a high average temperature all year round. Even in the night time the temperature was still above 20°C. So, Singapore's CCP was near to zero but CCD in the day time is high. This made the ratio very large for Singapore. The small amount of night time "cooling storage" required for long time running of the ventilation fan due to small CCD. Therefore, the night cooling strategy was not an efficient choice for the climate like Singapore.
- There was a range in which the saving increased significantly with the climate ratio from 1 to 2.2. The cities such as Atlanta and Alexandria were in this range. The relatively larger CCP and CCD made the night cooling ventilation effective in these places.
- The saving did not increase with the ratio of CCP to CCD after a certain point. The cities of Paris and Helsinki which had high ratio did not show any better than Atlanta and Alexandria. This is because in these cities, the temperature in the night was low but the buildings could be cooled too low to impact on the thermal comfort, i.e., the climate cooling potential was fully utilised.
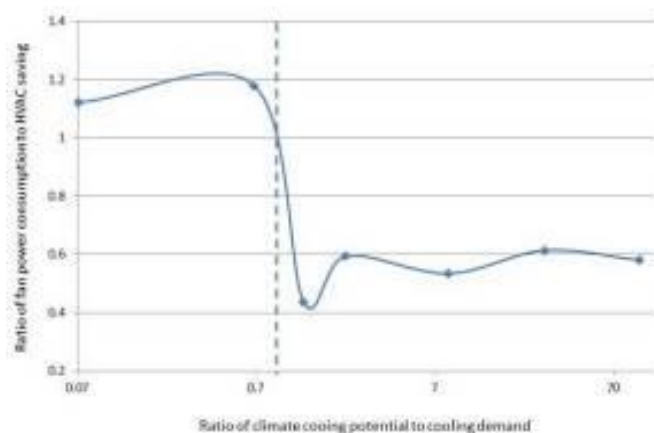
Figure 97 Applicable climate condition of night cooling ventilation in air conditioned buildings

From the discussion above, it can be seen that the effectiveness of night-time ventilation when it was combined with HVAC operation was not only dependent on the available climate cooling potential. The requirement for daytime thermal comfort could limit the use of climate cooling potential fully.

5 CONCLUSIONS

It can be found that the effectiveness of night cooling ventilation may not be similar in the same latitude range cities of west and east coast of the Pacific and the Atlantic. The night cooling ventilation may be more efficient in the east coast cities of ocean as they have lower average temperature during night and higher cooling potential in the summer time. The results show that among different locations, the reduction of building temperature when the night cooling ventilation implemented with passive cooling approach is linked with CCP as shown in Figure 6. However, for the active implement approach, it is found that the night cooling ventilation shows positive effect when the ratio of CCP to CCD is greater than 1, i.e., at this point, the reduction on HVAC energy consumption for cooling in daytime starts to outweigh the additional fan power consumed on night cooling from this point.

6   REFERENCES

[1] Leo SAMUEL, D.G.; Shiva Nagendra, S.M.; Maiya, M.P. 2013, "Passive alternatives to mechanical air conditioning of building: A review". *Building and Environment* **66**: 54–64. August

[2].http://www.architecture.com/SustainabilityHub/Designstrategies/Air/1-2-1-5-Nightventilationofthermalmass.aspx. Accessed on November 09, 2013. Nick Baker, *Night ventilation of thermal mass, The martin Centre*, University of Cambridge

[3] B. GIVONI, 1998, Effectiveness of mass and night ventilation in lowering the indoor daytime temperatures-Part 1:1993 experimental periods. Energy and Buildings.

[4] B. GIVONI, 1994, *Passive and low energy cooling of buildings*. New York: Van Nostrand Reinhold.

[5] B. GIVONI, 1992, Comfort, *climate analysis and building design guidelines*. Energy and Buildings, 1992, 18(1), pp. 11-23.

[6] ROAF S, Haves P, Orr J. 1998, *Climate change and passive cooling in Europe. In: Proceedings of "Environmentally friendly cities"*, PLEA 98 (passive and low energy architecture) conference, held Lisbon, Portugal, June 1998. UK: James & James Ltd.; 1988. p. 463–6.

[7] http://architecture2030.org/hot_topics/edward_mazria_senate_testimony. U.S. Energy consumption by sector, *Architecture 2030: Edward Mazria's Senate Testimony*

[8] http://wisegridsolutions.com/efficientlighting.html. Accessed on December 02, 2013. Building Energy Data Book, *why use efficient lighting,* wise grid

[9] LINDEN, P. F. 1999, "*The Fluid Mechanics of Natural Ventilation*". Annual Review of Fluid Mechanics **31**: 201–238.

[10] G.B. ZHOU, Y.P. Yang, X. Hong . 2011, Energy performance of a hybrid space-cooling system in an office building using SSPCM thermal storage and night ventilation. Solar Energy 85(2011)477-485.

[11] N. ARTMANN. H Manz, P. Heiselberg. 2007, Climatic potential for passive cooling of buildings by night-time ventilation in Europe. Applied Energy 2007; 84 pp. 187-201

[12] CR 1752 1998, Ventilation for buildings: design criteria for the indoor environment. CEN, Brussels;.

[13] OLESEN BW, Parsons KC. 2002, Introduction to thermal-comfort standards and to the proposed new version of EN ISO 7730. Energ Build 2002;34:537–4.

[14] BRAGER, G, S, de Dear, R, J. 2001, Climate, Comfort, & Natural Ventilation: A new adaptive comfort standard for ASHRAE Standard 55. Figure 3, Page 6.

[15]   http://apps1.eere.energy.gov/buildings/energyplus/weatherdata_about.cfm?CFID=739234&CFTOKEN=622a40312f286f10-1B10D739-CC6C-A2A9-7E034654CE94FE39&jsessionid=45B2D9642CDF8ADA26081014256F4EF8.eere. Accessed on March, 12, 2014. U.S. DEPARTMENT OF ENERGY. EnergyPlus Energy Simulation Software

259: Theoretical analysis of a membrane-based liquid desiccant system

ZIWEI CHEN[1], YUQI PAN[2], JIE ZHU[3]

[1] *Ziwei Chen, Department of Architecture and Built Environment, The University of Nottingham, University Park, Nottingham NG7 2RD, UK, ezxzc@nottingham.ac.uk*
[2] *Yuqi Pan, Department of Architecture and Built Environment, The University of Nottingham, University Park, Nottingham NG7 2RD, UK, layyp3 @nottingham.ac.uk*
[3] *Jie Zhu, Department of Architecture and Built Environment, The University of Nottingham, University Park, Nottingham NG7 2RD, UK, jie.zhu@nottingham.ac.uk*

Ventilation and air humidity are two important factors determining the thermal comfort of indoor environment. Liquid desiccant dehumidification has become one of the widely used dehumidification technologies with high efficiency and energy storage capability. Different from the conventional packed beds dehumidification, membrane-based dehumidification systems overcome the problem of liquid droplets from crossing over. Heat and mass transfer phenomena of the membrane-based dehumidification are much more complicated than the commonly well-investigated packed columns. Based on the literature studies, a simplified steady-state counter-flow mathematical model has been developed in this paper for a single layer membrane unit. The theoretical model can be used to carry out performance analysis and system design. The governing equations were solved iteratively by finite difference method. The performance analysis has been completed for a small-scale membrane-based dehumidification module consisting of 8 air channels and 8 solution channels. The influences of main design parameters on dehumidification effectiveness have been evaluated, including air and solution inlet conditions, air flow rate (NTU) and solution to air mass flow rate ratio (m*). The numerical results indicated the capabilities of the membrane-based unit to provide the dehumidified air under various climate conditions. The system NTU and solution to air mass flow rate ratio (m*) are two key parameters impacting the dehumidification performance, and they affect each other positively. Higher sensible and latent effectiveness can be achieved with larger NTU and m*. Suggestions for the system design and operation have been provided with performance evaluations.

Keywords: Dehumidification, Liquid Desiccant, Membrane-based, Heat and Mass Transfer, Numerical Model

1. INTRODUCTION

In recent years, innovative HVAC systems have been raising great concerns due to the significant energy consumption and ineffectiveness in independent humidity control for the conventional HVAC systems (Vakiloroaya et al., 2014). In hot and humid regions, air dehumidification plays an important role to control indoor thermal comfort. There are many available dehumidification approaches, such as cooling coils, solid and liquid desiccant dehumidification and electrochemical dehumidification (Zhang, 2008). Normally, cooling and dehumidification demands are achieved by mechanical vapour compression in which dehumidification is accomplished by cooling air to dew point temperature, and extra energy is consumed for re-heating the air to reach the designed supply temperature (Xiao et al., 2011). However, the associated risks appear, such as leakage, bacterial breeding, and fungi due to water condensation on the surface of the cooling coil. Alternatively, the liquid desiccant dehumidification technology has advantages in terms of addressing these drawbacks. The liquid desiccant dehumidification improves indoor supply air quality and thus prevents epidemic of respiratory disease (Zhang, 2012). Its higher dehumidification capability enables humidity control without extra energy consumptions in 'overcooling' and 're-heating' (Mei and Dai, 2008). Additionally, low-grade energy sources such as solar energy and waste heat can be utilized for liquid desiccants with low regeneration temperature.

The membrane-based liquid desiccant air dehumidification system has been attractive with elimination of crossover problems. In this system, the membrane acting as a selective barrier allows heat and moisture transfer between the solution and air stream while preventing the carryover of liquid desiccant or water (Huang and Zhang, 2013). To clarify the influences of design operating parameters and conditions precisely, intensive performance studies and optimisations have been carried out experimentally and numerically for different operational conditions. Koronaki et al. (2013) proved that the air inlet condition (i.e. air mass flow rate and air humidity ratio) and desiccant state (i.e. temperature and concentration) significantly influence dehumidification performance of a counter flow liquid desiccant dehumidifier. Ge et al. (2014) studied the performance of liquid-to-air membrane energy exchangers using experimental and analytical methods. They found the most significant dimensionless parameters affecting the dehumidification performance are NTU, solution to air thermal capacity ratio and solution operation ratio. The modelling methods have been well developed for traditional liquid desiccant devices using packed column and high-pressure liquid sprays. However, most of the traditional models are based on the assumptions which are not suitable for membrane-based systems. Unlike the constant desiccant concentration throughout dehumidification process for traditional packed-bed cooling tower, the vapour is transferred from air stream to desiccant solution, leading to the reduction in solution concentration which should be disclosed in a membrane-based system. Another difference is the "slug flow" assumption neglecting the transfer resistance between air stream and liquid desiccant in packed-bed systems. However, the membrane has more significant resistance for mass transfer, which should be taken into account in the mathematical model. Various mathematical models on membrane-based system have been developed over the years. Three most commonly adopted approaches are finite difference method, effectiveness NTU model, and simplified model using analytical solution or fitted curves. The studies mainly focus on the coupled heat and mass transfer characteristics and transient behaviour in membrane systems. Besides parametric studies, the basic mathematical model can provide fundamentals for further system design and optimization. Seyed-Ahmadi et al. (2009) presented a two dimensional transient numerical model for run-around heat and moisture exchanger system by applying the finite difference method. The analytical model was then adopted for assessment of the transient behaviour under different operating parameters and analysis of the storage volume of desiccant solution. Zhang (2010) proposed an analytical solution to conveniently estimate the sensible and latent effectiveness of a hollow fibre membrane contactor. The numerical approach is proved to be reliable for performance assessment based on the validation with experimental data. Huang et al. (2012) introduced a conjugate heat and mass transfer model in the membrane-formed parallel-plates channels. The boundary conditions of the membrane surface are identified to be much more complicated than the typical packed columns, which should not be simply assumed as constant heat flux (concentration) or surface temperature problems. However, some models are too complicated for basic system feasibility, performance and optimization analyses. A simpler mathematical model of a small-scale counter flow liquid-to-air membrane energy exchange system was developed by Ghadiri Moghaddam et al. (2013). Satisfactory agreement was presented between the numerical modelled coupled heat and mass transfers in the air, solution and membrane and experimental findings under different operating conditions.

The steady-state model has advantages in its simplicity and is efficient for predicting performance under various conditions. Based on the mathematical models of Seyed-Ahmadi et al. (2009), Huang et al. (2012) and Ghadiri Moghaddam et al. (2013), the modifications are adopted to develop a simplified numerical

model of coupled heat and mass transfer for a single-layer membrane unit using calcium chloride as the liquid desiccant in this paper. The membrane-based unit consists of an air and a solution channel arranged in parallel. Air and desiccant solution flow alternatively through a flat-plate in counter flow configurations. The steady-state effectiveness of the membrane-based liquid desiccant dehumidification system is numerically simulated with finite difference method. The performance analysis in this study focuses on the influences of various design parameters on dehumidification effectiveness, including air and solution inlet conditions, air flow rate (NTU) and solution to air mass flow rate ratio (m^*). Suggestions for further system design and operation are proposed together with performance evaluations.

2. MATHEMATICAL MODEL

A steady-state counter flow mathematical model is developed for a single-layer membrane unit as shown in Figure . Desiccant solution flows along x axis positive direction while air flows along negative direction. Air and solution flows are considered to be laminar since the Reynolds numbers are less than 2000 (Huang et al., 2012).

Height (H)	0.25m	Length (L)	0.30m
Membrane Thickness (δ)			0.0005m
Solution Channel Thickness (d_sol)			0.0016m
Air Channel Thickness (d_air)			0.005m
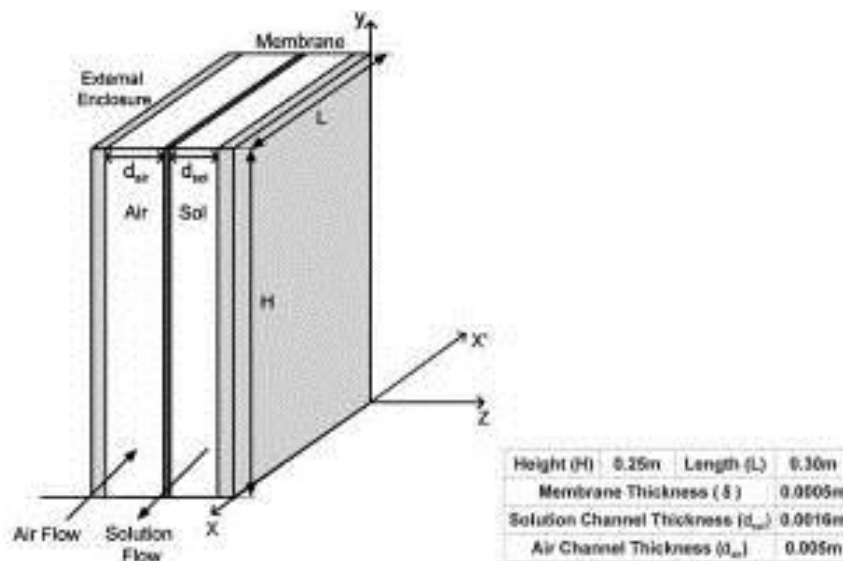
Figure 1 Schematic diagram of a counter flow single-layer membrane unit

The flowing assumptions are made to simplify the flow model:

1) The unit is well-insulated with negligible heat transfer taking place between membrane unit and ambient.
2) Thermodynamic and physical properties of air and solution flows are constant and independent of temperature and humidity.
3) Flows with uniform velocity are fully developed with negligible entrance effects.
4) The bulk properties (temperature, humidity) of two fluids are used; there is no temperature or concentration variation in y axis direction.
5) The membrane properties are uniform in the unit.
6) Heat and mass transfer only occur normally to the flow direction (z axis) and axial diffusion is neglected.
7) Water vapour is transferred in the membrane and condensed at the membrane-solution interface. The heat released during the process is added to the solution side since the convective heat transfer coefficient on solution side is much higher than that on air side.
8) The channel boundaries are flat with no fins or any heat transfer enhancements.

2.1 Governing equations

Solution and air channels governing equations

To model the heat and mass transfer between air and solution channels, a small control volume (CV) of the size *dx* by *dy* is determined. Graphs in Figure 2 show the incremental control volume for mass balance and energy balance in the solution and air channels respectively. Since air stream flows opposite to the solution flow, x' indicates the negative x direction. The specific humidity is used instead of vapour pressure since this property is more straightforward and the vaporisation heat can be easily derived. The equivalent specific humidity ratio of the desiccant solution is used in the analysis, which can be calculated with equilibrium state of air at the interfacial area. The empirical correlations between specific humidity and vapour pressure are adopted with reference to Cisternas and Lam (1991) and ASHRAE (2013). Hence, the membrane surface humidity governing the differential equations can be obtained from surface temperature and solution concentration. Explanations for parameters involving in the models are presented as follows:

- m_{salt} = mass of salt (kg)
- $\dot{m}_{air}$ = air mass flow rate (kg/s)
- $\dot{m}_{sol}$ = solution mass flow rate (kg/s)
- W_{air} = specific humidity of air (kg/kg)
- $W_{sol,mem}$ = specific humidity of solution on the membrane surface (kg/kg)
- $c_{p,sol}$ = solution specific heat (kJ/kgK)
- $c_{p.air}$ = air heat capacity (kJ/ kg K)
- h_{fg} = condensation heat of water (J/kg)
- T_{sol} = solution temperature (°C)
- T_{air} = air temperature (°C)
- $T_{sol,mem}$ = membrane surface solution temperature (°C)
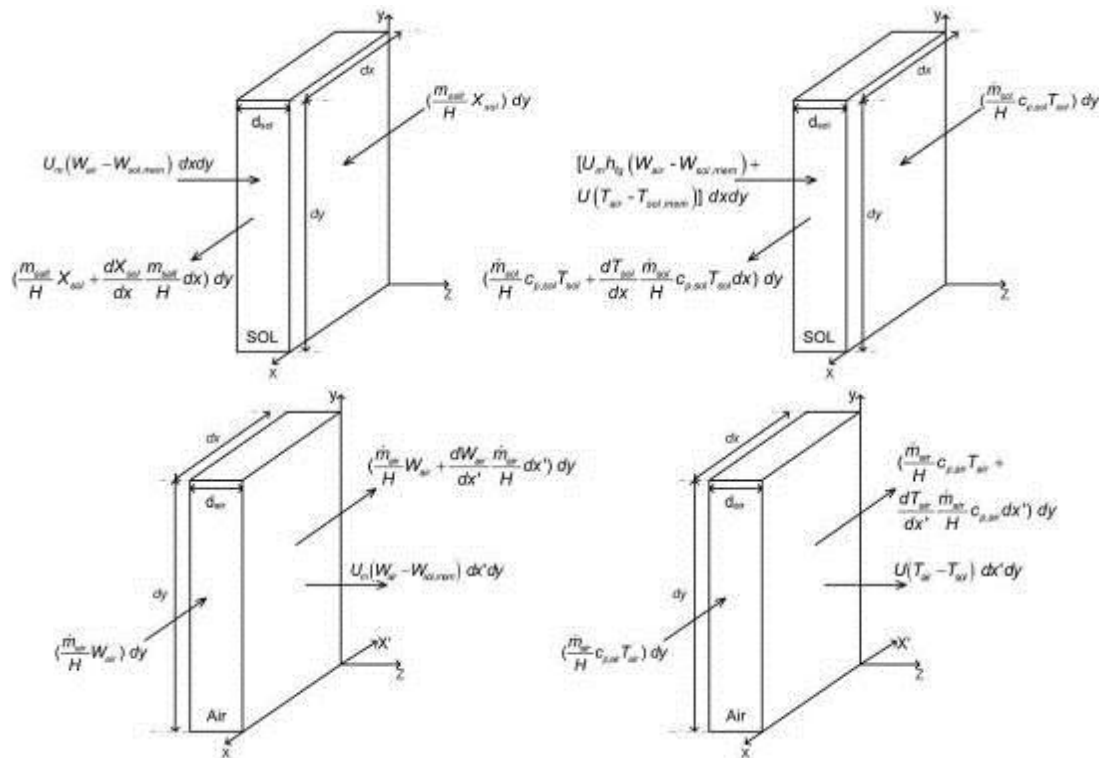
Figure 2. Control volumes for the mass balance and energy balance in the solution and air channels

The solution mass fraction (X_{sol}) is defined as the mass ratio between water and desiccant. The liquid desiccant solution concentration (C_{sol}) can be derived from the solution mass fraction.

Equation 1: Solution concentration.

$$C_{sol} = \frac{1}{1 + X_{sol}}$$

With regard to the heat and mass transfers in the two channels, overall convective mass transfer coefficient (U_m) and heat transfer coefficient (U) are defined respectively. To determine the overall transfer coefficients, mass and heat transfer coefficients can be derived from dimensionless Nusselt number and Sherwood number under conjugate transfer condition. Huang et al. (2012) validated their theoretical heat and mass

transfer models for various membranes with experiments. With referenced to the property tables, the corresponding *Nu* and *Sh* values under the defined conjugate transfer condition in this model are adopted.

Equation 2: Overall mass transfer coefficient.

$$U_m = \left(\frac{1}{h_{m,air}} + \frac{\delta}{k_{m,mem}} \right)^{-1}$$

Where:

- $h_{m,air}$ = air side mass transfer coefficient (kg/m²K)
- $k_{m,mem}$ = membrane mass conductivity (kg/ms)

Equation 3: Overall heat transfer coefficient.

$$U = \left(\frac{1}{h_{air}} + \frac{\delta}{k_{mem}} + \frac{1}{h_{sol}} \right)^{-1}$$

Where:

- h_{air} = air side heat transfer coefficient (W/m²K)
- k_{mem} = membrane conductivity (W/mK)
- h_{sol} = solution side heat transfer coefficient (W/m²K)

Membrane surface balance equations

The membrane heat and mass transfer is considered to occur at the membrane surface as the heat from vapour condensation is added to the solution side. The overall heat transfer coefficient (*U*) is used for heat transfer from air channel to membrane, which includes the resistance of convective heat transfer of the solution.

Equation 4: Mass balance in membrane surface.
$$U_m \left(W_{air} - W_{sol,mem} \right) = h_{m,sol} \left(C_{sol} - C_{sol,mem} \right)$$

Where:

- $h_{m,sol}$ = solution convective mass transfer coefficient (kg/m²s)
- $C_{sol,mem}$ = solution concentration on membrane surface

Equation 5: Energy balance in membrane surface.
$$\left(T_{sol,mem} - T_{sol} \right) = U \left(T_{air} - T_{sol,mem} \right) + h_{fg} U_m \left(W_{air} - W_{sol,mem} \right)$$

2.22. Normalization

The governing equations are then normalized to outline important parameters. The procedures are explained in Figure . NTU is obtained from minimum capacity ratio (i.e. $\dot{m}_{air} c_{p,air} < \dot{m}_{sol} c_{p,sol}$).
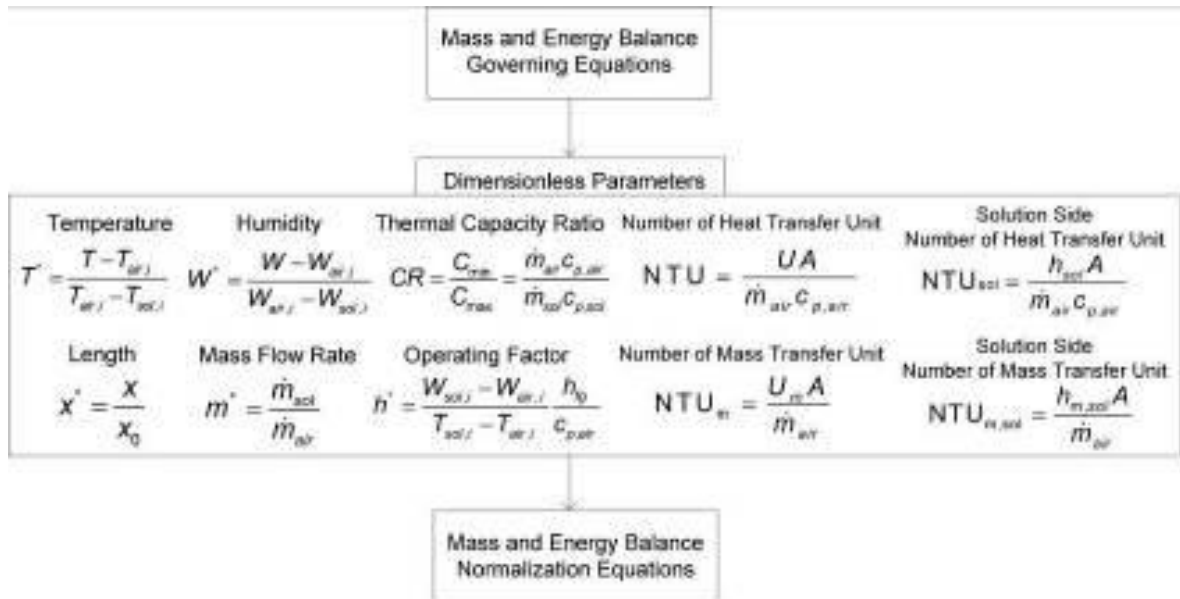
Figure 3. Normalization process with dimensionless parameters for governing equations

Equation 6: Solution side mass balance.

$$\frac{dX_{sol}}{dx^*} - \frac{1}{m^*} W_0 \text{NTU}_m \left(1 + X_{sol}\right)\left(W^*_{air} - W^*_{sol,mem}\right) = 0$$

Equation 7: Solution side energy balance.

$$\frac{dT^*}{dx^*} - \text{NTU}_m h^* CR\left(W^*_{air} - W^*_{sol,mem}\right) - \text{NTU} \cdot CR\left(T^*_{air} - T^*_{sol}\right) = 0$$

Equation 8: Air side mass balance.

$$\frac{dW^*_{air}}{x'^*} - \text{NTU}_m \left(W^*_{air} - W^*_{sol,mem}\right) = 0$$

Equation 9: Air side energy balance.

$$\frac{dT^*_{air}}{x'^*} - \text{NTU}_m \left(T^*_{air} - T^*_{sol}\right) = 0$$

Equation 10: Membrane mass balance equation.

$$\text{NTU}_m W_0 \left(W^*_{air} - W^*_{sol,mem}\right) = \text{NTU}_{m,sol}\left(C_{sol} - C_{sol,mem}\right)$$

Equation 11: Membrane energy balance equation.

$$\text{NTU}_{sol}\left(T^*_{air} - T^*_{sol,mem}\right) = \text{NTU}\left(T^*_{air} - T^*_{sol,mem}\right) - \text{NTU}_m h^*\left(W^*_{air} - W^*_{sol,mem}\right)$$

2.2 Solving procedure

Empirical correlations are applied to define the parameters for simulation. The constant properties are obtained directly from reference tables (Incropera et al., 2012, Conde, 2004, ASHRAE, 2013). In terms of boundary condition, the inlet condition of counter flow air and solution are defined as $X_{sol}\left(x = 0\right) = X_{sol,i}$, $T_{sol}\left(x = 0\right) = T_{sol,i}$ and $W_{air}\left(x = 1\right) = W_{air,i}$, $T_{air}\left(x = 1\right) = T_{air,i}$. The membrane module with 8 air channels and 8 solution channels is simulated for performance analysis. Finite difference method which approximates derivatives in terms of discrete differences is used to solve the governing differential equations (Jaluria, 2002). The equations are solved iteratively until the convergence is achieved (Figure

2.1). The convergence is defined by the percentage error between the current calculation results and previous ones. The tolerance is set to be error<1e-10. Afterwards, the temperature and humidity distributions in air and solution channels are obtained.
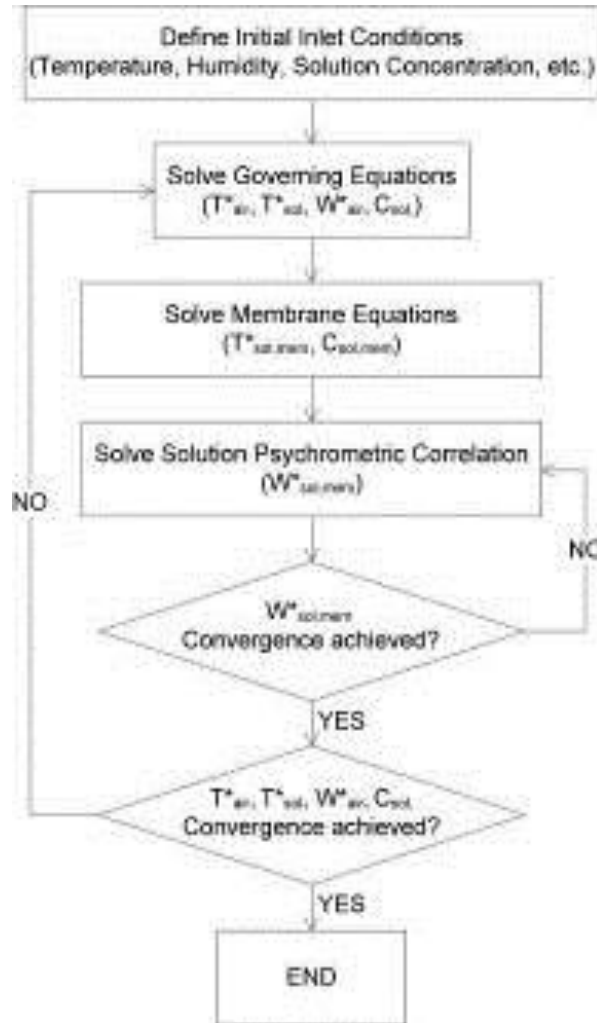
Figure 2.1 Solving procedure diagram

3. RESULTS AND DISCUSSIONS

The performance of the membrane-based dehumidification unit is studied under different operating conditions by adopting control variable method. The benchmark testing conditions are defined for simulation process as inlet air temperature of 30°C, specific humidity of 0.01728 kg/kg and inlet solution temperature of 16 °C and concentration of 35%. Basically, the system dehumidification performance is assessed by the sensitive, latent and total effectiveness, which are defined by taking inlet and outlet air temperatures (i.e. $T_{air,i}$ and $T_{air,o}$) and specific humidity (i.e. $W_{air,i}$ and $W_{air,o}$) into account (Isetti et al., 1997).

Equation 12: Sensible effectiveness.

$$\varepsilon_{sen} = \frac{T_{air,\,i} - T_{air,o}}{T_{air,i} - T_{sol,i}}$$

Equation 13: Latent effectiveness.

$$\varepsilon_{lat} = \frac{W_{air,\,i} - W_{air,o}}{W_{air,i} - W_{sol,i}}$$

Equation 14: Total effectiveness.

$$\varepsilon_{tot} = \frac{\varepsilon_{sen} - h^* \varepsilon_{lat}}{1 + h^*}$$

3.1 Inlet air effects

The system effectiveness varies not only with system design but also with local climate condition. The relative humidity (*RH*) is used as an indicator, which combines the effects of air temperature and specific humidity. The *RH* is defined from 50% to 90% with air temperature varying from 28.8 °C to 35.5 °C and specific humidity varying from 0.019 kg/kg to 0.023 kg/kg. Both sensible and latent effectiveness are influenced by inlet air condition as shown in Figure 3.1. Since the desiccant solution has low operating temperature than the air dew point, it is important to clarify the dehumidification process involves both cooling and absorption. There is only a slight variation in sensible effectiveness. In terms of the more complicated latent effectivness, the small but evident increase implies that better effectivenesss can be achieved at high relative humidity.

Moreover, the outlet air conditions are quite similar under different inlet conditions. This gives a good indication that the membrane dehumidification unit is reliable to provide relatively constant supply air under different outdoor design conditions. More accurate supply air states can be achieved by simple control of mass flow rate ratio or desiccant concentration level.
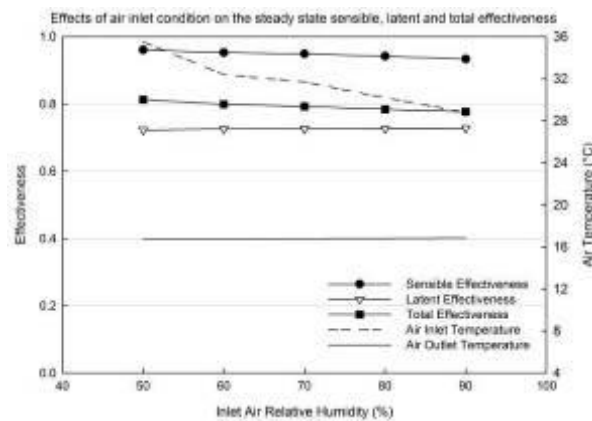
Figure 3.1 Effects of air inlet condition on the steady state sensible, latent and total effectiveness

3.2 Air flow rate (*NTU*) influences

NTU is selected to be investigated rather than the actual flow rate to eliminate the channel geometric influences. Particularly, NTU is modified by varying air and solution mass flow rates simultaneously for constant mass flow rate ratio (i.e. *m**=2). A clear correlation between the effectiveness and NTU at *m**=2 is shown in Figure 3.2. It can be observed that the total effectiveness lying between the sensible and latent effectiveness is dominated by latent effectiveness.
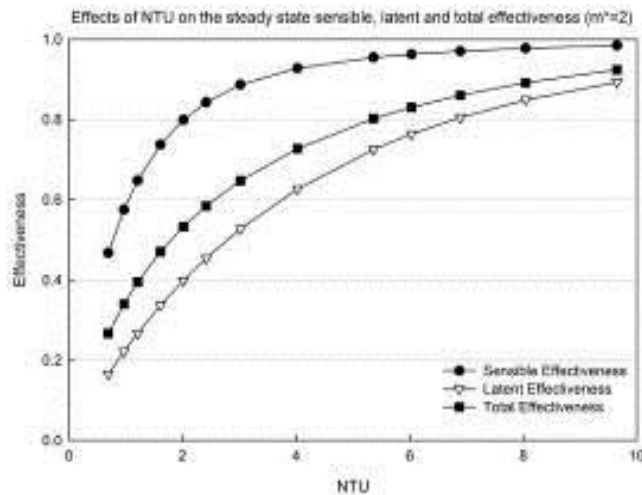
Figure 3.2 Effects of NTU on the steady state sensible, latent and total effectiveness (m*=2)
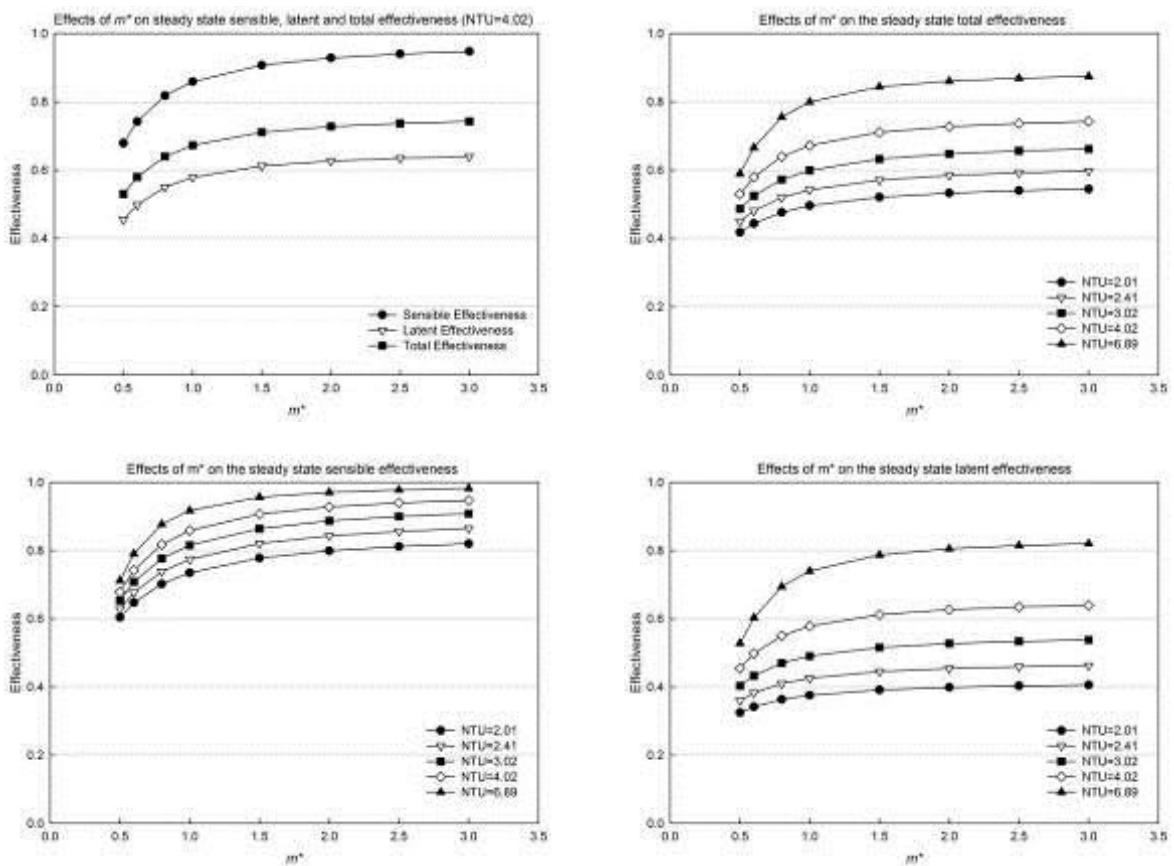
Figure 3.3 Effects of m* on the steady state sensible, latent and total effectiveness at different NTUs

The change in percentage increase for the sensible effectiveness is 89% as NTU increases from 1 to 3, while more significant increase rate can be found for the latent effectiveness (i.e. 219%). The gradual decrease in the gradient of effectiveness increase implies the less influence of NTU on the system performance. The sensible effectiveness approaches 1 at high NTU, this means that the membrane layer has little impact on heat transfer. On the contrary, the lower latent effectiveness is strongly influenced by the membrane vapour diffusion resistance. In theory, the latent effectiveness can be improved by decreasing vapour diffusion resistance (Mahmud et al., 2010). However, porous membrane would have risks in droplets carryover, which counteracts the advantages of using a membrane contactor. Therefore, the experimental investigations for the optimum membrane vapour diffusivity are needed in future research with regard to latent effectiveness and droplets carryover. Another reason restricting the increase of latent effectiveness is that the heat being transferred to the solution side increases solution temperature in a large extent and thus reduces solution concentration. As the solution equilibrium humidity is a function of solution

temperature and concentration, low humidity is associated with low temperature and high solution concentration. Owing to the constant solution mass flow rate through the process, heat transfer reduces the driving force by narrowing the gap between air humidity and solution concentration. In some conditions, the dehumidification effectiveness would start to reduce at high NTU level. In extreme cases with small mass transfer resistance and mass flow rate ratio (m^*), the sensible effectiveness may become less than latent effectiveness (Huang et al., 2014).

Solution to air mass flow rate ratio (m*) effects

The solution to air mass flow rate ratio (m^*) is a measurement of relative flow rate of two heat exchanging fluids. m^* is adjusted by modifying the solution mass flow rate with the fixed air mass flow rate for a constant NTU. The influences of m^* under different NTUs on the sensible, latent and total effectiveness are shown in Figure 3.3.

It is evident that the system effectiveness increases with m^* at constant NTU. The increase of latent effectiveness is more significant comparing to sensible effectiveness's. The variations of effectiveness at high *NTU* are more significant, especially for latent effectiveness. For example, the latent effectiveness increases 30% at NTU=6.89, while at NTU=2.01, only 8% increase is identified. It can be clearly seen that at low m^*, the effectiveness differences for different NTUs are very small, but the discrepancies become larger with m^*.

The reasons can be summarized as: the higher NTU results in high sensible and latent heat transfers and for the low solution mass flow rate, the solution is likely to be 'overheated' leading to temperature rise and transfer driving force decrease. With larger m^*, the temperature rise in solution is less significant and the system becomes more efficient at high NTU level. There is no common optimum value for m^* as other variables, but the COP of the system increases with m^* as less energy will be consumed for solution regeneration (Abdel-Salam et al., 2013). Huang et al. (2014) showed NTU significantly influences system performance. However, no benefit of high NTU is found with small m^*. Based on the numerical results, the latent effectiveness is found more sensitive to m^* than to NTU and this conclusion can be applied to cases where dehumidification is prior to cooling.

Solution temperature and concentration effects

The solution inlet temperature and concentration have great effects on the system performance since they are directly related to surface vapour pressure. Literately, low solution temperature and high solution concentration are desirable for cooling and dehumidification purposes. For analysis, the solution concentration is selected from 25% to 40%, which ensures dehumidification capabilities and avoids crystalize under the given temperatures. The sensible and latent effectiveness are considered for evaluation as shown in Figure 3.4.The sensible effectiveness is insensitive to neither solution temperature nor solution concentration. Only a slight decrease can be found, which is caused by the increased latent heat transfer. The solution at lower temperature has less impact by the latent heat transfers. On the other hand, the latent effectiveness is more strongly influenced by inlet solution temperature and concentration. And the variation is more significant at high solution temperatures. For example, 5% increase in the latent effectiveness is achieved at *T*=20.8°C, while only 2% increase at *T*=10.4°C. Moreover, at low solution concentration, the latent effectiveness is dependent on solution inlet temperature, and as the concentration increases, the dependence is getting weaker. When the concentration reaches 40%, the inlet temperature has nearly no effect on dehumidification performance. This suggests that the equivalent specific humidity of solution is less sensitive to temperature changes at high solution concentration.

Considering system dehumidification function, the low solution concentration may be not applicable. On the other hand, increasing the solution concentration, which strengths the advantage of low solution temperature would be a good way to improve dehumidification performance. However, the excessive highly concentrated solution may cause salt crystallization. Salt crystallization may lead to problems in fluid mal-distribution, blockage of the channels, high pumping pressure, and membrane fouling (Abdel-Salam et al., 2013). Therefore, the operating conditions need to be assessed carefully to avoid crystallization risks.
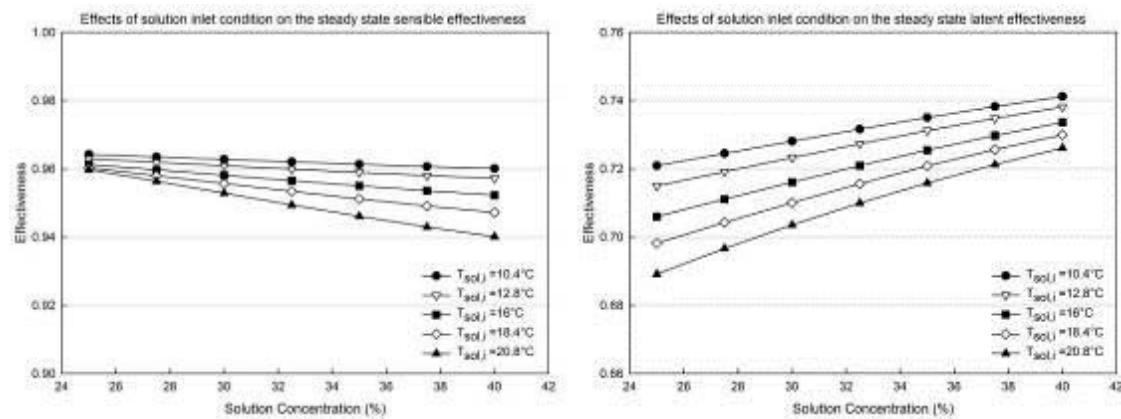
Figure 3.4 Effects of solution inlet condition on the steady state sensible and latent effectiveness

4. CONCLUSIONS

The performance of a membrane-based desiccant dehumidification unit was investigated through theoretical analysis. A counter flow steady-state numerical model was developed and solved iteratively to study dehumidification characteristics. The influences of various design parameters on dehumidification effectiveness were clarified, including air and solution inlet conditions, air flow rate (*NTU*) and solution to air mass flow rate ratio (*m**). The system performance was generally assessed by the sensible, latent and total effectiveness. Overall, the numerical results showed a good agreement with current literature data. The numerical analyses indicated that the system has much higher dehumidification capability than conventional systems. The system has the ability to provide the constant conditioned supply air under various climate conditions. The parameters with the largest influences on the system performance are air mass flow rate (NTU) and solution to air mass flow rate ratio (*m**). Higher sensible and latent effectiveness can be achieved with larger NTU and *m**. With fixed *m**, 51% improvement in the sensible effectiveness is achieved as NTU increasing from 1 to 8, while more significant increase can be observed for latent effectiveness (i.e. 68%). On the other hand, as *m** varies from 0.5 to 3, the latent effectiveness increases by 30% at constant NTU of 6.89, while at NTU of 2.01, only 8% increase is identified. The results implied that the two parameters are found to positively affect each other (i.e. the performance improves more significantly with increasing *m** at high NTU and vice versa). The solution temperature and concentration also have impacts on the system performance. Better sensible effectiveness is achieved at low solution concentration since the heat released to the solution side reduces temperature difference. Dehumidification effect is more significant with high concentration solution, and the effect of solution inlet temperature weakens at high solution concentration. It is possible that using high concentration solution offsets the disadvantages of relatively high solution temperature in dehumidification. The numerical results can be regarded as the fundamentals for further system optimization design.

5. REFERENCE

ABDEL-SALAM, A. H., Ge, G. & Simonson, C. J. 2013. Performance analysis of a membrane liquid desiccant air-conditioning system. *Energy and Buildings,* 62**,** 559-569.

ASHRAE 2013. 2013 ASHRAE Handbook - Fundamentals (I-P Edition). American Society of Heating, Refrigerating and Air-Conditioning Engineers, Inc.

CISTERNAS , L. A. & Lam, E. J. 1991. An analytic correlation for the vapour pressure of aqueous and non-aqueous solutions of single and mixed electrolytes. Part II. Application and extension. *Fluid Phase Equilibria,* 62**,** 11-27.

CONDE, M. R. 2004. Properties of aqueous solutions of lithium and calcium chlorides: formulations for use in air conditioning equipment design. *International Journal of Thermal Sciences,* 43**,** 367-382.

GE, G., Ghadiri Moghaddam, D., Abdel-Salam, A. H., Besant, R. W. & Simonson, C. J. 2014. Comparison of experimental data and a model for heat and mass transfer performance of a liquid-to-air membrane energy exchanger (LAMEE) when used for air dehumidification and salt solution regeneration. *International Journal of Heat and Mass Transfer,* 68**,** 119-131.

GHADIRI MOGHADDAM, D., Oghabi, A., Ge, G., Besant, R. W. & Simonson, C. J. 2013. Numerical model of a small-scale liquid-to-air membrane energy exchanger: Parametric study of membrane resistance and air side convective heat transfer coefficient. *Applied Thermal Engineering,* 61**,** 245-258.

HUANG, S.-M., Yang, M. & Yang, X. 2014. Performance analysis of a quasi-counter flow parallel-plate membrane contactor used for liquid desiccant air dehumidification. *Applied Thermal Engineering,* 63**,** 323-332.

HUANG, S.-M. & Zhang, L.-Z. 2013. Researches and trends in membrane-based liquid desiccant air dehumidification. *Renewable and Sustainable Energy Reviews,* 28**,** 425-440.

HUANG, S.-M., Zhang, L.-Z., Tang, K. & Pei, L.-X. 2012. Fluid flow and heat mass transfer in membrane parallel-plates channels used for liquid desiccant air dehumidification. *International Journal of Heat and Mass Transfer,* 55**,** 2571-2580.

INCROPERA, F. P., Dewitt, D. P., Bergman, T. L. & Lavine, A. S. 2012. *Principles of Heat and Mass Transfer*, John Wiley & Sons.

ISETTI, C., Nannei, E. & Magrini, A. 1997. On the application of a membrane air-liquid contactor for air dehumidification. *Energy and Buildings,* 25**,** 185-193.

JALURIA, Y. 2002. *Computational Heat Transfer,* Washington, Taylor & Francis Inc.

KORONAKI, I. P., Christodoulaki, R. I., Papaefthimiou, V. D. & Rogdakis, E. D. 2013. Thermodynamic analysis of a counter flow adiabatic dehumidifier with different liquid desiccant materials. *Applied Thermal Engineering,* 50**,** 361-373.

MAHMUD, K., Mahmood, G. I., Simonson, C. J. & Besant, R. W. 2010. Performance testing of a counter-cross-flow run-around membrane energy exchanger (RAMEE) system for HVAC applications. *Energy and Buildings,* 42**,** 1139-1147.

MEI, L. & Dai, Y. J. 2008. A technical review on use of liquid-desiccant dehumidification for air-conditioning application. *Renewable and Sustainable Energy Reviews,* 12**,** 662-689.

SEYED-AHMADI, M., Erb, B., Simonson, C. J. & Besant, R. W. 2009. Transient behavior of run-around heat and moisture exchanger system. Part I: Model formulation and verification. *International Journal of Heat and Mass Transfer,* 52**,** 6000-6011.

VAKILOROAYA, V., Samali, B., Fakhar, A. & Pishghadam, K. 2014. A review of different strategies for HVAC energy saving. *Energy Conversion and Management,* 77**,** 738-754.

XIAO, F., Ge, G. & Niu, X. 2011. Control performance of a dedicated outdoor air system adopting liquid desiccant dehumidification. *Applied Energy,* 88**,** 143-149.

ZHANG, L.-Z. 2008. Total Heat Recovery : Heat and Moisture Recovery from Ventilation Air, New York, NY, USA, Nova Science Publishers, Inc.

ZHANG, L.-Z. 2010. An analytical solution for heat mass transfer in a hollow fiber membrane based air-to-air heat mass exchanger. *Journal of Membrane Science,* 360**,** 217-225.

ZHANG, L.-Z. 2012. Progress on heat and moisture recovery with membranes: From fundamentals to engineering applications. *Energy Conversion and Management,* 63**,** 173-195.

284: Space cooling in buildings in hot and humid climates

A review of the effect of humidity on the applicability of existing cooling techniques

ADRIAN R KATILI, RABAH BOUKHANOUF, ROBIN WILSON

The University of Nottingham, University Park Nottingham NG7 2RD, ezxark@nottingham.ac.uk

The building sector is one of the biggest consumers of energy in many countries and in South East Asian region it accounts for around 30% of primary energy demand. This is mainly dominated by the use of air conditioning systems to provide space cooling for the building's occupants. Energy intensive vapour compression systems consume over 50% of total energy used in buildings, increasing to 80% at peak times. In addition, air dehumidification is achieved by reducing the ambient air temperature below its dew point, which is far lower than the required comfort conditions in buildings, causing more energy waste for air reheating.

In this paper various cooling techniques will be reviewed and their suitability to provide comfort cooling in the context of hot and humid climates discussed. Compared to vapour-compression system which offer good reliability and comfort control level, passive cooling techniques have also been developed as viable low carbon alternatives. Commonly, passive cooling technologies such as radiant cooling, ground cooling, evaporative cooling, etc. have been mainly used in dry and hot climate, however their adoption in humid climate poses a problem as ambient air moisture content is high. Techniques for water vapour removal from air using desiccant materials will be discussed as well the use of solar energy to reduce energy consumption.

Keywords: energy in buildings, humidity, space cooling

1. INTRODUCTION

Building sector is one of the main energy consumers in the world, contributing around 40% of the total energy consumption, with HVAC systems being the biggest contributors (Pérez-Lombard et al., 2008: page 395). In tropical and subtropical areas, cooling in buildings has become essential for thermal comfort, particularly in public buildings such as offices, supermarkets, sport centres, etc., where energy consumption accounts for over 50% of building's energy demands (Boukhanouf et al., 2013: page 1). It is also becoming increasingly popular even in European countries due to increasing level of thermal insulation and air tightness, and more recently to frequent warm weather patterns.

Similarly, concern on building energy consumption is being raised in developing countries, such as South East Asia. For example, in Indonesia and Malaysia, buildings account for a large proportion of total electricity sales; and energy consumption increased constantly due to heavily subsidized electricity, population growth and economic prosperity. Energy subsidies in Indonesia in the last ten years have contributed about 80% of total budget for social programs. There is therefore a strong interest to utilize energy resources and as efficiently as possible [(Kwong et al., 2014), (Setyawan, 2014)]. It is predicted that by 2020, the energy consumption in South East Asia countries will exceed that of developed countries. Figure 5 shows typical building energy consumption in South East Asian Countries.
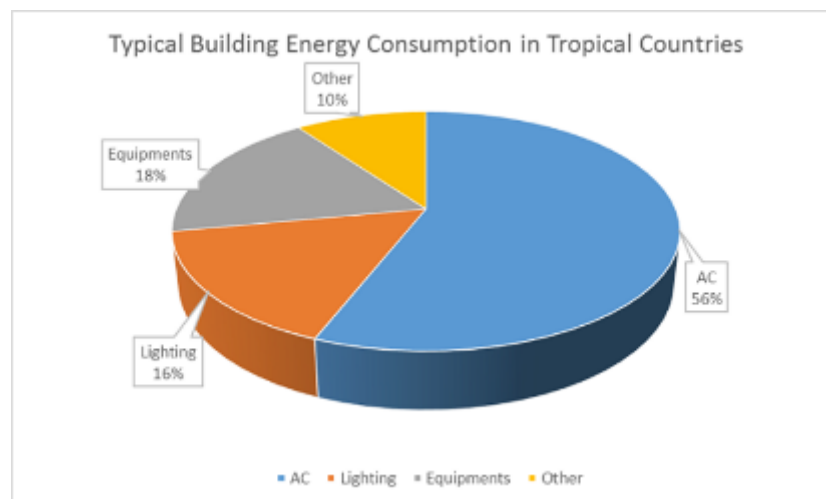
Figure 5: Typical Building Energy Consumption in Tropical Countries

The most dominant air conditioning system for building in the market today is the mechanical vapour-compression refrigeration system. This technology is quite popular because it has good stability in performance, long life cycle, reasonable energy performance, and is easy to control. However, it consumes large amount of electricity. Today, the use of mechanical HVAC system is widespread. Moreover, in hot and humid climate, the AC systems have to deal with indoor air humidity by reducing the air temperature below its dew point, resulting in even lower than the required temperature, thus further waste of energy. Therefore, it is important to understand the cooling requirement for tropical climates to determine the most efficient approach to provide comfort in building.

2. THERMAL COMFORT FOR HOT AND HUMID CLIMATE

2.1 Adaptive Thermal Approach

Thermal comfort model is necessary to determine proper boundaries / limitations to estimate the amount of heating or cooling that is required in buildings. The most common comfort model is PMV-PPD model developed by Fanger (Taleghani et al., 2013). In steady state models, ASHRAE 55 is usually used, where indoor air at 25°C and 50% RH is considered comfortable (especially for air-conditioned buildings). However, recent field studies have stated that the PMV models might not be applicable in all climates. Some field studies that were conducted in hot and humid climates have indicated that the PMV models often overestimate the thermal comfort range, especially in naturally-ventilated (free-running) building. For example, Feriadi and Wong calculated the thermal neutrality in naturally ventilated house, and it was found as 29.2°C (Feriadi and Wong, 2004: page 619). In areas with hot and humid climate, particularly when the air-conditioning system is not available, the acclimatisation of the people to the local climatic conditions

differ their thermal comfort requirement. Adjusting the set-temperature based on the adaptive model can reduce energy consumption. Tham investigated a building in Singapore and found that a reduction of 2˚C (from 27 to 25˚C) in thermostat set-point had increased the energy consumption by 11.8% (Tham, 2003: page 291). In Taiwan, Yang and Su found that 34.4% of energy use in buildings can be reduced by maintaining the indoor temperature at 2˚C higher than the conventional temperature setting (Yang and Su, 1997: page 29).

2.2 Effective Temperature Approach

In buildings where occupants are less able to control their environment, e.g. in highly occupied offices or commercial buildings with centralised air conditioning system, the concept of effective temperature (EP) is required. EP combines temperature and humidity into a single index so that two environments with same ET evoke the same thermal response even though they have different temperatures and humidity, but they must have the same air velocities. With this concept, thermal comfort in air-conditioned building can be maintained by adjusting between the air temperature and relative humidity. In hot and humid climate, similar EP can be achieved when the indoor temperature is increased without reducing comfort, by lowering the air humidity.

Wan et al. (Wan et al., 2009) investigated the energy saving potential by implying the EP concept. It was reported by increasing the indoor air temperature set point while lowering the air humidity set point, indoor cooling load was decreased; however, the fresh air cooling load was increased due to increase of latent load. In overall, the energy consumption is increased when maintaining the EP by increasing the indoor air temperature. In the other hand, indoor air humidity level in the building also has an impact on quality of air and comfort. Moisture can be considered as a source of occurrence of pathologies in buildings, such as bacteria, viruses, fungi and mites (Berger et al., 2012). It is proposed that optimum humidity level should be between 40% and 60%. It is therefore necessary to keep indoor air humidity low while reducing the energy consumption.

3 COOLING LOAD IN HOT AND HUMID CLIMATE

3.1 Sensible vs Latent Cooling Load

A significant amount of cooling load in buildings is attributed to dehumidifying air in the form of latent heat. Figure 6 shows an example of a daily profile of latent a sensible cooling loads in an apartment building in Hong Kong (Li et al., 2006), where it can be seen that latent heat load is comparable to sensible load during some periods of the day.
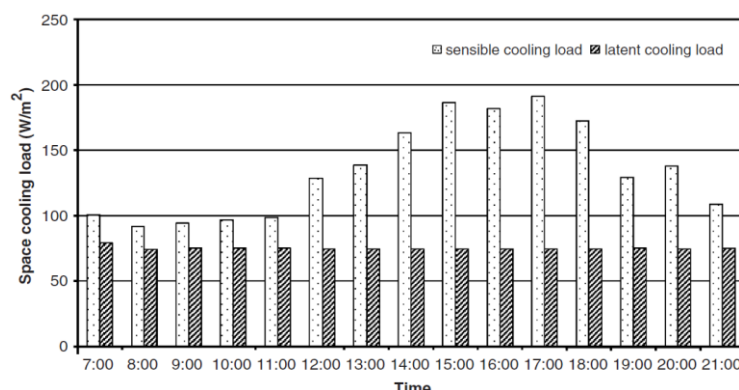
Figure 6: Distribution of sensible and latent cooling load throughout the day (Li et al., 2006)

The main part of the latent cooling load was contributed by humid fresh air whereas occupants' contribution is not as significant. The sensible cooling load, meanwhile, is dominated by heat gain through the building envelope and from as shown in Figure 7. Therefore, dehumidifying air requires large amount of electricity, and alternative low carbon cooling and dehumidifying process is necessary to assure comfort while reducing energy consumption.
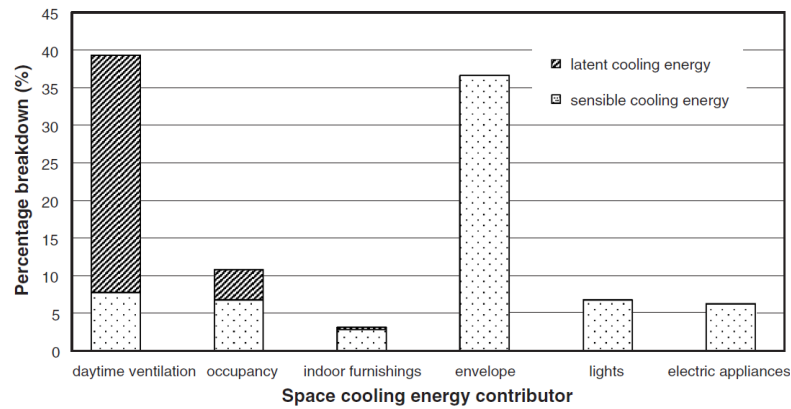
Figure 7: Contributor to building's cooling load (Li et al., 2006)

3.2 Latent Cooling Load in Hot and Humid Climate

The prevailing tropical weather conditions in most East Asian and South East Asian countries mean that latent cooling load of buildings is high with average outdoor air relative humidity higher than 70% and temperature range of 27 to 30°C (Figure 8). Assuming common standard for air conditioned building with space temperature of 24°C and relative humidity of 50%, the cooling system in South East Asian countries will need to reduce outdoor air relative humidity form over 70% to 50%, which requires significant amounts of mechanical energy for dehumidification and re-heating.
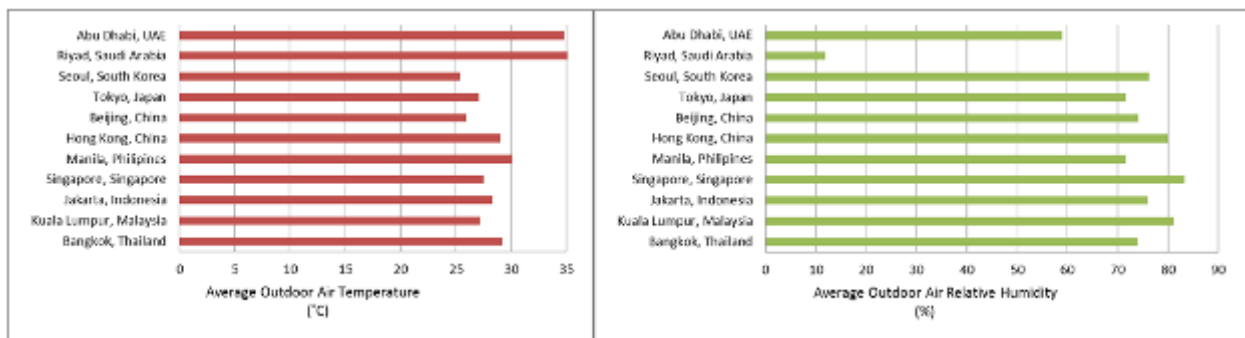
Figure 8: Monthly average outdoor condition for various climates in Asia during the hottest month of the year

4   ACTIVE COOLING TECHNIQUES

4.1 Mechanical vapour compression system

The market for air conditioning in buildings is dominated by mechanical vapour compression systems, as they have reliable performance and good comfort controllability. Individual air-conditioners are popular in residential buildings due to their easy installation and maintenance, while commercial buildings use centralised water chiller. The main air conditioning systems are:

Split/individual system

Individual air conditioners employ one condenser for one evaporator unit. The evaporator unit is usually mounted onto the wall inside the building, while the condenser unit is mounted on the external side. Generally, the individual air conditioners are distinguished by the placement of the condenser, whether it is put directly behind the evaporator and installed as a packaged unit (window type), or put elsewhere outside the cooled pace, connected by a refrigerant pipes (split type). Most of split type air conditioners use air-cooled condensers. However, these systems tend to have relatively low COP in hot and humid climate, ranging from 2.2 to 2.4 (Chen et al., 2008: page 1416). Water-cooled air-conditioning systems are often found in commercial buildings with centralised cooling system for better thermal efficiency. Chen et al. investigated the potential of using water-cooled condenser for split type air conditioners in residential buildings in Hong Kong, and found that the annual electricity consumption can be reduced by 8% (Chen et al., 2008: page 1423).

Centralised system

Typically, building with central air conditioning consists of a big cooling unit that will connected to ventilation ductworks connected to each room in the building. Chaiwongsa and Duangthongsuk (Chaiwongsa and Duangthongsuk, 2011) investigated heat recovery from the condenser to supply hot water in building in Thailand, and showed that energy saving are quiet important. On large scale systems, District Cooling System (DCS) have been adopted in many countries. A DCS is a centralized plant that can supply chilled water to a group of buildings, where central air conditioning systems were adopted. Incorporating the DCS could contribute to around 35% of energy saving in Hong Kong (Chen et al., 2008: page 1416). In addition, direct seawater-cooled plant utilizing water at 27˚C can achieve COP in the range of 4 to 5 (Yik et al., 2001: page 167). However this requires high initial cost, specific water treatment and/or equipment to avoid the corrosion of the piping. As in other air conditioners, latent heat load treatment still should be addressed to reduce the energy consumption of the compressor in hot and humid climate, either by replacing the compressor by a more energy-efficient system, or by integrating to other system to treat the latent load independently.

4.2 Absorption cooling system

In the absorption system, the mechanical compressor used in VC system, is replaced by a thermal compressor, which consists of an absorber, a generator, a solution pump, and an expansion valve. In the generator heat is added to separate the refrigerant vapour from the mixture of refrigerant-absorbent at high temperature. The attractive feature of the absorption system is that it can use various type of heat source such as solar thermal, waste heat and biomass. This makes absorption cooling system able to use low grade heat and make them less energy intensive than its mechanical vapour compression counterpart. Moreover, the absorption system can use less harmful refrigerant such as water/ammonia or LiBr/water working fluid pair (Ullah et al., 2013).

Thomas and Andre reported that combination of solar energy (with 142.3 m2) with absorption cooling system in an office building can reduce the energy consumption by 34.9% compared to conventional cooling system (Thomas and André, 2009: page 6). Hidalgo et al. carried out an experimental study using LiBr/water pair absorption system in Spain, using a 50 m^2 flat-plate solar collector to provide the regeneration heat, and reported that even though the solar energy only contributed to 56% of the cooling system operation during summer, the system still achieved saving up to 50% of primary energy (Hidalgo et al., 2008: page 1743).

4.3 Desiccant cooling system

Desiccant cooling (DC) systems are capable of treating sensible and latent load independently. Using materials with high capability of adsorbing water vapour in the air, desiccant dehumidifier systems can act as complementary component to either active/passive cooling systems, reducing latent load. DC systems mainly consist of three components: desiccant dehumidifier, cooling unit, and regeneration system. There are generally two types of desiccant materials used in DC systems: solid desiccants and liquid desiccants. Figure 9 presents a schematic of a DC system. In DC systems, incoming air stream is drawn through a desiccant material to partially remove its moisture content. The dried air is then passed to the cooling unit. For the systems to be able to work continuously, a regeneration process is required to drive out adsorbed/absorbed water vapour by heating the material.
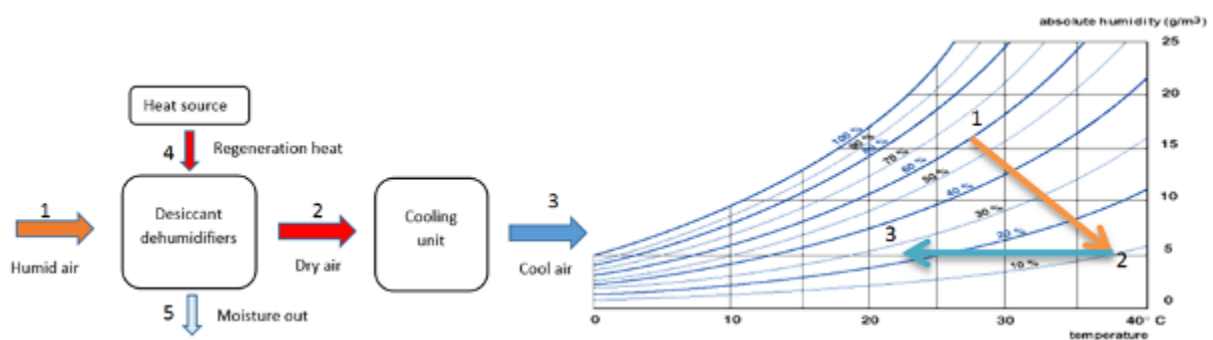

Figure 9: Schematic of DC system

Hirunlabh et al. performed an experimental study of a silica gel desiccant dehumidifier, combined with a split air conditioning system under the Thailand climate, and found that energy saving was up to 24% (Hirunlabh et al., 2007: page 576). In this study however, desiccant regeneration was not taken into consideration. Qi et al. (Qi et al., 2012) reported that if regeneration heat is provided by electricity, the DC system would consume almost twice as much energy than conventional cooling systems. Qi et al. also investigated the performance of solar-assisted desiccant dehumidifier combined with cooling coil driven by vapour compressor system in Hong Kong and found that the use solar energy reduced the energy consumption of the DC system by 50%. Overall, the solar-assisted DC system could save around 20% of energy compared to conventional system (Qi et al., 2012: page 514-515).

5 PASSIVE COOLING TECHNIQUES

5.1 Evaporative cooling techniques

Evaporative cooling system cools air through converting latent heat of water evaporation to sensible heat loss of the air, reducing its temperature towards wet-bulb temperature. The cooling capacity of evaporating cooling systems is often described by the difference between the dry bulb temperature (DBT) and the wet bulb temperature (WBT) of the air to be cooled. The WBT is usually used to define the climatic limitation for evaporative cooling techniques (Santamouris and Kolokotsa, 2013). An observation concluded that use of evaporative cooling has an upper climatic boundary lying along the 22°C WBT line up to a maximum of 42°C DBT (Lomas et al., 2004: page 664). Evaporative cooling techniques are generally divided into two types: direct and indirect evaporative cooling.

Direct system

Direct evaporative cooler (DEC) cools air by passing into a wetted material (usually porous material) causing the water to evaporate. As hot air passes over the wetted medium, some of sensible energy goes to evaporate the water, which releasing latent heat in form of water moisture. The air then leaves at the other side of the medium with lower temperature and higher humidity. Figure 10 shows the principles of DEC.
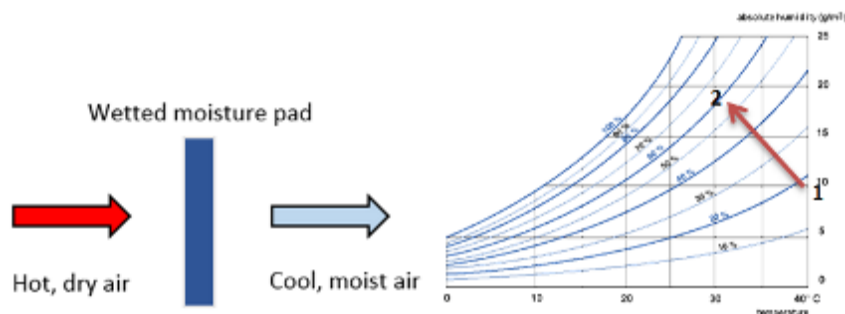
Figure 10: Schematic of DEC

Attempts have been made to integrate DEC in building to form a Passive Downdraught Evaporative Cooling (PDEC) system Ford et al. (Ford et al., 2010). PDEC mainly consist of a cooling tower (or more) which is attached to the building. In the cooling tower, the passing air is cooled directly by water evaporation, which then falls down through the tower due to buoyancy and enters into the adjacent building. In humid climate, the humidity of the air leaving the system can be increased to over 80%, which is not suitable for direct use in space, because it can cause rust and moisture sensitive materials (Xuan et al., 2012: page 3537).

Indirect system

In Indirect evaporative cooling (IEC) system, the cooling process is performed using a heat exchanger, where two airflows are utilized. The working air passes over a wetted side to generate evaporation, while the product/ supply air passes the opposite dry side. The working air is then cooled and humidified by the evaporation process, and at the same time absorbs heat from the dry air and thus cools the air in the dry side. The schematic of IEC is shown in Figure 11.
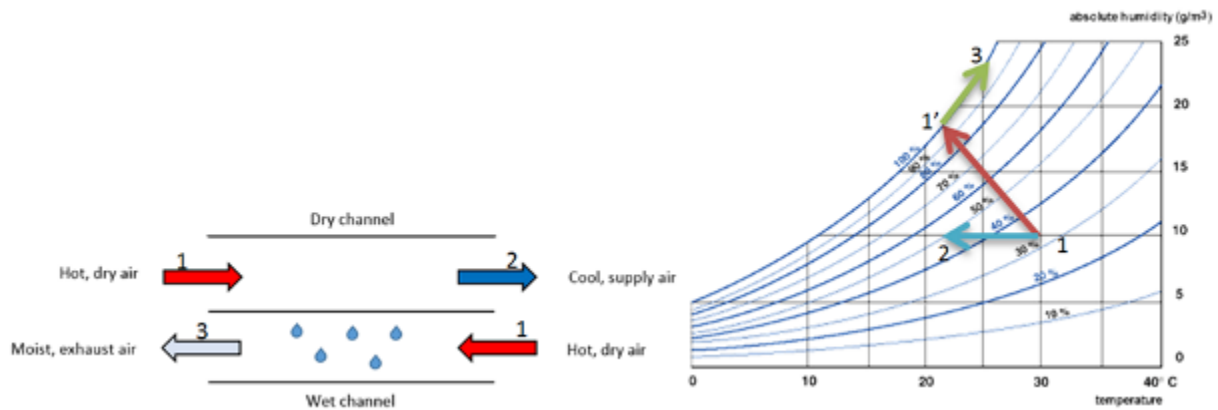
Figure 11: Schematic of IEC

Indirect evaporative cooling techniques are interesting for climate with low or moderate air humidity, as this configuration does not increase indoor air moisture content. However, the cooling potential in hot and humid climate is still limited due to smaller difference between the air's DBT and WBT. Maisotsenko Cycle (M-Cycle) has been developed to achieve supply air below its wet-bulb temperature (or close to its dew point). In M-Cycle arrangement, a part of cooled air in the dry channel is diverted to wet channel in counter flow arrangement to be cooled further. Figure 12 presents the schematic a sub-wet-bulb evaporative cooler.
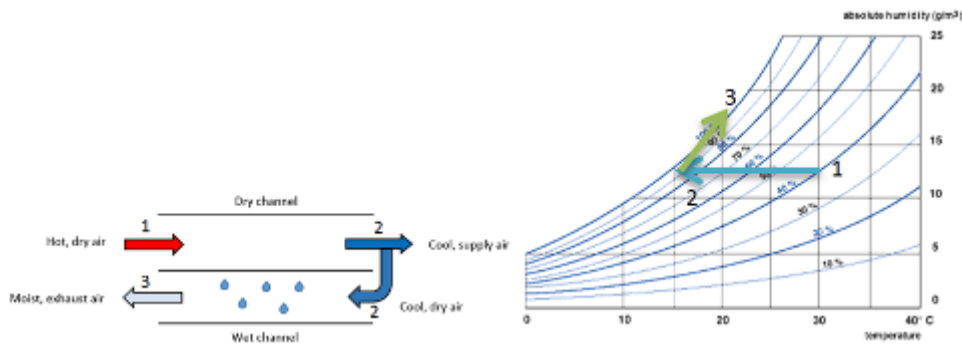
Figure 12: Schematic of sub-wet-bulb evaporative cooler

Boukhanouf et al. investigated the potential of the sub-wet bulb temperature evaporative cooler in hot and dry climate, and reported that with inlet air at dry bulb temperature of 30°C and relative humidity of 35% (WBT at 18.8°C and dew point of 12.5°C), the system was able to achieve temperature reduction to 16.9°C in dry channel (1.9°C below the WBT), while the air in the wet channel increased from 16.9°C to 19.8°C (Boukhanouf et al., 2013: page 7). In hot and humid climate, combination of M-Cycle evaporative cooler with desiccant air dehumidifier could be a very interesting proposition for energy saving in building.

5.2 Night ventilation

Night ventilation (NV) consists of over-ventilating the building during the night in order to evacuate accumulated heat in the building structure, reducing the building's cooling load for the following day. It is commonly used in office building, when the building is unoccupied during night. Blondeau et al. (Blondeau et al., 1997) studied NV application in La Rochelle, France, with constant airflow rate at 8 air change per hour. The NV allowed reduction of daytime temperature by 1.5-2°C, allowing reduction of 12-54% of the zone mechanical cooling energy. In tropical climate, however, the potential of NV is limited due to small day-night temperature difference, as well as condensation risk on the internal surface. A study in Malaysia by Kubota et al. reported that even though the application of NV could reduce the daytime peak temperature inside the building up to 2.5°C, indoor relative humidity was also increased (Kubota et al., 2009: page 833), thus indoor humidity control would be required.

5.3 Radiant cooling

The radiant cooling system provides cooling by supplying water to panels, usually installed on the ceiling of a room. The cool ceiling panels act as heat sinks through a radiation heat transfer process. On the other hand, convection heat transfer also occurs between the room air and the cool panels and creates

556

convection currents within the room. In this system, the supplied cooling water's temperature is maintained at above the indoor air dew-point temperature to avoid condensation of air's moisture on the panels. Vangtook and Chirarattaananon (Vangtook and Chirarattananon, 2006) performed a study of radiant cooling system with natural ventilation in Thailand with water temperature limited to 24°C and reported that the system performed inadequate in hot period. Seo et al (Seo et al., 2014) analysed the performance of radiant cooling system coupled with a dehumidified ventilation system and an outdoor air cooling in Seoul, South Korea with supply water temperature as low as 7°C with better cooling even in the hottest and most humid month in Korea, with operative temperature fluctuated between 25.84 and 26.92°C.

5.4 Ground Cooling

Ground cooling (GC) utilizes the advantage of ground temperature (usually between 1.5-3 m) that is relatively constant and lower than ambient air temperature in hot season/climate. Coupling between the building and the ground can be done either directly (taking outdoor air and pass it through underground pipes and deliver to building) or indirectly (recirculation of indoor air). As hot air is drawn to the pipes buried underground, the ground acts as heat sink for the passing air, providing sensible cooling to the air, reducing its temperature. The schematic of GC is shown in Figure 13.
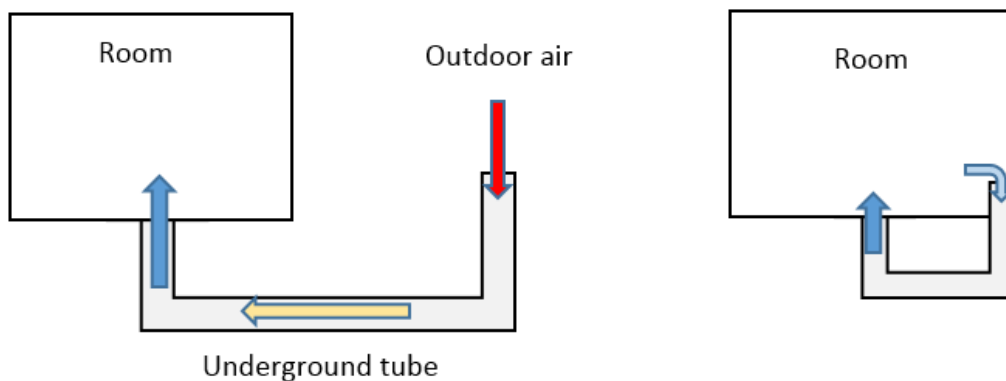
Figure 13: Schematic of ground cooling, direct (left) & indirect (right)

Several studies in European countries have shown that the GC offers promising alternative to conventional system. One case study in Germany showed that for ambient temperature close to 30°C, the air exiting the heat exchanger can be close to 18°C (Pfafferott, 2003). In areas with tropical climate, however, level of humidity should be taken into consideration, as condensation might appear in the underground pipes. In the other hand, indoor air humidity control will also be required. Sanusi et al. (Sanusi et al., 2013) conducted an experimental study of GC in Malaysia, and reported that even though the outlet air temperature was reduced by 5-6°C, the air relative humidity was increased to around 80%.

6   CONCLUSION

The increase of living standard and population growth in developing countries will lead to higher energy consumption and environmental impact. Energy consumption in buildings is one area which needs to be addressed in countries like South East Asian. With the hot and humid climates, cooling demand will contribute to the overall building energy consumption significantly. Particular attention should focus on addressing latent cooling load through energy efficient dehumidification system.

Off these, passive cooling techniques could be used as low-energy cooling alternative to conventional air conditioning systems. However, their application in humid climate is still limited. For example, the evaporative cooling technique, combined with desiccant dehumidification can overcome the issue of high humidity in tropical climate, however further research and development is required.

7   REFERENCES

BERGER, J., Tasca-Guernouti, S., Woloszyn, M. & Catherine, B. 2012. L'humidité dans les bâtiments : Pathologies et paramètres gouvernants. *XXXe Rencontres AUGC-IBPSA* Chambéry.

BLONDEAU, P., Spérandio, M. & Allard, F. 1997. Night Ventilation for Building Cooling In Summer. *Solar Energy,* 61**,** 327-335.

BOUKHANOUF, R., Alharbi, A., Ibrahim, H. G. & Kanzari, M. 2013. Investigation of a Sub-wet Bulb Temperature Evaporative Cooler for Buildings. *Sustanaible Building Conference.* Conventry University.

CHAIWONGSA, P. & Duangthongsuk, W. 2011. Hot Water Making Potential Using of a Conventional Air-Conditioner as an Air-Water Heat Pump. *Procedia Engineering,* 8**,** 165-170.

CHEN, H., Lee, W. L. & Yik, F. W. H. 2008. Applying water cooled air conditioners in residential buildings in Hong Kong. *Energy Conversion and Management,* 49**,** 1416-1423.

FERIADI, H. & Wong, N. H. 2004. Thermal comfort for naturally ventilated houses in Indonesia. *Energy and Buildings,* 36**,** 614-626.

FORD, B., Schiano-Phan, R. & Francis, E. 2010. The Architecture & Engineering of Downdraught Cooling - A Design Sourcebook, PHDC Press.

HIDALGO, M. C. R., Aumente, P. R., Millán, M. I., Neumann, A. L. & Mangual, R. S. 2008. Energy and carbon emission savings in Spanish housing air-conditioning using solar driven absorption system. *Applied Thermal Engineering,* 28**,** 1734-1744.

HIRUNLABH, J., Charoenwat, R., Khedari, J. & Teekasap, S. 2007. Feasibility study of desiccant air-conditioning system in Thailand. *Building and Environment,* 42**,** 572-577.

KUBOTA, T., Chyee, D. T. H. & Ahmad, S. 2009. The effects of night ventilation technique on indoor thermal environment for residential buildings in hot-humid climate of Malaysia. *Energy and Buildings,* 41**,** 829-839.

KWONG, Q. J., Adam, N. M. & Sahari, B. B. 2014. Thermal comfort assessment and potential for energy efficiency enhancement in modern tropical buildings: A review. *Energy and Buildings,* 68**,** 547-557.

LI, Z., Chen, W., Deng, S. & Lin, Z. 2006. The characteristics of space cooling load and indoor humidity control for residences in the subtropics. *Building and Environment,* 41**,** 1137-1147.

LOMAS, K. J., Fiala, D., Cook, M. J. & Cropper, P. C. 2004. Building bioclimatic charts for non-domestic buildings and passive downdraught evaporative cooling. *Building and Environment,* 39**,** 661-676.

PÉREZ-LOMBARD, L., Ortiz, J. & Pout, C. 2008. A review on buildings energy consumption information. *Energy and Buildings,* 40**,** 394-398.

PFAFFEROTT, J. 2003. Evaluation of earth-to-air heat exchangers with a standardised method to calculate energy efficiency. *Energy and Buildings,* 35**,** 971-983.

QI, R., LU, L. & Yang, H. 2012. Investigation on air-conditioning load profile and energy consumption of desiccant cooling system for commercial buildings in Hong Kong. *Energy and Buildings,* 49**,** 509-518.

SANTAMOURIS, M. & Kolokotsa, D. 2013. Passive cooling dissipation techniques for buildings and other structures: The state of the art. *Energy and Buildings,* 57**,** 74-94.

SANUSI, A. N. Z., Shao, L. & Ibrahim, N. 2013. Passive ground cooling system for low energy buildings in Malaysia (hot and humid climates). *Renewable Energy,* 49**,** 193-196.

SEO, J.-M., Song, D. & Lee, K. H. 2014. Possibility of coupling outdoor air cooling and radiant floor cooling under hot and humid climate conditions. *Energy and Buildings,* 81**,** 219-226.

SETYAWAN, D. 2014. Formulating Revolving Fund Scheme to Support Energy Efficiency Projects in Indonesia. *Energy Procedia,* 47**,** 37-46.

TALEGHANI, M., Tenpierik, M., Kurvers, S. & Van Den Dobbelsteen, A. 2013. A review into thermal comfort in buildings. *Renewable and Sustainable Energy Reviews,* 26**,** 201-215.

THAM, K. W. 2003. Conserving Energy Thermal Comfort Without. *Building and Environment,* 28**,** 287-299.

THOMAS, S. & André, P. Dynamic Simulation of a Complete Solar Assisted Conditioning System In an Office Building Using Trnsys. IBPSA2009 Building Simulation Glasgow, 2009.

ULLAH, K. R., Saidur, R., Ping, H. W., Akikur, R. K. & Shuvo, N. H. 2013. A review of solar thermal refrigeration and cooling methods. *Renewable and Sustainable Energy Reviews,* 24**,** 499-513.

VANGTOOK, P. & Chirarattananon, S. 2006. An experimental investigation of application of radiant cooling in hot humid climate. *Energy and Buildings,* 38**,** 273-285.

WAN, J. W., Yang, K., Zhang, W. J. & Zhang, J. L. 2009. A new method of determination of indoor temperature and relative humidity with consideration of human thermal comfort. *Building and Environment,* 44**,** 411-417.

XUAN, Y. M., Xiao, F., Niu, X. F., Huang, X. & Wang, S. W. 2012. Research and application of evaporative cooling in China: A review (I) – Research. *Renewable and Sustainable Energy Reviews,* 16**,** 3535-3546.

YANG, K. H. & Su, C. H. 1997. An Approach to Building Energy Savings Using the PMV Index. *Building and Environment,* 32**,** 25-30.

YIK, F. W. H., Burnett, J. & Prescott, I. 2001. A study on the energy performance of three schemes for widening application of water-cooled air-conditioning systems in Hong Kong. *Energy and Buildings,* 33**,** 167-182.

271: Economic evaluation of a CAES system for increased wind penetration to Egyptian grid

OMAR RAMADAN, SIDDIG OMER, SAFFA RIFFAT

[1] *University of Nottingham, University Park, Nottingham, NG7 2RD, laxor1 @nottingham.ac.uk*

Renewable Energy systems have gained growing interest especially in the last decade. However, there are serious issues that come with these systems, related to the intermittency of the renewable energy sources. Energy storage could play a big role to solve or at least minimize the issues related to the intermittency of the renewable energy systems. Compressed air energy storage (CAES), among many has the ability to have a considerable impact when it comes to large scale renewable energy systems as it can absorb and release large amount of energy (100's MW) for a long period of time (hours). An economic evaluation of CAES is important to establish its feasibility for large-scale renewable energy systems. An economic study is carried out in this paper taking Egypt as a case study for implementing CAES system as part of the proposed plans of increasing wind farms installation in Egypt by 2020.

1. INTRODUCTION

Energy demand is increasing worldwide on a yearly basis and has almost doubled over the last 30 years and is expected to grow steadily over the next few years (EIA, 2010). To meet the increase in demand, energy production needs to increase. On the upside, there exists large untapped potential in renewable energy resources, which are not only unlimited but could also help to meet the increase in demand and also reduce the environmental risks including greenhouse effects.

However, most of renewable sources are intermittent and may cause a considerable variation in electricity production, especially in the case of solar and wind energy. This poses both technical and economic challenges when these energy systems are integrated on a large scale. Therefore, innovative solutions are needed to accommodate the renewables intermittency effect on the grid. Many different technologies are being researched to minimize the effects of intermittency and help make renewables more reliable (Albadi, 2010). Energy storage systems play a big role for this application. For large-scale renewable energy systems such as wind energy; the most possible options are large scale storage systems which are mainly Compressed air energy storage (CAES) and Pumped hydro [Ibrahim, 2008]. For the CAES system, which is the focus of this paper, it is more suitable as it has large storage capacity and has a relatively shorter starting time and relatively lower capital cost (Greenblatt, 2007). On the other hand, CAES systems have some drawbacks which include the inevitable use of natural gas for heating for the expansion stage and the lower efficiency of the system compared to Pumped Hydro.

The CAES system working principle is quite simple, when the wind power is higher than the load demand meaning the supply is higher than the demand, the air is compressed using the compressors (charging period of the CAES unit); the air is stored in an underground air reservoir with minimal heat loss. When the wind power is low to meet the demand, then the compressed air is released from the underground air reservoir to power the turbines and generate electricity which is fed back to the grid (CAES unit is in discharging mode) to meet the demand.

The CAES system can be used for load levelling, hence improving the power supply from intermittent energy systems (eg. Solar and Wind). In that case, when the renewable energy source has excess in supply, the energy is stored and released to the grid in case of deficiency in power from the renewable energy sources. Another case is the use of CAES to improve the economic benefits of renewable energy systems; in this case the renewable energy systems store the energy in the CAES system when the price to sell electricity to the grid is low instead of supplying that power to the grid at low spot market prices (Madlener, 2011). When the spot market prices are high, the CAES system supplies the stored energy to the grid, hence increasing the income of renewable energy systems. In the Egyptian grid case, it is more practical to use the CAES system for load levelling issues as the Egyptian grid is weak and there are power cuts almost daily in Egypt. So improving the power output from the renewable energy sources seems more important than increasing the economic benefits from these systems.

2. METHODOLOGY

Dynamic programming is used to implement a simulation of the economic analysis of the system. The capital costs are calculated, and then the total fixed, variable annual costs and the annual revenues from the system are calculated. From that, the annual net profit/loss is found. Following these steps, the system is determined whether it is economically feasible. 2 systems are simulated in this case: 1st is the implementation of a wind farm without CAES, and the 2nd is the addition of a conventional CAES system. The system was modelled using MATLAB dynamic programming.

For each case scenario, the system net present value will be calculated on an annual basis . Also, sensitivity analysis was carried out on some of the input parameters to find out the effect of each on the net present value of the system and to give a better sense on how these parameters can change the economic feasibility of the system.

It is important to mention that there are also some constraints that govern the operation of CAES system when operating the CAES whether it is for load levelling or for economic optimization. The constraints have to do with the cavern air. The minimum and the maximum pressure have to be calculated at all times. Compression could be done only if the CAES cavern is not full (at max pressure). The expansion or selling electricity to the grid could only be done if the cavern is not empty (less than min pressure).

2.1 Base case: Wind power without CAES

The wind farm costs can be divided into capital costs and annual running costs which include labour work and maintenance.

The capital costs are mainly formed of

      a. wind turbines
      b. The foundation
      c.   Grid connection
      d. Planning

A cost breakdown of the capital cost is shown in Figure 1(IRENA, 2012).
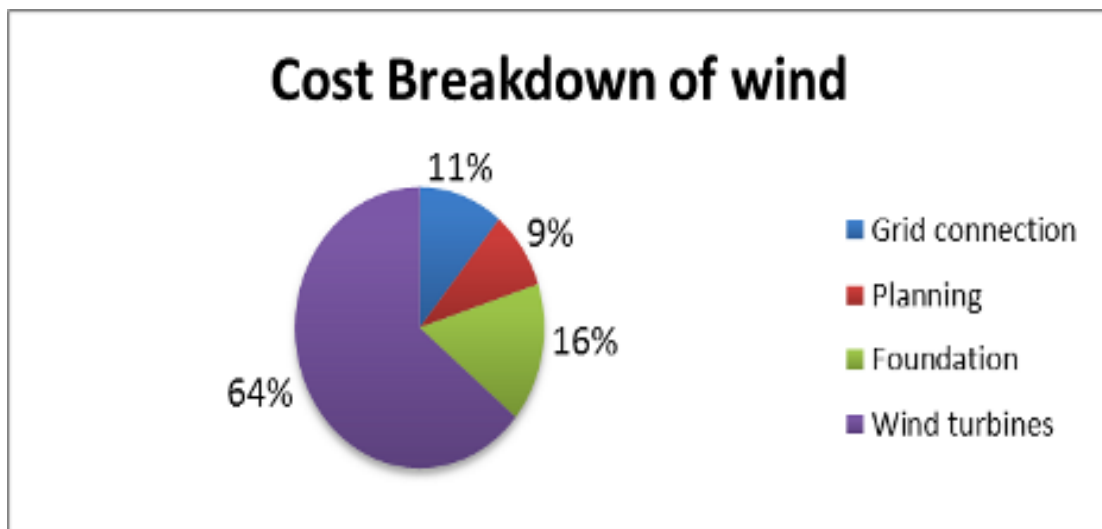
Figure 14 Cost break down of a wind farm

1. Running costs

    a. Fixed wind costs normally include insurance, administration, fixed grid access fees and service contracts for scheduled maintenance.
    b. Variable O&M costs typically include scheduled and unscheduled maintenance not covered by fixed contracts, as well as replacement parts and materials, and other labour costs.

The annual revenues from wind farms are calculated using Equation.(1) (Madlener, 2011)

$$R_w = \Sigma_{t=1}^{8760} P_w \times P_m \qquad\qquad \textit{Equation (1)}$$

Where P_w is energy supplied from wind and P_m is the market price

The Net present value of the system is calculated using Equation. (2)

$$NPV_w = -C_w + \Sigma_{t=1}^{T} \frac{(R_w - AC_w) \times e^{t-1}}{(i+1)^t} \qquad\qquad \textit{Equation (2)}$$

Where C_w is the capital cost of building a wind farm, AC_w is the annual cost of the wind farm, e is the escalation factor and i is the interest rate.

2.2 Second Case: Adding a conventional CAES plant

The economic feasibility of a CAES plant is based on the same procedure used in the wind. The capital cost of a CAES plant is calculated first, then the fixed and variable cost are added to the calculation. The

annual profit/loss are then calculated using the annual revenues, then the feasibility of the CAES system can be assessed.

Capital cost of a CAES plant

The capital cost of a CAES plant includes

a) The cost of building an underground storage
b) Cost of compressors
c) Cost of turbines
d) Other costs which include the cost of heat exchangers, pumps, transport of components cost and the installation costs (including pipe works).

The initial cost of installation of the CAES system is calculated using Equation 3 ((Zafirakis 2009)

$$IC_{CAES} = c_{cons} + c_t P_t + c_c P_c + other\ costs + Installation cost \qquad \qquad \textit{Equation (3)}$$

Where IC is the initial capital cost, c_{cons} is the construction cost per capacity of CAES ($/MW) , c_t is the specific turbine cost ($/MW) and P_t is the turbine power and c_c is the specific compressor cost ($/MW) and P_c is the compressor power.

Running Costs

Fixed cost of a CAES plant

The fixed is mainly the cost of labour, maintenance and fixed costs related to the operation of a CAES system. The fixed cost ($AFixed_{CAES}$) of the CAES plant is estimated as a factor of the initial capital cost of the CAES system. In the recent studies, the range of fixed cost of CAES range between 2-3% of total capital cost (Madlener,2011).

Variable cost of a CAES plant

The variable cost of a CAES plant is more complex than the fixed cost. It cannot be assumed as a factor of the total capital cost. Several factors affect the variable cost of a CAES system. First there is the cost of replacement of components in the system and secondly and most importantly is the natural gas price which is used in the expansion process (pre-heating the air before turbine stage). The fuel price is variable and changes on a yearly basis.

In the last 5 years the natural gas price have varied from around 2-6($/MMBTU) averaging around 4$/MMBTU.

The equation governing the annual payments of natural gas is

$$N_f = heat\ rate(MMBTU/KWhr) \times natural gas\ price\ (\$/MMBTU) \qquad \qquad \textit{Equation (4)}$$

Calculation of economic feasibility of CAES system

The method used in our calculations is to calculate the annual Revenues and costs without including the initial capital cost. The annual profits are then calculated and assessed as net present values. In this case, the cost of operating the CAES plant will be just the running costs: fixed and variable cost. The revenues will be selling the electricity to the grid. Therefore the total cost of operating the CAES system will not include the capital cost. The annual costs of CAES (AT_{CAES}) are calculated using Equation (6).

$$AT_{CAES} = AFixed_{CAES} + AN_f \qquad \qquad \textit{Equation (5)}$$

Revenues of CAES (R_{CAES}) can be calculated using

$$R_{CAES} = \sum_{t=1}^{t-turbine} P_{CAES} \times selling\ price \qquad\qquad Equation\ (6)$$

Annual Profit/Loss is calculated then using

$$\frac{P}{L} = R_{CAES} - AT_{CAES} \qquad\qquad Equation\ (7)$$

Then the Profit/Loss is assessed is net present value using

$$(P/L)_{NPV} = \sum_{t=1}^{t=n} \frac{P/L}{(i+1)^n} \qquad\qquad Equation\ (8)$$

Where n is the number of years of operation

After that the net present value is calculated by subtracting the initial capital cost (IC_{CAES}) with the annual Profit/Loss.

3.   RESULTS AND DISCUSSION

The wind farm costs per KW and also the annual fixed and variable costs vary in different developed countries. For the case of Egypt, the highest capital and annual costs from the data in (IRENA, 2012) are assumed for a developed country (Japan) as the wind energy production in Egypt is still low, so the highest capital and annual costs from a developed country is a valid assumption. The average economic life is around 25 years which is similar to that of the CAES system.

The geology of the Suez area close to the site of wind farms is formed of basement rocks. This type of geology is less favourable economically compared to molten salt for example as rocks excavation could cost around $30/kWh compared to $1/kWh for salt caverns. The cost of initial installation for a 300MW CAES is around $135M for a salt dome cavern which rises up to around $190M (EPRI , 2003) for the rock caverns ($30/kWh of excavation) where initial costs include acquisition, space and installation costs. The lifetime of a CAES reservoir is around 25 years.

Other installation costs regarding CAES system includes heat exchangers, addition of pumps, pipe works and transport of system components. Using different studies, the value of these other costs is around 350$/kW(Madlener, 2011).

The compressors life span is around 100,000 hours of operation. If that is taken into account of CAES operation and an estimated compressors operation of around 10hours/day, then the compressors life span will be around 27 years which is more than suitable for CAES and no variable cost of replacing the compressors during the 25 years operation of CAES is needed.

Compressors cost taken from different papers ranges from 300-450($/KW) (Safaei, 2013) (Madlener, 2011)(Zafirakis, 2009)

The turbine expanders normally should have life span of around 100,000 hours which should be suitable for the operation of CAES for 25 years. The turbine cost taken from different papers ranges between 300-500($/MW) Safaei, 2013) (Madlener, 2011)(Zafirakis, 2009)

Suez Egypt case study

In this case study, a CAES is modelled to have a capacity of around 250MW compressing The system could expand on full load of 331MW for 11 hours/day, thus having a capacity of around 3640MWhr. However in our simulation, the system would produce on average 128MW for 10 hours/day according to our previous calculation of installing CAES in the Suez area. The heat rate of the system is calculated as 3418 BTU/KWhr.

The Egyptian power trade market is very different to that of the European or the American system. Recently the government issued a new law for new tariffs for power produced from wind. For this law, the government

will buy wind power at a certain price unrelated to the selling time whether it's a peak time or not to encourage the growth of wind energy in Egypt.

According to the new governments tariffs in Egypt, grid will buy wind power for prices ranging for 68-82 (Egyptian piasters/KWhr) which is Equivalent to 89-108($/MWhr).Taking an assumption that the CAES system will sell electricity to the grid at the same rate for the new tariff system, so an assumed market price rate of selling at 100$/MWhr rate is chosen for this simulation. An interest rate of 5% is used in the simulation.

The case of the Suez area with the future plans of installation of 3 wind farms with different companies totalling 580MW (NREA ,2011). Figure 15 shows the expected wind power output compared to the expected load demand at 2020 when the wind plants are scheduled to be built.

The economic analysis for this case study is tackled in 2 scenarios.

1) Wind Farms costs and revenues (no Energy storage)
2) Wind farm with CAES
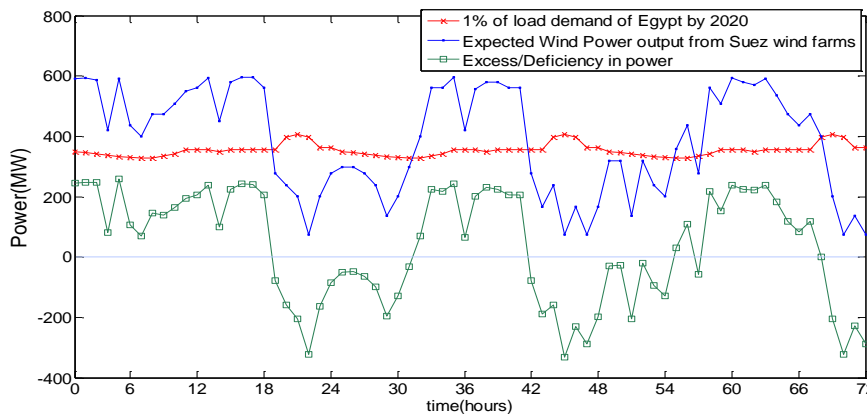
Figure 15 Expected wind power output and load demand for Suez case study

2.23. 3.1   Wind Farms without CAES

For this scenario the revenues will be divided into 2 cases. First when the wind supply is lower or equal to the load demand, then all the wind power will be sold to the grid. However, if the supply is higher than the wind demand, then wind will only supply the load demand amount and the extra surplus power will be ignored meaning that when the supply is higher than demand, a fraction of the wind farms will be assumed to be shut down (or the surplus output power will be dumped). Therefore in this case using the 3-day data available, a capacity factor of wind production is calculated to be 0.4. An annual interest rate (i) of 5% is used in this base case simulation. The fixed and variable costs are assumed to be of highest for developed country (IRENA, 2012)

Table1: base case parameters for Wind system

Wind without CAES (Egypt) base case parameters	
Selling price to grid	100$/MWhr
Interest rate (i)	5%
Fixed annual	70$/KW
Variable annual	38$/MWhr
Capital cost	2300$/KW

The NPV value is shown in Figure 4, where the NPV value increases from -1300Million$ to reach around -130Million$ by the end of the 25 years of operation for the selling price of 100$/MWhr set by the new Egyptian law for newly integrated wind turbines to the grid.

At year 0, the initial cost was 1334$Million, the NPV increases annually as the annual revenues are higher than the annual costs, so by the end of the 25 years for the base case simulation, the system would have recovered 90% of the invested money however it has not broken even. As mentioned earlier, it was

assumed that when wind is producing power more than the demand, the power would be dumped, however if that is not the case, then the wind would be making higher annual profits.

Table2: Calculated costs and revenues for wind for Suez

Wind without CAES (Egypt)	
Wind Capital cost (Million $)	1334
Fixed annual cost (Million $)	40.6
Annual Revenues (Million $)	203
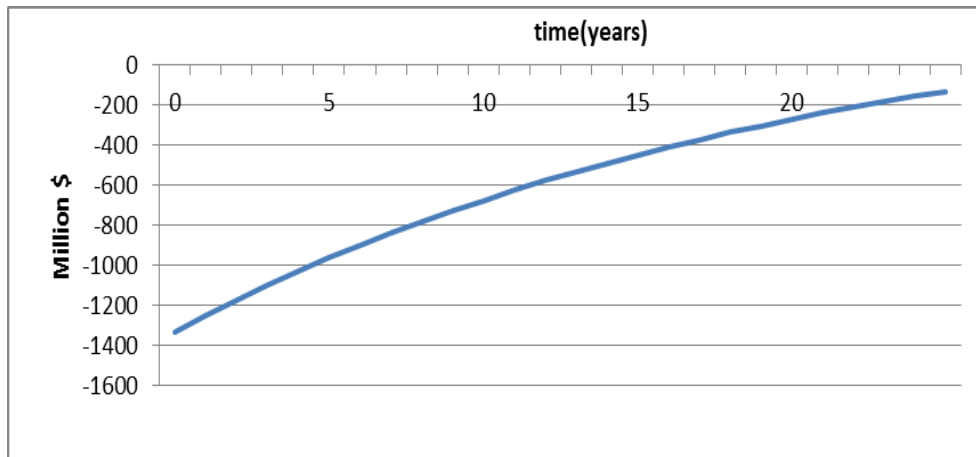
Figure 16 Net present value of System without CAES

2.24. 3.2   Wind with CAES

In this scenario the revenues will be considered to be at all power production time whether it is from the wind farm to the grid or from the CAES system to the grid. Therefore, the expected annual revenues are higher but with a higher capital cost. In this case, referring to previous simulation carried out for CAES case for Suez Egypt, the CAES would sell power to the grid at an average rate of 128MW for 30hours during a 72 hour data. Therefore, the CAES would have a capacity factor of 0.42

Table 3: CAES costs for Suez case study

CAES plant costs	
Construction cost(Million$)	119
Equipment cost(Million$)	267
Other costs (Million $)	117
Annual Fixed cost(Million$)	10
Annual variable cost(Million$)	9

In this simulation, the initial investment is around $1800Million. By the end of the 25 years of operation, the Wind +CAES case would recover around 96% of the initial investment for the base case of CAES assumptions.
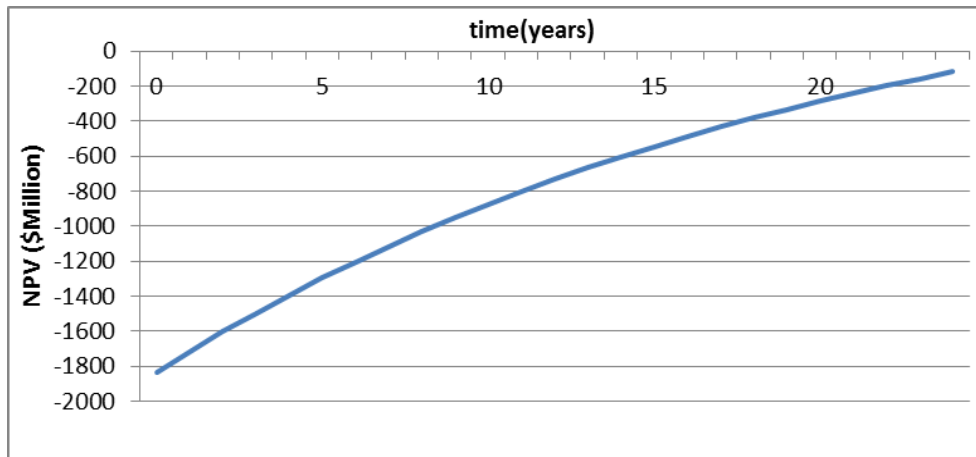
Figure 17 Net present value of system with CAES

For the base case of both Wind alone and Wind +CAES, the NPV value of the systems was below 0 which means that neither system could break even under base case values. However as mentioned earlier, some assumptions were made. For the wind alone, the assumptions are

a) If the Wind power is higher than the load demand, the Wind will only provide the load demand level. Any extra wind power will be dumped and not sold to the grid
b) If the Wind power is lower than the load demand, all the wind power will be sold to the grid.

For the Wind+CAES system, the assumptions are:

a) If the Wind power is higher than the load demand, the wind will sell to the grid the load demand level and will store the extra power in CAES
b) If the wind power is lower than the load demand, the system will sell to the grid the wind power +CAES power to satisfy the load

- Under the previous assumptions which should be valid in a normal grid system, for the wind alone, the system recovered around 90% of the initial investment, while for Wind+CAES, the system recovered around 96% of the initial investment. This means that adding a CAES system would improve the system economically in addition to improving the load-levelling of system. This recovery values were calculated for base cases mentioned earlier. The recovery value was calculated using the following:

$$Recovery\ value = \frac{Initial\ Investment - Final\ NPV\ value}{Initial\ Investment}$$

3.3 Sensitivity Analysis

Several parameters were varied to see the effect on the net present value of the whole system. The parameters that were test are:

a) Selling price to grid
b) Natural gas price
c) Initial capital cost of the whole system

The selling price will be varied from 89$ - 110$/ MWhr. The NPV results of the system are shown in Figure 18.

566
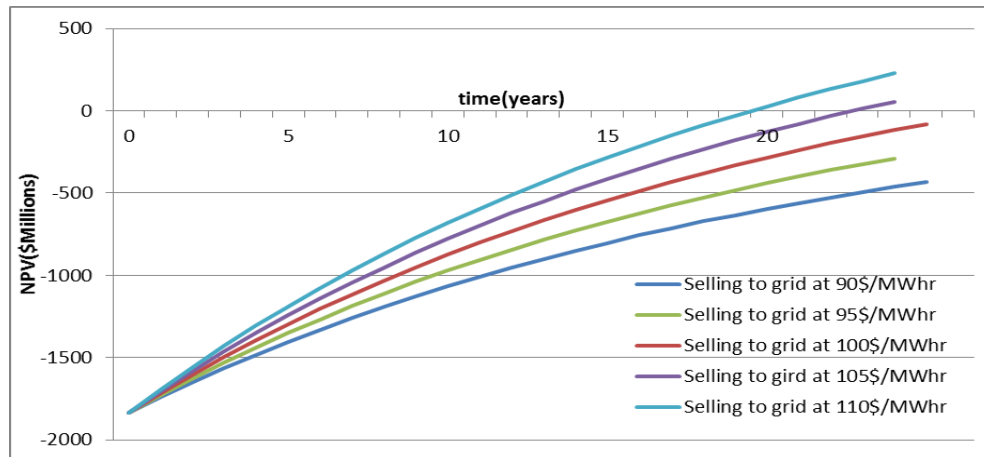
Figure 18 Annual NPV of system using different selling prices to the grid

A break even for the system is achieved after 19 years if the power is sold to the grid at a price of 110$/MWhr. The system also breaks even if it sells power to the grid at around 105$/MWhr. However, when the selling price becomes lower, the system does not break even. But in the worst simulation scenario at a price of 90$/MWhr, the system recovers around 76% of the initial investment after the 25 years of operation.

Natural gas price

An annual escalation rate of natural gas prices ranging from 0% to 10% is added to the simulation to see the effect on the net present value of the system. The results are shown in Figure 19.
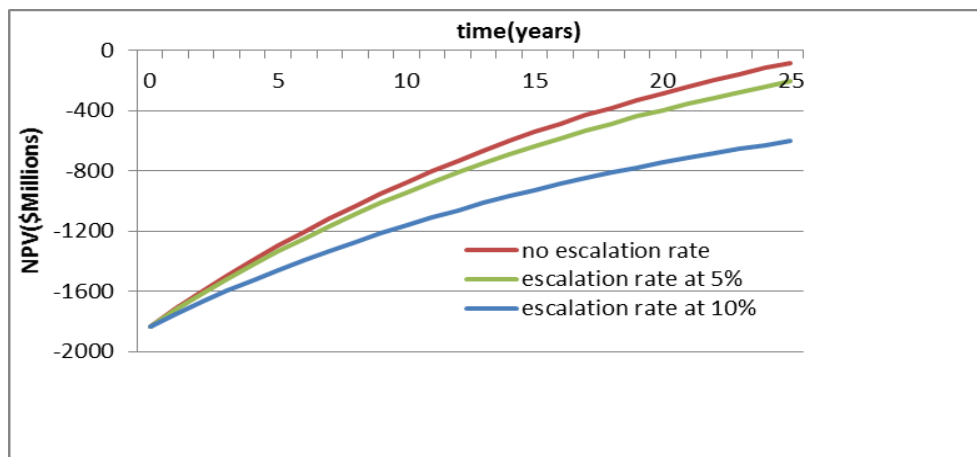
Figure 19 Annual NPV of the system adding an escalation rate factor of natural gas

Figure 19 shows that for an increase of escalation rate from 0% to 5% , there is not big effect on the final NPV of the system. However, increasing the escalation rate to 10% shows an obvious decrease in the NPV value with the system recovering only 67% of the total investment compared to the system recovering around 96% of the total investment if no value of the fuel escalation annual rate is added.

Initial Capital cost of the Wind+CAES

For this sensitivity analysis, the whole system (Wind+CAES) initial capital cost was varied from 80% to 110% which could be justified by government discount rates or variation in prices in the future of some of the components.

Figure 20 shows the effect of changing the initial capital cost of the whole system. In this simulation, the initial investment changed from around $1500Million to $2000Million for the range used in this sensitivity analysis. For the case of 20% discount on initial investment, the system breaks even after 17years. The system also breaks even when having 10% discount, while the system recovers 86% when there is an added cost of 10% to the system.

For the all the factors that were varied to test their effect on the system economic feasibility, the results showed a different effect that each would have on the annual NPV of the system.

a) Selling price to grid was varied from $90/MWhr to $/110MWhr, so a range 20% was used. The resulting NPV value changed from -$433Million to +$227Million giving total increase of -660$Million for 20% change of selling price.
b) Natural gas price was varied from 0% escalation rate to 10% escalation rate giving a change from -81$Million to -$602Million. Therefore an increase of 10% of annual fuel escalation rate gives a decrease of $521Million
c) Initial capital cost of the whole system was varied from 80% to 110% giving a change from +$314Million to -$279Million resulting in a decrease of 593$Million for 30% increase in capital cost of the whole system.

Therefore for 1% increase, the resulting values are shown next

a) Selling price to grid=33$Million
b) Natural gas price annual escalation=$$52.1Million
c) Initial capital cost of Wind+CAES= $19.8Million

Therefore in this case, the natural gas price escalation would have the highest effect out of the tested factors for sensitivity followed by the selling price to the grid followed by the initial capital cost of the system.
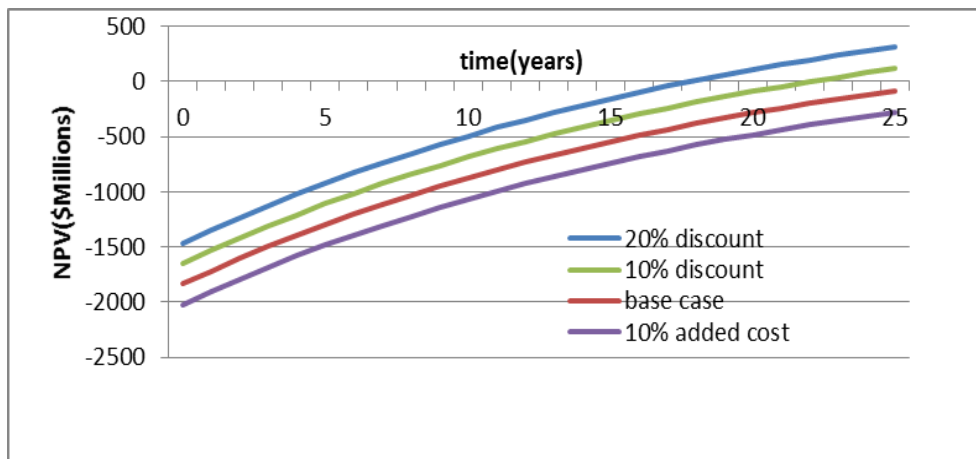
Figure 20 Annual NPV of system using different initial cost of Wind+CAES system

4   CONCLUSIONS

The simulations results carried out for the case study of Suez Area in Egypt show that the wind turbine installation with CAES is not profitable but it almost recovers most of the invested money for the base case conditions. The economic analysis was based on the market prices set by the new law of the government which is expected to change considerably in the coming years as the industry grows. CAES was found to slightly improve the economic feasibility of wind if the assumptions that extra power produced by wind are dumped. Variation of some of the parameters show that the wind turbines system alone and with the CAES become profitable whether higher selling price to the grid is possible through subsidies from the Egyptian government encouraging installation of new renewable energy systems.

5   REFERENCES

[1] EIA (2010) International Energy Outlook 2010. (March 2015, date last accessed).

[2] ALBADI M, El-Saadany E, 2010. Overview of wind power intermittency impacts on power systems. *Electrical Power Systems Research*, Volume 80, Pages 627–32

[3] IBRAHIM H, Llinca A, Perron J, 2008. Energy storage systems – characteristics and comparisons. *Renewable and Sustainable Energy Reviews* , Volume 12, Pages 1221–50.

[4] GREENBLATT Jeffery, Succar Samir, Denkenberger David, Williams Robert, Socolow Robert , 2007. Baseload wind energy: modelling the competition between gas turbines and compressed air energy storage for supplemental generation. *Energy Policy*, Volume 35, Pages 1474–92.

[5] MADLENER Reinhard, Jochen Latz, 2011. Economics of centralized and decentralized compressed air energy storage for enhanced grid integration of wind power. *Applied Energy,* Volume 101, Pages 299-309.

[6] International Renewable Energy Agency(IRENA), 2012. Renewable Energy Technology: Cost Analysis Series. Volume 1 Power Sector

[7] ZAFIRAKIS D, Kaldellis J, 2009. Economic evaluation of the dual mode CAES solution for increased wind energy contribution in autonomous island networks. *Energy Policy*, Volume 37, Pages 1958-1969

[8] EPRI-DOE handbook of energy storage for transmission & distribution applications. EPRI, Palo Alto, CA, and the U.S. Department of Energy, Washington, DC, 2003, 1001834.

[9] SAFAEI Hossein, Keith David, Hugo Ronald, 2013. Compressed air energy storage (CAES) with compressors distributed at heat loads to enable waste heat utilization. *Applied Energy*, Volume 109, Pages 165-179.

[10] NREA Annual Report 2010/2011. Available on website of New and Renewable Energy Authority (NREA). (October 2011, date last accessed).

351: A comparative analysis of the dairy milk cooling systems in selected farms in the Eastern Cape province of South Africa.

RUSSEL MHUNDWA[1], MICHAEL SIMON[2], STEPHEN TANGWE[3], EDSON MEYER[4]

1 Fort Hare Institute of Technology, University of Fort Hare, Alice Campus, Private Bag X1314, Alice 5700, South Africa,rmhundwa@gmail.com
2 Fort Hare Institute of Technology, University of Fort Hare, Alice Campus, Private Bag X1314, Alice 5700, South Africa, MSimon@ufh.ac.za
3 Fort Hare Institute of Technology, University of Fort Hare, Alice Campus, Private Bag X1314, Alice 5700, South Africa,STangwe@ufh.ac.za
4Fort Hare Institute of Technology, University of Fort Hare, Alice Campus, Private Bag X1314, Alice 5700, South Africa,emeyer@ufh.ac.za

Milk as a raw material is easily perishable since bacteria which contaminate it may multiply rapidly and render it non sanitary for processing and also unacceptable for human consumption. But however, the rate of multiplication of these bacteria can be reduced by refrigeration. This paper presents an overview of the milking process in selected dairy farms in the Eastern Cape Province of South Africa. A comparative analysis of dairy milk cooling systems was done through a survey. The aim of the survey was to establish the best dairy milk cooling technology which best suit the local conditions with special emphasis on the energy consumption during cooling of raw milk from 20 – 35^{0}C to the critical storage temperature of 4 – 4.5^{0}C for preservation before it can be processed. A simple multiple linear regression model was used to predict the cooling savings for a water to milk ratio of 2:1 with input parameters as water inlet temperature and milk outlet temperature for cooling savings as the output. An average cooling savings of 36 - 49% can be achieved using a pre-cooler which also translates to avoided CO2 and water usage. The refrigerant used in these systems was also evaluated on its thermo-physical properties in regards to the heat removal from the milk so as to meet the cooling load demand. The study will also lead to determining crucial parameters in the selection of an effective as well as efficient milk cooling system alongside its feasibility potential.

Keywords: Diary milk, Cooling system, Refrigeration, Cooling load,Refrigerant

1. INTRODUCTION

Milk as a raw material is easily perishable since bacteria which contaminate it may multiply rapidly and render it non sanitary for processing and also unacceptable for human consumption (Sapali *et al.,* 2014; Walstra *et al.,* 2006). But however, the rate of multiplication of these bacteria can be reduced by refrigeration. Bulk milk coolers (BMCs) are used to chill a given quantity of milk from the harvested temperature of approximately 30^0C – 35^0C to a required storage temperature of 4^0C within three hours of milking time (Ghewade *et al.,* 2007; Gotsa, 1995). In the Eastern Cape Province of South Africa, most dairy farms do not process milk on-site. They however produce the milk and sell to processing companies for further dairy processing into various products. As such there is bulk milk handling and storage on the farms before the milk can be collected hence BMCs are used. BMCs are designed to operate under first milking conditions and second milking conditions where by in the first instance within three hours they should be able to cool incoming raw milk from 35^0C to 4^0C and secondly from 19^0C to 4^0C at half-filled and completely filled scenarios respectively (Sapali *et al.,* 2014; Fabdec Cooling Systems, 2012). When the BMC is completely filled the system will shut down and the milk temperature will be maintained inside the tank through the use of insulation which lies between the two casings of the tank (Sapali *et al.,* 2014). In general, the BMC capacities range from 500 litres up to 30000 litres and they use different technologies to cool the milk. The direct expansion (DE) and ice-bank cooling systems are used for direct and indirect cooling of milk respectively (O'Keeffe, 2007). However, the focus of this comparison analysis is focused on two different configurations of the DE cooling systems using R22 as the refrigerant. Comparison was done for a system with milk pre-cooler with the one that is direct milk feed on their cooling energy saved.

1.1 Refrigeration cycle of the bulk milk coolers

Milk is cooled directly or indirectly using mechanical refrigeration cycle through the use of a refrigerant. An overview of the DE cooling system is shown in Figure 1 which illustrates the major components of the vapour compression cycle of the BMCs. The major components are compressor, evaporator, condenser and expansion valve.
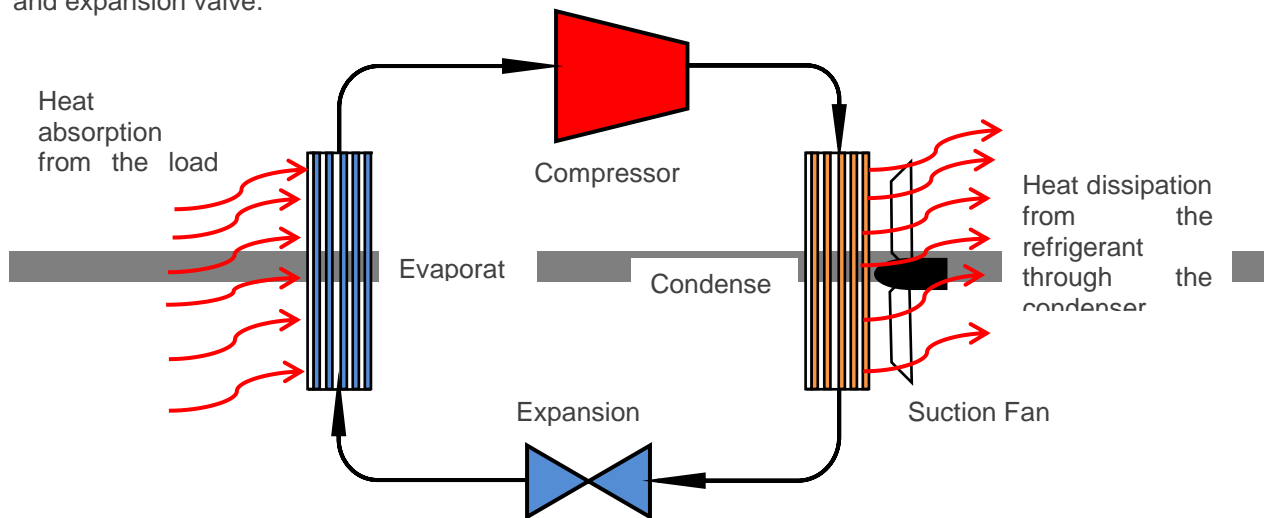
Figure 1: Schematic layout of the major components in a vapour compression refrigeration cycle of BMCs

The saturated refrigerant at the compressor enters the suction end of the compressor at low pressure and temperature state of approximately 482kPa and 4.4^0C respectively, an isentropic compression takes place through the work of the compressor causing the temperature to increase to about 43.3^0C and pressure to 1585kPa. The refrigerant flows to the condenser where it is cooled through a constant heat dissipation to the surroundings before it gets to the expansion valve where throttling takes place. At this stage the temperature and pressure of the refrigerant reduce to 4.4^0C and 482kPa and this is the temperature and pressure of the refrigerant as it flows into the evaporator. At the evaporator side the refrigerant absorbs heat from the cooling load, thus cooling the interior of the BMC. The evaporator for BMCs is integrated within the tank on the lower portion of the tank where the milk is in direct contact with.

2. METHODOLOGY

A survey was conducted on two dairy milk farms in the Eastern Cape province of South Africa. The selection criteria used included availability of data on herd size, and the ability and willingness of the farmer to collect and maintain accurate data. The aim of the survey was to establish the best dairy milk cooling technology which best suit the local conditions. The emphasis of the survey was on the energy consumption during cooling of raw milk from 35^0C to the critical storage temperature of 4 – 4.5^0C for preservation before it can be processed. A multiple linear regression model was used to predict cooling savings for 2:1 water to milk ratio pre-cooler. The refrigerant used in these systems were also evaluated on its thermo-physical properties in regards to the heat removal from the milk in relation to the quantity of milk produced per hour so as to meet the cooling load demand as well as on the global warming potential (GWP) and ozone depletion potential (ODP). The capacity of the BMCs used in this survey is 21 000 liters.

3. RESULTS AND DISCUSSION

3.1 Existing Different Configurations for the BMCs in the Eastern Cape

The following schematic diagrams show the different configurations of the BMCs from the findings of the survey. Figure 2 shows the layout of the BMC with a pre-cooler in the form of a plate heat exchanger which uses cold tap water as the coolant for the incoming raw milk. Raw milk leaves the cow udder at a temperature of approximately 35^0C (Murphy et al., 2013). As the milk passes through the heat exchanger it gives away heat to the cold water which in turn is channelled to the electric geyser where further heating of the water takes place to a temperature that is suitable for sanitary purposes. Depending on the water source, the temperature differential between the outlet raw milk temperature and the inlet water temperature also varies. The greater the temperature difference, so is the percentage cooling savings realised from the BMC. The use of the pre-cooler makes use of the waste heat from the milk and change it to useful heat, thus the electrical consumption for heating the sanitary water to 45 - 50^0C will be reduced as well as the cooling load on the refrigeration system since milk temperature will be reduced to about 18^0C – 20^0C as was reported by Sapali *et al.* (2014) and Fabdec Cooling Systems (2012), their findings were that without pre-heating of water, Plate heat n per month is used to heat up water to set point temperature for the cleaning of a dairy fac Exchanger em is being used at Seven Stars Dairy Trust.
(Pre-
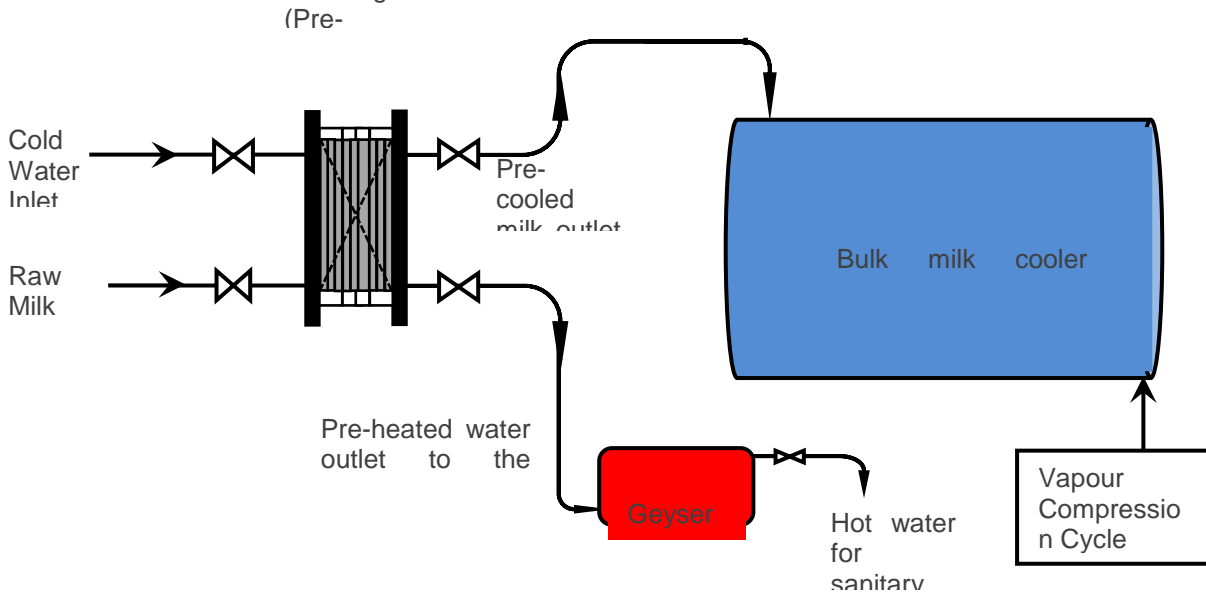
Figure 2: Schematic layout of the BMC with pre-cooler installation at Seven Stars Dairy Trust

Figure 3 below shows a direct system which is being used at the dairy farm at Fort Hare Dairy Trust. Raw milk from the milking machine is channeled directly to the BMC at 35^0C. The BMC will cool the milk to the required temperature of 4^0C. Water that is used for sanitary purposes in this plant is heated directly from the tap water by the electrical geyser. In this regard the performance of the refrigeration system will be compromised since the refrigerant has to remove all the heat from the milk. The main difference between these two systems is the pre-cooler in the form of a plate heat exchanger which also acts as a water pre-heater.
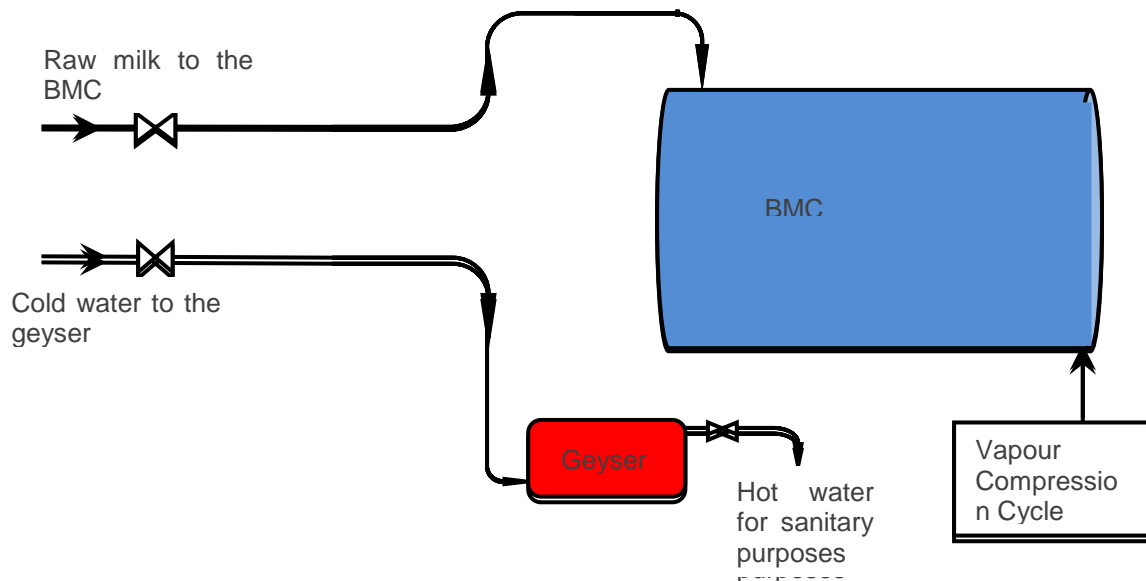
Figure 3: Schematic layout of a direct BMC system at Fort Hare Dairy Trust

3.2 Milk Blend Temperatures during Milking

There are basically two milking times in the Eastern Cape that is morning (between 05:00 and 06:00) and afternoon (between 15:00 and 16:00). Having these two milking times will have an impact on the blending temperature for the both cases where a pre-cooler is used and in the direct system. Experiments conducted by O'Keeffe (2007) revealed that pre-cooling of milk lowers the milk blend temperatures; hence bacterial growth is retarded unlike when the blend temperature of milk is high as in a direct system. Considering a system designed to cool milk in 2 hours, Table 1 below shows the milk blend temperatures for the pre-cooled and uncooled milk within 2 milking times.

Table 1: Milk Blending Temperatures during the two milking times (Adapted from O'Keeffe, 2007)

Milking time		Time in Minutes to cool the milk to given temperature		
		0	60	120
0500 - 0600	Uncooled Milk Temp	35	21	4.0
	Pre-cooled Milk	18	11	4.0
1500 - 1600	Uncooled Milk	4.0	11.8	4.0
	Pre-cooled Milk	4.0	7.1	4.0

Blending cooled milk with uncooled milk leads to an increase in the temperature of 7.8^0C during the second milking time as compared to a slight increase in temperature for pre-cooled milk of 3.1^0C. Thus the energy that will be required to cool the uncooled milk blend is higher than that of the pre-cooled milk blend. This is because the cooling load depends on the temperature of milk and the higher the milk temperature so is the cooling load (Murphy *et al.,* 2013).

3.3 Refrigerant used in the BMCs

Basically the design of any cooling system will solely depend on the type of refrigerant that will be used. Findings from the survey revealed that R22 is the commonly used refrigerant for the BMCs. This is because of its good thermo-physical properties and heat removal capability. R22 guarantees a good system performance over a wide temperature range and applications (Prapainop and Suen, 2012). The following Table 2 highlights the properties of R22, R410A and R407C.

Table 2: Properties of R22, R410A and R407C (Chen and Yu, 2008)

573

Refrigerant	Boiling Point at 1 atm (^{0}C)	Critical Temperature (^{0}C)	Critical Pressure (kPa)	ODP	GWP
R22	-40.75	96.1	4990	0.05	1860
R410A	-51.4	70.5	4810	0	2100
R407C	-43.6	85.8	4600	0	1800

As shown in Table 3 above, R22 has the highest critical temperature and pressure as compared to R410A and R407C, this implies that greater thermal energy can be removed from the load (raw milk) into the refrigerant without any distinctive phase change. The low boiling point of R22 enables it to continue to extract any heat from the milk irrespective of the milk temperature. Despite being a good refrigerant, R22 has an ozone depletion potential (ODP) value of 0.05 as compared to R410A and R407C which have zero ODP (Agrawal *et al.,* 2009; Zali *et al.*, 2011; Montreal Protocol, 2011). Based on this, R410A and R407C have a better environmental impact than R22 though it has a low global warming potential compared to other refrigerants. A study by Zali *et al.* (2011) recommended that R407C can be a suitable replacement of R22. Their findings revealed that if the distillation temperature is increased and evaporator temperature decreased, R407C exhibits the thermo-physical properties that are close to R22. However, replacing R22 with R410A or R407C is costly, but considering the sustainability of the environment it is ideal to consider the replacements.

3.4 Energy Savings through milk Pre-cooling

Pre-cooling of milk reduces milk cooling energy with approximately 40-65% (Pebbles *et al.,* 1993; O'Keeffe, 2007 and Murphy *et al.,* 2013) thus the energy for heating of water is also reduced. From our unpublished data the water inlet temperature and raw milk outlet temperature were used as predictors in a multiple linear regression model to predict the cooling savings for a dairy plant with a pre-cooler in the Eastern Cape Province of South Africa. Table 3 illustrates the percentage cooling savings through the use of 2:1 water to milk ratio pre-cooler;

Table 3: Percentage cooling savings for a 2:1 water to milk ratio pre-cooler

Cooling Water Inlet Temperature	Raw Milk Outlet Temperature	Percentage Cooling Savings (%)
9.44	14.44	63.95
10.03	15.03	63.94
15.39	19.39	51.26
15.77	19.77	51.26
10.98	15.98	63.93
16.32	20.32	51.25
23.08	26.08	38.55
24.81	27.81	38.53
25.36	28.36	38.53

The results in Table 3 show that the greater the temperature lift between the cooling water inlet temperature and the raw milk outlet temperature achieves high cooling savings. Likewise, if the temperature lift is so small, the cooling savings are also low. In this regard, the results presented in Table 1 are in agreement with O'Keeffe (2007) findings. Statistically it can be revealed that both predictors are all primary factors of almost equal contribution to the output, this implies that in order to get better savings the raw milk outlet temperature and the cooling water inlet temp should be at an optimum value which would lead to maximum temperature lift. Moreover, pre-cooling can also reduce the energy that is used to heat up sanitary water in a dairy facility.

4. CONCLUSIONS AND RECOMMENDATIONS

A comparison of two raw milk cooling systems was done through a survey. The findings from the survey indicated that using a pre-cooler in a dairy milk cooling system will lead to average energy savings of 36 – 49% in terms of milk cooling. The percentage savings also translate to the avoided percentage of carbon dioxide ejected into the environment as well as the volume of water intended to be used for the generation of electricity. The findings from the survey reveal that using a pre-cooler is the best cooling system for the local conditions. However, though the use of the pre-cooler will lead to savings it is recommended that;

- The pre-cooler must be well maintained and cleaned because it can be a harbor of milk contamination

- The room temperature where the BMC is installed must be air conditioned or well ventilated such that the ambient temperature does not affect the room temperature since if the pre-cooling process affected by an increase in the surrounding temperature.

5. REFERENCES

AGRAWAL A., Dave, R., and Shrivastava V., 2009. Replacing harmful refrigerant R22 in a bulk milk cooler Indian Journal of Science and Technology Vol.2 No. 9.

CHEN, J., and Yu, J., 2008. Performance of a new refrigeration cycle using refrigerant mixture R32/R134a for residential air-conditioner applications: Energy and Buildings 40, pp 2022-2027.

GHEWADE, D., Sapali, S., Kajale, S., 2007. Dynamic Modeling of Bulk Milk Cooler, 5th International Conference on Heat Transfer, Fluid Mechanics and Thermodynamics, Sun City, South Africa HEFAT 2007.

GOSTA, B., 1995. Dairy processing Handbook, Tetra Pak Processing Systems ABS-221 86 Lund, Sweden.

MURPHY, M., Upton, J., and O'Mahony, M., 2013. Rapid milk cooling control with varying water and energy consumption, Biosystems Engineering, 116, pp 15-22.

O'KEEFFE, J., 2007. Milk Cooling, Inservice Training Teagasc, Moorepark Research Centre Accessed on 7 May from http://www.teagasc.ie/advisory/farm_management/buildings/milkingEquipment/milk_cooling/MilkCoolingPresentation. pdf

PEEBLES, R., Reinemann D., and Straub, R., 1993. Analysis of milking center energy use, Presented at the 1993 Winter Meeting of the ASAE, Chicago, Illinois, ASAE

PRAPAINOP, R., and Suen, K., 2012. Effects of refrigerant properties on refrigerant performance comparison: A review International Journal of Engineering Research and Applications (IJERA) Vol. 2, Issue 4, pp.486-493.

SAPALI, S., Pise, S., Pise, A., and Ghewade, D., 2014. Investigations of waste heat recovery from bulk milk cooler Case Studies in Thermal Engineering 4, pp 136–143.

The Montreal Protocol in 2011. 23rd Meeting of the parties to the Montreal Protocol on substances that deplete the ozone layer, November 21–25, Bali, Indonesia, 2011.

WALSTRA, P., Wouters J., and Geurts, T., 2006. Dairy science and Technology. CRC Press/Taylor & Francis, Boca Raton

www.fabdec.com

ZALI, S., Rezai, H., and Mohammad, n., 2011. Performance Comparison of R407c and R22 in Off-Design Point Using Wilson-Plot Method Middle-East Journal of Scientific Research 9 (2): 177-183.

POSTER SESSION B

31: Novel two-stage high-solid anaerobic digestion of food waste and grass

WANGLIANGA LI[1], LOH KAI CHEE[2], TONG YEN WAH[*, 1, 2],
PENGHUI GAO[1], ZHANG JINXINA[1], LIM JUN WEI[1]

1 NUS Environment Research Institute, National University of Singapore, 5A Engineering Drive 1, Singapore 117411, Singapore
2 Department of Chemical and Biomolecular Engineering, National University of Singapore, 4 Engineering Drive 4, Singapore 117585, Singapore
Corresponding author at: NUS Environment Research Institute, National University of Singapore, 5A Engineering Drive 1, Singapore 117411, Singapore. Tel.: +65 6516 8467; fax: +65 6779 1936. E-mail address: chetyw @nus.edu.sg (Y.W. Tong).

A high-solid two-stage process was proposed to increase biogas yield, to improve the efficiency and to stabilize the digestion process of horticultural waste (HW) and food waste (FW). In this two-stage process, high-solid codigestion of FW and chicken manure (CM) was carried out in the first stage and then, transferred and codigested with grass in the second stage. When volatile solid (VS) ratio of FW, CM and grass was 4:5:5, after 70 days, the cumulative methane yield was about 203 mL/g VS. The optimized operation parameter for the two-stage is VS ratio of FW/CM/grass as 4:5:5, duration of first stage as 3 days. Compared with the codigestion of FW, CM and grass, the biogas yield of the two-stage process increased by 28% and the duration of digestion was 52 days, 18 days shorter. Under the optimal condition, the VS removal exceeded 55%. The composition analysis revealed that cellulose and hemicellulose contributed to the production of biogas.

Keywords: Food waste; Yard waste; High-solid; Digestion; Biogas

1. INTRODUCTION

Horticultural waste (HW), food waste (FW) and animal manure take up most of organic fractions of MSW, which are appropriate to be disposed with AD because of high organic content and moisture content. However, high-solid anaerobic digestion of HW is limited by low hydrolysis rates, low digestion efficiency, and inhibition of volatile fatty acids (VFAs), because its AD process is very easy to become acidified due to the accumulation of long chain fatty acids (LCFAs) and VFAs. Although FW is a promising organic substrate for AD due to its high potential for methane production, high organic matter content results in the failure of the single-phase AD because of the rapid production of large amounts of VFA at the initial stage. Digestate recycling can improve biogas yield and realize full utilization of organic waste, which can be realized in two-stage process.

The two-stage system has advantages over one-stage process since it can enrich different bacteria in each digester and increase the digestion stability. Therefore, compared with one-stage AD, the two-stage AD has better performance in acid production and methane yield and has a higher removal of suspended solids (SS) and chemical oxygen demand (COD) (ZHANG B., 2014;ZUO Z., 2014;YABU H., 2011.) Even though two-stage AD has been studied for many years, the two-stage process in solid state has never been reported. The new technology allows high organic loading rate and treatment capacity, meantime its biogas is a highly convenient bioenergy. After the solid-state AD, the solid residue can be disposed via further treated via thermal conversion if the residue has suitable heating value. The volume of waste is in fact greatly reduced and the solid residue of AD has low contents of organic matters and moisture after producing biogas and removing leachate via solid-state AD.

This study aims to develop a novel two-stage high-solid digestion process to dispose solid waste of FW, grass and CM economically and technically. The effect of different alkalis on the performance of the two-stage dry digestion was further studied by detecting the biogas yield and the variations in COD, ammonia nitrogen concentration and total solids (TS) of the substrate.

2. EXPERIMENT AND METHODS

2.1 High-solid codigestion of grass and chicken manure

Biogas and methane production of the cosubstrate with the mixture of grass, CM and FW was evaluated using batch experiment in 250 mL flask. The C/N ratio of grass/chicken manure was about 21.70. The flasks were sealed using rubber stoppers, and incubated at 35 ±1°C for up to 40 days. Biogas production was collected with Tedlar bags.

2.2 Two-stage bioreactors Configuration

Fig.1 Scheme of the semi-continuous two-stage system with recirculation.

The scheme of the two-stage digestion system was presented in Fig.1. Codigestion of FW and CM was carried out in first-stage digester. Then, the digestate was transferred to second-stage with a pump and mixed with grass. If necessary, the effluent produced in second-stage digester was recirculated back to the first-stage digester. In order to separate particulate matter from the effluent, the outlet of the second-stage digester was equipped with a sedimentation tank consisting of a filter, to separate and settle the large particles before pumping the liquid to the first-stage digester.

3   RESULTS AND DISCUSSION

3.1 Substrates characterization

Table 1 Physical properties of grass, FW and CM

Feed	Grass	CM	FW
C, %	41.08	28.16	50.48
N, %	1.02	3.48	2.84
C/N ratio	40.27	8.09	17.77
S, %	<0.50	1.09	<0.50
Total solid,%	89.58	72.26	29.32
Volatile solid ,%	77.61	38.38	26.03
Composition analysis			
Neutral detergent soluble, %	16.68	73.00	79.18
Cellulose, %	42.49	15.30	10.03
Hemicelluloses, %	27.14	4.07	2.33
Lignin, %	12.67	6.03	8.48
Ash, %	0.67	1.62	0.00

In this study, grass, FW and CM were used as the substrates. Physical properties of the substrates were measured in terms of TS, VS, elemental analysis and composition analysis, as shown in Table 1. For the three substrates, the organic fraction contributed to the major part of the biomass, representing a TS content of 89.86%, 72.26% and 29.32% in grass, CM and FW, respectively. VS of them are 77.61%, 38.38% and 26.03%, respectively. Based on elemental analysis, the C/N ratio of grass, CM and FW is 40.27, 8.09 and 17.77, respectively. The C/N ratios of all the different samples were not in the range of 20–30 which was proposed to be most suitable for optimum operation of the AD. While, from the composition analysis, we can see that the content of NDS, cellulose, hemicellulose, lignin and ash content of grass was 16.68%, 42.49%, 27.14%, 12.67% and 0.67%. While, for CM and FW, the content of NDS fraction was more than 70%. The contents of lignin and hemicellulose of them were only about 10%.

3.2 High-solid codigestion of FW, grass and CM

The VS ratio of grass, FW and CM is 4:4:5. Fig.2 showed the cumulative biogas yield, cumulative methane yield and methane concentration of codigestion. It can be seen that biogas was produced on the 1st day, then, no biogas produced until the 9th day. From the 9th day, biogas was produced until the 75th day. The cumulative biogas yield of cosubstrate was about 322 mL/g VS and the cumulative methane yield was about 203 mL/g VS. The pH value decreased from 7.03 to 5.49 in 5 days of digestion, which can inhibit the digestion process significantly. Then the pH value increased slowly since the 15th day. The possible reason is that the hydrolysis of FW is much faster than the digestion of CM. After the 15th day, ammonia was produced from the digestion of CM which has buffer effects and can increase the pH value. Thus, the pH value was in the range of 7.06 to 8.09 after the 25th day.

Fig.2 Cumulative biogas yield, methane yield and methane concentration of codigestion

3.3 HRT of first-stage on digestion performance

The effects of HRT of first-stage on total biogas yield of two-stage process were studied with TS 20%, VS ratio of FW: CM: grass as 4:5:5. The first-stage duration was chosen as 1 day, 2 days, 3 days, 4 days and 15 days. With the same total organic wastes, the FW/grass ratio on cumulative biogas yield and cumulative methane yield and HRT was tested. When the digestate of FW/CM was transferred on the 1st day, 2nd day, 4th day, 5th day and 7th day, the pH value of FW/CM digestion system was 6.50, 6.96, 6.96, 6.87 and 6.78. It can be concluded that the pH value decreased little after 7 days of codigestion. Codigestion with CM can make the digestion process more stable. Fig.5 showed the total biogas yield with different first-stage HRT. Fig.3 showed the total methane yield with different first-stage HRT. When first-stage HRT was 3 days, the biogas yield and methane yield were highest.

Fig. 3 HRT of first-stage on cumulative methane yield

4   CONCLUSIONS

1)   When FW was used as sole substrate, fast hydrolysis led to the sharp decrease of pH value to below 4.0 and thus, led to the failure of digestion within 3 days. The highest biogas yield and methane yield were obtained with the FW/grass ratio (VS ratio) 1:2.
2)   The hydrolytic retention time (HRT) 1 day, 2 day, 3 day, 4 day and 7 day of first stage on digestion performance was also studied. The optimal HRT of the first stage is 3 day.
3)   Biogas yield can be increased through two-stage process than codigestion.
4)   Under the optimal condition, the volatile solid (VS) removal efficiencies exceeded 55%.

5   ACKNOWLEDGEMENTS

6   REFERENCES

ZHANG B., HE P. He, 2014. Performance assessment of two-stage anaerobic digestion of kitchen wastes. Environ Technol, 35(10),1277–1285.

YABU H., Sakai C., Fujiwara T., et al. 2011.Thermophilic two-stage dry anaerobic digestion of model garbage with ammonia stripping. J Biosci Bioeng, 111 (3), 312–319.

ZUO Z., Wu S., Zhang W., Dong R., 2014. Performance of two-stage vegetable waste anaerobic digestion depending on varying recirculation rates. Bioresour Technol. 162, 266–272.

104: Application of biochar arising from gasification to rehabilitate soil of tropical secondary forest on degraded land

HANYU YANG [1, 2,] SHUN KAI KZOH [2], WEI CHENG NG [1], REUBEN C. J. LIM [3],
HUGH T. W. TAN [3], YEN WAH TONG [1, 2,] YANJUN DAI [4],
CLIVE CHONG [5], CHI-HWA WANG [1, 2]

1 NUS Environmental Research Institute, National University of Singapore,
1 Create Way, Create Tower #15-02, Singapore 138602
2 Department of Chemical and Biomolecular Engineering, National University of Singapore,
4 Engineering Drive 4, Singapore 117576
3 Department of Biological Sciences, National University of Singapore,
14 Science Drive 4, Singapore 117543
4 School of Mechanical Engineering, Shanghai Jiaotong University,
#800 Dongchuan Rood, Shanghai, China 200240
5 Bioplas Energy (Asia Pacific) Pte Ltd
9 Tuas South Street 15, Singapore 637077

Biochar arising from gasification is porous (surface area 77.2m2/g), alkaline (pH 9.0), rich in nitrogen (12100ppm), phosphorus (873.4ppm), potassium (4833.3ppm) and low in its carbon to nitrogen ratio (8:1), indicating its potential use as an amendment to the soil of adinandra belukar, a form of secondary forest on degraded land. Such soil is highly compacted (surface area 4.0m2/g), acidic (pH 4.0), poor in nitrogen (1120ppm), phosphorus (3.2ppm), potassium (29.9ppm) and high in its carbon to nitrogen ratio (14:1). In this study, the forest soil was mixed with biochar at 33.3, 50.0 and 66.7% by weight, and subsequently used to cultivate water spinach (Ipomoea aquatica). After 8 weeks of cultivation, water spinach grown in the forest soil mixed with 33.3% biochar grew the tallest (193.8mm, 4 times that of pure soil), had the heaviest stem dry weight (0.483g, 10 times that of pure soil) and the largest leaf surface area (100.6cm2, 30 times that of pure soil). Compared to commercially available water spinach, it had almost the same height, heavier stem dry weight and more leaf surface area, indicating the possibility of biochar to be used as an amendment to adinandra belukar soil.

Keywords: Biochar, Gasification, Secondary Forest, Degraded Land, Acidic Soil, Water Spinach.

1. INTRODUCTION

Acidic and nutrient-poor soil is found in adinandra belukar, a form of tropical secondary forest found on degraded land and this vegetation type is found in a 150-km radius around Singapore, and includes Peninsular Malaysia and the Riau Archipelago of Indonesia (Sim et al., 1992). This has a low pH range of 3.3–3.9 in the top 0–20 cm of surface, and low total nitrogen and phosphorus content (Sim et al., 1992). Gasification-derived biochar can potentially be used to address this problem. The gasification process allows the nutrient content such as nitrogen, potassium and phosphorus in the feedstock to be captured in the biochar at the end of reaction (Silber et al., 2010). Subsequent application of biochar to the soil allows these essential elements for plant growth to be released into the soil and improve nutrient level (MacKenzie and DeLuca, 2006). When applied in the appropriate condition, it raises the pH of acidic soil to 6.5–7.0 where cation exchange capacity is optimum for most essential elements for plant growth (Rice and Rice, 2006). The high surface area of biochar also helps to decrease the tensile strength of compacted adinandra belukar soil which hinders the healthy development of the root system (Chan et al., 2007).

2. MATERIALS AND METHODS

2.25. 2.1. Source of Soil and Biochar

The top 20cm of soil was collected from adinandra belukar at a hill slope along Kent Ridge Road, Singapore. For the cultivation study, biochar from Bioplas Energy (Asia Pacific) Pte Ltd was utilized. It was derived from the gasification of pure construction wood waste cut into 10mm long and 2mm wide pieces, at 900–1000°C in a 40-kW updraft gasifier. Soil and biochar were sent for testing at the Animal & Plant Health Laboratories of the Agri-Food & Veterinary Authority of Singapore (AVA) to characterize N, P, K content and C-to-N ratio, while the surface area was analysed using Brunauer–Emmett–Teller (BET) test.

2.26. 2.2. Water Spinach Cultivation

Water spinach (*Ipomoea aquatica*), a leafy vegetable commonly found in Southeast Asia, India, and southern China (Göthberg et al., 2002) was selected for this study. Seedlings germinated from seeds purchased from Ban Lee Huat Seed Pte Ltd, Singapore, were utilized. **Table 1** shows five treatments of substrate used for cultivation obtained by mixing biochar and soil in different ratios by weight, and their respective final pH values. Water spinach was cultivated in 5 replicates for each substrate, and critical growth indicators were recorded throughout and at the end of the 8-week long cultivation.

Table 1: Proportion of biochar and soil in each substrate treatment, and their final pH values

Substrate	Specification	Biochar Wt%	Soil Wt%	pH
A	pure soil (control)	0	100	4.02
B	2:1 soil-biochar	33	67	7.00
C	1:1 soil-biochar	50	50	7.28
D	1:2 soil-biochar	67	33	7.74
E	pure biochar	100	0	9.02

3. RESULTS AND DISCUSSION

2.27. 3.1. Analysis of Soil and Biochar

Table 2 shows that biochar has a higher pH value, a lower C-to-N ratio, a larger surface area, and N, P, K values approximately 10−100 times more compared to those of adinandra belukar soil. With an increase in pH as a result of mixing biochar with soil, phosphorus availability to water spinach was increased since phosphorus solubility in soil was enhanced in this pH range. Furthermore, at a higher pH, heavy metal solubility in the soil decreases sharply, thus making heavy metals less available for absorption by plants. Additionally, the large surface area of biochar owing to its porous structure improves the texture of soil, increases aeration, and facilitates cation exchange capacity.

Table 2: Characteristics of biochar and adinandra belukar soil

Item		Biochar	Adinandra Belukar Soil
pH		9.0	4.0
Elemental Analysis	N (ppm)	12100.0	1120.0
	P (ppm)	873.4	3.2
	K (ppm)	4833.3	29.9
	C:N	8.0	14.0
Surface Area (m2/g)		77.2	4.0

2.28. 3.2. Water Spinach Cultivation

Figure 1 shows that water spinach in pure soil and pure biochar grew the least with a final average height of only 46.0mm and 48.0mm, respectively. Meanwhile, water spinach grown in substrate mixtures (substrate B, C, and D) generally performed better than that in pure soil and pure biochar. Of substrates B, C and D, as the ratio of soil increased (with biochar decreasing correspondingly), the height of water spinach increased as well. Water spinach cultivated in substrate B (2:1 soil-biochar) displayed the best growth performance, reaching an average height of 193.8mm after 8 weeks of growth. This translates to almost a three-fold increase in final height as compared to pure soil and pure biochar. Additionally, the rate of growth as depicted by the gradient of the growth curve showed that water spinach cultivated in substrate mixtures (B,C, and D) grew at a much higher rate from the fifth week onwards compared to that in pure soil or biochar.

Figure 2 shows that water spinach cultivated in pure soil (substrate A) performed very poorly, with 0.109g dry weight of root, 0.0480g dry weight of stem and 2.86cm^2 leaf surface area, while water spinach cultivated in pure biochar (substrate E) performed equally poorly. Water spinach cultivated in 2:1 soil-biochar (substrate B) had the best performance, with 0.326g dry weight of root, 0.483g dry weight of stem and 100.6cm^2 leaf surface area, followed by substrate C with 0.215g dry weight of root, 0.318g dry weight of stem and 52.2cm^2 leaf surface area, and substrate D with 0.0996g dry weight of root, 0.154g dry weight of stem and 24.1cm^2 leaf surface area. Compared to commercial products such as the supermarket water spinach (SM) and the wet market water spinach (WM), water spinach cultivated in 2:1 soil-biochar (substrate B) displayed a comparable performance in terms of the dry weight of stem and the leaf surface area.
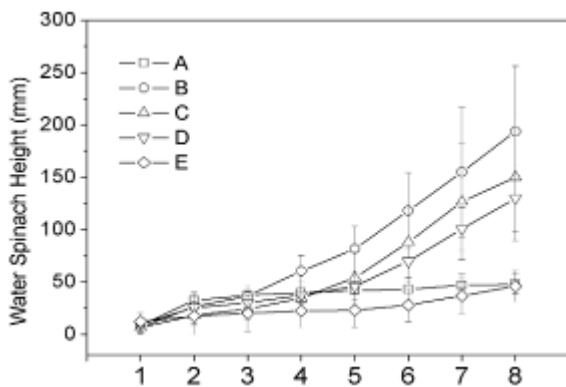
Figure 1: Stem heights of water spinach cultivated in each substrate from week 1 to week 8. A, B, C, D and E represents pure soil (control), 2:1 soil-biochar, 1:1 soil-biochar, 1:2 soil-biochar and pure biochar, respectively.
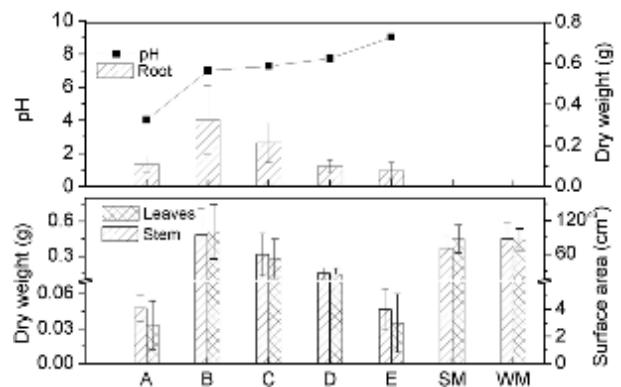
Figure 2: pH, dry weight of root and stem, and leaf surface area of each substrate. A, B, C, D, E, SM and WM represents pure soil, 2:1 soil-biochar, 1:1 soil-biochar, 1:2 soil-biochar, pure biochar, supermarket and wet market, respectively.

4. CONCLUSIONS

The physicochemical properties of gasifier-derived biochar indicate its potential in reversing detrimental effects of acidic and nutrient-poor soil to allow reforestation or agriculture. The addition of biochar as a soil amendment was able to improve soil texture, enhance nutrient availability, and raise the pH to more optimum levels for plant growth. Water spinach cultivated in 2:1 soil-biochar mixture yielded the best growth performance, with plants being approximately 4 times taller, 10 times heavier and 30 times larger in leaf surface area compared to plants grown in pure soil. Therefore, biochar may be used to rehabilitate the nutrient-poor acidic soil from secondary forest on degraded land.

5. ACKNOWLEDGEMENT

6. REFERENCES

CHAN, K. Y., Downie, A., Joseph, S., Meszaros, I. & Van Zwieten, L. 2007. Agronomic values of greenwaste biochar as a soil amendment. *Australian Journal of Soil Research,* 45**,** 629+.

G THBERG, A., Greger, M. & Bengtsson, B. E. 2002. Accumulation of heavy metals in water spinach (Ipomoea aquatica) cultivated in the Bangkok region, Thailand. *Environmental Toxicology and Chemistry,* 21**,** 1934-1939.

MACKENZIE, M. D. & Deluca, T. H. 2006. Charcoal and shrubs modify soil processes in ponderosa pine forests of western Montana. *Plant and Soil,* 287**,** 257-266.

RICE, L. W. & Rice, R. P. 2006. *Practical Horticulture,* 6th Edition**,** Pearson-Prentice Hall, New Jersey, USA. 482pp.

SILBER, A., Levkovitch, I. & Graber, E. R. 2010. pH-dependent mineral release and surface properties of cornstraw biochar: agronomic implications. *Environmental science & technology,* 44**,** 9318.

SIM, J. W. S., T, H. T. W. & Turner, I. M. 1992. Adinandra belukar: an anthropogenic health forest in Singapore. *Vegetation,* 102**,** 125-137.

74: Experimental evaluation of an integrated phase change material blind system for double skin façade buildings

YILIN LI [1], JO DAKWA [2], GEORGIOS KOKOGIANNAKIS [3]

[1] *Faculty of Engineering, The University of Nottingham, University Park, Nottingham, NG7 2RD,*
epxyl11@nottingham.ac.uk
[2] *Faculty of Engineering, The University of Nottingham, University Park, Nottingham, NG7 2RD,*
J.Darkwa@nottingham.ac.uk
[3] *School of Mechanical, Materials and Mechatronic Engineering, Sustainable Building Research Centre,*
University of Wollongong, Innovation Campus, Fairy Meadow, NSW 2519, gkg@uow.edu.au

Double skin facades (DSFs) have been widely recognised as sustainable design elements for reducing energy consumption in buildings. However overheating problems in DSFs in warm seasons and locations have been reported in various studies for contributing additional increase in cooling loads in buildings. Although strategies such as utilisation of shading devices and incorporation of thermal mass into DSFs have been investigated by some researchers, there are still some technical and scientific barriers to be overcome to ensure effective heat transfer processes in the systems. This paper focuses on the experimental evaluation of an integrated phase change material (PCM) blind system based on previous theoretical study. Detailed procedures for developing the integrated blind system based on laminated composite PCM have been established which cover series of screening tests on alternative materials. Temperature and airflow velocity data were monitored and collected from a typical DSF test facility equipped with a PCM blind prototype in the summer of 2014. The data analysis showed that the integrated PCM blind system was able to stabilise the cavity temperature to about 36oC during the hottest period which showed no significant increase as compared with the ambient temperature. Even though the developed system has demonstrated some level of capacity to mitigate the overheating phenomenon in DSF, there is the need for longer term investigations into the energy storage efficiency of the PCM due to repeated charging and discharging cycling.

*Keywords: Double skin facade, PCM blind system, Experimental evaluation*

1. INTRODUCTION

The building sector has been defined as one of the main contributors of total energy consumption. Globally, it has been stressed repeatedly that buildings are responsible for approximately 40% of the total world annual energy consumption (Omer, 2008). The energy situation in the building sector has raised the awareness for applying various sustainable design concepts with the aim of reducing energy consumption in buildings (Pacheco et al., 2012). As a form of envelop in modern buildings, double skin façade (DSF) has already become common architectural design feature for reducing energy consumption in buildings (Kim et al., 2012, Pasquay, 2004, Zhou et al., 2010). However in warm seasons DSFs often suffer from overheating problems which contribute to additional cooling energy in buildings (Darkwa et al., 2013). To this end, different types of thermal management strategies have been tried and investigated. For instance, shading devices such as venetian blinds combined with control management systems have been studied (Iyi et al., 2014, Gratia et al., 2007). Other strategies such as incorporation of thermal mass and energy storage devices into DSFs have also been proposed and evaluated (Fallahi et al., 2010, Mehling et al., 2008). Although the above systems have found to be promising, they do still have some technical and operational limitations and cannot be readily and effectively incorporated into DSFs.

In order to overcome these barriers, an integrated phase change materials (PCMs) blind system for DSF buildings was theoretically evaluated (Li et al., 2014) and found to have good potential. This paper therefore focuses on the experimental evaluation of that concept in a DSF building. It firstly introduces the concept and development of the proposed PCM blind system, then describes the experimental setup and data collection process in details. The results of experimental analysis are finally presented with key findings and recommendations for future research.

2. SYSTEM DESCRIPTION AND DEVELOPMENT

2.1 System description

Figure 62a shows the physical model of the integrated PCM blind system in a ventilated DSF with a number of blades demonstrated in Figure 62b. Previous literatures have proved that the laminated composite PCM with narrow phase-change zone was much more thermally effective compared with other randomly mixed PCMs (K. Darkwa, 2006, Darkwa et al., 2011). Thus in this study each PCM blade has a multilayer structure consisting of a laminated composite PCM layer and a substrate. The PCM layer is intended to absorb any excess solar heat through the external glass skin which may be trapped in the DSF cavity, and in this way prevents additional heat gain into the adjacent indoor area. When the temperature in the cavity drops below the PCM solidification temperature, the stored heat is then discharged and removed by means of natural or mechanical ventilation. Through this process the additional heat gain in DSF is shifted into the evening and the peak cooling load of the building can be significantly decreased.
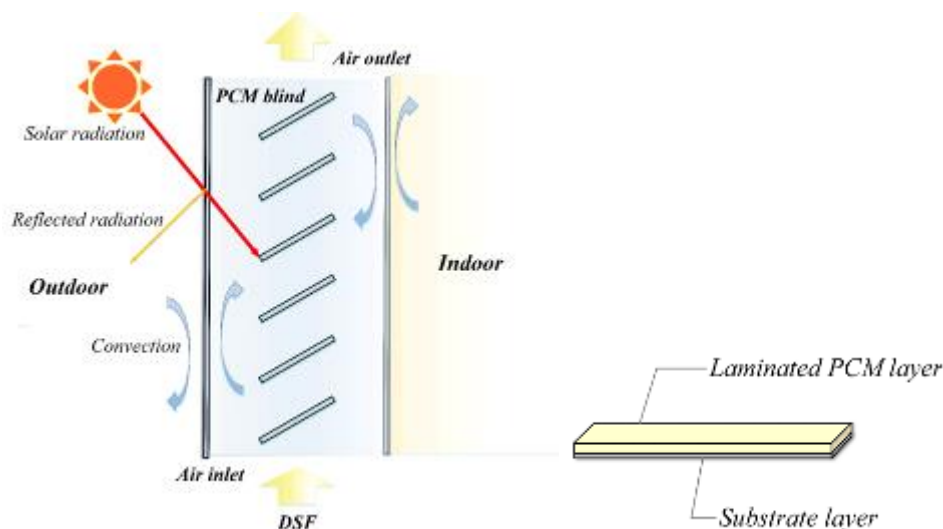
(a) Integrated PCM blind system in DSF   (b) Laminated PCM blade
Figure 21: Scheme of DSF integrated with the proposed PCM blind system

2.2 Prototype Development

Selected phase change material (PCM)

The raw PCM used for developing the laminated composite PCM was Rubitherm Company's microencapsulated powder PCM PX35 (2013). It consists of RT35 paraffin as phase change material and a hydrophilic silica powder as the secondary supporting structure. This microencapsulated PCM is able to maintain its solid form during phase change process and therefore can prevent leakage problem. It also has other advantages such as high thermal energy storage capacity over a relatively narrow temperature range, no supercooling effect, and stable performance through the phase change cycles. The technical data of the PX35 are presented in Table 1.

Table 1: Thermo-physical properties of PX35

Product	Melting point (°C)	Melting range (°C)	Heat of fusion (kJ/kg)	Specific heat capacity (kJ/kgK)	Density (kg/m^3)	Thermal conductivity (W/mK)
PX 35	35.00	29-36	100.00	1.60	650.00	0.10

Screening tests on adhesive materials

In order to choose suitable bonding materials for developing the laminated composite PCM, screening tests were conducted on different adhesive materials and PCM mixing proportions as shown in Table 2. The composite PCM material need to possess properties of high thermal storage capacity and mechanical stability, thus the proper adhesives should allow for high PCM content ratio in the mixture when bonding is completed.

Table 2: Composition of the PCM-adhesive samples

Composition	PCM-Epoxy AB				PCM-EP5138				PCM-PVA	PCM-EP5009
PCM ratio (wt%)	67%	75%	80%	83%	67%	75%	80%	83%	67%	50%

Among the tested PCM-adhesive samples, PCM mixed with common epoxy resin (PCM-epoxy AB, PCM-EP5138) had the highest PCM content ratio in the samples of nearly 83wt%. On the contrary the PCM ratio in the PCM-PVA and PCM-EP5009 conductive epoxy resin samples was only 67wt% and 50% respectively under the same experimental condition.

In terms of mechanical aspects, almost no shrinking problem was observed with the samples using epoxy resins as bonding materials (PCM-Epoxy AB, PCM-EP5138) after more than 24 hours curing process, whereas the PCM-PVA samples suffered severe shrinkage. With the same mixing proportion, samples using common epoxy resin adhesives also showed better bonding effect within the samples when compared with other adhesives (PVA) as boding materials.

Based on these outcomes epoxy resin adhesive was selected as the most suitable bonding material for developing the composite PCM, and the PCM content ratio in the composite could range from 67wt% to 83wt%.

3 EXPERIMENTAL SETUP AND MEASUREMENT

As shown in Table 3 and Figure 22, an experimental DSF test facility was built and installed on the third floor of an existing multi-storey DSF building located in Centre for Sustainable Energy Technologies (CSET), Ningbo, China. The test facility was a box (1.05 m x 0.95 m x 0.45 m) with two 5 mm flat float glass walls facing the south as the double skin and two wooden sidewalls. It was naturally ventilated with an open inlet and an open outlet. In total there were six PCM blades fixed in the middle of the box and at a tilt angle of 30°.

Table 3: Geometry and materials of DSF test facility and PCM blind

DSF test facility	DSF height	0.95m
	DSF cavity depth	0.45m
	Outer skin material	Flat float glass
	Outer skin thickness	5 mm
	Inner skin material	Flat float glass
	Inner skin thickness	5 mm
PCM blind	Blade number	6
	Blade width	150 mm
	Blade thickness	5 mm
	PCM layer material	Laminated composite PCM
	PCM layer thickness	3 mm
	Substrate material	Aluminium
	Substrate thickness	2 mm

(a) View of the DSF test facility   (b) Sensor installation spots

Figure 22: DSF test facility integrated with PCM blind (Tb: surface temperature of the blade; Tg: surface temperature of the glass; Ta: air temperature in DSF; Va: airflow velocity in DSF)

The DSF box was fully instrumented by sensors at different positions as shown in Figure 23. Twenty K-type thermocouples were installed in the test rig for measuring the surface temperature of the blades, surface temperature of the glass walls, and air temperature at different positions in the box. Two hotwire anemometers were set up to record the inlet and outlet airflow velocity in the DSF box.

The data being measured and their instrumentations are summarised as follow:

• Surface temperature of the PCM blind – K-type thermocouple
• Surface temperature of the glass wall – K-type thermocouple
• Air temperature in DSF box – K-type thermocouple
• Inlet and outlet airflow velocity of the DSF box – Hotwire anemometer
• Meteorological data – Weather station

All the sensors were calibrated before installation and were connected to a data logging system set up in an office of CSET building for continuous data acquisition. The temperature data were recorded throughout the day while the airflow velocity data were collected from 9:00 am to 17:00 pm. The time step of the data collection was 5 seconds. The continuous data collection was conducted in the summer of 2014 except for rainy days. Meteorological data include ambient temperature, solar radiation, and wind speed and direction were monitored and recorded by the weather station on the green roof of CSET building.

| (a) Front view | (b) Section view |

Figure 23: Demonstration of sensor installation spots (Red dot: thermocouples for measuring blade surface temperature; Yellow dot: thermocouples for measuring glass surface temperature; Blue dot: thermocouples for measuring air temperature; Blue square: anemometers for measuring the airflow velocity at the box inlet and box outlet)

4 RESULTS AND DISCUSSION

Figure 24 present the average temperature data of the DSF test cell on the warmest days during the summer of 2014. The air temperature in DSF was below 36°C for most of the days against a comparably high external glass surface temperature. The surface temperature of internal glass could be 2°C lower than the external glass due to the presence of PCM blind. The temperature difference of air close to external (Text) and internal glass skin (Tint) was 0.31°C while the temperature difference between the DSF outlet (Tout) and inlet (Tin) ranged within 0.1°C-1.0°C.The highest temperature for all the layers occurred on 12/7/2014 during the summer periods.
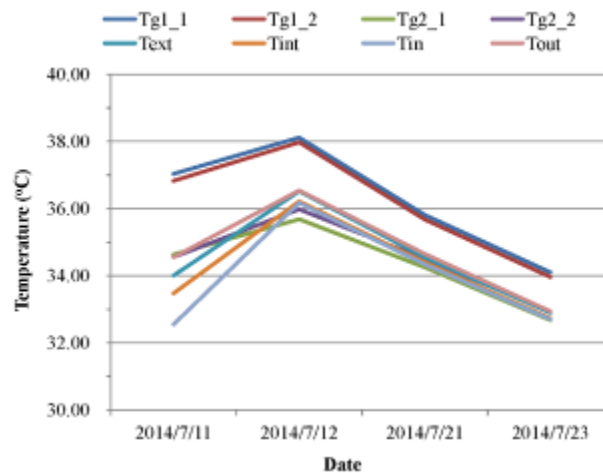
Figure 24: Temperature profiles of DSF test facility in summer 2014

As indicated in Figure 25 and Table 4, the surface temperature of PCM layer was only a little higher than the substrate with the largest difference of 0.65°C occurred to the highest PCM blade. The smallest temperature difference occurred on the third blade which may be due to the specific tilt angle of the blind.
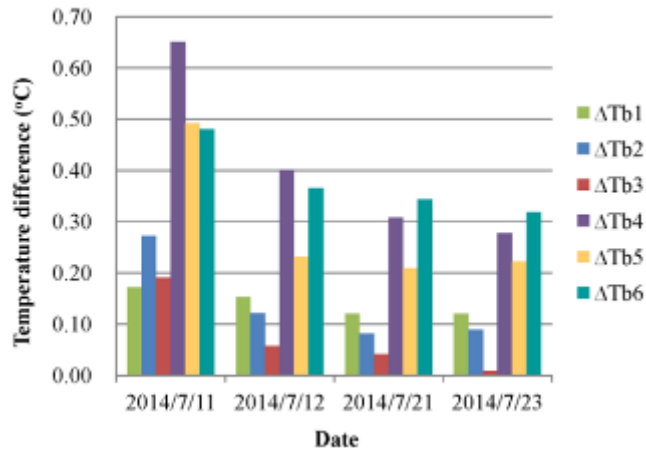
Figure 25: Temperature profiles of DSF test cell in summer 2014

Table 4: Temperature differences of the PCM layer (T_{bn_1}) and substrate (T_{bn_2}) in summer 2014 (Unit: ^oC)

($\Delta T_{bn}=T_{bn\_1}-T_{bn\_2}$; n=1, 2, 3, 4, 5, 6)

	ΔT_{b1}	ΔT_{b2}	ΔT_{b3}	ΔT_{b4}	ΔT_{b5}	ΔT_{b6}
2014/7/11	0.17	0.27	0.19	0.65	0.49	0.48
2014/7/12	0.15	0.12	0.06	0.40	0.23	0.37
2014/7/21	0.12	0.08	0.04	0.31	0.21	0.34
2014/7/23	0.12	0.09	0.01	0.28	0.22	0.32

The temperature variations in DSF test cell are demonstrated in Figure 26. It can be seen that all the temperature variations followed almost the same trend. The surface temperature of the PCM blind increased with the height of the DSF and responded to the environmental temperature in the DSF test cell. The air temperature in the DSF test cell did not exceeded 39^oC during the day time and was below 35^oC (its melting point) before 10:20 am and after 15:30 pm, which means the developed PCM blind system was able to undergo solidification process even on the hottest day in summer.
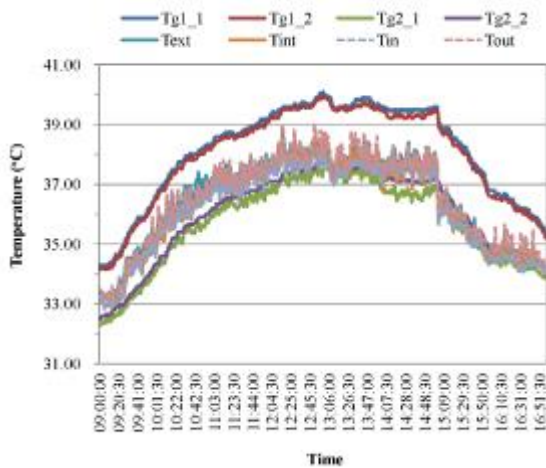
(a) Test cell environmental temperature
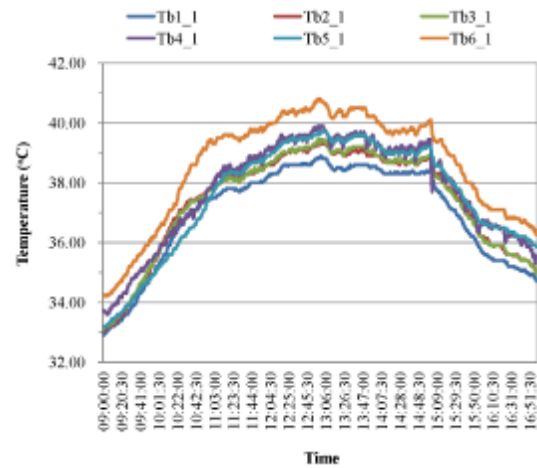
(b) Surface temperature of PCM layer
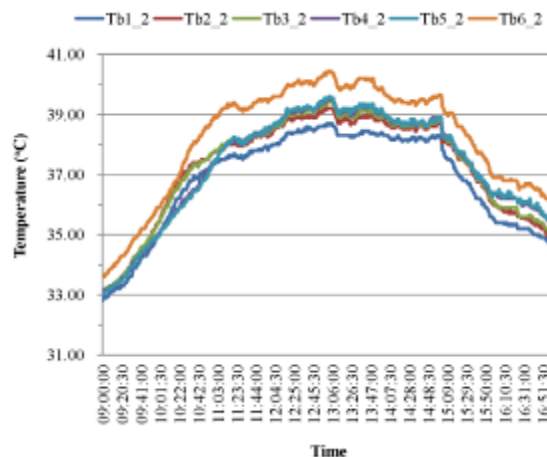
(c) Surface temperature of substrate

Figure 26: Temperature variations of DSF test cell, 12/7/2014

5   CONCLUSIONS

In this study, an integrated PCM blind system was developed and experimentally evaluated. The specific conclusions can be summarised as follow:

- For most of the days in summer period, the integrated PCM blind system was able to stabilise the average cavity temperature to about 36°C which showed no significant increase as compared with the ambient temperature. The surface temperature of internal glass could be 2°C lower than the external glass due to the presence of PCM blind.
- The air temperature in the DSF test cell did not exceed 39°C on the hottest day and was below 35°C (its melting point) before 10:20 am and after 15:30 pm.

Although the developed system has demonstrated some level of capacity of minimising the overheating phenomenon in DSF, there is the need for longer term investigations into the energy storage efficiency of the PCM due to repeated charging and discharging cycling. Besides, the effectiveness of the integrated system should also be tested under various climatic conditions and different operation modes of the DSF building.

6   REFERENCES

Data Sheet PX35. 2013.In: GMBH, R. T. (ed.).

DARKWA J., Li Y. & Chow, D. H. C. 2013. Heat transfer and air movement behaviour in a double-skin façade. Sustainable Cities and Society.

DARKWA J. & Zhou, T. 2011. Enhanced laminated composite phase change material for energy storage. Energy Conversion and Management, 52, 810-815.

FALLAHI, A., Haghighat, F. & Elsadi, H. 2010. Energy performance assessment of double-skin façade with thermal mass. Energy and Buildings, 42, 1499-1509.

GRATIA, E. & De Herde, A. 2007. The most efficient position of shading devices in a double-skin facade. Energy and Buildings, 39, 364-373.

MEHLING H, L. F. C. 2008. Applications for heating and cooling in buildings. In: DIETER MEWES, F. M. (ed.) Heat and cold storage with PCM An up to date introduction into basics and applications. Springer.

IYI, D., Hasan, R., Penlington, R. & Underwood, C. 2014. Double skin façade: Modelling technique and influence of venetian blinds on the airflow and heat transfer. Applied Thermal Engineering, 71, 219-229.

K. DARKWA, P. W. O. C., D. Tetlow 2006. Phase-change drywalls in a passive-solar building. Applied Energy, 83.

KIM, G., Schaefer, L. & Kim, J. T. 2012. Development of a Double-Skin Facade for Sustainable Renovation of Old Residential Buildings. Indoor and Built Environment, 22, 180-190.

OMER, A. M. 2008. Green energies and the environment. Renewable and Sustainable Energy Reviews, 12, 1789-1821.

PACHECO, R., Ordóñez, J. & Martínez, G. 2012. Energy efficient design of building: A review. Renewable and Sustainable Energy Reviews, 16, 3559-3573.

PASQUAY, T. 2004. Natural ventilation in high-rise buildings with double facades, saving or waste of energy. Energy and Buildings, 36, 381-389.

LI Y, Darkwa J, Kokogiannakis G. 2014. Modelling and Simulation of an Integrated Phase Change Material Blind System for Double Skin Façade Buildings. 13th International Conference on Sustainable Energy Technologies (SET2014), 25-28th August, 2014 Geneva, Switzerland.

ZHOU, J., Chen, Y. 2010. A review on applying ventilated double-skin facade to buildings in hot-summer and cold-winter zone in China. Renewable and Sustainable Energy Reviews, 14, 1321-1328.

85: Experimental investigation of open sorption pipe heat storage under North Cyprus climate conditions

DEVRIM AYDIN[1], SEAN CASEY[1], SAFFA RIFFAT[1]

[1]*Division of Infrastructure, Geomatics and Architecture, Faculty of Engineering, University of Nottingham, University Park, Nottingham, NG7 2RD, UK, ezxda4@nottingham.ac.uk*

Thermal energy storage systems have gained much attention in recent years as they are now seen as one of the most promising solutions to increase utilisation of solar energy and reduce greenhouse gas emissions. In the last decade, thermochemical versions of these systems have been widely researched for 'seasonal' storage of solar energy as they have the potential to store heat at ambient temperatures for extended periods of time without any degradation or heat loss. In this study an experimental analysis is carried out to investigate the applicability of thermochemical heat storage for space heating facilities under Northern Cyprus climate conditions. For this purpose a prototype sorption pipe was developed and the composite SIM-3a (Vermiculite – CaCl$_2$) was used as the absorption media. The discharging part of testing was conducted in a 12.4 m^2 test room whilst the charging process was conducted in an open environment with an integrated concentrating solar panel attached to the sorption pipe to dehydrate the material. According to the test result, a heat storage density (E$_d$) of 219 kWh/m^3 was achieved with a moisture sorption rate of 0.22 kg/h. The average thermal power output (Q$_{out}$) was found as 0.303W for a 9.38 h discharging period. During that period, the total thermal energy (E$_t$) provided by the heat storage was determined as 87% of the total heat load (E$_l$) of the test room. The charging period lasted 6 h with a desorption rate of 0.22 kg/h achieved using the solar energy. This corresponds to a drying ratio of 60%. In the discharging process encouraging results were achieved however for the charging process further improvement will be required to utilize the solar energy more effectively to fully dehydrate the absorbent.

Keywords: *North Cyprus, solar energy, heat load, thermochemical heat storage, theoretical and experimental analysis*

1. INTRODUCTION

Due to the ever increasing drive in technological and industrial developments coupled with increases in human population, environmental pollution is worsening. This phenomenon, alongside the rise in prices of fossil fuels has increased a large portion of current research towards new and improved renewable energy sources (Chiasson et al., 2000). For most populations across the world, solar energy is considered as a primary energy source for the future however, there are issues with its supply and demand which serve to limit its usability. Storing solar energy in a suitable way can provide some level of equilibrium between supply and demand. Energy storage systems can improve the utility of solar energy and also:

- contribute to energy conservation
- provide economical usage of fuel
- reduce the amount of wasted energy

Storage of solar energy in an appropriate way and developing systems to make it available on-demand must be a key mission of today's energy researchers (Sharma et al, 2009). Fossil fuels, which many national energy networks, including Cyprus are largely dependent on, are now limited and are predicted to be an insufficient and expensive energy source in the future (Grätzel, 2001). In addition to this, domestic energy demand continues to rise year on year. Increased energy demand is not only dependant on the rise in energy consumption, but also on environmental impacts such as climate change and atmospheric pollution (both are increasing).

Within this context, various international agreements such as Kyoto Protocol seek to address this problem (Zhou et al., 2012). As a result of the increasing awareness on the importance of renewable sources for reducing dependency on fossil fuels, the EU commission aims to increase the share of renewables to 20% by 2020 in member countries (Böhringer et al., 2009). Whilst Southern Cyprus is a member of EU, Northern Cyprus (NC) is not but there is still an onus on NC to develop infrastructure and strategies to increase usage of renewable sources as it has the potential to be a part of EU in the near future.
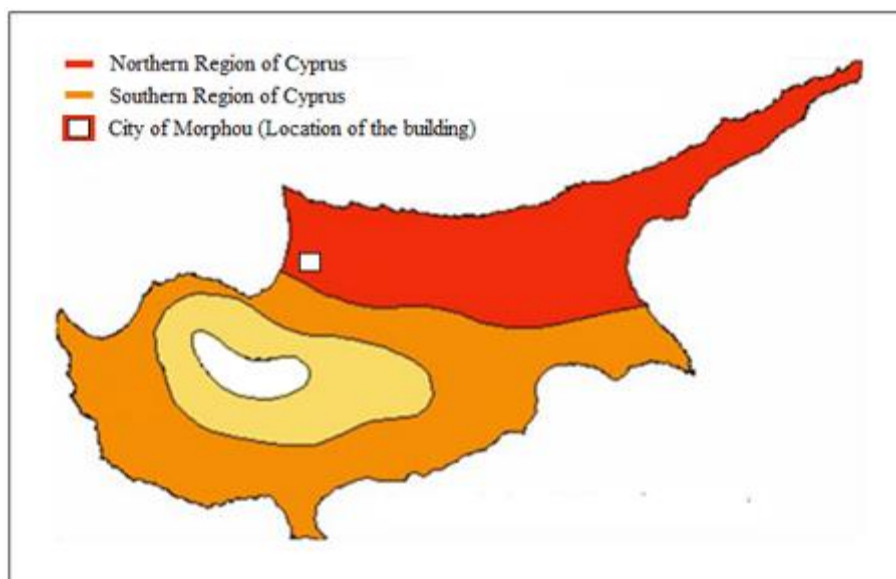
Figure 1: Map of Cyprus showing the geographical occurrence of solar radiation and location of the test building. Adapted from: (Evcil, 2012)

The island of Cyprus (see: Figure 1) has a remarkable solar potential (see: Figure 2) when compared with most of the developed EU countries. This abundance of dense solar radiation should be fully utilized, especially during the days when it is at its peak. Due to historically insufficient economical outlay, alongside the technical and managerial background of the country, usage of solar energy is largely limited to flat plate solar collector technology for water heating purposes (Ibrahim and Altunc, 2012). Generally, these systems can only be used from March to November as the solar availability in winter is inadequate to heat the water to a usable level (> 40 ºC). There are some cases where small size water storage tanks are used to store heat sensibly however, these tanks are rarely insulated and thus provide little or no advantage in utilizing the solar resource effectively. In NC, it is traditionally direct electrical heaters or air conditioners that are

employed for space heating purpose. Whilst water heating accounts for 45 % of end energy usage, space heating constitutes the second highest energy share (28%) in the residential sector (Atikol and Guven, 2003, Atikol, 1996) The reason for this can be due the large total area of residential buildings which, in general, can be 150 to 200 m^2 and usually consist of many uninsulated building components (*i.e.* walls, floors and roofs) with common usage of low efficiency single glazed windows.
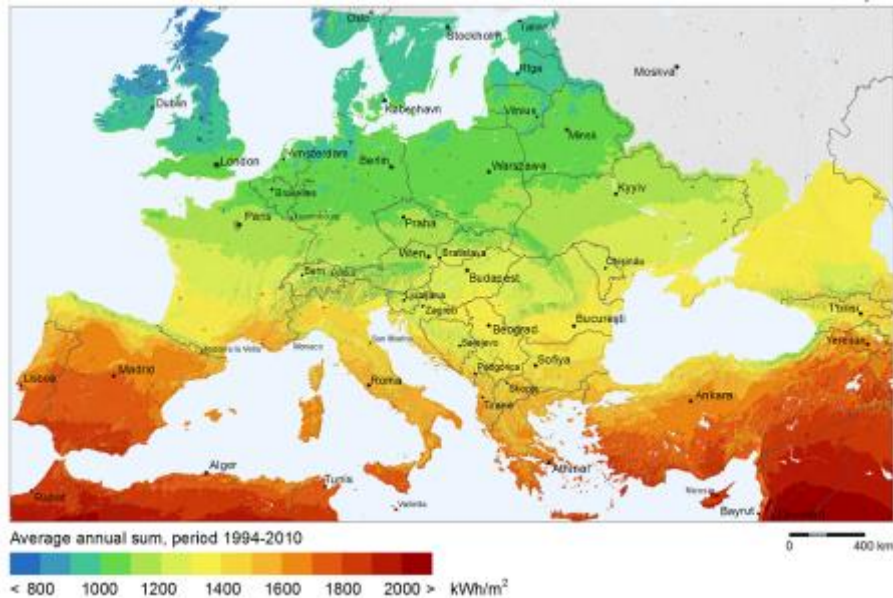
Figure 2: Global horizontal irradiation in European countries (Solargis, accessed on 2.5.2015)

There are currently no residential or commercial applications for utilizing solar energy for space heating during the winter months in NC (Evcil, 2012) and, even with the abundance of energy during the summer period, it cannot be employed in winter for this purpose because of the seasonal mismatch. Thermochemical heat storage (THS) systems should be the main driving force for storage of solar energy and usage of it during winter conditions. This will significantly contribute to reducing the usage of electricity and thus fossil based fuels in the residential sector for space heating applications. THS systems bring the advantage of storing solar energy, densely with very low heat loss and space requirements (Aydin, et al., 2015, Yu et al, 2013).

In this study, a single unit absorption pipe integrated with a solar concentrator is developed and tested. It is proposed to investigate both the sorption pipes design performance in discharging process and the integrated solar concentrator's performance in charging process. Within this study a compact heat storage unit that can be used for short term or seasonal (with multiple units) storage of solar energy is demonstrated. A small sized room, functioning as a farmhouse is used for experimentally testing the sorption pipe performance under realistic conditions. The heat load of the building during the testing period is analysed and compared with the supplied heat by the sorption pipe. Accordingly, to emphasize the critical role of THS, energy trends in NC (past and future) are discussed. The experimental procedure, methods and materials used for realizing the proposed study is discussed. In the final section, experimental results are presented and further improvements discussed. Achieving adequate storage of solar energy with absorption materials will allow to fulfil gap between heat load of the buildings and solar availability that can significantly reduce the usage of fossil fuels for heating the buildings.

2. ENERGY TRENDS IN NORTHERN CYPRUS

North Cyprus is part of a small island located in the eastern Mediterranean Sea. According to the census carried out in 2006 by the NC government the population is circa 265,000 with a total number of residential customers of ≈ 80,000 (KIBTEK, accessed on 28.04.2015). The rate of increase in demand for electricity has risen from ≈ 7 % in 2004 to > 30 % during recent years due to population and construction growth in all geographical regions. The total energy consumption, E_c in 2009 / 2010 for NC was 913 GWh whereas for 2011 / 2012 it was 1256 GWh corresponding to a 37% increase as shown in Figure 3.
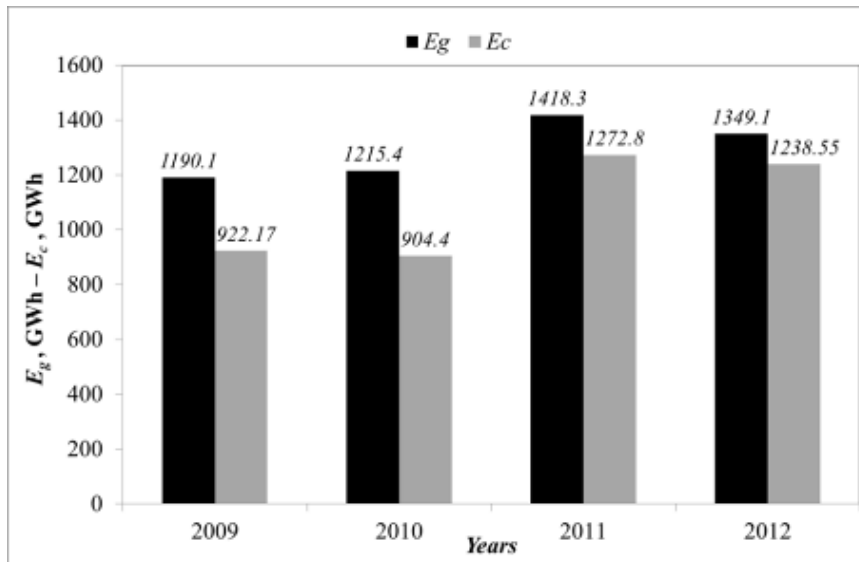
Figure 3: Total energy consumption and generation trend for Northern Cyprus

The residential sector in NC currently accounts for ≈35% of total national energy consumption (see: Figure 4a) with the share of water and space heating being the two heaviest loads at 45% and 28% respectively (see: Figure 4b). In total, 73% of the energy demand of a building in NC is thermal (*i.e.* space heating and hot water). As seen in Figure 2, the remarkable solar potential of Cyprus could be utilized to reduce fossil fuel consumption for space heating and hot water purposes. Feasibility studies on thermal energy storage systems for NC should be carried out as this technology has the potential to store solar energy and increase the solar fraction for building thermal energy consumption.
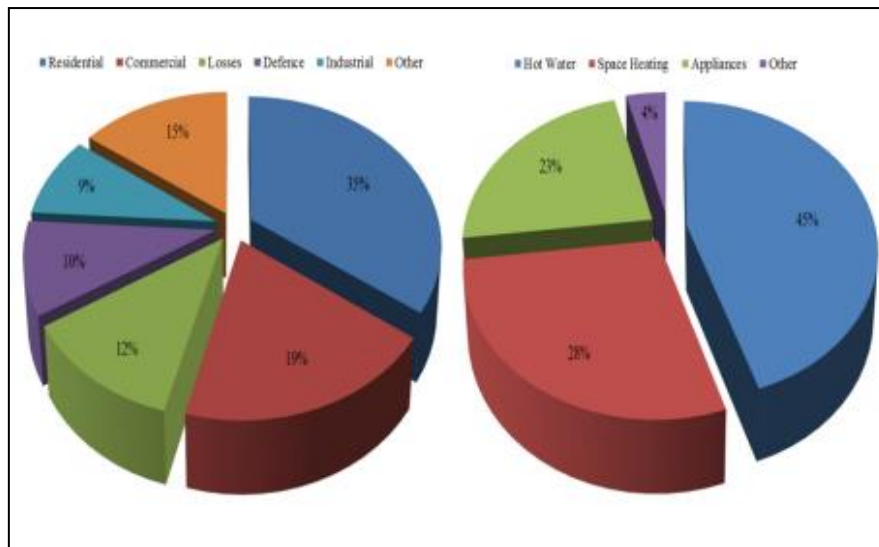
Figure 4: a)Share of national energy consumption in NC , b)Share of energy consumption in the residential sector in NC (Atikol and Guven, 2003).

The high share of overall energy consumption attributed to the residential sector is primarily due to the dependency on fossil fuels for domestic activities such as space and water heating with the majority of water heating in NC provided by either electricity or Liquefied Petroleum Gas (LPG). Central or district heating systems are rarely used in NC as a high percent of buildings are detached and winter climate conditions are not extremely cold. For this reason mainly air sourced heat pumps (HP) or direct electrical heaters are used to provide heating to each room of a dwelling separately. Additionally, in some dwellings, LPG sourced single heating units are also used. Although wood burning stove or fireplaces were popular in the past, these units are currently rarely used due to health and safety issues, environmental pollution and user heavy operating conditions such as temperature control.
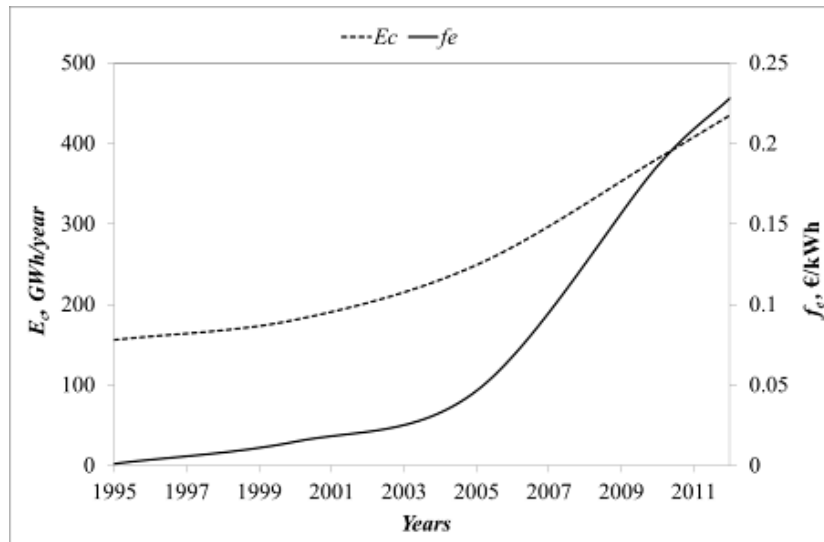
Figure 5: Energy consumption in residential sector and unit price trend for Northern Cyprus

NC does not have any oil or natural gas based fossil sources and imports all fuels types required for electricity generation, residential and commercial needs from other countries. Increases in population and recent industrial developments have caused a significant rise in demand for electricity and fossil fuel consumption (KIBTEK, accessed on 28.04.2015). There has also been a sharp rise in electricity unit prices. In 1990 electricity was 0.0008 €/kWh whereas the current unit price of electricity is 0.22 €/kWh, representing an increase of 275%. Energy consumption in residential buildings has also increased almost 4 fold from 112 GWh to 435 GWh over the same period (see: Figure 5).

NC has very good solar potential which should enable up to 100% of the thermal energy demand of a building to be met. Therefore the importance of the link (and mismatch) between solar energy and the heat load of a building should be understood and innovative methods to store heat with THS materials developed. This will start a transformation in NC towards a 'green' island and a cleaner and safer environment to live.

3. MATERIALS AND METHODOLOGY

In this study a novel absorption pipe integrated with a concentrating collector is developed and tested for solar thermal energy storage. Research on open thermochemical heat storage systems has gained momentum in the last decade as this method provides significant advantages over other heat storage methods. THS allows long term heat storage without any heat loss as well as provides higher energy storage density thereby it has a potential to increase solar share in space heating applications. However further research on THS systems is required especially on process/reactor design also on development of sorption materials. Although providing uniform moisture diffusion to extract the stored energy in THS is important, an effective design allowing efficient drying of THS material with solar energy is crucial. Therefore designs/concepts of THS should ease solar heat input to absorption media for removing the moisture without increasing the costs and complexity. In this context, conversely to the previous methods applied in the literature, a solar concentrator consisting of two mirrors for focusing the solar energy onto the absorption pipe is proposed for drying the absorbent (See: Figure 6a, 6b).The absorption pipe is made up of 0.7 mm thick stainless steel and has a diameter and length of d = 150 mm and l = 80mm respectively. It is painted black in order to maximize solar absorptivity. A perforated pipe, consisting of holes with a diameter of d_h = 3mm is placed at the centre of the absorption pipe. During the process, air enters from the bottom of the perforated pipe and rises vertically inside the pipe. As the top of the perforated pipe is sealed, compressed air diffuses in a horizontal direction and flows through the absorbent which is placed in between the absorption pipe and perforated pipe. A Vermiculite-CaCl$_2$ nano-composite absorbent (SIM-3a) is used as the absorption material as this material provided encouraging results in previous studies conducted by authors. (Casey et al., 2014, Casey et al., 2015, Aydin et al. 2015). Experimental investigation of the developed test rig consisted of two stages; discharging (humidification) in a small room (12.4 m^2 floor area) (See: Figure 6c) following charging (drying) in an open environment utilizing solar energy. The discharging process lasted 9 hours and due to the sufficient ambient relative humidity (RH ≈ 70%) during the testing period, no additional moisture was added to the inlet air. In this way, while the absorption pipe was providing heat to the room at the same time it allowed for maintaining the humidity level inside the room. A small

blower with the diameter of d_f = 40mm was used for providing air flow. Although previously a blower having larger diameter (d_f = 150 mm) incorporated with a reducer (150 mm→40 mm) was tested, a large pressure drop of air is observed. Therefore a smaller diameter blower was chosen to achieve sufficient air pressure for an effective diffusion through the absorbent. The discharging process was conducted on 28th December 2014 in the time range of 13:00-22:00. The charging process was carried out on 29th December 2014 between 10:30 -16:00. The measurement time interval was 15 minutes both for the discharging and charging processes. The volume of V-CaCl$_2$ used in the testing was 0.013 m^3. It is was dried for 48 hours at 150° in an electrical oven before the discharging process to ensure the removal of all residual moisture. The initial dry weight of the material was measured as 5.9 kg.

According to the experimental results the energetic performance of the tested absorption pipe was evaluated both for charging and discharging processes. A model (See: Figure 6c) was created in Ecotect software to simulate the heat load of the investigated building during the experimental period. By this way heat output of the absorption pipe was evaluated in comparison with the building heat load. Additionally, solar charging efficiency (charging) and mass uptake ratio, f, (charging and discharging) were also investigated. The equations used for analysing the experimental results are given in Table 1.

Table 1: Equations used in the analysis

Definition	Unit	Equation	Equation No.
Instantaneous heat gain	kW	$\dot{Q}_g = \dot{H}_o - \dot{H}_i$	1a
		$\dot{Q}_g = m_{dr}.c_p.(T_o - T_i)$	1b
Energy density	Wh/g	$E_d = \dfrac{E_{cum,dr}}{\Delta m}$	2
	kWh/m^3	$E_{d,dr} = \dfrac{E_{cum,dr}}{V_{ads}}$	3
Mass increase	g	$\Delta m = M_{wv} = M_w - M_d$	4
Mass uptake ratio	---	$f_{dr} = \dfrac{M_{ads,x} - M_{ads,d}}{M_{ads,d}}$	5
Absolute humidity	gr/kg	$w = 216.7.\left[\dfrac{\frac{RH}{100\%}.6.112.exp\left(\frac{17.62.t}{243.12+t}\right)}{273.15 + t}\right]$	6
Cumulative thermal energy generation	kWh	$E_{cum} = \dot{m}_{dr}.c_p.\displaystyle\int_0^{t_d}(T_o - T_i)dt$	7
Exergy gain	kW	$\dot{Ex}_g = (\dot{Ex}_o - \dot{Ex}_i)$	8a
		$\dot{Ex}_g = \dot{m}_{dr}.[(h_o - h_i) - T_a.(s_o - s_i)]$	8b
		$\dot{Ex}_g = \dot{m}_{dr}.c_p.[(T_o - T_i) - T_a.\ln\left(\frac{T_o}{T_i}\right)]$	8c
COP	---	$COP_{dr} = \dfrac{\dot{Q}_{g,ave}}{\dot{W}_f}$	9

Where:		Subscripts:	
C$_p$:	specific heat at constant pressure J/(kgK)	tr:	transferred
E$_d$:	energy density (kJ/kg	dr:	discharging
E$_{cum}$:	cumulative thermal energy (kWh)	a:	air, ambient
η$_I$:	1st law efficiency (–)	cr:	charging
η$_{II}$	2nd law efficiency (–)	ave:	average
Ex:	exergy (kW)	ads:	absorbent
f:	mass uptake ratio	w:	wet
h:	specific enthalpy (kJ/s)	i:	inlet
m:	mass (g, kg)	d:	dry
ma	mass flow rate of air (kg/s)	g:	gain
P:	pressure (Pa)	f:	fan
Q:	energy (kW)	x:	any time during discharging
RH:	relative humidity (%)	rxn:	reaction
S:	entropy (kJ/kg)	cum:	cumulative
t:	time (s, h)	o:	outlet
T:	temperature (∘C, K)	wv:	water vapour
V:	volume (m3)		
w:	absolute humidity (gr/kg)		

Figure 6: a)View of test unit during charging process, ,b)Schematic drawing of the absorption pipe integrated with solar concentrator c)Ecotect –schematic illustration of the test room

4. RESULTS AND DISCUSSION

4.1 Thermal Analysis of Discharging Process

Experimental results of discharging process are presented in Fig 7-8. Figure 7 represents the temperature and relative humidity variation of air during the experimental period. Inlet humidity varied in the range of 73%-63% whereas outlet relative humidity increased to 22% from 3%. In open thermochemical heat storage systems temperature lifting is dependent to the instantaneous moisture absorption of the absorbent.

601

Therefore both the reactor design to provide uniform air diffusion as well as properties of the thermochemical heat storage material have vital importance on temperature lifting. High moisture absorption rate, high thermal energy generation per unit mass of absorbed moisture (kWh/gr wv) and low regeneration temperature are desired outputs/properties of an effective heat storage system. In figure 7a temperature variation of inlet outlet and ambient temperature during the discharging process is given. Initially, resulting with the high absorption rate, the outlet temperature reached 40.1° C at the beginning of the experiment. At that time room temperature was 16° C while ambient/inlet temperature was 15.8° C. The mass flow rate of air was 0.021 kg/s during the experiment. Thermal power output varied in the range of 0.53 kW -0.37 kW. Figure 8a illustrates the increase of mass uptake and the mass uptake ratio (ratio of mass uptake to the initial dry mass of heat storage material). In total, 2.15 kg moisture is adsorbed in 9 hours testing where the initial dry mass of V-$CaCl_2$ was 5.9 kg. This result corresponds to $f = 0.37$ at the end of the testing while total energy output was 2.85 kWh at that time. Accordingly heat storage density is calculated as 1.32 kWh /kg wv while volumetric energy storage density was 219.2 kWh. Fig 8b shows the analysed heat load of the room and total thermal energy output during the experiment and as seen from the graph they are in close approximation. This phenomenon indicates that the supplied heat by the heat storage was sufficicient to keep room temperature at a comfortable level although the ambient temperature dropped sharply after 18:00 pm. Room temperature was 17.1 °C at the end of the experiment while ambient temperature was measured as 10.2° C. Applying insulatation to the building would allow to achieve higher room temperature as the heat losses would be minimized in that case. On the other hand a mismatch between supplied heat and the room heat load is observed after 9 pm as a result of the drop of ambient temperature and decrease in heat generation. This was an expected situation as wetting of the absorbent leads to a performance drop naturally. Therefore an effective method for drying the absorbent during daytime (9am - 4pm) would allow reusage of the absorption pipe over the following days. Thereby a sustainable, low cost heating method could be realized which will lead to minimize carbon emissions as well.
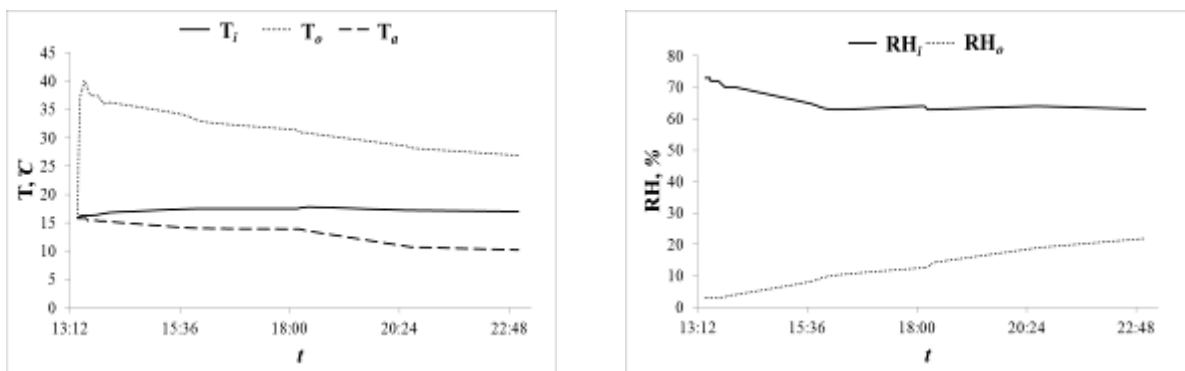
Figure 7: a)Temperature variation of air in discharging process (left), b) Ambient humidity and humidity variation of air in discharging process(right)
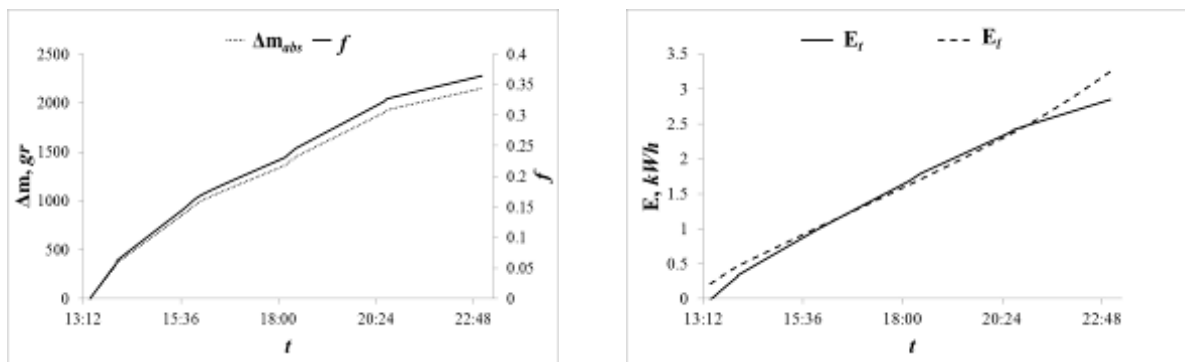
Fig 8: a)Moisture absorption and mass uptake ratio during discharging process(left), , b)Heat load of test room and supplied thermal energy to the room with absorption pipe in discharging process(right)

4.2 Thermal Analysis of Charging Process

In the charging process, a solar concentrator consisting of two mirrors is attached to the absorption pipe and the system is placed facing east with a tilt angle of 43 °C. It is aimed to heat the absorbent while ambient air is blown through it to enhance moisture removal via a convection effect. The absorption pipe is

painted black to increase heat absorption. The charging experiment lasted 6 hours between 10:00 - 16:00. Inlet and outlet temperature of air is given in Fig. 9. During the testing, ambient temperature reached to a peak of 27 °C while it was 20° C at the beginning and 18 °C at the end of experiment. At the same time the highest outlet air temperature from the absorption pipe was measured as 41 °C at 13:00 while it was 30 °C at 16:00 as a result of lowered solar radiation. Additionally the highest absorbent temperature is recorded as 67 °C during the experiment.

Figure 10b shows the relative and specific humidity of air at the inlet and outlet of the absorption pipe during the experiment. The main challenge of drying the absorbent in Cyprus' climate conditions is the high ambient relative humidity. This phenomenon reduces the drying efficiency as the inlet air already holds significant amount of moisture and it can remove limited amounts of moisture from the absorbent. It is seen from figure 10a that ambient RH, which is assumed equal to the inlet air humidity, was in the range of 56-63%. As the absorbent is heated with the solar concentrators, it provides a temperature increase of air. Thereby increasing the temperature of the air allows for a higher moisture holding capacity. Accordingly air leaves from the absorption pipe with lower RH but higher temperature than the inlet resulting with higher moisture output than the input instantaneously. Figure 10a also shows the inlet and outlet humidity content of air. As is seen at the beginning and at the end of charging, inlet air humidity content was higher than the outlet indicating that no moisture removal is provided in these short periods. Conversely it caused more moisture loading of the absorbent. This most probably happened as a result of the low temperature of absorbent from the beginning of the charging until its temperature reached to a sufficient level. Additionally after 3 pm, again, inlet specific humidity exceeds the outlet as a result of reducing solar irradiation. Finally it is calculated that the total amount of desorbed moisture was 1294 gr (See: Figure 10b) whereas the total amount of adsorbed moisture was 2150 gr in discharging process. These results correspond to a drying ratio of 60% which is achieved only with solar energy and 4W small blower. It is obvious that further improvement is required to achieve full dehydration of the absorbent with solar energy to achieve efficient cyclic usage of it. However the results demonstrate a potential for the designed system.

Fig 9:Temperature variation of air in charging process

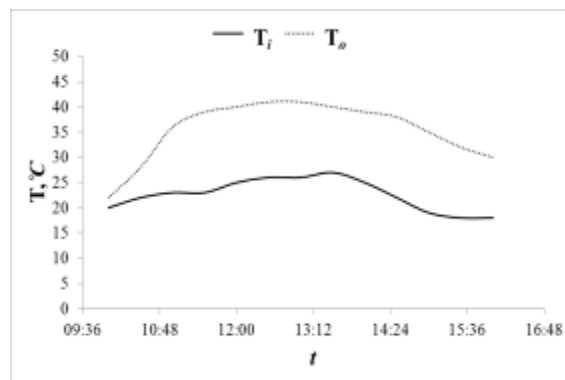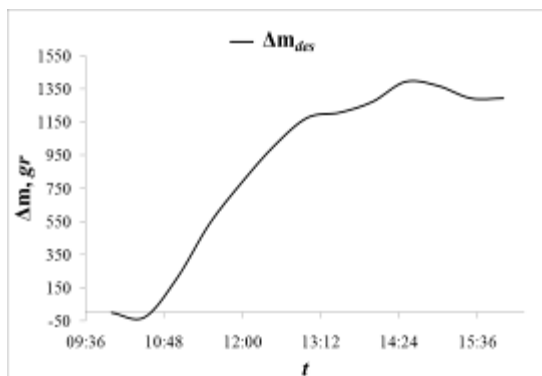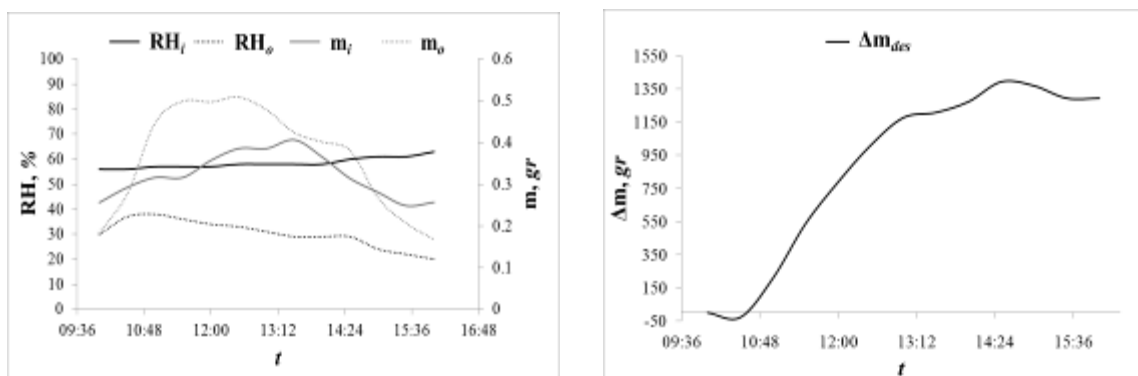Fig 10a: Relative humidity and vapour content of inlet-outlet air in charging process, Fig 10b: Moisture desorption in charging process

3.   CONCLUSION

In this study a novel open thermochemical heat storage system consisting of a sorption pipe and solar concentrator is experimentally investigated. It is aimed to present an alternative design / method for reactor design and efficient solar harvesting concept for open THS systems. In addition it is intended to examine the feasibility of heat storage in North Cyprus climate conditions. In general small portable heaters or air conditioners are mostly used in warm countries as heating loads are low. However it is overlooked that these are expensive and energy consuming methods especially when considering that year round free solar energy is available. Therefore benefitting from the heat storage methods for increasing solar share can both reduce costs for heating as well as carbon emissions while positively contributing the economic development.

Although research on open THS is ongoing, still there is a gap in the literature describing /investigating methods and concepts for regeneration of absorbents with solar energy. In addition there are a limited number of studies discussing novel methods for uniform air flow in large scale THS systems. Therefore a new concept addressing these issues is developed and tested in the present study. It is concluded that this design can provide the following advantages;

- Insufficient space is the main challenge for heat storage applications in many dwellings. Due to the compact nature of the presented system (integrated concentrator to absorption pipe) space requirement can be significantly reduced therefore wider usage of THS could be realized. Additionally the unit could be made up of light structural materials and could even be used as a portable heater. In that case it could be moved to any available location facing towards the solar light (*e.g balcony*, garden*)* for regeneration during daytime.
- The integrated solar concentrator and absorption unit could significantly reduce the heat losses and installation costs in comparison with separate installation of solar panels and heat storage tanks.
- The sorption pipe unit with the perforated pipe for air diffusion could provide uniform air diffusion both in the discharging and charging processes. This phenomenon will allow higher effectivity in usage of THS even in larger volumes.
- Design of THS as modular sorption pipe units will provide easier control and operation of heat storage in comparison with a single large tank filled with absorbent. For instance multiple units (*e.g 30 units)* could be designed in the way that each can provide enough heat for 2 days. In that case 60 days heating of 90 days of winter could be covered with solar energy.

According to the testing results 2.85 kWh thermal energy is achieved using 0.013 m^3 of absorbent corresponding to a 219.2 kWh energy storage density. Additionally thermal power output and discharging COP varied in the range of 0.53 kW-0.37 kW and 13-9 for a 9 hour discharging period respectively. During that time provided heat was sufficient to meet the heat load of the test room having floor area of 12.4 m^2. On the other hand 60% drying ratio is achieved during the charging process utilizng solar energy. It is concluded that high ambient humidity is the main challenge for drying the absorbent in NC climate conditions. However further improvement of the designed unit could allow it to achieve higher temperatures of absorbent. Thereby full dehydration could be achieved. Realizing this condition will lead to multi-cylic usage of the absorbent and the developed heat storage module. Thus an alternative low cost and sustainable method could be achieved for space heating applications.

5. REFERENCES

ATIKOL, U. and Guven, H., 2003. Feasibility of DSM-technology transfer to developing countries. Applied energy. 76, 197-210.

ATIKOL, U., 1996. Residential energy consumption survey. Eastern Mediterranean University Energy Research Centre Report ERC-96/001. Famagusta, N. Cyprus.

AYDIN, D., Casey, S.P., Riffat, S., 2015. The latest advancements on thermochemical heat storage systems. Renewable and Sustainable Energy Reviews. 41, 356-367.

AYDIN, D., Casey, S.P., Riffat, S., 2015. Numerical analysis od solar-assisted seasonal 'open'thermochemical heat storage. International Journal of Low Carbon Technologies.10(2), 131-138.

BÖHRINGER, C., Löschel, A., Moslener, U., Rutherford, T.F., 2009. EU climate policy up to 2020: An economic impact assessment. Energy Economics. 31, Supplement 2, 295-305.

BÖHRINGER, C., Rutherford, T.F., TOL, R.S., 2009. The EU 20/20/2020 Targets: An overview of the EMF22 assessment. Energy Economics. 31, 268-273.

CASEY, S.P., Elvins, J., Riffat, S., Robinson, A., 2014. Salt impregnated desiccant matrices for 'open' thermochemical energy storage—Selection, synthesis and characterisation of candidate materials. Energy and Buildings. 84, 412-425.

CASEY, S.P., Aydin, D., Riffat, S., Elvins, J., 2015. Salt impregnated desiccant matrices for 'open' thermochemical energy storage-Hygrothermal cyclic behaviour and energetic analysis by physical experimentation. Energy and Buildings. 92, 128-139.

CHIASSON, Andrew, Spitler, Jeffrey, Rees, Simon and Smith, Marvin, 2000. A model for simulating the performance of a pavement heating system as a supplemental heat rejecter with closed-loop ground-source heat pump systems. Journal of solar energy engineering. 122, 183-191.

EVCIL, A., 2012. An estimation of the residential space heating energy requirement in Cyprus using the regional average specific heat loss coefficient. Energy and Buildings. 55, 164-173.

GRÄTZEL, M., 2001. Photoelectrochemical cells. Nature. 414, 338-344.

IBRAHIM, D. and Altunc, M., 2012. Using Solar Energy in the Cleaning of Swimming Pools in North Cyprus. Journal of Sustainable Energy & Environment. 3, 31-34.

http://www.kibtek.com/Santrallar/santrallar.htm. (Accessed on 28.04.2015).

SHARMA, Atul, Tyagi, V., Chen, C., Buddhi, D., 2009. Review on thermal energy storage with phase change materials and applications. Renewable and Sustainable energy reviews. 13, 318-345.

http://solargis.info/doc/_pics/freemaps/1000px/ghi/SolarGIS-Solar-map-Europe-en.png. (Accessed on 2.05.2015).

YU, N., Wang, R., Wang, L., 2013. Sorption thermal storage for solar energy. Progress in Energy and Combustion Science. 39, 489-514.

ZHOU, D., Zhao, C.Y., Tian, Y., 2012. Review on thermal energy storage with phase change materials (PCMs) in building applications. Applied Energy. 92, 593-605.

86: Energy-efficient daylight devices

HELMUT KOESTER

Koester Lichtplanung, Karl-Bieber-Hoehe 15, D-60437 Frankfurt a. M.,
info@koester-lichtplanung.de

Daylight technology so far has received little attention in planning processes, despite the latest DIN EN recommendations. Quality characteristics of a design that take into account the reduced need for artificial lighting, are barely considered by any certification system like DGNB, LEED or BREEAM.

None of the certification systems rewards daylight systems designed to redirect daylight to improve the room illumination and thereby saving electric lighting. The goal of the developments is to achieve daylight autonomy without overheating the buildings.

The DIN sets guidelines for reducing the energy transmission in favour of cooling load reduction, but without simultaneously evaluating the required daylighting and visual transmission. Large glass facades are usually planned with darker sun protection glasses in Germany mostly in combination with exterior shading and interior glare protection to prevent buildings from overheating. The energy transmission is indeed reduced to a minimum, however, the lights must be lit to meet the lighting requirements, even when excessive daylight is available outside. The electric lighting, forces the power consumption, and additionally increases the internal cooling loads.

The paper will focus on daylight devices based on mirror optics and the light distribution characteristics as well as the g-values simultaneously achieved. The presentation will show different approaches in façade design by discussing finished high-rise projects implementing the latest daylight devices. Measurements concerning the energy consumption for lighting, heating and artificial illumination will be presented.

The following paper is an abstract of the book "Daylight Modulation – Strategies for Adaptive Facades" (KOESTER 2015).

Keywords: closed cavity façade, daylight autonomy, daylight blinds, daylight control, daylight systems, economic efficiency of daylight, energy efficient facades

1. INTRODUCTION

Daylight modulation is generated in the facade by using reflectors that regulate the brightness and glare-free light distribution in the interior. With the term "modulation" the author refers also to an "optical thermal control" by redirecting the sun to inside or outside with his developments of the RETRO-technology as well as the "optical energy transport", i.e. the energy distribution related to the redirected daylight in the interior (KOESTER, 2004).

The adaptively of daylight facades is the ability to adapt to different climates, latitudes, seasons, times of day and user needs. The facades adapt their protective function against overheating in summer and its supply function with light and solar heat in the winter.

The RETRO-systems patented by the author can be positioned outside, in front of the facade, interior, behind the facade, in the insulation glass or in the cavity of double-skin facades. This overview of different types of adaptive facades is structured by the technologies of light redirection and the application as external, internal or integrated systems.

This article might offer an overview to the reader of the optical systems that are either embossed or incorporated into the louvers to realize the requirements for building physics and daylighting by light redirection.

2. BASICS

The objective of integral dynamic daylight design consists in making the varying daylight conditions, the seasons, tangible within the building by light and shadows and to create the visual connection to the outside. To preserve the link with nature, to the sun, in the artificiality of our office world is most important.

Daylight technology should make it possible, by reflection direction, i.e. by irradiation direction and/or light redirection, to gain passive solar heating input and to ensure passive cooling power by minimizing the SHGC-values without losing the connection to outside (visual transmission) (Fig. 1).
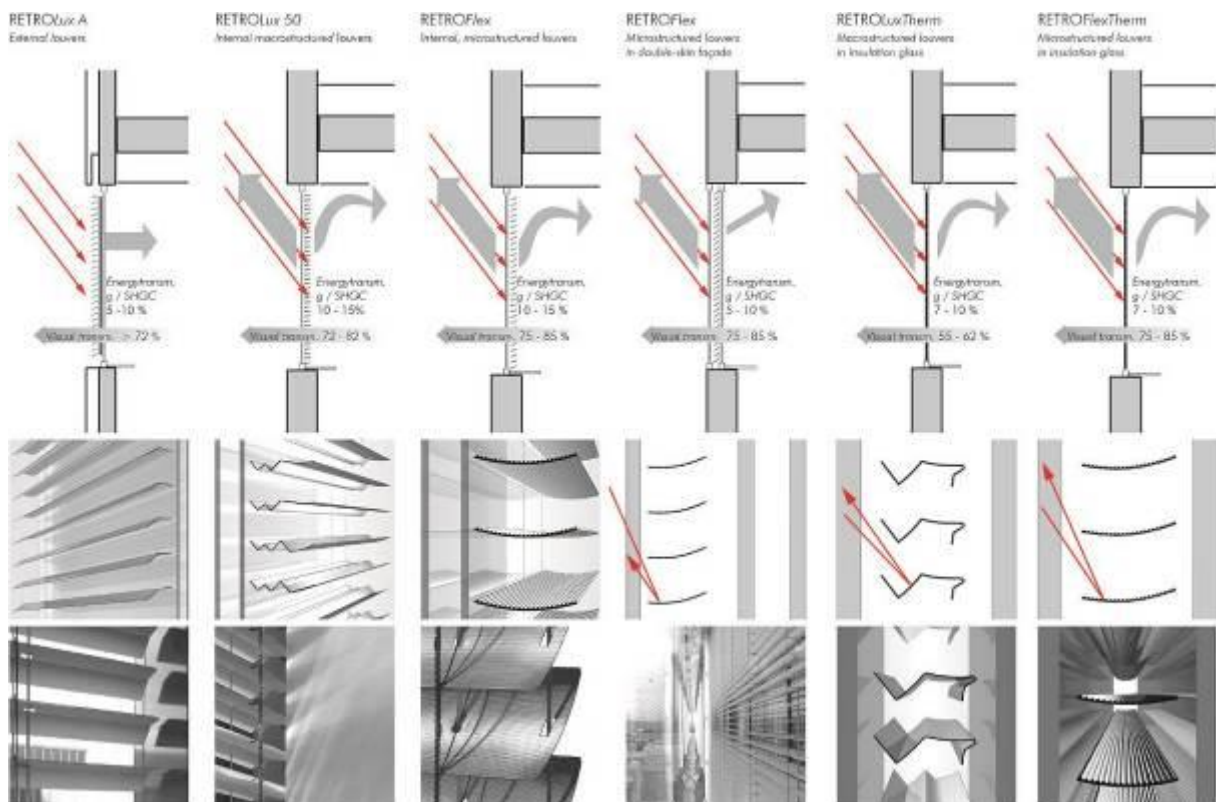
Figure 1: Adaptive façades

Intelligent daylight systems make use of the different sun incidence angles in winter and in summer for controlling the energy transmission (angle selective systems) (Fig. 2).

They are designed in accordance with the physical law "angle of incidence = angle of reflection". For manufacture, e.g. aluminium materials with special coatings are used.
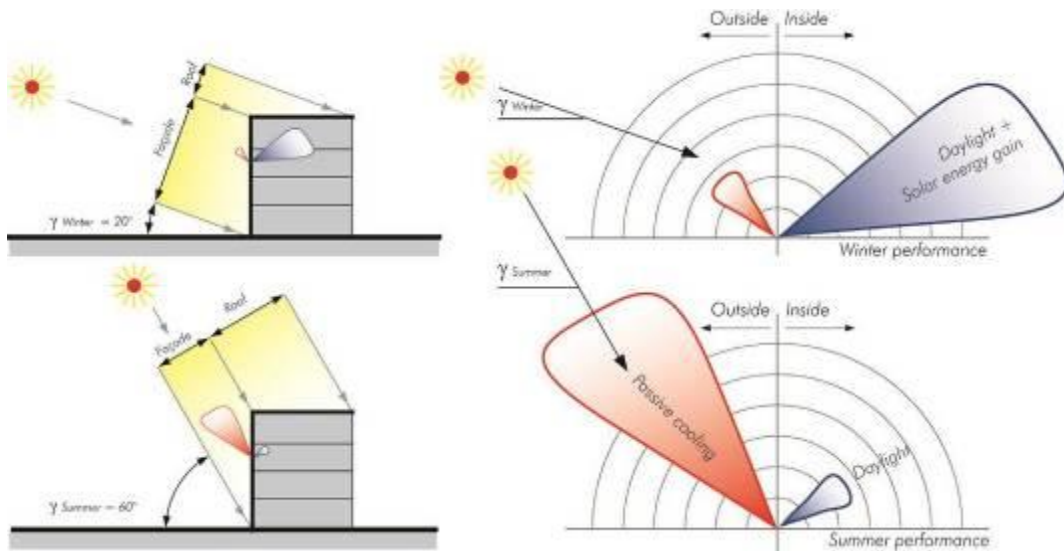
Figure 2: Thermal loads on roofs and façades in winter and in summer and the requests to an intelligent light redirecting system

By reflector technology, the daylight technology insures the supply of the inner rooms, particularly in the room depth, with daylight. This is achieved by a differentiated light redirection via particular louver shapes, i.e. in the upper window area, the light is deflected as flat as possible into the room depth, in the lower window area, the light should be guided steeper to the inner room ceiling in order to guarantee a glare free work place (Fig. 3).
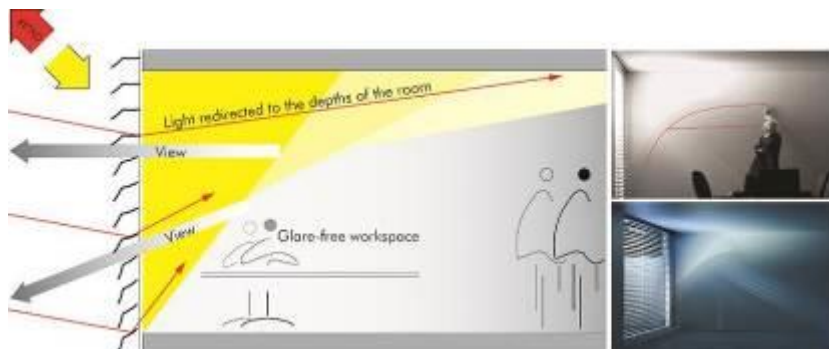
Figure 3: Glare-free light redirection: Room depth illumination through the upper window area

From the user's point of view, visual transmission or the outlook is considered the essential criterion and quality feature of the systems. Daylight technology is, therefore, developed so that good visual transmission through the systems is ensured independently from building-physics characteristics (g-values) and lighting requirements (τ-values).

3. ECONOMICS

Electric lighting energy consumption in conventional office buildings today is as much as 35 % of the total electric load - demands that are generated primarily during the day when daylight is abundant! Since the energy drawn for electric lighting is ultimately converted into heat, there is additionally a load on the cooling system. Proportional to the total energy used, electric lighting can add as much as 16 % to the cooling energy bill. Improved daylighting autonomy alone can reduce total energy use by as much as 25-30 %. RETRO-technology is therefore one of the most cost-effective investments for energy and carbon savings worldwide.

In the USA, the New Buildings Institute, Vancouver, Washington, calculates that daylight harvesting systems can generate lighting energy savings of 35-60 %. According to the US Department of Energy, daylight-response controls of skylights have demonstrated lighting energy savings in warehouses of 30-70 %, without consideration of the additional cooling energy benefits. In a controlled experiment, the Energy Centre of Wisconsin measured the additional cooling energy savings at 25 % (NBI, DOE; Wisconsin 2005).

Such savings are of economic significance. One kW of power on site uses approximately 3 kW of primary energy, with the rest lost as heat at the power plant. In conventional coal or oil fired power plants, only 35-40 % of the primary energy is converted into power with a further 6 % of the energy produced at the power plant lost in transmission. In developed economies such as USA, Japan, Germany, power plants are to be blamed for approximately 50 % of all CO_2 emissions! Over 40 % of each nation's total energy consumption in developed economies is used for heating, cooling, air conditioning, lighting, and other power requirements in buildings.

Therefore, the improved daylighting and an improvement in the g values take an important place in the context of energy efficiency measures.

The economic efficiency of the RETRO- systems is a very significant reduction in the total energy input while doubling the daylight input at the same time (Fig. 4). This is achieved by the precise light distribution on the louvers with monoreflective light redirection to inside and/or outside when the blinds are open.

Especially the use of optimized daylight technology allows energy savings in administration buildings of min. 30 % per year, even when considering workstations close by the window as they are in Germany.

In view of the reduced total energy input (SHGC-values), energy consumption for cooling is saved by the improved daylight illumination, additional considerably higher savings for electricity can, at the same time, be obtained. The economic efficiency of the improved daylight provision is obvious. The calculations also include the cooling loads caused by the electric lighting considering that the current used is completely converted to heat thus loading the air-conditioning system. Taking a façade of 1000 m², it is possible to save during the course of ten years, not considering energy costs increases, at a current price of 0.27 Euros/kWh, inclusive of the savings of maintenance costs (when installing the systems between the glass), as a mean value of all four geographic directions in our climate zone, about 168,000 Euros as compared to a sun protection provided exteriorly.   Taking in consideration an electricity cost increase of 5 % per annum, savings accumulated after 10 years will amount to 317,325.00 Euros, after 20 years to 991,497.00 Euros and after 30 years to 2,328,611.00 Euros per 1000 m² glass facade. The additional costs for the glass-integrated installation can, in most cases, be amortized within a period of five years. The present comparison refers to a competition between the insulation glass-integrated systems and traditional external blinds. The economic efficiency is even more distinct when comparing with standard interior louvers behind sun protection glazing (Fig. 6).
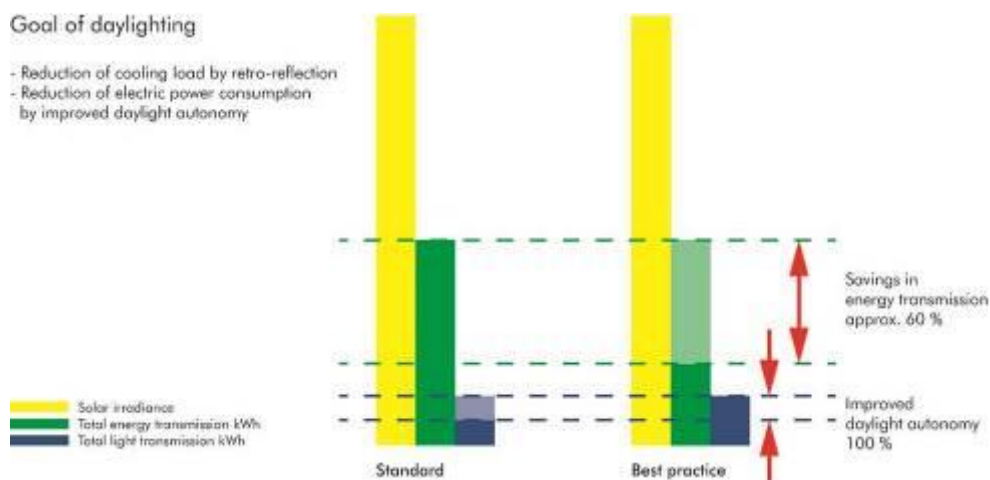
Figure 4: The RETRO-technology reduces the total energy input while improving at the same time the daylight illumination by light redirection.

Figure 5: Litex/Sopharma Triple Towers, Office buildings, Sofia, Bulgaria. Non-ventilated double-skin façade with Fresnel blinds of the RETROFlex 80 mm type, U value < 1.1 W/m²K, g-value ~ 0.05 - 1 in case of high summer sun and open blind.
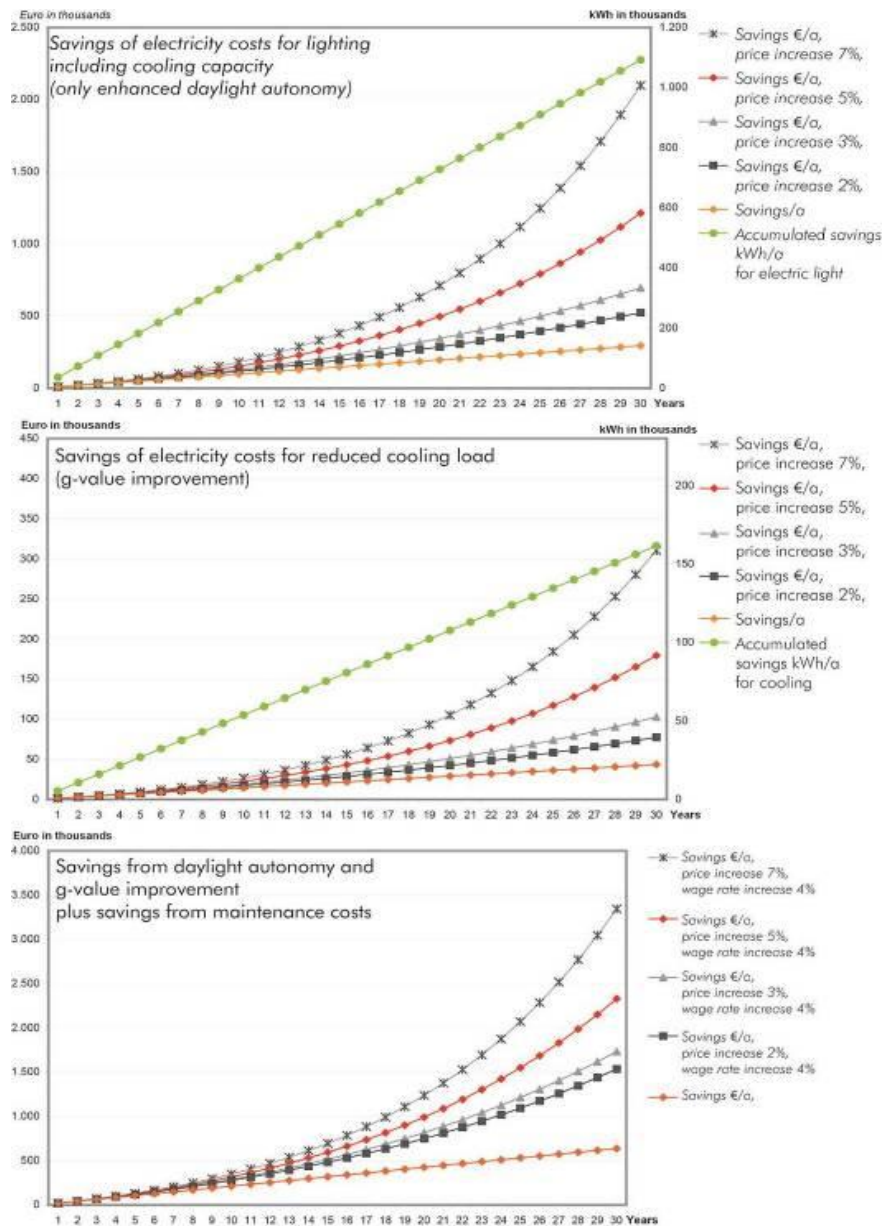
Figure 6: Energy saving potential of the RETRO-technology shown on the example of a school in Frankfurt, Germany, provided with a total of 1000 m² of glass area on the northern, eastern, southern and western façade. The energy savings for electric lighting and cooling as well as the additional savings for maintenance are calculated covering a period of 30 years for insulation glass integrated daylight technology as compared to traditional exterior sun protection (KOESTER, 2015: page 84 – 87).

4. APPENDIX - MEASUREMENTS

Figure 7: Measurements of RETROLuxTherm-louvers

Figure 8: Pharma 2020, New building; Production Department; Sulzbach-Laufen, Germany. About 2000 m² aluminium structure with daylight redirection of the RETROLuxTherm 20 mm type, in insulation glass in combination with a glazing 50/25; ideal for large-area façades

RETROLux O

Low-e glass
U = 1,1 W/m²K
g / SHGC = 52 %

Sun protection glass
τ = 63 %
g / SHGC = 32 %

Louver upper side
alu semi-spectral
total reflectivity R = 94 %
alternative R = 86 %
Louver lower side
white RAL 9010 or
alu glossy

RETROLux U

Horizontal β = 0°
β = tilt angle of the louver
Sun protection glass
$F_c = g_{tot}/g_{Glas}$

0,31 = 0,10 / 0,32

Visual transmission 74 %

50 mm

R = 94 % Low-e, clear glass
R = 86 % Low-e, clear glass
γ Measured values
R = 94 % Sun protection glass
R = 86 % Sun protection glass
R = Total reflectivity

Low-e, clear glass without RETROLux

Measured values for horizontal louver position

Sun protection glass 63/32 without RETROLux

Calculated values with low-e glass

Measured values with SPG 63/32

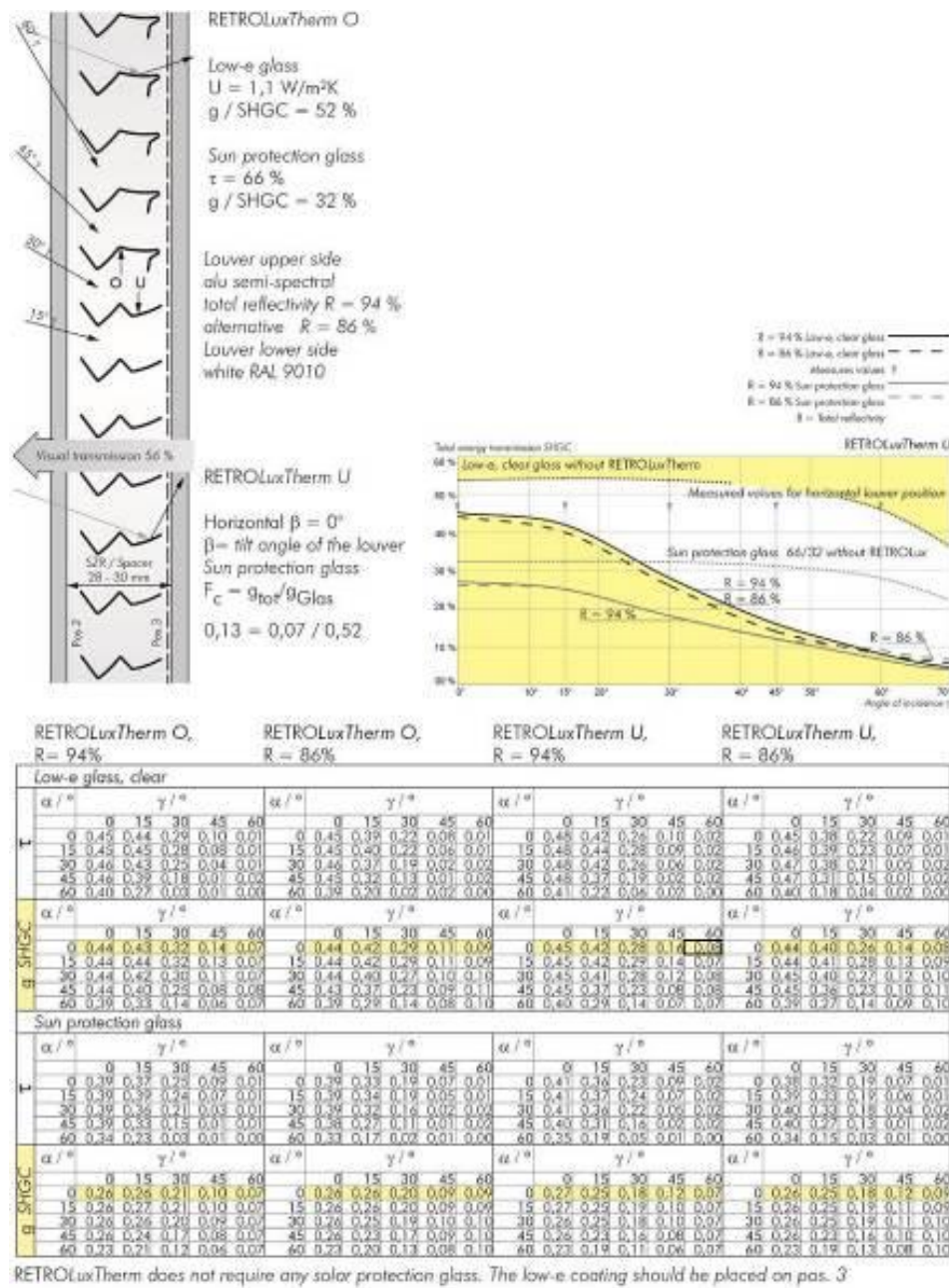| RETROLux O, R = 94%						RETROLux O, R = 86%						RETROLux U, R = 94%						RETROLux U, R = 86%					
Sun protection glass																							
α/°	γ/°					α/°	γ/°					α/°	γ/°					α/°	γ/°				
	0	15	30	45	60		0	15	30	45	60		0	15	30	45	60		0	15	30	45	60
0	0.50	0.42	0.26	0.07	0.04	0	0.49	0.35	0.19	0.05	0.02	0	0.50	0.40	0.21	0.07	0.03	0	0.50	0.36	0.18	0.05	0.02
15	0.50	0.42	0.24	0.06	0.04	15	0.49	0.34	0.18	0.04	0.03	15	0.50	0.41	0.20	0.05	0.03	15	0.49	0.37	0.17	0.03	0.02
30	0.49	0.40	0.20	0.03	0.04	30	0.48	0.31	0.15	0.02	0.03	30	0.49	0.45	0.17	0.02	0.02	30	0.49	0.40	0.15	0.01	0.02
45	0.48	0.36	0.14	0.03	0.03	45	0.47	0.27	0.10	0.02	0.02	45	0.49	0.33	0.13	0.02	0.02	45	0.48	0.28	0.11	0.02	0.01
60	0.42	0.23	0.02	0.03	0.03	60	0.39	0.15	0.02	0.03	0.00	60	0.43	0.18	0.02	0.02	0.00	60	0.41	0.14	0.01	0.02	0.00
α/°	γ/°					α/°	γ/°					α/°	γ/°					α/°	γ/°				
	0	15	30	45	60		0	15	30	45	60		0	15	30	45	60		0	15	30	45	60
0	0.29	0.29	0.23	0.11	0.11	0	0.30	0.28	0.21	0.14	0.14	0	0.29	0.29	0.22	0.11	0.10	0	0.29	0.28	0.23	0.14	0.14
15	0.29	0.28	0.24	0.11	0.10	15	0.29	0.28	0.23	0.13	0.14	15	0.29	0.29	0.23	0.11	0.10	15	0.30	0.29	0.23	0.13	0.14
30	0.29	0.28	0.23	0.12	0.10	30	0.30	0.28	0.22	0.14	0.14	30	0.29	0.28	0.22	0.12	0.10	30	0.29	0.28	0.23	0.15	0.14
45	0.28	0.26	0.20	0.10	0.09	45	0.29	0.26	0.20	0.13	0.12	45	0.29	0.26	0.19	0.10	0.09	45	0.29	0.26	0.20	0.13	0.12
60	0.24	0.23	0.14	0.08	0.09	60	0.24	0.23	0.16	0.11	0.12	60	0.25	0.23	0.13	0.08	0.09	60	0.25	0.23	0.16	0.11	0.12

α = Azimuth angle
γ = Elevation angle

Radiometric measured values
TU Berlin, Institut für Lichttechnik, Prof. Dr. Kaase, Dr. Aydinli

Figure 9: Measurements of RETROLux-louvers

Upper side of louvers: mirroring
Lower side: stone grey

Sun

No visual transmission
Darkening

Sun

Parabola

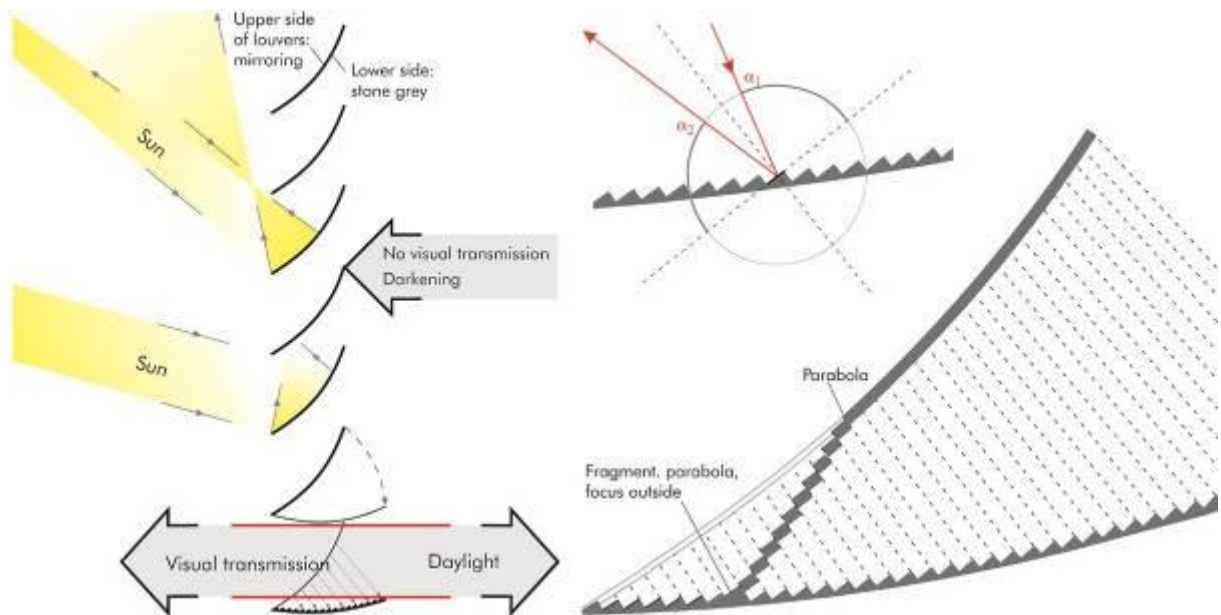Fragment, parabola, focus outside

Visual transmission   Daylight

Figure 10: Fresnel optics of RETROFlex louvers The optics of a closed mirror louver is reproduced by the microstructure on an open-positioned louver. Advantage: Better visual transmission and daylight redirection with the blinds in the open operational position.
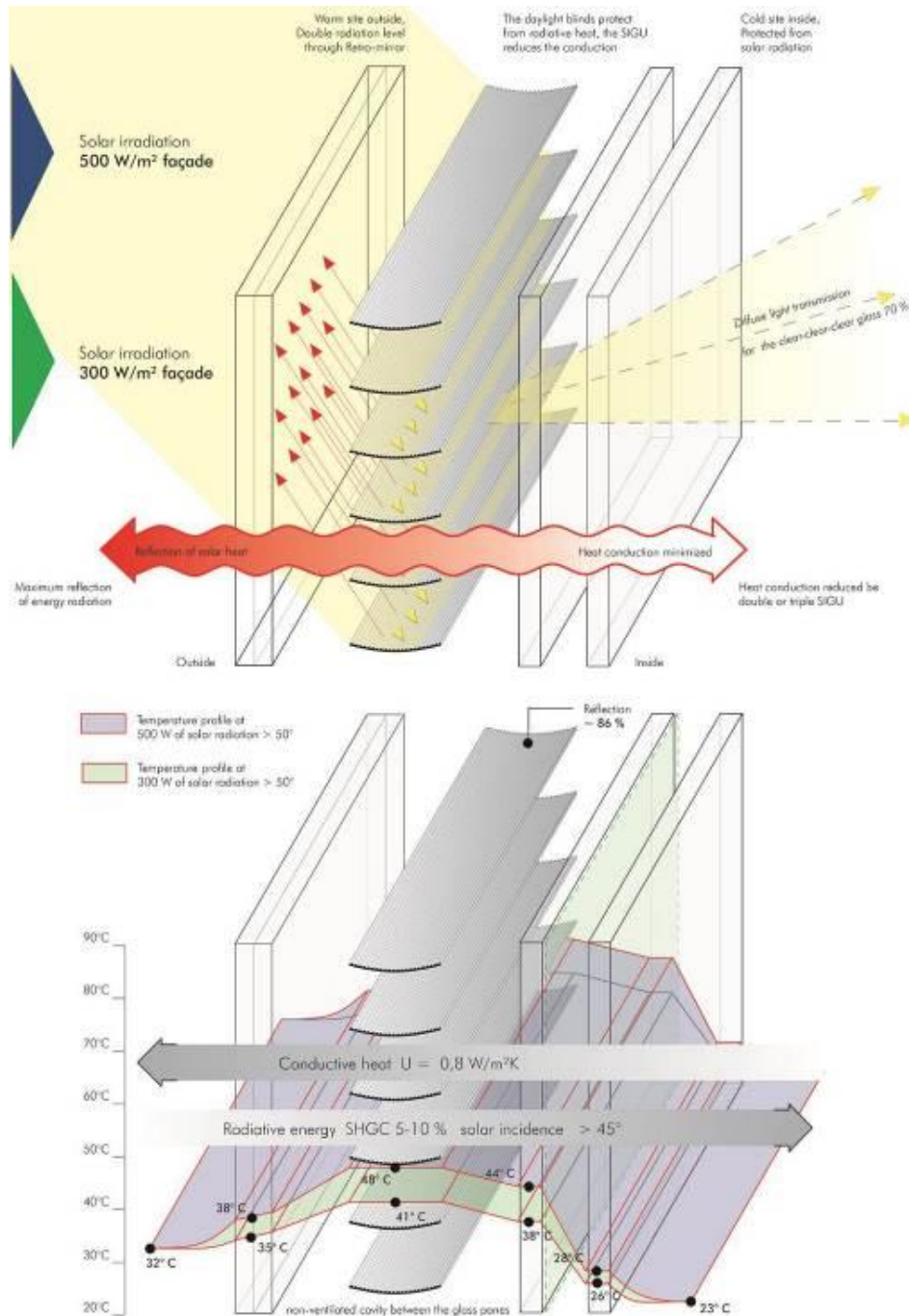
Figure 11: The outer pane is exposed to a double radiation load by incident and retro-reflected sun. The outer pane should therefore, be made from low-iron, colour-neutral glass to prevent absorption and heat generation. The lower the temperature of the outer glazing, the lower the heat radiation between the louvers will be on the inner glazing. The better the reflectivity of the light redirecting louvers, the lower the heat-up of the air space will be. Important: The sun irradiation must be reflected monoreflective, i.e. incident solar radiation has to be reflected with one single reflection into the outer space only to avoid ping-pong effects between the louvers. Only precise light control optics of the mirror louvers can achieve this quality. Diffuse scattering effects (e.g. with white louvers) results in much higher temperatures between the glass panes, since there are multiple reflections and thus increased absorptions. The temperature profile presented can be reached by RETROLux or RETROFlex blinds at angles of incidence > 45 ° and with horizontal louver position. The contour of the blinds is of crucial importance, because the low temperatures, the simultaneous visual transmission of 70-80% between the louvers and the simultaneous improved illumination of the room can only be realized with these louvers in a horizontal louver position. Maximum values of solar radiation are approx. 500-600 W/m². The maximum temperature of the inner glass pane will not extend 3 K above room temperature - and will be below 28° C. The temperatures in the cavity should not extend 60° C to ensure the longevity of the motors, plastic parts and fibres.
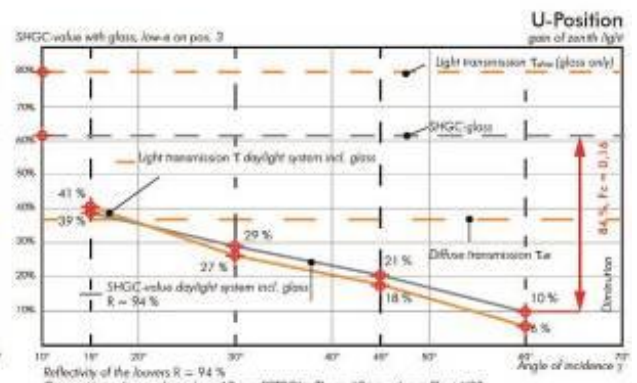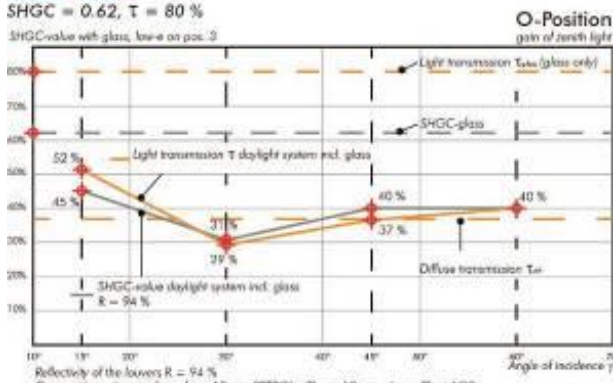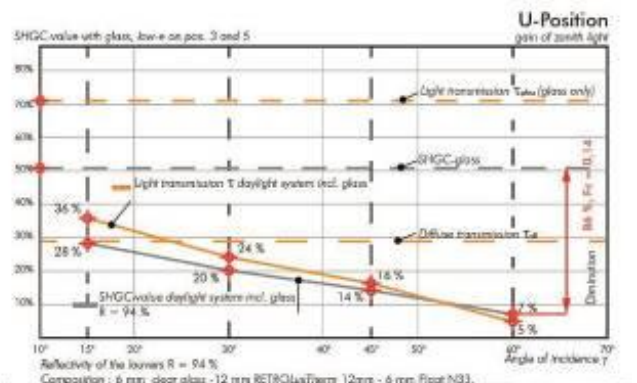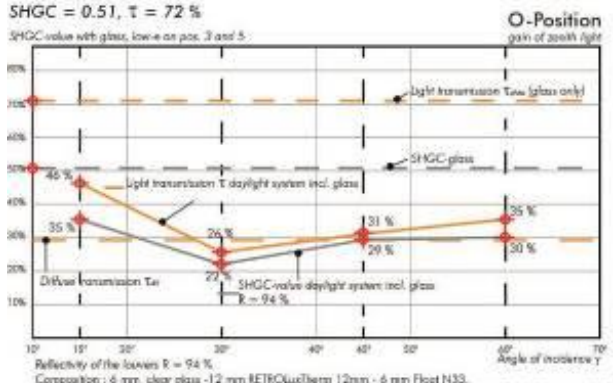
Figure 12: Measurements of RETROLuxTherm 12 mm-louvers

Figure 13: RETROLuxTherm 12 mm-systems regulate the solar incidence without tracking the louvers in favour of a uniform room illumination.

614
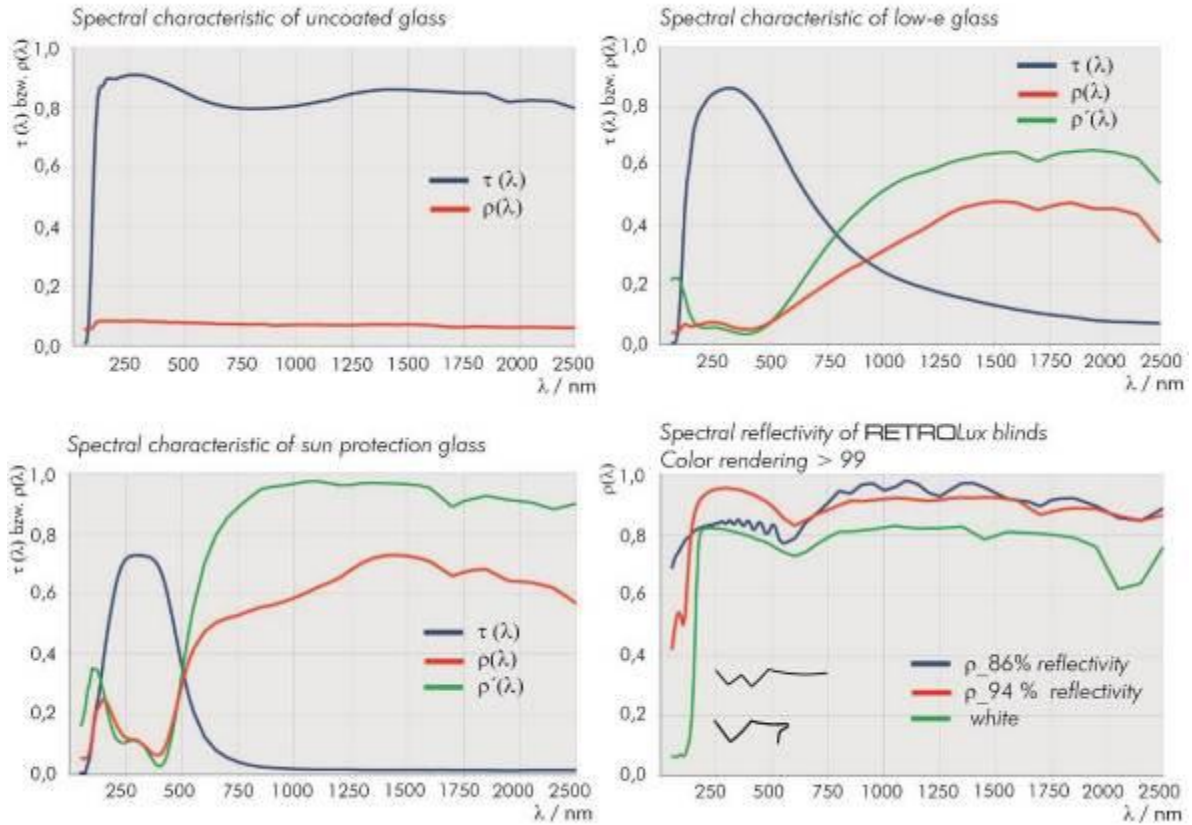
Figure 14: Spectral characteristics of glazing and RETRO-louvers
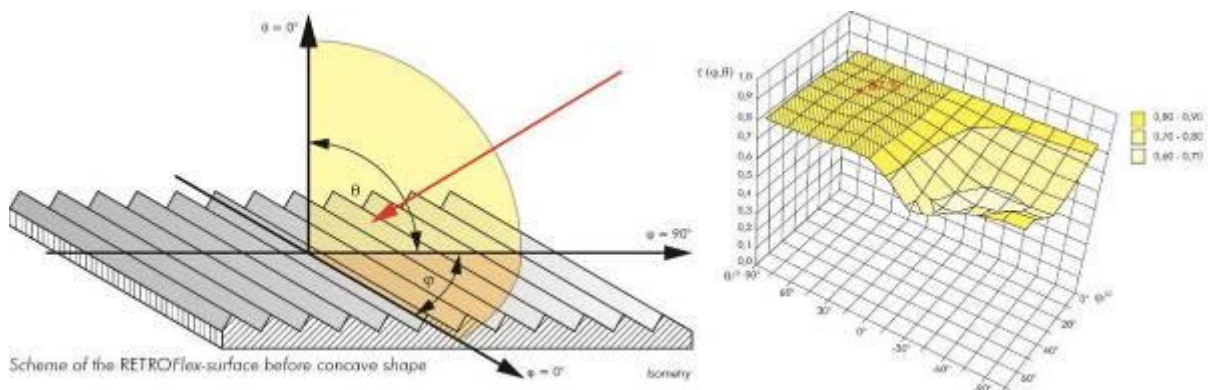
Figure 15: The measurement of total reflection of the RETROFlex surface as an average value under consideration of the sun's movement from East to West is ~ 86 %. The emissivity of upper surface is for 60°C 71.9%. The emissivity of the lower surface is for 60°C 84.2%

5. REFERENCES

KOESTER, Helmut, 2015. Daylight Modulation – Strategies for Adaptive Facades (dt./engl.). 1. Edition. Frankfurt a.M.: WITAG Verlag. ISBN 978-3-00-048400-1

KOESTER, Helmut, 2004. Tageslichtdynamische Architektur- Grundlagen, Systeme, Projekte. Basel: Birkhäuser Verlag. ISBN 3-7643-6729-6, Engl. edition: ISBN 3-7643-6730-X, Chinese edition: ISBN 9-78-7-5083-5110-0, Czech edition: ISBN 9-78-80-247-3049-3

KOESTER, Helmut, 2015. Energieeffiziente Tageslichtlenkung. Innovative Fassadentechnik, Ernst & Sohn-Special, Apr. 2015, A 61029, pp. 84 – 87

97: Deterministic and Bayesian approach to u-value measurements

Lia De Simon[1], Marco Iglesias[2], Edward Cooper[1],
David Tetlow[1], Christopher Wood[1]

1 Department of Architecture and built Environment, University Of Nottingham,
University Park, NG7 2RD, ezxld@nottingham.ac.uk
2 School of Mathematical sciences, University Of Nottingham,
University Park, NG7 2RD

In the framework of reducing building carbon emissions, more efficient building systems are designed to reduce heating and cooling loads in domestic premises. Extensive measurements are essential to evaluate the thermal qualities of the single building systems as well as monitoring the performance "as built" pre and post retrofit.

A series of experimental measurements have been carried out in a controlled environment with the aim of optimizing the analysis process in terms of time and reliability of the results.

The data have been examined with standard and innovative techniques, based on Bayesian statistical analysis. Initial investigation shows that the combination of accurate data collection and the employment of mathematical statistical tools in the analysis can produce reliable results also under non-steady conditions. Further advantages are the simultaneous estimation of a statistical error on the values obtained.

Keywords: Thermal mass, RC model, Bayesian Analysis, Insulation

1. INTRODUCTION

Reducing carbon emissions is a growing concern in the context of limiting the environmental impact of climate change. The building sector is responsible for approximately 25% of the UK carbon emissions, therefore it is essential to improve the energy efficiency of the UK building stock. (Dowson, Poole et al. , Government 2015)

For the purpose of estimating the carbon footprint of new and refurbished dwellings, several commercial software packages are available on the market, such as ANSYS, EnergyPlus and TAS, providing tools for whole building energy simulation. These packages use, in the calculation procedure, material specifications available from literature.

Lately it has been brought to attention that the accuracy of these assumptions might not be sufficient to produce reliable carbon saving estimates, (Hong, Oreszczyn et al. 2006, Cesaratto and De Carli 2013, Asdrubali, D'Alessandro et al. 2014). Li, Smith et al. (2014) measured mean U-values for solid walls of 1.3 ± 0.4 $Wm^{-2}K^{-1}$, compared to the assumed value of 2.1 $Wm^{-2}K^{-1}$ leading to an overestimated heating demand of 16%. Furthermore important differences have been observed between designed building performance and measured "as built" performance (Doran 2000, Lowe, Wingfield et al. 2007).

Experimental measurements are still the most reliable source of accurate information on building element characteristics. In situ measurements present some obstacles related to the impossibility of knowing the wall construction precisely and in most cases are season bound since the wall taken in consideration shouldn't be exposed to solar radiation and the temperature fluctuation should be minimal (Baker 2011). The monitoring procedure is described in detail in the BS-ISO9869-1:2014 (2014), and different analysis approaches can be followed to estimate the thermal resistance or thermal transmittance of the element taken in consideration.

1.1 Theory and calculation

Average method

The average method (Equation 61) is the direct computation method of the wall's R-value from the measured data, suggested by the ISO:9869. It assumes that the effects of the thermal mass are on average zero, due to the duration of the measurement campaign that requires a minimum of 3 days.

Equation 61: R-value calculated with the average method	$$R = \sum_{n=1}^{N}(T_{int}^n - T_{out}^n) \Big/ \sum_{n=1}^{N} q^n$$

Where:

- R is the thermal resistance,
- T_{int}^n and T_{out}^n are the instant internal and external temperatures respectively and
- q^n is the instant heat flux measured.

From the resistance R, the U-value can be calculated considering the internal and external surface resistance as shown in the equation below:

Equation 62: U-value calculation	$$U = \frac{1}{0.04 + R + 0.13}$$

RC networks

Another possibility is to use a dynamic method to analyse the data collected. An example of a dynamic model is the lumped-system model based on the RC circuit analogy. In this case the wall is discretized in a specified number of nodes, the nodes are connected by resistances and the thermal mass is "concentrated" in the internal nodes.

Dividing the element considered with two internal nodes as shown in Figure 27, leads to the discretization of the heat equation shown in below:
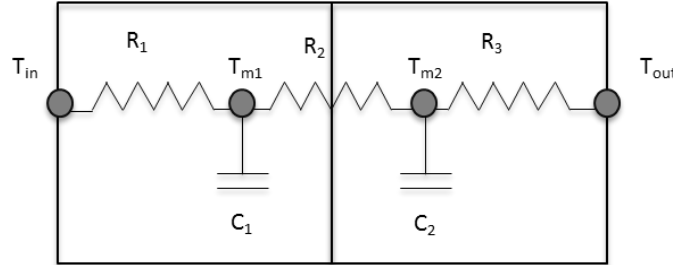

Figure 27: Diagram showing the wall discretization

Equation 63: Discretization of the heat equation
Equation 64: Discretization of the heat equation

$$C_1 \frac{T_{m1}^{n+1} - T_{m1}^{n}}{dt} = \frac{T_{in}^{n+1} - T_{m1}^{n+1}}{R_1} + \frac{T_{m2}^{n+1} - T_{m1}^{n+1}}{R_2}$$

$$C_2 \frac{T_{m2}^{n+1} - T_{m2}^{n}}{dt} = \frac{T_{m1}^{n+1} - T_{m2}^{n+1}}{R_2} + \frac{T_{out}^{n+1} - T_{m2}^{n+1}}{R_3}$$

Where:

- C is the thermal mass per unit area,
- T is the temperature, T_{in} and T_{out} are the indoor and outdoor temperatures respectively
- R is the resistance,
- dt is the time interval between two iterations
- n, n+1 indicate the time steps.

The internal heat flux can be determined via Equation 65, where q^n is the instantaneous heat flux at time step n.

Equation 65: Heat flux computation

$$q^n = \frac{(T_{in}^{n} - T_{m1}^{n})}{R_1}$$

The internal heat flux provided by this model is the quantity of interest that we compare against experimental data in order to infer the properties of the wall. Note that not only resistances and thermal mass but also the initial internal temperatures are unknown parameters of this RC model. In other words, the unknown is the vector

$$u = [R_1, R_2, R_3, T_{m1}^0, T_{m2}^0, C_1, C_2]$$

The external temperatures that appear in the previous expressions are measured data. Note that Equation 65 defines a forward map G that for a given vector u generates a vector $G(u) = [q_1, \dots, q_N]$ of time measurements of heat flux.

Unknown parameters in RC models could be potentially estimated by minimizing the residual difference between the model output $G(u)$ and the corresponding experimental measurements that we denote by y. This approach was, for example, followed by (Gutschker 2008) by means of the Downhill Simplex Method. However, the aforementioned approach does not provide a full characterization of the uncertainty that arises from the fact that unknown parameters cannot be uniquely identified from measurements often corrupted with observational noise. More recently, (Biddulph, Gori et al. 2014) has proposed to apply Bayesian inference in order to compute estimates of the unknown parameters as well as a proper measure of their uncertainty. The work of (Biddulph, Gori et al. 2014) uses the Bayesian approach with a similar model to the one previously described but with only one single thermal mass (STM).

In this paper, we extend the aforementioned work and consider the Bayesian approach to analyse experimental data with the double thermal mass (DTM) model described above. Our aim is to show that, for some type of complex walls, the STM model cannot properly characterise the heterogeneities in the material properties of the wall. As a result the Bayesian analysis applied to this model fails to provide accurate estimates of the unknown parameters that characterise these walls. In contrast, the Bayesian analysis with the proposed DTM model produces more realistic estimate as we show in the present work by comparing our methodology with the average method and the Bayesian approach applied to the RC network model with a single thermal mass (STM) node as proposed by (Biddulph, Gori et al. 2014)

The Bayesian approach for the estimation of unknown parameters

We consider a Bayesian Framework for the estimation of the unknown parameters u, of the model predictions $G(u)$, given measurement y . We assume that the following relation holds:

Equation 66 $$y = G(u) + \eta$$

where η is observational noise. In other words, we assume that additive observational noise corrupts our measurements of the heat flux. Furthermore we assume that η follows a Gaussian distribution with variance γ.

Equation 66, as well as the assumption of the noise, determines the likelihood of y given u that we denote by $P(y|u)$. "Likelihood" is used to describe a function of a parameter (in our case u) given a known outcome (y), "probability", instead, indicates of a function of the outcome assuming a given parameter.

We assume prior knowledge (before data) of u is available in terms of a prior probability distribution $P(u)$. In concrete, $P(u)$ is a product of uniform distributions defined for each of the component of u (recall $u = [R_1, R_2, R_3, T_{m1}^0, T_{m2}^0, C_1, C_2]$). The (posterior) uncertainty of the unknown u, given our observational data y, is quantified by the posterior distribution $P(u|y)$ which, from Bayes' theorem, we know is given by $P(u|y) \propto P(y|u)P(u)$.

An explicit expression of $P(u|y)$ is not available and so we provide a characterization by means of sampling with a Markov Chain Monte Carlo (MCMC) approach. More concretely, we consider a Metropolis-within-Gibbs algorithm based on prior-reversible proposals constructed from uniform distributions (Gelman, Carlin et al. 2014). The samples generated from this algorithm are then used to compute the expected value and the variance of u under the posterior distribution.

3. METHODOLOGY

The wall monitored is north-facing and shaded for most of the year due to the high vegetation growing nearby. The data collection started in March and it is still on going.

The wall construction comprises a steel frame core filled with 75mm PIR insulation boards and a 120mm external cladding of graphite enhanced EPS with white silicone render finish. The internal finish is plasterboard.

A preliminary investigation with an infrared camera revealed the position of the steel-frame structure. Seventeen heat flux meters (Hukseflux) were distributed between two metal studs. Next to each heat flux meter a RTD100 surface temperature sensor was positioned, as it can be seen in Figure 28. The external surface temperature was measured by means of a single RTD. A data logger DT85 was programmed to collect the data every minute. The installation and the monitoring were setup in accordance to what suggested by the ISO: 9869.
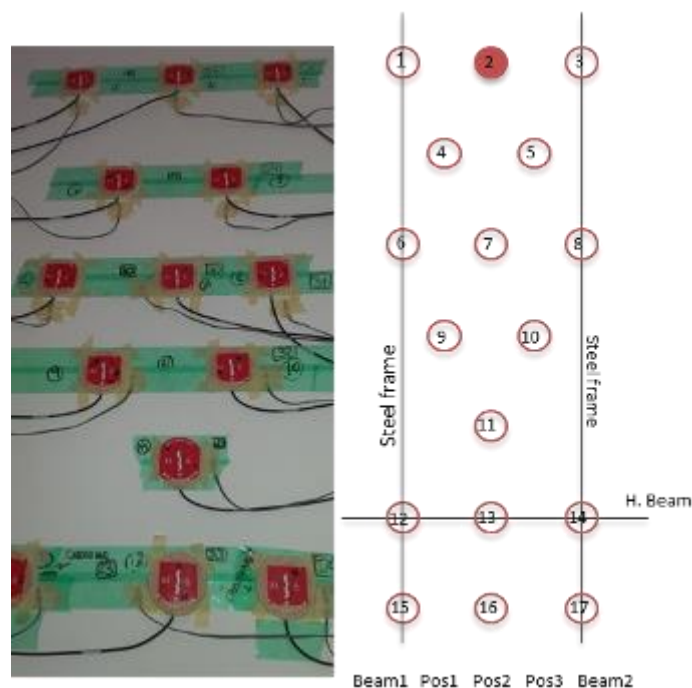
Figure 28: Diagram explaining the experimental setup

An initial guess of the wall properties was estimated by the BRE u-value calculator with the following results:

- Expected U-value: 0.16 W/m²K,
- Total resistance, including internal and external surface resistances of 0.13 and 0.04 m²K/W, 7.41 m²K/W,
- Thermal mass per unit area 13700 J/m²K

The thermal mass per unit area was also calculated separately for the metal frame and the insulation with the following results: 7590 J/m²K on the insulation (ρ_{PIR} = 38 kg/m³, ρ_{EPS} = 20 kg/m³, Cp_{PIR} = 1400 J/kg K, Cp_{EPS} = 1500 J/kg K), and 270225 J/m²K on the steel frame (ρ_{STEEL} = 7900 kg/m³, Cp_{STEEL} = 450 J/kg K).

Initially the data were analysed using the average method according to ISO:9869. The wall resistance was calculated in accordance with Equation 61 and the U-value has been calculated via Equation 62 .

Later the data were divided in 5 different groups: beam1, pos1, pos2, pos3 and beam2, according the position of the sensors on the wall, as shown in Figure 28:

- Beam1 contains the average data collected from position 1, 6, and 15.
- Pos1 contains the average data collected from position 4 and 9.
- Pos2 contains the average data collected from position 7, 11 and 16.
- Pos3 contains the average data collected from position 5 and 10.
- Beam2 contains the average data collected from position 3, 8 and 17.

These groups of data were used to infer the wall properties by means of the Bayesian model. The code was programmed to run 50000 iterations. The first 5000 iterations were discarded and the average and standard deviation for each parameter were calculated using the last 45000 values.

4. RESULTS

4.1 Average Method

At first, all the data from 17 March to 7 May (51 days) were analysed, by means of Equation 61 and Equation 62 the resulting U-values are shown in the diagram below, (Figure 29).
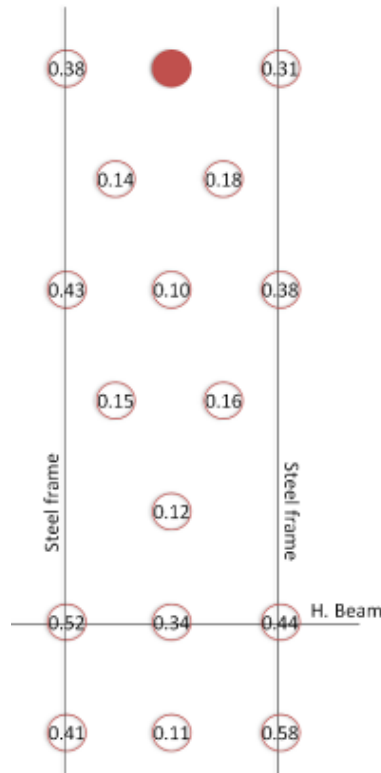
Figure 29: U-value [W/m^2K] in different wall positions, the black lines represent the steel frame construction; the red spot in the top line indicates that the sensor failed in that position.

The internal surface temperatures were averaged over the whole period in each position; the results are recorded in the table below:

Table 37: Average surface temperature measured during the whole monitoring period

	Beam 1	Pos 1	Pos 2	Pos 3	Beam 2
Average Surface Temperature [˚C]	20.4	20.8	20.9	20.7	20.5

According to ISO:9896, the final results need to meet two stability criteria:

1. The result obtained in the last 24h or the measurement campaign has to be within 5% of the result obtained 24h before
2. The result obtained using the last 2/3 of the data has to be within 5% of the result obtained using the first 2/3 of the data collected.

The results shown in Figure 29, meet the first criteria but present some issues with the second criteria: the measurements obtained in location 7 and 11 exceed the 5% limit showing a difference of 8%.

At a later stage, the data were divided in subgroups of 10, 12, 13, 14, 15 and 17 days each. The U values obtained agreed with the values presented in Figure 29 but, again, an analysis of the stability criteria showed that on the locations on the insulation presented more challenges to meet the second criterion.

Besides, the duration of the interval considered did not affect the result: grouping the data in four 12 day groups produced stable results in all locations while dividing the data in groups of 13, 15, days produced instability in some locations.

Considering that the U-value obtained in the centre of the insulation is 0.11 W/m²K, a 5% margin on such value requires that the transmittance does not oscillate more than ± 0.006 W/m²K.

4.2 RC Networks

In this case, to reduce the time required by the simulations, the data collected between 6th-13th April have been analysed. During the time window considered, the average external surface temperature was 10.3 ˚C, while the average internal surface temperature was 20.9˚C.

STM model

The results obtained using the STM model have been summarised in Table 38. R_{tot} represents the sum of R1, R2 and the internal and external resistances, 0.13 and 0.04 respectively. U is the reciprocal of R_{tot}.

Table 38: Results obtained with the STM model

	R1 [m2K/W]	R2 [m2K/W]	Tm [˚C]	C [J/m2K]	Rtot [m2K/W]	U [W/m2K]
Beam1	0.11	2.10	22.4	8.62 104	2.38	0.42
Pos1	2.68	2.07	18.84	7.78 105	4.92	0.20
Pos2	2.68	1.90	20.03	9.32 105	4.75	0.21
Pos3	2.74	2.79	17.20	9.29 104	5.70	0.18
Beam2	0.12	2.00	22.35	8.79 104	2.29	0.44

Table 39: Standard deviation on the values obtained from the STM model

	σR1 [m2K/W]	σR2 [m2K/W]	σTm [˚C]	σC [J/m2K]
Beam1	0.02	0.05	0.17	4.33 103
Pos1	0.26	0.67	0.71	5.23 105
Pos2	0.26	0.66	0.65	4.80 105
Pos3	0.22	0.28	1.25	1.92 105
Beam2	0.02	0.05	0.18	4.43 103
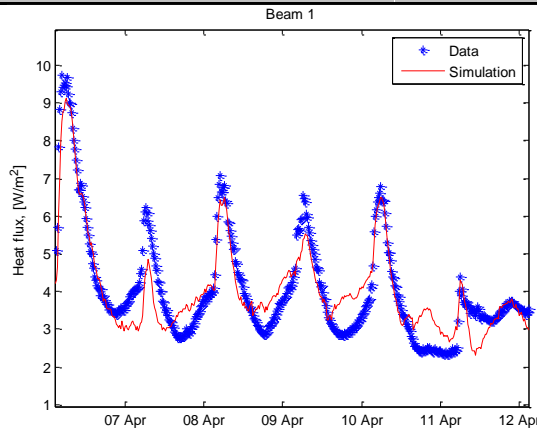
Figure 30: Simulation results and data for the STM model, for Beam 1
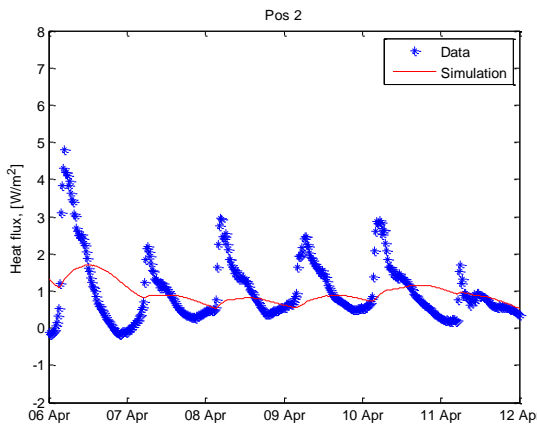
Figure 31: Simulation results and data for the STM model, Pos 1

Looking at the data displayed in Table 38 and Table 39, it can be seen that the U-values calculated from the R-values computed by the STM model are in range with the U-values expected from literature but the STM model cannot reproduce the subtle difference between the values measured at the centre of the insulation (Pos2) and the quarters (Pos1 and Pos3), besides, comparing Figure 30 and Figure 31, it can be

seen that, in the case of Pos2, the heat flux predicted by the STM model doesn't match with the data collected, while in the case this is true for the data collected on the steel frame.

Furthermore the estimated thermal mass temperature shown in Table 38, presents a counter intuitive pattern since it is higher on the metal frame and lower on the insulation while the opposite behaviour was expected. Finally the values obtained for the thermal mass are out of scale compared to the expected results.

DTM Model

The results obtained from the DTM model have been presented in Table 40 and Table 41.

Table 40: Results obtained with the DTM model

	R1	R2	R3	T1	T2	C1	C2	R_{tot}	U-value
Beam1	0.14	1.47	0.76	22.49	9.25	$4.41\ 10^4$	$5.31\ 10^4$	2.54	0.39
Pos1	0.12	2.87	2.87	24.43	15.38	$3.39\ 10^4$	$2.17\ 10^4$	6.03	0.17
Pos2	0.08	2.81	2.81	23.57	19.94	$2.57\ 10^4$	$1.67\ 10^5$	5.87	0.17
Pos3	0.31	2.68	2.49	22.97	12.94	$3.00\ 10^4$	$4.22\ 10^4$	5.65	0.18
Beam2	0.13	1.48	0.66	22.55	9.30	$4.05\ 10^4$	$6.68\ 10^4$	2.44	0.41

Table 41: Standard deviation on the values obtained from the DTM model

|	σ_{R1}	σ_{R2}	σ_{R3}	σ_{T1}	σ_{T2}	σ_{C1}	σ_{C2}
Beam1	0.04	0.50	0.49	0.25	4.98	$9.60\ 10^3$	$4.30\ 10^4$
Pos1	0.05	0.12	0.12	0.18	4.05	$6.37\ 10^3$	$2.53\ 10^4$
Pos2	0.03	0.17	0.16	0.13	0.70	$3.25\ 10^3$	$2.60\ 10^4$
Pos3	0.65	0.24	0.67	1.27	4.52	$7.65\ 10^3$	$1.16\ 10^5$
Beam2	0.04	0.48	0.46	0.25	4.76	$7.72\ 10^3$	$4.73\ 10^3$

Figure 32: Simulation results and data for the DTM model, for Beam 1

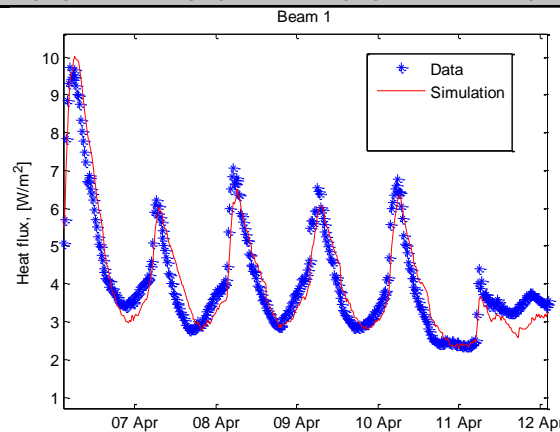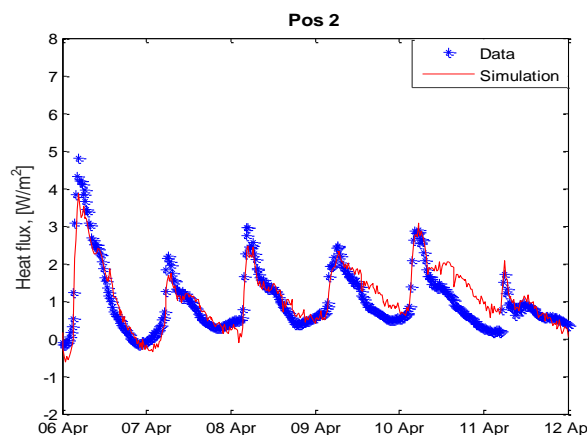*Figure 33: Simulation results and data for the DTM model, for Pos2*

As it can be seen comparing Figure 33 and Figure 32, the DTM model reproduces the heat flux measured faithfully also on the insulation layer.

5. DISCUSSION

From the data presented in Figure 29, the impact of the steel frame in the wall construction can be clearly seen: the U-value on the studs is roughly 4 times higher than the U-value on the insulation layer. The results obtained via the BRE U-value calculator are in reasonable range compared with the U-values obtained on the insulation but cannot account for the high variability of the thermal transmittance across the wall surface. Furthermore, a surface temperature difference of roughly 0.5°C has been measured between the locations on the insulation and the locations on the metal frame.

Together, these two facts contribute to characterise the thermal bridge effect due to the studs. The implications of this can be seen on the long run where this temperature difference could give rise to condensation on the metal studs allowing dust and dirt to stick to the frame and insulation thus creating dark lined and stains on the wall.

The results presented in Table 38 obtained from the STM model show that for the locations Pos1, Pos2 and Pos3 there is a large variability in the values obtained for the model parameters: i.e. R2 varies from 1.90 to 2.79 m^2K/W, the estimated initial thermal mass temperature varies between 17.20 to 20.03°C and the thermal mass per unit area spans between 9.29 10^4 and 9.32 10^5 J/m^2K. Still the U-values obtained vary between 0.18 and 0.21 W/m^2K. In other words, there is more than one set of data that gives the same answer. This indicates that the results produced by this model might satisfy the mathematical problem but don't necessarily reflect the real physical properties of the wall.

All the previous observations and the remarks presented in the results section on the STM suggest that the model might not be accurate enough to simulate the data collected on the insulation layer, therefore the DTM model is proposed and analysed. Figure 33 shows that the DTM is capable of reproducing the heat flux measured realistically. Still, looking at the results presented in Table 40, similar conclusions to the STM model can be drown: the results produced by the DTM model are quite consistent on the metal steel frame but are variable on the insulation.

The main difference across the wall considered in this work and a solid wall is the wall composition. Locations Beam1 and Beam2 and a solid wall present high mass per unit area while the insulation between the steel beams presents much lower thermal mass, when compared to the previous constructions. At the same time, the resistance offered by the insulated steel frame construction is much higher than the resistance of a brick wall. Furthermore, the wall construction in this case comprises two layers, introducing a discontinuity in the thermal conductivity of the element considered at the interface point.

These observations suggest that a discretization of the heat equation on a single point might not be sufficient to characterize the wall and adding a second capacitor enables the DTM to model the heat flux fairly well. Still, the results displayed in Table 40 show some peculiarities: the resistance values are not uniformly distributed, but the first resistance in one order of magnitude lower than the other two. The values obtained for C1 and C2 are in the expected order of magnitude but C2 presents a large standard deviation, as it can be seen from Table 41.

6. CONCLUSIONS

The work described here compares an innovative approach for analysing experimental data with the average method described in the ISO:9869.

Both models analysed, DTM and STM, are able to reproduce accurately the heat flux measured on the metal steel frame locations but, as it can be evinced comparing Figure 31 and Figure 33, for some types of wall construction, in this case two layers of insulation, the STM might not be appropriate, and the DTM appears to be a better model. Furthermore, the statistical tools employed allow estimating the accuracy of the results obtained.

The advantages offered by the STM and DTM models consist in the possibility of obtaining information on the construction of the wall considered. This can be exploited to investigate an unknown wall construction such as non-standard constructions or historical building since these models can produce information on the layering of materials or non-uniformities of the wall that cannot be determined by visual inspection or

without an intrusive approach. For example, if fitting the data requires more than one capacitor this is an indication that the wall composition comprises several layers.

In the same way this kind of analysis can be used to monitor the performance of an element "as built" and highlight the differences between the expected design performance and real life performance.

Still, some work needs to be carried out to perfection these methods. Discretization of the whole wall thickness in only two nodes is still a coarse approximation and therefore it might be worth extending these models, enabling them to cope with finer meshes, introducing a resistance function and a capacitance function over the wall thickness rather than discrete resistances and capacitances.

Further work needs to be done on analysing the errors produced by the model, and estimate the accuracy of the experimental measurements to verify the possibility of measuring U-values with precision $\pm$ 6 mW/m^{2}K.

7. REFERENCES

ASDRUBALI, F., F. D'Alessandro, G. Baldinelli and F. Bianchi (2014). "Evaluating in situ thermal transmittance of green buildings masonries—A case study." Case Studies in Construction Materials 1: 53-59.

BAKER, P. (2011). "U--values and traditional buildings: in situ measurements and their comparisons to calculated values." Historic Scotland Technical Paper 10.

BIDDULPH, P., V. Gori, C. A. Elwell, C. Scott, C. Rye, R. Lowe and T. Oreszczyn (2014). "Inferring the thermal resistance and effective thermal mass of a wall using frequent temperature and heat flux measurements." Energy and Buildings 78: 10-16.

BS-ISO9869-1:2014 (2014). Thermal insulation -- Building elements -- In-situ measurement of thermal resistance and thermal transmittance

CESARATTO, P. G. and M. De Carli (2013). "A measuring campaign of thermal conductance in situ and possible impacts on net energy demand in buildings." Energy and Buildings 59: 29-36.

DORAN, S. (2000). "Field investigations of the thermal performance of construction elements as built." Building Research Establishment report 78132.

DOWSON, M., A. Poole, D. Harrison and G. Susman (2012). "Domestic UK retrofit challenge: Barriers, incentives and current performance leading into the Green Deal." Energy Policy 50(0): 294-305.

GELMAN, A., J. B. Carlin, H. S. Stern and D. B. Rubin (2014). Bayesian data analysis, Taylor & Francis.

Government, D. f. c. a. l. (2015, 7 May 2015). "2010 to 2015 government policy: energy efficiency in buildings." Retrieved 1 June, 2015, from https://www.gov.uk/government/publications/2010-to-2015-government-policy-energy-efficiency-in-buildings/2010-to-2015-government-policy-energy-efficiency-in-buildings#appendix-6-energy-performance-of-buildings.

GUTSCHKER, O. (2008). "Parameter identification with the software package LORD." Building and Environment 43(2): 163-169.

HONG, S. H., T. Oreszczyn, I. Ridley and W. F. S. Group (2006). "The impact of energy efficient refurbishment on the space heating fuel consumption in English dwellings." Energy and Buildings 38(10): 1171-1181.

LI, F. G., A. Smith, P. Biddulph, I. G. Hamilton, R. Lowe, A. Mavrogianni, E. Oikonomou, R. Raslan, S. Stamp and A. Stone (2014). "Solid-wall U-values: heat flux measurements compared with standard assumptions." Building Research & Information(ahead-of-print): 1-15.

LOWE, R., J. Wingfield, M. Bell and J. Bell (2007). "Evidence for heat losses via party wall cavities in masonry construction." Building Services Engineering Research and Technology 28(2): 161-181.

116: Software to determine the energy and light transmission of glass facades in conjunction with special daylight redirecting systems

YANG LI[1], HELMUT KÖSTER[2], BERND BRUEGGE[3]

1 Technische Universität München, Boltzmannstr. 3, Munich, Germany, yang.li@in.tum.de
2 Köster Lichtplanung, Karl-Bieber-Höhe 15, Frankfurt/Main, info@koester-lichtplanung.de
3 Technische Universität München, Boltzmannstr. 3, Munich, Germany, bruegge@in.tum.de

There is a lack of angle-selective evaluation of sun protection devices in rating systems. In particular, the visual transmission of the blinds, which deals with visual comfort, has not yet been addressed. In this paper we look at a specific light distribution of the transmitted sunlight, to improve daylight illumination in the depth of the room under consideration of daylight autonomy.

In order to make a qualitative assessment of shading devices and daylight systems, it is necessary to evaluate the technological structure of facades in their energetic consequence by a simultaneous evaluation of energy transmission, light transmission, room depth illumination and visual transmission with respect to latitude, orientation, climate, and sunshine hours.

We developed a software simulator based on 3D ray-tracing to meet these needs. The software allows to define a glass facade in its optimum size (light entry surface) and its technological specifications, by calculating the quantitative functional diagram and supporting an optimization of glass assemblies and glass coatings in combination with light redirecting structures.

This paper presents the development and features of the 3D ray-tracing simulation software, 3D-RayTracer. We have used the 3D-RayTracer to simulate light transmission. The results of two different daylighting systems are described (RetroLuxTherm 20 mm and RetroFlex introduced by company RetroSolar, developed and patented by Dr. Helmut Koester). The paper finishes by discussing energy savings and further development of the 3D-RayTracer.

Keywords: daylight technology, simulation, software development, daylight redirecting systems

1. INTRODUCTION

Since the last 15 years we have witnessed significant growth of the glass coating industry. Glass coating is mainly used to save energy for cooling in office buildings with solar protective coatings and for heating in residential buildings with low-e coatings. The challenge is to develop glass combinations and coatings with high light transmittance and low solar factor. Currently such glasses vary between a light transmittance of 80% and a g-value of 60% to a light transmittance of 30% and a g-value of 15% and less. The use of such glasses affects the energy consumption of buildings. When g-value is low, the cooling costs are reduced. When both g-value and light transmission are low, this increases the energy consumption for artificial lighting, which leads to higher costs and additional cooling loads since the light us finally converted into heat.

Another rapid advancement is the development of new surfaces and light redirecting contours with angle-selective properties in blinds and daylight control systems. The surface characteristics differ in terms of specular reflection, its total reflectance and emissivity and its gloss. The light and energy transmission in buildings is determined by these surfaces and particularly through the innovative lamella contours, in addition to specific glasses / glass coating properties.

In the further development of light-directing lamellar structures, in combination with different materials and coated glasses, the geometry of daylight systems and their physical models become more and more complex. It is difficult to assess and understand how the sunlight is transmitted and how much energy is consumed using different daylight systems with such complexity. Therefore, there is a need for a software system that simulates light transmission and energy transmission into the complex geometries, and evaluates the performance of daylight systems with respect to different sun-angles. The software can also generate performance profiles with "meaningful" variants to determine lighting and energetic characteristics. These characteristics can then serve as the basis for various calculations, such as for building simulation or for the planning and installation of low-energy buildings.

To meet these needs, in this paper, we describe the simulation software, 3D-RayTracer. The objective of the software is to help define facades in its optimum size (light entry surface) and its technological specifications, by calculating the quantitative functional diagram and supporting an optimization of glass assemblies and glass coatings in combination with light redirecting structures. The simulation of light and energy transmission in other software has been realized in various ways. For example, RADIANCE is a widely used simulation engine that implements both ray tracing and radiosity. Reinhart and Walkenhorst (Reinhart and Walkenhorst, 2001) applied RADIANCE for daylight simulation in a test office with external venetian blinds. However, RADIANCE focuses on the optical simulation but not on the computation of energy transmission. Kuhn et al. (Kuhn et al., 2001 and Kuhn et al., 2011) have developed angle-dependent determination of total solar energy transmittance in even complex facades. The software program is implemented in ESP-r (Clarke, 2001) and has been validated. While Kuhn et al.'s method is promising, its implementation cannot avoid usability difficulties that are inherited from ESP-r. In comparison to other light planning software, our goal is to help users understand the complex geometries and assess light and energy performances with regard to different glass, daylighting systems and sun angles.

The rest of the paper is organized as follows. Section 2 introduces main features of the software, 3D-RayTracer. Then in Section 3 we show the simulation results of three different redirecting systems using 3D-RayTracer. Section 4 discusses energy management and further development of the software.

2. THE SIMULATION SOFTWARE

We develop a 3D-simulation software system, 3D-RayTracer, to help assess shading devices and daylight systems. Prior to the development, it was known to use a 2D-RayTracer to calculate the light and energy transmission perpendicular to the facade. The 2D-RayTracer calculates the different angles of incidence. Such software was already developed in 2002 by Koester and Velkovsky to calculate complex geometries and their thermal and visual behaviour in combination with glass also considering the reflecting and absorbing characteristics of the glass, glass coatings and surface properties of the louvers. It is also possible to calculate the light distribution in the CC-level with this software. 3D-RayTracer simulates the light and energy transmission of various glass facades in combination with light redirecting structures. It employs a 3D ray-tracing algorithm that supports a more precise simulation in comparison to the known 2D methods. This allows analysing the thermal and visual behaviour of the façade while the sun moves from east to west. Given the location and orientation of a building, date and time, we can determine the sun's

elevation and azimuth angles to simulate the sun path. In contrast to 2D methods that simplify the problem to a 2D world, this is more precise and closer to reality. Moreover, our algorithm promotes the simulation of fine structures of light redirecting systems, such as structures at millimetre levels.

In 3D-RayTracer, users can define scenes of different combinations of glass facades and blinds (Figure 1). Users specify properties of glass and louver materials such as reflectance, diffusion and absorption factors. Geometries of facades are also specified, for example, slope and rotation angles of louvers and glass. In each scene, various simulations can be run for given sun angles. Thus, users can easily evaluate and compare different sun protection systems with selective sun angles (Figure 2).

Figure 34: Define a scene that consists of a glass pane and LuxTherm Louvers
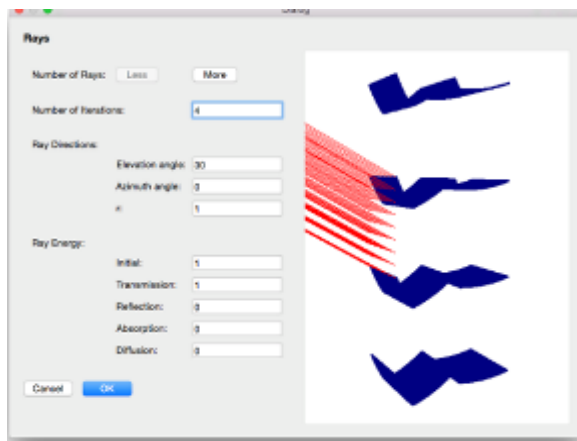
Figure 35: Define sun angles (rays)
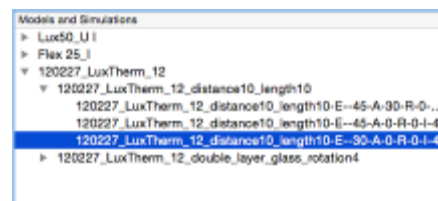
Figure 36: A workspace in 3D-RayTracer that defines different facades and sun angles

After scenes and simulations are specified, light transmission and light reflection are simulated and visualized. 3D-RayTracer uses a workspace schema (Figure 3). Each workspace contains multiple simulations. Users can reload previous simulations in a workspace and compare simulation results. Users can also replay the reflection step by step, to understand how the light redirecting systems work. For instance, Figure 6 illustrates a replay of reflections in three steps. Each step represents a reflection in the system.

Furthermore, the total energy gain (g-value), the percentage of direct light transmission, the percentage of retro-reflection and the percentage of redirected light transmission are calculated. These are important

factors that are used to identify solar gain and illumination of a room using different glass facades and blinds. Light distribution is also calculated and is visualized in a 3D plot (Figure 4). 3D-RayTracer calculates the light distribution through (Andersen 2005)

$$BTDF(\theta_1,\phi_1,\theta_2,\phi_2)=\Phi_2^{norm}/(\Delta\theta_2^{rad}\times\Delta\phi_2^{rad}\times\sin\theta_2\cos\theta_2),$$

where (θ_1,ϕ_1) are the polar coordinates of the incoming light flux, (θ_2,ϕ_2) are the polar coordinates of the transmitted light flux.

Finally, 3D-RayTracer also enables easy report generation. Screenshots of light visualization, simulation results such as g-value together with the description of the daylight systems can be exported into a report. Therefore, the comparison can be easily documented and used in other activities in the planning process.
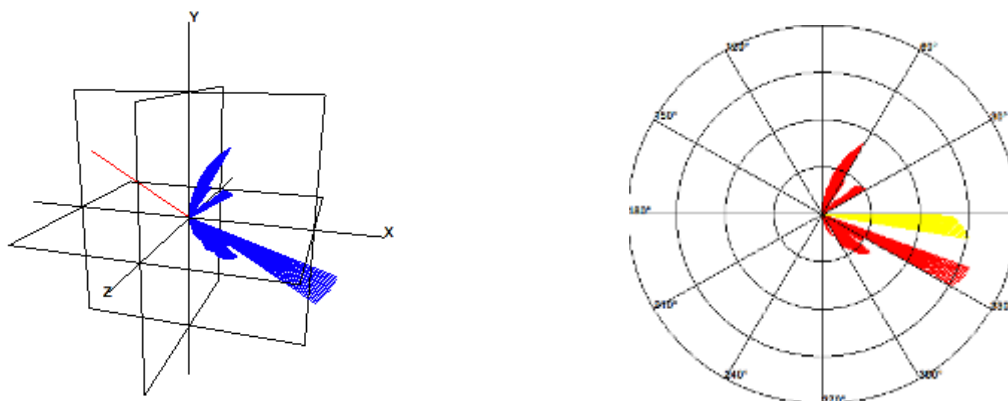
Figure 37: Plots of light distribution. Left: plot in 3D. Right: polar plot along the plane C0-C180 and C90-C270.

3. RESULTS

In the following we show the results of using 3D-RayTracer to simulate light transmission in three different daylight systems, namely, mirror blinds, RETROFlex, and RETROLuxTherm.

3.1 Mirror Blinds

Traditionally, users close the mirror blinds to reflect the sunlight when the sun glares. Protection from glaring sun is only achieved when the blinds are closed. The redirected solar rays are partially absorbed and transformed into heat on the lower side of the blinds. For example, when the sun elevation angle is 45 degrees, and azimuth angle is 0 degree, we rotate the mirror blinds to 45 degrees to reflect the sunlight to the outside (Figure 5). However, in this scenario, there is no visual transmission.

Another problem of using mirror blinds is passive solar heating. For instance, Figure 6 illustrates light transmission of 25-degrees rotated mirror blinds. Through the first reflection on the mirror blinds, about 50% sunlight is transmitted to the inside of rooms. The other half sunlight is redirected to the inside via the second reflection. Almost all sunlight is transmitted to the inside of rooms. Therefore, rooms are overheated in summer.

Figure 38: Visualize simulated light transmission and light reflection of mirror blinds with smooth surface in 3D-RayTracer
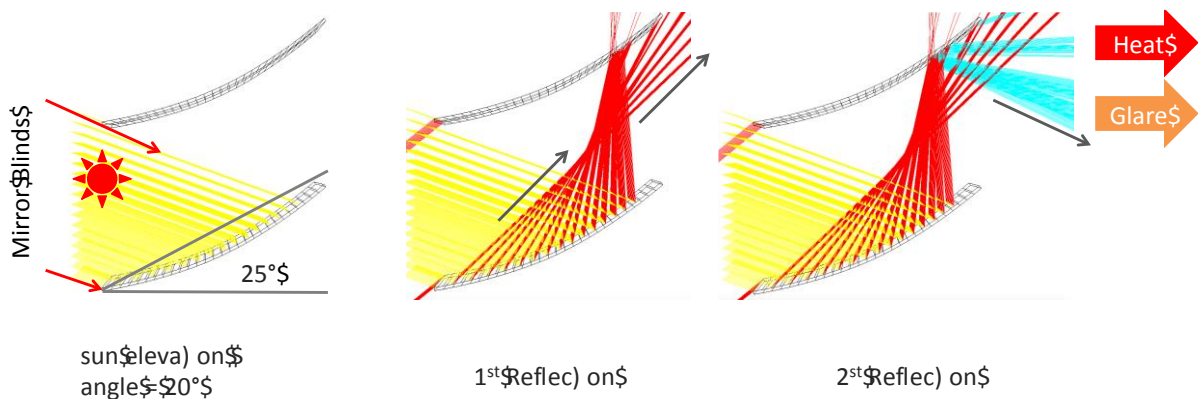
Figure 39: Visualize simulated light transmission of mirror blinds with smooth surface in 3D-RayTracer (blinds rotation angle = 25 degrees, sun elevation angle = 20 degrees, sun azimuth angle = 0 degree)
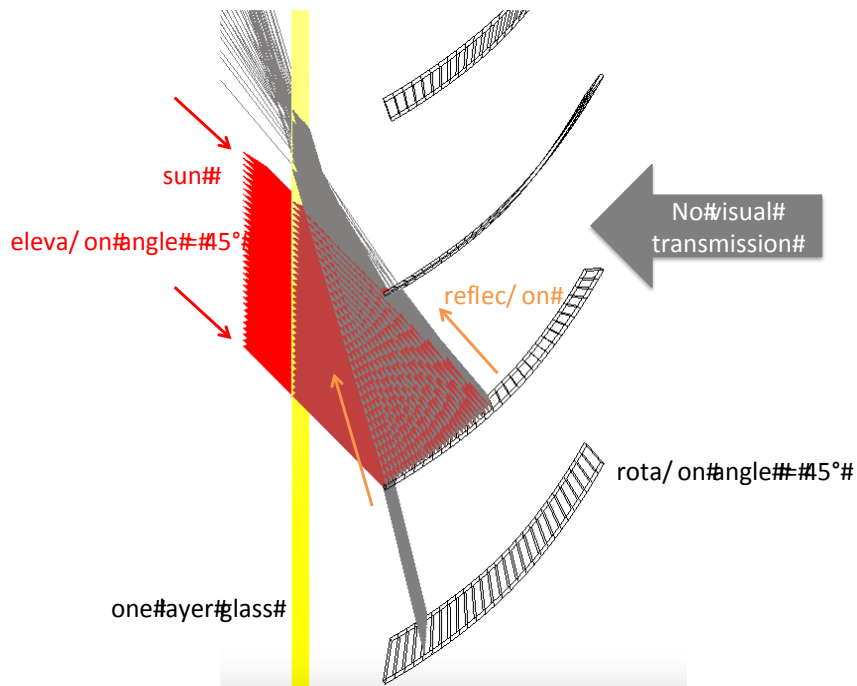
3.2 RETROFlex

To address the problem of no visual transmission using traditional mirror blinds, Köster Lichtplanung has developed RETRO*Flex* (Köster, 2015). The upper side of the louver has a microstructure following a Fresnel mirror with a focal point outside. The microstructure retro-reflects the sunlight as if the blind's louvers were closed - but still the blind is open for daylighting and viewing. As illustrated in Figure 7 and Figure 8, only partial sunlight is redirected onto ceilings, which is enough to illuminate rooms with open blinds. Most part of sunlight is retro-reflected back to the outside. This protects rooms from overheating summer sun, but still provides good visual transmission. Through 3D-RayTracer, users can explore and interact with different daylighting systems. This for example helps users understand how exactly the microstructures works to redirect sunlight.

In particular, Figure 7 also shows a comparison between light redirection with RETROFlex in reality and in simulation. We can see that our simulation matches to the optics in reality. It is worth noting that the two models of RETROFlex (Figure 7 vs. Figure 8) although have similar structures, the tooth size in microstructures does make a difference in light redirection. With a smaller microstructure, more light can be redirected into ceilings (Figure 8). Therefore, using model 2 in combination with composite windows, it provides good lighting conditions interior, while secondary heat radiation is minimized.
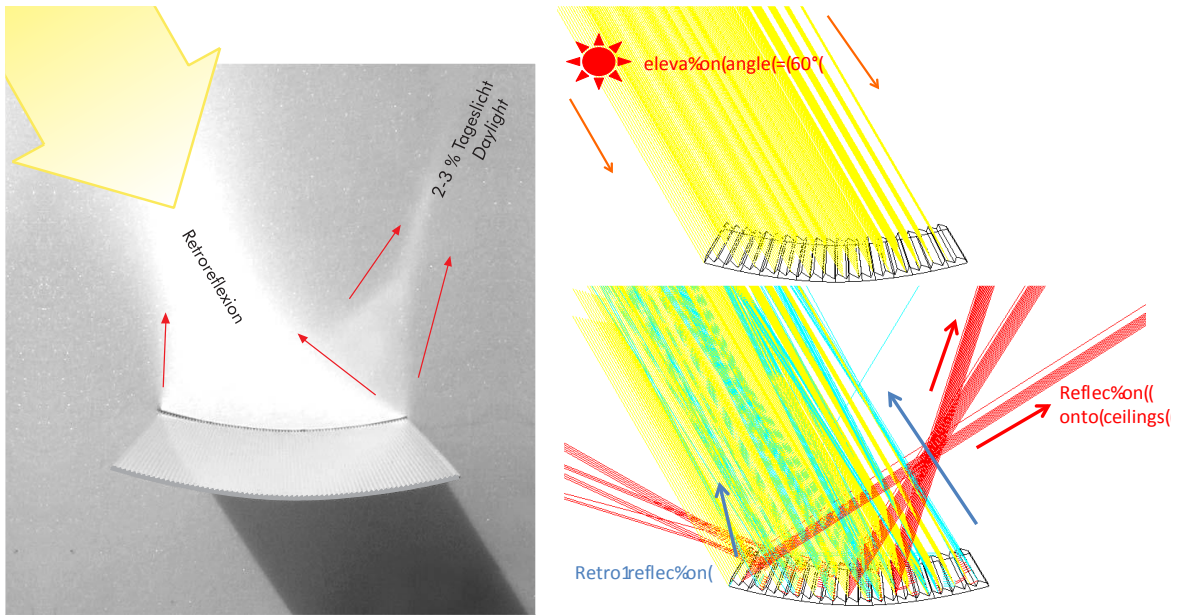
Figure 40: Left: Optics of the daylight system RETROFlex model 1. Right: Visualization of simulated light transmission in RETROFlex model 1 with microstructured mirror surface with Fresnel optics.
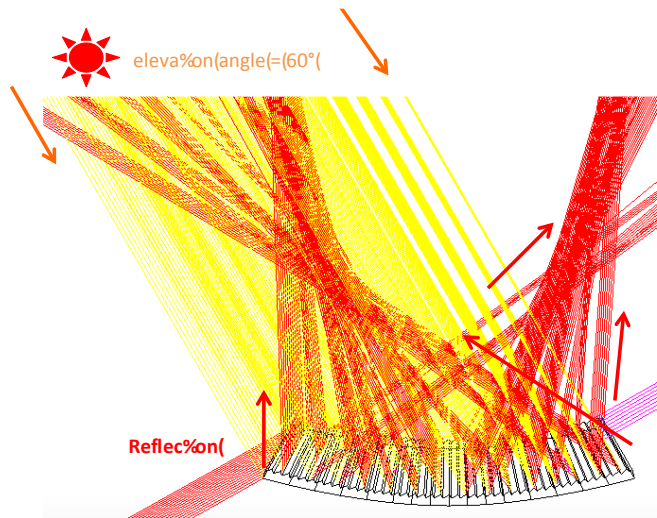
Figure 41: Visualization of simulated light transmission in RETROFlex model 2 (model 2 has a smaller microstructure in comparison to model 1).

3.3 RETROLuxTherm

RETROLuxTherm louvers are produced as readymade insets for installation between the panes of double or triple insulation glass units. The thickness of the glazing and their functional layers are dimensioned according to structural calculations and building physics. These aluminium louvers have two sections: a V-shaped retro-reflective area for protection from the overheating summer sun, and a second section that functions as a light shelf to improve the interior daylighting.

RETROLuxTherm O louvers are installed in the upper part of a window. The light shelves in these louvers redirect the daylight inside, illuminating the depths of large interiors. RETROLuxTherm U louvers redirect the daylight onto the ceiling for glare-free illumination of the workplace. Figure 9 shows the light redirection in RETROLuxTherm O and RETROLuxTherm U louvers. The louvers are semi-spectral and highly reflective on their upper side. The lower side may have either a white or a high-tech glossy aluminium surface. With a white lower side, the facade may be used as a media screen, with projections beamed from street level. RETROLuxTherm U louvers also function as Venetian blinds.

Furthermore, lab experiments have been conducted to study the energy performance of this daylighting system. We compare our simulation results with the lab results. We have run the simulation for various sun

angles. For example, Figure 10 visualizes simulated light reflection in the system when the sun elevation angle is 45 degrees and azimuth angle is 30 degrees. Table 1 shows the comparison between lab and simulation results. We found that our simulation results are in general close to the lab results. However, there are still differences of 2% -- 8%.

Figure 42: Left: Illustration of RETROLuxTherm O and U. Right: Visualization of simulated light transmission in 3D-RayTracer.

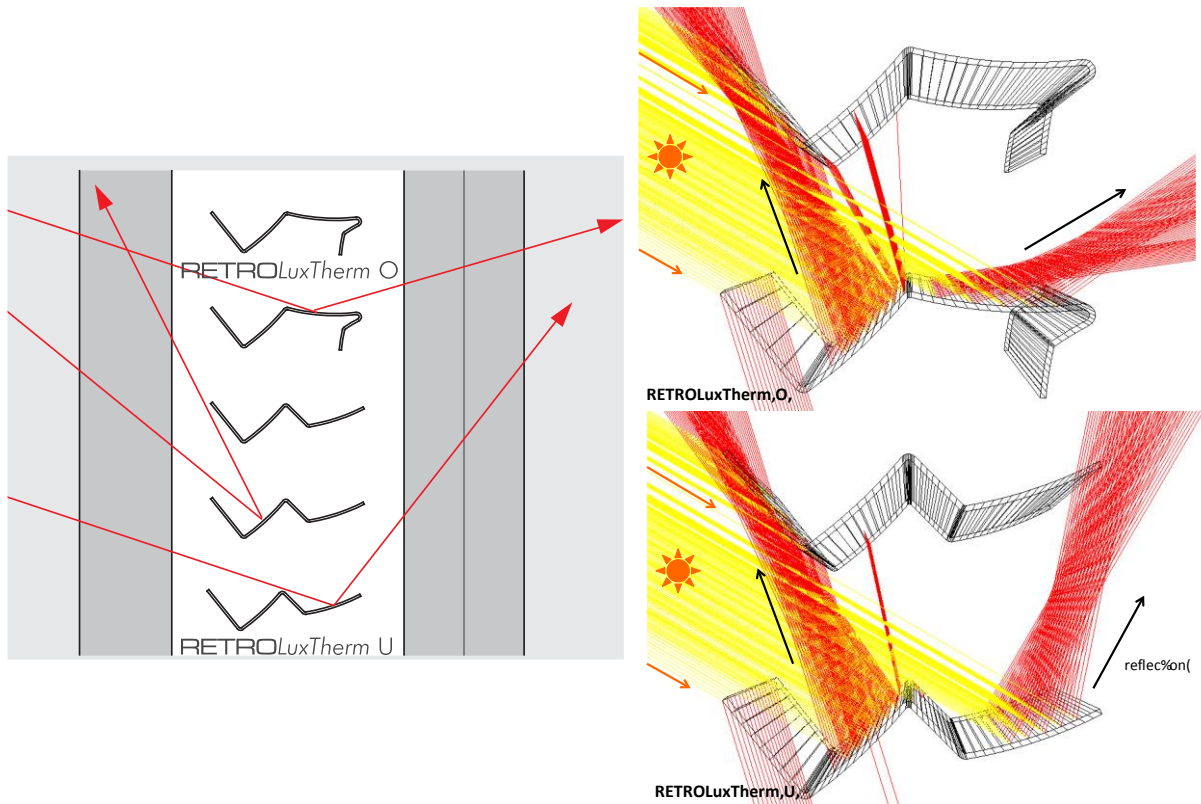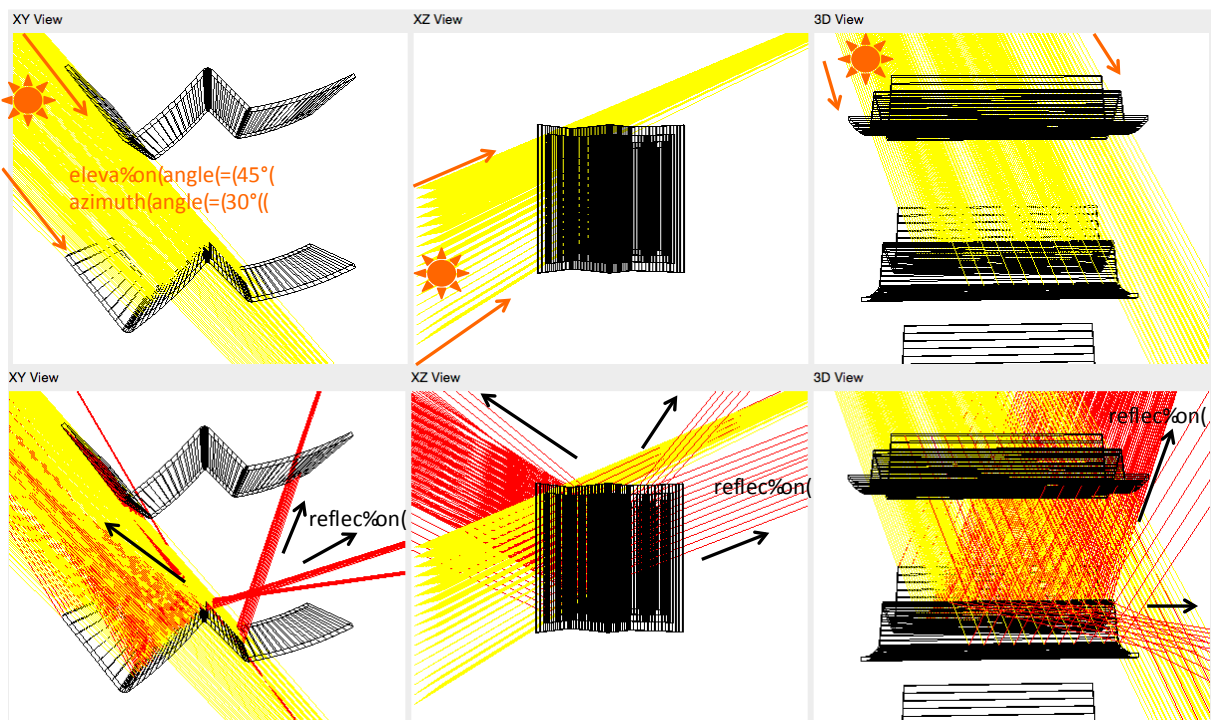*Figure 43: Visualization of simulated light reflection in RETROLuxTherm U*

632

Table 42: Comparison of g-values computed based on simulation and lab measurements (RETROLux U with SSV sun protection glass)

Azimuth	Elevation	g-value (based on simulation)	g-value (based on lab measurement)
0	15	0.30	0.28
0	30	0.28	0.20
30	45	0.20	0.12
30	60	0.15	0.07
45	60	0.12	0.06

4   DISCUSSION

In the following, we discuss energy saving with daylight systems. We also describe our plans for further development of the 3D-RayTracer.

4.1 Energy Saving

There are more and more distinctive heating and especially cooling periods in the European climate. The goal of an intelligent daylight technology should be to achieve solar energy gains in winter and to achieve a passive cooling, especially in summer. These two conflictive goals are achieved by the RETRO-technology we have presented in Section 3 through utilization of the sun's changing angles of incidence.

For instance, Figure 11 illustrates both summer and winter performance of a daylight redirecting system. In summer, sun angles are higher. The low g-values with respect to high sun angles help passive cooling of rooms. This in turn reduces the cooling cost substantially. In winter, sun angles are lower. The corresponding higher g-values help solar gain into rooms. Additionally, redirected sunlight illuminates rooms without the glare of the sun. The cost of artificial lightings can be reduced substantially.

The g-values calculated by 3D-RayTracer provides a good basis to further study and compare the impact of different daylighting systems on energy savings, while other factors can be still taken into account, such as locations and requirements on visual effects. In the next step, we plan to enable comparative studies of energy savings for rooms and buildings, not only at the facade level. The software system should be able to simulate the total energy consumption for heating, cooling, lighting for facades and buildings over a year. The software should also be able to simulate the energy consumption, to provide forecasts for users, to predict the CO_2 reduction, and to provide the basis for accurate simulation. The goal is to obtain energy certification by official building certification programs, such as German Sustainable Building Council (DGNB, 2015) and the U.S. Green Building Council (LEED, 2015).
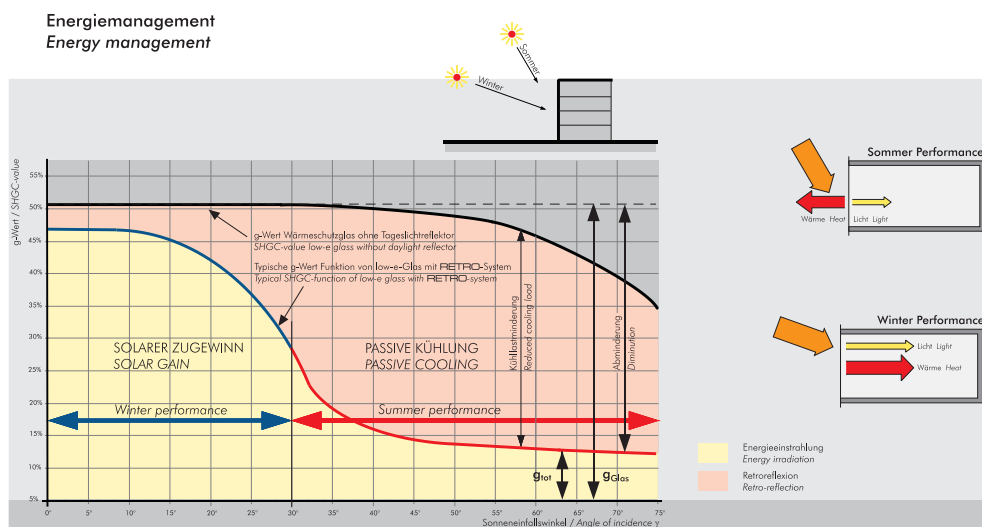

Figure 44: Illustration of energy management in summer and in winter

4.2 Further Software Development

Besides energy management, to better support decision-making and evaluation of sun protection systems, with reference to location and time, the next step of our development is to integrate the functionalities of location and time selection. Furthermore, in order to improve the simulation precision, more parametric studies must be conducted to improve our selection of parameters. The computation of energy consumption and CO_2 emission should also be included in the simulation.

In the next step of development, we will also focus on improving the software usability. A goal of our software is to support better understanding and decision making for users, which include architects, building physicists, glass manufacturers etc. In order to support the different user groups, the presentation of simulation results needs to be tailored towards their needs. The complexity of the simulation also brings another challenge: how to avoid information overload? We need to know what kind of information is most interesting to a user group and present it accordingly.

5   CONCLUSION

A new software system for simulating light and energy transmittance in complex facades has been presented. It consists of two main parts:

- Visualization of light transmission and reflection in daylighting systems. Unlike many existing simulation software that often miss an easy-to-use user interface, 3D-RayTracer facilitates interactive 3D visualization, so that users can easily understand how different daylighting systems work with respect to different sun angles.
- Calculation of angle-dependent light distribution and g-values. They are important factors for designers to compare different glass and louver systems with reference to buildings' location, orientation and other optical requirements (e.g. media facades).

The development of 3D-RayTracer is still in progress. Through the presented simulation results, we see the benefits of 3D-RayTracer in helping qualitative assessment of shading devices and daylight systems. We have identified features we are planning to realize in the future. We hope to improve the simulation precision and also provide good user experience to support energy management.

6   REFERENCES

ANDERSEN, M., Rubin, M., Powles, R., & Scartezzini, J. L., 2005. Bi-directional transmission properties of venetian blinds: experimental assessment compared to ray-tracing calculations. Solar Energy, 78(2), Elsevier, pp. 187-198.

CLARKE, J., 2001. Energy Simulation in Building Design (2nd ed.), Routledge, Taylor and Francis Group

DGNB, 2015, German Sustainable Building Council, http://www.dgnb.de/en/council/dgnb/

KUHN, T.E., Bühler, C. and Platzer, W.J., 2001. Evaluation of overheating protection with sun-shading systems, Solar Energy, 69(6), Elsevier, pp. 59–74

KUHN, T.E., Herkel, S., Frontini, F., Strachan, P., and Kokogiannakis, G., 2011. Solar control: A general method for modelling of solar gains through complex facades in building simulation programs, Energy and Buildings, 43(1), pp. 19-27

KÖSTER, H., 2005. *U.S. Patent No. 6,845,805*. Washington, DC: U.S. Patent and Trademark Office.

LEED, 2015. U.S. Green Building Council, http://www.usgbc.org/leed#certification

REINHART, C.F. and Walkenhorst, O., 2001. Validation of dynamic RADIANCE-based daylight simulations for a test office with external blinds, Energy and Buildings, 33 (7), pp. 683–697

180: The state of the art: superinsulation construction materials under the UK's domestic energy building

Aerogel and vacuum insulation technology applications

MAHMOUD SHATAT*, THEO ELMER, DAVID TETLOW, SAFFA RIFFAT

Institute of Sustainable Energy Technology, University of Nottingham, Nottingham, NG7 2RD, UK
*Email: mahmoodshatat@hotmail.com

The concept of building retrofit has become a top priority for many countries and especially in the European Union in order to meet the world Kyoto protocol to reduce carbon dioxide emissions. Consequently, the EU is committed to reduce the energy of heating in buildings and the greenhouse gases by 50% and 80% respectively compared to 1990 levels by 2050. This translates to one house being retrofitted every minute. A viable solution in achieving this target is to increase the amount of insulation in the building stock. Numerous materials have therefore been introduced to the market during recent decades. Until recently aerogel has been used in the space and chemical industry, while VIPs have been used in the refrigeration and cold shipping industry. Their use in the building environment has been limited, and the challenging factor causing this is high cost. However, this can be offset by the high thermal insulation properties that provide a thinner final construction profile. This advantage could create new opportunities for architects and construction engineers to design energy efficient buildings. This paper presents innovative superinsulation materials of very low thermal conductivity, and their application under the UK's building energy codes. The thermal performance and energy saving capacity of aerogel and vacuum insulation panels (VIPs) are covered in addition to the economic, health and safety aspects. Additionally, their application in domestic homes to achieve the UK's Code for Sustainable Homes level four and six ratings is discussed.

Keywords: Climate change, Insulation material, Aerogel, Vacuum insulated panels, thermal conductivity

<div align="center">NOMENCLATURE</div>

q_{tot}	Total heat transfer (W/m^2)	HDD	Heating degree day
q_{cd}	Solid skeleton conduction heat transfer (W/m^2)	C_f	Fuel cost
q_g	Gas conduction heat transfer (W/m^2)	C_{ins}	the cost of insulation material
q_{cv}	Gas convection heat transfer (W/m^2)	$C_{A,exies}$	the annual heating cost with existing U-value
q_r	Radiation heat transfer (W/m^2)	$C_{A,imp}$	the annual heating cost with improved U-value
λ_{tot}	Total thermal transport (W/m.k)	η	the efficiency of the heating system
λ_{cd}	Solid skeleton thermal transport (W/m.k)	U	Average heat loss (W/m2K)
λ_g	Gas conduction thermal transport (W/m.k)	PWF	Discounting factor
λ_{cv}	Gas convection thermal transport (W/m.k)	N	life time
λ_r	Radiation thermal transport (W/m.k)	H_v	Heating value of fuel
C_A	Annual cost	H	Heating system efficiency
K	Thermal conductivity (W/m.K)	VIP	Vacuum insulated panel
R	thermal resistance of material (m^2.K/W)	EPS	Expanded polystyrene
d	layer thickness (m)	CoP	Centre of panel
HDD	Heating degree day	TER	Target emission rate

1. INTRODUCTION

Domestic housing sector represents over 30% of UK energy consumption (DTI, 2010). Targets such as the UKs commitment to an 80% reduction in greenhouse gas (GHG) emissions compared to 1990 levels by 2050 will be challenging, and the domestic sector will play a central role in achieving this (DECC, 2008).

Improved energy efficiency in buildings is paramount to reduce energy consumption in order to achieve a corresponding cut in greenhouse gas (GHG) emissions. Around 57% of energy use in domestic buildings is for space heating (Simmler et al., 2005), therefore residential and domestic insulation has been found to be one of the most cost effective ways of improving the energy efficiency of buildings, thus lowering its associated emissions (McKinsey, 2009). If a reduction in heat loss from the building's interior to its surroundings can be achieved, a corresponding reduction in the energy required to heat the building is achieved. A lower heat requirement means lower energy consumption. Approximately 35% of buildings heat loss results from the walls. Insulation of buildings has become a top priority for the government and decision makers in the UK in order to meet the national 2050 emission targets.

Current UK building regulations (HMG, 2010) state opaque building elements (walls) need to have a U-Value (Total Thermal Transmittance) of 0.3 W/m2.K. PassivHaus – a leading research authority and world standard in zero-carbon building design state a U-Value of 0.1 - 0.15 W/m2.K is required to achieve PassivHaus status (BRE, 2010). This shows the current benchmark of zero-carbon U-Value standards.

An issue associated with trying to improve the thermal insulation of the building envelope is the play-off between improved insulation and total wall thickness. A very low U-value could be achieved with a much thicker multi-layered wall construction; however this approach has three limitations; one, a loss in internal floor area, two, an increased building footprint and three, a more complex building design (Lyons, 2007). Insulation placed internally will result in the occupants having less living space, a particular problem in retrofit scenarios. Insulation applied externally, will result in the housing development taking up more land space for the same internal floor area. In a development of a few hundred houses this could be a large increase in total land area required, resulting in further costs for land and materials.

The challenge is how to design walls to achieve very low U-Values (of less than 0.1) without incurring the penalties of loss in internal floor area, increased building footprint and building complexity. As Fricke and Emmerling (1992) state the use of air as an insulator has reached its limit; a new approach to building insulation is required, aerogels or VIPs or a combination of the two may be a viable solution of addressing this challenge.

The purpose of this state-of-the-art review is to give an up to date summary of the present use of aerogels and VIPs in the building industry, predominately as wall insulation. The main areas covered are; residential thermal performance and energy properties of aerogel and VIPs, economic, health and safety aspects. Case studies focused on the use of aerogel and VIPs to reduce the thermal bridge effect caused by wall ties and the use of aerogel as a wall insulation in domestic homes to achieve the UK's Code for Sustainable Homes level four and six ratings has also been discussed.

1.1   Properties of High Performance Insulators

This section will examine the main thermal transport mechanisms in aerogels and VIPs.

Total heat transfer (q_{tot} – W/m^2) through a conventional insulation material is due to three heat transfer processes;

(i)   Radiation (q_r)
(ii)   Conduction through the solid skeleton (q_{cd})
(iii)   Heat transfer through the gas inside the material – gas conduction (q_g) and gas convection (q_{cv}).

The total heat flow rate can be expressed as in Equation 1 (Baetans et al., 2010).

$q_{tot} (W/m^2) = q_r + q_{cd} + q_g + q_{cv}$ (1)

The **thermal transport** through a material according to the temperature gradient can be quantified by the materials thermal conductivity (Baetans et al., 2010).

Gas heat transfer

$\lambda_{tot} (W/m.k) = \lambda r + \lambda cd + \lambda g + \lambda cv$ (2)

Gas heat transfer
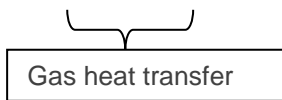
Currently, the major challenge in building insulation materials is that all these parameters should be minimised to achieve a low thermal conductivity.

1.2   The Use of a Partial Vacuum and Micro-Porous Core in Insulating Materials

The most effective way of improving the insulation properties of a material is to reduce its gaseous thermal conductivity. To achieve the most effective reduction in the gaseous thermal conductivity (λg) a perfect vacuum would have to be introduced, in this case λg = 0. To eliminate thermal conductivity due to convection of gas within the insulation material, a perfect vacuum would also have to be present, λcv = 0. There would be a space empty of matter, thus only radiation heat transfer and conduction around the outer boundary enclosure could occur, these thermal transport mechanisms can only be minimised not eliminated.

Baetans et al. (2010) state that the gaseous thermal conductivity of a porous material at lower pressure is determined by (1) the number of gas molecules (2) the number of obstructions for the gas on the way from the hot to cold side.

A reduction in the gaseous thermal conductivity of an insulating material is achieved by (1) creating a reduction in pressure, thus less particles are in a given volume of space thus the mean free path between collisions of particles is increased, and (2) introduce a nano-structured core material so that the mean free path of the gas molecules reaches values in the same order of magnitude as the largest pores in the nano-structured core material. When the pore diameter of the material becomes less than the average free length of the path of gas molecules, the molecules will only collide with the pore surfaces without transferring

energy, this known as The Knudsen Effect (Figure 45). Therefore with the introduction of pressure reduction within a nano-structured core material a reduction of the gas heat transfer element in Equation 2 can be achieved (Figure 46).

Baetans et al. (2010) states that increasing the Knudsen number (Kn) beyond 1 by reducing the pressure (mean free path length increases) in conjunction with decreasing the cell dimensions is a very efficient way of reducing the thermal conductivity of an insulating material, showing the potential for very effective thermal insulation with evacuated systems particularly those with micro-porous structures evident in the use of aerogel and VIPs as high quality insulators (Figure 46).
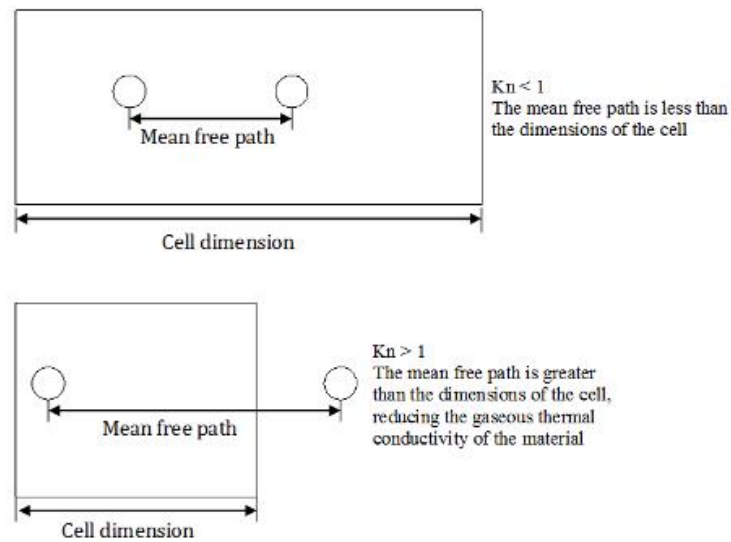
Figure 45: The Knudsen effect on gaseous thermal conductivity

Achieving and maintaining conditions close to a near perfect vacuum are not feasible when trying to commercialise a product for building insulation applications because of increased complexity of production and robustness in operation. Therefore it has been shown that it is advantageous to use a partial vacuum in conjunction with the micro-porous structure to lower the thermal conductivity. The inclusion of a porous material is mainly due to the Knudsen effect and the fact that a perfect vacuum is not feasible. Gaseous conduction and convective heat transfer will occur if no core material is used.

Figure 46 shows how by both reducing the avergae pore size of the insulator core and the gaseous pressure, reduces the thermal conductivity, this is partly due to the Knudsen Effect and is the reason aerogel and VIPs are effective insulators.
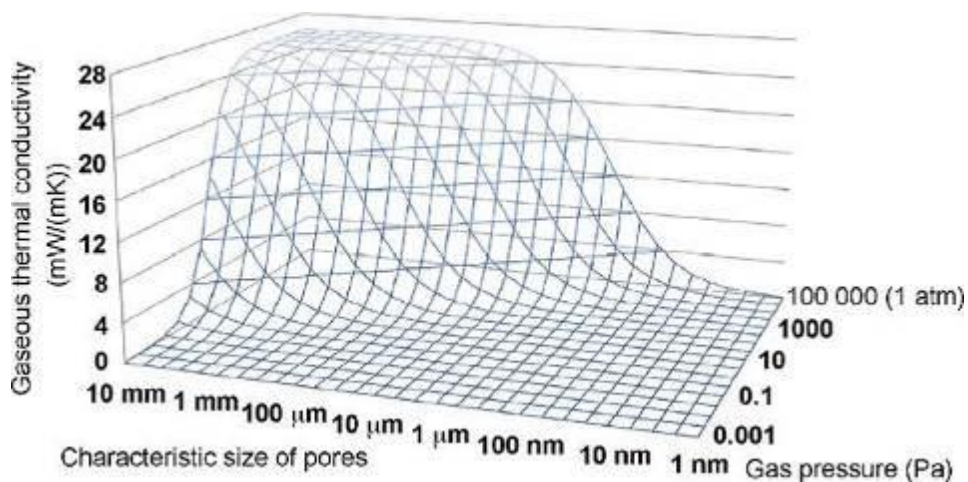
Figure 46: Gaseous thermal conductivity of air as a function of pore size and pressure (Baetans et al. 2010)

2   AEROGELS

Aerogels are a novel high performance thermal and acoustic insulation material. Currently their greatest application is as thermal insulation in the building industry namely wall insulation and as translucent / transparent light panels; this literature will focus on their application as novel insulation materials for opaque elements i.e. walls. Aerogels are also used as absorbents, shock absorbers, nuclear waste storage and in batteries.

Aerogels are dried gels with a very high porosity, high specific surface area and low density. Silica aerogels are synthesised firstly by traditional low-temperature sol-gel chemistry, they are then dried by supercritical drying to remove moisture and replace it with a gas, maintaining the porous texture of the wet stage. The synthesis process is complex and is described in depth by Baetans et al. (2011) but in essence the process comprises three main steps; gel preparation, ageing and drying.

2.1   Properties of Silica Aerogels

Silica aerogels consist of a cross linked structure of SiO_2 (Silicon dioxide) chains with a large number of air filled pores. Silica aerogel pore sizes range from 5 to 70nm, this will equate to 85 – 99.8% of the total volume of the aerogel volume, depending on the purity of the aerogel and the fabrication process (Bommel et al., 1997; Zeng et al., 1994). It is due to the small pore size and high porosity silica aerogels can achieve such impressive thermal and acoustic properties (Section 1.1). The bulk density of silica aerogels can be as low as 3 kg/m3; however in building applications they have densities of around 150kg/m3 (Hunt et al., 1991). Silica aerogels have low mechanical and tensile strength; however they are load bearing with high compression strengths of up to 3 bar. If aerogels come into contact with moisture it can demolish the aerogel structure thus eradicating the high thermal insulation properties of the material (Jensen et al., 2004). Therefore silica aerogels need to be well hydrophobised to prevent this and are normally encapsulated within a vacuum, which in turn helps reduce the thermal conductivity of the material further. For commercial applications such as building wall insulation, silica aerogel is incorporated into a fibre matrix, to produce an aerogel blanket, such as the Spaceloft® product produced by Aspen aerogel. This composition helps remove the issue of the low tensile strength of the aerogel and makes the integration of the aerogel into a buildings structure simpler as the aerogel blanket resembles similar properties to that of conventional roll out rock-wool insulation.

Figure 47: Aspen Aerogels Spaceloft® blanket insulator

Thermal Conductivity

High performance insulation materials of a very low thermal conductivity (W/m.K) are required. The thermal conductivity of the fumed silica skeleton is roughly 0.004 W/m.K. A complete silica aerogel panel can achieve thermal conductivities of 0.008 W/m.K under a pressure of 50mbar or less and 13 W/m.K at atmospheric pressure. The increase in thermal conductivity from the core thermal conductivity to the quoted value used in the application is due to the envelope material or fibre matrix (Baetens, 2011). Current manufacturers of silica aerogel for building wall insulation such as Aspen aerogel with their Spaceloft® product quote thermal conductivities of 13.5 W/m.K in use. This is roughly 2.5 times lower than rockwool insulation, which has a thermal conductivity of 0.034 W/m.K. The thermal conductivity of silica aerogel is

largely unaffected up to temperatures of 200°C; however as stated previously water inclusion degrades the thermal conductivity dramatically. The low thermal conductivity can be explained by the Knudsen effect discussed in the previous section.

Due to this literature review focussing on the application of aerogels for opaque thermal insulation applications, the acoustic and optical properties will not be discussed, for a complete review see Baetans et al. (2011). However silica aerogels have properties that make them of particular interest for highly insulated light panels (translucent elements) or acoustic barriers.

Economic benefits of silica aerogel as a building wall insulator

The main advantages associated with the use of silica aerogel as an insulator in building applications is its extremely low thermal conductivity (0.014 W/m.K) coupled with its minimal thickness (10-20mm), this means an entire building element can achieve a minimal U-Value with a low total wall thicknesses. For a conventional insulation material such as rock wool to provide an equivalent level of insulation it would need to be roughly 2.5 times thicker than the aerogel, this poses the issue of internal or external loss of floor area. Advantages of aerogels in the form of a flexible blanket such as the Spaceloft® product over other new novel insulating materials such as vacuum insulation panels is their degree of robustness, workability, capacity to be cut and fitted on site and ease of installation. This is illustrated in both Case Study One and Two in Section 2.4. Also aerogel, particularly when incorporated into a blanket like design does not suffer the same issues of thermal bridging such as a VIP, this is because the aerogel insulator is made up of a single homogenous material, thus heat flux through the material is continuous. Also because of its flexibility in its application it means it can be added to many parts of a building design, thus potentially minimising thermal bridge effect (Section 2.4.2). Another advantage associated with aerogel is the degree of commercialisation it has achieved. Aerogel is not a material that is still based in the lab; it has made it out and penetrated the insulation market; between 2003 and 2008 the global market for aerogels tripled to 83 Million US$, and is expected to reach 646 Million US$ by 2013 (Cagliardi, 2009). This rapid expansion of the aerogel market illustrates the definite benefit of using aerogel. It can be expected with continued research and development within the aerogel industry the costs of the material can be reduced further.

There are limitations associated with the use of silica aerogels, most significant is cost. Aerogel manufacturers now place much of the emphasis of R+D into the reduction of the cost of aerogels now that technologically the material works effectively as a building insulation material. Aspen Aerogel's Spaceloft® costs around £21/m2, compared to rock wool which costs roughly £5/m2 (Cavity Slab Insulation, Wickes) this large difference in cost represents a significant barrier to the full market penetration of aerogels as building insulators. Until aerogels become cost competitive with conventional building insulation materials the building industry will not realise a full switch over to the use of aerogel (or any other novel insulation materials), even considering the cost and energy savings such materials can help achieve. The high costs are mainly due to the production and manufacturing process, in particular the energy costs associated with the supercritical drying of the gel. Aspen aerogels had a breakthrough in speeding up the solvent extraction process, thus cutting costs, now they are a worldwide leader in the production of aerogel. However further cost reductions are still required in order to produce effective market penetration. These cost savings may be achievable through improved/more efficient production and manufacturing techniques or the use of other materials not silica, these may include carbon or alumina; however this would depend on these materials suitability to thermal insulation applications.

2.2   Health and Safety

Issues such as health, safety and fire protection need addressing when investigating the use of novel insulation materials. The handling of aerogel insulation sheets can create a lot of fine dust; this can cause irritation in the throat and chest. The International agency for Research on Cancer (IARC) classifies synthetic amorphous silica as not being carcinogenic to humans. Studies into the effect of long term exposure to synthetic silica show no evidence of it causing silicosis; test on animals show that amorphous silica particles can be completely removed from the lungs. Aerogels have a treated (CH3) surface for hydrophisation to remove moisture in order to prevent the degradation of the aerogel structure. If this hydrophobe comes into contact with skin or eyes it can cause severe drying and irritation. Therefore aerogels should be treated with caution and correct protective equipment should be worn; gloves, mask, goggles and overcoat, in order to reduce the risk of it coming into contact with bare skin. Aerogels can be considered safe as insulation materials once installed, especially if prolonged, unprotected contact with them is avoided. Issues such as skin irritation and respiratory problems caused by the handling of aerogels

can be addressed by wearing correct protective equipment when handling the material or the development of a way of encasing the aerogel in something to protect the user from direct contact (Merget, 2004).

Silica aerogels such as Aspen Aerogel's Spaceloft® consists of SiO_2 with a CH_3 hydrophobe; these materials are considered non-flammable and non-reactive, thus suitable for domestic home application.

The MSDS that accompanies the Aspen Aerogel's Spaceloft® material states that it is not classified as a dangerous material, mechanical irritation and drying may be caused if it comes into contact with skin and eyes. In the event of fire, normal fire extinguishing media suitable for the surrounding environment may be used on the aerogel, avoiding the inhalation of the smoke and gases produced.

2.3   Silica aerogel insulation: Building applications

A leading manufacturer of aerogel insulation materials for commercial applications is Aspen Aerogel, Inc. with their Spaceloft® insulator (Figure 47). This flexible aerogel blanket is available in either 5mm or 10mm thicknesses. Blankets can be placed together to produce a module of a desired thickness (or thermal resistance). Aspen Aerogels quote a thermal conductivity of 15 mW/m.K for the product, this equates to a 2.5 times reduction compared to traditional insulators. Because the Spaceloft® product is a textile like blanket it is flexible in its application, reasonably robust and can be cut onsite. Aerogel can be used as both the main insulation element in a wall, replacing conventional insulators such as glass wool or retrofitted internally. Aerogel can also be used as a way of reducing thermal bridges created by wall ties. However as discussed later in the advantages and disadvantages of the use of aerogel insulation, cost, at £21/m2 is nearly ten times more expensive than conventional insulators, however where space is an issue it is a very viable insulation option.

Two case studies using Aspen Aerogel's Spaceloft® will be presented to show real application of aerogel products and the benefits they can provide.

Case One: Aerogel insulation fitted on the internal skin of a housing apartment (UK)

The aim of the project was to, in accordance with UK government's policy, upgrade insulation in public housing apartments. The insulation was to improve the U-Value of the entire wall, creating energy savings (AA, 2011a). Due to the project being a retrofit, the insulation material needed to be of minimal thickness in order to lessen the loss of internal floor area.

Two layers of 10mm Spaceloft® aerogel insulation were placed together and fastened to a building facing board; these were then screwed directly into the internal skin of the building as shown in Figure 48. This process was 50% faster than the installation of conventional insulation material as no framing was needed, the panels were easily installed around windows and other fixtures. The module had a total thickness of 30mm; three times thinner than the closest cost-competiveness option and cost effectively the aerogel insulation met all energy targets set.

Figure 48: Spaceloft® aerogel used for building wall insulation (AA, 2011a)

With the installation of the aerogel the U-Value of the apartment wall fell from 0.63 W/m2.K to 0.35W/m2.K, a 44% reduction in thermal transmittance. This equated to a reduction of 900 kWh/year energy use and 400kg/year in carbon abatement (AA, 2011).

2.4   Aerogel Summary

This short review has shown the ability of aerogels to provide incredibly high insulation values (Code level 4 and 6) at minimal wall thicknesses. There are many advantages and disadvantages of using aerogels. Current products such as Aspen Aerogels Spaceloft insulation blanket are flexible in their application to buildings, however at nearly £21/m2, they are not currently cost competitive with conventional insulators such as rockwool, thus there integration and uptake within the building industry to date has been for cases of special interest where high insulation values are required at minimal thickness. Thus for aerogel insulation to make the large contribution it is capable of improving the thermal efficiency of buildings, it first needs to become cost competitive.
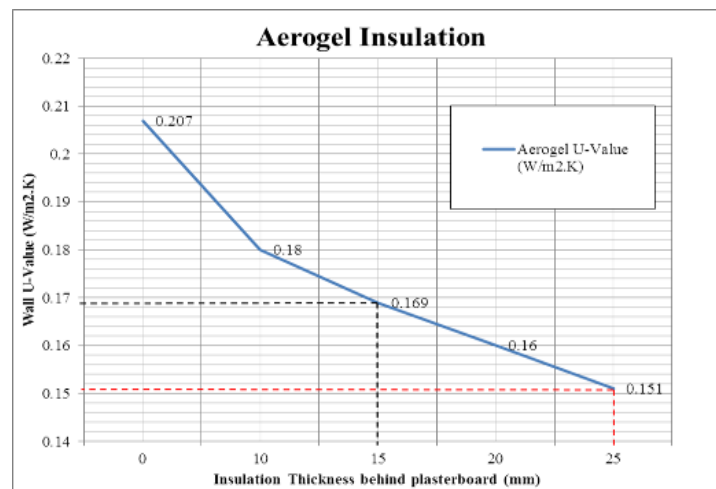

Figure 49: Aerogel providing Code Level 4 and 6 U-Values (BRE, 2010and CLG, 2006)

To conclude thus far; aerogel as a wall insulation material is a viable option to achieve Code Level 4 status within the Energy and CO2 category; at nominal increases in total wall thicknesses compared to conventional house walls. However when used to try and achieve Code Level 6 standards the total wall thickness exceeds the 300mm mark, and thus is not considered as a viable option due to the penalties created by increasing wall thickness. However what could be introduced is a complete improvement to the whole wall, in this case Level 6 status may be achievable at thicknesses less than 300mm with the use of aerogel.

3   VACUUM INSULATED PANELS (VIPS)

Vacuum Insulation Panels consist of an evacuated foil-encapsulated envelope with an open micro-porous interior, operating as high performance thermal insulating materials. By using a vacuum, conductive and convective heat transfer is minimised; but not eliminated due to the VIP not being a perfect vacuum. The internal core helps increase the Knudsen number above 1, thus reducing the gaseous thermal conductivity described in Section 1.1. However the internal core structure of the panel and the envelope as shown in Figure 50 do provide a path for heat flow and is the subject of much research in how to improve the performance of VIPs (Simmler, 2005; Kwon et al., 2009).

The next two sections will discuss the two main components of VIPs; the core and the envelope.
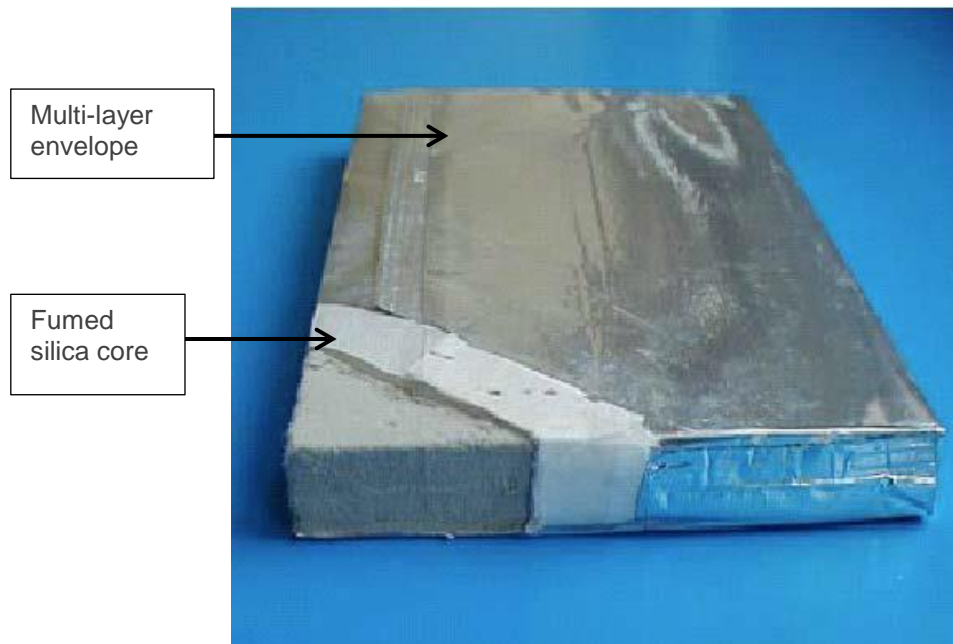
Figure 50: Vacuum Insulation Panel

3.1   Vacuum insulation core

The core in a VIP panels provides a basis for low gaseous thermal conductivity, but also some mechanical strength. Because of this, the core material needs to meet four main requirements.

1) Material pore diameter needs to be very small. Ideal is 10nm or less, this reduces gaseous conductivity to zero at atmospheric pressure
2) Material needs a 100% open cell structure, so that it can be evacuated
3) Material needs to be resistant to compression (due to evacuated core)
4) Material needs to be impermeable to infrared radiation, use of opacifers

Figure 51 illustrates if conventional insulation materials are to be used as the core in VIPs a very high standard of vacuum is required (0.1mbar). In order to achieve this higher level of vacuum, the envelope material must be of a higher quality to maintain the vacuum however this will also have a higher thermal conductivity.

A material that works very well as a core material is fumed silica. Fumed silica consist of a cross linked structure of SiO2 chains with a large number of air filled pores. Fumed silica pore sizes range from 5 to 70nm, this equates to 85–99.8% of the total volume of the aerogel (Bommel et al., 1997; Zeng et al., 1994). Fumed silica has both an intrinsic low pore size and very high porosity, thus the low gaseous thermal conductivity will have a large effect on the overall thermal conductivity of the VIP. Gaseous thermal conductivity will be strongly reduced at ambient pressure due to the Knudsen effect in fumed silica (Baetans et al. 2011) thus a high level of vacuum will not be required to achieve good thermal conductivity of the whole panel (Figure 51). The gaseous thermal conductivity of VIPs is eliminated due to the reduced pressure (~0.1mbar) and small pore size of the core, heat transfer at the centre of the panel is due to the thermal conductivity of the fumed silica core, this is roughly 0.004 W/m.K.

In order to maintain the life of VIPs getters are added to the VIP core to absorb gases and desiccants to absorb water vapour. These additives prevent the increase in internal gas and vapour pressure, both damaging to the longevity of the vacuum and the complete VIP service life. The internal gas and water vapour pressure will not increase until the capacity of the getters and desiccants are reached. Thus they prevent an increase in thermal conductivity of the panel even if there is an inclusion of gas and water vapour into the core.
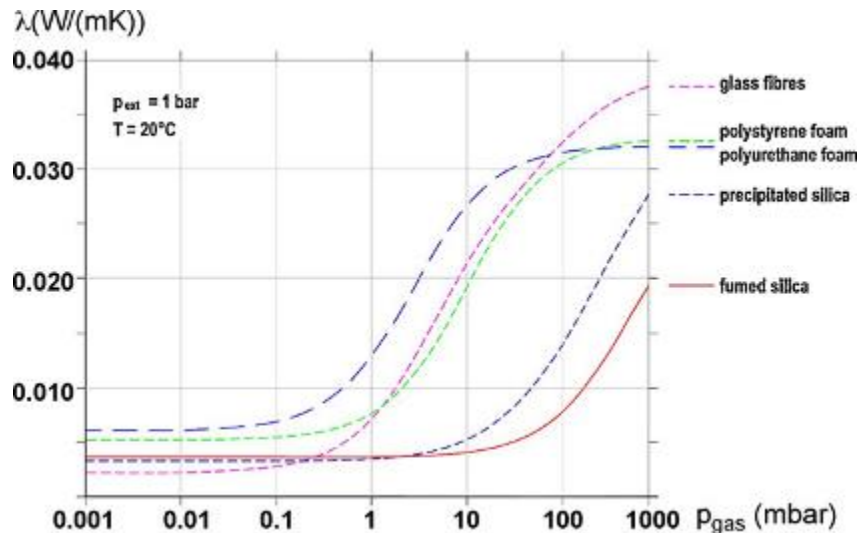
Figure 51: Thermal conductivity of different insulation materials at different pressures (Simmler et al., 2005)

3.2   The VIP envelope

The outer envelope of VIPs is a critical element to the complete material; it helps maintain the vacuum and prevent permeation of gases and water vapour into and within the delicate internal micro-porous structure. If moisture is allowed to enter into the VIP it can destroy the internal structure, thus significantly increasing the thermal conductivity of the panel. Thus the envelope needs to have high gas and water vapour tightness and the lowest thermal conductivity possible. As a general rule the pressure within a VIP should not rise above 100mbar after 30-50 years of operation (Simmler et al., 2005).

Multi-layered aluminium foils 100-200µm thick are commonly used due to their low gas and water vapour permeation. However aluminium has a very high thermal conductivity (237 W/m.K). Therefore the thermal conductivity of the encapsulated micro-porous material within the aluminium foil envelope will have higher heat flux at its edges compared to its centre.

Envelope design is a balancing act between achieving a sufficient seal, and also minimising thermal conductivity at the panels' edges.

Several configurations of envelope design exist (Baetens, 2010), these include

   1) Metal foils, with a central aluminium barrier layer laminated between two PET layers
   2) Metallised films, three layers of aluminium coated PET films with an inner PE sealing
   3) Polymer films, different plastic layers laminated together, more permeable that 1 and 2

Because of the increased thermal conductivity experienced at the edges of the panel an average value of the complete panels thermal conductivity is used λeff.

3.3   The economic and benefits of using VIPs as a building wall insulator

VIPs are still at the research, development and demonstration stage. There are many pros and cons with their current use in the building sector.

The main advantage of using VIPs as wall insulators is there incredibly low thermal conductivity, the effective (panel average) value is around 0.008 W/m.K, this is nearly half that of aerogel. Such a low thermal conductivity value illustrates the vast potential VIPs have in achieving incredibly low U-Values and assisting in reducing energy demand in the building sector. Using Equations 3 and 4, the equivalent thickness of insulation material required to achieve a specific U-Value was calculated, the results are shown in Figure 52, VIPs can achieve a similar level of insulation performance as a conventional wall insulator such as rockwool at less than a quarter of the thickness (Tenpierik et al., 2007). This is of particular interest for retrofit applications where the insulation value of a wall wants to be improved at minimal cost to loss in internal floor area. However, such an advantage is also applicable to new builds; particularly in large scale

multiple building developments. If for example to achieve the same insulation value using a conventional insulator meant that the building footprint was increased by 1m2 compared to the same building utilising VIPs, for a 500 house development, this would equate to a 500m2 increase in land area required for the development. Thus not only an increase in the cost of land would be incurred using conventional insulators, but also more materials and potentially increased building complexity would be incurred. **Error! Reference source not found.** illustrates the space saving benefits of using VIPs over both aerogel and rockwool insulation.

U-Value = 1 / R   *(3)*
R = d / k   *(4)*

Where:

R = thermal resistance of material (m2.K/W)

d = layer thickness (m)
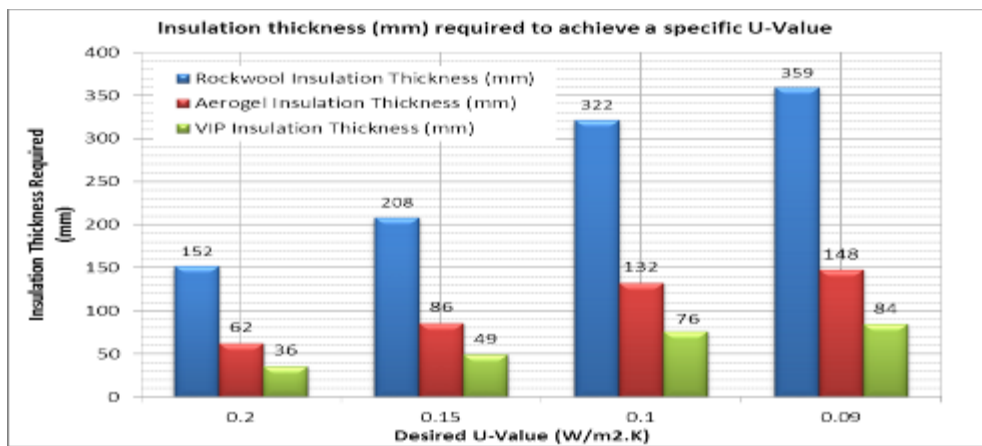
K = material thermal conductivity (W/m.K)

Figure 52: Insulation thicknesses required to meet predetermined U-Value targets

Baetans et al. (2010) state that VIPs are the only insulating material currently on the market that only 40mm is required in order to meet most national building regulations.

Although there are some strong benefits to the use of VIPs, there are many disadvantages however it is hoped with the wider use and application of this novel technology through time some of these will be ameliorated/eliminated. These disadvantages can be categorised into technical and commercial.

3.4   Insulation costs:

Material cost is one of the most important factors governing choice of insulation material and the manufacturing process has a strong influence of material cost. For example organic foams are now well established, and mass production allows their production at low unit cost (Omer, Riffat et al. 2007). However vacuum insulation, still presents manufacturing challenges and this is reflected in product cost. In addition to the cost of the insulation material itself, it is also important to consider the cost of energy saved during the lifetime of the insulation material. This may favour a relatively expensive but efficient insulation material compared with a cheaper, but less thermally insulating material.

Alam, Singh et al. (2011) determined the economic feasibility of VIP applications in buildings by calculating the payback period as:

$$\text{Payback period} = C_{ins}/(C_{A,exies} - C_{A,imp} \qquad (5)$$

The annual costs of heating can ve calculated as:

$C_A = (86400 \times HDD \times C_f \times U \times PWF)/ (H_v \times ń)$ (6)

$PWF = N/ (1+ i)$ (7)

Where:

HDD is the heating degree day;

C_f is the cost of fuel;

C_{ins} is the cost of insulation material

$C_{A,exies}$ is the annual heating cost with existing U-value

$C_{A,imp}$ is the annual heating cost with improved U-value

ń =the efficiency of the heating system

U is the average heat loss (W/m^2.K);

PWF is the discounting factor N/(1+i) where N is the life time in years and i is the inflation rate;

H_v is the heating value of fuel;

H is the efficiency of the heating system

Alam, Singh et al. (2011) found VIPs can achieve a considerably shorter payback period when the economic value of the potential space saving due to thinner VIP is considered, as shown in
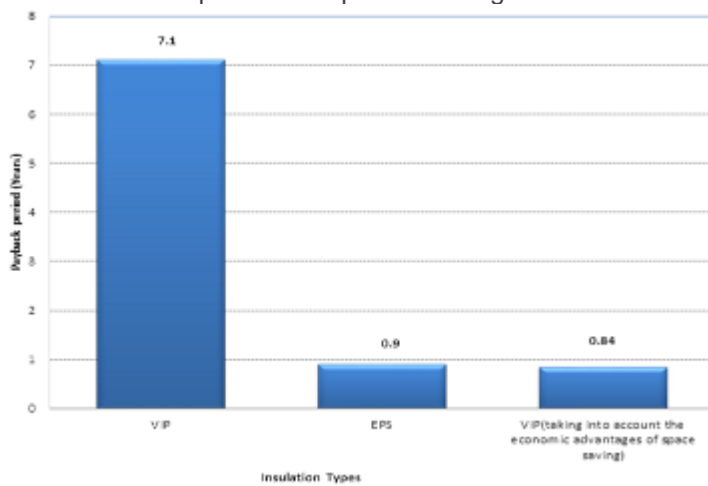
Figure 53. London was taken as the location for the analysis and the assumptions for the calculation of payback period are given in Table 43.

Table 43: Data used to calculate payback period.(Alam, Singh et al. 2011)

Average building U-value	0.24 (W/ m^2 /K)
(VIP) Thickness	60 mm
Cost	£80/ m^2
(EPS) Thickness	256 mm
Cost	£ 10.78/ m^2
Fuel	Natural gas
Emission conversion factor	0.20
HDD	1931 °C day

Cost fuel	£ 0.40/m^3
Efficiency of heating system (ή)	0.9
Heating value per annum (Hv)	39.5×10^6 (Jm^{-3})
Life time service (N)	25
Inflation rate (i)	10%

Payback period of VIPs and expanded polystyrene (EPS) boards based on scenarios from Table 1. The calculations were performed by using a base rent of €506/m2
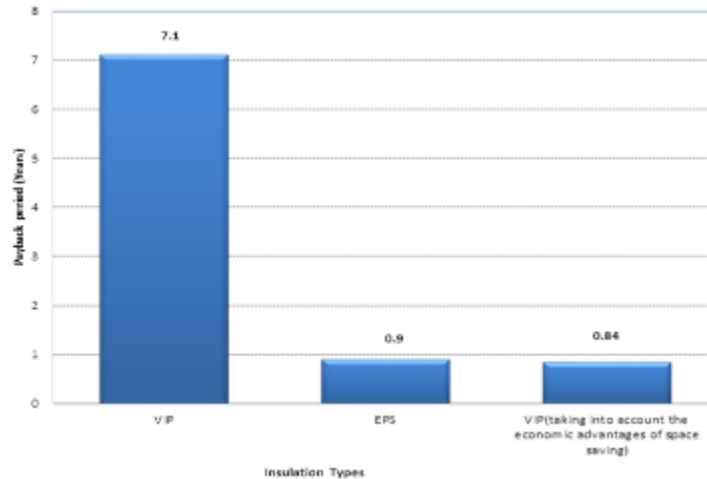
Figure 53: Payback period for VIPs compared to EPS taking into account the economic advantages of space saving (Alam, Singh et al. 2011)…

3.5   VIP building applications

Because of VIPs very low thermal conductivity; roughly 5-10 times better than conventional insulation, there application to a variety of scenarios in the built environment are possible, enabling similar or better insulation values to be achieved at much slimmer profiles, creating space saving advantages. However careful consideration before planning and implementation of VIPs is needed, this is due to the major limitation (discussed in 3.2) of their rigidity in terms of on-sight adjustments (cannot be cut). VIPs have four major applications within the built environment. Case studies will also be used to illustrate VIP applications.

Interior and exterior insulation

VIPs can be placed on the inside i.e. the warm side of the wall (Ghazi, 2005; Bundi, 2003) or VIPs can be installed as exterior insulation placed on the outside of the load bearing structure (Willems et al., 2005b; Winkler et al., 2005; Zwerger et al., 2005; Binz et al., 2005) for both existing (retrofits) and new builds. Because of VIPs superior thermal conductivity to thickness ratio it means loss in internal floor for interior installations is minimised. For exterior installations the increase in the buildings footprint is also minimised. Thus VIPs are of equal interest to both renovations where space saving is critical and new builds where space use wants to be minimised. If an existing wall of 280mm with a U-Value of 0.43 W/m2.K, has a 20mm interior VIP applied behind the plasterboard, the U-Value falls to 0.21 W/m2.K (51% improvement). This equates to only a 0.8m2 loss in internal floor area.

3.6   Code for Sustainable Homes – meeting specific standards

It has already been outlined in Section 2.5 what the Code for Sustainable Homes is; how it is assessed and where improved wall insulation sits within the assessment. This Section will be used just to illustrate how VIPs can help achieve Code Level 4 and 6 standards. Specifically meet particular U-Values at certain wall thicknesses. The similar wall make-up is used as in 2.5.1: 100m brick, 60mm VIP, 100mm brick then 13mm plasterboard (thickness = 275mm). A second layer of VIP is inserted behind the plasterboard at 5mm increments staring from 10mm finishing at 25mm i.e. until total wall thickness = 300mm

Code level 4

As determined in Section 2.5.1 a U-value of 0.168 W/m2.K is required to meet Code Level 4 standards, Figure 3.7 shows that to meet Code Level 4 a VIP layer behind the plasterboard is not required; it is only needed in the cavity. This equates to a total wall thickness of 275mm. In terms of total wall thickness this is 5.5 % improvement over aerogel. It may be more desirable to have insulation such as rockwool in the cavity and VIP on the inside behind the plasterboard because of ease of installation and cost. These values are purely indicative in order to demonstrate the potential of VIP as high performance building insulators.

Code level 6

Code Level 6 refers to a carbon-zero home. As in Section 2.5.1 the PassivHaus standard will be used as the guide; a wall U-Value of 0.15 – 0.1 W/m2.K (or below) is required.
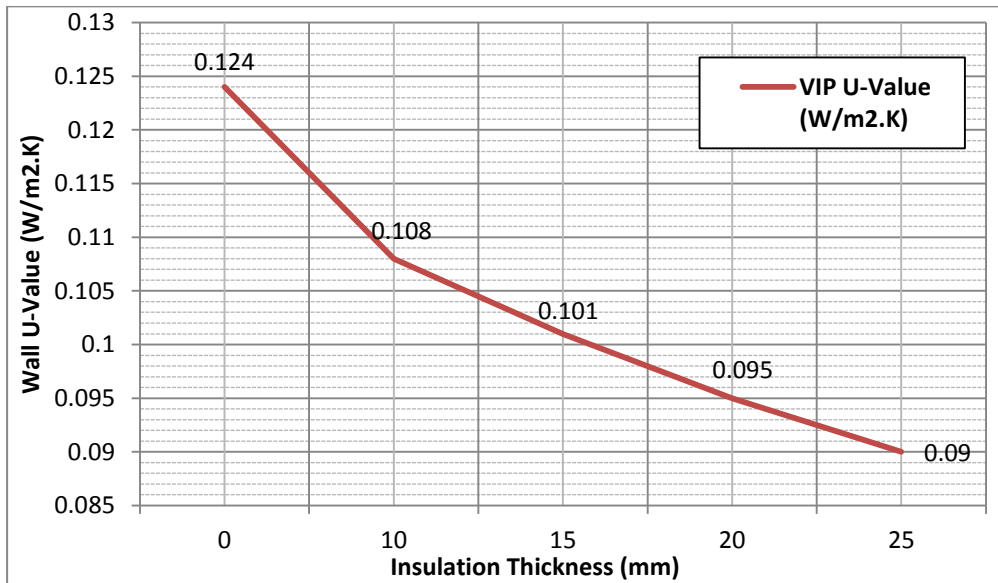
Figure 54 shows that to meet Code Level 6 a VIP layer of 15mm needs to be placed behind the plasterboard to achieve the lower end of the PassivHaus standard, this equates to a total wall thickness of 290mm.
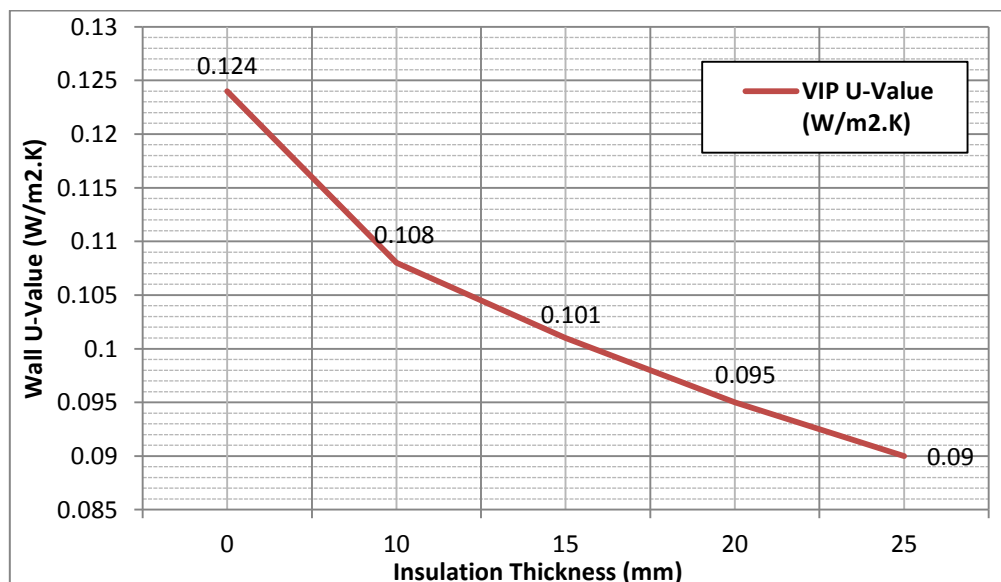
Figure 54: VIPs providing Code Level 4 and 6 U-Values

4   CONCLUSIONS AND OUTLOOK

The large market potential for high performance building insulation materials (aerogel and VIPs) within the EU has been effectively presented with the knowledge of the basic heat transfer mechanisms and the ways

of reducing the thermal conductivity of a material (Simmler et al., 2005). As of 1995 there were 150 million dwellings in the EU, 32% were built pre-1945 and 50% are un-insulated. Although these figures are 15 years old they still illustrate the vast potential and benefit improved insulation can provide in reducing energy demand for space heating and cooling thus reducing CO_2 emissions. Simmler et al., (2005) also state that the energy consumption of the dominating old building stock can be reduced three fold with the installation of high performance insulators such as aerogel or VIPs, this equates to an EU CO_2 reduction of 8%, the agreed amount the EU pledged to in the Kyoto Protocol.

This study has also illustrated the capacity VIPs can provide in achieving incredibly low insulation at minimal wall thicknesses, to an even greater degree than aerogels. VIPs can achieve Code Level 4 and 6 standards at lower total wall thickness than aerogel, illustrating the superior insulating properties. However VIPs do have many costs associated with their current use, more so than aerogels. These are predominantly monetary cost compared to other insulators (even aerogels), their rigidity in application (cutting onsite), and delicate nature (degradation of vacuum through time and vulnerability to perforation).

The large effect of these novel insulating materials can provide is dependent upon their fast, wide spread uptake; this uptake is largely dependent upon the materials applicability to a variety of building scenarios. Currently the use of these novel insulation materials is limited to special cases such as renovations where space saving is critical. Yet aerogel and VIPs can provide a level of insulation beneficial to all building scenarios. However these materials are still in their infancy and the production procedures and distribution networks are not yet optimised. The evident differences in prices between aerogel/VIPs and conventional insulators such as rock wool illustrate this difference. Nevertheless the relatively high material costs of aerogel and VIPs in particular may be partially compensated by the good insulation properties they can provide. It is not proposed aerogel and VIPs will replace conventional insulators, but supplement them in order to try to reduce energy demand in buildings by improving their thermal efficiency. With VIPs and aerogel insulators the wall thickness can be reduced by about 78.7% and 62.5 % respectively compared to the conventional insulation materials such as Rockwool insulation.

The payback period may appear relatively expensive as (Alam, Singh et al. 2011) mentioned, but if we take into account the economic advantages of space saving then the VIPs will be a valuable choice as insulation especially for solid walls.

The rapid R&D in addition to the greater use of these novel insulating materials would significantly reduce the prices and, permitting more effective market penetration, allowing these material to provide the insulating benefits they are capable of.

5   ACKNOWLEDGMENT

6   REFERENCES

HUNT, A.J. Jantzen, C.A.. Cao W, (1991) 'Aerogel – a high performance insulating material at 0.1 bar', in: R.S. Graves, D.C. Wysocki (Eds.), ASTM STP 1116, Insulation Materials: Testing and Application, Proceedings of the Symposia for Committee 16 on Insulation Materials, Gatlinburg, October 10–12, vol. 2, pp. 455–463.

ALAM, M., H. Singh, et al. (2011). "Vacuum Insulation Panels (VIPs) for building construction industry – A review of the contemporary developments and future directions." Applied Energy 88(11): 3592-3602.

Aspen Aerogels (AA) (2011a) Aerogel Interior Wall Insulation Reduces U-Values by 44%, Lowers Energy Use and Carbon Emissions, Northborough USA

Aspen Aerogels (AA) (2011b) Wood Framing Insulated With Aerogel Improves Energy Efficiency by 15%, Northborough USA

BAETENS, R, Jelle, B, Gustavsen, (2011) 'Aerogel insulation for building applications: A state-of-the-art review' Energy and Buildings, vol. 43, 761-769

BAETENS, R, Jelle, B, Thue, JV, Tenpierik, MJ, Grynning, S, Uvslokk, S, Gustavsen, A (2010) 'Vacuum insulation panels for building applications: A review and beyond' Energy and Buildings, vol. 42, pp 147-172

BOMMEL, M.J, Engelsen, C.W, Miltenburg, J.C (1997) 'Thermoporometry study of fumed silica/aerogel composites', Journal of Porous Materials, vol. 4, pp 143–150.

BRE (2010), Passiv Haus Institut, Passiv Haus Primer

BRUNNER, S, Simmler, H (2008) 'In situ performance assessment of vacuum insulation panels in a flat roof construction', Vacuum, vol. 82, pp 700–707.

BUNDI, R, Ghazi, K, Frank, Th (2003) 'Vacuum insulated panels in building applications', in: Int. Conference, CISBAT, EPFL, Lausanne.

CAGLIARDI, M (2009) Aerogels Report AVM052B, BCC Reserach

Communities and Local Government (CLG) (2006) Code for Sustainable Homes, A Step-change in Sustainable Home Building Practice, Communities and Local Government, Crown Copyright

DECC (2008) Climate Change Act 2008. The Climate Change Act 2008 2013, Electronic article.

Department of Trade and Industry (DTI) (2010), Energy Consumption in the United Kingdom http://webarchive.nationalarchives.gov.uk/+/http://www.berr.gov.uk/files/file11250.pdf (viewed 20th November 2011).

FRICKE, J, Emmerling, A (1992) 'Aerogels – preparation, properties, applications', Structure and Bonding, vol.77, pp 37–87

GHAZI, K, Bundi, R, Binder, B (2004) 'Effective thermal conductivity of vacuum insulation panels', Building Research and Information, vol. 32 (4) pp 293–299.

GHAZI, K, Nussbaumer, T, Bundi, R (2005) 'Thermal performance of VIP assemblies in building constructions', in: M. Zimmerman (Ed.), Proceedings of the 7th International Vacuum Insulation Symposium, EMPA, Duebendorf, Switzerland, 28–29 September 2005, pp. 131–138.

HAWKES, A., Staffell, Iain., Brett, Dan., Brandon, Nigel, Fuel cells for micro-combined heat and power generation. Energy & Environmental Science, 2009. 2(7).

HM Government (HMG) (2010) The Building Regulations 2000 (amended), Approved Document L1A Conservation of fuel and power in new dwellings, London, NBS

JENSEN K.I., Schultz J.M.,. Kristiansen F.H (2004) 'Development of windows based on highly insulating aerogel glazings', Journal of Non-Crystalline Solids, vol. 350, pp 351–357.

KWON, J.S, Jang, C.H, Jung, H, Song, T.H (2009) 'Effective thermal conductivity of various filling materials for vacuum insulation panels', International Journal of Heat and Mass Transfer, vol. 52, pp 5525–5532

LYONS, A (2007) Insulation Materials, in: Materials for architects and builders, third ed., Butterworth-Heinemann, Oxford, pp. 308–322.

MERGET, R, Bauer, T, Küpper, H, Philippou, S, Bauer, H, Breitstadt, R, Bruening, T (2002) 'Health hazards due to the inhalation of amorphous silica', Archives of Toxicology, vol. 75, pp 625–634.

McKinsey & Company (2009) Pathways to a Low-Carbon Economy – Version 2 of the Global Greenhouse Gas Abatement Cost Curve.

NUSSBAUMER T, Bundi, R, Tanner, Ch, Muehlebach, H (2005) 'Thermal analysis of a wooden door system with integrated vacuum insulation panels', Energy and Buildings, vol. 37, pp 1107–1113.

OMER, S. A., S. B. Riffat, et al. (2007). "Thermal insulations for hot water cylinders: A review and a conceptual evaluation." Building Services Engineering Research and Technology 28(3): 275-293.

QUENARD, D, Sallee, H (2005) 'From VIP's to building facades: three levels of thermal bridges', in: M. Zimmerman (Ed.), Proceedings of the 7th International Vacuum Insulation Symposium, EMPA, Duebendorf, Switzerland, 28–29 September 2005, pp. 113–120.

SCHWAB, H, Stark, C, Watchel, J, Ebert, H.P, Fricke, J (2005) 'Thermal bridges in vacuum insulated building facades', Journal of Thermal Envelope and Building Science, vol. 28, pp 345–355.

SIMMLER, H, Brunner, S, Heinemann, U, Schwab, H, Binz, A, Moosman, A, Steinke, G, Schonhardt, U, Frenan, F, Ghaz, K, Bundi, R, Cauberg, H, Tenpierik,M, Johannesson, G, Thorsell, T Erb, M, Nussbaumer, B (2005) 'Vacuum Insulation in the Building Sector Systems and Applications, Final Report for the IEA/ECBCS Annex 39 HiPTI-project', High Performance Thermal Insulation for Buildings and Building Systems.

SIMMLER, H, Brunner, S (2005b) Vacuum insulation panels for buildings—basic properties, ageing mechanisms AND service life, Energy and Buildings 37 1122–1131.

WITTKOPF, S.K. (Eds.), Proceedings of the 24th International Conference on Passive and Low Energy Architecture, PLEA/NUS, Singapore, September 22– 24, 2007, pp. 303–310

TENPIERIK, M.J, Cauberg, J.J.M (2007) 'VIP integrated facade designs: the advantage of combining high thermal performance with limited construction thickness', in: B.K. Tan,.

WILLEMS, M.K, Schild, K, Hellinger, G (2005a) 'Numerical investigation on thermal bridge effects in vacuum insulating elements', in: M. Zimmerman (Ed.), Proceedings of the 7th International Vacuum Insulation Symposium, EMPA, Duebendorf, Switzerland, 28–29 September 2005, pp. 145–152.

WILLEMS, W.M, Schild, K (2005b) 'Vacuum insulated constructions in detail', in: Proceedings of the 7th Symposium on Building Physics in the Nordic Countries, IBRI, Reykjavik, June 13–15, 2005, pp. 928–936.

WINKLER, H, Mainka, G.W (2005) 'Development and first experiences of a prefabricated VIP-sandwich element for fast and secure application on building surfaces', in: M. Zimmerman (Ed.), Proceedings of the 7th International Vacuum Insulation Symposium, EMPA, Duebendorf, Switzerland, 28–29 September 2005, pp. 121–130.

ZENG, S.Q., Hunt, A.J., Cao, W, Greif, R (1994) 'Pore Size Distribution and Apparent Thermal Conductivity of Silica Aerogel', Journal of Heat Transfer, vol. 116, pp 756–759.

ZWERGER, M, Klein, H (2005) 'Integration of VIP's into external wall insulation systems', in: M. Zimmerman (Ed.), Proceedings of the 7th International Vacuum Insulation Symposium, EMPA, Duebendorf, Switzerland, 28–29 September 2005, pp. 173–179.

205: An office study of lighting energy-demand savings conducted using a purpose built, intuitive building energy management system interface

Thomas Whiffen[1], Sophie Naylor[2], Dainius Alonderis[3], Mark Gillott[4], Christopher Wood[5], Saffa Riffat[6]

University of Nottingham, Dept. of Architecture and Built Environment, University Park, Nottingham, NG7 2RD, [1]thomas.whiffen@nottingham.ac.uk, [2] laxsjn@nottingham.ac.uk, [3] ezxda3@nottingham.ac.uk, [4]mark.gillott@nottingham.ac.uk, [5] christopher.wood@nottingham.ac.uk, [6] saffa.riffat@nottingham.ac.uk

To date, building energy management systems (BEMS) have been well established in the large scale non-domestic field as an energy saving technology, contributing towards sustainable future cities. They utilise complex control interfaces, with control signals passed through purpose built communication wiring. Estimated end-use energy savings, due to BEMS addition, can reach up to 50%, with associated financial savings for building users. The intelligent control, featured in BEMS, enables buildings to adapt; optimising operation based on weather forecast data. Traditionally they have been complex to install and operate, requiring trained personnel to maintain. Alternatively domestic BEMS are growing in popularity, monitoring and controlling the simple heating functions of a house.

This work outlines the development of a novel BEMS for the small to medium sized non-domestic market. The market features a variety of building types, sizes and uses therefore an adaptable and intuitive system is required to facilitate energy savings within the sector. From initial concept, through a brief review of the market, this work finally presents a viable BEMS to reduce end-use energy in non-domestic buildings. Having showcased the development of an intuitive monitoring GUI, the energy saving results from a single-occupancy office trial found PIR control more beneficial than daylight illuminance threshold control, for the office trial context. Combining the two control methods achieved 67% savings during the test period.

Keywords: Building energy management systems, intelligent building control, low energy buildings, intuitive GUI, office energy savings

1.   INTRODUCTION

Worldwide, in 2011, the built environment accounted for 118 exa-joules, 34% of global energy consumption. 30 exa-joules (equivalent to 717Mtoe) were consumed within service sector buildings, 26% of total built environment consumption (International Energy Agency (IEA), 2014). Assessing the end-use energy demand in such buildings (Figure 55), 33% of end-use energy was consumed through space heating and cooling, with a further 14% used on lighting. The demand for energy is projected to rise (Houssin, 2013), putting extra stress on energy markets and the environment, yet the energy intensity (energy consumption divided by contribution to GDP) has not improved since the late 1980s, suggesting a lack of improvement in energy-efficiency (Wade, 2003). To meet the UK government climate change targets (80% CO_2 reduction by 2050), energy-efficient measures, throughout the service sector built environment, are an essential feature in future cities (Davey, 2012).
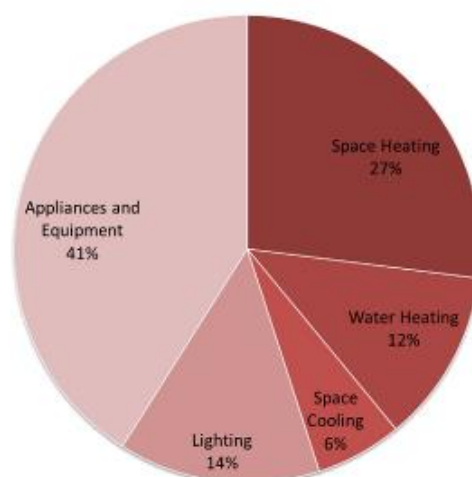

Figure 55 - Service-sector Built Environment End-use Energy Breakdown for 2011 (International Energy Agency (IEA), 2014)

Energy saving strategies, such as Building Energy Management Systems (BEMS) target energy reduction in all energy use areas within the service-sector built environment. BEMS make energy savings possible by removing inefficient impacts of user behaviour on the building energy demand. Studies have shown that the automation of lighting and appliance use – processes often left purely to occupant control - can save energy consumed by up to 21% (Park et al., 2013), 22% (Milenkovic and Amft, 2013), 25% (Garg and Bansal, 2000), 34% (Xu et al., 2011) and 50% (Harle and Hopper, 2008) respectively. The exact savings made depend heavily on the building application and the level of responsiveness to occupant needs.

Since the energy price rise observed in the 1970's, automated control systems to manage energy intense aspects within the built environment have been developed (de Dear and Brager, 2001). Building energy management systems (BEMS) seek to maintain occupant comfort in the controlled space, whilst minimising the energy consumption (Dounis and Manolakis, 2001). Central to each system developed are; the methods for specifying occupant comfort, and the energy-cost function (Figueiredo and Sá da Costa, 2012).

Traditionally the complex design, installation, optimisation and operation of BEMS have resulted in systems for large commercial buildings only. In recent years the domestic market has hosted a wave of 'smart' BEMS that incorporate advances in self-learning technology. To date still, little is focused on the small to medium sized non-domestic (SMSND) market due to the diversity and complexity of buildings in the sector. In addition to the different building usage; tight budgets, rental arrangements, an uneducated work force and smaller energy bills (compared to the large commercial buildings) have all inhibited the research and development of technologies for the market (National Energy Foundation, 2015).

The work reported set out to develop an intuitive interface to an adaptable BEMS. The hardware utilises power-line communication (PLC) to avoid additional wiring. Combining the hardware and software solutions enabled the development of a low-cost, easy-to-use BEMS; suitable for SMSND buildings.

2.   INTERFACE

To date the interface has been developed to operate with two test facilities, the Nottingham HOUSE on University Park and a custom-built desktop rig, referred to herein as "T1A". The developed solution was informed from market research (National Energy Foundation, 2015), expert understanding and multidisciplinary collaboration. The interface features several windows with increasing complexity in each window (Figure 2). The uninformed user can gain snapshot information from the *'home'* window, where responsive energy saving strategies are suggested. The informed user can interrogate the source of excessive energy usage or comfort deviation through *'conditions'* and *'usage'* windows. Further historical analysis and high-level assessment can be conducted through the *'analysis'* and *'portfolio'* windows. Finally, control and action can be taken remotely through the *'settings'* and *'control'* windows (Figure 3).
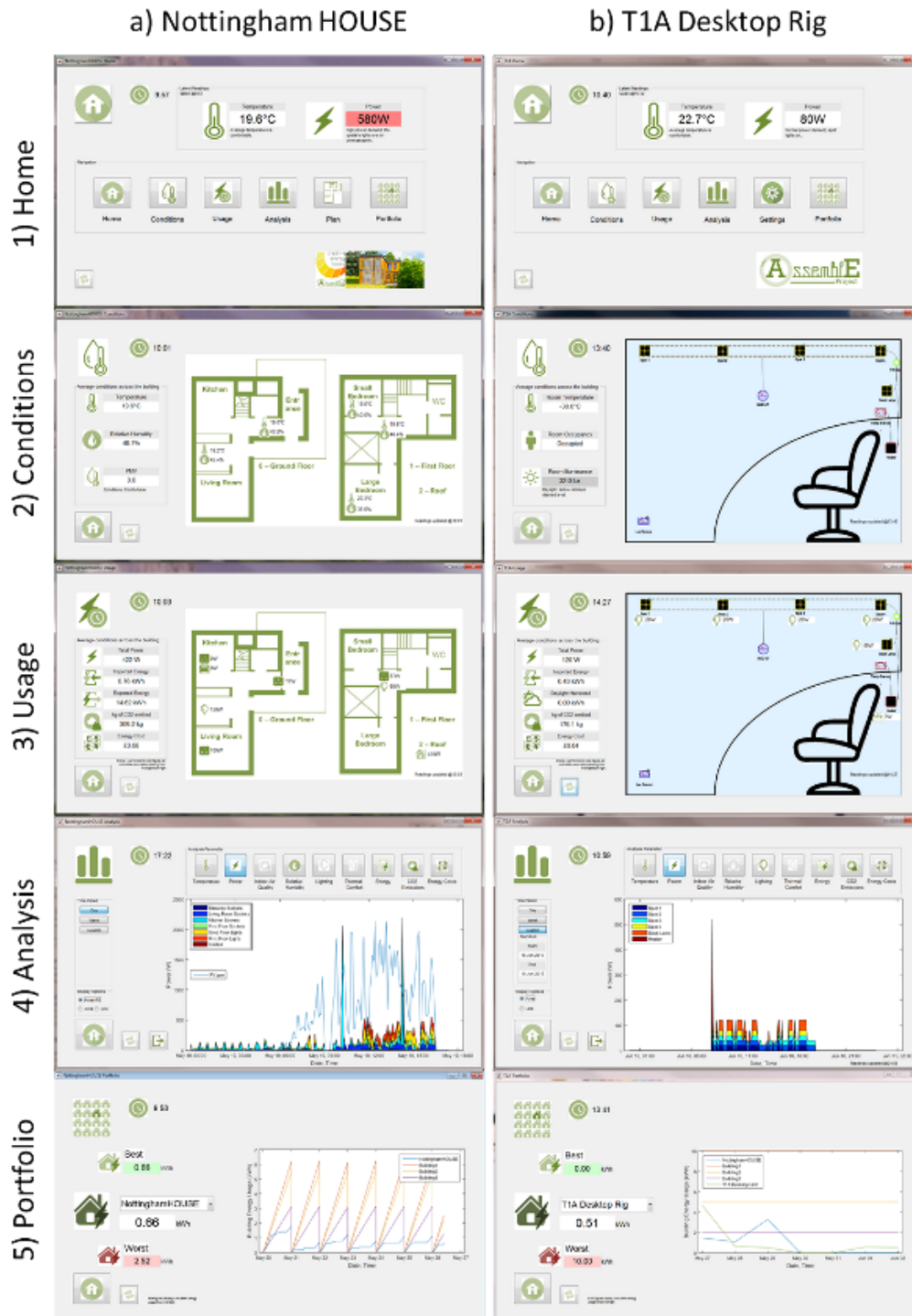
Figure 2 - BEMS Interface Windows: a) Nottingham HOUSE b) T1A Desktop Rig
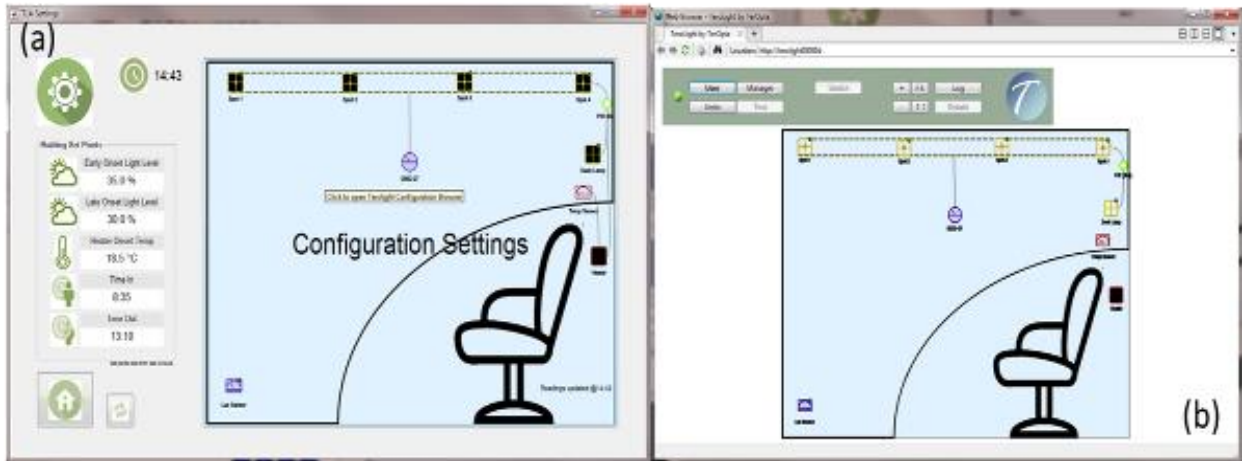
Figure 3 - Interface (a) settings and (b) control windows

3. METHOD

Practically the hardware and software were tested to determine potential energy savings using the system. Office energy demand for lighting was investigated using the desktop rig, in a single-occupancy office scenario. Further, three BEMS strategies were investigated to determine the relative merits of controlling lights using; PIR control, a daylight illuminance threshold (DIT) control and a combined PIR-DIT method. A fourth light was controlled manually to act as the reference case. Figure 56 conveys the electronic configuration set up in the 'control' window.

The 13.5m^2 office had a single outside window facing south-west, accounting for 16.5% of the 7.4m^2 south-western wall. The office was fitted with the T1A BEMS controlling four 20W halogen spot lights, each controlled by manual, PIR or illuminance sensors. The illuminance sensor was placed on the window sill and PIR sensor mounted on the desktop (Figure 57). Since the desk was placed in the north-westerly corner a high DIT of 71% was set to ensure sufficient illuminance was maintained at the work station. A five-minute PIR delay was set for each light. The Cambridge, UK office was occupied intermittently between 8am and 6pm, for three consecutive days in mid-June, by a sole occupant.
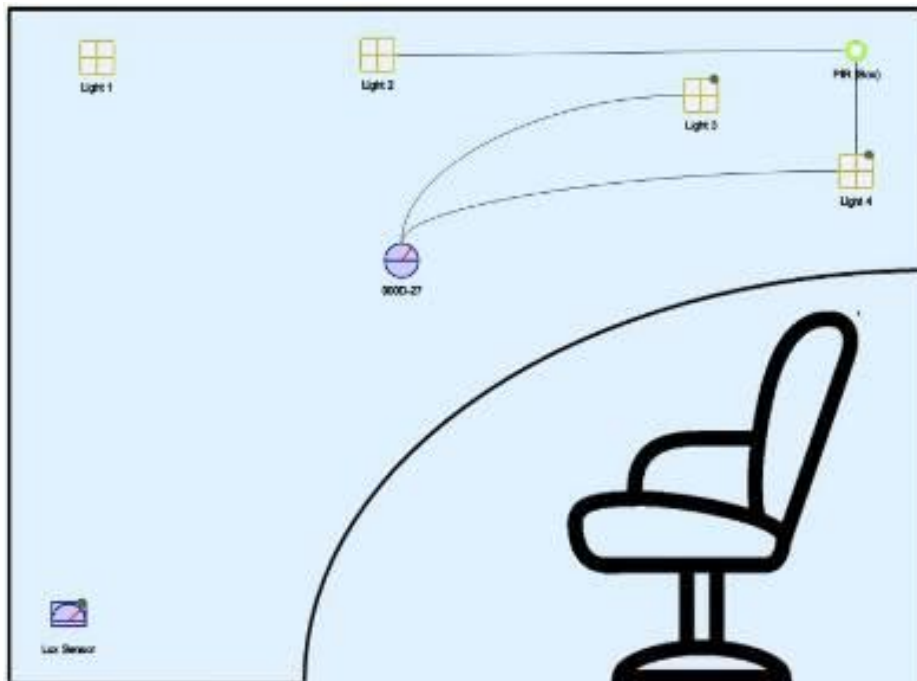
Figure 56 - Software view of the light and sensor configuration

Figure 57 - Office setup: (a) Lux sensor position, (b) desk configuration, (c) T1A hardware

2.29. 3.1 Test Methodology

Following desktop rig set up, as shown in Figure 57, the light and sensors controls were configured using the T1A system as shown in Figure 56; Light 1 – manual on/off control, Light 2 – PIR controlled (5 minute delay), Light 3 – DIT controlled (71% Illuminance level) and, Light 4 – PIR and DIT controlled. Subsequently the interface and data storage process were initiated. Throughout the test the occupant sw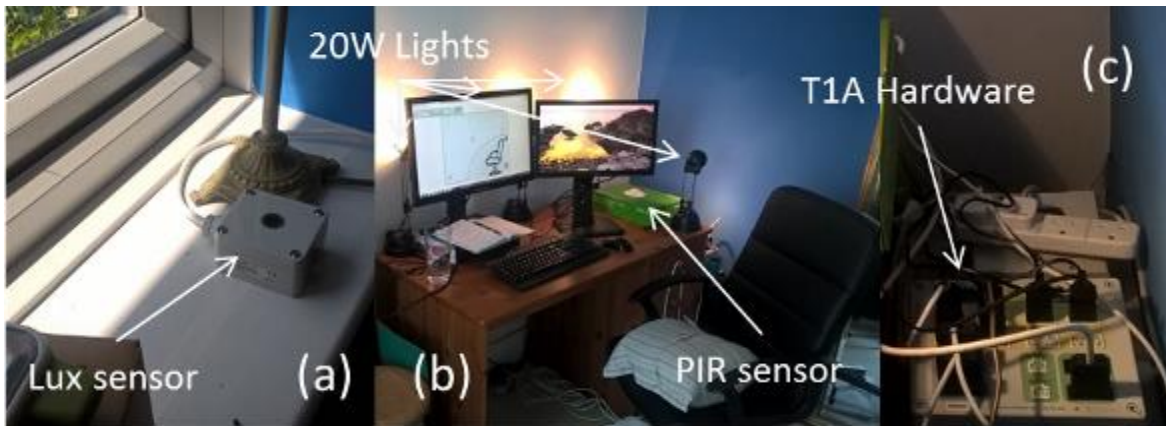itched on Light 1 at 8am until 6pm daily, whilst using the office as usual. After the test period the data was exported and energy analysis conducted.

4. RESULTS AND DISCUSSION

Weather forecast data was gathered prior to the investigation for the occupied period of the day. Further, Table 44 documents the approximate solar PV generation from the office solar array. These figures along with the *Daylight Percentage Reading* line on Figure 58 characterise the solar resource available to the test office during the test period. Late afternoon provided the greatest opportunity for daylight harvesting due to the weather pattern and orientation of the office. Where the blue solid line exceeds the red dashed line (in Figure 58) Light 3 was switched off by the BEMS. Over the test period, through the hours of 8am to 6pm, there was sufficient daylight 29% of the time. The noisy green dotted line in Figure 58 represents the occupancy profile throughout the day. In total, based on PIR measurement, the office was occupied 42% of the available time between 8am and 6pm.

Table 44 - Weather data from Met Office between June 9th and 11th 2015, at Cambridge NIAB

Time of Day	Day 1	Day 2	Day 3
	Conditions, Temperature (°C), Chance of Rain (%)		
7am	10°C, <5%	9°C, 20%	10°C, <5%
10am	10°C, 20%	13°C, 20%	17°C, <5%
1pm	14°C, 20%	15°C, <5%	20°C, <5%
4pm	14°C, 20%	17°C, <5%	21°C, <5%
7pm	13°C, <5%	16°C, <5%	☀ 20°C, <5%
Office PV generation	~13 kWh	14 kWh	26 kWh

The energy usage for each light was reviewed over the test period. Figure 59 represents the breakdown of energy consumption and savings due to PIR or daylight threshold control. The reference light (Light 1) consumed 580Wh, whilst the PIR controlled light (Light 2) saved 55% and the DIT controlled (Light 3) saved 26%. Combined, the BEMS (Light 4) was capable of saving 67% of energy throughout the test.
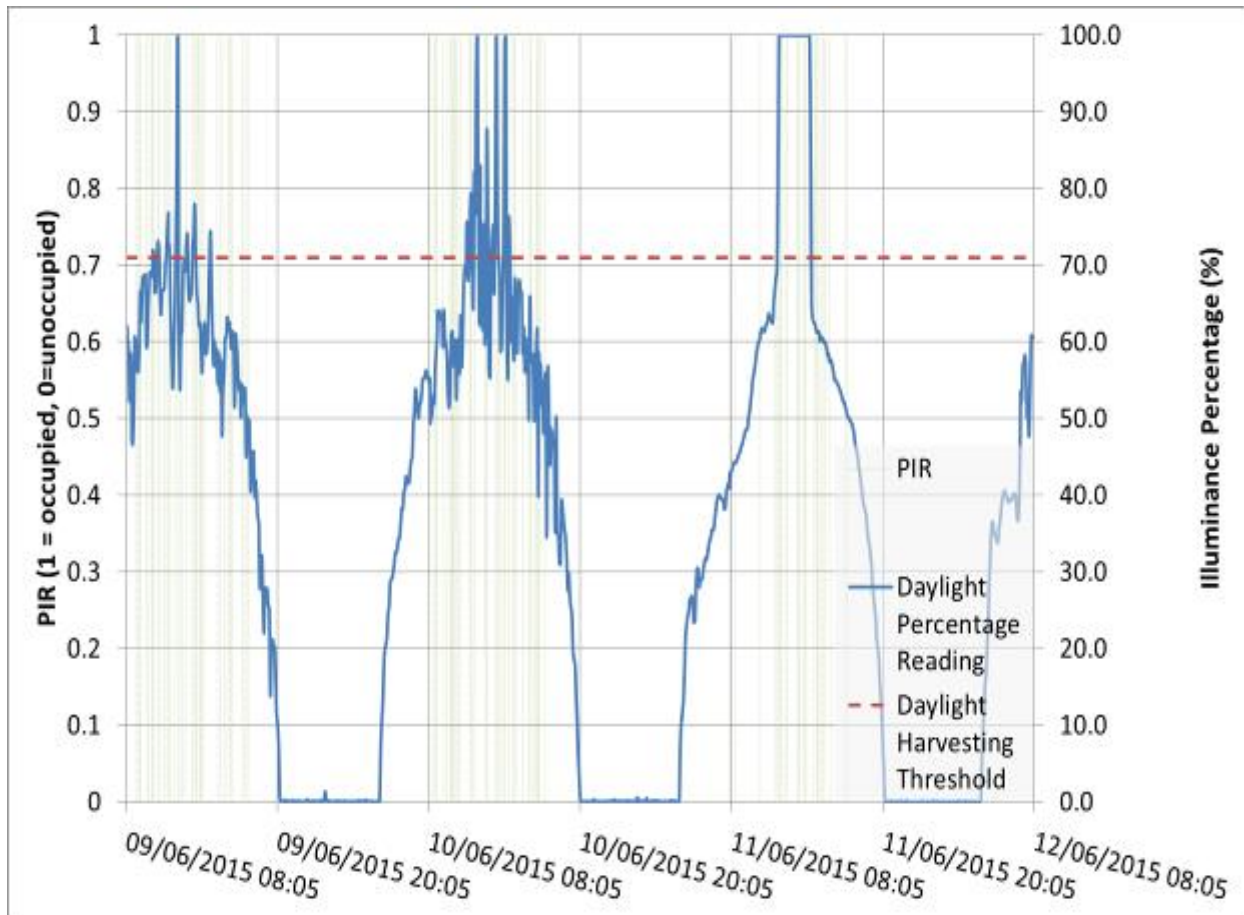
Figure 58 - Occupancy and Illuminance Profiles for the three day test period

	Light 1 - no control	Light 2 - PIR	Light 3 - DIT	Light 4 - PIR&DIT
PIR Savings (kWh)	0.00	0.32	0.00	0.32
Daylight Savings (kWh)	0.00	0.00	0.15	0.07
Usage (kWh)	0.58	0.26	0.43	0.19

Figure 59 - Energy usage and savings for each light over the three day test

5. CONCLUSIONS AND FURTHER WORK

In the sole-occupancy office PIR control offered more than double the savings of the DIT control. Sole-occupancy offices are likely to benefit more greatly from PIR control than multiple occupancy offices due to the greater variation in presence profiles. In addition, the DIT control savings observed benefited from a high-solar resource during the third day. Further study to investigate the comparative benefits of the control methods under higher density office occupation and greater levels of glazing would be of benefit. Further work that investigates occupant satisfaction under differing daylight thresholds would be of interest to optimise the DIT control benefits. Finally, additional work assessing the methods over a longer time-period would be beneficial for developing year-round savings projections.

6. ACKNOWLEDGEMENTS

7. REFERENCES

DAVEY, E. 2012. The Energy Efficiency Strategy: The Energy Efficiency Opportunity in the UK. In: CHANGE, D. O. E. A. C. (ed.).

DE DEAR, R. & Brager, G. S. 2001. The adaptive model of thermal comfort and energy conservation in the built environment. International Journal of Biometeorology, 45, 100-108.

DOUNIS, A. I. & Manolakis, D. E. 2001. Design of a fuzzy system for living space thermal-comfort regulation. Applied Energy, 69, 119-144.

FIGUEIREDO, J. & Sá Da Costa, J. 2012. A SCADA system for energy management in intelligent buildings. Energy and Buildings, 49, 85-98.

GARG, V. & Bansal, N. K. 2000. Smart occupancy sensors to reduce energy consumption. Energy and Buildings, 32, 81-87.

HARLE, R. K. & Hopper, A. The potential for location-aware power management. 2008 2008. 302-311.

HOUSSIN, D. International Energy Agency Webinar. 2013.

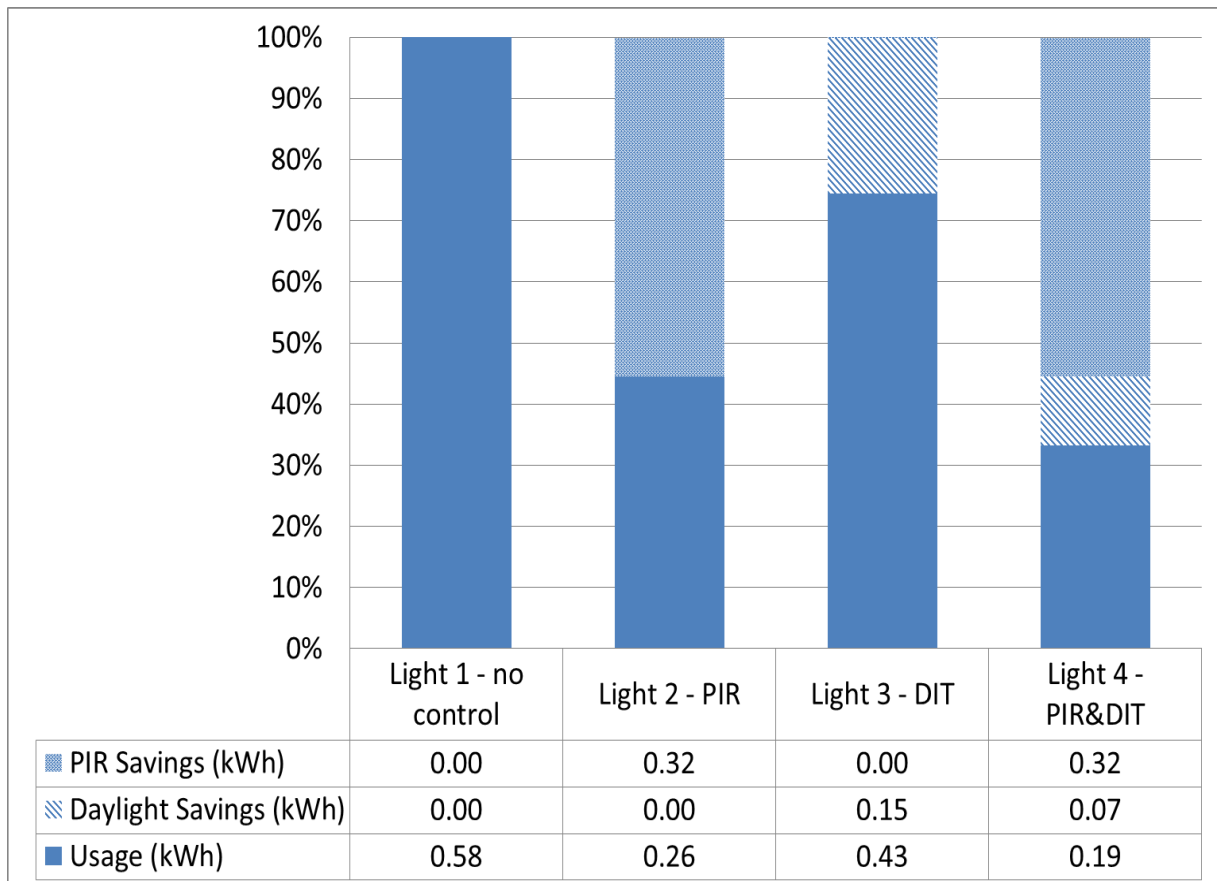INTERNATIONAL ENERGY AGENCY (IEA) 2014. Energy Technology Perspectives.

MILENKOVIC, M. & Amft, O. An opportunistic activity-sensing approach to save energy in office buildings. 2013 2013. 247-258.

NATIONAL ENERGY FOUNDATION 2015. Project ASSEMBLE: Market Review Report.

PARK, S., Choi, M.-I., Kang, B. & Park, S. 2013. Design and Implementation of Smart Energy Management System for Reducing Power Consumption Using ZigBee Wireless Communication Module. Procedia Computer Science, 19, 662-668.

WADE, J., Pett, J., Ramsay, L., 2003. Energy efficiency in offices: Assessing the situation. The Association for the Conservation of Energy.

XU, Y., Stojanovic, N., Stojanovic, L., Anicic, D. & Studer, R. 2011. An approach for more efficient energy consumption based on real-time situational awareness. The Semantic Web: Research and Applications. Springer.

212: Improvements in glazing technologies to reduce building heat losses

Abdulelah ALOTAIBI [1], Saffa B. RIFFAT [2]

1 University of Nottingham, University of Nottingham, Dept. of Built Environment, ezxata@exmail.nottingham.ac.uk
2 University of Nottingham, University of Nottingham, Dept. of Built Environment, saffa.riffat@nottingham.ac.uk

This paper offers a review of the existing and emerging glazing technologies for windows. Windows account for up to 60% of the heat losses in buildings. The commercially available window systems on the market are double glazing, triple glazing, suspended films, vacuum glazing and smart glazing systems. Double glazing window systems can rarely meet the new energy standards while the other systems are expensive and not always reliable. Often, they require use of low-e coatings and inert gases which substantially increase cost of production. Recently, new glazing systems have been explored with the focus on window cavity filling and the novel combinations of materials in multiple cavities. Aerogel and PCM glazing systems represent the first segment of this research. While offering better U-values, such systems still have disadvantages such as material fragility (in case of aerogel), visibility (in case of PCM) and some other relevant parameters. Novel glazing designs such as solar pond and air sandwich also allow increasing thermal performance of the systems, but their applications are still in their infancy. PV systems represent a very promising direction in this regard. They are based on combining the existing proven technologies, and while showing higher U-values than other advanced glazing systems, they generate electricity to at least partially offset energy spending on heating and cooling. Optimisation of PV glazing system parameters is considered one of the major factors that could make them a product of choice in the nearby future.

Keywords: windows, glazing, energy, heat transfer, photovoltaics

1.   INTRODUCTION

Windows perform many useful functions in buildings ranging from natural lighting and outdoor vision to ventilation and an emergency exit in critical situations such as fire. One major drawback of windows, however, is their high relative heat transmittance which attributes to a substantial amount of heat loss. On average, a standard conventional window has the U-value of 2.00 W/m^2K whereas roof, floor and external walls have the average values of 0.16 W/m^2K, 0.25 W/m^2K and 0.30 W/m^2K respectively (Cuce and Riffat, 2015). Consequently, while buildings reportedly consume 40% of all energy in European Union, windows contribute up to 60% of this amount (Jelle et al., 2012). With the uncertainty surrounding global energy prices, European governments are seeking to increase energy efficiency in buildings, and reducing heat loss through windows will play an important role in this. While energy consumption standards for buildings vary at national levels, the standards set by Passivhaus Institute are widely recognised as the key recommendation framework in Europe. According to these standards, in order to be considered efficient, energy consumption for heating and cooling in buildings should not exceed 15 kWh/m^2 on an annual basis (Passivhaus Institute, 2014). Based on this, it is estimated that U-values of windows would have to be around 0.85 $W/m^2 K$ which is much lower than the existing average values of conventional windows (Zero Carbon Hub, 2014).

It is clear that attaining the goals of energy efficiency in buildings is largely dependent on whether it will be possible to reduce heat losses through windows. This can be achieved by application of energy efficient window technologies. The reduction of heat losses through windows should not only lead to lower energy consumption but also provide more comfortable thermal conditions for the buildings' inhabitants. The focus of the paper is on window glazing which due to its application to the largest portion of a window has the most significant impact on its U-value. Application of novel glazing technologies is expected to produce higher thermal insulation, better solar gain control and natural lighting solutions (Jelle et al., 2012; Sadineni et al., 2011). The paper offers a thorough review of the existing and emerging glazing technologies to demonstrate where improvements in reducing heat losses can be achieved. A particular attention among the emerging technologies is given to photovoltaic (PV) glazing that has a comparative advantage over the other glazing types through the ability to generate additional energy. With the potential that PV glazing offers, it is one of the most promising technologies that can become widespread in the nearby future.

2.   EXISTING WINDOW GLAZING TECHNOLOGIES

Window glazing should be considered as a system that consists of glazing materials, glazing layers, cavities between the layers and gas filling the cavities. Commercially available glazing technologies include single, double and triple glazing with various combinations of glass material, cavity gases and window coatings (Carmody, 2012; Cuce and Riffat, 2015; Ghoshal and Neogi, 2014; Jelle et al., 2012). Figure 1 presents some glazing solutions available on the market.
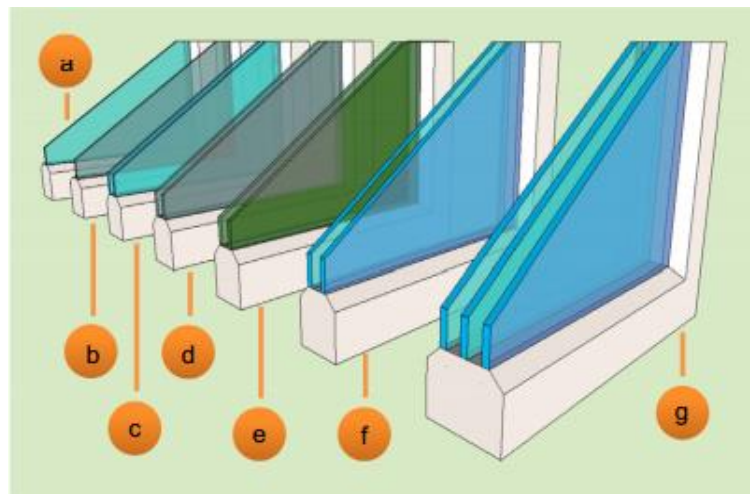

Figure 1. Commercially available glazing technologies: (a) single clear glass, (b) single glazing with gray tint, (c) double clear glass, (d) double glazing with gray tint, (e) double glazing with selective tint, (f) double glazing with low-e and (g) triple glazing with low-e (Cuce and Riffat, 2015, p. 698)

Thermal insulation performance of the different glazing technologies depends on the number of glazing layers, size of a cavity, type of gas used to fill the cavity and presence of a low emissivity coating (low-e) on the glass. It is generally recognised that thermal properties of windows are enhanced with larger number of glazing layers, larger cavity size, filling the cavity with inert gases and applying low-e coating to glass panes (Nicholls, 2004). Existing experimental studies confirm this. Carmody (2012), for example, showed that single pane glazed windows could offer U-values as low as 0.84 W/m^2 K; double pane glazed windows 0.49 W/m^2 K without low-e coating and 0.34 with low-e coating; and triple pane glazed windows with low-e coating could offer as U-values as low as 0.28 W/m^2 K. Ander (2014) experimentally found that application of low-e coating for single pane glazed window improves U-value from 1.09 W/m^2 K to 1.06 W/m^2 K; application of low-e coating for double pane glazed windows improves U-value from 0.48 W/m^2 K to 0.33 W/m^2 K, while replacing air with argon in double pane glazed window further reduces U-value to 0.26 W/m^2 K.

2.1 Double Glazing

Double pane glazing technologies currently represent the largest share of the window market in Europe (Cuce and Riffat, 2015). The production process for such windows is well developed and cost effective due to economies of scale. Schematic representation of a conventional double glazed window unit is shown in Figure 2.
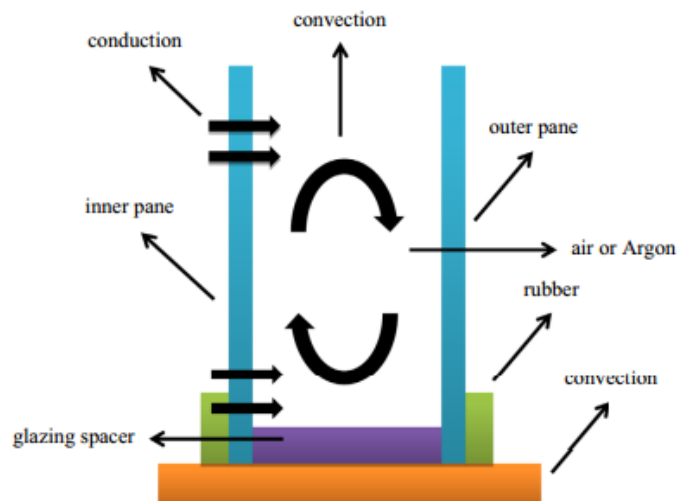
Figure 2. A Conventional double glazed window unit (Cuce and Riffat, 2015, p. 699)

For better energy performance, standard double glazed windows are sometimes produced with low-e coatings and inert gases. Low-e coatings are usually made of metal or metal oxide and come in either soft or hard form (Jelle et al., 2012). Soft coatings have better light transmittance; however, they are less durable and, therefore, require more protective layers (Chiba et al., 2005; Redinger et al., 2009). While coated double glazed windows have better thermal performance, cost of their production is substantially higher in comparison to standard double glazed windows. Cost is also a significant factor in application of inert gases. Cuce and Riffat (2015) argued that the use of inert gases in double pane glazed windows is justifiable when practicality and thermal performance are more important than costs associated with production. The cheapest of inert gases used in glazing systems is argon, although its thermal conductivity (0.018 W/mK) is two times lower than that of Krypton and Xenon respectively. Still, it is believed that argon will remain the most commonly used filler to improve energy performance of windows due to a good balance of cost-effectiveness and performance (Cuce and Riffat, 2015; Jelle et al., 2012).

2.3 Multilayer Glazing

Multilayer glazing refers to window systems where more than two glazing layers are combined with air or inert gases in the cavities with optional addition of low-e coating. Triple glazing window systems are the most common among the mass produced multilayer glazing technologies (Jelle et al., 2012). Such windows are also considered the most energy efficient systems on the market (Jelle et al., 2012). Provided below is the table of triple glazed window products offered on a mass commercial basis. U-values of these systems range from low 0.230 to high 0.79 W/m^2 K, which is explained by the different configuration types. Along

with U-values, visible solar transmittance (V_t) and solar heat gain coefficient (SHGC) are given, showing that the systems provide adequate solar light and energy transmittance rates.

Higher energy efficiency of triple glazing windows in comparison to double glazing systems can be explained by more elements influencing this parameter (more panes and cavities); however, presence of more elements also makes these systems larger and heavier. Application of inert gases helps to reduce cavity size without sacrificing thermal properties of windows (Jelle et al., 2012). This helps to partially address the window thickness issue; however, such windows are also more expensive. Another common disadvantage is their lower light transmittance because of an additional glass pane.

Table 45: Examples of commercially available triple glazing systems

System	Manufacturer	Reported U-value W/m^2 K	SHGC	V_t
ClimaGuard 80/70 Triple glazed: 3.0mm Clr, 5/16" Gap, 3.0mm Clr, 5/16" Air Space, 3.0mm: Air and 90% Argon/10% Air Filled Units	Guardian	0.230	0.580	72%
Guardian Neutral Triple glazed: 3.0mm Clr, 5/16" Gap, 3.0mm Clr, 5/16" Air Space, 3.0mm: Air and 90% Argon/10% Air Filled Units	Guardian	0.227	0.391	55%
iPlus 3E Triple glazed with low-e coating and 2x14 mm space width, air filled	Interpane	0.49	0.47	71%
iPlus 3L Triple glazed with low-e coating and 2x16 mm space, air filled	Interpane	0.53	0.55	72%
Velfac 200 Triple glazed, argon gas filled cavities,	Velfac	0.79	0.50	76%

NOTE: all descriptions and values are taken from the companies' websites or by personal contact

2.4 Suspended Films

Some commercially available window glazing systems incorporate suspended films (SF) in their design. The SFs are usually made of thin polymers and serve to replace the inner glass pane of found in triple glazing systems (Cuce and Riffat, 2015; Jelle et al., 2012). Because SCF are lighter and thinner than a glass pane, their application allows reducing the system's weight on the one hand and increasing the cavity space on the other. At the same time, they provide advantage over double glazing units by creating additional cavities and improving thermal performance. Although not as popular as double and triple glazing systems, SF glazing units have been actively offered on the market. Table 2 provides descriptions and relative parameters of three SF glazing systems on the market. The products offered by Hurd and Serious Materials offer lower U-values largely because they use Xenon instead of air to fill the cavities. Ander (2014) reported that experimentally achieved U-values for double suspended coated films with Krypton could achieve U-value as low as 0.10 W/m^2 K. All manufacturers offer possibilities for multiple SFs with options for inert gases to fill the cavities all of which correspondingly decrease U-values. However, they also make window units substantially more expensive.

Table 2: Examples of commercially available suspended films glazing systems

System	Manufacturer	Reported U-value W/m^2 K	SHGC	V_t
Ultra-R Dual pane, nanocoated polymer used for film with Xenon fill, low-e coating applied	Hurd	0.21	0.15	21%
1125 Serious Widow Dual pane, low SHG film with Xenon fill, low-e coating applied	Serious Materials	0.28	0.17	23%
Series 204 Dual pane, air fill, low-e coating applied	Visionwall Solutions	0.62	0.30	50%

NOTE: all descriptions and values are taken from the companies' websites or by personal contact

While SF glazing units offer relatively low U-values, their main disadvantage is in correspondingly low SHGC and V_t. In terms of costs, these units are also in the higher range because low-e coatings and inert gases are almost always applied to enhance their thermal performance. Finally, there are questions related to their durability.

2.5 Vacuum Glazing

A typical vacuum glazing system is based on the idea that the vacuum eliminates conduction and convection of heat. The first vacuum glazing system was produced at the University of Sydney by Robinson and Collins (1989), and the major principles behind manufacturing has remained largely the same: air is removed from the space between the panes which are connected by a number of small grids, and the edges are welded to provide an air tight envelope (Figure 3). Because even a small amount of vacuum is sufficient to reduce heat transfer, the gap between the panes can be minimised. This allows to achieve good thermal performance with relatively thin units.
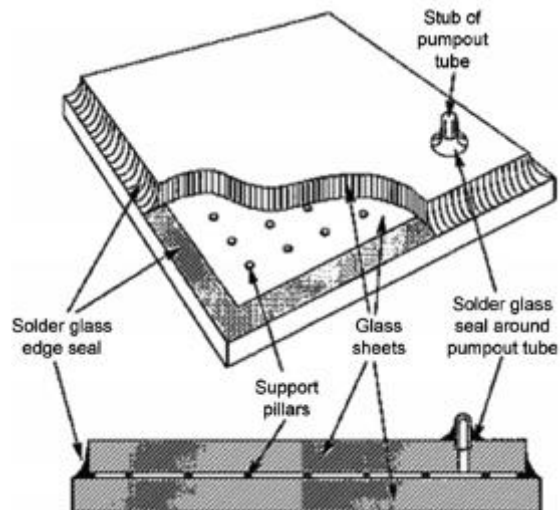
Figure 3. A vacuum glazing schematic (Cuce and Riffat, 2015, p. 701)

Low-e coating can serve as an additional component to enhance the performance of vacuum glazed windows. This was theorised by Collins and Simko (1998) and later experimentally confirmed by a number of studies. Fang et al. (2015) who showed that low-e coating application in two vacuum gaps of a triple glazing system can reduce U-value to 0.24 W/m2 K. Manz et al. (2006) used a model with four low-e coatings and stainless steel support pillars to obtain similar results.

The commercial applications of vacuum glazing have been around for several years. The leading producer of vacuum glazing windows is Pilkington. Its SPACIA-21 is a 21 mm thin system that represents a combination of evacuated and low-e coated glass sheets with a reported U-value of 0.70 W/m2 K, SHGC of 0.32 and V_t of 53%. The evident advantages of such system are space economy due to slim design and relatively high HISG and V_t in comparison to FS glazing units. However, production of evacuated glazing windows on a mass scale is stalled by engineering problems including air and thermal pressures, reduced visibility due to pillars used and maintenance of a vacuum seal along the window perimeter.

2.6 Smart Glazing

Smart glazing is the technology that allows windows to change lighting and heating properties based on indoor and outdoor conditions thereby reducing heating and cooling energy costs (Jelle et al., 2012). The principle behind smart glazing is that application of certain materials to glass makes it reactive to heat, light or voltage and change between transparent and translucent states (Baetens et al., 2010). While this technology has been existent for some time, its commercial applications started emerging only in the end of the past decade. Three types of coatings - liquid crystals, suspended particles and chromic materials – have been researched, and chromic materials have been found the most promising of them (Granqvist, 1991; Baetens et al., 2010). Electrochromic windows found commercial applications. In such windows, glass is covered with chromic materials which are linked to an electric current. As voltage is applied to the coating, it changes from transparent to opaque. The transparent state allows to achieve high natural light permeability while opaque state allows to reflect up to 98% of the light thereby reducing heat coming indoors. Some of the commercially available electrochromic glazing windows are listed in Table 3.

Smart glazing windows provide competitive U-values at more or less acceptable SHGC and V_t. They also offer better control over sunlight which can be in form of an electrical switch or a sunlight sensor. At the

same time, the power consumption is not high: according to the US Department of Energy's National Renewable Energy Laboratory, 100 typical electrochromic glazing windows consume energy equivalent to just one incandescent lamp. Another important advantage of electrochromic glazing is that it can be applied to the conventional windows thereby saving on glazing production from scratch (Granqvist, 1991; Jelle et al., 2012). However, as with the other advanced glazing systems reviewed earlier, smart glazing windows are expensive. They also cannot provide full control of some direct sunlight effects, and their durability is usually shorter than in the traditional glazing systems (Cuce and Riffat, 2015; Jelle et al., 2012; Piccolo and Simone, 2009). Finally, the manufacturer specified times for changing between the glass states are several minutes which does not provide the level of light control that many would expect.

Table 3: Examples of commercially available electrochromic glazing systems

System	Manufacturer	Reported U-value $W/m^2 K$	SHGC*	V_t*
CoolView Blue Double glass, air filled, Li ions as electrocrhomic material	SageGlass	1.59	0.48-0.09	62%-3.5%
Classic Triple glass, Krypton filled, Li ions as electrochrmic material, additional low-e coating applied	SageGlass	0.62	0.38-0.05	52%-3%
ConverLight Double glass, a patented multilayer electrochromic structure consisting of polyester, transparent conductors of ITO, NiO/WO electrochromic layer and ion-conducting electrolyte	ChromoGenics	0.48	0.75-0.06	46%-2.5%

* The range values are given for transparent and opaque states respectively. NOTE: all descriptions and values are taken from the companies' websites or by personal contact

3. EMERGING WINDOW GLAZING TECHNOLOGIES

Following from the review of the existing common and advanced window glazing systems available on the market today, it is clear that a good balance between cost and performance is yet to be found. Research in glazing technologies for windows has recently produced several promising systems which have not yet received wide commercial applications. Among such systems are aerogel glazing, phase change material (PCM) glazing, solar pond, air sandwich and PV glazing.

3.1 Aerogel Glazing

Aerogels are light weighted materials with extremely low density which, due to high porosity, have much lower thermal conductivity than still air (Cuce and Riffat, 2015). Because of these properties, aerogels are regarded as one of the most promising emerging materials for residential building retrofitting. Applied to window glazing as an insulation material, aerogels promise greater solar thermal transmittance combined with high visibility. Available research on aerogel glazing describes granular and monolithic silica aerogel systems. Shultz et al. (2005) investigated performance of a window system with a 15 mm evacuated monolithic silica aerogel encapsulated between two low iron glass layers and reported U-values below 0.70 $W/m^2 K$ with V_t at 76%. Jensen et al. (2004) managed to achieve a U-value of 0.66 $W/m^2 K$ and thermal transmittance of 0.85 for a 13.5 mm thick system combining vacuum glazing and evacuated monolithic aerogel. Monolithic aerogel systems show better performance than granular aerogel systems. Reim et al. (2005) created and tested two prototype window glazing systems with granular aerogel to achieve U-values of 0.88 $W/m^2 K$ and 0.53 $W/m^2 K$. In a comparative study involving monolithic and granular aerogel glazing systems Buratti and Moretti (2012) found that the best combination of optical and thermal performance was achieved with a double glazed monolithic vacuum aerogel system with U-value of 0.60 $W/m^2 K$ and V_t of 62%. Granular aerogel system showed U-values of slightly over 1 $W/m^2 K$ and relatively low Vt of 27% (Buratti and Moretti, 2012).

Because monolithic aerogel glazing window systems show better performance than granular aerogel systems, they are the best candidate for wide commercial applications in the nearby future. Such systems offer good U-value without much sacrifice of V_t factor. At the same time, aerogels are notable for their fragility due to extremely low tensile strength (Cuce and Riffat, 2015). In addition to tensile stress, aerogel glazing systems have to be well protected against water which may easily destroy the aerogel structure.

3.2 PCM Glazing

PCM materials transform from solid state to liquid when absorbing heat and change from liquid to solid state when releasing stored heat energy. These properties of PCM make them attractive for energy saving

purposes in windows. Considerations of PCM applications in fenestration were explored by Demirbas (2006), Baetens, Jelle and Gustavsen (2010) and Khudhair and Farid (2004) with some promising results. Several numerical and experimental studies involving PCM filled window glazing systems showed the possibility of substantial U-value reduction in comparison to the conventional double glazing systems. Ismail et al. (2008) showed that two pane window systems with PCM filled cavity performed better than the systems with gas-filled cavities. Goia and colleagues performed a number of studies involving paraffin wax as a PCM in a double glazing window system showing improvements in thermal properties (Goia et al., 2012; Goia et al., 2013). Overall, use of PCM as cavity filler in window glazing systems allows the reduction of U-value up to 0.50 W/m^2 K (Grynning et al., 2013). However, challenging points remain. For example, paraffin, which is considered one of the most promising PCMs for glazing due to low cost, has low thermal conductivity value and large volume variation during phase shifting process (Cuce and Riffat, 2015). Another remaining challenge is relatively low V_t (Grynning et al., 2013).

3.3 Solar Pond and Air Sandwich

Solar pond and air sandwich are some of the most recent products following from research developments in window glazing. Both systems represent multiple sections of materials and gases to provide windows with the integrated solutions for effective lighting, heat collection storage and preservation as well as sunlight control. The solar pond is a closed, transparent window body equipped with several transparent sections (Figure 4). The inner and outer layers of the solar pond are filled with transparent thermal insulation liquid and the inter layer(s) is filled with water, gas or vacuum. An air filled solar pond was been recently tested at the University of Nottingham, and it was shown that an optimised system may achieve U-value as low as 0.40 W/m^2 K (Cuce and Riffat, 2015). Air Sandwich is a similar concept being developed by Sekisui Company in Japan. The system is a combination of multiple thin plastic films with air filling the cavities in between them (Figure 4). Experiments showed that the number of air filled cavities leads to increasing reduction in U-value without any sacrifice in terms of V_t factor (Cuce and Riffat, 2015).
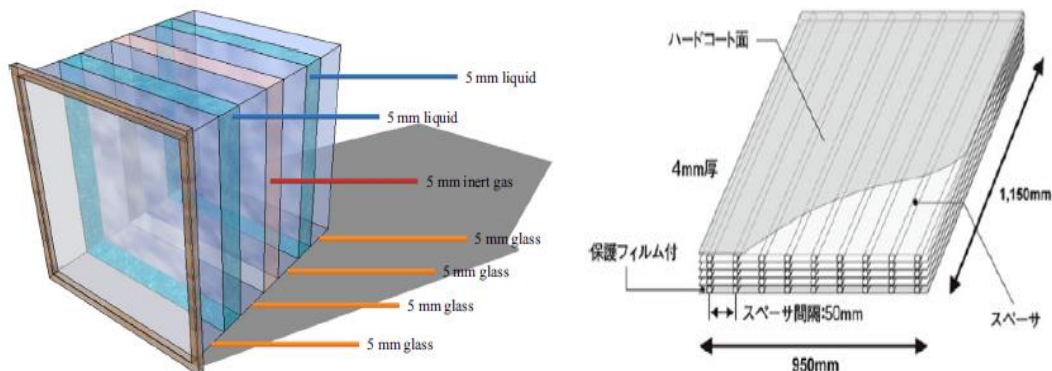
Figure 4. Multilayer Solar Pond and Air Sandwich systems (Cuce and Riffat, 2015, p. 701)

4. NOVEL PHOTOVOLTAIC GLAZING TECHNOLOGY

Photovoltaics (PV) refers to a method of producing electricity by using materials with photovoltaic effect to convert solar energy (Branker et al., 2011). Power generation takes place in solar cells – electrical devices made of photovoltaic materials (silicon based or non-silicon based). The cells are put together to form solar panels while thin film materials such as amorphous silicon, can be directly sputtered on the surface of a module and interconnected with a laser (Jelle et al., 2012). Protection of the cells in a PV module is based on a transparent cover and waterproof backing such as low iron content glass lamination in the front side and a polymer sheet on the rear side.

While PV has been a popular direction in energy and building research for some time, its applications for windows have not received much attention until recently. Solar glazing modules, however, can be attractive in window systems because they enable capturing and transforming solar energy which is mostly wasted in the other window glazing systems. The technology of combining PV and glazing involves creation of a nanoparticle coating on the window glass by means of spraying (Jelle et al., 2012). The desired transparency and energy generation levels will dictate the distance between the cells which can be between 3 to 50 mm. Because the space between the solar cells diffuses daylight, electricity production is combined with both natural light and shading. Shading and electricity generation make total glazing area parameter a very important factor (Fung and Yang, 2008). Another important factor is the PV material. The

conventional crystalline (c-Si) cells have relatively high efficiency in terms of capturing solar power; however, they have high opacity levels which makes them rather inefficient for residential building applications (Lewis et al., 2009). Development of the amorphous silicon (a-Si) cells partially resolved this problem. The relationship between power generation and V_t, however, remains adverse, and it is regulated by adding tiny holes in the cells and regulating the size of these holes (Cuce and Riffat, 2015). Figure 5 shows a possible PV glazing window system with a-Si thin film solar cells.

There is an active ongoing research in PV glazing systems seeking to increase power generation while at the same time reducing U-value and increasing V_t. In a comprehensive review of the available research on PV glazing technologies, Skandalos and Karamanis (2015) reviewed studies on the basis of outcomes related to thermal performance of PV glazing units, their optical performance and their performance in terms of other relevant parameters such as cost reduction, energy saving potential and environmental benefits. The vast majority of the reviewed studies demonstrated that the most notable contributions of PV glazing systems are in electricity savings, reduction of cooling and heating loads and lighting. Skandalos and Karamanis (2015) concluded that the best performance results for PV glazing systems arise from optimum selection of the building integration parameters such as design, climatic characteristics and so forth). There are also new promising areas of research which focus on development of dye-sensitised solar cells and organic solar cells for windows (Kim et al., 2012; Yoon et al., 2011). These new types of solar cells may further reduce cost of production and enhance the relevant parameters of PV glazing windows' performance.
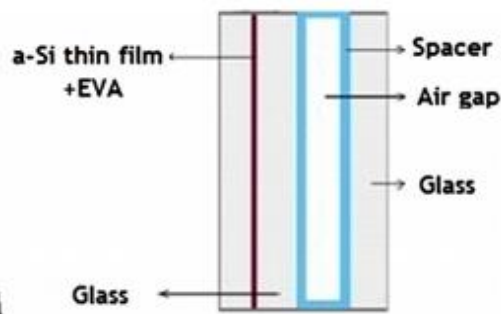

Figure 5. An a-Si PV glazing system (Skandalos and Karamanis, 2015, p. 308)

5. CONCLUSIONS

The aim of this paper was to review the existing and emerging window glazing technologies and identify the most promising areas of improvements. At present, double glazing window systems dominate the market with the some presence of triple glazing, suspended films, vacuum glazing and smart glazing systems. Double glazing window systems can rarely meet the new energy standards while the other systems are expensive and not always reliable. Often, they require use of low-e coatings and inert gases which substantially increase cost of production. Recently, new glazing systems have been explored with the focus on window cavity filling and the novel combinations of materials in multiple cavities. Aerogel and PCM glazing systems represent the first segment of this research. While offering better U-values, such systems still have disadvantages such as material fragility (in case of aerogel), visibility (in case of PCM) and some other relevant parameters. Novel glazing designs such as solar pond and air sandwich also allow to increase thermal performance of the systems, but their applications are still in their infancy. PV systems represent a very promising direction in this regard. They are based on combining the existing proven technologies, and while showing higher U-values than other advanced glazing systems, they generate electricity to at least partially offset energy spending on heating and cooling. Optimisation of PV glazing system parameters is considered one of the major factors that could make them a product of choice in the nearby future.

6. REFERENCES

ANDER, G. 2014. Windows and glazing. National Institute of Building Sciences. <http://www.wbdg.org/resources/windows.php> [accessed 19.06.15].

BAETENS, R., Jelle, B. and Gustavsen, A. 2010. Properties, requirements and possibilities of smart windows for dynamic daylight and solar energy control in buildings: a state-of-the-art review. Solar Energy, Materials and Solar Cells, 94: 87–105.

BRANKER, K., Pathak, M. and Pearce, J. 2011. A Review of solar photovoltaic levelized cost of electricity. Renewable and Sustainable Energy Reviews, 15(9): 4470–4482.

BURATTI, C. and Moretti, E. 2012. Experimental performance evaluation of aerogel glazing systems. Applied Energy, 97: 430-437.

CARMODY J. 2012. High performance windows and facades. Centre for Sustainable Building Research (CSBR), University of Minnesota. <http://www.csbr.umn.edu/outreach/presentations_carmody.html> [accessed 19.06.15].

CHIBA, K., Takahashi, T., Kageyama, T. and Oda, H. 2005. Low-emissivity coating of amorphous diamond-like carbon/Ag-alloy multilayer on glass. Applied Surface Science, 246: 48–51.

COLLINS, R. and Simko, T. 1998. Current status of the science and technology of vacuum glazing. Solar Energy, 62(3): 189–213.

CUCE, E. and Riffat, S. 2015. A state-of-the-art review of innovative glazing technologies. Renewable and Sustainable Energy Reviews, 41: 695-714.

DEMIRBAS, M. 2006. Thermal energy storage and phase change materials: An overview. Energy Sources, 1: 85–95.

FANG, Y., Hyde, T., Arya, F., Hewitt, N., Wang, R. and Dai, Y. (2015). Enhancing the thermal performance of triple vacuum glazing with low-emittance coatings. Energy and Buildings, 97: 186-195.

FUNG, T. and Yang, H. 2008. Study on thermal performance of semi-transparent building-integrated photovoltaic glazing. Energy and Buildings, 40 :341–350.

GHOSHAL, S. and Neogi, S. 2014. Advance glazing system – energy efficiency approach for building: A review. Energy Procedia, 54: 352-358.

GOIA, F., Perino, M. and Serra, V. 2013. Improving thermal comfort conditions by means of PCM glazing systems. Energy and Buildings, 60: 442-452.

GOIA, F., Zinzi, M., Carnielo, E. and Serra, V. 2012. Characterisation of the optical properties of PCM glazing system. Energy Procedia, 30: 428-437.

GRANQVIST, C. 1991. Solar energy materials – overview and some examples. Applied Physics Annals, 52: 83–93.

GRYNNING, S., Goia, F., Rognvik, E. and Time, B. 2013. Possibilities for a characterization of a PCM window system using large scale measurements. International Journal of Sustainable Built Environment, 2(1): 56-64.

JELLE, B., Breivik, C. and Rokenes, H. 2012. Building integrated photovoltaic products: A state-of-the-art review and future research opportunities. Solar Energy, Materials and Solar Cells, 100: 69-96.

JELLE, B., Hynd, A., Gustavsen, A., Arasteh, D., Goudey, H. and Hart, R. 2012. Fenestration of today and tomorrow: a state-of-the-art review and future research opportunities. Solar Energy Materials and Solar Cells, 96: 1–28.

KHUDHAIR, A. and Farid, M. 2004. A review on energy conservation in building applications with thermal storage by latent heat using phase change materials. Energy Conservation Management, 45: 263–275.

KIM, Y., Sachse C., Zakhidov, A., Meiss, J., Müller-Meskamp L, et al. 2012. Combined alternative electrodes for semi-transparent and ITO-free small molecule organic solar cells. Organic Electronics, 13(11): 2422–2428.

LEWIS, J., Zhang, J. and Jiang, X. 2009. Fabrication of organic solar array for applications in microelectromechanical systems. Journal of Sustainable Renewal Energy, 1: 013301.

MANZ, H., Brunner, S. and Wullschleger, L. 2006. Triple vacuum glazing: Heat transfer and basic mechanical design constraints. Solar Energy, 80(12):1632–1642.

NICHOLLS, R. (ed). 2004. The green building bible: The low energy design technical reference. London: Green Building Press, vol. 2.

PICCOLO, A, and Simone, F. 2009. Effect of switchable glazing on discomfort glare from windows. Building Environment, 44: 1171–1180.

REIDINGER, M., Rydzek, M., Scherdel, C., Arduini-Schuster, M. and Manara, J. 2009. Low- emitting transparent coatings based on tin doped in diumoxide applied via a sol–gel routine. Thin Solid Films, 517, 3096–3099.

REIM, M., Korner, W., Manara, J., Korder, S., Arduini-Schuster, M., Ebert, H, et al. 2005. Silica aerogel granulate material for thermal insulation and daylighting. Solar Energy, 79: 131–139.

ROBINSON, S. and Collins, R. 1989. Evacuated windows-theory and practice. In: ISES Solar World Congress, International Solar Energy Society. Kobe, Japan.

SADINENI, S., Madala, S. and Boehm, R. 2011. Passive building energy savings: a review of building envelope components. Renewable and Sustainable Energy Review, 15: 3617–3631.

SCHULTZ, J., Jensen, K. and Kristiansen, F. 2005. Superinsulation aerogel glazing. Solar Energy, Materials and Solar Cells, 89: 275–285.

SKANDALOS, N. and Karamanis, D. 2015. PV glazing technologies. Renewable and Sustainable Energy Reviews, 49: 306-322.

Zero Carbon Hub. 2014. Fabric energy efficiency for zero carbon homes: A flexible performance standard for 2016, <www.zerocarbonhub.org> [accessed 19.06.15].

483: Maintainability: a best-practice approach to building design

OWAJIONYI L. FRANK[1] AND SADDIQ OMAR[2]

[1] Department of Architecture, Rivers State University of Science and Technology, Port Harcourt, Nigeria
[2] Department of Architecture and Built Environment, University of Nottingham, United Kingdom

The development of varying unconventional low carbon and low energy technologies to meet current demands for sustainable solutions and to make our 'buildings feel good' call for good consideration to the maintenance of these buildings and the fitted technologies from design inception. It is more so when we realise that building elements, components and materials are also exposed to the fast changing environmental vagaries which cause wear and tear and ageing. Maintainability is a design characteristic which incorporates function, accessibility, reliability, and ease of servicing and repairs into all active and passive system components, that maximizes costs and benefits of expected life-cycle value of a facility". This paper therefore looks at maintainability design approach as a best-practice approach to low carbon, green and sustainable building designs. It draws data from a research conducted by the authors to explore a best practice approach to operability and maintainability of low carbon buildings (LCBs) in the UK. A mixed method research approach involving across-method and within-method triangulation (interviews, surveys and case studies) were adopted. The study concluded that building designers need to prove the maintainability and operability of their designs before they are constructed, and in so doing will give due attention to how the facilities would be maintained, when they are designing.

Keywords: architects, building design, life cycle, operability and maintainability, sustainable maintenance.

1. INTRODUCTION

Maintainability is an emerging research subject in the built environment, particularly as it relates to low carbon and sustainable technologies in buildings. It is a discipline within the science of engineering; it was pioneered by the United States Military service in 1954, (Blanchard and Lowery, 1969). The discipline was initiated to provide designers with a source of specialized skills and knowledge related to the support and maintenance of equipment and systems (Ibid). Maintainability is described by the US Institute of Technology and Science as; "*a characteristic of design and installation, expressed as the probability that an item will be retained in or restored to a specified condition within a given period of time, when the maintenance is performed in accordance with prescribed procedures and resources*" (ITS, 1996). BusinessDictionary.com defines it as a "*Characteristic of design and installation which determines the probability that a failed equipment, machine, or system can be restored to its normal operable state within a given timeframe, using the prescribed practices and procedures*" (Businessdictionary.com, n.d.). Dunston and Williamson (1999) also defined maintainability to mean "*The design characteristic which incorporates function, accessibility, reliability, and ease of servicing and repair into all active and passive system components, that maximizes costs and benefits of expected life-cycle value of a facility*". Dunston and Williamson related the definition more to buildings (facilities), with emphasis on maximizing costs and benefits of expected life-cycle value of the facility. Blanchard and Lowery (1969) makes it more explicit; "*Maintainability is a characteristic of equipment design and installation which is expressed in terms of ease and economy of maintenance, availability of the equipment, safety, and accuracy in the performance of maintenance actions.*" Chew (2010) defines it as "*the ability to achieve the optimum performance throughout the lifespan of a facility within the minimum life cycle cost*".

Deducing from the above definitions, maintainability can simply be described as a design characteristic; qualifying a design with respect to ease, safety and cost that will be involved in maintaining the designed building, after it has been built. So, 'maintainability in building design' would be said to mean 'a design that is conscious of the ease, safety and cost of maintenance, not compromising standards and quality, but ensures that building elements and components are kept in their continued good appearance and functional state, through the building life-cycle'. The outcome of maintainability will be a maintainable design; a maintenance conscious design.

Although the term 'maintainability' is deemed to have originated in the 1950s, but its principles has been an age-long traditional theory of architecture; that from inception of design, the architect is expected to give considerations to maintenance possibilities and cost (Seeley 1976; Mills 1994; Lush 1994). As far back as 1895, Ruskin (1895) identified the need for designers and builders to be conscious of the durability (maintainability) of their works. There is no gainsaying that the degree of durability of a structure is determined by the materials used and how they are used (constructed). These of course will be determined at the detail design and specification stage of the design phase of the structure. However, maintainability in building designs seems to still stand as theory rather than practice. CIRIA (2009) corroborates this assertion as it states that the obligation for designers to deliver assets that may be safely and economically maintained is already enshrined in the law, but it is often not well done, and that there is a lack of practical guidance*.* Dunston and Williamson (1999) noted also that maintenance problems in facilities are heavily attributed to design limitations, among other issues. Seeley (1987) noted that designers must ask themselves these 4 questions as they design each element or component of a building: how can it be reached; how can it be cleaned; how long will it last and how can it be replaced? Unfortunately, most designers are often more concerned with aesthetics of the elements than their maintenance requirement (Zubairu 2010). In a study carried out of 211 large building design firms in the United States to investigate the relationship between design practices and maintenance considerations it was concluded that

   i)   ease of repair and replacement, access to cleaning area and ease of cleaning were ranked by designers to be among the least important design factors considered during design,
   ii)   among the complains designers reported receiving from clients and tenants, maintenance related complains ranked much higher(Arditi and Nawakorawit 1999a),

It is therefore obvious that designers are largely responsible for the huge cost of operation and maintenance of buildings and should consequently be liable to finding an enduring solution. According to CIRIA (2009), the obligation for designers to deliver safely and economically maintained buildings is already enshrined in law. However, this is often not well done, and there is a lack of practical guidance (Ibid)*.* Dunston and Williamson (1999) noted also that maintenance problems in facilities are heavily attributed to design limitations, among other issues.

So one question this study sets out to answer is if in the recent years there have been some improvements in designers' attitudes to maintainability, and if not, what should be the appropriate method (best practice approach) that will ensure that designers adhere reasonably to this age-long requirement – maintainability?

The key findings that emerged were that building designers attitude to maintainability is still very poor, and in most cases clients were never aware of the maintenance implication of their proposed buildings before they are erected. The findings also show that if designers are made to prove the operability and maintainability of their designs before they are constructed, they will for certain be maintainability conscious and the clients will be fully abreast of the maintenance requirements of their proposed building and be able to make informed choices at their own risk.

2. BACKGROUND TO RESEARCH

2.1 Current Demands for Sustainable Solutions in Building Designs

With the realities of climate change confronting us, building designers all over the world are being called upon to create buildings that are sustainable; buildings that are energy efficient, functional and economical, comfortable and safe, with reduced or no harm to the macro environment and the future generation. This has thus resulted in substantial rise in technology which has become a mixed blessing to humanity; whereas it provides us with comfort, it also increased the amount of energy required to drive these technologies (Hensen and Lamberts, 2011). It is also widely understood that this increased energy usage has led to critical environmental problems (Ibid) – increased CO_2 and other greenhouse gasses emission (RIBA, 2009). Globally, efforts are being made to cut down on the use of fossil fuel in driving these technologies. Joe Clarke in Hensen and Lamberts (2011) noted some of these efforts which among others include: deployment of energy efficiency measures and a switch to new and renewable sources of energy. In the building industry, this has given rise to varying low carbon and renewable technologies, also referred to as sustainable technologies, green technologies or energy efficient technologies gradually replacing the conventional high fossil fuel driven technologies in buildings, in order to meet up with the World scientific consensus on Carbon emissions target of 80% reduction by the year 2050 (Avis, 2011).

The driving objective of LCB building designs is to reduce the overall impact of the built environment on human health and the natural environment by:

> ➢ Efficiently using energy, water, and other resources
> ➢ Protecting occupants health and improving employee productivity
> ➢ Reducing waste, pollution and environmental degradation.

It is common in literature that buildings and associated uses account for a substantial part of the environmental load caused by anthropogenic activities (U.S.DOE, 1999; Szokolay, 2008; BRE, n.d.). The United States Department Of Energy (DOE), 1999 reports that buildings in the U.S alone consume roughly: 37% of the nation's primary energy, 67% of the total electricity used each year, 35% of CO_2 emission in the US and 9% global CO_2 emission. Szokolay, 2008 looks at the figures at a global perspective; reports that building and associated uses are responsible for: 42% of all energy consumption, 40% of all atmospheric emissions, 30% of all raw material usage, 25% of solid wastes, 25% of water usage, 20% of liquid wastes. Szokolay also added that all these can be strongly influenced by architects and designers. The question is how?

Some of the common answers in literature are:

1. To ensure that buildings they design are energy efficient, meeting the nation's standards for zero carbon designs(U.S.DOE, 1999)
2. To address the issue (of ensuring zero carbon) from all the stages of the building life; from early sketch design, via detailed design to construction, commissioning, operation, control and maintenance of new builds and existing one (Hensen and Lamberts, 2011).
3. Similar to point 2 above is advocacy for whole-life assessment concept. RIBA, 2009 has criticized the conventional concept of Whole life Assessment termed life-cycle costing (LCC) or whole-life costing (WLC), noting that this is money-based measurement. It further explained that whereas the initial construction cost could be estimated with reasonable accuracy, the cost-in-use (operation and maintenance cost) could be more difficult to estimate due to future uncertainty. RIBA further

advocates for life-cycle analysis (LCA) which is based on the whole life assessment of its environmental impact as a better approach.

However, Joe Clarke in Hensen and Lamberts (2011) questioned the rationale of accepting the widespread deployment of micro-CHP within the urban environment if the global carbon emission reduction target is attained at the expense of reduced local air quality and increased maintenance cost?" Implying that the cost implication of running a building cannot be divorced from the environmental impact globally and locally; within the building.

From the foregoing, it seems proper to conclude that whereas it is difficult to calculate near-actual operating and maintenance cost from inception, it is possible to put forward a rough guide in the form of maintenance needs of the design from the very early stage of the project. This is to say that designers should ensure that the buildings they design are maintainable long into the future, so that need for new build and the accompanying energy need, emissions, materials and water needs as well as the associated wastes are minimized. So if the environment must be safe guarded, demand is placed not only for a reduction in new-build activities, but also in maintenance works.

2.2 Growing Concern for Building Maintenance

Issue of maintenance has become of growing concern not only to researchers but to government bodies and practitioners. This has led to the adoption of various procurement routes in the building industry. In the UK, the Design & Build (or Develop and Build) and the Design, Build & Operate, otherwise known as the Private Finance Initiatives (PFI) systems or Public Private Partnership (PPP) in other countries, seem be tops on the preferred list of procurement systems by public or corporate clients. PFI's primary principle is to transfer the responsibilities and associated risks of funding, designing, building, operating and maintaining public infrastructure to the private sector over a period of usually 25 to 30 years (Harris 2004, Smith 2004 and Pretorius et al 2008). By this arrangement, a private sector firm, usually the contractor or ProjectCo; the consortium of main contractor and private sector funders (House of Commons HC 68, 2010) undertakes the responsibility of sourcing for funds for the project, produces designs - in-house or outsource designers (Smith 2004), constructs, operates and maintains the building from which quality public services are delivered. According to Pretorius et al 2008, the expectations of the public sector for a PFI scheme is to achieve Value for Money (VfM). One way of achieving this VfM and in fact the key benefit of PFI is the requirement for buildings to be maintained to high standards over the life of the contract (HC 631, 2011).

However, there have also been growing concerns within Government, researchers and the general public, suggesting that the PFI cannot ensure maintainability or sustainable maintenance practice. It is also believed that the PFI arrangement is far too expensive; a means of transferring debts to future generation, mortgaging the nation's future and not providing good value for money (Smith, 2004; Monbiot, 2010; Norman, 2010). HC 631 (2011) noted that there was no clear and explicit justification and evaluation found for the use of PFI in terms of value for money (VfM). It was seen as a back-door form of privatization. In terms of maintenance, HC 631 (2011) noted that the requirement for buildings being maintained to high standards over the life of the contract is supposed to be a key benefit of PFI, yet some hospital Trusts were not satisfied with the maintenance services. In addition, Smith (2004) noted that the argument of the PFI advocates that long-term savings would be achieved through cheaper maintenance and running costs, and more efficient facilities management, sounds convincing in theory, but yet to be proven in practice. Similarly, HC 68 (2010) reports that "there is no clear evidence to conclude whether PFI has been demonstrably better or worse value for money for housing and hospitals than other procurement options. In many cases local authorities and Trusts chose the PFI route because the Departments offered no realistic funding alternative".

The National Audit Office study of the performance management of hospital PFI contracts consisting of 76 such operations in England noted among others, the following key findings:

a) cleaning, laundering and portering costs are about the same with non PFI hospitals.
b) hospitals with PFI buildings spend more on maintenance annually
c) Trusts'(client) assessment of ProjectCo's and contractors' performance by service shows on the average, a satisfactory score card but Estates Maintenance was seen to be area of service with highest score of dissatisfaction, followed by ProjectCo in managing the services (general operation management)

Figure 1 show clearly the number of Trusts who stated that performance is less than satisfactory. Here maintenance services and general Management topped the scale.
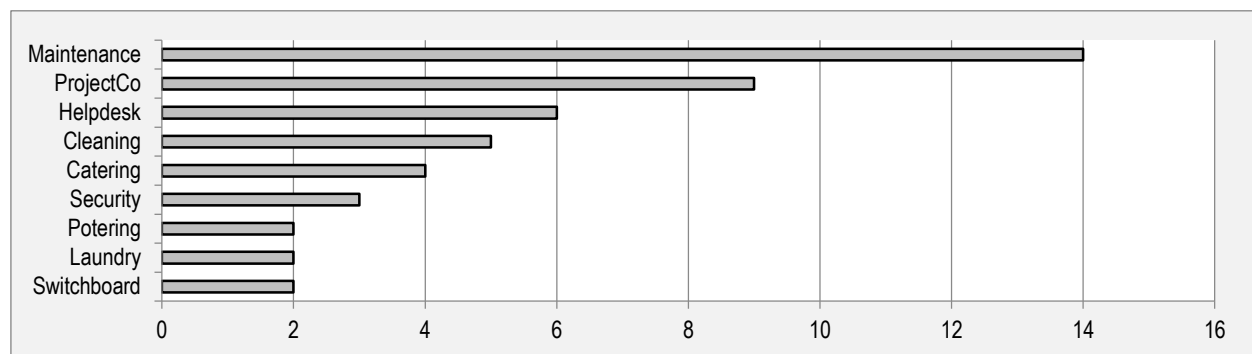

Figure 1: Number of Trusts who stated that performance is less than satisfactory (Source: National Audit Office 2010, pp.22)

Whereas the PFI/PPP procurement route may ensure high standard of maintenance; it cannot guarantee maintainability and sustainable maintenance practice, if maintainability factors were not considered during design.

Studies reported in Frank (2011) show that no procurement route can adequately ensure maintainability if maintainability is not factored into the design. The House of Commons Report HC631 concludes that *"there are no mechanisms built into generic PFI contracts to test the continued value for money of maintenance work during the contract period".* This mechanism is indeed what this paper sought to explore.

> 2.3 Maintainability and the Concept of 'Duty of Care'

In the English law of tort, a duty of care is a legal obligation which is imposed on an individual, requiring that they adhere to a standard of reasonable care while performing any acts that could foreseeably cause injury to others. The law states thus; (Speaight and Stone, 2010). The term `injury' in this case is explained by P.J. Derbney, Partner, Cartwright and Lewis, Solicitors (1998) to mean *"primarily physical injury and consequential financial loses".*

By the concept of 'Duty of Care', a designer is expected to take reasonable care to ensure that his client or the third party users do not incur any foreseeable physical injury or economic loss as a consequence of his action or in-action. Section 13 of the Sales of Goods and Services Act 1982 as amended by the Sale and Supply of Goods Act 1994 of the English law and statute provides that the designer must carry out the design services with reasonable skill and care (Designing Buildings, 2013). According to the Architects' Legal Handbook (Speaight and Stone, 2010), Everyone who offers a service to others and claims expertise to do what he offers has a responsibility to society in general and to his clients in particular.

Blanchard and Lowery (1969) opined that, by applying the principles of maintainability, the problems of product support and maintenance of complex systems can be reduced, if not eliminated. They also added that *"the decisions made by the line manager in implementing a maintainability programme have much to do with the competitive success or failure of his firm".* Aligning this statement to building design, one would say – 'the decisions made by the building designer in implementing a maintainability programme have much to do with the competitive success or failure of his practice'. It therefore becomes imperative to put in place workable principles and procedures that can facilitate compliance to maintainability considerations, so that clients do not suffer the burden of high cost of maintenance and general under-performance in terms of energy savings and indoor air quality; thereby achieving good value for money.

3. METHODOLOGY

The paper draws data from an earlier study undertaken by the authors to explore a best practice approach to operability and maintainability of LCBs in the UK. A mixed method research involving across-method and within-method triangulation (interviews, surveys and case studies) were adopted; supported by extensive literature search.

The interview was populated by 5 very experienced professionals who were, sitting at the top management level of their respective organizations. 80% of them (4 out of 5) had over 30 years' experience in their respective fields of practice as shown in table 1. The small sized interviewed population provided opportunity for detailed insight into the subject. Similar work reported in Dawood et al, 2013 which was directed at understanding current architectural design practices with respect to low carbon designs in the UK was also informed by interviews involving five participants drawn from large architectural practices in the country.   Although the spread of interviewees in this study did not go through all the built environment professional disciplines, it covered a wide range of stakeholders in the built environment; clients, Designers, facilities managers and built environment researchers, as discussed in Frank and Daminabo (2014). Secondly, the vast years of experience they have acquired in working with other building professionals provides a good level of reliability in their opinions. In addition, because most of the participants sit at the top decision making bodies of their organization, they receive and work with feedbacks from other experts. The interviews were conducted using a semi-structured qualitative interview format; adopting the interview protocol discussed in Creswell (2009). The data collected was analysed using the thematic content analysis method as discussed in (Burnard, 1991; Aronson, 1994 and Marks and Yardley, 2004). The analysis method involved the use of coding or themes drawn from existing theoretical ideas that the researchers brought to the data (deductive coding) and from the raw data itself (inductive coding) as discussed in Marks and Yardley 2004.

Table 1: Summary of Building Professionals who took part in the Interviews

S/no	Code No. of Participant	Years of Experience	Professional Background	Professional groups according to the nature of job
1	001	30	Engineer	Client & Facilities Manager
2	002	Less than 10	Planning & Development Surveyor	Client
3	003	30	Building Surveyor	Facilities Manager
4	004	30	Architect	Building Design Practitioner & Academic Researcher
5	005	37	Architect	Academic Researcher

After the interviews were conducted, transcribed and analysed, a structured questionnaire in web format was developed and the link was sent to some professionals who were not able to make out time for a one-on-one interview. It was also published on the RIBA knowledge community blog. A hard copy format was also developed, to reach facilities managers principally, since they are directly involved with the day to day running of buildings. The purpose of the surveys was to reach a wider population of participants and also to allow for quantitative analysis of data. It was also designed to complement the results of the interview; to further explore possible case studies and the associated O&M challenges of the specific buildings the participants may have been involved with. The web format survey was collected and analysed using the 'SurveyMonkey' (online survey software) for data collection and analysis, while the data collected through the hard copy survey were manually fed into the SurveyMonkey for analysis.

Galvin (2015) validates this study design. It reports results of the study which aimed at offering guidance for qualitative researchers to improve result reliability. The study surveyed 54 recent papers in six prominent building and energy journals. The result shows that researchers in building energy consumption often use semi-structured interviews to produce qualitative data and that the interview samples are typically small, but inferences are often made for interventions in the light of the findings, on the assumption that these are somehow transferable to wider populations.

4.   FINDINGS AND DISCUSSIONS

The concept and principles of maintainability as discussed in section 1.0 is an age-long traditional theory of architecture which requires building designers to give considerations to maintenance issues and cost from the design inception. The obligation for designers to deliver safely and economically maintained buildings is already enshrined in law, but this however, is often not well done. It also presented Dunston and Williamson (1999) argument that maintenance problems in facilities are heavily attributed to design limitations, among other issues. So one question this study sets out to answer is if in the recent years there have been some improvements in designers' attitudes to maintainability, and if not, what should be the best practice to ensuring that designers adhere reasonably to this age-long requirement – maintainability? Findings emerging from the study indicate that most architects; building designers attitude to maintainability is still very poor, and in most cases clients were never aware of the maintenance implication of their proposed buildings before they are constructed. The findings also show that if designers are made to prove the operability and maintainability of their designs before they are constructed, they will certainly be

maintainability conscious and the clients will be fully abreast of the maintenance requirements of their proposed building and be able to make informed choices at their own risk from the onset; before designs are concluded.

4.1 Designers Attention to Maintainability

Questions on designers' attention to maintenance consideration during design featured both in the online and manual surveys. The online respondents which consist of nearly 70% of building designers (58.3% of architects and 8.3% of architectural technologists) were asked the question; *"From your experience as a professional in the building industry, how would you agree or disagree with the statement – most architects pay less attention to issues of maintenance and operation challenges in their designs?"* The result is reflected in figure 2. This could be said to reflect architect's opinion, since architects constitutes nearly 70% of the study population. In Figure 3 the result of the manual survey is presented. 50% of the study population were made up of facilities managers (FMs). Other professionals are just 1 participant each except the quantity surveyors which are 2 participants. So it may also seem proper to say that this reflects the opinion of those who directly experience the building in use; the facilities managers.
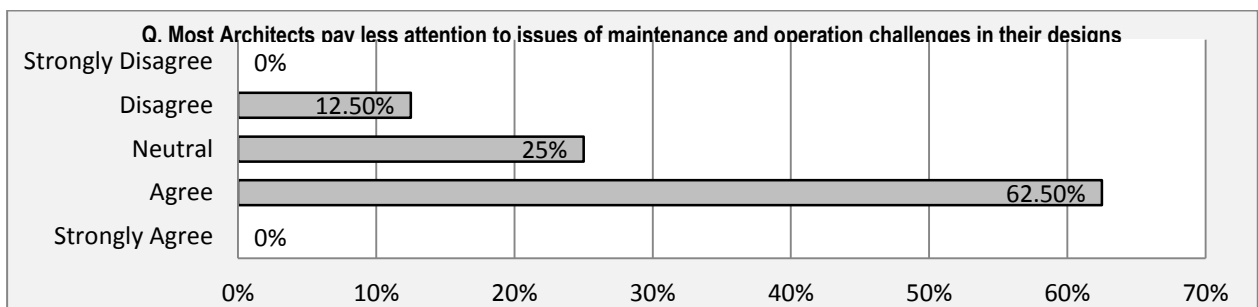

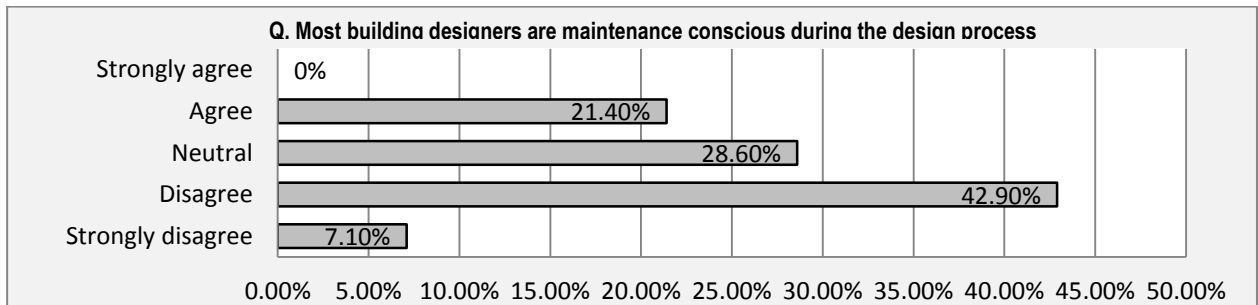Figure 2: Attitudes of Architects towards Maintainability (Architects opinions)

Figure 3: Attitudes of building designers towards Maintainability (FMs opinions)

Both results show that architects do not give attention to maintainability. While over 60% of architects agree that most architects or building designers pay less attention to maintenance and operation issues during design, 50% of facilities managers corroborate this by disagreeing and strongly disagreeing that building designers are maintenance conscious during the design process. In both cases the percentage of neutrality are 25% and 29% respectively.

The interview result also returned 60% of the interviewees agreeing that most architects do not pay attention to maintenance and operation considerations during design. The question was put thus; 'there is an opinion that most architects are not maintenance conscious while making their designs. What do you think about that? It is interesting to quote their answers directly:

> ➢ *"Absolutely right!"* (Code no. 004). Interestingly, this participant is an architect with 30years experience in both private practice and in teaching and research in the UK.
> ➢ "I think it is very variable, there is a school of thought that signature architects pay less attention to the issue of maintenance and operation challenges of the building in use". (Code no. 001). This participant also has 30 years' experience and also involved in managing building procurement processes as well as managing the buildings in operation.

➢ *"It is not their primary concern how the building operates after construction".* (Code no. 002). Although this participant is less than 10 years in the industry, he sits on the management side of a renowned building developer company that has won several awards for the several buildings they have been involved with.

All three (3) study tools; the interviews, online and manual surveys, concluded that most architects do not give sufficient attention to issues of operation and maintenance in their designs.

4.2 Clients Awareness of O&M Implications

Following the strategy of inductive coding described by Marks and Yardley (2004), which involves drawing themes from the raw data itself, a comment from one of the interviewees was found to be interesting and worth further probing. Interviewee 001 represented a client body. The question about how as a client he would ensure that the building delivered to him was maintainable was put to him. His answer suggested that a skilled member of his team is usually assigned to work with the design team. This member uses his experience to identify any concern on the proposal as regards maintenance or operational challenges that are reasonable. Furthermore, a project management group, responsible for all of the individual projects will receive regular reports and presentations from the design team, and will use their collective skills also to voice out any concern regarding the proposals. This suggested that this client is usually armed with the operation and maintenance implications of his proposed buildings before they are constructed. So the online questionnaire was designed to also find out when LCB owners became aware of the maintenance implications of the buildings delivered to them. Participants were asked to indicate when the client for the exemplar LCB became aware of the maintenance implication of the technologies and when, by their respective experiences they think is best for the client to be aware.

Although opinion was varied, however, results indicated that about 37% of clients became aware of the maintenance implications during the design stage (RIBA stage C – E), 25% became aware while the building is in operation. If the client became aware of the maintenance implication of his proposed technology at the design stage, then it is most likely that the information would have been passed on to the design team, or even emanating from the design team. So to validate this result, the question was reframed and included in the hard copy survey. Reframing the question became necessary because facilities managers whom the survey was targeted at are seldom involved in the design process. The reframed question reads; *"From your experience as a building professional, do you think that clients are usually aware of the operation and maintenance implications of their proposed building before construction?"* Figure 4 presents the results. In this result, only about 29% of the population (mainly facilities managers) agree that clients are usually aware of the maintenance implications while over 71% said no.
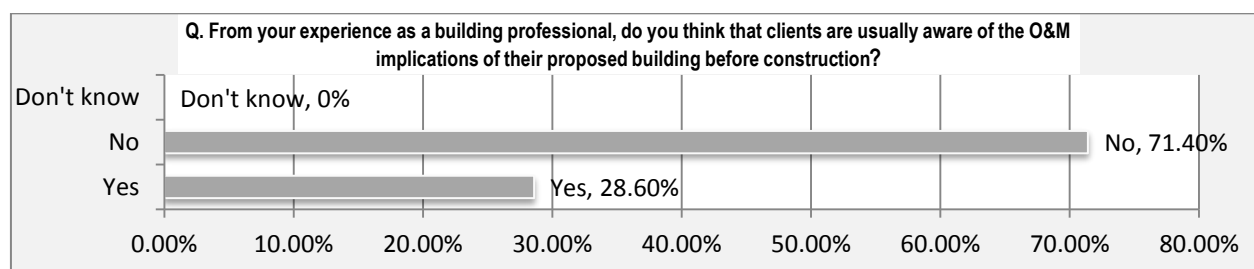
Q. From your experience as a building professional, do you think that clients are usually aware of the O&M implications of their proposed building before construction?								
Don't know	Don't know, 0%							
No							No, 71.40%	
Yes	Yes, 28.60%							

Figure 4: Clients' Awareness of O&M Implications before construction (Hard Copy Survey)

However, it is also noteworthy that the result of the first survey also shows that 25% of participants (mainly architects) indicate that clients became aware while the building is in operation. Another 25% said it was either during construction or during handing-over/commissioning and 12.5% do not know when. So the conclusion here would be that, in most cases clients are not aware of the maintenance implications of their proposed buildings before construction. 50% of the respondents in the online survey suggested that it would be best practice for clients to be aware of the maintenance implications of their proposed developments at the RIBA stage C – E of the design process. Another 37.5% opined that the pre-construction/ tender stage (RIBA stage F – H) will be the best period. Both stages are before the construction stage. That means 87.5% are of the opinion that clients should be aware of the O&M implications of the design before construction.

4.3 Proof of Maintainability

Commenting freely on what could be done to make architects think maintenance while designing, 60% of the interviewees said it will be necessary to prove how the building will be operated and maintained, before it is constructed. Interviewee code no. 004 commented thus;

"The first thing that is going to happen is that as the standards for low carbon buildings gets tighter, then architects will be required to prove that their buildings are going to perform and I suspect what is going to happen is that the building regulations will start to incorporate a maintenance regime or some kind of test after a year to see how it is working. The rest is how people feel in the building and that I think is bound to change". Interviewee 003 suggested that the architects need to demonstrate how the building operates "before it is up".

The second survey, directed at facilities managers was used to validate this opinion mainly because the facilities managers are those who engage with the building longer than other built environment professionals. In most cases, they represent the client, and in economic terms, they are consumers of the designers' and contractors' products. Tunstall (2006) argued that the consumer is in the best position to judge the success or failure of a product, and that their level of expectation is crucial. The result is shown on figure 5. In total about 93% of the study population agree or strongly agree that building designers need to demonstrate that the buildings they design will be maintainable (safely and economically maintained) before it is constructed.
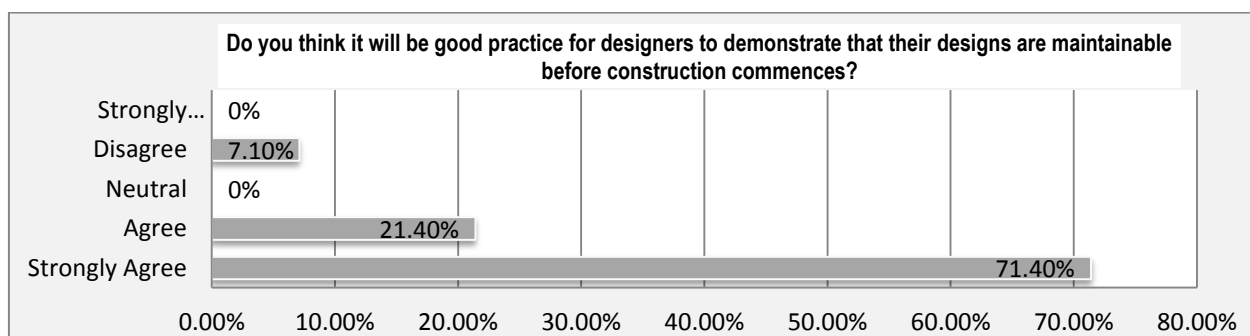
Do you think it will be good practice for designers to demonstrate that their designs are maintainable before construction commences?

Response	Percentage
Strongly…	0%
Disagree	7.10%
Neutral	0%
Agree	21.40%
Strongly Agree	71.40%

Figure 5: Need to Prove Maintainability

In the opinion of Interviewee 001, this is already a requirement by law; "*the CDM regulations require designers to think through these things* (operation and maintenance), *the issue is how well do they do this?"* The question of how well they do this seems to have been answered in the previous sections. Section 6.6.1 concludes that most architects do not give sufficient attention to issues of maintenance. In section 6.6.2 it was noted that most clients are never aware of the maintenance implications of their buildings before they are built, which by extension could imply that the designers never communicated that to the clients, probably because it was neither part of the clients' brief nor the design brief. The issue of how well the law is being obeyed suggests that the best solution to improving designers' attitude to operability and maintainability should not end in legislation, but should extend to a cultural or process change. This change is inevitable if low carbon buildings need to be delivered to clients' satisfaction and to achieve value for money.

CIRIA (2009) corroborates the stands of interviewee 001. It argued that the obligation for building designers to provide their clients with safely and economically maintained and repaired assets, as well as whole-life considerations are already enshrined in law. However, it is often not well done and there is no practical guidance to this effect (Ibid). CIRIA (2009) also suggested a *'cultural shift in work attitudes and thinking';* on the part of both clients and designers.

This suggests that there has to be a change in what clients expect from designers, and designers need to re-orientate themselves in the way they design. When clients constantly demand from their design consultants what the maintenance and operational implications would be (in terms of 'how' and 'how much'), then designers will sit up to their social responsibility of providing buildings with *'commodity, delight and firmness'* (Vitruvius in Strelitz, 2008). Tunstall, (2006) describes firmness to refer to 'Constructability and Durability'. Meaning that, designers need to design buildings and their fixtures to be both constructible and durable.

5. CONCLUSION

The results outlined in this study reinforce the principle of duty of care, discussed in section 2.3. The principle places duty on designers to take reasonable care to ensure that their clients do not suffer the burden of high cost of maintenance and general under-performance in terms of energy savings and indoor air quality; thereby achieving good value for money. Meeting this requirement entails ensuring maintainability in design as deduced from the findings of this study. By applying the principles of maintainability, the problems of product support and maintenance of complex systems can be reduced, if not eliminated as opined by Blanchard and Lowery (1969).

Also, by the concept of 'right first time' discussed also in Frank (2014) and Sharma (2013), it is imperative for designers and their clients to take steps early enough to get the building right at the outset, to avoid the extra cost that will be involved in early replacement of components and unnecessary repairs. Therefore putting in place a system or process that can facilitate compliance to maintainability considerations will no doubt enhance a re-orientation in designers' attitudes towards maintainability as discovered from the results of this study. Designers need to prove the operability and maintainability of buildings they have designed, before construction and clients need to demand this proof in order to be able to make informed decisions on the Operation and maintenance implications of their proposed buildings before they are erected.

6. REFERENCES

ARDITI, D. & Nawakorawit, M., 1999a. Designing buildings for maintenance: designers' perspective. *Journal of Architectural Engineering,* 5(4), pp. 107 - 116.

ARONSON, J., 1994. *A Pragmatic View of Thematic Analysis.* [Online] Available at: http://www.nova.edu/ssss/QR/BackIssues/QR2-1/aronson.html [Accessed 11 December 2012].

AVIS, 2011. *World Carbon Reduction Targets.* [Online] Available at: http://www.avis.ca.za/main.aspx?ID=1634 [Accessed 24 Nonember 2011].

BLANCHARD Jr., B. S. & Lowery, E. E., 1969. *Maintainability- Principles and Practices.* s.l.:McGraw-Hill.

BRE, n.d.. *Low Carbon Development in East England.* [Online] Available at: http://www.rudi.net/node/20144 [Accessed 29 november 2011].

BURNARD, P., 1991. A Method of Analysing Interview Transcripts in Qualitative Research. *Nurse Education Today,* Volume 11, pp. 461 - 466.

BusinessDictionary.com, n.d.. *Maintainability.* [Online] Available at: http://www.businessdictionary.com/definition/maintainability.html [Accessed 11 April 2011].

CASSIDY & Pinkard Colliers, n.d.. *Sustainable Building Operation and Maintenance.* [Online] Available at: http://www.cassidypinkard.com/wmspage.cfm?parm1=9446 [Accessed 10 April 2010].

CHEW, M.Y.L, 2010. *Maintainability of Facilities for Building Professionals.* Singapore: World Scientific Publishing Co. Pte. Ltd..

CIRIA - Construction Industry Research and Information Association, 2009. *C686 - Safe Access for Maintenance Repair: Guidance for Designers,* London: CIRIA.

CRESWELL, J. W., 2009. Research Design - quantitative, qualitative, and mixed method approaches. 3rd ed. London: SAGE Publications Ltd..

DAWOOD, S., Crosbie, T., Dawood, N. & Lord, R., 2013. Designing Low Carbon Buildings: A framework to reduce energy consumption and embed the use of renewables. *Sustainable Cities and Societies,* Volume 8, pp. 63 - 71.

DESIGNING BUILDINGS LTD, 2013. *DESIGN LIABILITY.* [ONLINE] Available at: http://www.designingbuildings.co.uk/wiki/Design_liability [Accessed 27 March 2013].

DUNSTON, P. S. & Williamson, C. E., 1999. Incorporating Maintainability in Constructibility Review Process. *Journal of Management in Engineering,* 15(5), pp. 56-60.

FRANK, O.L, 2011. Exploring the Potential of the O&M Manual as the Designers' Tool for Solving Maintenance Problems of Public Buildings in Nigeria. Hong Kong, Faculty of Construction and Land Use, The Hong Kong Polytechnic University, pp. 2-9.

FRANK, O. L., 2014. Exploring a best practice approach to oprability and maintainability of low carbon buildings in the UK, s.l.: University of Nottingham.

FRANK, O. L. & Daminabo, F. F., 2014. *The Role of architects in ensuring sustainable maintenance of public buildings in Nigeria.* Geneva Switzerland, World Society of Sustainable Energy Technologies.

HARRIS, S., February 2004. Public Private Partnerships: Delivering Better Infrastructure Services. Washington DC, s.n.

HC - House of Commons, 17 June, 2010. HC 68 - The Performance and Management of Hospital PFI Contracts: Report by the Comptroler and Auditor General (session 2010-2011), London: The Stationary Office.

HENSON, J. L. & Lamberts, R., 2011. *Building Performance Simulation for Design and Operation.* Abingdon, Oxen: Spon Press.

House of Commons Committee of Public Accounts, 18 January 2011. *HC 631 PFI in Housing and Hospitals (Fourteenth Report of Session 2010 - 11),* London: The Stationary Office Limited.

ITS - Institute for Telecomunication Science, 1996. *Definition: Maintainability.* [Online] Available at: www.its.bldrdoc.gov/fs-1037/dir-022/_3198.htm [Accessed 11 April 2011].

LUSH, D., 1994. Services Design and Maintenance. In: E. D. Mills, ed. *Building Maintenance and Preservation - A Guide to Design and Management.* 2nd ed. Oxford: Butterworth-Heinemann Ltd., pp. 63 - 75.

MARKS, D. F. & Yardley, L., 2004. *Research Methods for Clinical and Health Psychology.* s.l.:SAGE Publishers.

MILLS, E. D., 1994. Design and Building Maintenance. In: E. D. Mills, ed. *Building Maintenance and Preservation - A Guide to Design and Management.* 2nd ed. Oxford: Butterworth Heinemann, pp. 1 - 15.

MONBIOT, G., 2010. The bill for PFI contracts is an outrage. Let us refuse to pay this odious debt. *guardian.co.uk*, 22 November.

National Audit Office, 25 June, 2010. HC 71- PFI in Housing: Report by the Comptroller and Auditor General (Session 2010 - 2011), London: The Stationary Office.

NORMAN, J., 2010. PFI Firms should shair thier gains. *guardian.co.uk*, 25 November.

Office of Research Facilities (ORF), 2006. *Policy for Post Occupancy Evaluation.* [Online] Available at: http://orf.od.nih.gov/PoliciesAndGuidelines/ORFPolicies/POEPolicy.htm [Accessed 04 May 2011].

P.J. DERBNEY, Partner, Cartwright and Lewis, Solicitors, 1998. *Duty of Care: Common Law Negligence,* s.l.: The Student Activities Safety Association, Leeds University Union.

PRETORIUS, f. et al., 2008. *Project Finance for Construction & Infrastructure.* Oxford: Blackwell Publishing Ltd..

RIBA - Royal Institute of British Architects, 2009a. *Climate Change Toolkit: 01 Climate Change Briefing,* London: RIBA.

RUSKIN, J., 1895. *The Seven Lamps of Architecture.* 6th ed. London: George Allen.

SEELEY, I. H., 1976. *Building Maintenance.* 1st ed. London: Macmillan Press Ltd..

SEELEY, I. H., 1987. *Building Maintenance.* 2nd ed. London: Macmillan Press.

SHARMA, K., 2013. *The concept of doing something "FIRST TIME RIGHT".* [Online] Available at: http://www.speakingtree.in/spiritual-blogs/seekers/self-improvement/the-concept-of-doing-something-first-time-right [Accessed 20 April 2013].

SMITH, C. S., 2004. PFI Culture. *ARQ - Architectural Research Quarterly,* 8(1), pp. 7 - 8.

SPEAIGHT, A. & Stone, G., 2010. *Architect's Legal Handbook- The Law for Architects.* Oxford: Elsevier - Architectural Press.

SZOKOLAY, S. V., 2008. Introduction to Architectural Science: the basis for sustainable design. 2nd ed. Oxford: Elsevier.

US. Department of Energy (DOE), 1999. *Low Energy Building Design Guidelines.* [Online] Available at: http://www.eren.doe.gov/femp/ [Accessed 24 November 2011].

ZUBAIRU, S., 2010. The National Building Maintenance Policy for Nigeria - The Architects' Perspective. Abuja, Architects Registration Council of Nigeria, pp. 1 - 12.

234: Theoretical investigation of soil-based thermal energy storage system for greenhouses

Erdem Cuce[1], Yate Ding[1],
Saffa Riffat[1], Chungui Lu[1]

1 Department of Architecture and Built Environment, Faculty of Engineering,
University of Nottingham, University Park, NG7 2RD Nottingham, UK

Abstract: In this short communication, a novel thermal energy storage system for greenhouses is presented. The novel system is based on directly heating a particular mass of soil through the solar power and utilizing the energy stored in critical months such as November, December, January and February. The target mass of soil is placed beneath the greenhouse with a height of 2m and the boundaries are well-insulated via vacuum insulation panels to provide adiabatic conditions yielding to no heat loss from the edges. Through electric heaters placed inside the target mass of soil, thermal energy is stored inside the soil via the power coming from photovoltaic (PV) panels fixed on the roof of the greenhouse. A specific thin film PV glazing technology called heat insulation solar glass (HISG) is preferred for the power input to the greenhouse. As the first aim of the research, heating demand of the greenhouse is determined for each month. Temperature difference and overall heat transfer coefficient between indoor and outdoor environment are considered to be independent variables in the analyses. Secondly, soil-based thermal energy storage system is introduced and its potential contribution to the heating demand is discussed. The preliminary results indicate that the soil mass is a dominant parameter in soil temperature and hence the thermal energy storage capacity. For a soil mass of 250 tonne, around 600K soil temperature is achieved by the end of year, which is very remarkable.

Keywords: Greenhouses, energy consumption, heating demand, thermal energy storage, solar power

1. INTRODUCTION

In this short communication, a novel thermal energy storage system for greenhouses is presented. The novel system is based on directly heating a particular mass of soil through the solar power and utilizing the energy stored in critical months such as November, December, January and February. The target mass of soil is placed beneath the greenhouse with a height of 2m and the boundaries are well-insulated via vacuum insulation panels to provide adiabatic conditions yielding to no heat loss from the edges. Through electric heaters placed inside the target mass of soil, thermal energy is stored inside the soil via the power coming from photovoltaic (PV) panels fixed on the roof of the greenhouse. A specific thin film PV glazing technology (heat insulation solar glass) is preferred for the power input to the greenhouse [1-4].

2. METHODOLOGY

Within the scope of this short communication, theoretical investigation of this novel energy storage system is given. As the first aim of the research, heating demand of the greenhouse is determined for each month. Temperature difference and overall heat transfer coefficient between indoor and outdoor environment are considered to be independent variables in the analyses. Monthly heating demand of the greenhouse is determined as illustrated in Figure 1 depending on the aforesaid independent variables. As it is understood from the 3D graphs that the critical months in heating demand are December, January and February as expected for Nottingham. The calculations are made with respect to characteristic climatic conditions of Nottingham given in Figure 2 and 3 for ambient temperature and relative humidity, respectively.

3. RESULTS AND DISCUSSION

The main governing equation of the heat loss from the greenhouse is given by:

$$Q = U A \Delta T$$

where U is the overall heat transfer coefficient between indoor and outdoor environment, A is the heat transfer surface area and ΔT is the temperature difference. In Figure 4, maximum solar power and its available part are illustrated for the climatic conditions of Nottingham. The figures are provided for per m^2 for easier understanding and data utilization. Although Nottingham does not have abundant solar energy potential, there is a remarkable potential in the summer time to be considered for thermal energy storage. In the second part of the research, soil temperatures are calculated for each month and for various amounts of soil. The driving governing equation to determine the soil temperatures is given by:

$$Q = m \, c_p \, \Delta T$$

where m is the mass of soil, c is the specific heat capacity of soil and ΔT is the temperature difference. As considering the potential soil mass beneath the greenhouse, the soil mass as an independent variable is varied from 250 to 2000 tonne and the soil temperatures are calculated as shown in Figure 5. As it is clearly seen from the results that the soil mass is a dominant parameter in soil temperature and hence the thermal energy storage capacity. For a soil mass of 250 tonne, around 600 K soil temperature is achieved by the end of year, which is very remarkable.

4. CONCLUSIONS

This short communication clearly indicates that solar powered soil-based thermal energy storage for greenhouses is attractive and can be preferred to contribute in reducing operational costs of greenhouses.

5. REFERENCES

1.   Cuce E, Young CH, Riffat SB. Thermal insulation, power generation, lighting and energy saving performance of heat insulation solar glass as a curtain wall application in Taiwan: A comparative experimental study. Energy Conversion and Management 2015; 96: 31–38.

2.   Cuce E, Young CH, Riffat SB. Thermal performance investigation of heat insulation solar glass: A comparative experimental study. Energy and Buildings 2015; 86: 595–600.

3.   Cuce E, Riffat SB. A state-of-the-art review on innovative glazing technologies. Renewable and Sustainable Energy Reviews 2015; 41: 695–714.

4.   Cuce E, Young CH, Riffat SB. Performance investigation of heat insulation solar glass for low-carbon buildings. Energy Conversion and Management 2014; 88: 834-841.
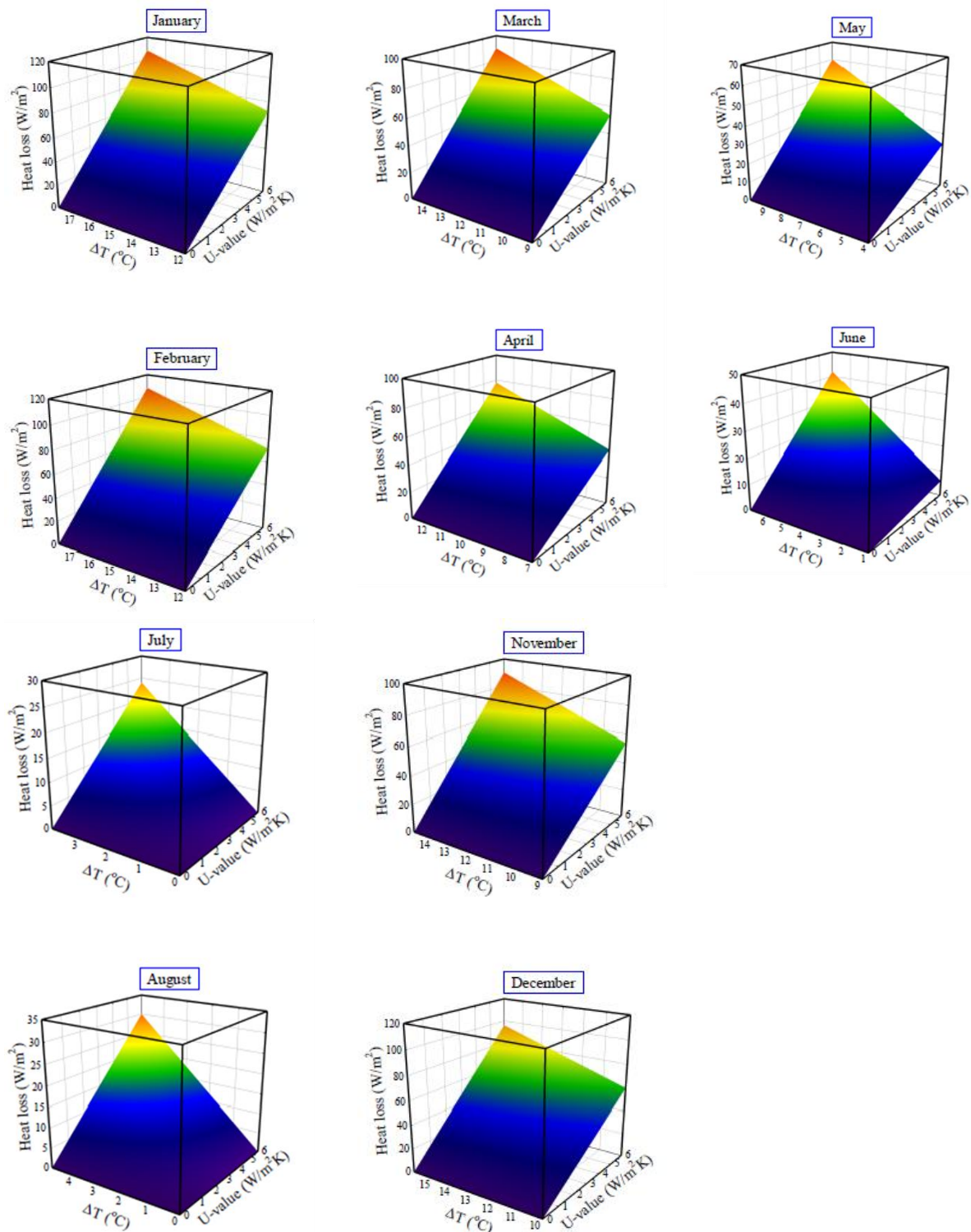

Figure 60: Monthly heating demand of the greenhouse for various temperature differences and overall heat transfer coefficients.
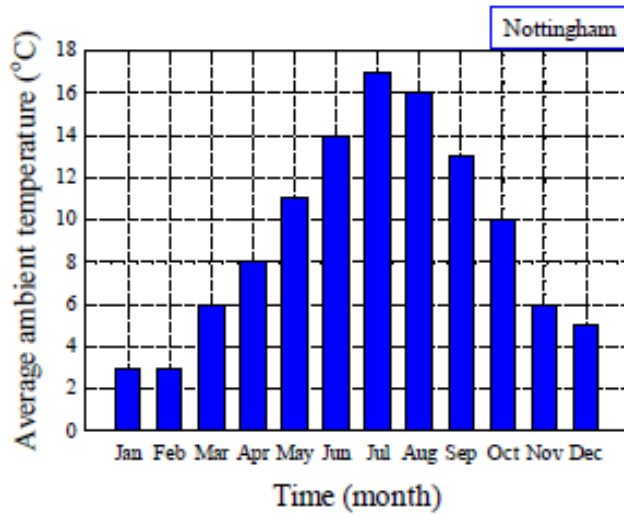
681

Figure 2: Monthly average ambient temperatures for Nottingham.
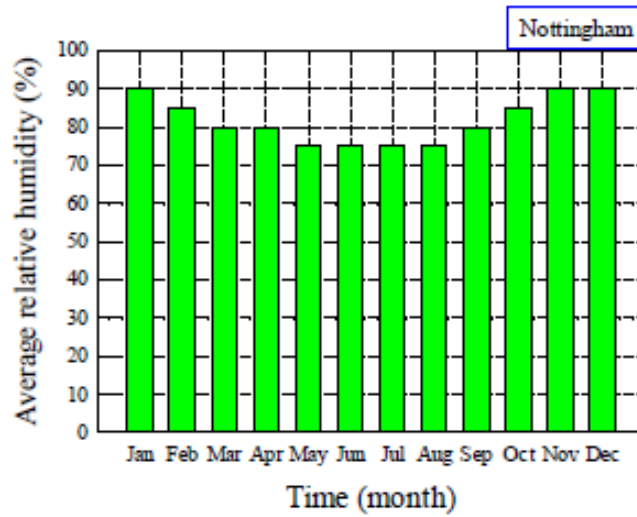

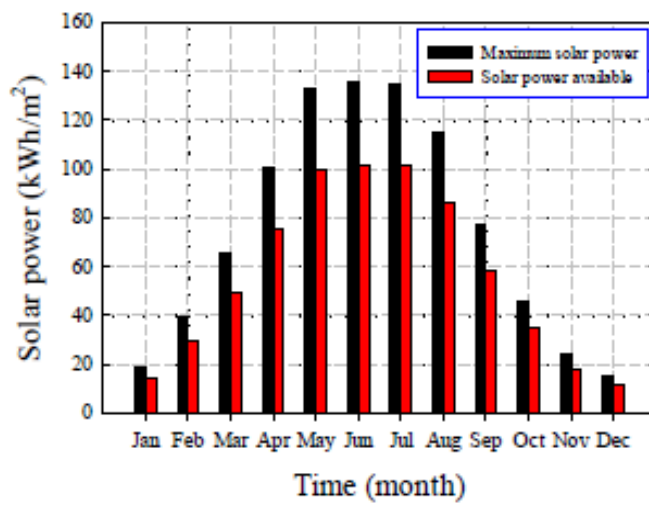Figure 3: Monthly average relative humidity values for Nottingham.

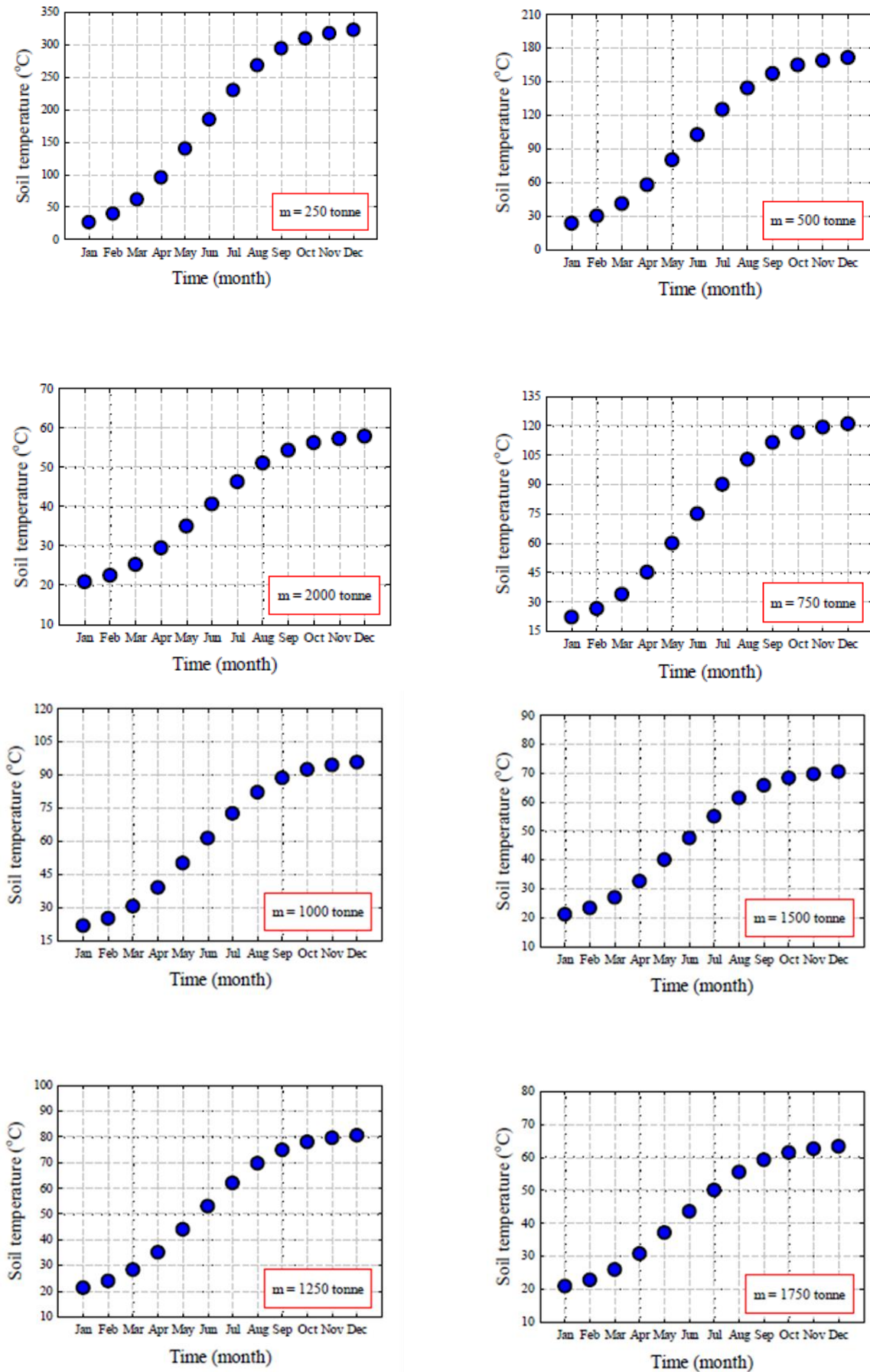Figure 4: Monthly solar power potential and available power for Nottingham.

Figure 5: Monthly average soil temperatures achieved through seasonal thermal energy storage system.

312: Kinetics of direct CO_2 capture from ambient air Using K_2CO_3/Al_2O_3 composite sorbent

Janna VESELOVSKAYA[1], Vladimir DEREVSCHIKOV[2], Aleksey Okunev[3]

1 Boreskov Institute of Catalysis, Pr. Ak. Lavrentieva, 5, Novosibirsk, 630090, Russia; Novosibirsk State University, Pirogova str., 2, Novosibirsk, 630090, Russia; Research and Educational Center for Energy Efficient Catalysis in Novosibirsk State University, Pirogova str., 2, Novosibirsk, 630090, Russia, jvv@catalysis.ru
2 Boreskov Institute of Catalysis, Pr. Ak. Lavrentieva, 5, Novosibirsk, 630090, Russia; Novosibirsk State University, Pirogova str., 2, Novosibirsk, 630090, Russia; Research and Educational Center for Energy Efficient Catalysis in Novosibirsk State University, Pirogova str., 2, Novosibirsk, 630090, Russia
3 Novosibirsk State University, Pirogova str., 2, Novosibirsk, 630090, Russia, Boreskov Institute of Catalysis, Pr. Ak. Lavrentieva, 5, Novosibirsk, 630090, Russia

The composite material $K2CO3/Al2O3$ is a promising solid absorbent for direct $CO2$ capture from ambient air. In the current work the kinetics of $CO2$ absorption by this composite material was studied in the perfectly mixed reactor. The dependence of $CO2$ absorption rate on temperature and characteristic grain size of the composite sorbent was investigated. It was revealed that the total $CO2$ uptake decreases in the temperature range from 50 to 80oC. Comparison of $CO2$ absorption kinetics of by fractions of the composite with characteristic grain sizes of 0.8-1.0 mm and 1.6-2.0 mm showed that the initial rate of $CO2$ absorption inversely depends on characteristic grain size of the composite material, which indicates that the absorption process is limited by mass transfer. The results obtained are of interest for the capture of air-borne $CO2$ with subsequent renewable methane production using H2 from alternative sources of energy.

Keywords: renewable energy storage, direct air capture, carbon dioxide, potassium carbonate, alumina

1. INTRODUCTION

The major challenge of our time is filling the gap between energy supply and demand with clean, reliable and inexpensive energy. Given depletion of fossil fuels, renewable energy technologies will need to play a bigger role in the future. However, there are still some unresolved problems that prevent these technologies from being economically viable on a large scale.

One of the main issues of power systems based on renewables, such as wind and solar energy, is volatility of the power supply. Hence, a storage technology is needed for electrical energy, produced by these fluctuating sources. The use of excess renewable electricity for production of synthetic fuels offers a realistic solution to this challenge, which enables an offsetting in the time gap between power production and its consumption.

The surplus electricity generated by renewables can be used for water electrolysis in order to produce hydrogen: $2H_2O \xrightarrow{electrolysis} 2H_2 + O_2$.

Hydrogen is considered to be a perspective fuel for low-carbon economy, but there are still unresolved safety problems regarding its transportation and storage. Therefore, it is reasonable to use the generated hydrogen for production of a conventional hydrocarbon fuel, e.g. methane, which can be obtained by Sabatier process: $CO_2 + 4H_2 \rightarrow CH_4 + 2H_2O$. The synthetic renewable methane, which corresponds to chemically normal natural gas, can be injected into the existing gas network or stored and utilized on demand.

It is very important for sustainable development that renewable methane can be produced using carbon dioxide captured from ambient air. It is well known that CO_2 is the major anthropogenic greenhouse gas which contributes to global climate change. Direct CO_2 capture from ambient air (a.k.a. "direct air capture", DAC) offers more flexibility compared to conventional source point capture and can potentially be "carbon negative" if a renewable energy source is used to drive the process. Incorporation of the DAC unit with into the energy storage system offers an opportunity to use anthropogenic carbon dioxide as a valuable feedstock for the production of renewable methane which can be utilized in the heating market or as a fuel for transportation.

Carbon dioxide capture from ambient air is more challenging than conventional carbon capture from flue gases because of very low concentration of CO_2 in air (~ 400 ppm) and the necessity to operate in the presence of moisture excess at ambient temperature and pressure. The most developed DAC technologies are based on carbon dioxide absorption by aqueous alkali solutions. The major drawback of this approach is that the regeneration of these solutions is generally multi-stage and energy intensive.

Potassium carbonate is a well-known solid inorganic chemisorbent which reacts with atmospheric CO_2 in the presence of water vapour forming potassium bicarbonate: $K_2CO_3 + H_2O + CO_2 \rightarrow 2KHCO_3$.

The main problem with using bulk potassium carbonate for CO_2 absorption purposes is low carbonation rate (Okunev, 2000, p. 355). This problem can be solved by dispersing K_2CO_3 particles inside a porous support material. Composite materials "potassium carbonate inside a porous matrix" are known to be effective sorbents for capturing carbon dioxide from wet flue gases (Hayashi, 1998, p. 185; Lee, 2006, p. 385, Okunev, 2000, p. 355; Zhao, 2006, p. 4683).

Recently, it was also shown that K_2CO_3/γ-Al_2O_3 composite is a promising material for CO_2 capture directly from ambient air (Veselovskaya, 2013, p. 332). The composite was able to absorb CO_2 directly from ambient air without any pretreatment (such as drying) and showed great thermal stability in multiple temperature-swing absorption (TSA) cycles. However, a room for improvement of the composite materials CO_2 absorption properties still exists. The aim of this work was to study kinetics of CO_2 absorption form ambient air by K_2CO_3/γ-Al_2O_3 composite material in order to understand which factors define the rate of CO_2 capture.

2. MATERIAL AND METHODS

2.1 Composite Sorbent Preparation and Characterization

Composite sorbent K_2CO_3/γ-Al_2O_3 was prepared by dry impregnation method, described in detail in (Veselovskaya, 2013, p. 333). Granular γ-Al_2O_3 (A-64) produced by JSC «Angarsk Catalysts and Organic Synthesis Plant» was used as a host matrix. Cylindrical alumina granules with diameter of 3 mm and typical length of 4-6 mm were filled with 40 wt. % aqueous solution of potassium carbonate, dried at 100°C for 24 h and then calcinated at 300°C for 2 h. Potassium loading for the composite sorbent determined by means of atomic absorption spectroscopy is 12.5 wt. %, which is equivalent to 22.1 wt. % of K_2CO_3. The resulted product was crushed and sieved to obtain the desired particle size range fractions: 1.6-2.0 mm and 0.8-1.0 mm.

The phase composition for the samples of the composite sorbent was determined from powder X-ray diffraction (XRD) patterns which were obtained on a Brucker D8 Advance diffractometer using Cu K$_\alpha$ radiation. Diffraction intensities were measured with the LynxEye position sensitive detector (2.9° angular range). XRD patterns were collected in 2θ range 10-70°, with 0.02° step size and 2s collection time. Variation of the phase composition of the composite sorbent owing to heating and cooling of the composite sorbent in air were studied by XRD analysis *in situ* by Siemens D-500 X-ray diffractometer equipped with graphite monochromator on the diffracted beam using Cu K$_\alpha$ radiation. Diffraction patterns were detected in the 10°-50° (2θ) region by points with the 0.05° (2θ) step.

2.2 CO_2 absorption in the perfectly mixed reactor

CO_2 absorption kinetics by the composite material was studied using the perfectly mixed laboratory reactor), schematically shown in Figure 1. In a perfectly mixed reactor, concentrations and temperature are uniform and a high gas velocity around the particles of the sorbent allows avoiding interparticle transport limitations.
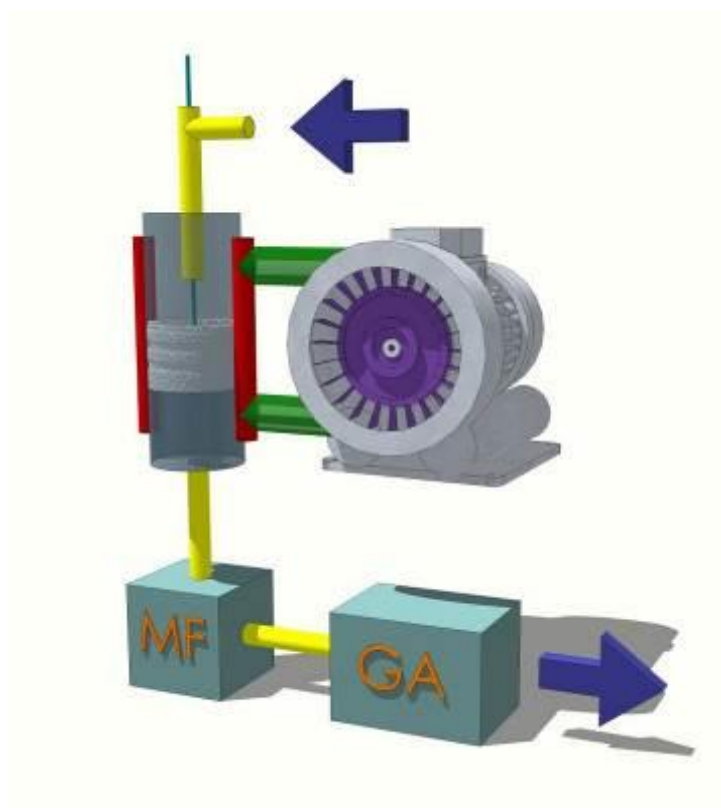

Figure 1. The perfectly mixed reactor for measuring CO_2 absorption from air (MF = mass flowmeter, GA = gas analyser).

The mixture of sorbent particles and quartz balls (D = 3 mm) was placed into a cylindrical steel tube reactor 18 mm ID located inside an electrical heater. Quartz balls were used for the improvement of heat and mass transfer in sorbent bed. The typical mass of the composite material loaded was 0.2 g.

Before the measurement of CO_2 absorption from air, a sample of the composite sorbent was regenerated at 300°C inside the reactor, as the air from compressed air line was purged directly through the reactor without any mixing. After that, the reactor was cooled down with no air purging. This temperature was maintained constant during the absorption experiments. Temperature monitoring during the whole experiment was carried out using a thermocouple, installed in the centre of the bed.

During the absorption experiment air from compressed air line was preliminarily humidified by passing it through a water evaporator, placed inside a thermostat at T=25°C. The outlet flow rate of air during the isothermal absorption experiment was controlled by the mass flowmeter SMC PFMV-5 and maintained 0.4 dm^3/min. Perfect mixing in the reactor was achieved by circulating air by means of the external pump. The rate of gas mixing in the reactor was 12 times more than outer flow rate. The initial CO_2 concentration in the air was 530-560 ppm. The outlet CO_2 concentration was measured by gas analyzer OPTOGAZ-500.4C.

3. RESULTS AND DISCUSSION

3.1 The effect of the characteristic grain size

CO_2 absorption kinetic curves for the samples with different characteristic grain size were measured in the perfectly mixed reactor at T=50°C (Figure 2). One can see that the minimal value of outlet CO_2 concentration differs significantly in these experiments, which indicates that the initial rate of CO_2 absorption depends on characteristic grain size of the sorbent.
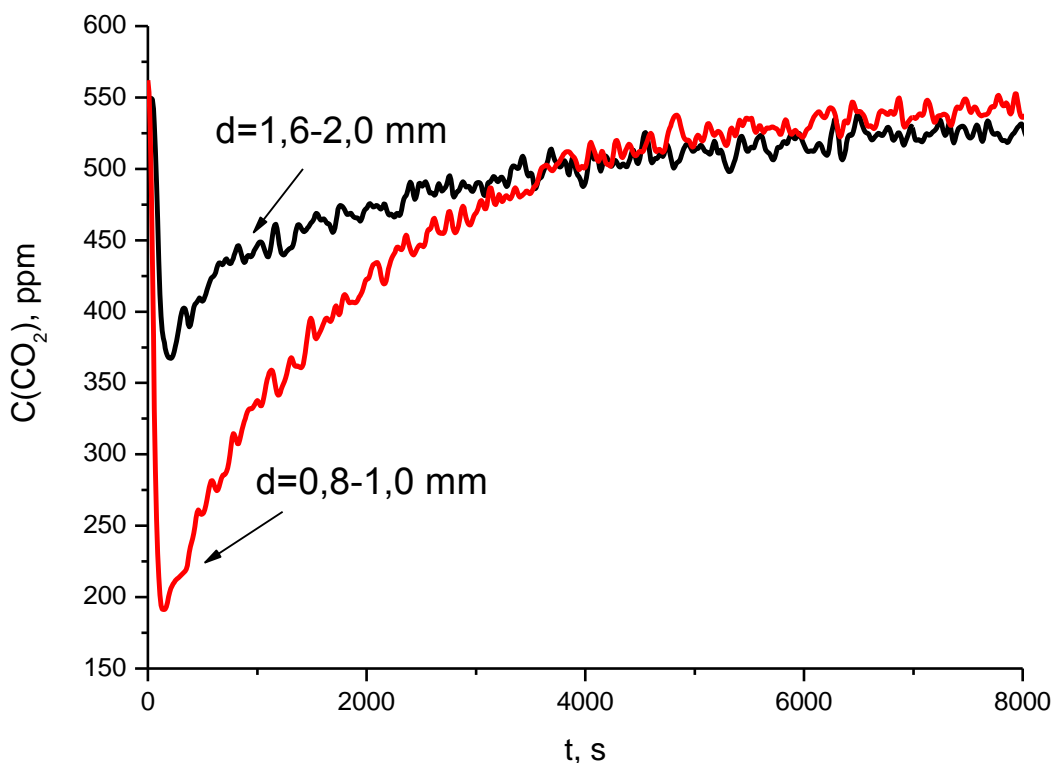

Figure 2. CO_2 absorption curves for the samples with different characteristic grain size (T=50°C, U=0.4 dm^3/min).

The maximal rate of CO_2 absorption was calculated as follows:

Equation 67: The maximal rate of CO₂ absorption

$$W_{max} = \frac{U \cdot (C_o - C_{min})}{m_s}$$

Where:

- W_{max} = the maximal rate of absorption for the sample (in $cm^3(CO_2)/min/g$)
- U = flow rate (in cm^3/min)
- C_0 = inlet CO_2 concentration (in vol.%/100%)
- C_{min} = minimal outlet CO_2 concentration (in vol.%/100%)
- m_s = mass of the sample (in g)

It was demonstrated that the maximal rate of absorption is inversely proportional to the characteristic grain size (Figure 3). The strong dependence of the rate of absorption on characteristic grain size indicates that the process of CO_2 absorption by the composite material is limited by mass transfer within the composite grain.
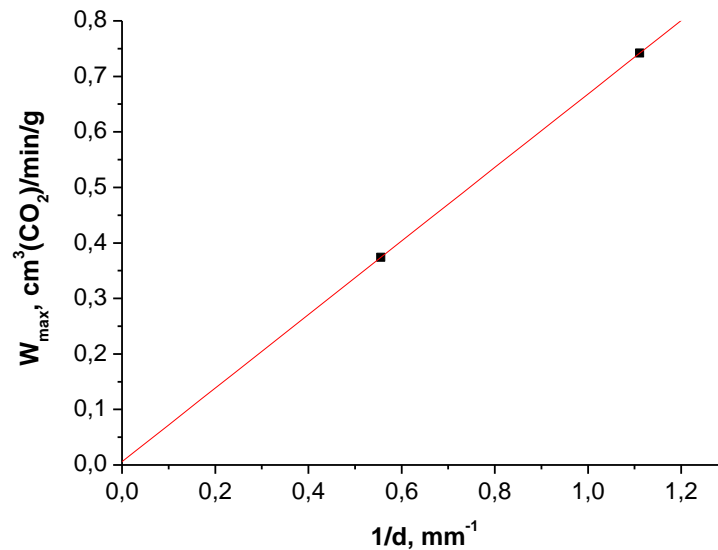
Figure 3. Maximal rate of CO2 absorption versus reciprocal characteristic grain size of the composite particles (experimental conditions: T = 50oC, U = 400 cm3/min, ms = 0.2 g)

CO_2 uptake by the composite material was calculated as follows:

Equation 2: CO₂ uptake calculation

$$a(t) = \frac{U \cdot M_{CO_2}}{V_m \cdot m_s} \int_0^t (C_0 - C(t))dt$$

Where:

- a(t) = CO_2 uptake (in wt.%)
- U = flow rate (in cm^3/min)
- C_0 = inlet CO_2 concentration (in vol.%)
- $C(t)$ = outlet CO_2 concentration (in vol.%)
- m_s = mass of the sample (in g)
- t = time (in s)
- V_m = the molar volume of the ideal gas at the standard conditions (24.4 dm^3/mol)
- M_{CO_2} is molar weight of CO_2 (44 g/mol)

The kinetic curves illustrating CO_2 uptake temporal evolution for the samples with different characteristic grain size are presented in Figure 4. One can see both samples reach the same level of total CO_2 uptake but the time of saturation is much shorter for the sample with characteristic grain size of 0.8-1.0 mm. Thus, reduction of the characteristic grain size allows shortening the duration of the absorption step in the TSA cycle, which is preferable for practical applications.

Figure 4. Kinetic CO_2 uptake curves for the samples with different characteristic grain size: d=0.8-1.0 mm and d=1.6-2.0 mm (T=50ºC, U=0.4 dm³/min)

3.2 The effect of temperature

The effect of temperature on CO_2 absorption behaviour of the composite was studied for the sample with the characteristic grain size of 0.8-1.0 mm. CO_2 absorption curves were measured in the temperature range from 40 to 80ºC. Integral kinetic CO_2 uptake curves calculated from experimental data are presented in Figure 5.
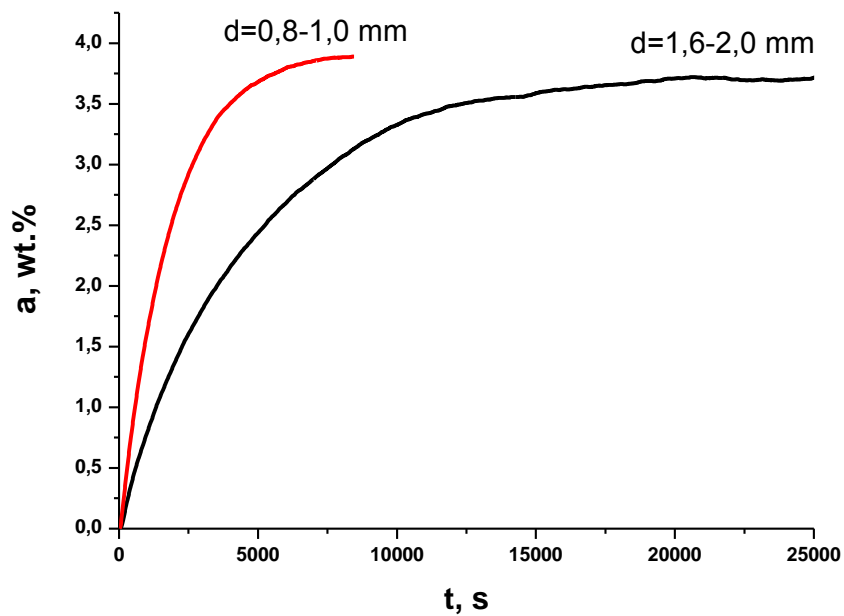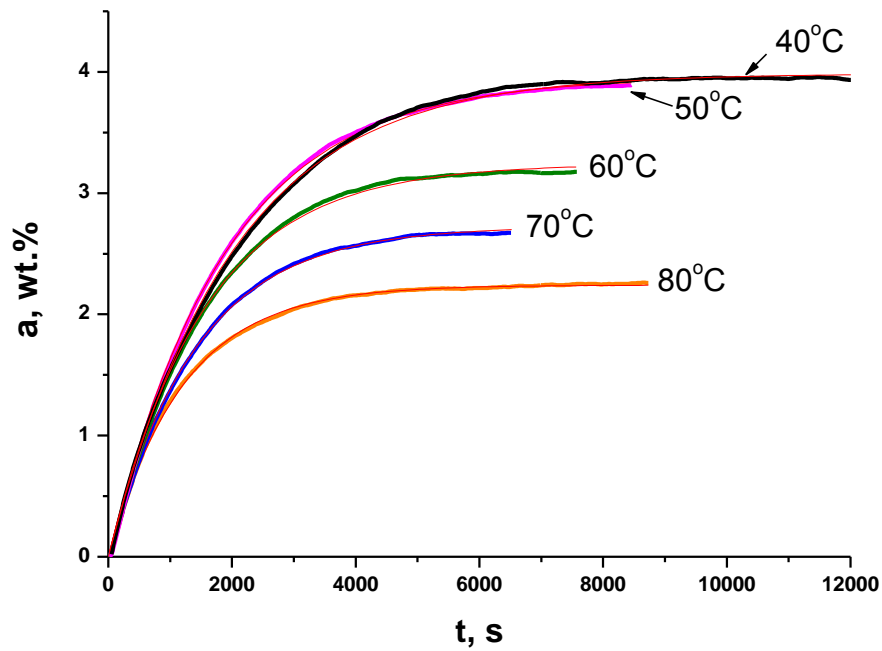
Figure 5. Kinetic CO_2 uptake curves for the samples with different characteristic grain size: d=0.8-1.0 mm and d=1.6-2.0 mm (T=50ºC, U=0.4 dm³/min)

All the curves were approximated by exponential law:

Equation 3: CO_2 uptake approximation
$$a(t) = a_{tot} \cdot (1 - e^{-kt})$$

Where:

- $a(t)$ = CO_2 uptake (in wt.%)
- a_{tot} = total CO_2 uptake (in wt.%)
- k = rate constant (in s^{-1})
- t = time (in s)

The values of a_{tot} и k for all the experiments at different temperatures are presented in Table 1.

Table 46: The values of total CO_2 uptake and rate constant for different absorption temperatures

Temperature of absorption, ºC	a_{tot}, wt.%	$k*10^4$, s^{-1}
40	4.0	5.0
50	4.0	5.3
60	3.2	6.4
70	2.7	7.1
80	2.2	8.3

It was demonstrated that total CO_2 uptake of the sample monotonously decreases in the temperature range from 50 to 80ºC. On the other hand, the values of the total CO_2 uptake are the same for experiments conducted at T=40ºC and T=50ºC. Apparently, the total amount of CO_2 captured by the composite material is defined by absorption equilibrium in the system. In order to reach a maximal saturation of the material with CO_2 the absorption process should be conducted at temperature no higher than 50ºC.

The crystalline products of CO_2 absorption at different temperatures have been characterized by means of XRD analysis (Table 2). It was demonstrated that phase composition is not the same for the samples saturated with CO_2 at 40 and 80ºC. After CO_2 absorption at 40ºC the crystalline phases of potassium bicarbonate $KHCO_3$ and potassium dawsonite $KAlCO_3(OH)_2$ are present in the sample, which is in line with our previous results (Veselovskaya, 2013, p. 335). On the other hand, XRD pattern for the sample after CO_2 absorption at 80ºC does not show characteristic reflections for potassium bicarbonate or potassium dawsonite. The only crystalline phase detected for the latter sample is highly defected potassium carbonate K_2CO_3. Thus, the products of CO_2 absorption are X-ray amorphous if the absorption process takes place at 80ºC. The observed difference in phase composition between these 2 samples confirms the hypothesis that absorption equilibrium in the system defines the value of CO_2 uptake at given temperature.

Table 2: Phase composition for samples of the composite (d=0.8-1.0 mm) after CO_2 absorption at different temperatures

Temperature of absorption, oC	Crystalline phases
40	KHCO3, KAlCO3(OH)2
80	K2CO3 (defected)

4. CONCLUSIONS

Kinetics of CO_2 absorption by K_2CO_3/Al_2O_3 sorbent was studied in the perfectly mixed reactor. Two fractions of the sorbent (d=0.8-1.0 mm and d=1.6-2.0 mm) were investigated in order to study the grain size effect on kinetic performance of the material. It was shown that the maximal rate of CO2 absorption inversely depends on characteristic grain size of the composite material. Accordingly, the time of saturation with CO_2 (the end of absorption) is much shorter for smaller particles of the sorbent.

The effect of absorption temperature was studied for the sample with characteristic grain size of 0.8-1.0 mm. It was shown that total CO_2 uptake is stable in the temperature range 40-50ºC and is decreasing in in the temperature range 50-80ºC. Apparently, the observed dependence of total CO_2 uptake on temperature is defined by absorption equilibrium of the material with CO_2.

By means of XRD analysis it was shown that temperature of CO_2 absorption also strongly affect phase composition of the composite material. Formation of the crystalline phases of potassium bicarbonate $KHCO_3$ and potassium dawsonite $KAlCO_3(OH)_2$ was observed as a result of CO_2 absorption at T=40ºC. However, these crystalline phases were not formed after CO_2 absorption at T=80ºC.

5. ACKNOWLEDGMENT

6. REFERENCES

HAYASHI, H., Taniuchi, J., Furuyashiki, N., Sugiyama, S., Hirano, S., Shigemoto, N., Nonaka, T., 1998. Efficient recovery of carbon dioxide from flue gases of coal-fired power plants by cyclic fixed-bed operations over K_2CO_3-on-carbon, *Ind. Eng. Chem. Res.* 37, p. 185-191.

LEE, S.C., Choi, B.Y., Lee, T.J., Ryu, C.K., Ahn, Y.S., Kim, J.C., 2006. CO_2 absorption and regeneration of alkali metal-based solid sorbents, *Catal. Today* 111, p. 385-390.

OKUNEV, A.G., Sharonov, V.E., Aristov, Yu.I., Parmon, V.N., 2000. Sorption of carbon dioxide from wet gases by K_2CO_3-in-porous matrix: influence of the matrix nature, *React. Kinet. Catal. Lett.* 71, p. 355-362.

VESELOVSKAYA, J.V., Derevschikov, V.S., Kardash, T.Yu., Stonkus, O.A., Trubitsina, T.A., Okunev, A.G., 2013. Direct CO_2 capture from ambient air using K_2CO_3/Al_2O_3 composite sorbent, *Int. J. Greenhouse Gas Control*, 17, p. 332-340.

ZHAO, C., Chen, X., Zhao, C., 2009. CO_2 absorption using dry potassium-based sorbents with different supports, *Energy Fuels*, 23, 4683-4687.

341: Experimental investigation of impact of diesel particulate filter on performance and emissions of a bharat stage-1 C.I. engine

Pradeep Kumar Gupta[1],[*], Dilip Sharma[1], Shyam Lal Soni[1], Rahul Goyal[1], Dheeraj Kishor Johar[1], Ashok Singh Tanwar[2], Anmesh Kumar Srivastava[1]

1Mechanical Engineering Department, MNIT Jaipur, J L N Marg, Jaipur (Rajasthan), India.
2Carriage Workshop, Indian Railways, Ajmer (Rajasthan), India
Corresponding author. Tel.: +91-9928257700. E-mail: pkrgupta@gmail.com

Automobile emissions are the main source of GHG accumulation in environment. With an increasing concern for world environment, it is of great importance to analyze the reasons for vehicle emissions and to figure out the ways to minimize these emissions without sacrificing vehicle performance. Since old engines produce more emissions and it will be difficult to entirely stop their usage especially in developing and under-developed nations, it is desired that appropriate emission reduction technologies are tested on such old engines to see if these technologies could reduce the emissions from such engines substantially with economical acceptability. This study tried to fulfill this requirement by testing an uncoated wall-flow type ceramic DPF with a Bharat Stage-1, variable speed, direct injection, water cooled, 4 cylinder, C.I. engine in laboratory in India. Engine was run at 1500, 2000, 2500 and 3000 rpm at 0, 25, 50, 75 and 90 Nm torque, both with and without the DPF. Gas analyzer and smoke meter were used to measure emissions. The results, in form of engine performance (BSF and BTE) and smoke, NO_x, CO and CO_2 emissions, were analyzed and conclusions were drawn. It was found that using DPF, particulate matter emissions (smoke) were almost entirely eliminated, without impacting the engine performance adversely, and this was the biggest need. Also, it does not involve a big investment and the regeneration cost is also small. Off-board regeneration was done for maximum effectiveness by taking out and heating the DPF in an electrical resistance furnace at 650oC for 10 hours

Keywords: Diesel Particulate Filter; Particulate matter; Exhaust emissions; Automotive emissions; Emission reduction

1. INTRODUCTION

Old engines will continue to be used in India and other developing / under-developed nations because of the prevailing life-style and low cost of living. Road worthiness is tested as per the year of manufacture and old vehicles will continue to ply on roads fulfilling the emission norms of their respective year of manufacture. These old diesel engines of Bharat Stage I, II and III periods produce lots of harmful emissions, especially smoke or particulate matter, limits for which are substantially reduced in Bharat Stage IV and V standards. Pundir (2001) stated that the air quality in developing countries like India has already reached an alarmingly low level and that most cities in India have already exceeded the National Ambient Air Quality (NAAQ) standards. Nesamani (2010) observed that particulate matter (PM) is a major concern in Indian cities since 60 out of 62 metropolitan cities have already exceeded World Health Organization (WHO) standards (24-h ambient air quality standards) and that one of the leading causes of death in India is air pollution. Pundir (2001) further stated that the increase in this PM concentration is primarily due to automotive emissions which according to him have increased at a faster rate than any other sector. He also commented that 60% of vehicular pollution in India is from the 20% poorly maintained vehicles. Automotive internal combustion engines contribute to 70% of air pollution in city like Delhi.

Ramanathan and Carmichael (2008) informed that black carbon, a major PM component, is reported to be the second strongest contributor to current global warming, after carbon dioxide (CO_2). Bergmann et al. (2009) considered the environmental impact and suspected adverse health effects of PM as the main cause for continuously tightened emission limits for diesel vehicles throughout the world. They felt that implementation of diesel particulate filters (DPF) seems to be essential in light of these regulatory changes and the increasing demand for environment friendly vehicles capable of complying with future regulations. They recommended wall-flow DPF systems to effectively reduce PM mass as well as the number of particles at all sizes, including ultrafine particles.

Numerous epidemiological and toxicological studies have concluded that there are adverse health effects of exposure to ambient particulate matter (PM) (e.g. Pope, 2000; Oberdörster, 2000). Regulatory authorities worldwide are consistently enforcing stricter PM emission limits in the vehicle certification procedure considering the fact that automotive exhaust has long been identified as one of the major contributors to anthropogenic PM. PM, due to its ultrafine size, can easily enter lungs during inhalation which may lead to serious breathing problems. Installation of the best available DPF systems in all diesel vehicles registered after 2011 has been mandated in light of the increasing evidence of the toxicity of diesel PM (which was already classified as carcinogenic) and the proven robustness of the DPF systems (Jeuland et al., 2004; COM, 2005; Mamakos et al., 2013).

Diesel Oxidation Catalyst (DOC), Diesel Particulate Filter (DPF), Selective Catalyst Reduction (SCR) and Exhaust Gas Recirculation (EGR) are some of the pre/after treatment systems designed to chemically treat the exhaust gases of diesel engines, especially PM and NOx. Of these, DOC and DPF technology is widely accepted as it usually removes 90% or more of the PM (soot). Since the particulate filter gets filled with accumulated ash, it needs to be cleaned to keep up the performance. This process of cleaning the DPF is called 'regeneration' in which the collected soot is burnt off at high temperature to leave only a tiny residue of ash. It is done either by passive regeneration which takes place automatically through the use of a catalyst when the exhaust temperature is high or by active regeneration where the electronic control unit (ECU) takes control of the process (Khatri and Sangtani, 2013).

Hence, to minimize the emissions from such old C.I. engines belonging to Bharat Stage III or earlier emission standards, feasibility of use of technologies like DPF needed to be tested with the fuel standards of today. However, it was observed that the biggest challenge to accomplish this would be the regeneration of DPF.

Active regeneration would be difficult and expensive by Indian standards or similar cultural habitats. Regeneration can also be accomplished off-board by heating the DPF at 650^0C in a furnace for 10 hours which was done during this study. This kind of regeneration requires 4 hours for cooling the DPF after regeneration. When numerous people with similar set-up will be there, there will be businesses setting up furnaces for commercial off-board regeneration of DPFs as is being done in advanced countries like the USA. Volvo, in 2010, suggested a Volvo Reman service exchange program covering the DPF, which according to them was the most cost- and time-effective solution. Under this program, their extensive dealer network would store processed filters, for exchange with choked filters for regeneration, in order to keep

uptime to a maximum. They claimed that with this service, the change of DPF will take approx. 1 hour (Volvo, 2010).

DPF may be classified as wall-flow and flow-through depending on their respective filtration mechanism. Flow-through type filters create a smaller pressure drop since they are made of ceramic foam, wire mesh or metal wool. This helps in betterment of fuel efficiency but at the cost of lower filtering efficiency, often below 60%. In contrast, to fulfill the current PM regulations, wall-flow type filters are the most commercialized DPF. Wall-flow type DPF are honeycomb monoliths made of ceramic materials such as cordierite and silicon carbide which consist of a series of parallel channels alternatively plugged at each end to force the exhaust gas flow through the porous filter wall. Hence, porosity of the substrate, the mean diameter of pores and the wall thickness are the main factors deciding the efficiency of wall-flow DPF (Lapuerta et al., 2012).

This study tried to fulfill the requirement of PM reduction by testing an uncoated wall-flow type ceramic DPF with a Bharat Stage-1 C.I. engine in a laboratory set-up in India. It was found that using this DPF, particulate matter emissions (smoke) was almost entirely eliminated (reduced by 79-99%), without impacting the engine performance adversely, and this was the biggest need.

Though there are other pre/after-treatment devices such as DOC, EGR and SCR to control the emission from diesel engines, this paper will focus on Diesel Particulate Filter (DPF) since the device is able to filter out more than 95% of soot particles.

2. EXPERIMENTAL SET-UP

In the current study, a Bharat Stage-1 diesel engine of Mahindra Jeep in India was used in the laboratory set-up. The specifications of the engine are given in table 1. To artificially load the engine and to measure the torque accurately and reliably, an eddy current brake dynamometer (absorption type dynamometer) was coupled to the engine so that the engine RPM and dynamometer RPM was same (1:1). The reaction torque in this dynamometer was sensed by using a load cell with digital indicator. Schematic diagram of the complete laboratory set-up is shown in fig. 1 and the laboratory set-up is shown in fig. 2.

A mild steel cylinder cage was fabricated to hold the DPF. To connect this cage with the exhaust pipe a mild steel cone was fabricated and was joined to the cylinder using 9 bolts. Similarly on the other end of the cylinder, another mild steel cone was joined to connect it to the final exhaust pipe to the atmosphere. To keep DPF tightly intact in the cage as also to reduce the outside temperature of DPF cage, glass wool packing was used between DPF and DPF cage wall. Since the DPF was getting choked after a few hours of running, a strainer was made and welded in the DPF cage as shown in fig. 3. Specifications of the DPF used are shown in table 2.
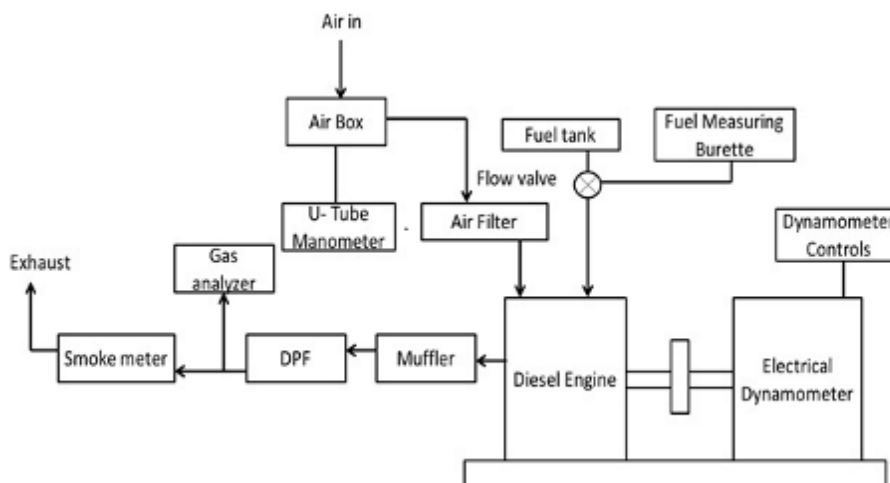

Fig. 1: Schematic diagram of the complete laboratory set-up

Fig. 2: Laboratory set-up showing the diesel engine, dynamometer, DPF cage, muffler and dynamometer panel.

Table 1: Specifications of the engine

S. No.	Particular	Unit	Description
1.	Type of engine	-	C.I. engine
2.	Make and Model	-	Mahindra & Mahindra, XDP 4.90
3.	Valves	-	Overhead, rocker arm operated
4.	Timing	-	Gear operated
5.	Cooling	-	By water
6.	Cylinders	-	4 (in-line arrangement)
7.	Operating cycle	-	4 stroke (order: 1-3-4-2)
8.	Bore	mm	90
9.	Stroke	mm	83
10.	Cubic capacity	cc	2112
11.	Compression Ratio	-	22.4 : 1
12.	Max. Power	bhp	62 at 4500 rpm
13.	Max. Torque	kg.m (Nm)	12.3 (120.5) at 2000 rpm

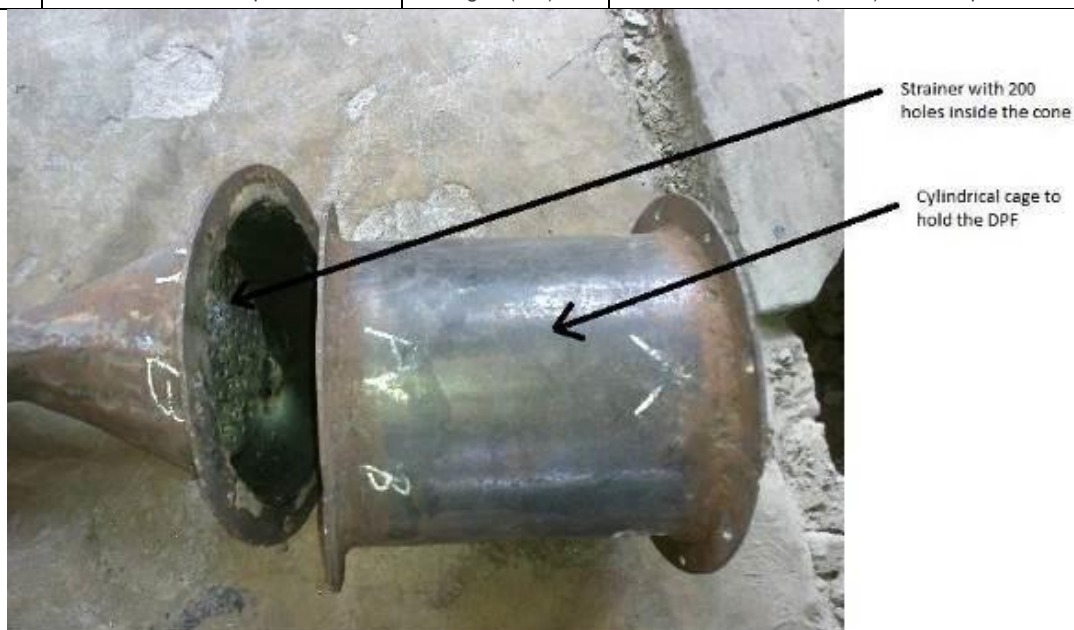*Fig. 3: Cylindrical DPF cage and cone with strainer welded inside.*

Table 2: Specifications of the DPF used

S. No.	Particular	Description
1.	Dimensions	Diameter: 5.66", Length: 6"
2.	Cells per square inch	300 cpsi
3.	Wall thickness	13 mil (1 mil = 10^{-3} inch)
4.	Open Frontal Area	37.1% on inlet
5.	Filtration surface area	1.093 m^2
6.	Coating	Uncoated
7.	Material	Ceramic
8.	Type	Wall-flow type

A cabinet provided for the control panel of the dynamometer had the following instruments:

a) Digital torque indicator (in Nm)
b) Digital RPM indicator (same as engine RPM in this case)
c) Electronic, eddy current dynamometer controller (torque control rotating knob)
d) Excitation current indicator (Amp.) (with 6 Amp. MCB for safety)

To measure the intake air-flow of the engine and for pulsation of intake air, an air-box with a 50 mm orifice was attached to the set-up with a U-tube manometer.

AVL make DITEST (AVL DiGas 4000 light) 5 gas analyzer was used to analyze the exhaust emission from the engine. The 5 gases included NO_x, CO, HC, CO_2 and O_2, out of which CO, HC and CO_2 were measured by NDIR Technique and NO_x and O_2 were measured by electrochemical sensors. It gave HC and NO_x emissions in PPM and that of other gases in percentage. Smoke in exhaust was measured with the help of AVL 437 smoke meter.

3. METHODOLOGY

The experimental investigation of impact of diesel particulate filter on performance and emissions of a Bharat Stage-1 C.I. engine was divided into two steps. In the first step, a series of tests were carried out to evaluate the engine performance and emissions when it was run without DPF (base case). In the second step, DPF was added after the muffler, and the same tests were conducted again to evaluate the engine performance and emissions. For both the steps, observations for performance and emissions were taken for 0, 25, 50, 75 and 90 Nm torque with 1500, 2000, 2500 and 3000 RPM for each torque. Engine could not be run at 3000 rpm with 90 NM torque for 15 minutes as the exhaust temperature rose quite high and the exhaust pipe became red hot. As a precautionary measure, it was decided not to go beyond 90 Nm torque and not to cross 3000 RPM at any torque.

The torque was varied by rotating the emf control knob on the dynamometer panel. RPM was varied by rotating the accelerator wheel on the engine panel. The engine was run for 15 minutes to reach steady state condition before taking the reading at each load and RPM. To measure BSFC and BTE at each load condition, time for 50 ml of diesel consumption was noted. For each load condition, the emissions were noted using AVL 5 gas analyzer and AVL smoke meter.

After recording relevant data, Brake Specific Fuel Consumption (BSFC) and Brake Thermal Efficiency (BTE) were calculated, and graphs were plotted for various performance and emissions parameters against RPM for various loads comparing the same for base case against the case with DPF. Results were then analyzed and conclusions drawn.

Since it was a Bharat Stage-I diesel engine, it produced quite high amount of smoke and the DPF got choked during the test. Hence, it was necessary to regenerate the DPF to continue with the tests. Hence, the DPF was heated in a muffle type, electric resistance furnace (size: 6" X 6" X 12", maximum temperature: 1000°C), at 650°C for 10 hours. After that it required 4 hours for cooling, after which the DPF was again used. DPF, before and after regeneration, is shown in fig. 4(a) and 4(b).

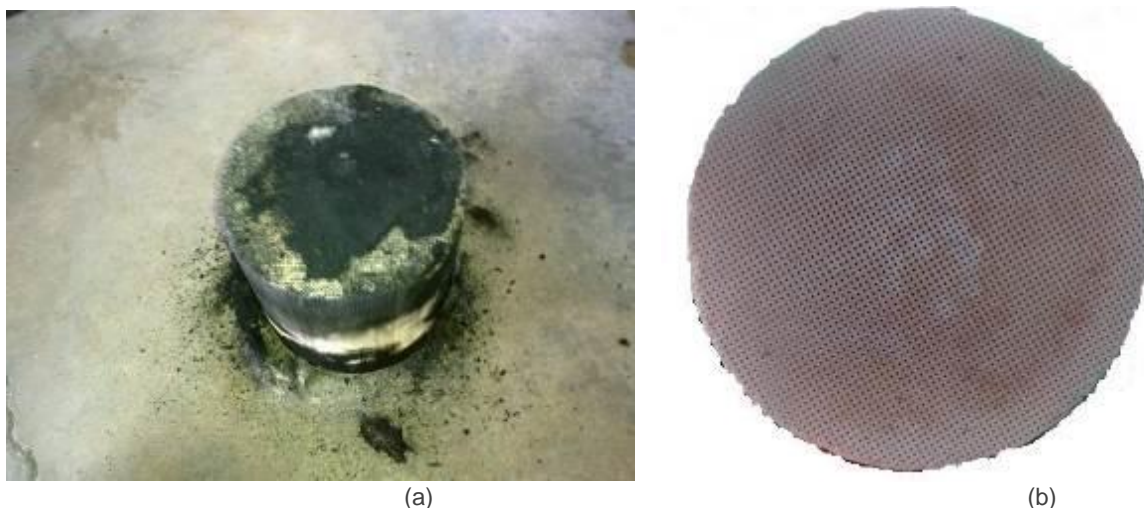<div align="center">(a)   (b)</div>

Fig. 4: (a) DPF before regeneration (b) DPF after regeneration

4. RESULTS AND DISCUSSIONS

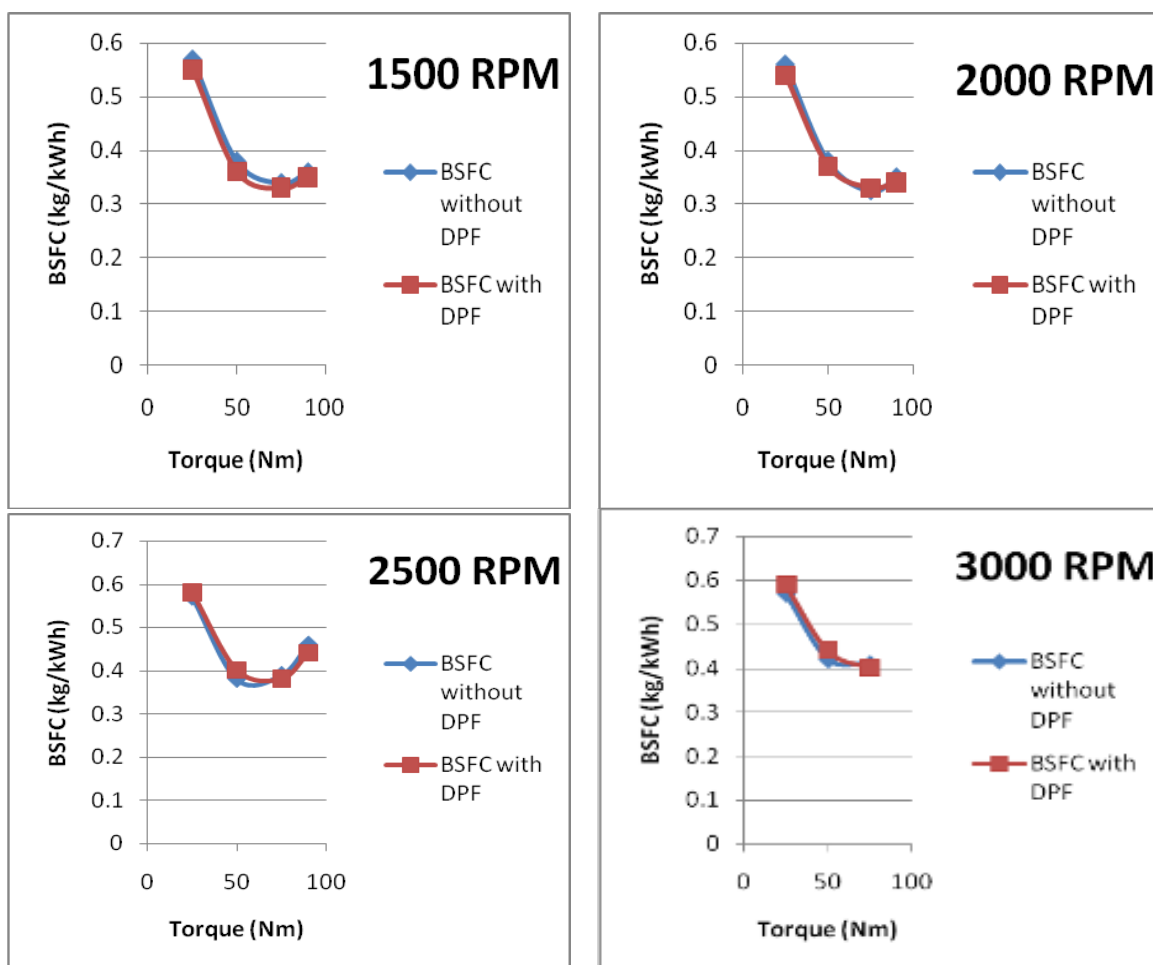4.1 Engine Performance with and without DPF:

(a) BSFC

Fig. 5: Variation of BSFC with torque for various RPM with and without DPF
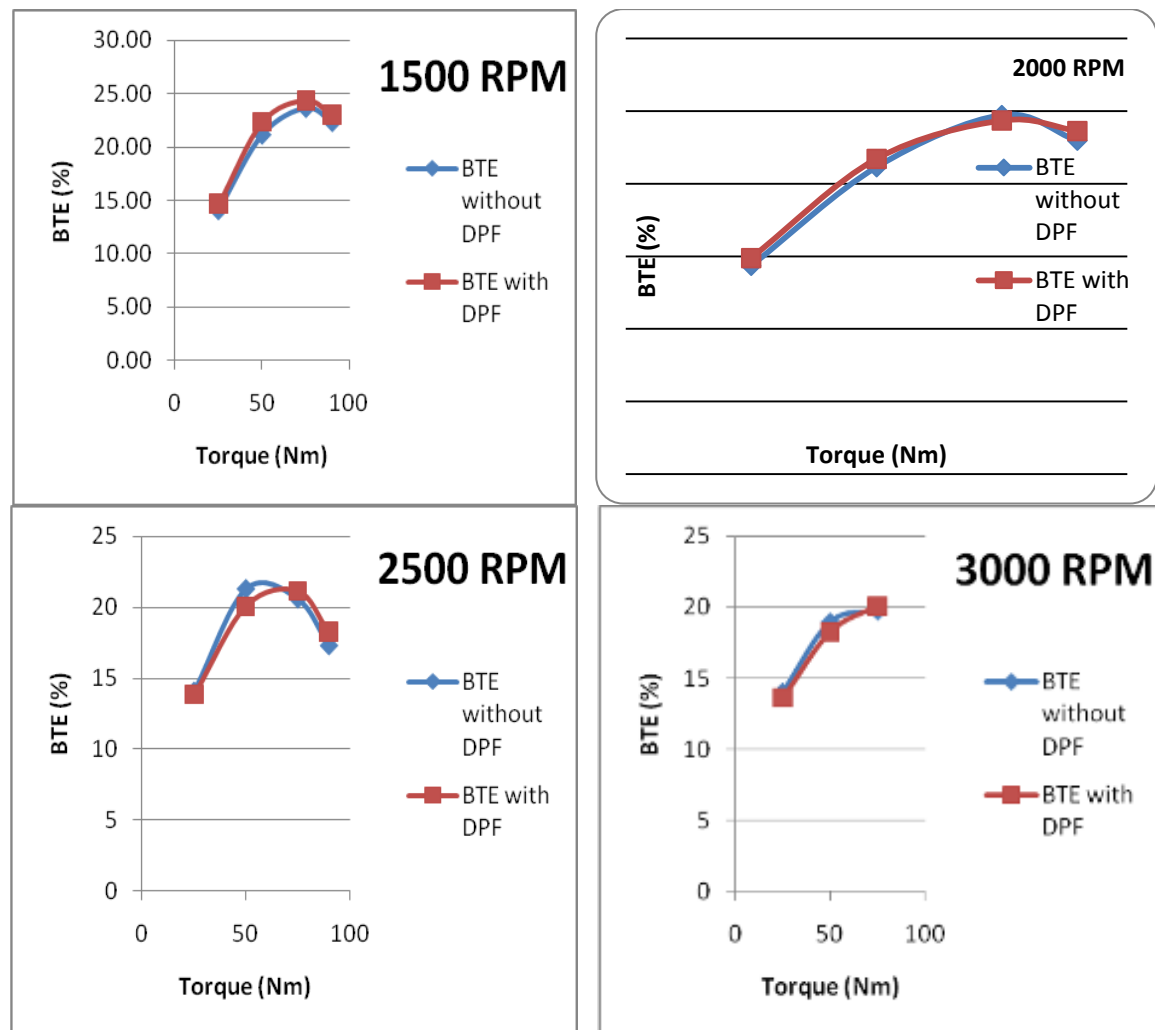
(b) BTE

Fig. 6: Variation of BTE with torque for various RPM with and without DPF

From fig. 5 and fig. 6, it is observed that installation of DPF did not have any significant impact on engine performance. However, when the DPF gets sufficiently choked, it develops high back pressure, which adversely impacts BSFC and BTE, resulting in an increased consumption of fuel. Hence, it becomes all the more important to either have a feasible and economically viable periodical DPF regeneration mechanism. Boger et al. (2011) anticipated that next generation DPF designs shall be as fuel consumption neutral as possible by providing ultra-low restriction and supporting engine thermal management needs in cold start and regeneration operations.

3.3 Smoke reduction with DPF

Reduction of smoke or particulate matter is the most desirable function of installation of DPF and from the graphs in fig. 7 it is evident that almost all (79-99%) of smoke is absorbed by the porous cells of the DPF, emitting negligible amount of smoke.

3.1 Impact of DPF on NOx emissions

As is seen from fig. 8, NOx emission increased at all loads at all RPMs with DPF. This is because with DPF, some back pressure is formed and exhaust is trapped between the engine and DPF for a considerable amount of time. The three major causes of formation of NOx are (i) high combustion temperature, (ii) availability of excess oxygen and (iii) duration of availability of excess oxygen. When the exhaust is trapped between the engine and DPF, it gets more time and excess oxygen, which reacts with N_2 present in exhaust to form NOx. This also reduces O_2 percentage in exhaust as is evident from similar curves plotted for O_2 in this section.
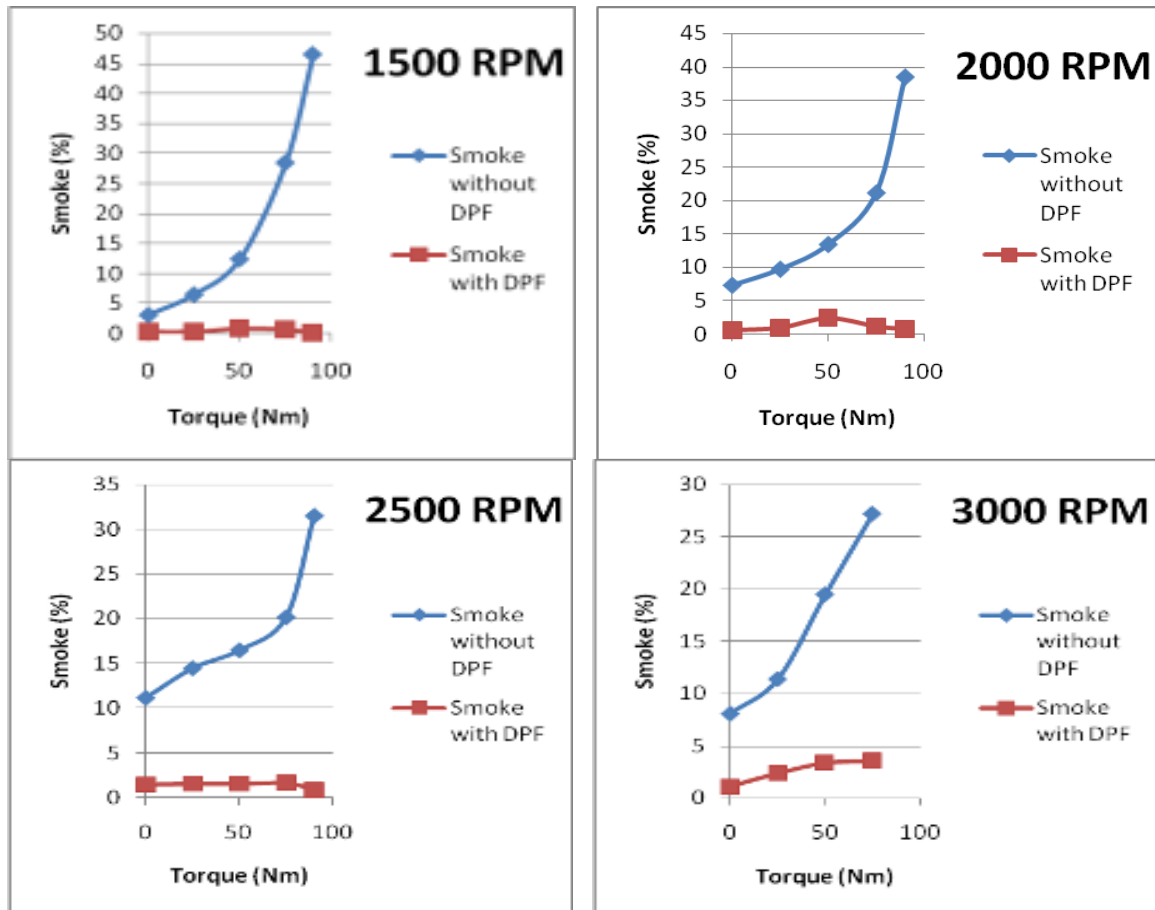
Fig. 7: Variation of smoke emission with torque for various RPM with and without DPF
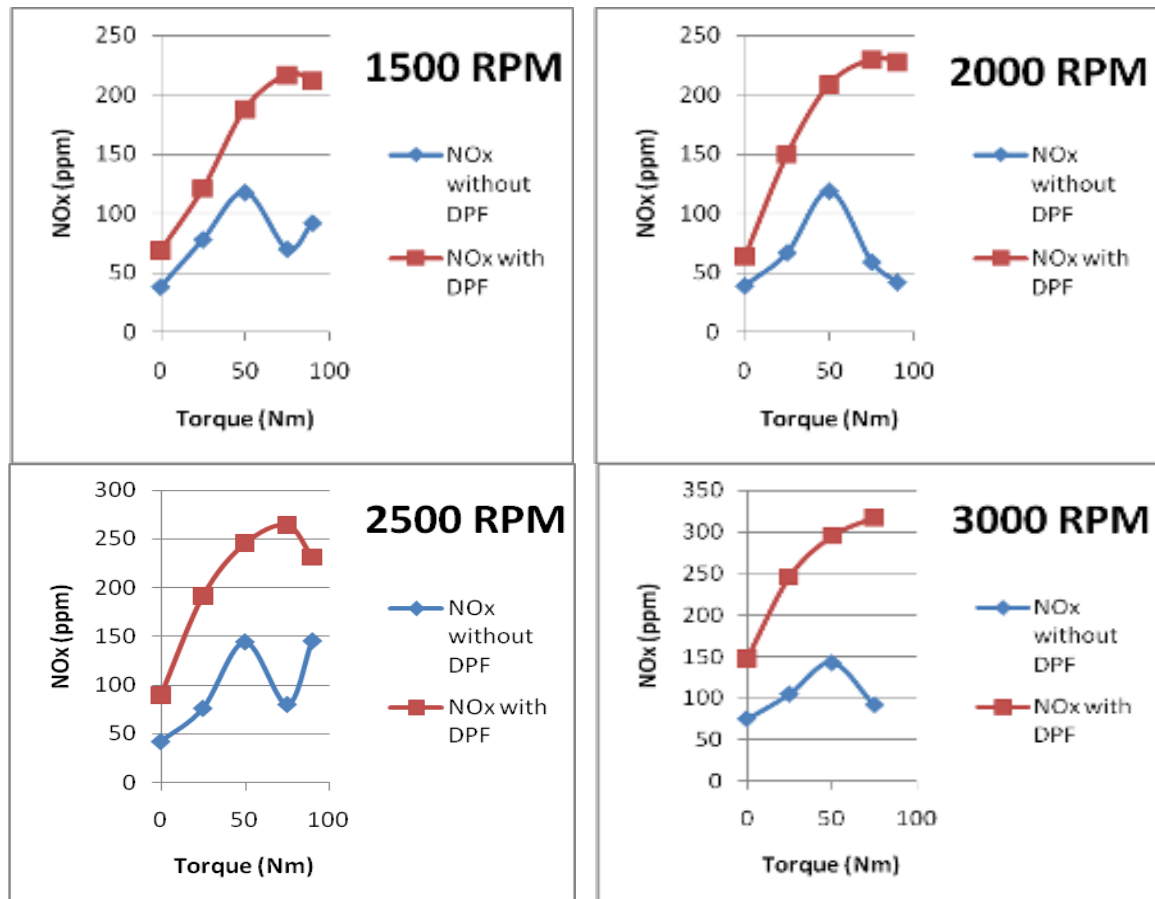

Fig. 8: Variation of NOx emission with torque for various RPM with and without DPF
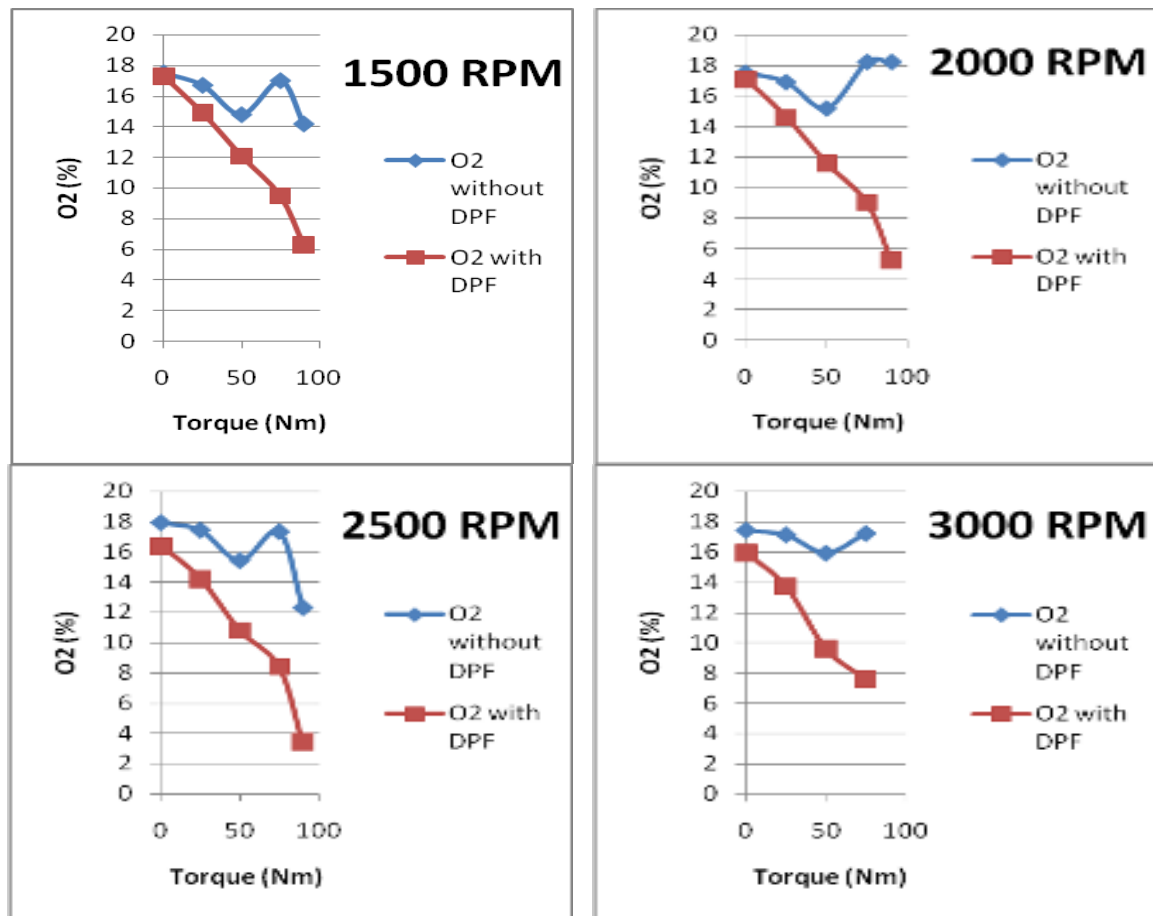
3.2 Impact of DPF on O2 in exhaust

Fig. 9: Variation of O2 (in exhaust) with torque for various RPM with and without DPF

It is clearly seen from the graphs in fig. 9 that O_2 percentage in exhaust decreased substantially with DPF at all loads and all RPMs. The primary reason for this is oxidation of soot (particulate matter) in DPF to form CO and CO_2, and oxidation of N_2 present in exhaust to form NOx. The increase in NOx with DPF has already been discussed above in this section.

5. CONCLUSIONS

An uncoated wall-flow type ceramic DPF was installed on a Bharat Stage-1 C.I. engine in a laboratory set-up in India and its impact on performance and emission was observed. The following conclusions could be drawn from the results obtained.

(i)   There was a great reduction (79-99%) in smoke emission with DPF bringing it to almost nil.
(ii)   It was observed that there is no adverse impact of DPF on engine performance. However, it is of utmost importance to keep DPF clean so as to avoid back pressure which shall impact fuel consumption and thermal efficiency adversely.
(iii)   DPF installation adversely effects NOx emission and to counter this negative impact, suitable actions need to be taken, e.g. catalytic reduction, EGR, etc.

6. REFERENCES

BERGMANN M., Kirchner U., Vogt R., Benter T., 2009. On-road and laboratory investigation of low-level PM emissions of a modern diesel particulate filter equipped diesel passenger car. Atmospheric Environment 43 (2009), 1908-1916. DOI:10.1016/j.atmosenv.2008.12.039.

BOGER T., He S., Collins T., Heibel A., Beall D., Remy C., 2011. A next generation cordierite diesel particle filter with significantly reduced pressure drop. SAE International 2011-01-0813, DOI:10.4271/2011-01-0813.

CHAPMAN L., 2007. Transport and climate change: a review. Journal of Transport Geography 15, 354-367. DOI:10.1016/j.jtrangeo.2006.11.008.

COM, 2005. Thematic strategy on air pollution. Communication from the commission to the council and the European parliament 446 final.

JEULAND N., Dementhon J.B., Gagnepain L., Plassat G., Coroller P., Momique J.C., Belot G., Dalili D., 2004. Performances and durability of DPF (diesel particulate filter) tested on a fleet of Peugeot 607 taxis: Final results. SAE Technical Paper, 2004-01-0073. DOI:10.4271/2004-01-0073.

KHATRI D.S., Sangtani F., 2013. Development and evaluation of an ECU for DPF regeneration system. International Journal of Mechanical Engineering and Research 6 (2013), 617-622.

LAPUERTA M., Fernández J.R., Oliva F., 2012. Effect of soot accumulation in a diesel particle filter on the combustion process and gaseous emissions. Energy 47 (2012) 543-552. DOI:10.1016/j.energy.2012.09.054

MAMAKOS A., Steininger N., Martini G., Dilara P., Drossinos Y., 2013. Cost effectiveness of particulate filter installation on Direct Injection Gasoline vehicles. Atmospheric Environment 77 (2013), 16-23. DOI:10.1016/j.atmosenv.2013.04.063.

NESAMANI K.S., 2010. Estimation of automobile emissions and control strategies in India. Science of the Total Environment 408 (2010), 1800–1811. DOI:10.1016/j.scitotenv.2010.01.026.

OBERDÖRSTER G., 2000. Toxicology of ultrafine particles: in vivo studies. Philosophysical Transactions of the Royal Society Series A 258, 2719-2740.

POPE III C., 2000. Epidemiology of fine particulate air pollution and human health: biologic mechanisms and who's at risk? Environmental Health Perspectives 108, 713-723. DOI:10.1289/ehp.00108s4713.

PUNDIR B.P., 2001. Vehicular air pollution in India: recent control measures and related issues. In: Morris S, editor. India Infrastructure Report 2001. New Delhi: Oxford University Press; 2000, 260–263.

RAMANATHAN V., Carmichael G., 2008. Global and regional climate changes due to black carbon. Nature Geoscience 1, 221-227. DOI:10.1038/ngeo156.

TENTE H., Gomes P., Ferreira F., Amorim J.H., Cascão P., Miranda A.I., Nogueira, L., Sousa S., 2011. Evaluating the efficiency of diesel particulate filters in high-duty vehicles: Field operational testing in Portugal. Atmospheric Environment 45 (11), 2623-2629. DOI:10.1016/j.atmosenv.2011.02.069.

Volvo Construction Equipment, 2010. Exhaust emissions reduction – towards 'stage IIIB/Tier 4 interim' non-road diesel exhaust emission standards – Questions and Answers, April 2010.

356: Working fluids and technologies to cool and power the future

SAFFA RIFFAT[1], DEVRIM AYDIN[1], RICHARD POWELL[1], YIJUN YUAN[1]

1Division of Infrastructure, Geomatics and Architecture, Faculty of Engineering, University of Nottingham, University Park, Nottingham, NG7 2RD, UK, saffa.riffat@nottingham.ac.uk

Energy technologies and energy management strategies has been gaining attention in the last decade as energy is vital for a safer and sustainable future. Dependency on energy is much higher than the past due to the industrial growth, increasing population as well as the comfort demand. However, recognising that global energy demand is rising but the world can burn only 20% its established fossil fuel reserves by 2050 if global warming is not to exceed 20C represents a major threat to the future of all humans (Berners-Lee and Clark, 2013). The present rate of fossil consumption means that this will be achieved by ~2030.

Yet domestic sector is count as the leading energy consumer as more people around the world aspire to comfort living standards which will drive the demand for air conditioning and electric power. Urgent solutions are required not only to increase share of renewable resources but also more efficient usage of fossil fuels which could be achieved with innovative power, air conditioning and refrigeration cycles utilising "Long term sustainable" (LTS) fluids, especially air, water and CO_2.

In the paper we provide a rational approach to the future use of working fluids based on our interpretation of the available technical evidence. We consider it self-evident that volatile fluids will continue to play major role in cooling and power generation, however new technologies will be needed that optimise energy efficiency and safety with minimum environmental impact. Concordantly we discuss the past and current situation of volatile fluids and look at four innovative technologies for future, using natural refrigerants including dew point cooling, combined heat and power generation, heat networks and heat storage systems.

Keywords: working fluids, sustainability, dew point cooling, combined heat and power, heat networks, heat storage systems.

1. INTRODUCTION

Like the majority of scientists, the authors accept the scientific evidence that humans are causing global warming. Despite the uncertainty that still remains about the sensitivity of the atmosphere to greenhouse gas emissions, notably CO_2, which affects the onset and frequency of adverse weather events, we consider that cooling, heat pumping and power generation technologies to reduce greenhouse gas emissions need to be developed now. Delaying until the anticipated effects of global warming are pronounced will be too late. While totally agreeing that the greenhouse gases must be urgently reduced we believe that considerable confusion has been created over the past 15 years, not least as the result of political lobbying. In the paper we provide a rational approach to the future use of working fluids based on our interpretation of the available technical evidence…We have no remit from either the fluorinated fluid or the "natural" fluid industries to defend their positions. While we consider it self-evident that volatile fluids will continue to play major roles in cooling and power generation, new technologies will be needed that optimise energy efficiency and safety with minimum environmental impact. This paper explores available options. Refrigeration and air conditioning currently contribute to global warming directly by the release of high GWP HFC refrigerants and indirectly by carbon dioxide emissions from fossil fuel power stations producing electricity to drive compressors. Yet as more people around the world quite properly aspire to the living standards of the developed world, the demand for cooling will increase. Ironically, higher global temperatures will drive the demand for air conditioning and thus the demand for electric power, which, if satisfied by fossil fuels, increases global, warming in a positive feed-back loop. Organic Rankine Cycle systems, although less numerous than cooling units, in many cases depend upon similar fluorinated fluids. By optimising heat recovery from low temperature sources, including CHP and thermal solar energy, they help reduce dependence on fossil fuels. But this benefit needs to be compared to global warming generated by fluorinated working fluid leaks.

2. THE PAST

Even in antiquity refrigeration and air conditioning was valued. The Egyptians produced ice by exposing shallow trays of water overnight in locations where a breeze would cause evaporation resulting in freezing. The Babylonians, Romans, the Persians and Chinese transported ice from mountainous regions and stored it in ice houses prior to distribution. Seasonal ice storage become of increasing importance until the introduction of mechanical refrigeration in the last quarter of the 19th century. In the 1870s the UK was importing ice from as far away as North America and Norway. British stately homes often had ice houses, many of which still exist, where ice harvested from lakes in the winter was stored for summer use. The Babylonians cooled their houses by splashing water over the walls. Islamic gardens created a millennium ago incorporated fountains to create cool areas for the comfort of their wealthy owners. Water clearly was the first refrigerant.

In 1805 Oliver Evans, an early American steam engineer and inventor, was the first to propose the vapour compression cycle, with ether as the working fluid, but did not build a working device. Pioneers of early refrigeration included the following:

In 1835 Jacob Perkins was the first who patented the vapour compression for a practical refrigeration system. In the early 1850s Australian James Harrison was the first to produce a practical commercial refrigeration machine producing ice and using ether as working fluid (Figure 1) (Zolfagharifard, 2011). Units were rapidly adopted by breweries in Australia and Britain.In 1851 John Gorrie, an American medical doctor, developed an ice-making machine providing cold air for cooling fever patients. Intriguingly, he combined a/c with coolth storage and was the undisputed father of air conditioning, but his work was way ahead of its time. Air conditioning attracted little attention until the seminal work of Carrier in the early 20th century.Truly modern industrial refrigeration began in the early 1870s with the development of ammonia vapour compression systems by Carl von Linde, a technology that has endured and has been progressively developed to the present day. Although the first carbon dioxide refrigeration was explored around the same time as Linde's ammonia development, the technology began to make an impact from 1890 onwards when British manufacturer J.E. Hall started manufacturing industrial units. These were especially favoured for refrigerated food ships because of the low toxicity and non-flammability of CO_2 compared to ammonia and other refrigerants (SO_2, methyl chloride, and hydrocarbons) available in late 19th century and early 20th century. In the 1930s 80% of the British chilled food fleet used CO_2 as the refrigerant.

Figure 1: Harrison's ice making machine (Zolfagharifard, 2011)

With the increasing availability of electric power and of small electric motors, SO_2 based refrigerators were developed for domestic and small commercial applications. Their popularity grew after the WW_1, especially in the USA, but not-infrequent leaks led to adverse press reports. General Motors, the owner of Frigidaire, recognised that to expand further refrigeration needed new and safe refrigerants. Engineer Thomas Midgley and chemists Albert Henne and Robert McNary, tasked with finding replacements, scanned the chemical literature and decided that the CFCs and HCFCs, discovered by Belgian chemist Frederick Swarts in the 1890s, provided the right combinations of boiling points and safety. Du Pont and General Motors set up Kinetic Chemicals in 1930 to manufacture the new fluids. CFCs R114, R11 and R12 were among the first to be manufacture followed by R22. These non-flammable, low toxicity fluids allowed the refrigeration to develop rapidly, especially after WW_2 when rising standards, first in the USA and then in the rest of the developed world increased demand for food refrigeration and air conditioning. Not surprisingly the same trend is being seen in developing world since cooling demand and living standards are inter-related. After nearly 30 years of near-exponential growth after WW_2 and against a background of increasing environmental awareness, the fate of CFCs in the atmosphere started to be questioned (Powell, 2002). Lovelock showed that CFCs persisted in atmosphere (Lovelock et al, 1972). In 1972, against a background of, the CFC/HCFCs producers themselves began to question what was happening to the CFCs/HCFCs being freely released in to atmosphere? The answer was they had no idea since there appeared to be no natural sinks for these compounds. The fundamental break-through was the landmark paper by Rowland and Molina suggesting that CFC and HCFC omissions could result in the destruction of stratospheric ozone, which shields the biosphere from harmful UV radiation, caused considerable concern (Molina and Rowland, 1974). The industry jointly funded independent academics to check the Rowland and Molina thesis...The intention was to find the truth, not just excuses to rubbish the thesis. Simultaneously the industry looked for alternatives to CFCs/HCFCs which had similar performance and efficiency low toxicity and non-flammability. From these programmes the HFCs, notably R134a emerged. By 1980 atmospheric science and the modelling of the effects of CFCs/HCFCs indicated there was a potential problem, but the effect would take decades to have a serious impact. Although the manufacturers were prepared to replace CFCs/HCFCs with non-ozone depleting HFCs these results combined with the global recession removed the political will to legislate against ozone depleting substances. The situation changed in 1985 with discovery by the British Antarctic Survey of the so-called "ozone hole" during the Antarctic spring (Farman et al., 1985) which was subsequently shown to be the result of chlorine containing compounds condensing on stratospheric clouds trapped in the polar vortex. As the sun rose after the polar winter the clouds evaporated releasing a chlorine pulse and hence causing a rapid decrease of ozone over the South Pole. Subsequent scientific studies proved that man-made chlorine compounds were largely responsible. Under the auspices of the Montreal Protocol (1987) UN member states agreed to limit the manufacture and release of ozone depleting substances, notably CFCs/HCFCs. The Protocol also made provision for ongoing scientific work to understand the severity of the problem and to allow restrictions to be tightened. By the mid-1990s it was clear that to prevent continuing stratospheric ozone depletion CFCs/HCFCs would need to be phased-out completely. The Protocol was amended; the CFCs would go because they had highest ozone depletion potential, followed by the HCFCs. Developed countries, which were more economically able make the transition, were required to phase out more quickly than the poorer countries. Europe unilaterally banned the manufacture of CFCs after 1995. HCFCs, notably R22, were banned as a refrigerant after the end of 2014, including the recycling of existing material. HFCs replaced CFCs/HCFCs in many applications combining comparable efficiencies, non-ozone depletion, low toxicity and non-flammability.

2.1 Unravelling Confusion…

The HFCs have solved ozone depletion caused by CFCs and HCFCs, although it will take until ~2100 for the "ozone hole" to disappear. But the HFCs themselves have now come under increasing pressure as potent global warming gases. The new question now is "what replaces the HFCs?" In the authors' view

trying to answer this question has caused considerable confusion since science, technology and politics have become muddled.

How much do the HFCs contribute to global warming? The scientifically authoritative sources of information are the IPCC reports on global warming published by the UNEP (Intergovernmental Panel on Climate Change, 2013). At present HFCs contribute ~1% to global warming, which appears "trivial" compared to the major greenhouse gases, notably CO_2 and methane. Their 15% per annum growth is the problem, which if unchecked would result in an estimated 0.5 K increase in global warming by 2100. HFCs also contribute to global warming indirectly when used as refrigerants via the CO_2 emitted by fossil fuel power stations to supply the power to generate the electric power to drive refrigerators and air conditioners. Obviously replacements for HFCs should not result in significantly lower energy efficiencies otherwise the contribution of fossil-fuelled cooling equipment to global warming will increase, not decrease. If hydro fluorocarbon, such as R245fa, is used to generate electric power from "waste" heat or in a CHP unit then it reduces CO_2 emissions, provided these are greater than the global warming caused by HFC leaked from equipment.

3. "CHEMICAL & NATURAL REFRIGERANTS"?

While supporting the move from hydrocarbon fluids (HFCs) to so-called "natural" fluids to reduce potential global warming, we consider that these have issues, which although well-known and not denied by industry, are not being properly communicated to the general public. In particular the use of term "natural" is misleading, especially since it is often contrasted with "synthetic" or "chemical" as opprobrious descriptors for HFCs. To combine the low toxicity and non-flammability of the HFCs with low environmental impact and long term sustainability the choice of working fluids is restricted to water, air and CO_2. Clearly, this is relevant to domestic applications and has informed the technologies described in this paper. For applications where inventories are small or in large installations, where engineering supervision is continuous and public exposure limited, then hydrocarbons and ammonia are acceptable. We suggest that "natural" fluids might be more accurately as "long term sustainable" fluids. In both the technical and non-technical literature, fluorine-containing (HFC) refrigerants are increasingly referred to as "chemical" or "synthetic" refrigerants in contrast the so-called "natural" refrigerants. In part at least, this is a reaction against the Chemical Industry which is perceived to be contaminating the environment in its unremitting pursuit of profit despite the fact that it an essential contributor to the living standards of developed nations. "Chemical" is now seen by some as being "bad" and is contrasted with "natural", which implies good. Even a leading UK national newspaper, The Daily Telegraph, noted for its sceptical articles on the existence of man-made global warming (Booker, 2015), in 2006 pointed out that "*everything is made of chemicals, and so claims that products are "chemical-free" are not true*" (Fleming, 2006), yet in 2012, published an article entitled "*The green guide to chemical free beauty*" (Jones, 2012) extolling the merits of "natural" products, which chemist recognise as being chemicals. If a Telegraph, with its reputation for quality journalism, can publish articles that differ about the meaning of "chemical" then the confusion between so-called "chemical" and "natural" refrigerants is perhaps not surprising. The scientific community acknowledges that communicating clearly with the general public is essential; this requires a consistent terminology, and resisting its distortion for commercial or ideological reasons.

In the context of refrigerants what is meant by the term "chemical"? The major fluorochemical fluids are R32 (CH_2F_2), R125 (CF_3CF_2H), R143a (CF_3CH_3), R134a (CF_3CH_2F), R227ea (CF_3CHFCF_3), R152a (CHF_2CH_3) and R245fa ($CHF_2CF_2CH_2F$). The "natural" refrigerants are water (R718), air, R714 (ammonia), carbon dioxide (R744), R290 (propane, C_3H_8), R600a (methylpropane), R600 (n-butane, $CH_3CH_2CH_2CH_3$), n-pentane, R601a (2-methylbutane) and cyclo-pentane. Whether they are HFCs or "natural" refrigerants, all can be synthesised by chemical reactions and all can undergo chemical reactions. In other words they are self-evidently all chemicals. Patent refers, correctly in our view, to these compounds, whether fluorine-containing or not, as chemical refrigerants to distinguish them from thermoelectric devices, a distinction which is valid (Ravji et al., 2012). But the distinction between "chemical" refrigerants and "natural" refrigerants is technically meaningless in terms of their properties.

Water, air, carbon dioxide and some hydrocarbons ammonia are "natural" in the sense that they are present in the biosphere. But this, in itself, does not necessarily make them desirable as refrigerants. Sulfur dioxide could be described as "natural", and, pedantically at least, this might be extended to dichlorodifluoromethane (CFC-12), which has reportedly been detected in volcanic gases (Isidorov et al., 1990) Both are now rightly rejected as refrigerants, although both were used in the past. Ammonia and carbon dioxide used as refrigerants are manufactured from methane ("natural" gas) in large chemical plants, so they are just as much "synthetic chemicals" as the fluorocarbons. The point is that by calling carbon

dioxide and ammonia "natural" in contrast to the "synthetic", fluorocarbons makes a generic distinction in terms of their origin is also meaningless. If the carbon dioxide is recovered from biomass fermentation, for example bioethanol manufacture, then it might reasonably be termed "natural", or at least "biochemical". Perhaps a better term is "sustainable". Ammonia obtained from putrefying animal wastes would be "natural", although we would question whether the process would be economic. More sensibly, ammonia might be manufactured from hydrogen obtained from the electrolysis of water using renewable energy and atmospheric nitrogen via conventional technology. Even more exciting, is the potential for low temperature ammonia production (Lan et al., 2013). In principle this approach is sustainable, although it involves a "chemical synthesis", so the ammonia thus produced should be described as "synthetic" or "chemical" not "natural".

The hydrocarbon fluids are typically obtained from natural gas purification plants and oil refineries, which are chemical plants primarily operated to produce refined fossil fuels and chemical industry feedstocks. If the hydrocarbon refrigerants were simply recovered by distillation from natural gas then they could with reasonably be described as "natural". But when fossil fuels are finally phased-out then they will no longer available from this source. To be "sustainable" they might be obtained from biomass processing (European Biofuels Technology Platform, 2011). The hydrocarbons thus obtained would be "synthetic chemicals" and could not honestly be described as "natural", but they would be sustainable. Methoxymethane (dimethyl ether, CH_3OCH_3), already manufactured on a substantial scale as an aerosol propellant, is a promising low global warming refrigerant. We cannot find any reports of biological sources, so it cannot be regarded as "natural", in the sense of occurring in nature. Although clearly "synthetic, it is being developed as a second generation bio-fuel (Olah et al., 2009) especially for use in low-pollutant diesel engines and thus will be available as a "sustainable" but "synthetic chemical" refrigerant. Some may consider the above discussion is pedantic suggesting that "natural" is just a convenient label to identify a group of refrigerants that have low direct environmental impact. Although lacking precision this might be perhaps acceptable as "jargon" for those working in the refrigerants field. But this would be to miss the point. Bearing in mind that the scientific and technical communities is often criticised for not communicating their work clearly to the general public we should remember the adjective "natural" conveys a specific meaning to the non-technical general public, essentially as defined by The Oxford Dictionary; "natural" as: *existing in or derived from nature; not made or caused by humankind*. The term "natural" applied to refrigerants is an obfuscation. At present all fluids marketed as refrigerants, whether fluorochemical or so-called "natural", are derived from petrochemical feedstocks, none of which are sustainable. The ultimate target must be "sustainable", albeit "synthetic", refrigerants manufactured from bio-renewable resources by environmentally low-impact processes based on green chemical technologies, consistent with the ethos of circular manufacturing technology (EUR-Lex, 52014DC0398R(01)). We suggest calling these products "Long Term Sustainable" refrigerants, or more broadly working fluids since they might be employed in ORC systems; these are listed in Table 1.

3.1 Hazards

Starting in the 1930s, the desire for low toxicity and non-flammability drove the move away from the LTS fluids to the CFCs and HCFCs. By returning to these fluids means accepting the hazards they entail, which are not trivial. Ammonia, a refrigerant that has been used since the beginning of modern refrigeration in the 1870s, still causes serious accidents and fatalities. A listing of 99 refrigerant incidents compiled by the European Fluorocarbons Technical Committee (EFCTC) from March 2006 to October 2013 records 981 injured, 236 severely injured and 95 fatalities with 16772 evacuated (EFCTC, 2013). By far the greater majority resulted from ammonia leaks. Three incidents resulted from hydrocarbon leaks (1 injured, 11 severely harmed, 1 death.) Five CO_2 incidents were recorded although one had no data. (40 injured, 1 severely harmed, 200 evacuations). One fluorocarbon leak was noted (1 injured, 1 death). Since the data originated from an organisation with an explicit interest in promoting fluorocarbons against LTS fluids, a selection of the links to the original data sites were checked and found to be correct. Using the search terms "ammonia + accident" an internet search generated additional, more recent examples of ammonia releases causing problems. "hydrocarbon + accident + refrigerant" generated a recent report by the London Fire Brigade concerning the fire hazard of domestic freezers related especially the flammable cyclopentane blowing agent. EU and American legislation restricts the hydrocarbon charges in appliances with heat exchangers in rooms to a maximum of 150 g. This information reinforces what was already known, that is ammonia and hydrocarbons are potentially hazardous, especially when used on the large scale without adequate supervision. The Singapore government is sufficiently concerned to restrict their applications (Cooling Post, 2014). We are not arguing for the phasing out ammonia and hydrocarbon, merely suggesting that their range of applications will be limited, because with tens of millions of installation world-wide accidents will inevitably happen.

Table 1: Long Term Sustainable Fluids

Chemical Structure	Chemical name	ASHRAE number	Normal BP (^{o}C)
	air		
H_2O	water	R718	100
NH_3	ammonia	R414	-33.4
CH_3CH_3	ethane	R170	-88.6
$CH_3CH_2CH_3$	propane	R290	-42.1±2
$CH_3CH(CH_3)CH_3$	iso-butane (methylpropane)	R600a	-11.7
$CH_3(CH_2)2CH_3$	butane	R600	0 ±1
CH_3OCH_3	methoxymethane (dimethyl ether)	R170E	-24
$CH_3(CH_2)3CH_3$	normal-pentane	R601	36.1±2
$CH_3CH(CH_3)CH_2CH_3$	iso-pentane (2-methylbutane)	R601a	27.7
$CH_2CH_2CH_2CH_2CH_2$	cyclo-pentane	R407c	49

While accepting that hydrocarbons are acceptable for applications where less than 150 g charge is adequate, and, with ammonia, for big installations that can be properly monitored by appropriately skilled engineers, we suggest for larger domestic, commercial and industrial applications, which are not routinely monitored, then safer refrigerants are essential. With the phase-out fluorinated refrigerants because of environmental concerns then fluid choice is driven back to water, carbon dioxide and possible air. In looking for technologies, whether air conditioning, refrigeration, heat pumping or low temperature power generation/CHP the authors have therefore focused on water and air based systems, which in some cases can be advantageously coupled with vapour compression transcritical CO2 systems.

Examples of cooling/air conditioning, heat pumping, power generation and energy storage systems are presented in the following sections:

4. DEW POINT COOLING

Market research completed in 2013 on the usage of air conditioning indicated the industry gains £55 billion in revenues globally. China alone accounts for £18 billion of this sum, while the UK accounts for £600 million. Mechanical vapour compression systems dominate the cooling sector making up 80% of the above market share. However, evaporative cooling (EC) market is expected to experience fast growth over the next ten years from £5.5 billion in 2013 to £20 billion in 2024. This is due to the increasing attention gained by EC using the natural refrigerants water and air. Use of water as cooling medium and air as a heat transporter (air/water cycles) is a promising alternative to electrically powered heat pumps. The basic idea of air conditioning has been refined through centuries of evolution. The ancient Egyptians hung wet mats in their doors and windows in order to allow wind to blow through them to cool the air. This can be considered the first attempt at air conditioning. Mechanical fans were introduced in the 16th century to provide air movement, and by the 19th century cooling towers with fans were introduced to blow water-cooled air inside factories. Evaporative coolers are the innovative technology of the 20th century (Western Environmental Services Corporation, 2015).

EC basically adds water vapour to the air and can be considered a simple, efficient and cheap method to decrease the temperature. However, direct evaporative cooling (DEC) is a cause of concern given that the resulting high humidity both reduces thermal comfort and causes mold growth that could cause several allergic problems and diseases (Figure 2). In addition DEC has low efficiency in humid climates, as only limited amount of water could be added to the air. Desiccant systems can be integrated to evaporative coolers to overcome this problem. However necessities of desiccant regeneration also complex system design are the main barriers for this cooling method to compete with heat pumps. Alternatively to DEC, IEC

technology has developed based on novel core (heat exchanger) technology, enabling to cool air without moisture addiction (Figure 2). With indirect evaporative cooling (IEC), a secondary (scavenger) air stream is cooled by water in wet channel. The cooled secondary air stream goes through a core, where it cools the primary air stream flowing in the dry channel. IEC does not add moisture to the primary air stream. Both the dry bulb and wet bulb temperatures are reduced. However, IEC systems still have technical drawbacks including the limitations in air temperature drop and the large dependency on the ambient air conditions, where the lowest temperature that could be attained is the intake air wet-bulb temperature. In addition, efficiency of IEC is 60-70% whereas direct evaporative cooling (DEC) efficiency is usually 90%. This is because in DEC cooling is achieved with adding moisture to the air and new temperature is found on wet bulb gradient. In IEC new temperature is found on dry bulb gradient as a result of a temperature drop without moisture addiction. In order to overcome the stated drawbacks of IEC, a breakthrough step was taken in the last decade and dew point EC has been developed based on M-Cycle (Maisotsenko et al., 2003). M-Cycle based dew point cooling is a revolutionary thermodynamic process that utilizes the psychometric energy (or the potential energy) available from the latent heat of water evaporating into the air and uses atmospheric air as a renewable source of energy. The performance of any evaporative cooling system is largely dependent on the structure and design of the heat and mass exchanger. Thereby modifying the exchanger of the IEC system, air could be cooled below its wet bulb temperature and towards the dew point temperature (Zhao et al., 2009) (Figure 2) which lies behind the remarkable performance of Dew point coolers. Authors carried out several studies on dew point cooling technology ((Zhao et al., 2008) and reported that counter-flow exchanger for M-Cycle dew point cooling provides greater (around 20% higher) cooling capacity, as well as greater (15% - 23% higher) dew-point and wet-bulb effectiveness when equal in physical size and under the same operating conditions. However it is indicated that cross flow system, however, had a better (10% higher) energy efficiency (COP) (Zhan et al., 2011). Theoretically with dew point coolers, product (primary) air could be cooled until saturation line, which will significantly increase efficiency up to 90%. Dew point cooling can be considered a breakthrough technological advancement as it provides larger intake-supply air temperature difference than any other evaporative cooling method without any moisture addiction to supply air.
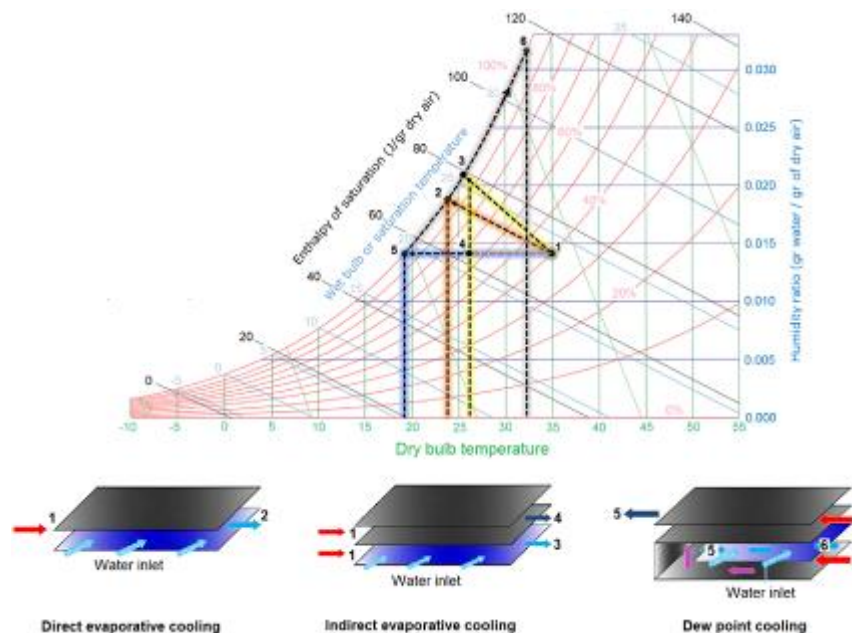

Figure 2: Evaporative cooling technologies

A dew point evaporative cooler is introduced to the market by Coolerado Corporation using Maisotsenko cycle (M-Cycle) (Coolerado Corporation, 2006) which is basically benefitting from latent heat of evaporation of water to cool the product air up to dew point. System uses a cross flow heat exchanger core, has COP value of 16 and a payback period of <2 years. As an example of the latest status of cooling cycles with air/water couple, this system will be a revolutionary step towards green energy. Future developments will be heat exchanger design and material for further enhancement of dew point cooler efficiency. Currently single intake – counter flow and double intake – cross flow are favourable core designs. On the other hand in terms of material, sandwich aluminium-foil/fibre and cellulose fibre with water proof coating on one side are promising heat exchange surface materials for effective dew point cooling performance.

5. COMBINBED HEAT AND POWER GENERATION

Combined heat-power (CHP) system is a promising way of utilizing solar energy and waste heat from industry, power plants and other commercial buildings. CHP is a proven technology with technical, economic and environmental benefits using the low-grade heat for both electrical and thermal power supply. Authors agree that the key to reduce future energy consumption-fossil fuel dependency lies on maximum utility from low-grade heat. According to Bradley (Bradley, 2014), every year 10 gigawatts of potential power is squandered as waste heat from industrial processes—enough to light 10 million homes. However, the high installation cost of CHP systems is an obstacle and government stakeholders have a key role in this just like other renewable energy applications. As an example, the Danish government mandated expansion of CHP as a national policy beginning in the 1980s, requiring grid operators to pay for the power generated at a set rate (Lindey, 2009). The guaranteed ability to sell electricity stimulated the construction by private entities of relatively small-scale CHP plants. The same strategy lies behind the rapid growth of wind and solar power in Denmark and in Germany as well. In Germany CHP contributed 13% of electricity generation in 2009. The German government has a target to increase CHP to 25% of generating capacity by 2020. Furthermore, USA is targeting 50% increase in CHP capacity by 2020, which would correspond to around 12% of US generating capacity (Department of Energy and Climate Change, 2013).

With combined heat and power (CHP) / co-generation systems, heat that might be lost as a by-product of electricity generation is captured for power generation also space and water heating. Locally supplied electricity incurs lower transmission losses than the national grid, looses 40% of its supply. Payback periods of four to ten years are possible (Mayer, 2007). CHP can also produce a 30-50% reduction in carbon dioxide emissions, as well as, be incorporated with absorption chillers or desiccant coolers for space cooling called "tri-generation."

Organic Rankine Cycle (ORC) has been widely researched for CHP systems as it is suitable for small and large scale heat and power generation with utilizing low grade heat. However health and environmental concerns on refrigerants will be a barrier on further development and implementation of ORCs. On the other hand moist air cycles for CHP, will be a new trend as they use natural refrigerants, work in lower pressures and enable to recover high amount of heat as a result of moisture condensation. Buyadgie reported a newly developed CHP system using moist air and called "Solar Low-Pressure Turbo-Ejector M-Power System" (SLTE-MPS) (Buyadgie, 2014). System replaces compressor with ejector and utilizes a serial HMX core, produced by Coolerado for air-conditioning through Maisotsenko Cycle (M-cycle) for equalizing counter flows' pressures at the same atmospheric or sub-atmospheric level. It is claimed that system converts solar thermal energy into electrical power with thermal efficiency of 30-40% which is 11-18% for steam-water Rankine Cycle. Buyadgie says that: "In the Brayton power cycle, mechanical compressor consumes useful work. When ejector replaces compressor, the system's efficiency increases 2-2.5 times since ejector does not consume work and serves to optimize pressure after the turbine.

Another promising technology proposed by the authors for refrigeration and air conditioning as an alternative to the conventional heat pumps could be ice heat pump using open air/water cycle. The system uses air compressor and expander units and a water atomising nozzle. Water, which is injected at the expander inlet of the heat pump, is converted into ice at the outlet of the expander. The use of air and water, as natural refrigerants, will result in a highly efficient and environmentally-friendly heat pump system for ice and heat production.

Figure 3 shows the ice heat pump working principal. The ice heat pump system is an energy saving device. It harnesses heat from ambient air, water vapour/steam under low temperatures to solidify and release a large amount of latent heat. The heat is converted to mechanical work through the expander to offset compression work, thereby improving the COP of the heat pump.

In the system ambient air enters the air compressor and it is compressed to a high pressure. The high pressure/high temperature air is then passed through the heat exchanger/condenser unit and releases heat that could be used for space heating. At the inlet of the expander unit, water is injected using an atomizing nozzle. The air/water-vapour mixture is then expands through the expander unit producing ice. The expander outlet is connected to an ice-water separator/tank. An ice agitator powered by an electric motor could be used to break the ice into ice slurry. The ice slurry could be used for space cooling or refrigeration.

The proposed technology uses air and water as the working fluids. The utilisation of the sensible heat of dry air and sensible heat/latent heat of water would maximise the absorption of energy from ambient air

and water. The water phase change contains a large amount of energy and therefore the ice heat pump will have a great advantage compared to conventional heat pumps using HFCs.
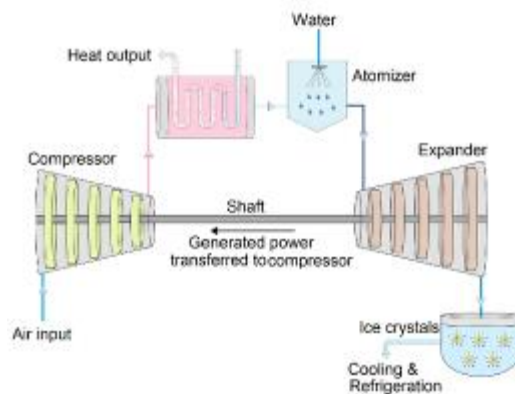

Figure 3: Schematic diagram of ice heat pump

5.1 What is the Benefit of CHP

Combined heat and power (CHP) can offer a variety of economic benefits for large energy users. Considering the sharply increasing demand of electricity, local power generation with CHP could be reducing the stress on electricity grid. Additionally it can provide security of supply, making energy go further, through more efficient use of fuel – regardless of whether the fuel is renewable or fossil (The Association for Decentralised Energy, 2015). Alternatively, reduction in the cost of energy with CHP will improve the competitiveness of industry and business, helping alleviate fuel poverty and lowering cost in delivery of public services (United States Environmental Protection Agency, 2015).

5.2 Do We Have the Luxury to Ignore the Heat Demand?

The supply of heat is largely ignored in the energy and climate change debate, despite heat representing nearly half the world's final energy consumption. According to IEA report (International Energy Agency, 2014) in 2009, heat represented 47% of final energy consumption, compared with 17% for electricity, 27% for transportation, and 9% for 'non-energy (raw material usage of fuel) use. Oil, coal and gas account for more than two-thirds of the fuels used in meeting this significant demand for heat. Currently thermal power plants operating based on Rankine cycle, only convert the 30% of fuel energy to electricity as a final product meaning that rest of the energy is wasted as low-grade heat. Conversely potential of CHP lies behind providing the maximum benefit from the energy source and delivering not only electricity but also heat, which allows efficiency to reach 90-95%. According to a report by Pöyry Energy Consulting (Jha, 2008) for Greenpeace, the energy produced by power plants that provide both heat and electricity could be almost tripled in the UK. So-called CHP plants are far more efficient than conventional power stations because they harness heat that is normally wasted, by piping it to industrial or domestic users with heat networks. Heat networks have a key role in order to benefit from CHP technology, and many sources of heat that are currently not being used. They provide a means of transporting waste heat from industrial processes and some commercial buildings.

5.3 Heat Networks: The Key to Save the Waste Heat

Heat networks are gaining attention in the last decade as they act as a bridge between the waste heat sources (*e.g,* industrial, power plants) and the residential sites. Heat networks are commonly used in Eastern Europe, Germany, South Korea, USA, Canada, and Scandinavia. Approximately 61% of the customers in Denmark, receive their heat via heat networks (Department of Energy and Climate Change, 2013).

Heat networks will prove to be the key for waste heat recovery in the future. Similar to the electricity grid, effective heat networks will allow central production - distribution, and will bring many advantages such as balancing the heat-supply demand, reducing the heating costs, investment costs (on heating systems), CO_2 emissions, and wasted energy. However, heat networks should be cost effective including low investment and operational costs in order to easily integrate with other systems. Water is mainly used as the heat transfer fluid, which requires a high pumping pressure. High pressure pumps would be expensive to run

and also water pumping could results in leakage problems. On the other hand, heat transport with air is not feasible as a result of low specific heat of air. According to authors using moist air which will significantly reduce the required duct size and allow long distance effective heat transport called "Moist air system" (MAS) (Figure 4) will be more practical. Assuming Q kW heat is transferred from heat source A to the heat sink B with a well-insulated (Qloss ~ 0) duct line by using i) dry air as heat transfer fluid, and ii) humid (moist) air as heat transfer fluid; the heat transport capacities of dry air, and humid (moist) air were analysed considering several parameters including density, pressure, enthalpy and humidity. Results of analysis revealed that the required duct size (diameter) for the transport of equal amounts of heat is much lower when moist air is used as the heat transfer medium than when dry air is utilised. An example of transporting 1 kW heat from A to B, at the same air velocity, the required duct diameter for dry air is found to be about 210 mm whereas only 14 mm is required for moist air.
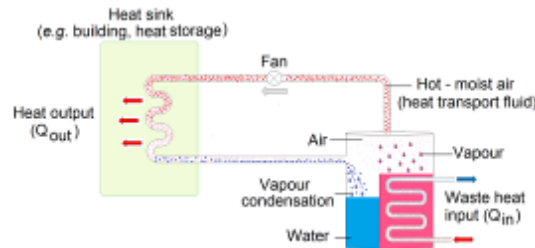

Figure 4: Moist air system

5.4 Moist Air System: A better Way to Transport the Heat

MAS is a unique and novel heat transfer system, which utilises a network of highly insulated small flexible ducts containing flowing air and moisture as the heat transfer medium. Recovered waste heat as well as the generated useful heat (solar) will be efficiently transported to the CHP plant and customer building network via MAS. This will allow the harness of low grade waste heat (100-150°C) released from waste incineration, biomass and industrial plants for heat production and electricity generation, thereby making more efficient use of waste heat recovery (Figure 5). Localised waste heat-driven CHP-MAS system will be future's promising technology for sustainable heat and power generation at reduced cost.

MAS system would be effective for transferring waste heat from different locations to buildings. Solar heat could easily be utilised using MAS as medium for connecting different devices such as hot water tanks and power generation units operating at low temperature heat. Alternatively MAS system could be integrated to HVAC systems used to supply heating and cooling via radiation panel, fan coil etc. in buildings and would be compatible with the building structure as it does not require a large space. Additionally heat transfer coefficient, (W/m^2K) for moist air and water are in a close approximation, therefore usage of moist air instead of water in central heating applications does not bring any disadvantage/obstacle in terms of overall heat transfer to the building from the radiator.

 MAS system has the potential to replace the conventional heat transport methods especially in multi-storey buildings and towers due to the given advantages and its light, low cost, low pressure and flexible nature.
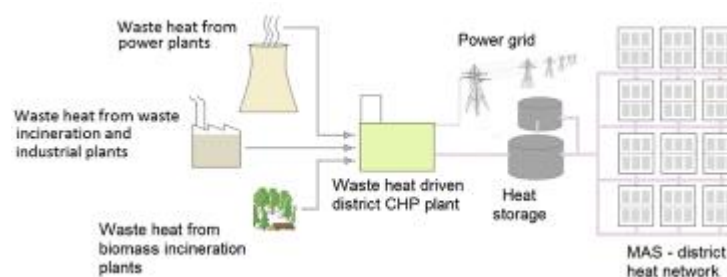

Figure 5: Schematic diagram showing MAS - heat networks between waste heat sources, centralised CHP plant and residential site

6. ENERGY STORAGE: PATHWAY TO SOLAR HEATING

In order to fully benefit from renewable sources, technological development in renewable energy industry leads to energy storage which is crucial for bringing a balance to supply and demand.

The main drawback of renewable sources is that they are not steady and climatic conditions are difficult to determine. Although it is clear that we already developed technologies to harvest power from renewables, we are still struggling to store and accumulate these energies. Unfortunately weather conditions are changing continuously and giving unpredictable outputs. Therefore to harvest energy generated as a result of natural events, we must urgently develop energy storage technologies in order to contribute to our sharply rising renewable energy demand. We can save the solar energy in summer to use in winter or during daytime to use night. This condition will both compensate the mismatch between supply and demand, as well as, dramatically reduce the payback period of renewable energy technologies (Aydin et al., 2015).

Electrical storage is on the target in the last decade especially for bringing the PV technology to a cost effective level. In addition there are an increasing number of large scale electricity storage applications especially in hydroelectric form in Northern Europe, China, Japan, and USA and in many other countries. Compressed air storage also has been gaining attention and currently small and large scale compressed air storage systems are available in the market. On this context Lindey (Lindey, 2010) critically investigated the possible ways to storage of electrical energy and looked at a number of technologies for storage in the form of potential energy (hydroelectricity), pressure (compressed air), kinetic energy (flywheels) and with using batteries or ultra-capacitors. Although some significant advancements have been achieved on storing electricity, unfortunately thermal energy storage is highly ignored. However as mentioned previously, thermal energy constitutes almost half of world total energy demand. Still combustion of natural gas, coal and oil is primary drivers for space and water heating purposes in buildings. Usage of these fuels should be restricted only for power generation considering their high carbon emissions, less availability and high energy potential. Utilizing fossil fuels for domestic heating (low temperature) purposes is briefly wasting their potential by using them to generate low quality energy. Consequently, in developed countries highest energy consumption is in building sector with %27. Also %70 of atmospherical emissions including greenhouse gas sourced from building sector (Parameshwaran et al., 2012). This problem requires an immediate solution which is linked to storage of solar energy.

Sensible heat storage (SHS) is a mature technology for short term storage and latent heat storage (LHS) is showed a potential for balancing the mismatch between day and night as well. However with these technologies it seems highly unlikely to reach the goal of long term heat storage due to the heat loss. A possible way for seasonal storage of solar energy will be the thermochemical heat storage (THS) based on vapour adsorption-desorption of zeolites, silica gels and salt hydrates. Due to the nature of these materials, as long as they kept hygrotermally insulated in dry form they are able to store heat independent of the time without any heat loss. Thereby solar energy could be used for drying these materials in summer for generating heat in winter (Figure 5). THS materials have approximately 8–10 times higher storage density over SHS, and two times higher over LHS materials when compared on a like for like storage volume basis. However in thermochemical heat storage vapour or moist air transfer is the prime mover which is not an issue in sensible or latent heat storage. This condition brings a requirement for innovative reactor design in order to provide effective vapour diffusion through the adsorbent. Additionally regeneration temperature is another important parameter for efficiently drying the adsorbents with solar energy in summer. Although Zeolite and Silica Gel have satisfy most of the requirements to be a candidate material, they seem highly unlikely to regenerate with solar energy as Zeolite requires 250-300°C and Silica Gel requires 150-200 °C for complete regeneration. Thereby Salt hydrates came into question as some salt hydrates ($CaCl_2$, $LiNO_3$, LiBr, $MgCl$, $MgSO_4$, LiCl) demonstrated remarkable adsorption properties since they are highly hygroscopic and generate heat due to vapour adsorption (Casey et al., 2014, Casey et al., 2015). However the drawback of salt hydrates is that they turn into an aqueous solution as a result of vapour adsorption therefore a host matrix is required to hold the solution. Our research showed that vermiculite could be a promising candidate with its nano-porous nature, low cost, low density, high permeability and high mass uptake. We have tested several nano-composite adsorbents based on salt hydrate impregnated vermiculite. Results revealed that composite $CaCl_2$ – Vermiculite has a great potential as it provides 30 °C temperature lifting of air, heat storage density of 250 kWh/m^3 and has a regeneration temperature of 80 °C which is achievable with solar energy in summer conditions. The composite matrix is also cost effective as unit price is found as \$540/m^3.

Future developments on thermochemical heat storage will focus on reactor design, enhancing heat heat/mass transfer and innovative integration of solar collectors and heat storage systems. This heat storage method demonstrated a potential to be a solution for long term heat storage which will enable us to efficiently utilize solar energy as well as any kind of waste heat. A future target for reduction of building sourced energy consumption and greenhouse gas emission should be achieving centralised large scale – MW level heat storage systems which will collect and distribute the heat to the buildings via heat networks by utilizing moist air system.
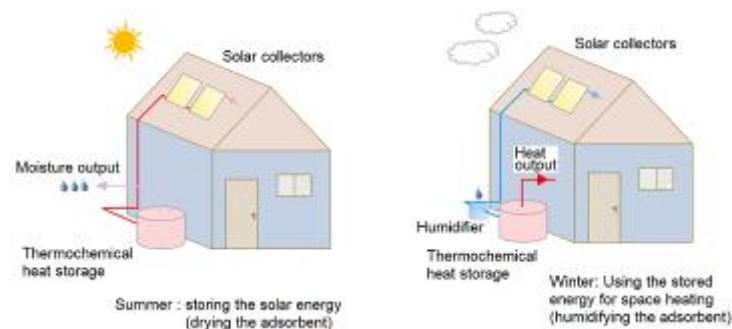
Figure 6: Schematic diagram of seasonal thermochemical heat storage

7. CONCLUSION

Future energy security and minimal environmental impact of energy generation and consumption could be achieved with focusing on innovative technologies using "natural" fluids for power, heat and coolth generation. We have presented the historical evolution of working fluids with providing technical evidence in order to overcome the confusion on their environmental impact. Later we focused on four innovative technologies using air / water. From our point of view, volatile fluids will continue to play major roles in cooling and power generation in the future. However presented new technologies using air / water couple will be the key to optimise energy efficiency - safety also optimal usage of volatile fluids with minimal environmental impact.

8. REFERENCES

AYDIN. D., Casey, S. P., Riffat, S., 2015. The latest advancements on thermochemical heat storage systems. Renew Sustain Energy Rev, 41, 356–367.

BERNERS-LEE, M. and Clark, M.D., 2013. The Burning Question: We can't burn half the world's oil, coal and gas. So how do we quit? Profile Bokks LTD, London.

BOOKER, C., 2015. Was 2014 really "the hottest year ever"? The Telegraph.http://www.telegraph.co.uk/comment/11337317/Was-2014-really-the-hottest-year-ever.html

BRADLEY, L., 2014. Batteries could capture low grade waste heat. Scientific American . http://www.scientificamerican.com/article/batteries-could-capture-low-grade-waste-heat/

BUYADGIE, O., 2014. Solar low-pressure turbo-ejector M-Power system for electricity, heating, cooling and distillation. 13th International Conference on Sustainable Energy Technologies, Geneva, Switzerland.

CASEY, S. P., Elvins, J., Riffat, S., Robinson, A., 2014. Salt impregnated desiccant matrices for 'open' thermochemical energy storage—Selection, synthesis and characterisation of candidate materials. Energy and Buildings , 84, 412–425.

CASEY S. P., Aydin, D., Riffat, S., Elvins, J., 2015. Salt impregnated desiccant matrices for 'open' thermochemical energy storage–hygrothermal cyclic behaviour and energetic analysis by physical experimentation. Energy and Buildings, 92, 128-139.

Climate Change 2013, The Physical Science Basis. Working Group I Contribution to the Fifth Assessment Report of the Intergovernmental Panel on Climate Change. Edited by STOCKER, T. H., QIN, D., PLATTNER, G. K., TIGNOR, M. M. B., ALLEN, S. K., BOSCHUNG, J., NAUELS, A., XIA, Y., BEX, V., MIDGLEY, P. M. Cambridge University Press, New York, 2013.

Coolerado HMX (heat and mass exchanger) brochure. Arvada, Colorado, USA: Coolerado Corporation (2006). http://www.coolerado.com/products/hmx/

Department of Energy and Climate Change. The Future of Heating: Meeting the challenge, 2013.https://www.gov.uk/government/uploads/system/uploads/attachment_data/file/190149/16_04-DECC The_Future_of_Heating_Accessible-10.pdf

EFCTC , 2013. https://www.fluorocarbons.org/uploads/Modules/Library/efctc_fs_ii_accidents-db_2013_references_03.12.2013l.pdf

European Biofuels Technology Platform, 2011. Liquid, synthetic hydrocarbon. http://www.biofuelstp.eu/factsheets/synthetic-hydrocarbons-fact-sheet.pdf

Evaporative Cooling Basics, 2015. Western Environmental Services Corporation. http://www.wescorhvac.com/Evaporative%20cooling%20white%20paper.htm

FARMAN, J. C., Gardiner, B. G., Shanklin, J. D., 1985. Large losses of total ozone in Antarctica reveal seasonal ClOx /NOx interaction. Nature, 315, 207–210. doi:10.1038/315207a0.

FLEMING, N., 2006. Debunking of detox. http://www.telegraph.co.uk/news/uknews/1506912/Debunking-of-detox.html .

International Energy Agency (IEA). Topic: Heat, 2014. http://www.iea.org/topics/heat/

ISIDOROV, V. A., Zenkevich, I. G., Ioffe, B. V.,1990. Volatile organic compounds in solfataric gases. Journal of Atmospheric Chemistry, 10(3), 329-340 .

JHA, A., 2008. Heat and power plants could triple their energy output , report says . The Guardian. http://www.theguardian.com/environment/2008/jun/19/renewableenergy.energyefficiency

LAN, R., Irvine, J. T. S., TAO, S., 2013. Synthesis of ammonia directly from air and water at ambient temperature and pressure. Nature Scientific Reports. 3(1145), 1-7. doi:10.1038/srep01145.

LINDLEY, D., 2010. The energy storage problem. Nature, 464, 18-20. http://www.nature.com/news/2009/090311/pdf/458138a.pdf

LINDEY, D., 2009. The energy should always work twice. Nature, 458, 138-141. http://www.nature.com/news/2009/090311/pdf/458138a.pdf

LOVELOCK, J.E., Maggs, R. J., Wade, R. J., 1973. Halogenated hydrocarbons in and over the Atlantic. Nature 241, 194 - 196.

JONES, J., 2012. The green guide to chemical-free beauty. http://fashion.telegraph.co.uk/beauty/news-features/TMG9598248/The-green-guide-to-chemical-free-beauty.html

MAISOTSENKO, V., Gillan, L. E., Heaton, T. L., Gillan, A. D., 2003. Method and plate apparatus for dew point evaporative cooler. Patent No: US 6581402 B2 .

MAYER, P., 2007. What it costs: CHP (combined heat and power systems) . http://www.building.co.uk/what-it-costs-chp-%28combined-heat-and-power-systems%29/3092455.article

Molina, M. J. & Rowland, F. S., 1974. Stratospheric sink for chlorofluoromethanes: chlorine atom catalysed destruction of ozon. Nature, 249, 810-812.

OLAH, G. et al., 2009. J. Org. Chem. 74 (2), 487–498. http://www.biofuelstp.eu/factsheets/dme-fact-sheet.html

PARAMESHWARAN, R., Kalaiselvam, S., Harikrishnan, S., Elayaperumal A., 2012. Sustainable thermal energy storage technologies for buildings: a review. Renew Sustain Energy Rev 16(5), 2394–433.

POWELL, R. L., 2002. CFC phase-out: have we met the challenge? Journal of Fluorine Chemistry 114, 237–250.

RAVJI, S. J. & Delande, B. S. H., 2012. Container having ingredients for preparing a frozen confection, container holder and device for preparing a frozen confection. Patent No: US20120096876.

Singapore issues HC refrigerant warning, 2014. Cooling Post . http://www.coolingpost.com/world-news/singapore-issues-hc-refrigerant-warning/

The Association for Decentralised Energy. Benefits of CHP, 2015. http://www.theade.co.uk/advantages--benefits-of-chp_183.html

United States Environmental Protection Agency (EPA). Combined Heat and Power Partnership, 2015. http://www.epa.gov/chp/basic/economics.html

ZHAN, C., Duan, Z., Zhao, X., Smith, S., Jin, H., Riffat S., 2011. Comparative study of the performance of the M-cycle counter-flow and cross-flow heat exchangers for indirect evaporative cooling - Paving the path toward sustainable cooling of buildings. Energy, 36, 6790-6805.

ZHAN, C., Zhao, X., Smith, S., Riffat, S. B., 2011. Numerical study of a M-cycle cross-flow heat exchanger for indirect evaporative cooling. Building and Environment , 46, 657-68 .

ZHAO, X., Yang, S., Duan, Z. & Riffat, S. B., 2009. Feasibility study of a novel dew point air conditioning system for China building application. Building and Environment, 44, 1990–1999 .

ZHAO, X., Li, J. M., Riffat, S. B., 2008. Numerical study of a novel counter-flow heat and mass exchanger for dew point evaporative cooling. Applied Thermal Engineering, 28, 1942-51.

ZHAO, X., Liu, S., Riffat, S. B., 2008. Comparative study of heat and mass exchanging materials for indirect evaporative cooling systems. Building and Environment , 43, 1902-10 .

ZOLFAGHARIFARD, E., 2011. Harrison's ice making machine. The Engineer . http://www.theengineer.co.uk/in-depth/classic-archive/harrisons-ice-making-machine/1008228.article

52014DC0398R(01) Communication From The Commission to The European Parliament, The Council, The European Economic and Social Committee and the Committee of The Regions Towards a Circular Economy: A zero waste programme for Europe /* COM/2014/0398 final/2 */, http://eur-lex.europa.eu/legal-content/EN/TXT/?uri=CELEX:52014DC0398R%2801%29

361: An application of homotopy perturbation method for efficiency and effectiveness assessment of longitudinal porous fins

Erdem CUCE[1], Pinar MERT CUCE[2]

[1] University of Nottingham, NG7 2RD, Nottingham, UK, Email:Erdem.Cuce@nottingham.ac.uk
[2] University of Nottingham, NG7 2RD, Nottingham, UK, Email: ezxapm@nottingham.ac.uk

In our previous research, thermal performance investigation of straight fins has been carried out in detail and dimensionless analytical expressions of fin efficiency and fin effectiveness have been presented for the first time in literature via homotopy perturbation method. In this work, previous works have been extended to porous fins. Governing equations have been formulated by utilizing Darcy's model. Dimensionless temperature distribution along the length of porous fin has been developed as a function of porosity and convection parameters. The ratio of porous fin to solid fin heat transfer rate has also been investigated as a function of thermo-geometric fin parameter. The results have been compared with those of finite difference method for a specific case and an excellent agreement has been obtained. The expressions developed are beneficial for thermal engineers for preliminary assessment of thermophysical systems.

Keywords: Homotopy perturbation method, heat transfer, thermal performance, porous fins

1. **INTRODUCTION**

Enhancement of heat transfer through fins is an attractive area of research on account of its wide concept and rapidly developing applications [1]. Fins are extensively used to improve the rate of heat dissipation from a hot surface especially in thermal engineering applications [2,3]. Their areas of usage are not limited with the conventional applications such as air conditioning, refrigeration, chemical processing equipment and internal combustion engines [4]. They are also very promising in heat dissipation systems of space vehicles and in cooling of electronics [5]. As a consequence of the growing significance of efficient, cost-effective heat dissipation systems with smaller weights and volumes, an accurate analysis and interpretation of the heat transfer from extended surfaces has been of vital importance, and hence extensive research has been carried out to date in this area. It is unequivocal from the literature review that the research has been greatly focused on the theoretical [6-10] and experimental [11-14] thermal analysis of solid fins with different profiles and thermophysical properties. However, heat transfer in porous fins has attracted attention of researchers with a wide range of applications especially in recent years.

Heat transfer in porous media appears in many different thermal engineering applications such as reactor cooling, heat exchangers, and solar collectors [15]. The concept of porous fin has been firstly introduced by Kiwan and Al-Nimr [16] as considering Darcy's model in formulation [17]. Several attempts have been made so far for accurate understanding of heat transfer in extended surfaces made of porous materials. Saedodin and Sadeghi [18] have analysed the heat transfer in a cylindrical porous fin through fourth order Runge–Kutta method and they have revealed that the heat dissipation rate from a porous fin is greater than that of a solid fin. Turkyilmazoglu [9] has presented exact solutions to the heat transfer in straight fins with variable cross sectional area and temperature-dependent thermal conductivity. He has found that the exponential fin profiles dissipate much more heat compared to the rectangular fins. A similar output has been obtained by Cuce and Cuce [6] in their CFD work on parabolic fins. They have investigated the effects of concavity level on temperature distribution, efficiency and effectiveness of longitudinal fins under the influence of natural convection and radiation. Their results have indicated that the heat loss per unit mass remarkably increases with increasing concaveness. Kiwan and Al-Nimr [16] have studied the thermal performance of straight porous fins for three different cases as the infinite fin, finite fin with insulated tip and finite fin with uninsulated tip. In their work, all the geometric and flow parameters affecting the temperature distribution along the fin length have been expressed with only one term S_h. The results have indicated that the heat transfer rate from porous fins increases with increasing values of S_h as a consequence of the enhancement in Darcy and Rayleigh numbers. Gorla and Bakier [2] have conducted a theoretical work on thermal analysis of porous fins. The nonlinear governing equations of the problem have been solved using the fourth order Runge–Kutta method. The temperature distribution and heat transfer rate have been determined with respect to changes in radiation parameter and ratio of thermal conductivity. Domairry and Fazeli [19] have studied the rectangular fins with temperature-dependent thermal conductivity via homotopy analysis method, and developed an efficiency expression. They have compared the results with those of the exact solution and Adomian's decomposition method and very good agreement has been obtained. Hatami and Ganji [20] have evaluated thermal performance of circular convective–radiative porous fins with different section shapes and materials. Darcy's model has been utilized to simulate the heat transfer in porous medium. Governing equations have been solved via Least Square Method and fourth order Runge–Kutta method. The results have revealed that the porous fin with exponential shape and made of silicon nitride dissipates the greatest amount of heat compared to the other fin profiles and materials. Kundu et al. [21] have presented a theoretical work for performance assessment of porous fins with various profiles. They have found that the exponential fin profile dissipates the greatest amount of heat. Also, they have stated a significant increase in heat transfer through porous fins for any geometric fin compared to that of solid fins for a low porosity and high flow parameter. Torabi and Zhang [22] have theoretically investigated the thermal efficiencies of four different fin profiles (rectangular, triangular, convex and exponential). Their results have revealed that the rectangular fin profile has the highest surface temperature and therefore the highest fin efficiency. Similarly, Nguyen and Aziz [23] have compared the heat transfer rates from convecting–radiating fins for different profile shapes, but they have utilized finite difference method in their analyses. Taludkar and Mishra [24] studied the effect of combined radiation and convection heat transfer in a porous channel bounded by isothermal parallel plates. They have underlined that the heat transfer is significantly enhanced via the insertion of a porous solid matrix. Popiel et al. [25] have conducted a numerical study to analyse the combined effects of natural convection and radiation on fin efficiency.

As it is unequivocal from literature review that extensive research has been done so far on comparative performance evaluation of solid and porous fins both theoretically and experimentally. It is understood from the overview that various numerical approaches have been utilized for thermal performance assessment of porous fins. However, very few attempts have been made with homotopy perturbation method since the

equations become much more elaborative depending on the nonlinearity and number of term. In addition, no research to date has aimed at developing analytical expressions for the efficiency and the effectiveness of porous fins although it is compulsory for a thorough performance assessment. Therefore in this study, homotopy perturbation method is applied to thermal analysis of rectangular porous fins. Dimensionless temperature distribution, efficiency and effectiveness expressions are developed for longitudinal porous fins.

2. **GOVERNING EQUATIONS**

Figure 1 illustrates the schematic of the rectangular porous fin profile considered in this study. The dimensions of the porous fin are represented by L, w and t which correspond to the length, the width and the thickness of the fin, respectively. For the rectangular fin profile, the cross section area is constant. The porous nature enables the flow of infiltration through the fin. Some assumptions are made for the governing equations of the prescribed problem. The porous medium is assumed to be isotropic and homogenous, and it is saturated with single-phase fluid. The surface radiant exchange is assumed to be negligible. The thermophysical properties of both fluid and solid matrix are considered constant. The temperature inside the porous fin changes only across the fin length. The temperature variation across the fin thickness is considered to be insignificant. The solid matrix and fluid are at local thermal equilibrium with each other. Darcy formulation is utilized for the simulating the interactions between the porous medium and the fluid. If energy balance equation is applied to the differential slice segment shown in Figure 1, one gets:

$$q_x - q_{x+dx} = \dot{m}c_p(T(x) - T_\infty) + hA(T(x) - T_\infty) \tag{1}$$

where q is the heat flux, $\dot{m}$ is the mass flow rate of the fluid passing through the porous material, c_p is the specific heat capacity of the fluid, h is the convective heat transfer coefficient, A is the heat transfer surface area, T is the fin temperature and T_∞ is the ambient temperature. The velocity of fluid passing through the fin any point which is given with V at the fin profile can be determined from Darcy's model [20] as follows:

$$V = \frac{gk\beta(T(x) - T_\infty)}{\upsilon} \tag{2}$$

where g is the gravitational acceleration, k is the thermal conductivity of the fluid, β is the volumetric thermal expansion coefficient and υ is the kinematic viscosity of the fluid. The mass flow rate of the fluid passing through the fin can be given by:

$$\dot{m} = \rho V w dx \tag{3}$$

where ρ is the density of the fluid. The heat transfer surface area of the differential slice segment is obtained from the fin profile as:

$$A = (2w + 2t)dx \tag{4}$$

Substitution of equations (2), (3) and (4) into equation (1) as $dx \to 0$ yields:

$$\frac{dq}{dx} = \frac{\rho c_p gk\beta w}{\upsilon}(T(x) - T_\infty)^2 + h(2w + 2t)(T(x) - T_\infty) \tag{5}$$

From Fourier's law of conduction one can write:

$$q = -k_e wt \frac{dT}{dx} \tag{6}$$

where

k_e is the effective thermal conductivity of the porous fin and given by:

$$k_e = \phi k_f + (1 - \phi)k_s \qquad (7)$$

where ϕ is the porosity variable, k_f is the thermal conductivity of the fluid and k_s is the thermal conductivity of the solid. Substitution of equations (6) and (7) into equation (5) yields:

$$\frac{d^2T}{dx^2} - \frac{\rho c_p g k \beta}{v t k_e}(T(x) - T_\infty)^2 - \frac{h(2w + 2t)}{w t k_e}(T(x) - T_\infty) = 0 \qquad (8)$$

By introducing the following dimensionless parameters

$$\theta = \frac{T(x) - T_\infty}{T_b - T_\infty} \qquad (9)$$

$$\psi = \frac{x}{L} \qquad (10)$$

one gets:

$$\frac{d^2\theta}{d\psi^2} - \xi\theta^2 - \zeta^2\theta = 0 \qquad (11)$$

where ξ is the porous parameter and ζ is the convection parameter, which are defined as follows:

$$\xi = \frac{Da \times Ra}{k_r}\left(\frac{L}{t}\right)^2 \qquad (12)$$

$$\zeta = \left(\frac{h(2w + 2t)L^2}{w t k_e}\right)^{1/2} \qquad (13)$$

In equation (12); Da, Ra and k_r are the Darcy number, the Rayleigh number and the thermal conductivity ratio, which are given by:

$$Da = \frac{\varsigma}{t^2} \qquad (14)$$

$$Ra = \frac{g\beta t^3}{va}T(x) - T_\infty \qquad (15)$$

$$k_r = \frac{k_e}{k_f} \qquad (16)$$

where ς is the permeability of porous fin and a is the thermal diffusivity. In equation (11), ξ represents the influence of the permeability of the porous medium as well as buoyancy effects. In this respect, greater values of ξ indicate higher permeability of the porous medium. On the other hand, ζ is the convection parameter which shows the impact of the surface convecting of the porous fin. The case of finite-length fins with insulated is considered within the scope of this paper. As the fin tip is insulated, no heat transfer occurs at the insulated tip, and hence the boundary conditions of the governing differential equation are as follows:

$$\left.\frac{d\theta}{d\psi}\right|_{\psi=0} = 0 \qquad (17)$$

$$\theta|_{\psi=1} = 1 \qquad (18)$$

3. HOMOTOPY PERTURBATION METHOD

Homotopy perturbation method provides an approximate analytical solution to differential equations in the form of an infinite power series. The method was first introduced by the Chinese mathematician He [29-31].To illustrate the basic ideas of this method, the following general nonlinear differential equation can be considered:

$$\mathcal{B}(u) - f(r) = 0, \quad r \in \Omega \tag{19}$$

with boundary conditions

$$\mathfrak{I}\left(u, \ \frac{\partial u}{\partial n}\right) = 0, \quad r \in \ell \tag{20}$$

where $\mathcal{B}$ is a term of differential operator, $\mathfrak{I}$ a term of boundary operator, $f(r)$ an analytic function and ℓ the boundary of the domain Ω. The operator $\mathcal{B}$ is separated into linear and nonlinear parts namely L and N. Thus, equation (19) can be organized as follows:

$$L(u) + N(u) - f(r) = 0 \tag{21}$$

Then a homotopy $v(r,p)\colon \ \Omega \times [0,1] \rightarrow R$ is constructed which satisfies

$$\mathcal{H}(v,p) = L(v) - L(u_0) + pL(u_0) + p[N(v) - f(r)] = 0 \tag{22}$$

where $p \in [0,1]$ is an embedding parameter and u_0 the first approximation that satisfies the boundary condition. The process of changes in p from zero to unity is that of $v(r,p)$ changing from u_0 to $u(r)$. On the other hand, v is considered as follows:

$$v = v_0 + pv_1 + p^2v_2 + p^3v_3 \tag{23}$$

The method assumes that v_0, v_1, v_2, ... v_j are calculated via the functions obtained in the methodology. But, this might not be available all the time. As a consequence, the approximation for solution is given by:

$$u = \lim_{p \to 1} v_0 + v_1 + v_2 + \cdots + v_j \tag{24}$$

It is unequivocal that there is a great variety of physical systems in heat transfer science governed by various differential equation systems whether linear or strong nonlinear. It needs to be noted that the homotopy perturbation method can be applied to a great majority of the cases in heat transfer.

4. ANALYSIS

$$\mathcal{H}(\theta,p) = L(\theta) - L(u_0) + pL(u_0) + p[N(\theta) - f(r)] = 0 \tag{25}$$
$$\theta = \theta_0 + p\theta_1 + p^2\theta_2 \tag{26}$$

If homotopy equation is rearranged by the following terms

$$L(\theta) = \frac{d^2\theta}{d\psi^2} - \zeta^2\theta \tag{27}$$
$$N(\theta) = -\xi\theta^2 \tag{28}$$
$$L(u_0) = \frac{d^2u_0}{d\psi^2} - \zeta^2u_0 \tag{29}$$

one gets:

$$(\theta_0 + p\theta_1 + p^2\theta_2)'' - \zeta^2(\theta_0 + p\theta_1 + p^2\theta_2) - p\xi(\theta_0 + p\theta_1 + p^2\theta_2)^2 = 0 \tag{30}$$

Through the power of p terms

$$p^0 : \theta_0'' - \zeta^2\theta_0 = 0 \tag{31}$$

$$\left.\frac{d\theta_0}{d\psi}\right|_{\psi=0} = 0 \tag{32}$$

$$\theta_0(1) = 1 \tag{33}$$

$p^1 :$

$$\theta_1'' - \zeta^2\theta_1 - \xi\theta_0^2 = 0 \tag{34}$$

$$\left.\frac{d\theta_1}{d\psi}\right|_{\psi=0} = 0 \tag{35}$$

$$\theta_1(1) = 0 \tag{36}$$

$$p^2 : \theta_2'' - \zeta^2\theta_2 - 2\xi\theta_0\theta_1 = 0 \tag{37}$$

$$\left.\frac{d\theta_2}{d\psi}\right|_{\psi=0} = 0 \tag{38}$$

$$\theta_2(1) = 0 \tag{39}$$

It is possible to improve the accuracy as increasing the number of terms. However in most cases, two terms are able to provide sufficient accuracy for the problem. Hence this work considers homotopy perturbation method with two terms, and the reliability of the method is verified by the results obtained from another numerical technique. Solving equations (31) and (34) via a simple MATLAB code yields:

$$\theta_0 = sech(\zeta)cosh(\zeta\psi) \tag{40}$$

$$\theta_1 = -\frac{1}{6}\frac{\exp(\zeta\psi)\left(\frac{2\xi}{\exp(2\zeta)} - 12\xi + 2\xi\exp(2\zeta)\right)}{\zeta^2\left(\frac{1}{\exp(\zeta)} + \exp(\zeta)\right)^3} - \frac{1}{6}\frac{\frac{2\xi}{\exp(2\zeta)} - 12\xi + 2\xi\exp(2\zeta)}{\zeta^2\exp(\zeta\psi)\left(\frac{1}{\exp(\zeta)} + \exp(\zeta)\right)^3}$$

$$-\frac{1}{24}\frac{\exp(\zeta\psi)\left(\frac{6\xi}{\exp(\zeta\psi)} - 3\xi\exp(\zeta\psi) + \frac{\xi}{\exp(3\zeta\psi)}\right)}{\zeta^2\left(\frac{1}{2}\frac{1}{\exp(\zeta)} + \frac{1}{2}\exp(\zeta)\right)^2}$$

$$-\frac{1}{24}\frac{6\xi\exp(\zeta\psi) - \frac{3\xi}{\exp(\zeta\psi)} + \xi\exp(3\zeta\psi)}{\zeta^2\exp(\zeta\psi)\left(\frac{1}{2}\frac{1}{\exp(\zeta)} + \frac{1}{2}\exp(\zeta)\right)^2} \tag{41}$$

After all, the solution is achieved as follows:

$$\theta = \theta_0 + \theta_1 = sech(\zeta)cosh(\zeta\psi)$$

$$-\frac{1}{6}\frac{\exp(\zeta\psi)\left(\frac{2\xi}{\exp(2\zeta)} - 12\xi + 2\xi\exp(2\zeta)\right)}{\zeta^2\left(\frac{1}{\exp(\zeta)} + \exp(\zeta)\right)^3} - \frac{1}{6}\frac{\frac{2\xi}{\exp(2\zeta)} - 12\xi + 2\xi\exp(2\zeta)}{\zeta^2\exp(\zeta\psi)\left(\frac{1}{\exp(\zeta)} + \exp(\zeta)\right)^3}$$

$$-\frac{1}{24}\frac{\exp(\zeta\psi)\left(\frac{6\xi}{\exp(\zeta\psi)}-3\xi\exp(\zeta\psi)+\frac{\xi}{\exp(3\zeta\psi)}\right)}{\zeta^2\left(\frac{1}{2}\frac{1}{\exp(\zeta)}+\frac{1}{2}\exp(\zeta)\right)^2}$$

$$-\frac{1}{24}\frac{6\xi\exp(\zeta\psi)-\frac{3\xi}{\exp(\zeta\psi)}+\xi\exp(3\zeta\psi)}{\zeta^2\exp(\zeta\psi)\left(\frac{1}{2}\frac{1}{\exp(\zeta)}+\frac{1}{2}\exp(\zeta)\right)^2} \tag{42}$$

The efficacy of the presented method is checked through a specific case ($\xi=\zeta=1$) and the accordance is given in Figure 2. There is an excellent agreement between the results of compared methods. As previously emphasized, the performance of the homotopy perturbation method can easily be improved as increasing term number. However, only two terms are capable of producing excellent results in most cases which is unequivocal in Figure 2. This characteristic feature of homotopy perturbation method makes is attractive for rapid and accurate preliminary assessment of thermophysical systems.

5. RESULTS AND DISCUSSION

5.1 Temperature Distribution

In this section, results obtained from homotopy perturbation method are presented in detail. As the first step of the analyses, the temperature distribution along the length of longitudinal porous fin is presented with respect to changes in porous and convection parameter. Figure 3 depicts the dimensionless temperature distribution within porous fin with respect to changes in convection parameter (ζ) while the porous parameter remains constant ($\xi=1$). Similarly, porous parameter dependency of the dimensionless temperature distribution is illustrated in Figure 4 whereas the convection parameter is constant ($\zeta=1$). It can be easily observed from each graph that the temperature of porous fin rapidly decreases and the fin quickly reaches the surrounding temperature while the porous and convection parameters increase. This is an expected consequence of the natural convection phenomenon and verified by the results of Saedodin and Shahbabaei [32].

Determination of dimensionless temperature distribution enables to compare the heat transfer rates from porous and solid fin. Heat transfer rates from porous and solid fin can be given by equations (43) and (44), respectively:

$$q_p=-k_e wt\frac{dT}{dx}\bigg|_{x=0} \tag{43}$$
$$q_s=hPL(T_b-T_\infty) \tag{44}$$

If the heat transfer ratio is determined as considering the dimensionless terms, equation (45) is obtained as follows:

$$\frac{q_p}{q_s}=\gamma=\tau\frac{d\theta}{d\psi}\bigg|_{\psi=1} \tag{45}$$

where τ is the thermo-geometric fin parameter and given by:

$$\tau=-\frac{k_e wt}{hPL^2} \tag{46}$$

In this respect, Figure 5 shows the ratio of porous fin to solid fin heat transfer rate for different values of porous parameter. It is observed that the dimensionless heat transfer rate **(γ)** increases linearly with increasing thermo-geometric fin parameter (τ). In addition to that, for any constant value of τ, the ratio of heat dissipation rate between porous and solid fin increases with porous parameter (ξ). A similar tendency is found in the results of Gorla and Bakier [2].

5.2 in efficiency

As reported by Bergman et al. [33] efficiency of an extended surface is given by the following equation:

$$\eta = \frac{Q_f}{Q_m} \tag{47}$$

where Q_f is the heat transfer rate from the extended surface and Q_m is the maximum heat transfer rate that can be achieved from the extended surface. The heat dissipation from the fin can be calculated through Newton's law of cooling:

$$Q_f = \int_0^L hP\left(T(x) - T_\infty\right)dx \tag{48}$$

where P is the fin perimeter. On the other hand, maximum heat transfer is calculated where the fin base temperature is remained the same throughout the fin as follows:

$$Q_m = hPL(T_b - T_\infty) \tag{49}$$

where T_b is the fin base temperature. If equation (47) is rearranged with equations (48) and (49), one gets:

$$\eta = \frac{\int_0^L hP\left(T(x) - T_\infty\right)dx}{hPL(T_b - T_\infty)} = \int_{\psi=0}^1 \theta(\psi)d\psi \tag{50}$$

By integrating equation (50), the dimensionless expression of fin efficiency is achieved as given below:

$$\eta = \frac{\begin{pmatrix} -\frac{5}{2}exp(3\zeta)\xi cosh(\zeta) + exp(6\zeta)\zeta^2 + \frac{1}{6}\xi cosh(\zeta)exp(\zeta) \\ -exp(2\zeta)\zeta^2 + \frac{5}{2}exp(5\zeta)\xi cosh(\zeta) - \frac{1}{6}exp(7\zeta)\xi cosh(\zeta) \\ +\frac{1}{2}exp(8\zeta)\zeta^2 - \frac{1}{2}\zeta^2 \\ -2\xi cosh(\zeta)exp(5\zeta)\zeta - 2\xi cosh(\zeta)exp(3\zeta)\zeta \end{pmatrix}exp(-\zeta)}{\left(\zeta^3 cosh(\zeta)\left(1 + 3exp(2\zeta) + 3exp(4\zeta) + exp(6\zeta)\right)\right)} \tag{51}$$

Figure 6 shows the variation of fin efficiency with respect to changes in porous and convection parameter. It is noted that the fin efficiency considerably reduces with increasing porous and convection parameter. This finding can be attributed to the lower fin temperatures due to the higher cooling influence of ξ and ζ at greater values. Cuce and Cuce [1] have previously demonstrated the similar tendency for their theoretical work on rectangular solid fins. It is observed that the homotopy perturbation method is very effective for evaluating the thermal efficiency of porous fins as a function of thermophysical properties.

5.3 Fin effectiveness

The effectiveness of an extended surface is determined by the following equation [33]:

$$\varepsilon = \frac{Q_f}{Q_{fb}} \tag{52}$$

where Q_{fb} corresponds to the heat loss from the fin base. Assuming the width of the fin (w) is notably greater than the fin thickness (t), Q_{fb} can be given by:

$$Q_{fb} = \frac{hPt}{2}(T_b - T_\infty)$$ (53)

If equations (48) and (53) are substituted into equation (52), one gets:

$$\varepsilon = \frac{\int_0^L 2hP\,(T(x) - T_\infty)dx}{hPt(T_b - T_\infty)}$$ (54)

Efficiency expression can be rearranged as follows:

$$\varepsilon = \int_{\psi=0}^{1} \omega\theta(\psi)d\psi$$ (55)

where $\omega = 2L/t$. Through integration, the dimensionless expression of fin effectiveness is found as given in equation (56). As it is clear in Figure 7 that the fin effectiveness exponentially decreases with increasing convection parameter. However, it increases with increasing values of fin length/fin thickness ratio. Cuce et al [3] have previously developed an effectiveness expression for longitudinal solid fins, and if convection parameter is neglected ($\xi = 0$), the results show an excellent agreement with those of they obtained.

$$\varepsilon = \frac{\begin{pmatrix} -\frac{5}{2}exp(3\zeta)\xi cosh(\zeta) + exp(6\zeta)\zeta^2 + \frac{1}{6}\xi cosh(\zeta)exp(\zeta) \\ -exp(2\zeta)\zeta^2 + \frac{5}{2}exp(5\zeta)\xi cosh(\zeta) - \frac{1}{6}exp(7\zeta)\xi cosh(\zeta) \\ +\frac{1}{2}exp(8\zeta)\zeta^2 - \frac{1}{2}\zeta^2 \\ -2\xi cosh(\zeta)exp(5\zeta)\zeta - 2\xi cosh(\zeta)exp(3\zeta)\zeta \end{pmatrix}exp(-\zeta)\omega}{\left(\zeta^3 cosh(\zeta)\left(1 + 3exp(2\zeta) + 3exp(4\zeta) + exp(6\zeta)\right)\right)}$$ (56)

Within the scope of this paper, the competitiveness of the proposed method with the well-known commercial codes [34] developed by experts in applied mathematics such as Ascher, Mattheij and Russell has also been evaluated. Their pioneer works on the numerical solution of boundary value problems for ordinary differential equations [35-38] have been utilized for a sensitive assessment of the HPM. In this regard, the results of the dimensionless temperature distribution along the fin length have been calculated and compared as illustrated in Table 1. It can be concluded from the results that there is an excellent agreement between their commercial FORTRAN code and the HPM.

6. CONCLUSION

In the present study, our previous works on theoretical and experimental investigation of longitudinal solid fins have been extended to porous fins. Temperature distribution along the length of porous fin, fin efficiency and fin effectiveness have been determined as a function of porous and convection parameter. A dimensionless expression of fin effectiveness as a function of fin length/fin thickness ratio has been firstly introduced. The results have revealed that the homotopy perturbation method is a very practical and reliable approach that presents an accurate approximate solution without any linearization. The expressions developed might be very significant for thermal engineers for preliminary assessment of thermophysical systems instead of consuming time in heat conduction problems governed by strongly nonlinear differential equations. In further works, homotopy perturbation method is expected to apply to porous fins with variable cross-sectional area for a more elaborative investigation. Moreover, alternative solution techniques such as Adomian's decomposition method and Galerkin method can be compared with homotopy perturbation method in terms of applicability, reliability and simplicity for various applications of thermal science.
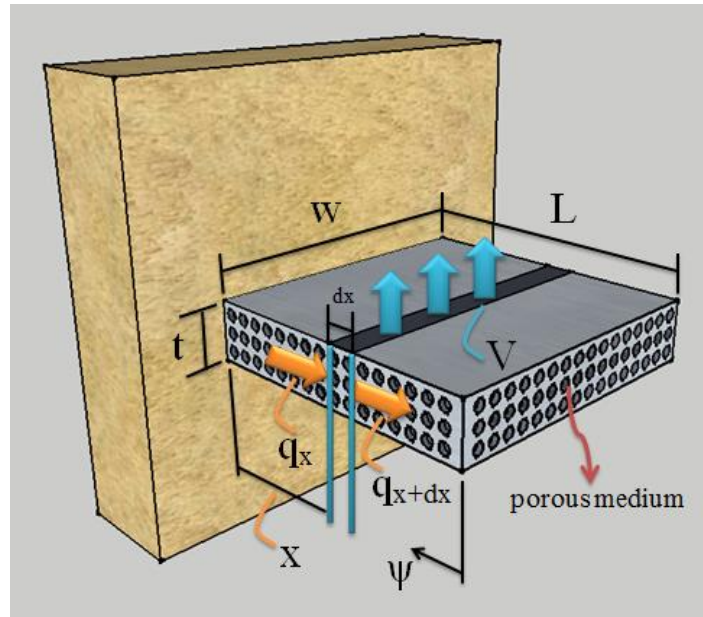
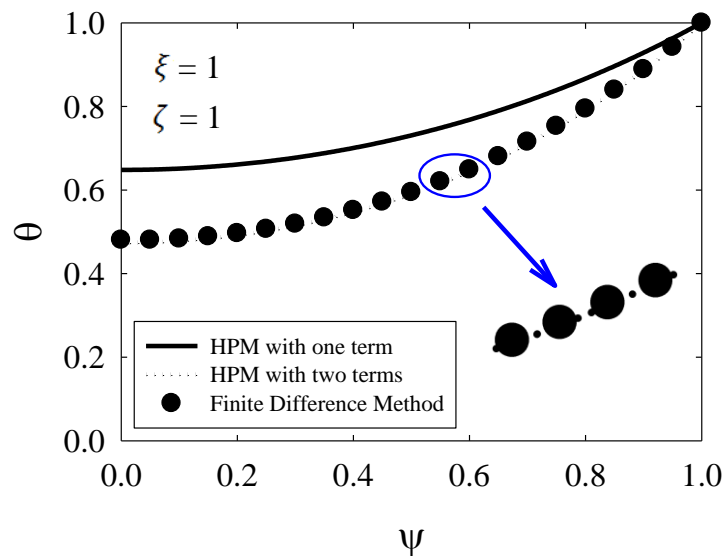***Figure 1***. *Schematic of the rectangular porous fins.*

Figure 2. *Accuracy of the results from HPM for a specific case.*
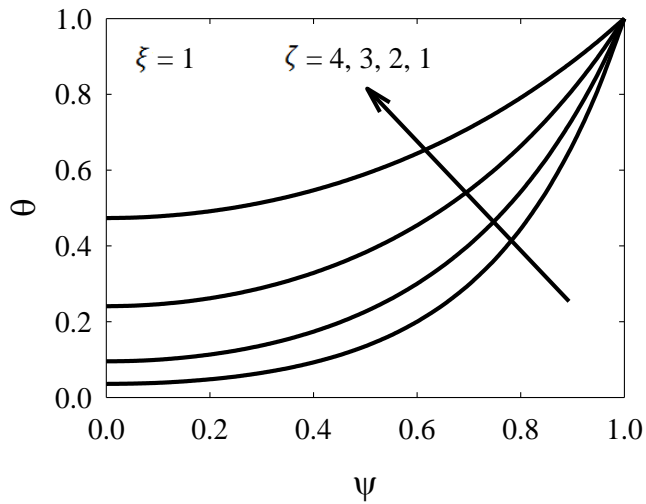
Figure 3. Dimensionless temperature distribution along the length of porous fin for different values of convection parameter.
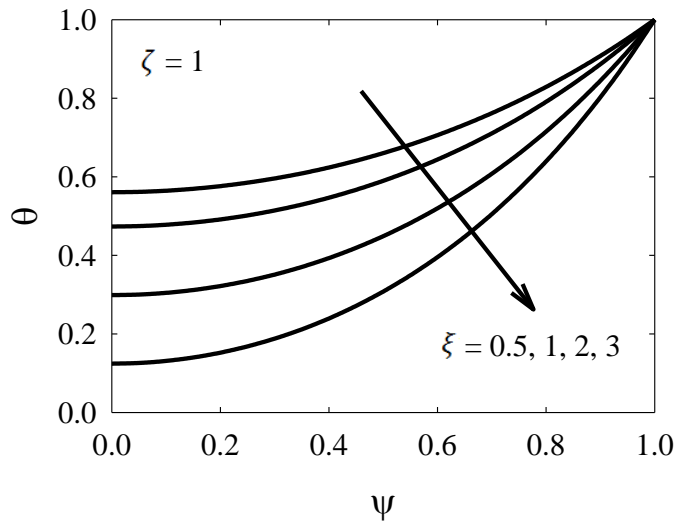

Figure 4. Dimensionless temperature distribution along the length of porous fin for different values of porous parameter.
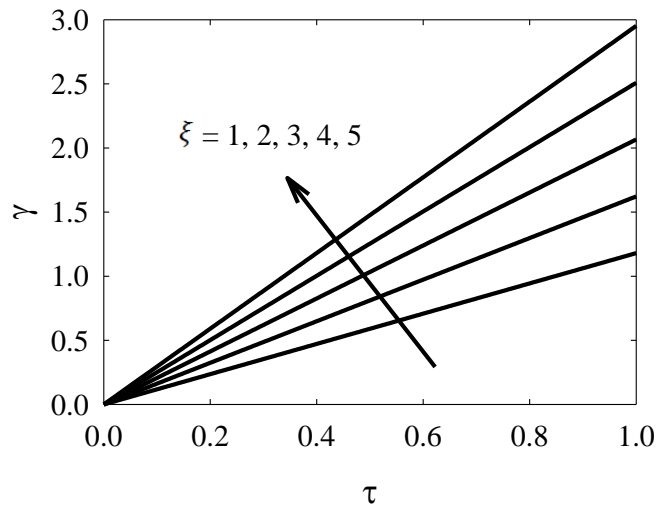

Figure 5. Thermo-geometric fin parameter dependency of the ratio of porous fin to solid fin heat transfer rate for different values of porous parameter.
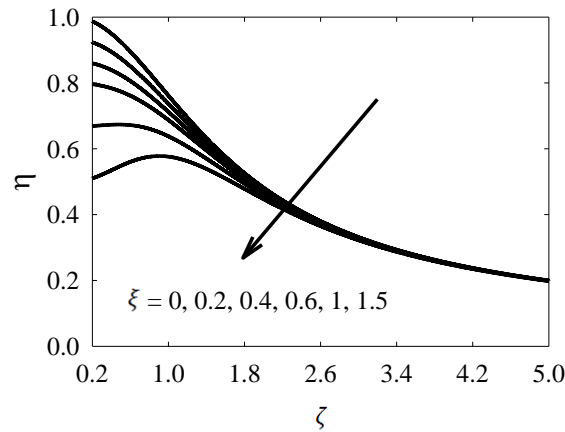
*F**igure 6**. Efficiency of porous fin for different values of porous and convection parameter.*
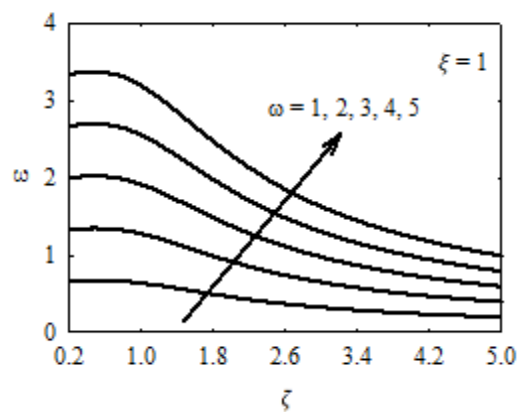

Figure 7. *Effectiveness of porous fin for different values of convection parameter and as a function of fin length/fin thickness ratio.*

Table 1.   The competiveness of the proposed method with a well-known commercial code: Comparison of the dimensionless temperature distribution (θ) along the fin length

ψ	two-term HPM	twpbvp.f [34]
0.0000	0.4735	0.4804
0.0500	0.4746	0.4804
0.1000	0.4780	0.4833
0.1500	0.4836	0.4886
0.2000	0.4915	0.4963
0.2500	0.5017	0.5064
0.3000	0.5143	0.5190
0.3500	0.5293	0.5340
0.4000	0.5468	0.5516
0.4500	0.5670	0.5718
0.5000	0.5898	0.5946
0.5500	0.6154	0.6203
0.6000	0.6440	0.6488
0.6500	0.6757	0.6803
0.7000	0.7106	0.7150
0.7500	0.7489	0.7529
0.8000	0.7909	0.7944
0.8500	0.8368	0.8396
0.9000	0.8867	0.8887
0.9500	0.9410	0.9421
1.0000	1.0000	1.0000

7. REFERENCES

[1]   CUCE E, Cuce PM. Homotopy perturbation method for temperature distribution, fin efficiency and fin effectiveness of convective straight fins with temperature-dependent thermal conductivity. Proceedings of the Institution of Mechanical Engineers, Part C: Journal of Mechanical Engineering Science 2013; 227(8): 1754–60.

[2]   GORLA RSR, Bakier AY. Thermal analysis of natural convection and radiation in porous fins. International Communications in Heat and Mass Transfer 2011; 38: 638–45.

[3]   CUCE PM, Cuce E, Aygun C. Homotopy perturbation method for temperature distribution, fin efficiency and fin effectiveness of convective straight fins. International Journal of Low-Carbon Technologies 2014; 9(1): 80–4.

[4]   ZHANG HG, Wang EH, Fan BY. Heat transfer analysis of a finned-tube evaporator for engine exhaust heat recovery. Energy Conversion and Management 2013; 65: 438–47.

[5]   AZIZ A, Nguyen H. Two dimensional performance of convecting–radiating fins of different profile shapes. Waerme and Stoffuebertrag 1993; 28: 481–7.

[6]   CUCE PM, Cuce E. Effects of concavity level on heat loss, effectiveness and efficiency of a longitudinal fin exposed to natural convection and radiation. International Journal of Numerical Methods for Heat and Fluid Flow 2013; 23(7): 1169–78.

[7]   ARSLANTURK C. Analysis of thermal performance of annular fins with variable thermal conductivity by homotopy analysis method. Isi Bilimi ve Teknigi Dergisi – Journal of Thermal Science and Technology 2010; 30(2): 1–7.

[8]   ARSLANTURK C. Optimization of straight fins with a step change in thickness and variable thermal conductivity by homotopy perturbation method. Isi Bilimi ve Teknigi Dergisi – Journal of Thermal Science and Technology 2010; 30(2): 9–19.

[9]   TURKYILMAZOGLU M. Exact solutions to heat transfer in straight fins of varying exponential shape having temperature dependent properties. International Journal of Thermal Sciences 2012; 55: 69–75.

[10]   GANJI DD, Rahimi M, Rahgoshay M. Determining the fin efficiency of convective straight fins with temperature dependent thermal conductivity by using homotopy perturbation method. International Journal of Numerical Methods for Heat and Fluid Flow 2012; 22(2): 263–72.

[11]   KIM HJ, An BH, Park J, Kim DK. Experimental study on natural convection heat transfer from horizontal cylinders with longitudinal plate fins. Journal of Mechanical Science and Technology 2013; 27(2): 593–9.

[12]   GAWAI US, Mathew VK, Murtuza SD. Experimental investigation of heat transfer by pin fin. International Journal of Engineering and Innovative Technology 2013; 2(7): 202–4.

[13]   ALIABADI MK, Hormozi F, Zamzamian A. Experimental analysis of thermal–hydraulic performance of copper–water nanofluid flow in different plate-fin channels. Experimental Thermal and Fluid Science 2014; 52: 248–58.

[14]   DONG JQ, Zhang Y, Li GT, Xi WW. Experimental study of wavy fin aluminum plate fin heat exchanger. Experimental Heat Transfer 2013; 26(4): 384–96.

[15]   ALKAM MK, Al-Nimr MA. Solar collectors with tubes partially filled with porous substrate. Journal of Solar Energy Engineering 1999; 121: 20–4.

[16]   KIWAN S, Al-Nimr M. Using porous fins for heat transfer enhancement. Journal of Heat Transfer 2001; 123(4): 790–5.

[17]   KIWAN S. Effect of radiative losses on the heat transfer from porous fins. International Journal of Thermal Sciences 2007; 46(10): 1046–55.

[18]   SAEDODIN S, Sadeghi S. Temperature distribution in long porous fins in natural convection condition. Middle-East Journal of Scientific Research 2013; 13(6): 812–7.

[19]   DOMAIRRY G, Fazeli M. Homotopy analysis method to determine the fin efficiency of convective straight fins with temperature-dependent thermal conductivity. Communications in Nonlinear Science and Numerical Simulation 2009; 14: 489–99.

[20]   HATAMI M, Ganji DD. Thermal performance of circular convective–radiative porous fins with different section shapes and materials. Energy Conversion and Management 2013; 76: 185–93.

[21]   KUNDU B, Bhanja D, Lee KS. A model on the basis of analytics for computing maximum heat transfer in porous fins. International Journal of Heat and Mass Transfer 2012; 55: 7611–22.

[22]   TORABI M, Zhang QB. Analytical solution for evaluating the thermal performance and efficiency of convective–radiative straight fins with various profiles and considering all non-linearities. Energy Conversion and Management 2013; 66: 199–210.

[23]   NGUYEN A, Aziz A. The heat transfer rates from convecting-radiating fins for different profile shapes. Heat and Mass Transfer 1992; 27(2): 67–72.

[24]   TALUKDAR P, Mishra SC, Trimis D, Durst F. Combined radiation and convection heat transfer in a porous channel bounded by isothermal parallel plates. International Journal of Heat and Mass Transfer 2004; 47: 1001–13.

[25]   POPIEL CO, Blanch R, Wojtkowiak J. Efficiency of the horizontal fin subjected to free convection and radiation heat transfer. Heat Transfer Engineering 2007; 26(4): 299–309.

[26]   GANJI DD, Ganji ZZ, Ganji HD. Determination of temperature distribution for annual fins with temperature-dependent thermal conductivity by HPM. Thermal Science 2011; 15: 111–5.

[27]   KIWAN S, Zeitoun O. Natural convection in a horizontal cylindrical annulus using porous fins. International Journal of Numerical Methods for Heat and Fluid Flow 2008; 18(5): 618–34.

[28]   HATAMI M, Hasanpour A, Ganji DD. Heat transfer study through porous fins (Si_3N_4 and AL) with temperature-dependent heat generation. Energy Conversion and Management 2013; 74: 9–16.

[29]   HE JH. Homotopy perturbation technique. Computer Methods in Applied Mechanics and Engineering 1999; 178: 257–62.

[30]   HE JH. A coupling method of a homotopy technique and a perturbation technique for non-linear problems. International Journal of Non-Linear Mechanics 2000; 35: 37–43.

[31]   HE JH. Homotopy perturbation method: a new nonlinear analytical technique. Applied Mathematics and Computation 2003; 135: 73–9.

[32]   SAEDODIN S, Shahbabaei M. Thermal analysis of natural convection in porous fins with homotopy perturbation method (HPM). Arabian Journal for Science and Engineering 2013; 38: 2227–31.

[33]   BERGMAN TL, Lavine AS, Incropera FP, DeWitt DP. Fundamentals of heat and mass transfer. 7th ed. Danvers, MA: John Wiley & Sons, 2011.

[34]   http://www.netlib.org/ode/. (Last access is on 18.04.2014).

[35]   ASCHER UM, Mattheij RMM, Russell RD. Numerical solution of boundary value problems for ordinary differential equations. Philadelphia, PA 19104-2688, USA, 1987.

[36]   ASCHER U, Christiansen J, Russell RD. Collocation software for boundary-value ODEs. ACM Transactions on Mathematical Software (TOMS) 1981; 7(2): 209–22.

[37]   BADER G, Ascher U. A new basis implementation for a mixed order boundary value ODE solver. SIAM Journal on Scientific and Statistical Computing 1987; 8(4): 483–500.

[38]   ASCHER U, Christiansen J, Russell RD. A collocation solver for mixed order systems of boundary value problems. Mathematics and Computation 1979; 33: 659–79.

203: Engine performance and emission characterization of modelled biodiesel fuels from hybridised moringa oleifera and jatropha curcas seed oils

Andrew C. ELOKA-EBOKA[1], Freddie L. INAMBAO [2]

1 Green Energy Solutions Research Group, Discipline of Mechanical Engineering, University of KwaZulu-Natal, Howard College, Durban 4041, South Africa, fatherfounder@yahoo.com, eloka-ebokaa@ukzn.ac.za

Biodiesel fuels are one of the easiest alternative fuels to be utilized in compression ignition engines. They are renewable, environmentally friendly and produce less gaseous and exhaust emissions. A variety of biodiesel feedstocks have been experimented with using different engine types and for various performance evaluations. In this study, overall engine performance tests and gaseous/emission characterizations were conducted in a four stroke versatile internal combustion engine (TD 300) over a wide range of throttle from the feedstocks of Moringa and Jatropha biodiesel and their resultant biodiesel hybrids. The hybrid compositions were J50M50, J40M10, J30M20, J20M30, and J10M40 from crude oil samples (in situ) and: BM50J50, BM40J10, BM30J20, BM20J30 and BM10J40 from produced biodiesel (ex situ). The biodiesel hybrids were produced by transesterification at specific optimization protocols and subjected to a novel approach in biodiesel development and hybridization using in situ and ex situ processes as reported in our earlier studies (Eloka-Eboka and Inambao [16]). The single stock biodiesel of Moringa and Jatropha and their hybrids performed favourably in comparison to AGO following ASTM standardized procedures. The torque, air consumption, ambient air temperature and pressure, specific fuel consumption, brake thermal and mechanical efficiency, brake power, engine noise, exhaust temperature and smoke opacity were determined. Also, gaseous emission was conducted using an online sampler which was subjected to a GC-MS spectrophotometer interacting with a flame induced detector (FID) for all comparisons. Results show greater improvement in performance from the hybrids and Moringa biodiesel with close similarity to AGO. The emissions were however insignificant to the immediate environment as against those of AGO. Biodiesel development continues to be currently researched until the much needed breakthrough is achieved globally.

Keywords: Engine, performance, emission, characterization, biodiesel, Moringa, Jatropha, seed oil, hybrids, hybridization, in situ, ex situ

1. INTRODUCTION

The civilization of any country has come to be reckoned on the basis of the number of automotive vehicles being used by the populace of the country. The tremendous rate at which population explosion is taking place imposes expansion of cities to larger areas and the common person is forced to travel long distances even for his/her routine work [1-3]. This in turn is causing an increase in vehicular population at an alarming rate thereby creating huge pressures for different governments in raising substantive foreign exchange for the import of crude petroleum products to meet the fuel requirements of automobiles and engines. The large amount of pollutants from the exhausts of engine applications running on fossil fuels have drastically increased in proportion to the number of vehicles on roads [4]. In view of the need and heavy demand for diesel fuel involved in transport in the domestic, industrial and agricultural sector and also the fast depletion of unevenly distributed fossil fuels, the search for alternate fuels has become pertinent apart from effective fuel utilization which has been the concern of the engine designers and manufacturers, developers, users and researchers involved in fuel, renewable and alternate fuel research and combustion [5-7].

When Rudolf Diesel [8] first invented the diesel engine, about a century ago, he demonstrated the principle by employing peanut oil and hinted that vegetable oil would be the future fuel in diesel engines. However, the higher viscosity and chemical composition of unprocessed oils and fats have been shown to cause problems in a number of areas: (i) piston ring sticking; (ii) injector and combustion chamber deposits; (iii) fuel system deposits: (iv) reduced power; (v) reduced fuel economy and (vi) increased exhaust emissions. The above mentioned problems can be solved once vegetable oils are converted chemically into biodiesel [6, 7]. Biodiesels derived from vegetable oils present a very promising alternative to diesel fuel since biodiesels have numerous advantages compared to fossil fuels as they are renewable, biodegradable, provide energy security and foreign exchange savings besides addressing environmental concerns and socio-economic issues [9-14]. These biodiesels have lower viscosity, density, molecular weight and ratio of carbon to hydrogen. Experiments were conducted [5-9] with conventional engine fuelled with biodiesel and it was reported that performance was comparable with conventional engines [10, 11, 13]. The drawbacks associated with biodiesel for use as fuels in compression ignition engines call for improvement in biodiesel production and processes [14, 15].

Biodiesel as mono-alkyl ester made from natural and renewable vegetable oil and animal fats based feedstock can be improved upon by chemical processes such as hybridization [16, 17]. Biodiesel is an environmentally friendly alternative diesel fuel consisting of the alkyl esters of fatty acids which are expected to play a significant role in reducing overall CO_2 emissions which will in turn clean and sustain the environment [14, 15]. Biodiesel is produced commercially by a chemical reaction, transesterification, which lowers the viscosity of the vegetable oils, breaks the poly-unsaturated nature of the bonds and improves its performance, combustion and atomization in the combustion chambers. Since biodiesel is an oxygenated, sulphur-free fuel, it typically reduces engine and gaseous emissions except for the oxides of nitrogen (NOX) which are slightly higher than fossil diesel [14, 15]. The chemical and physical properties of the fatty acids, as well as the effect of molecular structure determine the overall properties of biodiesel fuel. Investigations into the impact of FAME properties on diesel engines are highly topical, as hybrids of different feedstocks and higher blends with automotive gas oil (fossil diesel) of biodiesel are introduced [12, 18].

1.1 Emission Effects

Global warming is considered to be one of the greatest environmental threats facing our modernized and technological world. Climate change has mainly been caused by the increase in atmospheric greenhouse gases due to human activities since the start of the industrial era which includes burning fuel to run engines [18]. When fuels are burnt, the exhaust products contain gaseous, solid, and liquid emissions. For internal combustion (IC) engines, there are just a few basic types of emissions to consider: Carbon (IV) oxide, oxides of Nitrogen (NOx), oxides of Sulphur (SOx), Carbon (II) oxide (CO), hydrocarbons (HC), and particulate matter (PM). In addition to these primary pollutants, reactions in the atmosphere generate secondary pollutants, namely acid rain, photochemical smog and tropospheric ozone [18]. Many of these pollutants have serious implications on human health, safety and the environment. Consequently, many countries have established strict environmental regulations that must be met by all automobile manufacturers and fuel developers.

1.2 Status and legislation of biodiesel use in South Africa

Legislation has driven research to satisfy increasingly stringent emission requirements such as improving the combustion process and utilizing advanced after-treatment systems. Another approach has been to develop and popularize electrically powered vehicles and hybrids, and the use of alternative fuels. Of most recent and still at developmental stage is the process of hybridization of different feedstocks of biodiesel to improve general biodiesel fuel properties which this paper is related to. Studies are at top gear at the Biofuel Research Laboratories of the Green Energy Solutions Research group at the University of KwaZulu-Natal, Howard College, Durban, South Africa to make the required breakthrough. Different feedstocks are being experimented with to ascertain fuel properties and performance characterization [16]. Biofuels are expected to play a significant role in reducing overall CO_2 emissions [4]. Also, the possibility of substituting cleaner burning alternative fuels for gasoline and diesel has drawn increasing attention over the past decade [16]. Biofuels produced from sugar cane, corn or other vegetable oils are attracting interest as renewable energy sources that do not increase CO_2 levels [17]. That is why the South African government granted a reduction of 30% fuel tax for biodiesel thus encouraging its utilization in the country [19]. In terms of legislation, the South African Bureau of Standards (SABS) drafted a provisional biodiesel standard (SANS 1935:2011) [20] edition 2 as comparable to the ASTM D6751:2 which was based on European standards with some modification in parameters like the iodine value, and allowing the use of other esters as well [19]. Feedstocks of specific interests include soya oil, corn and physics nuts (Jatropha). Some studies were conducted with the objective of determining the influence of biodiesel development and application on the South Africa's economy without interfering with food production. The outcome was positive with the assessment that biodiesel especially from non-edible sources could replace 20% of imported diesel in the country [19].

1.3 Engine performance

Cetane Index (CN) is one of the main indicators of the ignition quality and combustion miscibility in diesel engines. It is a dimensionless descriptor for the ignition delay time of a fuel upon injection into the combustion chamber. The higher the cetane number, the shorter the ignition delay time and vice versa. It is an acceptable fact that the CN of biodiesel is generally higher than fossil diesel fuel due to the absence of aromatic compounds and unburnt hydrocarbons [20] and better amongst biodiesel hybrids [16,17]. The European standard for biodiesel (EN 14214:2003) specifies the minimum requirements for CN to be 51, since too low cetane number might cause very rapid and incomplete combustion. Like other properties, Cetane number/index number is affected by the molecular structure of the source material FA [21-23]. The CN of biodiesel depends on the distribution of fatty acids in the original oil or fat from which it was produced. The longer the straight chain FA and the more saturated the molecules in the fuel, the higher the CN [7, 10, 20].

Higher Cetane numbers of the fuel was also correlated with reduced NO exhaust emissions for conventional diesel fuel as stated by Knothe and Steidley [22], however this is not always true for all types of engine technologies, as modern engines that are equipped with more sophisticated injection systems that control the rate of injection are less sensitive to CN variations [20, 22-23]. In addition, several other properties of biodiesel are important for determining its suitability as an alternative to petroleum diesel fuel. It is generally known that biodiesel fuels have lower heat release values than petroleum diesel. Fuel density and number of double bonds also have an effect on the fuel's calorific value but not significantly. Hybridization alters this structural sequence to suit desired fuel needs. A review conducted by some biodiesel researchers concluded that the FAMEs have slightly higher combustion efficiency than baseline diesel fuel due to the structural oxygen content of the biodiesel which improves the combustion process, as also and similar observations reported by Lapuerta et al. [24-26].

Lubricity properties of fuel are very critical for reducing friction wear in engine components which are normally lubricated by the fuel rather than crankcase oil. Mechanical wear and fuel leaks can cause many problems in the engine fuelling system, as fuel pumps and injectors depend on the fuel for lubrication of moving parts. It has been known that biodiesel improves the lubricity of diesel fuel, and it is a common practice among most of the diesel fuel producers to add 1-5% of biodiesel in the ultralow Sulfur diesel (ULSD) fuel to improve its lubrication quality [19, 22]. Particulate Matter (solids or liquids) emissions have been of considerable concern with the manufacturers of diesel engines, as it is very visible and often contains some carcinogenic aromatic hydrocarbons such as benzene. According to an EPA technical report issued in 2002 [12, 14], the particulate matter emissions of B100 and B20 are less than petroleum diesel by 47%, and 12% respectively. Lapuerta et al. [24] reported that particulate matter emissions were investigated by a few authors and their results did not show any significant correlation either with the chain

length or with the unsaturation level. But Monyem and Van Gerpen et al. [27, 28] reported an increase in particulate matter with increasing number of double bonds in the fatty acid and no significant impact of FA chain length was observed. NOx formation is influenced by the oxygen concentration in the fuel, combustion duration, and mixture richness in the combustion chamber [2]. The formation of NOx emissions is also effected by fuel properties, such as cetane number, aromatics content and iodine number. Lapuerta et al. [24] reported that the use of biodiesel fuels leads to a slight increase in NOx emissions, especially in the case of highly un-saturated biodiesel fuels.

1.4 Improvement consideration in biodiesel feedstock

When considering the total amount of greenhouse gas emissions it is therefore important to consider the whole production process and what indirect effects such production might cause. The effect on carbon dioxide emissions is highly dependent on production methods and the type of feedstock used. Calculating the carbon intensity of biofuels is a complex and inexact process, and is highly dependent on the assumptions made in the calculation. A calculation usually includes:

1.   Emissions from growing the feedstock (e.g. petrochemicals used in fertilizers);

2.   Emissions from transporting the feedstock to the factory;

3.   Emissions from processing the feedstock into biodiesel.

Based on these, production methodology of biodiesel as a whole is as important as quality of the biodiesel. In cases where there is incomplete transesterification process, the end product(s) may be undesirable for utilization in the engines which may also affect the environment

1.5 Specific study objectives

Engine testing facilities are commonly used in engine development and catalyst performance research laboratories to achieve further emission reductions. A variety of biodiesel feedstocks have been experimented with using different engine types and for various performance evaluations but the aim of this study is overall engine performance tests and gaseous/emission characterizations on a four stroke versatile internal combustion engine (TD 300) over a wide range of throttle from the feedstocks of Moringa and Jatropha biodiesel and their resultant biodiesel hybrids produced by transesterification, at specific optimization protocols and subjected to a novel approach in biodiesel development, viz. a viz hybridization using *in situ* and *ex situ* processes as reported in our earlier studies [16].

In this study, the single stock biodiesel of Moringa and Jatropha and their hybrids were subjected to standardized procedures and compared with AGO. The torque, air fuel ratio, ambient air temperature and pressure, specific fuel consumption, brake thermal and mechanical efficiency, brake power, exhaust temperature and smoke opacity and their individual effects were determined with significant differences; gaseous emissions were also measured to ascertain the level of improvement in performance.

2.   MATERIALS AND METHODS

2.1 Development and application of biodiesel production model

The biodiesel production model that was adopted in this study was derived from the production protocol of CSIR-CSMCRI, Bhavnagar [30] for Jatropha biodiesel production patented in the US which was re-evaluated and modified to suit variable feedstocks in this study. The working principle was the free fatty acid neutralization through base wash. The processes involved are a form of oil pre-treatment which conditioned the crude oil for transesterification. The free fatty acid composition of any crude vegetable oil and its neutralization is the main thrust of reaction. Oil with lower free fatty acids requires less treatment procedures and less materials of reaction. The modified model is preceded by several stoichiometric calculations which are then applied in the experimental reactions. The model encompasses a dual way process consisting of two main reactions: base wash/neutralization reaction using strong base, in this case, aqueous solutions of sodium hydroxide (NaOH) was used for base-wash in the first phase while methyl-

esterification reaction was performed in the second phase using methanol in the presence of potassium hydroxide (KOH) as catalyst. NaOH interacts better in aqueous medium hence the choice in the base wash while the solubility of KOH in organic solvent makes it the choice in esterification. The effervescence reaction with NaOH in water enhances the dissolution and therefore proper pre-treatment of the crude vegetable oil. The calculations were adopted in excel spreadsheets and values imputed to give required compositions for the reaction simply by changing the quantity of oil to be transesterified (in kg) and the fatty acid composition. The model generated the required NaOH and water for dissolution and also the required KOH needed to convert the neutralized oil to biodiesel. Expounding on this model is well beyond the scope of this present study.

Before adopting the model, four important experimental and numerical determinations were required:

Determination of the average molecular weight of fatty acids usually adopted for any member of the carboxylic acid family; determination of the weight of the crude oil to be transesterified (in kg): determination of the free fatty acid composition of the crude oil using any method; and determination of the total free fatty acids.

From the experimental and numerical calculations of this model, the following will be determined: The amount of sodium hydroxide (NaOH) required for neutralization/ base wash for any quantity and type of crude vegetable oil; the amount of water (H_2O) needed to dissolve the required sodium hydroxide; the amount of potassium hydroxide required as catalyst for transesterification and the amount of methanol (alcohol) required for the total transesterification of vegetable into biodiesel (methyl esters).

The engine test performance and emission analysis test which followed the model experimentation was conducted at the Biofuels laboratory of the Petroleum Processing Engineering Technology of Petroleum Training Institute, Effurun, Nigeria. A TD 300, a versatile engine test bed with instrumentation for comprehensive investigations into the features and operating characteristics of internal combustion engines was used for the study. It enables a wide range of investigations into the characteristics of four-stroke single-cylinder petrol and diesel engines. For use with engines up to 10 kW: four-stroke diesel and four-stroke petrol engines ideal for group demonstrations and student projects; Includes comprehensive control console and instrumentation; Optional ancillaries available to extend the range of study even further; Quick, convenient and accurate engine mounting and changeover; Test bed includes anti-vibration mounts; Uses four-quadrant drive to start and load the engine, giving excellent stability; Self-sealing couplings enable quick and efficient connection and disconnection of fuel lines with minimum loss or spillage of fuel; Works with TecQuipment's Versatile Data Acquisition System (VDAS®).

The main components of the system are: a heavy fabricated floor-mounting bed; an instrument console with instrument frame; a fuel tank support frame that supports the fuel tank and optional fuel gauge. The bed is held on anti-vibration mounts. It includes a robust trunnion-mounted d.c. machine. An electronic load cell connected to the machine measures the driving torque of the test engine. The engines are supplied pre-mounted on a sturdy precision base plate. When the engine is initially mounted onto the test bed or exchanged with an alternative engine, dowels and slots locate the engine quickly, accurately and reliably. Each engine includes a colour-coded fuel tank with self-sealing couplings. The couplings ensure the engines can be connected and disconnected quickly and efficiently with minimum loss or spillage of fuel. For convenience and safety, the fuel tank can be removed for filling or for storage in a fuel locker when not in use. Removing the fuel tank also prevents unauthorized use of the equipment.

The control has an electrical cabinet which houses a four-quadrant drive to start and load the engine. The motor can also be used to drive the engine while the fuel and ignition are off, so students can establish frictional losses. The control includes an air-box and orifice plate to enable students to measure air flow. The instrumentation and display units are mounted on a sturdy frame, which is part of the control. The control also includes a convenient work top for use as a writing desk, or for positioning other equipment such as a computer. The control and test bed are separate in order to avoid vibration being transmitted from the engine to the measuring devices. In addition, it allows the instrumentation to be thermally and acoustically screened from the test bed, using suitable shielding or a wall. The engines (available separately) include an exhaust thermocouple, dynamometer coupling, colour-coded fuel tank, hoses and fittings. They have modified cylinder heads and cranks for connection to TecQuipment's Engine Cycle Analyzer (ECA100 available separately). An Exhaust Gas Calorimeter (TD300a) is also available to enable students to measure energy lost through exhaust gases and to determine the energy balance of the engine.

2.2 Power, torque and rotational speed relationship employed

THE RELATIONSHIP OF POWER, TORQUE AND ROTATIONAL SPEED ACCORDING TO SERWAY AND JEWETT [29] AND GENERAL ENGINE TECHNOLOGY IS CRUCIAL TO ENGINE PERFORMANCE. MATHEMATICALLY FOR ROTATION ABOUT A FIXED AXIS OR POINT, THE EXPRESSION IS GIVEN BY:

$$W = \int_{\theta 1}^{\theta 2} \tau \, d\theta \qquad\qquad (5.1)$$

WHERE W = WORK, τ = TORQUE, Θ_1 AND Θ_2 ARE INITIAL AND FINAL ANGULAR POSITIONS. FROM THE THEORY OF WORK-ENERGY AND POWER, W IS EQUAL TO CHANGE IN ROTATIONAL KINETIC ENERGY, ΔE WHICH IS GIVEN BY;

$$\Delta E = \frac{1}{2} I \, \omega^2 \qquad\qquad (5.2)$$

WHERE I IS THE MOMENT OF INERTIA AND Ω IS THE ANGULAR SPEED (RPM).

$$P = \tau . \omega \qquad\qquad (5.3)$$

P = POWER, T = TORQUE AND Ω = ANGULAR VELOCITY.

THE POWER INJECTED BY THE TORQUE DEPENDS ON INSTANTANEOUS ANGULAR SPEED AND THE POWER OUTPUT [29] IS DETERMINED BY THE TORQUE APPLIED TO THE ENGINE GENERATOR AS SCHEMATICALLY PRESENTED IN FIGURE 5.1.

$$P = \tau \times \pi \times \omega \qquad\qquad (5.4)$$

2.3 Emissions Determination

The temperature attained at different time and speeds were recorded using the thermocouple and the digital meter. The fuel consumption per sample for the period of the tests (40 minutes) was also recorded. This was accomplished by taking the difference of the volume of the initial fuel used for each run and the final volume after runs for 40 minutes. The amount of flue gas emitted (O2, CO, NO2 and VOCs) at each interval of time, temperature and speed for each sample was recorded in parts per million (ppm) and compared. All the data collected were analyzed, compared and graphs plotted. Inference statistics were used for this analysis and applied for the purpose of this study. The experimental setup used in the present work is shown in Figure alongside portable diesel smoke meter (opacimeter). The engine was loaded with an eddy current dynamometer. The mass flow rate of intake air was measured with an orifice meter connected to a manometer. A surge tank was used to damp out the pulsations produced by the engine, for ensuring a steady flow of air through the intake manifold. The fuel consumption rate was determined using the glass burette and stop watch. The engine speed was measured using a digital tachometer. An AVL 444 Di gas analyzer was used for measuring the exhaust gas components such as CO, HC, and NOx. The smoke density was measured using an AVL 413 smoke meter. The exhaust gas temperature was measured with a k-type thermocouple.
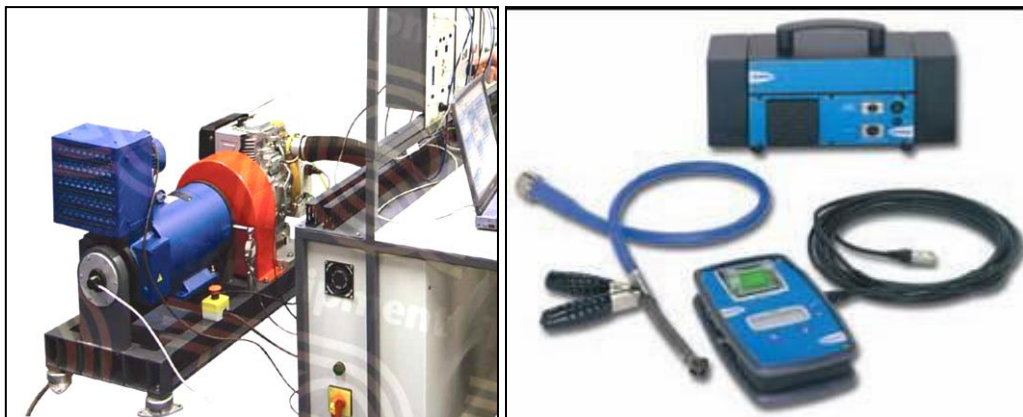
Figure 1: Experimental setup (TD 300/302) Engine test set up and portable diesel smoke meter

Before starting the measurements, some important points were considered in order to get meaningful data from the experiments. The engine was warmed up prior to data acquisition. The lubricating oil temperature was monitored to confirm that the engine was in a sufficiently warmed-up situation. Ambient conditions should be maintained for different engine runs because the ambient pressure and temperature have an effect on intake air drawn into the engine cylinder, thereby changing the fuel-air mixing as well as combustion process. All the engine test runs were carried out in fair constant ambient conditions. During the tests with hybrids biodiesel, the engine was started with AGO until it warmed up. Then fuel was switched to biodiesel and hybrids. After finishing the tests with biodiesel B100 the fuel was always switched back to diesel and the engine was run until the hybrids biodiesel had been purged from the fuel line, injection pump, and injector in order to prevent starting difficulties at later time.

At the start of each test the test engine was operated with base fuel-diesel for about 30 minutes to attain a normal working temperature condition after that base line data were generated and the corresponding results were obtained. The engine was then operated with hybrids of biodiesel in situ (J50M50, J40M10, J30M20, J20M30, and J10M40) and ex situ (BM50J50, BM40J10, BM30J20, BM20J30 and BM10J40). At every operation the engine speed was checked and maintained constant. All the measurements were repeated thrice, and the arithmetic mean of these three readings was employed for calculation and analysis. The different performance and emission parameters analyzed in the present investigation were brake thermal efficiency (BTE), brake-specific fuel consumption (BSFC), exhaust gas temperature (EGT), carbon monoxide (CO), unburned hydro-carbons (HC), nitrogen oxide (NO), and smoke. Smoke opacity was measured using portable diesel smoke meter (Figure 5.4) according to SAE J1667 standards as adopted by South African National Standards [20].

3. RESULTS AND DISCUSSION

The results show that crude Moringa oil properties which include some chemo-physical properties which are determinants in its characteristics as a feedstock for biodiesel. The chemo-physical and thermal properties have been presented in our previous paper. As this study is primarily concerned with the engine performance and emission characteristics, parameters such as brake specific fuel consumptions (BSFC) on engine loads, brake specific thermal efficiencies (BSTE) on engine loads, exhaust gas temperatures on engine loads, smoke opacity on engine loads were evaluated. Also expressed are the comparisons of thermal and mechanical efficiencies, composition of gaseous emissions and the effects of engine loads on them. These are presented in Table 1, Figures 2 to 8. As can be seen in Table 1, the average biodiesel (B100 and the acceptable biodiesel bend, B20) was compared with conventional AGO for regulated and non-regulated emissions. The emissions of CO, PM and NOx were significantly reduced in biodiesel compared to AGO and B20 (80% of AGO). Sulphates, PAHs and nPAH which were non-regulated also followed the same trend of non-pollution in biodiesel. This was as established by the National Biodiesel Board of the US and was employed as the benchmark (standard/control) for comparison of the hybrids performance of this study. The effects of engine loads on thermal efficiency in Figures 2 and 3 when AGO and biodiesel hybrids were used to power the engine exhibited close comparison with the AGO. The efficiencies increased as the engine load was increased for all the hybrids utilized.

Table 1: Average biodiesel (B100 and B20) emissions compared to conventional diesel

Emission Type	B100	B20
	Emissions in relation to conventional diesel	
Regulated		
Total Unburned Hydrocarbons	-67%	-20%
Carbon Monoxide	-48%	-12%
Particulate Matter	-47%	-12%
NOx	+10%	+2% to -2%
Non-Regulated		
Sulfates	-100%	-20%[a]
PAH (Polycyclic Aromatic Hydrocarbons)[b]	-80%	-13%
nPAH (nitrated PAH's)[b]	-90%	-50%[c]
Ozone potential of speciated HC	-50%	-10%

Source: National Biodiesel Board, Biodiesel Fact Sheets, Emissions

Figure 2: Effects of engine loads on brake thermal efficiencies of biodiesel and hybrids

Figure 3: Effects of engine loads on brake specific fuel consumption of biodiesel and hybrids

The difference in the response of AGO and biodiesels was quite insignificant even though AGO performed better. At full load, AGO produced 40% thermal efficiency while the hybrid biodiesel fuels produced between 35% and 40%. BM50J50 and BM40J10 were as high as 38%. The presence of oleic acid and the higher oxidative stability of Moringa as a hybridization agent may be responsible for this improved performance. This was due to the higher percentage in brake power as loads are applied. The high presence of dissolved oxygen and complete combustion of the biodiesel hybrids were also responsible which enabled proper atomization of the fuel molecules. Fuel consumption (Figure 3) is also related to the thermal efficiencies

which decreased as the loads increased. Biodiesel and hybrids combusted more than AGO so had a lesser consumption rate with superior heating/calorific value, lesser specific gravity and lower mass flow injected into the engine [19]. Viscosity as a property also played a significant role in the atomization of fuel in the combustion chambers. At full load, the specific fuel consumption of AGO was as low as 0.28 kg/kWh while the hybrid biodiesel recorded between 0.30 kg/kWh to 0.42 kg/kWh.

This is quite an improvement from non-hybridized conventional biodiesel fuels as recorded by other researchers. The mono-unsaturated oleic acid which is very prominent in the Moringa hybridizing agent with fatty acid profile of 74.0% as indicated in our earlier studies [16, 17] also made a significant contribution. Oils with high oleic acid content are desirable and give biodiesel fuels a reasonable balance or compromise of fuel properties. Considering that the other saturated fatty acid methyl esters (C20:0 and C22:0) in Moringa biodiesel as well as C22:1 likely have high cetane numbers, a high cetane number of Moringa biodiesel is anticipated [16, 17]. Figures 4 and 5 show the trend of events of the exhaust gas temperature and smoke opacity with increased engine loads. There was a general increase in smoke opacity and exhaust temperature as the engine loads increased. But in comparison to AGO, the biodiesel and the hybrids performed better. At peak load, AGO recorded 380 HSU while the hybrids fell between 290 and 320 HSU; what this means is that AGO produced more smoke than the biodiesel and hybrids. Density/opacity of smoke is used to measure the efficiency of combustion of fuel in the engine. The lower the better and higher is the environmental protection it offers. The exhaust gas temperature is also closely linked with the former. Fossil AGO recorded higher temperatures than the biodiesel hybrids. At peak load, it was 395°C while the hybrids were between 320°C to 375°C. Biodiesel and hybrids with lesser emissions and lower exhaust gas temperatures are not prone to tail pipe and exhaust corrosion compared to AGO. It must be noted that the quantity of fuel injected into the engine increases with engine load to maintain the power output and therefore the heat released rises proportional to the exhaust gas temperature as the load increases which is also indicative of combustion quality in the chamber.
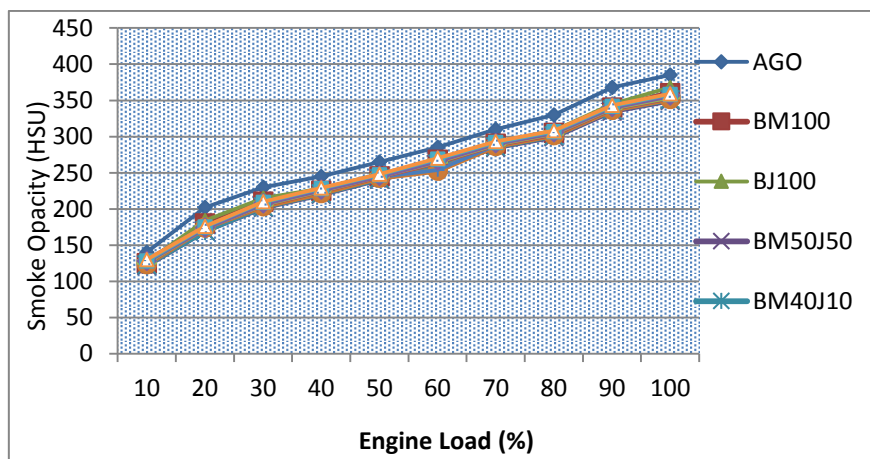

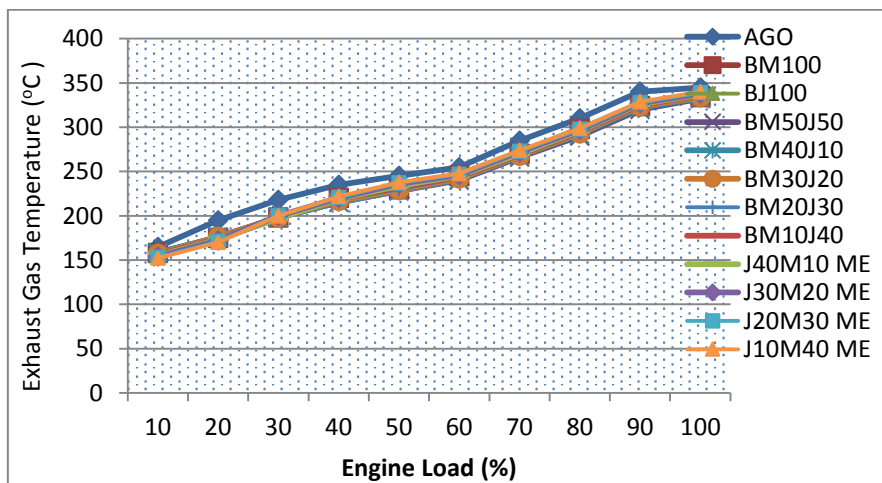Figure 4: Effects of engine loads on smoke opacity of biodiesel and hybrids

Figure 5: Effects of engine loads on exhaust gas temperature of biodiesel and hybrids

For all the emissions, CO, CO_2, NOx, VOCs as evaluated in Figures 6, 7 and 8 with AGO, there was a general trend with respect to engine loads. At constant load, there was slight variation with respect to hybrids which was very wide compared to AGO (0.035 and 0.018 %) vol composition of CO_2 at 100 and 50% load respectively while the hybrids fell between 0.02 to 0.017 and 0.008 to 0.02% vol at 100 and 50% respectively. Figures 6 shows that AGO produced a wider variation in composition of CO than biodiesel and hybrids while Figure 7 compared mechanical and thermal efficiencies. The same trend is also observable in Tables 2 with respect to torque, temperature and rotational speed, v in rpm. Between the speed of 1000 rpm to 200 rpm, the torque, and temperature with increase in time from 5 minutes to 40 minutes, the emissions of CO, NOx, CO, VOCs and O_2 increased for AGO and for the hybrids at 50 and 100% load respectively.

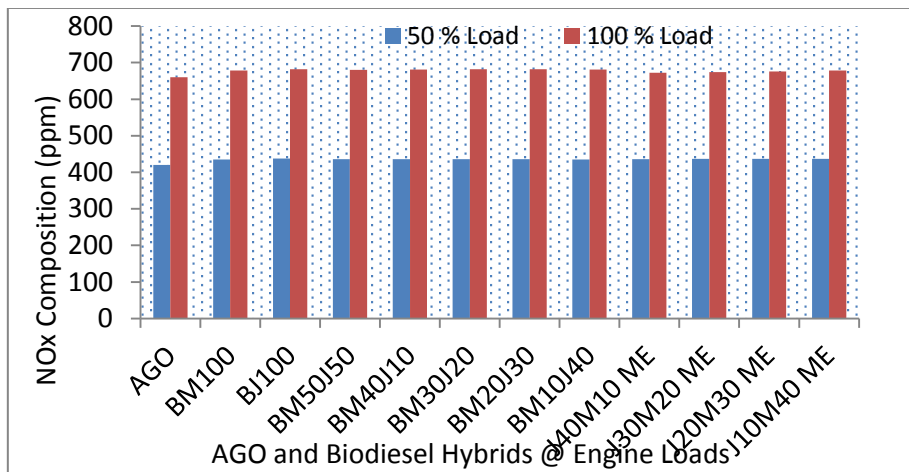*Figure 6: Effect of CO emission composition of the hybrids at different loads*

Figure 7: Effect of NOx emission composition on the hybrids at different loads
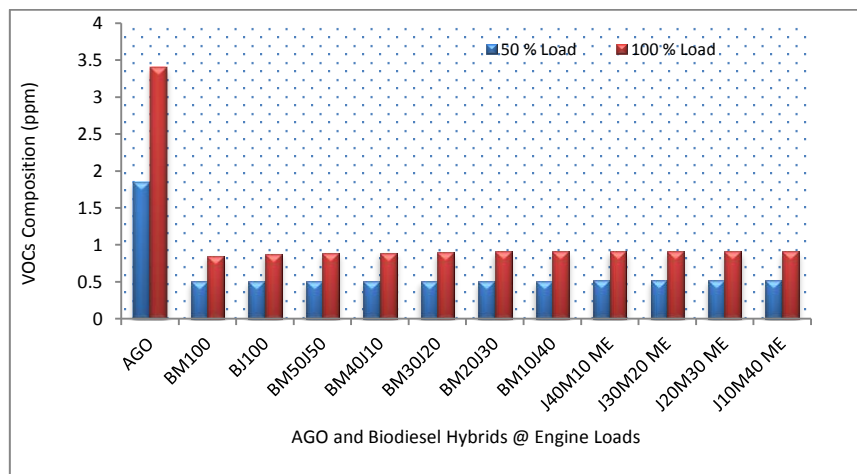

Figure 8: Effect of VOCs emission composition on biodiesel and hybrids at different loads

4. CONCLUSION

The aim of this investigation was to evaluate engine performance and usability of Moringa and Jatropha hybridized biodiesel fuels produced by the model of improved method and by hybridization as a new approach in biodiesel improvement and to characterize the emission from compression ignition engines in accordance to ASTM standards and to compare with AGO (Control). Moringa biodiesel appears to be a biodiesel fuel with one of the highest cetane numbers ever reported as biodiesel fuel. There is no doubt that Moringa is a potentially valuable oil seed crop and that its oil appears to be a viable and promising feedstock for biodiesel production and as a hybridization agent. The performance of the hybrids of Jatropha and Moringa seed oil in the CI engine was very close to the performance of the petroleum diesel (AGO). Therefore, they can be used in CI engines for any diesel engine application without modification both in rural areas and for meeting the energy requirement in various agricultural operations such as irrigation, threshing, grinding and general farm operations. The CI engine ran successfully during the tests conducted. The hybrids characterized for their improved chemo-physical and stable thermal properties performed favourably compared with conventional diesel (AGO). The specific fuel consumption, thermal and mechanical efficiencies, exhaust gas emission were close to the value obtained from AGO. The overall smoke density produced during combustion were less than those produced by AGO while also all the emissions produced were better and more environmentally friendly, achieving higher energy efficiencies from hybridisation of biodiesel feedstock. All the hybrids showed improved properties compared to the non-hybridised or single stock biodiesel. Recommendation is that other feedstocks should be experimented with hybridisation either *in situ* or *ex situ*. This study has also pointed a direction to researchers to look at other forms of hybridisation of feedstocks such as hybridising not just two feedstock oils (bi-hybridisation) but also poly-hybridisation.

5. ACKNOWLEGEMENT

6. REFERENCES

[1] KOFFMAN, D., Weiner, R., Pfeiffer, A. and Chapman, S. (2010). Funding the public transportation needs of an aging population: TCRP Project J-11, Task 8, Transit Cooperative Research Program, Nelson\Nygaard Consulting Associates, San Francisco, California.

[2] RAJA, S.A., Robinson, D.S. and Lindon, C.R.L. (2011). Biodiesel production from Jatropha oil and its characterization. Research Journal of Chemical Sciences, 1(1); 81-87.

[3] RAHMAN, K.M., Mashud, M., Roknuzzaman, M.D. and Asadullah, Al G. (2010). Biodiesel from Jatropha oil as an alternative fuel to diesel engine, IJMME-IJENS, 10(3): 1-6.

[4] IBRAHIM, J.S. and Eloka-Eboka, A.C. (2012). Evaluation of levels of automobile exhaust gas pollution in selected cities of Benue State. Advances in Science and Technology, 8(1): 14-18.

[5] AGARWAL, A.K. (1999). Performance evaluation and tribological studies on a biodiesel fuelled compression ignition engine. Ph.D. Thesis, Indian Institute of Technology, Delhi, India.

[6] AJIWE, V.I.E., Ajibola, V.O. and Martins, C.M.O.A. (2001). Vegetable diesel fuels from Castor oil, its methyl-ester and ester-diesel blends. Journal of Applied Sciences, 3(4): 1471-1487.

[7] AJIWE V.I.E., Ajibola, V.O. and Martins, C.M.O.A. (2002). Pentadetha macrophylla (oil bean) oil, its methyl-ester and ester-diesel blends. Alternative source of diesel. Nnamdi-Azikiwe University, Awka. African Journal of Science, 3(2): 587-600.

[8] REDDY, V.S., Ranjan, K.R., Sharma, V.K. and Tyagi, S.K. (2011). Experimental investigation of a diesel engine fuelled with Jatropha curcas L. seed oil, International Journal of Sustainable Energy, 30: sup1, S4-S10.

[9] VAN GERPEN, J.H., Peterson, C.L. and Goering, C.L. (2007). Biodiesel: an alternative fuel for compression ignition engines. Presentation at the 2007 Agricultural Equipment Technology Conference Louisville, Kentucky, USA 11-14 February.

[10] ASTM. (2002). D 6751 Standard specification for biodiesel fuel (B100) blendstock for distillate fuels. West Conshohocken, Penn.: ASTM International.

[11] ASTM. (2006). Standard Specification for Diesel Fuel Oils. West Conshohocken, Penn.: ASTM International.

[12] VAN GERPEN, J.H. 2005. Biodiesel processing and production. Fuel Processing Technology 86: 1097-1107.

[13] MIRUNALINI, T., Anand, R. and Mahalakshmi, N.V. (2006). Jatropha oil as a renewable fuel in a diesel engine. Proceedings of the 3rd BSME-ASME International Conference on Thermal Engineering, 20-22 December, 2006, Dhaka, Bangladesh.

[14] KNOTHE, G. Gerpen, J.H. and Jurgen, K. (2005). The biodiesel handbook. Champaign, Ill: AOCS Press.

[15] IGBUM, O.G., Eloka-Eboka, A.C., Ubwa, S.T. and Inambao, F.L. (2014). Evaluation of environmental impact and gaseous emissions of biodiesel fuels and blends of selected feed-stocks. International Journal of Global Warming, Inderscience Publication Series, Volume 6 No 1: 99-112.

[16] ELOKA-EBOKA, A.C. and Inambao, F.L. (2014a). Hybridisation of feedstocks – a new approach in biodiesel development: A case of Moringa and Jatropha seed oils. Energy Sources Part A (Taylor and Francis) (Accepted and in Press).

[17] ELOKA-EBOKA, A.C. and Inambao, F.L. (2014b). Blending of feedstocks – a new approach in biodiesel development: A case of Moringa and Jatropha seed oils. Proceeding of 22nd Domestic Use of Energy Conference, Cape Peninsula University of Technology, Cape Town, 31st March - 2nd April, 2013: 189-196. (Published in IEEE Explore).

[18] KRISHNA, M.V.S., Chowdary, R.P., Kishen, T., Reddy, K and Murthy, P.V.K. (2013). Performance, emissions and combustion characteristics of waste fried vegetable oil in based biodiesel in high grade low heat rejection diesel engine. British Journal of Applied Science & Technology, 3(4): 1345-1367.

[19] KORBITZ, W. (2005). Status of biodiesel in Asia, the Americas, Australia and South Africa. In: Knothe, G. (Ed.). The Biodiesel Handbook. National Centre for Agricultural Utilization Research, Agric Research Service, USDA, Illinois, USA.

[20] South Africa National Standard (SANS 1935:2011) (2011). Automotive biodiesel – fatty acid methyl esters (FAME) for diesel engines – requirements and test methods. Pretoria: SABS Standards Division.

[21] VAN GERPEN, J.H., Peterson, C.L., Goering, C.E. (2007). Biodiesel: an alternative fuel for compression ignition engines. Presentation at the 2007 Agricultural Equipment Technology Conference Louisville, Kentucky, USA 11-14 February 2007.

[22] KNOTHE, G. and Steidley, K.R. (2005). Lubricity of components of biodiesel and petrodiesel: the origin of biodiesel lubricity. Energy and Fuels, 19: 1192-1200.

[23] AGARWAL, A.K. (2007). Biofuels (alcohols and biodiesel) applications as fuels for internal combustion engines. Progress in Energy and Combustion Science, 33: 233-271.

[24] LAPUERTA, M., Armas, O. and Rodríguez-Fernández, J. (2008). Effect of biodiesel fuels on diesel engine emissions. Progress in Energy Combustion Science, 34: 198-223.

[25] LAPUERTA, M., Armas, O., Ballesteros, R. and Fernández, J. (2005). Diesel emissions from biofuels derived from Spanish potential vegetable oils. Fuel, 84: 773-780.

[26] LAPUERTA, M., Rodriguez-Fernandez, J. and Agudelo, R. (2008). Diesel particulate emissions from used cooking oil. Biodiesel. Bioresour. Technol. 99: 731-740.

[27] MONYEM, A.; Gerpen, J.V. (2001). The effect of biodiesel oxidation on engine performance and emissions. Biomass Bioenergy, 20, 317-325.

[28] MONYEM, A., van Gerpen, J.H. and Canakci, M. (2001) The effect of timing and oxidation on emissions from biodiesel-fueled engines. Transactions of the ASAE, 44: 35-42.

[29] SERWAY, R.A. and Jewett, Jr, J.W. (2003). Physics for scientists and engineers. 6th ed. Pacific Grove, CA: Brooks Cole.

[30] SRINIVASAN, K., Sankaranarayanan, S. and Antonyraj, C.A. (2012). Improved process for the preparation of fatty acid alkyl esters (biodiesel) from triglyceride oils using eco-friendly solid base catalysts. Goggle patents.

POSTER SESSION C

220: Numerical simulation of a new biomass/solar micro-cogeneration ORC system

Ana I. Palmero-Marrero[1], João Soares[2] and Armando Oliveira[3]

[1] University of Porto, Dept Mech.Eng., Rua Dr. Roberto Frias, 4200-465, Porto, Portugal, apalmero@fe.up.pt

[2] University of Porto, Dept Mech.Eng., Rua Dr. Roberto Frias, 4200-465, Porto, Portugal, joaosoares@fe.up.pt

[3] University of Porto, Dept Mech.Eng., Rua Dr. Roberto Frias, 4200-465, Porto, Portugal, acoliv@fe.up.pt

This paper presents numerical simulation results for a new prototype of a 6 kWe solar/biomass system. The system uses a micro-cogeneration Organic Rankine Cycle (ORC), driven by a combination of solar thermal and biomass sources. Both sources may be used separately or combined. The solar thermal energy is obtained through medium-temperature concentrating compound parabolic solar collectors (CPC) with evacuated tubes. This system is able to generate electrical energy and useful heat at two different temperature levels. The computer model of the overall system was developed by combining EES (Engineering Equation Solver) with TRNSYS software. EES was used for the power cycle calculation and TRNSYS for simulating the solar circuit and overall system. The ORC/power cycle model consists of a set of algebraic equations representing the thermodynamic behaviour of each ORC component. The ORC simulated by EES includes the following components: evaporator, expander, generator, regenerator, condenser and pump. For an electrical output equal to 6 kW, a fluid inlet temperature in the ORC evaporator of 180ºC was assumed, achieved with the solar collectors and biomass boiler. The ORC is expected to operate at nearly steady-state conditions, as the cycle driving temperature is kept approximately constant. However, TRNSYS is needed to take into account the transient behaviour of solar energy. The TRNSYS model includes the following components: solar collector, boiler, thermal storage, economizer, pumps and control systems. The system is under development and a prototype will be installed and tested in Benguerir (Morocco), in the framework of the REELCOOP project, funded by the EU. For solar resource assessment purposes, Meteonorm software was used to generate climatic data of Benguerir. Results of system simulation under different operating conditions are presented. Annual solar fraction and annual global electrical efficiency for different collector areas and storage capacities were calculated.

Keywords: organic Rankine cycle, micro-cogeneration, solar energy, biomass

1. INTRODUCTION

Micro-generation is the decentralised production of electricity, through different means (micro-turbines, fuel cells, Stirling engines, small internal combustion engines, PV cells) with an electrical power output up to 50 kW. Micro-cogeneration, or micro-CHP, is the combination of micro-generation with useful heat. The use of solar energy with conventional energy sources, for combined heat and power (CHP) in buildings, reduces pollutant emissions and offers energy savings. Distributed power generation in small, decentralised units, is expected to help reducing emissions and saving grid capacity, while also providing opportunities for renewable energy. It could thus form a constituent part of a more sustainable future (Pehnt *et al.*, 2006).

Among the several existing technological solutions for micro-cogeneration, Organic Rankine Cycle (ORC) systems are an interesting solution in cases where the heat demand is significantly larger than electricity needs, which is the case of residential and also other buildings (Oliveira *et al.*, 2014). Micro-ORC systems driven by renewable energy sources have attracted the attention of many researchers. Either theoretical or experimental works have been carried out, including developments and improvements in system components (Facão *et al.*, 2008), (Palmero-Marrero and Oliveira, 2009), (Quoilin *et al.*, 2011), (Qiu *et al.*, 2011), (Twomey *et al.*, 2013), (Jradi *et al.*, 2014).

In the present paper, a micro-cogeneration ORC system driven by a combination of solar thermal and biomass sources is simulated. Both sources may be used separately or combined. High efficiency vacuum-CPC solar collectors are used, and the power cycle uses a highly efficient rotary lobe expander. The system is under development and a prototype is being built, under the framework of the REELCOOP project, funded by the EU (REELCOOP, 2015). Preliminary simulation results were presented in the SET 2014 (Oliveira *et al.*, 2014). In the next sections, detailed numerical simulations for specific climatic and operational conditions are presented.

2. DESCRIPTION OF THE SYSTEM AND MODEL

In this work, the computer model of the overall system was developed by combining EES (Engineering Equation Solver) (EES, 2015) with TRNSYS (TRNSYS, 2013). EES was used for the power cycle calculation and TRNSYS for simulating the solar circuit and overall system.

In this system, the power cycle is based on the Organic Rankine Cycle (ORC) and is driven by solar thermal energy and biomass combustion. The operating temperature of the solar thermal collector varies between 100ºC and180ºC, and the utilization of the biomass boiler guarantees an evaporator inlet temperature of 180ºC.The first step was the development of the ORC / power cycle model in EES. The model consists of a set of algebraic equations representing the thermodynamic behaviour of each ORC component, under steady state. The developed program may be used in connection with TRNSYS, as discussed later, or as a standalone program, able to predict ORC efficiency and output electrical power, besides relevant cycle properties, using as inputs the useful heat input and the efficiencies of several components such as expander, generator or heat exchangers.

Concerning the development of the TRNSYS model, for solar resource assessment purposes METEONORM (Meteotest, 2015) was used to generate data of Global Horizontal Irradiation, GHI [kWh/m2], solar azimuth and height [º] and ambient temperature [ºC], on an hourly basis for a typical year. The chosen location was Benguerir (Morrocco), where the prototype will be installed and tested. For this city, the data from Meteonorm and local data were compared - see Fig. 1. In this case, the Meteonorm data were obtained with interpolation from nearby meteorological stations.

The major differences between Meteonorm and local data concern horizontal global irradiation (G) and ambient temperature (Ta) for July, August and September (difference lower than 10% for these months).
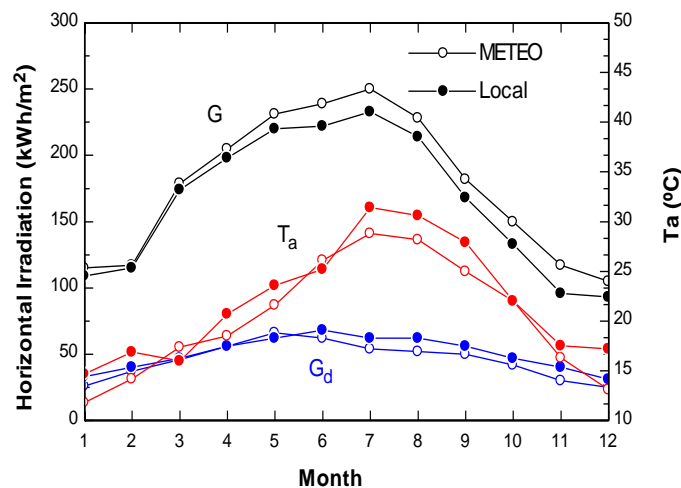
Figure 1: Global (G) and diffuse (Gd) solar radiation on horizontal surface and ambient temperature (Ta) with Meteonorm data and local data for Benguerir.

2.1 Definition of system components

The system was presented and schematically represented in Oliveira *et al*., 2014.

The solar circuit was simulated by TRNSYS and included these components: solar collector, thermal storage, boiler, economizer, pumps and control systems. The solar collector is a new CPC collector with evacuated tubes developed in the framework of the REELCOOP project.

The Organic Rankine Cycle (ORC) was simulated by EES and included these components: evaporator, expander, generator, regenerator, condenser and pump. The expander was connected to a generator with a power output of 6 kW. It is assumed that the ORC operates under steady-state conditions, as the cycle driving temperature will be kept approximately constant. Even if the condenser temperature changes, due to changes in ambient temperature, this is a reasonable simplification due to the low system inertia.

Different working fluids are used in the system: thermal oil for the solar sub-system, water for the condenser, and Solkatherm (SES36) fluid for the ORC. The Solkatherm fluid is a non-flammable refrigerant with low toxicity. Another important reason for using SES36 in the ORC system is the possibility of using energy at a relatively low temperature.

The characteristics of each component simulated in TRNSYS are taken as follows:

- Solar collector. This is a medium-temperature non-tracking concentrating compound parabolic solar collector (CPC) with evacuated tubes. The CPC collectors have an external reflective concentrator located behind an evacuated tube which houses the absorber and heat transfer fluid. The performance is obtained by interpolating bi-axial IAM data.

- Thermal storage. The thermal storage was modelled by assuming that the tank consists of N (N = 6) fully-mixed equal volume segments. The degree of thermal stratification is determined by the value of N. The performance of the fluid-filled sensible energy storage tank was obtained considering negligible heat losses (perfect insulation). The fluid is oil (TERMOL 5HT).

- Boiler. The boiler is a heater that uses biomass as combustible to elevate the temperature of a fluid using external proportional control. External proportional control (an input signal between 0 and 1) is in effect as long as a fluid set point temperature is not exceeded. In this case, the fluid is oil, the set point temperature is 180ºC and the boiler efficiency is 0.9.

- Economizer. The economizer was modelled as a zero capacitance counter-flow sensible heat exchanger. The cold side input was assumed to be water. The effectiveness was calculated by using the overall heat transfer coefficient (UA).

- <u>Pumps</u>. The pump model computes a mass flow rate using a variable control function and a fixed maximum flow capacity. For the solar circuit simulated in TRNSYS, two pumps are considered: one between the thermal storage tank and the solar collectors and another between the Organic Rankine Cycle (ORC) circuit and solar circuit.

- <u>Control system</u>. The on/off differential controller generates a control function which can have a value of 1 or 0. The value of the control signal is chosen as a function of the difference between upper and lower temperatures, compared with two dead band temperature differences. In the solar circuit two control functions are considered. One control allows the flow between the solar collector and storage tank, when the collector outlet temperature is higher than the temperature of the fluid at the bottom of the storage. Another control acts between the boiler and storage tank. In this case, the boiler is running when the tank outlet temperature is lower than 180ºC.

The inputs of TRNSYS components and EES components are shown in Table 1.

 As can be seen in Table 1, the solar collector areas selected for the numerical simulation were 100, 168.3 and 200 m^2, being that 168.3 m^2 will be the collector area installed in the Benguerir prototype (in Morocco).

Table 1: Definition of the inputs for each component.

Programs	Components	Inputs
TRNSYS	Climatic data (Meteonorm)	Local: Benguerir
	CPC collector with evacuated tubes	Concentration factor (C) = 2.5 Efficiency curve parameters: η_0=0.68; a_1=0.4 W/m^{2}K; a_2=0.004 W/m^{2}K^2 Flow rate = 0.020 kg/s/m^2 Collector area: 100 m^2, 168.3 m^2, 200 m^2 Collector tilt: adjusted seasonally (twice per year) in the range of solar height values (at solar noon in the solstices).Tilt = 9ºN in Summer and 56ºN in Winter Collector azimuth = 0º Fluid specific heat = 2610 J/kgºC (oil TERMOL 5HT) IAM data: file created through the numerical simulation of the novel CPC collector
	Thermal storage	Tank volume (V_{tank}): 2 m^3, 5 m^3, 8 m^3 Stratified: 6 fully-mixed equal volume segments Tank losses: negligible Cold-side temperature (from Evaporator) : varies with evaporator heat Cold-side flow rate (from Evaporator)= 0.20 kg/s
	Boiler	Rated capacity = 60 kW Set point temperature = 180ºC Boiler efficiency = 0.9
	Economizer	Overall heat transfer coefficient of exchanger (UA) = 2.8 W/K
	Pump	Maximum power = 0.6 kW
EES	Evaporator	Useful heat: varies with expander efficiency (45.5 kW, 42.5 kW and 40 kW) Outlet temperature = 145ºC Superheating = 5ºC
	Expander	Efficiency (η_{exp}): 0.65, 0.70, 0.75
	Generator	Efficiency = 0.95 Net electrical power = 6 kW
	Regenerator	ΔT_{min} = 10ºC Efficiency = 0.82
	Condenser	Condenser temperature = 45ºC

3. SIMULATION RESULTS

Using the EES program, different ORC cycle outputs depending on expander efficiency were obtained, as shown in Table 2. The ORC cycle efficiency can be defined as net electricity divided by evaporator heat.

Table 2: Outputs of the ORC cycle

Components	Outputs		
	$\eta_{exp} = 0.65$	$\eta_{exp} = 0.70$	$\eta_{exp} = 0.75$
Condenser ($\dot{Q}_{cond}$)	39.16 kW	36.17 kW	33.66 kW
Regenerator ($\dot{Q}_{reg}$)	13.84 kW	12.31 kW	11.01 kW
Evaporator ($\dot{Q}_{evap}$)	45.5 kW	42.5 kW	40 kW
Expander ($\dot{P}_{Exp}$)	6.70 kW	6.66 kW	6.65 kW
Generator ($\dot{P}_{G}$)	6.37 kW	6.33 kW	6.31 kW
ORC cycle effic. ($\eta_{elec,NET,ORC}$)	0.13	0.14	0.15

For TRNSYS, the input values shown in Table 1 were considered. The monthly and annual performances for different collector areas are shown in Table 3, with: a) A_{col}=100 m², b) 168.3 m², and c) 200 m², in all cases with an expander efficiency (η_{exp}) equal to 0.75 and a tank volume of 5 m³ . The tables contain values of incident solar radiation on the collector surface (G_{coll}), useful heat gain on the solar collector fluid (Q_{usef_coll}), energy obtained by the boiler (Q_{aux}) and solar fraction (f, defined as the ratio between the useful solar heat and total heat provided to the power block).

For the calculations, a collector tilt equal to 9º was used for the summer period (from April to September) and 56º for the winter period (from January to March and from October to December). The operating time considered for the system was equal to 24 hours/day. Note that if the system operates during a shorter daily period, as in the case where electrical needs are not continuous, the solar fractions will be much higher, assuming the system is run during sunshine hours. For instance, with A_{col}=100 m² and operation during 16 hours/day, the annual solar fraction would increase from 0.14 to 0.21. If the operating period was 12 hours/day, the annual solar fraction would increase to 0.28 for this collector area.

Table 3.a): Monthly and annual performance results for A_{col} = 100 m² (η_{exp} = 0.75, V_{tank} = 5 m³)

Month	G_{coll} (MWh)	Q_{usef_coll} (MWh)	Q_{aux} (MWh)	$f = \dfrac{Q_{usef_{coll}}}{Q_{usef_{coll}} + Q_{aux}}$
Jan	20.18	4.69	25.07	0.16
Feb	16.62	3.48	23.40	0.13
Mar	20.35	3.21	26.55	0.11
Apr	21.18	3.29	25.51	0.11
May	23.07	4.28	25.48	0.14
Jun	23.63	4.73	24.07	0.16
Jul	24.78	5.01	24.75	0.17
Aug	23.24	4.15	25.61	0.14
Sep	19.26	2.66	26.14	0.09
Oct	19.41	3.73	26.03	0.13
Nov	19.09	4.48	24.32	0.16
Dec	19.46	4.51	25.25	0.15
Annual	250.27	48.23	302.17	0.14

Table 3.b): Monthly and annual performance results for A_{col} = 168.3 m² (η_{exp} = 0.75, V_{tank} = 5 m³)

Month	G_{coll} (MWh)	Q_{usef_coll} (MWh)	Q_{aux} (MWh)	$f = \dfrac{Q_{usef_{coll}}}{Q_{usef_{coll}} + Q_{aux}}$
Jan	33.96	7.68	22.08	0.26
Feb	27.97	5.54	21.34	0.21
Mar	34.25	5.16	24.60	0.17

Apr	35.64	5.34	23.46	0.19
May	38.82	6.30	23.46	0.21
Jun	39.77	7.12	21.68	0.25
Jul	41.70	7.76	22.00	0.26
Aug	39.12	6.81	22.95	0.23
Sep	32.41	4.47	24.33	0.16
Oct	32.66	5.80	23.96	0.19
Nov	32.13	7.28	21.52	0.25
Dec	32.76	7.36	22.40	0.25
Annual	421.20	76.62	273.78	0.22

Table 3.c): Monthly and annual performance results for $A_{col} = 200\ m^2$ ($\eta_{exp} = 0.75$, $V_{tank} = 5\ m^3$)

Month	G_{coll} (MWh)	Q_{usef_coll} (MWh)	Q_{aux} (MWh)	$f = \dfrac{Q_{usef_{coll}}}{Q_{usef_{coll}} + Q_{aux}}$
Jan	40.36	6.25	23.51	0.21
Feb	33.23	6.40	20.48	0.24
Mar	40.70	6.09	23.67	0.20
Apr	42.36	6.26	22.54	0.22
May	46.13	7.27	22.49	0.24
Jun	47.26	8.39	20.41	0.29
Jul	49.56	9.14	20.62	0.31
Aug	46.49	8.02	21.74	0.27
Sep	38.51	5.24	23.56	0.18
Oct	38.81	6.35	23.41	0.21
Nov	38.19	8.43	20.37	0.29
Dec	38.93	8.57	21.19	0.29
Annual	500.53	86.43	263.97	0.25

For each expander efficiency, the solar fractions for the different collector areas were calculated. The results show that the annual solar fractions for each collector area are practically constant for the different expander efficiencies (f_{annual}=0.14 for A_{col}=100 m², f_{annual}=0.22 for A_{col}=168.3 m² and f_{annual}=0.25 for A_{col}=200 m²). This is due to a decrease in the tank inlet temperature (from the evaporator) with the decrease of expander efficiency (η_{exp}), leading to an increase in collector useful energy (Q_{usef_coll}). Q_{usef_coll} and the auxiliary energy from the boiler (Q_{aux}) increase as η_{exp} decreases, resulting that the annual solar fraction (f_{annual}) remains practically constant with expander efficiency, for each collector area.

The annual thermal performance can be related to the annual net electricity generation of the power block. Assuming that the solar driven CHP plant is running non-stop throughout the year (helped by the boiler), the annual net generated electricity value is 52.6 MWh, with an operating period of 24 h/day. One could define an average "solar electrical efficiency", defined as the net electricity divided by auxiliary energy, with the values shown in Table 5.

Table 5: Annual auxiliary energy, annual solar fraction and annual average solar electrical efficiency ($\eta_{sol,electr}$) for different collector areas and V_{tank}= 5 m³.

A_{col} (m²)	Q_{aux_annual} (MWh)	f_{annual}	$\eta_{sol,electr}$
100 m²	302.17	0.138	0.174
168.3 m²	273.78	0.219	0.192
200 m²	263.97	0.247	0.199

For each solar collector area, different storage capacities (2 m³ and 8 m³) were also analysed. For a collector area of 100 m², the variation of storage capacity has a small influence on the solar fraction and on the solar electrical efficiency. For a higher collector area, the solar fraction and solar electrical efficiency decreased considerably when the tank volume changed from 5 to 2 m³. For V_{tank}=2 m³, when A_{col}=168.3

m^2, f_{annual}=0.178 and $\eta_{sol,electr}$=0.183; when A_{col}=200 m^2, f_{annual}=0.180 and $\eta_{sol,electr}$=0.183. Note that in this case (A_{col}=200 m^2), the tank volume of 2 m^3 is insufficient for the utilization of incident solar radiation.

The annual global electrical efficiency ($\eta_{electr,annual}$) is defined as the total electrical energy generated during one year, divided by the sum of all annual energy inputs – boiler input energy plus solar incident radiation. Figure 2 shows the calculated values for different collector areas for V_{tank}=8 m^3.
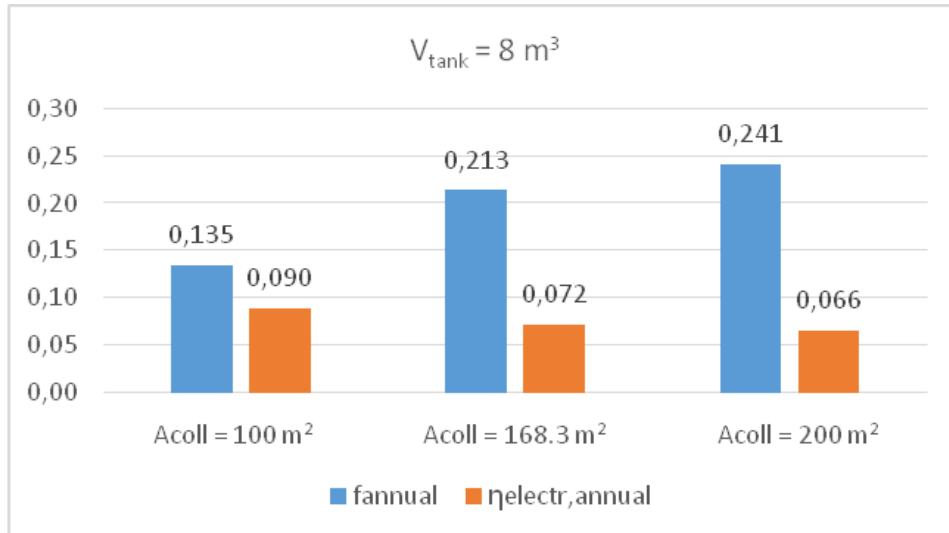
Figure 2: Annual solar fraction (f_{annual}) and annual average global electrical efficiency ($\eta_{electr,annual}$) for different collector areas with V_{tank}=8 m^3.

We may note that the average (annual) electrical efficiency may reach 9%, with the best expander efficiency value considered (η_{exp} = 0.75) and the lower collector area. The results show that it is not interesting to use higher collector areas, as the efficiency drops. In fact, the increase in incident solar energy, which is proportional to collector area, is not translated into useful energy, as a significant part is dumped (energy excess). This excess could be reduced by increasing storage capacity. Nevertheless, areas above 168 m^2 are not recommendable, additionally when they represent a significant increase in the system initial cost.

Figure 3 shows the daily variation of the incident solar radiation on the collector surface (G_{coll}), useful heat gain on the solar collector fluid (Q_{usef_coll}), energy supplied by the boiler (Q_{boiler}) and electrical efficiency (η_{electr}), for 21st December (a) and 21st June (b), when A_{col} = 168.3 m^2 and V_{tank} = 8 m^3. Note that the tilt of the collector was optimized for the solstices (tilt=56° in December and 9° in June); therefore, the maximum incident solar radiation on the collectors are similar for both days (approximately 670 MJ/h)

Note that with an operating period of 24 h/day, the higher electrical efficiency was achieved when the boiler was running without solar radiation (between 8 pm and 6 am). The utilization of biomass as combustible in the boiler for this biomass/solar micro-cogeneration ORC system is very important for the full day operation.

Figure 4 shows the results (solar fraction and average global electrical efficiency) for different storage capacities with A_{col}=168.3 m^2.
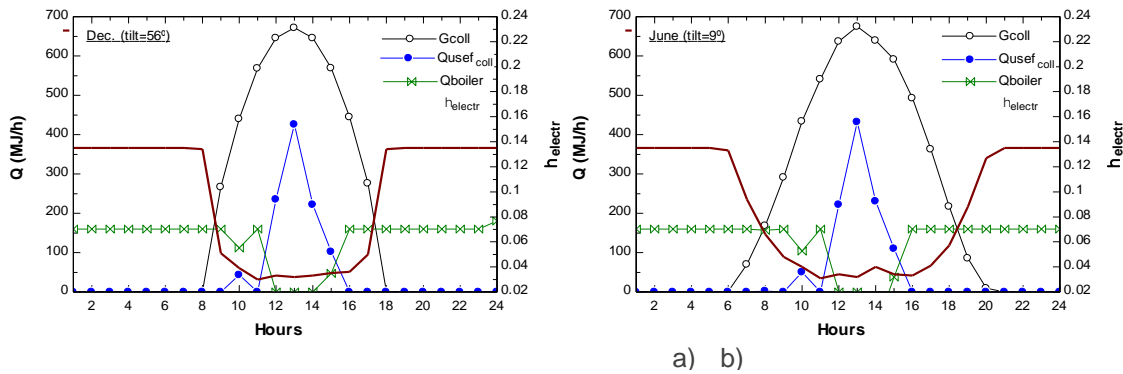
a)   b)

Figure 3: Incident solar radiation (G_{coll}), useful heat gain (Q_{usef_coll}), energy supplied by the boiler (Q_{boiler}) and electrical efficiency (η_{electr}), for: a) 21st December and b) 21st June, when $A_{col} = 168.3\ m^2$ and $V_{tank}=8\ m^3$.
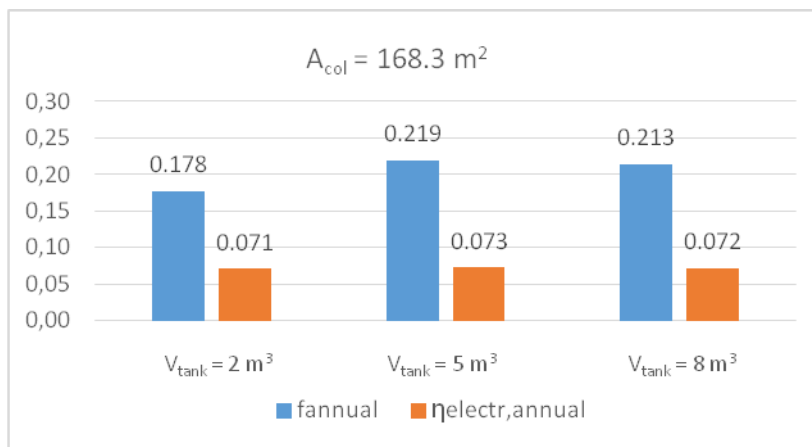

Figure 4: Annual solar fraction and annual average global electrical efficiency ($\eta_{electr,annual}$) for different storage capacity with $A_{col}=168.3\ m^3$.

Increasing storage capacity implies a decrease in collector inlet temperature, leading to an increased collector efficiency and annual solar fraction. However, excessive storage capacities don't improve system performance. Also, when the storage capacity varied between 2 to 8 m^3, no significant effect on $\eta_{electr,annual}$ was obtained, as can be seen in Figure 4.

4.   CONCLUSION

In the present paper, the numerical simulation of a novel hybrid biomass/solar micro-cogeneration ORC system was presented. It uses a rotary lobe expander coupled to a generator for electricity generation. Its nominal electrical power is equal to 6 kW, and the ORC, using SES36 as working fluid, is driven by thermal oil at a maximum temperature of 180ºC. This temperature is achieved by a combination of two renewable energy sources: solar energy, through the use of highly efficient novel vacuum-CPC thermal collectors, and a biomass boiler.

The monthly and annual performances for different collector areas (100 m^2, 168.3 m^2 and 200 m^2) and different expander efficiencies (0.65, 0.70 and 0.75) were calculated. The results showed that the annual solar fractions (f_{annual}) for each collector area were practically constant for the different expander efficiencies. When the operating period considered for the system was 24 hours/day and with a storage capacity of 5 m^3, $f_{annual}=0.14$ for $A_{col}=100\ m^2$, $f_{annual}=0.22$ for $A_{col}=168.3\ m^2$ and $f_{annual}=0.25$ for $A_{col}=200\ m^2$.

For each solar collector area, different storage capacities (2 m^3 to 8 m^3) were studied. Increasing storage capacity implies a decrease in collector inlet temperature, leading to an increased collector efficiency and annual solar fraction. However, excessive storage capacities don't improve system performance. Also, for a given collector area, when the storage capacity varied between 2 to 8 m^3, no significant effect on the average (annual) electrical efficiency ($\eta_{electr,annual}$) was obtained. For the higher storage capacity and the best expander efficiency value considered ($\eta_{exp} = 0.75$), $\eta_{electr,annual}$ may reach 9%, with the lower collector area. The results show that it is not interesting to use higher collector areas, as the efficiency drops. Nevertheless, areas above 168 m^2 are not recommendable, additionally when they represent a significant increase in the system initial cost.

A prototype of the system is under construction and will be tested in Morocco in 2016/17. More complete results, namely comparison between numerical and experimental results for the operating conditions, will be presented in the near future.

5. ACKNOWLEDGMENTS

6. REFERENCES

EES - Engineering Equation Solver, Program Manual, F-Chart Software (available at http://www.fchart.com), 2013.

FACÃO, J., Palmero-Marrero A., Oliveira A.C., 2008, Analysis of a Solar Assisted Micro-Cogeneration ORC System, International Journal of Low Carbon Technologies, vol.3 n.4, pp.254-264.

JRADI, M., Li J., Liu H., Riffat S., 2014, Micro-Scale ORC-Based Combined Heat and Power System Using a Novel Scroll Expander, International Journal of Low Carbon Technologies, Advance Access published February 20, 2014, available online (doi:10.1093/ijlct/ctu012).

Meteotest, Meteonorm Handbook, Parts I, II and III. Bern, Switzerland (available at http://www.meteotest.ch), 2015.

OLIVEIRA, A.C. et al., 2014, Presentation and Preliminary Simulation of a Biomass/Solar Micro-Cogeneration ORC System, Proceedings SET2014.

PALMERO-MARRERO, A., Oliveira A.C, 2009, Economic Analysis of a Solar Assisted Micro-cogeneration Organic Rankine Cycle System, Proceedings SET2009.

PEHNT, M., Cames M., Fischer C., Praetorius B., Schneider L., Schumacher K., Voβ Jean-P., 2006, Micro Cogeneration: Towards decentralized energy systems, Ed. Springer, Germany.

QIU, G., Liu H., Riffat S., 2011, Expanders for Micro-CHP Systems with Organic Rankine Cycle, Applied Thermal Eng, vol.31, pp.3301-3307.

QUOILIN, S., Orosz M., Hemond H., Lemort V., 2011, Performance and Design Optimization of a Low-Cost Solar Organic Rankine Cycle for Remote Power Generation, Solar Energy, vol.85, pp.955-966.

REELCOOP project: http://www.reelcoop.com, 2015.

TRNSYS 17 - A Transient System Simulation Program, Solar Energy Lab, University of Wisconsin-Madison, (available at http://sel.me.wisc.edu/trnsys), 2013.

TWOMEY, B., Jacobs P.A., Gurgenci H., 2013, Dynamic Performance Estimation of Small-Scale Solar Cogeneration with an Organic Rankine Cycle Using a Scroll Expander, Applied Thermal Eng, vol.51, pp.1307-1316.

238: Solar-panels-assisted heat pump - a sustainable system for domestic low-temperature space heating applications

Elamin A R.MOHAMED[1], SAFA. RIFFAT[2], Siddig. Omer[3]

1 University of Nottingham, University of Nottingham, Dept. of Built Environment,
amin_eissawi@alumni.nottingham.ac.uk
2 University of Nottingham, University of Nottingham, Dept. of Built Environment,
saffa.riffat@nottingham.ac.uk]
3 University of Nottingham, University of Nottingham, Dept. of Built Environment,
siddig.omer@nottingham.ac.uk

Direct expansion solar panels assisted heat pump systems (DX SAHP) have been extensively used in many applications. In the DX-SAHP systems the solar collector and the heat pump are combined into one unit so as to convey the solar energy to the refrigerant. The current work is aimed at examining the use of the DX-SAHP for low temperature space heating applications. The solar collector is used as the evaporator, where refrigerant is directly vaporized due to solar energy input. The thermal performance is examined at the laboratory and also modelled in parallel using computer program. Results point out that the DX-SAHP using solar panels for space heating systems when compared to the conventional solar-assisted heat pump systems, where two components used for one single purpose (DX-SAHPs combine two processes; absorbing solar energy and vaporize refrigerant) is promising as substitute in terms of both energy conserving as well as economic viability. This innovative design results in higher heat transfer coefficient in solar collector-evaporator, lower system losses due to low evaporating temperature and reduces overall system cost.

Keywords: Solar-panels-assisted; Heat pump; Space heating; Economic viability; Low temperature applications.

1. INTRODUCTION

In the past few decades, the mainstream of global energy consumption has risen significantly. The conventional fossil fuel is energy source regarded as a major part of global energy consumption. However energy consumed worldwide in 2004 was 15 TW (=1.5× 10^{13} w) 86.5% of it from fossil fuel [1]. Combustion of fossil fuels contains production notably of carbon dioxide and other gases that cause the greenhouse impact and deleterious to the environment, which leading to global warming. Moreover the use of conventional systems involves carbon emission. As a result, rising demand for petroleum-based fossil fuels has oriented to concerns that may be exhausted in the next forthcoming decades to the stage that would cause a considerable disruption in the energy supply chain. Furthermore, due to the oil price volatility and dissipation of fossil fuel resources and future markets are subject to unstable price changes. Extensive public and private researches and development efforts to achieve technological breakthroughs have made to bring these technologies to use [2-3]. Recent findings pointed out alternatives sources that are environmentally friendly as well as clean such as solar and wind, which led to the development of renewable energy sources.

Direct solar radiation is considered to be one of the most prospective sources of energy. The total solar energy supply is sufficient to answer the total demand of energy in dwellings [4]. The yearly heat demand of 20GJ for typical, well-insulated dwelling can be delivered by about 20m² of solar collectors [5]. Buildings energy consumption is at critical stake, as 40% of energy demand in Europe is used in buildings [6]. Devices are not only essential to reach the ''3E'' objectives, conciliating clean Environment, sustainable Energy policy, solid Economy and social development. But also motivate a dramatic paradigm shift toward capital cost and their intermittent nature in power production. Among the solar energy technologies, flat-plate collectors are the most prevalent devices that can be utilize for heating of residential and public buildings. One of the purposes which are deemed by designers is the surge of outlet temperature of the solar collectors [7]. It is worthwhile to look at alternative new refrigerants that operate with reduced or very little CO^2 emission. Using Refrigerant-fluid may be solution to enhance of outlet temperature in solar collector. It concluded that refrigerants can be an important factor in the increase of collector efficiency so that when it is close to the isoelectric point the efficiency is maximized. In recent years, in order to improve the COP of the heat pump, many technical combinations are possible and many designs for heat pumps and supplementary systems have been suggested and investigated. Technology that combine a low temperature side of the heat pump to solar source are becoming promising today, and seem to be reasonable to get high COP, great reliability, simplexes and reduce both cost and maintenance costs[8]. These combinations systems have been based on the following principals: a) Heat pump with solar-assisted evaporator; b) Classical heat pump coupled to standard thermal solar collectors; c) Multifunction appliance combining an air-source heat pump, a thermal-regenerative Controlled Mechanical Ventilation (CMV) and a thermal solar collector for house heating [10].

2. THE PROPOSED SYSTEM AND SCOPE OF STUDY

In the current study, a direct expansion solar-assisted SAHP system is used for space heating applications as an alternative to natural gas or electric heating. The operational aspects and its theory of this system have been depicted in the readers can find details in Refs [11]. The current study is concentrated on the thermal analysis of the SAHP system to evaluate the energy conservation potential of particular design. System effectiveness aspects pertaining to the resource utilization as characterized by the primary energy ratio are analysed.

The direct expansion SAHP heating system (DX-SAHP) is integration of ternary solar-collector connected on series and a heat pump in which the collector/plates also acts as heat pump evaporator. Such combination is cost effective owing to elimination of a heat exchanger required in convention SAHP systems. It is worthwhile that the use of refrigerant as both in quenching of the collector and as working fluid of the heat pump. This situation causes the collector to operate at low temperature by which to raise the solar energy collection efficiency. After which, it is high enough to boost the heat pump performance. This has impact on both reduced capital cost of the solar collector as well as minimized heat pump operating costs owing to enhanced heat pump coefficient of performance (COP_H) compared to the conventional air source heat pump. A refrigerant with low boiling point, R-407c, is employed as the working fluid in the cycle shown schematically in [Figure-1] and on a T_s diagram (Figure-1), experimentally and in modelling and R-1234yf is modelled to compute the cycle performance. The fin-tube-sheet evaporator is exposure directly to simulator-lighting by which is simulates the sun intensity in different levels. The incident solar energy ends up being absorbed by the fluid refrigerant after which the liquid makes its way via the fin part between the tubes that convey the refrigerant. Hence process 1-2 entails constant pressure evaporation of sub-

cooled fluid into saturated vapour at first part. In the process 3-4, the liquid is compressed from evaporator pressure to condensing pressure. This process is followed by the constant pressure operate between part 4-1 in which the fluid is DE-superheated and condensed to the saturation refrigerant state. After this the condenser process, the liquid passes through a throttle (expansion valve). The thermal analysis of the DX-SAHP system performances of ternary bare none-covered solar-collectors comparatively is lower cost. In this study we have used a non-cover ternary flat plate solar collector.
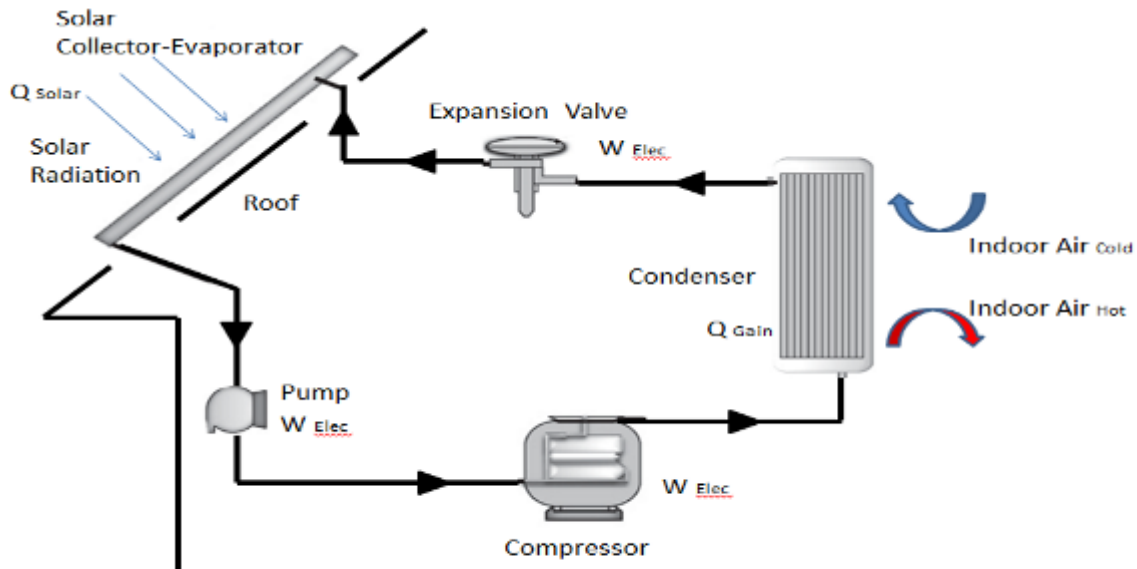
Figure 1: Schematic of DX expansion solar-assisted heat pump system
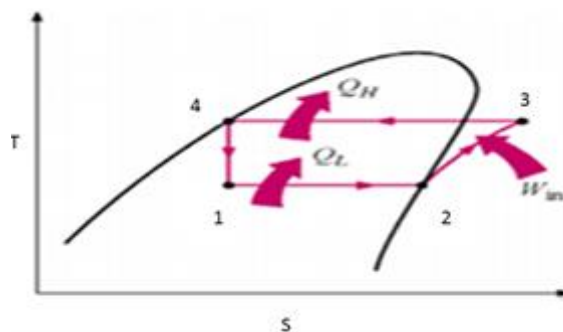
Figure 2: T_s diagram for the solar assisted heat pump system

3. FIRST LAW THERMAL ANALYSIS

When the solar radiation with intensity of (I) falls on the solar collector, a main part of the radiation (I), strikes to the aluminium absorber plate electroplated with black paint selective coating. A part of solar radiation is absorbed by the working fluid (Q$_{evaporator}$) and the remained part is dissipated through top and bottom of the absorber plate to the surrounding. By other words to compute the outlet temperature and efficiency of the solar collector, first the heat losses to surrounding should be calculated. The rate of useful energy extracted by the collector experimentally (Qevp) expressed as the a rate of extraction under steady state condition is proportional to the rate of useful energy absorbed by the collector , less the amount lost by the collector to its surrounding. The relation between the absorbed heat and heat losses are of which are as follows:

$$Q_{evaporate} = Ac * \left[\tau \propto I - U_L (T_p - T_a) \right] \qquad (1)$$
$$= F' Ac \left[\tau \propto I - U_L (\check{T} - T_a \right] \qquad (2)$$

- – Where:
- – Ac: Solar collector surface area m²
- – ε: The collector absorption rate0.9
- – I: The intensity of solar radiation (W/m²)

- U_L The collector overall loss coefficient (W/m²)
- T_p: the collector/evaporator temperature °C
- Ta: Ambient temperature °C
- F': Solar collector efficiency factor which is depended on tube-and-sheet
- Ť: Mean refrigerant temperature in the collector/evaporator (c°)

By assuming that the losses of the plates/collectors occur to a common sink temperature T_a, parameter U_L that is the overall heat loss coefficient can be determined as [12]:

$$U_L = U_t + U_b + U_e \qquad (3)$$

Where U_t the heat loss coefficient from the top/plate, U_b is the heat loss coefficient from the bottom/plate, and U_e is the heat loss coefficient from the edges of the collector. To calculate U_t, the following correlation can be used [13]:

$$U_{top} = \left(\frac{N}{\frac{C}{Tp}\left[\frac{Tp-Ta}{(N+f)}\right]^e} \right)^{-1} + \frac{1}{h_w} + \frac{\sigma(Tp+Ta)(Tp^2+Ta^2)}{\frac{1}{\varepsilon_{p}+0.0091Nh_w}+\frac{2N+f-1+0.113\varepsilon_p}{\varepsilon_p}-N} \qquad (4)$$

Where N is the number of glass covers that for present paper is 0, σ is Stefan-Boltzmann constant, and ε_p is emittance plate, the parameter of h_w is the wind heat transfer coefficient and V_w is wind velocity and L is the length of collector can be calculated by:

$$h_w = \frac{8.6V_w^{0.6}}{L^{0.4}} \qquad (5)$$
$$C = 520 * (1 - 0.0000\beta^2) \; for \; 0° < \beta < 70°; for \; 70° < \beta < 90°, use \; \beta = 70° \quad (6)$$
$$f = (1 + 0.89h_w - 0.1166h_w\varepsilon_p)(1 + 0.07866N) \; In \; which \; \beta \; is \; the \; collector \; slope. \quad (7)$$

Note that the main heat losses occur from the top. To determine the heat losses from edges not applicable in the paper and the bottom one can use the following equations:

$$U_{bottom} = \frac{1}{\frac{t_b}{k_b}+\frac{1}{h_{b.a}}} \qquad (8)$$

Where k_b and t_b are the thermal conductivity and thickness of insulators bottom edges respectively and $h_{b.a}$ is convection heat transfer coefficient bottom and edges, and their values are assumed to be the same and equal to $=h_w=5$ W/m²°c for still air. As seen, to calculate U_t, and, thus U_L, the value of T_p should be determined at first. For this purpose, an initial value of T_p is measured experimentally, and the quantities of U_L and Q_{solar} are calculated. Also can be computed through modelling via refrigerant enthalpy chart:

Where $\quad Q_{evaporator} \; via \; experiment \; laboratory \; experiment \; \simeq \; Q_{Solar} \; via \; modelling$

$$Q_{Solar} = ṁ_r * (h_{refout} - h_{refin}) \quad (9)$$
$$Q_{Solar,ref} = ṁ_r * (h_2 - h_1) \qquad (10)$$

Where:

$$\dot{m}_r: Collector \; mass \; flow \; rate \; (k_g/s), \; ṁ_r = Q * \rho \; wherein \; Q = \frac{\pi}{4}D^2 * V \quad (11, 12)$$

$Q: The \; volumetric \; flow \; rate \; (m^3/s)$

$D: Outer \; tube \; diameter \; of \; risers \; (m)$

$\rho: Fluid \; density \; (k_g/m^3)$

$V = The \; mean \; velocity \; of \; the \; fluid \quad (m/s)$

h_{refout}: $Refrigerant/Collector\ outlet\ enthalpy\ (k_J/k_g)$

h_{refin}: $Refrigerant/\ Collector\ inlet\ enthalpy\ (k_J/k_g)$

For this work, it is not necessary to develop a completely new analysis for the tube-sheet relation situation, Hottel-Whilliar-Blis have developed the collector efficiency factor F'(Duffi & Beckman, 2006[*]), for the tube-sheet relation in the formula as following:

$$F' = \frac{1}{W\left[\frac{1}{[D+(W-D).F]} + \frac{W.U_L}{\pi D_i hf_i}\right]}$$ (13) Where:

W: $Pitch\ between\ the\ serpentine\ tubes\ of\ the\ collector$

D: $Outer\ tube\ diameter\ of\ risers$

D_i: $Inner\ tube\ diameter\ of\ risers$

F : $Fin\ efficiency\ factor\ of\ the\ collector\ plate = \frac{tanh[m(W-D)/2]}{m(W-D)/2}$ (14)

m= $\sqrt{U_L/k_m * \delta_m}$ (15)

Where:

k_m: Thermal conductivity of the collector/evaporator flat plate (211 W/m°c)

δ_m: Thickness of the absorber collector/evaporator flat plate (0.002 mm)

To obtain the internal heat transfer coefficient (h_{fi}), the definition of the Nusselt number must be applied:

$$hf_i = \frac{Nu * k_{ref}}{D_i}$$ *(16)*

Where:

N_u: Nusselt number a dimensionless parameter used in calculations of heat transfer between a moving fluid and a solid body

k_{ref}: Refrigerant thermal conductivity (W/m°c)

To calculate the Nusselt number, Gnielinski correlation is used that is valid for $3000 \leq Re \leq 5 \times 10^5$ and $0.5\ Pr \leq 2000$, this correlation is expressed as [11]:

$$N_u = \frac{(f/8)(R_e - 1000) * P_r}{1 + 12.7(f'/8)^{0.5} * (P_r^{0.6} - 1)}$$ *(17)*

Where: f:

is the Darcy friction factor and can be obtained by Petukhov's formula for evaluating it, assuming that any quality change in the collector/evaporator is largely due to enthalpy change and neglecting the quality difference due to pressure drop. This result is good for turbulent flow in smooth pipes:

$$f' = \frac{1}{[0.790 I_n(R_e) - 1.64]^2}$$ *(18)*

The relation is valid for the Reynolds numbers between 4000 and 10^8, Reynolds and Prandtl numbers described as:

$$R_e = \frac{4\dot{m}_r}{\pi.D_i.\mu_{ref}} \qquad (19)$$

$$P_r = \frac{\mu_{ref}.C_{p_{ref}}}{k_{ref}}$$

It should be noted that the Reynolds numbers is in terms of mass flow rate in any riser ($\dot{m}_r$) where (μ_{ref}) refrigerant viscosity ($k_g/m\ s$)

4. THE EVAPORATOR/COLLECTOR SECTION

The collector model is used to determine the value of outlet collector temperature T_2 for given values of ambient temperature Ta and *Icoll*, refrigerant properties h_1 and h_4 and the heat pump parameters (specific volume v_1 and the displacement volume rate (VD). The net energy absorbed by the fluid circulating via the collector/evaporator equals incident solar radiation minus the heat loss from the collector/evaporator and accordingly the outlet fluid temperature T_2 can be calculated through the steady state energy balance on the collector/evaporator in modelling part, expressed by thereby:

$$\frac{VD}{v_1}(h_2 - h_4) = F'Ac * [I_{coll}(\tau \propto) - U_L(T_2 - T_a) \quad (20)$$

From the above equation one can solve for T_2 as:

$$T_2 = T_a + \frac{I_{coll}.(\tau\alpha)}{U_L} - \left(\frac{VD}{v_1}\right) * \frac{(h_2 - h_1)}{U_L.F'.A_c} \qquad (21) \quad \text{(For modelling part)}$$

For a given location (Nottingham, UK), all the data explained (Table: 1) are provided as inputs. The value of the collector/evaporator temperature at given time of the day is measured experimentally and compared to those assumed values of enthalpies at state points 2 and 1 which are modelled and computed from the polynomial fit for the refrigerant properties. A new value of T_2 according to circulated process is compared with the previously measured experiment results and modelled values of T_2. The values of these parameters are incorporated over a given month. The thermal energy produced by the heat pump Q_H (W) is calculated from the following equation [..];

Table 47: Standard system parameters for thermal analysis

Parameter	Value
1 Condensing temperature	86 °c(variable)
2 Collector area	4.22 m²
3 Collector efficiency factor	0.947 (variable)
4 Transmittance-absorptance product	0.9
5 Collector heat loss coefficient= 9.999 W/°c m²	
6 Compressor efficiency	0.75 (variable)
7 Compressor displacement=7.84E-04 m³/s	

$$Q_{H\_ref} = \dot{m}_{coll\_ref}(h_3 - h_4)(22)$$
$$Q_{H\_air} = \dot{m}_{air} * C_{p\_air}(T_{out} - T_{in})(23)$$

Where m_{coll_ref} and m_{air} are the collector refrigerant and condenser rejected air mass flow rate respectively, whereas CP $_{air}$ the air specific heat capacity. Consequently the efficiency of the solar-collector η_{coll_ref} can be defined both experimentally and in model part as expressed can be below.

$$\dot{m}_{coll\_ref} = \frac{V_D}{v_1} \ (kg/_s) \quad (24)$$
$$\dot{m}_{air} = \rho * V * A \ (kg/_s) \ (25)$$

Where ρ is density of flowing air (k_g/m^3), V is the air flow velocity ($m/_s$) and A the flow area (m^2)

$$\eta_{coll\_ref} = \frac{Q_{solar}}{I_{coll}*A_c} \qquad \text{For modelling part} \quad (26)$$

$$\eta_{coll\_ref} = \frac{Q_{evaporator}}{I_{coll}*A_c} \quad \text{For experiment part} \quad (27)$$

5. THE COMPRESSOR SECTION

The compressor work W_{comp} or compressor power $W_{power} = \mathfrak{m}_{refrigerant} * W_{comp}$ for a given pressure ratio P_2/P_1 is determined for model part from expression;

$$W_{comp} = \frac{P_1 v_1}{\eta_{comp}} \left(\frac{k}{k-1}\right) \left[\frac{P_2}{P_1}\right]^{\frac{k-1}{k}} - 1\right] \text{ or } W_{comp} = \mathfrak{m}_r(h_3 - h_2) \text{ For model part (28)}$$

$W_{comp} = \frac{Work_{electronic}}{\eta_{comp}}$ for experiment part the compressor and auxiliary power devices electricity-consumption displayed on the power-meter was recorded. (29)

Where[k] is the ratio of specific heats, and for R-407c it has a value of 1.14. The assumption of ideal gas behaviour during the compression process appeared to be reasonably acceptable since the compressor work computed in this way is slightly overestimated in comparison with the compressor work calculated instantly through the experiment work. While p_2/p_1 can be determined through measured high side and low side pressure respectively at experiment and via refrigerant thermodynamic polynomial chart for modelling section. The work compressor also relied on the efficiency of the compressor which is variable related to fluid condition (entropy) and temperature of the collector outlet fluid T_2 (enthalpy).

$\eta_{comp} = \frac{T_{2i}-T_2}{T_{2a}-T_2}$ (30) (Efficiency of compressor), therefore the iteration of calculated η_{comp} and their repetitions in turn depend yet again on fluid state arising out of T_2 variation, and have applied to define exact compressor(η_{comp})The situation here changes very rapidly when T_{2i} isontropic (CTD calculated) and T_{2a} each of which changes its temperature:

$$T_{2i} = T_2 * \left[\frac{P_2}{P_1}\right]^{0.28571} \quad (31)$$

$$T_{2a} = T_{3'} = T_2 \left[\frac{P_2}{P_1}\right]^{\left[\frac{n-1}{n}\right]} \quad (32)$$

Where n=k while T_3"discharge compressor temperature °C" and η_{comp} is neglected. To determine the liquid temperatures after compressor T_3 operation can be calculated of which are as follows whereas the compressor η_{comp} were provided previously according to variable solar radiation incidents.

$$T_3 = T_2 \left[1 + \frac{\left[\frac{P_2}{P_1}\right]^{\left[\frac{k-1}{k}\right]} - 1}{\eta_{comp}}\right] \quad (33)$$

Calculating modelling section T_3 is determined to count energy provided by compressor as stated aforementioned, since the coefficient of performance of the heat pump (COP$_H$) inversely dependent on compressor work is calculated from equation listed below.

$$COP_{heatpump} = \frac{Q_H}{Work_{comp}} (34)$$

Q_H The thermal energy produced by the heat pump which is the condenser work (Q$_{conden}$) and will be discussed in the next section.

6. THE CONDENSER SECTION

The air velocities were measured so as to further obtain the air flow rate at the outlet of condensation fan and the heating capacity. The operating performance of a heat pump is fairly related to the temperature that namely the difference between the temperature of the heat source and the output temperature of the heat pump. Therefore the COP $_{heat\ pump}$ determined solely by the condensation temperature and the

temperature lift (condensation-evaporation temperature).The real heating capacity is obtained from equation [35] by measuring the air temperature difference between inlet and outlet of and the air mass flow rate at outlet orifice.

$$Q_{condenser_{air}} = \mathfrak{m}_{r_{air}} * c_{p_{air}}(T_{out.condeser} - T_{in.condenser}) \quad (35)$$

Since the system requires auxiliary energy owing to intermittency during night-time or absence of available solar energy, the effective coefficient of performance and seasonal performance factor are determined as:

$$COP_{effective} = \frac{Q_{condenser\,(air)}}{Work_{electronic}} (36)$$

From the above equation one can solve for

$$Effectiveness = \frac{Q_{heatpump}}{Q_{heatpump} * Q_{electronic}} = \frac{Q_H}{W} \quad (37)$$

$$SPF = \frac{Heat\ energy\ output\ (kWh)}{Total\ input\ energy\ (kWh)} \quad (38)$$

7. PRIMARY ENERGY RESOURCE UTILIZATION

In competing systems for domestic space heating (DSH) applications, one can use the primary energy ratio (PER) which is defined as the ratio of the thermal energy produced to the primary energy consumed, a parameter that characterizes the overall efficiency of a number of interconnected energy transformation process, for example in the DSH applications, so as to determine the (PER) one must track the energy flow the way back to the primary energy source (natural gas, oil ,coal ,etc.) to define how many kJ of thermal energy are produced for end-use for every kilo joules of primary energy utilized. The ratio of the provided thermal energy and the primary energy is known as the primary energy ratio (PER) in reality there are emissions of global warming gases such as CO_2 and other pollutants attributed to electric devices for each kWh of electrical energy used in it. The SAHP system operates in the solar only system mode.

$$PER = COP_{heat\ pump} * \mathfrak{n}_{evporator} \quad (39)$$

$$PER = \frac{useful\ heat\ delivered\ by\ heat\ pump}{primary\ energy\ consumed} \quad (40)$$

$$SPF = \frac{Heat\ energy\ output\ (kWh)}{Total\ input\ energy\ (kWh)} \quad (41)$$

8. DISCUSSION OF RESULTS SYSTEM PERFORMANCE

Zeotropic refrigerant R407c was used experimentally and theoretically in modelling. In order to accomplish this, computer programmes MATLAB were used. Also, new refrigerant such as 1234yf (Figure:11-12)) were also analysed so as to present a comparative analysis. In this section, the effectiveness of enlarge the collector area played a major role in this research. Refrigerant enters collector/evaporator plates at $-19\,°C$ passed through each panel upwards and came out with liquid temperatures between 24-30°C, where the surrounding energy were absorbed [Figure:3-4] It should be noted that since the plates connected together on series this showed impact on the outlet collector temperature by lifting less temperature as the evaporating temperature rises. It shows the variation of the coefficient of thermal performance for collector temperatures ranging within the limits-11 to 24°C for R407c. The condensing temperature is maintained at $86\,°C$ while the rejected air reaches27°C. Results were obtained for range of solar incident, specified of collector area 4.22m²and compressor displacement volume of7.84E-04m³/s. The research also sheds light on compressor electricity consumption and its efficiency triggered by liquid thermodynamic state and equally important liquid collector-outlet temperature bring about efficiency changes swing between0.47-0.75 %. It is clearly seen that the effects of evaporation temperature impact in which compressor lifts less work according to relatively high evaporation temperature[Figure:8]. As illustrated (Figure:6) R407C yields the highest value of 3.6 COP$_H$ within available solar radiation. R1234yf simulation is conducted to carry out thermal and coefficient of performance which covers the experimental working conditions of heat pumps in this study [Figure:12]. It is obvious that COP$_{1234yf}$ drop gradually from 4-5 to 3-4 as the condensing temperature rises in the simulation context at an average around 3.5%[Figure:

11-12]. The change of COP is much more significant than that of condensing temperature due to steeper variation curve. This happens because smaller the temperature difference between $T_{evaporator}$ and $T_{ccondenser}$, the greater COP the heat pump system can achieve due to less compressor work W_{comp}. To describe this, the lowest and highest COP for $1234yf$ refrigerant emerges at the maximum $(T_{evapo}\,0°C, T_{cond}\,55°C$) and minimum $(T_{evapo}\,20°C, T_{cond}\,25°C)$ temperature difference.

9. CONCLUSION

This presented study indoor thermal performances analysis of the potential for a DX-SHP system to provide space heating. The investigation was based on the steady-state modelling of the thermodynamic vapour compression cycle. The tests were operated at solar collector/evaporator temperatures greater than room temperature. The heat was extracted from the condenser and used to heat space according to the demand. The experimental results were compared with the theoretical model predictions and they showed minor differences between the ideal and real situations. The analysis results of the $SAHP$ system indicates that the system is an appropriate match for space heating applications and have an excellent agreement between present data and the numerical data. This system reveals are both promising economical as well as energy conserving solutions compared to the electricity-only heating systems. It should be mentioned that although of favourable results provides an opportunity for further investigations to improve and optimise the performance of DX-SHP. It is found that parallel connection would be more likely have better heat pump performance by reducing the fluid temperature by$±13°C$. However, reduced consumption of electricity and the capture of renewable solar energy through collectors should have convenient environmental effect since diminished carbon emission would result if this system is used as an alternative to the electric-only systems. Economic cost-efficiency benefit analysis should be considered in a future study.
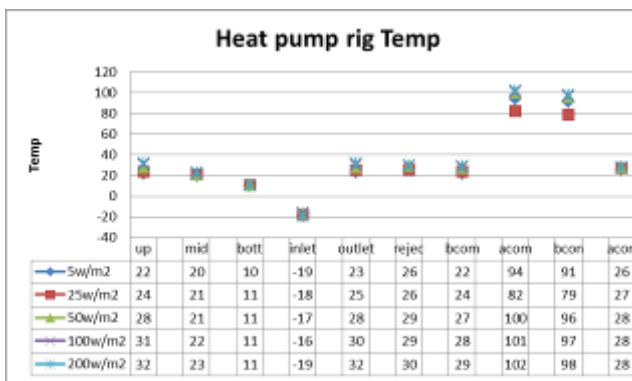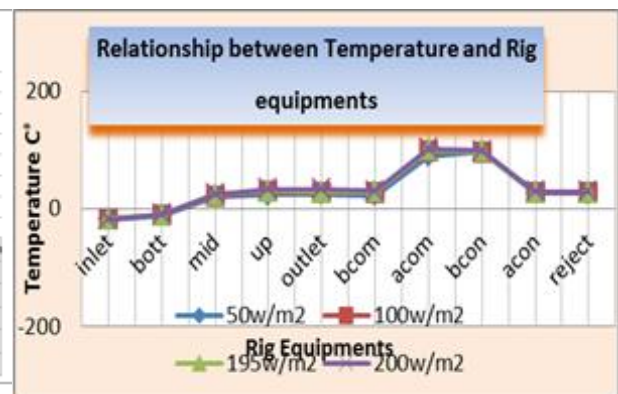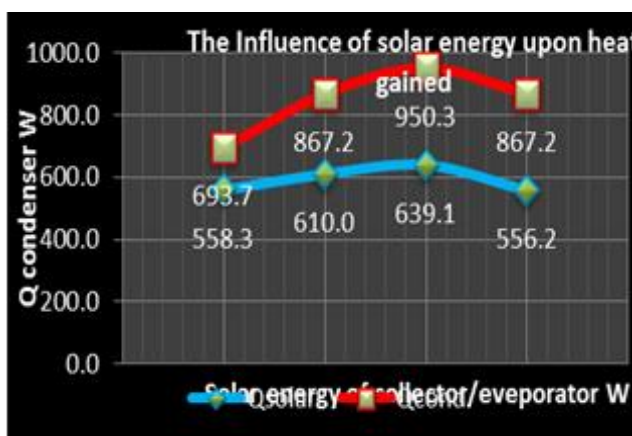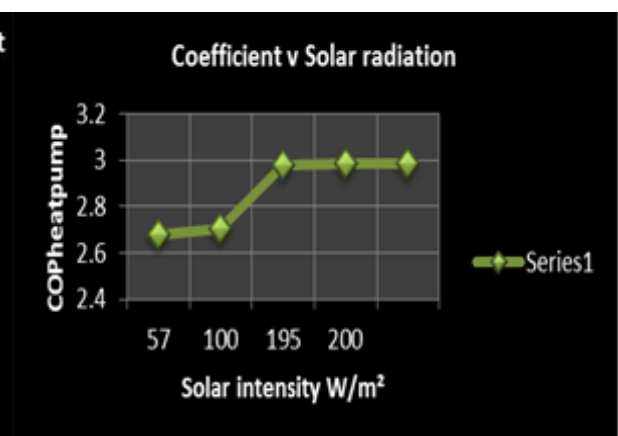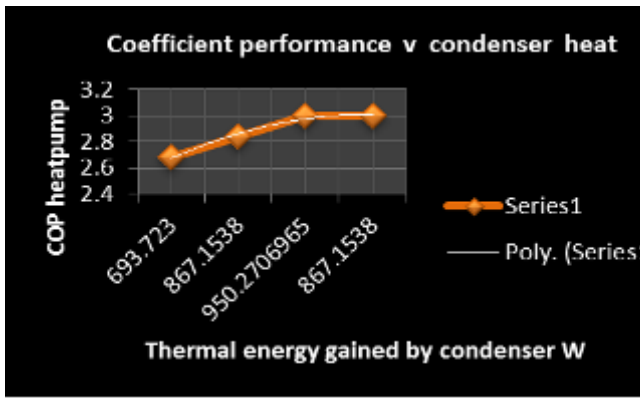

Figure 3

Figure 4

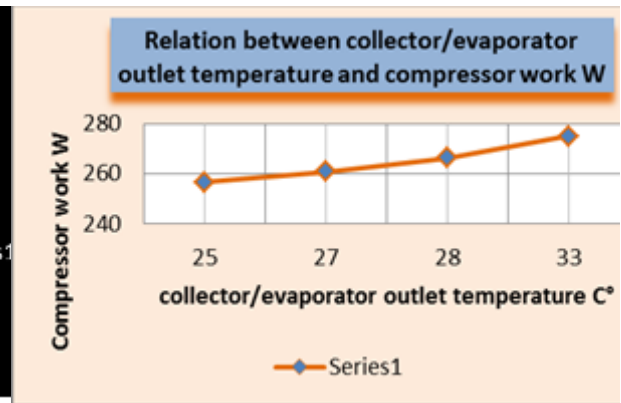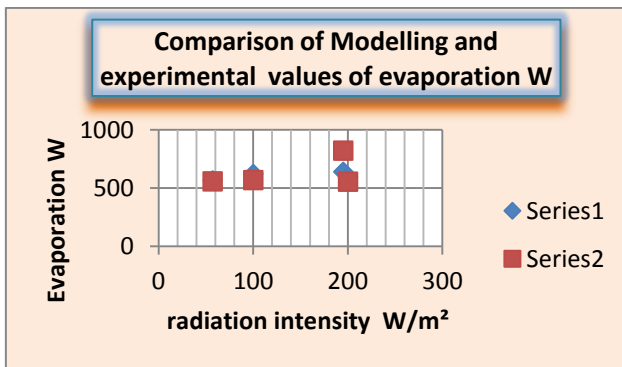*Figure 5*

Figure 6

Figure 7
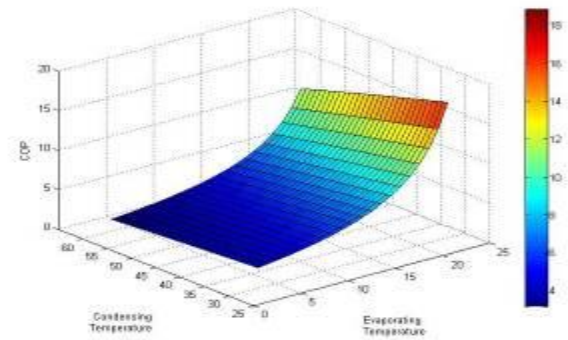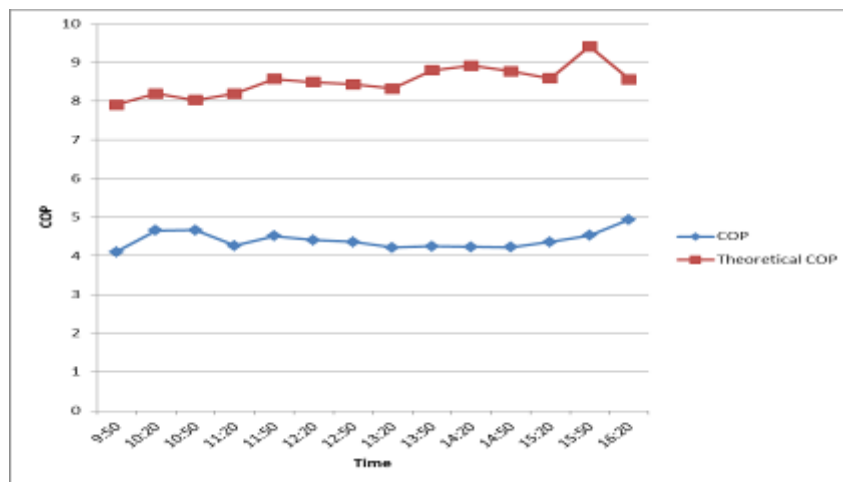

Figure 8

Figure 9

Figure 10

Figure 11

10. REFERENCES

[1]World consumption of primary energy by energy type and selected country groups. Energy Information Administration, U.S. Department of Energy; 2006.

[2] F.Diaz-Gonzaleza.SUMPER, O,G.Bellmunt, R.V.Robles, A review of energy storage technologies for wind power applications, Renewable and Sustainable Energy Review Reviews 16 (2012) 2154-2171.

[3] R.M. DELL, DA.J Rand, Energy storage- a key technology for global energy sustainable, Journal of power sources 100 (1-2) (2001) 2-17.

[4] HERMANS, J, Energy Survival Guide; 2008.

[5] HERMANS, J, Energy Survival Guide; 2008.

[6] La Region Wallonne. La consummation energetique de nos batiments, unenjeu crucial pour l'avevir; 2006. http://energie.wallonie.be.

[7]http://en.wikipedia.org/wiki/Global...warming.

[8] Blaise. M, Investigations of Novel Heat Pump Systems for Low Carbon Homes, Nottingham UK, 2011.

[9] Haafs S. HENRICI H. Refrigeration technology. Ullmann's encyclopaedia of industrial chemistry. Wiley- 2002.

[10] WANG S. Handbook of air conditioning and refrigerant. 2nd ed. McGraw-Hill Professional; 2000.

[11]KUSH BA Performance of heat pump at elevated evaporating temperatures with application to solar input.Sol 1980:102:203-10

[12] F.B Gorozabel CHATA, S.K. chaturvedi, A. Almogbel Norfolk, Virginia, USA,2005, Analysis of direct expantion solar assisted heat pump using different refrigerant, Elsevier Ltd.

308: Energy performance assessment of market available photovoltaic module technologies under Kuwait climate condition

Ahmed Hamza H Ali[1] AND Hassan M.G. Alfadhli[2]

1 Mechanical Engineering Department, Faculty of Engineering, Assiut University, Assiut 71516, Egypt (ah-hamza@aun.edu.eg)

2 Engineering Projects Department, Ministry of Interior, Mirqab, Kuwait City, Kuwait

Energy performance assessment of the two main photovoltaic technologies available in 2015 market operates under hot arid climatic conditions for the state of Kuwait is carried out. For the case of one MWp PV plant, the study investigated the influence of climatic parameters on energy production and performance ratio based on the daily, monthly and yearly energy produced from crystalline silicon based and thin film technology photovoltaic technologies. The assessed technologies are monocrystalline, polycrystalline and thin-film of cell types of cadmium telluride (CdTe) and CdS/CdTe semiconductor. The assessment is based on the manufacture provided PV modules characteristics and 30 years average hourly values of the ambient air dry temperatures, horizontal solar radiation and average wind speed for the state of Kuwait. The main results of this study are: For same maximum power for all investigated technologies compared with Polycrystalline one the Monocrystalline technology plant requires extra area by 3.696%, thin-film cadmium telluride (CdTe) requires extra area by 4.34% and thin-film cadmium sulphide (CdS)/cadmium telluride (CdTe) (CdS/CdTe) requires extra area by 16.1% respectively. While, referenced to the net energy produced from Polycrystalline PV technology: the Monocrystalline technology plant produces extra annual net energy by 0.552%, thin-film cadmium telluride (CdTe) technology produces extra annual energy by 0.43% and thin-film CdS/CdTe technology produces extra annual energy by 0.62%, respectively. The CdS/CdTe PV technology has the higher performance ratio values of the all-over the hot months of the year for the state of Kuwait. Modules with tilting angle of 30 degree with the horizontal have the higher yearly average incident solar energy of 2157.49 kWh/m2 for the state of Kuwait.

Keywords: PV technologies energy performance, PV systems in hot arid areas, PV module efficiency

1. INTRODUCTION

Solar energy radiation reaching the earth's surface represents thousand times of the current primary energy needs by earth inhabitants. The current utilization of solar energy resource represents less than 1% of the total electricity generated from all renewable energy resources. Instead of the use of photovoltaic systems has been increasing steadily for the last 20 years, solar energy conversion technologies still suffer from some weaknesses that make those technologies weakly competitive with fossil fuels energy market such as high capital cost, modest conversion efficiency, and large scale field daily maintenance. From the research and development point of view, development of new technologies with higher conversion efficiencies at higher ambient temperature, anti-dust coated for use in desert areas and low production costs is a key requirement for enabling the deployment of solar energy technologies at a large scale in hot arid sandy areas. In the open literature, the plane for solar energy resource utilization, to generate electrical energy, based on the conversion technologies for the state of Kuwait are not clearly articulated, report of IRENA (2014). It can be clearly recognized from this report that the recent state of the art for the state of Kuwait is mainly dependent on the fossil fuels for electricity generation. In addition, the electricity consumption is increasing highly without introducing an alternative portion to be generated from renewable energy resources such as the solar energy. The geographic location of Kuwait exposed to the higher value of the incident solar energy per square meter KISR (2015). It is well known that the performance of any solar energy conversion system into useful form depends on various environmental factors such as ambient temperature, solar irradiation intensity, and wind speed at installation sites. There are few studies in the open literature investigated the photovoltaic systems performance under the state of Kuwait climate condition such as Al-Otaibi et.al (2015) for the case of schools' rooftop with two small-scale, grid-connected photovoltaic (PV) systems. Aldihani et al. (2014) investigated the performance of solar PV panel based on heterojunction with intrinsic thin layer (HIT) silicon cells under Kuwait environment and assessed the effect of cooling in reducing the impact of dust on the PV power output. Ghoneim (2012) evaluated the role of PV grid connected in reducing the total and peak load demand in Kuwait as well as the assessment of the environmental impacts of grid connected PV system. Al-Hasan el al. (2004) evaluated the role of grid connected PV in reducing the total and peak load demand in Kuwait at different PV system sizes. Abdullah et al. (2002) investigated the feasibility of implementing grid connected PV systems in Kuwaiti climate. Ghoneim et al. (2002) examined the economic feasibility of photovoltaic-powered solar water heating systems in Kuwait. It is known that PV cell performance decreases with increasing the ambient air temperature, as the cell operating temperature plays a key role in the photovoltaic conversion process. Therefore, the PV module electrical efficiency and the output power are depending on the environment variables as well as PV material dependent characteristics. Ali (2005), Ali et al. (2010) and Ali et al. (2013) reported that, increasing the PV module temperature is one of the hindrances to its rated performance in hot arid areas. There are many studies in the open literature represent module electrical efficiency equations, which can be applied to PV modules or PV arrays, mounted on free air-standing frames installation and/or building integrated PV arrays. Skoplaki and Palyvos (2009) presented tabulations for most known correlations expressing the PV cell/module electrical efficiency as a function of PV cell temperature and weather variables such as the ambient temperature, wind speed and the solar radiation flux (irradiance), with material dependent properties. Aste et al. (2014) carried out experimentally under real operating conditions a performance comparison of three different and representative PV technologies in temperate climatic conditions In particular, investigation the influence of climatic parameters on energy production, with a focus on the thermal and spectral analysis. Cañete et al. (2014) carried out a comparative analysis of the efficiency of different PV module technologies under the climatic conditions at southern of Spain and proposed an empirical model to estimate the daily energy performance. Tossa et al. (2014) proposed a new approach to estimate the performance and energy productivity of photovoltaic modules under real operating conditions. Ya'acob et al. (2014) developed a correlation model between the ambient temperatures, solar radiation and wind speed variables and the cell temperature for a PV system installed in a specific location in Malaysia. Their correlation model is derived based on new weather conditions for measuring the Normal Operating Cell Temperature (NOCT).

Clearly, many previous studies show that the energy produced by different photovoltaic module technologies depends mainly on the specific climate conditions of each location. In addition, most of the presented PV module energy performance results were based on the module manufacture information at the standard test condition (STC) as most of these studies were carried on moderate climate. While, in hot arid areas the manufacture technical information at Normal Operating Cell Temperature (NOCT) for photovoltaic systems need be used as a base for initial sizing of PV plant in hot arid area in order to investigate the system performance. Therefore, the location weather data such solar irradiation, ambient air dry bulb temperature and wind speed with maker provided material characteristics technical data at NOCT need to be used. From the available literature, clearly, the energy performances of different

photovoltaic modules market available technologies under severs hot arid conditions for the state of Kuwait climate is not available.

Therefore, the aim of this study is to carry out comparison between the two main representative photovoltaic technologies available in 2015 market in hot arid climatic conditions, in particular, the influence of climatic parameters on energy production to assess the daily, monthly and yearly energy produced from crystalline silicon based and thin film technology photovoltaic technologies. These technologies are monocrystalline, polycrystalline and thin-film of cell types of cadmium telluride (CdTe) and cadmium sulphide (CdS)/cadmium telluride (CdTe) (CdS/CdTe) semiconductor. This is based on the manufacture provided PV modules characteristics and 30 years average hourly values of the ambient air dry temperatures, horizontal solar radiation and average wind speed for the state of Kuwait.

2. METHODOLGY FOR ENERGY PERFORMANCE ASSESSMENT

To evaluate the performance of different photovoltaic modules technologies, hourly, daily, monthly and yearly produced energy values based on the module efficiency as a function of ambient air-dry temperatures, solar radiation and average wind speed is performed. However, one must be careful in applying a particular expression for PV module efficiency because each equation has been developed with a specific mounting geometry or building integration. Skoplaki and Palyvos (2009) presented tabulations for most known correlations expressing the PV cell/module electrical efficiency for various mounting geometry as a function of PV cell temperature and other weather data such as the ambient air dry bulb temperature, wind speed and the solar irradiance with module material characteristics dependent properties. However, the study aim is to investigate the electrical energy performances of market available photovoltaic modules technologies under severs hot arid conditions for PV power generation plant with modules installed on frame mountain in open air. The PV module hourly efficiency value for PV module installed in open air and maintained over frames is presented in Skoplaki and Palyvos (2009) and given by

$$\eta_h = \eta_{ref}\left\{1 - \beta\left[T_a - T_{ref} + \left(\frac{9.5}{5.7 + 3.8V_w}\right)(T_{NOCT} - T_a)\frac{G_T}{G_{NOCT}}\right]\right\}$$

(1)

Where:

- η_h= hourly value efficiency of PV module
- η_{ref}= PV module reference efficiency provided by the manufacture at Stander Test Condition STC
- β= PV module temperature power coefficient provided by the manufacture (K^{-1})
- T_a = ambient air dry bulb temperature (K^{-1})
- T_{ref} = reference temperature value at the reference condition provided by the manufacture (K^{-1})
- V_w = wind speed at monitored surface (m/s)
- T_{NOCT}= module temperature at Normal Operating Cell temperature provided by the manufacture (K^{-1})
- G_T= total solar radiation flux (irradiance) on module tilted plane (W/m^2)
- G_{NOCT}= solar radiation flux (irradiance) at Normal Operating Cell temperature provided by the manufacture (W/m^2)

The value of G_T is obtained from the total horizontal solar irradiance at plant location by using the equation given in Duffie and Beckman (2006) for northern hemisphere as follows:

$$G_T = G_H\left(\frac{\cos |\Phi - \delta - B|}{\cos |\Phi - \delta|}\right)$$

(2)

Where:

- G_H = total solar radiation flux (irradiance) on the horizontal (W/m^2)

- Φ= location Latitude (degree)
- δ= solar declination angle, and it is calculated using equation given in Duffie and Beckman (2006) (degree)
- B= PV module slope angle with horizontal (degree)

The hourly average value of the solar irradiance on the horizontal plan, G_H, is obtained from the generated hourly weather file data by using ENER-WIN (2007) software for a weather station with WBAN number as average of the station recorded over 30 years in the software database for a target location.

To calculate the hourly value of the net produced energy in Watt-hour (WH) from PV module of different PV technologies considering the overall system losses percentage is calculated by:

$$E_h = \eta_h \times G_T \times \Delta t \times \eta_g \times A_{modules}$$

(3)

Where:

- η_h= hourly value efficiency of PV module
- E_h = hourly value of the produced energy (Wh)
- Δt= time interval (s)
- η_g= overall useful energy factor
- $A_{modules}$= PV modules apparent area (m^2)

The daily, monthly or yearly values of produced energy (E) can be obtained by summation of the net hourly energy value through a certain period either one day, a month or a year.

To compare between different photovoltaic module technologies under specific climate conditions the performance ratio (PR) is a measure of the quality of a PV plant in general as it is independent of the location. It is described as a quality factor that can be used to as a comparison indicator of different technologies. The performance ratio describes the relationship between the actual and theoretical energy outputs of the PV plant. It thus shows the proportion of the energy that is actually available for supply to the grid after deduction of energy loss and of energy consumption for plant operation. Therefore, the performance ratio indicate how energy efficient technologies and reliable for a PV plant under same operating conditions and the status of your PV plant over a period of time. In this study, the hourly performance ratio (PR) over a year can clearly indicates the comparison of the different PV modules. It is calculated as reported in the literature such as Cariete et al. (2014) as follow:

$$PR = \left(\frac{E_h \times I_{STC}}{G_T \times \Delta t \times P_{max}} \right)$$

(4)

Where:

- PR= performance ratio
- E_h = hourly value of the produced energy (Wh)
- I_{STC}= Irradiance at Stander Test Condition STC (W/m^2)
- G_T = total solar radiation on module tilted plane (W/m^2)
- Δt= time interval (s)
- $A_{modules}$= PV modules apparent area (m^2)
- P_{max}= module nominal power provided by the manufacture at Stander Test Condition STC (W)

Photovoltaic module manufacturers provide data sheet with their product having a series of characteristic parameters, including their efficiency. These parameters are calculated under standard test conditions (STC) and cannot be used to accurately to establish how much energy such module will produce under actual specific climate conditions and on the spectral response of each technology. Therefore, a selection from the market available photovoltaic module technologies is done based on the two main commercial technologies which are crystalline silicon based modules such as monocrystalline, polycrystalline and thin

film technology modules such as cadmium telluride (CdTe) and cadmium sulphide (CdS)/cadmium telluride (CdTe) (CdS/CdTe) semiconductor. The main characteristics of the investigated modules in this study are given in table (1). Clearly, the modules have different efficiencies different power temperature coefficients and different spectral response.

Comparison between different photovoltaic modules technologies available in the market is based on their energy performances when installed in hot arid areas such as the state of Kuwait climate condition. In ENER-WIN (2007) the available recorded of for the state of Kuwait for weather and solar radiation flux hourly data is only for Kuwait Int'l Airport, WBAN Station I.D.: 40582, (Latitude= 29.2267°N and Longitude = 47.9800°E). The hourly data is generated by using ENER-WIN (2007) software for WBAN Station I.D.: 40582. The energy generation factor value is set based on the assumption that PV module overall system losses percentage are as follows: losses due to Soiling 2%, Shading 3%, Mismatch 2%, Wiring 2%, Connections 0.5%, Light-Induced Degradation 1.5%, Nameplate Rating 3%. Therefore, the overall useful energy factor, η_g, used in this study is 0.86.

3. RESULTS AND DISCUSSION

Energy performance assessment of market available photovoltaic module technologies under Kuwait climate condition is carried out based on the initial design of a small photovoltaic plant with maximum power (P_{max}) of one MWp. The plant sizing is calculated based on the module Maximum power at Nominal Operating Cell Temperature (NOTC). The calculated required area based on the PV module characteristics shown in table (1) are as follow: Monocrystalline technology is 8529 m^2, Polycrystalline is 8225 m^2, thin-film cadmium telluride (CdTe) is 8582 m^2 and thin-film cadmium sulphide (CdS)/cadmium telluride (CdTe) (CdS/CdTe) is 9549 m^2, respectively. However, the less required area is found for Polycrystalline PV technology.

Table1: Specifications of the investigated photovoltaic module technologies extracted from the manufacturers data sheet

Type of module cell material	Monocrystalline	Polycrystalline	Thin-film cadmium telluride (CdTe)	Thin-film cadmium sulphide (CdS)/cadmium telluride (CdTe) (CdS/CdTe)
Module frame dimension, m	1.956x0.992x 0.04	1.956x0.992x 0.04	1.2x0.6x 0.0068	1.2x0.6x 0.0068
Performance specifications at Stander Test Condition STC (Irradiance of 1000 W/m² (I_{STC}), temperature 25 °C and AM of 1.5)				
Maximum power (P_{max}), Wp	310	320	112.5	100
Tolerance value of power %	±3	±3	±5	±5
Maximum power point voltage (V_{mpp}), V	36	36.8	70.2	46.8
Maximum power point current (I_{mpp}), A	8.61	8.7	1.6	2.14
Open circuit voltage (V_{oc}), V	44.9	45.02	87.7	58.8
Short circuit current (I_{sc}), A	8.91	9.34	1.75	2.33
Module efficiency η, %	>15.99	>16.49	15.625	13.89
Performance specifications at Nominal Operating Cell Temperature NOTC (Irradiance of 800 W/m², Ambient temperature of 20°C and Wind speed 1 m/s)				
Maximum power (Pmax), Wp	227.5	235.91	83.9	75.4
Tolerance value of power %	±3	±3	±5	±5
Maximum power point voltage (V_{mpp}), V	32.63	33.51	65	43.7
Maximum power point current (I_{mpp}), A	6.97	7.01	1.29	1.73
Open circuit voltage (Voc), V	40.5	42.52	82.6	55.5

Short circuit current (Isc), A	7.26	7.71	1.41	1.88
Nominal Operating Cell Temperature (NOTC), °C	45±2	45±2	45	45
Temperature coefficient (TC) of V_{OC}	(-0.31%/°C)	(-0.32%/°C)	(-0.29%/°C)	(-0.29%/°C)
Temperature coefficient (TC) of I_{SC}	(-0.03%/°C)	(-0.034%/°C)	(-0.04%/°C)	(-0.04%/°C)
Temperature coefficient (TC) of P_{max}	(-0.4%/°C)	(-0.4%/°C)	(-0.34%/°C)	(-0.29%/°C)

Therefore, clarification of the extra areas percentage for other technologies is based on Polycrystalline PV technology area. For a plant having equal maximum power for all technologies, the Monocrystalline technology plant requires extra area by 3.696%, thin-film cadmium telluride (CdTe) requires extra area by 4.34% and thin-film cadmium sulphide (CdS)/cadmium telluride (CdTe) (CdS/CdTe) requires extra area by 16.1% respectively.

The solar irradiance on module-tilted plane (G_T) required determining the hourly value of the produced net energy (WH) for PV module installed in open air and maintained over frames having slope angel with the horizontal is obtained from generated total solar irradiance on the horizontal, GH, by eq. (2). The value of G_T is for determined for Latitude angle of 29.2267degree, solar declination angle that calculated as in Duffie and Beckman (2006). The module-tilting angle with horizontal is investigated to define the tilting modules angle provides the maximum value of yearly average incident solar energy on modules tilted plane. The yearly total energy on the module with fixed tilted angle for different titling angles with the horizontal is shown in figure (1). Clearly, from the figure, modules with tilting angle of 30 degree with the horizontal have the higher yearly average incident solar energy of 2157.49 kWh/m^2 for the state of Kuwait. Therefore, the tilting angle of 30 degree with the horizontal is base in this study.
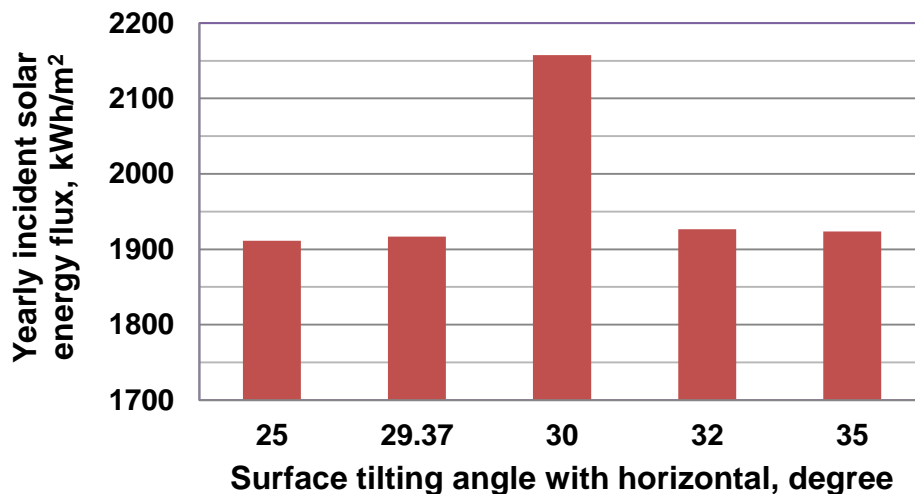

Figure 1: Yearly average incident solar energy on module fixed tilted plane at different tilting angle.

3.1 Hourly Performance of Different PV Modules Technologies

The generated hourly value weather and solar radiation flux data for the state of Kuwait indicated that the highest ambient air dray bulb temperature might occur on 4th of August. Therefore, this day data is used as a case to present the hourly-obtained values for the efficiencies, net energy produced and performance ratio of different PV modules technologies and the obtained results are shown in table (2). As can be seen from the table, during sunshine hours the average hourly value of ambient air-dry bulb temperature is ranged between 32 to 48.8 °C, wind speed average hourly values ranged from 4.1 to 9.9 m/s and the average solar radiation on horizontal at noon is 1.006 kW/m^2. The correspondence values for modules efficiencies, net energy produced and performance ratio Also, from the table clearly show that thin-film cadmium sulphide (CdS)/cadmium telluride (CdTe) (CdS/CdTe) PV technology has slightly higher value than other technology. Another hourly performance parameter shown in the table (1) to compare the different PV technologies is the performance parameter. In addition, the CdS/CdTe PV technology has a slightly higher value of the performance ratio. As per the material characteristic shown in table (1),

CdS/CdTe PV technology has a lower value of the maximum power temperature coefficient. This explains the enhancement on the performance of CdS/CdTe PV technology when operated under hot arid environment. However, as the data in the table (1) is for one day only, PV plant designer cannot depend on this result. Therefore, the obtained hourly values over a year for the performance ratio for each of the selected PV modules technologies used in this study are shown in figure (2). Clearly, from the presented results in the figure, the CdS/CdTe PV technology has the higher performance ratio values all over the hot months of the year for the state of Kuwait.

3.2 Plant Monthly and Yearly Net Energy Produced by Different PV Modules Technologies

The results of the total monthly produced net energy for the selected different PV modules technologies used in this study is shown in figure (3). Clearly, from the figure the results show that the monthly produced total net energy from CdS/CdTe PV technology is slightly higher value. Quantitative results of total annual net energy produced from one MWp plant assessed PV modules technologies under climate condition of the state of Kuwait are shown in figure (4). From the figure, the results of the annual net energy produced with MWp with Monocrystalline technology plant is 2289.28 MWh, Polycrystalline is 2276.71 MWh, thin-film cadmium telluride (CdTe) is 2286.4 MWh and thin-film CdS/CdTe is 2290.8 MWh, respectively. As the compression of the required different module area was based on the Polycrystalline PV technology; therefore, the total net annual energy produced form a plant with different PV modules technologies is also based on the net energy produced from Polycrystalline PV technology. The results show that the produced net annual energy from one MWp PV plant capacity referenced to the net energy produced from Polycrystalline PV technology are as follows. The Monocrystalline technology produces extra annual net energy by 0.552%, thin-film cadmium telluride (CdTe) technology produces extra annual energy by 0.43% and thin-film CdS/CdTe technology produces extra annual energy by 0.62%, respectively.
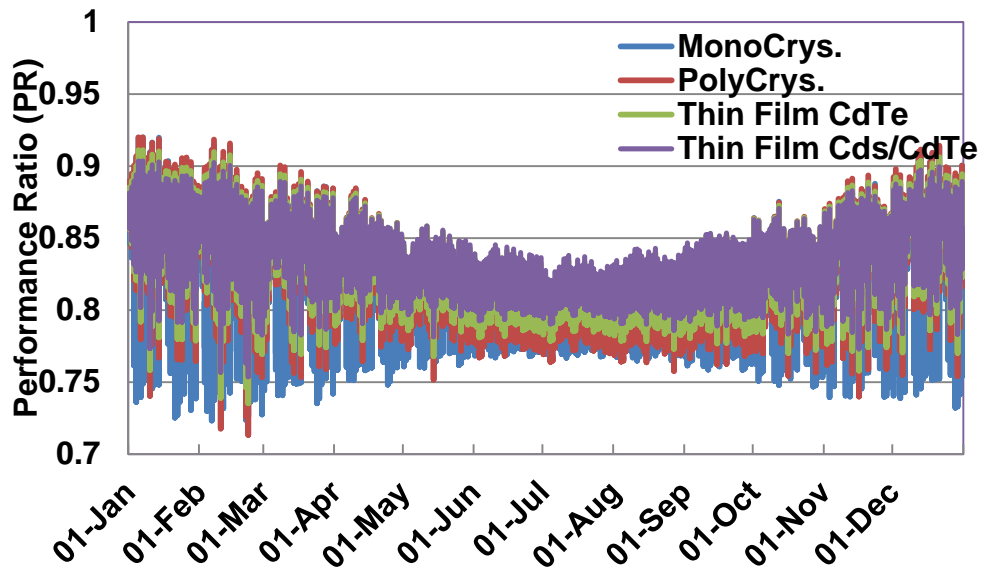
4. CONCLUSION

Energy performance assessment of the two main photovoltaic technologies available in 2015 market operates under hot arid climatic conditions for the state of Kuwait is carried out. For the case of one MWp PV plant, the study investigated the influence of climatic parameters on energy production and performance ratio based on the daily, monthly and yearly energy produced from crystalline silicon based and thin film technology photovoltaic technologies. The assessed technologies are monocrystalline, polycrystalline and thin-film of cell types of cadmium telluride (CdTe) and cadmium sulphide (CdS)/cadmium telluride (CdTe) (CdS/CdTe) semiconductor. The assessment is based on the manufacture provided PV modules characteristics and 30 years average hourly values of the ambient air dry temperatures, horizontal solar radiation and average wind speed for state of Kuwait. The main conclusions of this study are as follows:

- For same maximum power for all investigated technologies compared with Polycrystalline as a base of minimum required modules area, the Monocrystalline technology plant requires extra area by 3.696%, thin-film cadmium telluride (CdTe) requires extra area by 4.34% and thin-film cadmium sulphide (CdS)/cadmium telluride (CdTe) (CdS/CdTe) requires extra area by 16.1% respectively.
- Modules with tilting angle of 30 degree with the horizontal have the higher yearly average incident solar energy of 2157.49 kWh/m^2 for the state of Kuwait.
- The CdS/CdTe PV technology has the higher performance ratio values of the all-over the hot months of the year for the state of Kuwait.
- For same maximum power for all investigated technologies referenced to the net energy produced from Polycrystalline PV technology are as follow: the Monocrystalline technology plant produces extra annual net energy by 0.552%, thin-film cadmium telluride (CdTe) technology produces extra annual energy by 0.43% and thin-film CdS/CdTe technology produces extra annual energy by 0.62%, respectively.

Table 2: Hourly value of the weather and solar radiation flux data and the correspondence result values of the efficiencies, energy produced and performance ratio of different PV modules technologies for 4th of August under state of Kuwait weather condition.

	HOURLY WEATHER AND SOLAR DATA: (SI Units), LOCATION: Kuwait Int'l Airport											Performance calculated parameters											
	WBAN Station I.D.: 40582, Average of 30 years from: 1982-2012 Date Aug. 4																						
Time hr	DB Temp °C	WB Temp °C	Sun alt.	Sun azimuth	Direct Normal (Wh/m²)	Direct Horiz (Wh/m²)	Diff. Horiz (Wh/m²)	Total Horiz G_H (Wh/m²)	Cloud Cover (%)	Wind Speed (m/s)	Stn PB (kPa)	Total Rad. on tilted surf by B=30 G_T (Wh/m²)	Hourly PV module efficiency (η_h) with wind cooling factor, eq. (1)				$E_h= \eta_h *G_T*\eta_g * A_{modules}$				Performance Ratio (PR)			
													Mono Crys.	Poly Crys.	Thin Film CdTe	Thin Film Cds/CdTe	Mono Crys. MWh	Poly Crys. MWh	CdTe MWh	Cds/CdTe MWh	Mono Crys.	Poly Crys.	CdTe	Cds/CdTe
1	35	17.2	0	0	0	0	0	0	0	8.1	99.8													
2	33.8	17.1	0	0	0	0	0	0	0	4.1	99.46													
3	32.9	16.9	0	0	0	0	0	0	0	6	99.26													
4	32.1	16.8	0	0	0	0	0	0	0	9	99.15													
5	31.7	16.7	0	0	0	0	0	0	0	4.3	99.09													
6	31.5	16.7	9.4	76	516	84	47	130	0	5.7	99.07	197.13	0.151806	0.156553	0.149527	0.133792	0.219503	0.218297	0.217542	0.216593	0.8138	0.8178	0.8242	0.8295
7	32	16.8	22.2	83	815	308	73	381	0	6.5	99.09	577.7	0.150348	0.15505	0.148316	0.132874	0.637106	0.633606	0.632374	0.630399	0.7987	0.8122	0.8194	0.8254
8	33.5	17	35.3	89	918	530	93	623	0	4.5	99.15	944.6	0.147647	0.152263	0.146072	0.131173	1.023008	1.017387	1.018345	1.017561	0.7843	0.801	0.8099	0.8173
9	35.9	17.5	48.3	97	966	722	109	831	0	4.8	99.26	1259.94	0.146093	0.150661	0.144782	0.130194	1.350133	1.342715	1.346272	1.347104	0.7744	0.793	0.803	0.811
10	38.7	18.1	61.1	109	991	867	121	989	0	9.9	99.4	1499.4	0.146283	0.150857	0.14494	0.130314	1.608854	1.600014	1.603916	1.604631	0.7703	0.7899	0.8005	0.8092
11	41.7	18.7	72.5	132	1003	957	129	1085	0	7.3	99.56	1644.89	0.144788	0.149315	0.143698	0.129372	1.746893	1.737295	1.74444	1.747583	0.771	0.781	0.7929	0.803
12	44.5	19.3	77.6	188	1006	983	131	1113	0	4.1	99.73	1687.25	0.143929	0.148429	0.142984	0.128831	1.781255	1.771469	1.780485	1.785098	0.774	0.7746	0.7875	0.7981
13	46.8	19.8	70.5	234	1002	944	128	1072	0	1.5	99.9	1625.02	0.144708	0.149232	0.143631	0.129322	1.724838	1.715361	1.722571	1.725801	0.7765	0.7744	0.7873	0.798
14	48.3	20.1	58.7	254	987	843	119	962	0	7.5	100.1	1458.20	0.142868	0.147335	0.142103	0.128163	1.528098	1.519702	1.529296	1.534766	0.7766	0.7662	0.7804	0.7921
15	48.8	20.2	45.8	264	959	687	106	794	0	5.5	100.2	1203.49	0.142785	0.14725	0.142035	0.128111	1.260445	1.25352	1.261554	1.266163	0.7742	0.7653	0.7796	0.7914
16	48.6	20.4	32.7	272	904	489	89	578	0	4.7	100.3	876.04	0.142624	0.147084	0.141901	0.12801	0.916472	0.911437	0.917449	0.92094	0.771	0.765	0.779	0.791
17	48.1	20.3	19.7	279	781	263	68	331	0	9.9	100.7	501.65	0.1422	0.146646	0.141548	0.127743	0.523244	0.520369	0.52406	0.526263	0.7683	0.7642	0.7786	0.7906
18	47.1	20.1	6.9	285	389	47	37	84	0	5.7	100.4	127.30	0.142641	0.147101	0.141915	0.12802	0.133192	0.13246	0.133332	0.133837	0.7682	0.767	0.781	0.793
19	45.9	19.8	0	0	0	0	0	0	0	4.7	100.4													
20	44.4	19.5	0	0	0	0	0	0	0	8.1	100.3													
21	42.7	19	0	0	0	0	0	0	0	6.3	100.2													
22	40.9	18.6	0	0	0	0	0	0	0	6.3	100.1													
23	39	18.2	0	0	0	0	0	0	0	5.5	99.9													
24	37.2	17.8	0	0	0	0	0	0	0	9	99.73													
Total																	14.45304	14.37363	14.43164	14.45674				

Figure 2: A year hourly average value of the performance ratio for different PV modules technologies used in this study.

Figure 3: Total monthly produced net energy for the selected different PV modules technologies used in this study
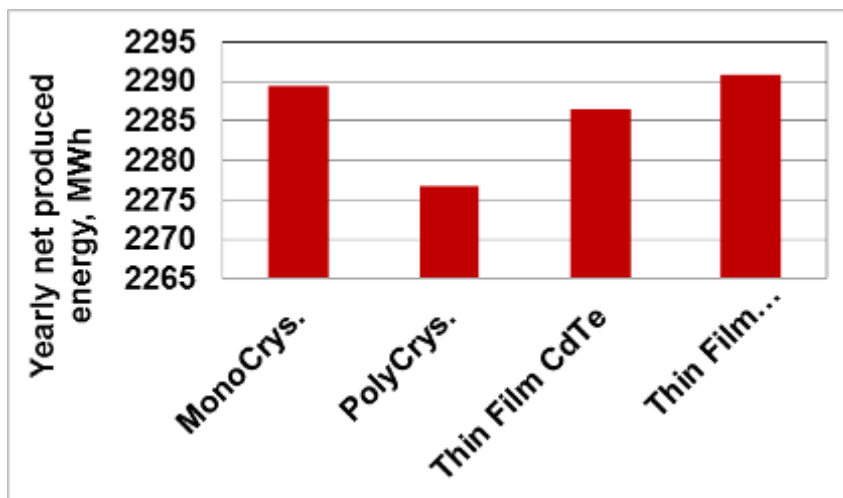
Figure 4: Total annual net energy produced from one MWp plant with different PV modules technologies used in this study

5. REFERENCES

ABDULLAH, Ali H., Adel A. Ghoneim and Ahmad Y. Al-Hasan (2002). Assessment of grid-connected photovoltaic systems in the Kuwaiti climate. Renewable Energy vol. 26 pp.189–199

ALDIHANI, A., A. Aldossary, S. Mahmouda and R.K.AL-Dadah (2014). The effect of cooling on the performance of photovoltaic cells under dusty environmental conditions. Energy Procedia vol.61, pp. 2383 - 2386

AL-HASAN, A.Y., A.A. Ghoneim and A.H. Abdullah (2004). Optimizing electrical load pattern in Kuwait using grid connected photovoltaic systems. Energy Conversion and Management vol.45, 483-494

ALI, Ahmed Hamza H., Ahmed, M., and S. M. Abdel-Gaied (2013). Investigation of Heat Transfer and Fluid Flow in Transitional Regime inside a Channel with Staggered Plates Heated By Radiation for PV/T System PV/T System. Energy; vol. 59(15), pp. 255-264.

ALI, Ahmed Hamza H., Ahmed, M., and Youssef, M. S. (2010). Characteristics of heat transfer and fluid flow in a channel with single-row plates array oblique to flow direction for photovoltaic/thermal system. Energy vol. 35 (9), pp. 3524-3534.

ALI, Ahmed Hamza. H. (2005). Characteristics of flow and heat transfer for in-line plate segments inside channel used for photovoltaic modules thermal regulation. Applied Thermal Engineering; vol. 25 (8-9), pp. 1381-1401.

AL-OTAIBi, A., A. Al-Qattan, F. Fairouz and A. Al-Mulla (2015). Performance evaluation of photovoltaic systems on Kuwaiti schools' rooftop. Energy Conversion and Management vol. 95, pp.110-119

ASTE, Niccolo`, Claudio Del Pero, Fabrizio Leonforte (2014). PV technologies performance comparison in temperate climates. Solar Energy vol. 109, pp.1-10.

CAÑETE, Cristina, Jesús Carretero and Mariano Sidrach-de-Cardona (2014). Energy performance of different photovoltaic module technologies under outdoor conditions. Energy vol. 65, pp. 295-302.

DUFFIE, J.A. and Beckman, W.A., (2006). Solar Engineering of Thermal Processes. Third ed., John Wiley & Sons, New York.

ENER-WIN (2007). Software for building energy analyses. Degelman Engineering Group, Inc., College Station, Texas

GHONEIM, Adel A. (2012), Environmental impacts of grid connected photovoltaic system adapted for peak load reduction in Kuwait, Chemical Engineering Transactions, vol. 29, pp.1213-1218

GHONEIM, Adel A., Ahmad Y. Al-Hasan and Ali H. Abdullah (2002). Economic analysis of photovoltaic-powered solar domestic hot water systems in Kuwait. Renewable Energy vol.25, pp.81–100

IRENA 2014, Pan-Arab renewable energy strategy 2030- Roadmaps of actions for implementation. http://www.rcreee.org/sites/default/files/irena_pan-arab_strategy_june_2014.pdf

KISR 2015, Kuwait Institute for Scientific Research. http://www.kisr.edu.kw/en/research/energy-and-building/programs/innovative-and-renewable-energy-program

SKOPLAKI, E. and J.A. Palyvos (2009). On the temperature dependence of photovoltaic module electrical performance: A review of efficiency/power correlations. Solar Energy vol. 83, pp.614-624

TOSSA, Alain K., Y.M. Soro, Y. Azoumah and D. Yamegueu (2014). A new approach to estimate the performance and energy productivity of photovoltaic modules in real operating conditions. Solar Energy vol.110, pp.543-560.

YA'ACOB, M. Effendy, Hashim Hizam, Tamer Khatib, M. Amran M. Radzi, Chandima Gomes, M. Bakri A., M. Hamiruce Marhaban and Wilfried Elmenreich (2014). Modelling of photovoltaic array temperature in a tropical site using generalized extreme value distribution. J. of Renewable and Sustainable Energy (AIP), vol. 6(3), pp.1-7

313: Investigation of the PV self-cleaning

Sami Alsaleh[1] , Siddig A OMER[2] AND Rabah BOUKHANOUF [3]

1 Institute of Sustainable Energy Technology, University of Nottingham, University Park, Nottingham, UK, NG7 2RD, ezxsa1@exmail.nottingham.ac.uk

2 Institute of Sustainable Energy Technology, University of Nottingham, University Park, Nottingham, UK, NG7 2RD, siddig.omer@nottingham.ac.uk

3 Institute of Sustainable Energy Technology, University of Nottingham, University Park, Nottingham, UK, NG7 2RD, lazrb@exmail.nottingham.ac.uk

This study focuses on the investigation and development of PV self –cleaning and its impact on dust removal, that would enable a wider deployment of solar photovoltaic systems in the Middle East and Gulf region which enjoys abundant solar radiation throughout the year, and where sand storm dust and elevated ambient temperature persist. The dust reduces the power generated by the solar devices or hinders the visibility through windshields. The research intends to combine a number of technologies to assist and improve the operational performance of photovoltaic (PV) systems. This investigation covered some of systems which employed PV self-cleaning techniques including application of Titanium Oxide (TiO2) coatings to remove the particles of dust from the PV panel surface.

Regular cleaning of the panels is often necessary to prevent serious degradation of their performance, especially in regions with dusty climates. However, manual cleaning of solar panels, especially in the context of large installation, can be a labour-intensive process and thus often prohibitively costly. Even in small buildings, cleaning a PV system can involve complicated issues of access that might require the intervention of specialist staff. Some of the technologies involve the use of electrodynamic screens for electrostatic dust removal, robotic cleaning tools, vibrating mechanisms featuring piezo-ceramic actuations, as well as TiO2-treated chemical or nano-films. Nevertheless, none of these technologies has to date been able to establish itself as an industry standard and achieve the necessary commercial breakthrough. In light of the above, self-cleaning technologies could present the perfect solution to these issues and help address many of the obstacles preventing solar panel technology from becoming more widely adopted. This would help reduce dependence on the fossil-fuel based energy resources which can be devoted to generation of national revenues and also leads to a reduction of CO2 emissions to the environment.

Keywords: PV, Self –Cleaning, Dust

1. INTRODUCTION

Over the past decades, the explosion in global population combined with the advent of modernisation to wider parts of the globe has meant that the demand for energy has continued to grow, most of which continues to be based on fossil fuel sources. However, in the context of the high pollution levels caused by fossil-fuel extraction, and an increasing awareness and alarm over the dangers of climate change, the search for alternative renewable energy sources that are lasting, reliable and cost-effective has become more urgent and critical than ever. Over recent years, four main forms of such alternative energy sources have emerged: wind, solar, hydroelectric and geothermal energy, the adoption of which has varied greatly across the globe due to geographical, topological and other factors. For instance, hydroelectric dams are harder to build in non-mountainous regions and solar panels are not suited to cloudy weather. While some regions, such as Japan, Australia and many African countries have naturally given prominence to solar energy, the US, Denmark or Germany have seen the emergence of wind turbines (Ishengoma and Norum, 2002) (2005). Meanwhile, a number of European nations have been increasingly integrating photovoltaic and wind energy into their future infrastructure plans (Blanco, 2009, 2013). In this context, one particular factor that has proven problematic for the use and implementation of solar panels has been the sedimentation of dirt and/or dust deposits on their surfaces, which can significantly hamper the performance and longevity of the panels, even leading to their failure (Sarver et al., 2013). In terms of Solar *Photovoltaic (PV) Energy,* while wind and water-based energy sources have been exploited for centuries, photovoltaic power has been a relatively modern development which has been gathering momentum steadily over the past few decades. At the basic level, solar panel technology involves electricity production by panels of serially-connected photovoltaic cells. The cells use captured photons to create a stable current by freeing electrons (Penick and Louk, 1998). As such, a panel's performance depends both on the materials and the process adopted in its construction, with more efficient materials being costlier. There are three main categories of solar panels: amorphous, monocrystalline, and polycrystalline (Messenger and Ventre, 2002). A panel's design, notably its size and the choice of components used (such as converters and solar trackers), depends principally on the power needs it is expected to address. By definition, panels produce fluctuating and irregular levels of outputs (e.g. affected by changes in the sun's position, the panel's composition and environmental conditions). As such, converters help maximise the panel's performance by converting its variable output into constant voltages (Penick and Louk, 1998). Moreover, since panels can only accumulate power during sunlight hours, using their output at night requires the use of a storage solution, whether by transferring the output to the power grid or using a battery. However, the performance of PV solar collectors might be reduced by the rise of the cells temperature and the accumulation of the dust on the tops of PV panels. Hence, cooling and cleaning methods should be applied in PV system to improve the efficiency of PV cells. In this report, several approaches applied to do the self-cooling and self-cleaning on PV panels are introduced.

2. FACTORS AFFECTING PV SYSTEM PERFORMANCE

In terms of PV performance, solar panels performance are clearly affected by environmental factors, especially those relating to weather conditions, such as cloud presence and movements, temperatures and the sun's position, many of which change on a seasonal basis. For instance, the light intensity is greater during the summer than in the winter due to changes in the sun's position (2005, BOLLINGER, 2007, Sarver et al., 2013). A solar panel's positioning and angles are hugely consequential for its performance, though most panels use fixed-angle mounts positioned for a specific season or at an average angle based on summer and winter outputs. As such, in order to increase the number of hours a panel can generate power at peak efficiency levels, a power tracker is needed to adjust the panel's angle in accordance with the sun's changing movements. Moreover, changes in the temperature have a significant impact on photovoltaic cells, with increases in temperature leading to decreases in panel efficiency (although higher temperatures coincide with higher illumination levels) (2005). Moreover, a system's design should clearly take into account key parameters such as the size of the panel, the type of converters, as well as the different storage options under various seasonal weather patterns (Ishengoma and Norum, 2002).
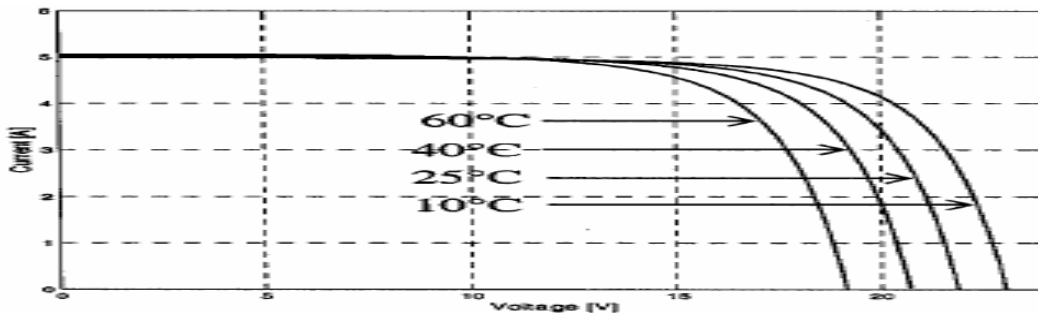
Figure 61 Voltage and Temperature Variations of a Photovoltaic Cell (Ishengoma and Norum, 2002)

Meanwhile, Figure 1 above shows the relationship between voltage and temperature, with a reduction in voltage as temperatures rise. The figure also shows that the generated power is proportional to the temperature. As such, when establishing the maximum energy for a specific time of year, the effect of temperature must be taken into account. Figure 2 shows the points where maximal power and voltage are achieved, which correspond to maximal cell outputs (Messenger and Ventre, 2002).
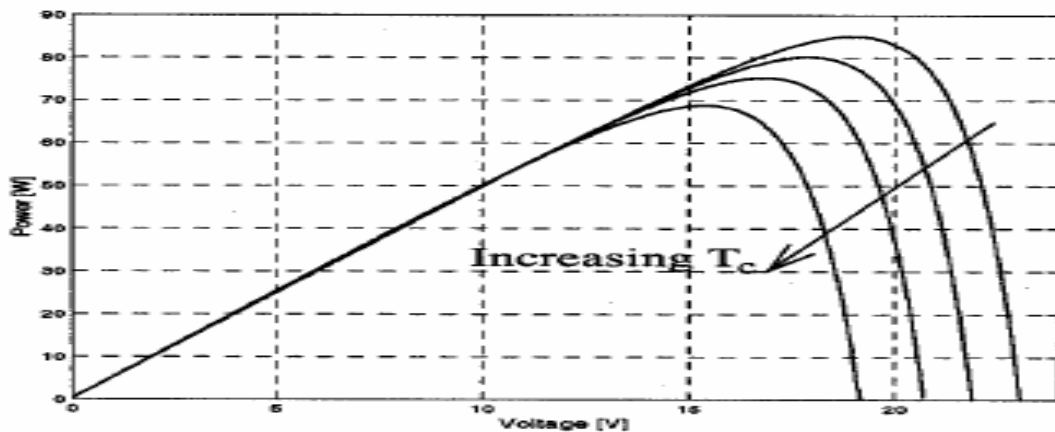
Figure 62 Output Power and the Effects of Temperature(Messenger and Ventre, 2002)

3. DUST EFFECT

Although numerous factors are usually considered when examining PV system performance, one of the most significant factors is one that is often ignored, namely the presence of dust and dirt. As is to be expected, a number of studies confirm that the impact of dust is greater in some regions of the globe than others. Areas of greater impact include the Middle East, North Africa and Asia, where arid winds can accentuate the impact of the problem. Indeed, hours of exposure to dust in these areas produce the same level of damage to PV performance than usually occurs over months in other regions with milder climates. This is highlighted in Figure 3 which illustrates panel performance levels over time in the United States, Oman and Egypt as example (Sarver et al., 2013).
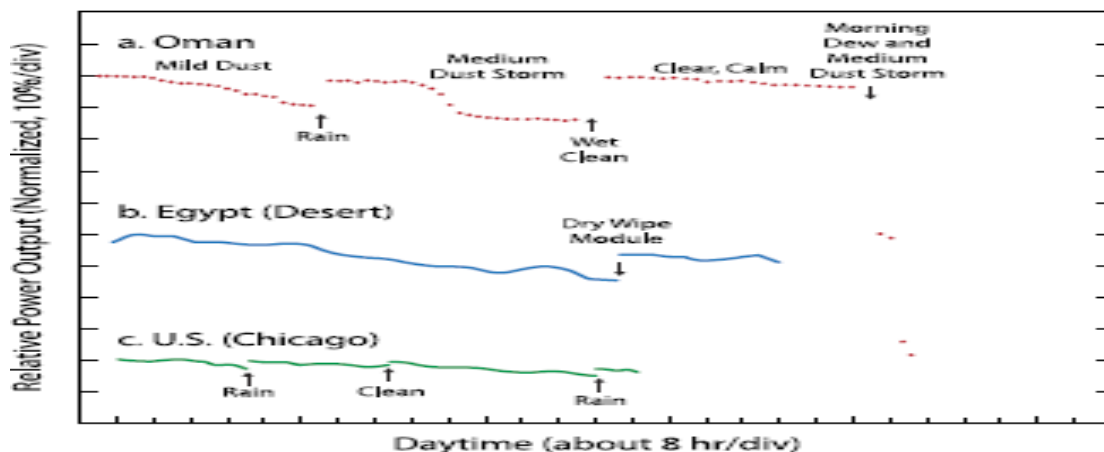
Figure 63 Comparison of PV module performances under various dusts(Sarver et al., 2013)

Manifestations of hazards to PV panels are numerous, and include bird droppings, dust deposits and water stains, all of which can degrade significantly the PV panel's performance. Indeed, PV module efficiency is estimated to be reduced by 10–25% as a result of losses related to damage to the inverter, the wiring, or the soiling of the module with dust and debris (Mani and Pillai, 2010). Of course, the susceptibility of PV panels to the damaging impact of dust reduces their appeal as an alternative energy source. As such, a thorough understanding of this phenomenon is essential in helping enhance PV technology's robustness in resisting the effects of dust. However, research on the topic remains limited, partly due to the complexities of the phenomena involved.

Broadly defined, the term 'dust' refers to solid particles that can be found in the atmosphere and are less than 500 µm in diameter (Mani and Pillai, 2010). Examples include dust lifted into the air by urban traffic, airborne particles caused by pollution, and particles emitted by volcanic eruptions. In the context of this study, dust can also refer to pollens (such as bacteria) and microfibers (from fabrics, carpets etc.) that are ubiquitous in the atmosphere. The two key factors that determine the characteristics of dust settlement on PV systems are the local environment and dust particle properties. Aspects of the local environment include weather conditions, environmental features (e.g. vegetation), and built environment characteristics (height, orientation and surface finish). Dust properties include chemical, biological and electrostatic properties; particle size, shape and weight; as well as dust aggregation or accumulation characteristics. Moreover, the surface finish of the PV panel surface is of great import, since a sticky surface (i.e. one that is rough, furry, has electrostatic build-up or contains adhesives residues) presents a greater likelihood of dust accumulation than otherwise. In terms of the effect of gravity, horizontal surfaces are more liable to collecting dust than vertical or inclined ones, although this depends greatly on wind conditions. Moreover, dust settlement tends to be hampered by high-speed wind and aggravated by low-speed wind. However, the distribution of dust settlement at specific locations of the PV panel can be influenced by the PV system's orientation relative to the wind movement, with dust likelier to settle in low-pressure areas of the panel (brought about by high-speed wind movements impacting on inclined or vertical surfaces). Meanwhile, dust dispersal is determined by the properties of the dust particles (notably weight, size, type) (Mani and Pillai, 2010).In light of the above, Figure 4 below illustrates the various factors influencing dust settlement (Mani and Pillai, 2010)
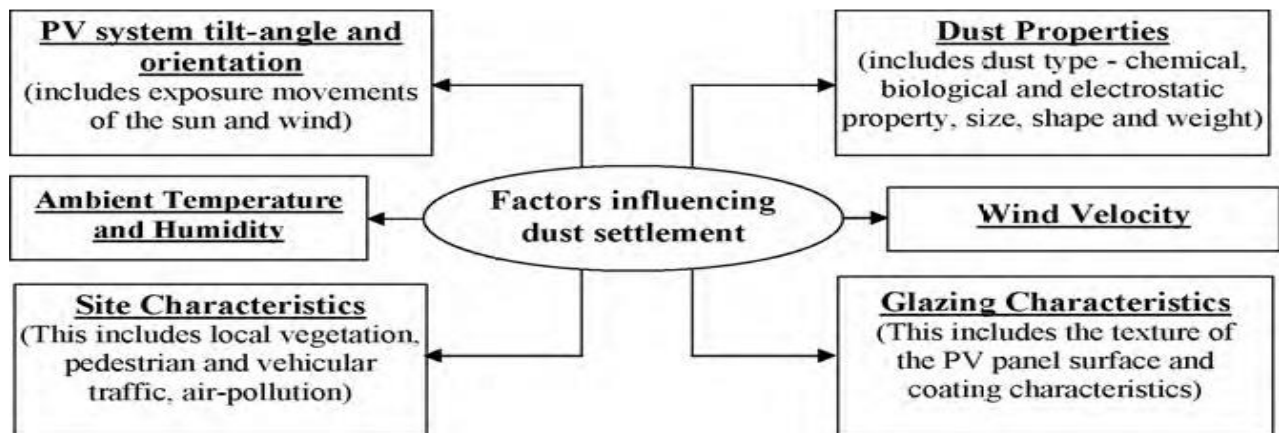
Figure 64 Factors influencing dust settlement.(Mani and Pillai, 2010)

In terms dust ,the mechanisms through which soil gets deposited were studied by Cuddihy (Cuddihy and Willis, 1984, Cuddihy, 1983, Cuddihy, 1980), who divided them into four primary mechanisms, as shown in Figure 5. These are: cementation by water or soluble salts, organic material deposition, surface tension, and particle energetics. Inorganic and organic particulates, often containing water soluble and insoluble salts, can often be found in atmospheric dust. As such, in high humidity conditions, microscopic droplets of salt containing insoluble particles are formed on surfaces. As a result, when these dry the precipitated salts cement the insoluble particles onto the surface of the panel. Moreover, the fact that the surface tends to be first coated by an ultrathin layer of deposited organic material renders removing the salt deposits especially challenging, necessitating a complex cleaning processes.
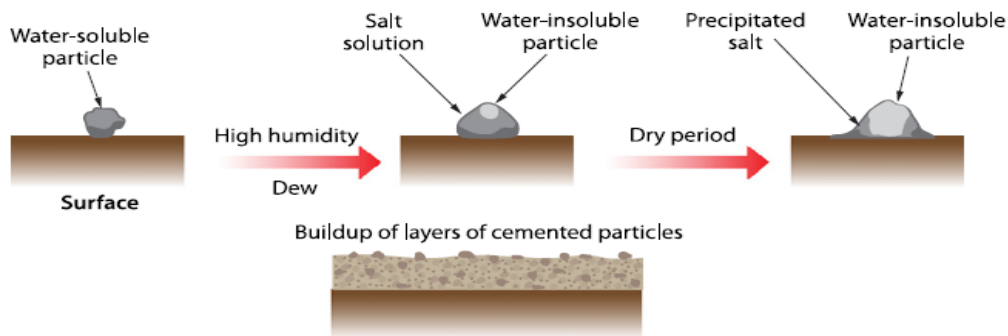
Figure 65 Dust–Moisture Cementation Process(Sarver et al., 2013)

A number of research studies have been undertaken on dust settlement and its impact in a solar PV systems context. For instance, at a solar village near Riyadh, in Saudi Arabia, Salim et al. (Salim et al., 1988), devised a PV test system to investigate the impact on PV energy output of long term dust accumulation. Using an array tilted at a fixed angle of 24.6^0, the team compared the difference in monthly energy outputs between an array that was cleaned daily and one that was left to gather dust, finding a drop of 32% between the two after eight months. However, not only were the test site's dust levels and dust particle properties not investigated in the study, the results were arguably misleading since energy reductions usually would occur within weeks in such highly polluted sites, rather than 8 months. Indeed, Hassan et al. (Hassan et al., 2005) found that PV panel degradation takes place quickly, usually within the initial 30 days of exposure. Moreover, the results obtained by Salim et al. seem to suggest that while the panel's efficiency decreases by 33.5% after 30 days, it actually subsequently rises to 65.8% after a six month period despite no cleaning taking place. For his part, Garg (Garg, 1974), while undertaking a similar examination, established that over a 30-day period, the normal transmittance (of direct radiation through glass) for a horizontally-mounted system had fallen from 90% to 30%. Meanwhile, in Kuwait, Sayigh et al.(Sayigh et al., 1985) investigated reductions in transmittance at tilt angles of 0^0, 15^0, 30^0, 45^0 , and 60%, obtaining reduction rates of 64%, 48%, 38%, 30% and 17% respectively after a 38-day-long exposure period to the environment. However, an accurate and useful interpretation of Sayigh's results presents a number of issues. In particular, the tests on clean and dirty panels were conducted on different days, and therefore under different insolation conditions. In this context, the study undertaken by El-Shobokshy and Hussein (El-Shobokshy and Hussein, 1993) seems to be the most complete to date. El-Shobokshy and Hussein conducted a laboratory investigation into the impact of different physical properties of five dust varieties on PV cell performance and used three types of dirt: limestone (commonly found as dust in the atmosphere), cement (key construction material) and coal (present in industrial environments). Three different sizes of limestone were used, bringing the total number of dirt varieties tested to five. Figure 6 have shown the variation in short circuit intensity according to that in the amount of deposited dust was measured for the five varieties of dirt. The dirt particles were characterised based on their diameter and density (El-Shobokshy and Hussein, 1993).The authors established that the reduction in PV performance chiefly depends on the accumulated dust's density as well as on the type of powder involved and its size distribution. They also concluded that the greater effect was produced by the finest particles of dust rather than the thick ones. This was explained as the result of the more even distribution of finer particles, which leaves little spaces between them for the light to pass through. Figure 9 shows the relationship between the density of dust deposited and the power produced.
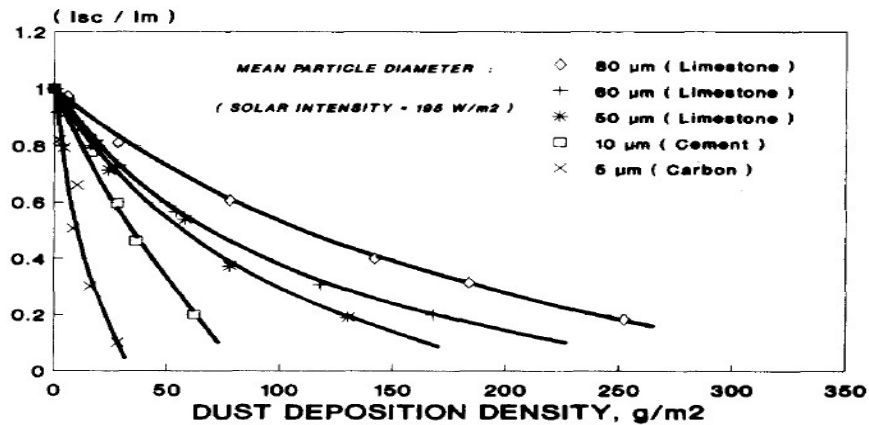
Figure 66 Variation circuit current with dust for the five types of dirt used(El-Shobokshy and Hussein, 1993)

As such, the study offers a number of key conclusions. Not only does dust accumulation affect PV cell performance, it is important to establish accurate information about the dust variety, particularly the type of material involved, its density and size distribution, in order to assess its effect on power output. Furthermore, a study by Elminir et al. (Elminir et al., 2006), conducted in Cairo, Egypt, examined the influence of natural soil dust on the transmittance of glass covers of 3-mm thickness, commonly used in solar collectors and at seven tilt angles (0^0, 15^0, 30^0, 45^0, 60^0, 75^0 and 90^0). The monthly averages of suspended particles obtained in the study are shown in Fig. 7, which seems to confirm that the more acute the tilting angle, the likelier it is that dust particles would roll off the surface. Moreover, increases in accumulated dust levels reduce the transmittance of the transparent cover, thus affecting the panel's energy yield amount. Figure 8 shows average decreases in transmittance caused by various levels of dust deposition densities
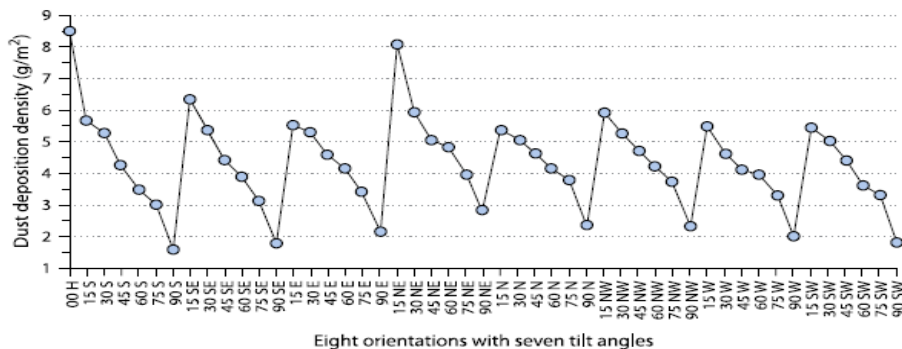
Figure 67 Quantity of dust accumulate on glass samples installed in eight different orientations with seven tilted angles in an arid location(Elminir et al., 2006).

In this context, the decrease in transmittance is calculated as the difference between that of a clean sample and a dust-covered one, and Figure 8 seems to confirm that this reduction is caused by dust accumulation on the surface of the sample. However, a law of diminishing returns seem to be in operation in that the reduction in transmittance increases at a progressively smaller rate until the reduction reaches an upper plateau beyond which additional dust levels no longer result in further reductions in transmittance.

778
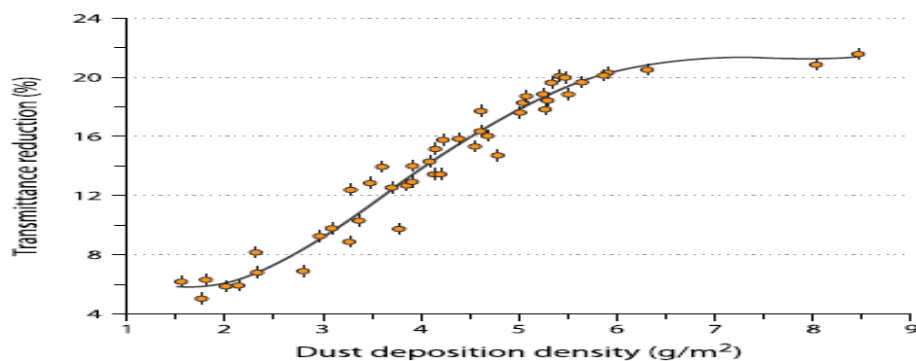
Figure 68 Reduction in transmittance as a function of dust deposition density(Elminir et al., 2006)

4. SELF-CLEANING TECHNIQUES

As has been mentioned in the previous section, the effect of dust accumulation on PV panels can be quite damaging. As such, regular cleaning of the panels is often necessary to prevent serious degradation of their performance, especially in regions with dusty climates. However, manual cleaning of solar panels, especially in the context of large installation, can be a labour-intensive process and thus often prohibitively costly. Even in small buildings, cleaning a PV system can involve complicated issues of access that might require the intervention of specialist staff. Self-cleaning technologies could present the perfect solution to these issues and help address many of the obstacles preventing solar panel technology from becoming more widely adopted.

A number of solar panel self-cleaning technologies have been explored (He et al., 2011, Sarver et al., 2013). Some of the technologies involve the use of electrodynamic screens for electrostatic dust removal, robotic cleaning tools, vibrating mechanisms featuring piezo-ceramic actuations, as well as TiO2-treated chemical or nano-films.

4.1 Self-Cleaning Nano-Film

Covering the surface of solar panels with a pellucid self-cleaning nano-film - made of a super-hydrophilicity material or super-hydrophobic material would – has been shown to be quite effective in keeping the surface clean of dust. Nano-film technology involves the following two strategies:

Super-hydrophilcityfilm - Following a photocatalytic process, the TiO2 film reacts to UV light by breaking up accumulated organic dirt. The film's hydrophilcity then induces rainwater to diffuse across the entire panel surface, rinsing the dust away. However, because of its reliance on rainfall, this method is unsuitable for desert regions, (He et al., 2011) and research has been focused on how best to prepare, dope and modify the material. Using TiO2-based nano-films has generated a significant level of interest after proving quite successful both in terms of research and in terms of practical implementation (Pilkington, 2014, Wheal, 2005). The technology combines two processes. First, a photocatalyst process uses ultraviolet light and water molecules to disintegrate organic dirt by converting it into a gaseous carbon dioxide. A second process than deploys a hydrophilic effect to wash out the dust and dirt particles by inducing rain water to propagate across the PV system glass. This technology, by its very nature, is ideal for use in regions with regular and sufficient rainfall levels. By contrast, use in regions with dry climate or insufficient levels of precipitation would render these processes quite ineffective.

Super-hydrophobic film - Studies have been conducted on the development of superhydrophobic surfaces using special microstructures or nanostructures that can enhance the contact angle (CA) to higher than 150^0, in order to ensure falling Water droplets quickly roll off the surface, carrying dust away in the process. While research on superhydrophobic films has mostly focused on improving their non-wettability, doubts remain over the technique's applicability in desert circumstances. Further research is clearly needed to truly investigate such real world applications (Park et al., 2011, Zhu et al., 2009, Niu et al., 2009).

4.2 Electrostatic Dust Removal

In this regard, a technology that has been of particular interest to researchers is electrostatic dust removal (He et al., 2011, Mani and Pillai, 2010, Sarver et al., 2013), which involves using electrostatic and dielectric forces to displace charged and uncharged dust and dirt particles (Atten et al., 2009). However, although

this process can remove dirt and dust deposits quite effectively, a significantly high-voltage is required by the electric curtain (film). This can significantly affect solar transmission and reduce the output of the solar panel by up to 15% (Sharma et al., 2009). The notion of 'electric curtain', put forth by Tatom and collaborators (1967), and later further developed by Masuda (Aoyoma and Masuda, 1971) is the most popular of electro dust removal methods, and has been shown to be effective in using electrostatic and dielectrophoretic forces to displace charged and uncharged particles (Calle et al., 2008).Electric curtains are constituted of parallel electrodes embedded in a dielectric surface, across which oscillations in the electrode potentials are transmitted, Figure 9 shown Electric curtain basic structure.
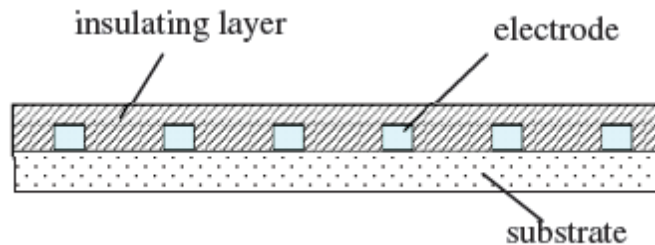
Figure 69 Electric curtain basic structure(Matsunaga et al., 1985)

When connected to a single-phase AC voltage, the electrodes cause a traveling-wave electric curtain to be excited, as Figure 10 illustrates. The charged particles, under the right frequency and amplitude conditions, are prevented from settling but are instead dragged across the surface following the electric field, keeping the surface clean (Liu and Marshall, 2010).
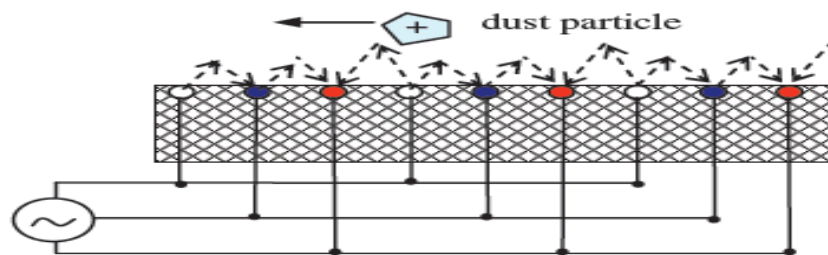
Figure 70 Three-phase electric curtain(Liu and Marshall, 2010)

4.3   Mechanical PV Panel Vibration

Another technology that has been the subject of recent examination is PV panel vibration techniques, which usually deploy piezo-ceramic actuators. The technology remains at an early stage of development, and has been mostly considered in the context of space technology missions, such as probes to Mars, where the impact of dust on solar panel performance is both significant and of critical consequences. Nevertheless, this technology has been investigated in a number of studies, notably by Williams et al (Williams et al., 2007) who established the effectiveness of higher vibration resonances, which can restore up to 95% of the generating capacity of the Panel's output power. However, it must be noted that the study does not specify the power consumption requirements involved in operating the actuators (Williams et al., 2007).

4.4   Electrodynamic Screens

A number of studies have examined the effectiveness of cleaning methods in improving the performance of PV panels. For instance, Biris et al. (Biris et al., 2004) investigated the use of electrodynamic screens to remove contaminant particles and found that higher voltages correspond to a better dust removal rate. Meanwhile, Biris et al. (Biris et al., 2004) ,examining the role of surface mass density on electrodynamics dust removal, found that phased voltage renders the surface dust particles electro-statically charged, allowing for them to be removed using an alternating electric field. Using this method resulted in 90% of deposited dust being removed within 2 minutes. For their part, Bock et al. (Bock et al., 2008) and Sims et al. (Sims et al., 2003), investigating an efficient power management approach for self-cleaning PV panels featuring integrated electro-dynamic screens, confirmed that voltage was the decisive parameter, with higher voltages producing better dust removal performance. In this light, electro-dynamic screen-based cleaning, in addition to the high initial and operating costs it involves, can only be deployed in a limited range of applications due to the fact it doesn't use any liquids, and cannot be used for the removal of muddy or the sticky particles.

4.5   Mechanical Removal of Dusts

Robotic cleaning - A robotic device was developed by Anderson (Anderson et al., 2010) et al. for the purpose of cleaning PV panel arrays using water spray. The robot-sprayed water was found to cool the panels during the cleaning, increasing the array's performance by 15% in the process. Meanwhile, Moreno et al. (Fernández et al., 2007), in their examination of the effects of low-mass robotic dust wiper technology on the MSL rover, found that the robotic dust wiper can enhance the PV panel's efficiency by 7%. However, robotic-based technology involves significant initial and operating costs; as well as complex mechanical and control design requirements.

Washing Surfaces - Moharram et al. (Moharram et al., 2013) describes the adoption by a PV power plant in Cairo, Egypt, of a combination of non-pressurised water and the surfactant developed by Abd-Elhady et al. (Abd-Elhady et al., 2011) for its PV cleaning so as to examine the efficacy of this technology. Three experiments, illustrated in Figure 11, were conducted, subjecting each of the panels to 45 days under one of the following cleaning regimes: no cleaning, cleaning using non-pressurised water, and cleaning using pressurised water and surfactant. At the end of the experiment, as Figure 11a shows, panels in the first regime had accumulated a thick dust layer, panels under the second regime (water) had significantly lesser dust accumulation, while the dust on the panels in the third experiment (surfactants) was practically negligible. Fig. 11b highlights that while regular cleaning is mandatory in dusty areas, using non-pressurized water is not enough and a mix of cationic and anionic surfactants should be used as an effective cleaning solution (Moharram et al., 2013).
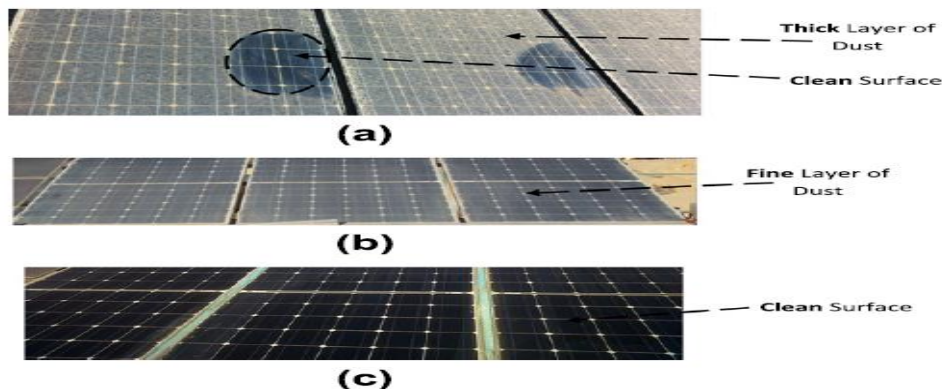
Figure 71 The solar modules under different cleaning mechanisms, (a) no cleaning, (b) cleaning by water, and (c) cleaning by surfactants after 45 days of operation(Moharram et al., 2013)

Moreover, as Figure 12 highlights, the performance of PV panels that undergo non-pressurised water cleaning is reduced by an average of 0.14%/day and thus by 50% after 45 days, which confirms that this cleaning option is not sufficiently effective.
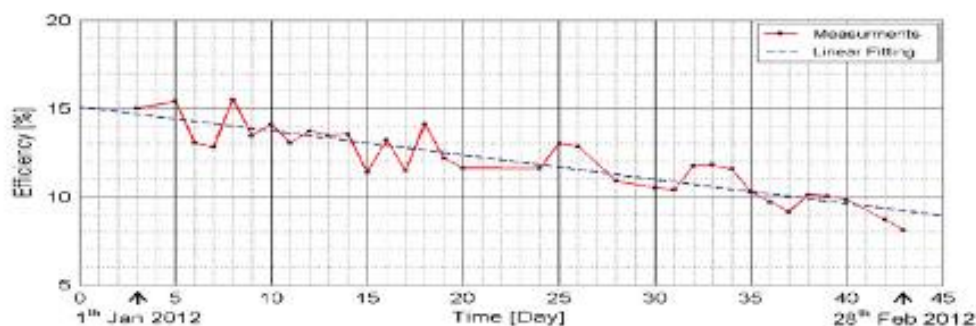
Figure 72 The efficiency of the PV panels versus time due to cleaning using water(Moharram et al., 2013)

4.6   Forced Air

Schumacher et al. (1979) designed several devices using air flow and air vibrations to clean solar collectors and tested their abilities for removing dust from mirror surfaces. To identify a suitable cleaning method, two approaches were investigated in the experiment. The first approach tested several nozzles, including

vortex-generating nozzles which imparted the rotational and translational motion to air and converging nozzles which allowed the air directly flow to the surface.

The second approach applied a mechanical transducer to provide ultrasonic energy through the air to the surface. Results indicated that vortex nozzle and converging could present a good performance for the cleaning of the mirror, while providing ultrasonic energy to the air flow could give a better performance for the surface cleaning. Meanwhile, a number of water-based PV cleaning systems were presented by Kandil and Elsherif (Elsherif and Kandil, 2011), featuring a range of devices such as a sliding brush, sliding nozzles, rotating brushes and fixed nozzles. Programmable logic controllers (PLCs) and sensors were used on all systems to control and monitor their operations. In the fixed nozzles version, the surface is cleaned by high-speed water jets released through a set of nozzles (fixed onto a manifold mounted atop the PV panel). In the sliding nozzles version, the manifold was adapted so that it could move across the surface of the panel to ensure a uniform cleaning process. In the moving brush version, the fixed-nozzles system was supplemented with a moving brush, one variant of this system used a moving brush while another had a sliding brush. The system's ability to clean all varieties of dirt ensured its performance was superior. This confirms that water-based cleaning improves the performance of PV panels but that it requires pressurised water or the use of a brush to deal especially persistent dirt such as mud.

5. CONCLUSION

This paper have discussed factors affecting PV system performance including environmental factors, especially those relating to weather conditions, such as dust, temperatures and the sun's position. The effect of dust accumulation on PV panels can be quite damaging. Hence, regular cleaning of the panels is often necessary to prevent serious degradation of their performance, especially in dusty climates. Self-cleaning technologies could present the perfect solution to these issues and help address many of the obstacles preventing solar panel technology from becoming more widely adopted. Nevertheless, none of these technologies has to date been able to establish itself as an industry standard and achieve the necessary commercial breakthrough.

6. BIBLIOGRAPHY

2005. Intusoft Newsletter, Newsletter Issue 78 [Online]. Available: http://www.intusoft.com/nlhtm/nl78.htm [Accessed 25/03 2014].

2013. INTELLIGENT ENERGY , PV PARITY PROJECT, HOW TO SUPPORT DIFFERENT PHOTOVOLTAIC APPLICATIONS IN THE ACHIEVEMENT OF COMPETITIVENESS AND BEYOND. INTELLIGENT ENERGY

ABD-ELHADY, M., Zayed, S. & Rindt, C. Year. Removal of dust particles from the surface of solar cells and solar collectors using surfactants. In: Proceedings of the Eurotherm international conference on heat exchanger fouling and cleaning IX, Crete, Greece, 2011. 5-10.

ANDERSON, M., Grandy, A., Hastie, J., Sweezey, A., Ranky, R., Mavroidis, C. & Markopoulos, Y. P. 2010. ROBOTIC DEVICE FOR CLEANING PHOTOVOLTAIC PANEL ARRAYS.

AOYOMA, M. & Masuda, S. Year. Characteristics of electric dust collector based on electric curtain. In: Proceedings of the General Conference of the Institute of Electronic Engineers in Japan, 1971.

ATTEN, P., Pang, H. L. & Reboud, J.-L. 2009. Study of dust removal by standing-wave electric curtain for application to solar cells on mars. Industry Applications, IEEE Transactions on, 45, 75-86.

BIRIS, A., Saini, D., Srirama, P., Mazumder, M., Sims, R., Calle, C. & Buhler, C. Year. Electrodynamic removal of contaminant particles and its applications. In: Industry Applications Conference, 2004. 39th IAS Annual Meeting. Conference Record of the 2004 IEEE, 2004. IEEE, 1283-1286.

BLANCO, M. I. 2009. The economics of wind energy. Renewable and Sustainable Energy Reviews, 13, 1372-1382.

BOCK, J. P., Robinson, J., Sharma, R., Zhang, J. & Mazumder, K. Year. An efficient power management approach for self-cleaning solar panels with integrated electrodynamic screens. In: Proc. ESA Annual Meeting on Electrostatics, 2008.

BOLLINGER, J. 2007. APPLICATIONS OF SOLAR ENERGY TO POWER STAND-ALONE AREA AND STREET LIGHTING. MASTER OF SCIENCE IN ELECTRICAL ENGINEERING, UNIVERSITY OF MISSOURI-ROLLA.

CALLE, C., Mcfall, J., Buhler, C., Snyder, S., Arens, E., Chen, A., Ritz, M., Clements, J., Fortier, C. & Trigwell, S. Year. Dust particle removal by electrostatic and dielectrophoretic forces with applications to NASA exploration missions. In: Proceedings of the electrostatics society of America Annual meeting, Minneapolis, 2008. 17-19.

CUDDIHY, E. & Willis, P. B. 1984. Antisoiling technology: theories of surface soiling and performance of antisoiling surface coatings, The Administration.

CUDDIHY, E. F. 1980. Theoretical considerations of soil retention. Solar energy materials, 3, 21-33.

CUDDIHY, E. F. Year. Surface soiling: theoretical mechanisms and evaluation of low-soiling coatings. In: Proceedings of the Flat-Plate Solar Array Project Research Forum, 1983. 379-396.

EL-SHOBOKSHY, M. S. & Hussein, F. M. 1993. Effect of dust with different physical properties on the performance of photovoltaic cells. Solar Energy, 51, 505-511.

ELMINIR, H. K., Ghitas, A. E., Hamid, R. H., El-Hussainy, F., Beheary, M. M. & Abdel-Moneim, K. M. 2006. Effect of dust on the transparent cover of solar collectors. Energy Conversion and Management, 47, 3192-3203.

ELSHERIF, H. & Kandil, H. Year. Fully automated cleaning systems for Photovoltaic panels and reflectors. In: GUC Workshop on Renewable Energies and Smart Grid, 2011. 25-26.

FERNÁNDEZ, D., Cabás, R. & Moreno, L. Year. Dust wiper mechanism for operation in Mars. In: Proceedings of 12th European Space Mechanisms & Tribology Symposium (ESMATS), 2007.

GARG, H. 1974. Effect of dirt on transparent covers in flat-plate solar energy collectors. Solar Energy, 15, 299-302.

HASSAN, A., Rahoma, U., Elminir, H. & Fathy, A. 2005. Effect of airborne dust concentration on the performance of PV modules. J Astron Soc Egypt, 13, 24-38.

HE, G., Zhou, C. & Li, Z. 2011. Review of Self-Cleaning Method for Solar Cell Array. Procedia Engineering, 16, 640-645.

ISHENGOMA, F. M. & Norum, L. E. Year. Design and implementation of a digitally controlled stand-alone photovoltaic power supply. In: Nordic Workshop on Power and Industrial Electronics, 2002. 12-14.

LIU, G. & Marshall, J. 2010. Effect of particle adhesion and interactions on motion by traveling waves on an electric curtain. Journal of Electrostatics, 68, 179-189.

MANI, M. & Pillai, R. 2010. Impact of dust on solar photovoltaic (PV) performance: Research status, challenges and recommendations. Renewable and Sustainable Energy Reviews, 14, 3124-3131.

MATSUNAGA, T., Tomoda, R., Nakajima, T. & Wake, H. 1985. Photoelectrochemical sterilization of microbial cells by semiconductor powders. FEMS Microbiology Letters, 29, 211-214.

MESSENGER, R. A. & Ventre, J. 2002. Photovoltaic systems engineering, New York, CRC press.

MOHARRAM, K. A., Abd-Elhady, M. S., Kandil, H. A. & El-Sherif, H. 2013. Influence of cleaning using water and surfactants on the performance of photovoltaic panels. Energy Conversion and Management, 68, 266-272.

NIU, J. J., Wang, J. N. & Xu, Q. F. 2009. Synthesis of superhydrophobic silicon oxide nanowires surface on silicon wafer. Journal of nanoscience and nanotechnology, 9, 1819-1824.

PARK, Y.-B., Im, H., Im, M. & Choi, Y.-K. 2011. Self-cleaning effect of highly water-repellent microshell structures for solar cell applications. Journal of Materials Chemistry, 21, 633-636.

PENICK, T. & Louk, B. 1998. Photovoltaic power generation. Final report presented to Gale Greenleaf on December, 4.

PILKINGTON. 2014. Self cleaning glass [Online]. Available: http://www.pilkingtonselfcleaningglass.co.uk/default1.htm [Accessed 10/03 2014].

SALIM, A., Huraib, F. & Eugenio, N. Year. PV power-study of system options and optimization. In: EC photovoltaic solar conference. 8, 1988. 688-692.

SARVER, T., AL-QARAGHULI, A. & KAZMERSKI, L. L. 2013. A comprehensive review of the impact of dust on the use of solar energy: History, investigations, results, literature, and mitigation approaches. Renewable and Sustainable Energy Reviews, 22, 698-733.

SAYIGH, A., AL-JANDAL, S. & AHMED, H. Year. Dust effect on solar flat surfaces devices in Kuwait. In: Proceedings of the workshop on the physics of non-conventional energy sources and materials science for energy, 1985. 2-20.

SCHUMACHER, J., HANSEN, J. & NEVENZEL, J. 1979. Preliminary design report: New ideas for heliostat reflector cleaning systems. NASA STI/Recon Technical Report N, 80, 23809.

SHARMA, R., WYATT, C. A., ZHANG, J., CALLE, C. I., MARDESICH, N. & MAZUMDER, M. K. 2009. Experimental evaluation and analysis of electrodynamic screen as dust mitigation technology for future Mars missions. Industry Applications, IEEE Transactions on, 45, 591-596.

SIMS, R., BIRIS, A., WILSON, J., YURTERI, C., MAZUMDER, M., CALLE, C. & BUHLER, C. Year. Development of a transparent self-cleaning dust shield for solar panels. In: Proceedings ESA-IEEE joint meeting on electrostatics, 2003. 814-821.

WHEAL, R. 2005. Photocatalytic solar chimney for pre-heating air and the removal of VOCs, Thesis (Ph.D.), University of Nottingham.

WILLIAMS, R. B., REBEKAH, T., ANDRANIK, S. & STEPHEN, F. 2007. Vibration Characterization of Self-Cleaning Solar Panels with Piezoceramic Actuation. 48th AIAA/ASME/ASCE/AHS/ASC Structures, Structural Dynamics, and Materials Conference. American Institute of Aeronautics and Astronautics.

ZHU, J., HSU, C.-M., YU, Z., FAN, S. & CUI, Y. 2009. Nanodome Solar Cells with Efficient Light Management and Self-Cleaning. Nano Letters, 10, 1979-1984.

321: Heat transfer and fluid flow studies in helical–spiral coils of modified cavity receiver for solar dish process heat system

K. S. REDDY[1], T. Srihari VIKRAM[2],

[1,2] *Heat Transfer and Thermal Power Laboratory, Department of Mechanical Engineering, Indian Institute of Technology Madras, Chennai – 600036, INDIA; Email: [1]ksreddy@iitm.ac.in Tel: +91 44 2257 4702; Fax: +91 44 2257 4652*

The present study deals with the heat transfer and fluid flow characteristics of heat transfer fluid in helical coil of modified cavity receiver of solar dish collector. A 3-D numerical model is developed to study the effect of fluid flow rate, DNI and opening ratios on the heat transfer and fluid flow from the receiver. The variation of average fluid temperature along the coil, Nusselt number and friction factor has been estimated for the fluid flow along the helical coil under different conditions. At DNI of 500 W/m2 and diameter ratio of 0.48, the rise in average fluid temperature for 100 lph is about 160K and about 17 K for 1000 lph. A steep increase in the average fluid temperature is observed in the spiral section whereas in the bottom helical section, it varies linearly and in the top helical section, the variation is very less. Nusselt number varies between 25 to 75 in the spiral section and 50 to 200 in the helical section for different flow rates. Nusselt number along the coil decreases in the spiral part and oscillates along the helical section. The oscillation of Nusselt number in the helical section is due to the secondary flow developed and the geometry of the coil. It can be noted that the heat transfer rate is comparatively higher in the helical section than the spiral section. The friction factor drastically drops in the spiral section and remains constant in the helical section. The friction factor ranges between 0.01 to 0.05 in spiral section and 0.01 to 0.02 in the helical section for different flow rates. The figure of merit is estimated in terms of ratio of pressure drop and heat transfer rate and it varies between 1 and 540 for different flow rates and DNI. The thermal efficiency of the receiver is found in the range of 70 - 80%. The present model can be used to estimate heat transfer/gain and pressure drop across the helical-spiral coil receiver of solar dish collector used for process heat applications.

Keywords: Solar dish, helical receiver, pressure drop, process heat

1. INTRODUCTION

The process heat requirements in various sectors like industrial, commercial and domestic sectors contributes to a major fraction of total fossil fuel energy consumption for its applications. These thermal needs can be met with usage of solar energy which is abundant. India has a good solar energy potential of about 5 to 7 kWh/m²day as it lies in the tropical zone. A substantial amount of India's low to medium temperature process heat requirements could be met by concentrating solar heat technology systems by combination with suitable process integration. This would reduce global CO_2 emissions, local air pollution, and India's growing dependence on expensive oil imports. The use of solar energy for process heat applications have been utilised in India for variety of applications such as dairy, industry etc. The concentrating solar systems are used for both process heat and power generation applications. The concentrating solar systems are classified into linear Fresnel systems, solar parabolic trough systems, central power tower and solar parabolic dish systems. These technologies have been used for both solar thermal and power applications widely. Out of the available four technologies, solar parabolic dish system has high solar – thermal conversion efficiency ranging between 0.85 and 0.9 (LOVEGROVE et al., 2007). The solar parabolic dish has been utilised for process heat applications (SHARMA et al., 2006) and demonstrated for power applications (LOVEGROVE et al., 2007). The receiver is the key component for conversion of solar energy into thermal energy. The efficient and effective design of the receiver reduces the losses from the system thereby increasing the useful energy. There are two types of receivers for solar parabolic dish system namely: external receivers and cavity receivers. The cavity receivers are the most preferred receivers than external receivers as they have higher conversion efficiencies. The cavity receiver consists of coil/tube wound in the shape of cavity, which forms the shape of helical coils. The shape of the helical coil depends on the geometry of the receiver. Helical coils are preferred for their higher heat transfer rate and volume to surface area.

Various studies have been carried out on different shapes and sizes of receiver coil to evaluate the performance of coil for variety of applications ranging from heat transfer equipment to solar thermal receivers. A detailed survey of literatures by VASHISTH et al. (2008) discusses the application of different shapes and geometries of coil for wide range of applications ranging from the laboratory scale to industry considering the flow and thermal parameters and discussed the recent developments in this area. A compendium of correlations for single and two-phase flows in the coiled geometry are discussed in detail. PAWAR et al. (2011) presented critical review on heat transfer through helical coils of circular cross section. Several experimental and numerical studies have been carried out to characterise the usage of coil thermally and hydrodynamically. JAYAKUMAR et al. (2010) carried out CFD analysis to study the vertically oriented helical coils considering the parameters such as tube pitch, pitch circle diameter, tube diameter on heat transfer characteristics and developed Nusselt number correlations. Experimental and numerical studies on heat transfer and flow characteristics of horizontally spiral coils have been studied by NAPHON (2011). KE et al. (2011) carried out numerical investigation of heat transfer studies in conical spiral tube bundles used in heat exchangers. The effect of tube diameter and shape of the coil are discussed. It has been shown that the cone angle and cross section have significant effect when compared to tube pitch on heat transfer. WU et al. (2009) carried out numerical investigation of turbulent flow, heat transfer and entropy generation in helically coiled tube with larger curvature ratio. Based on the studies, it is found that coil pitch, curvature ratio and Reynolds number have different effect on Nusselt number, friction factor and entropy generation have been discussed. KURNIA et al. (2011) studied the heat transfer performance of helical coils of non-circular cross sections with different geometries such as in-plane spiral, helical spiral and conical ducts. The results are compared with straight pipe of same length. The advantages and limitations of using coiled tubes are also discussed in light of numerical analysis.

The studies on heat transfer and flow in solar receivers have been performed and are limited. The heat transfer characteristics and performance of conically wound, single layer, monotube receiver for concentrating solar collector have been investigated by RICE et al. (1981). The effect of various parameters such as tube diameter, pitch etc., on the performance of the solar collector are discussed and a method for improvement in efficiency is also discussed. BANNISTER (1991) studied the maximisation of exergy gain in solar thermal receivers by the suitably selecting the pipe radius. The optimum trade-off between heat transfer and pumping power has been investigated considering water and steam as working fluid. MAY and DONOVAN (2010) performed analysis of helical coil heat exchanger for solar thermal application. Parametric studies have carried out considering the flow and geometrical parameters. REDDY et al. (2014) presented the design and analysis of helical coil for desalination applications. The helical receiver aims at increasing the heat transfer by Dean flow effect. Based on the analysis, optimum design parameters have been arrived. ZAPATA et al. (2013) developed a transient model for heat exchange in solar once-through

cavity receiver. The heat loss calculations from mono-tube cavity receiver, calculation of receiver exit mass flow rate, improved dynamic model have been discussed.

The heat transfer and flow analyses of different shapes and geometries of helical coil have been analysed. Several results cannot be generalised as they are pertained to certain applications and geometry. Hence, in the present study, the heat transfer and flow characteristics of helical coil for modified cavity receiver have been investigated. The effect of various parameters such as flow rate, length of the coil, DNI etc. on Nusselt number and friction factor have been investigated.

2.   MODELLING OF HELICAL COIL RECEIVER FOR SOLAR PARABOLIC DISH COLLECTOR

The solar parabolic dish system consists of concentrator, receiver, tracking and control systems. The concentrator focuses the incident solar energy towards the receiver placed at the focal point into useful heat. The tracking and control system tracks the system throughout the day to focus the sun. The receiver consists of metallic tube wound in the shape of hemisphere at the top part and spiral in the bottom part as shown in Figure 1. The helical receiver is insulated at the outer surface and covered with metal sheet over it. In the present study, the diameter of the tube is considered as 8×10^{-3} m and the distance between the two turns are considered as 1×10^{-3} m. The helical coil diameter (D) is considered as 0.305 m based on the flux distribution analysis of fuzzy focal solar parabolic dish collector (REDDY et al. 2015). The diameter of the cavity opening (d) is varied to suit the different diameter ratios (d/D) such as 0.24, 0.48, 0.77 and 1(Figure 2). The number of turns in spiral part (aperture) of 0.24, 0.48, 0.77 are 12, 8 and 3
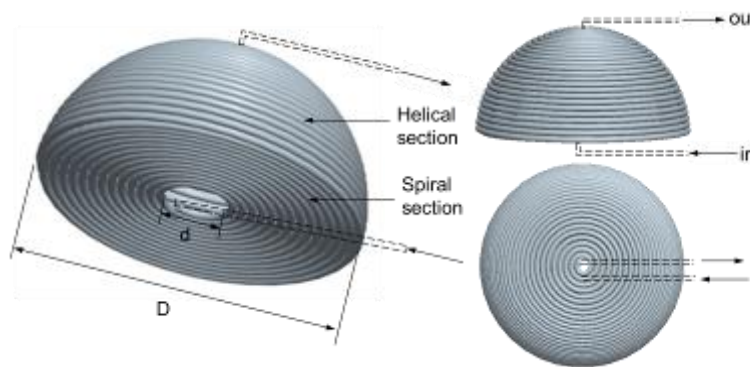
Figure 1: Geometry of helical – spiral modified cavity receiver
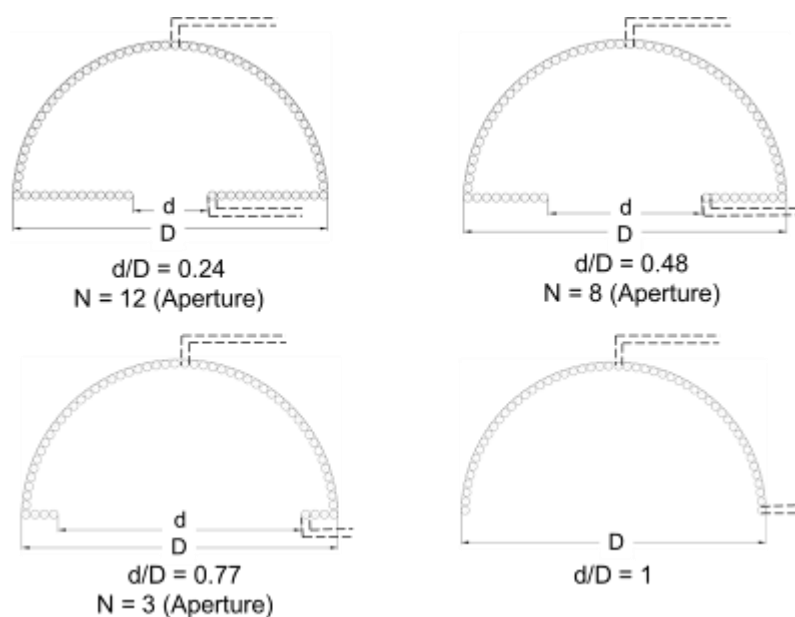
Figure 2: Helical – spiral modified cavity receiver with different diameter ratios

2.1 Mathematical model

The flow and heat transfer simulations were based on the simultaneous solution of the system of equations describing the conservation of mass, momentum and energy.

Equation 68: Continuity equation	$\nabla \cdot \vec{V} = 0$
Equation 2: Momentum equation	$\vec{V} \cdot \nabla(\rho \vec{V}) = -\nabla p + \mu.\nabla^2 \vec{V} + \rho \vec{g} + \vec{F}_c$
Equation 3: Energy equation	$\vec{V} \cdot \nabla(\rho C_p T) = k\nabla^2 T$

Where:

- $\vec{V}$ = Velocity vectors
- ρ = Density (kg/m^3)
- p = Pressure (Pa)
- g = Acceleration due to gravity (m/s^2)
- $\vec{F}_c$ = Centrifugal force (N)
- C_p = Specific heat capacity (J/kgK)
- k = Thermal conductivity (W/mK)
- T = Temperature (K)

2.2 Boundary conditions

The concentrated solar radiation is incident on the inner surface of the receiver. Hence, heat flux value is imposed on the inner surface of the receiver. The outer surface is insulated to minimise the heat loss from the receiver. Hence zero heat flux is applied on the outer surface the helical coil. The fluid enters the helical coil with inlet velocity of u$_{in}$. The pressure outlet is specified at the outlet of the coil. The boundary conditions applied for the helical coil receiver is shown in Figure 3 (a). The working fluid considered in the present study is therminol 72 which is a high temperature heat transfer fluid with excellent stability upto 653 K (EASTMAN, 2010). The properties of the fluid are considered as the function of temperature.

2.3 Numerical Procedure and Validation

The helical coil receiver is modelled in Pro Engineer V4.0. The meshing of the geometry is carried out using ANSYS Workbench 14.5. The computational domain of helical and spiral section of the receiver coil is shown in Figure 3(b). The sweep mesh of element size 2.5 x 10^{-3} m is generated with the face mesh size of 0.4 x 10^{-3} m. The numerical simulations are carried out using ANSYS 14.5. The numerical simulations are carried out considering SIMPLEC algorithm for pressure and velocity coupling in momentum equation. The second order upwind scheme has been considered for discretizing the equations. The present numerical procedure is validated with two different models (i) conical tube bundle and (ii) spiral coil. The fluid flow and heat transfer characteristics of conical tube bundle has been studied by KE et al, 2011. The heat transfer and heat transfer coefficient obtained by KE et al (2011) for the inlet flow velocity of 0.1 m/s has been compared with the present numerical procedure and the results are tabulated (Table 1) and shows good agreement. The heat transfer and flow characteristics of spiral coil carried out by NAPHON (2011) is compared at flow rate of 0.05 kg/s. Table 1 shows the comparison of experimental and numerical results for heat transfer rate and outlet temperature of the spiral coil. The deviation of heat transfer is within 10%, when compared with NAPHON (2011)

Table 48: Validation of numerical procedure

Parameter	KE et al, 2011	Present numerical procedure	NAPHON, 2011	Present numerical procedure
Heat transfer coefficient (W/m2K)	150	152.46	-	-
Heat transfer (W)	307.45	310.35	2785.25	3031.72
Outlet fluid temperature (K)	-	-	307.65	308

(a)   (b)
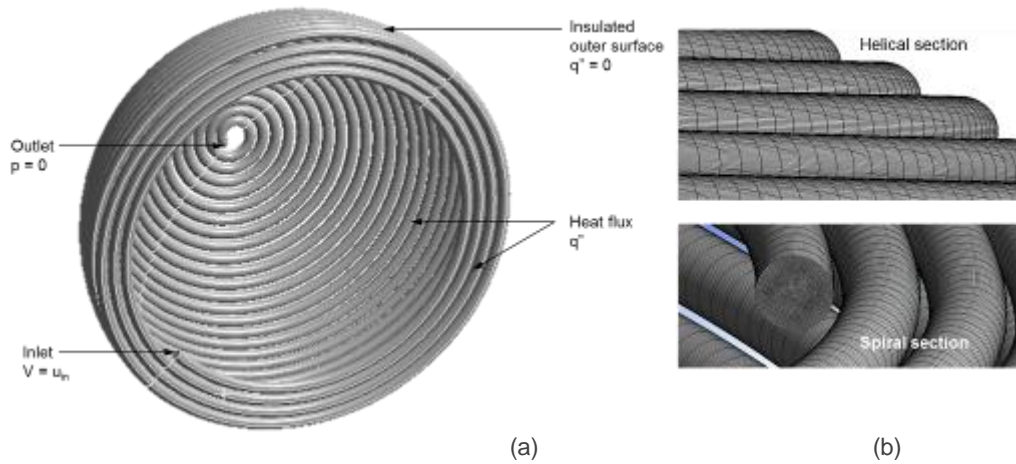
Figure 3: (a) Boundary conditions of helical-spiral coil receiver
(b) Computational domain of helical and spiral section of helical coil

2.4 Grid Independence Studies

The effect of cell size is important in numerical modelling for accuracy and time taken for the simulation. The grid independent studies have been carried out considering various cell sizes and the results are tabulated in Table 2. Considering the parameters and the secondary flow, the model with 79,81,000 cells have been considered for further studies.

Table 2: Grid independence studies

No. of cells	Fluid outlet temperature (K) @ 500W/m2 and 100 lph	Secondary flow observed	Heat transferred to the fluid (kW)
33,20,000	468.08	No	8.565
46,57,500	467.43	No	8.571
79,81,500	466.95	Yes	8.573
1,01,50,000	465.97	Yes	8.575

3. FLUID FLOW AND HEAT TRANSFER CHARACTERISTICS OF HELICAL COIL

3-D numerical simulations have been carried out to estimate the various parameters such as average fluid temperature, Nusselt number and friction factor of the helical coil.

3.1 Average fluid temperature

The average fluid temperature or the bulk fluid temperature is the area weighted average temperature of the fluid along the helical coil. The average fluid temperature is used to estimate the thermal characteristics of the fluid along the helical coil. The average fluid temperature along the helical coil is estimated using equation given below.

Equation 4: Average fluid temperature
$$T_f = \frac{\int_0^A wTdA}{\int_0^A wdA}$$

Where:

- T_f = Average fluid temperature (K)
- w = Velocity component in flow direction (m/s)
- dA = Elemental area (m^2)

788

3.2 Nusselt number

Nusselt number of the fluid plays important role to determine the performance of the coil. The average Nusselt number along the cross section of the tube of helical coil is estimated using equation given below.

Equation 5: Average Nusselt number
$$Nu_{avg} = \frac{q'' d_t}{k(T_w - T_f)}$$

Where:

- q" = Heat flux (W/m^2)
- d_t = Diameter of the tube (m)
- k = Thermal conductivity of the fluid (W/mK)
- T_w = Wall temperature of the helical coil (K)

3.3 Friction factor

The average friction factor along the cross section of the tube of helical coil is estimated using equation given below.

Equation 6: Average friction factor
$$f_{avg} = \frac{2\tau_w}{0.5 \cdot \rho \cdot u_{in}^2}$$

where:

- τ_w = Wall shear stress (N/m^2)
- u_{in} = Inlet velocity of the fluid (m/s)

4. RESULTS AND DISCUSSION

The fluid flow and heat transfer characteristics of helical coil of modified cavity receiver considering the effect of various parameters such as DNI (ranging from 250 W/m^2 to 1000W/m^2 in the steps of 250 W/m^2), fluid flow rate (100, 250, 300, 500, 750, 1000 lph) and length of the coil (corresponding to the d/D ratios of 0.24, 0.48, 0.77 and 1) are discussed below.

4.1 Temperature distribution and pressure drop across helical coil

- The average fluid temperature and wall temperature of the helical coil for flow rate of 100 lph at different DNI and different diameter ratio is shown in Figure 4. Figure 4 (a) shows the temperature distribution for the diameter ratio of 0.24 at different DNI.

The temperature rise can be divided into three segments where, the fluid temperature increases drastically in the spiral section, gradual increase in middle part of the helical section and remains constant in the top part of the helical section. The temperature rise of 84K, 170K, 254K and 307K are observed for DNI values of 250, 500, 750 and 1000W/m^2. The increase in flow rate increases the secondary flow inside the coil and the average fluid temperature oscillates along the coil (Figure 4 (b)). Similarly, the variation of average fluid temperature and wall temperature (Figure 4 (c)) is estimated for the different diameter ratios say 0.24, 0.48, 0.77 and 1 at flow rate of 100 lph and DNI of 1000 W/m^2. The temperature rise depends on the diameter ratios. Four different profiles of average fluid temperature can be seen initially in the spiral and helical section of the receiver. The outlet temperature of 607 K is observed for diameter ratio of 0.24. However, for other diameter ratios, the outlet temperature remains same at 590 K.

(a)

(b)

(c)
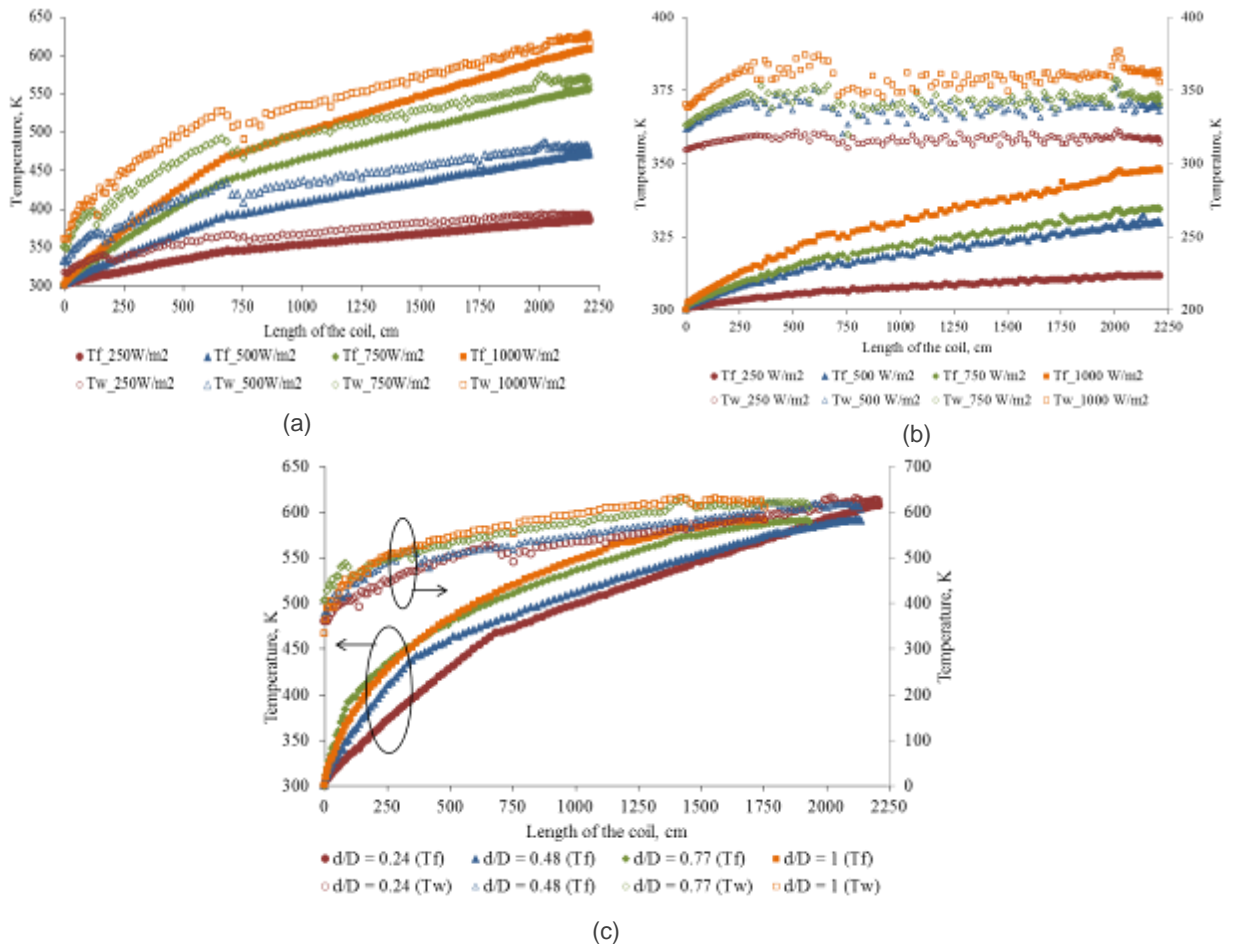
Figure 4: Temperature distribution in helical coil receiver (a) different DNI at flow rate of 100 lph ; (b) different DNI at flow rate of 750 lph (c) different diameter ratio at flow rate of 100 lph

(a)   (b)
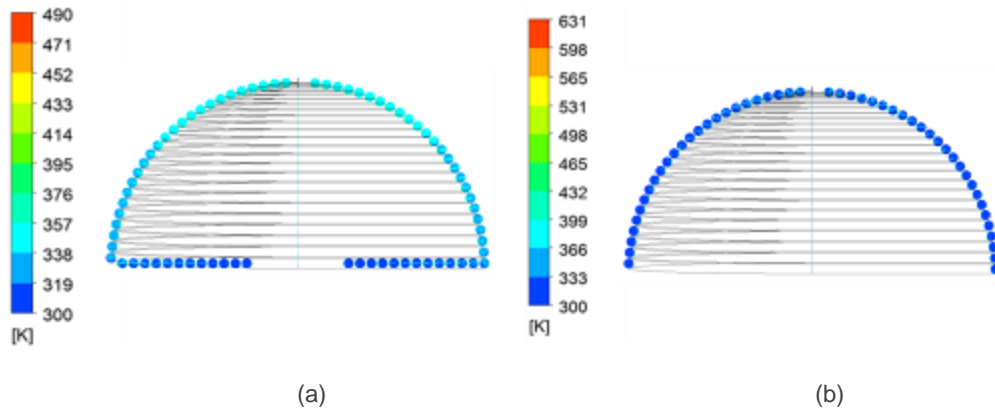
Figure 5: Temperature contours along the vertical plane for different diameter ratio (a) d/D = 0.24 (b) d/D = 1
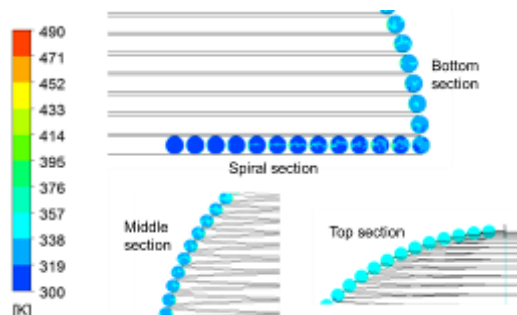
Figure 6: Detailed view of temperature contours in different sections for coil d/D = 0.24

The temperature contours along the vertical plane for diameter ratios 0.24 and 1 are shown in Figure 5 (a) and (b) respectively. The temperature increases in the spiral part and continues till the middle section of the helical part and in the top section of the coil The development of secondary flow along the coil is shown in Figure 6. The Dean vortices are set up in the bottom section i.e., spiral section and it develops as the fluid flows along the coil. The fluid undergoes drastic change in geometry. The pressure distribution along the length of the coil is shown in Figure 6. For the diameter ratio of 0.24, the pressure drop of 0.15 to 0.4 bar is observed for different DNI at flow rate of 100 lph (Figure 7 (a)). The pressure drop varies between 0.15 to 14 bar for DNI of 1000 W/m^2 and different flow rates (Figure 7 (b)).
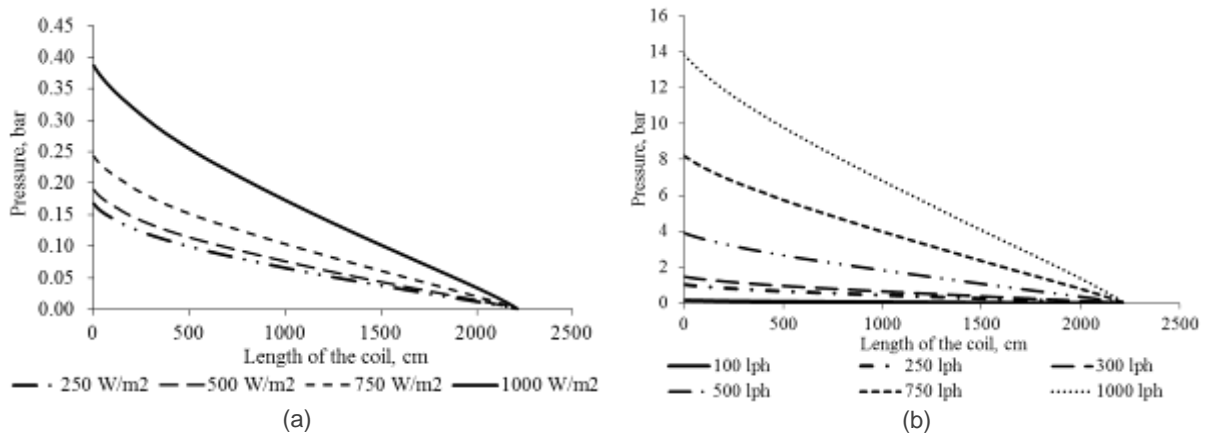
Figure 7: Pressure distribution in helical coil receiver for diameter ratio of 0.24
(a) different DNI (b) different flow rates

4.2 Effect of DNI

The average outlet temperature of the fluid at flow rate of 100 lph and DNI of 500 W/m^2 and 1000 W/m^2 are 470 K and 607 K respectively. The variation of Nusselt number along the length of the coil is shown in Figure 8. It can be observed that the Nusselt number is lower in the spiral section compared to that of helical section. In the helical section, the Nusselt number increase slowly and reaches higher value at the top section.
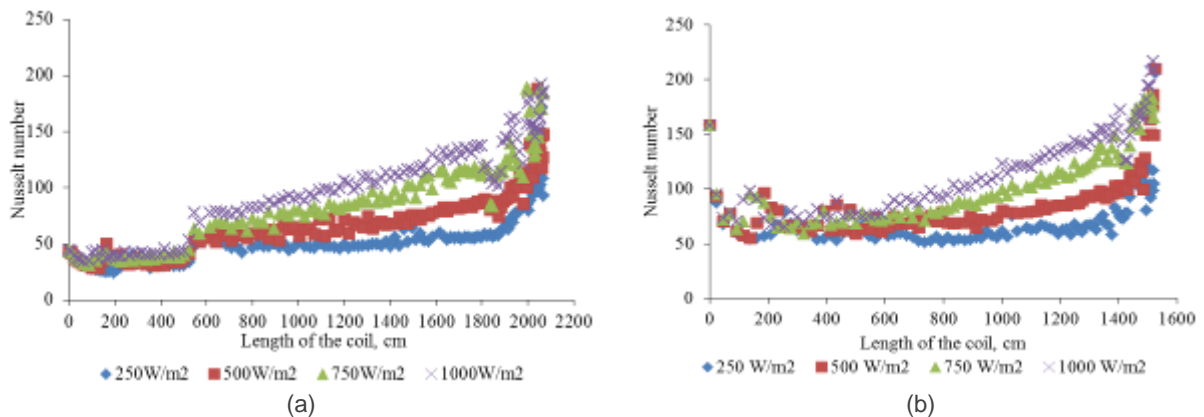
Figure 8: Variation of Nusselt number along helical coil receiver for different diameter ratio (a) d/D = 0.48
(b) d/D = 1

The variation of friction factor along the length of the coil is shown in Figure 9. The friction factor decreases along the coil drastically in the spiral section and decreases in the middle helical section and increases in top section.

791

(a)

(b)
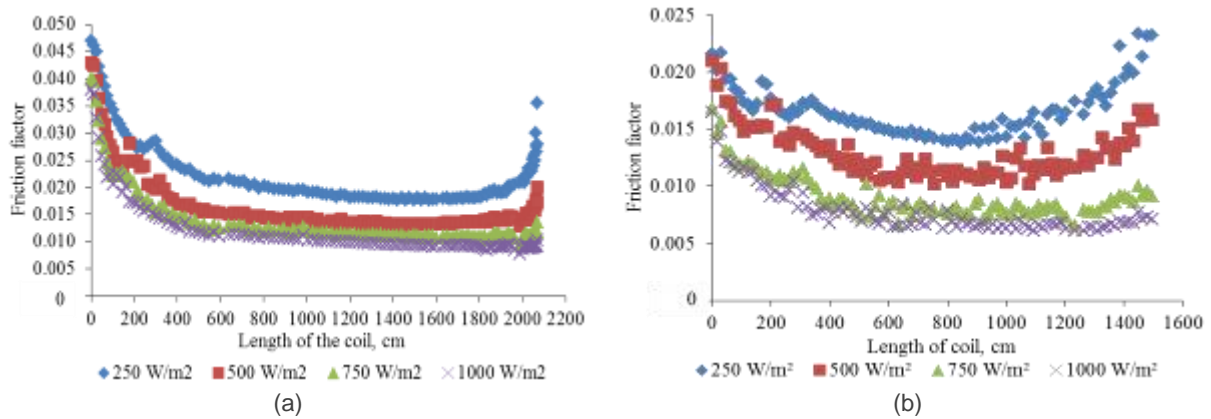
Figure 9: Variation of friction factor along helical coil receiver for different diameter ratio (a) d/D = 0.48 (b) d/D = 1

4.3 Effect of diameter ratio of coil

The effect of diameter ratio on Nusselt number and friction factor is shown in Figure 10. It is observed that, the Nusselt number remains constant along the spiral section and there is increase in Nusselt number along the helical section. The variation of friction factor in the developing region is higher when compared to that of helical section.

(a)

(b)
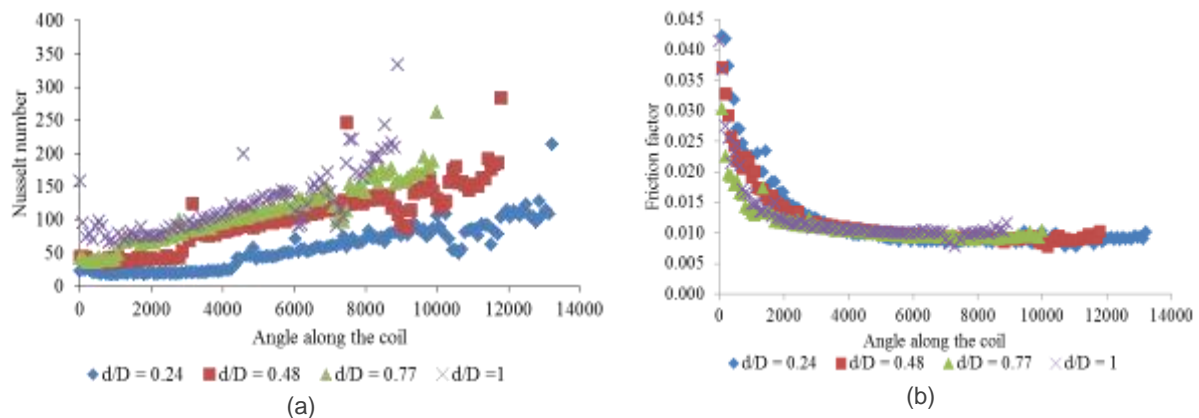
Figure 10: Variation of (a) Nusselt number and (b) friction factor along helical coil receiver for different diameter ratios

4.4 Effect of flow rate

The effect of flow rate on heat transfer and flow is evaluated based on Nusselt number and friction factor along the coil length. The variation of flow rate drastically influences the heat transfer and fluid flow. At lower flow rates, say 100 lph, the average outlet fluid temperature is about 607 K, 435 K, 415 K, 370 K, 348 K and 336 K respectively for diameter ratio of 0.24 and flow rates of 100, 250, 300, 500, 750 and 1000 lph. The variation of Nusselt number and friction factor for diameter ratio of 0.48 and 1 are shown in Figure 11 and 12 respectively.

The friction factor decreases drastically when the fluid is developing in the spiral section. When the fluid is fully developed, the variation of friction factor along the helical coil remains constant. At the exit of the helical section, due to the drastic change in geometry, there is an increase in friction factor.

(a)

(b)
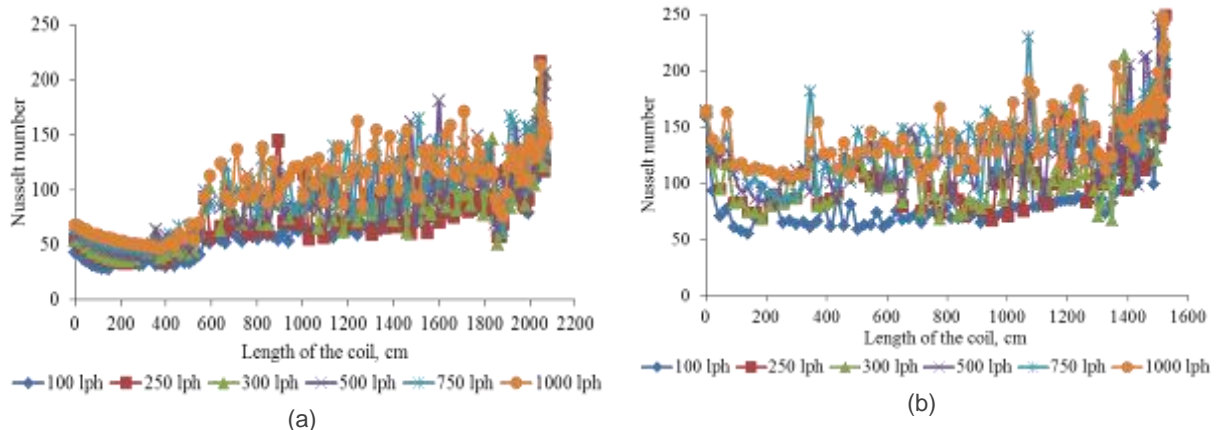
Figure 11: Variation of Nusselt number along helical coil receiver for different diameter ratio (a) d/D = 0.48 (b) d/D = 1

(a)

(b)
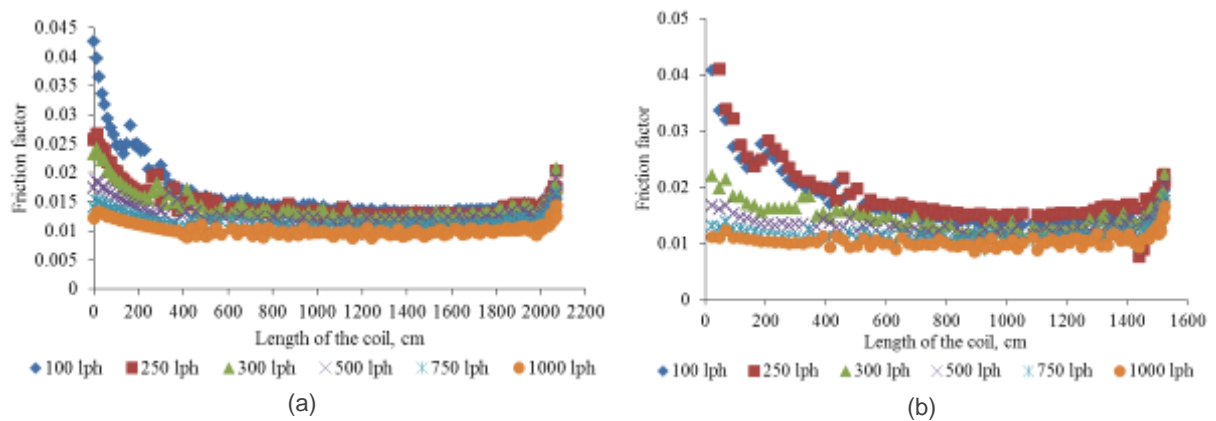
Figure 12: Variation of friction factor along helical coil receiver for different diameter ratio (a) d/D = 0.48 (b) d/D = 1

4.5 Performance analysis of helical-spiral coil

The performance analysis of the coil is estimated based on the figure of merit. It is defined as the ratio of the pressure drop across the coil to the heat transfer rate. The figure of merit of the helical-spiral coil varies between 1 and 320 for different diameter ratios at DNI of 1000W/m². Similarly for the diameter ratio of 0.24, it varies between 1 and 540; for diameter ratio of 1, it varies between 1 and 510 at different DNI values. Based on the numerical simulation, the thermal efficiency of the modified cavity receiver varies between 70 and 80%.

5. CONCLUSION

The 3-D numerical investigation of heat transfer and fluid flow through the helical coil of modified cavity receiver for solar parabolic dish has been carried out. The effect of various parameters such as DNI, flow rate and diameter ratio have been studied. The average fluid temperature of the fluid for various conditions has been estimated. The DNI has a significant effect on the performance of the helical coil. The average outlet temperature of the fluid at flow rate of 100 lph and DNI of 500 W/m² and 1000 W/m² are 470 K and 607 K respectively. Nusselt number and friction factor have been estimated for the helical-spiral coil to ascertain the performance of the coil under different conditions. Nusselt number varies between 25 to 75 in the spiral section and 50 to 200 in the helical section for different flow rates. The drastic increase of the parameter at the top helical section may be due to the sudden geometrical change. When the flow rate is less, the variation along the helical section remains more or less constant. When the flow rate is higher, the oscillating behaviour of the fluid is observed due to the secondary flow. The friction factor ranges between 0.01 to 0.05 in spiral section and 0.01 to 0.02 in the helical section for different flow rates. The figure of merit (ratio of pressure drop and heat transfer rate) varies between 1 and 10 for flow rate of 100 lph and DNI of 250 W/m². The present model can be used to estimate heat transfer/gain and pressure drop across the helical coil receiver of solar dish.

6. ACKNOWLEDGEMENTS

7. REFERENCES

BANNISTER, P., 1991. Maximisation of exergy gain in high temperature solar thermal receivers by choice of pipe radius, ASME Journal of Heat transfer, 113, 337-340

JAYAKUMAR, J. S., Mahajani, S. M., Mandal, J. C., Iyer, K. N., Vijayan, P. K., 2010. CFD analysis of single-phase flows inside helically coiled tubes, Computers and Chemical Engineering, 34, 430-446

KE, Y., Pei-Qi, G., Yan-CaI, S., Hai-Tao, M., 2011. Numerical simulation on heat transfer characteristic of conical spiral tube bundle, Applied Thermal Engineering, 31, 284-292

KURNIA, J. C., Sasmito, A. P., Mujumdar, A. S., 2011. Evaluation of the heat transfer performance of helical coils of non-circular tubes, Zhejiang University- Science A, 12 (1), 63-70

LOVEGROVE, K., Zawadski, A., Coventy, J., 2007. Paraboloidal dish solar concentrators for multi-megawatt power generation, In: ISES Solar World Congress, Beijing, China, September 18 – 22, 2007

MAY, A., Donovan, T. S., 2010. 14th International Heat Transfer Conference/ Convective heat transfer in helical coil solar thermal collector, 491-497

NAPHON, P., 2011. Study on heat transfer and flow characteristics in a spiral-coil tube, Intl Comm in Heat and Mass Transfer, 38, 69-74

PAWAR, S. S., Sunnapwar, V. K., Mujawar, B. A., 2011. A critical review of heat transfer through helical coils of circular cross section, Journal of Scienctific and Industrial Research, 70, 835-843

REDDY, K. S., Mallick, T. K., Vikram, T. S., Sharon, H., 2014. Design and optimisation of elliptical hyperboloid concentrator with helical receiver, Solar Energy, 108, 515–524

REDDY, K. S., Natarajan, K. S., Gumtapure, V., 2015. Experimental performance investigation of modified cavity receiver with fuzzy focal solar dish concentrator, Renewable Energy, 74, 148-157

RICE, M P, Modest, M F, Borton, D N, Rogers, W E, 1981. Heat transfer analysis of receivers for a solar concentrating collector, Chemical Engineering Communications, 8, 353-364

SHARMA, V. R., Bhosale, S. J., Kedare, S. B., Nayak, J. K., 2006. Field tests of the performance of paraboloid solar concentrator ARUN160 at Latur, In : Proceedings of NCAER2006 - National Conference on Advances in Energy Research, Indian Institute of Technology Bombay, India, December 4-5, 2006, 182-187

THERMINOL 72, 2010, Eastman Chemical Company, US

VASHISTH, S., Kumar, V., Nigam, K. D. P.,2008. A Review on the Potential Applications of Curved Geometries in Process Industry, Industrial and Engineering Chemistry Research, 47, 3291-3337.

WU, S. Y., Chen, S. J., Li, Y. R., 2009. Numerical investigation of turbulent flow, heat transfer and entropy generation in a helical coiled tube with larger curvature ratio, Heat and Mass Transfer, 45, 569-578

ZAPATA, J. I., Pye, J., Lovegrove, K., 2013, A transient model for the heat exchange in a solar thermal once through cavity receiver, Solar Energy, 93, 280-293

354: Improving illumination and temperature distribution uniformity in high concentrating solar cells

Abdulrahman ALDOSSARY[1], Abdulmaged ALGAREU[1], Adel ALDIHANI[1], Raya. AL-DADAH[1], Saad. MAHMOUD[1]

[1]University of Birmingham, Edgbaston, Birmingham, United Kingdom. B15-2TT,axa281@bham.ac.uk

High concentrating Photovoltaic (HCPV) has the potential to replace the expensive PV material with cheaper optical elements. The use of high solar concentration ratios with the triple junction III-V solar cells offers potential of high solar cell efficiency and power output. However, non-uniformity of the incident flux is detrimental to the CPV technology as this tends to cause hot spots and current mismatch leading to reduced electrical efficiency of the system and degrade the life of the solar cell. In this work, a point focus Fresnel lens was developed and the influence of using a small square reflector placed above the PV surface as a Secondary Optical Element (SOE) in alleviating the non-uniform illumination and temperature distribution was investigated. Also, the SOE height and material reflectivity influence on the optical performance was examined. This was done by implementing optical and thermal simulations using advanced ray tracing method and Multi-physics finite element software respectively. Incident rays distribution uniformity was evaluated using the standard deviation from the mean value. A low standard deviation indicates that most received rays by the solar cell are close to the mean value i.e. more uniform. Results show that a combination of introducing a short SOE (60mm) made from 95% reflective material above the PV and increasing the distance between the PV and the Fresnel lens (l) to 500mm significantly improve the surface illumination uniformity. The achieved uniformity standard deviation is less than 3 with minimum loss in received power i.e. 48.25W in case of introducing SOE and l=500mm compared to 49.07W where receiver placed at focus point.

Keywords: Multi-junction PV, optical efficiency, high concentration, Fresnel lens, non-uniform illumination

1. INTRODUCTION

Global warming, increased fuel prices, worldwide conflict, and increased environmental awareness are major factors of encouraging intensive research and development of renewable energy. Solar energy technologies including solar heating, solar photovoltaic, and solar thermal electricity can contribute solving energy problems in the world (Hoeven 2011: page19). PV is a promising technology which has the advantage of converting sunlight directly into electricity. Solar PV power has been one of the fastest growing renewable energy technologies and it is anticipated that this technology will play a major role in the future of global electricity generation (Twidell & Weir 1986: page182). The new technology, III-V generation multi-junction solar cells, offer high efficiencies exceeding 43% compared to traditional solar cells made of a single layer of semiconductor material (Micheli et al. 2013: page01). The main challenge of promoting PV is the high initial cost when compared to electricity generated from conventional sources (Mah 1998: page02). Concentrated PV systems offer advantages where space and cost are reduced as the expensive PV can be replaced with cheap optical lenses.

A typical CPV system consists of one or more optical element which could be either reflective or refractive (Madhugiri 2012: page1381). The Fresnel lens is a known refractive optical element as a concentrator with many advantages such as compact size, lower weight and material cost (Pan et al. 2011: page4283). The main goal of the concentrators is to increase the concentration ratio (CR). However, concentrators produce high surface temperature as well as non-uniform distribution of illumination on the receiver which can ultimately degrades life of the solar cell (Baig et al. 2012: page5890). A classical method to reduce the non-uniform illumination and improve the uniformity is introducing a SOE to a HCPV (Baig et al. 2012; Benítez et al. 2010; Hernández et al. 2008; Victoria et al. 2013).

In this work, the effect of varying the distance between the receiver and the Fresnel lens (*l*) and inserting SOE above the receiver are examined using ray tracing software. Moreover, the influence of SOE material reflectivity on the optical efficiency was also investigated. Finally, irradiation distribution from this software is imported to COMSOL Multiphysics and thermal simulation is executed to demonstrate the resulted temperature profile on the PV surface.

2. FRESNEL LENS MODELLING
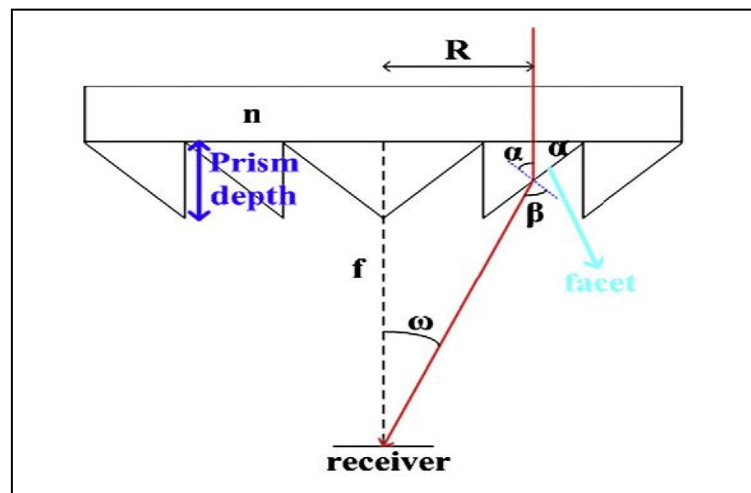
Figure 1: schematic of planar Fresnel lens (Pan et al. 2011)

Figure 1 shows schematic of planar Fresnel lens. Each Fresnel lens consists of serial pitches of Fresnel lens facets. The following equations describe each pitch of the Fresnel lens (Leutz & Suzuki 2001: page67).

$$n \sin \alpha = \sin \beta \tag{1}$$

$$\tan \omega = \frac{R}{f} \tag{2}$$

$$\beta = \alpha + \omega \tag{3}$$

$$\tan \alpha = \frac{R}{n\sqrt{R^2 + f^2} - f} \tag{4}$$

Groove pitch of Fresnel lens here is upside down (grooves in) which is suitable for dusty environment as dust can deposit within these grooves and cause shadows on the PV (Leutz & Suzuki 2001: page70). Snell's law is applied on the incident ray as shown in figure 1 where R is the distance between incident ray and the centre axis of the Fresnel lens, n is the refractive index of the Fresnel lens, ω is an angle between the normal of the receiver and the refractive ray, β is an angle between the normal direction of the Fresnel lens's facet and the refractive ray, and *f* is the focal length (Pan et al. 2011: page4285).

In this investigation, the developed Fresnel lens has a focal length (*f*) of 460mm, the Groove pitch of 3 mm, Fresnel lens thickness of 3mm, and F number of 1.3. The modelled Fresnel lens is made from Polymethyl Methacrylate (PMMA) with a refractive index of 1.49. The area of this Fresnel lens and the receiver is 62500 mm^2 and 100 mm^2 respectively resulting in a geometry concentration ratio of 625X where X is the solar radiation received taken as 1000 W/m^2.
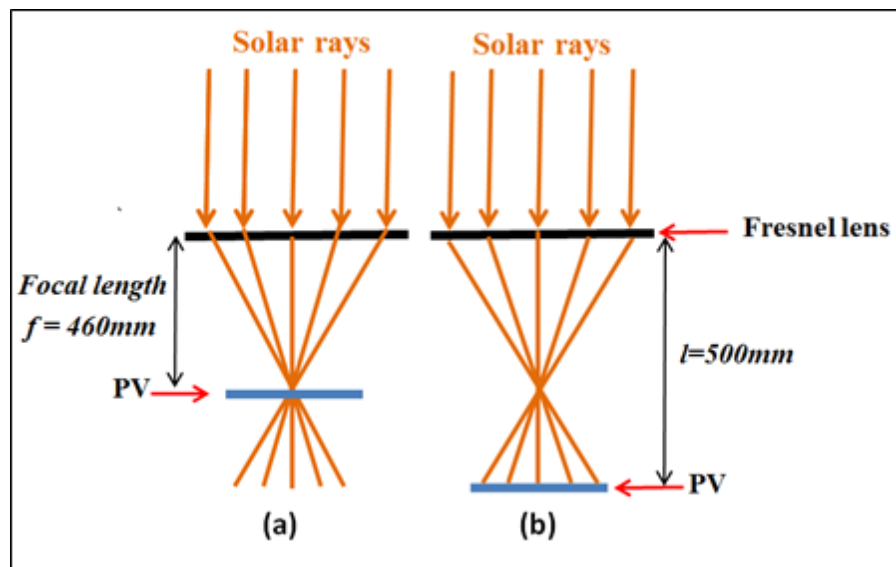
Figure 2: Receiver (Solar cell) at: a) focal point & b) l=500mm

Optical efficiency and illumination uniformity are two important parameters that need to be considered during the development of Fresnel lens. In order to evaluate the optical performance of above Fresnel lens, it is simulated using advanced ray tracing engineering software called Optisworks. Figure 2 shows how the rays are refracted by the groove facet angles of the Fresnel lens to the PV at the focus point and at a distance away from the focus point (l).

3. RESULTS

Incident rays uniformity was evaluated using the standard deviation. A low standard deviation indicates that most received rays by the solar cell are close to the mean value i.e. uniform.

Figure 3 shows the received ray distribution at the surface of the PV cell placed at the focus point (figure 2a). It can be seen that the developed Fresnel lens produces high energy concentration at the centre of the PV cell between -0.5 to +0.5mm region exceeding $55x10^6$ W/m^2. This will create a hot spot on the receiver which can reduce the conversion efficiency due to the current mismatch as well as the reliability of the solar cell.
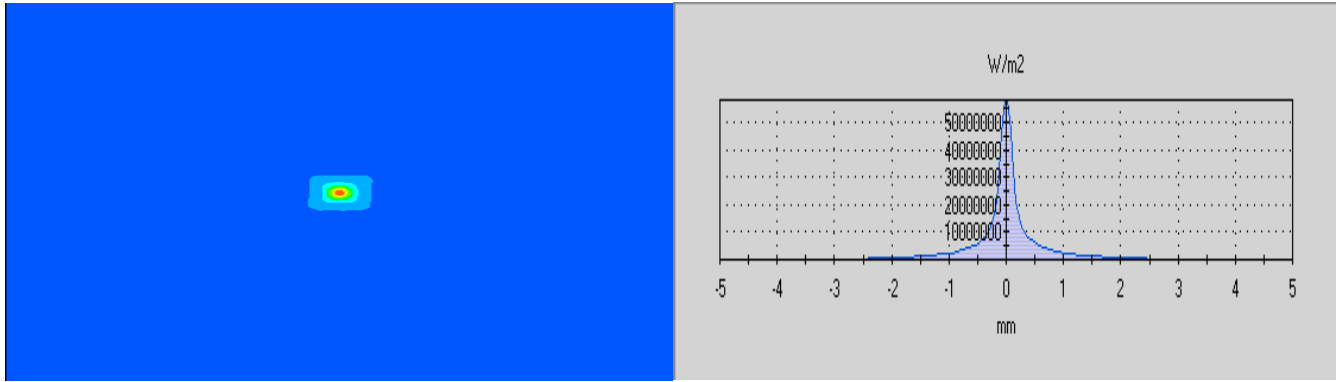
Figure 3: Irradiance distribution on the solar cell
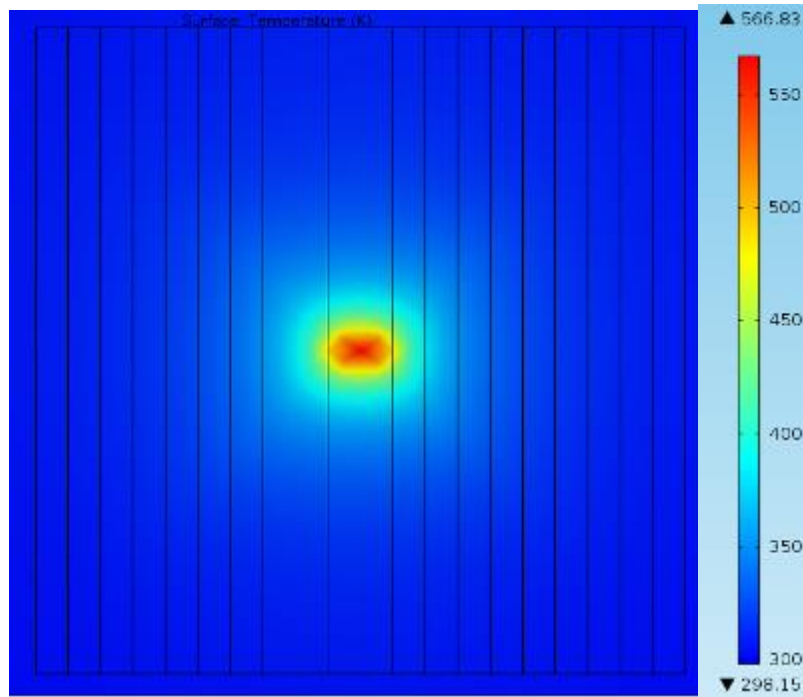
Figure 4: 2D image of temperature distribution on the solar cell

Thermal modelling of AZUR 3C42A (Average & Data 2014: page1) III-V multi-junction PV cell made of GaInP-GaInAs-Ge and area of $1cm^2$ to predict its temperature distribution was carried out. Assuming ambient and cooling water temperature of 298.15 K, the cell was placed above a cooling channel with hydraulic diameter of 8.47×10^{-3} m where water flows at a velocity of 0.25m/s. The solar radiation energy received by the PV cell is partially used to generate electricity and the rest is converted to heat. Kerzmann and Schaefer method was used to calculate the amount of input energy that is converted to heat (q_{heat}) as per equation 5 (Kerzmann & Schaefer 2012: page258):

$$q_{heat} = q_{rad} (1 - \eta_{pv}) \tag{5}$$

where q_{rad} is solar radiation incident on the surface of the PV cell, η_{pv} is the cell average electrical efficiency given as a function of thermal coefficient ($\beta_{thermal}$) at each concentration, efficiency at reference temperature (41.4%), and average PV surface temperature (T_{pv}) as shown in equation 6 (Skoplaki & Palyvos 2009: page617):

$$\eta_{pv} = 41.4\% - [\beta_{thermal} (T_{pv} - 298.15)] \tag{6}$$

This converted heat is transferred through the PV cell solid layers by conduction to the water channel where it was dissipated using forced convection. Also, some of this heat is radiated back from the cell to the ambient. Conjugate heat transfer physical model in COMSOL was used to solve the heat conduction and convection simultaneously.

798

Figure 4 shows the resulted temperature profile using the radiation distribution of the Fresnel lens shown in figure 3; the hot spot on the surface is clear. Although active cooling is applied, the maximum surface temperature reaches to about 567K. Without cooling, the surface temperature of the PV at this level of concentration can reach to 1500K (Min et al. 2009: page03; Theristis et al. 2012: page263). This high temperature is detrimental for any solar cell.

3.1 Effect of increasing the distance between the Fresnel lens and the receiver

Figure 2b shows placing the PV cell further away from the focus point allow the rays to spread over the cell surface. For the receiver located at the focus centre, the predicted Fresnel lens optical efficiency is 78.5% which produces concentration ratio of 491X with received power of 49.07W. Figure 5 shows the variation of received power and the non-uniformity of rays distribution on the surface of the cell with distance from the Fresnel lens. It can be seen that increasing the distance from the lens reduces the non-uniformity but results in significant reduction of the power received.
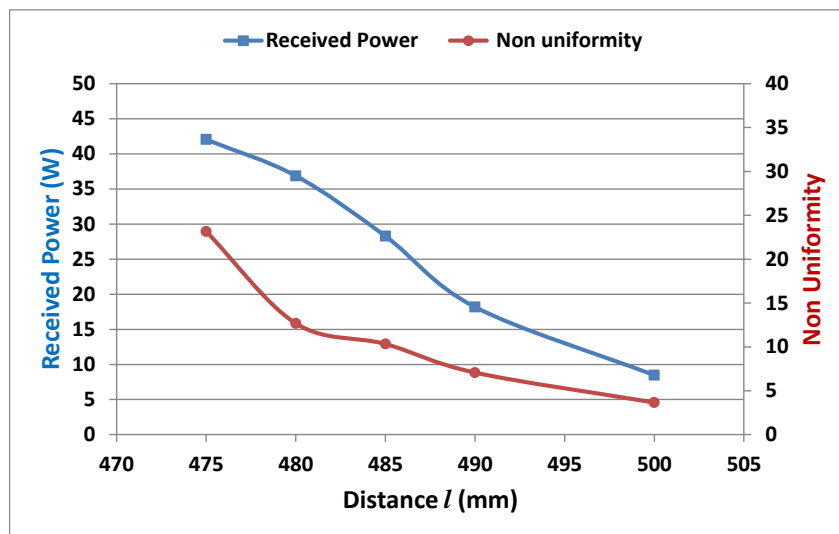
Figure 5: the effect of increasing (l) on received power and uniformity

3.2 Effect of using secondary optical element

A 60mm Squared Miniature Concentrator (SMC) with 95% reflectivity is simulated as a secondary optical element placed above the receiver at l=500mm for further improvement (figure 6). Figure 7 shows the rays distribution over the surface of the PV cell placed at l=500mm with the SOE. It can be seen that the energy flux received increased significantly from 8.47W to 48.25W whereas the non-uniformity of rays distribution remained low at 2.79.

Using SOE increased the received power while maintaining the non-uniformity at low value. Table 1 lists the received power, non-uniformity, optical efficiency and concentration ratio obtained with the PV placed at different distances from the Fresnel lens and with the SOE.

Figure 8 shows the resulted temperature profile with the ray distribution of the designed Fresnel lens after increasing l to 500mm and adding SOE; the temperature distribution is more uniform. The calculated optical efficiency is 77.2% which produces concentration ratio of 481X. The maximum surface temperature is less than 316K and the average temperature is significantly lower than the case with the PV placed at the focal point.

Figure 9 shows the effect of the secondary optical element height on the uniformity and received power in case of l=500mm. It can be seen that increasing the SOE height resulted in decreasing the non-uniformity to reach minimum level at SOE height of 60 mm. Further increase of the SOE height resulted in increasing the non-uniformity. As for the received power, it increased from 40 to 48W with increasing SOE height from 15 to 30mm and remained around 48W until SOE height of 60mm and then decreased with further SOE height increase. 60mm reflector is the ideal height where the surface rays non-uniformity is minimal and received power is maximal.
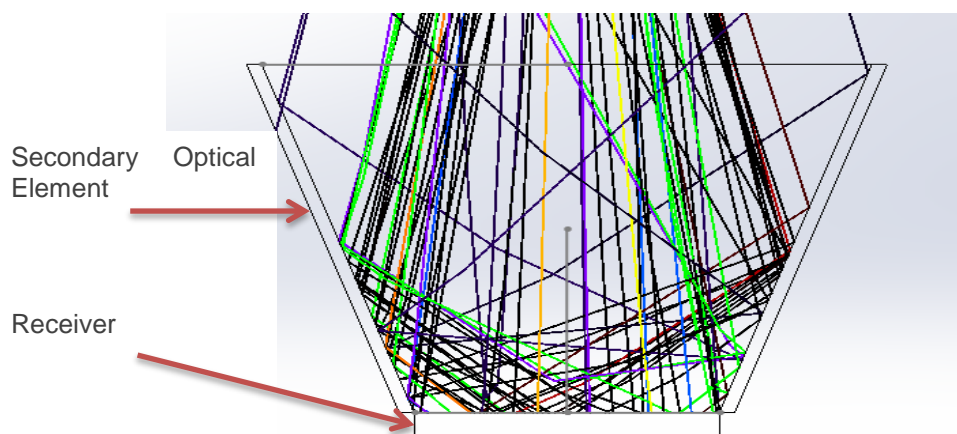
Figure 6: Rays reflected to the receiver by SOE
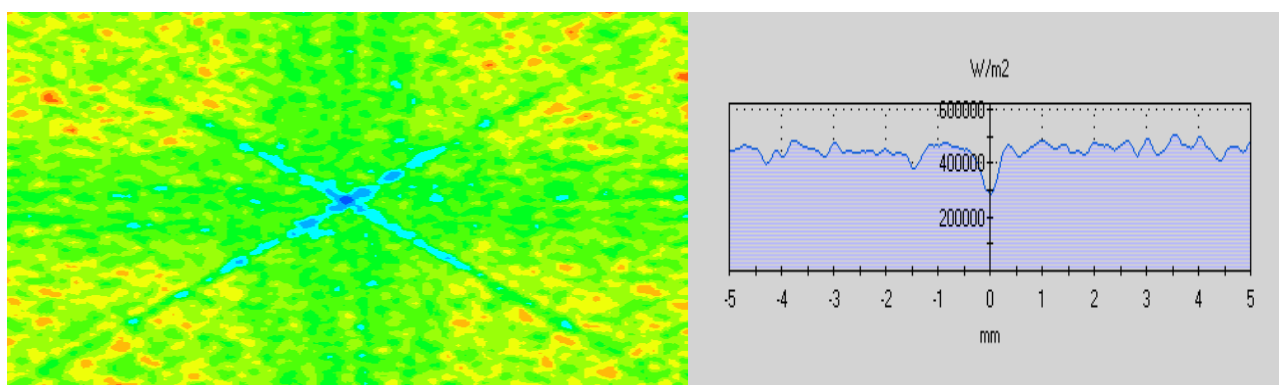
Figure 7: irradiance distribution for l= 500mm including 60 mm height reflector
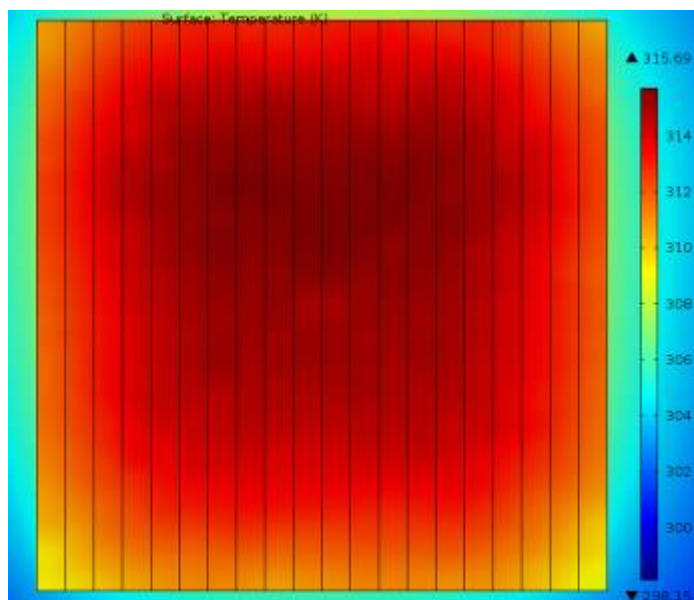
Figure 8: 2D image of temperature distribution on the solar cell

Table1: Simulation results

Case	Received Power (W)	Non-uniformity standard Deviation	Optical efficiency (%)	Resulted CR
original design (f = 460mm)	49.07	842.92	78.5%	491X
l =475mm	42.04	23.15	67.0%	420X
l =480mm	36.86	12.68	59.0%	369X
l =485mm	28.27	10.33	45.0%	283X
l =490mm	18.18	7.07	29.0%	182X
l =500mm	8.47	3.66	14.0%	85X
l = 500mm and 60mm height SMC	48.25	2.79	77.2%	481X

3.3 Effect of Secondary Optical Element height
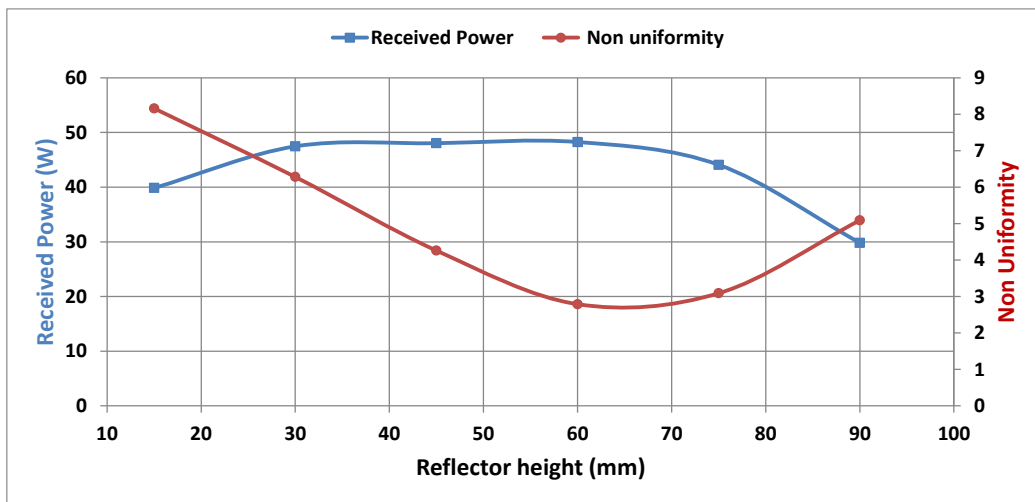
Figure 9: Reflector height vs Received power & non uniformity

3.4 Effect of Secondary Optical Element material reflectivity

Figure 10 shows that increasing the SOE material reflectivity would enhance the received power and as a result the total optical efficiency. The received power increased from about 25 to 50W by increasing the SOE material reflectivity from 50 to 95%. Similarly, the optical efficiency increase from about 40 to 80% by increasing the SOE material reflectivity from 50 to 95%.
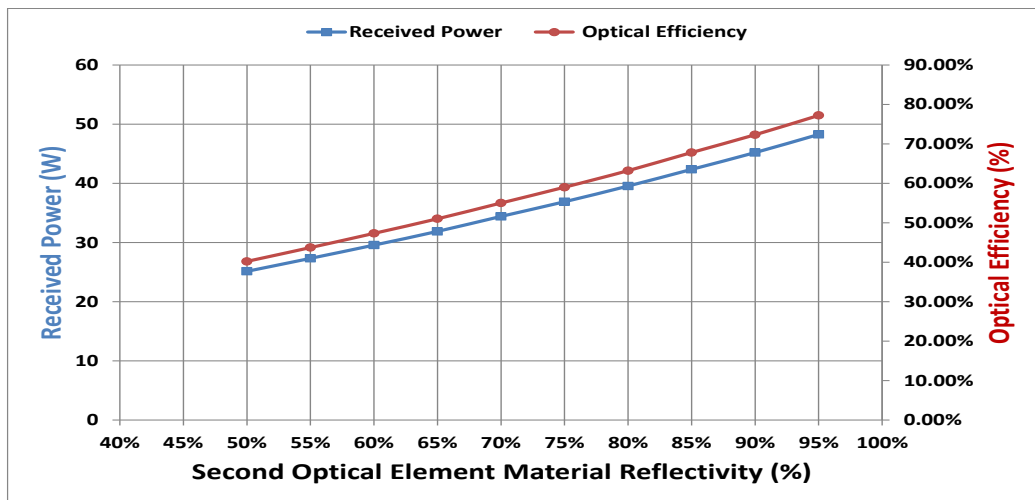
Figure 10: SOE material reflectivity vs Received power & Optical efficiency

4. CONCLUSIONS

Concentrating solar radiation on PV cells has the potential of reducing the number of PV cells used. Received radiation uniformity and hot spot are challenging issues in CPV which needs to be considered when using the Fresnel lens. Ray tracing using advanced engineering software is a powerful tool to analyse the optical performance of solar concentrators and optimise their designs. In this work the effect of varying the distance between the Fresnel lens and the receiver with and without SOE in terms of optical efficiency and illumination uniformity on the solar cell surface was investigated. The optical simulation results showed that increasing the gap between the Fresnel lens and the solar cell from focus position at 460 to 500mm and placing a small square reflector above the PV significantly improve the surface illumination uniformity. Also, simulation results showed that 60mm height SMC made from 95% reflective material is the optimal reflector that can be integrated with the developed Fresnel lens as a secondary optical element. Moreover, higher reflective material for SOE leads to a better optical efficiency and received power by the PV as shown in figure 10. Thermal simulation results demonstrated that PV surface average temperature is much lower after introducing the SOE due to the more uniform energy distribution unlike the case where energy is concentrated in a very small area leading to hot spot.

5. REFERENCES

AVERAGE, T. & Data, E., 2014. Enhanced Fresnel Assembly - EFA Type: 3C42A – with 10x10mm^2 CPV TJ Solar Cell Application: Concentrating Photovoltaic (CPV) Modules. , pp.0–3.

BAIG, H., Heasman, K.C. & Mallick, T.K., 2012. Non-uniform illumination in concentrating solar cells. *Renewable and Sustainable Energy Reviews*, 16(8), pp.5890–5909.

BENÍTEZ, P. et al., 2010. High performance Fresnel-based photovoltaic concentrator. *Optics express*, 18(9), pp.A25–40.

HERNÁNDEZ, M. et al., 2008. High-performance Kohler concentrators with uniform irradiance on solar cell. In *Optical Engineering+ Applications*. p. 705908.

HOEVEN, M., 2011. *Solar Energy Perspectives*, International Energy Agency.

KERZMANN, T. & Schaefer, L., 2012. System simulation of a linear concentrating photovoltaic system with an active cooling system. *Renewable Energy*, 41, pp.254–261.

LEUTZ, R. & Suzuki, A., 2001. Nonimaging Fresnel lenses: design and performance of solar concentrators, Springer.

MADHUGIRI, G.A., 2012. High solar energy concentration with a Fresnel lens : A Review. , 2(3).

MAH, O., 1998. Fundamentals of photovoltaic materials. *National Solar Power Research Institute*, pp.1–10.

MICHELI, L. et al., 2013. Opportunities and challenges in micro- and nano-technologies for concentrating photovoltaic cooling: A review. *Renewable and Sustainable Energy Reviews*, 20, pp.595–610.

MIN, C. et al., 2009. Thermal analysis and test for single concentrator solar cells. *Journal of Semiconductors*, 30(4), p.044011.

PAN, J.-W. et al., 2011. High concentration and homogenized Fresnel lens without secondary optics element. *Optics Communications*, 284(19), pp.4283–4288.

SKOPLAKI, E. & Palyvos, J. a., 2009. On the temperature dependence of photovoltaic module electrical performance: A review of efficiency/power correlations. *Solar Energy*, 83(5), pp.614–624.

THERISTIS, M. et al., 2012. Design and numerical analysis of enhanced cooling techniques for a high concentration photovoltaic (HCPV) system. *27th European Photovoltaic Solar Energy Conference and Exhibition*, pp.260–265.

TWIDELL, J. & Weir, T., 1986. *Renewable Energy Resources*, Abingdon, UK: Taylor & Francis.

VICTORIA, M. et al., 2013. Characterization of the spatial distribution of irradiance and spectrum in concentrating photovoltaic systems and their effect on multi-junction solar cells. *Progress in Photovoltaics: Research and Applications*, 21(3), pp.308–318.

355: Effect of dusty environment on the electrical performance of different photovoltaic modules

ADEL ALDIHANI[1], ABDULRAHMAN ALDOSSARY[1], RAYA AL-DADAH[1],
SAAD MAHMOUD[1], AYMAN AL-QATTAN[2]

1 University of Birmingham, School of Mechanical Engineering, AXA178@student.bham.ac.uk
2 Kuwait Institute for Scientific Research, energy and building research centre, aqattan@kisr.edu.kw

With high solar radiation during most parts of the year (7.65 kWh/m2.day), Kuwait is showing increased interest in solar energy technology. Despite the high solar radiation, Kuwait suffers from dust and high ambient temperature. This work experimentally investigates the performance of two types of solar PV modules based on monocrystalline and polycrystalline silicon cells under Kuwait environment. The effects of dust and ambient temperature on the PV modules performance were investigated over a period of 12 months where measurements of input solar radiation, voltage, current, cell surface temperature and accumulated dust were carried out. Measurements at two different days where ambient temperatures are 41°C and 15°C with similar radiation level of 1000 W/m2 revealed that the percentage power output reduction of dusty polycrystalline module was higher than dusty monocrystalline module compared to the clean testing. Compared to the clean PV, the monocrystalline dusty module has shown 21% and 19.5% reduction in power output while the polycrystalline dusty modules showed 28% and 25% loss in power output at hot and cold day, respectively, therefore, the monocrystalline is more suited for hot and dusty environments like Kuwait.

Keywords: crystalline PV cell, dust, irradiance, Kuwait

1. INTRODUCTION

Solar energy is a main form of renewable energy and is receiving global interest due to increasing energy needs and concerns of environmental impacts. Kuwait is located on latitude of 29.22^0N and enjoys high solar radiation and ambient temperature in most parts of the year. However, Kuwait suffers from the dust and sand storms as a result of its dryness, very little vegetation, weightless-textured surface soil and frequent unstable airstreams (Al-hurban and Al-ostad, 2009, p. 3). In many applications, the efficiency of PV modules efficiency in outdoor set up are mainly reduced near 10 - 25% because of failures in wiring, inverters, and soiling "dust" (Mani And Pillai, 2010, p. 1). Salim et al. (SALIM et al., 1988, p. 2) measured the PV modules power output in Saudi Arabia (similar environment to Kuwait) over 12 months period where 32% drop in the power output was noticed. The airborne dust accumulated on PV module surfaces decreases their transmittance and causes a decline in their power output performance. Wakim et al. (Wakim, 1981, p. 4) reported a decrease in PV power by 17% because of sand deposition on PV modules in Kuwait after one week. Additionally the study also implied that the effect of dust on PV performance would be higher in summer than in winter. In another study on the impacts of dust on PV modules in Germany (SCHILL et al., 2015, p. 4), it was stated that the dust on PV module only caused a 17-20% efficiency reduction compared to clean module. PV modules performance clearly affected when dust grains are accumulated on the modules surfaces mainly due to the dust affecting the absorption, reflection, and transmission of the incident solar irradiance on the module surface creating temperature variations (Mekhilef et al., 2012, p. 3). Catelani et al. (Catelani et al.,2012, p.2), showed that the dust causes a drop of the transmittance of PV cell coating which led to a significant degradation of PV cell electrical current.

This work experimentally investigates the effect of dust accumulation and ambient temperature on the performance of two PV modules namely monocrystalline and polycrystalline in the harsh climatic conditions of Kuwait. All relevant parameters like voltage, current, module temperature and irradiance which determine the characteristics and the power output of the modules were monitored on a continuous basis throughout the measurement period. These measurements were taken for clean and dusty PV module with time on a daily basis over a period of one year. Throughout this period of measurement no planned cleaning procedure was applied to the dusty one while the clean one was kept clear through daily cleaning process. The test methods and procedures chosen for this purpose are based on consensus standards of relevant committees of the Institute of Electrical and Electronics Engineers (IEEE) and the American Society for Testing and Materials (ASTM). The purpose of this investigates is to compare the performances of PV technologies (monocrystalline and polycrystalline) under the impact of Kuwait environment.

2. KUWAIT ENVIROMENT

The global hemispherical solar radiation data on horizontal plane was obtained from the Environment Public Authority of Kuwait (see figure 1).
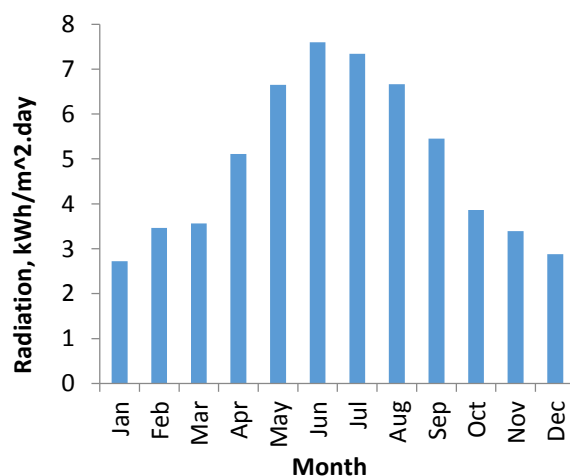
Figure 1: Monthly average global radiation on horizontal plane in Kuwait (Environment Public Authority of Kuwait).

Figure 1 shows that Kuwait receives abundant solar radiation exceeding 7000 Wh/m²day in June and the duration of sunshine is very long. Meanwhile, in January the total solar radiation received is below 3000

Wh/m²day. The yearly average received solar radiation reach up to 5500 Wh/m²day. As a result of its low topographic position and with little or no vegetation, Kuwait is vulnerable to sand storms where airstreams discharge silt, clay and sand particles from ground and carry them through the storms. The storms crossing Kuwait carries substances of sediment containing 85% sand, clay and the rest is silt (Al-dousari et al., 2012, p. 5). Normally, dust movement in Kuwait is low throughout winter, rises in March-April, and reaches highest in July as shown in figure 2.
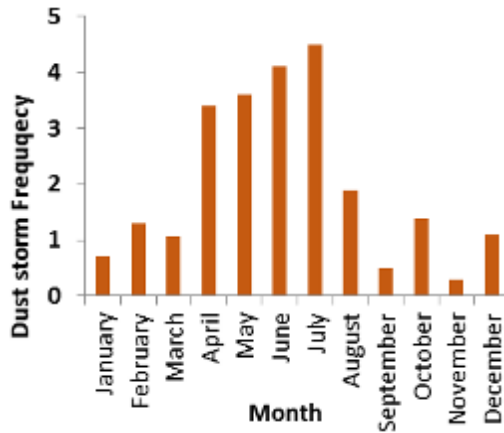
Figure 2: Number of dust storm days in Kuwait in monthly average (2011-2013).

During summer, average daily high temperatures range from 40 to 48 °C. The maximum ever temperature reported in Kuwait was 53.9 °C at west area on July 2012 which is the highest reported temperature in Asia and besides the third highest in the world (Al-dousari et al., 2012, p. 4). Figure (3) illustrate the average ambient temperature in Kuwait for one year.
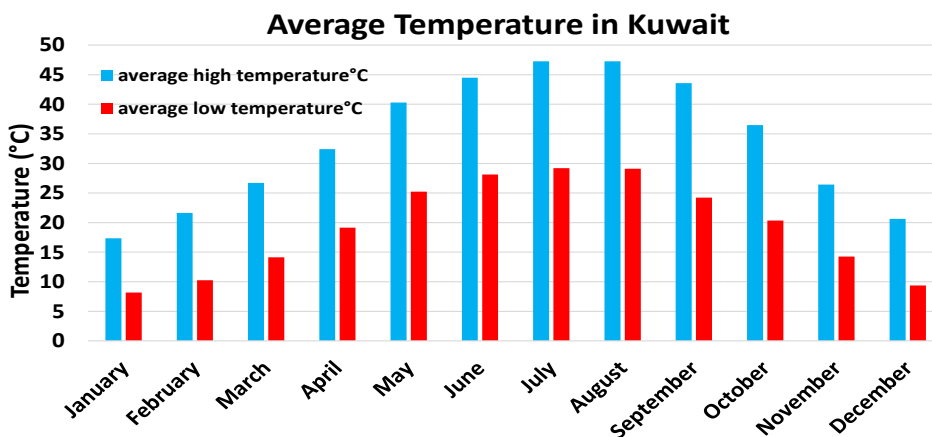
Figure 3: average high and low temperature in Kuwait (2011-2013).

3. EXPERIMENTAL WORK

The outdoor measurements were performed in the site of Kuwait Institute of Scientific Research (KISR) 30ºN latitude. The system consists of two pairs of PV modules made from two different cell technologies monocrystalline and polycrystalline. The mounting structure was installed facing true south and tilted 30º which corresponds to the estimated latitude of Kuwait (optimal inclination angle for Kuwait). As the main objective of this work is to investigate the effect of dust and temperature on module performance, the PV module current (I), voltage (V), Power, module temperature as well as the ambient temperature and in plane module radiation were measured. Table 1 shows the performance of the two PV modules under Standard Testing Conditions (STC) of solar irradiance 1000 W/m², air mass (AM) of 1.5 and cell temperature of 25 °C.

Table 1: Modules technical data as STC.

Technology	Monocrystalline	Polycrystalline
No. of cells	72 in series	60 in series

Module efficiency	16.4%	14.4%
Nominal Power	210 W	240 W
Nominal Voltage	41.3 V	30.2 V
Nominal Current	5.09 A	8.02 A
Open circuit Voltage	50.9 V	37 V
Short circuit Current	5.57 A	8.61 A
Power Temperature Coefficient	-0.30%/C	-0.46%/C

The experimental setup was equipped with a range of instrumentation including a Kipp & Zonen pyranometer with sensitivity of 7 to 14 µV/W/m^2, -40 ^{o}C to +80 ^{o}C operational temperature and +/-10 W/m^2 error for measurement of the solar radiation on the module plane. The pyranometer was mounted on the inclined plane of the PV modules (30°) and cleaned on daily basis. Also, the temperature of each module was measured with temperature sensors attached on the back sheet of the PV modules centre investigated. The temperature sensors are thermally attached by a thermal conducting adhesive and isolated from the ambient temperature impact. The temperature sensor is PV-PT100 with Temperature Range of -50/+300 °C and +/- 0,6°C accuracy. Temperature sensors are coupled to specialised custom-built IV tracer/maximum power tracker units designed by National Instruments for this task. These tracer units were assembled to supply the specific data needed for the monitoring system. They read a 200-point IV data sweep in every minute, along with maximum power tracking of the module within the sweeps, which holds the modules performing at maximum power point continuously. The IV tracer maximum voltage and current readings are 250V and 10A with sweep speed of < 5 seconds per channel at 50 steps. The monitoring equipment preforms real time measurement of PV modules IV characteristics repeatedly recorded. The measurement plan was to obtain continuous measurements of V, I, P and module temperature during 12 months periods. These were determined from continuous IV measurements of the installed units. A planned data backup collection was taken every 1 month in addition to the regular data recording to indicate any non-uniformity of the modules outputs. The measured module and meteorological data were transferred to a data acquisition system held at KISR renewable energy building. The flow chart in figure 4 shows the measurement system of the installed units.
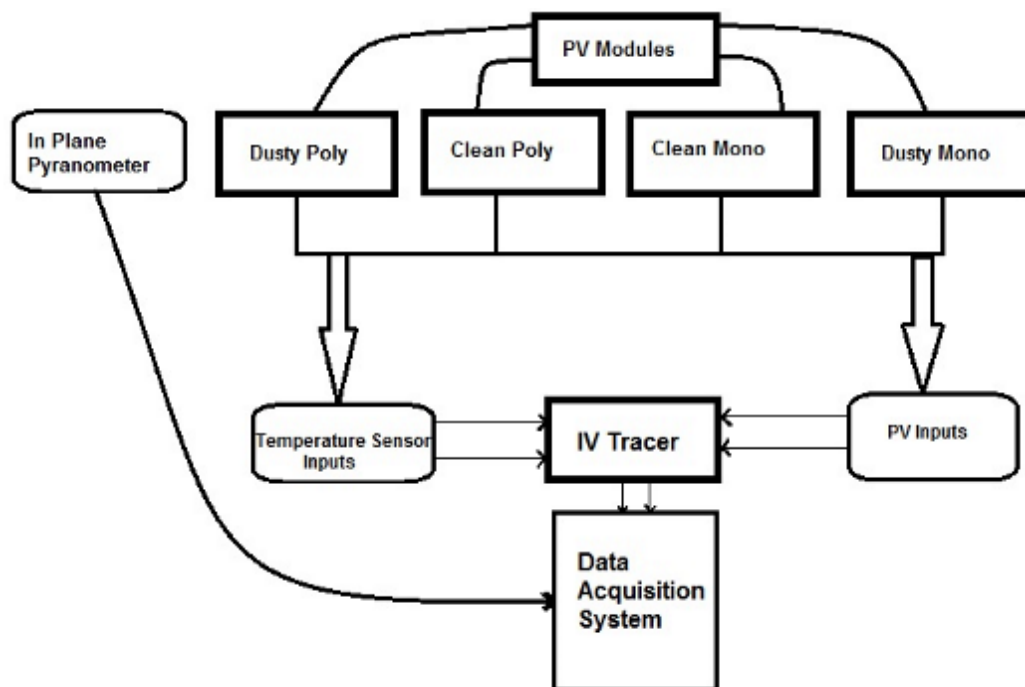
Figure 4: experimental data acquisition system at KISR

The PV modules installed in (KISR) are shown in figure 5 where the dust accumulated on one of the PV modules surface after 12 months without cleaning. The PV modules installed next to each other and exposed to similar environment conditions. One module of each PV type was kept clean for comparison purpose.

Figure 5: Accumulated dust on PV modules installed in Kuwait, from the left, dusty polycrystalline, clean polycrystalline, dusty monocrystalline and clean monocrystalline.

The maximum power is evaluated from the maximum product of voltage times current. The measured IV, radiation, module temperature, date and time are stored on the database and gathered for all records of all modules. In this investigation an average of 10 minutes data sampling in a period of 12 months were used. The maximum power output point data sets that appeared once the solar radiation was between 100 and 1000 W/m² , were chosen with the purpose of minimising the effect of large AM during the morning and the evening. The data was investigated during 20 of December 2013 and 1 of July 2013 with conditions of stable sunlight and calm airstreams around midday.

4. RESULTS AND DISCUSSION

The PV Module output depends upon solar radiation in addition to module temperature. As illustrated in the figures 6 (a, b, c and d) the highest in plane solar radiation and variation of modules temperature in hot and cold day. Meanwhile, the average ambient temperatures in the hot day is 41°C and cold day is 15°C. The module temperature showed an increasing movement with solar radiation. The highest radiation intensity was recorded at midday when sun ray is perpendicular on the surface of PV module. The monocrystalline modules temperature remains below the polycrystalline module temperature at all time. The ranges of recorded values are 300 W/m^2 in the morning and as well as late afternoon while at midday equal 1000W/m² .

 Figure 6 (a,b) shows solar radiation measurement per hour in hot and cold day. Figure 6(b) shows radiation intensity duration is lower during a cold day than those in hot day especially in the midday. Solar radiation hours also changes according to seasons, in winter the sun hours becomes low and high in summer because sun ray's angle changes due to the earths tilt angle (Duffie and Beckman, 2006, p. 96). According to the below figures 6 (a and b) can be conclude that the solar radiation is sufficient to develop a PV system in Kuwait.

Before 7 am and After 4 pm, the module temperature becomes low, the reason behind this is decreasing of solar radiation which reduces the photovoltaic process and module temperature. The module temperature is higher in midday due to high solar radiation. As showed in the figure 6(c, d) the hourly measured module temperature for clean and dusty PV panels at the hot and cold day. Furthermore, the dusty panels produce lower heat than the clean panels by up to 3 degrees at noontime because of the dust accumulated layer reduces the radiation rays on the module surface. Where, the measured accumulated dust layer on PV module is 0.15 mm

The characteristics of PV module based on four main factors are: solar radiation, module temperature, and the module and cells connection. The solar radiation has slighter impact than module temperature on the voltage; in opposite way, the current varies according to changes in the irradiation, increasing as this increases because of the collection and generation of high- generated carriers as stated by Bunea et al (2006, p. 1). The differences in the solar radiation lead to variation in the measured current which affects the power output. As illustrated in figure 7 30% has dropped for dusty polycrystalline and 22% for dusty monocrystalline at hot day. Moreover, at the peak hours approximately 2 amp and 1 amp for dusty polycrystalline and dusty monocrystalline, respectively. In another hand, for cold day dusty polycrystalline current dropped 28% while the dusty monocrystalline dropped 18% at midday because that the daylight times are minimal.
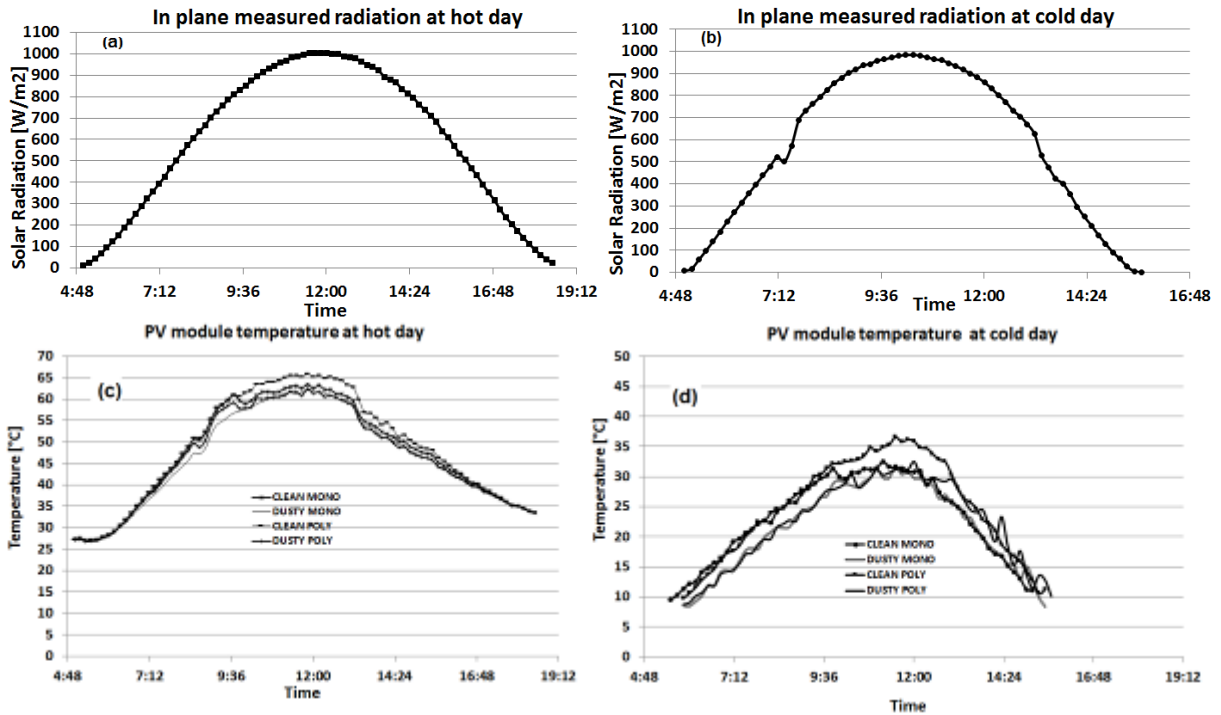
Figure 6: Hourly measured in plane radiation (a, b) and PV module temperature (c, d) of clean and dusty (polycrystalline and monocrystalline) during hot and cold day.
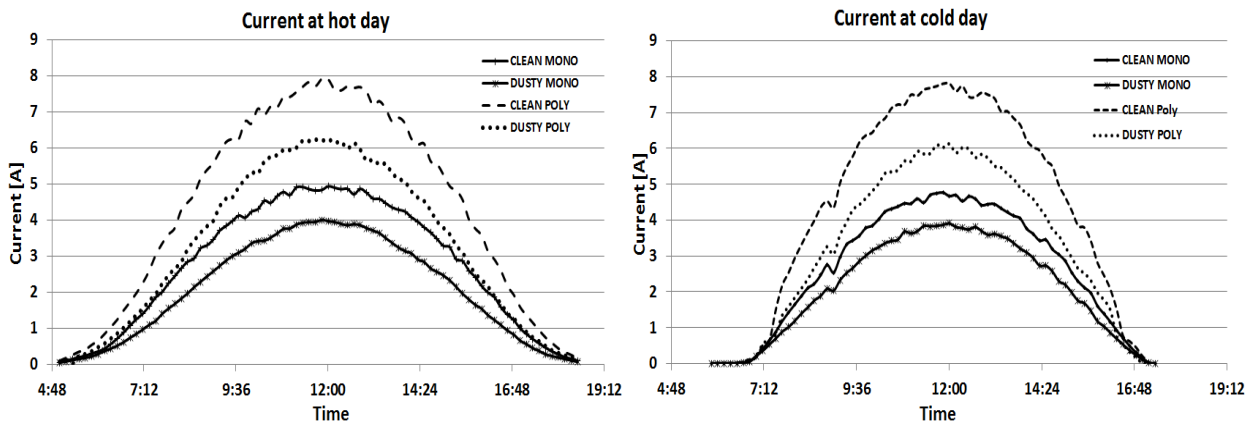
Figure 7: Hourly measured current of clean and dusty (polycrystalline and monocrystalline) PV modules at hot and cold day.

Figure 7 shows the comparison of the produced current of all modules clean and dusty in the hot and cold day. The current percentage drop of monocrystalline modules are lower than polycrystalline module at all times. Due to its better light absorbing characteristic, this result supported by Schaefer-Tec (2015, p. 2). Module temperature has small effect on the measurement of the current. Opposite, the module temperature is proportional to the voltage, otherwise, if the module temperature increased the voltage will be decreased. (Jiang et al, 2011, p. 3).

The module area has effect on the measurement of the voltage, because the PV cells are connected in series that leads to improve the voltage, despite of the available current has not affected by the series connection (see table 2). As illustrated in the figure 8 the voltage is highest drop in the noon hours where the radiation and module temperatures are maximum for all PV modules. In another hand, the voltage peaks in the morning (around 7 am) and afternoon (around 3 pm) at all days (hot and cold), when the radiation and module temperature are moderate (not high and not low). In addition to, the dusty modules produce higher voltage in the clean module, in more specific, 3 voltage in the hot day and 2 voltage in the cold day at midday. In conclusion, the causes behind these results are the dust layers lead to decrease the radiation rays and heat distribution on the panel surface.
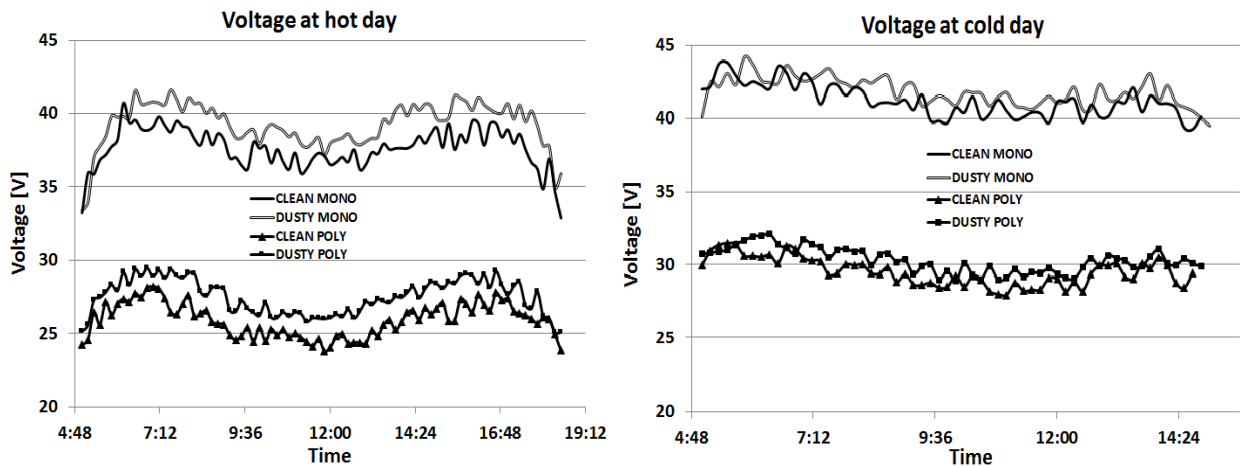
Figure 8: hourly measured voltage of (polycrystalline and monocrystalline) PV modules at hot and cold day.

From figure 8 can be noticed that the voltage for all PV modules (clean and dusty) have revers relationship with the module temperature in both days. Moreover, all the voltage values for PV modules are lower than STC in the both days as illustrated in table 3.

Table 3: Measured voltage value of Monocrystalline and polycrystalline at noon time compared STC.

PV modules	Hot Day Voltage	Cold Day Voltage	STC Voltage
Clean Monocrystalline	38	41	41.3
Dusty Monocrystalline	36	40	41.3
Clean polycrystalline	26	28	30.4
Dusty Polycrystalline	23.5	29	30.4

The output of PV modules power in the outdoor conditions is differ from STC according to unsteady outdoor conditions. The hourly measured module power output in hot and cold day for all modules is shown in Figure 9. The modules power output has presented similar relation with solar radiation. In parallel, at noon time, output power of the modules were highest corresponding to the highest solar radiation. The percentages were decreased in the module power, specifically, in the dusty monocrystalline equal 21% while in the dusty polycrystalline is 28% in the hot day. Whereas, the percentages for cold day were 19.5% and 25% respectively. These results were measured in the noon time compared to clean modules when the radiation is high. The monocrystalline modules have lower power temperature coefficient than polycrystalline modules (see table 1).
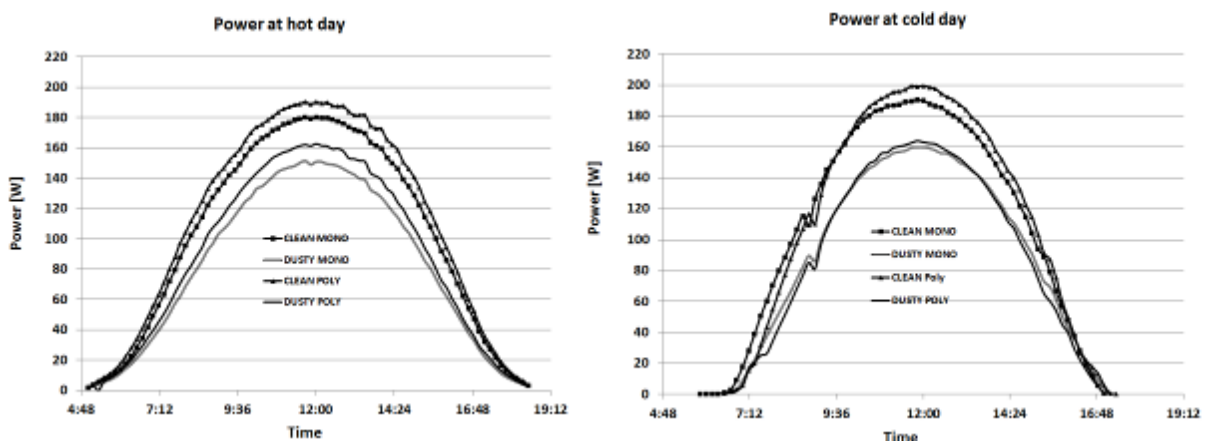
Figure 9: Hourly measured power output of (polycrystalline and monocrystalline) PV modules during hot and cold day.

The monocrystalline dusty modules has shown 28% and 23% lower percentage module power loss than 35% and 31% of polycrystalline dusty modules power loss in hot and cold day, respectively, compared to the standard testing conditions (see figure 9 and table 1). The polycrystalline module was low because the high power temperature coefficient compared to monocrystalline module in all conditions (dusty and clean) in both days (hot and cold) (see table 1).

5. CONCLUSION

The effect of dust deposition on the surfaces of photovoltaic modules was experimentally studied under Kuwait environment. Two PV technologies (monocrystalline and polycrystalline silicon) were exposed during 12 months on the site of Kuwait Institute for Scientific Research (KISR). The results indicated that performance of PV modules decreased progressively with dust deposited on its surface and high PV module temperature. During the hot day, the output power of dusty monocrystalline and dusty polycrystalline PV modules showed reduction of 21% and 28% respectively compared to the clean ones. The dusty modules power output during cold day showed a lesser degradation compared to the hot day where, the percentage power output reduction was 19.5% for the monocrystalline module and for the polycrystalline module it was 25%. Therefore both PV modules require continuous cleaning to reduce the power output losses. However, monocrystalline PV suffer less in dusty environment as that of Kuwait with lower losses at colder environments.

6. REFERENCES

AL-DOUSARi, A., Al-Awadhi, J. and Ahmed, M. (2012). Dust fallout characteristics within global dust storm major trajectories. Arab J Geosci, 6(10), pp.3877-3884.

AL-HURBAN, A. and Al-Ostad, A. (2009). Textural characteristics of dust fallout and potential effect on public health in Kuwait City and suburbs. Environmental Earth Sciences, 60(1), pp.169-181.

BUNEA, G., Wilson, K., Meydbray, Y., Campbell, M. and De Ceuster, D. (2006). Low Light Performance of Mono-Crystalline Silicon Solar Cells. 2006 IEEE 4th World Conference on Photovoltaic Energy Conference, 2, pp.1312 - 1314.

CATELANI M, Ciani L, Cristaldi L, Faifer M, Lazzaroni M, Rossi M (2012). Characterization of photovoltaic panels: The effects of dust. Instrumentation and Measurement Technology Conference (I2MTC), 2012 IEEE International. 9-12 September, 2012, pp 45-50.

DUFFIE, J. and Beckman, W. (2006). Solar engineering of thermal processes.3rd edition New York: Wiley.

JIANG, H., Lu, L. and Sun, K. (2011). Experimental investigation of the impact of airborne dust deposition on the performance of solar photovoltaic (PV) modules. Atmospheric Environment, 45(25), pp.4299-4304.

MANI, M. and Pillai, R. (2010). Impact of dust on solar photovoltaic (PV) performance: Research status, challenges and recommendations. Renewable and Sustainable Energy Reviews, 14(9), pp.3124-3131.

MEKHILEF, S., Saidur, R. and Kamalisarvestani, M. (2012). Effect of dust, humidity and air velocity on efficiency of photovoltaic cells. Renewable and Sustainable Energy Reviews, 16(5), pp.2920-2925.

SALIM A, Huraib F, Eugenio N (1988). PV power-study of system options and optimization. In Proceedings of the 8th European PV Solar Energy

Schaefer-tech, 2015. [Online] Available at: http://www.schaefer-tec.com/fileadmin/user_upload/sortiment/3d-profilometer/Sensofar/App_Notes--_Solar_Cells.pdf. [Accessed 1 May 2015].

SCHILL, C., Brachmann, S. and Koehl, M. (2015). Impact of soiling on IV-curves and efficiency of PV-modules. Solar Energy, 112, pp.259-262.

WAKIM F (1981). Introduction of PV power generation to Kuwait. Kuwait Institute for Scientific Research, Kuwait City. Report no.440.

357: Optical analysis of flux uniformity and efficiency in low concentrating PV systems

Abdulmaged ALGAREU[1] ,Abdulrahman ALDOSSARY[1],
Saad. MAHMOUD[1], Raya. AL-DADAH[1]

1University of Birmingham, Edgbaston, Birmingham, United Kingdom. B15-2TT, aoa124@bham.ac.uk

Solar concentration has the potential to replace the expensive PV cells with cheaper optical elements and enhancing the overall output. Two main types of concentrators are used in CPV systems which are either reflective or refractive (Fresnel lens). One of the advantages can be achieved from using refractive concentrators is compact height which is not available in reflective concentrators especially in high concentration ratios. But the main problem with refractive concentrators is the hot spot generated at the centre of the PV cell. In this paper, different Fresnel lens parameters affecting the optical efficiency and flux distribution have been investigated, including groove width, draft angle, focal length, f/number, lens thickness and PV cell position beneath the Fresnel lens. Then, a Square Fresnel Lens (SFL) of Concentration Ratio (CR = 10) and design focal length (f = 145 mm), was compared with a reflective Square miniature Concentrator (SMC) with the same CR in terms of uniformity, optical efficiency and compactness. Results showed that optical efficiency increases with the decrease of groove width and draft angle. Simultaneously, optical efficiency is fixed with different lens concentration ratios of the same f / number, and decreases if the focal length is fixed to different concentration ratios. The best position of the PV cell for the square Fresnel lens of a focal length of 145 mm that gives good uniformity (with Standard Deviation = 3.38) is 185mm beneath the Fresnel lens with optical efficiency of 76.46% compared to the 79.47% achieved at the focal distance of 145mm but with point concentration. As for the reflective concentration with CR = 10, the optical efficiency achieved is 76.56% which is comparable to that of the Fresnel but with larger height of 230mm.

Keywords: Optical efficiency, low concentration, reflective concentrator, flux uniformity, Fresnel lens.

1. INTRODUCTION

Different types and configurations of solar concentrators have been demonstrated to exploit solar energy using concentrated thermal and photovoltaic systems during the past decades. Concentrator geometries can be classified as reflective concentrators such as Dish concentrators (Zhu, Boehm et al. 2011, p: 2264), 3D Elliptical Hyperboloid Concentrator EHC (a/b=1) (Saleh Ali, O'Donovan et al. 2013, p57), V-trough concentrator (Sangani, C.S et al. 2007, p:343) and compound parabolic concentrators (CPC) (Guiqiang, Gang et al. 2012, p:343), or refractive concentrators such as groove in and groove out Fresnel lenses (Leutz and Suzuki 2001p.p: 67-68), and flat, roof and curved Fresnel lenses (Lorenzo and Luque 1981, p: 2941).

Investigations have been carried out on solar concentrators in terms of flux uniformity, optical efficiency and compactness. The lack of uniformly distributed flux incident on CPV system has a negative effect leading to hot spots, electrical current mismatch and consequently drop in the overall system efficiency (Baig, Heasman et al. 2012, p:1088), and may lead to damage the PV cells (Munoz, Alonso-García et al. 2011, p: 1090). A hybrid Fresnel-based concentrator was presented by (Zhuang and Yu 2014, p: 1105) with improved uniformity irradiance distribution on the solar cell without using secondary optical element (SOE) in CPV, and results showed a flux uniformity of less than 16.2 % and f-number less than 0.59. Algareu et al. have investigated the optical performance of low concentration ratio reflective and refractive concentrators for photovoltaic applications (Algareu, Mahmoud et al. 2014, p: 1107). Results showed that both types of concentrators have similar optical efficiency for concentration ratios up to 10. For concentration ratios above 10, the performance of reflective concentrators has deteriorated significantly while the refractive concentrators have retained their high optical efficiency highlighting the potential of refractive concentrators. This paper presents an optical analysis using ray-tracing technique to develop an efficient Square Fresnel lens (SFL) of Concentration Ratio (CR= 10) and investigate the effect of PV cell position relative to it. Also, the performance of such lens was compared to reflective concentrator with the same CR in terms of uniformity, optical efficiency and compactness.

2. METHODOLOGY

Ray tracing technique one of the techniques used nowadays for determining the incoming radiation to the concentrator aperture reflected or refracted rays in the concentrator, absorbed rays by the receiver, as well as the distribution of radiation on the receiver. Using OPTISWORKS software, different Fresnel lens parameters and their effect on lens optical efficiency have been investigated in this paper, such as the groove width, draft angle, fixed focal length at different concentration ratios, fixed f-number at different concentration ratios and lens material thickness. In figure 1 a schematic diagram shows the main parameters affecting Fresnel lens optical efficiency.
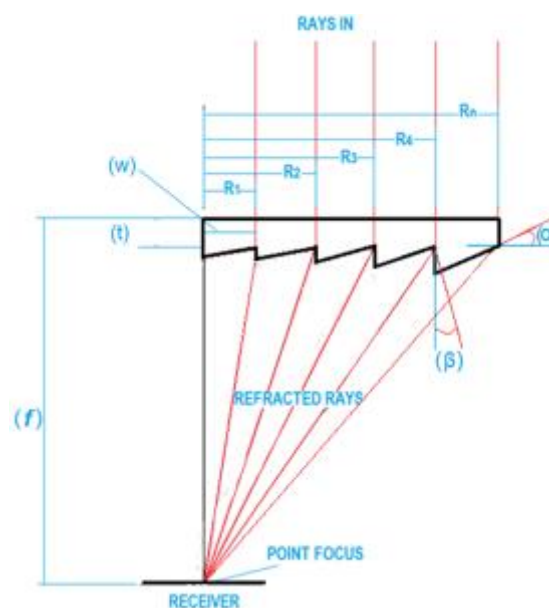
Figure 1 Different Fresnel Lens design parameters

Where R1, R2, R3, R4….Rn: represent the distance of extreme paraxial ray from the optical axis in Fresnel lens, P1, P2 and P3 is the PV cell different investigated positions, f is the focal length, W is the groove width, t is the Fresnel lens thickness excluding groove height, β is the draft angle and α is the groove facet angle which is calculated by the following equation (Leutz and Suzuki 2001, p: 68):

$$\tan \alpha = \frac{R}{n\sqrt{R^2 + f^2} - f}$$

Where *n* is the refraction index for Fresnel lens and in this case is the PMMA refraction index (*n* = 1.49).

According to the equation of suitable groove width (pitch) (Davis and Kühnlenz 2007) which is:

$$Groove\ Width = 1.5 * \sqrt{\lambda * f}$$

And λ is the wavelength, five different wave lengths have been chosen in investigating the effect of groove width on the lens optical efficiency with CR= 10, *f* = 43.32 mm and D = 36.8 mm as shown in table 1.

Table 1 Calculated groove width values based on focal length and different wavelengths

Wave type	Wave length λ (nm)	Focal length *f* (mm)	Lens diameter D (mm)	Groove width (mm)
Ultraviolet	250	43.32	36.8	0.16
Visible light	550 (centre of Visible light)	-	-	0.23
Infra-red	3217	-	-	0.56
-	higher	-	-	1.12
-	higher	-	-	2.26
-	higher	-	-	4.52

Draft angle (shown in figure 1) is the angle specified with respect to the normal of lens (Davis and Kühnlenz 2007, p: 52), and it is made for the mould release and avoid production difficulty (3M 2009, p: 1). Draft angle has been investigated, in terms of its effect on the lens optical efficiency, by changing the angle from 0º which is normal to the lens plane to 2º in interval of 0.5º.

Fixed focal length (*f*) of 20 mm was used in designing Fresnel lenses with different concentration ratios for a receiver of 100 mm^2 to investigate the effect of concentration ratio in the case of fixed focal length on the optical efficiency.

F / number is the ratio of the focal length to the lens diameter, and is calculated by the following equation (Leutz and Suzuki 2001, p: 66):

$$f\ /\ number\ = \frac{f}{2R}$$

Table 2 shows the calculated focal length values for different Fresnel lens concentration ratios at fixed chosen   f / number of 1.2.

Table 2 Calculated minimum focal length at F-number 1.2 and different concentration ratios (CR: 2- 10).

CR (PV CELL =10*10 mm)	F-number	Lens diameter (D=2R mm)	Focal length
2	1.2	15.8	18.96
4	1.2	22.5676	27.08112
6	1.2	27.08	32.496
8	1.2	31.6	37.92
10	1.2	36.10	43.32

The effect of Fresnel lens thickness on the optical efficiency is investigated by changing the lens thickness (excluding the groove height) by 1 mm, starting from 1mm thickness to 5 mm.

Then, two different concentrators reflective SMC with a height (H) of 230 mm and surface reflectivity of 95% with PMMA transparent cover (transmittance 88 %), and Square Fresnel Lens SFL with a focal length (*f*) of 145 mm to be used in PV system with geometric concentration ratio of 10 have been in investigated in terms of received flux uniformity on 50 mm x 50 mm PV cell area, optical efficiency and compactness.

Figure 2 shows the SMC and Square Fresnel Lens (SFL) geometries used in investigating the flux uniformity and concentrator optical efficiency.
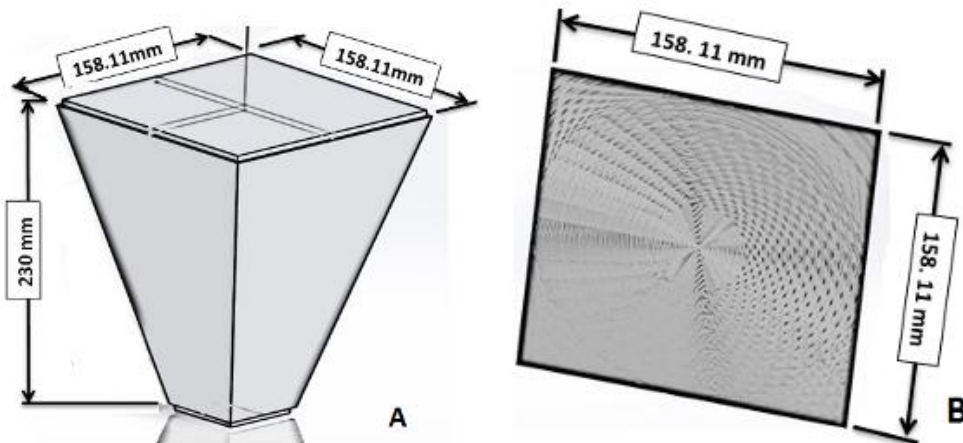
Figure 2 Reflective and refractive concentrators: A Square Miniature Concentrator (SMC) and B Square Fresnel Lens (SFL)

Simulation was carried out at irradiance of 340 W/m^2 to investigate the parameters mentioned. For the comparison of Fresnel lens, flux distribution and optical efficiency were investigated at different distances from the PV cell to determine which distance gives the optimum flux distribution and efficiency, in intervals of 5 mm above and below the focal length, and a fixed SMC optimum height shown in figure 2.

3. RESULTS

3.1 Effect of groove width on Fresnel lens optical efficiency

Depending on the suggested groove width values it is clear from figure 3 that the optical efficiency decreases as the groove width increases, but width groove width between 0.16 mm and .56 mm the drop in efficiency is not that significant.
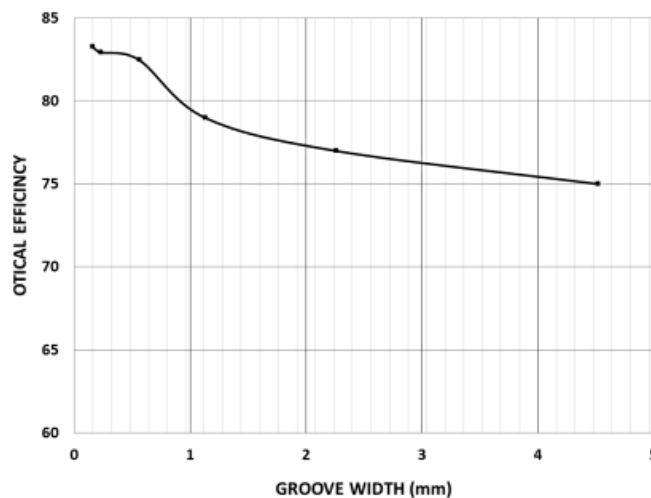
Figure 3 effect of Fresnel lens groove width on the optical efficiency

2.30. 3.2 Effect of Draft angle on Fresnel lens optical efficiency

For the draft angle effect, the Fresnel lens optical efficiency is dropped for about 3 % when the draft angle increased (from 0o to 0. 5o). For draft angle more than 0.5o there is no significant drop in the optical efficiency, even with the increase of draft angle up to 2°.
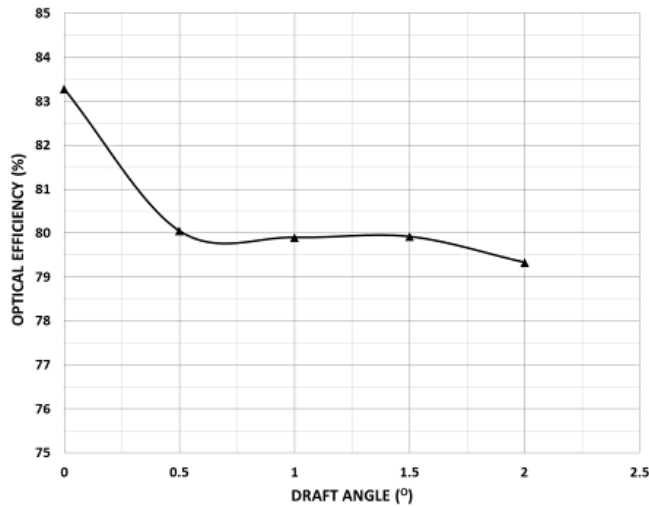
Figure 4 effect of draft angle on the optical efficiency

2.31. 3.3 Fixed focal length (f) at different concentration ratios

It is clear from figure 4 that the optical efficiency decreases with the increase of concentration ratio, if the effective focal length is fixed, reaching the Fresnel lens maximum efficiency at the one with lower concentration ratio and the minimum with higher concentration ratio, even with changing the receiver position.
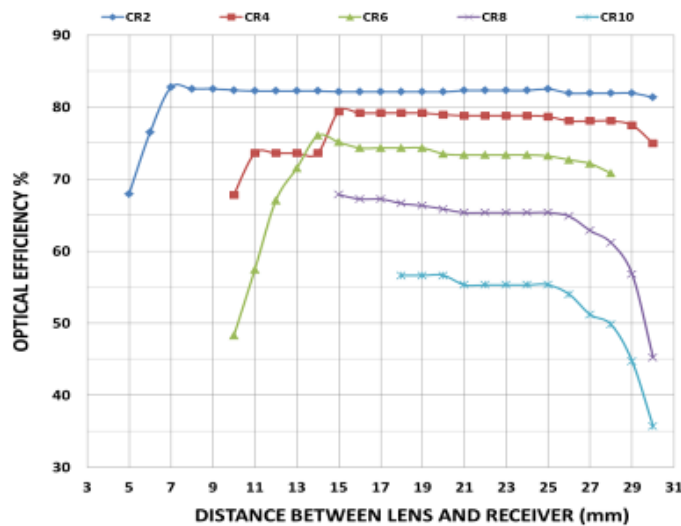
Figure 5 Optical efficiency of different Fresnel lens concentration ratios at a fixed focal length.

2.32. 3.4 Fixed f/number at different concentration ratios

In figure 6, it is noticeable that all Fresnel lenses with different concentration ratios give close optical efficiency values at a fixed f / number. This means that the driver of the optical efficiency is the ratio of focal length to the lens diameter and there is no change in the lens optical efficiency with the change of concentration ratio, even with changing the receiver position to a certain distances.
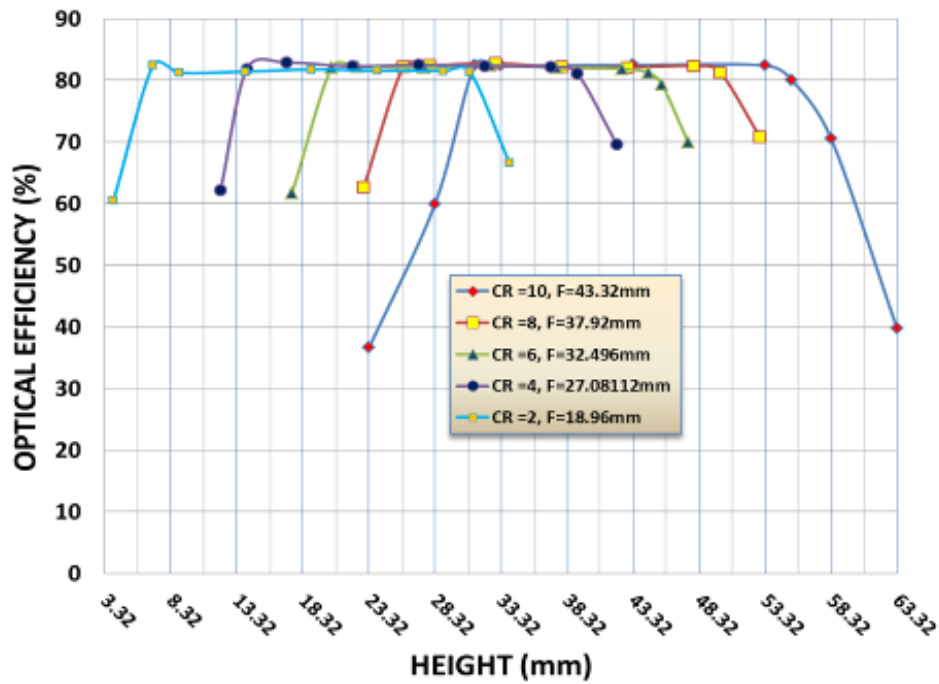
Figure 6 Optical efficiency of different Fresnel lens concentration ratios at a fixed f/ number.

2.33. 3.5 Effect of thickness on Fresnel lens optical efficiency

For the lens thickness effect, the Fresnel lens optical efficiency is dropping as the lens material thickness increases, reach its maximum of over 82 % at 1 mm thickness and the minimum of about 76 %. Figure 7 shows the effect of Fresnel lens thickness on its optical efficiency.
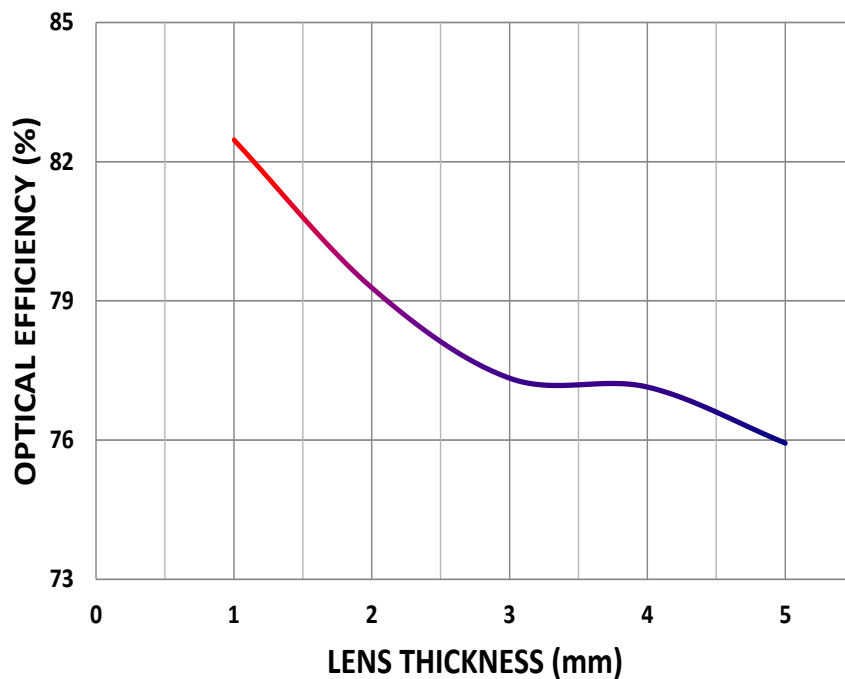
Figure 7 effect of Fresnel lens thickness on the optical efficiency

2.34. 3.6 Flux uniformity

Standard deviation (SD) for the flux distribution was calculated at all PV cell distances (105 mm to 185 mm) to determine the highest value that represents the extreme non-uniform flux distribution and lowest values

which represents the optimum flux distribution for the used Fresnel lens design. Figure 8 presents the SD calculation results and received flux distribution showing the highest SD value when the PV cell is located at the focal length (distance of 145 mm) of Fresnel lens which means large SD value from the received flux, while the PV cell distances 185mm and 105 mm showed the lowest SD values of 3.38 and 4.30 respectively. At the same time, 2D flux distribution results showed that the SMC flux in figure 8A is concentrated in a circular shape with a crossed shape of lower intensity at the centre of the PV cell with an average of 2000 W/m^2. In Fresnel lens, flux distributions at three lens distances (105 mm, 145 mm and 185 mm) are shown in figure 8 B, C and D, respectively. In figure 8B, the flux is distributed all over the PV cell showing good uniformity but with higher flux intensity (over 12000 W/m^2) at the centre of the PV cell. Figure 8C show a highly concentrated flux at a very small point (diameter of 3 mm) presenting the point focus distribution at the focal length distance. While in a distance of 185 in figure 8D showed good uniformity with an average of about 2000 W/m^2 and lower intensity at the centre of the PV cell making this PV cell distance (185 mm) and the SMC are the most suitable concentrators for the PV cells that there is no hot region at the centre of the cell. But for the compactness a Fresnel lens with distance of 185 mm is more compact than the reflective concentrator with 230 mm.
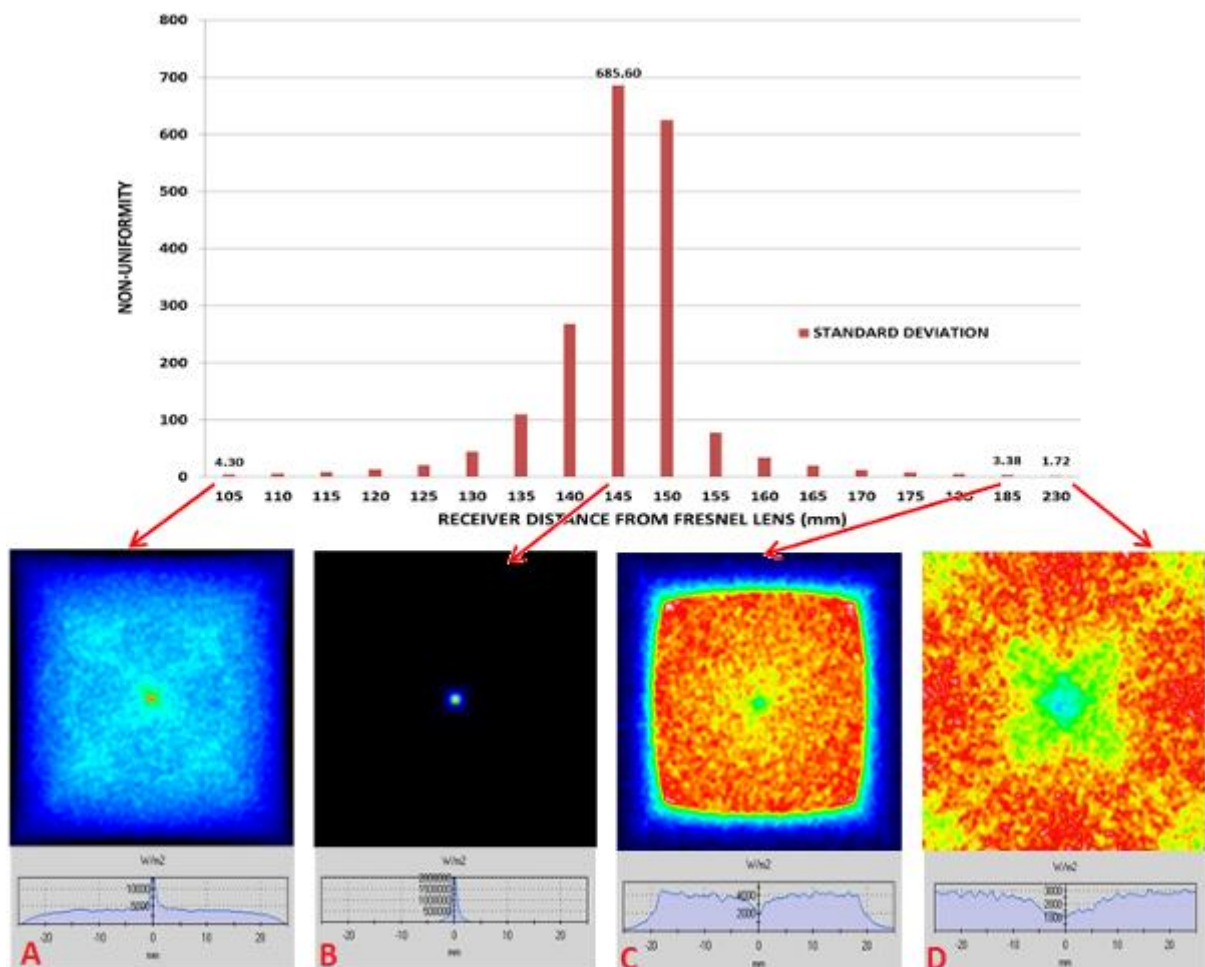
Figure 8: Standard deviation and 2D flux distribution for : A SMC (H = 230 mm), B SFL at 105 mm distance from

3.7 Optical efficiency

Simulation results showed that the four cases have a good optical efficiency with higher efficiency for the distances 105 mm and 145mm (at the focal length) of about 79 %while the gain optical efficiency at the distance 185mm and the reflective concentrator SMC is about 76% for both. Figure 9 shows the optical efficiency for the Fresnel lens at the three distances and the reflective concentrator.
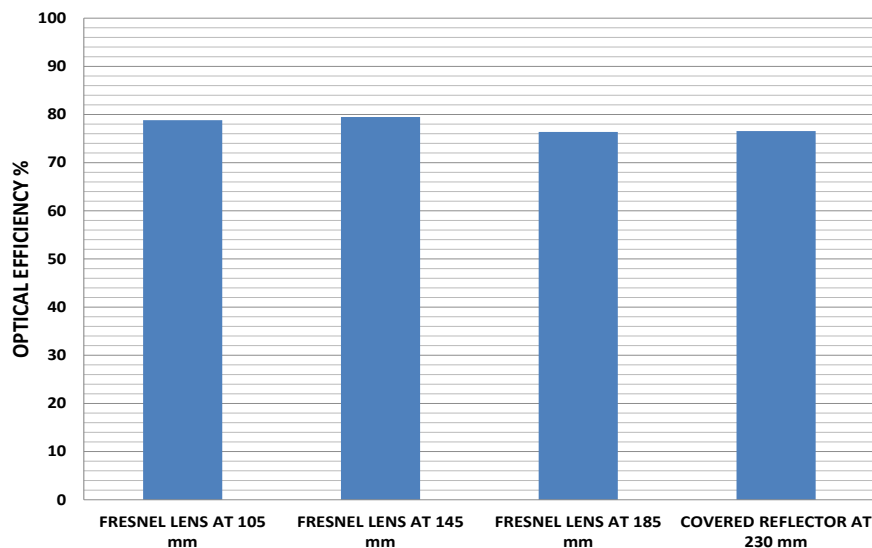
Figure 9 Optical efficiency of Fresnel lens at the three distances and the reflective concentrator.

4. CONCLUSION

An optical analysis for a refractive PV concentrator (Fresnel lens) using ray-tracing technique is presented. Different Fresnel lens parameters affecting the optical efficiency and flux distribution have been investigated, including groove width, draft angle, focal length, f/number, lens thickness and PV cell position beneath the Fresnel lens. Then, a Square Fresnel Lens (SFL) of Concentration Ratio (CR = 10) and design focal length (f = 145 mm), was compared with a reflective Square miniature Concentrator (SMC) with the same CR in terms of uniformity, optical efficiency and compactness. Results showed that optical efficiency increases with the decrease of groove width and draft angle. Simultaneously, optical efficiency is fixed with different lens concentration ratios of the same f / number, and decreases if the focal length is fixed to different concentration ratios. The best position of the PV cell for the square Fresnel lens of a focal length of 145 mm that gives good uniformity (with Standard Deviation = 3.38) is 185mm beneath the Fresnel lens with optical efficiency of 76.46% compared to the 79.47% achieved at the focal distance of 145mm but with point concentration. As for the reflective concentration with CR = 10, the optical efficiency achieved is 76.56% which is comparable to that of the Fresnel but with larger height of 230mm.

5. REFERENCES

3M (2009). Factors Influencing the Optical Efficiency of Fresnel Lens Concentrators. M. company. St. Paul, USA.

ALGAREU, A., S. Mahmoud, et al. (2014). "Optical Performance of Low Concentration Ratio Reflective and Refractive Concentrators for Photovoltaic Applications." Energy Procedia 61(0): 2375-2378.

BAIG, H., K. C. Heasman, et al. (2012). "Non-uniform illumination in concentrating solar cells." Renewable and Sustainable Energy Reviews 16(8): 5890-5909.

DAVIS, A. and F. Kühnlenz (2007). "Optical Design using Fresnel Lenses." Optik & Photonik 2(4): 52–55.

GUIQIANG, L., P. Gang, et al. (2012). "Preliminary study based on building-integrated compound parabolic concentrators (CPC) PV/thermal technology." Energy Procedia 14(0): 343-350.

LEUTZ, R. and A. Suzuki (2001). Nonimaging Fresnel Lenses, Springer, UK.

LORENZO, E. and A. Luque (1981). "Fresnel lens analysis for solar energy applications." Applied Optics 20(17): 2941-2945.

MUNOZ, M. A., M. C. Alonso-García, et al. (2011). "Early degradation of silicon PV modules and guaranty conditions." Solar Energy 85(9): 2264-2274.

SALEH Ali, I. M., T. S. O'Donovan, et al. (2013). "An optical analysis of a static 3-D solar concentrator." Solar Energy 88(0): 57-70.

SANGANI, C.S, et al. (2007). Experimental evaluation of V-trough (2 suns) PV concentrator system using commercial PV modules, Elsevier B.V.

ZHU, L., R. F. Boehm, et al. (2011). "Water immersion cooling of PV cells in a high concentration system." Solar Energy Materials and Solar Cells 95(2): 538-545.

ZHUANG, Z. and F. Yu (2014). "Optimization design of hybrid Fresnel-based concentrator for generating uniformity irradiance with the broad solar spectrum." Optics & Laser Technology 60(0): 27-33.

406: A study on the optical separation of highly concentrated solar radiation using hot mirror

Yeongmin Kim[1], Young Soo Lee[2], Seung Jin Oh[3], Wongee Chun[4]

1 Department of Nuclear and Energy Engineering, Jeju National University, km820426@jejunu.ac.kr
2 Energy Efficiency Research Division, Korea Institute of Energy Research, yslee@kier.re.kr
Department of Mechanical Engineering, National University of Singapore, mpeohsj@nus.edu.sg
4 Department of Nuclear and Energy Engineering, Jeju National University, wgchun@jejunu.ac.kr

Highly concentrated solar radiation obtained from a solar concentrator mounted on a solar tracker can be divided into infrared and visible regions before its actual applications. That is, solar rays are separated into infrared and visible regions as they are reflected off the first and second reflectors and channelled into an optical unit called a "hot mirror." The infrared rays could be applied for thermoacoustic applications, while visible rays may be utilized for indoor lighting. This work introduces the separation of two different sources of light; sunlight and artificial light. As for the artificial light, its wavelength extended from 400 ㎚ to 720 ㎚ in the visible region and 620 ㎚ to 940 ㎚ in the infrared region. A series of tests revealed that the hot mirror used in this work was capable of separating solar radiation whose wavelength extended from 460 ㎚ to 680 ㎚ in the visible region. For the artificial light, its wavelength ranged from 620 ㎚ to 940 ㎚.

1. INTRODUCTION

Solar energy is classified according to a wavelength in the x-ray, gamma ray, ultraviolet, visible, infrared, and so on. And it is different depending on the wavelength range of application fields. X-rays, gamma rays, ultraviolet rays, visible light such as the wavelength is relatively shorter than the infrared region is utilized for the electric energy production and solar lighting systems using the photoelectric effect, the infrared of the longest wavelength is used thermoacoustic laser. Therefore, in order to implement two or more features are combined by the optical system, it is necessary to apply a separate method for utilizing the properties of the wavelength range.

In this study, the development of the tracking solar tracking system using the hot-mirror that separating the infrared ray region and visible light region, a basic experiment was carried out to confirm this. The wavelength of the visible light range is separated to take advantage of solar light through the light system and the infrared range may use a thermoacoustic system.

2. EXPERIMENTAL DEVELOPMENT

2.1 Solar Tracking System Based on AVR

In this study, we developed a two-axis solar tracking system based on AVR in order to maximize the utilization efficiency of solar energy. The system was used ATmega128 AVR series microcontroller. And GPS, tilt sensor, compass sensors, etc. were used. The system altitude and azimuth of the site sun by ATmega123 CPU to perform the control of high precision, and calculates the sunset Sunrise times, the time from the GPS by UART communication, real-time date, latitude, longitude data and it is supplied to. In the current system, small reflection module is mounted of 30 cm, and is used as a heat source of the light source and the thermo-acoustic laser of natural light in sunlight is focused to.

2.2 The Optical Separation System Using the Hot-Mirror

The optical separation system consists of the concentrated sunlight incoming part, hot-mirror that separates the incoming sunlight and part of the separated visible light and infrared ray. Hot-mirror is selectively reflect a certain wavelength band of visible light and infrared rays and transmits ultraviolet rays. Hot-mirror installed on this system is allowed to pass through the wavelength range of visible light and ultraviolet rays, and reflects the infrared ray. Visible light part was produced to be connected to an optical fibre to use a solar lighting and some of the reflected infrared ray, it was fabricated to the shape of the resonance tube to use a thermoacustic system. The size of the optical separation system is designed as a compact to connect the solar tracking system.

Figure 1 shows the optical separation solar tracking device developed in this study. The size of the device is the width 40 ㎝, vertical 30 ㎝ and height 60 ㎝, and is excellent in portability and compact size is not dependent on the location.
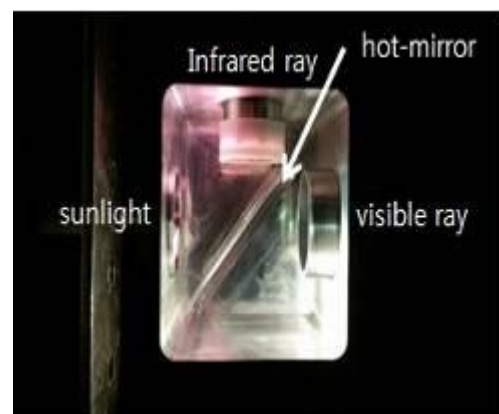
(a) Hot mirror   *(b) Optical Separation System*
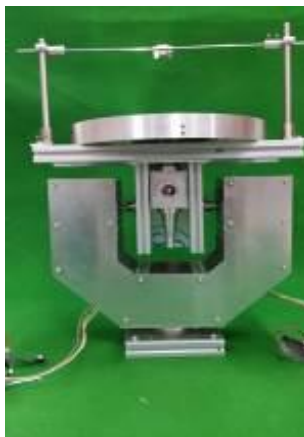
(c)Optical Separation Solar Tracking System

*Figure 1: Optical Separation Solar Tracking System*

3. EXPERIMENTAL METHOD AND RESULT

3.1 Experiments and the Results of the Light Separating Solar Tracking System Utilizing the Light Source Generator

In this experiment, the incidence of artificial light generated from the light source device using a optical fiber cable directly to the hot-mirror was confirmed that the visible light and infrared ray are separated. Figure 2 shows the optical separation experiments using artificial light source using a spectrophotometer light around the wavelength of the artificial light source and the light separation after separation were measured with visible light wavelength and infrared ray wavelength.

(a) Light Source
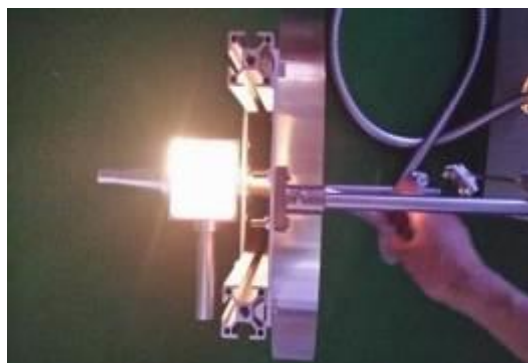
(b) Experiment of the Light Source

Figure 2: Experiment of the optical separation using the light source
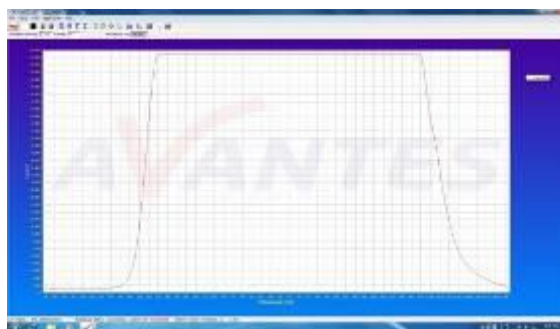
(a) Wavelength of the light source
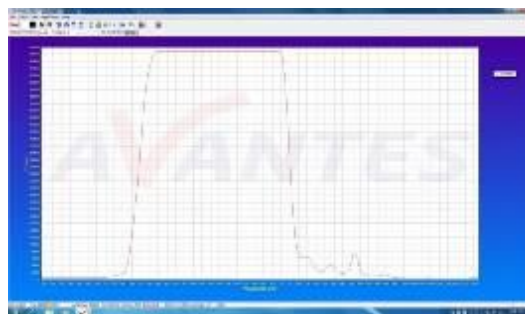
(b) Wavelength of visible light in the light source
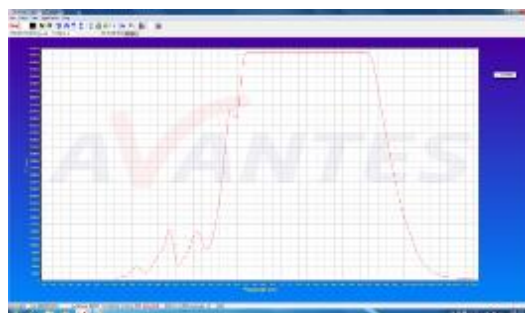
(c) Wavelength of infrared ray in the light source

Figure 3: Experiment results of the optical separation using the light source

The wavelength range of visible light is from 380 ㎚ to 750 ㎚ and the wavelength range of infrared region is from 780 ㎚ to 1400 ㎚. Figure 3 (a) shows that the wavelength of the light pre-separation of the artificial light sources is measured, the wavelength range can be confirmed that the visible light region and the infrared region are not separated until 1000 ㎚ from 400 ㎚. Figure 3(b), 3(c) is an artificial separation using a hot-mirror. Wavelength range of Figure 3(b) shows the visible light region from 400 ㎚ to 720 ㎚ and wavelength range of Figure 3(c) has an infrared ray range from 620 ㎚ to 940 ㎚.

3.2 Experiments and the results of the light separating solar tracking system utilizing the sunlight

The experiment was a light separation experiment applying the solar tracking device to evaluate the wavelength of the focused sunlight. Figure 4 shows an optical separation solar tracking system and the light separation phenomenon by the hot-mirror.

(a) Experiment of optical separation solar tracking system

(b) Optical separation by the hot-mirror

Figure 4: Experiment of the optical separation with the solar Tracking system

Figure 5 shows the visible light region and the infrared ray wavelength range by applying experiment solar tracking system. The wavelength range of visible light after separating the focused solar light is from 460 nm up to 680 nm, it can be confirmed in Figure 5(a). Furthermore, the wavelength range of infrared ray after separating is from 660 ㎚ to 920nm, it can be confirmed in Figure 5(b). Compared with the light source

generator and sunlight experimental results, the wavelength range of visible light has a difference of about 60nm, the wavelength range of infrared ray have a difference of approximately 20nm. The wavelength range of infrared ray and the wavelength range of visible light have a slight error, but all are included in the wavelength range of visible light and infrared ray, that using the hot-mirror are separated and the combined sunlight wavelength range it is possible to ensure that it is possible.
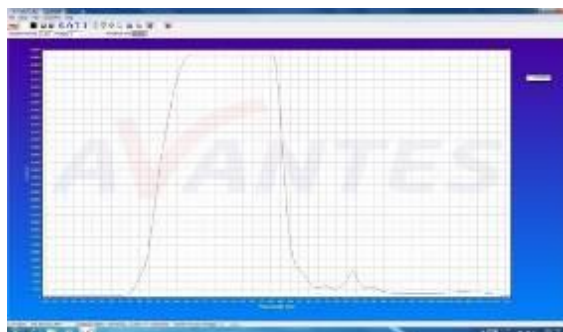
(a) Wavelength of visible light by the optical separation solar tracking system
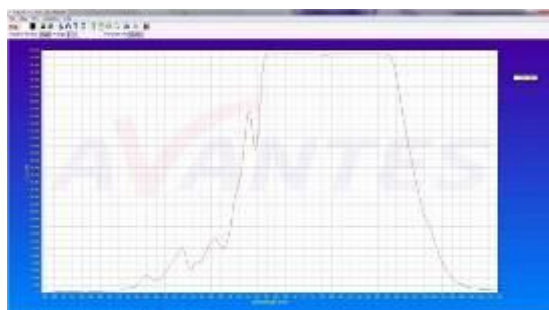
(b) Wavelength of infrared ray by optical separation solar tracking system

Figure 5: Experiment results of the optical separation with the solar tracking system

4. CONCLUSIONS

In this experiment, the light source generator and concentrated sunlight by using the hot-mirror experiments were carried out to split the visible light region and the infrared ray region. Conclusions are as follows:

(1) Visible light region by the light separation experiment using the light source generator was measured from 400 nm to 720 nm, and the infrared region was measured from 620 nm to 940 nm.

(2) Infrared ray region by the sunlight separation experiment applying the solar tracking system was measured from 460 nm to 720 nm, and the infrared region was measured from 660 nm to 920 nm.

(3) Two experiments the visible light region and show a difference of about 40 nm~60 nm, the infrared region may indicate a slight difference in 20 nm~40 nm, it can know that all are included in the respective regions.

Optical separation solar tracking system is simultaneously available system of the visible light region and the infrared ray region. If that visible light region in the separated solar is utilized for room lighting, and infrared region is utilized for thermoacoustic energy, it can not only be energy saving but also to take advantage of the solar energy in a variety of applications.

5. ACKNOWLEDGMENTS

6. REFERENCES

PANSONI P, et al., Design and development of compact solar collectors, IRT 2004.

SYMKO, O. G., Using sound to turn heat into electricity, News Center, University of Utah, 2007.

SYMCO et al., Microelectronics Journal, 35-2, 2014, pp.185 ~ 191.

SEUNG Jin Oh, Yoon Joon Lee, Kuan Chen, Young Min Kim, San Hoon Lim, Wongee Chun. Development of an embedded solar tracker for the enhancement of solar energy utilization, International Journal of Energy Research, 36, 2012, pp.249 ~ 258.

KUAN Chen, Seung Jin Oh, Yoon Joon Lee, Won Jong Oh, Ki-Hong Kim, Wongee Chun. Acoustic energy output and coupling effect of a pair of thermoacoustic lasers, International Journal of Energy Research, 36, 2012, pp.477 ~ 485.

SEUNG Jin Oh, Muhammad Burhan, Kim Choon Ng, Yeongmin Kim, Wongee Chun. Development and performance analysis of a two-axis solar tracker for concentrated photovoltaics(CPV), International Journal of Energy Research, 2014.

SEUNG Jin Oh, Won Jong Oh, Nam Jin Kim, Yoon Joon Lee, Kuan Chen, Wongee Chun. A Study on the Design and Development of Solar Powered TAL(Thermoacoustic Laser), Journal of Energy & Climate Change, 5, 2010, pp.165 ~ 174.

SEUNG Jin Oh, Yoon Joon Lee, NamJim Kim, Joon Ho Hyun, Sang Hoon Lim, Wongee Chun, Development of an AVR MCU-based Solar Tracker, Journal of Energy Engineering, 20-4, 2011, pp.353 ~ 357.

440: Off-design thermodynamic performances of a typical solar hybrid coal-fired power plant in China

Hui Hong[1],*, Wei Han[1], Shuo Peng [1,2,] Hongguang Jin[1]

1 Institute of Engineering Thermophysics, Chinese Academy of Sciences, Beijing 100190, China
2 University of Chinese Academy of Sciences, Beijing 100049, China

The concept of solar-hybrid coal-fired power plant is to use concentrated solar thermal energy to replace the extracted steam in regenerative Rankine power cycle. In this way, solar heat is capable of assisting coal-fired power plants to increase generating capacity with the same consumption of fuel, or remaining the same generating capacity but reducing its green house gas emissions within the same range. The advantages of a solar-hybrid coal-fired power plant in terms of design have been discussed by many researchers. However, off-design thermodynamic performances have not been well discussed yet. In this study, a typical 330 MW coal-fired power plant in Sinkiang of China is selected as the case study to denote the off-design thermodynamic performance. Influences of three main factors including solar radiation, incident angle and turbine load, on key parameters such as solar-to-electricity efficiency and net solar power ratio are discussed. Annual thermodynamic performances are discussed. The results obtained in this study could provide some guidance for the design and construction of solar-hybrid coal-fired power plant.

Keywords: Solar hybrid coal-fired power plant; Off-design; Thermodynamic performances

1. INTRODUCTION

Solar-hybrid coal-fired power plant could utilize concentrated solar heat below 300 °C to replace the extracted steam in regenerative Rankine power cycle to heat the feed water. Through this process, the steam that was to be extracted can efficiently expand in the steam turbine to generate electricity [1]. The plant can operate at a fully rated output during low irradiation periods without an energy storage device, thus reducing cost and simplifying the system. Besides, the steam can be more effectively converted into work with the aid of the relatively larger capacity units of the coal-fired plant with higher turbine efficiency than solar-only thermal power plant

In general, the early work started in 1975 with Zoschak and Wu [2] studying seven methods of absorbing solar energy as the direct thermal input to an 800 MW fossil-fuelled central station steam power plant. The first experimental solar-hybrid coal-fired power plant was built in Colorado in 2010, which integrate a previously existing 44 MW coal-fired power plant and a 4 MW CSP installation [3]. Yang et al. contributed to the thermodynamic advantages analysis of the solar-hybrid coal-fired power plant by analysing the overall efficiencies of the solar-hybrid coal-fired power plant with different solar replacements for the extraction steam. The results indicated that the solar thermal to electricity conversion efficiencies of the solar-hybrid coal-fired power plant are higher than those of a solar-only power plant at the same temperature of solar input [4-5]. Replacement of higher grade extraction steam facilitates better thermal performance and efficiency [6]. Zhai et al. [7] have studied a conventional 600 MW coal-fired power plant and a 600 MW solar-aided coal-fired power plant by using the First and Second Laws of Thermodynamics principles. Suresh et al. [8] analysed the energy, exergy, economic, and environmental impacts of hybrid solar-coal-fired subcritical and supercritical power plants in India using the Cycle Tempo software. Hong et al. [9] investigated the exergy destruction of a solar-hybrid coal-fired power plant using an energy-utilization diagram (EUD) methodology. Zhao et al. [10] proposed a hybrid power system combining mid-temperature solar heat and a coal-fired power plant to capture CO_2.

The objective of the present study were to discuss the influences of three main factors including solar radiation, incident angle and turbine load, on key parameters such as solar-to-electricity efficiency and solar power ratio, to disclose the annual thermodynamic performances of the hybrid system.

2. SYSTEM DESCRIPTION

A typical 330 MW reheat coal-fired power plant in Sinkiang, China was selected as the case study, as shown in Figure 1. Its state parameters are shown in Table 1. The coal-fired power plant has three low-pressure feed water heaters (L3, L2, L1), a deaerator (DE), and three high-pressure feed water heaters (H3, H2, H1). After hybridization, a solar-driven feed water heater (SWH in Figure 1) is added in parallel with the first-stage heater (H1). When the solar irradiation is sufficient, the first stage extracted steam is cut off, and the feed water is heated in the solar-driven feed water heater. When solar irradiation is insufficient to totally replace the first-stage extracted steam, the total flow of the feed water at the inlet of the first feed water heater is separated into two parts. One part is introduced into the previous H1, whereas the other flows into the solar feed water heaters (SWH). In this way, the feed water can be simultaneously heated by the extracted steam of the turbine and the concentrated solar heat. The outlet temperature of both the SWH and the H1 reaches the required inlet temperature of the boiler by changing the flow rate of both the thermal oil and the feed water into the solar receiver.

The Changji City is located at latitude of 44.1°N, with annual solar radiation of 1319 kWh/m². The weather data of Changji City was offered by NREL's standard system advisor model library (SAM). It is found that annual average solar irradiation is about 613 W/m2. Therefore, we choose this value as the design solar irradiation. The actual operational data in 2011 of the original 330 MW coal-fired power plant in Changji City is used here to simulate the solar-hybrid coal-fired power plant. It is found from the operational data that the annual turbine load of this plant is about 75%. Therefore, we choose the operational state of 75% turbine load as design condition.

The Luz LS-3 collector is selected in the solar-hybrid coal-fired power plant. N-S axis tracking mode is used. Dowtherm_A thermal oil is selected as the HTF in solar receiver. At design condition, the inlet and outlet temperature of solar field are separately 249 °C and 271 °C to match with the feed water temperature. The parabolic trough collector aperture area was assessed to be 70650 m², with a row spacing of 15 m. The solar field is composed of 50 loops each of which is made up of six solar collector assemblies. Each assembly is an independent tracking group of 10 parabolic trough solar collectors.
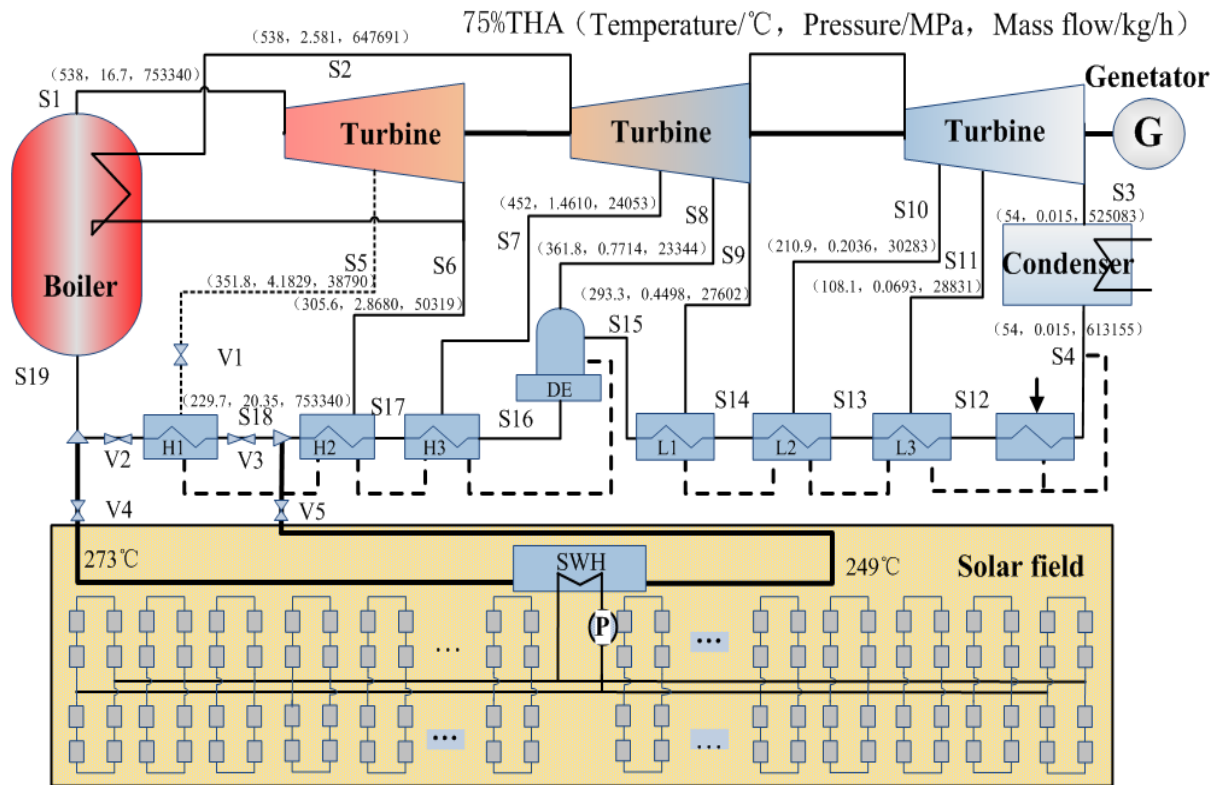
Figure 1. Schematic diagram of the solar-hybrid coal-fired power plant

Table 1. State parameters of solar aided coal-fired power plant

Items	Temperature (100%/75%/50% load, °C)	Pressure (100%/75%/50% load, MPa)	Mass flow (100%/75%/50% load, kg/h)
1	538/538/538	16.7/16.7/16.7	1034601/753340/499300
2	538/538/538	3.472/2.581/1.751	875791/647691/435982
3	54/54/54	0.015/0.015/0.015	688877/613155/418291
4	54/54/54	0.015/0.015/0.015	822023/613155/418291
5	380.1/351.8/344	5.7114/4.1829/2.8226	61830/38790/21686
6	329.7/305.6/299.4	3.8574/2.8680/1.9459	75873/50319/28926
7	451/452/453.9	1.9557/1.4610/0.9993	36195/24053/12774
8	359.9/361.8/364.8	1.0278/0.7714/0.5301	33892/23344/14351
9	290.8/293.3/396.9	0.5969/0.4498/0.3104	40170/27602/17012
10	208/211/215	0.2558/0.1934/0.1340	43210/30283/19129
11	106/108/111	0.0873/0.0658/0.0454	48378/28831/13144
12	93.1/85.6/76.2	1.724/1.724/1.724	822023/613155/418291
13	125.4/116.4/105.2	1.724/1.724/1.724	822023/613155/418291
14	153.9/143.2/130.2	1.724/1.724/1.724	822023/613155/418291
15	182.7/170.1/155.8	16.7/16.7/16.7	1034601/753340/499300
16	209.7/195.6/178.5	16.7/16.7/16.7	1034601/753340/499300
17	246.4/229.7/209.4	16.7/16.7/16.7	1034601/753340/499300
18	272.1/252.8/230.4	16.7/16.7/16.7	1034601/753340/499300

3. ROLE OF KEY PARAMETERS ON THERMODYNAMIC PERFORMANCES

Solar irradiation, incident angle, turbine load are three important parameters to influence the thermodynamic performances of the solar hybrid coal-fired power plant. Therefore, these three parameters are discussed in this section.

3.1 Solar irradiation

Figure 2 denotes the variation of solar-to-electricity efficiency under different turbine load. For a certain turbine load, solar-to-electricity efficiency rises as the increase of DNI. As the DNI continues rising, the further efficiency improvement is limited by the required heat capacity of the feed water heater. To keep the required inlet temperature of the boiler, the excess solar heat is abandoned and the work output stays still, leading to the reduction in the solar-to-electricity efficiency. It is also found that the required DNI for peak solar-to-electricity efficiency rises as the increase of turbine load. This phenomenon depends on the decrease of heat duty in H1 under part load operation. Therefore, more solar heat is needed for the peak value.

Solar power ratio is defined as the ratio of net solar power to the total power output of the hybrid system. Figure 3 denotes the variation of the solar power ratio as DNI changes. As the increase of DNI, the ratio first increases and then keeps constant under all the three turbine loads. That is because the absorbed solar heat increases as the DNI. Therefore, the net solar power output increases, leading to the increase of the solar power ratio. When the absorbed solar heat could totally replace the first stage extracted steam, solar power output reach the peak value and remains constant as the increase of DNI, so does the solar power ratio. It is also shown that as the turbine load increases, the required DNI for the peak solar power ratio increases. That is due to the increase of the required solar heat as the turbine load increase, leading to a higher DNI value for peak solar power ratio.

Figure 4 shows the variation of the heat consumption rate with solar irradiation. For a given turbine load, the absorbed solar heat increases as the rise of DNI. As a result, the extracted steam flow decreases, leading to the increase of output power. Therefore, the heat consumption decreases. After the absorbed solar heat could totally replace the extracted steam, the heat consumption keeps constant.

3.2 Incident angle

Figure 5 denotes the variation of solar-to-electricity efficiency when the incident angle changes from 0° to 70°. As the increase of incident angle, the solar-to-electricity efficiency first keeps constant then decreases. When the incident angle is smaller than 50°, solar-to-electricity efficiency rises as the increase of turbine load. The inflection point of these three turbine loads is 10°, 30°, 50°, respectively. That is because when the incident angle is relatively small, the cosine loss of the solar field is correspondingly small. In this case, the absorbed solar heat reach the design value and remains constant, leading to the stable of solar-to-electricity efficiency. With the increase of incident angle, the absorbed solar heat may be less than the design value, resulting in the declination of solar-to-electricity efficiency. As the decrease of turbine load, the required solar heat correspondingly decreases, leading to a larger inflection point value of incident angle. It also can be seen that, 75% turbine load and 100% turbine load achieve higher solar-to-electricity efficiency than 50% turbine load. However, the solar-to-electricity efficiency under 75% turbine load keeps stable when incident angle changes between 0° to 40°, which is the usual variation range during a year. From the viewpoint of system stability, running under 75% turbine load is better than other two turbine load.

Figure 6 shows that solar power ratio first keep constant and then decrease for all the three turbine loads. As the incident angle varies from 0° to 40°, solar power ratio under 75% turbine load is higher than the other two turbine loads. That is because the required solar heat of 50% turbine load is much lower than 75% turbine load. Therefore the solar power is correspondingly lower, leading to a lower solar power ratio. Although the design net solar power under 100% turbine load is higher, the value cannot be reached for all the considered solar incident angle, resulting in a smaller solar power ratio as well.

Figure 7 shows the variation of the heat consumption rate with incident angle. For a given turbine load, the absorbed solar heat increases as the decrease of incident angle. As a result, the extracted steam flow decreases, leading to the increase of output power. Therefore, the heat consumption decreases. After the absorbed solar heat could totally replace the extracted steam, the heat consumption keeps constant.
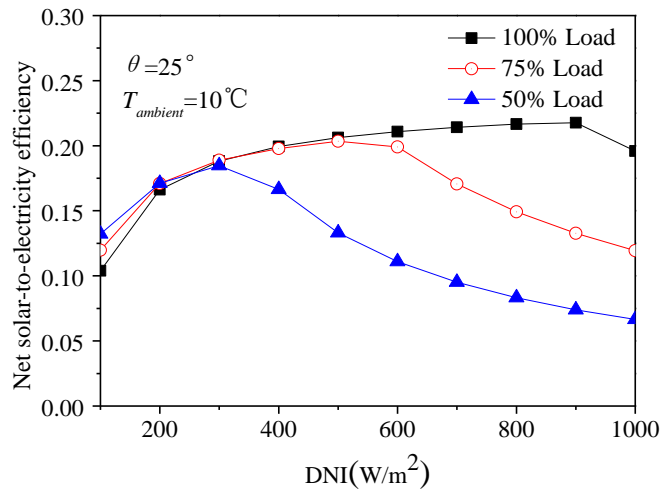
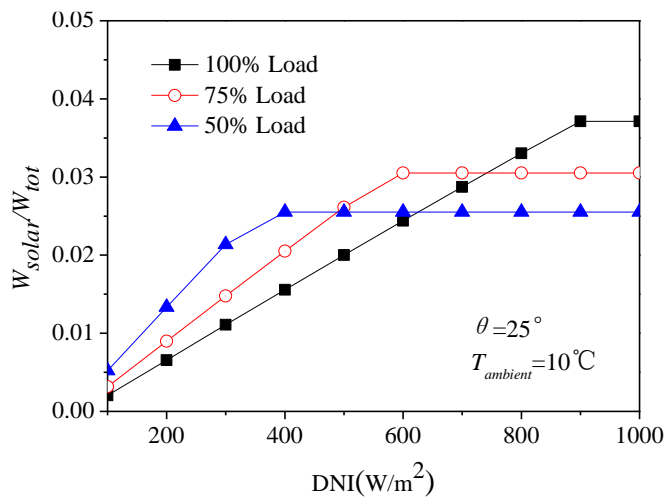Figure 2. Solar-to-electric efficiency variation with DNI change

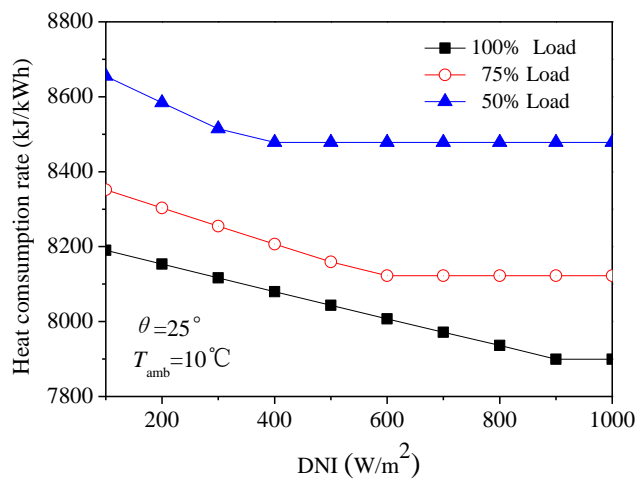Figure 3. Net solar power ratio variation with DNI change

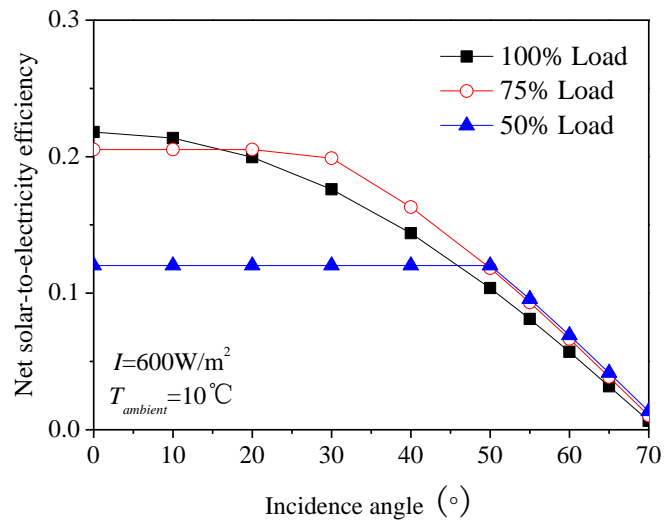Figure 4. Heat consumption rate variation with DNI change

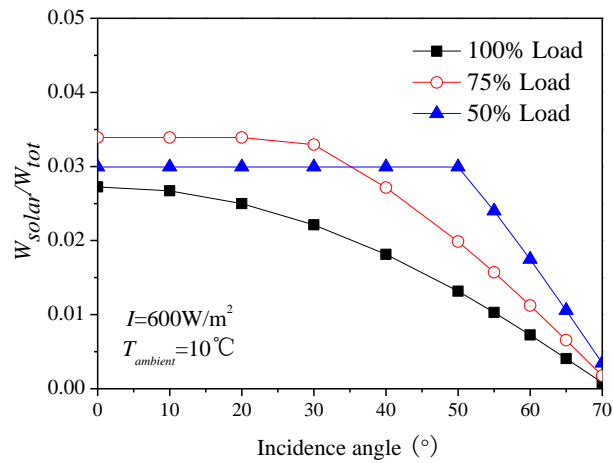*Figure 5. Solar-to-electric efficiency variation with incident angle*

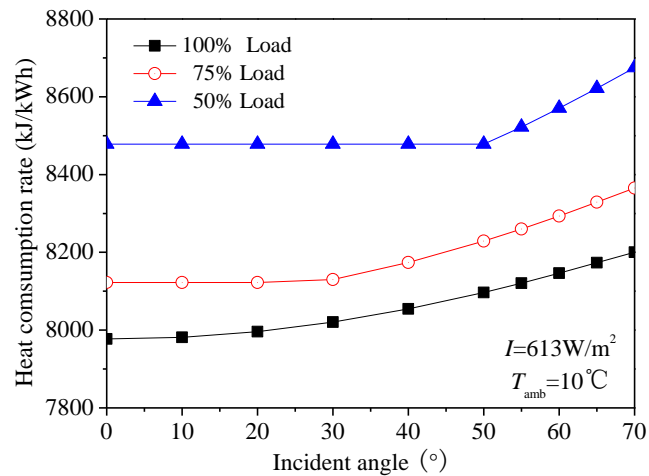*Figure 6. Net solar power ratio variation with incident angle*

Figure 7. Heat consumption rate variation with incident angle change

3.3 Turbine load

Figure 8 denotes the variation of solar-to-electric efficiency with turbine load. When the absorbed solar heat could totally replace the first stage extracted steam, the absorbed solar heat increases as the turbine load increase. For a certain DNI and solar incident angle, the solar field efficiency simultaneously increases. Besides, the turbine efficiency also increases as the turbine load increase. Therefore, the solar-to-electric efficiency correspondingly increases. When the absorbed solar heat could not totally replace the first stage extracted steam, the absorbed solar heat keeps constant for a certain DNI and solar incident angle. As the increase of turbine load, the average temperature of HTF increases, leading to the decrease of solar-to-electric efficiency.
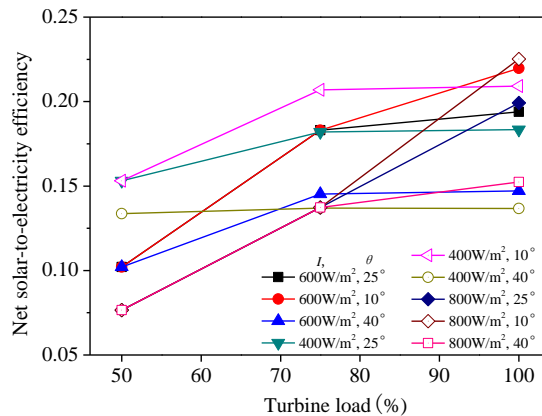
Figure 8. Solar-to-electric efficiency variation with turbine load change

Figure 9 denotes the variation of solar power ratio for different turbine load. When the absorbed solar heat could totally replace the first stage extracted steam (I=800W/m2, θ= 10° in Figure 9), the net solar power increases as the turbine load increase, leading to the increase of the solar power ratio. When the absorbed solar heat could not totally replace the first stage extracted steam (I=400W/m2 and θ = 40° in Figure 9), the solar power ratio declines as the increase of turbine load. That is because the absorbed solar heat is constant for a certain DNI and solar incident angle. Therefore, the distinction of the net solar power for different turbine load is not much. On the contrary, the distinction of the total work output is large.

Figure 10 shows the influence of turbine load on the heat consumption rate. It is found that the heat consumption rate decreases as the increase of turbine load. If the turbine load rises from 75% to 100%, the heat consumption rate decreases by about 2%. If the turbine load rises from 50% to 75%, the heat consumption rate decreases by about 4%.
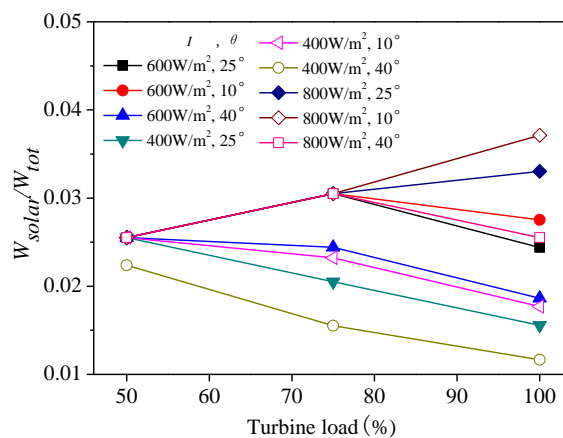

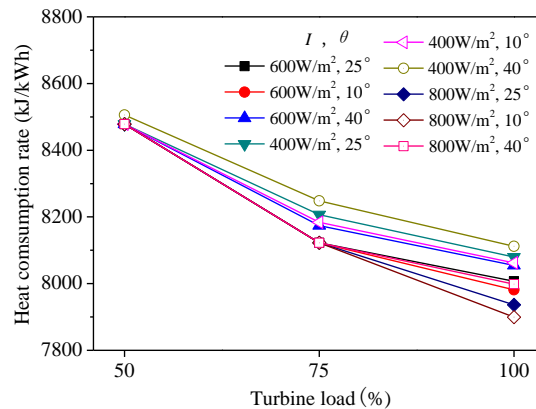*Figure 9. Net solar power ratio variation with turbine load change*

Figure 10. Heat consumption rate variation with turbine load change

4   ANNUAL THERMODYNAMIC PERFORMANCES

Figure 11 depicts the net solar-to-electricity efficiency on typical days of different seasons under full load. For 100% turbine load, the peak net solar-to-electricity efficiency in summer can reach up to 25%. As the DNI continues rising, the further efficiency improvement is limited by the required heat capacity of the feed water heater. To keep the required inlet temperature of the boiler, the excess solar heat is abandoned and the work output stays still, leading to a reduction in the net solar-to-electricity efficiency. In spring and autumn, although slightly lower than in summer, peak net solar-to-electricity efficiency can still reach as high as 20%~22%. In winter, the peak net solar-to-electricity efficiency is only 11% owing to the decrease of DNI and the increase of solar incident angle. When the turbine load is down to 75% and 50%, the net solar-to-electricity efficiency drops sharply as DNI rises, especially in summer. That is because the total flow rate of feed water decreases as turbine load decline, in order to match the decreased output power. In this way, the heat duty of FWH1 under part load operation correspondingly decreases. Therefore, more solar heat is abandoned as the increase of DNI, leading to the decline of the net solar-to-electricity efficiency.

It is found from the operational data of the coal-fired power plant that the annual turbine load of is about 75%. For simplicity, we suppose the coal-fired power plant operate at 75% turbine load all year round. Figure 12 shows the annual net solar power and the solar-to-electricity efficiency of the hybrid system. It is found that the annual net solar power of the hybrid system is about 28 GW. The annual solar-to-electricity efficiency can reach to 19%, which is about 5 percent higher than the solar-only thermal power system.

5   CONCLUSION

A typical 330MW solar-hybrid coal-fired plant in Sinkiang Province was evaluated in this study. Based on the weather condition of Changji City and actual operating data of the original coal-fired power plant, the off-design thermodynamic performances of the solar-hybrid coal-fired power plant is simulated under different solar radiation conditions and three different turbine loads. The three main parameters that influence system performance are direct normal solar irradiation, incident angle and turbine load. For a certain turbine load, solar-to-electricity efficiency reaches to a peak value as the increase of DNI. As the increase of incident angle, the solar-to-electricity efficiency first keeps constant, and then decreases. Annual thermodynamic performances are discussed. It is found that annual solar-to-electricity efficiency of the solar hybrid coal-fired power system can reach to 19%, which is about 5% higher than the solar-only thermal power system. The results obtained in this study could provide some guidance for the design and construction of solar-hybrid coal-fired power plant.
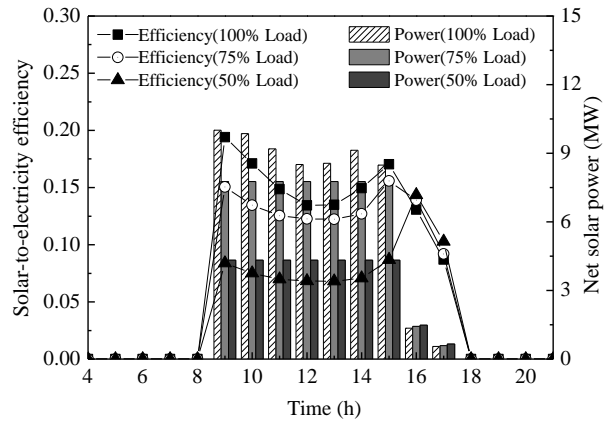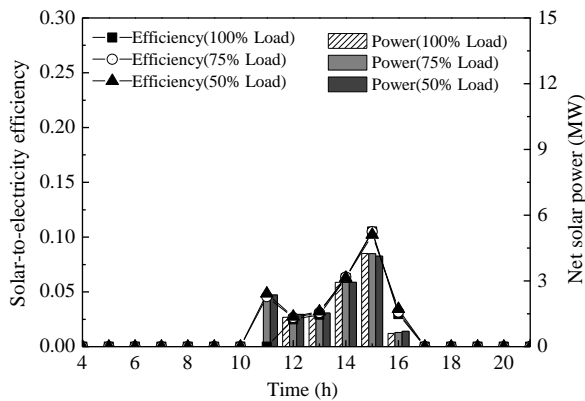
(a) Spring Equinox
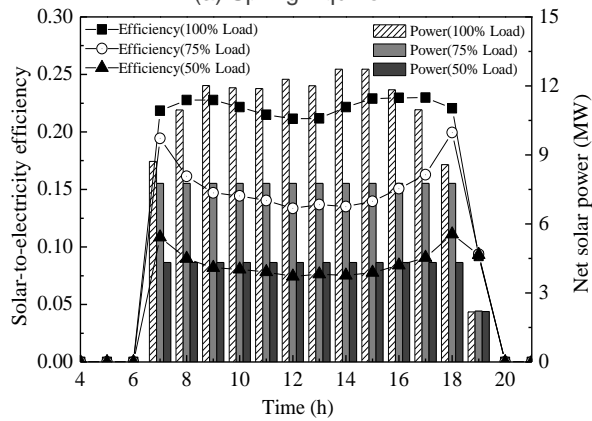
(b) Summer Solstice
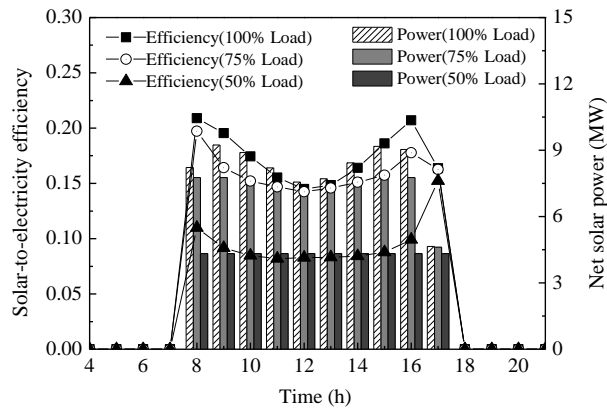
(c) Autumn Equinox

(d) Winter Solstice

Figure11. Variation of net solar-to-electric efficiency and net solar power
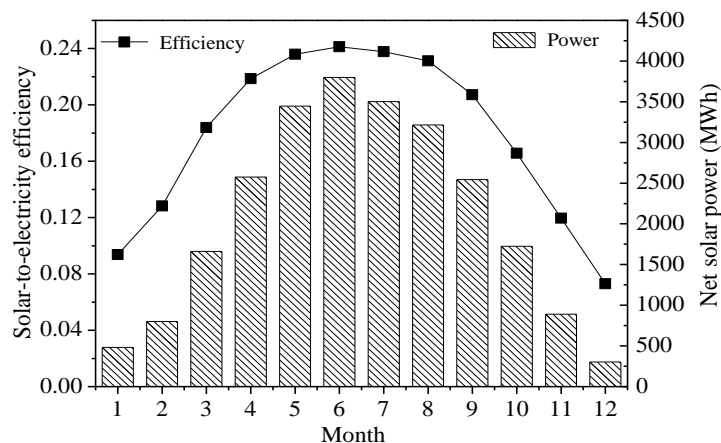
Figure 12. Annual net solar power and solar-to-electricity efficiency

6   ACKNOWLEDGEMENTS

7   REFERENCES

[1] HU E, Yang YP, Nishimura A, Yilmaz F, Kouzani A, Solar thermal aided power generation. Applied Energy, 2010, 87: 2881-2885.

[2] ZOSCHAK RJ, Wu SF., Studies of the direct input of solar energy to a fossil-fueled central station steam power plant. Solar Energy, 1975, 17: 297–305.

[3] National renewable energy laboratory, 2010, http://www.nrel.gov/csp/news/2010/870.html.

[4] YAN Q, Yang YP, Nishimura A, Kouzani A, Hu E, Multi-point and Multi-level Solar Integration into a Conventional Coal-Fired Power Plant. Energy Fuels, 2010, 24 (7): 3733-3738.

[5] YANG Y, Yan Q, Zhai R, et al, An Efficient Way to Use Medium-or-Low Temperature Solar Heat for Power Generation-Integration into Conventional Power Plant. Applied thermal engineering, 2011, 31: 157-162.

[6] HOU HJ, Mao J, Yang YP, Luo N. Solar-Coal Hybrid Thermal Power Generation- an Efficient Way to Use Solar Energy in China, International Journal of Energy Engineering, 2012, 2(4): 137-142

[7] ZHAI R, Zhu Y, YangY, Tan K, Eric Hu, Exergetic and Parametric Study of a Solar Aided Coal-Fired Power Plant, Entropy, 2013, 15 (3): 1014-1034.

[8] SURESH M., Reddy KS, Kolar AK., 4-E (energy, exergy, environment, and economic) analysis of solar thermal aided coal-fired power plants. Energy for Sustainable Development 2010, 14: 267-79.

[9] HONG H, Zhao Y, Jin H. Proposed Partial Repowering of a Coal-Fired Power Plant Using Low-Grade Solar Thermal Energy. International J. Thermodynamics, 2011, 14(1): 21-28.

[10] ZHAO Y, Hong H, Zhang X, Jin H, Integrating mid-temperature solar heat and post-combustion CO2-capture in a coal-fired power plant. Solar Energy, 2012, 86: 3196-3204.

485: Economic and environmental analyses of a BIPV-PCM-slurry based energy system

Zhongzhu Qiu [1, 2,*], Xudong Zhao[1], Xiaoli Ma[1], Peng Li[3]

1 School of Engineering, University of Hull, Cottingham Road, Hull, UK, Xudong@hull.ac.uk
2School of Energy and Mechanical Engineering, Shanghai University of Electric Power, Shanghai, China, Z.qiu@hull.ac.uk
3School of Mechanical Engineering, Tongji University, Shanghai, China, lipeng99@tongji.edu.cn

In this paper, the economic & environmental benefits of the new BIPV-PCM-slurry energy system for use in European buildings were investigated. This involved (1) analyses of the capital and operational cost of the BIPV-PCM-slurry energy system; (2) calculation of increase in the capital cost and saving in operational cost of the system relative to the conventional BIPV, PV/water and conventional heat & power systems; and (3) estimation of the payback period and life cycle cost saving of the system relative to the conventional ones. Furthermore, the carbon emission reduction potential of the system for the use as a replacement of the conventional heat and power systems, BIPV or BIPV/water systems across the European regions was analysed.

It is concluded that the BIPV-PCM-slurry energy system is more suitable for use in the southern Europe region than in the northern Europe region. The economic benefits of the BIPV-PCM-slurry, BIPV/water and BIPV are highly dependent upon its application area and local climatic condition. Among the three comparable systems, BIPV-PCM-slurry type presented the greatest potential in obtaining the quickest economic return in investment.

The environmental benefits of the three systems are also climatic dependant, having more favourite outcome in Southern Europe than in Northern Europe. Again, the BIPV-PCM-slurry system presents the greatest potential in cutting the carbon emission to the environment, over the other two comparable systems.

Keywords: MPCM suspension, solar PV/T module, energy system, economic analyses, environment benefits

1. INTRODUCTION

The commonly used fluids for cooling the PV cells in a PV/T module are air, water and refrigerant. Phase Change Materials (PCMs) are chemical substances that change phase from solid to liquid when absorbing heat from an energy source or from liquid to solid when releasing heat to an energy sink, whilst the temperature of the materials remain constant. The PCMs normally have higher thermal capacity owing to the latent heat contained in the heat transfer process and are therefore, suitable for use in PVs' heat collection. PCMs are broadly classified as organic materials (e.g., paraffin and non-paraffin) and inorganic materials (e.g., salt hydrates, eutectics pentaerythiol and pentaglycerine); both classes contain materials with phase change temperatures in the range 15 to 30℃, which is the desired controlling temperature for PV cells. However, the thermal conductivities of existing PCMs are very low (0.1 to 1.8 W/m·K) [1], which would significantly impair the heat transfer process and consequently, affect the temperature control against the PV cells.

In recent years, a new way dealing with PCMs has been developed in industries e.g. BASF and EPS [2, 3]. In this process, the PCM particles are encapsulated by polymer shells of size 1 to 100μm. These encapsulated particles are then mixed with a carrier fluid (e.g., water) with the selected additives (i.e. dispersing agents), thus forming a MPCM slurry. Use of such a slurry enables much higher thermal conductivity of the fluid owing to the movement of the carrier fluid and smaller size of the MPCM particles. Besides the function as the energy storage, the slurry can also serve as a heat carrier allowing heat received from a heat source to be taken away and delivered to a place where heat is required.

Although the MPCM slurries have been found notable applications in HVAC systems, use of such slurries in PV/T based energy systems has not yet been explored. To understand the features (merits and disadvantages) of a MPCM slurry for application in the PV/T systems, a novel serpentine piping incorporated PV/T module was proposed by the authors. This module would allow the MPCM slurry to be completely melted on the outlet of the serpentine piping, thus achieving a relatively lower PV surface temperature, and higher thermal, electrical and overall efficiencies.

The objective of this paper is to evaluate economic and environmental impact of the technology to Europe and analyse its adaptability within the European regions.

2. REGIONAL ACCEPTANCE ANALYSES

2.1 Summary of the characteristic parameters of the system's components

By using the experiment-validated computer model developed in [4], the annual operational performance of the BIPV-PCM-slurry energy system under real weather conditions will be predicted in this task. The thermal and geometrical parameters of the major components of such a system are listed in Table 1.

2.1 Analyses of the EU weather data

Weather data for a typical design year relevant to different locations of the EU countries were extracted from the energy-plus database [5], and analysed accordingly. Assuming that the BIPV-PCM-slurry energy system is installed on the south-facing building envelope in Stockholm and Madrid, which have the typical northern and southern European climatic conditions, the hourly solar irradiance and ambient temperature from 09:00:00 to 17:00:00 on a typical day for each month of the year and the average daily wind velocity are summarised . The instant figures of the former two parameters could be calculated using the interpolation approach. The average daily wind velocity derived from the energy-plus database.

2.2 Brief analysis of the energy outputs of the BIPV-PCM-slurry system

By applying the above weather data into the established models in tasks 2 & 3, the monthly and annual electricity and heat yields of the BIPV-PCM-slurry system in Madrid and Stockholm were calculated and presented in Tables 2 and 3 respectively. It is seen that the system had 367 kWh of electricity and 1986 kWh of heat annually in Madrid, and 203 kWh of electricity and 1035 kWh of heat annually in Stockholm. This indicated that the system is more energy productive in southern Europe than that in northern Europe, mainly owing to the higher solar radiation and ambient temperature of southern part relative to the northern part.

Table 1 The thermal and geometrical parameters of the major components of the system

No	Item	Size /type	Structure	Capacity/thermal properties	Remarks
1	BIPV-PCM-Slurry module	1600*800mm	1.Glazing cover 2.PV lamination 3.Serpentine pipe 4. Insulation 5. Frame set	heat output:0.735 kW electricity: 150W U-value:<0.172W/m2.℃ slurry flow rate:40-87.5 kg/h flow resistance:265-280kPa	
2	Slurry-to-refrigerant heat exchanger	206*76*55mm/Stainless steel plate type	20 Flat plates	>3000W	light, compact, low resistance, low cost
3	compressor	1kW	n/a	Heat output: 4000W	Condensing temperature:50-75℃ evaporation temperature:-15-25℃
4	Heat storage	100L, cylinder storage tank for a BIPV module	1. stainless steel wall; 2. >150mm mineral wool insulation	>2660kJ storage capacity	Size, type, storage capacity and insulation performance are to be confirmed by the following modelling and experimental wok
5	Condenser	Copper coil, Ø 9.52×0.8, L=3.5m	Copper coil	Heat transfer rate:4000W	
6	Water tank	200L	Cylinder, Stainless steel	-	

Table 2 Summary of monthly electricity and heat yields of Madrid

Month of the year	Electricity yield (kWh)	Heat yield (kWh)
Jan	20.6	84.7
Feb	25.1	115.2
Mar	34.5	176.9
Apr	34.1	178.7
May	36.2	205.3
Jun	40.0	235.6
Jul	42.9	264.3
Aug	39.8	243.7
Sep	31.0	179.9
Oct	26.7	142.8
Nov	22.0	104.9
Dec	14.5	54.0
Annual energy yield	367.4	1986.3
Annual energy income(€)	77.27	417.89

Table 3 Summary of monthly electricity and heat yields of Stockholm

Month of the year	Electricity output (kWh)	Heat output (kWh)
Jan	3.5	2.3
Feb	8.5	25.7
Mar	15.0	59.2
Apr	26.6	132.7
May	31.2	175.0
Jun	29.0	168.1
Jul	28.3	167.0
Aug	22.7	134.4
Sep	16.7	92.4
Oct	11.1	52.7
Nov	6.4	20.3
Dec	3.8	5.2
Annual energy yield	202.7	1034.8
Annual energy saving(€)	42.64	217.73

It should be noted that the heat output of the systems was seen to be provided by an electrical boiler. And the following economic analysis based on the electricity unit rate €1.2104 per kWh.

3. ECONOMIC ANALYSIS

In order to understand the economic feasibility of converting this kind of BIPV-PCM-slurry energy system into a commercial product, an economic analysis of this system was carried out through a parallel comparison with the conventional BIPV and BIPV/water systems.

3.1 Estimated capital cost

This type of system was considered to have a life span of 25 years [6]. Its capital cost comprises the individual component costs, the appropriate sale profit and Value Added Tax (VAT) [7]. It should be noted that the unit costs of the system components were quoted from the selected product catalogue[8]. Details of the system cost breakdown are presented in Table 4, and it can be seen that the initial cost of such a dedicate sized system is €1737.98. Apart from the battery which has life cycle of 5 years, all other components of the system have life cycle of 25 years.

Table 4. Capital cost of the BIPV-PCM-Slurry system

System components	Unit price (€)	Quantity	Cost (€)	life period
BIPV-PCM-Slurry module	785.60	1	785.60	25
Micro-Compressor	51.24	1	51.24	25
Flat-plate heat exchanger	27.65	1	27.65	25
Storage Tank	66.44	1	66.44	25
Expansion valve	26.98	1	26.98	25
Pipe lines	4.92	10 m	49.24	25
Microencapsulated slurry	18.79	8.6kg	160.36	25
Micro-inverter	134.90	1	134.90	25
Battery	101.18	2	202.35	5
Accessories	N/A	N/A	75.23	25
installation and commissioning	N/A	N/A	157.99	25
Capital cost (€)			1737.98	

The conventional BIPV and BIPV/water systems have the same life cycle period as to the BIPV-PCM-slurry system [9]. Compared to this new system, the BIPV and BIPV/water systems are simpler and easier to install, thus remaining the relatively smaller capital costs, i.e., €1444.91 and €1011.55 respectively[10]. The cost breakdowns of the conventional systems are presented in Tables 5 & 6.

Table 5 Capital cost of the BIPV/water system

System components	Unit price (€)	Quantity	Cost (€)
BIPV/water module	785.60	1	785.60
Tank	132.88	1	132.88
Pipe lines	4.92	10 m	49.24
Micro-inverter	80.94	1	80.94
Battery	101.18	2	202.35
Accessories	N/A	N/A	62.55
installation and commissioning	N/A	N/A	131.35
Capital cost (€)			1444.91

Table 6 Capital cost of the BIPV system

System components	Unit price (€)	Quantity	Cost (€)
BIPV Panel	628.48	1	628.49
Micro-inverter	44.96	1	44.96
Battery	101.18	2	202.35
Accessories	N/A	N/A	43.79
installation and commissioning	N/A	N/A	91.96
Capital cost (€)			1011.55

3.2 Operational Cost

The annual operational cost of the BIPV-PCM-slurry system covers two parts: the electricity cost for operation of the compressor & pump and the system maintenance cost. The electricity consumption and cost of the system are presented in Table 7; while its maintenance cost, calculated on basis of 2% of initial cost[11], is presented in Table 8.

Table 7. Annual Electricity cost of the BIPV-PCM-slurry system

Month	Electricity use(kWh)	
	Madrid	Stockholm
Jan	20.40	2.00
Feb	26.40	9.70
Mar	38.40	17.90
Apr	38.60	33.20
May	43.20	40.90
Jun	48.60	39.30
Jul	53.30	38.90
Aug	49.60	32.70
Sep	38.00	24.80
Oct	31.30	15.70
Nov	24.20	7.80
Dec	14.20	3.30
Annual electricity use	426.00	266.20
Annual electricity cost(€)	89.63	56.01

Table 8. Annual operational cost of the BIPV-PCM-slurry system (€)

Items	Madrid	Stockholm
Annual electricity cost	89.63	56.01
Annual maintenance cost	34.76	34.76
Annual operational cost	124.39	90.76

3.3 Payback Period

The experimental results [9] obtained at the Mediterranean climatic condition indicated that the Building Integrated Photovoltaic module (BIPV) had 13oC higher rear temperature than the open-air PV modules. This led to around 4% reduction in the PVs' power output, equivalent to around 0.3% lose in efficiency per degree rise in the module's temperature.

Comparison among three BIPV modules, i.e., open-air type (Fig. 1), ventilated type (Fig. 2) and non-ventilated type (Fig. 3) was carried out under the equivalent operational condition. The peak temperatures of the three PV modules were 65.5 oC , 73.3 oC , and 78.8 oC respectively, while their electrical efficiencies are 4.67%, 2.33% and 1.68%; indicating that the temperature and electrical efficiency were in adverse relationship.[12]
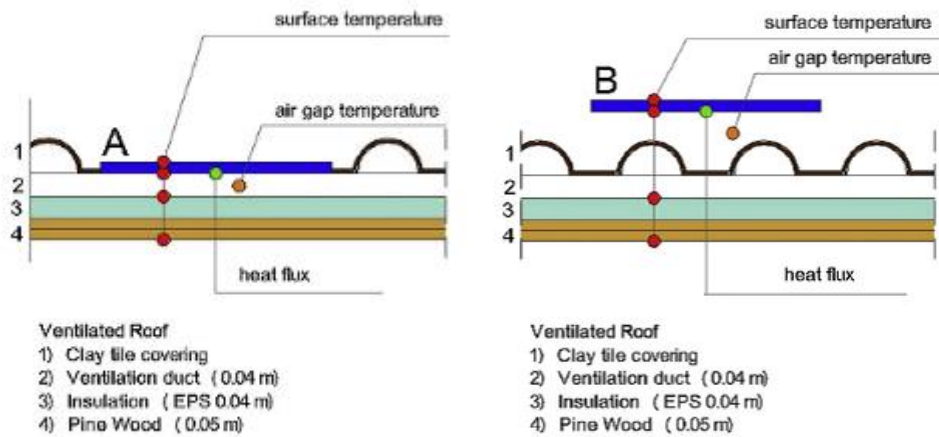
Fig. 1. Schematic of the open-air module [9]   Fig. 2. Schematic of the ventilated type module
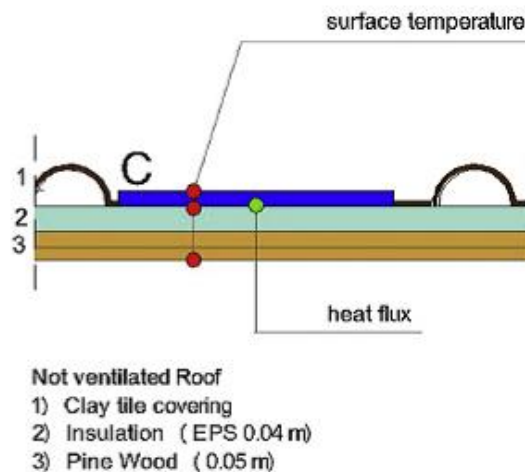
Fig. 3. Schematic of the non-ventilated type module

Compared to the BIPV system, the BIPV/water system, when operating at the equivalent condition, could achieve a reduction in PV cells' temperature by around 14.4 oC, which consequently led to an increase in PVs' electrical efficiency by 4.33%.

Compared to the BIPV and BIPV/water systems, our BIPV-PCM-slurry system, when operating at the equivalent condition, could achieve even lower PV cells' temperature, 31.1 oC and 16.7 oC lower than above two systems respectively. This consequently led to the increase in PVs' electrical efficiency by 9.33% and 5.0% respectively.

Taking into account the cost difference of the three BIPV systems, as well as their thermal and electrical efficiency gap caused by the PVs' temperature variation, the payback periods for investing these three systems in Madrid were calculated and the results were presented in Table 9. Compared to the BIPV and BIPV/water systems, the new BIPV-PCM-slurry system could achieve 36.5 and 2.9 years less payback years, which are very efficient in terms of return for investment.

Table 9. The payback period of the three systems in Madrid (€)

System components	BIPV	BIPV/water	BIPV-PCM-slurry
Initial capital cost(€)	1011.55	1444.91	1737.98
Annual Operational cost(€)	0.00	28.90	124.39
Annual electricity saving(€)	24.51	47.23	77.27
Annual heat saving(€)	0.00	172.13	417.89
payback time(annum)	41.3	7.6	4.7

Note: The feed in saving is not covered because it varies with countries

For Stockholm climatic condition, the payback periods for investing these three systems were also calculated and the results were presented in Table 10. Compared to the BIPV and BIPV/water systems, the new BIPV-PCM-slurry system could achieve 68.4 and 6.5 years less payback years.

Table 10 The payback period of the three systems in Stockholm (€)

System components	BIPV	BIPV/water	BIPV-PCM-slurry
Initial capital cost(€)	1011.55	1444.91	1737.98
Annual Operational cost(€)	0.00	28.90	90.76
Annual electricity yield saving(€)	12.87	24.81	42.64
Annual heat yield saving(€)	0.00	90.42	217.73
payback period(annum)	78.6	16.7	10.2

Note: The feed in saving is not covered because it varies with countries

3.4 Life Cycle Cost (LCC) per kWhe Generated

Life Cycle Cost (LCC) per kWhe generated can be calculated using the following correlation,

$$LCC_{kWe} = \frac{LCC}{25*Ee} \qquad (1)$$

Where, 25 represents the PV system's life cycle, the system's LCC can be calculated using the following equation,

$$LCC = PC_i + PC_r + PC_m + PC_e - PS_e - PS_s \qquad (2)$$

where, PC_i is the present value of the initial capital cost, PC_r present value of battery replacement cost, PC_m present value of maintenance cost, PC_e present value of energy cost, PS_e present value of energy saving, PS_s present value of system's salvage.

The PV system's life cycle is usually considered as 25 years while the battery has only 5 years payback period. In this case, the PC_r can be calculated using the following equation,

$$PC_r = C_{bat} * \frac{(1+f)^5}{(1+i)^5} + C_{bat} * \frac{(1+f)^{10}}{(1+i)^{10}} + C_{bat} * \frac{(1+f)^{15}}{(1+i)^{15}} + C_{bat} * \frac{(1+f)^{20}}{(1+i)^{20}} \qquad (3)$$

where, C_{bat} is annual cost of the battery; i fixed value of the interest rate,10%, f inflation rate, 5%.

Similarly,

$$PC_m = C_m * \sum_{n=1}^{25} \frac{(1+f)^n}{(1+i)^n} \qquad (4)$$

where, C_m is annual cost of maintenance

$$PS_e = S_e * \sum_{n=1}^{25} \frac{(1+f)^n}{(1+i)^n} \qquad (5)$$

where, S_e is annual saving of energy

$$PS_s = S_s * \frac{(1+f)^{25}}{(1+i)^{25}} \qquad (6)$$

where, S_s is saving of energy system's salvage; this is ignored hereby.

The life cycle costs per kWhe output in the three systems were therefore calculated using the equations (1) – (6), and the results are presented in Tables 11 and 12. In terms of the Madrid operational condition, the LCCs per kWhe output for the BIPV, BIPV/water and BIPV-PCM-Slurry systems are €0.39, €-0.15, and €-0.34 respectively. The minus signs appeared hereby implied that fossil fuel savings owing to the implementation of the system have exceeded its investment. The BIPV-PCM-slurry system can obtain the greater benefits in terms of the return-for-investment than the other two systems.

Table 11. The Life Cycle Cost per kWhe in Madrid

Present value upon 25 years life cycle	BIPV	BIPV/water	BIPV-PCM-slurry
Initial capital cost(€)	1011.55	1444.91	1737.98
Operational cost(€)	0.00	417.15	1795.78
Battery replacement cost(once every 5 years) (€)	467.94	467.94	467.94
Electricity and heat yield saving(€)	353.86	3166.80	7148.45
Cost per kWhe(€/kWhe)	0.39	-0.15	-0.34

In terms of the Stockholm operational condition, the LCCs per kWhe output for the BIPV, BIPV/water and BIPV-PCM-Slurry systems are €85, €23, and €0.05 respectively. Again, the BIPV-PCM-slurry system can obtain greater benefits in terms of the return-for-investment than the other two systems.

Table 12. The Life Cycle Cost per kWhe in Stockholm

Present value upon 25 years life cycle	BIPV	BIPV/water	BIPV-PCM-slurry
Initial capital cost(€)	1011.55	1444.91	1737.98
Operational cost(€)	0.00	417.15	1795.78
Battery replacement cost(once every 5 years) (€)	467.94	467.94	467.94
Electricity and heat yield saving(€)	185.78	1663.55	3758.84
Cost per kWhe(€/kWhe)	0.85	0.23	0.05

4   ENVIRONMENTAL BENEFIT

The annual CO_2 emission reduction could be determined on basis of the annual electrical and thermal energy savings of the three systems over the current heat and electrical grid systems, by multiplying a conversion factor [8].

$$PS_s = S_s * \frac{(1+f)^{25}}{(1+i)^{25}} \qquad\qquad (7)$$

where, the is CO2 emission reduction; electricity to CO2 emission conversion factor; system's energy output; sytem's energy use. It is known that 1 kWh of grid electricity contains 0.54522 kg of CO_2[13], it should be noted that the thermal energy output of three systems were seen to be provided by an electrical boiler.

The CO2 Emission Reductions in Madrid and Stockholm are presented in Tables 13 and 14 respectively. In terms of the Madrid climatic condition, carbon emission reduction values of the three systems relative to the conventional heat and power systems are 1.6 tons, 14.2 tons, and 26.3 tons per annum respectively, indicating that BIPV-PCM-slurry system had the highest potential in cutting the carbon emission to the environment.

Table 13 CO2 Emission Reduction in Madrid

	BIPV	BIPV/water	BIPV-PCM-slurry
Annual Energy Yield(kWh)	116.5	1042.7	2353.7
Annual Energy Use(kWh)	-	-	426.0
Annual Energy Net Output(kWh)	116.5	1042.7	1927.7
Annual CO2 Emission Reduction (tons/annum)	0.1	0.6	1.1
Life Cycle CO2 Emission Reduction (tons/annum)	1.6	14.2	26.3

In terms of Stockholm climatic condition, carbon emission reduction values for the three systems relative to the conventional heat and power systems are 0.8, 7.5, and 13.2 tons tons per annum respectively, which are less than that in Madrid climatic condition. Again, BIPV-PCM-slurry system had the highest potential in cutting the carbon emission to the environment.

Table 14 CO2 Emission Reduction in Stockholm

	BIPV	BIPV/water	BIPV-PCM-slurry
Annual Energy Yield (kWh)	61.2	547.7	1237.5
Annual Energy Use (kWh)	-	-	266.2
Annual Energy Net Output (kWh)	61.2	547.7	971.3
Annual CO2 Emission Reduction (tons per annum)	0.0	0.3	0.5
Life Cycle CO2 Emission Reduction (tons per annum)	0.8	7.5	13.2

5   CONCLUSIONS

5.1 Feasibility

The new BIPV-PCM-slurry system is more suitable for southern European region than northern. The energy output of the system in the northern part is much less than that in southern part. Taking the Madrid and Stockholm as the examples that can represent the typical southern and northern European climatic conditions respectively, the annual electricity and heat yields of the system in Madrid are 367.4 kWh and 1986.3 kWh respectively; while the system yields in Stockholm are only 202.7 kWh and 1034.8 kWh. This indicates that the system is more energy productive in southern Europe than that in northern Europe, mainly owing to the higher solar radiation and ambient temperature of southern part relative to the northern part.

5.2 Economic and environmental benefits

For a Madrid building with the potential to install the BIPV, BIPV/water and BIPV-PCM-slurry systems, the relevant payback periods are 41.3, 7.6 and 4.7 years respectively. For a Stockholm building with the potential to install the BIPV, BIPV/water and BIPV-PCM-slurry systems, the relevant payback periods are 41.3, 7.6 and 4.7 years respectively. Both cases in combination indicated that the BIPV-PCM-slurry system demonstrated that greater economic benefits than the other two systems.

The life cycle costs (LCCs) per kWhe output in the three systems varied with the climatic conditions. In Madrid which has a typical southern European climatic condition, the LCCs per kWhe output for the BIPV, BIPV/water and BIPV-PCM-Slurry systems are €0.39, €0.15, and €0.34 respectively. In Stockholm which has a typical northern European climatic condition, the LCCs per kWhe output for the three systems are €0.85, €0.23, and €0.05 respectively. Compared to the other two systems, the BIPV-PCM-slurry system can obtain the greater benefits in terms of return-for-investment.

6 REFERENCES

Vineet Veer TYAGI, D. Buddhi, 2007. PCM thermal storage in buildings: a state of art. Renewable and Sustainable BASF Factbook 2010, BASF, Ludwigshafen, Germany, 1-20, June 2010.

PCM Products Catalogues, EPS Ltd, Cambridge shire, UK, 1-6, October 2010.

Zhongzhu QIU, Xudong Zhao*, Peng Li, Xingxing Zhang, Samira Ali. 2015. Theoretical Investigation of the Energy Performance of a Novel MPCM Slurry Based PV/T Module. Energy, 87, 686–698.

BALARAS, Constantinos A., et al. 2007. European residential buildings and empirical assessment of the Hellenic building stock, energy consumption, emissions and potential energy savings. Building and environment, 42(3) , 1298-1314.

Benefits of electric heating. http://www.dimplex.co.uk/corporate_information/benefits_of_electric_heating.htm. accessed on 28/05/2015

D'ORAZIO, M., C. Di Perna, and E. Di Giuseppe.2014. Experimental operating cell temperature assessment of BIPV with different installation configurations on roofs under Mediterranean climate. Renewable Energy, 68, 378-396.

Economic benefits.http://thermotechs.com/Advantages_and_Costs.php. accessed on 28/05/2015

How long do solar electric PV panels last? http://info.cat.org.uk/questions/pv/life-expectancy-solar-PV-panels. accessed on 28/05/2015

Retail price index: Fuels components monthly figures (QEP 2.1.3). http://www.decc.gov.uk/en/content/cms/statistics/prices/prices.aspx. accessed on 28/05/2015

S. KALOGIROU, Economic analysis of solar energy systems using spreadsheets,1996.Proceedings of the World Renewable Energy Congress IV, Denver, Colorado, US, 1303-1307

Solar water heating, http://www.energysavingtrust.org.uk/Generate-your-own-energy/Solar-water-heating. accessed on 25/05/2015

2010 guidelines to Defra/DECC's GHG conversion factors for company reporting, http://www.carbontrust.co.uk/cut-carbon-reduce-costs/calculate/carbon-footprinting/Pages/conversion-factors.aspx. accessed on 28/05/2015

488: Research on the development of a small-scale supercritical carbon dioxide power cycle experimental loop with a high-speed turbo-generator

JUNHYUN CHO, HO-SANG RA, GILBONG LEE, HYUNGKI SHIN, YOUNG-JIN BAIK

1 Thermal Energy Conversion Laboratory, Korea Institute of Energy Research, 152, Gajeong-ro, Yuseong-gu, Daejeon, Korea

A supercritical carbon dioxide power cycle which is known as one of promising power cycle for a concentrating solar power (CSP) has technical challenges of operation near critical point and under high pressure/temperature conditions, and challenges of turbomachinery and bearing technology. Therefore, a small-scale simple supercritical carbon dioxide power cycle experimental loop was designed and manufactured to obtain diverse basic data of operational characteristics, control and stability of this power cycle, and to utilize these data for following scale-up research. As the first step, 1 kWe-class high speed turbo-generator and experimental loop for a 200 oC of supercritical carbon dioxide were designed and manufactured. A carbon dioxide is pressurized up to 130 bar by piston-type pump and heated up by an immersion electric heater, then drive a turbo-generator. A diameter of turbine wheel and rotational speed was designed to 22.6 mm and 200,000 rpm respectively. A commercial angular contact ball bearing was applied to the turbo-generator

1. INTRODUCTION

A supercritical carbon dioxide power cycle has been focused as a promising power cycle due to the compactness, a high efficiency and a wide applicability. A turbo-alternator-compressor unit (TAC) using a radial compressor is used in a several published 10-100 kW-class supercritical carbon dioxide power cycle test loop to configure a brayton power cycle. Due to a high energy density near the critical point, a size of the TAC unit becomes very small in a lab-scale test loop. Therefore, the TAC unit has a minimum size to obtain proper efficiency and manufacturability. Then, system components such as a heater, the heat exchangers, a chiller, valves, pipes and other parts have to be large to build a test loop, thus it is hard to build, control and handle the system.

2. DESIGN OF THE EXPERIMENTAL TEST LOOP

A supercritical fluid refers to a substance whose temperature and pressure are above its critical point; under such conditions, the fluid possesses both liquid and gas properties. The critical point of CO_2 is 30.98°C and 7.377 MPa, above which all of the processes of the supercritical cycle occur.

2.1 Design of the Cycle

In this study, using a small size of piston-type carbon dioxide pump, a multi-purpose 1 kW-class supercritical carbon dioxide power cycle test loop which operates as a simple recuperated Brayton cycle at a temperature of 500 °C and at a pressure of 135 bar, and as a transcritical cycle at a temperature of 200 °C is designed to concentrate on the characteristics of the cycle, control and stability issues of a supercritical carbon dioxide power cycle.

Figure 1 shows a full schematic of an experimental test loop and its transcritical operating conditions which turbine inlet temperature is a 200 °C. Two piston-type carbon dioxide pumps (Catpump, USA) which mass flow rate are 0.023 kg/s and 0.046 kg/s respectively were used to pressurize liquid carbon dioxide at a temperature of 20 °C and at a pressure of 5729 kPa up to 13000 kPa which is a supercritical state. An immersion type electric heater heats supercritical carbon dioxide up to 200 °C and then, hot CO_2 drives a radial type turbine. After expansion at a turbine, a supercritical carbon dioxide is cooled to a liquid state by coolant water at a brazing plate heat exchanger (BPHE).

When system is operated as a simple recuperated Brayton cycle, a turbine inlet temperature goes up to 500 °C and a printed circuit heat exchanger (PCHE) type recuperator is used to preheat a working fluid using remained heat after a turbine outlet. Instead of a BPHE, a PCHE type cooler is used because a pressure of a carbon dioxide is still high at a cooling process (above 7400 kPa). Using several valves and bypass loop, these two cycles are configured by one test loop facility.
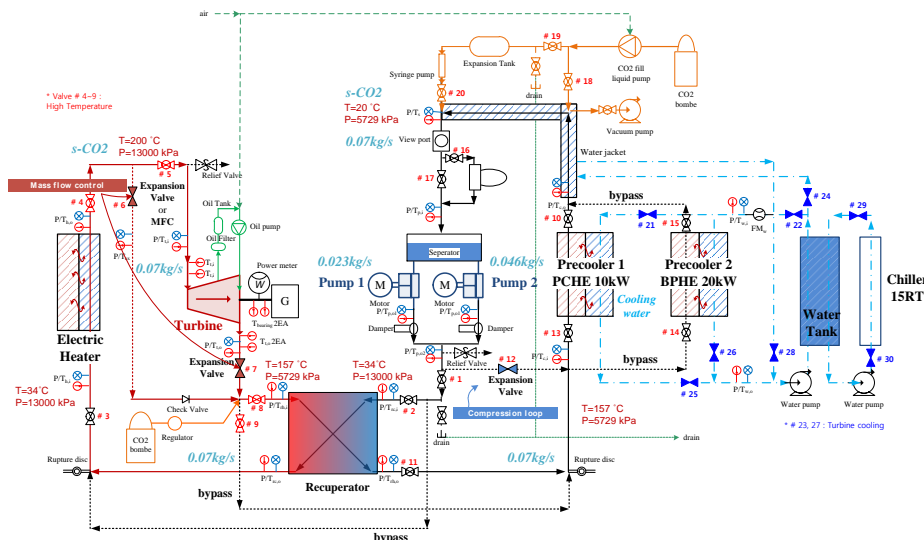

Figure 73: Schematic diagram of an experimental test loop (200°C operating condition)

2.2 Design of a High-Speed Turbo-Generator

As a first step, a transcritical carbon dioxide power cycle is designed which a turbine inlet temperature is 200 °C. Because a mass flow rate is so small (0.07 kg/s), it is difficult to design radial-type turbine. In our operating condition, an optimal radial turbine has a diameter of 22.6 mm and a rotating speed of 800,000 rpm. Since it is nearly impossible to drive 800,000 rpm turbine, a partial admission nozzle is adopted to manufacture and operate a turbo-generator in an experimental test loop. By using only one channel of a nozzle, 200,000 rpm rotating speed condition is designed as shown in Figure 2.
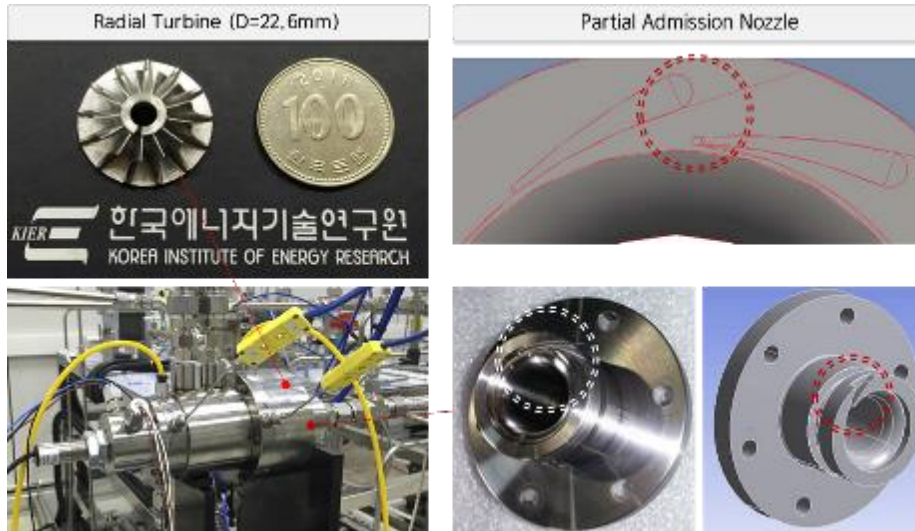
Figure 2: A high-speed turbo-generator using a radial turbine and a partial admission nozzle

In particular, a commercial angular contact ball bearing (SKF) is used to overcome technical problems of the gas foil journal and thrust bearings shown in results of the advanced research groups such as Sandia National lab. Due to thrust balancing and high temperature operation, a gas foil bearing has operation limits. Thus, in this study, bearing room is separated from a turbine room by a several labyrinth seal in order to make atmospheric pressure condition to operate oil-lubricated ball bearing. In this design, inevitable leakage loss through the labyrinth seal occurs, so a compensation loop of the carbon dioxide from the additional CO_2 tank is also designed in the test loop.

2.3 Design of Heat Source, Heat Sink, Heat Exchanger and BOPs
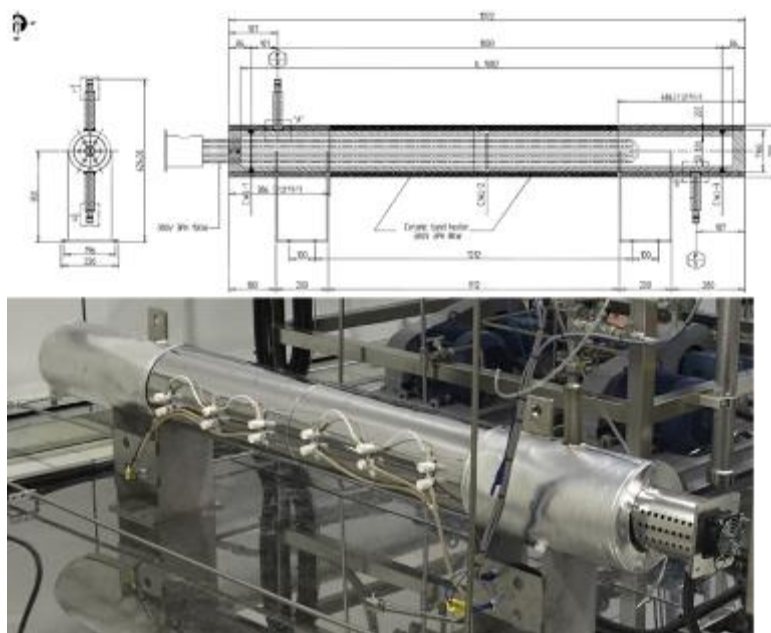
Figure 3: A 30 kW electric heater composed of a 10 kW immersion heater and a 20 kW ceramic band heater

A 30 kW electric heater was designed to use as a heat source. To focus on cycle operation and control, an electric heater is chosen because it is simple and easy to control compared to a boiler type. To endure a high pressure operating condition of a 13,000 kPa at a high temperature of 500 ^{o}C, an immersion type heater was designed and manufactured. In this study, electric heater consists of the 10 kW immersion heater and the 20 kW ceramic band heater. A capacity of 20 kW band heater was attached on the shell side surface of the immersion heater to increase total heat capacity as shown in Figure 3.

A 15 RT chiller which is composed of 5 RT and 10 RT chiller using a scroll compressor and 10 kW electric heater is designed and manufactured to make cooling water. With two chiller and heater, a temperature of a cooling water can be sophisticatedly controlled.

As shown in Figure 4, the printed circuit heat exchangers (PCHEs) were used as a recuperator and a cooler in a Brayton cycle operation for exchanging heat between the low temperature CO_2 and high temperature CO_2 in a recuperator, CO_2 and cooling water in a cooler, respectively. Through the use of multiple heat-exchanging plates consisting of micro-channels, PCHEs are able to reduce their volume and withstand high pressures and high temperatures. All PCHEs in this experimental test loop were fabricated by SUS316L material.

In transcritical operation by using a turbo-generator described in previous section, a brazing plate heat exchanger (BPHE) was designed because cheap BPHE can be applied due to lower pressure of the CO_2 side than the Brayton cycle operation.
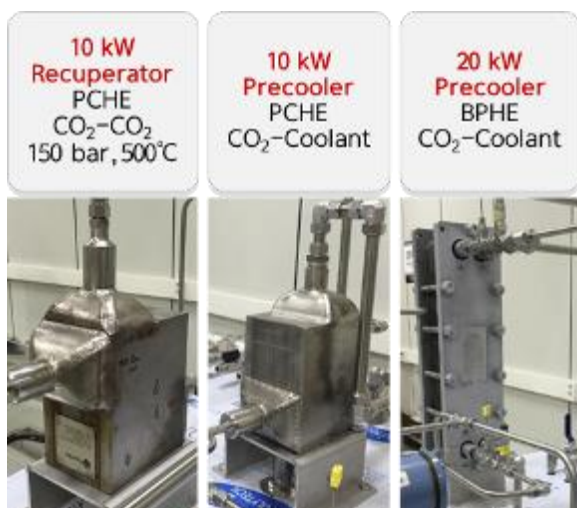
Figure 4: A 10 kW PCHE recuperator, a 10 kW PCHE cooler and a 20 kW BPHE cooler

Finally, balance of plants (BOPs) were designed or chosen. A liquid CO_2 pump to fill the CO_2 into the system, an expansion tank for separation of gas and liquid phase of CO_2, a syringe pump for regulating pressure of the closed system, a CO_2 compensation loop, the high temperature/pressure valves, the safety systems and instrumentation were designed and manufactured.

3.   PRELIMENARY OPERATION

After assembling each components, as a first step, balancing process of the turbo-generator was conducted. In wide-open atmospheric condition called as cold-run, a turbo-generator was driven by external electric power source. A level of vibration of the rotor and temperatures of the bearings were monitored. A 160,000 rpm of cold-run was successful, but some bearing operational problems were observed. After detail adjustment of the rotating parts, power generating operation will be conducted.

4. CONCLUSION

In summary, a small-scale supercritical carbon dioxide power cycle test loop was designed and manufactured to test both transcritical cycle and Brayton cycle. By using small piston-type pumps instead of a centrifugal compressor, mass flow rate of the cycle could be reduced. A high-speed turbo-generator which is composed of a radial type turbine wheel and a partial admission nozzle was developed. In addition, an immersion electric heater, the PCHEs, chiller and BOPs were fabricated.

5. ACKNOWLEDGMENT

6. REFERENCES

DOSTAL, V., Driscoll, M., Hejzlar, P., 2004. A supercritical carbon dioxide cycle for next generation nuclear reactors. Massachusetts Institute of Technology. Dept. of Nuclear Engineering, Cambridge, MA 2004; MIT-ANP-TR-100.

WRIGHT, S.A., Radel, R.F., Rochau, G.E., Pickard, P.S., 2010. Operation and analysis of a supercritical CO2 Brayton cycle. SANDIA REPORT 2010; SAND2010-0171.

POSTER SESSION E

172: The influence of the primary refrigerant thermo-physical properties on the performance of a domestic air source heat pump water heater

Stephen TANGWE[1], Michael SIMON[2], Edson MEYER[3]

1 Fort Hare Institute of Technology, University of Fort Hare, P.B X1314 Alice, South Africa, stangwe@ufh.ac.za   2 Fort Hare Institute of Technology, University of Fort Hare, P.B X1314 Alice, South Africa, msimon@ufh.ac.za
3 Fort Hare Institute of Technology, University of Fort Hare, P.B X1314 Alice, South Africa, emeyer@ufh.ac.za

The domestic air source heat pump is a reliable and energy efficient system in the production of sanitary hot water. It generates sanitary hot water by harnessing the low grade aero-thermal energy during the process of vapour compression refrigerant cycles. The primary refrigerant in the domestic air source heat pump water heater is responsible for the transportation of the useful high grade thermal energy from the evaporator to the condenser where is dissipated to heat up water to the desired set point temperature (55oC) during the vapour compression refrigerant cycles. The study focused on the critical monitoring of the thermodynamic properties of the distinctive refrigerants (R407C and R417A) used by two identical split type air source heat pump water heaters and under dynamic heating modes. The experimental data that displayed the temperature profiles from the installed temperature sensors at the compressor suction and discharge lines as well as the condenser inlet and outlet ends in conjunction with the electrical energy consumption were fully analysed to evaluate the refrigerant impact on the performance of the air source heat pump water heater. The preliminary results from the two split air source heat pumps retrofitting 150 liters high pressure geyser under the first hour heating rating and controlled simulated hot water drawn off demonstrated that the system with refrigerant R417A performed better than the other with R407C although there was no significant mean difference in their coefficient of performance. The coefficient of performance of the both systems under the different heating up scenarios was above 2. The REFPROP simulation software was used to give an analytical comparison of the two refrigerants. The results obtained from the study can be applied in the selection of an excellent thermo-physical refrigerant to be utilized as a primary fluid in a domestic air source heat pump water heater.

Keywords: Split type air source heat pump water heater, Vapour compression refrigerant cycles, Refrigerant thermo-physical properties, REFPROP simulation software, coefficient of performance

1. INTRODUCTION

The domestic air source heat pump (ASHP) water heater is an efficient and renewable device for sanitary hot water production (Morrison *et al.,* 2004). The special characteristic of the domestic ASHP water heater responsible for the excellent performance is known as the coefficient of performance (COP) (Petit and Meyer, 1997). ASHP COP can range from 2 to 4 and depends on the thermo-physical properties of the primary refrigerant and also the design of its components (evaporator, compressor, condenser and expansion valve) that make up the close loop circuit of the vapour compression refrigerant cycle close loop circuit (Levins, 1982; Bodzin, 1997). The ASHP water heater COP can be defined as the ratio of the useful thermal energy gained by the stored water to the electrical energy required to operate the system. It is worthy to allude that the performance of an ASHP can further be optimized by the efficient installation of the system (Baxter *et al.,* 2005). The domestic ASHP water heater COP can be determined by an experimental method whereby the thermal and electrical energy are quantitatively measured and also by used of TRNSYS software whereby the COP is derived using this simulation application (Tangwe *et al.,* 2015 ; Kline *et al.,* 2000). The domestic ASHP water heater can be classified into the split type and the integrated system. The split type ASHP water heater is composed of an ASHP unit retrofitting a hot water cylinder (geyser with its element disable). In a split type ASHP water heater, the ASHP unit is connected to the water storage tank by pipes or tubes and the ASHP unit is situated at a lower position. More specifically, the split type ASHP water heater can also be divided into the single pass system and the recirculation system. The integrated ASHP water heater is a compact system with the ASHP unit situated at the top of the system. The primary refrigerant thermo-physical properties are crucial in the selection of an excellent refrigerant to be employed in a domestic ASHP water heater. The popular and commonly use refrigerant R22 is widely replaced with azeotropic or zeotropic blend refrigerants (R407C, R417A and R410A) due to their zero ozone depletion potential (ODP) and tolerable global warming potential (GWP) as can be depicted in table 1 (Roberts and Pearson, 1996). The GWP and the ODP of these refrigerants make them the favourite refrigerants in ASHP.

Table 49: Some key properties of common refrigerant in ASHP

Refrigerant	Molecular mass (kg)	Boiling point (°C)	Critical temperature(°C)	Critical pressure (MPa)	ODP	GWP
R22	86.47	-40.86	96.15	4.99	0.05	1700
R410A	72.58	-51.58	72.5	4.93	0.00	2100
R407C	86.60	-43.56	86.74	4.62	0.00	1610
R417A	106.75	-39.12	87.04	4.04	0.00	2346

It can be depicted from the table 1 that the thermo-physical properties of R407C and R417A refrigerants are comparable in terms of the critical temperature, boiling point and critical pressure. This thermodynamics properties make the refrigerants very suitable as a primary fluid in ASHP water heater. Based on the lower boiling point and the higher critical temperature of these refrigerants (R407C and R417A), it is possible to absorb substantial aero-thermal energy at the evaporator in the form of latent heat which is later compressed to high grade thermal energy before transported to the condenser where the thermal energy in the refrigerant is dissipated.

1.1 The vapour compression refrigerant cycle of ASHP unit

The major components of an ASHP unit that make up the close circuit of the vapour compression refrigerant cycle are the evaporator, compressor, condenser and expansion valve as well as the primary refrigerant. The figure 1 illustrates the schematic block diagram of the component connection in the closed loop circuit of a vapour compression refrigerant cycles. During a typical vapour compression refrigerant cycles, the refrigerant (R407C or R417A) picks up aero-thermal energy from the ambient at the evaporator. The extracted aero-thermal energy is converted as latent heat of evaporation to change the refrigerant to a low pressure and temperature vapour. The process occurring at the evaporator is isothermal. This refrigerant vapour enters the compressor via the suction line and is compressed to a high pressure and temperature super-heated steam and then transported to the condenser through the discharge line. The process occurring at the compressor is isentropic. In the condenser, the refrigerant dissipates the absorbed thermal energy to the secondary fluid (water) and it becomes a low temperature and high pressure refrigerant liquid. The process is an isobaric condensation. Finally, the refrigerant flow passes a thermal expansion valve where the pressure is reduced due to the process of throttling. The process occurring at the expansion valve is isenthalpic. Electrical energy is required to sustain the vapour compression refrigerant cycle as the heat flows from a low temperature source (evaporator) to a high temperature sink (condenser). There are

also auxiliary components that consumed electrical energy (such as the water circulation pump and the propeller axial fan) incorporated into the ASHP unit intended to retrofit an electric high pressure geyser with its element disabled.
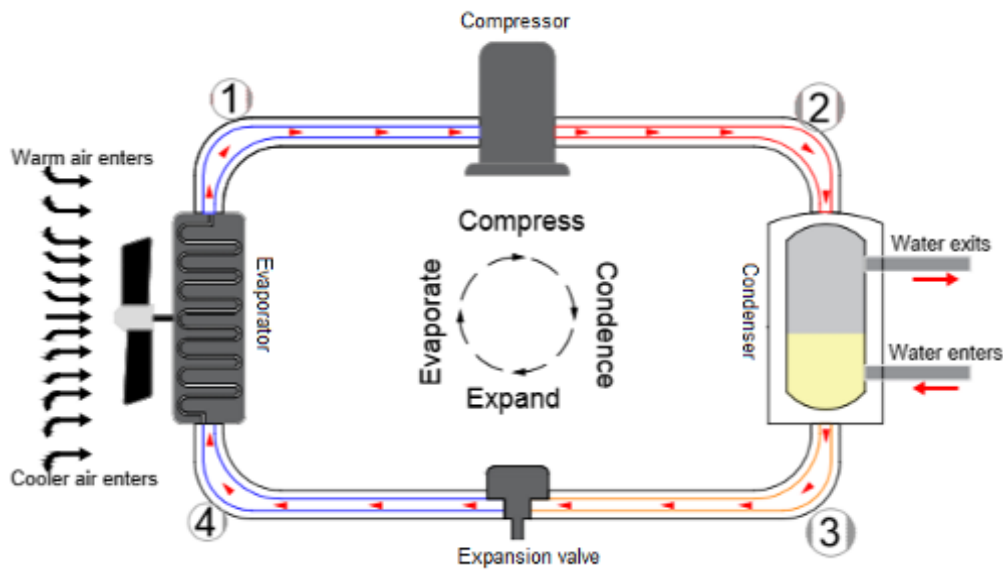

Figure 1: Shows the schematic diagram of the close loop circuit in a VCRC

1.2 The saturated vapour temperature and entropy plots

REFPROP is a recognized and accredited refrigerant simulation application used to simulate the thermodynamic properties of refrigerant (Lemmon *et al.,* 2013). The plots of temperature against entropy for R407C and R417A were generated using the REFPROP simulation software and are shown in figures 2 and 3 respectively. The saturated vapour plots for the temperature and entropy for the both refrigerants compare to that of R22 and hence make them the suitable replacement candidates for R22. It can also be observed from the plots that the critical temperature for the refrigerants are almost equal. The critical temperature is the maximum temperature in the saturated vapour temperature and entropy graph and correspond to the point where the liquid and vapour phase of the refrigerant becomes indistinguishable.
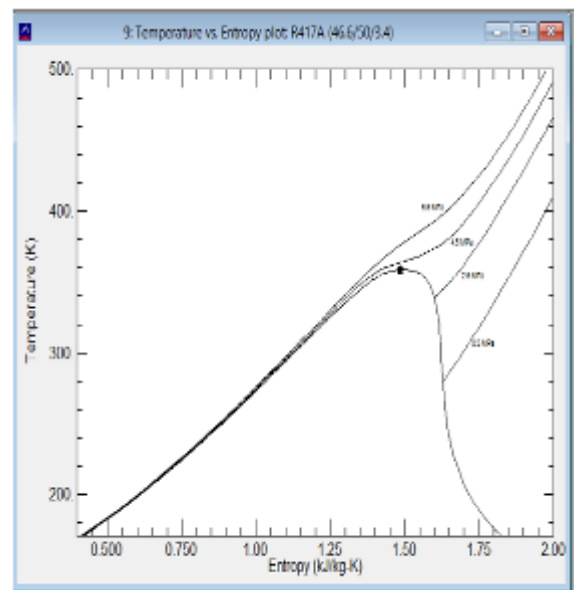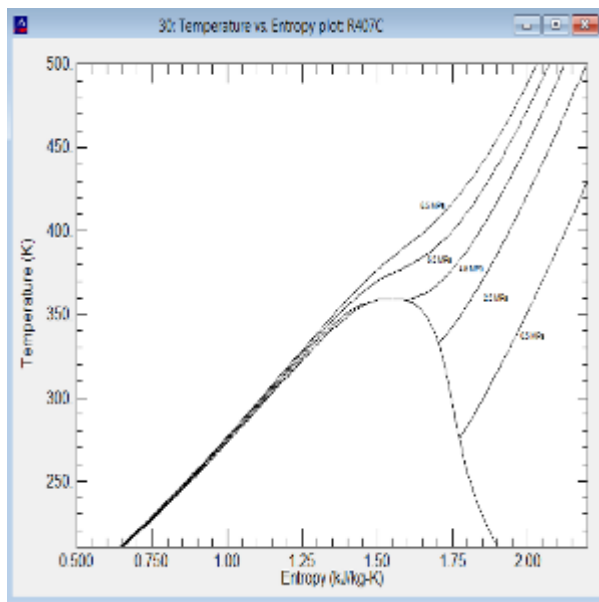
.*Figure 2: Graph of temperature vs entropy for R407C* *Figure 3: Graph of temperature vs entropy for R417A*

1.3 The saturated vapour pressure and enthalpy plots

The figures 4 and 5 illustrate the pressure and enthalpy graphs for R407C and R417A and were generated using the REFPROP simulation software. The critical pressures for the refrigerants are almost equal and comparable to that of R22. The saturated vapour pressure and enthalpy graphs for the above refrigerants are identical and mimic that of R22. This identical representation of the pressure and enthalpy plots of the blend (R417A and R407C) to R22 provided sufficient evidence of using the R407C and R417A as the ideal refrigerant for ASHP water heaters.
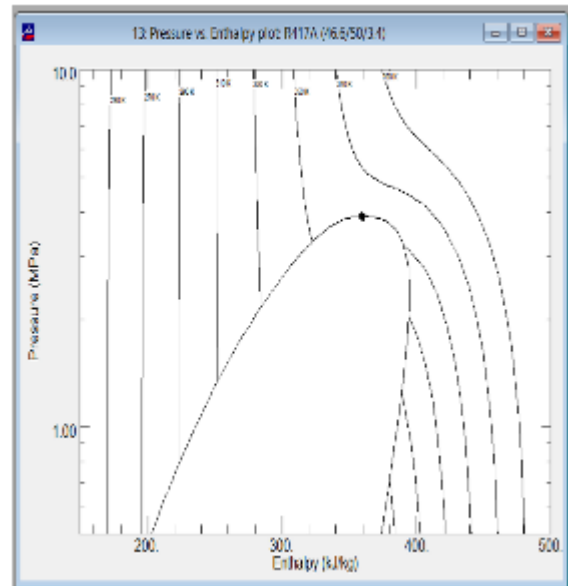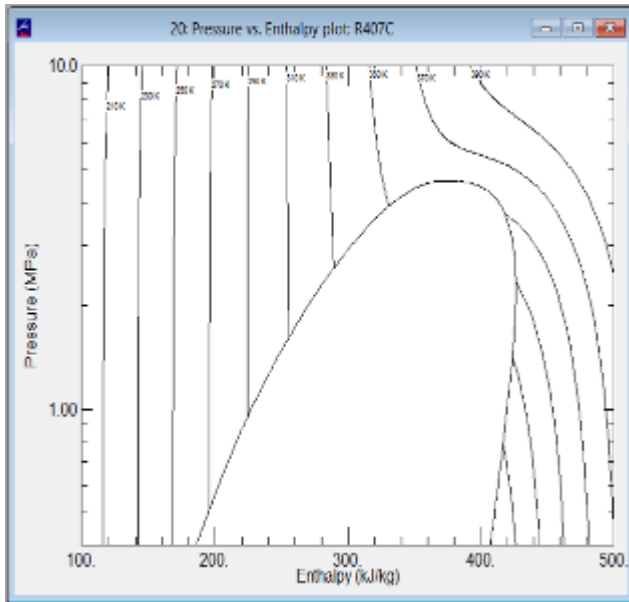
Figure 4: Graph of pressure vs enthalpy for R407C   Figure 5: Graph of pressure vs enthalpy for R417A

1.4 Specification of the split type ASHP units and the installation of the ASHP water heaters

The figure 6 illustrates the installation setup of the split type domestic ASHP water heaters that were employed for the study. It comprised of an ASHP unit (with R407C and R417A as the refrigerant) and a 150 litres geyser. In addition, a data logger is incorporated that monitored the thermodynamics temperature profiles for the refrigerant during the vapour compression refrigerant cycles, the volume of water heated and the electrical energy consumption of the systems.

Figure 6: Illustrates the ASHP water heater and data logger installation setup

Table 2 shows the specifications of the two split type ASHP water heater used for the study, according to the manufacturer's nameplates details with the initial cold water temperature ranging from 16 -24 $^{\circ}$C and the hot water set point temperature of 55°C. The minimum ambient temperature should be greater than 4°C according to manufacturer standards.

Table2: ASHP water heaters specifications

	Kwikhot ASHP water heater	SIRAC ASHP water heater
Refrigerant	407C	R417A
Rated heating capacity (kW)	3.5	4.7
Rated input power (kW)	1.43	1.30
Auxiliary electrical power (kW)	0.00	0.00
Voltage supply/Frequency/Phase	230V/50Hz/1PH	230V/50Hz/1PH
Noise level (dB)	49	50

2. OBJECTIVES

The primary focuses of the study were as follows;

To monitor the coefficient of performance of the two split type ASHP water heaters under distinctive heating up scenarios (firstly, under the first hour heating rating and secondly during a 50 litres and 100 litres controlled hot water drawn off from the storage tank).

To compare the electrical power consumption profiles of the two systems during the respective vapour compression refrigerant cycles in relation to the scenarios.

To perform a comparative analysis of the temperature profiles of the vapour compression refrigerant cycles for the different ASHP water heaters.

3. MATERIALS AND METHODS

The table 3 presents the list of devices and sensors used for the experimental setup.

Table 3: Materials used for the experimental setup

Devices and sensors	Purpose
Kwikhot ASHP unit (R407C)	To retrofits one of the 150 liters geyser tank
SIRAC ASHP unit (R417A)	To retrofits one of the 150 liters geyser tank
Two 150 litres geysers	To serve as hot water storage tank for the retrofits
Two power meters	To measure the electrical power consumption of both systems
Twelve temperature sensors	To measure the temperatures at different locations of the two systems
Ambient and relative humidity sensor	To measure the ambient temperature and relative humidity
Two flow meters	To measure the water flow rate into the inlet of the ASHP unit

Two temperature sensors were installed on the inlet and outlet pipe of each ASHP unit to measure the temperature of water flowing into the ASHP unit and also the water exiting from the unit. Four temperature sensors were installed on the compressor suction and discharge lines as well as the condenser inlet and outlet ends for each of the ASHP units. These temperature sensors measured the refrigerant temperatures at the installed locations. A flow meter is connected to the inlet pipe of the ASHP unit to determine the hot water flow rate during a heating up cycle. The temperature sensors, flow meters and the power transducers were configured to log every one minute interval. The ambient temperature and relative humidity sensor were also configured and logging in one minute interval.

4. CALCULATIONS AND THEORY

The useful output thermal energy gained by the stored water is given by equation 1

$$Q = mc\Delta T \qquad\qquad (1)$$

Where:

Q = Useful thermal energy gained by water in kWh

m= mass of water heated in kg = volume of water heated in L

c = specific heat capacity of water = 4.2 kJ/kg^{o}C

Δ T = temperature difference between ASHP outlet and inlet water temperature

The input electrical energy consumed by the ASHP water heater is given by equation 2

$$E = Pt \qquad\qquad (2)$$

Where:

E = Input electrical energy in kWh

P = Electrical power consumption in kW

t = 5 minutes time interval

The coefficient of performance of the ASHP water heater is the ratio of the output useful thermal energy and the input electrical energy and is given by equations 3 and 4.

$$COP = Q / E \qquad\qquad (3)$$
$$COP = mc\Delta T / Pt \qquad\qquad (4)$$

Where:

COP = coefficient of performance of the ASHP water heater

5. RESULTS AND DISCUSSIONS

The results and discussions in this study were broken down into the electrical and thermodynamics performance of the two split type ASHP water heaters under the distinctive heating up scenarios.

5.1 First hour heating rating COP for the ASHP water heater

Table 4 shows the first hour heating rating performance for the ASHP water heaters for three specific periods in a day; namely during the morning hours from 8:00, during the afternoon hours from 14:00 and during the evening hours from 18:00. The first hour heating rating is a heating up cycle whereby the hot water in the stored tank is completely drawn off and cold water allow to fill the tank while the ASHP water heater is force to heat up the water to the set point temperature (55 ^{O}C) (Tangwe *et al.*, 2014). The results delineated that, although both systems were operating under the same conditions, the COP of the SIRAC ASHP water heater using R417A is slightly better than that for the Kwikhot ASHP water heater using R407C. It should be emphasized that the initial cold water temperature as well as the average ambient temperature and relative humidity under the operating condition of both systems were the same, since the both systems were filled up with water from the same source and switch on without any time lap. In all the first hour heating up scenarios, the SIRAC ASHP water heater took over two hours to attain the set point

temperature while the Kwikhot system uses almost three hours. This is attributed to the better COP and the higher average input power consumption of the SIRAC system.

Table 4: COP of systems with respect to water temperatures and ambient conditions

Heating up period	Initial water temperature (oC)	Water set point temperature (oC)	Ambient temperature (oC)	Relative humidity (%)	System COP R407C	R417A
Morning	16.5	55.0	20.0	72.0	2.78	2.90
Afternoon	20.0	55.0	23.5	56.3	2.53	2.58
Evening	17.0	55.0	17.0	81.0	2.54	2.74

The Table 5 confirms that the input power consumption for the Kwikhot system is smaller than that of the SIRAC ASHP water heater for all the first hour heating up scenarios. Despite, of the smaller power consumption, the electrical energy consumption for the Kwikhot system is greater than that of the SIRAC system. It can be observed from both tables 4 and 5 that the COP during the first our heating rating is greater than 2 and agree with literatures regarding the coefficient of performance of domestic ASHP water heaters [3; 4].

Table 5: COP of systems with respect to water temperatures and ambient conditions

Heating up period	Average power consumption (kW) R407C	R417A	Total electrical energy consumes (kWh) R407C	R417A	Total thermal energy gain (kwh) R407C	R417A	System COP R407C	R417A
Morning	0.87	1.34	2.45	2.35	6.80	6.80	2.78	2.90
Afternoon	0.93	1.42	2.41	2.37	6.13	6.13	2.53	2.58
Evening	0.89	1.35	2.67	2.48	6.80	6.80	2.54	2.74

5.2 First hour heating rating compressor and condenser temperature profiles

The figures 7 and 8 show the temperature profiles for the ambient temperature, compressor suction and discharge lines temperatures and the condenser inlet and outlet end temperatures for the two ASHP water heaters as they undergo vapour compression refrigerant cycles during a typical first hour heating rating. The figure 7 demonstrated that the compressor suction temperature is lower than the ambient temperature and hence aero-thermal energy will be extracted by the refrigerant at the evaporator. There exist no marginal difference between the compressor discharge temperature profile and that of the condenser inlet temperature profile in the figure 7 owing to the efficient insulation that prevented heat losses. The figure 7 also shows a smaller temperature difference between the condenser inlet temperature and the outlet temperature for the refrigerant throughout the vapour compression cycles. This insinuates a lower COP when compared to the temperature lift in figure 8. Furthermore, there is a marginal difference in the compressor discharge temperature profile to that of the condenser temperature as shown in figure 8. The difference in the condenser inlet and outlet temperature during a vapour compression refrigerant cycles is a measure of the useful thermal heat dissipated.

1.1 First hour heating rating power consumption

Figures 9 and 10 shows the profiles for the input electrical power consumption during a typical first hour heating rating scenario for the two ASHP water heaters. It can be depicted that the input power consumption increases as the heating up cycle progresses. The power consumption does not depend on the relative humidity as during the heating up process the relative humidity decreases while power consumption increases. The power consumption depends principally on the hot water heating load and the initial temperature of the water intended to be heated. From the figure 9, the power of the Kwikhot ASHP water heater varies from 0.7 kW to 1.1 kW, while in the figure 10, the power of the SIRAC ASHP water heater varies from 1.4 kW to 1.7 kW.
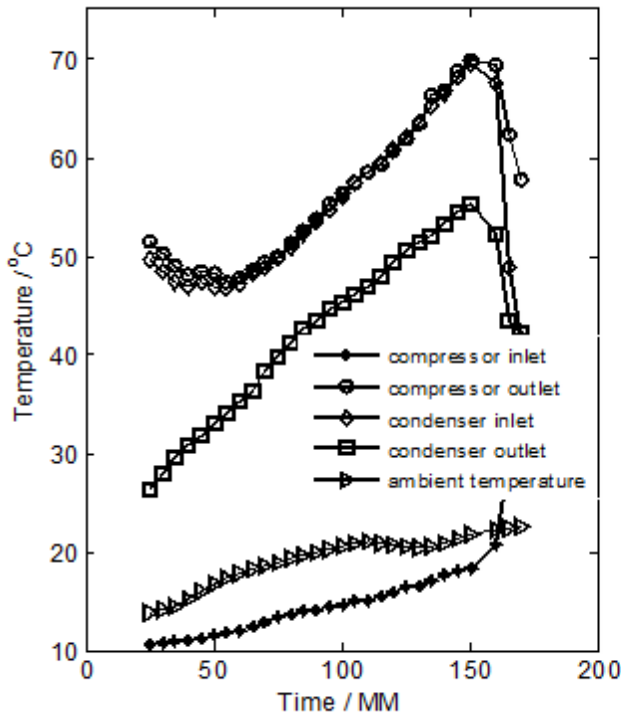
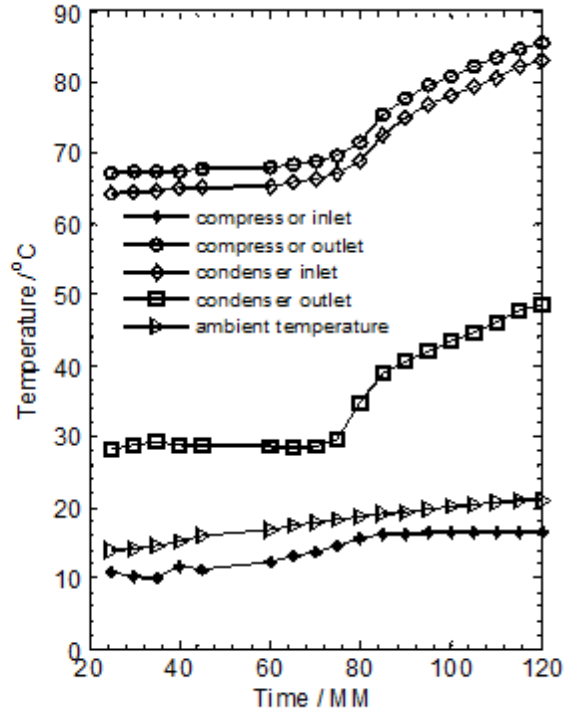*Figure 7: Temperature profiles for R407C ASHP*

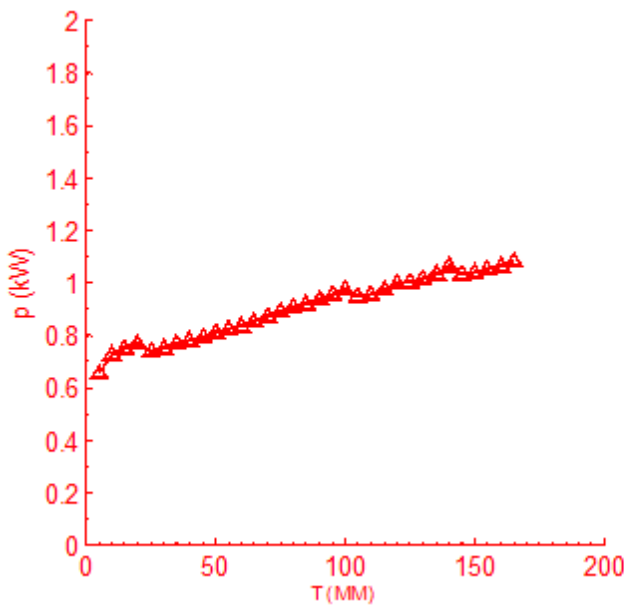*Figure 8: Temperature profiles for R417A ASHP*

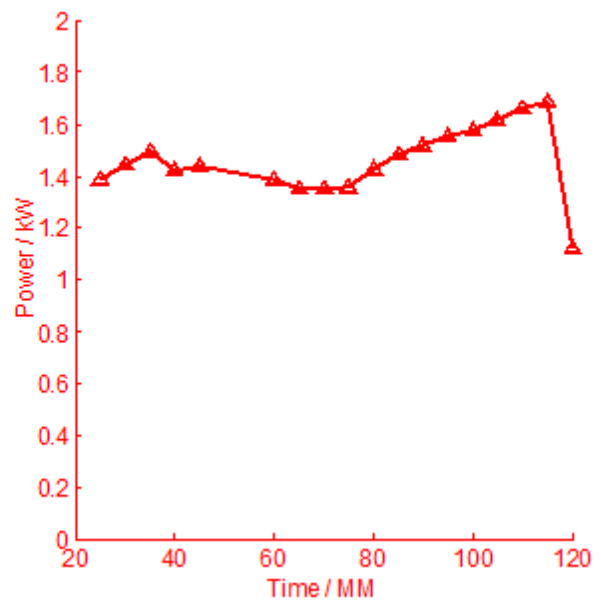*Figure 9: Power consumption profile for R407C system Figure 10: Power consumption profiles for R417A system*

2.35. 5.4 Simulated controlled water drawn off heating up cycles

The table 6 shows the ambient conditions and the initial temperature of water associated with the reported COP for the Kwikhot and SIRAC ASHP water heaters after a 100 liters and 50 liters hot water drawn off in the morning and afternoon for a typical day. It can be observed that with a much volume of hot water drawn off from the tank, the initial water temperature was lower. The lower the initial water temperature (21.5 °C registered after the 100 litres hot water drawn off) the better the COP when compared to a scenario of higher initial water temperature (39.0 °C registered after a 50 litres hot water drawn off).

Table 6: COP of systems with respect to water temperatures and ambient conditions

Heating up period	Initial water temperature (oC)	Water set point temperature (oC)	Ambient temperature (oC)	Relative humidity (%)	System COP	
					R407C	R417A
Morning	21.5	55.0	17.0	70.0	2.62	2.78
Afternoon	39.0	55.0	22.5	50.0	2.01	2.74

The higher COP recorded by the SIRAC system in either of the controlled hot water drawn off scenarios were due to the smaller electrical energy consumption during the vapour compression refrigerant cycles. These smaller electrical energies consumed by the SIRAC system can be clearly depicted from table 7.

Table 7: COP of systems with respect to water temperatures and ambient conditions

Heating up period	Average power consumption (kW)		Total electrical energy consume (kWh)		Total thermal energy gain (kwh)		System COP	
	R407C	R417A	R407C	R417A	R407C	R417A	R407C	R417A
Morning	0.93	1.46	2.08	2.08	5.77	5.77	2.62	2.78
Afternoon	0.80	1.54	1.21	1.03	2.41	2.40	2.01	2.33

2.36. 5.5 Compressor and condenser temperature profiles for simulated hot water drawn off

Figures 11 and 12 show the ambient temperature, compressor suction and discharge temperature and condenser inlet and outlet temperature for the refrigerant during the vapour compression refrigerant cycles initiated by a 100 litres hot water drawn off on both the Kwikhot and SIRAC systems. It can be deduce that, though hot water drawn off does not correspond to a full drawn off (150 litres), the respective profiles pattern mimics that of the first hour heating rating. The duration of the heating up cycles is less as compared to the first hour heating rating. Furthermore, it can be observed that the Kwikhot system took over two hours to heat up water to the set point temperature while the SIRAC system use below 1.5 hours. In this scenario, it can also be depicted that the temperature difference during the vapour compression refrigerant cycles for the condenser inlet and outlet temperatures are higher for the SIRAC as oppose to the Kwikhot system. This also implies greater thermal energy is dissipated by the SIRAC ASHP water heater during the VCRC. Base on the temperature lift for the both systems, it can be alluded that the SIRAC system exhibit a higher temperature lift and hence justify the reason for the system better COP.
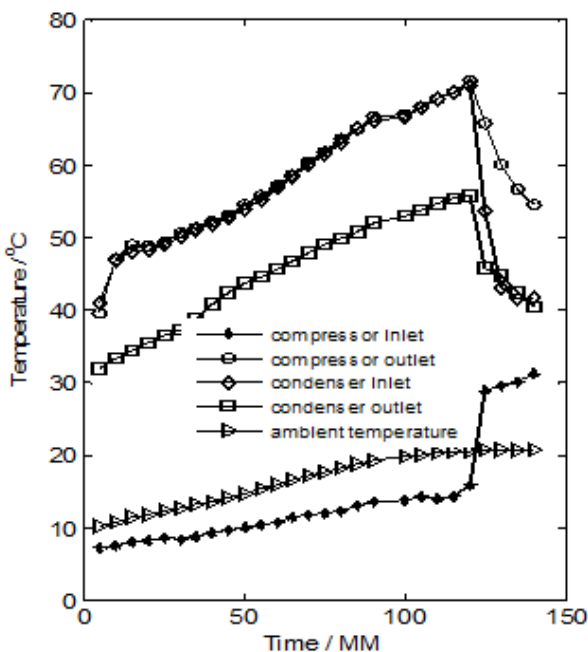

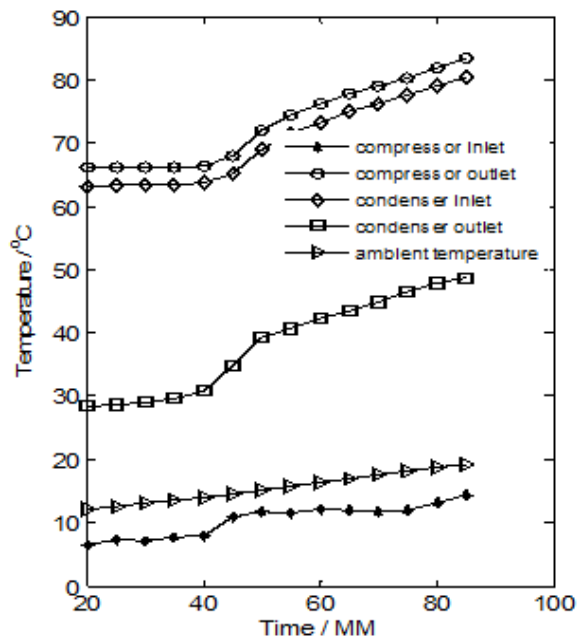*Figure 11: Temperature profiles for R407C system for a 100 litres drawer*

Figure 12: Temperature profiles for R417A system for a 100 litres drawer

5.6 Power consumption profiles for the simulated hot water drawn off

The figures 13 and 14 show the profiles of the electrical power consumption owing to the heating up cycles initiated by a 100 liters hot water drawn off from both of the ASHP water heaters. The power consumption increases with an increase in the heating up period. This can also be confirmed that despite the power consumption increases with an increase in the hot water heating load, it also turns to increase with a rise in the ambient temperature. The slight increase in the average power consumption under this heating up mode on the both systems is partly due to the rise in the average initial water temperature as presented in table 6.
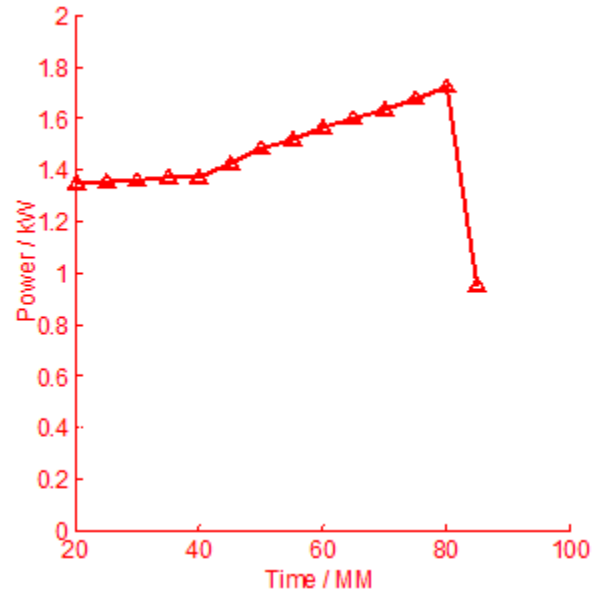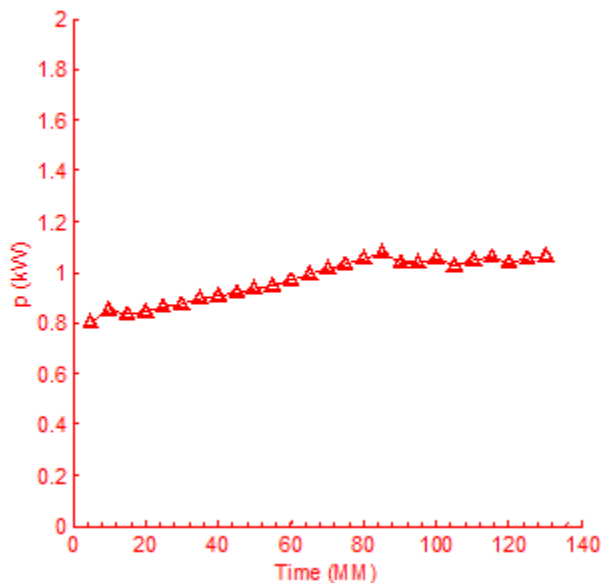
Figure 13: Power consumption profile for R407C system Figure 14: Power consumption profiles for R417A system

2. CONCLUSION

Conclusively, the ASHP water heater using the refrigerant R417A has a slightly better thermo-physical properties than the one with refrigerant R407C. The refrigerant R417A, can attain up to an average of 70°C as the condenser inlet temperature while R407C condenser average inlet temperature can only range from 50-60°C in a typical refrigeration cycle whereby hot water set point temperature was 55°C. Furthermore, the difference in the condenser inlet and outlet temperature during a vapour compression refrigerant cycles is over 30°C for the R417A system and just above 10°C for the R407C system. This higher temperature difference translates to a greater enthalpy change which is responsible for the amount of thermal energy dissipated by the refrigerant at the condenser side.

3. REFERENCES

BAXTER, V. D., Tomlinson, J. J., Murphy, R.W., Ashdown, B.G., and Lapsa, M. V. 2005. Residential Heat Pump Water Heater Development Status USA www.ornl.gov/~webworks/cppr/y2001/pres/122293.pdf.

BODZIN, S. 1997. "Air-to-Water Heat Pumps for the Home". Accessed July/August 1997. www.homeenergy.org/show/article/nav/hotwater/page/8/id/1315

DOUGLAS, J (2008). Demonstrations Encourage Wider Use of Efficient Technologies. EPRI Journal, 15-17.

LEMMON, E W.., Huber, M L.., and McLindea, M O.., 2013. NIST Reference Fluid Thermodynamic and Transport Properties REFPROP, Applied Chemicals and Materials Division, National Institute of Standards and Technology, Colorado.

LEVINS, W.P. 1982. "Estimated Seasonal Performance of a Heat Pump Water Heater Including Effect of Climatic and In-House Location." Oak Ridge National Laboratory, Oak Ridge, TN. National Technical Information Service. Vergina, USA. A03 Microfiche A01.Pp 24-36.

MORRISON, G.L., Anderson, T., and Behnia M. 2004. "Seasonal Performance Rating of Heat Pump Water Heaters." Energy Conservation & Management 76:147-52.

ROBERTS, N. A and Pearson, S. F, 1996. High Efficiency R22 replacement, International Refrogeration and Air Conditioning Conference, Paper 456. http://docs.lib.purdue.edu/iracc/456.

PETIT P.J and Meyer J.P. 1997, A techno-economic analytical comparison of the performance of air coupled and horizontal-ground coupled air conditioners in South Africa. International Journal of Energy Research 1997:21(11):1011-21.

TANGWE, S., Simon, M., and Meyer, E., 2014. Mathematical modeling and simulation application to visualize the performance of retrofit heat pump water heater under first hour heating rating, Renewable Energy, vol. 72, issue C, pages 203-211

TANGWE, S., Simon, M., and Meyer, E., 2015. Quantifying residential hot water production savings by retrofitting geysers with air source heat pumps, 23rd International Conference on Domestic Us of Energy, Cape Town, South Africa, pp 235-241.

211: Investigation on the performance of air source heat pump system with new environment friendly refrigerants for a low carbon building

Yate Ding[*], Erdem Cuce, Saffa Riffat, Chungui Lu

Institute of Sustainable Energy Technologies, Department of Architecture and Built Environment, University of Nottingham, Nottingham NG7 2RD, UK
*Corresponding Author E-mail Address: yate.ding@nottingham.ac.uk

Energy is an important development factor. It is consumed in different format from different sources in daily human activities. Solar energy, as the most fundamental renewable energy resource, serves in a clean, domestic and environmentally friendly way with minimum impact on surroundings. Due to the ability of transferring heat from low temperature to high temperature, heat pump systems can make great use of natural resources and waste heat resources for the purpose of space heating. Based upon this theoretical principle, this paper presents an investigation on the performance of air source heat pump (ASHP) system with new environment friendly refrigerants, such as R1233zd(E), R1234YF, R1234ze(Z) and R1234ze(E). At the same time, some conventional refrigerants (R134a, R245fa and R123) have been investigated as well for results comparison. A MATLAB program has been developed with the assistance of the database of CoolProp. The results show that the use of some selected environment friendly refrigerants in air source heat pump system for building application alongside other refrigeration applications in strongly recommended.

Keywords: heat pump, refrigerants, air source

1. INTRODUCTION

Due to the ability of transferring heat from low temperature to high temperature, heat pump systems can make great use of natural resources and waste heat resources for the purpose of space heating. With the assistance of external power, a heat pump accomplishes the work of transferring energy from the heat source to the heat sink. Ground Source Heat Pump (GSHP) systems, also known as geothermal heat pumps, generally have higher efficiencies since they draw heat from ground soil which is at a relatively constant temperature throughout the year. Air source heat pump (ASHP) is another branch of heat pumps, but draws heat from low temperature ambient air and boosts it to a higher temperature. Heat in the air is absorbed at low temperature into a fluid, which then passes through a compressor where its temperature is increased, and transfers its higher temperature heat to the heating and hot water circuits of the residence. Although the efficiency of ASHP may be lower, it also presents various merits over water or ground source heat pump, involving lower maintenance and easier installation. An ASHP system can provide a full central heating solution and domestic hot water up to 80°C if it is correctly specified.

2. CONCEPT AND PRINCIPLE OF OPERATION

The theoretical model and simulation of new refrigerants are based on the reversed Carnot Cycle and heat transfer laws in different form, which relate the environmental variables with the thermal energy absorbed by the collectors and the mechanical compression refrigeration cycle. The refrigerant thermodynamic cycle of heat pump systems is indicated by Figure 1, which includes four processes: compression to condensing pressure in compressor (1 to 2s theoretically or 1 to 2 practically), isobar condensation to saturation liquid state in condenser (2 to 3), isenthalpic expansion through TEV or capillary tube (3 to 4) and constant isothermal evaporation. Therefore, the model and simulation allow one to obtain the operating temperatures and parameters starting from the following conditions: temperature, wind speed and PV/heat insulation solar glass power input (solar radiation).
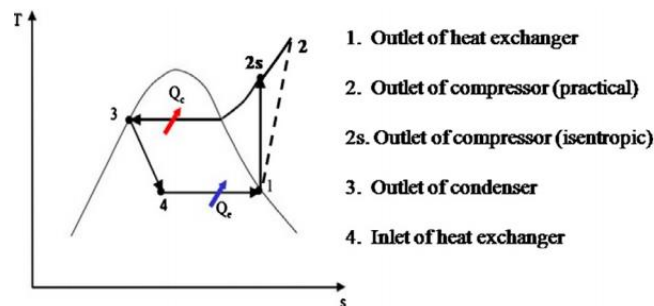

1. Outlet of heat exchanger
2. Outlet of compressor (practical)
2s. Outlet of compressor (isentropic)
3. Outlet of condenser
4. Inlet of heat exchanger

Figure 74: Indication of the heat pump thermodynamic cycle in T-s diagram

2.1 Condenser and evaporator model

When simulating the performance of innovative refrigerants, the energy rate absorbed at the evaporator and released at the condenser can be determined in terms of the refrigerant enthalpy changes in Eq. (1) and (2) respectively.

$$Q_{evap,ref} = m_r \cdot (h_1 - h_4) \qquad\qquad (1)$$
$$Q_{cond,ref} = m_r \cdot (h_2 - h_3) \qquad\qquad (2)$$

However, in the process of actual ASHP system test, the real heating and cooling capacity are obtained from Eq. (3) by measuring the air temperature difference between inlet and outlet of condenser and evaporator, and the air mass flow rate at the same time.

$$Q_{cond,air} = m_a \cdot c_p \cdot (T_{air,out} - T_{air,in}) \qquad\qquad (3)$$

2.2 Compressor model

The compressor work, W_{comp} for a given pressure ratio P_2/P_1 can be determined by from the following equation:

$$W_{comp} = \frac{P_1 v_1}{\eta_{comp}} \left(\frac{k}{k-1}\right) \left[\left(\frac{P_2}{P_1}\right)^{\frac{k-1}{k}} - 1\right] \qquad (4)$$

Where k is the ratio of specific heat. The assumption of ideal gas behavior during the compression process is found to be fairly reasonable, because the compressor work expressed in this method is somewhat overestimated compared with the value obtained directly from the refrigerant property table. Since the coefficient of performance of the heat pump is inversely related to the compressor work, this will lead to conservative or underestimated values of COP. The compressor indicated power can be calculated in terms of the enthalpy change of the refrigerant from the inlet and outlet of the compressor as in Eq. (5).

$$W_{comp} = m_r(h_2 - h_1) \qquad (5)$$

To simplify the calculation process, when doing simulation of refrigerant thermal performance on the basis of property chart, the enthalpy value of refrigerant at compressor outlet is replaced by the enthalpy value at the temperature of 5℃ or 10℃ higher than the condensing temperature.

2.3 Coefficient of performance

The relationship between the heat rejected by condenser and the work consumed by compressor is defined as coefficient of performance (COP) of the heat pump, which can be calculated from Eq. (6)

$$COP = \frac{Q_{cond}}{W_{comp}} = \frac{m_r \cdot (h_2 - h_3)}{m_r \cdot (h_2 - h_1)} = \frac{h_2 - h_3}{h_2 - h_1} \qquad (6)$$

However, the COP expressed above is a theoretical situation that only takes into account the enthalpy change of refrigerant. In reality, some auxiliary equipment, such as refrigerant pump, water pump (in water tank system) or fan, consumes electrical energy to run the system. Therefore, the effective coefficient of performance can be established by the following equation which replaces the compressor consumption by electrical input,

$$COP_{effective} = \frac{Q_{cond}}{W_{elec}} \qquad (7)$$

3. WORKING FLUIDS: ENVIRONMENT FRIENDLY REFRIGERANTS

3.1 Hydrofluoro Olefin (HFOs)

The Investigation of halogenated olefins with fluorinated propane isomers is currently endured as potential low GWP replacements for R134a in automotive applications. This effort is mainly related to the European F-gas regulations that do not allow the use of refrigerants with GWP greater than 150 in new models starting from January 2011 and new manufactured vehicles on January 2017. Amongst HFOs, R1234yf is identified as the promising alternative of R134a in automotive applications [1]. R1234ze(Z) and R1234ze(E) are other HFO refrigerants that have been developed to substitute R134a in refrigeration applications where sink temperature is as high as 70°C [1, 2]. Yet, R1234ze's has been commercially available as foam blowing agent [3]. The performances of HFOs are reported to be similar to R134a and with similar system size and operation pressures. Moreover they are compatible with available R134a components. Unlike 134a, both R1234yf and both R1234ze types have mild flammability where they are classified as class two refrigerants. However, to ignite a class two refrigerant, significantly large energy is required [4].

3.2 Hydrochloroflouroolefins (HCFOs)

Particularly R1233zd(E), was developed by Honeywell as a foam blowing agent and cleaning solvent to replace CFCs and HFCs and HCFCs [5]. However, the refrigerant has been promoted by the developers as the promising alternative for R123 and R245fa in ORC applications, high capacity chillers, and high

temperature applications [6]. Although R1233zd(E) has chlorine, the refrigerant is non-flammable, non-toxic, has negligible ODP, very low GWP, and very short atmospheric life time of 26 days [7]

The very recent undergoing investigations of new working fluids such as HFO's and HCFO R1233zd(E) gained attention. However few of HFOs has been evaluated theoretically for ORC applications such as R1234yf and R1234ze(E) in [8]. The rest of these emerging refrigerants were not seen in either theoretical or real ORC applications. Most importantly, the promising HCFO R1233zd(E) which still unavailable commercially and with thermodynamic properties that are still not publicly available.

In this section the thermodynamic performance of selected HFO's and HCFO R1233zd(E) whose properties were supplied privately are evaluated in a heat pump system to supply space heating from PV/heat insulation solar glass. The performances of the new refrigerants were also compared to conventional refrigerants. Table 1 presents the evaluated refrigerants alongside their critical and environmental properties.

Table 50: Environment friendly and conventional refrigerants thermodynamic information

Refrigerant	Molecular weight [kg/kmol]	Critical Temperature [K]	Critical pressure [bar]	GWP	ODP	ASHRAE standard 34 and EN378 [9]
Environment friendly refrigerants						
R1233zd(E)	130.496	438.75	35.709	>5 [7]	0 [10]	A1
R1234YF	114.042	367.85	33.822	4[8]	0	A2L
R1234ze(Z)	114.042	423.27	35.33	6 [1]	0	A2L
R1234ze(E)	114.042	382.52	36.3625	6[8]	0	A2L
Conventional refrigerants						
R134a	102.03	374.21	40.59	1430	0	A1
R245fa	134.05	427.15	36.51	1030	0	B1
R123	152.93	456.82	36.70	77	0.02	B1
Keys: A1: Non-flammable and has very low toxicity. A2L: Moderate flammability and low toxicity. B1: Non-flammable, and has higher toxicity.						

4. HEAT PUMP SYSTEM

The schematic diagram of the simulated heat pump is shown in Figure 2 and Figure 3, which include four main components: compressor, condenser, capillary tubes (operates as expansion valve) and evaporator with some proposed refrigerants (see Table 1) flowing inside as working fluid. Both condenser and evaporator are finned heat exchanger and two fans are installed besides the condenser and the evaporator for the purpose of exchanging heat with these two components through the circulation of air.
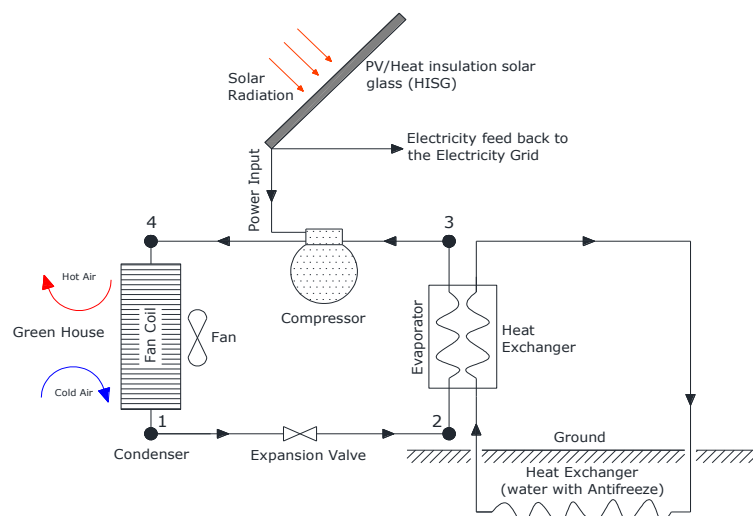

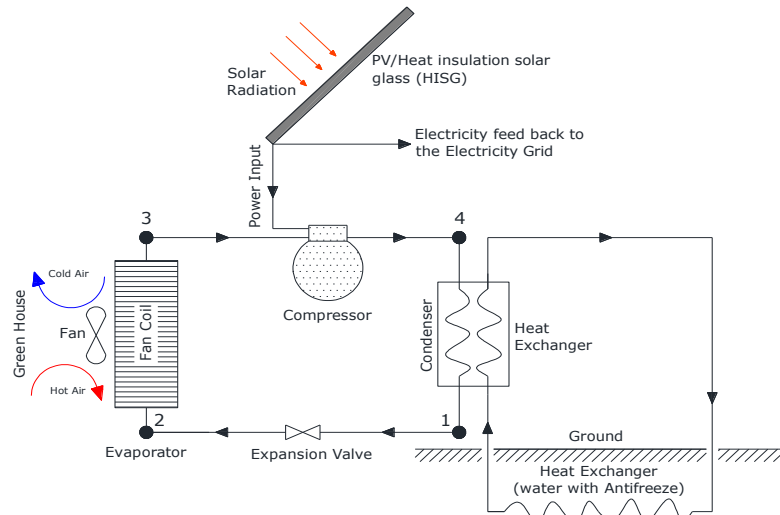*Figure 2: Heat pump system for green house (winter)*

Figure 3: Heat pump system for green house (summer)

5. SIMULATION RESULTS AND ANALYSIS

The simulation is conducted within the range of condenser temperature varies from 25°C to 95°C and evaporator temperature sets at 5°C (winter) and 15°C (summer) to compare the environment friendly new refrigerants to conventional refrigerants. An average scroll compressor isentropic efficiency reported in literatures of 80% was used for the heat pump system. External PV/heat insulation solar glass power input is set up to 1kW. After simulation with the assistance of MATLAB and refrigerant thermodynamic properties chart from CoolProp, the comparison of thermal performance and coefficient of performance on these proposed refrigerants (R134a, R245fa, R123, R1233zd(E), R1234yf, R1234ze(Z) and R1234ze(E)) have been carried out, as shown in Figure 4 to Figure 7.
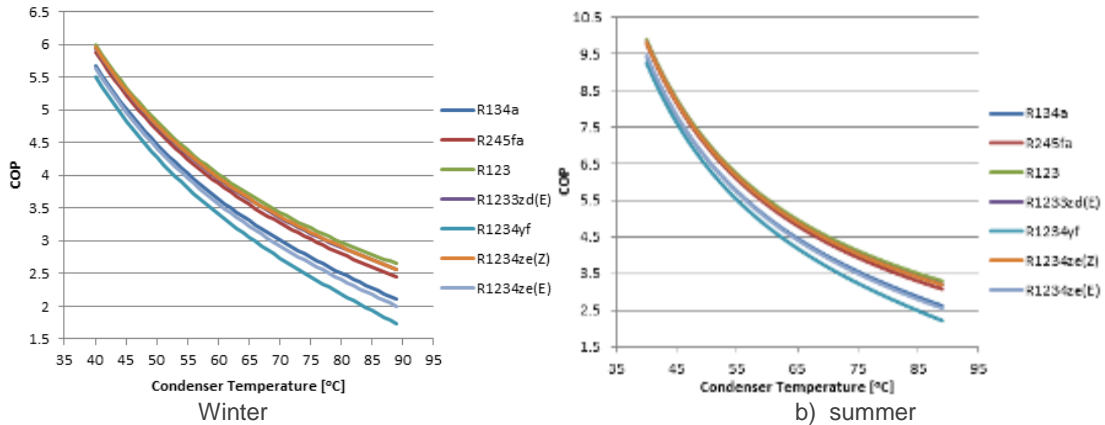
Winter   b) summer

Figure 4: COP variations of refrigerants under different condenser temperature
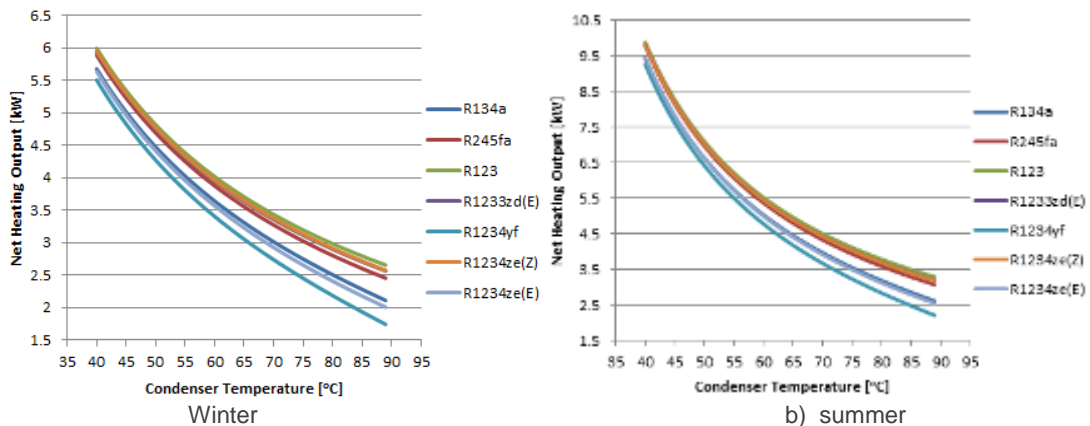
Winter   b) summer

Figure 5: Heating outputs of refrigerants under different condenser temperature
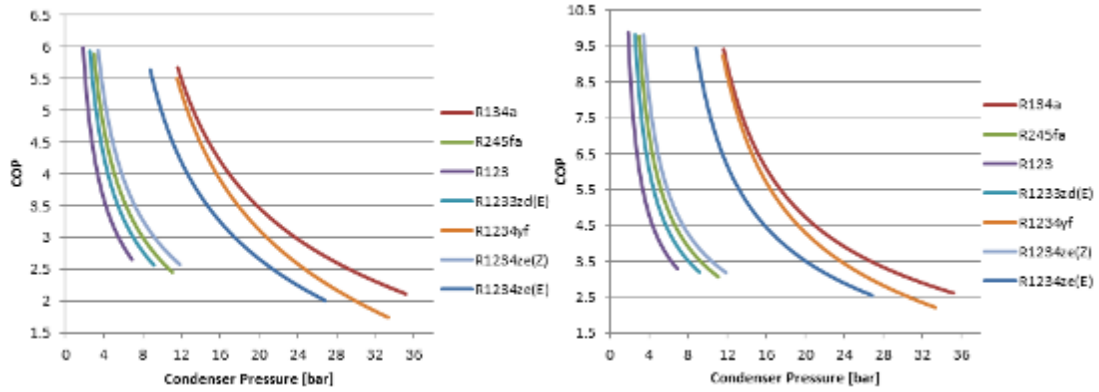
a) Winter   b) summer

Figure 6: COP variations of refrigerants under different condenser pressure
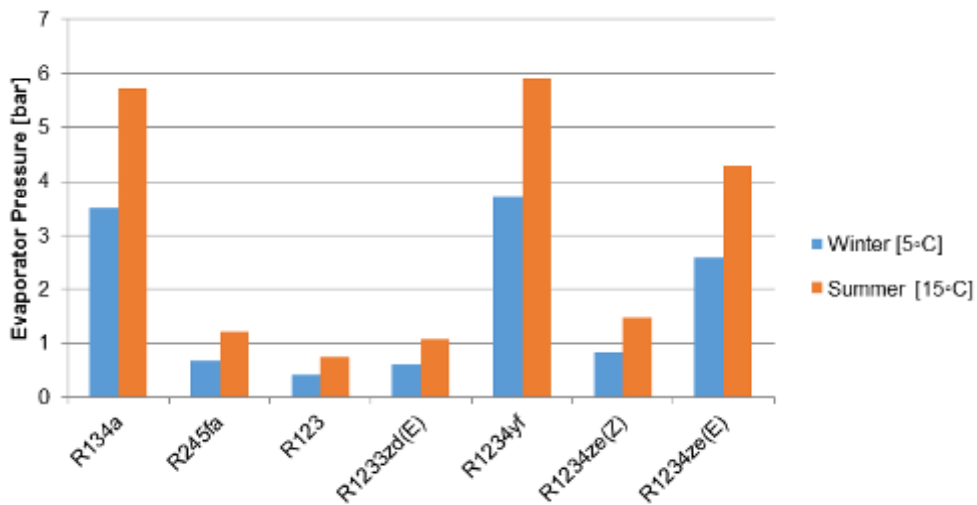
Figure 7: Evaporator pressures of refrigerants for winter and summer

In the Figure 4, the results indicate that the highest coefficient of performance (COP) is achieved by the conventional R123 refrigerant followed closely by the environment friendly R1234ze(Z). The environment friendly R1233zd(E) achieved the third highest COP with almost identical performance to the R1234ze(Z). The conventional R245fa refrigerant has the fourth highest COP. All the proposed refrigerants showed to cluster together and follow similar trend. The environment friendly R1234ze(E) and the conventional very popular R134a showed almost identical performance. R1234yf has lowest COP during simulated cases (winter and summer). As shown in Figure 5, the net heating output showed the similar linear trend of COP and the R1234ze(Z) and R1233zd(E) achieved higher heating output in their environment friendly refrigerants group. Figure 6 illustrates the heat pump COP, for different refrigerants, as a function of condenser pressure and Figure 7 shows evaporator pressures of refrigerants under different seasons of winter and summer. At lower condenser pressures (under 12 bar), R245fa, R123, R1233zd(E) and R1234ze(Z) achieved similar linear trend of COP during condenser temperature range (25°C to 95°C). On the other hand, R134a, R1234yf and R1234ze(E) have higher condenser pressures range (12 bar to 36 bar) in terms of condenser temperature range (25°C to 95°C), which is the same as evaporator pressures requirements.

6.   CONCLUSION

This paper presented an overview of the heat pump system covering key aspects such as the selection of working fluids which mainly characterise the performance of the system. The report presented the results of conducted simulation on various conventional and new emerging environment friendly refrigerants. The simulation results revealed the capability of the new refrigerants to replace conventional refrigerants. R1233zd(E) and R1234ze(Z) showed outstanding performance that is similar to R123 while R1234ze(E) showed similar performance to R134a. However, R1234yf showed the lowest performance with higher

condenser and evaporator pressures than others. Therefore, the use of some selected environment friendly refrigerants (R1233zd(E) and R1234ze(Z)) in heat pump system for green house alongside other refrigeration applications is strongly recommended.

7. ACKNOWLEDGMENT

8. REFERENCES

BROWN, J.S., C. Zilio, and A. Cavallini, The fluorinated olefin R-1234ze(Z) as a high-temperature heat pumping refrigerant. International Journal of Refrigeration, 2009. 32(6): p. 1412-1422.

BIGONHA, Tibiriçá, C., G. Ribatski, and J. Richard Thome, Flow Boiling Characteristics for R1234ze(E) in 1.0 and 2.2 mm Circular Channels. Journal of Heat Transfer, 2011. 134(2): p. 020906-020906.

BEATTIE, R.J. and J.A. Karnaz, Investigation Of Low GWP Refrigerant Interaction With Various Lubricant Candidates, in The International Refrigeration and Air Conditioning Conference. 2012: Purdue University, West Lafayette, Indiana, USA.

BROWN, Steven, J., HFOs: New low globar warming potential refrigerants ASHRAE journal, 2009.

Honeywell. Honeywell Solstice® 1233zd(E) Technical Information. [cited 2014 12 April 2014]; Technical Information]. Available from: http://www.honeywell-blowingagents.com/?document=solstice-lba-technical-brochure&download=1.

Honeywell. Solstice Range of Refrigerants. [Brochure] 2012 [cited 2014 15 April 2014]; Solstice Refrigerants Brochure]. Available from: http://www.honeywell-refrigerants.com/europe/?document=the-future-begins-with-solstice&download=1.

HULSE, R.J., et al., Physical Properties of HCFO-1233zd(E). Journal of Chemical & Engineering Data, 2012. 57(12): p. 3581-3586.

BALA VARMA, D. and B. Joost. Organic Rankine Cycle System Analysis for LowGWP Working Fluids. in The International Refrigeration and Air Conditioning Conference. 2012. Purdue University, West Lafayette, Indiana, USA.

WALTER, B., Refrigerants: Now And In The Future (Presentation), in Carrier's Sustainability Symposiums. 2012: SYRACUSE, N.Y, USA.

SCHMIDT, T., et al., Biotransformation of trans-1-chloro-3,3,3-trifluoropropene (trans-HCFO-1233zd). Toxicology and Applied Pharmacology, 2013. 268(3): p. 343-351.

385: Modulating vs on/off heat pump systems for residential heating: sizing strategies based on annual energy analysis

Giacomo BAGARELLA [1], Renato Lazzarin [2], Marco Noro [3]

[1] Department of Management and Engineering, University of Padua, Str. S. Nicola 3, 36100, Vicenza, Italy, bagarella@gmail.com
[2] Department of Management and Engineering, University of Padua, Str. S. Nicola 3, 36100, Vicenza, Italy, renato@gest.unipd.it
[3] Department of Management and Engineering, University of Padua, Str. S. Nicola 3, 36100, Vicenza, Italy, marco.noro@unipd.it

Abstract: In recent years the use of heat pumps for space heating has spread widely. The technology development allows building of very efficient heat pumps equipped with inverter driven variable speed compressors.

Though several studies were carried out in the past comparing on-off and modulating strategies in heat pump units, only few works considered the whole heat pump system (which includes also heat source, tank, building and climate). Moreover, because of lack of knowledge about cycling losses, most of comparisons between modulating and on-off strategies did not consider the effects of the reduced COP of a system at start-up.

In this work simulations were carried out considering both on-off and modulating air-to-water heat pump systems in a single family house located in Padua (North-East of Italy). The aim of this study is to evaluate how the heat-pump sizing, the tank sizing and the cycling losses phenomenon can influence the SPF of both the systems (on-off and modulating). To investigate what are the conditions which let modulating heat pump plants having better performances than on-off heat pumps is another main objective of the study.

Keywords: heat pump, regulation, heating plant, thermal energy tank, cycling losses

1. INTRODUCTION

In recent years the use of heat pumps for space heating has spread widely. This is mainly due to the evolution of the technical features of devices, of their performances and of the electricity generation system efficiency. The technology development allows to build and market very efficient heat pumps equipped with inverter driven variable speed compressors.

From the theoretical point of view several issues are to be considered when a fixed speed heat pump is compared to a variable speed one. When a heat pump serves a building for space heating, it must be remarked that the peak heating load happens only at the outdoor design temperature (e.g. -5 °C). For most of the time the required heating power is supposed to be a fraction of the design one. So the heat pump is asked to face a space heating part load.

Even if an on-off heat pump unit is undersized, in order to face the full load at a bivalent temperature (UNI EN 14825, 2012: page 8) of 0 °C or 2 °C, the heating system would also face this peak load for a small fraction of the heating season (Lazzarin, 2012, page 64) and the number of on-off cycles would bring down the efficiency of the fixed speed unit. A variable speed unit, on the other hand, could run continually for a larger amount of time, so reducing cycling losses, considered as those inefficiencies which reduce the performances of a unit during the transient period (Bagarella *et al.*, 2013, page 2111). However, the inverter is an electricity consuming device that is definitely not negligible in the overall energy balance.

From the energy balance it is possible to guess that a modulating unit could be more efficient than an on-off unit of the same nominal heating capacity. In case of a part load operation, a fixed capacity unit would produce the same amount of heat of the modulating unit, but in half of the time. So the temperature of the secondary fluid, during the on period, will be higher for the fixed capacity unit. As it can be seen in Figure 1, the outlet water temperature of the modulating unit can be considered similar to the average water temperature of the on-off one ($t_{m,cycle}$), which is much lower than the average water temperature of the on-off unit during the on period ($t_{m,on}$). This will affect the condensation temperature the same way, leading the modulating heat pump to operate with a lower condensation temperature and a higher *COP*.
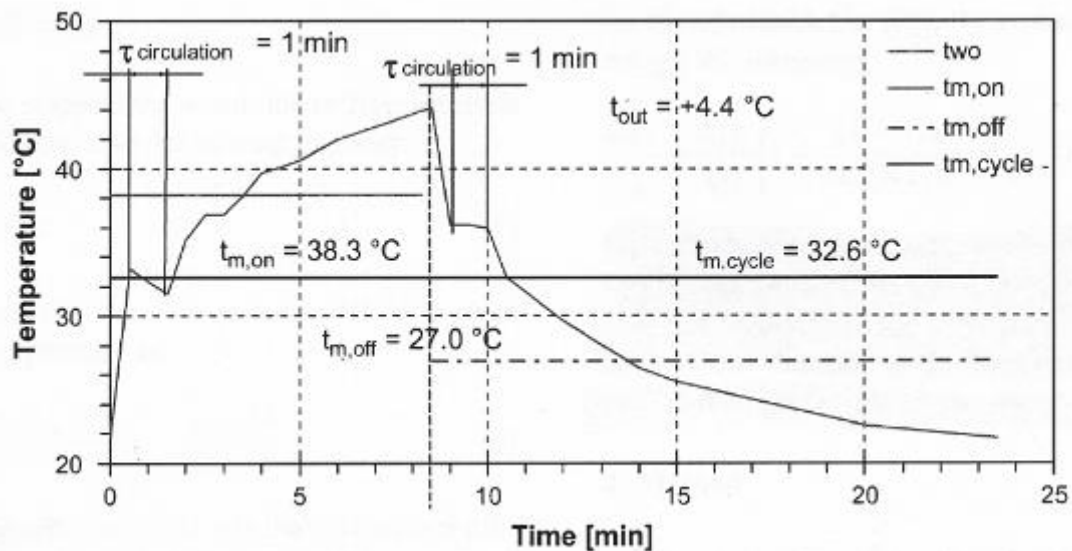

Figure 75: Outlet water temperature profiles in on-off heat pump system (Fahlen and Karlsson, 2005, page 2).

From the previous rationale one could expect a meaningful increase in thermodynamic efficiency when considering a variable capacity heat pump towards a fixed one.

Aprea, Mastrullo and Renno (2006, page 983) compared an on-off air-water heat pump with a modulating unit and found a 20 % electric energy reduction with the second one. Energy savings were mainly attributed to the reduction of the compression ratio during the modulation phase (Aprea *et al.*, 2006, page 991).

Though several studies have been carried out in the past comparing on-off and modulating strategies in single heat pump units, only few studies analysed the whole heat pump system, which includes not only the single heat pump unit, but also the heat source, the heat sink, the heating distribution system, the thermal storage tank, the liquid pump and the auxiliary heaters, as explained in section 2.

How does the *SPF* (Seasonal Performance Factor) of both on-off and capacity controlled heat pump systems behave along the year when climatic conditions change? What are the conditions which let modulating heat pump systems having better performances than on-off heat pumps?

Madani, Claesson and Lundqvist (2011a, pages 1934-1942) answered to these questions simulating the annual operation of both on-off and modulating geothermal heat pumps with the typical thermal loads of a single house located in Stockholm (Sweden). Considering an electric auxiliary heater they concluded that the modulating heat pump led to better performances only when the on-off heat pump was sized to cover less than 65 % of the heating peak demand. On the other hand, when the on-off heat pump presented a higher capacity, no energetic savings were found because benefits coming from a lower mean compression ratio with the modulating heat pump, were completely compensated by the energy consumption of both inverter and pumps.

In this paper several simulations were carried out considering an on-off and a variable capacity air-to-water heat pump system with the typical thermal loads of a single family house located in Padua (North-East of Italy). Being unusual the utilization of electric auxiliary heaters in Mediterranean climates, a condensing (modulating) boiler was considered.

Finally, because of lack of knowledge about the cycling losses phenomenon, most of the comparisons between modulating and on-off strategies found in literature do not consider the effects of the reduced *COP* of a system at start-up. In this paper cycling losses penalizations have been considered too.

2. METHODOLOGY

To simulate the annual behaviours of both on-off and variable capacity heat pumps, the system was firstly modelled.
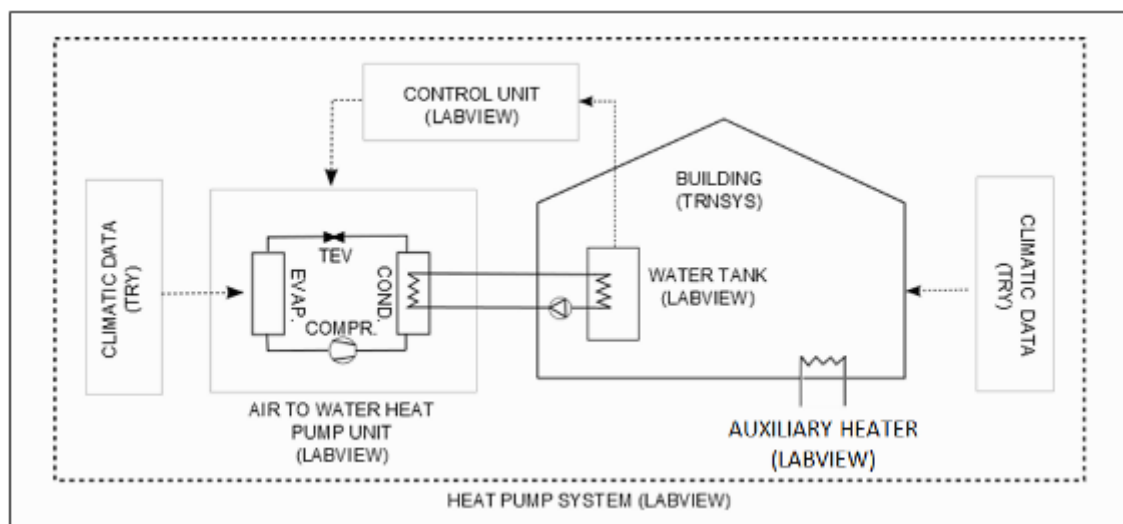

Figure 2: Schematic overview of the heat pump system (TEV=Thermostatic Expansion Valve; TRY=Test Reference Year).

Figure 2 shows a schematic overview of the modelled heat pump system. The air-to-water heat pump unit supplies heat to the building and is modelled by linking together the sub-models of condenser, expansion valve, evaporator and compressor as in Madani, Claesson and Lundqvist (2011b, pages 1338-1347). Some technical data of the considered heat pump unit are summarized in Table 1. REFPROP 9.0 was used to estimate the properties of the refrigerant in each operating condition. Heat transfer coefficients of both evaporator and condenser were set according to results obtained by tests done with an equivalent experimental unit. The modelled unit was validated comparing its behaviour against those of the real modulating one. Superheating and subcooling were considered constant as in Cecchinato, Chiarello and

Corradi (2010, page 1778). The global electric consumption of the system was calculated summing up those of compressor, inverter, pump and fan. The compressor consumption was estimated basing on manufacturers' data for each operating conditions. Pump and fan consumption (0.03 kW and 0.06 kW) were assumed constant. The inverter efficiency was considered to be in a range between 88 % and 95 %, depending on the compressor speed, as specified by the manufacturer. Cycling losses were measured thanks to specific experimental tests as described in Bagarella, Lazzarin and Lamanna (2012, page 2114) and results were included in the model. Despite the compressor manufacturer ensures a maximum number of hourly on-off cycles up to 12, with a minimum 2 minutes on-time, the maximum number of startups considered in the simulations was 5, in order not to excessively reduce the compressor life cycle.

A simplified method to account for frost formation and the defrost cycle consumption was also implemented in the model. The average fin temperature is estimated from the evaporation temperature and the evaporating power. When the fin temperature allows for frost formation (fin temperature below 0 °C and below outdoor air dew point), frost starts building up. Once the frost has reached its upper bound, the heat pump reverses the cycle providing the heat to melt the frost.

The building (Table 2) was modelled in TRNSYS 16.0 and was used to estimate the thermal loads basing on the annual climatic data (TRY) of Padua (Italy). The design temperature is -5 °C and Heating Degree Days are 2381. The thermal properties of the building envelope are those compliant to the present National Regulations for new buildings' standards. The thermal load of the building and the thermal capacity of the heat pump unit were used to continuously calculate the temperature of the blended hot water tank.

The thermal storage decouples the heat produced by the heat pump from the heat required by the building. The tank protects the heat pump unit from an excessive number of on-off cycles and ensures the thermal comfort inside the building avoiding excessive variations in the air temperature during defrosts. A low temperature radiant heating distribution system was considered. The set-point of the hot tank was set at 35 °C.

The control unit allows the heat pump to work either with on-off cycles or with a capacity control algorithm. The temperature of the tank was given as input to the control. In the case of on-off strategy a 2 °C dead band around the set-point of the water tank was used while in the capacity controlled unit a PID algorithm was used to set the compressor speed.

When the heating capacity of the heat pump unit was not enough to cover the heating demand a condensing boiler auxiliary heater having 0.96 thermal efficiency (Lazzarin, 2012, page 65) was considered.

The climatic conditions have a double effect on the system; lower air temperatures correspond to lower evaporation temperatures (so lower *COPs*) and to higher building heating powers.

The global algorithm of the heat pump system was implemented in LABVIEW 8.5 environment by linking together the sub-models of the elements following the approach in Figure 2.

Table 1: Heat pump unit data.

Component	Information
Condenser	Plate heat exchanger Heat exchange surface: 0.79 m2 Plates: 20
Evaporator	Finned coil
Refrigerant	R410A
Nominal heating capacity (UNI EN 14825, 2012)	7.2 kW
Expansion valve	TEV Kv = 0.066 m3 h-1
Compressor	BLDC Twin-rotary Displacement: 1.3 l

Table 2: Building data.

Parameter	Information
Vertical structures transmittance	0.28 W m-2 K-1
Horizontal structures transmittance	0.24 W m-2 K-1
Floor transmittance	0.27 W m-2 K-1
Windows transmittance	1.60 W m-2 K-1
Building type	Single family house (2 floors)
Building volume	363.5 m3
Building height	5.5 m
Ventilation rate	109 m3 h-1
Set point temperature	20 °C

3. COP VARIATIONS AND MODULATION CAPACITY OF THE VARIABLE SPEED UNIT

Once the models of both heat pump units (fixed speed and modulating) and heat pump systems were built, the attention was at first focused on the performances of the capacity controlled unit. The influence of outside air temperature and heating demand on the heat pump COP was investigated.

For a better understanding of the results, compressor isentropic efficiencies (calculated basing on manufacturer data) at different frequencies are reported in Figure 3. The maximum isentropic efficiency of the compressor is obtained for frequency from 50 Hz to 70 Hz. Similar results were found by Madani, Ahmadi, Claesson and Lundqvist (2010, page 6). The isentropic efficiency lowers for higher pressures ratios. However, for very low condensation temperatures (e.g. T_c = 28 °C), the behaviour is reversed, probably because the used twin-rotary compressor was not optimized for really low pressures ratios.

Figure 4 represents the *COP* of the modulating unit as a function of the thermal load of the building.

The capacity at the nominal frequency (120 Hz) lowers for decreasing outside air temperatures. The maximum *COP* point shifts toward lower capacities too because the heat pump unit is optimized for a determined volumetric flow rate and thus, excluding the clearance volume, for a determined compressor frequency (50-70 Hz). The most important feature of the curves in Figure 4 is the significant decrease of the *COP* (after the maximum value) moving toward higher capacities.

The modulation ability of an inverter driven heat pump unit should not be overrated. When the nominal frequency of the compressor is 120 Hz, its velocity can be reduced till to 20-30 Hz. Thereafter a strong reduction in volumetric efficiency takes place, even if the pressure drop at suction is much lower for the lower flow rates. As a matter of fact, at low rotation speeds, the lubrication does not assure a good tightness against the return of refrigerant to the suction. Moreover, the electric motor efficiency usually reduces for lower frequencies. Yet the *COP* reduction, at low rotation speed, demands a higher electric power by the compressor, mainly transferred to the refrigerant. Summarizing: the modulation ability is far from being proportional to the reduction in rotational speed of the compressor. This ability is further decreased when the outside temperature is higher, as the heat pump capacity increases just when an effective modulation would be welcome.

It should be noticed that the minimum capacity of a heat pump depends not only on the minimum compressor frequency considered, but also on the PID parameters of the compressor controller. For instance, the higher the reactivity of the controller, the higher the overshoot of the compressor frequency (as depicted in Figure 5), thus the higher the minimum capacity of the heat pump unit. On the other hand, the higher the stability of the control, the lower the overshoot, the lower the minimum capacity of the heat pump.

Table 3 reports the capacity ratio of the considered compressor (minimum frequency set to 30 Hz) when the parameters of the PID controller are set in order to let the heat pump to operate in stable conditions.
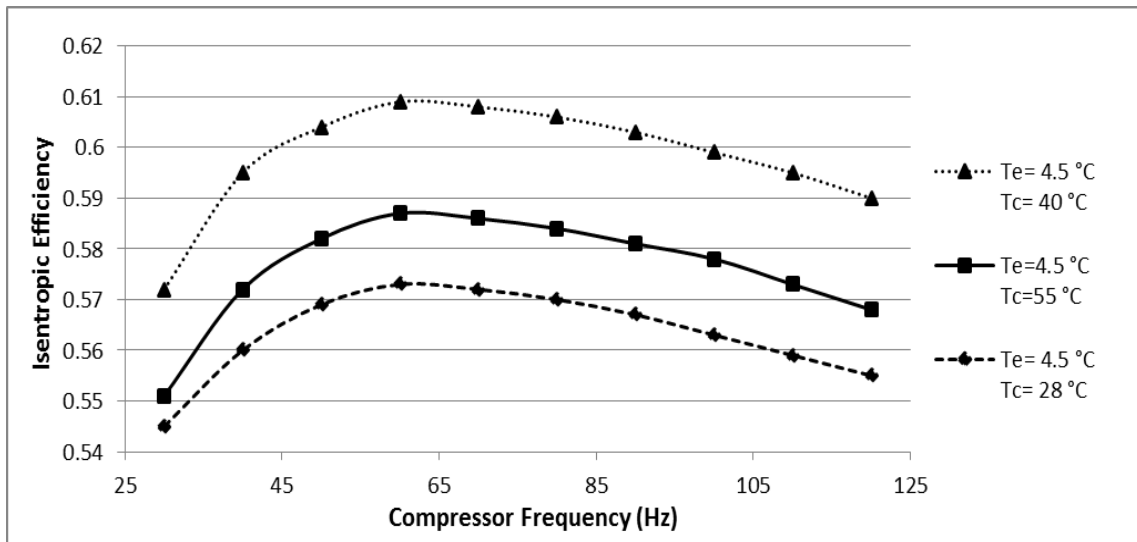
Figure 3: Compressor isentropic efficiency at different frequencies and evaporation (T_e) and condensation (T_c) temperatures.
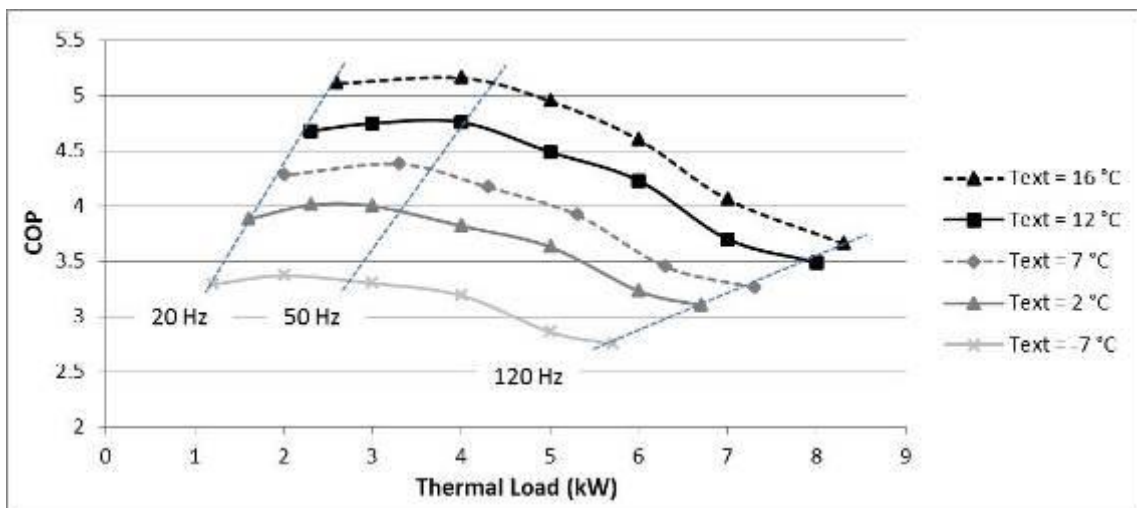

Figure 4: Heat pump unit COPs at different temperatures of the external air (T_{ext}) and for different thermal loads.
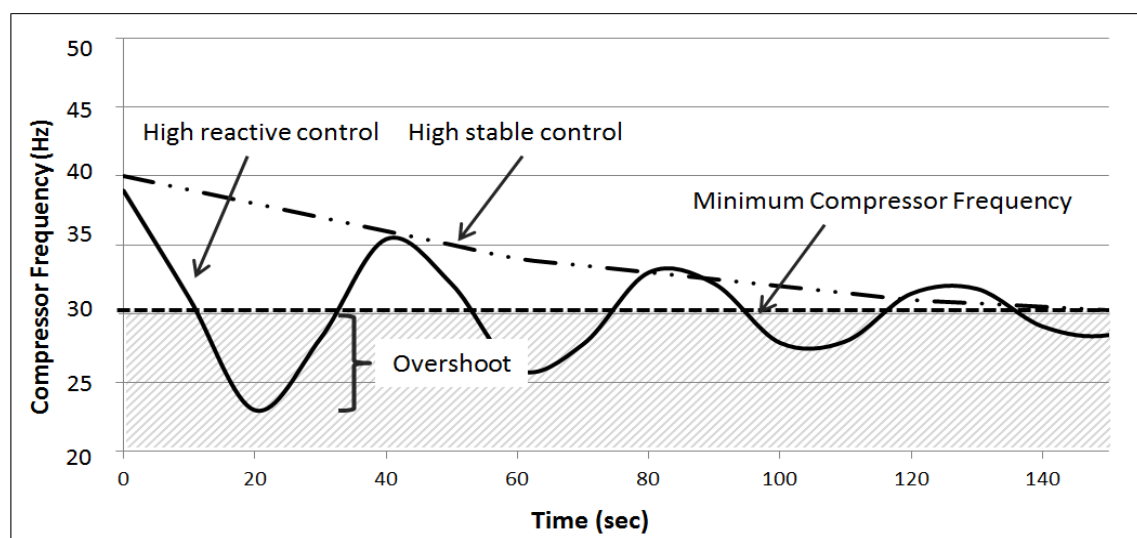

Figure 5: Behaviour of both high reactive and high stable compressor controls.

Table 3: Capacity ratio of the heat pump unit at different temperatures of the external air.

Text (°C)	Maximum capacity (kW)	Minimum capacity (kW)	Capacity ratio %
16.0	8.2	4.4	53.8 %
12.0	8.0	4.0	50.0 %
7.0	7.2	3.3	46.5 %
2.0	6.7	2.9	42.9 %
-7.0	5.8	2.2	38.2 %

4. AN ANNUAL COMPARISON

The comparison of the performances of the plant equipped with on-off and variable capacity air-to-water heat pump was realized by dynamic simulations with a 15 minutes time step. Firstly a 150 litres tank for both on-off and variable capacity heat pump was considered. In the first simulation the two systems were sized to cover the 91.4 % of the maximum thermal load required for heating up the house. This size of both heat pumps corresponds to a -4 °C bivalent temperature, as reported in Figure 6. From a theoretical perspective the bivalent temperature is the temperature of the external air which let the heating capacity of the heat pump to be equal to the required heating load. When the outside air temperature is lower than the bivalent temperature the auxiliary energy is required, otherwise the heat pump operates either modulating or in on-off, depending on the modulation strategy.

Figure 7 shows the different annual profiles of the monthly SPF of both capacity controlled and on-off heat pump systems. For most of the time the heating load required is less than the heating capacity of the heat pump. Thus the capacity controlled heat pump unit can work with higher SPF than the on-off one. The differences in the SPF values of the two systems are higher in spring and autumn, when is higher the need for modulation. In fact in those periods the capacity controlled unit can work with lower compressor frequencies and thus with reduced pressures ratios and reduced compressor specific works. On the other hand, the differences in the SPF values are lower when the heating loads are similar to the heating capacity of the capacity controlled heat pump unit. In those cases the capacity controlled heat pump unit is forced to work at full capacity, without the benefits coming from modulation. Figure 7 also shows the cumulative number of on-off cycles with both heat pump systems. Though the capacity controlled system let a drastic reduction of on-off cycles, its modulation capacity decreases when the outdoor air temperature is higher. This phenomenon is confirmed by the profile of the cumulative on-off cycles, whose slope increases in spring and autumn with respect to the coldest periods.

Figure 8 shows the magnitude of the contribution of the different elements to the total electric energy absorbed by the systems. The variable speed unit electric consumption is 1662 kWh, 13.2 % less than the on-off unit that consumes 1915 kWh.

The pump and the fan consumptions are higher in the capacity controlled system because they operate for a longer time. Moreover, in the capacity controlled system there is one more contribution to the total energy consumption due to the need of an inverter.

In the specific conditions of the simulation, defrost energies of both the systems are similar. From the Introduction paragraph one could expect the defrosting energy to be lower in the modulating unit than in the on-off unit. This is not confirmed in this specific case. This could be attributed to the fact that the modulating unit operates for longer during the heating season than the on-off one.

Finally, the cycling losses phenomenon is considerably lower in the capacity controlled heat pump case thanks to the reduction of the total number of on-off cycles described in Figure 7. Figure 8 suggests that, if the annual performances of the systems are compared, the cycling losses phenomenon has to be considered because its contribution can influence the comparison itself. In this specific case the effect of the cycling losses has been estimated to be 3.4 % and 8.3 % of the total electric consumption respectively for the modulating and the on-off heat pump systems. These values are higher than the 2.1 % efficiency loss reported by Uhlmann and Bertsch (2012, page 2146), who considered a maximum number of 3 hourly startups. This probably happens because, in this simulation, the maximum number of hourly on-off cycles obtainable was set at 5.
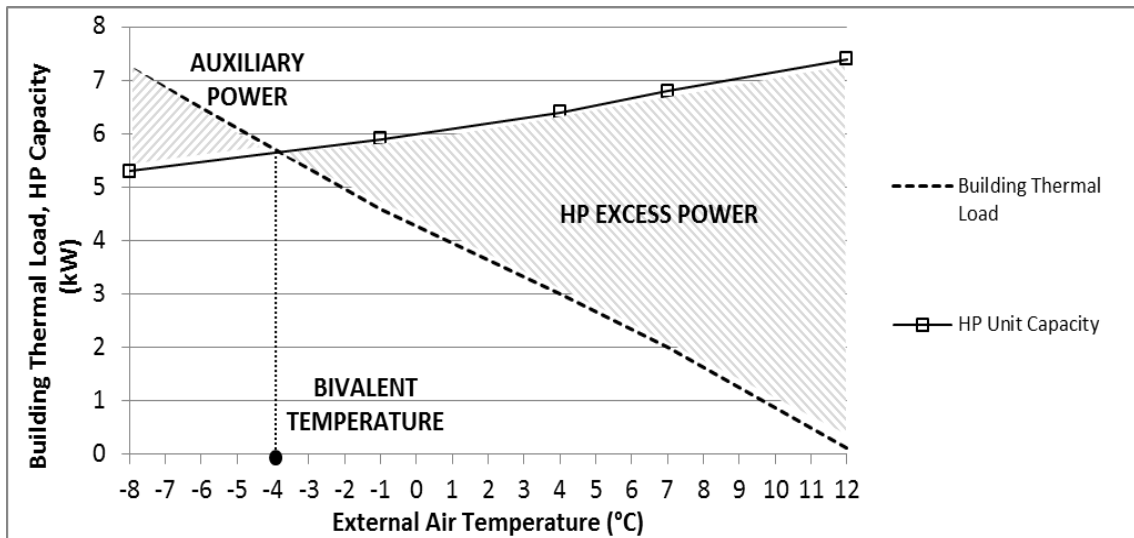
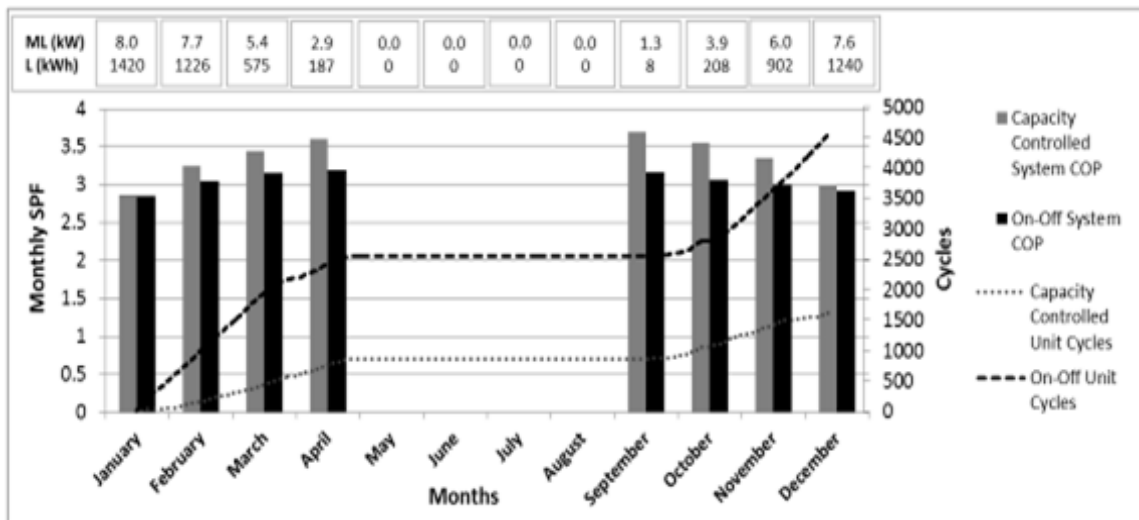*Figure 6: Bivalent temperature of the considered heat pump (HP).*

Figure 7: Annual profiles of the monthly SPF and cumulative on-off cycles of both capacity controlled and on-off heat pump systems. Monthly thermal energy needs (L) and monthly maximum loads (ML) are reported too.
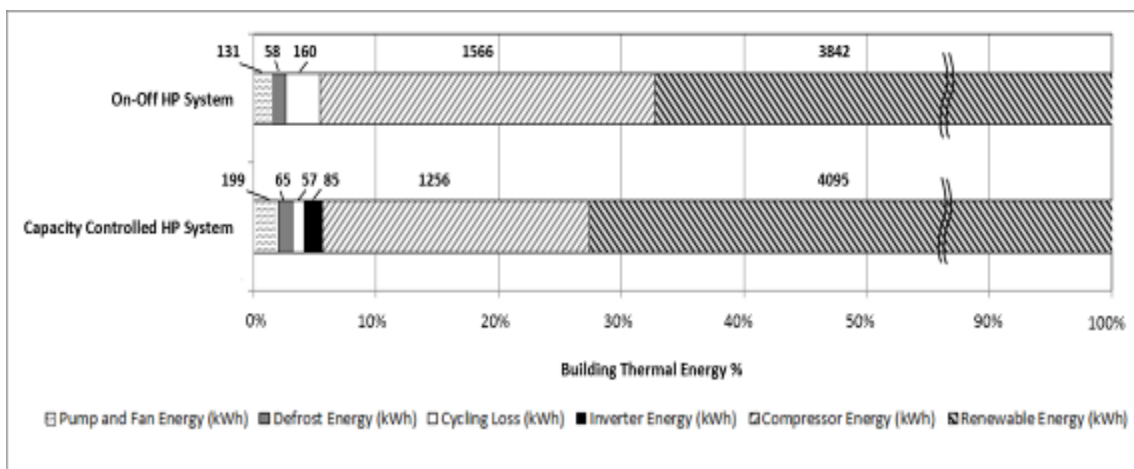

Figure 8: Absolute and percentage contribution of different elements to the total building thermal energy with both on-off and capacity control heat pump systems.

5. ANALYSIS OF MAIN VARIABLES INFLUENCING THE SEASONAL PERFORMANCES

5.1 The influence of the unit size

To analyse how the sizing of the on-off heat pump can influence the performances of the system, several simulations were run varying the maximum heating capacity of the on-off heat pump. As in Figure 9, to a higher heating capacity corresponds a lower bivalent temperature, thus a lower auxiliary energy required. Simulations were run varying the sizing of the on-off heat pump, covering the annual heating demand from 74.3 % to 99.8 %. On the contrary the nominal capacity of the inverter driven heat pump was at first kept constant.
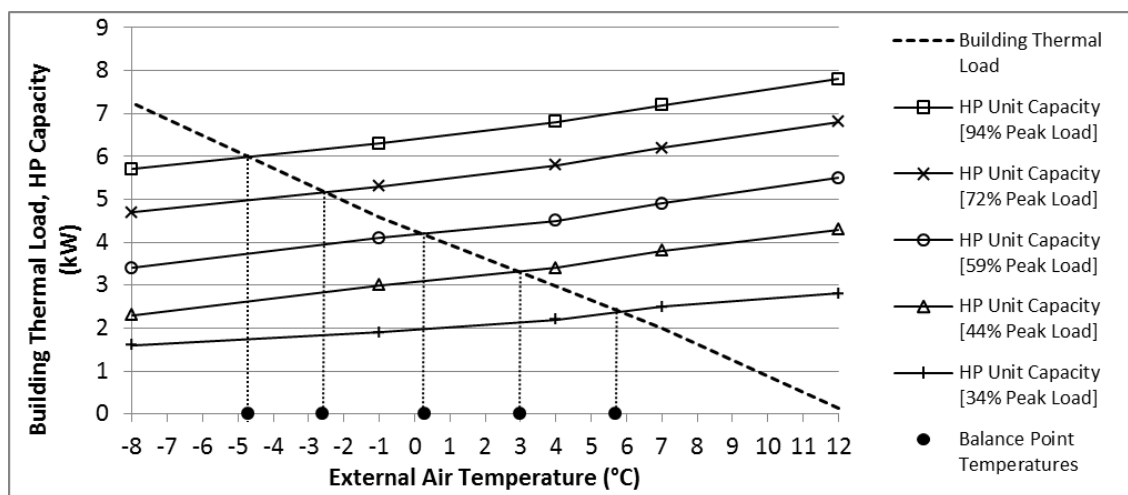
Figure 9: Bivalent point temperature depending on the heating capacity of the heat pump unit (HP).

Table 5: Total energy, on-off cycles, SPF of the unit, SPF of the system and percentage energy savings of the capacity controlled system for different annual heating demand (or peak load) coverings of the on-off heat pump system.

Annual heating demand covering %	99.8%	99.7%	98.4%	97.1%	94.9%	91.9%	87. %	81.7%	74.3%
Peak load covering %	94.0%	91.4%	72.1%	65.7%	59.2%	54.1%	43.8%	38.6%	33.5%
On-off cycles	4837	4574	3896	3542	3140	2700	2233	1725	1237
Auxiliary energy (kWh)	5	9	41	75	132	210	321	473	666
Cycling losses (kWh)	169	160	136	124	110	95	78	60	43
Total energy consumption (kWh)	1932	1924	1909	1906	1909	1914	1931	1956	1994
SPF on-off HP unit	3.04	3.05	3.09	3.12	3.14	3.18	3.22	3.27	3.34
SPF on-off HP system	2.98	3.00	3.02	3.02	3.02	3.01	2.99	2.95	2.89
Inverter HP savings	13.5%	13.1%	12.5%	12.3%	12.4%	12.7%	13.4%	14.6%	16.2%

Table 5 shows that the lower the heating capacity of the on-off heat pump, the lower the number of on-off cycles and thus the lower the cycling losses. The lower values of the cycling losses when the heat pump is undersized led to an increase of the SPF of the unit. On the other hand, the less the heating capacity of the heat pump considered, the higher the auxiliary energy used. Thus the weight of SPF of the auxiliary heater over the SPF of the whole system is greater. In this case the optimum SPF of the system was obtained for a covering percentage of the annual heating demand from 95 % to 98 % which corresponds (in the specific climatic conditions of Padua) respectively to a 59 % - 72 % covering of the peak thermal load of the considered building.

Figure 10 and the last row of Table 5 explain that, when comparing the performances of the capacity controlled and the on-off heat pump systems, the energy savings obtained by the former are higher the higher is the level of undersizing of the on-off unit (that is the best on-off sizing is the one that minimize the

energy saving of the inverter solution with respect to on-off). Several simulations were run varying the nominal capacity of the inverter driven heat pump too but lower performances of the heat pump system have been obtained by reducing the heat pump unit sizing. The reason is that, when the size of the inverter driven heat pump was decreased, the reduction of the cycling losses phenomenon was not enough to compensate the higher energy required by the auxiliary heater.
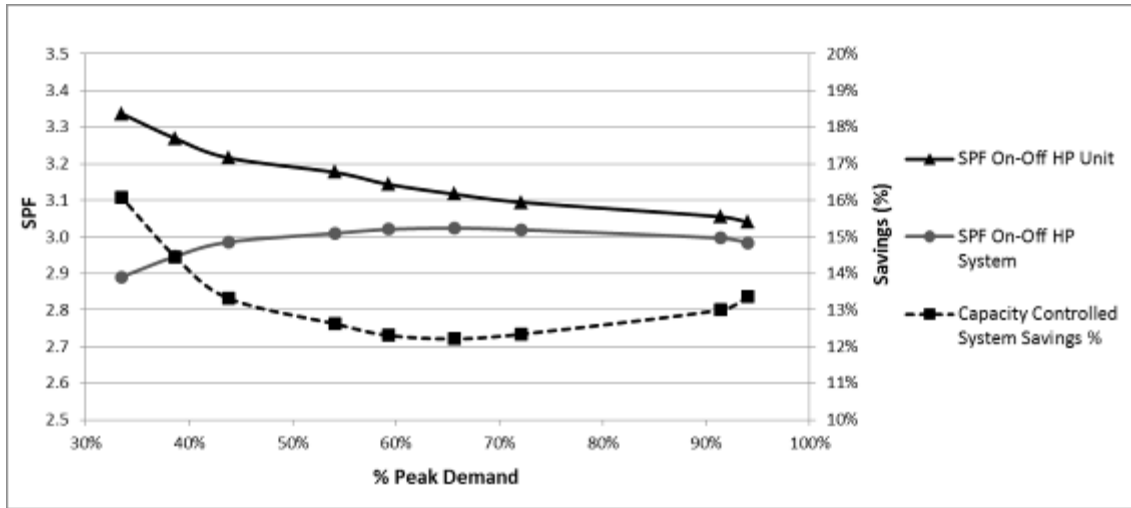

Figure 10: SPF profiles for different covering of the annual peak demand of the on-off heat pump (HP) unit and system. Energy savings of the capacity controlled heat pump compared with the on-off HP are reported too.

2.37.5.2.   The influence of the storage volume

The role of the tank size in this comparison was investigated too. Simulations were run keeping the capacity of the heat pump units constant and varying the volumes of the tanks of both inverter driven and on-off heat pump systems. In the simulations the thermal losses of the tanks have been considered according to UNI EN 15316-4-3 (2008). Water storage volumes higher than 100 litres were considered, in order to avoid more than 5 startups per hour and to avoid extreme variations in the water outlet temperatures during the off periods of the units.
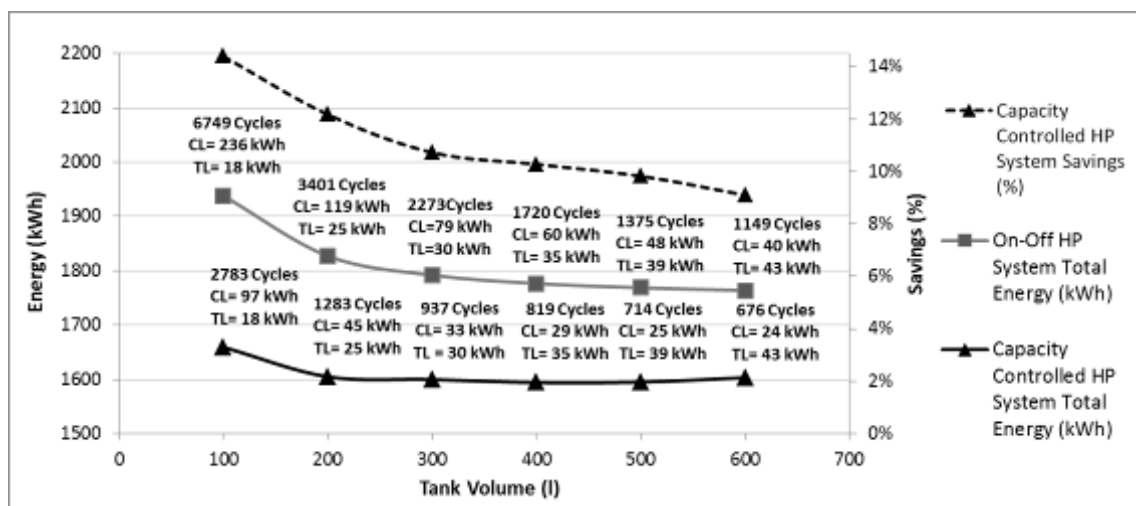

Figure 11: On-off cycles, cycling losses (CL), tank thermal losses (TL) and total energy saving of the modulating unit toward the on-off one as a function of the tank volume.

Figure 11 shows that, for both the systems, the higher the volume of the tank, the lower the number of on-off cycles. With the on-off heat pump system, when the volume of the tank increases, the increased tank losses are overcompensated by the reduction of cycling losses. By increasing the water tank volume from 100 litres to 600 litres, the cycling losses penalization is reduced from 12.1 % to 2.2 %. The storage thermal

losses are the same for both the on-off and the modulating system, so these losses do not affect the comparison. For tank volumes exceeding 300 litres, there is no further meaningful reduction in cycling losses for the on-off unit, so the savings of the modulating unit are almost constant.

6. CONCLUSIONS

In this work simulations were run considering both on-off and modulating air-to-water heat pump systems in a single family house located in Padua (Italy). The analyses of the annual performances of these systems demonstrated that the higher the need for modulation, the higher the advantages of the modulating system over the on-off one. Anyway, the magnitude of the advantages of the modulating system over the other one strongly depends on the sizing of both the on-off unit and the thermal storage. The maximum *SPF* of the on-off system was obtained with the heat pump unit sized to cover the 59 % - 72 % of the building peak load, which corresponds to 95 % - 98 % covering of the annual heating demand. Moreover, the higher the volume of the thermal storage, the lower the cycling losses magnitude and thus the higher the performances of the on-off system.

One of the main conclusions of this paper is that, when evaluating the advantages of a modulating system, the attention should be not only focused on the comparison of the energy performances of the modulating unit with those of the on-off one. In fact, the reader should be aware that there are many other variables such as the sizing of both the unit and the thermal storage that might strongly influence the comparison itself.

Finally, it is not always correct to evaluate the annual energy performances of a heat pump neglecting cycling losses. When an on-off system is sized to cover a high percentage of the building peak load and the volume of the thermal storage is small, simulations showed that the cycling losses phenomenon can significantly increase (up to 12.1 %) the electric consumption of the whole system.

7. REFERENCES

APREA, C., Mastrullo, R., Renno, C., 2006. Experimental analysis of the scroll compressor performances varying its speed, *Applied Thermal Engineering*, 26: 983-992.

BAGARELLA, G., Lazzarin, R. M., Lamanna, B., 2013. Cycling losses in refrigeration equipment: An experimental evaluation, *International Journal of Refrigeration,* 36 (8): 2111-2118.

CECCHINATO, L., Chiarello, M., Corradi, M., 2010. A simplified method to evaluate the seasonal energy performance of water chillers, *International Journal of Thermal Sciences*, 49: 1776-1786.

FAHLEN, P., Karlsson, F., 2005. Optimizing and controlling media flows in heat pump systems. Eighth IEA Heat Pump Conference. Las Vegas, USA.

LAZZARIN, R. M., 2012. Condensing boilers in buildings and plants refurbishment, *Energy and Buildings*, 47, 61-67.

MADANI, H., Ahmadi, N., Claesson, J., Lundqvist, P., 2010. Experimental analysis of a variable capacity heat pump system focusing on the compressor and inverter loss behaviour. International Refrigeration and Air Conditioning Conference. Purdue.

MADANI, H., Claesson, J., Lundqvist, P., 2011a. Capacity control in ground source heat pump systems part I: modelling and simulation, *International Journal of Refrigeration,* 34: 1338-1347.

MADANI, H., Claesson, J., Lundqvist, P., 2011b. Capacity control in ground source heat pump systems part II: Comparative analysis between on/off controlled and variable capacity systems, *International Journal of Refrigeration,* 34: 1934-1942.

TEST REFERENCE YEAR, TRY, Data Sets for Computer Simulations of Solar Energy systems and energy consumption in buildings, Commission of the European Communities, Directorate general XII for Science, Research and Development.

UHLMANN, M., Bertsch, S., 2012, Theoretical and experimental investigations of startup and shutdown behaviour of residential heat pumps*, International Journal of Refrigeration*, 35: 2138:2149.

UNI EN 14825, 2012. Air conditioners, liquid chilling packages and heat pumps, with electrically driven compressors, for space heating and cooling – Testing and raring at part load conditions and calculation of seasonal performance.

UNI EN 15316-4-3, 2008, Method for calculation of system energy requirements and system efficiencies – Heat generation systems, thermal solar systems.

287: Field performance of air-source heat pump in low-temperature region of north China

Songhui AI[1], Baolong WANG, Xianting LI, Wenxing SHI[*]

[1] Department of Building Science, Tsinghua University, Beijing, China, hu_tu_tu@126.com
[*]Department of Building Science, Tsinghua University, Beijing, China, wxshi@mail.tsinghua.edu.cn

As the rapid development of economics and the deterioration of environment, development of sustainable energy is of vital importance. In north China, the traditional heating form in winter is boiler which has resulted in severe air pollution. The air-source heat pump, as a clean and efficient form of heating source, could be used as a new form of heating source. However, the running performance drops sharply as the outdoor temperature decreases, especially in winter of north China. As the development of compressor technology, several technologies have been utilized to solve this problem. The quasi two-stage compression with refrigerant injection is an effective method, which can decrease the discharge temperature and increase the coefficient of performance. Several site tests have been conducted during a long period in this paper.

To investigate the operating performance of air-source heat pump applied in low-temperature region, several parameters were measured, including the energy consumption, the heating capacity and the outdoor temperature. Thus, the running performance is analyzed.

The testing result shows that the coefficient of performance maintains above 2.8kW/kW when the outdoor temperature is -8℃ in Beijing. In Taiyuan of Shanxi province, the average heating capacity of an air-source heat pump water heater during the coldest month is 24.5kW, which is close to 75% of the rated heating capacity under much mild 7/6℃ working condition. The average hourly heating performance is 2.71kWh/kWh. The average hot water temperature is about 45.5℃.The testing data above proves that the air-source heat pump with scroll compressor of quasi two-stage compression shows great running performance in the cold region of north China, which could be a reasonable choice of heating device applied in north China.

Keywords: air-source heat pump, low-temperature, site test, running performance

1. INTRODUCTION

In the north urban of China, energy consumption of space heating has been increasing sharply in recent years[1]. As it is shown in Fig1, until 2008, the energy consumption of space heating has increased to 156 million tce per year, which is more than twice of that in 1996, and 70% of them are consumed by district heating. Around half of heat for the district heating are provided by the combined heat and power systems, and the other half are provided by coal and gas boilers[2], which consume large amount of energy[3]. Meantime, burning coal has resulted in severe air pollution, such as haze, which is extremely severe in north China in these years. Thus, clean and efficient heat source is urgently required as a substitute for burning coal.
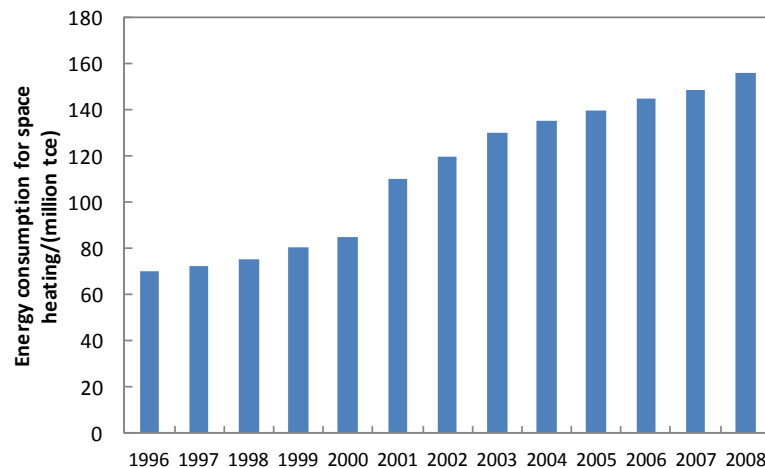
Figure 1: Energy consumption for space heating in the north urban of China(data from[4])

Air source heat pump (ASHP) is a facility which is driven by electricity, to produce cold/hot air or water using ambient air as thermal source. Compared with burning coal, it is clean and environment-friendly. The ASHP is usually applied in the middle and lower reaches of Yangtze River[5]. As the climate is mild there, thus, it shows great running performance during the whole year. However, winter in north China is pretty cold, the lowest temperature may below -30℃, which may lead to the sharp decrease of heating capacity. And with the rapid increase of discharge temperature, the ASHP may not work effectively and safely, which may lead to the shut off of the ASHP[6]. Many researchers have proposed different technologies to solve this problem, such as two stage compression[7], quasi two stage compression[8], two stage coupling system and cascade cycle[9-10]. By utilizing the methods above, the discharge temperature can be decreased effectively, and the running performance can be improved at the same time.

And as the improvement of ASHP technology, ASHP has been applied in cold region. Stefan S[11] has simulated a two-stage heat pump with R410a as refrigerant, and also tested the operating performance. The testing result shows that it could work under -30℃, and the COP could reach 2.1. W.Wang[12] has reported a double-stage heat pumps, which couples an ASHP with a water source heat pump. And the system has been field tested in Beijing. The result shows that the performance has been improved a lot, and it can work well in cold region. Ma Guoyuan[8] has proposed a new sub-cooling system with a supplementary inlet on the compressor. He has made a dynamic model of the system. The outcome shows that the system could work well under -15℃.Wang BL[13-14] has proposed a precise model for the scroll compressor with refrigeration injection. And the result has shown that this kind of compressor could improve the operating performance to a large extent. Although the technologies of low ambient temperature ASHP have been widely researched in laboratory, the field environment is more complicated than the lab. Thus, the actual running performance must be measured before the confirmation of the real performance of the ASHP in low temperature ambient. According to the paper survey, there is still lack of site test of the ASHP, especially long period site test. Thus, in this paper, two site tests of ASHP with quasi two stage compression have been conducted in north China, one is ASHP applied in an office building in Beijing, the other one is ASHP domestic water heater applied in a hotel in Taiyuan of Shanxi province. The running performance is analyzed by long-period monitoring on site.

2. METHOD

2.1 Schematic of ASHP with quasi two stage compression

Fig.2 is the schematic diagram of ASHP with an economizer. When it works on heating condition, the air-cooled heat exchanger works as the evaporator, and the plate heat exchanger works as the condenser. The liquid refrigerant at the outlet of the condenser with high pressure and high temperature (point 3) goes through electric expansion valve (a). After that, it turns into the middle pressure state (point 4) flowing into the economizer. Liquid refrigerant with middle pressure Ge (point 5) goes through electric expansion valve (b) . After throttling, it (point 7) flows into evaporator, absorbs heat from ambient air, then flows back to the compressor (point 1). While, the gas refrigerant with middle pressure Gi (point 6) is injected to the compressor through the gas injection inlet of the compressor. As the temperature of the injection gas is lower compared with that in the compression pocket, the discharge temperature of the compressor is decreased. Through twice throttling, the refrigerant flowing into the evaporator is almost liquid, which enhances the cooling effect by increasing the refrigerant enthalpy difference in the evaporator. So the running performance of ASHP is enhanced.
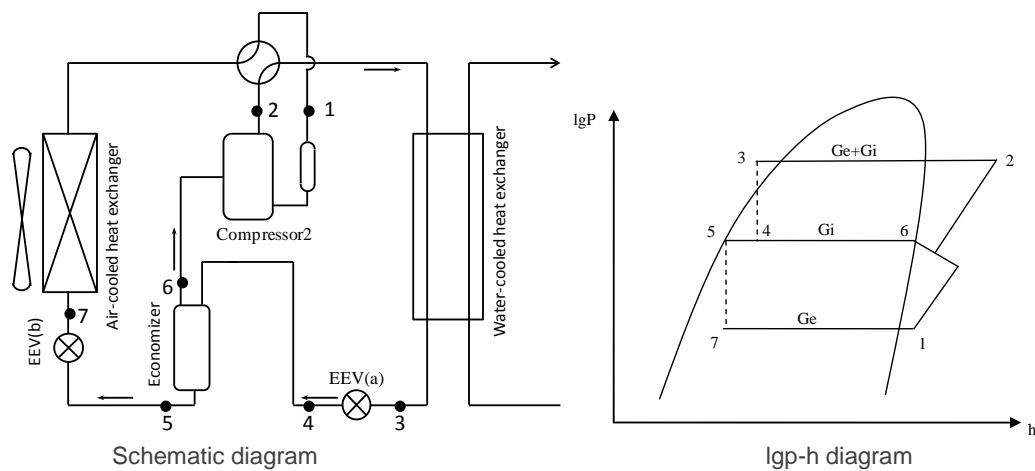

Figure 2: Schematic of the ASHP with quasi two stage compression

2.2 Performance parameters

In order to analyze the long-term running performance of the ASHP, some parameters should be monitored in real time, including heating capacity, energy consumption and the ambient temperature. According to the parameters above, some performance parameters are calculated to illustrate the operating performance of the heat pump.

Energy consumption

The energy consumption of the heat pump includes the energy consumption of the compressor, the fan of the evaporator and the controller. A power meter which can make real-time record and long-distance transmission, exports real-time power and accumulated energy consumption every 15 minutes, which is denoted as $W_{15\text{min}}$, after four times of record, the hourly energy consumption is attained. After accumulation of 24hours, the daily energy consumption is attained. The accumulation of the daily energy consumption of the whole heating season is the seasonal energy consumption.

Heating capacity

As the ASHPs we have tested both use water as thermal media in the condenser side. Thus, measuring the heating capacity from the water side is much easier than that from the air side or the refrigerant side. In order to measure the heating capacity, the flow rate of the water and the temperature of the inlet and the outlet of the heat pump should be measured.
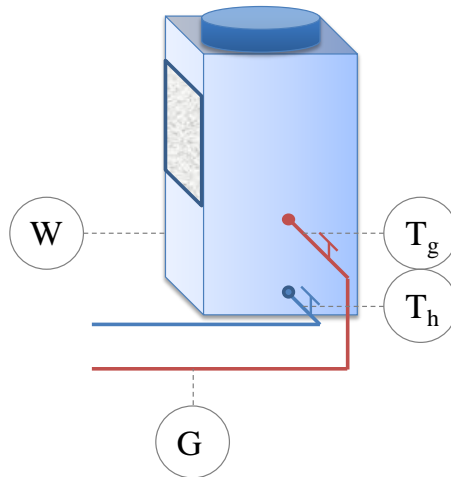
Figure 3: Measuring points arrangement on the heat pump unit

The measuring points are shown in Fig3. T_g is the outlet temperature of the heat pump unit, T_h is the inlet temperature of the heat pump unit. G is the flow meter which is used to monitor the flow rate of the water. W is the power meter which is used to monitor the energy consumption of the heat pump unit.

Performance parameters

According to the hourly heating capacity, hourly energy consumption, daily heating capacity, daily energy consumption, seasonal heating capacity and seasonal energy consumption, the average coefficient of performance (COP) could be calculated hourly, daily and seasonal, respectively.

The hourly heating performance could be calculated as follow:

Equation 1: Hourly heating performance

$$\frac{Q_{hour}}{W_{hour}} = \frac{\sum\limits_{p=1}^{4} Q_{15min}}{\sum\limits_{p=1}^{4} W_{15min}}$$

The daily heating performance could be calculated as follow:

$$\frac{Q_{day}}{W_{day}} = \frac{\sum\limits_{q=1}^{24}\sum\limits_{p=1}^{4} Q_{15min}}{\sum\limits_{q=1}^{24}\sum\limits_{p=1}^{4} W_{15min}}$$

Equation 2: Daily heating performance

The seasonal heating performance could be calculated as follow:

Equation 3: Seasonal heating performance

$$\frac{Q_{seasonal}}{W_{seasonal}} = \frac{\sum\limits_{k=1}^{89}\sum\limits_{q=1}^{24}\sum\limits_{p=1}^{4} Q_{15min}}{\sum\limits_{k=1}^{89}\sum\limits_{q=1}^{24}\sum\limits_{p=1}^{4} W_{15min}}$$

Among the formula, p represents the 4 quarters in an hour, q represents the 24hours around one day, and k represents the number of days around the heating season which is about 89 days.

2.3 Measuring instruments

As the measuring parameters mentioned above, some measuring instruments are arranged on the heat pump unit. The temperature sensors are used to measure the inlet and outlet temperature of the water, and the ultrasonic flow meter is used to measure the flow rate of the water. The power meter is used to monitor the real-time power and the accumulated energy consumption. The measuring ranges and the accuracies are shown in Table 1.

Table 1: Measuring range and error of the instruments

	Measuring parameters	Measuring instruments	Measuring range	Instrumental error
Heating capacity	Outlet water temperature	Temperature sensor	-40 ~ 100ºC	0.2 ºC
	Inlet water temperature	Temperature sensor		
	Flow rate	Ultrasonic flow meter	0 ~±30m^3/s	±1%
	Ambient temperature	Temperature sensor	-40 ~ 100ºC	0.2 ºC
Energy consumption	Real-time power Accumulated energy consumption	Power meter	0 ~ 106 kWh	0.5 kWh

All the temperature sensors have been validated before measurement. The sensors have been strapped together inside and outside the house successively. The error is within ±0.2ºC.

3. RESULTS AND COMPARISONS

3.1 ASHP in Beijing

We have measured an ASHP applied in an office building in Beijing, where the ASHP is used as the space heating source in heating season of winter. The site test nearly lasts for 3 months, from Dec 17th 2013 to Mar 15th 2014. The rated parameters are listed in Table 2.

Table2: Rated parameters of the ASHP

	Rated working condition	Cooling(heating) capacity/kW	Power input/ kW	COP /(kW/kW)	Flow rate of the plate heat exchanger/(m3/h)
Cooling	Ambient dry bulb temperature:35oC	66.0	18.8	3.51	
	Temperature of supply water:7 oC				11.4
Heating	Ambient dry bulb temperature/ambient wet bulb temperature:7/6 oC	70.0	19.5	3.59	
	Temperature of supply water:45 oC				

(a) Daily energy consumption
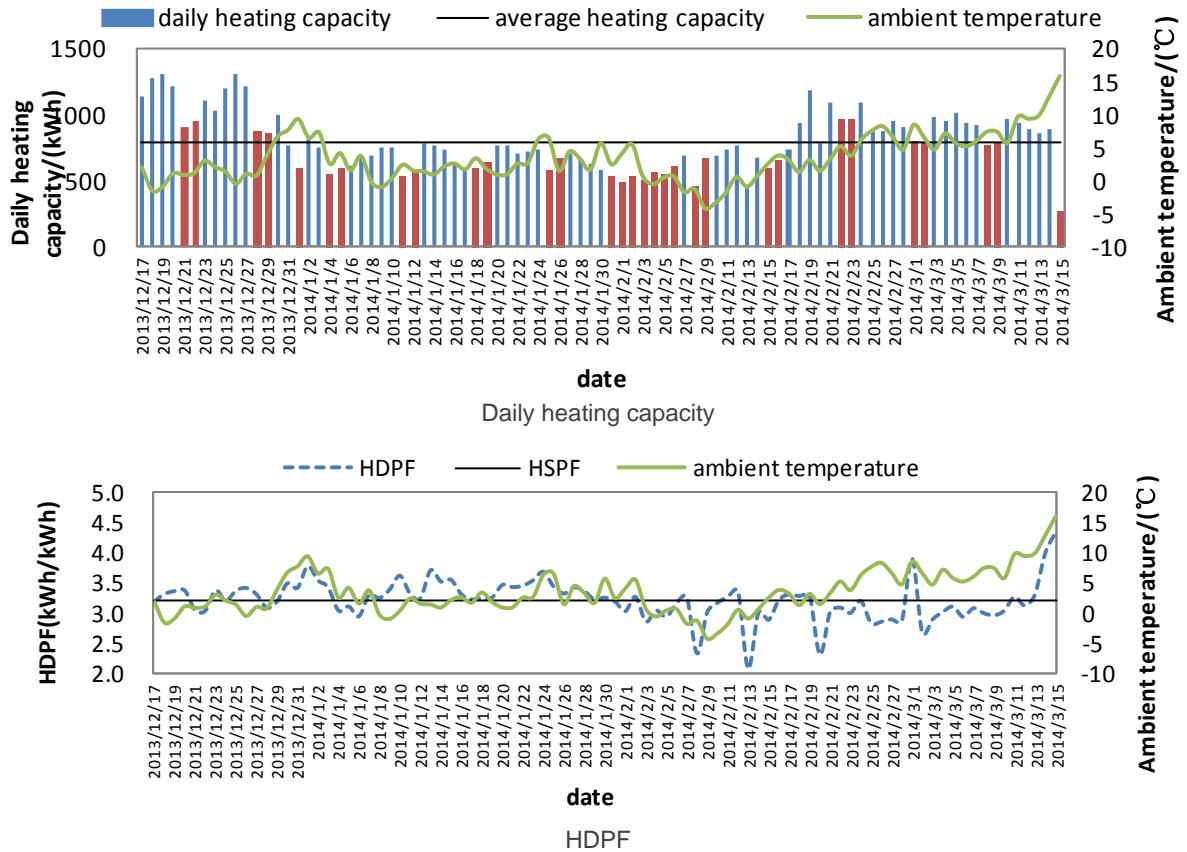
Daily heating capacity

HDPF
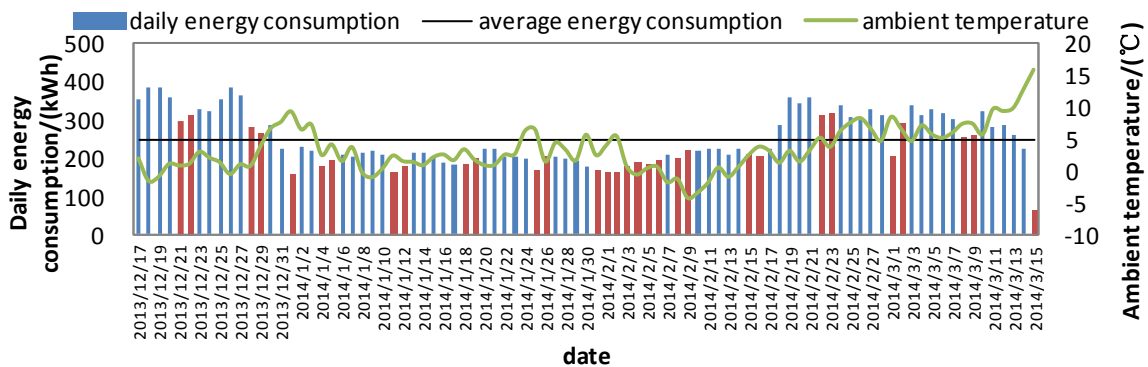
Figure 4: Heating performance for the ASHP in heating season

As it is shown in Fig4, the red column represents the parameters tested on weekends, including the statutory holidays. As far as we have investigated before, there are few people working in the office building during the weekend. Thus, the heat pump is set into the anti-freeze mode which means the temperature of the supply water can be decrease. In that way, the energy will be saved to a large extent.

From Fig4(a), it shows that during nearly 3 months, the average daily energy consumption is about 247.81kWh. To some extent, the energy consumption changes as the ambient temperature changes. As the ambient temperature increases, the heating load decreases, thus, the energy consumption decreases, which is similar to the heating capacity. The average daily heating capacity is about 792.21kWh. According to the energy consumption and heating capacity measured above, the daily heating performance is calculated. From the figure, it is concluded that the ASHP runs steadily during the heating season, and the heating performance changes regularly as the ambient temperature changes. As the ambient temperature rises, the heating performance improves meantime. During the testing period, the heating seasonal performance is about 3.20kWh/kWh.
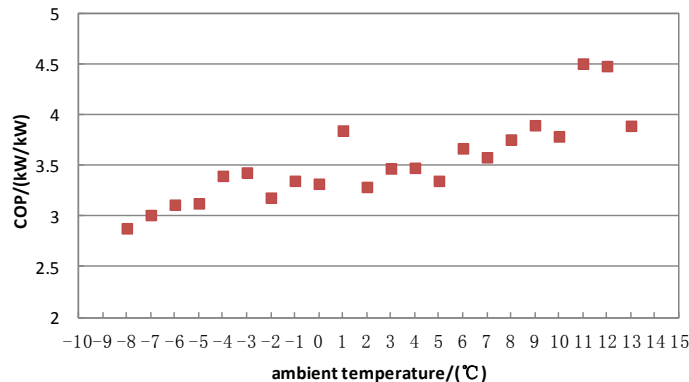

Figure 5: COP VS the ambient temperature

According to the statistics of COP under different ambient temperature, it is concluded, from Fig.5, that as the ambient temperature rises, the COP increases at the same time. When the temperature is -8℃, the COP could reach 2.8kW/kW, which illustrates that the ASHP works well in Beijing.

3.2 ASHP water heater in Taiyuan

An ASHP water heater is applied in a hotel in Taiyuan, Shanxi province, to provide domestic hot water. The measurement has lasted for one month, from Jan 18th 2014 to Feb 17th 2014, which is the coldest month of a year in Taiyuan. The compressor of the water heater is a scroll compressor with quasi two stage compression with gas injection. The rated parameters are shown in Table 3.

Table 3: Rated conditions of ASHP water heater

	Working condition		Heating capacity/(kW)	Power input/(kW)	COP(kW/kW)
	Air side	Water side			
Rated condition 1	Ambient dry bulb temperature/wet bulb temperature=20/15℃	Flow rate=7.5 m³/h, Temperature of supply water=55℃	42	9.8	4.29
Rated condition2	Ambient dry bulb temperature/wet bulb temperature =7/6℃		33	9.5	3.47

There is a water tank attached to the ASHP water heater. When the heating load for hot water is low, hot water is stored in the water tank, to supply hot water when the heating load is high. When the average temperature in the water tank is lower than 45℃, the ASHP starts, when the average temperature is higher than 50℃, the ASHP stops.

Fig6(a) is the temperature of supply water during one month, as shown in the figure, the temperature of supply water keeps almost steadily which doesn't change a lot as the ambient temperature changes. The average temperature of supply water is about 45.5℃, which could satisfy the demand for hot water. From Fig.6(b) and (c), it is concluded that the heating capacity and the hourly heating performance changes as the ambient temperature changes. The average heating capacity reaches about 24.5kW during the coldest month, which is close to 75% of the rated heating capacity under much mild 7/6℃ working condition. The heating hourly performance changes in a large range, as the heat pump starts and stops frequently. The average hourly COP reaches 2.71kWh/kWh.

According to the statistics of COP (Fig.7), it is concluded that as the ambient temperature rises, the COP increases to some extent. The lowest temperature in Taiyuan is about -6℃, and the COP could reach 2.1kW/kW.

4. CONCLUSION

ASHP is a clean and efficient heat source as a substitute of coal. The long-term performance is measured in this paper. According to the testing result, the ASHP with quasi two stage compression could work steadily and effectively in cold region of north China. The testing result shows that the COP maintains above 2.8kW/kW when the outdoor temperature is -8℃ in Beijing. In Taiyuan of Shanxi province, the heating capacity of an air-source heat pump water heater is around 75% of the rated heating capacity when the outdoor temperature is -5℃. The average hot water temperature can reach 45.5℃.
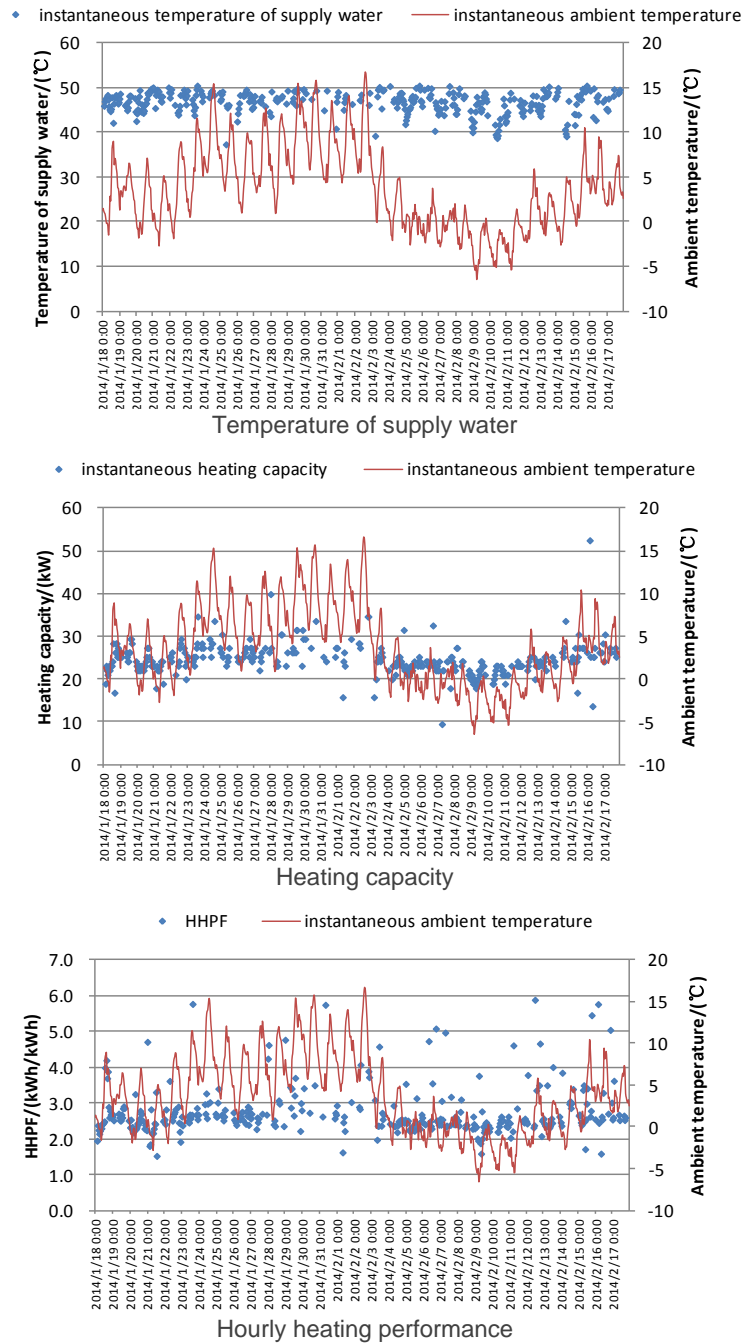
Temperature of supply water

Heating capacity

Hourly heating performance

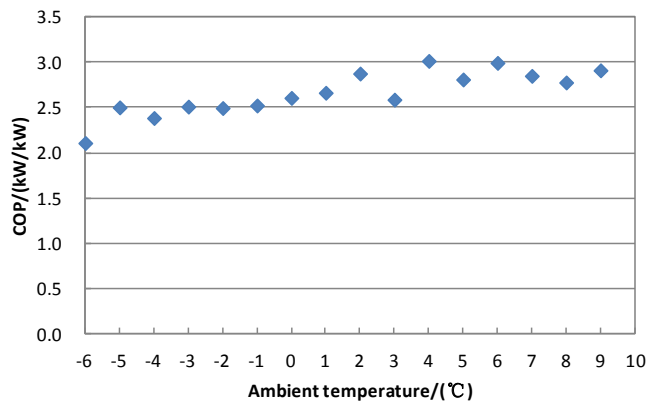*Figure 6: Running performance of ASHP water heater*

Figure 7: COP changing as the ambient temperature

5. REFERENCES

JIN, Zhanyong, 2010. Research on economic incentives for energy-efficiency renovation for existing residential buildings in northern heating areas[D]. Harbin: Harbin Institute of Technology.

JIANG, Yi, 2011. Research on energy saving of existing buildings in China north urban heating regions[J]. Energy of China, 33(9), 6-13.

CAO, Xiaoli, 2010. Research on major problems and suggestions of energy efficiency retrofit of existing buildings in northern heating areas of China[D]. Xian: Xian University of Architecture and Technology.

TSINGHUA building energy research center, 2010. Annual Report on China Building Energy Saving and Development[M]. 1. Beijing: China Building Materials Press.

LONG, Weiding, Fan, Cunyang, 1995. Feasibility analysis of using the ASHP chiller in Shanghai area[J]. HVAC, 25(5): 3-7.

GUO, J.J, WuJ, Y,Wang R.Z, 2011. Experimental research and operation optimization of an air-source heat pump water heater[J]. Applied Energy, 88 (11) :4128–4138.

TIAN, Changqing, Shi, Wenxing, Wang, Sen, 2004. Research on inverter air source heat pump with two-stage compression applied in cold regions [J]. Solar Energy, 25 (3): 388-393.

MA, Guoyuan, Chai, Qinhu, Jiang, Yi, 2003. Experimental investigation of air-source heat pump for cold regions[J]. International Journal of Refrigeration, 26(1): 12-18.

MA, Zuiliang, Yang, Ziqiang, Yao, Yang, Yu, Yinping, 2001. Analysis of using air-source heat pump water chiller-heater units in the cold regions[J]. HVAC, 31(3): 28-31.

YU, Yinping, Ma, Zuiliang, 2002. The feasibile analysis of double stage coupling heat pump appling in the cold field[J]. Power DSM, 4(2): 39-42.

BERTSCH, Stefan S, Groll, Eckhard A, 2008. Two-stage air-source heat pump for residential heating and cooling applications in northern US climates[J]. International Journal of Refrigeration, 31(2008): 282-292.

WANG, W, Z, Ma, Y, Jiang, Y, Yang, S, Xu, Z, Yang 2005. Field test investigation of a double-stage coupled heat pumps heating system for cold regions[J]. International Journal of Refrigeration, 28(2005): 672-679.

WANG, Baolong, Shi, Wenxing, Li Xianting, Yan, Qisen, 2008. Numerical research on the scroll compressor with refrigeration injection[J]. Applied Thermal Engineering, 28(5-6): 440-449.

WANG, Baolong, Shi, Wenxing, Li, Xianting, 2009. Numerical analysis on the effects of refrigerant injection on the scroll compressor[J],.Applied Thermal Engineering, 29 (1): 37-46.

486: Research on the compressor test rig for refrigerant drop-in experiment

GILBONG LEE, JOO-SANG KIM, JUNHYUN CHO, HO-SANG RA AND YOUNG-SOO LEE

1 Thermal Energy Conversion Laboratory, Korea Institute of Energy Research, 152, Gajeong-ro, Yuseong-gu, Daejeon, Korea

This study is on the compressor test rig for refrigerant change test. Increasing the production temperature is one of the main research topics of heat pump and for that compressor plays the key role. To ensure the reliability of compressor, both analytic and experimental approaches would be used. This study takes the experimental approach to check the reliability. Steam generation is the target operation condition. R245fa is selected as working fluid since it has good characteristics under the temperature range for steam generation. For effective experiments test rig based on bypass cycle is constructed. Long term experiment on refrigerant change is under operation. Change of lubricant will be scheduled later.

Keywords: Compressor, Heat pump, Steam Generation

1. INTRODUCTION

Many researches have been conducted to apply heat pump technology for the energy saving in industrial heat demands. Low and mid pressure steam occupy the largest portion in industrial heat demand. However most of heat pump systems in the market generate hot water up to 90oC. Kobe Steel reported the world 1st steam generation heat pump system (SGH120, SGH165) in 2011 but it still takes very minor portion of market. To expand the application of heat pumps in industrial field, there must be sufficient examinations on the technical breakthrough points and risk issues concerned with steam generation application. Since one of the most important components of heat pump is compressor, researches on that component would have top priority. This also means that there should be enough evidences that compressor operation under steam generation conditions guarantee the same reliability quality as under other commonly known operation conditions.

The most common causes of compressor failure are refrigerant flood back, flooded starts, liquid slugging, overheating, lack of lubrication, etc. Refrigerant flood back occurs when refrigerant is not heated up to superheated phase in the evaporator. This is caused by low evaporation load or failure of evaporator. Under compression with refrigerant flood back, foaming phenomenon in oil of compressor is generally occurred. Flooded start is when compressor starts its initial operation with a large amount of liquid refrigerant within the compressor shell. This happens when the system is over-charged with refrigerant or the system is stayed for a long period. Under flooded start, massive and instant exit of lubricant occurs. This causes temporal lack of lubrication of compressor. Overheating operation is caused by high compression ratio, low suction pressure, high superheat, etc. High compressor temperature causes negative effect to lubrication. Generally, a system tends to be overheated when the compressor is operated beyond operation map suggested by manufacturers.

To produce steam with heat pump, the condensation temperature should rise up to 130oC. This high temperature would increase the risk level of compressor caused by overheating and lubrication deterioration. When compressor stops operation refrigerant in system might crawls to the compressor since the surrounding temperature of compressor becomes lower than the working temperature conditions of heat exchangers. As the amount of refrigerant in compressor increases, the risk of liquid compression also increases. Furthermore the refrigerant should be changed since the required operation temperature is beyond the critical temperature of R134a, R407C or R410A which are most commonly used HFC refrigerants in current market. The change of working fluid would affect response time of suction superheat and require redesign of control logic. Reference performance test and long-term operation are required to verity these issues.

Performing full cycle experiment for long-term operation is inefficient since it will take a lot of energy and cost. More efficient approach for long-term operation of compressor is required in this point. Discharge-
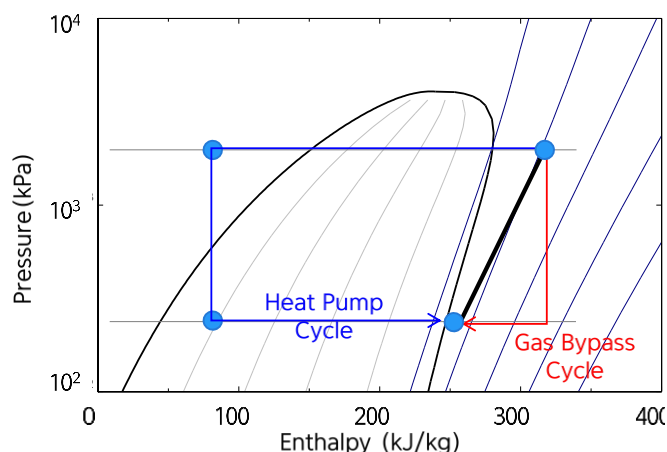

Figure 1. Heat pump cycle vs. gas bypass cycle

bypass cycle is a cycle that first expands the exiting gas of compressor and then cools the gas down to the inlet condition of compressor through gas cooler. This cycle requires less energy and time since it does not have condensation and evaporation processes. Therefore, about 1/3 of capacity is needed compared to

the facility for full cycle experiment. This paper will show construction of compressor reliability test rig based discharge bypass cycle

2. DESIGN OF COMPRESSOR TEST RIG

Working fluids for steam generation cycle should have critical temperature over 130oC. R1234ze(Z), R245fa and R365mc satisfy this requirement. Among them R245fa was chosen since it has no flammability and is easily purchased. Table 1 gives characteristics of refrigerant candidates.

Table 1. Properties of refrigerant candidates

Refrigeratnt	GWP	Flammability	T_c [℃]	P_c [MPa]
R134a	1430	-	101.1	4.06
R744	1	-	31.0	7.38
R1234yf	4	Low	94.7	3.38
R1234ze(E)	6	Low	109.4	3.64
R1234ze(Z)	<10	Low	153.7	3.97
R245fa	1030	-	154.0	3.65
R365mfc	794	Low	186.9	3.27

The purpose is to check reliability issues with refrigerant change and operation temperature increase. As for compressor, R134a screw compressor was selected. The cooling capacity of discharge bypass cycle is determined by the power consumption of compressor. Therefore estimation of compressor power as to the refrigerant change is required to determine the capacity of test rig. Estimation was based on the operation data of compressor of R134a. The manufacturer offers simulation tools for its compressor line-ups. First, volume flow rate and isentropic efficiency were correlated with pressure ratio for the case of R134a. The correlations were later used to estimate power consumption for the case of R245fa. Since there are large discrepancy in working temperatures of two refrigerants, the working pressures were matched during the estimation process. The estimated value was then applied to determine the specification of heat exchanger. The heat exchanger is a brazed-type plate heat exchanger and its specification was determined by SPP G7 software of SWEP. The processes are summarized in Fig. 2.
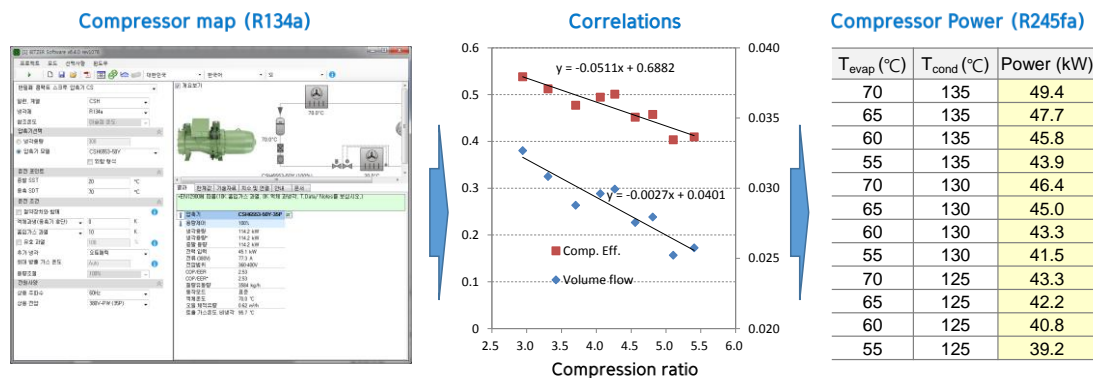

Figure 2. Estimation processes for compressor power in case of R245fa

The test rig was designed to cover various types of compressors. For this purpose, compressor unit is separated to other components unit. Furthermore both R134a and R245fa cycles would be operated at the same time with the same heat source. There would be two paths in bypass cycle. One is expansion-cooling path and the other is cooling-expansion path. Considering the general working conditions of R134a's hot water heat pump and R245fa's steam heat pump cycle, the condensation temperature of R134a is located near to the evaporation temperature of R245fa. This implies that expansion-cooling path is suitable for

R245fa and cooling-expansion path for R134a. Refrigerant circuit was designed to cover both paths. Fig. 3 shows the two paths and system layout which was used in this study.

Fig. 4 shows test rig constructed. Two screw compressors can be operated at the same time. The right test rig was constructed based on basic bypass cycle suggested by Purdue University. Under basic cycle all of the refrigerant in the system is in vapour state. Therefore the system becomes more sensitive to refrigerant charge than conventional heat pump system. To improve this, gas cooler of left test rig was designed as to make the exit status of refrigerant 2-phase. Reheating heat exchanger was added to ensure suction superheat.
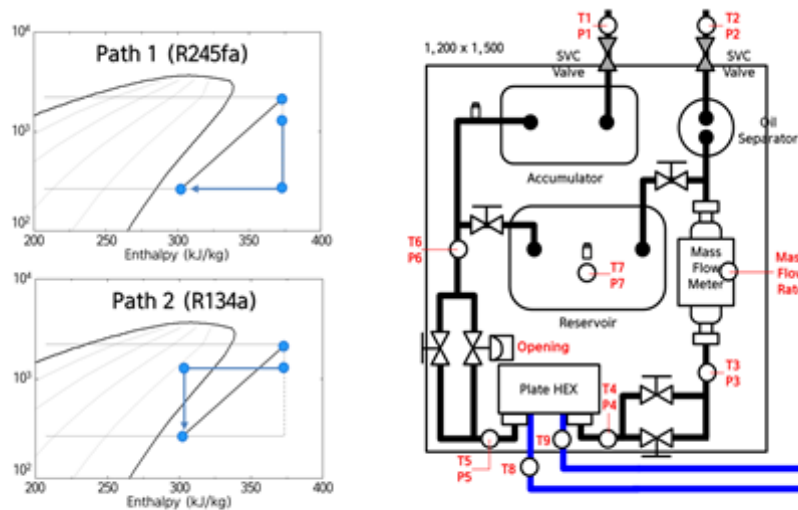
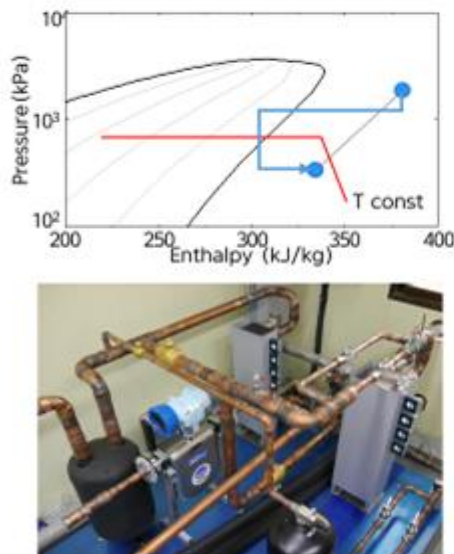Figure 3. Two paths of discharge bypass cycle and system layout


Figure 4. Compressor reliability test rig

3. TEST RESULTS

The results of refrigerant change test are presented in Fig. 5. The temperature of heat source was 30°C. R134a and R245fa took different cycle paths. The controllable variables of test rig are opening of expansion devices, flow rate of secondary fluid and the amount of refrigerant charge. Sensitiveness tests of above factors were performed and the results are presented in Fig. 6. System showed more sensitive response to the refrigerant charge than other two factors. This is because the state of refrigerant in system is gas phase. To reduce sensitiveness to refrigerant charge, refrigerant circuit was modified so that the refrigerant

at the exit of gas cooler would be in 2-phase state and then be expanded into lower temperature level and finally be heated up to compressor inlet conditions with the same heat source.

Fig. 7 shows cycle values and surface temperature of compressor under steam cycle. When suction temperature increased over 80oC, discharge temperature rose around 140oC. In this point, the surface temperature of compressor rotor part measured by thermal imaging camera was around 150oC.

When suction temperature went beyond 100oC, there occurred deformation in supporting part of motor. Under room temperature start-up, the risk of dispositioning of rotor axis was increased due to liquid compression and extremely low suction pressure. Since lubrication performance declines as temperature increases, reliability test for viscosity change of lubricant will be performed later.
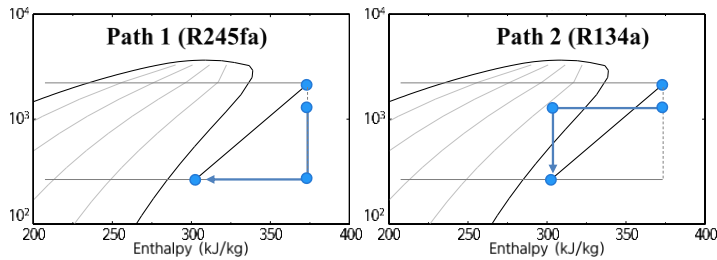
Item		R134a	R245fa
Suction	Temp.[℃]	35.8	53.7
	Pres.[bar]	6.19	2.44
Discharge	Temp.[℃]	100.6	102.8
	Pres.[bar]	25.18	9.61
Suction Superheat[℃]		13.2	14.4
Mass flow rate[kg/s]		0.54	0.25

Figure 5. Refrigerant change test of bypass cycle
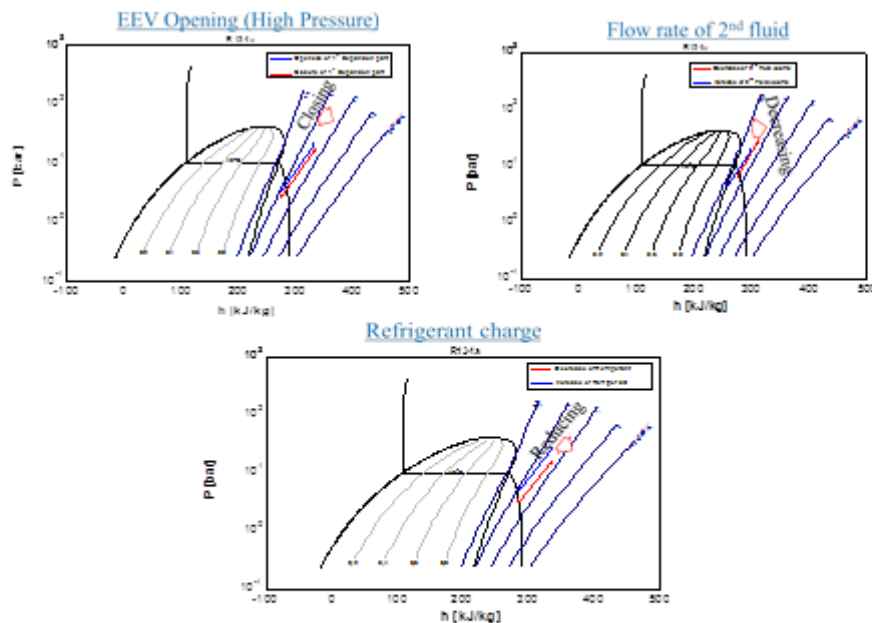
Figure 6. Controllable parameter tests of bypass cycle

Item	Suction		Discharge			DT$_{suc.sh}$ [℃]	DT$_{dis.sh}$ [℃]
	Temp. [℃]	Press. [bar]	Temp. [℃]	Press. [bar]	T$_{cond}$ [℃]		
25%	76.3	4.12	115.4	10.97	94	20.2	21.4
50%	78.3	3.7	123.5	12.41	99	25.8	24.5
75%	81.9	3.48	133.2	14.01	105	31.5	28.2
100%	86.5	3.27	145.9	15.94	110	38.1	35.9
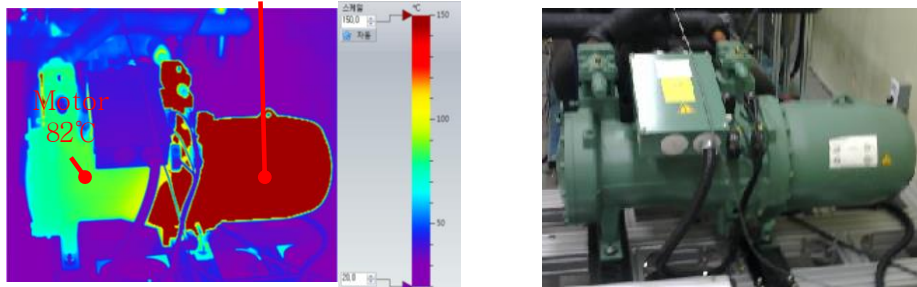
Figure 7. Compressor capacity variation test under steam generation condition

4. CONCLUDING REMARKS AND FUTURE WORKS

Currently, heat pump is trying to find its opportunities in industrial application, especially in generating high temperature steam. To widen the application range, compressor, heat exchangers, refrigerants and other components of heat pump should satisfy the new operation requirement. Among the components compressor plays the key role. To ensure the reliability of compressor, both analytic and experimental approaches can be used. This study is on the experimental approach to obtain the reliability.

Steam generation condition is the target operation condition. R245fa was selected as working fluid since it has good characteristics under the required operation temperature range. For effective experiments test rig based on bypass cycle was constructed. The approach is changing working fluid and lubricant of commercial compressor of R134a. First test on working fluid change is under operation. Change of lubricant will be executed later.

Since operation temperature increases about 30 to 40oC with R245fa compared to R134a, there may be clearance risks resulted by thermal expansion of each components in compressor. The first compressor tested had failure due to contact between journal bearing and rotors. This means larger gap is required for the case of high temperature operation. During long term test run, other reliability issues might occur and such issues would be design criteria for steam heat pump system.

5. ACKNOWLEDGMENT

6. REFERENCES

[1]   DANFOSS, Why compressors fail part 1-7, http://danfoss.com.

[2]   DIRLEA, R., Hannay, J., e Lebrun, J., Testing of refrigerant compressors without condensation, Purdue Conference, USA, 1996.